2012 EUROPEAN FREQUENCY AND TIME FORUM

Chalmers University of Technology
April 23-27, 2012, Gothenburg, Sweden

PROCEEDINGS

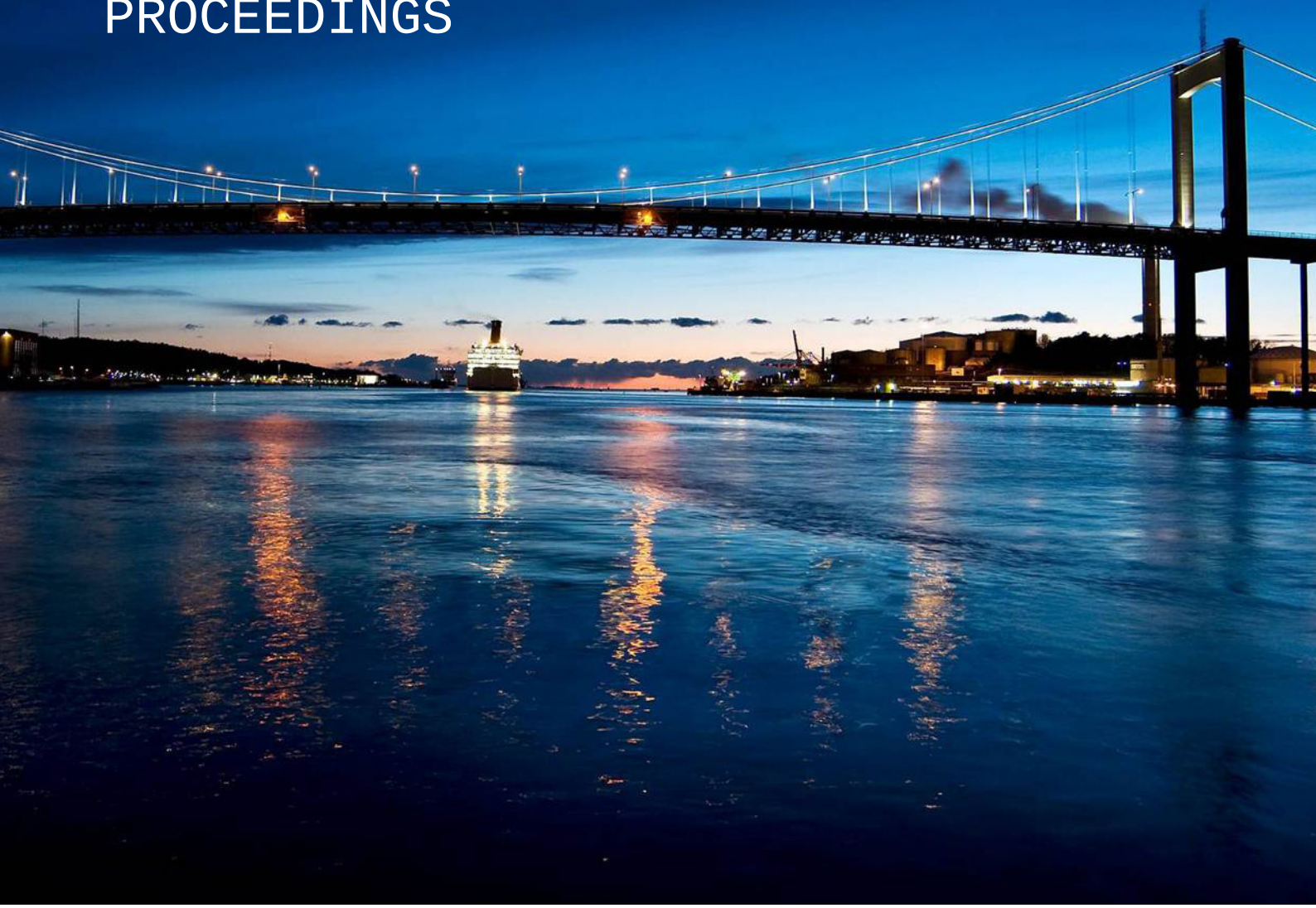

TABLE OF CONTENTS

Not all presented papers have been submitted as full papers in Proceedings. Links to those submitted are given below, and also in the Session Schedule, and in the Attendee List.

Tuesday, April 24 **09:00 - 10:40**

Session: Cryogenic Sources & Fine Tuning Synthesisers
Room: RunAn
Session Chair: Jeremy Everard, University of York

Tuesday, April 24 **09:00 - 10:40**

Session: Primary Frequency Standards
Room: The Palmstedt hall
Session Chair: Sebastian Bize, SYRTE

Investigation of Rapid Adiabatic Passage in the Fountain PTB-CSF2
Vladislav Gerginov, PTB
Michael Kazda, PTB
Nils Nemitz, PTB
Stefan Weyers, PTB

Improved Tests of the Stability of Fundamental Constants Using the SYRTE-FO2 Rb/Cs Dual Fountain

Jocelyne Guéna, SYRTE - Observatoire de Paris
Michel Abgrall, SYRTE - Observatoire de Paris
Philippe Laurent, SYRTE - Observatoire de Paris
Daniele Rovera, SYRTE - Observatoire de Paris
Peter Rosenbusch, SYRTE - Observatoire de Paris
Michael Tobar, University of Western Australia
André Clairon, SYRTE - Observatoire de Paris
Sébastien Bize, SYRTE - Observatoire de Paris

Tuesday, April 24 **11:10 - 12:50**

Session: Lattice Clocks
Room: RunAn
Session Chair: Ekkehard Peik, PTB

INVITED: Prospects for Frequency Comparison of Optical Lattice Clocks Toward 10-18 Fractional Uncertainties
Hidetoshi Katori, University of Tokyo

Tuesday, April 24 **11:10 - 12:50**

Session: Time Scales & Time Transfer
Room: The Palmstedt hall
Session Chair: Laurent Guy Bernier, METAS

Tuesday, April 24 **14:00 - 15:40**

Poster Session: Materials, Resonators, & Resonator Circuits
Room: Poster Area

Tuesday, April 24 **14:00 - 15:40**

Poster Session: Timekeeping, Time & Frequency Transfer, GNSS & Applications I
Room: Poster Area

Tuesday, April 24 **14:00 - 15:40**

Poster Session: Optical Frequency Standards & Applications I
Room: Poster Area

Reducing Thermal Noise in Ultra-Stable Optical Resonators
Sana Amairi, QUEST, PTB
Jannes Wuebbena, QUEST, PTB
Olaf Mandel, QUEST, PTB
Piet Schmidt, Quest,PTB

Absolute Frequency Measurement of 1S0 (F = 1/2) - 3P0 (F = 1/2) Transition of 171Yb in One-Dimensional Optical Lattice at KRISS
Dai-Hyuk Yu, KRISS
Chang Yong Park, KRISS
Won-Kyu Lee, KRISS
Sang Eon Park, KRISS
Taeg Yong Kwon, KRISS
Sang-Bum Lee, KRISS
Jongchul Mun, KRISS

Towards an Optical Clock on the Isomer Transition in 229^{Th} Nucleus
Georgy Kazakov, Vienna University of Technology
Matthias Schreitl, Vienna University of Technology
Winkler Georg, Vienna University of Technology
Schumm Thorsten, Vienna University of Technology
Litvinov Andrey, St. Petersburg State Polytechnic University
Romanenko Viktor, Institute of Physics, Nat. Acad. Sci. of Ukraine
Romanenko Aleksander, Kyiv National Taras Shevchenko University
Yatsenko Leonid, Institute of Physics, Nat. Acad. Sci. of Ukraine

Room-Temperature Ultraviolet Extended Cavity Diode Laser for Laser Cooling of 171Yb+
Steven King, National Physical Laboratory
Rachel Godun, National Physical Laboratory
Patrick Gill, National Physical Laboratory

Chien-Ming Wu, Department of Physics, National Central University
Tze-Wei Liu, Department of Physics, National Central University
You-Huan Chen, Department of Physics, National Central University
Shinn-Yan Lin, Telecommunication Laboratories, Chunghwa Telecom
Wang-Yau Cheng, Department of Physics, National Central University

Tuesday, April 24 **14:00 - 15:40**

Poster Session: Sensors & Transducers
Room: Poster Area

Tuesday, April 24 **16:10 - 17:50**

Session: Sensor Development & Design
Room: RunAn
Session Chair: Bernard Dulmet, ENSMM

Tuesday, April 24 **16:10 - 17:50**

Session: Frequency and Time Transfer by Optical Fibers I
Room: The Palmstedt hall
Session Chair: Harald Schnatz, PTB

Wednesday, April 25 **09:00 - 10:40**

Session: PLENARY
Room: RunAn
Session Chair: Patrick Gill, NPL

Listening to the Universe: Gravitational Wave Detection on the Ground and in Space
Karsten Danzmann, Max Planck Institute for Gravitational Physics, (Albert-Einstein-Institut) and Institute for Gravitational Physics, Leibniz Universität Hannover

Onsala Space Observatory: Overview of its activities
Hans Olofsson, Onsala Space Observatory, Swedish National Facility for Radio-astronomy at Chalmers University of Technology

Wednesday, April 25 **11:10 - 12:50**

Session: Resonator Design & Characterisation
Room: RunAn
Session Chair: Mike Underhill, Underhill Research Ltd

Wednesday, April 25 **11:10 - 12:50**

Session: Ion Clocks
Room: The Palmstedt hall
Session Chair: Davide Calonico, INRIM

INVITED: Single-Ion Optical Frequency Standards Based on 171Yb+
C. Tamm, Physikalisch-Technische Bundesanstalt
M. Okhapkin, Physikalisch-Technische Bundesanstalt
B. Lipphardt, Physikalisch-Technische Bundesanstalt
S. Weyers, Physikalisch-Technische Bundesanstalt
N. Huntemann, Physikalisch-Technische Bundesanstalt
E. Peik, Physikalisch-Technische Bundesanstalt

Optical Frequency Measurements in a Single Ion of 171Yb+
Rachel Godun, National Physical Laboratory
Steven King, National Physical Laboratory
Stephen Webster, National Physical Laboratory
Helen Margolis, National Physical Laboratory
Luke Johnson, National Physical Laboratory
Krzysztof Szymaniec, National Physical Laboratory
Patrick Baird, University of Oxford
Patrick Gill, National Physical Laboratory

Minimizing Time-Dilation in Ion Traps - Towards an Optical Clock with Coulomb Crystals
Tanja Mehlstäubler, PTB
Karsten Pyka, PTB
Jonas Keller, PTB
Norbert Herschbach, PTB
David Meier, PTB
Kristijan Kuhlmann, PTB

Strontium Ion Optical Frequency Standard at 445 THz
Geoffrey Barwood, National Physical Laboratory
Patrick Gill, National Physical Laboratory
Guilong Huang, National Physical Laboratory
Hugh Klein, National Physical Laboratory

Wednesday, April 25 **14:00 - 15:40**

Session: Frequency Combs
Room: RunAn
Session Chair: Helen Margolis

Wednesday, April 25 **14:00 - 15:40**

Session: Algorithms
Room: The Palmstedt hall
Session Chair: Demetrios Matsakis, US Naval Observatory

Wednesday, April 25 **16:10 - 17:50**

Poster Session: Oscillators, Synthesizers, Noise, & Circuit Techniques
Room: Poster Area

Wednesday, April 25 **16:10 - 17:50**

Poster Session: Microwave Frequency Standards II
Room: Poster Area

STE-Quest: Testing the Einstein Equivalence Principle with Atomic Sensors in Space

Luigi Cacciapuoti, European Space Agency
Kai Bongs, University of Birmingham
Philippe Bouyer, University of Bordeaux
Matin Gehler, European Space Agency
Luciano Iess, University of Rome "La Sapienza"
Philippe Jetzer, University of Zurich
Arnaud Landragin, SYRTE, Observatoire de Paris, CNRS, LNE, UPMC
Ernst Rasel, University of Hannover
Stephan Schiller, Heinrich-Heine-Universität Düsseldorf
Uwe Sterr, PTB
Guglielmo Maria Tino, University of Firenze
Philip Tuckey, SYRTE, Observatoire de Paris, CNRS, LNE, UPMC
Pierre Waller, European Space Agency
Peter Wolf, SYRTE, Observatoire de Paris, CNRS, LNE, UPMC

Vinu Venkatraman, Ecole Polytechnique Fédérale de Lausanne
Yves Pétremand, Ecole Polytechnique Fédérale de Lausanne
Christoph Affolderbach, University of Neuchâtel
Gaetano Mileti, University of Neuchâtel
Nico de Rooij, Ecole Polytechnique Fédérale de Lausanne
Herbert Shea, Ecole Polytechnique Fédérale de Lausanne

Accuracy Evaluation of NICT Atomic Fountain CsF2

Motohiro Kumagai, NICT
Clayton R Locke, NICT
Hiroyuki Ito, NICT
Masatoshi Kajita, NICT
Yuko Hanado, NICT
Mizuhiko Hosokawa, NICT

Wednesday, April 25 **16:10 - 17:50**

Poster Session: Timekeeping, Time & Frequency Transfer, GNSS & Applications II
Room: Poster Area

Zhiheng Jiang, Bureau International des Poids et Mesures (BIPM)
Wlodzimierz Lewandowski, Bureau International des Poids et Mesures (BIPM)

Amale Kanj, Observatoire de Paris
Joseph Achkar, Observatoire de Paris
Daniele Rovera, Observatoire de Paris

Accurate Time/Frequency Comparison and Dissemination Through Optical Telecommunication Networks

Harald Schnatz, Physikalisch-Technische Bundesanstalt
Davide Calonico, Istituto Nazionale di Ricerca Metrologic
Erik Dierikx, Dutch Metrology Institute
Gesine Grosche, Physikalisch-Technische Bundesanstalt
Per Olof Hedekvist, Technical Research Institute of Sweden
Alexander Kuna, Institute of Photonics and Electronics
Giuseppe Marra, National Physical Laboratory
Mikko Merimaa, Centre for Metrology and Accreditation
A. Niessner, Bundesamt für Eich - und Vermessungswesen
Giorgio Santarelli, LNE-SYRTE
Vladimir Smotlacha, CESNET
Christian Chardonnet, Université Paris 13

Davide Calonico, INRIM
Cecilia Clivati, Politecnico di Torino, INRIM
Giovanni A. Costanzo, Politecnico di Torino
Filippo Levi, INRIM
Alberto Mura, INRIM
Aldo Godone, INRIM
Marco Prevedelli, Università di Bologna
Guglielmo M. Tino, Università di Firenze
Nicola Poli, Università di Firenze, LENS

Wednesday, April 25 **16:10 - 17:50**

Poster Session: Optical Frequency Standards & Applications II
Room: Poster Area

Comparison of Reference Cavities for an Optical Clock with Improved Short-Term Stability

Jonas Keller, Physikalisch-Technische Bundesanstalt
Stepan Ignatovich, Institute of Laser Physics, Novosibirsk
Maksim Okhapkin, Institute of Laser Physics, Novosibirsk
Stephen Webster, National Physical Laboratory
David-Marcel Meier, Physikalisch-Technische Bundesanstalt
Karsten Pyka, Physikalisch-Technische Bundesanstalt
Tanja Mehlstäubler, Physikalisch-Technische Bundesanstalt

Experimental Validation of a Simple Approach to Determine the Laser Linewidth from the Frequency Noise Spectrum

Nikola Bucalovic, LTF, UniNE
Vladimir Dolgovskiy, LTF, UniNE
Christian Schori, SpectraTime
Pierre Thomann, LTF, UniNE
Gianni Di Domenico, LTF, UniNE
Stéphane Schilt, LTF, UniNE

Finite Element Analysis of Support-Area-Insensitive Position in Cutout Optical Cavity for Yb Optical Lattice Clock

Sang Eon Park, KRISS
Won-Kyu Lee, KRISS
Dai-Hyuk Yu, KRISS
Chang Yong Park, KRISS
Sang-Bum Lee, KRISS
Taeg Yong Kwon, KRISS

Comparison of Ultra-Stable Lasers at PTB

Christian Grebing, Physikalisch-Technische Bundesanstalt
Thomas Legero, Physikalisch-Technische Bundesanstalt
Thomas Kessler, Physikalisch-Technische Bundesanstalt
Christian Hagemann, Physikalisch-Technische Bundesanstalt
Stefan Vogt, Physikalisch-Technische Bundesanstalt
Sebastian Häfner, Physikalisch-Technische Bundesanstalt
Uwe Sterr, Physikalisch-Technische Bundesanstalt
Sebastian Raupach, Physikalisch-Technische Bundesanstalt
Gesine Grosche, Physikalisch-Technische Bundesanstalt
Nils Huntemann, Physikalisch-Technische Bundesanstalt
Christian Tamm, Physikalisch-Technische Bundesanstalt
Burghard Lipphardt, Physikalisch-Technische Bundesanstalt
Jonas Keller, Physikalisch-Technische Bundesanstalt
Tanja Mehlstäubler, Physikalisch-Technische Bundesanstalt
Harald Schnatz, Physikalisch-Technische Bundesanstalt

Impact of the Coupling Between the Two Servo-Loops in a Self-Referenced Er:Fiber Optical Frequency Comb

Vladimir Dolgovskiy, Laboratoire Temps-Frequence, Universite de Neuchatel
Nikola Bucalovic, Laboratoire Temps-Frequence, Universite de Neuchatel
Christian Schori, Laboratoire Temps-Frequence, Universite de Neuchatel
Pierre Thomann, Laboratoire Temps-Frequence, Universite de Neuchatel
Gianni Di Domenico, Laboratoire Temps-Frequence, Universite de Neuchatel
Stephane Schilt, Laboratoire Temps-Frequence, Universite de Neuchatel

Strontium in an Optical Lattice As a Portable Frequency Reference

Ole Kock, University of Birmingham
Steven Johnson, University of Birmingham
Yeshpal Singh, University of Birmingham
Kai Bongs, University of Birmingham

A Fiber Delay Stabilized Laser with Low Frequency Sensitivity to Vibrations

Bérengère Argence, LNE-SRTE - Observatoire de Paris
Tang Li, Key Laboratory of Quantum Optics
Jean-Laurent Dournaux, GEPI - Observatoire de Paris
Cecilia Clivati, INRIM
Pierre Lemonde, LNE-SRTE - Observatoire de Paris
Giorgio Santarelli, LNE-SRTE - Observatoire de Paris

Klaus Döringshoff, Humboldt-Universität zu Berlin
Matthias Reggentin, Humboldt-Universität zu Berlin
Moritz Nagel, Humboldt-Universität zu Berlin
Evgeny Kovalchuk, Humboldt-Universität zu Berlin
Anja Keetman, University of Applied Sciences Konstanz
Thilo Schuldt, University of Applied Sciences Konstanz
Claus Braxmaier, University of Applied Sciences Konstanz
Achim Peters, Humboldt-Universität zu Berlin

Thursday, April 26 **09:00 - 10:40**

Session: Frequency and Time Transfer by Optical Fibers II
Room: RunAn
Session Chair: Giorgio Santarelli, OBSPM

Gesine Grosche, Physikalisch-Technische Bundesanstalt
Osama Terra, Physikalisch-Technische Bundesanstalt
Sebastian Raupach, Physikalisch-Technische Bundesanstalt
Uwe Sterr, Physikalisch-Technische Bundesanstalt
Harald Schnatz, Physikalisch-Technische Bundesanstalt
Andre Pape, Institut fuer Quantenoptik Hannover
Jan Friebe, Institut fuer Quantenoptik Hannover
Matthias Riedmann, Institut fuer Quantenoptik Hannover
Ernst Rasel, Institut fuer Quantenoptik Hannover
Stefan Droste, MPQ Garching
Katharina Predehl, MPQ Garching
Ronald Holzwarth, MPQ Garching
Thomas Udem, MPQ Garching

Ultra-Stable Frequency Dissemination on a Dedicated Frequency Channel of the Telecommunication Network

Olivier Lopez, LPL-CNRS-Université Paris 13
Adil Haboucha, LNE-SYRTE
Bruno Chanteau, LPL-CNRS-Université Paris 13
Anthony Bercy, LKB-UPMC-CNRS-ENS
Christian Chardonnet, LPL-CNRS-Université Paris 13
Anne Amy-Klein, LPL-Université Paris 13-CNRS
Giorgio Santarelli, LNE-SYRTE

Thursday, April 26 **09:00 - 10:40**

Session: Microwave Clocks
Room: The Palmstedt hall
Session Chair: Steve Lecomte, CSEM

A Cold Rubidium Frequency Standard for the Fundamental Physics Mission STE-Quest

Christoph Affolderbach, LTF, University of Neuchâtel
Geoffrey Barwood, NPL
Sébastien Bize, LNE-SYRTE, Observatoire de Paris
Kai Bongs, University of Birmingham
Ingo Ernsting, Heinrich-Heine-Universität
Benoit Faure, CNES
Patrick Gill, NPL
Olivier Grosjean, CNES
Jocelyne Guéna, LNE-SYRTE, Observatoire de Paris
Kenneth Jaldehag, SP
Stefan Kundermann, CSEM
Philippe Laurent, LNE-SYRTE, Observatoire de Paris
Steve Lecomte, CSEM
Thomas Legero, PTB
Thomas Lévèque, CNES
Per-Olof Lindqvist, RUAG Space AB
Michel Lours, LNE-SYRTE, Observatoire de Paris
Didier Massonnet, CNES
Gaetano Mileti, LTF, University of Neuchâtel
Alexander Nevsky, Heinrich-Heine-Universität
Nicola Poli, Universita' di Firenze, LENS, INFN
Marco Prevedelli, Universita' di Bologna
Stephan Schiller, Heinrich-Heine-Universität
Harald Schnatz, PTB
André Stefanov, University of Bern
Uwe Sterr, PTB
Guglielmo Tino, Universita' di Firenze, LENS, INFN
Philip Tuckey, LNE-SYRTE, Observatoire de Paris
Stephen Webster, NPL

Miniature Trapped-Ion Frequency Standard with 171Yb+

Heather Partner, Sandia National Laboratories / University of New Mexico
Peter Schwindt, Sandia National Laboratories
Yuan-Yu Jau, Sandia National Laboratories
Adrian Casias, Sandia National Laboratories
Darwin Serkland, Sandia National Laboratories
Ronald Manginell, Sandia National Laboratories
Matthew Moorman, Sandia National Laboratories
Robert Boye, Sandia National Laboratories
Tony Statom, Sandia National Laboratories
John Prestage, Jet Propulsion Laboratory
Nan Yu, Jet Propulsion Laboratory
Sheng Chang, Symmetricom
Taye Gebrewold, Symmetricom

Thursday, April 26 **09:00 - 10:40**

Session: Sensor Systems
Room: Scania hall
Session Chair: Svenja Knappe, NIST

Thursday, April 26 **11:10 - 12:50**

Session: Stable Lasers
Room: RunAn
Session Chair: Ernst Rasel, University of Hannover

INVITED: Characterization and Application of a Cryogenic Silicon Cavity with Fractional Frequency Stability of 1E-16
Thomas Kessler, PTB
Christian Hagemann, PTB
Thomas Legero, PTB
Christian Grebing, PTB
Gesine Grosche, PTB
Uwe Sterr, PTB
Fritz Riehle, PTB
Michael Martin, JILA
Jun Ye, JILA

Sebastian Raupach, PTB
Thomas Legero, PTB
Andreas Bauch, PTB
Thomas Kessler, PTB
Andreas Koczwara, PTB
Burghard Lipphardt, PTB
Harald Schnatz, PTB
Uwe Sterr, PTB
Gesine Grosche, PTB

Bruno Chanteau, LPL-Université Paris 13-CNRS
Olivier Lopez, LPL-CNRS-Université Paris 13
Wei Zhang, LNE-SYRTE Observatoire de Paris
Gorgio Santarelli, LNE-SYRTE Observatoire de Paris
Yann Le Coq, LNE-SYRTE Observatoire de Paris
Frédéric Auguste, LPL-Université Paris 13-CNRS
Benoît Darquié, LPL-Université Paris 13-CNRS
Christian Chardonnet, LPL-Université Paris 13-CNRS
Anne Amy-Klein, LPL-Université Paris 13-CNRS

Thursday, April 26 **11:10 - 12:50**

Session: Two-Way Time & Frequency Transfer
Room: The Palmstedt hall
Session Chair: Dirk Piester, PTB

Thursday, April 26 **11:10 - 12:50**

Session: Compact Microwave Clocks
Room: Scania hall
Session Chair: Gaetano Mileti, Université de Neuchâtel

Thursday, April 26 **14:00 - 15:40**

Session: Oscillators & Noise Processes
Room: RunAn
Session Chair: Philippe Guillemot, CNES

Thursday, April 26 **14:00 - 15:40**

Session: GNSS and Applications
Room: The Palmstedt hall
Session Chair: Kenneth Jaldehag, SP

Thursday, April 26 **14:00 - 15:40**

Session: Optical Standards & Applications
Room: Scania hall
Session Chair: Rodolphe Le Targat, SYRTE

Welcome to EFTF 2012

With great pleasure, we welcome all attendees to the 26th European Frequency and Time Forum in Gothenburg, which combines the leading international technical conferences for research, development, and applications of timing and frequency control. The conference will offer attendees and exhibitors a great opportunity to disseminate and interact both technically and socially.

Since 2007, we have held joint conferences with the International Frequency Control Symposium (IFCS) in odd years, with a very successful joint meeting last year in San Francisco. For the even years, we have our standard EFTF-only format and it promises to exceed expectation. We have 215 papers scheduled, larger than all previous EFTF-only venues. In addition, this year, we have constructed an invited speaker programme made up from a combination of pre-invited speakers and invitations to some of the Authors of submitted papers. This has allowed us to formulate a strong lecture schedule, with leading inputs from around the world.

We have a great plenary session with two very distinguished researchers in fundamental physics and space research. Professor Dr Karsten Danzmann will talk about the quest to observe gravity waves both terrestrially and in space in the future LISA science mission. Professor Hans Olofsson will talk about the Onsala Space Observatory, where delegates will have the opportunity to visit on the Friday 27th April after the conference. The observatory is targeted on radio-astronomy and geoscience, with ongoing or planned contributions to ALMA, European VLBI, and the square kilometre array projects.

Monday 23rd April is the tutorial day, with a full programme of tutorial speakers. The main conference opens on Tuesday 24th. Tuesday and Wednesday include two parallel lecture sessions plus a poster session on each day. Thursday includes three parallel lecture sessions throughout the day. The programme covers all aspects of the scientific scope, from oscillators, MEMS resonators and microwave clocks through to optical oscillators, frequency standards and frequency combs. An extensive programme of papers using microwave or optical techniques address the problem of high accuracy remote time and frequency comparison. There is also an exhibition presented by leading manufacturers of Frequency Control and Precision Timekeeping Equipment. During the Tuesday poster session, the posters selected for the student poster competition will be assessed, with a best poster selected for groups 1/2 combined, 3, 4, 5 and 6. The winners will be announced at the EFTF Awards Ceremony, during the Conference Dinner, along with the EFTF2012 Young Scientist Award and EFTF Award.

The Local and Scientific Committee Chairs and committee members are dedicated to providing a stimulating and educational technical program for all attendees. Finally, we would like to thank the various sponsors of EFTF2012 from the Time & Frequency community, both industrial companies and research institutes, many of whom provided support to the conference student / postdoc financing scheme. This has allowed us to help some 40 young attendees.

Looking forward to seeing all of you in Goteborg and we hope that you all enjoy a stimulating and productive week at the conference.

Jan Johansson	Giorgio Santarelli	Patrick Gill
EFTF2012 Local	EFTF Executive	EFTF2012 Scientific
Organising Chair	Committee Chair	Programme Chair

COMMITTEES

EFTF Executive Committee

Elected Members

Giorgio Santarelli - Observatoire de Paris - SYRTE, France, Chair
Ekkehard Peik - Physikalisch-Technische Bundesanstalt, Germany, Vice Chair
Bernard Dulmet - ENSMM - LCEP, France
Jeremy Everard - University of York, United Kingdom
Patrick Gill - National Physical Laboratory, United Kingdom
Pascal Rochat - Spectratime SA, Switzerland
Wolfgang Schäfer - TimeTech, Germany
Patrizia Tavella - INRIM Istituto Nazionale di Ricerca Metrologica, Italy
Michael J. Underhill - Underhill Research, United Kingdom
Francois Vernotte - Observatoire de Besançon, France

Ex Officio Members

Rémi Brendel - SFMC, France
Jan Johansson - SP Technical Research Institute of Sweden
Clark T.-C. Nguyen - University of Berkeley, United States of America
Gaetano Mileti - Laboratoire Temps Fréquence, University of Neuchatel, Switzerland

EFTF 2012 Local Organisation Committee

Jan Johansson - SP Technical Research Institute of Sweden, Chair
Kenneth Jaldehag - SP Technical Research Institute of Sweden
Per Olof Hedekvist - SP Technical Research Institute of Sweden
Anna Axelsson - SP Technical Research Institute of Sweden
Gunnar Elgered - Chalmers University of Technology, Sweden

EFTF 2012 Scientific Committee

Jean-Pierre Aubry
Sylvain Ballandras
Andreas Bauch
Laurent Guy Bernier
Sebastien Bize - Chair Group 6
Rodolphe Boudot
Pierre-Yves Bourgeois
Luigi Cacciapuotti
Anne Curtis
Pascale Defraigne
Jerome Delporte
Bernard Dulmet - Chair Group 1
Chris Ekstrom
Jeremy Everard - Chair Group 2
Stephen Feltham
Mike Garvey
Patrick Gill - Programme Chair
Gesine Grosche
Philippe Guillemot
Jorg Hahn
Michito Imae
Eugene Ivanov
Kenneth Jaldehag
Jan Johansson
Svenja Knappe
Steve LeComte - Chair Group 3
Filippo Levi
Luca Lorini
Louis Marmet
Demetrios Matsakis
Gaetano Mileti
Eamonn Murphy
Bernd W. Neubig
Ekkehard Peik
Dirk Piester - Chair Group 5
Nicola Poli
Maria Ramos
Leo Reindl - Chair Group 4
Fritz Riehle
Enrico Rubiola
Clemens Ruppel
Christophe Salomon
Giorgio Santarelli
Wolfgang Schaefer
Ashwin Seshia
Patrizia Tavella
Pierre Thomann
Philip Tuckey
Pierre Uhrich
Mike Underhill
Pierre Waller
Peter Wolf
Victor Zhang

PLENARY SESSIONS

Tuesday, April 24 **08:30 - 08:55**

Session: Plenary
Room: RunAn
Session Chair: Giorgio Santarelli, SYRTE

Welcome, acknowledgements and information
Technical program information
2013 IEEE-UFFC joint symposia announcement
Logistical conference information

Wednesday, April 25 **09:00 - 10:40**

Session: Plenary
Room: RunAn
Session Chair: Patrick Gill, NPL

09:00 – 10:00

Listening to the Universe: Gravitational Wave Detection on the Ground and in Space
Prof. Dr. Karsten Danzmann, Max Planck Institute for Gravitational Physics, (Albert-Einstein-Institut) and Institute for Gravitational Physics, Leibniz Universität Hannover

10:00 – 10:40

Onsala Space Observatory: Overview of its activities
Prof. Hans Olofsson, Onsala Space Observatory, Swedish National Facility for Radio-astronomy at Chalmers University of Technology

2012 EFTF AWARDS

EFTF Award

The award, which is open to anyone working in the fields traditionally associated with the European Frequency and Time Forum (EFTF), recognizes exceptional contributions in all fields covered by the EFTF either for fundamental advances or important applications. The significance of contributions includes the degree of initiative and creativity, the quality of work, the degree of success obtained as well as the worldwide scientific impact on the Time and Frequency Community. This award is sponsored by the Société Française des Microtechniques et de Chronométrie. The recipients are selected by the Executive Committee of the EFTF.

2012 EFTF Award:

Dr. Pascale Defraigne, Observatoire Royal de Belgique

Citation: "For seminal contribution in the use of geodetic GNSS techniques for time and frequency transfer".

EFTF Young Scientist Award

The EFTF Young Scientist Award is conferred in recognition of a personal contribution that demonstrated a high degree of initiative and creativity and lead to already established or easily foreseeable outstanding advances in the field of time and frequency metrology. A prerequisite is that the work to be taken under consideration has been published in the Proceedings of the European Frequency and Time Forum. The award honours a person under the age of 40 at the date of the opening session of the 2012 EFTF conference. The goal is to encourage scientific endeavour and competition and to help young scientists along their career paths. This award is sponsored by the Société Française des Microtechniques et de Chronométrie. The recipients are selected by the Executive Committee of the EFTF.

2012 EFTF Young Scientist Award:

Dr. Gesine Grosche, *Physikalisch-Technische Bundesanstalt*

Citation: "In recognition of prominent contributions to several fields of frequency metrology associated with the dissemination of optical frequencies over optical fibers".

STUDENT PAPER COMPETITION

This year, students were encouraged to enter their papers in a Student Paper Competition. From the nearly 40 papers submitted to the competition, 3 or 4 from each technical group (except for Groups 1 and 2 which have been merged) were selected as finalists. From these finalists one winner was chosen for each group. Judging of the winners was based on:

(1) clarity of student's presentation,
(2) depth of student's knowledge,
(3) degree of the student's contribution to the project, and
(4) relevancy of the work to the field.

Student paper competition Finalists: EFTF 2012

Groups 1/2: Materials, Resonators & Resonator circuits/ Oscillators, Synthesisers, Noise & Circuit techniques

Modelling of BVA Resonator for Collective Fabrication
Alexandre Clairet, Rakon France

Theory and Design of Intrinsic Zero-Group Velocity Thin Film Resonators
Lilia Arapan, Uppsala University, Sweden

Using Quartz Resonators for Maximizing Wake-Up Range in Wireless Wake-Up Receivers
Gerd Ulrich Gamm, University of Freiburg, Germany

Winner: Lilia Arapan, Uppsala University, Sweden

Group 3: Microwave Frequency Standards

Wall-Coated Cells for Rb Atomic Clocks: Study of the Ripening Process by Double-Resonance Spectroscopy
Matthieu Pellaton, University of Neuchatel, Switzerland

Towards First Active Clock Based on Mode-Locked InGaN VECSEL with Rubidium Vapor Cell Saturable Absorber
Xi Zeng, Centre Suisse d'Électronique et de Microtechnique (CSEM), Switzerland

Narrow Linewidth, Micro-Integrated Extended Cavity Diode Lasers for Quantum Optics Precision Experiments in Space
Erdenetsetseg Luvsandamdin, Ferdinand-Braun Institut Leibniz-Institut fuer Hoechstfrequenztechnik, Germany

Miniature Trapped-Ion Frequency Standard with $^{171}Yb^{+}$
Heather Partner, Sandia National Laboratories, University of New Mexico, USA

Winner: Xi Zeng, Centre Suisse d'Électronique et de Microtechnique (CSEM), Switzerland

Group 4: Sensors & Transducers

Mixed Orthogonal Frequency Coded SAW RFID Tags
Mark Gallagher, University of Central Florida, USA

Loosely Coupled Wireless Sensing of Measuring Open Loop Micro Coils
Adnan Yousaf, Institute of Microsystems Engineering IMTEK, Germany

Eight Channel Embedded Electronic Open Loop Interrogation for Multi Sensor Measurements
David Rabus, FEMTO-ST, France

Tilted C-Axis Thin-Film Bulk Wave Resonant Pressure Sensors with Improved Sensitivity
Emil Anderås, Uppsala University, Sweden

Winner: Emil Anderås, Uppsala University, Sweden

Group 5: Time-keeping, Time & Frequency Transfer, GNSS Applications

An Integrity Monitoring Algorithm for Satellite Clock Based on Test Statistics
Xinming Huang, Satellite Navigation R&D Center, National Univ. of Defense Technology, China

Time Transfer on Optical Fiber Development at INRIM
Cecilia Clivati, Politecnico di Torino, INRIM, Italy

Characterization of OP TWSTFT Stations in colocation Based on the Combined Use of Code and Carrier Phase Data
Amale Kanj, LNE-SYRTE, Observatoire de Paris, France

Two Way Time Transfer with Picoseconds Precision and Accuracy
Jan Kodet, Czech Technical University in Prague, Czech Republic

Winner: Jan Kodet, Czech Technical University in Prague, Czech Republic

Group 6: Optical Frequency Standards and Applications

Mid-IR Frequency Measurement Using an Optical Frequency Comb and a Long-Distance Remote Frequency Reference
Bruno Chanteau, LPL-Université Paris 13-CNRS, France

Importance of the Carrier-Envelop-Offset Dynamics in the Stabilization of an Optical Frequency Comb
Nikola Bucalovic, Laboratoire Temps-Fréquence, Université de Neuchâtel , Switzerland

Room-Temperature Ultraviolet Extended Cavity Diode Laser for Laser Cooling of 171Yb+
Steven King, National Physical Laboratory, UK

A Sub-40 mHz Linewidth Laser Based on a Silicon Single-Crystal Optical Cavity
Christian Hagemann, Physikalisch-Technische Bundesanstalt, Germany

Winner: Steven King, National Physical Laboratory, UK

TUTORIALS

On Monday, 23 April 2012, there were a series of tutorials covering a wide range of related topics. The tutorials included both the fundamental topics of frequency and timing at a level suitable for practitioners new to the field, and more advanced and specialized topics related to specific areas. As such, the tutorials aim to provide useful knowledge to the beginners in the community, as well as those with extensive experience.

EFTF Tutorial Program, Monday 23rd April 2012

08.30-10.00 **Optical Oscillators, Frequency Standards and Clocks**,
by Stephen Webster (NPL, Teddington, UK)

10.00-10.30 Coffee break

10.30-12.00 **Femtosecond Combs for Frequency Metrology**,
by Yann Le Coq (Observatoire de Paris, CNRS, UPMC)

12.00-13.30 Lunch

13.30-15.00 **Clock and Time transfer Statistics and Analysis Techniques**,
by John Davis (NPL, Teddington, UK)

15.00-15.15 Coffee break

15.15-16.45 **Frequency & Time Transfer using Optical Fibres**,
by Gesine Grosche (PTB, D)

16.45-17.00 Coffee break

17.00-18.30 **Low Phase Noise Oscillators: Theory, Design and Measurement**,
by Jeremy Everard (University of York, UK)

08.30 - 10.00
Room: The Palmstedt hall

Optical Oscillators, Frequency Standards and Clocks

Stephen Webster
National Physical Laboratory, Teddington, UK
Email: stephen.webster@npl.co.uk

Over the past 50 years, atomic clocks have been based on microwave frequencies and primary standards have demonstrated uncertainties at the level of a few parts in 10^{16}. Optical clocks are a new generation of atomic clock, in which the frequency of *light* is the signal used for timing. They are based on "forbidden" atomic transitions for which light is absorbed over a very narrow range of frequencies. Depending on the particular atomic species and transition used, the ratio of the frequency to the frequency width (Q-factor) ranges from 10^{14}-10^{23}, thus, these transitions constitute very precise frequency references. They are also insensitive to external electromagnetic fields and can be highly reproducible and it is anticipated that optical clocks will reach uncertainties of a part in 10^{18}. Further, given that the frequency of light is ~100,000 times higher than that of microwaves, the same level of precision as a microwave atomic clock may be reached in a much shorter time. As optical clocks come of age and prove the stability and reproducibility predicted of them, the prospect will open up for a redefinition of the second in terms of an optical frequency.

The atomic absorber in an optical clock takes one of two forms: it is either a single ion confined in an electro-dynamic trap (Paul trap), or an ensemble of neutral atoms held in an electric dipole force trap (optical lattice). The atomic absorbers are laser cooled so that they are nearly at rest and, to first order, do not experience a Doppler shift on interaction with the light used to probe the atomic transition. To make use of the high-Q of the atomic transition, the probe light must also have a very narrow frequency width and this is achieved by stabilizing a laser to a secondary reference, a high-finesse Fabry-Pérot etalon. A mode-locked femtosecond-pulsed laser (femtosecond comb) converts the very rapid oscillations of the light from some 100's of THz down to a radio frequency so that output of the optical clock can be counted by commercial electronics and compared to the SI second and the outputs of other optical clocks.

This tutorial will give an overview of the essential elements of an optical clock: the atomic reference, the ultra-stable laser and the femtosecond comb. It will describe how each of these elements is realized in practice and the experimental challenges involved in operating such an apparatus. The methods by which the performance of optical clocks are measured and how one makes comparisons between clocks will be considered. The current state-of-the-art will be reviewed including the improvements that are likely to occur over the next few years.

10.30 - 12.00
Room: The Palmstedt hall

Femtosecond Combs for Frequency Metrology

Yann Le Coq
LNE-SYRTE, Observatoire de Paris, CNRS, UPMC
Email : yann.lecoq@obspm.fr

In this tutorial, I will cover the basics of optical frequency combs, in the context of frequency metrology. I will introduce the physics, concepts and technical implementations related to femtosecond lasers for metrology, concentrating on the work-horses of metrology laboratories (Ti:Sapphire and Er-doped fiber lasers). I will show how these lasers are used routinely to measure and compare optical frequency standards in research laboratories.

I will further describe the concepts and technology that are used nowadays for realizing efficient servo-locking of optical frequency combs, as well give an overview of the “transfer oscillator technique” which is a servo-loop free alternative to phase-locking techniques. I will also comment on the various counters technology (pi-counter, lambda counters, dead-time,…) and a few statistical tools for frequency metrology (Allan variance, modified-Allan variance, time variance). Some words will be said about the current limitations of the optical frequency combs technology (narrow-linewidth regime, residual noise, amplitude-phase conversion in photodetection,…) and the research which are being led worldwide to overcome them.

I will finish by describing briefly some open perspectives of the domain, like whispering gallery modes frequency combs, direct frequency comb spectroscopy, astro-combs,…

13.30 - 15.00
Room: The Palmstedt hall

Clock and Time Transfer Statistics and Analysis Techniques

John Davis
National Physical Laboratory, Teddington, UK

Atomic clocks and time transfer techniques produce a range of noise processes that are observed when making clock difference and time transfer measurements. This has given rise to a unique set of second difference statistics that is used to characterise these measurements.

This tutorial examines the power law noise processes, periodic instabilities, deterministic processes and other sources of instabilities that are observed in both clock difference and time transfer measurements. The choice of statistics used to analyse a set of measurements depends on the noise processes present. The concept of stationary and non-stationary noise processes is examined, including the rationale for using second and third difference statistics. Detailed presentations are given of the Allan Deviation (ADEV), Modified Allan Deviation (MDEV), Time Deviation (TDEV) and Hadamard Deviation (HDEV), including their characteristics and confidence intervals. More complex second difference statistics are also reviewed including the Total Deviation and the Dynamic Allan Deviation.

Less well used statistics for characterising atomic clocks and time transfer techniques are examined, including the use of Fourier Transforms, auto- correlation functions, Prediction Error Deviation (PED), and the Maximum Time Interval Error (MTIE) that is employed in telecommunications applications.

A review is also presented of techniques used to analyse clock and time transfer data. These include least squares and Kalman filters, and other less well known techniques including wavelet analysis. The models used in these techniques to describe clock and time transfer noise are examined, including treatment of the memory occurring in flicker noise processes and periodic instabilities.

15.15 - 16.45
Room: The Palmstedt hall

Frequency & Time Transfer using Optical Fibres

Gesine Grosche
PTB, D

Ever more accurate clocks and frequency references are being developed in dedicated laboratories around the world, reaching astonishingly low instability and high accuracy, currently near 1 part in 10 to the 17. Yet, making the ultra-stable output of these powerful instruments available beyond the walls of the metrology laboratory, to enable physics experiments, remains a challenge.

In the wake of the optical telecommunication revolution, transfer techniques that make use of optical fibre have greatly developed: within one decade, improvements of more than three orders of magnitude in precision have been achieved. Frequency transfer accuracy at the level of 1 part in 10 to the 19, and, for 1 km-scale links, synchronisation at the level of femtoseconds has been reported. Fibre based transfer of frequency and time is now reaching 1000 km scale, allowing international comparisons and joint experiments.

In this tutorial I will illustrate advantages and challenges of using optical fibre as a transmission medium for precision metrology. This will cover basic concepts, techniques and limitations, focussing on optical telecommunication fibre (1.5 μm), which is both cheap and optimised for low loss, making it suitable for long-distance transfer. The tutorial will give an overview and comparison of different frequency and time transfer techniques, including methods based on radio-frequency modulation, on using the optical carrier phase, and on the transmission of fs-pulses generated by modelocked lasers.

17.00 - 18.30
Room: The Palmstedt hall

Low Phase Noise Oscillators; Theory, Design and Measurement

Jeremy Everard
University of York, UK
Email: jeremy.everard@york.ac.uk

Low phase noise signal generation is key in setting the ultimate performance limit of communications and radar systems. It is therefore essential to develop simple accurate models and theories for the phase noise in both feedback and negative resistance oscillators to enable simple high performance designs to be developed.

This tutorial will describe simplified models and theories which use simple transfer function feedback techniques (at the operating frequency - not at baseband) to accurately predict the phase noise in oscillators. These theories are then used to produce some key topologies, design rules and circuits for oscillators.

Oscillator topologies including the Amplifiers, phase shifters, resonators and coupler circuits will then be presented and some designs offering the very best performance currently available will be briefly described.

A battery powered design labkit which offers 5 experiments for the design of a fixed frequency and VCO will be described and where possible demonstrated. This has been used in a one day short course (run for the last three years) at the IEEE International Microwave Symposium. The software provided with the labkit will also be demonstrated.

STUDENT AWARD SPONSORS

LNE (Laboratoire National de Métrologie et d'Essais)

SPECTRATIME

T4SCIENCE

GMV Aerospace and Defence SAU

SELEX Galileo S.p.A.

RAKON France SAS

CSEM SA (Centre Suisse d'Electronique et de Microtechnique)

NOISE XT SAS (Noise eXtended Technologies)

TIMETECH GmbH

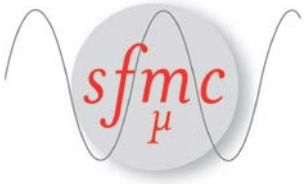

SFMC (Société Française des Microtechniques et de Chronométrie)

NPL (National Physical Laboratory)

SODERN

MENLOSYSTEMS GmbH

UNINE (Université de Neuchâtel)

IDIL FIBRES OPTIQUES

VREMYA-CH

TECHNICAL TOURS

On the last day of the conference, Friday April 27th, tours to the National Metrology Institute at SP and to the Onsala Space Observatory were held.

EXHIBITION

An exhibition of Time and Frequency instrumentation at the conference was held during Tuesday 24th April and Wednesday 25th April.

LIST OF EXHIBITORS

Chronos Technology Ltd, Booth A2. Time and timing solutions, Test measurements and monitoring solutions.

Informasic AB, Booth A8. Informasic has developed Time Transfer Unit TTU for precise time transfer over high speed fiber optic lines. The system is using a passive method that does not interfere with the data transmitted over the OC-192 SDH protocol. This new technology was developed together with SP to provide the necessary equipment that allows for a wide distribution of precise time signals. Informasic is specialized high tech design house developing customized systems based on FPGAs and CPUs/MCUs particularly in the high speed communications area. Other areas of focus are wireless communication and security. The company is highly recognized for its development skills and has won 1st price best national embedded system product in the prestigious contest "Swedish Embedded Award".

GuideTech, Booth B1. GuideTech's new generation of High Precision "UFC" Universal Frequency Counters & "CTIA" Continuous Time Interval Analyzers Measurement Instruments with 2ps resolution is now available to show attendees with up to 50% discount and as an introductory promotion for a limited time and quantity. GuideTech is a leading provider of High Precision Timing Test & Measurement instruments for scientific laboratories, development and volume manufacturing applications. GuideTech's multi-channel timing test systems substantially improves test throughput through parallel & fast measurement rates, greater accuracy, and through critical high-speed timing test coverage. GuideTech sells its computer-based timing instruments since 1988 to NIST, NASA, CERN, US Naval Observatory, Northrop Grumman, Rolls Royce and other respected organizations worldwide. Our instruments are based on GuideTech's 24 patents portfolio of "Continuous Time Interval Analyzer" (CTIA) technology. GuideTech's Computer-based products and test systems are available in ISA, PCI & PXI as well as standalone systems.

Lange electronic GmbH, Booth A7. In addition to timing and frequency sources, time distribution and time monitoring systems developed in-house, Lange-Electronic GmbH also provides satellite simulation systems and telemetry systems. Nowadays high precision timing is crucial for labelling data blocks to ensure correct correlation of data at all times. This is relevant for measurement data in research as well as data blocks in big computer networks transporting security or time dependent data, such as banks or insurances where the time tag of transactions may strongly influence the revenues. Overlaying video signals with time and date is also in this category. Our distribution systems for timing and frequency have been developed for applications requiring the same time simultaneously at different locations. Having been designed with redundancy they are synchronized via external frequency sources such as GPS. In addition we are offering alarm and control options for monitoring all inputs and outputs.

Morion Inc, Booth B2. Morion, Inc. is well-known both in Russia and as a worldwide designer and manufacturer of quartz frequency control products (FCP) - quartz oscillators, filters and crystals dedicated for various applications such as telecommunications, navigation, test & measurement, digital broadcasting, search and rescue systems, etc.

Noise XT, Booth A10. Phase noise analyzers and low noise oscillators.

Rakon, Booth A10. Rakon is the world leader in the design and manufacture of frequency control solutions. With unique, innovative products and a dynamic approach to business, Rakon is the chosen partner for many of the world's leading electronics manufacturers. Whether it be deep down in the infrastructure, satellites in space, navigation devices or smart phones and tablets - Rakon products enable connectivity.

Oscilloquartz SA, Booth B3. For more than 60 years, Oscilloquartz (OSA) is a world leader and pioneer in the supply of precision time and frequency technology. Today, Oscilloquartz continues to be one of the most advanced manufacturers of frequency sources, such as quartz crystal oscillators, GPS receivers or Cesium clocks for telecommunication and metrology applications. Oscilloquartz is also a leading provider of turnkey sync solutions and services. For quartz crystal oscillators, our flagship technology is the ultra-stable BVA® resonator. Our BVA line highlights our capability to manufacture, in industrial quantities, the best quartz oscillator ever manufactured in this world. Furthermore, a third generation with even better shot term stability performance (6E-14 at 1 to 10 seconds) has now been demonstrated. Behind this symbol of perfection, we also manufacture a complete range of Oscillator products, including high end, single oven and double oven oscillators, fulfilling the demanding synchronization specifications of mobile base stations and other telecommunication equipment. Since 2009, OSA has commercialized a new generation of entirely European made Cesium Clocks. Today we are on track to release a new optically pumped Cesium for advanced Metrology applications in 2013. Oscilloquartz's activities also cover the generation of primary references clocks, the distribution of this reference throughout telecom networks, together with the local regeneration and distribution of clocking references. We also provides a full range of OEM products form Manufacturers and System Integrators based on GPS receivers and Time & Frequency Sources including the latest IEEE 1588v2 Precise Time Protocol.

Pascall Electronics Ltd, Booth A3. Pascall Electronics is a leading supplier of specialist RF & Microwave systems, sub-systems & components and both standard and custom power supplies. The RF division has established Pascall as a quality supplier of RF & Microwave components and sub-systems for applications which include Radar, ELINT and SIGINT. The RF division has particular expertise in ultra low noise frequency sources including Pascall's industry leading ultra low noise VHF OCXO range and customised multi-channel fast switching synthesisers.

PIKtime, Booth A9. PikTime Systems specializes in high quality time and frequency equipment

---

Quartzlock Ltd, Booth A6. Time and frequency references, distribution, conversion and measurement.

SP Technical Research Institute of Sweden, Booth B5. SP Technical Research Institute of Sweden is a leading international research institute. We work closely with our customers to create value, delivering high-quality input in all parts of the innovation chain, and thus playing an important part in assisting the competitiveness of industry and its evolution towards sustainable development.

Symmetricom, Booth A1. Symmetricom® is the world's leading source of highly precise timekeeping technologies, instruments and solutions. We provide timekeeping in GPS satellites, national time references, and national power grids as well as in critical military and civilian networks, including those that enable next generation data, voice, mobile and video networks and services. We assist customers in over 90 countries to generate, distribute and apply time. We develop the technology, build the products, optimize the solutions to strict customer requirements and provide post-implementation training, maintenance, engineering and technical support. Our product offering — among the industry's broadest — includes atomic clocks, hydrogen masers, timescale systems, GPS instrumentation, synchronous supply units, standards-based clients and servers, performance measurement and management tools and embedded subsystems that generate, distribute and apply precise frequency and time.

T4 Science, Booth B7 – B8. T4Science offers iPrecision maser and clock solutions.

SpectraTime, Booth B7 – B8. Spectratime offers iPrecision timing and clock solutions.

SpectraCom, Booth B7 – B8. Spectracom offers synchronizing critical operations.

TimeTech GmbH, Booth B4. TimeTech GmbH is sole European manufacturer of Two-Way Satellite Time and Frequency Transfer modems (SATRE TWSTFT), used by European and North-American Institutes to compare high accuracy clocks. Our space activity includes design, development and manufacturing of space systems in particular for satellite position location and high performance intercontinental time transfer.

Toptica, Booth A4. Grating stabilized narrow linewidth laser, femtosecond fiber lasers and wavelength meters.

ULISS and Femto-ST Booth A11. ULISS is a business unit of FEMTO-ST lab located in Besançon (France), which is in charge of the development and commercialization of an ultra-stable CSO (Cryogenic Sapphire Oscillator). The ULISS technology is the only one able to provide relative frequency stability better than $1x10^{-14}$ for integration times ranging from 0.1 s to 1 day (a few $1x10^{-15}$ under 1000s). The first autonomous CSO (called ELISA), has already been in operation since June 2009. It has been designed and built in collaboration between FEMTO-ST Institute, the National Physical Laboratory (UK) and TimeTech GmbH (D).

Zurich Instruments, Booth A5. Technology-leader Zurich Instruments (ZI) designs and manufactures high performance dynamic signal analysis instruments for advanced scientific research and leading industrial applications. ZI products include lock-in amplifiers, phase-locked loops, instruments for electrical impedance spectroscopy, and application specific pre-amplifiers. Headquartered in Zurich, Switzerland, ZI is a technology spin-off from the Swiss Federal Institute of Technology (ETH Zurich). ZI customers are scientists and engineers in leading research labs and organizations worldwide.

PARALLEL ORAL SESSION SCHEDULE

Tuesday, April 24 09:00 - 10:40			
	RunAn	**The Palmstedt hall**	
	Cryogenic Sources & Fine Tuning Synthesisers	**Primary Frequency Standards**	
Session Chairs:			
	Jeremy Everard, University of York	**Sebastian Bize, SYRTE**	
09:00 - 09:40	**INVITED: High Q-Factor Cryogenic Resonators and Applications** *Michael Tobar, The University of Western Australia*	**INVITED: Fountain Clock Accuracy** *Kurt Gibble, The Pennsylvania State University*	
09:40 - 10:00	**Ultra-Stable Low-Phase-Noise 11.2 GHz Signal Measured by Comparing Two cryocooled Sapphire Microwave Oscillators** *John Hartnett, et al., University of Western Australia, University of Science and Technology of China*	**Investigation of Rapid Adiabatic Passage in the Fountain PTB-CSF2** *Vladislav Gerginov, et al., PTB*	
10:00 - 10:20	**Cryogenic Quartz Frequency Sources: Problems and Perspectives** *Maxim Goryachev, et al., FEMTO-ST*	**Improved Tests of the Stability of Fundamental Constants Using the SYRTE-FO2 Rb/Cs Dual Fountain** *Jocelyne Guéna, et al., SYRTE - Observatoire de Paris, University of Western Australia*	
10:20 - 10:40	**Charactherization of an Auxiliary Offset Generator for Steering of H-Masers** *Daniele Rovera, et al., LNE-SYRTE / OP CNRS UPMC, SKK electronics*		

Tuesday, April 24 11:10 - 12:50			
	RunAn	The Palmstedt hall	
	Lattice Clocks	Time Scales & Time Transfer	
Session Chairs:			
	Ekkehard Peik, PTB	Laurent Guy Bernier, METAS	
11:10 - 11:30	INVITED: Prospects for Frequency Comparison of Optical	**UTCr: a Rapid Realization of UTC** *Felicitas Arias, et al., BIPM*	
11:30 - 11:50	**Lattice Clocks Toward 10-18 Fractional Uncertainties** *Hidetoshi Katori, University of Tokyo*	**Strategies for Steering UTC(NPL) Using the Caesium Fountain Primary Frequency Standard** *Peter Whibberley, et al., NPL*	
11:50 - 12:10	**Comparison of Two Strontium Optical Lattice Clocks in Agreement at the 10-16 Level** *Rodolphe Le Targat, et al., LNE-SYRTE, INRIM, Nicolaus Copernicus University*	**Time and Frequency Transfer with a Microwave Link in the Aces/PHARAO Mission** *Pacôme Delva, et al., SYRTE, UPMC, Observatoire de Paris*	
12:10 - 12:30	**Blackbody Radiation Shift Correction of an Optical Lattice Clock from dc Stark Shift Measurements** *Thomas Middelmann, et al., Physikalisch-Technische Bundesanstalt (PTB)*	**Ground to Ground Time Transfer by Laser Link T2L2** *Etienne Samain, et al., oca, CNES*	
12:30 - 12:50	**Reaching the 10-15 Accuracy Range with a Hg Optical Lattice Clock** *John J. McFerran, et al., SYRTE*		

Tuesday, April 24 16:10 - 17:50			
	RunAn	The Palmstedt hall	
	Sensor Development & Design	Frequency and Time Transfer by Optical Fibers I	
Session Chairs:			
	Bernard Dulmet, ENSMM	Harald Schnatz, PTB	
16:10 - 16:30	**INVITED: Phononic Crystal Sensors** *Ralf Lucklum, Otto-von-Guericke-University*	**Real-Time Phase Stable One-Way Frequency Transfer Over Optical Fiber** *Per Olof Hedekvist, et al., SP Technical Research Institute of Sweden*	
16:30 - 16:50		**Microwave Frequency Transfer with Optical Stabilisation** *Sascha Schediwy, et al., University of Western Australia, AARNet, Australian National University, Macquarie University, National Measurement Institute*	
16:50 - 17:10	**Tilted C-Axis Thin-Film Bulk Wave Resonant Pressure Sensors with Improved Sensitivity** *Emil Anderås, et al., Uppsala University*	**One-Way Two-Color Fiber Link for Frequency Transfer** *James Hanssen, et al., U.S. Naval Observatory*	

Continue on next page

Tuesday, April 24 16:10 - 17:50			
	RunAn	The Palmstedt hall	
	Sensor Development & Design	Frequency and Time Transfer by Optical Fibers I	
Session Chairs:			
	Bernard Dulmet, ENSMM	Harald Schnatz, PTB	
17:10 - 17:30	**An Optimal 2D and 3D Modelling of Finite SAW and BAW Devices Based on Perfectly Matched Layer Method** *Karim Dbich, et al., TDK-EPC, CNRS*	**Calibrated Time Transfer Through a 73 km Optical Fiber Link by Means of Spread Spectrum Signals** *Michael Rost, et al., Physikalisch-Technische Bundesanstalt, Institut für Quantenoptik*	
17:30 - 17:50	**Temperature Insensitive Displacement Transducer Based on a Dual Mode Microwave Sapphire Resonator** *Fabio Stefani, et al., Dipartimento di Fisica, Università di Pisa, Dipartimento di Ingegneria dell'Informazione*	**Time and Frequency Fiber Optic Link Between AOS and Gum. Calibration and First Results** *Jerzy Nawrocki, et al., Space Research Centre, AGH University of Science and Technology, Central Office of Measures*	

Wednesday, April 25 09:00 - 10:40			
	RunAn		
	PLENARY		
Session Chairs:			
	Patrick Gill, NPL		
09:00 - 10:00	**Listening to the Universe: Gravitational Wave Detection on the Ground and in Space** *Professor Dr. Karsten Danzmann, Max Planck Institute for Gravitational Physics, (Albert-Einstein-Institut) and Institute for Gravitational Physics, Leibniz Universität Hannover*		
10:00 - 10:40	**Onsala Space Observatory: Overview of its Activities** *Professor Hans Olofsson, Onsala Space Observatory, Swedish National Facility for Radio-astronomy at Chalmers University of Technology*		

Wednesday, April 25 11:10 - 12:50			
	RunAn	**The Palmstedt hall**	
	Resonator Design & Characterisation	**Ion Clocks**	
Session Chairs:			
	Mike Underhill, Underhill Research Ltd	**Davide Calonico, INRIM**	
11:10 - 11:50	**INVITED: The Fairy World of Quartz MEMS** *Olivier Le Traon, ONERA -The French Aerospace Lab*	**INVITED: Single-Ion Optical Frequency Standards Based on 171Yb+** *C. Tamm, et al., Physikalisch-Technische Bundesanstalt*	
11:50 - 12:10	**New Electrostatically-Excited Single Crystal Silicon Resonator Vibrating in a Thickness-Extensional Mode** *Mihaela Ivan, et al., FEMTO-ST*	**Optical Frequency Measurements in a Single Ion of 171Yb+** *Rachel Godun, et al., National Physical Laboratory, University of Oxford*	
12:10 - 12:30	**Theory and Design of Intrinsic Zero-Group Velocity Thin Film Resonators** *Lilia Arapan, et al., Uppsala University, Technical University of Sofia, Smartcom Bulgaria AB*	**Minimizing Time-Dilation in Ion Traps - Towards an Optical Clock with Coulomb Crystals** *Tanja Mehlstäubler, et al., PTB*	
12:30 - 12:50	**Investigation of Drive Level Dependencies of Higher Overtones in SC Quartz Resonators** *Vladimir Stofanik, et al., FEI STU*	**Strontium Ion Optical Frequency Standard at 445 THz** *Geoffrey Barwood, et al., National Physical Laboratory*	

Wednesday, April 25 14:00 - 15:40			
	RunAn	The Palmstedt hall	
	Frequency Combs	Algorithms	
Session Chairs:			
	Helen Margolis, NPL	Demetrios Matsakis, US Naval Observatory	
14:00 - 14:40	**INVITED: Direct Frequency Comb Metrology Up to PHz Frequencies** *T.J. Pinkert, et al., VU University, Max Born Institute, Ludwig-Maximilians-University*	**INVITED: The New Prediction Algorithm for UTC: Application & Results** *G. Panfilo, BIPM*	
14:40 - 15:00	**High Contrast, Low Noise Selection and Amplification of an Individual Optical Frequency Comb Line** *Erik Benkler, et al., PTB, Cosigno, Imagine Optic Spain S.L.*	**Kinematic Positioning Improvements with Stochastic Clock Modeling** *Kan Wang, et al., ETH Zurich*	
15:00 - 15:20	**Importance of the Carrier-Envelop-Offset Dynamics in the Stabilization of an Optical Frequency Comb** *Nikola Bucalovic, et al., Laboratoire Temps-Fréquence, Université de Neuchâtel, UniNE, Institute of Quantum Electronics, ETH Zurich, SpectraTime*	**Development of a Clock Ensemble Algorithm Incorporating Data from NPL's Caesium Fountain** *Setnam Shemar, et al., National Physical Laboratory*	

Continue on next page

Wednesday, April 25 14:00 - 15:40			
	RunAn	**The Palmstedt hall**	
	Frequency Combs	**Algorithms**	
Session Chairs:			
	Helen Margolis, NPL	**Demetrios Matsakis, US Naval Observatory**	
15:20 - 15:40	**Investigation of an Optical Frequency Comb with intra-Cavity EOM and Optimization of Microwave Generation** *Wei Zhang, et al., LNE-SYRTE, Observatoire de Paris, CNRS, UPMC, MenloSystems GmbH*	**Real-Time Assessment of Dynamic Allan Deviation and Dynamic Time Deviation** *Andrzej Dobrogowski, et al., Poznan University of Technology*	

Thursday, April 26 09:00 - 10:40			
	RunAn	**The Palmstedt hall**	**Scania hall**
	Frequency and Time Transfer by Optical Fibers II	**Microwave Clocks**	**Sensor Systems**
Session Chairs:			
	Giorgio Santarelli, OBSPM	**Steve Lecomte, CSEM**	**Svenja Knappe, NIST**
09:00 - 09:20	**INVITED: Frequency Dissemination at the 19th Decimal Place** *Gesine Grosche, et al., Physikalisch-Technische Bundesanstalt, Institut fuer Quantenoptik Hannover, MPQ Garching*	**A Microwave Frequency Standard Based on the Laser Cooled 113Cd+ Ions** *Jianwei Zhang, et al., JMI*	**Correlator Time Delay Extraction for Wireless Acoustic Sensors** *Donald Malocha, University of Central Florida*
09:20 - 09:40		**Narrow Linewidth, Micro-Integrated Extended Cavity Diode Lasers for Quantum Optics Precision Experiments in Space** *Erdenetsetseg Luvsandamdin, et al., Ferdinand-Braun Institut Leibniz-Institut fuer Hoechstfrequenz-technik Berlin, Humboldt-Universitaet zu Berlin*	**High-Speed Reader for Wireless Resonant SAW Sensors** *Victor Kalinin, et al., Transense Technologies plc*
09:40 - 10:00	**Ultra-Stable Frequency Dissemination on a Dedicated Frequency Channel of the Telecommunication Network** *Olivier Lopez, et al., LPL, CNRS, Université Paris 13, LNE-SYRTE, LKB, UPMC, ENS*	**Measurement of the Electric Polarizability of the Cs Ground State for the Blackbody Radiation Shift Correction in Primary Frequency Standards** *Jean-Luc Robyr, et al., University of Fribourg*	**Eight Channel Embedded Electronic Open Loop Interrogation for Multi Sensor Measurments** *David Rabus, et al., FEMTO-ST, SENSEOR*

Continue on next page

Thursday, April 26 09:00 - 10:40			
	RunAn	**The Palmstedt hall**	**Scania hall**
	Frequency and Time Transfer by Optical Fibers II	**Microwave Clocks**	**Sensor Systems**
Session Chairs:			
	Giorgio Santarelli, OBSPM	**Steve Lecomte, CSEM**	**Svenja Knappe, NIST**
10:00 - 10:20	**Fiber Optic RF Frequency Transfer on the Distance of 480 km with Active Stabilization of the Propagation Delay** *Lukasz Sliwczynski, et al., AGH University of Science and Technology*	**A Cold Rubidium Frequency Standard for the Fundamental Physics Mission STE-Quest** *Christoph Affolderbach, et al., LTF, University of Neuchâtel, NPL, LNE-SYRTE, Observatoire de Paris, University of Birmingham, Heinrich-Heine-Universität, CNES, SP, PTB, RUAG Space AB, Universita' di Firenze, LENS, INFN, Universita' di Bologna, University of Bern*	**Indoor-Localization System Using a Micro Inertial Measurement Unit (IMU)** *Fabian Hoeflinger, et al., University of Freiburg*
10:20 - 10:40	**Dissemination of an Optical Frequency Comb Over Fiber with 3×10-18 Fractional Accuracy** *Giuseppe Marra, et al., National Physical Laboratory, Optoelectronics Research Centre, University of Southampton*	**Miniature Trapped-Ion Frequency Standard with 171Yb+** *Heather Partner, et al., Sandia National Laboratories / University of New Mexico, Jet Propulsion Laboratory, Symmetricom*	**Laser Gyroscopes for Very High Sensitivity Applications** *Jacopo Belfi, et al., Dip. Fisica Università di Pisa, INFN sezione di Pisa*

Thursday, April 26 11:10 - 12:50			
	RunAn	**The Palmstedt hall**	**Scania hall**
	Stable Lasers	**Two-Way Time & Frequency Transfer**	**Compact Microwave Clocks**
Session Chairs:			
	Ernst Rasel, University of Hannover	**Dirk Piester, PTB**	**Gaetano Mileti, Université de Neuchâtel**
11:10 - 11:30	**INVITED: Characterization and Application of a Cryogenic Silicon Cavity with Fractional Frequency Stability of 1E-16** *Thomas Kessler, et al., PTB, JILA*	**Study on Carrier-Phase TWSTFT Using Ku Band Signals** *Miho Fujieda, et al., NICT*	**Studies of a Short and Long – Term Stability of an Active H-Maser** *Nikolay Demidov, et al., Vremya-CH, National Research Institute for Physical-Technical and Radio technical*
11:30 - 11:50		**State-of-the-Art Time Link Calibration with a Mobile TWSTFT Station** *Thorsten Feldmann, et al., TimeTech GmbH, PTB*	**Laser-Pumped High-Performance Compact Gas-Cell Rb Standard with <3E-13 Tau-1/2 Stability** *Thejesh Bandi, et al., Laboratoire Temps-Fréquence (LTF), University of Neuchâtel, Istituto Nazionale di Ricerca Metrologica (INRIM), Laboratory of electromagnetics and acoustics, École Polytechnique Fédérale de Lausanne*
11:50 - 12:10	**A Small-Linewidth Absolute Optical Frequency Source** *Sebastian Raupach, et al., PTB*	**A Delay Calibration System for a TWSTFT Station** *Faisal Ali Mubarak, et al., VSL*	**First Metrological Signals from a Compact Cold-Atom CPT Frequency Standard** *Francois-Xavier Esnault, et al., NIST*

Continue on next page

Thursday, April 26 11:10 - 12:50			
	RunAn	**The Palmstedt hall**	**Scania hall**
	Stable Lasers	**Two-Way Time & Frequency Transfer**	**Compact Microwave Clocks**
Session Chairs:			
	Ernst Rasel, University of Hannover	**Dirk Piester, PTB**	**Gaetano Mileti, Université de Neuchâtel**
12:10 - 12:30	**Mid-IR Frequency Measurement Using an Optical Frequency Comb and a Long-Distance Remote Frequency Reference** *Bruno Chanteau, et al., LPL, Université Paris 13, CNRS, LNE-SYRTE*	**Characterization of OP TWSTFT Stations in colocation Based on the Combined Use of Code and Carrier Phase Data** *Amale Kanj, et al., Observatoire de Paris*	**Trapped Atom Clock on a Chip (TACC)** *Wilfried Maineult, et al., LNE-SYRTE, LKB*
12:30 - 12:50	**Cr:ZnSe Laser with 0.03 Hz/Hz1/2 Frequency Noise for Compact Methane Based OFS** *Mikhail Gubin, et al., Lebedev Physical Institute, Bauman Moscow State Technical University*	**Two Way Time Transfer with Picoseconds Precision and Accuracy** *Ivan Prochazka, et al., Czech Technical University in Prague, Academy of Sciences of the Czech Republic, Technical University Munich, Wettzell Observatory*	**Interferometry with Chip Based Atom Lasers** *Ernst Maria Rasel, QUEST/LUH*

Thursday, April 26 14:00 - 15:40			
	RunAn	The Palmstedt hall	Scania hall
	Oscillators & Noise Processes	GNSS and Applications	Optical Standards & Applications
Session Chairs:			
	Philippe Guillemot, CNES	Kenneth Jaldehag, SP	Rodolphe Le Targat, SYRTE
14:00 - 14:20	**INVITED: The Opto-Electronic Oscillator (OEO): Review and Recent Progress** *Lute Maleki, OEwaves Inc.*	**Review of GLONASS Time Transfer** *Zhiheng Jiang, et al., Bureau International des Poids et Mesures (BIPM)*	**Permanent Magnet Zeeman Slowers and a Narrow-Linewidth Clock Laser for a Strontium Optical Lattice Frequency Standard** *Ian Hill, et al., NPL*
14:20 - 14:40		**On the Impact of Group Delay Variations on GNSS Time and Frequency Transfer** *Tobias Kersten, et al., Institut für Erdmessung, Universität Hannover*	**Interrogation Laser with 5e-16 Instability for a Magnesium Optical Lattice Clock** *Andre Pape, et al., Leibniz Universität Hannover*
14:40 - 15:00	**Long Duration Performance of Quartz Oscillators and Rb Clocks in Space** *Thomas McClelland, et al., Frequency Electronics, Inc., Lockheed-Martin, The Aerospace Corporation*	**Very Precise Synchronization of Distributed Pseudolites** *Werner Lange, Lange-Electronic GmbH*	**Characterization of an Ultra-Stable Optical Cavity Developed in the Industry for Space Applications** *Bérengère Argence, et al., LNE-SRTE, Observatoire de Paris, SODERN, CNES Centre National d'Etudes Spatiales*

Continue on next page

Thursday, April 26 14:00 - 15:40			
	RunAn	The Palmstedt hall	Scania hall
	Oscillators & Noise Processes	GNSS and Applications	Optical Standards & Applications
Session Chairs:			
	Philippe Guillemot, CNES	Kenneth Jaldehag, SP	Rodolphe Le Targat, SYRTE
15:00 - 15:20	**Asymmetric Spectra of Phase Modulated Transitions of Square Waves** *Michael Underhill, Underhill Research*	**Study and Development of a New GNSS Receiver for Time and Frequency Transfer** *Kun Liang, et al., National Institute of Metrology(NIM), Beijing Trust GPS Science&Technology Development Co., Ltd*	**An Ultra-Stable Optical Frequency Reference for Space Applications** *Thilo Schuldt, et al., University of Applied Sciences Konstanz, Humboldt-University Berlin, Astrium GmbH - Satellites*
15:20 - 15:40		**Smartphone Application for the Near-Real Time Synchronization and Monitoring of Clocks Through a Network of GNSS Receivers** *Ricardo Píriz, et al., GMV, INRIM*	**Narrow, Long-Term Stable Spectral Holes in a Eu3+:Y2SiO5 Crystal for Application to Laser Frequency Stabilization** *Alexander Nevsky, et al., University of Düsseldorf*

Some Future Applications of Cryogenic High-Q Resonant Cavities

Michael E. Tobar, Daniel L. Creedon, Maxim Goryachev, Karim Benmessai, Jean-Michel le Floch, Eugene N. Ivanov
ARC Centre of Excellence for Engineered Quantum Systems
University of Western Australia
Crawley WA 6009, Australia
Email: michael.tobar@uwa.edu.au

Warwick P. Bowen
ARC Centre of Excellence for Engineered Quantum Systems
University of Queensland
St. Lucia QLD 4072, Australia

Serge Galliou, Roger Bourquin
Department of Time and Frequency
FEMTO-ST Institute, ENSMM
25000, Besançon, France

***Abstract*— Some future applications for high-Q resonant cavities at cryogenic temperatures lie in the discipline of hybrid quantum systems. In this paper we review our recent work in this discipline, which investigates spins in sapphire resonators and the unique property of quartz at low temperatures.**

I. Introduction

Traditionally high-Q cryogenic resonators have been used to generate very stable [1] and low noise signals [2]. At the University of Western Australia the majority of our work has utilised cryogenic sapphire resonators operating in Whispering Gallery Modes (WG), which exhibit very high Q-factors ($> 10^9$) at microwave frequencies. High stability is only possible due to the additional inclusion of residual paramagnetic impurities that annul the frequency-temperature dependence of sapphire [3]. More recently, the residual Fe^{3+} impurities with parts-per-billion concentration within the lattice have been shown to create a three level system corresponding to the spin states of the ion. By pumping at 31.3 GHz, a stable 12.04 GHz maser signal with stability of parts in 10^{15} may be created [4], [5], [6]. Moreover, sapphire loop oscillators, stabilised by Pound or interferometer circuits form a mature now commercial technology, which are fast approaching their best limit of performance (for further information see the other papers in this proceedings by UWA and FEMTO authors and references therein).

Also, recently cryogenic quartz BAW resonators have shown very high Q-factors at low temperature with a research program at FEMTO to build oscillators from these devices [7]. In this paper we look at our recent work to adapt such technology to hybrid quantum systems with the aim at observing the properties of these devices at the quantum limit.

II. Nonlinear Effects of Electron Paramagnetic Resonance in High-Q Cryogenic Sapphire Microwave Resonators

Since the development of the first laser [8], a multitude of nonlinear effects have been observed in optical systems. Optical second- [9] and third-harmonic generation [10], [11], optical sum-frequency generation [12], optical parametric oscillation and amplification[13], [14], Raman lasing [15], and two-photon absorption [16] are all well-characterised nonlinear effects which have been instrumental in the development of the past few decades of modern optics. High quality optical cavities allow the effect of the nonlinearity to be greatly enhanced, and have lead to many new applications including the implementations of frequency combs through parametric frequency conversion effects [17], [18], [19]. Optical nonlinearities are crucial for switching and modulation in modern communications technology, and are an enabling capability for future implementations of optical computer technologies, including the possibility of a quantum computer based on encoded single photons [20]. Recently, dramatic progress has been made in using microwave systems for quantum information and measurement, with nonlinearities playing a critical role. Josephson junctions in particular, which operate at microwave frequencies, act as a nonlinear inductor which permits uneven spacing of energy levels, leading to individual addressability of energy states using an external field. This, and other strongly nonlinear systems are currently of considerable interest for a new generation of quantum measurement experiments including quantum-limited amplification [21], single quadrature squeezing with tunable nonlinear Josephson metamaterials [22], readout of superconducting flux qubits [23], and frequency conversion with quantum-limited efficiency [24]. An addressable quantum memory with coherence times long enough for quantum computing applications could potentially be achieved through the manipulation of

electron spins in a crystal lattice host, which typically occurs at microwave frequencies, and can have characteristic relaxation times of order seconds. This, along with the potential for large collective couplings, have provoked great interest in electron spins in solids as potential quantum memories for superconducting qubits. In particular, nitrogen-vacancy (NV) centers in diamond [25], Cr^{3+} spins in sapphire [26], and nitrogen spins in fullerene cages & phosphorous donors in silicon [27] have been well studied in circuit Quantum Electrodynamics (QED) experiments coupling superconducting resonators to electron spin ensembles.

Here, we demonstrate the resonant enhancement of the weak nonlinear $\chi^{(3)}$ paramagnetic susceptibility present in a parts-per-billion concentration of electron spins in sapphire [28]. To the authors' knowledge, this is the first observation of a paramagnetic nonlinear process purely at microwave frequencies in a crystalline host. Degenerate Four Wave Mixing (FWM) is achieved with the application of only a single pump field, with the pump and idler frequencies enhanced by ultra-high Q-factor WG mode resonances. FWM is an enabling process for both frequency comb generation and many quantum computing and metrology applications. Our system is further suited to these applications due to the extremely low dielectric loss tangent at millikelvin temperature, which persists even at single photon input power [29].

The experimental system consists of a cryogenic sapphire resonator-oscillator [4], [5], [6], [30], [31], [32] as shown in Fig. 2(a). The system is cooled to liquid helium temperature and pumped with microwave power to excite WG mode resonances. As a result of the manufacturing process, paramagnetic Fe^{3+} ions are included in the sapphire lattice at a concentration of 150 ppb ($\sim 10^{16}$ spins in the lattice) [32]. The crystal field splitting results in an inhomogeneously broadened electron spin resonance (ESR) with 27 MHz linewidth [33] at

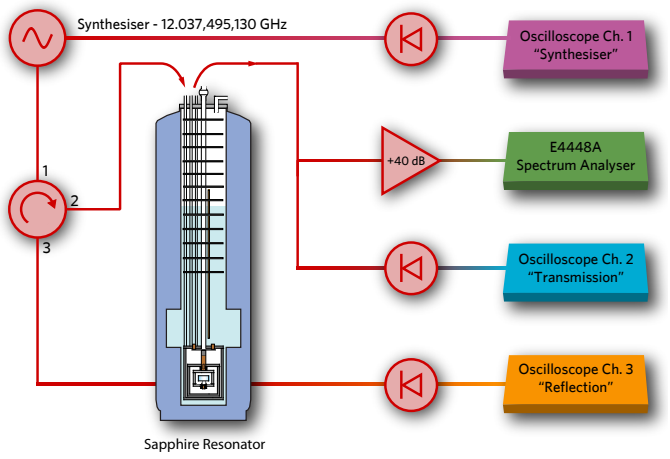

Fig. 1. Schematic of the detection circuit. The sapphire resonator is mounted in a vacuum chamber at the end of an insert in a liquid helium dewar, with a detailed cross section of the resonator in its cavity shown in Figure 2(a). Herotek DT8016 detectors are used to generate a voltage proportional to incident microwave power as input for the oscilloscope.

zero applied DC magnetic field, corresponding to the spin-$|1/2\rangle$, $|3/2\rangle$, and $|5/2\rangle$ states of the ion. Within the system a complex interaction occurs between the microwave input field, a dilute paramagnetic Fe^{3+} spin system, and ^{27}Al lattice ions, which ultimately results in the production of signal and idler photons equally spaced in frequency, characteristic of degenerate FWM. The resonator-oscillator geometry is such that two microwave resonances exist within the ESR bandwidth, as shown in Fig. 2(b), which act to resonantly enchance both the pump and idler fields. The pump resonance frequency of $\omega_0 = 12.0375$ GHz is co-incident with the $|1/2\rangle \rightarrow |3/2\rangle$ transition residing at the maximum of the ESR, and the idler resonance frequency of $\omega_- = 12.0298$ GHz is in the wings of the ESR. No WG mode exists within the ESR bandwidth at the signal frequency ω_+.

At low pump powers, excitation was only observed at the pump frequency. However, as is characteristic of degenerate four-wave mixing, after a threshold power level is surpassed, continuous excitation of the signal and idler fields is also found to be present, with the signal and idler frequencies equally spaced $\Delta\omega = 7.669$ MHz from the pump frequency, and the idler frequency clamped to its whispering gallery mode resonance. Remarkably, signal and idler excitation was observed to appear anywhere from instantaneously to $\sim$7.5 seconds after application of the pump, with the delay being strongly dependent on the pump power and its detuning from resonance. Figure 3 shows the transmitted power through the resonator as a function of time for two different cases, with insets showing the spectrum analyser trace before (Fig. 3(a)(i)) and after applying the synthesizer signal. In the first case, when the synthesizer is switched on (Fig. 3(a)(ii)) the transmitted power remains constant for 7.58 seconds, after which time the signal and idler appeared simultaneously (Fig. 3(a)(iii)) and the total output power detected was seen to rise. In contrast, in the second example the signal and idler appear significantly faster, but relax over a period of several seconds before reaching a steady-state transmitted power level.

The complex time dynamics of the interaction can be qualitatively understood as being due to the slow seeding of the parametric process due to energy transfer in the Fe^{3+} spin system. Upon application of the pump field, the sub-set of Fe^{3+} ions within the ESR at the pump frequency begin to absorb energy. The hyperfine lattice interaction between the individual Fe^{3+} spin packets, and the ^{27}Al nuclear spins then slowly transfers power through a cross-relaxation process from the pump mode frequency, down to the idler resonance frequency thus seeding the signal. A similar behaviour has been observed in optical systems, where Raman scattering from the pump into the signal seeds the parametric process, and significantly reduces the threshold power for observation four-wave mixing[34], [35]. In the optical case, the Raman scattering occurs virtually instantaneously. Here, by contrast, the time constant of the hyperfine lattice interaction can be extremely long, with previous studies with Cr^{3+} doped sapphire [36] recording transient relaxation times on the order of 5 seconds. We attribute the complex dynamics observed

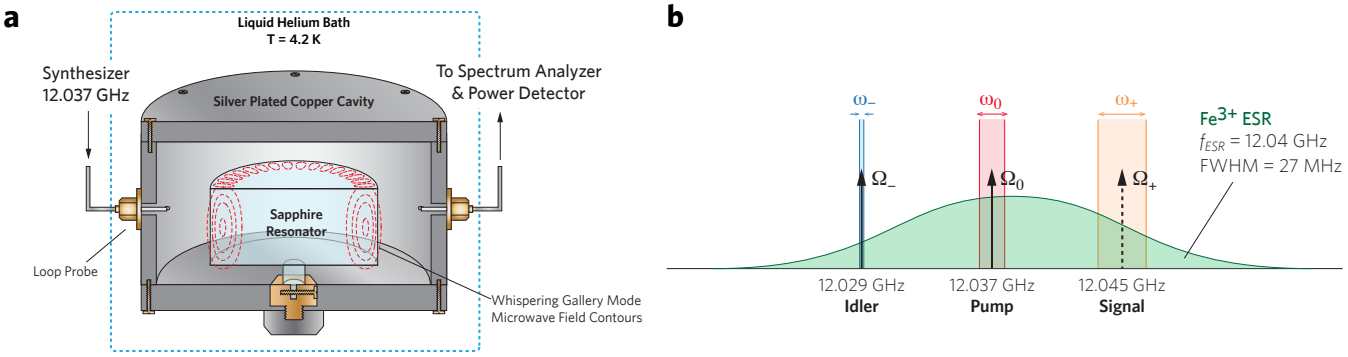

Fig. 2. **(a)** Cross section of the experimental package. The sapphire resonator is shown in its cavity, which is mounted in a vacuum chamber at the end of an insert in a liquid helium dewar. Herotek DT8016 power detectors are used at the output to generate a voltage proportional to incident microwave power, measured with an oscilloscope. **(b)** (Not to scale.) Schematic of the system described by our theoretical model. Ω_0 and Ω_- represent fixed microwave WG mode resonances in the sapphire resonator with bandwidths of order 10 Hz. Ω_+ models a lossy resonance at $\Omega_+ = 2\Omega_0 - \Omega_-$ as no WG mode exists at 12.045 GHz. The applied pump frequency ω_0 can be selected in a range of over 4 kHz around Ω_0 to successfully result in the generation of ω_- whose frequency only changes over a narrow range <40 Hz, and ω_+ with a frequency range of order 8 kHz.

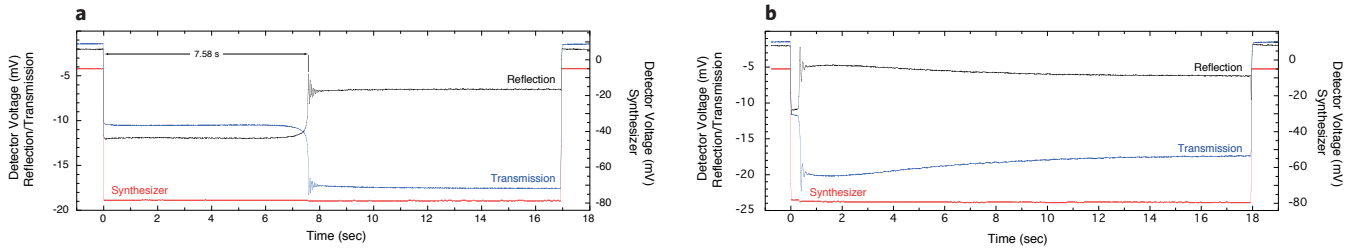

Fig. 3. Power detected in transmission through the resonator when (a) the 12.037 GHz pump signal is offset 2.671 kHz above resonance, and (b) when the 12.037 GHz pump is offset 2.659 kHz above resonance. In both cases, the excitation signal was switched on at zero seconds.

over long time scales in our experiment to this fact.

The four-wave mixing operates for pump frequencies over a range spanning 4 kHz, corresponding to ∼400 times the linewidth of the pump WG resonance. Four-wave mixing is a phase sensitive process, and we observe an apparent strong phase-mismatch when the pump frequency tunes closely to pump WG mode resonance. A large enough phase mismatch ensures that four-wave mixing is effectively suppressed. Due to the resonant enhancement of the idler field, it's frequency is clamped strongly to the signal resonance frequency, varying by less than 36 Hz over the full pump frequency range as shown in Fig. 4. This allows the signal frequency to be widely and predictably tuned by tuning the pump frequency. The tunable bandwidth decreases with pump power and is, for example, only several hundred Hertz at a pump power of 5 dBm.

The full model of the parametric process including cross-relaxation induced seeding is beyond the scope of this article. Here we instead neglect the seeding process, and estimate the parametric nonlinearity through a simple three mode picture with Hamiltonian:

$$H = \hbar\Omega_0\hat{a}_0^\dagger\hat{a}_0 + \hbar\Omega_-\hat{a}_-^\dagger\hat{a}_- + \hbar\Omega_+\hat{a}_+^\dagger\hat{a}_+ + i\hbar g\hat{a}_0^2\hat{a}_-^\dagger\hat{a}_+^\dagger - i\hbar g^*\hat{a}_0^{\dagger 2}\hat{a}_-\hat{a}_+, \quad (1)$$

where the terms on the first line are the rest energy of the system, while those on the second account for the nonlinear interaction, with g being the nonlinear interaction strength. The annihilation operator $\hat{a}_j$ describes the field amplitude in mode j, with $\langle a_j^\dagger a_j\rangle$ being the mean photon number in the mode and the subscripts 0, $+$, and $-$ respectively denoting the pump, signal and idler modes. Ω_j is the resonance frequency of mode j. The splitting of the $\mathrm{WGH}_{17,0,0}$ mode at Ω_0 is neglected since the splitting frequency is far smaller than the spacing of the pump, signal, and idler frequencies, and thus it is expected not to contribute significantly to the physics.

Applying the quantum Langevin Equation to Eqn. 1 [37], one can then find equations of motion for the pump, idler and signal. In the rotating frame, this yields the expectation value equations

$$\dot{\alpha_0} = -2g\alpha_0^*\alpha_-\alpha_+ - (\gamma_0 + i\Delta_0)\alpha_0 - \sqrt{2\gamma_{0,\mathrm{in}}}\alpha_{0,\mathrm{in}} \quad (2)$$

$$\dot{\alpha_-} = g\alpha_0^2\alpha_+^* - (\gamma_- + i\Delta_-)\alpha_- \quad (3)$$

$$\dot{\alpha_+} = g\alpha_0^2\alpha_-^* - (\gamma_+ + i\Delta_+)\alpha_+. \quad (4)$$

where $\alpha_j = \langle a_j\rangle$, γ_j and Δ_j are, respectively, the decay rate and detuning from resonance of field j, $\gamma_{0,\mathrm{in}}$ and $\alpha_{0,\mathrm{in}}$ are the input coupling and amplitude of the incident pump field, and since the idler and signal are not pumped, $\alpha_{-,\mathrm{in}} = \alpha_{+,\mathrm{in}} = 0$. Expressed in terms of half-bandwidths, $\gamma_- = 6$ Hz, $\gamma_{0,l} = 5$ Hz, and $\gamma_{0,u} = 6.7$ Hz. Consistent with our experiments, we model the signal resonance as a lossy resonance such that the signal dynamics are fast compared with the pump and idler dynamics. Hence, γ_+ represents a lossy damping and is related

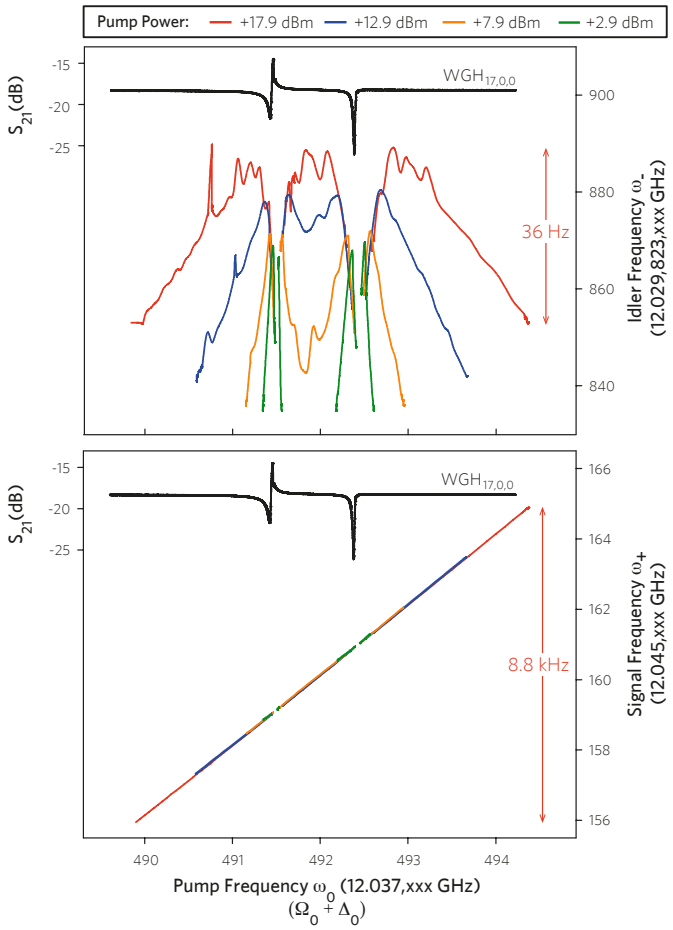

Fig. 4. Output frequency of the idler (top), and signal (bottom) as the input pump frequency is swept over the $\mathrm{WGH}_{17,0,0}$ resonance at 12.037 GHz. The gradient of the 'signal' slope is 2.00, meaning $\Delta_+ \approx 2\Delta_0$. The frequency of the idler (ω_-) is strongly locked to the WG mode frequency Ω_- as the frequency shift is more than two orders of magnitude smaller.

to the ratio of the amplitudes $\gamma_+ = \gamma_- \frac{a_-^2}{a_+^2}$. Equation (4) can then be adiabatically eliminated, giving an equation of motion for the signal:

$$\dot{\alpha_-} = -\left[\gamma_-\left(1 - g'|\alpha_0|^4\right) + i\left(\Delta_1\left(1 - g'\frac{\Delta_2\gamma_-}{\Delta_1\gamma_+}|\alpha_0|^4\right)\right)\right]\alpha_- \tag{5}$$

The effective nonlinearity g' can be related to the intrinsic nonlinearity g, and expressed in terms of only the pump parameters, given by:

$$g' = g\frac{\gamma_+}{\gamma_-}\frac{1}{\sqrt{\gamma_+^2 + \Delta_2^2}} \tag{6}$$

$$= \frac{\gamma_0^2 + \Delta_0^2}{2\gamma_{0,\mathrm{in}}}\frac{\hbar\Omega_0}{P_{\mathrm{in}}^{\mathrm{thresh}}} \tag{7}$$

Here, the steady-state intracavity pump amplitude α_0 is related to the threshold power by $P_{\mathrm{in}}^{\mathrm{thresh}} = \hbar\Omega_0|\alpha_{0,\mathrm{in}}^{\mathrm{thresh}}|^2$.

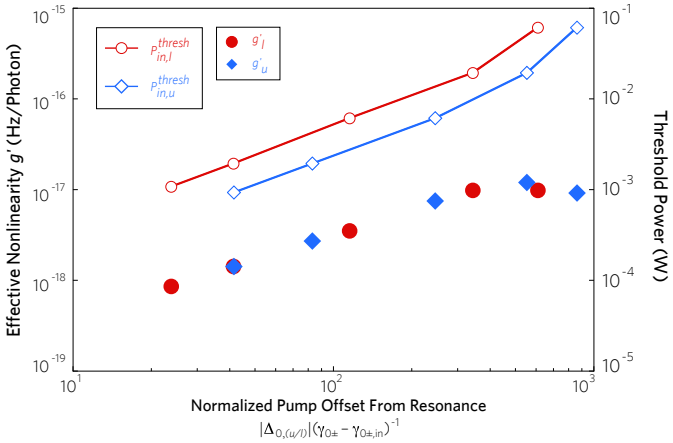

Fig. 5. Effective nonlinearity and threshold power as a function of the normalised detuning from resonance. The subscripts u and l refer respectively to the upper doublet of the $\mathrm{WGH}_{17,0,0}$ mode (for positive detuning), and lower doublet (for negative detuning). Here, g' ranges between 10^{-18} and 10^{-17}, and decreases as the pump tunes towards resonance, with FWM turning off between 20 and 40 unloaded half bandwidths (HBWs) from resonance. A maximum in g' occurs around 500 unloaded HBWs, with an associated inflection in the required $P_{\mathrm{in}}^{\mathrm{thresh}}$ to enable FWM.

Figure 5 shows the effective nonlinearity and threshold power as a function of normalised detuning from resonance, calculated using the parameters of our system.

In summary, we have demonstrated that a strong $\chi^{(3)}$ nonlinearity at microwave frequencies, arising from only a parts-per-billion concentration of paramagnetic ions, leads to degenerate four-wave mixing in a cryogenic sapphire resonator when pumped with only a single frequency. Long characteristic times on the order of several seconds were observed due to slow cross-relaxation and interaction with lattice ion nuclear spins, and broad tunability can be achieved by altering the pump frequency. Our system has the potential for application in a host of future quantum computing and metrology experiments where low microwave loss and strong nonlinearity is desirable, such as measurement of qubits in circuit QED setups, single quadrature amplification and squeezing, quantum-limited parametric amplification, or potential use in nanoscale magnetometry [38] with the benefit of having the necessary amplification and nonlinearity integrated within a single device.

III. Extremely High Q-Factor Quartz Bulk Acoustic Wave Resonators at Millikelvin Temperature

Low-loss, high frequency acoustic resonators cooled to millikelvin temperatures are a topic of great interest for application to hybrid quantum systems. When cooled to 20 mK, we have shown that resonant acoustic phonon modes in a Bulk Acoustic Wave (BAW) quartz resonator demonstrate exceptionally low loss (with Q-factors of order billions) at frequencies of 15.6 and 65.4 MHz, with a maximum $f.Q$ product of 7.8×10^{16} Hz [39]. Given this result, we have shown

that the Q-factor in such devices near the quantum ground state can be four orders of magnitude better than previously attained [39]. Such resonators possess the low losses crucial for electromagnetic cooling to the phonon ground state, and the possibility of long coherence and interaction times of a few seconds, allowing multiple quantum gate operations.

To achieve the operation of hybrid mechanical systems in their quantum ground state, it is vital to develop acoustic resonators with very low losses at temperatures approaching absolute zero. The frequencies accessible using mechanical systems are low, and thus a lower temperature is required (governed by $\hbar\omega > k_B T$) to reach the equilibrium ground state. The average number of thermal phonons should follow the Bose-Einstein distribution

$$n_{TH} \sim \frac{1}{e^{\frac{\hbar\omega}{k_B T}} - 1} \tag{8}$$

where $\hbar$ is the reduced Planck constant, and T and k_B are the temperature and Boltzmann's constant respectively. For example, at 10 mK a frequency of greater than 144 MHz is required to have $n_{TH} < 1$, which increases proportionally with temperature. Aside from conventional thermodynamic cooling, the ground state or Standard Quantum Limit could potentially be reached by exploiting an extremely low loss resonance, where the mode can be cold damped through feedback or a parametric processes. In the ideal case the ratio Q/T remains constant, where the acoustic Q-factor is reduced as the mode amplitude is then damped and electromagnetically cooled to a lower temperature. Alternatively, if the change in state of the resonance can be measured at a rate faster than the dissipation rate γ, the bath noise is filtered by the high-Q resonance, which is no longer in equilibrium with the bath. In such a case, the effective noise temperature is reduced so that a change in state of order one acoustic phonon could be measureable. The effective temperature, T_{eff}, is then related to the physical temperature, T, by $T_{eff} = T\tau\gamma/2$, where τ is the measurement time. With these techniques in mind, the development of cold, high frequency, ultra-low-loss acoustic resonators represents a crucial step in overcoming the challenge of maintaining long coherence times in systems occupying their quantum ground state.

In this work, we measure a quartz BAW resonator designed with non-contacting electrodes down to 18 mK, and show that the Q-factor continues to increase beyond 10^9, albeit with a smaller power law exponent. The resonator is a state-of-the-art resonator (SC-cut, BVA technology) designed for room temperature operation in its shear mode (5 MHz with a frequency-temperature turn-over point at 80 deg. C), a schematic of which is shown in Fig. 6. To allow the acoustic modes to be trapped between the electrodes at the centre of the resonator, isolating the mode from mechanical losses due to coupling to the support ring, the resonator is manufactured with a planoconvex shape. The longitudinal overtones are the most strongly trapped and thus exhibit particularly high quality factors. Here, we present measurements characterising

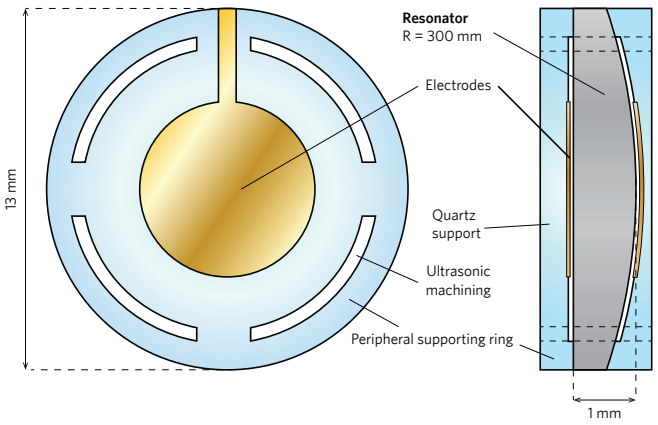

Fig. 6. Schematic of the quartz Bulk Acoustic Wave (BAW) resonator manufactured by BVA Industries with non-contacting electrodes. The radius of curvature of the resonator is 300 mm. Vibrations are trapped in the area of the resonator between the electrodes attached to the quartz support structure.

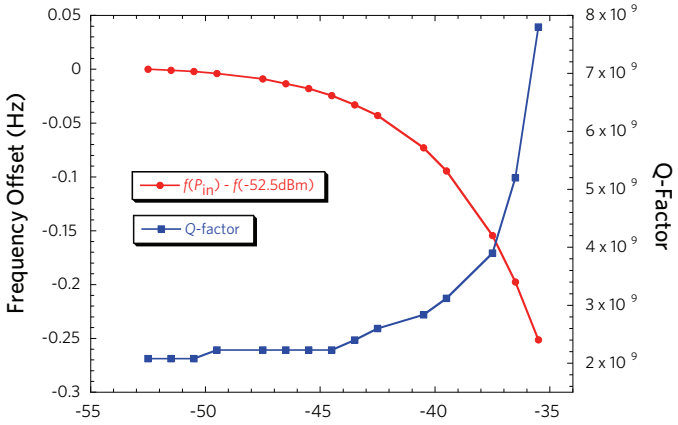

Fig. 7. Frequency offset versus input power, $f\,(P_{\text{in}})$, at 18 mK for the 5th overtone with respect to the frequency at -52.5 dBm, $f\,(-52.5)$ =15,597,316.3845 Hz

the 5th and 21st overtones with effective mode masses of order 5 and 0.7 milligram respectively (total resonator mass of 220 mg) at frequencies 15.6 and 65.4 MHz respectively, which exhibit Q-factors exceeding 10^9 corresponding to decay times of order tens of seconds.

Our experiment was cooled using a cryogen-free Dilution Refrigerator (DR) system, with the quartz resonator thermally connected via an oxygen-free copper mount to the mixing chamber of the DR and cooled to ∼20 mK. To measure the intrinsic Q-factor of the quartz BAW resonators, a passive method was employed using an Agilent E5061B-005 Impedance Analyzer with a frequency resolution of 0.02 mHz. For BAW devices at low temperatures, this measurement method is preferable to traditional bridge methods because of the significant temperature induced changes in the resonator that result in impedance mismatching of the usual π-network. A distinctive feature of the impedance analyzer method is a need for compensation of the long connecting cables. For

this purpose, three calibration references (an open circuit, short circuit and a 50 Ω standard) are placed close to the quartz resonator at the end of nominally identical cables. The purpose of the calibration is to remove cable effects from measurement results. Once the calibration is performed under cryogenic conditions for a given frequency range, amplitude, number of points and sweep rate, the magnitude and phase of the resonator motional branch impedance are measured in the vicinity of the resonance. The data is then approximated by a neural network model, and the resonator parameters are obtained through a complex admittance representation of the approximated data.

As at 4K [7], the longitudinal mode exhibits superior Q-factors to both slow and fast shear modes. For example the 5th overtone of the fast shear mode at 9.2 MHz exhibits a Q-factor of 2.2×10^8, while the 5th overtone of the slow shear mode exhibits a Q-factor of 3.1×10^8. Many overtones and anharmonics were measured, with the highest Q-factor observed in the 5th overtone longitudinal mode at 15.6 MHz. At high input powers, the resonator undergoes a frequency shift and a significant increase in Q-factor, as shown in Fig. 7 . No distortion of the line shapes was seen in this power range from -52.5 to -35 dBm. At higher powers still, close to 0 dBm, nonlinear effects typical in BAW quartz resonators were seen. The Q-factor at -35 dBm rose to more than 8 billion. This effect is due to a parametric effect that comes from the nonlinearity of a shunt capacitance formed by the resonator electrodes, which are separated by a quartz disk and two gaps. We observe a strong dependence on the excitation level, which has been never been observed at room or liquid helium temperatures in these resonators. Harmonic balance simulations of the corresponding lumped resonator with a nonlinear shunt capacitance model the effect very well, and show an almost exponential increase of the Q-factor with a corresponding reduction in frequency.

At powers below -50 dBm, the Q-factor remained constant. At this power level, we measured both the 5$^{\text{th}}$ and 21$^{\text{st}}$ overtones as a function of temperature. Figure 8 shows the frequency shift and Q-factor below 2 K in temperature. In this regime of such high Q-factor, the loss introduced by the support structure is likely to become important and should be considered. It is also interesting to note that for both modes, the frequency of the overtones exhibit a turning point just below 1 K. At this temperature with such high Q-factor and the annulment of the frequency-temperature dependence, a frequency-stable oscillator could be built, which is a point of future investigation. At lower temperatures there are multiple annulment points and no clear dependence of Q-factor, although both overtones have peak values between 100 and 300 mK. We also note that in various temperature regions, both overtones exhibit a $T^{-0.36}$.

With such extraordinary Q-factors at mK temperatures, quartz BAW resonators are eminently suitable for electromagnetic cooling techniques such as parametric

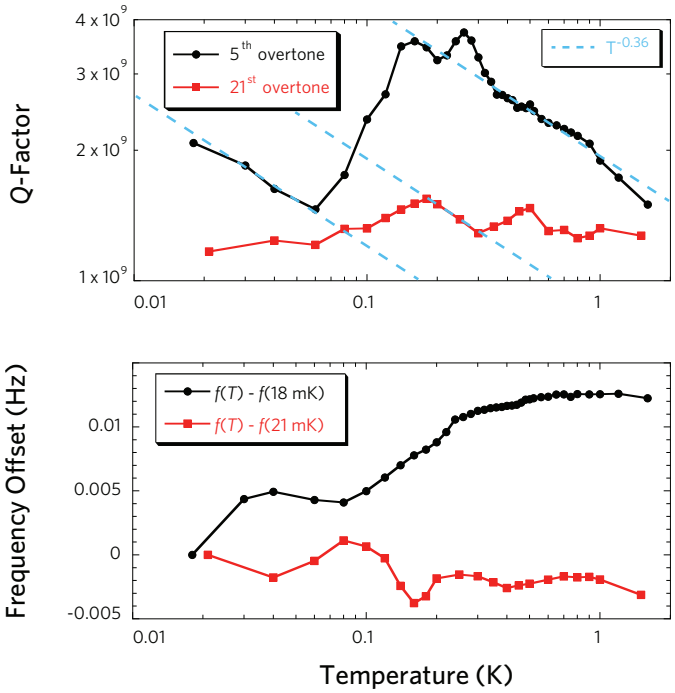

Fig. 8. Q-factor and frequency offset versus temperature, $f(T)$, for the 5^{th} and 21^{st} overtones with respect to the frequency at 18 and 21 mK respectively, at -52.5 dBm input power. Dashed lines show a $T^{-0.36}$ dependence for both overtones in various temperature regions.

cold damping or feedback cooling. We anticipate that these techniques could be used to prepare the resonator in an ultra-cold quantum state, potentially allowing the resonator to enter the acoustic phonon ground state while maintaining a damped Q-factor of more than four orders of magnitude bigger than previously achieved (as suggested in [39]), which corresponds to acoustic decay times of order a few seconds. Also, the resonator exhibits strong electromechanical coupling to mechanical modes through the piezoelectric effect at these temperatures, meaning that a hybrid quantum system is readily achievable. Thus, using BAW technology, single phonon quantum control could be achievable allowing coherence times significantly longer than previously attained, which could allow many more coherent gate operations before coherence is lost with wide ranging implications for quantum information, computing, and control.

ACKNOWLEDGMENT

This work was funded by Australian Research Council grant numbers FL0992016 and CE11E0082. Collaboration between FEMTO-ST and UWA was also supported by ISL grant number FR100013.

REFERENCES

[1] Locke C. R., Ivanov E. N., Hartnett J. G., Stanwix P. L., Tobar M. E., "Invited article: Design techniques and noise properties of ultrastable cryogenically cooled sapphire-dielectric resonator oscillators," *Rev. Sci. Instrum.* **79**(8), 051301 (2008).

[2] Tobar, M. E., and Blair, D. G. "Phase noise analysis of the sapphire loaded superconducting niobium cavity oscillator, " *IEEE Trans. on MTT* **42**(2), 344-347 (1994).

[3] Benmessai, K., Creedon, D. L., Le Floch, J-M., Tobar, M. E., et al., "Controlling the frequency-temperature sensitivity of a cryogenic sapphire maser frequency standard by manipulating Fe^{3+} spins in the sapphire lattice," *Physical Review B* **85**, 075122 (2012).

[4] Bourgeois, P. Y., Bazin, N., Kersalé, Y., et al., "Maser oscillation in a whispering-gallery-mode microwave resonator," *Applied Physics Letters* **87**, 224104 (2005).

[5] Benmessai, K., Bourgeois, P.-Y., Kersalé, Y., et al., "Frequency instability measurement system of cryogenic maser oscillator," *Electronics Letters* **43**, 1436 (2007).

[6] Benmessai, K., Creedon, D. L., Tobar, M. E., et al., "Measurement of the fundamental thermal noise limit in a cryogenic sapphire frequency standard using bimodal maser oscillations," *Physical Review Letters* **100**, 233901 (2008).

[7] Galliou, S., Imbaud, J, Goryachev, M, et al., "Losses in high quality quartz crystal resonators at cryogenic temperatures," *Applied Physics Letters* **98**, 091911 (2011).

[8] Maiman, T. H., "Stimulated optical radiation in Ruby," *Nature* **187**, 493–494 (1960).

[9] Franken, P. A., Hill, A. E., Peters, C. W., and Weinreich, G., "Generation of optical harmonics," *Physical Review Letters* **7**(4), 118–119 (1961).

[10] Terhune, R. W., Maker, P. D., and Savage, C. M., "Optical harmonic generation in Calcite," *Physical Review Letters* **8**(10), 404–406 (1962).

[11] Carmon, T. and Vahala, K., "Visible continuous emission from a silica microphotonic device by third-harmonic generation," *Nature Physics* **3**, 430–435 (2007).

[12] Bass, M., Franken, P. A., Hill, A. E., Peters, C. W., and Weinreich, G., "Optical mixing," *Physical Review Letters* **8**(1), 18 (1962).

[13] Wang, C. C. and Racette, G. W., "Measurement of parametric gain accompanying optical difference frequency generation," *Applied Physics Letters* **6**(8), 169–171 (1965).

[14] Kippenberg, T., Spillane, S., and Vahala, K., "Kerr-nonlinearity optical parametric oscillation in an ultrahigh-Q toroid microcavity," *Physical Review Letters* **93**(8), 0839041–0839044 (2004).

[15] Spillane, S. M., Kippenberg, T. J., and Vahala, K. J., "Ultralow-threshold Raman laser using a spherical dielectric microcavity," *Nature* **415**, 621–623 (2002).

[16] Kaiser, W. and Garrett, C. G. B., "Two-photon excitation in CaF_2:Eu^{2+}," *Phys. Rev. Lett.* **7**(6), 229–231 (1961).

[17] Kippenberg, T., Holzwarth, R., and Diddams, S., "Microresonator-based optical frequency combs," *Science* **332**, 555–559 (2011).

[18] Del'Haye, P., Arcizet, O., Gorodetsky, M., Holzwarth, R., and Kippenberg, T., "Frequency comb assisted diode laser spectroscopy for measurement of microcavity dispersion," *Nature Photonics* **3**, 529–533 (2009).

[19] Del'Haye, P., Schliesser, A., Arcizet, O., Wilken, T., Holzwarth, R., and Kippenberg, T., "Optical frequency comb generation from a monolithic microresonator," *Nature* **450**, 1214–1217 (2007).

[20] O'Brien, J. L., "Optical quantum computing," *Science* **318**(5856), 1567–1570 (2007).

[21] Laflamme, C. and Clerk, A. A., "Quantum-limited amplification with a nonlinear cavity detector," *Physical Review A* **83**, 033803 (2011).

[22] Castellanos-Beltran, M. A., Irwin, K. D., Hilton, G. C., Vale, L. R., and Lehnert, K. W., "Amplification and squeezing of quantum noise with a tunable Josephson metamaterial," *Nature Physics* **4**(12), 929–931 (2008).

[23] Lupaşcu, A., Driessen, E. F. C., Roschier, L., Harmans, C. J. P. M., and Mooij, J. E., "High-contrast dispersive readout of a superconducting flux qubit using a nonlinear resonator," *Physical Review Letters* **96**(12), 127003 (2006).

[24] Ramirez, D., Rodriguez, A., Hashemi, H., Joannopoulos, J., Soljačić, M., and Johnson, S., "Degenerate four-wave mixing in triple resonant Kerr cavities," *Physical Review A* **83**, 033834 (2011).

[25] Kubo, Y., Ong, F. R., Bertet, P., Vion, D., Jacques, V., Zheng, D., Dréau, A., Roch, J.-F., Auffeves, A., Jelezko, F., Wrachtrup, J., Barthe, M. F., Bergonzo, P., and Esteve, D., "Strong coupling of a spin ensemble to a superconducting resonator," *Physical Review Letters* **105**, 140502 (2010).

[26] Schuster, D. I., Sears, A. P., Ginossar, E., DiCarlo, L., Frunzio, L., Morton, J. J. L., Wu, H., Briggs, G. A. D., Buckley, B. B., Awschalom, D. D., and Schoelkopf, R. J., "High-cooperativity coupling of electron-spin ensembles to superconducting cavities," *Physical Review Letters* **105**, 140501 (2010).

[27] Wu, Hua and. George, R. E., Wesenberg, J. H., Mølmer, K., Schuster, D. I., Schoelkopf, R. J., Itoh, K. M., Ardavan, A., Morton, J. J. L., and Briggs, G. A. D. D., "Storage of multiple coherent microwave excitations in an electron spin ensemble," *Physical Review Letters* **105**, 140503 (Sep 2010).

[28] Creedon, D. L., Benmessai, K., Bowen, W. P., and Tobar, M. E., A. D. D., "Four-wave mixing from Fe^{3+} spins in sapphire," *Physical Review Letters* **108**, 093902 (Sep 2012).

[29] Creedon, D. L., Reshitnyk, Y., Farr, W., Martinis, J. M., Duty, T. L., and Tobar, M. E., "High Q-factor sapphire whispering gallery mode microwave resonator at single photon energies and milli-Kelvin temperatures," *Applied Physics Letters* **98**(22), 222903 (2011).

[30] Benmessai, K., Bourgeois, P. Y., Tobar, M. E., et al., "Amplification process in a high-Q cryogenic whispering gallery mode sapphire Fe^{3+} maser," *Measurement Science & Technology* **21**, 025902 (2010).

[31] Benmessai, K., Tobar, M. E., Bazin, N., et al., "Creating traveling waves from standing waves from the gyrotropic paramagnetic properties of Fe^{3+} ions in a high-q whispering gallery mode sapphire resonator," *Physical Review B* **79**, 174432 (2009).

[32] Creedon, D., Benmessai, K., Tobar, M., et al., "High-power solid-state sapphire whispering gallery mode maser," *IEEE Transactions on Ultrasonics, Ferroelectrics, and Frequency Control* **57**(3), 641–646 (2010).

[33] Symmons, H. and Bogle, G., "On the exactness of the spin-Hamiltonian description of Fe^{3+} in sapphire," *Proceedings of the Physical Society (London)* **79**(3), 468–472 (1962).

[34] Freitas, J., Costa e Silva, M., Lüthi, S., and Gomes, A., "Raman enhanced parametric amplifier based S–C band wavelength converter: Experiment and simulations," *Optics Communications* **255**(4-6), 314 – 318 (2005).

[35] Dahan, D. and Eisenstein, G., "Tunable all optical delay via slow and fast light propagation in a Raman assisted fiber optical parametric amplifier: a route to all optical buffering," *Optics Express* **13**(16), 6234–6249 (2005).

[36] Makhov, G., Terhune, R., Lambe, J., and Cross, L., "Memorandum of Project Michigan: Electron-nuclear interaction in Ruby and its effect on the Ruby maser," tech. rep., Willow Run Laboratories, The University of Michigan (July 1960).

[37] McRae, T. G. and Bowen, W. P., "Time-delayed entanglement from coherently coupled nonlinear cavities," *Physical Review A* **80**, 010303(R) (2009).

[38] Hatridge, M., Vijay, R., Slichter, D. H., Clarke, J., and Siddiqi, I., "Dispersive magnetometry with a quantum limited SQUID parametric amplifier," *Physical Review B* **83**(13), 134501 (2011).

[39] Goryachev, M., Creedon,D. L., Ivanov, E. N., Galliou, S., Bourquin, R., Tobar, M. E., "Extremely low-loss acoustic phonons in a quartz bulk acoustic wave resonator at millikelvin temperature," arXiv:1202.4556 (2012).

Cryogenic Quartz Frequency Sources: Problems and Perspectives

Maxim Goryachev, Philippe Abbé and Serge Galliou
Frequency and Time Department
FEMTO-ST Institute, UMR CNRS 6174
26 Chemin de l'Epitaphe, 25000 Besançon, France
Email: maxim.goryachev@femto-st.fr

***Abstract*—This work presents the results of investigation of frequency sources based on cryogenic BAW quartz resonators. Two systems are considered: a passive feedback frequency stabilisation system and a fully cryogenic oscillator. The first approach improves the long-term frequency stability implementing a minimal number of electronic components at liquid helium temperatures. The second one is a BAW oscillator designed for 4K temperatures based on field-effect and bipolar transistors.**

I. Introduction

Nowadays, in the category of low-volume frequency sources, the best short-term frequency stability performance is still achieved with quartz crystal oscillators. But it is generally believed that this family of frequency sources is almost in saturation and could not lead to considerable stability improvement with reasonable efforts in the future. So, are further investigations in the field of bulk acoustic wave (BAW) sources worth trying or will they be squeezed out by MEMS? To figure out the future potential of the BAW systems, their cryogenic implementation has been proposed. Indeed, quality factors of over than 400×10^6 for 68 MHz at 4K have been reported for these devices [1], [2]. Such an increase in the resonator quality factor potentially leads to a frequency stability improvement of greater than 100. Although source frequency stability could be limited by other factors, such as environmental limitations.

The work starts with a short description of the cryocooler system with a discussion of corresponding environmental instabilities. Then, the resonator properties at liquid helium temperatures are briefly summarized. Third, the feedback passive reference system is presented. The frequency stability results are discussed. And, finally, the behavior of several types of fully cryogenic oscillators is demonstrated and explained.

II. Cryogenic System

The cryogenic environment for devices under test is created with a two-stage pulse-tube cryocooler. The cryocooler is shielded with two protection screens: a vacuum chamber and an anti-radiation shield. The air pressure of about 10^{-7} mBar is created inside the chamber which is at room temperature. Both primary and secondary pumps are cut off from the chamber during the whole measurement time. The anti-radiation shield is attached to the first cryocooler stage and its temperature is about 50K.

The cryocooler second stage temperature can go down to almost 3K in the unloaded configuration. The thermal losses are mainly introduced with connecting cables needed for measurements and environmental control as well as the DUT heat dissipation. Nominally, the cryocooler absorbs up to 1 W at this stage at 4K.

Two main environmental sources of instabilities for the DUT are thermal instabilities and vibrations. The detailed discussions of these instabilities could be found in [3], [4]. The temperature fluctuations are reduced using a passive filter (introduced between the second stage and the oxygen-free copper block with the DUT) and active temperature control (implemented with a 332 Temperature Controller from Lake Shore, a CERNOX sensor and a 20 Ohms heating resistor). The PSD of temperature fluctuations of the DUT is an almost white noise in the $10^{-4} - 10^{1}$ frequency range with clear spurious frequencies of 1.7 Hz and its harmonics.

Another type of cryocooler environmental disturbances is vibration. The measurement suggests that the DUT is subject to f^{-1} instabilities in the frequency range of $10^{-2} - 10^{1}$ Hz due to external vibration in the vertical axis. It has to be noted that no vibration compensation system is installed for the presented measurements. Instead the proper installation angle between device and cryocooler axes is chosen as suggested in [3].

III. Summary of Quartz Resonator Characteristics at Liquid Helium Temperatures

In past decades, quartz crystal resonators were tested at very low temperatures [5]–[10]. Although some increase in device quality factors has been reported, these studies remain to be unsystematic observations. In addition, the authors used some obsolete approaches to cryogenic experiments based on cryostat approach which imposes several limitations on practical utilisation of DUTs. Recently, the investigations have been resumed based on modern cryocooler techniques (see previous section). In these experiments 5 or 10 MHz BAW SC-cut [11] and LD-cut BVA (Boîtier à Vieillissement Amélioré) [12] as well as some LGT resonators have been investigated in the temperature range $3.5 - 20$K [1]–[4], [13], [14].

The useful for this work results are as follows:

- quality factors of shear (longitudinal respectively) mode increase as T^{-4} (close to T^{-6} respectively) in the $5-20$K

range and exhibit very slight increase in the $3.5-5$K range;
- the highest measured Q-values among 5th overtones of the three modes are 325×10^6 for the A-mode, 50.5×10^6 for the B-mode, 1.99×10^6 for the C-mode;
- the characterized modes does not exhibit any turning points in their frequency-temperature characteristics in the temperature range $3.5-20$K with a minimal sensitivity of 2×10^{-9} K^{-1} for the A-mode, 3×10^{-9} K^{-1} for the B-mode and 1×10^{-8} K^{-1} for the C-mode, obtained at the lowest temperatures;
- A-modes of SC-cut resonators demonstrate very high power dependence leading to considerable distortion of resonance shapes for dissipating powers greater than 1 μW;
- quartz crystal resonators demonstrate rather high phase noise which comes from acceleration and temperature instabilities.

For more details, please, see the references given above.

IV. Feedback Frequency Reference System

This section present the main results of investigation of frequency stabilisation system based on cryogenic quartz resonator. This is a supersystem approach, when the commercial Voltage Controlled Oscillator (VCO) and cryogenic passive resonator are used as building blocks for a higher level system. It is this higher level system that leads to stability improvement. The advantage of this approach is that it requires a minimal number of electronic components at the cold level and has no problems related to oscillation conditions, mode selection, etc.

The block diagram of the investigated system is shown in Fig. 1. The system works as follows. The frequency of the output carrier signal from the VCO is multiplied by a commercial frequency synthesiser to one of the crystal resonance frequencies. Then, this signal is split into two paths, one of which is fed into a quartz crystal π-network and another one into a $\frac{\pi}{2}$ phase shifter with identical cables. After that, a double balanced mixer is used to extract a phase error information stored in signal frequency difference. The DC voltage from the mixer output is filtered, amplified and used for correction of the VCO frequency. In fact, the $\pi-network$, phase shifter and the mixer form a frequency discriminator converting the error stored in the phase into voltage. The efficiency of the transformation depends on the crystal loaded Q-factor and resonator own noise. It is shown theoretically, that the long-term frequency stability of the system in terms of the Allan deviation is proportional to the loaded Q. In the same time, short-term stability is defined by the VCO.

Results of the closed-loop system locked on the following resonance modes are shown in Fig. 2: for the 5th overtone of the A-mode (curve(2)), the 3rd overtone of the A-mode (curve(3)) and the 5th overtone of the B-mode (curve(4)). Results are compared with the stand-alone voltage controlled oscillator (curve(1)) used as a signal source in the loop. All

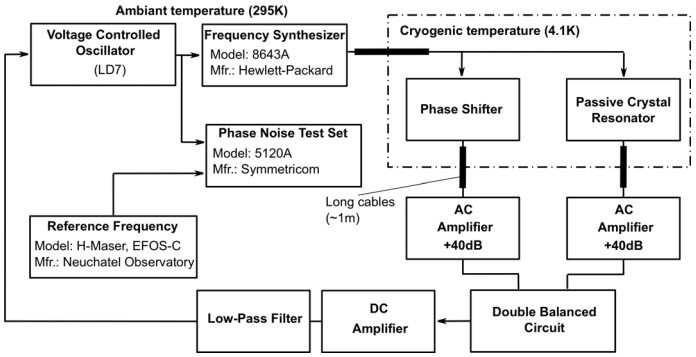

Fig. 1. Block diagram of the closed loop frequency stabilization system based on a cryogenic quartz crystal resonator

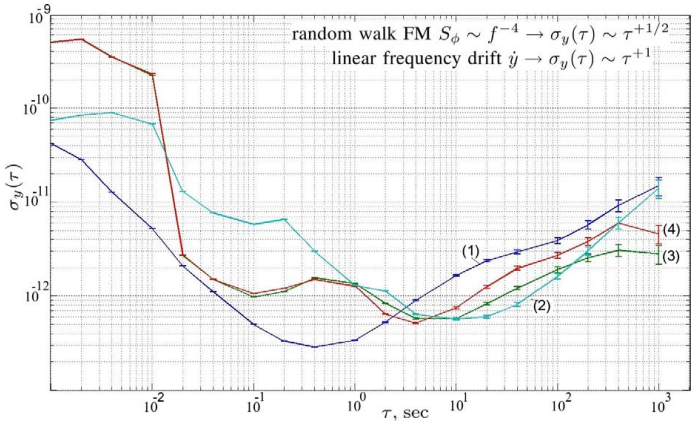

Fig. 2. Allan deviation of the closed-loop frequency stabilization system locked at (2) - the 5th overtone of the A-mode, (3) - the 3rd overtone of the A-mode, (4) - the 5th overtone of the B-mode and a stand-alone oscillator (1)

three measurements show degradation of the frequency stability for small averaging times ($\tau < 0.1$ s) and improvement for large averaging times ($\tau > 10$ s). Also, in the latter region, modes 3A and 5B demonstrate the same slope as the stand-alone oscillator, i.e. $\tau^{+1/2}$. This slope of the Allan deviation curve corresponds to the f^{-4} phase noise (random-walk frequency modulation). As opposed, the 5th overtone of the A-mode shows τ^{+1} law, which is a deterministic linear frequency drift. The frequency stability deterioration for small values of τ is due to the additional noise of the closed loop electronic components as well as the short-term cryogenic resonator phase noise. The main difference between two cases is that the resonator working at the 5th overtone of the A-mode is in a nonlinear regime due to the amplitude-frequency effect (the Q-factor of this mode is much higher).

Stability measurements shown in Fig. 3 are for the closed-loop system locked on the 5th overtone of the A-mode. In these measurements, the frequency stability has been examined as a function of the amount of time of permanent operation of the resonator inside the cryocooler. So, Fig. 3 presents the Allan deviation measured during the first 12 hours (curve (2)) and after at least 60 hours of permanent operation (curve (3)). Both results can be compared with the stand-alone oscillator

stability (curve (1)). As expected, the closed loop degrades the system frequency stability for small averaging times τ, but improves it for large averaging times. In the same time, for large τ, curve (3) exhibits the same slope as the stand-alone oscillator, i.e. $\tau^{+1/2}$, which corresponds to the f^{-2} phase noise (phase random-walk). On the other hand, after just 12 hours of operation, the system shows a τ^{+1} law, that is a deterministic linear frequency drift. This drift is due to a rapid aging of a resonator in the first hours after the cooling process which changes its mechanical properties.

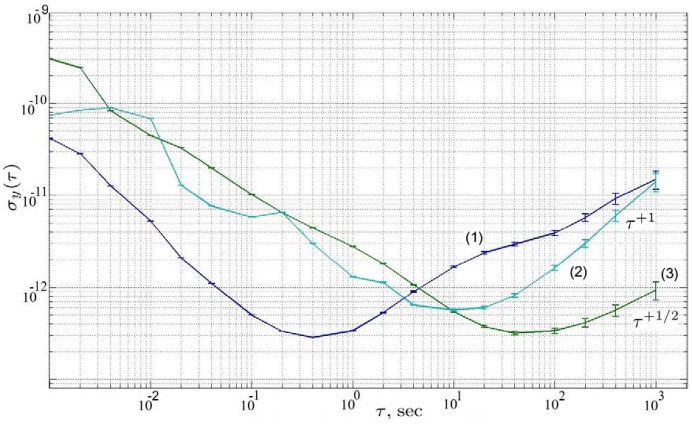

Fig. 3. Allan deviation of the closed-loop frequency stabilization system locked on the 5th overtone of the A-mode, and measured (2) at first 12 hours of resonator operation inside the cryocooler, (3) after at least 60 hours of resonator permanent operation in cryogenic environment and compared with the stand-alone oscillator (1), i.e. the VCO

The practical implementation of the loop is related with several problems. Briefly speaking, the design requires a compromise between requirements to the loaded quality factor, signal-to-noise ratio and nonlinearities. Since these requirements are contradictory and SC-devices are very nonlinear, the system operation is achieved by significant reduction of the loaded Q-factor. A possible solution is LD-cut resonators, devices that are specially designed for exhibiting low nonlinearities. Though the latter crystals have a lower value of unloaded Q-factor, a higher active resistance and a lower sensitivity to the dissipation power (see [14]), allow to design a cryogenic part of the feedback system with a higher loaded quality factor.

Schematics of the cryogenic part of the system is the same as in the previous case. The loaded quality factor for the implemented system achieved 34.6% of is unloaded value. This corresponds to $Q_L = 33.6 \cdot 10^6$. The resulting frequency stability in terms of the Allan deviation is shown in Fig. 4. The corresponding phase noise power spectral densities are presented in Fig. 5. The frequency stability improvement is achieved for the Fourier frequencies below 4 Hz. A PSD increase between 4 Hz and 1 kHz is due to synthesiser phase noise. For higher Fourier frequencies the stability is limited by the VCO.

The tested feedback stabilization systems achieves frequency stability of $4 \cdot 10^{-13}$ at 100 seconds and has stability better than 10^{-12} between 1 and 2000 seconds. It is concluded

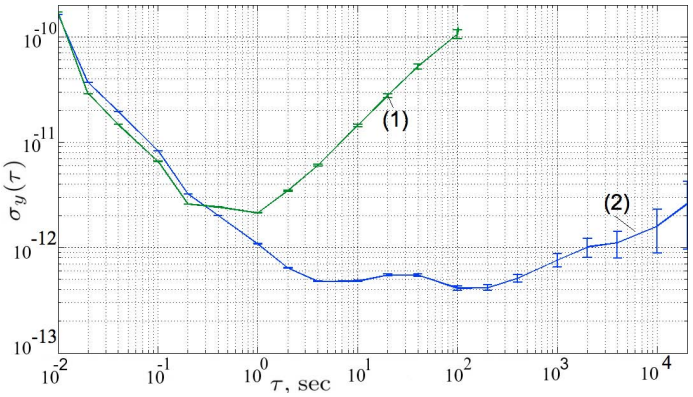

Fig. 4. Allan deviation of the VCO (1) and the closed-loop frequency stabilization system locked on the 5th overtone of the A-mode of a LD-cut resonator (2)

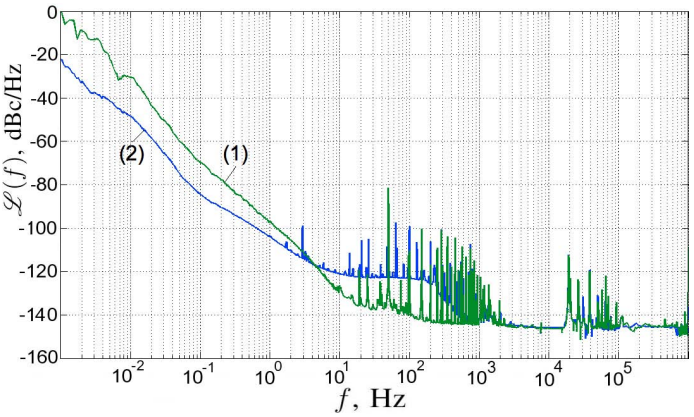

Fig. 5. Phase noise PSD for the VCO (1) and the closed-loop frequency stabilization system locked on the A-mode of 5th overtone of the LD-cut resonator (2)

that the long-term frequency is limited by relatively high temperature sensitivity and second stage temperature fluctuations that bypass the thermal filter through the connecting cables.

The open loop variant of the considered system allows to measure the quartz resonator phase noise and identify its sources [3].

V. Cryogenic BAW Oscillators

Another approach to source frequency stability improvement is based on subsystem consideration, when the better system performance is achieved by optimising oscillator elements, topology, etc. The advantage of cryogenic oscillator is at higher values of the cryogenic resonator quality factor provides narrower resonator bandwidth, which leads to a better close-to-carrier noise performance. However, such unusually high values of quality factors lead to severe problems with oscillator modeling and optimization which are important stages for cryogenic oscillator design. Indeed, since any modification of the device require the warm up of the cryogenerator and a consequent cooling (at least 24 hours in total), the behaviour of the device should not be studied by trial and error. Instead, a careful simulation procedure is needed. The solution is pro-

posed in [15]. This problem is related to another one. The oscillator design requires fulfilment of oscillation (Barkhausen) conditions for a particular mode. At room temperature this is done manually for each sample with a very precise choice of components for a selective filtering. For obvious reasons, this is not possible at liquid helium temperatures. The second major problem of this approach is that the fully cryogenic oscillator requires that all electronic components should work at 4 K. That makes extremely difficult their choice, characterisation and simulation. So, the development process of cryogenic electronic system (and oscillators in particular) is a very time-consuming and exhausting process comparing to the room temperature situation. Moreover, cryogenic devices are much less reliable, their behavior is much less predictable, and the environmental influences are much less known.

Another feature of the cryogenic oscillator development is the necessity to design a corresponding thermo-mechanical structure. This requirement is a consequence of the many issues concerning resonator and transistor temperatures, dissipated power, temperature instabilities etc. For all prototypes presented here, an oxygen-free copper is used as a holder. The resonators are placed vertically inside the holder with a direct thermal and mechanical contact. The electronic components are soldered on the insulator surface mounted on the holder.

The first oscillator prototype was design based on MOSFET active device. The corresponding schematic diagram is shown in Fig. 6. This is an one-loop Collpits oscillator with one MOSFET transistor in an oscillating loop and another one in the output buffer stage (source-follower). Both transistors are biased separately, in order to achieve the best performance (since all samples have unique properties). In fact, bias voltages are the only means for oscillator adjustment at cryogenic temperatures.

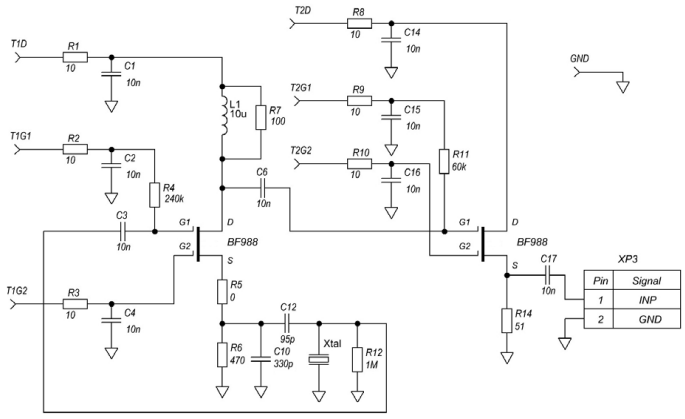

Fig. 6. Schematic diagram of a cryogenic crystal oscillator based on a MOSFET transistor

The experiments show that the oscillator could be excited on different crystal modes depending on the voltage biases. These modes are 5.489680 MHz (the 3rd overtone of the B mode), 4.992987 MHz (the 3rd overtone of the C mode), 8.4430359 MHz (probably, an anharmonic mode), 11.853208 MHz (probably an anharmonic mode). Unfortunately, no A-mode overtone could be excited. The best frequency stability performance is measured for the 8.4430359 MHz mode (see Fig. 7).

Fig. 7(b) shows that the closest to the carrier slope of the phase noise PSD is less (about f^{-2}) than the second one from the carrier (f^{-4}). This phenomenon could be explained theoretically by introducing the amplitude-to-phase noise conversion into the oscillator phase noise model [4].

Another type of oscillator is built with a SiGe heterojunction bipolar transistors. The measurement and simulations of these devices are presented in [16]. The schematics of this device is also a one-transistor Colpitts oscillator with a buffer output stage and external separated bias. This oscillator has been excited on the 3rd overtone of the C mode (4.992984 MHz) and the 3rd overtone of the B mode (5.489793 MHz). The corresponding frequenty stability measurement results are presented in Fig. 8.

The oscillator development for liquid-helium temperatures is a very time consuming task. Despite the rigorous models of electronic components and sophisticated analysis methods and, the actual behavior of cryogenic oscillators leaves many unpredictable phenomena. Nevertheless, it seems that for excited modes, the practical frequency stability limits are achieved for the MOSFET-based oscillator (about $2 \cdot 10^{-12}$ between 1 and 1000 seconds). In addition, it has to be noted that oscillators based on LD-cut resonators exhibits much worse frequency stability.

VI. Conclusion

The design of frequency sources based on cryogenic quartz resonators is associated with several problems. These problems are clearly stated in the previous sections. The main conclusion is that these problems and limitations do not allow to design ultra-stable frequency sources such as predicted. Indeed, without a turning point it is impossible to achieve a sufficient temperature stability of a frequency source system. And, considerable nonlinear effects suggest to work with lower signal levels which worsen the signal-to-noise ratio. These problems are aggravated by the instabilities of the cryogenic environment. Nevertheless, some ways for further developments could be proposed:

- device structure optimization can further increase resonator quality factor down to the limits of the material losses;
- investigation at milikelvin temperatures showed several turn-over points in herms of the frequency-temperature sensitivity, as well as considerable increase of the Q-factor;
- design of a new optimized crystal cut may provide a turning point in the temperature-frequency characteristic at the liquid helium temperatures;
- optimization of LD-cut resonators is a probable solution to the problem of high nonlinear effects, since this is a special cut designed for this purpose at room temperatures;

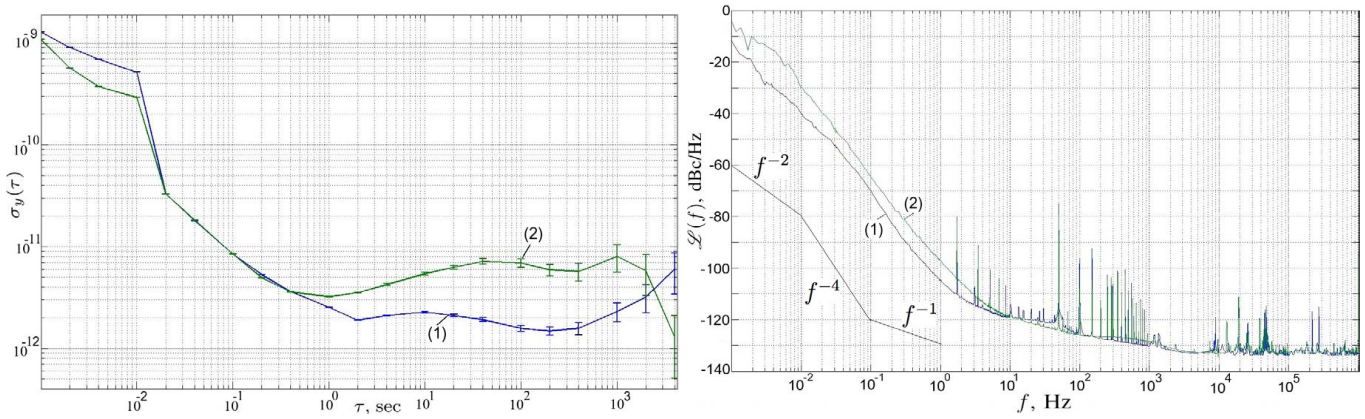

(a) Allan deviation (b) Phase noise PSD

Fig. 7. MOSFET-based liquid helium oscillator stability measurement results: improved ref. X1_A7 8.4430359 MHz and ref. X3_A8 8.443156 MHz

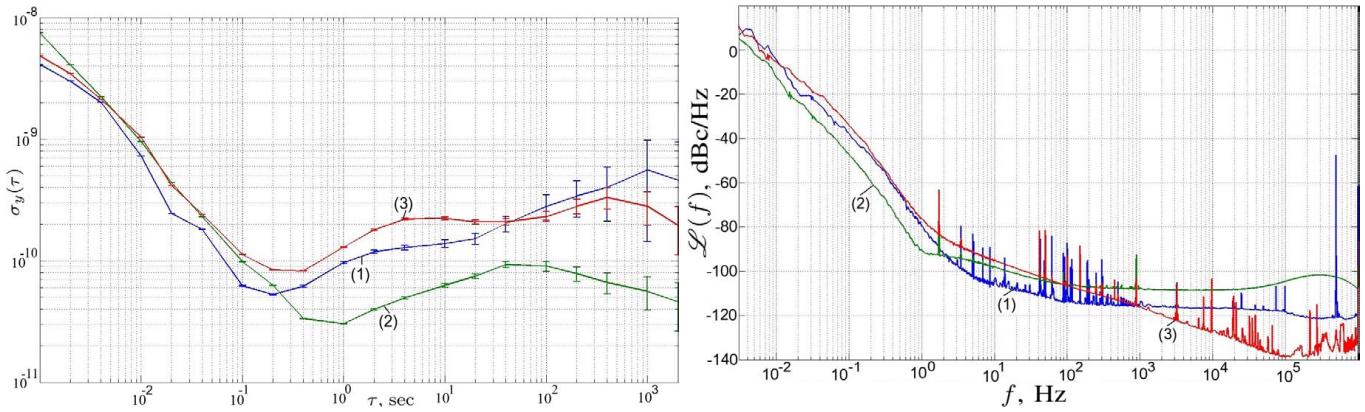

(a) Allan deviation (b) Phase noise PSD

Fig. 8. HBT-based liquid helium oscillator stability measurement results for different voltage biases

- DUT environment improvements (active and passive temperature stabilization systems as well as active vibration compensation) are needed to ensure better results;
- further investigations in cryogenic SiGe HBTs (probably, another package or on-wafer devices) may help to find more reliable devices of this kind;
- further improvement of simulation and optimization methods for liquid-helium temperature.

ACKNOWLEDGMENT

This work is supported by Conseil Régional de Franche-Comté (Convention No. 2008C_16215). The authors wish to thank the council for its grant and financial support as well as the staff of the Time and Frequency Department of FEMTO-ST Institute, Besançon, France for the help and fruitful discussions.

REFERENCES

[1] S. Galliou, J. Imbaud, M. Goryachev, R. Bourquin and Ph. Abbé, "Losses in high quality quartz crystal resonators at cryogenic temperatures," *Appl. Phys. Lett.*, vol. 90, 091911, 2011.

[2] M. Goryachev, S. Galliou, J. Imbaud, R. Bourquin, B. Dulmet and P. Abbé, "Recent investigations on BAW resonators at cryogenic temperatures," *IFCS-EFTF Joint Symp.*, San Francisco, 2011.

[3] M. Goryachev, S. Galliou, Ph. Abbé, P.-Y. Bourgeois, S. Grop and B. Dubois, "Quartz resonator instabilities under cryogenic conditions," *IEEE Trans. Ultrason., Ferroelect., Freq. Contr.*, vol. 59, no. 1, pp. 21-29, 2012.

[4] M. Goryachev, S. Galliou, J. Imbaud and Ph. Abbé, "Advances in development of liquid helium BAW oscillators," *IEEE Trans. Ultrason., Ferroelect., Freq. Contr.*, under review.

[5] N. Smagin, "Quartz crystal resonators with quality factors of about $120 \cdot 10^6$ at 2K," *Izmeritel Tekh. SSSR*, no. 9, 1960.

[6] G. Mossuz, "Study and achievement of a quartz crystal oscillator at very low temperature," *UFC PhD Thesis*, July 1975.

[7] G. Robichon, J. Groslambert, J.J. Gagnepain, "Frequency stability of quartz crystal at very low temperatures: preliminary results," in *38th Annual Freq. Contr. Symp.*, 1984, pp. 201-205.

[8] A. El Habti, "Study of resonators and oscillators at very low temperatures," *UFC PhD Thesis*, Jan. 1993.

[9] J. J. Suter, "Acoustic loss phenomena in alpha quartz resonators over the $1.4 - 77$K temperature range," *J. appl. Phys.*, vol. 63, no. 11, pp. 5594-5595, June 1988.

[10] A. El Habti, F. Bastien, "Low temperature limitation on the quality factor of quartz resonators," *IEEE Trans. Ultrason., Ferroelect., Freq. Contr.*, vol. 41, no. 2, pp. 250-255, 1994.

[11] E. P. Eernisse, "Quartz Resonator Frequency Shifts Arising from Electrode Stress," *Proc. 29th Ann. on Freq. Contr. Symp.*, Fort Monmouth, NJ, pp. 1-4, 1975.

[12] R. J. Besson, "A new electrodeless resonator design," *Proc. 31th Ann. on Freq. Contr. Symp.*, Fort Monmouth, NJ, pp. 147-152, 1977.

[13] S. Galliou, J. Imbaud, R. Bourquin, N. Bazin, P. Abbé, "Outstanding Quality Factors of Bulk Acoustic Wave Resonators at Cryogenic Temperature," in *Proc. EFTF 2008*, Toulouse, France, April 2008.

[14] M. Goryachev, *Cryogenic Bulk Acoustic Wave Resonators and Oscillators*, LAP Lambert Academic Publishing GmbH, 2012.
[15] M. Goryachev, S. Galliou and Ph. Abbé, Oscillator Phase Noise Modeling and Optimization, *Proc. 24th EFTF*, Noordwijk, Netherlands, April 2010.
[16] M. Goryachev, S. Galliou and Ph. Abbé, Cryogenic Transistor Measurement and Modeling for Engineering Applications, *Cryogenics*, vol. 50, pp. 381-389, 2010.

Characterization of an Auxiliary offset Generator for steering of H Masers

G. D. Rovera, M. Abgrall, M. Siccardi†
LNE-SYRTE, Observatoire de Paris - LNE - CNRS - UPMC, France
†SKK Electronics, Cuneo, Italia
e-mail: daniele.rovera@obspm.fr

***Abstract*— We report the characterization of the first prototype of an new Auxiliary offset Generator developed for steering the 100 MHz output of H Masers.**

INTRODUCTION

It is very common in time and frequency laboratories to use a 5 MHz or a 10 MHz output of a Hydrogen Maser as the local frequency reference. This output is steered by a micro phase stepper to generate the best local realization of the Hertz, and then divided down to 1Hz pulses to obtain the Local UTC signal. Since the H-Maser and the micro phase stepper are quite sensitive to the environmental conditions, they are usually located in a remote and quiet place; then their output signals are sent via coaxial lines or optical fiber links to the laboratory where the frequency reference is effectively used. With the dramatic improvement of performances of atomic fountains and optical frequency standard this configuration operating at 5 MHz or 10 MHz might be the bottleneck for high quality frequency comparisons.

On the other hand, almost all H-maser have one of more output at 100 MHz. The possibility of setting up a frequency reference based on one of those outputs will greatly improve the overall performances. Up to now we have no knowledge of the availability of a commercial micro phase stepper operating at 100 MHz and so we have designed one. Principal characteristics of the device is to preserve the spectral purity of the signal produced by a high quality H-maser and to preserve the long term stability of the best atomic frequency standard available. To avoid the issue shown by traditional micro phase stepper, where the noise depends on the amount of frequency shift, we have realized a device that mix between a frequency synthesizer and a micro phase stepper. This solution allows to combine tunability and low noise. The low noise synthesizer has a resolution of about 20 nHz, while the phase stepper can introduce discrete steps smaller than $1 \cdot 10^{-16}$ s. The first prototype of the device shows an instability smaller than $2 \cdot 10^{-14}$ for integration time of 1 s.

I. ARCHITECTURE

The architecture of the offset generator is shown in Fig. 1. The 100 MHz input signal is up-converted to 1 GHz and then down-converted back to 100 MHz and distributed to the output stages. In each frequency conversion is introduced a small frequency offset, on the order of 10^{-4} which is applied

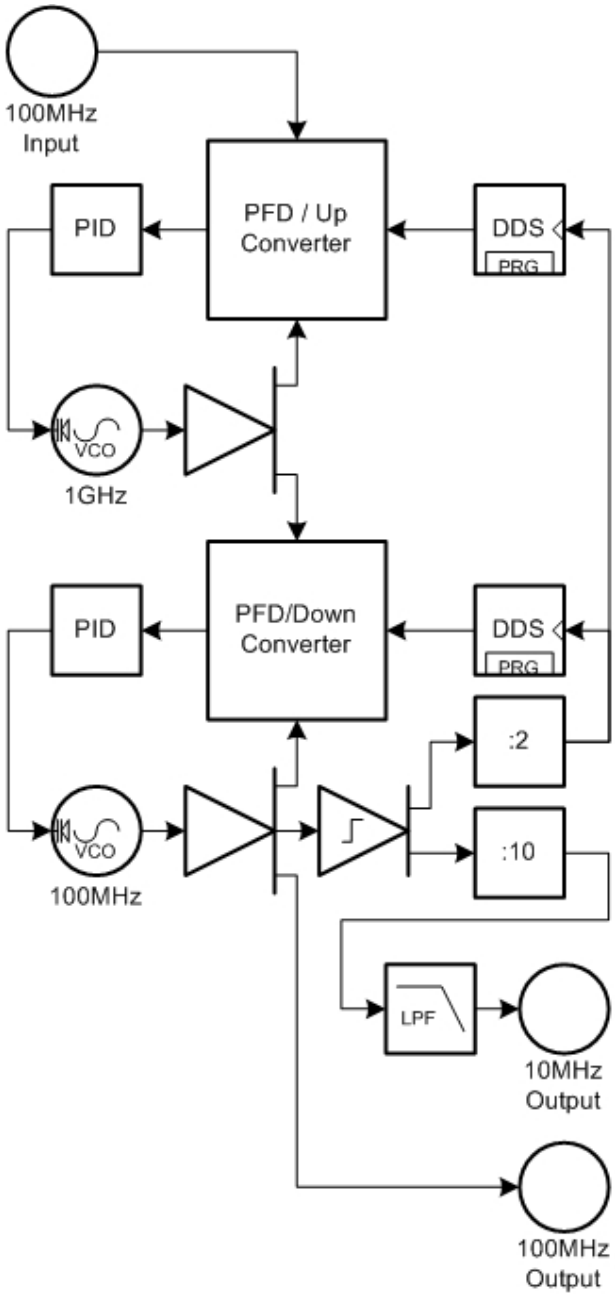

Fig. 1. Simplified diagram of the Offset Frequency Generator

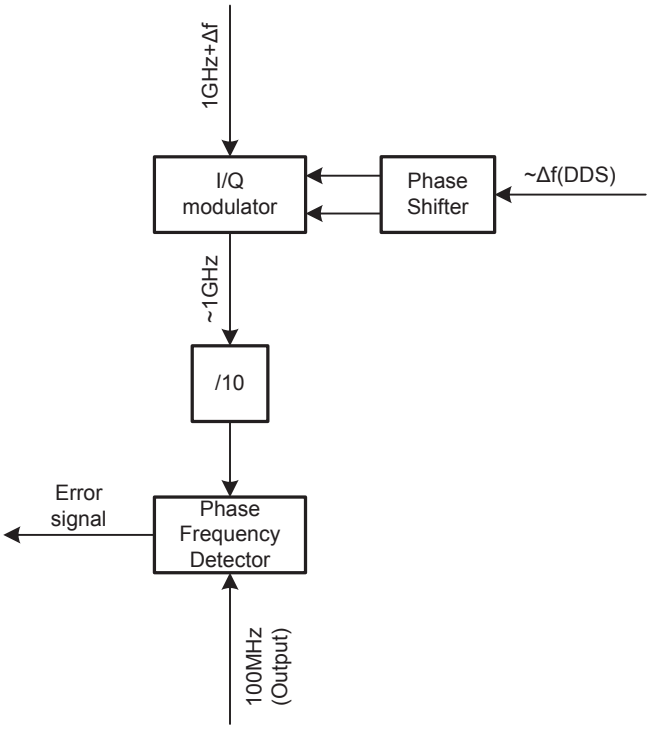

Fig. 2. Down-converter details

by the converters in opposite directions, such that the output frequency of the device is the difference of the offsets. A VCO is used to regenerate the output signal of each conversion block. The 100 MHz sine-wave output of the offset generator is a buffer. The 10 MHz output is a divider-by-10 followed by a low-pass filter. A micro-controller with LAN capabilities programs the offset generator.

The up-converter and the down-converter stages are very similar, being basically a PLL with an arbitrary frequency offset. The down-converter stage is shown in Fig. 2. It is made by a phase comparator and by a single-sideband mixer that allows to introduce the frequency offset on the high frequency path. In between the two there is a factor 10 prescaler, which makes the comparison frequency equals. The PLL loops are closed with an active PID controller. The single-sideband mixer is made by an integrated I/Q modulator. The 1 GHz distributor is a power splitter, while the 100 MHz distributor is an active OPAMP splitter. The offset generators are 48 bit DDS that are clocked with a 50 MHz signal derived directly from the 100 MHz output. The frequency resolution of the device is around 1e-16.

II. Measurement

The device generates 13 dBm signals, which harmonic contents is smaller than -45 dBc at 100 MHz and -65 dBc at 10 MHz. The isolation between 100 MHz output and input is better than 80 dB. The test of the noise generated by the frequency offset generator has been tested in a typical operational configuration. A signal from one output of a low noise 100 MHz distribution amplifier is used as input of

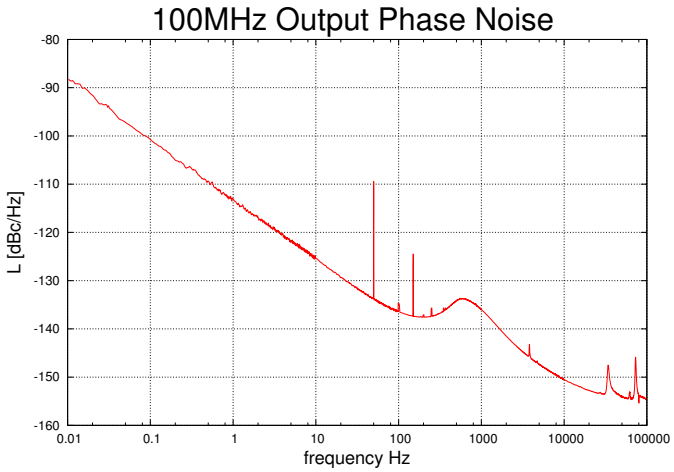

Fig. 3. Output phase measured with a $2.1 \cdot 10^{13}$ offset

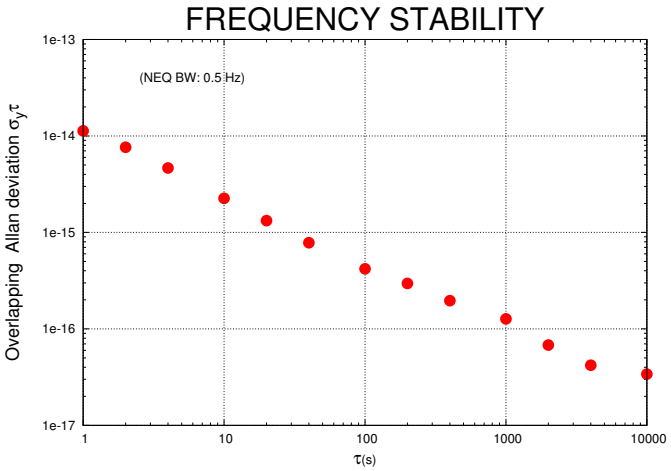

Fig. 4. Allan Deviation measured with a $2.1 \cdot 10^{13}$ offset

the frequency offset generator. The output, shifted with an offset of about 2e-13, is analyzed by a 5125A Test Set from Symmetricom, by using a second output of the distribution amplifier as reference signal. The 100 MHz phase noise measured with this configuration is shown in Fig. 3. The Allan standard deviation measured by the same setup is shown in Fig. II. The thermal sensitivity of the main output has only been roughly estimated with an hair-dryer and will not exceed the design value of 3 ps/K. A test of the software interface has been carried out during one month by steering the frequency offset generator with a simple algorithm calculating the correction from the frequency data of the mobile fountain.

Conclusion

A measure of the relevant characteristics of the frequency offset generator designed to steer the 100 MHz output of a high performance H maser has been carried out at LNE-SYRTE. This measure confirm that the device is well suited to generate a low noise 100 MHz signal for the practical realization of the definition of Hertz.

Fountain Clock Accuracy

Kurt Gibble
The Pennsylvania State University, Department of Physics
State College, PA 16802, USA

***Abstract*—We give a review of recent advances in the accuracy of atomic fountain clocks. The new features are improved experimental and theoretical treatments of distributed cavity phase shifts and a full modeling of microwave lensing. Here we highlight that state selection is often highly non-uniform when Rabi flopping is used instead of an interrupted adiabatic frequency chirp. We show that detuning the state-selection microwave field as well as changing its amplitude can give a much more homogeneous state selection. A spatially inhomogeneous state selection corrupts the density extrapolation because the density distribution changes, which also mixes effects from distributed cavity phase and microwave lensing. This is expected to be important for the microgravity clock PHARAO on ACES, and can also improve fountain clocks.**

I. INTRODUCTION

The highest accuracy of atomic fountain clocks has improved by nearly a factor of two over the last two years [1-4]. Significant progress was made by first evaluating distributed cavity phase (DCP) errors [5,6], and secondly, the first full treatments of the biases due to the microwave lensing of atomic wavepackets by the dipole forces in the clocks' Ramsey cavities. DCP errors are fundamentally a Doppler shift that result because the cavities have small traveling waves and the atoms do not exactly retrace their upward and downward fountain trajectories through the clock cavity. Properly evaluating the DCP uncertainty lowered the SYRTE-FO2 uncertainty to 2.8×10^{-16} [1]. With a smaller DCP uncertainty, the microwave lensing uncertainty stood out and a full modeling of it for NPL-CsF2 reduced its uncertainty from 4.1×10^{-16} to 2.3×10^{-16} [2]. The DCP and microwave lensing model was subsequently applied to PTB-CSF2 and the entire SYRTE fountain ensemble, lowering SYRTE-FO2's uncertainty to 2.1×10^{-16} [3,4]. In the next section, we summarize and discuss a recipe to evaluate DCP uncertainties [1-4]. We refer the reader to [2-4] for the treatments of microwave lensing.

With smaller DCP and microwave lensing uncertainties, the frequency shift due to ultracold collisions [7] contributes more prominently to the overall uncertainty of fountains. For many fountains, it is the largest contribution. To extrapolate the clock's frequency to zero density, it is important to change the atomic density without changing the spatial density distribution. One solution is an interrupted adiabatic frequency chirp, which can precisely select half the atoms [8]. A number of clocks are not currently able to use this technique, including the planned PHARAO clock as part of the ACES project [9]. These clocks instead use power-dependent Rabi flopping to change the density. Here we explicitly show that the changing the power gives a large variation in the selection probability, which changes the density distribution. This in turn introduces systematic errors into the density extrapolation, and also convolves it with the systematic DCP and microwave lensing errors. The transverse variation of the selection can be intentionally varied [10] and here we show that detuning the state selection field can give much more homogeneous state selection.

Finally, one of the next largest sources of uncertainty for many clocks is background gas collisions. We briefly discuss these collisions and the differences between room-temperature collisions and the scattering of room-temperature atoms off of ultra-cold atoms.

II. DCP EVALUATION

Our models of DCP errors [5,6] were stringently verified with three fountains without any free parameters [1-3]. Here we briefly review and discuss a procedure to evaluate DCP uncertainties.

The key step in our treatment is to decompose the loss fields in the cavities into an azimuthal Fourier series $\cos(m\phi)$ [5,6]. This reduces the calculation of the 3D cavity field near the cavity axis to a sum of 2D finite-element solutions for m=0,1, and 2. Higher m are trivial because the fields are proportional to ρ^m for $\rho\rightarrow0$. This Fourier series also dictates the symmetry of the fountain perturbations that produce DCP shifts.

The m=0 DCP errors are small at optimal microwave amplitude and can be accurately calculated. The m=0 phase variations are predominately longitudinal, which leads to a large dependence of the DCP shift on microwave amplitude. The m=2 DCP shifts are quadrupolar and also quite small, of order 1×10^{-16}. Here, detection laser non-uniformity and the uncertainty in the centering of the cloud's launch point gives the errors. These can also be modeled sufficiently well that conservative limits are adequate.

This work was financially supported by the NASA, NSF, ONR, Penn State, and la Ville de Paris.

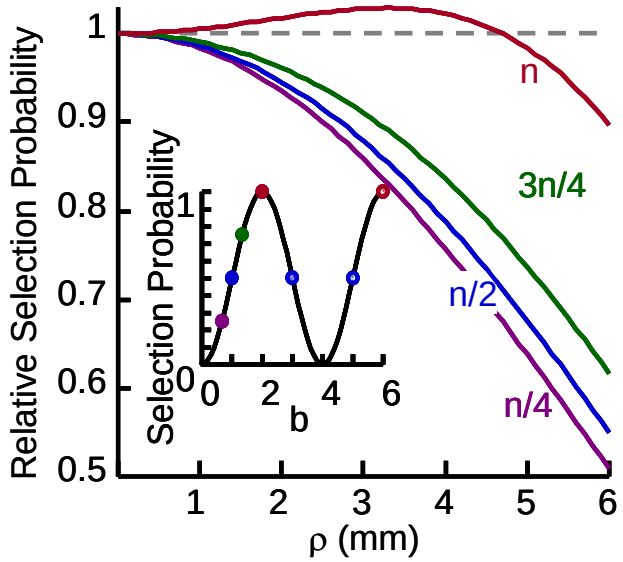

Fig. 1. State selection probability for different pulse areas. For a field on resonance that is not pulsed, the selection probability is $\sin^2(\theta/2)$ where $\theta(\rho)= \theta(\rho=0)J_0(k\rho)$, which is independent of the selection cavity geometry [6]. The inset depicts selecting the various density fractions with several pulse areas.

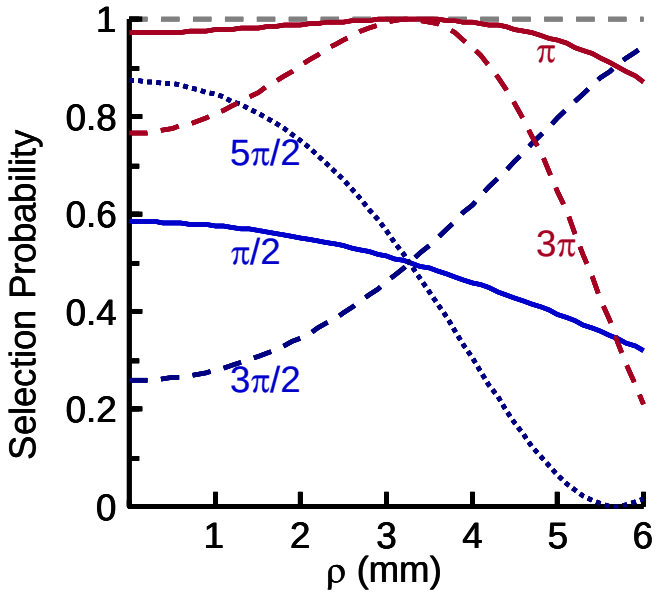

Fig. 2. Changes in the shape of the state selection probability for different pulse areas. Selecting ½ the atoms, 3π/2 pulses give a larger variation with the opposite curvature. Operating the clock alternately with π/2, 3π/2, and 5π/2 state selection pulses probes the effect of state selection inhomogeneity on the clock's frequency [10].

The m=1 DCP errors are due to phase gradients across the cavity, for example due to imbalances in the power fed from opposite sides of the cavity. These have a large scale size – they can easily be 10^{-14} for a single-sided cavity feed and a fountain tilt of 2 mrad. The clock cavity should be tuned to resonance so that phase imbalances of the feeds do not produce DCP errors [6]. Then, the feeds should be balanced at optimal amplitude so that there is no linear change in fountain frequency when the fountain is tilted to move the atoms along the feed axis [1]. Then, the fountain can be aligned to be vertical, for example by comparing frequency differences between feeding only one feed or the other at different elevated microwave amplitudes [1, 11]. Note that measuring the tilt sensitivity with two 5π/2 pulses does not help to establish the m=1 DCP uncertainty [1,6]. Inhomogeneous cavity surface resistances can give dramatically different microwave amplitude dependences of the DCP shifts.

The fountain can also be tilted to move the atoms perpendicular to the feeds. Here, it is more difficult to be sure of true vertical for m=1 DCP errors [1-4]. For this reason, future cavity designs prefer to have at least 4 independent feeds that are distributed equally in ϕ [6]. Optimizing the feed positions and cavity shape should lead to negligible DCP uncertainties, even at high microwave amplitudes [6].

III. State Selection

Driving a π/2 pulse on resonance in a state selection cavity is a common way to change the atomic density to evaluate the ultracold collision frequency shift. If the state selection field is applied for the entire traversal of the atoms through the cavity, instead of a short pulse while the atoms are in the middle of the cavity, the transition probability as a function of position is shown in Fig. 1. As illustrated in the inset, all or half of the atoms can be selected with a number of pulse areas, e.g. π/2, 3π/2, and 5π/2 [10]. Selecting with a 3π/2 instead of a π/2 pulse reverses the curvature of the selection probability and

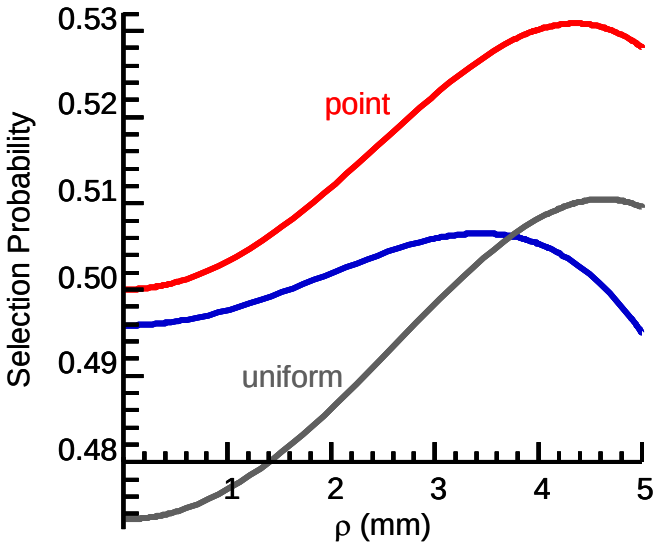

Fig. 3. State selection probability for pulse areas that give a selection probability with the smallest variation (blue), ±1%, and by operating where the transition probability is independent of amplitude for a point source on axis (red), and a uniform density (gray). For these, the detunings are (1.0029, 1.0048, 1.0422) $\Delta\nu_{HWHM}$ and pulse areas (0.7915, 0.8478, 0.8500)π. Here we use the PTB-CSF2 clock cavity as an example. Thus, these results include the mode perturbations due to the holes in the cavity endcaps.

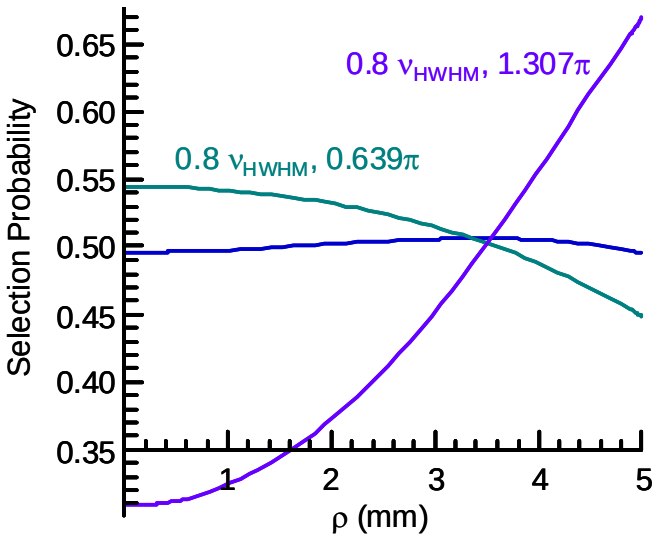

Fig. 4. The selection inhomogeneity can be intentionally increased by a modest amount. Detuning to $0.8\Delta\nu_{HWHM}$ and selecting half the atoms gives modest and opposite selection curvatures (aqua and purple). The blue curve is the same as in Fig. 3

also exaggerates the variation as shown in Fig. 2. Using $5\pi/2$ gives even more dramatic variations.

In Fig. 3, we show that the selection probability can be very flat, varying by ±1%, by detuning the selection cavity field to 1.0029 $\Delta\nu_{HWHM}$ and giving a 0.7915 π pulse. Here $\Delta\nu_{HWHM}$ is the half-width at half-maximum of a π pulse for a small cloud of atoms passing through the cavity on axis. (For a uniform cloud, $\Delta\nu_{HWHM}$ is 6.68% wider than for a point source.) In Fig. 3 for reference, we also show the selection probability for the case of a very small cloud launched through the selection cavity and the transition probability maximized with respect to microwave amplitude, where the detuning is set to give a transition probability of ½ (red). Here, the detuning is 1.00484 $\Delta\nu_{HWHM}$ and the pulse area is 0.8478 π. Similarly, for a uniform density distribution, e.g. for a cloud passing downward through the selection cavity, gives 1.04222 $\Delta\nu_{HWHM}$ and 0.8500 π (gray). In essence, by operating such that the transition probability is independent of power and at the detuning that gives the desired density ratio, the selection probability is far more uniform. In Fig. 4, the variation can be easily exaggerated and the shape reversed by choosing different detunings and pulse areas, but with more modest variations than in Fig. 2.

IV. Background Gas Collisions

A number of clocks assign a frequency uncertainty of 1×10^{-16} for collisions with background gas atoms. The coefficients that are used were measured in room-temperature Cs collisions in vapor cell clock [12]. In a fountain, even a small scattering angle with a room-temperature atom or molecule will expel the Cs atom from being detected. The range of scattering angles that are detected are well within the quantum mechanical diffractive scattering cone - only of order 1% of the diffractive cone is detected. Therefore the measured frequency shifting rate coefficients in [12] are not applicable. Further, the interference of the scattered and the unscattered parts of the atoms' wave functions can be expected to dominate the frequency shift cross section. More attention to this systematic error is clearly required.

Acknowledgment

We acknowledge many discussion and contributions from collaborators at LNE-SYRTE, NPL, and PTB, and especially Ruoxin Li at Penn State.

References

[1] J. Guéna, R. Li, K. Gibble, S. Bize, and A. Clairon, "Evaluation of Doppler Shifts to Improve the Accuracy of Primary Atomic Fountain Clocks," Phys. Rev. Lett. vol. 106, 130801 (2011).

[2] R. Li, K. Gibble, K. Szymaniec, "Improved accuracy of the NPL-CsF2 primary frequency standard: evaluation of distributed cavity phase and microwave lensing frequency shifts," Metrologia vol. 48, pp. 283-289, (2011).

[3] S Weyers, V Gerginov, N Nemitz, R Li, K Gibble, "Distributed cavity phase frequency shifts of the caesium fountain PTB-CSF2," Metrologia vol. 49, pp. 82-87, (2012).

[4] J. Guéna, M. Abgrall, P. Laurent, B. Chupin, M. Lours, G. Santarelli, P. Rosenbusch, M. E. Tobar, R. Li, K. Gibble, A. Clairon, and S. Bize, "Progress in atomic fountains at LNE-SYRTE," IEEE Trans. Ultrasonics, Ferroelectrics, and Freq. Control, vol. 59, 391-410 (2012).

[5] R. Li and K. Gibble, "Phase variations in microwave cavities for atomic clocks," Metrologia vol. 41, pp. 376-386 (2004).

[6] R. Li and K. Gibble, "Evaluating and minimizing distributed cavity phase errors in atomic clocks," Metrologia vol. 47, pp. 534-551 (2010).

[7] K. Gibble and S. Chu, "A laser cooled Cs frequency standard and a measurement of the frequency shift due to ultra-cold collisions," Phys. Rev. Lett. Vol. 70, pp. 177-180 (1993).

[8] F. Pereira Dos Santos, H. Marion, S. Bize, Y. Sortais, A. Clairon, and C. Salomon, "Controlling the Cold Collision Shift in High Precision Atomic Interferometry," Phys. Rev. Lett. Vol. 89, 233004 (2002).

[9] P. Laurent et al., "Design of the cold atom PHARAO space clock and initial test results," Appl. Phys. B vol. 84, 683 (2006).

[10] C. Fertig and K. Gibble, "Measurement and cancellation of the cold collision frequency shift in an ^{87}Rb fountain clock," Phys. Rev. Lett. vol. 85, 1622-1625 (2000).

[11] F. Chapelet et al., Proceedings of the 20th European Frequency and Time Forum, 2006 (EFTF, Braunschweig, 2006), p. 160.

[12] C. W. Beer and R. A. Bernheim, "Hyperfine pressure shift of 133Cs atoms in noble and molecular buffer gases," Phys. Rev. A vol. 13, pp. 1052-1057 (1976).

Comparison of two Strontium optical lattice clocks in agreement at the 10^{-16} level

Rodolphe Le Targat
LNE SYRTE
Observatoire de Paris
61, Avenue Denfert-Rochereau
75014 Paris, France
Email: rodolphe.letargat@obspm.fr

Luca Lorini
INRIM
Strada delle Cacce 91
10135 Torino, Italy

Mikhail Gurov
LNE SYRTE
Observatoire de Paris
61, Avenue Denfert-Rochereau
75014 Paris, France

Michal Zawada
Institute of Physics
Nicolaus Copernicus University
Grudziadzka 5
87-100 Toruń, Poland

Rafal Gartman
Institute of Physics
Nicolaus Copernicus University
Grudziadzka 5
87-100 Toruń, Poland

Bartłomiej Nagórny
Institute of Physics
Nicolaus Copernicus University
Grudziadzka 5
87-100 Toruń, Poland

Pierre Lemonde
LNE SYRTE
Observatoire de Paris
61, Avenue Denfert-Rochereau
75014 Paris, France

Jérôme Lodewyck
LNE SYRTE
Observatoire de Paris
61, Avenue Denfert-Rochereau
75014 Paris, France

***Abstract*— Two optical lattice clocks operated on the transition $^1\mathrm{S}_0 - ^3\mathrm{P}_0$ of the ^{87}Sr atom are now operational at the LNE-SYRTE laboratory, their comparison aims at demonstrating that no systematic effect has been overlooked in their respective accuracy budgets. In this proceeding we focus only on trapping effects, we discuss technical aspects of the calibration of the lattice induced light shifts, and we show the observation of the second order light shift. Data resulting from the comparisons are reported and discussed.**

I. Introduction

The research on Optical Lattice Clocks (OLCs) has been so fruitful in the last 10 years that state-of-the-art experiments in this field are henceforth more accurate than the microwave standards ([1], [2], [3]). But only a direct comparison of two OLCs operated with the same atomic element can bring the indisputable demonstration that no systematic effect has been omitted.

We have therefore built two clocks based on the $5s^2\,{}^1\mathrm{S}_0 - 5s5p\,{}^3\mathrm{P}_0$ transition of ^{87}Sr neutral atoms, referred to as Sr1 and Sr2. The comparisons of these two clocks imply the study of a large number of systematics, but in this proceeding we focus only on the calibration of the lattice induced shifts (first and second orders), and on the influence of the spectral purity of the lasers feeding the lattices (sec. II). We also report the results of the direct comparisons and discuss the influence of the light shifts calibrations (sec III).

II. Characterization of the optical lattices

The optical lattice is the keystone of this type of clock: on one hand, it confines atoms so tightly that they are in the Lamb-Dicke regime [4], and the other hand the operation of the trap at the magic wavelength [5] prevents the atomic motion from resulting in a systematic effect when the clock transition is probed. The performance of the clock is therefore directly linked to the level of control on the lattice.

A. Description of the traps

In our setup, the lattice of each clock is formed in a Fabry-Perot cavity so that the effective potential experienced by the atoms is increased. But in order to demonstrate that the comparison of the two clocks is robust against technical features, their respective traps have been purposely designed in a very different fashion:

- Sr1: The enhancement cavity is rather long (32 cm), the resulting standing wave features a large waist of 90 μm, so that the maximum depth U_0 of the potential U_0 is equal to $500\,\mathrm{E}_r$ (where $\mathrm{E}_r = h \times 3.44$ kHz is the recoil energy of a ^{87}Sr atom absorbing a photon at the magic wavelength $\lambda_m = 813.427$ nm). An intracavity mirror at 45 degrees incidence ensures the purity of the polarization (more than $99.9\,\%$ in terms of electric field [6])
- Sr2: The short (6 cm) linear cavity helps decreasing the conversion of frequency noise of the laser into amplitude noise in the cavity, and a smaller waist allows to reach a potential as deep as $5000\,\mathrm{E}_r$. Nevertheless, in this configuration, the 2 polarization eigenmodes are degenerate and it is necessary to add waveplates before the cavity to control the quality of the polarization.

B. Magic wavelength and residual light shift

Even if the trapping light frequency ν_{lat} is very close to the magic value, the residual light shift must nevertheless be calibrated and taken into account [7]. For a π transition and neglecting the (M1) and (E2) interactions, it is expressed as:

$$\Delta\nu = \Delta\kappa U_0 + \Delta\gamma U_0^2 + ... \quad (1)$$

$$= \left[\Delta\tilde{\kappa}^s(\nu_{lat} - \nu_m) + \Delta\kappa^v\, m_F\, i\,(\vec{\epsilon}\times\vec{\epsilon}^{\,*})\,.\vec{e}_B + \Delta\kappa^t\,\beta\right] U_0 + \Delta\gamma U_0^2 + ... \quad (2)$$

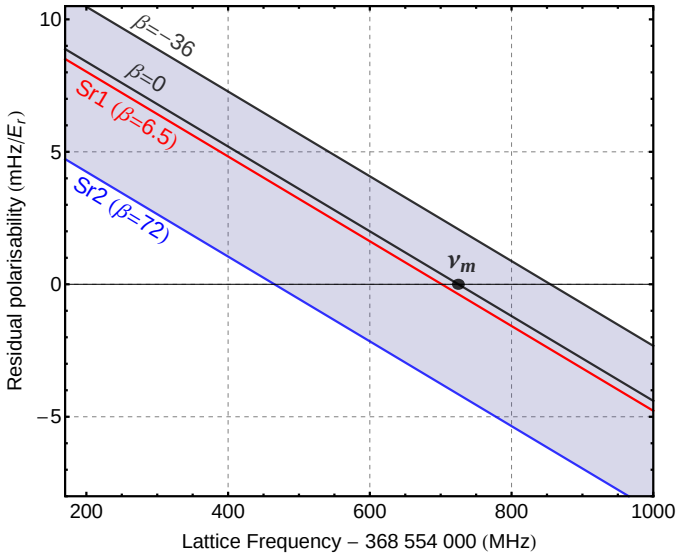

Fig. 1. Residual polarizabilities $\Delta\tilde{\kappa}^s(\nu_{lat}-\nu_m)+\Delta\kappa^t\,\beta$ as a function of the lattice frequency. The coefficient β ranges from -36 to 72, the shaded area corresponds to the accessible values.

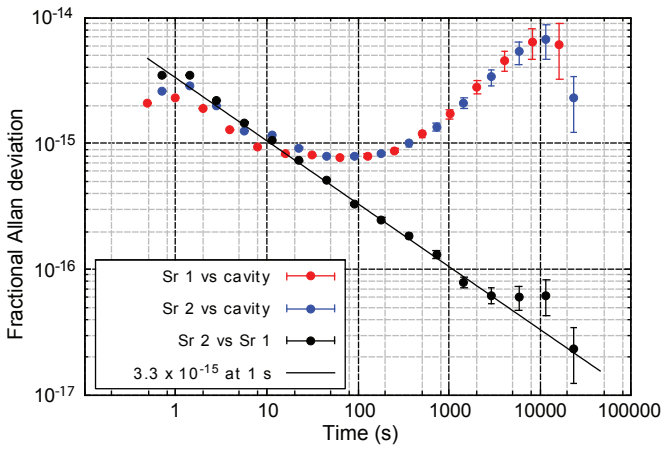

Fig. 2. Stability of the clocks versus the clock laser reference cavity (red points: Sr1, blue points: Sr2), and the two clocks versus each other (black points).

where $\vec{\epsilon}$ and $\vec{e}_B$ are unitary vectors describing the polarization of the lattice and the orientation of the quantization axis. The coefficients $\Delta\kappa^v = \pm 0.22(5)\,\mathrm{Hz/E}_r$ and $\Delta\kappa^t = -0.0577(23)\,\mathrm{mHz/E}_r$ have been measured experimentally [7], the coefficient $\Delta\tilde{\kappa}^s = -0.0155(11)\,\mathrm{mHz/E}_r\mathrm{/MHz}$ results from the fit of light shift measurements spanning over more than one year. The first contribution to the polarizability $\Delta\kappa$ is a scalar term with a zero crossing at the magic frequency $\nu_m = 368\,554\,725(3)$ MHz. The second term, the vectorial contribution, can be cancelled by using a lattice beam with an ellipticity $|\vec{\epsilon}\times\vec{\epsilon}^*|$ equal to zero or by interleaving measurements based on the Zeeman states $F = 9/2, m_F = 9/2$ and $F = 9/2, m_F = -9/2$. Finally, the tensorial term scales as a factor β ranging from -36 to 72: $\beta = \beta_\epsilon.\beta_m$ where $\beta_\epsilon = (3|\vec{\epsilon}.\vec{e}_B|^2 - 1)$ is a geometric factor and $\beta_m = (3m_F^2 - F(F+1))$ an atomic factor. This coefficient β is different for the two clocks ($\beta_1 = 6.5$ for Sr1, $\beta_2 = 72$ usually for Sr2), which simply results in a shift of the effective magic frequency (figure 1).

C. Calibration of the clocks

The calibration of each clock is performed by interleaving measurements of the clock frequency for various lattice depths, while the other clock is operated at constant depth and used as a reference. The stability of a single clock is rapidly limited by the thermal noise of the ultrastable cavity on which the clock laser, shared between the two clocks, is stabilized (figure 2). In contrast, the frequency difference between Sr1 and Sr2 keeps decreasing as $1/\sqrt{\tau}$ after several hours of integration, which demonstrates that all the systematics are correctly handled even on such long timescales. A resolution of 5×10^{-17} is reached after one hour of integration.

The optical setup to generate the trapping light consists in an extended cavity laser diode, locked on a transfer cavity that is itself referenced to the narrow cooling $^1\mathrm{S}_0{-}^3\mathrm{P}_1$ transition. This ensures the control on the frequency ν_{lat}, not only during each measurement, but has allowed a permanent monitoring over the years. This master laser injects two Tapered Amplifiers (TAs), each of them feeding the lattice of one of the two clocks.

A reliable way to control the lattice depths is to keep the current of the TAs constant, and to use liquid crystal waveplates and polarizing beamsplitters to attenuate the optical power at will. A typical result is shown on fig. 3, the residual polarizabilities for Sr1 (3.9 (5) mHz/E_r) and Sr2 (-0.41(27) mHz/E_r) are compatible with the expected 3.8 mHz/E_r polarizability difference between the configurations $\beta_1 = 6.5$ and $\beta_2 = 72$ for two lattices operated at the same frequency (about $\nu_m - 250\,\mathrm{MHz}$ in this case).

It is important to mention that a second calibration method, consisting in ramping down directly the current of the TAs, can lead to very deceiving results, as it is shown by the discrepancy observed on fig. 3 for both clocks. Apart from an offset resulting from technical reasons, the two curves should have exactly the same behavior. For Sr2 it appears clearly that they are similar at high lattice depth, but a significant difference comes into play below 1500 recoils. For Sr1, this approach leads to a senseless result. A likely interpretation of this discrepancy is a spurious background in the TAs spectrum appearing at low current, and evading the safeguards in place: frequency filters (interference filters at the output of the TAs, Fabry-Perot cavities forming the lattices) and spatial filters (optical fibers between the TAs and the cavities). The influence of this issue on the clocks comparisons will be discussed in section III.

D. Hyperpolarizability

Only the first order light shift cancels at the magic wavelength, the second order term, due to the hyperpolarizability $\Delta\gamma$ (eq. 1) of the atoms needs to be calibrated. So far, only

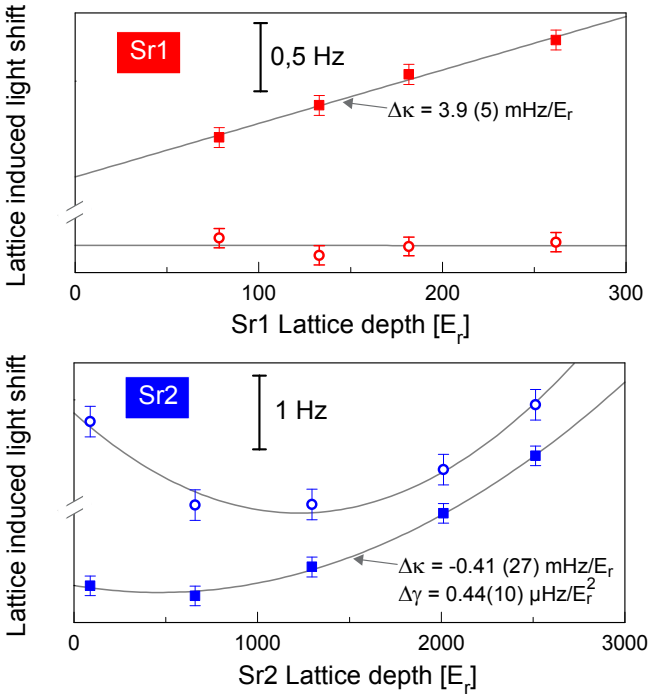

Fig. 3. Clock frequency plotted as a function of the lattice depth U_0, and fitted by a straight line for the clock Sr1 (top graph) and a parabola for Sr2 (bottom graph). For each clock, the two sets of data correspond to controlling the lattice depth by changing the current of the TA (circles) or by keeping the current constant and using a crystal liquid waveplate (squares).

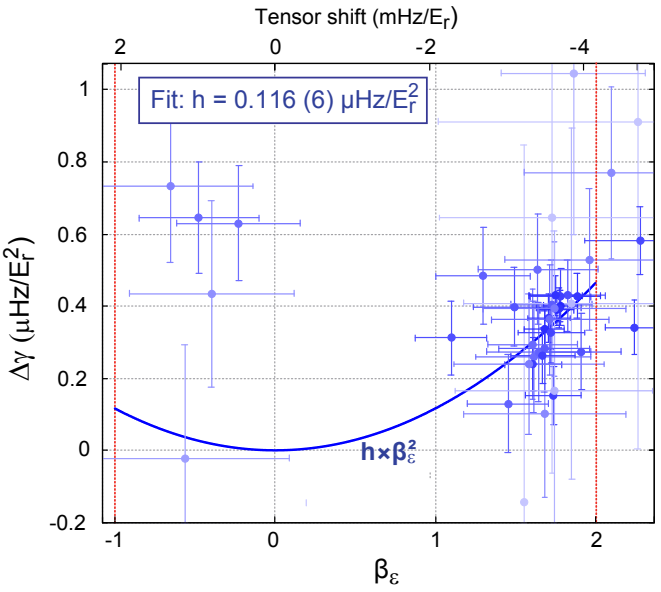

Fig. 4. Hyperpolarizability coefficients resulting from the fit of 42 different calibrations of the Sr2 clock. The smaller the error bar is, the darker the color coding is, and the solid line corresponds to the fit by a parabola. The β_ϵ coefficient is inferred from the calibration of the tensorial part of the polarizability. Only to the case of a linearly polarized lattice has been investigated so far, β_ϵ is changed by turning the polarization $\vec{\epsilon}$ and keeping the quantization axis defined by $\vec{\epsilon}_B$ fixed.

an upper bound had been set [8] [7] but in the data reported for Sr2 on fig. 3, the quadratic behavior is a clear signature of the hyperpolarizability, observed here with an unprecedented resolution with an OLC. The theoretical expression of $\Delta\gamma$ is fairly complex, but the terms involving the two-photon coupling elements are expected to predominate. A complete calculation [9] shows that a reasonable first guess for the hyperpolarizability in the case of a linearly polarized beam is a behavior scaling as β_ϵ^2. A fit of the data acquired so far (figure 4) results in:

$$\Delta\gamma^{\text{fit}} = 0.116(6)\beta_\epsilon^2 \ \mu\text{Hz/E}_r^2 \qquad (3)$$

Even for extreme values of β_ϵ, the uncertainty on the systematic shift introduced by the hyperpolarizability would still be compatible with a 10^{-18} relative accuracy for a clock operated with a $100\,\text{E}_r$ deep lattice.

III. Comparison of the 2 Strontium Clocks

The accuracy budget of our clocks has been established to be 1.4×10^{-16} and will be published in a detailed form in a near future. Nevertheless, the ultimate test to demonstrate that no systematic effect has be omitted is to compare directly two clocks based on the same transition, since only then the expected difference is known to be zero. For instance, the clock Sr2 was originally showing a 10^{-13} discrepancy with Sr1 [6], due to patch charges accumulated on the mirrors of the cavity forming the optical lattice. Such a shift would have been impossible to detect in first place with differential or absolute frequency measurements performed on this clock alone.

To the best of our knowledge, it is the first time that two state-of-the-art OLCs with accuracies better than the state-of-the-art microwave fountains are compared. An important number of comparisons has been performed in the last year, the frequency difference is shown on the figure 5. The initial measurements were compatible with 0, until a sudden shift ($\sim 0.4\,$Hz) appeared. The TAs were identified to be the cause of this anomaly: the sign of the discrepancy inverted when the 2 TAs feeding the 2 lattices were swapped, and the value of the shift changed immediately and amounted to more than 1 Hz when a new TA was used for Sr1. Not only the calibration performed via the current of the TAs can lead to an erroneous extrapolation of the light shift to zero depth (see sec. II-C), but the error can change from one TA to another, and even seems to depend on the aging of a given TA. Nevertheless, the calibration via a control of the trapping depth done at constant TA current lead to data points compatible again with the accuracy budget (final blue points of fig. 5).

IV. Conclusion

In conclusion, we have studied in detail the effects of the optical lattice on the clock transition spectroscopy. The master laser seeding the Tapered Amplifiers generating the lattice beams is locked on a transfer cavity to ensure the control of the detuning from the magic frequency $\nu_m = 368\,554\,725(3)$ MHz. A reliable calibration of the light shift necessitates to

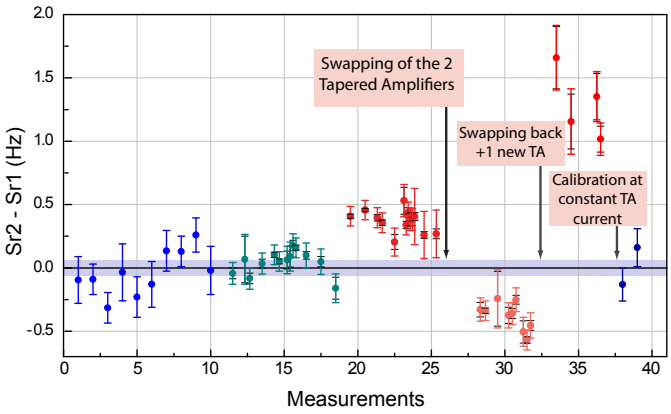

Fig. 5. Comparison between the clocks Sr1 and Sr2. The data points in blue colors are considered to be in good agreement with 0 (within the accuracy budget represented by the shaded area), whereas the points in red colors are not. Black error bars: statistics, colored error bars: statistics+systematics.

keep the spectrum of the TAs unchanged and to vary the trapping depths with the help of controllable attenuators. Only this strategy leads to a good agreement between the two clocks, ongoing measurements should reinforce this statement. Finally, to the best of our knowledge, the second order term has been resolved for the first time in a Strontium clock thanks to the very deep trap (up to $5000\,\mathrm{E}_r$) of Sr2, a fit of the data obtained so far shows that the shift should not exceed $0.464(25)\ \mu\mathrm{Hz/E}_r^2$ for a linearly polarized lattice.

Acknowledgment

We thank Yann Le Coq for the magic frequency measurements. This work has received funding from the LNE, as well as from CNES, ESA and IFRAF.

References

[1] S. Falke, H. Schnatz, J. V. Winfred, T. Middelmann, S. Vogt, S. Weyers, B. Lipphardt, G. Grosche, F. Riehle, U. Sterr, and C. Lisdat, "The 87-Sr optical frequency standard at PTB," *Metrologia*, vol. 48, p. 399, 2011.

[2] G. K. Campbell, A. D. Ludlow, S. Blatt, J. W. Thomsen, M. J. Martin, M. H. G. de Miranda, T. Zelevinsky, M. M. Boyd, J. Ye, S. A. Diddams, T. P. Heavner, T. E. Parker, and S. R. Jefferts, "The absolute frequency of the 87 Sr optical clock transition," *Metrologia*, vol. 45, p. 539, 2008.

[3] J. Guéna, M. Abgrall, D. Rovera, P. Laurent, B. Chupin, M. Lours, G. Santarelli, P. Rosenbusch, M. Tobar, R. Li, K. Gibble, A. Clairon, and S. Bize, "Progress in atomic fountains at LNE-SYRTE," *Ultrasonics, Ferroelectrics and Frequency Control, IEEE Transactions on*, vol. 59, no. 3, pp. 391–410, 2012.

[4] R. H. Dicke, "The Effect of Collisions upon the Doppler Width of Spectral Lines," *Physical Review*, vol. 89, pp. 472–473, 1953.

[5] H. Katori, M. Takamoto, V. G. Pal'chikov, and V. D. Ovsiannikov, "Ultrastable Optical Clock with Neutral Atoms in an Engineered Light Shift Trap," *Phys. Rev. Lett.*, vol. 91, p. 173005, 2003.

[6] J. Lodewyck, M. Zawada, L. Lorini, M. Gurov, and P. Lemonde, "Observation and cancellation of a perturbing dc stark shift in Strontium optical lattice clocks," *IEEE Trans. Ultrason., Ferroelect., Freq. Contr.*, vol. 59, no. 3, p. 411, 2012.

[7] P. G. Westergaard, J. Lodewyck, L. Lorini, A. Lecallier, E. A. Burt, M. Zawada, J. Millo, and P. Lemonde, "Lattice-Induced Frequency Shifts in Sr Optical Lattice Clocks at the 10^{-17} Level," *Phys. Rev. Lett.*, vol. 106, p. 210801, 2011.

[8] A. Brusch, R. Le Targat, X. Baillard, M. Fouché, and P. Lemonde, "Hyperpolarizability Effects in a Sr Optical Lattice Clock," *Phys. Rev. Lett.*, vol. 96, p. 103003, 2006.

[9] J. Lodewyck *et al.*, "Polarizabilities and hyperpolarizabilities of the Strontium clock transition," *In preparation*.

Reaching the 10^{-15} accuracy range with a Hg optical lattice clock

J.J. McFerran, L. Yi, S. Mejri, R. Tyumenev, Z. Xu, S. Di Manno, W. Zhang, J. Guéna, Y. Le Coq and S. Bize

SYRTE, 61 avenue de l'Observatoire, 75014 Paris, France

Following previous work on neutral atom lattice clocks [1-4], we have presented work regarding a 3rd neutral atomic species, namely mercury. We have carried out absolute frequency measurements of the (6s2) $^1S_0$ — (6s7s) $^3P_0$ clock transition frequency in ^{199}Hg against a Cs fountain primary reference and achieved a fractional uncertainty of 5.7 parts in 10^{15}, nearly three orders of magnitude lower than previously measured [5].

The ^{199}Hg atoms are confined in a vertical lattice trap with light at the newly determined magic wavelength of 362.5697±0.0011 nm and at a lattice depth of $20E_R$. The uncertainty on the magic wavelength is a 100-fold improvement on our previous measurements [6,7]. The atoms are loaded from a single stage magneto-optical trap with cooling light at 253.7 nm. Altogether, only three laser wavelengths are used for the cooling, lattice trapping and probing (265.6 nm). A quality factor, Q, of 10^{14} is obtained for the clock transition spectrum when using a probe pulse of 80 ms duration and the linewidth is Fourier transform limited. The frequency of the clock transition is determined to be 1 128 575 290 808 162.0 ± 6.4 (systematic) ± 0.3 (statistical) Hz, where the statistical uncertainty arises from data recorded over a period of three months. Neither an atom number nor second orders Zeeman dependence have been observed at the present level of resolution.

When stabilizing the ultra-stable laser to the atomic clock signal, we measure a fractional frequency instability of 6×10^{-15} at 1s, adhering to an inverse square-root tau dependence out to 400s where it becomes limited by the counterpart against which it is measured i.e. a Fabry-Perot stabilized ultra-stable laser and/or LNE-SYRTE cryogenic sapphire based ultra-stable reference [8,9].

These results, which establish the potential of ^{199}Hg as a highly accurate frequency standard, are published in [10,11].

References

[1] Takamoto et al., J. Phys. Soc. Jpn., 75, 104302 (2006).

[2] A. Ludlow et al., Science 319, 1805 (2008).

[3] N. D. Lemke et al., Phys. Rev. Lett. 103, 063001 (2009).

[4] P. G. Westergaard et al., Phys. Rev. Lett. 106, 210801 (2011).

[5] M. Petersen et al, Phys. Rev. Lett. 101, 183004 (2008).

[6] L. Yi, et al., Phys. Rev. Lett. 106, 073005 (2011).

[7] S. Mejri, J. J. McFerran, L. Yi, Y. Le Coq, and S. Bize, Phys. Rev. A 84, 032507 (2011).

[8] S. Dawkins, et al., Appl. Phys. B 99, 41 (2010).

[9] J. Millo, et al., Phys. Rev. A 79, 053829 (2009).

[10] J. J. McFerran, et al., Phys. Rev. Lett. 108, 183004 (2012).

[11] J. J. McFerran, et al., *submitted*.

UTCr: a rapid realization of UTC

G. Petit, F. Arias, A. Harmegnies, Z. Jiang, H. Konaté,
W. Lewandowski, G. Panfilo, L. Tisserand
Time Department, BIPM
92312 Sèvres France
gpetit@bipm.org

***Abstract*— Considering the evolving needs of time metrology and the convenience of allowing the contributing laboratories access to a realization UTC more frequently than through the monthly *Circular T*, the BIPM Time Department has started to implement the computation of UTCr, a rapid realization of UTC published every week and based on daily clock and time transfer data. Results of the first weeks of a pilot experimentation of this new product are presented.**

I. INTRODUCTION

At present the Coordinated Universal Time UTC is calculated with one-month data batches, and is available monthly in the BIPM *Circular T* [1] under the form of [*UTC*-*UTC*(*k*)], where *UTC*(*k*) is a local realization of UTC by participating laboratory k, at five-day intervals. Extrapolation of values over 10 to 45 days based on prediction models is necessary to many applications. UTC, as published today, is not adapted for real and quasi-real time applications. A more rapid realization would benefit e.g. to the following:

- UTC contributing laboratories would have more frequent assessing of the *UTC*(*k*) steering, and consequently better stability and accuracy of *UTC*(*k*) and enhanced traceability to UTC;
- Users of *UTC*(*k*) would access to a better "local" reference, and indirectly, better traceability to the UTC "global" reference;
- Users of Global Navigation Satellite Systems would get a better synchronization of GNSS times to UTC, through improved UTC and *UTC*(*k*) predictions: this is the case of UTC(USNO) for GPS, UTC(SU) for GLONASS, and of the UTC(k) to be used in the generation of Galileo, BeiDou and Gagan system times.

For these reasons, the BIPM has proposed to provide UTCr, a new realization of UTC available with a reduced delay. The paper presents the algorithm used and the main characteristics of UTCr in Section II, then reports in Section III on its implementation in a Pilot experiment initiated in January 2012. Comparisons of UTCr with the final UTC for the first months of 2012 are discussed in Section IV.

II. CHARACTERISTICS AND REALIZATION OF UTCr

A. Main characteristics of UTCr

UTCr is based on daily data reported daily by contributing laboratories. The solution is calculated every week over an interval of about 4 weeks of data, i.e. a sliding solution in which the reference at the beginning of the computation interval ensures continuity with UTC, when available. It is disseminated through daily values of [*UTC*r – *UTC*(*k*)] published at one-week intervals on the Wednesday afternoon, providing access to results up to the preceding Sunday.

The stability of UTCr is expected to be about comparable to that of UTC because the interval of calculation covers one month approximately, the weighting procedure is the same as for UTC, and the participating laboratories are expected to represent at least about 50% of the clocks in UTC and 70% of the total clock weight in UTC. Finally the accuracy is ensured by steering to UTCr to UTC based on the differences observed over the most recent common interval. The process can be summarized as follows:

- A stability algorithm provides an ensemble scale that we here name EALr;
- UTCr is derived from EALr by a steering function f.

$$UTC\mathrm{r} = EALr + f(\mathrm{t}) \qquad (1)$$

The computation can be split in four steps, which are briefly described in the following sections.

B. Data reporting and checking

UTCr is based on daily data, both for clock and time transfer, which must be reported daily by contributing laboratories, in practice the data of day D must be uploaded before day D+2, 12:00 UTC. Each laboratory uses an individual account on the ftp server, which is different from the account used for UTC, and is created when the laboratory indicates its intention to participate. Standard file naming conventions must be respected, see ftp://tai.bipm.org/UTCr/Documents/ for guidelines.

In operational use, it is expected that no interaction should happen with laboratories for data correction, etc…. Therefore a number of tasks are automatically carried out in this step:

- detect the input data and check the format of data file, as recognized through the file names.
- report on unknown or new data file. Detection of new files triggers a manual intervention to allow the inclusion of the new data in the data set;
- report on known data file.

C. *Computation of the time links*

For the computation of UTCr, time links are so far based only on GNSS code data provided in the CGGTTS format [2]. They may be expanded later to include Two Way satellite time transfer and possibly GNSS phase and code solutions. GNSS code data are processed using the Rapid Precise Orbits and clocks products of the International GNSS Service (for GPS) and of the IAC analysis center (for GLONASS), all of which are available in less than one day. Procedures have been developed to allow automatic treatment, particularly for what concerns the detection and correction of possible time steps to avoid interpolation errors.

D. *Stability algorithm*

The stability algorithm is similar to ALGOS [3, 4, 5] used for TAI. The ensemble scale EALr is

$$EALr - h_j(t) = \sum_{i=1}^{N} w_i \left[h_i'(t) - x_{i,j}(t) \right] \qquad (2)$$

where N is the number of participating clocks, w_i the relative weight of clock H_i, $h_j(t)$ is the reading of clock H_j at time t, $x_{ij} = h_j - h_i$, and $h'_i(t)$ is the prediction of the reading of clock H_i that serves to guarantee the continuity of the timescale. At this stage, only a linear prediction has been implemented, a marked difference with ALGOS for which a quadratic prediction has been in use since August 2011 [6].

The computation interval is between 27 and 31 days, as it starts with a "TAI standard date" (i.e. a Modified Julian Day ending with 4 or 9) and it ends with the last day of the week under computation. Similar to the ALGOS algorithm, the clock weights are determined from the clock instability computed over the computation interval and (up to) eleven 30-day intervals preceding it. Three other rules are applied, that modify the weights obtained from the computed instability:

- If less than four past intervals are available, a null weight is attributed to the clock;
- The maximum weight of a clock is set at $2.5/N$;
- A test for "abnormal behavior" is implemented, similar to the one in ALGOS.

After these rules have been applied, the weights are renormalized and the procedure is iterated until convergence.

E. *Steering to UTC*

The steering of UTCr to UTC is based on a weighted average of the differences $D(t_j)$ between UTC and UTCr computed at the dates t_j as:

$$D(t_j) = \sum_{k=1}^{N} W_k \left([UTCr - UTC(k)](t_j) - [UTC - UTC(k)](t_j) \right) \qquad (3)$$

where W_k is the total weight of the laboratory k in the UTCr calculation. The steering function $f(t)$ is a linear function adjusted to the ensemble of $D(t_j)$. It is planned that each month, when UTC is available, a new function $f(t)$ is calculated and is then applied until the next UTC calculation becomes available. This steering procedure is under study and will be reviewed after the experimentation period of UTCr computation.

III. IMPLEMENTATION OF UTCr

The announcement for a pilot experiment was sent to all contributing laboratories in September 2011. By the end of November 2011, 48 laboratories representing 86% of the clock weight in UTC indicated their intention to participate by sending daily clock and time transfer files.

The regular data reports started on January 1st 2012, and the first weekly computation was carried out for the 5th week of 2012, labeled 1205 (the label YYWW identifies the WW th week of year 20YY), and was published on February 27, 2012. "Operational" publication started with week 1208, published the next Wednesday on February 29th 2012, and has continued since that time. The results are published every Wednesday before 18:00 UTC on the web page ftp://tai.bipm.org/UTCr/Results/.

The calendar of publication of UTC is monthly and follows the list of standard dates (MJD ending by 4 or 9), while that of UTCr is weekly and follows the civil week, see an illustration in Figure 1. This has some implications on the steering of UTCr which must be based on an extrapolation of the observed past differences between UTC and UTCr, see an example in the results given in Section IV-A.

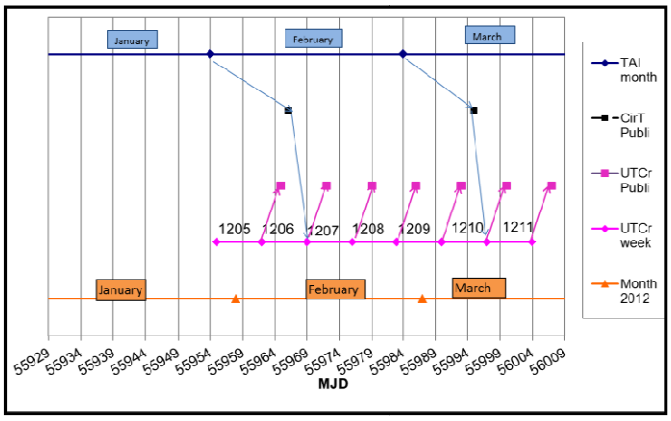

Figure 1. Sequence of events for the computation of UTC and UTCr. The second line from bottom indicates the week numbers for UTCr computation and their date of publication. The top line shows the TAI months in 2012 where the standard dates are indicated in the vertical grid. The line below indicates the date of publication of the corresponding Circular T, e.g. showing that the January Circular is available for the 1206 UTCr computation, and the February Circular for the 1210 UTCr computation.

IV. COMPARISONS OF UTCr WITH UTC

In the following sections, we report comparisons of UTCr with UTC based on the first weeks of UTCr computation.

A. Comparison of the results

The direct comparison of UTCr to UTC is based on the $D(t_j)$ values as given in (3). Figure 2 shows this direct comparison for three months (February to April 2012). In the first two months, a drift can be clearly seen. It is due to the absence of steering in the first weeks of the UTCr computation, until MJD 55989 in week 1209. Subsequently, a default in the steering function which was computed from the February UTC values and applied in March failed to correct the drift, affecting all values from MJD 55994 until MJD 56024 in week 1214. This was corrected only for the week 1215, when the March UTC values became available. The drift is thought to be due partly to the linear prediction used in UTCr whereas a quadratic prediction is used for UTC [6], but also partly to the intrinsic instability of the clock ensemble used for UTCr, which varies from week to week. Therefore it can be expected that using a quadratic prediction in UTCr could reduce the difference between UTCr and UTC, as well as using a steering function experimentally determined as indicated in Section II-E. The steering procedure is one of the main topics to be studied during the pilot experiment phase.

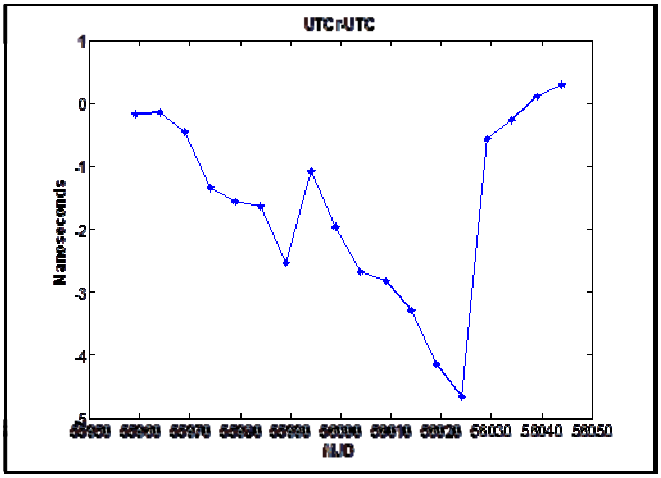

Figure 2. Comparison of UTCr to UTC over three months (see text for details)

B. Comparison of weights

Based on the UTCr computations in four weeks in February 2012, some 32 to 36 laboratories participate to UTCr (vs. 69 in UTC) and more than 25 have some weight in UTCr (vs about 50 in UTC). From Figure 3, we see that many of the laboratories which have a significant weight in both UTC and UTCr have a larger relative weight in UTCr, as expected because each clock has a larger weight due to the reduced number of clocks in UTCr compared to UTC.

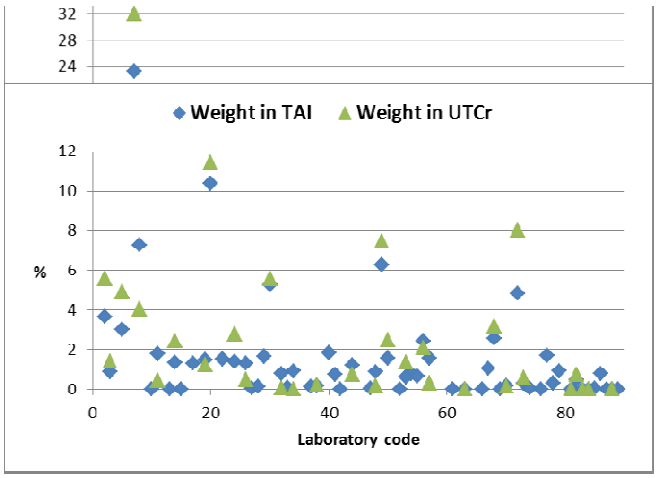

Figure 3. Average weights of the laboratories participating to the four UTCr computations in February 2012 (triangles) compared to their weight in the February UTC computation (diamonds).

C. Comparison of the clock ensemble

Comparing the clock populations and statistics for UTCr in four weeks in February 2012 and for the February UTC computation, we note that:

- 32 UTC laboratories, which clocks make 86% of the UTC weight in February, participated to the four UTCr computations;
- Some 60% of the UTC clocks are in UTCr (note that their total weight in the February UTC computation is lower than the 86% mentioned in the preceding bullet, because not all UTC clocks are reported for UTCr);
- The maximum weight w_{max}, which is computed with the same formula as 2.5/N, is therefore higher in UTCr than in UTC;
- The proportion of clocks reaching w_{max} is slightly lower in UTCr than in UTC;

TABLE I. CHARACTERISTICS OF THE CLOCK ENSEMBLES FORMING UTCR AND UTC IN FEBRUARY 2012

	UTCr	UTC
N clocks for weight	210	360
Max weight w_{max}	1.2%	0.7%
1-month stability at w_{max}	$4.5\text{-}4.7\times10^{-15}$	4.8×10^{-15}
Total weight @ w_{max}	31-37%	40%

We can infer that UTCr is about 20% less stable than UTC, considering that it is based on 60% of the clocks with similar characteristics (see [7] for an estimation of the 1-

month instability of UTC). Table I summarizes some comparisons of the clock ensembles of UTCr and UTC over February 2012.

V. CONCLUSION

UTC contributing laboratories have been invited to participate on a voluntary basis to a pilot experiment to generate a rapid realization of UTC named UTCr. The pilot experiment started in January 2012, with the target of producing a report for the 19th meeting of the Consultative Committee for Time and Frequency in September 2012. A final decision on the routine production of UTCr will be taken end of 2012.

The first weeks of the pilot experiment have shown that it is possible to perform an automatic computation and a rapid publication of UTCr, while maintaining metrologic quality of the rapid realization.

UTC continues to be calculated and published as before the advent of UTCr, however, it will benefit from UTCr through a shorter latency of publication due to anticipated data checking and pre-processing and a possible better quality of data from contributing laboratories from an early detection of problems.

ACKNOWLEDGMENT

We thank the time laboratories for their participation to the UTCr pilot experiment.

REFERENCES

[1] http://www.bipm.org/jsp/en/TimeFtp.jsp?TypePub=publication

[2] Allan D.W., Thomas C., "Technical directives for standardization of GPS time receiver software", Metrologia 31, pp. 69-79, 1994.

[3] Guinot B and Thomas C., "Establishment of international atomic time" Annual Report of the BIPM Time Section 1, 1988.

[4] Thomas C., Wolf P., and Tavella P, "Time scales", BIPM Monographie 94/1, 1994.

[5] Panfilo G. and Arias E-F., "Algorithms for TAI" UFFC 57 (1) 140-150, 2010.

[6] Panfilo G., Harmegnies A., Tisserand L., "A new prediction algorithm for the generation of International Atomic Time". Metrologia, 49, n. 1, pp. 49-56, 2012.

[7] Petit G., "The long-term stability of EAL and TAI (revisited)", *Proc. EFTF-FCS'07 meeting*, 391–394, 2007.

Time and frequency transfer with a MicroWave Link in the ACES/PHARAO mission

P. Delva*, F. Meynadier, C. Le Poncin-Lafitte, P. Laurent and P. Wolf
LNE-SYRTE, Observatoire de Paris, CNRS et UPMC,
61 avenue de l'Observatoire, 75014, Paris, France
*Email: Pacome.Delva@obspm.fr

***Abstract*— The Atomic Clocks Ensemble in Space (ACES/PHARAO mission), which will be installed on board the International Space Station (ISS), uses a dedicated two-way MicroWave Link (MWL) in order to compare the timescale generated on board with those provided by many ground stations disseminated on the Earth. Phase accuracy and stability of this long range link will have a key role in the success of the ACES/PHARAO experiment. SYRTE laboratory is heavily involved in the design and development of the data processing software : from theoretical modelling and numerical simulations to the development of a software prototype. Our team is working on a wide range of problems that need to be solved in order to achieve high accuracy in (almost) real time. In this article we present some key aspects of the measurement, as well as current status of the software's development.**

I. Introduction

The ACES/PHARAO mission is an international metrological space mission aiming at realizing a time scale of high stability and accuracy on board the International Space Station (ISS). Relative frequency stability (ADEV) should be better than $\sigma_y = 10^{-13} \cdot \tau^{-1/2}$, which corresponds to $3 \cdot 10^{-16}$ after one day of integration (see fig.1); time deviation (TDEV) should be better than $2.1 \cdot 10^{-14} \cdot \tau^{1/2}$, which corresponds to 12 ps after one day of integration (see fig.2). Absolute frequency accuracy should be around 10^{-16}.

This mission is an international cooperation of more than 150 people. PI laboratories are SYRTE/Paris Observatory, LKB/ENS and Neuchâtel Observatory, and leading space agencies are the European Space Agency and CNES, the French space agency. Many industrial partners are involved, the main ones being EADS/Astrium, EADS/Sodern and TimeTech. All are working together to meet the scientific objectives of the mission:

- Demonstrate the high performance of the atomic clocks ensemble in the space environment and the ability to achieve high stability on space-ground time and frequency transfer.
- Compare ground clocks at high resolution on a worldwide basis using a link in the microwave domain. In common view mode, the link stability should reach around 0.3 ps after 300 s of integration; in non-common view mode, it should reach a stability of around 7 ps after 1 day of integration (see fig.2).
- Perform equivalence principle tests. It will be possible to test Local Lorentz Invariance and Local Position Invariance to unprecedented accuracy by doing three types of tests: a test of gravitational redshift, drift of the fine structure constant and of anisotropy of light.

Besides these primary objectives, several secondary objectives can be found in [1]. For example, if the theory of general relativity is considered as exact, then the measurement of gravitational redshifts can be used to measure gravitational potential differences between different clock locations. It is a new type of geodetic measurements using clocks called relativistic geodesy.

In this article we describe in details the MicroWave Link (MWL) used in the ACES/PHARAO mission, and developed by TimeTech (TT) and EADS/Astrium. First we describe one-

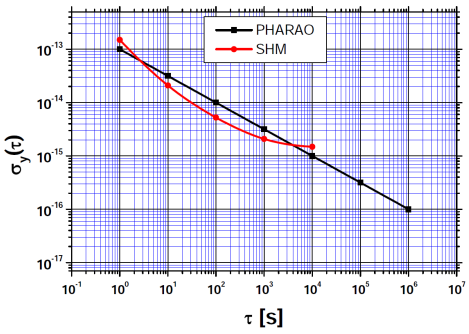

Fig. 1. PHARAO (Cesium clock) and SHM (hydrogen maser) expected performances in Allan deviation.

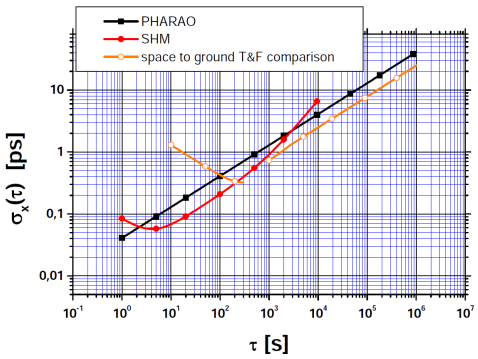

Fig. 2. Performance objective of the ACES clocks and the ACES space-ground time and frequency transfer expressed in time deviation.

way and two-way links theoretically and introduce the SYRTE Team (ST) observables. In the second part we describe how works the TT modem, and what is the link between the modem observables (TT observables) and the ST observables. Finally we present the status of the data analysis software and of the simulation we are developing.

II. The MicroWave Link (MWL)

The MicroWave Link (MWL) will be used for space-ground time and frequency transfer. A time transfer is the ability to synchronize distant clocks, i.e. determine the difference of their displayed time for a given coordinate time. The choice of time coordinate defines the notion of simultaneity, which is only conventional. A frequency transfer is the ability to syntonize distant clocks, i.e. determine the difference of clock frequencies for a given coordinate time. Here we suppose that all clocks are perfect, i.e. their displayed time is exactly their proper time. Proper time τ is given in a metric theory of gravity by relation:

$$c^2 \mathrm{d}\tau^2 = -g_{\alpha\beta} \mathrm{d}x^\alpha \mathrm{d}x^\beta, \tag{1}$$

where $g_{\alpha\beta}$ is the metric, c the velocity of light, $\{x^\alpha\}$ the coordinates and Einstein summation rule is used. We use in this article the notation $[.]$, which is the coordinate / proper time transformation obtained from eq.(1), and $T_{ij} = t_j - t_i$ for coordinate time intervals[1].

The MWL is composed of three signals of different frequencies: one uplink at frequency $\simeq$ 13.5 GHz, and two downlinks at $\simeq$ 14.7 GHz and 2.2 GHz. Measurements are done on the carrier itself and a code that modulates the carrier at 100 Mchip/s. The link is asynchronous, i.e. the uplink is independent of the downlink. Measurements are provided at 80 ms intervals and can be interpolated in order to choose any particular configuration, e.g. emission of the downlink signal simultaneously with reception of the uplink signal at the spacecraft antenna (so-called Λ configuration).

In the following we give a formal description of one-way and two-way links for code observables. The principle for carrier observables is the same except that periods cannot be identified, leading to a phase ambiguity.

A. One-way link

1) Experiment: let's consider a one-way link between a ground and a space clock represented respectively by subscript g and s. The sequence of events is illustrated on fig.3. At time coordinate t_1, clock g displays time τ_1 and modem Mg produces a code C^1. This code modulates a sinusoidal signal of frequency f and sent at coordinate time t_2 by antenna g. The delay between the code production and its transmission by antenna g is $\Delta^g = [T_{12}]^g$, expressed in local frame of clock g. Antenna s receives signal C^1 at coordinate time t_3, and transmit it to modem Ms and clock s which receives it at coordinate time t_4, with a delay $\Delta^s = [T_{34}]^s$. Clock s displays

[1]e.g. $[T_{12}]^A$ is the transformation of coordinate time interval T_{12} in proper time of clock A, and $[\Delta\tau^A]^t$ is the transformation of proper time interval $\Delta\tau^A$ of clock A in coordinate time t.

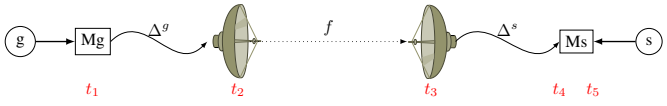

(a) Sequence of events

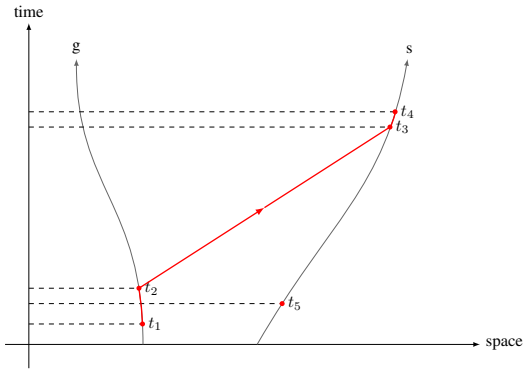

(b) Space-time diagram

Fig. 3. Schematic representation of the one-way link.

time τ_1 and modem Ms produces the code C^1 at coordinate time t_5.

We use superscript g or s on proper times τ for clocks g or s, and we express proper time as a function of coordinate time. Then we can write

$$\tau_1 = \tau^g(t_1) = \tau^s(t_5). \tag{2}$$

We define the ST (SYRTE Team) observable $\Delta\tau^s$ given by modem Ms with:

$$\Delta\tau^s(\tau^s(t_4)) = \tau^s(t_5) - \tau^s(t_4). \tag{3}$$

This observable is dated with proper time of clock s when this clock receives code C^1 from antenna s. It can be interpreted as the difference between the time of production of code C^1 by clock s, and time of reception of same code C^1 sent by clock g, all expressed in proper time of clock s.

2) Desynchronisation: desynchronisation between clock g and s is written in an hypersurface characterized by coordinate time t = constant. From eqs.(2)-(3) it is straightforward to deduce it for coordinate time t_4:

$$\tau^s(t_4) - \tau^g(t_4) = -\Delta\tau^s\left(\tau^s(t_4)\right) - \left[T_{23} + [\Delta^g + \Delta^s]^t\right]^g \tag{4}$$

Similar formulas can be obtained for the desynchronization at coordinate times t_1 and t_5. This expression has been obtained for the uplink, from ground to space. To obtain the desynchronisation with downlink observables, all you have to do is replace g and s in eq.(4).

B. Two-way link

1) Experiment: let's consider now a link which is composed of two one-way links, between a ground and a space clock represented respectively by subscript g and s. The two sequences of events are illustrated on fig. 4. The uplink (from ground to space) has a frequency f_1 and is represented by

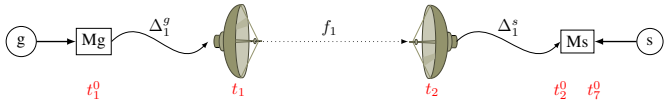

(a) Uplink sequence of events

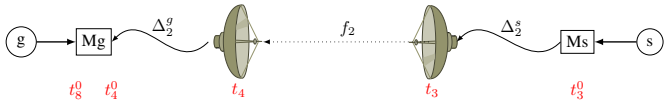

(b) Downlink sequence of events

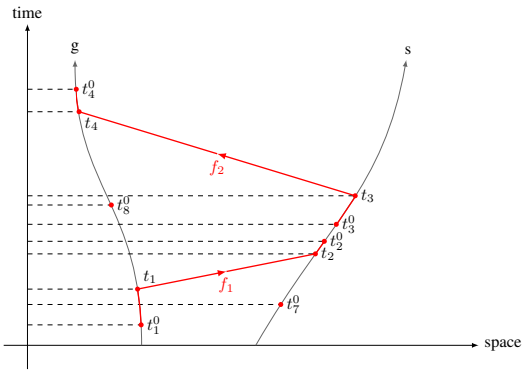

(c) Space-time diagram

Fig. 4. Schematic representation of the two-way link.

coordinate time sequence $(t_1^0, t_1, t_2, t_2^0, t_7^0)$ (fig.4(a)). This link is defined with the relation:

$$\tau^g(t_1^0) = \tau^s(t_7^0).$$

The downlink has a frequency f_2 and is represented by coordinate time sequence $(t_3^0, t_3, t_4, t_4^0, t_8^0)$ (fig.3(b)). This link is defined with the relation:

$$\tau^s(t_3^0) = \tau^g(t_8^0).$$

2) Desynchronisation in a two-way configuration: a two-way configuration is defined by $\tau^g(t_1^0) = \tau^s(t_3^0)$, i.e. the code C^1 of link f_1 is the same as code C^2 of link f_2, and they are locally produced and sent at the same time: $t_1^0 = t_8^0$ (at clock g) and $t_3^0 = t_7^0$ (at clock s). Then we calculate desynchronisation between clocks g and s at coordinate time t_1^0 as:

$$\tau^s(t_1^0) - \tau^g(t_1^0) = \frac{1}{2}\left[\left[\Delta\tau^g_{\text{mo}}(t_4^0) - \Delta\tau^s_{\text{mo}}(t_2^0)\right]^t + T_{34} - T_{12}\right]^s \tag{5}$$

where we introduced the *corrected* observables $\Delta\tau^g_{\text{mo}}$ and $\Delta\tau^s_{\text{mo}}$:

$$\begin{aligned} \Delta\tau^g_{\text{mo}}(t_4^0) &= \Delta\tau^g\left(\tau^g(t_4^0)\right) + \Delta_2^g + \Delta_2^s \\ \Delta\tau^s_{\text{mo}}(t_2^0) &= \Delta\tau^s\left(\tau^s(t_2^0)\right) + \Delta_1^g + \Delta_1^s. \end{aligned} \tag{6}$$

3) Desynchronisation in a Λ configuration: in the ACES/PHARAO mission we use the so-called Λ configuration. This configuration minimizes the error coming from the uncertainty on ISS orbitography (in [2] it has been shown that in this configuration the requirement on ISS orbitography is around 10 m). The Λ configuration is defined by $t_2 = t_3$, i.e. code C^2 is sent at antenna s when code C^1 is received at this antenna. This configuration is obtained by interpolating the observables. Then it can be shown that desynchronisation between clocks g and s at coordinate time t_2 is:

$$\tau^s(t_2) - \tau^g(t_2) = \frac{1}{2}\left(\Delta\tau^g_{\text{mo}}(t_4^0) - \Delta\tau^s_{\text{mo}}(t_2^0) + [T_{34} - T_{12}]^g\right). \tag{7}$$

C. Approximations

1) Coordinate / proper time transformation: in equation (7) remains one transformation from coordinate to proper time. We know that $T_{12} \sim T_{34} \sim 1$ ms. During this time interval we can consider that the gravitational potential and velocity of the ground station are constant. Therefore we can do the approximation:

$$[T_{34} - T_{12}]^g = (1 - \epsilon_g(t_2))\,(T_{34} - T_{12}), \tag{8}$$

where

$$\epsilon_g(t) = \frac{GM}{r_g(t)c^2} + \frac{v_g^2(t)}{2c^2},$$

M is the Earth mass, $r_g(t)$ and $v_g(t)$ are the radial coordinate and the coordinate velocity of the ground clock at coordinate time t. Orders of magnitude of these corrective terms are:

$$\begin{aligned} \frac{GM}{r_g c^2} T_{34} &\sim 0.6 \text{ ps} \\ \frac{v_g^2}{2c^2} T_{34} &\sim 0.002 \text{ ps} \end{aligned}$$

The gravitational term is just at the limit of the required accuracy. The velocity term is well below, so we can neglect it. Final formula for desynchronisation is then:

$$\begin{aligned} \tau^s(t_2) - \tau^g(t_2) = \frac{1}{2}\Big(&\Delta\tau^g_{\text{mo}}(t_4^0) - \Delta\tau^s_{\text{mo}}(t_2^0) \\ &+ \left(1 - \frac{GM}{r_g(t_2)c^2}\right)(T_{34} - T_{12})\Big). \end{aligned} \tag{9}$$

2) Λ configuration: in the Λ configuration we suppose that $T_{23} = 0$. However, this will never be exactly 0 and it will be known with a precision δT_{23}. This will add a supplementary delay $\delta(\tau^s - \tau^g)$ to desynchronisation (7):

$$\delta(\tau^s - \tau^g)(t_2) = (\epsilon_g(t_2) - \epsilon_s(t_2))\,\delta T_{23}$$

Orders of magnitude are:

$$\begin{aligned} \frac{GM}{c^2}\left(\frac{1}{r_g} - \frac{1}{r_s}\right) &\sim 2.8 \cdot 10^{-11} \\ \frac{v_g^2 - v_s^2}{2c^2} &\sim -3.3 \cdot 10^{-10} \end{aligned}$$

With the required accuracy on the MWL, $|\delta(\tau^s - \tau^g)| \lesssim 0.3$ ps, we deduce the following constraint on δT_{23}:

$$\delta T_{23} \lesssim 0.9 \text{ ms}.$$

This constraint is much less constraining than the one coming from orbitography, which is $\delta T_{23} \lesssim 1$ μs (see [2]).

D. Atmospheric delays

The downlink is composed of two one-way links of frequencies f_2 and f_3, represented respectively by coordinate time sequence $(t_3^0, t_3, t_4, t_4^0, t_8^0)$ and $(t_5^0, t_5, t_6, t_6^0, t_9^0)$. These two links are affected by a ionospheric delay that depends on their respective frequencies, whereas the tropospheric delay does not depend on the link frequency (we neglect dispersive effects at this stage). We write:

$$T_{12} = \frac{R_{21}}{c} + \Delta_{12}^{\text{iono}}(f_1) + \Delta_{12}^{\text{tropo}} + \Delta_{21}^{\text{Shapiro}} \tag{10}$$

$$T_{34} = \frac{R_{34}}{c} + \Delta_{34}^{\text{iono}}(f_2) + \Delta_{34}^{\text{tropo}} + \Delta_{34}^{\text{Shapiro}} \tag{11}$$

$$T_{56} = \frac{R_{56}}{c} + \Delta_{56}^{\text{iono}}(f_3) + \Delta_{56}^{\text{tropo}} + \Delta_{56}^{\text{Shapiro}} \tag{12}$$

where $R_{ij} = |\vec{x}_g^{\text{a}}(t_j) - \vec{x}_s^{\text{a}}(t_i)|$ is the range, $\vec{x}_s^{\text{a}}$ and $\vec{x}_g^{\text{a}}$ are respectively position vectors of space and ground antennas, $r_s^{\text{a}} = |\vec{x}_s^{\text{a}}|$, $r_g^{\text{a}} = |\vec{x}_g^{\text{a}}|$ and:

$$\Delta_{ij}^{\text{Shapiro}} = \frac{2GM}{c^3} \ln\left(\frac{r_s^{\text{a}}(t_i) + r_g^{\text{a}}(t_j) + R_{ij}}{r_s^{\text{a}}(t_i) + r_g^{\text{a}}(t_j) - R_{ij}}\right) + \mathcal{O}(c^{-4}) \tag{13}$$

Ionospheric and tropospheric delays are around or below 100 ns, whereas Shapiro delay (term in c^{-3}) is below 10 ps for the ACES/PHARAO mission (see [3] and fig.8).

1) Ionospheric delay: in order to deduce ionospheric delays, we combine the two ground observables to be free of tropospheric delays. We obtain:

$$\begin{aligned}&\Delta\tau^g(\tau^g(t_0^6)) - \Delta\tau^g(\tau^g(t_0^4)) = [T_{34} - T_{56}]^s \\ &+ \left[T_{46}^0\right]^s - \left[T_{46}^0\right]^g + \Delta_2^s - \Delta_3^s + \left[[\Delta_2^g - \Delta_3^g]^t\right]^s\end{aligned} \tag{14}$$

Here we impose that $T_{46}^0 = 0$, i.e. both f_2 and f_3 measurements are done at the ground station at the same local time. However, this will never be exactly zero, there will be a remaining δT_{46}^0 introducing a timing error $\delta T \simeq \left(\epsilon_s(t_4^0) - \epsilon_g(t_4^0)\right)\delta T_{46}^0$. With a required accuracy $\delta T \lesssim 0.3$ ps, we obtain the following constraint:

$$\delta T_{46}^0 \lesssim 0.9 \text{ ms}.$$

We expect that $|T_{34} - T_{56}| \lesssim 100$ ns (see [3]); therefore we can neglect the coordinate to proper time transformation in eq.(14). We can also neglect this transformation for the delays. Then eq.(14) is equivalent to:

$$\Delta\tau_{\text{mo}}^g(t_6^0) - \Delta\tau_{\text{mo}}^g(t_4^0) = T_{34} - T_{56} \tag{15}$$

From eqs.(11), (12) and (15) we obtain:

$$\Delta_{56}^{\text{iono}}(f_3) - \Delta_{34}^{\text{iono}}(f_2) = \Delta\tau_{\text{mo}}^g(t_4^0) - \Delta\tau_{\text{mo}}^g(t_6^0) + \frac{R_{34} - R_{56}}{c} \tag{16}$$

where we neglected the difference of the Shapiro delays between the two downlinks, which can be shown to be completely negligible.

Now we can calculate S the Slant Total Electron Content (STEC). The ionospheric delay affects oppositely code (co) and carrier (ca) and may be approximated as follows (with S.I. units):

$$\Delta_{\text{co}}^{\text{iono}}(f) = \frac{40.308}{cf^2}S + \frac{7527}{f^3}\int N_e\left(\vec{B}\cdot\vec{k}\right)\mathrm{d}L \tag{17}$$

$$\Delta_{\text{ca}}^{\text{iono}}(f) = -\frac{40.308}{cf^2}S - \frac{7527}{2f^3}\int N_e\left(\vec{B}\cdot\vec{k}\right)\mathrm{d}L \tag{18}$$

where N_e is the local electron density along the path, STEC $S = \int N_e \mathrm{d}L$, $\vec{B}$ is the Earth's magnetic field and $\vec{k}$ the unit vector along the direction of signal propagation. It has been shown that higher order frequencies effect can be neglected for the determination of desynchronisation [3].

We suppose that for a triplet of observables $\{\Delta\tau^s(\tau^s(t_2^0)), \Delta\tau^g(\tau^g(t_4^0)), \Delta\tau^g(\tau^g(t_6^0))\}$, the direction of signal propagation and of the magnetic field along the line of sight do not change, and $|\vec{B}| \simeq B_0$. Then:

$$\Delta_{\text{co}}^{\text{iono}}(f) = \frac{40.308}{cf^2}S\left(1 + \frac{7527c}{40.308f}B_0\cos\theta_0\right) \tag{19}$$

$$\Delta_{\text{ca}}^{\text{iono}}(f) = -\frac{40.308}{cf^2}S\left(1 + \frac{7527c}{80.616f}B_0\cos\theta_0\right), \tag{20}$$

where θ_0 is the angle between $\vec{B}$ and the direction of propagation of signal f_2 and f_3. Then we obtain:

$$\begin{aligned}\left[\Delta_{56}^{\text{iono}}(f_3) - \Delta_{34}^{\text{iono}}(f_2)\right]_{\text{co}} &= \frac{40.308}{c}\left(\frac{1}{f_3^2} - \frac{1}{f_2^2}\right)S \\ &\times\left[1 + \frac{7527c}{40.308}\frac{f_2^3 - f_3^3}{f_2 f_3\left(f_2^2 - f_3^2\right)}B_0\cos\theta_0\right]\end{aligned} \tag{21}$$

$$\begin{aligned}\left[\Delta_{56}^{\text{iono}}(f_3) - \Delta_{34}^{\text{iono}}(f_2)\right]_{\text{ca}} &= -\frac{40.308}{c}\left(\frac{1}{f_3^2} - \frac{1}{f_2^2}\right)S \\ &\times\left[1 + \frac{7527c}{80.616}\frac{f_2^3 - f_3^3}{f_2 f_3\left(f_2^2 - f_3^2\right)}B_0\cos\theta_0\right]\end{aligned} \tag{22}$$

These equations, together with equation (16), give the STEC S. The value of S can then be used to correct the uplink ionospheric delay.

2) Tropospheric delay and range: by adding ground and space observables of links f_1 and f_2 we obtain:

$$\begin{aligned}&\Delta\tau^s(\tau^s(t_2^0)) + \Delta\tau^g(\tau^g(t_4^0)) + \Delta_1^g + \Delta_2^g \\ &+ \left[[\Delta_1^s + \Delta_2^s]^t\right]^g = \left[T_{23}^0\right]^s - \left[T_{23}^0\right]^g - [T_{12} + T_{34}]^g\end{aligned}$$

As in the previous section, it can be shown that $\left[T_{23}^0\right]^s - \left[T_{23}^0\right]^g = 0$ if T_{23}^0 is known with a precision $\delta T_{23}^0 \lesssim 0.9$ ms. We neglect the coordinate to proper time transformations for delays and obtain:

$$T_{12} + T_{34} = -\left(1 + \frac{GM}{r_g(t_2)c^2}\right)\left(\Delta\tau_{\text{mo}}^s(t_2^0) + \Delta\tau_{\text{mo}}^g(t_4^0)\right),$$

Then, from eqs.(10)-(11) we obtain:

$$\begin{aligned}\frac{R_{21} + R_{34}}{c} &= -\left(1 + \frac{GM}{r_g(t_2)c^2}\right)\left(\Delta\tau_{\text{mo}}^s(t_2^0) + \Delta\tau_{\text{mo}}^g(t_4^0)\right) \\ &- \left(\Delta_{12}^{\text{iono}}(f_1) + \Delta_{34}^{\text{iono}}(f_2) + \Delta_{12}^{\text{tropo}} + \Delta_{34}^{\text{tropo}} + \Delta_{21}^{\text{Shap}} + \Delta_{34}^{\text{Shap}}\right)\end{aligned}$$

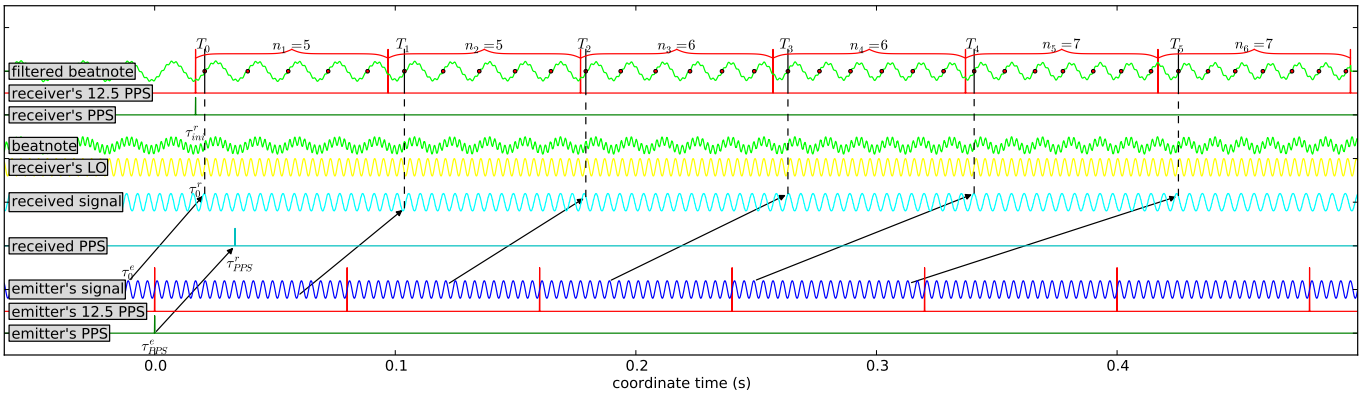

Fig. 5. Both emitter's and receiver's signals are represented against coordinate time scale. Red dots on the filtered beatnote indicate zero crossings on ascending edge. n_m is the number of red dots between two 12.5 PPS pulses. T_{m-1} is the proper time of the first red dot in the same sequence. Propagation times are represented by black arrows. Here signal frequency is much lower than in reality, and Doppler effect is strongly magnified in order to show variation of n_m.

where Shapiro delay is added for completeness; practically it should be negligible compare to the error of the tropospheric model. This equation shows that range and tropospheric delays are degenerated. Range can be calculated with a model for tropospheric delay, and tropospheric delay can be calculated from an estimation of range.

III. MicroWave Link modems

We explain here basic principles of the ground/space modems developed by TimeTech/Astrium for the ACES/PHARAO mission, that will be linked to the clocks and the antennas. This principle is illustrated on fig.5. At emitter and receiver are generated a PPS signal (one Pulse Per Second), a 12.5 PPS (one pulse every 80 ms, the period of measurements), and a periodic signal (either code at 100 MHz or carrier). Let e be the emitter and r the receiver. A PPS impulsion sent at local time τ^e_{pps} of the emitter is received at local time τ^r_{pps} of the receiver. Local time τ^r_{pps} is recorded by the modem for each received PPS.

When received, the periodic signal (blue) is mixed with a local oscillator (yellow) which frequency is not far from the received frequency, and filtered to obtain the low frequency part of the beatnote (green). The beatnote frequency is around 195 kHz for code and 729 kHz for carrier. The receiver modem records the time of the first ascending zero-phase of the beatnote signal after the 12.5 PPS signal. We call this observable T_m, where m is the number of the 80 ms sequence. Finally, the modem counts the number of ascending zero-phase n_m during sequence m.

τ^r_{pps}, T_m, n_m and m are the basic observables of the modem, which we call TT observables, and are recorded for code and carrier signals. The modem internal clock is reset every 4 s. However the observables are also roughly dated in UTC, which allows resolving the 4 s ambiguity between resets.

A. From TT to ST observables

Let $\phi_e(\tau^e)$ and $\phi_r(\tau^r)$ be respectively the phase of emitted and received signals, changing with local time of emitter and receiver. Let's consider two signals: one emitted at emitter local time τ^e_0 and received at receiver local time τ^r_0, and another one, emitted at τ^e_1 and received at τ^r_1 (see fig. 6). The phase increase between these two signals is equal at emitter and receiver:

$$\phi_e(\tau^e_1) - \phi_e(\tau^e_0) = \phi_r(\tau^r_1) - \phi_r(\tau^r_0). \tag{23}$$

The received signal is mixed with a local oscillator signal such that the beatnote phase is:

$$\phi_{\text{b}}(\tau^r) = \begin{cases} \phi_{\text{L.O.}}(\tau^r) - \phi_r(\tau^r) & \text{(for code)} \\ \phi_r(\tau^r) - \phi_{\text{L.O.}}(\tau^r) & \text{(for carrier)} \end{cases} \tag{24}$$

Signs are different for code and carrier; we will write subsequent formulas in a compact way with the sign in black for code and red for carrier. We assume $\phi(\tau) = \omega\tau + \text{cst}$, where ω is the pulsation of the considered signal. Then, from eqs.(23) and (24) we deduce:

$$\tau^e_1 - \tau^e_0 = \frac{\omega_{\text{L.O.}}}{\omega_e}(\tau^r_1 - \tau^r_0) \overset{+}{-} \frac{1}{\omega_e}(\phi_{\text{b}}(\tau^r_1) - \phi_{\text{b}}(\tau^r_0)) \tag{25}$$

We introduce the ST observable, which links local time of emission to local time of reception: $\Delta\tau^r(\tau^r) = \tau^e - \tau^r$. From

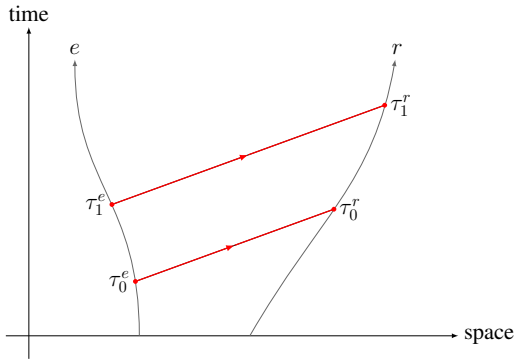

Fig. 6. Link between phase, emitter and receiver local times.

eq.(25) we get:

$$\begin{aligned}\Delta\tau_1^r(\tau_1^r) - \Delta\tau_0^r(\tau_0^r) = \quad & \left(\frac{\omega_{\text{L.O.}}}{\omega_e} - 1\right)(\tau_1^r - \tau_0^r) \\ & + \frac{1}{\omega_e}(\phi_{\text{b}}(\tau_1^r) - \phi_{\text{b}}(\tau_0^r))\end{aligned} \tag{26}$$

Let's apply this formula to the MWL modem by introducing the TT observables: $\tau_0^r = T_{m-1}$ and $\tau_1^r = T_m$. From definition of T_m and n_m observables we know that $\phi_{\text{b}}(T_m) - \phi_{\text{b}}(T_{m-1}) = 2\pi n_m$. Then we deduce from eq.(26):

$$\begin{aligned}\Delta\tau_m^r(T_m) = \quad & \Delta\tau_{m-1}^r(T_{m-1}) \\ & + \left(\frac{\omega_{\text{L.O.}}}{\omega_e} - 1\right)(T_m - T_{m-1}) \\ & + \frac{2\pi n_m}{\omega_e}\end{aligned} \tag{27}$$

where $\Delta\tau_m^r$ is the ST observable corresponding to sequence m. This recursive formula allows to find all ST observables from TT observables, if the first term $\Delta\tau_0^r(T_0)$ is known. We notice than in case of zero Doppler, the last two lines of the equation cancel, and the ST observable $\Delta\tau^r$ should be constant with local time.

Relative accuracy of ST observables during one passage of ISS is:

$$\begin{aligned}\delta(\Delta\tau_m^r) \quad & \sim \quad \left|\frac{\omega_{\text{L.O.}}}{\omega_e} - 1\right| \cdot \delta T_m \\ & \sim \quad \begin{cases} \frac{195 \text{ kHz}}{100 \text{ MHz}} \cdot 10 \text{ ns} \sim 20\ ps & \text{(code)} \\ \frac{729 \text{ kHz}}{13.5 \text{ GHz}} \cdot 10 \text{ ns} \sim 0.5\ ps & \text{(carrier)} \end{cases}\end{aligned}$$

where accuracy of T_m observables, $\delta T_m \sim 10$ ns, can be deduced from modem internal clock, which frequency is around 100 MHz. However, δT_m is underestimated here because other noise sources than the internal clock may count. The goal here is not to do a precise accuracy budget but rather get a lower limit.

B. Initial term determination

What is the first term of the iterative series (27)? Our goal is to determine $\Delta\tau_0^r(T_0)$ with an absolute accuracy < 100 ps, which is required for ground-space time transfer. For frequency transfer, we should be able to bridge the gap between two passages with an accuracy depending on the duration between them, which can be read on fig.2 (e.g. 1.5 ps for two passages separated by one orbital period).

Let

$$\Delta\tau_{\text{pps}}^r(\tau_{\text{pps}}^r) = \tau_{\text{pps}}^e - \tau_{\text{pps}}^r = \tau_{\text{ini}}^r - \tau_{\text{pps}}^r \tag{28}$$

be the ST observables linked to TT observables τ_{pps}^r, and τ_{ini}^r be the receiver local time of generation of the PPS, which is by definition of the experiment equal to the local time of emission of the same PPS signal τ_{pps}^e. As τ_{pps}^e can be guessed from a UTC tag, $\Delta\tau_{\text{pps}}^r(\tau_{\text{pps}}^r)$ is known and can be linked to $\Delta\tau_0^r(\tau_0^r)$ with the help of eq.(26):

$$\begin{aligned}\Delta\tau_0^r(\tau_0^r) = \quad & \Delta\tau_{\text{pps}}^r(\tau_{\text{pps}}^r) + \left(\frac{\omega_{\text{L.O.}}}{\omega_e} - 1\right)(\tau_0^r - \tau_{\text{pps}}^r) \\ & - \frac{1}{\omega_e}(\Phi_{\text{b}}(\tau_0^r) - \Phi_{\text{b}}(\tau_{\text{pps}}^r))\end{aligned} \tag{29}$$

From the values of T_m and n_m one can determine the beatnote phase at τ_{pps}^r. The uncertainty in that determination is $\delta\Phi_b(\tau_{\text{pps}}^r) \sim \omega_b \cdot \delta T_m \sim 0.012$ rad. The uncertainty of the two last terms on the right side of the equation is then ~ 20 ps, which is sufficient. However, $\Delta\tau_{\text{pps}}^r$ is known with the modem internal clock accuracy, i.e. $\delta(\Delta\tau_{\text{pps}}^r) \sim 10$ ns. Even averaging on a complete data set is not sufficient, reaching ~ 580 ps accuracy with 300 points. Then we need a method to obtain a precise PPS observable.

1) Precise PPS observable: the emitter PPS is phase coherent with the code phase and the receiver PPS is phase coherent with the local oscillator phase. Then we can use the internal counter and the code phase observables to follow the phase precisely and derive a more accurate pps observable that we call $\Delta\tau_{\text{ppps}}^r$.

The receiver local oscillator is phase coherent with the receiver PPS (it has a zero crossing at τ_{ini}^r), then:

$$\Phi_{\text{L.O.}}(\tau_{\text{ini}}^r) = 2\pi N_{\text{L.O.}} \tag{30}$$

where $2N_{\text{L.O.}}$ is an integer. Similarly the emitted (and received) code is phase coherent with the emitted (received) PPS, so we have

$$\Phi_e(\tau_{\text{pps}}^e) = \Phi_r(\tau_{\text{pps}}^r) = 2\pi N_B \tag{31}$$

where N_B is an integer. Using eqs.(24), (28), (30) and (31) we obtain:

$$\Delta\tau_{\text{ppps}}^r(\tau_{\text{pps}}^r) = \frac{1}{\omega_{\text{L.O.}}}\left(2\pi N - \phi_{\text{b}}(\tau_{\text{pps}}^r)\right), \tag{32}$$

where $2N = 2(N_{\text{L.O.}} - N_B)$ is an integer. Provided we can determine the integer $2N$ exactly, the uncertainty on $\Delta\tau_{\text{ppps}}^r$ is $\delta\phi_{\text{b}}/\omega_{\text{L.O.}} \sim 20$ ps. The value of N is determined by using the direct measurement $\Delta\tau_{\text{pps}}^r(\tau_{\text{pps}}^r)$ in eq.(32) above:

$$N = \frac{1}{2\pi}\left(\omega_{\text{L.O.}}\Delta\tau_{\text{pps}}^r(\tau_{\text{pps}}^r) + \Phi_{\text{b}}(\tau_{\text{pps}}^r)\right) \tag{33}$$

Uncertainty of the second term in (33) is $\sim 0.012/(2\pi) \sim 2 \cdot 10^{-3}$, therefore negligible. However, uncertainty of the first term is $\sim \omega_{\text{L.O.}} \cdot 10 \text{ ns}/(2\pi) \sim 1$, which is insufficient. One solution is to average over all PPS measurements of a continuous passage, which should be sufficient for realistically useful passages (e.g. > 50 s).

Finally using the precise PPS observable $\Delta\tau_{\text{ppps}}^r(\tau_{\text{pps}}^r)$ calculated from eq.(32) in eq.(29) reaches the required accuracy for time transfer.

2) Bridging the gap: to perform ground-space frequency comparisons on long term one needs to link observables from two different ISS passages. It is then necessary to determine precisely the time elapsed from one passage to another thanks to the TT observables. Let's call $\Delta\tau_0(\tau_0)$ and $\Delta\tau_0'(\tau_0')$ the

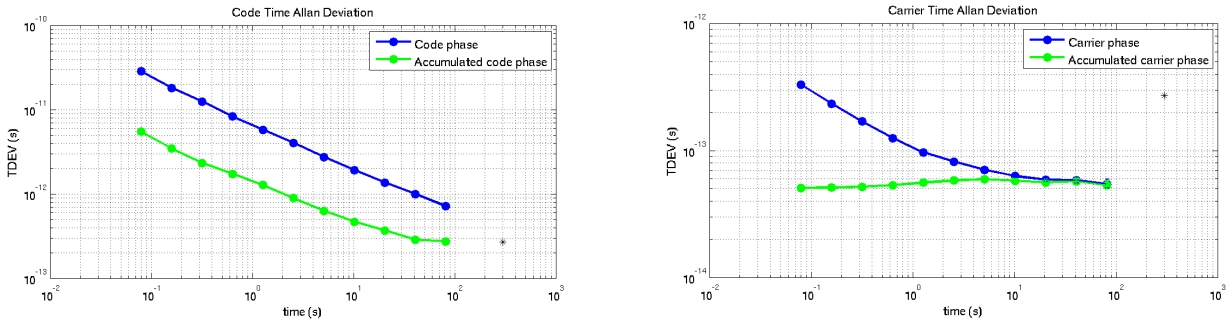

(a) Code observables

(b) Carrier observables

Fig. 7. Short term stability (TDEV) of ST observables, derived from either code/carrier phase or accumulated code/carrier phase.

initial terms of two different passages (in this section we omit the r indices on ST observables $\Delta\tau^r$ and on local time τ^r). The error on their absolute determination is ~ 20 ps. However we want to reach $\delta\left(\Delta\tau'_0(\tau'_0) - \Delta\tau_0(\tau_0)\right) \lesssim x$, where x is a specification that depends on the duration separating the two passages and can be read from fig.2 (e.g. 1.5 ps for one orbital period separation). From eq.(26) we deduce:

$$\begin{aligned}\phi_{\mathrm{b}}(\tau'_0) - \phi_{\mathrm{b}}(\tau_0) = \quad & -\omega_e(\Delta\tau'_0(\tau'_0) - \Delta\tau_0(\tau_0)) \\ & + (\omega_{\mathrm{L.O.}} - \omega_e)\,(\tau'_0 - \tau_0)\end{aligned} \tag{34}$$

Moreover, we know that $\phi_{\mathrm{b}}(\tau'_0) - \phi_{\mathrm{b}}(\tau_0) = 2\pi N_g$, where N_g is an unknown integer. We deduce that:

$$\begin{aligned}N_g = \frac{1}{2\pi} \quad & (-\omega_e(\Delta\tau'_0(\tau'_0) - \Delta\tau_0(\tau_0)) \\ & + (\omega_{\mathrm{L.O.}} - \omega_r)\,(\tau'_0 - \tau_0))\end{aligned} \tag{35}$$

It can be shown that the accuracies of the different terms in this equation are sufficient to determine N_g without ambiguity. Then we deduce:

$$\Delta\tau'_0(\tau'_0) - \Delta\tau_0(\tau_0) = \left(\frac{\omega_{\mathrm{L.O.}}}{\omega_e} - 1\right)(\tau'_0 - \tau_0) - \frac{2\pi N_g}{\omega_e} \tag{36}$$

This equation links ST observables from two passages to ~ 20 ps, which is not sufficient as can be seen from fig.2. Using several pairs of code observables to determine this quantity will not increase the accuracy, as the error for each data pairs will be correlated. Two solutions can be envisioned. One can use carrier phase observables. However, it remains to be seen if the phase ambiguity (integer N_g) can be solved for carrier phase. This will be studied in another article. Second solution would be to use another observable from the MWL modem: the accumulated phase T_m^{acc}, which is the sum of all dates of ascending zero-phase during sequence m.

In fig.7 is shown the short-term stability of ST observables, calculated either using T_m or T_m^{acc} observables, for code (fig.7(a)) and carrier (fig.7(b)). It can be seen that using T_m^{acc} observables increases measurements accuracy. However, code accuracy is still not sufficient to bridge the gap between two passages: we assume that ST observables uncertainty is $\delta(\Delta\tau) \sim 3 \times \mathrm{TDEV}_0$, where TDEV_0 is the Time deviation for $\tau = 0.08$ s, the period of measurements. Then, from fig. 7(a), $\delta(\Delta\tau) \sim 90$ ps for code phase and $\delta(\Delta\tau) \sim 18$ ps for accumulated code phase. This is not sufficient to bridge any gap. From fig. 7(b) we deduce $\delta(\Delta\tau) \sim 0.9$ ps for carrier phase and $\delta(\Delta\tau) \sim 0.15$ ps for accumulated carrier phase. Any of these two observable is sufficient to bridge a gap of 30 mn or larger. It remains to be seen how to solve the phase ambiguity for carrier phase, which will be studied in another article.

IV. Simulation and Data Analysis

The SYRTE team writes an independent data analysis software, in order to make the most of the ACES/PHARAO mission data. This software is written in Python language. In order to test it, we wrote a simulation that generates (noisy) TT observables, as well as theoretical ST observables. This simulation is written in Matlab language, and is as much as possible independent from the data analysis software.

A. Simulation

The simulation takes as input orbitography of the ISS and one Ground Station (GS) in a Celestial Reference System. From orbitography files it simulates the proper times given by ISS and GS clocks, and the time transfer between these

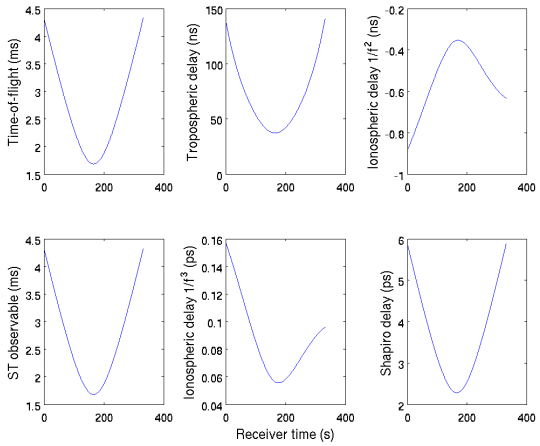

Fig. 8. Contribution of atmospheric and Shapiro delays in the simulated time-of-flight of the f_1 signal for carrier observables.

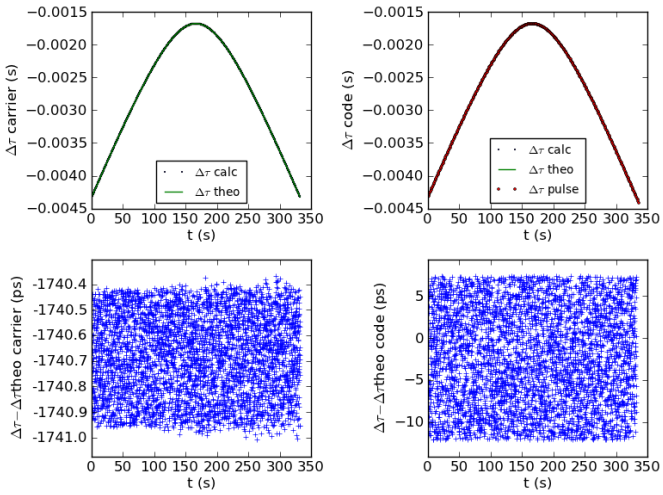

Fig. 9. Pre-processing software: comparison between ST observables calculated from simulated TT observables, and theoretical ST observables, for carrier (left) and code (right).

two clocks, using a modelization of the MWL. Observables are given in terms of TT and ST observables. Moreover, theoretical values of the scientific products are given in order to test the data analysis software.

In fig.8 we have plotted different contributions included in the signal time-of-flight of signal $f_1 \simeq 13.5$ GHz. Minimum elevation of ISS is taken as 10°, and atmospheric parameters are temperature $T = 298$ K, pressure $p = 1$ bar and water vapor pressure $e = 0.5$ bar. A sinusoidal variation is added to atmospheric parameters, with a period of 24 hours, and a Chapman layer model is used to calculate the STEC.

Tropospheric delay is dominant in the time-of-flight, with a value of several 10 ns. We used here a Saastamoinen model, which is not really reliable at low elevation of ISS. The dispersive part of troposphere has not been taken into account, and it remains to be seen if this is necessary. Ionosphere is dispersive such that ionospheric delay can be separated in two contributions: an effect that scales with $1/f^2$ and one that scales with $1/f^3$ (see eqs.(17)-(18)). The second order contribution is around 1 ns and the third contribution around 0.1 ps, below mission accuracy. However these effects are much larger for the $f_3 = 2.25$ GHz signal: around 40 ns for second order term and 20 ps for third order term. Then third order terms cannot be ignored. Finally the Shapiro delay of several ps is slightly over the required accuracy.

B. Data analysis

An independent pre-processing software has been written, using equations from sec.III. It takes TT observables from the simulation, transforms them to ST observables and compares the result to the theoretical ST observables coming from the simulation. One example can be seen on fig.9. It can be seen that ST observables are well recovered, with a noise which is coherent with previous estimations. However here the noise is underestimated because all noise sources have not been

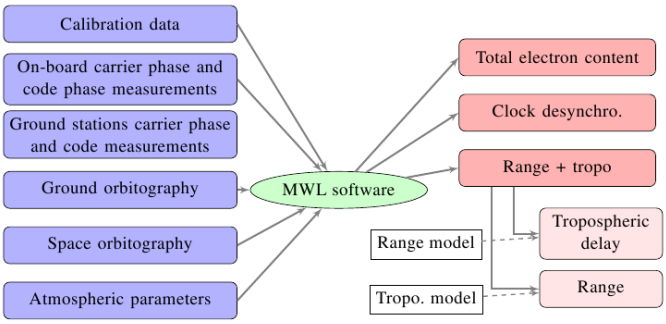

Fig. 10. Full data analysis software: illustration of inputs and outputs.

included (only the modem internal clock noise). The absolute value of the ST code observable is found thanks to the method of the initial term determination, with an uncertainty less than 20 ps (explaining why the data cloud is not centered on 0). The phase ambiguity for carrier observable has not been solved, explaining the constant bias between the recovered and the theoretical ST carrier observables.

The full data analysis software is being written but not finished yet. We explain its basic principle on fig.10. A special care is taken for file naming, data classifying, file formats and conventions. Indeed many data from several different sources will have to be used and these issues can be critical. Current implementation has a modular design and is currently being developed.

V. Conclusion

We have written a theoretical description of one-way and two-way satellite time and frequency transfer and developed a model of the MicroWave Link in the frame of the ACES/PHARAO mission. This description has been used to write a data analysis software and a simulation to test it. The simulation is written in its first version, and used to assess our pre-processing software. The design of the data analysis software has been done in a modular way, and most of the building blocks are ready.

Several questions remain: how to solve the phase ambiguity for the carrier observable, what is the dispersive effect of the troposphere?

References

[1] L. Cacciapuoti and C. Salomon, "Aces mission objectives and scientific requirements," ESA, Tech. Rep., 2010, aCE-ESA-TN-001, Issue 3 Rev 0.

[2] L. Duchayne, F. Mercier, and P. Wolf, "Orbit determination for next generation space clocks," *Astronomy and Astrophysics*, vol. 504, pp. 653–661, Sept. 2009.

[3] L. Duchayne, "Transfert de temps de haute performance : le lien micro-onde de la mission ACES," Ph.D. dissertation, Observatoire de Paris, France, 2008. [Online]. Available: http://tel.archives-ouvertes.fr/tel-00349882/fr/

T2L2 : Ground to ground Time Transfer

Etienne Samain, Myrtille Laas-Bourez, Clément Courde, Pierre Exertier, Jean-Marie Torre, Nicolas Martin, Jean-Louis Oneto, Mourad Aimar, Francis Pierron.
GeoAzur, Observatoire de la Côte d'Azur
Grasse, France
mailto:Etienne.Samain@oca.eu

Philippe Guillemot
CNES – French Space Agency
Toulouse, France
philippe.guillemot@cnes.fr

Sylvie Leon
CNES – French Space Agency
Paris, France

Abstract

T2L2 (Time Transfer by Laser Link), developed by both CNES and OCA permits the synchronization of remote ultra stable clocks over intercontinental distances. The principle is derived from laser telemetry technology with a dedicated space equipment deigned to record arrival times of laser pulses at the satellite. Using laser pulses instead of radio frequency signals used in classical time transfer techniques (GPS, TWSTFT), T2L2 permits to realize some links between distant clocks with time stability of a few picoseconds and accuracy better than 100 ps.

From the launch in 2008, several campaigns were done to demonstrate both the ultimate time accuracy and time stability capabilities. It includes some experiments implemented in collocation to directly compare T2L2 time transfer residuals with the direct link between the stations, and some ground to ground time transfer between ultra stable clocks.
After reminding the principle and the objectives of the mission, this paper will give a description of a non common view campaign performed between OCA and Tahiti, will give some results for a collocation campaign led at OCA and will present the next experiment which will permit to evaluate the long term time stability of T2L2.

I. INTRODUCTION

T2L2 is a time transfer technique based on an international laser ranging network (roughly 40 laser stations) and a dedicated space segment implemented on-board the altimeter satellite Jason 2. The project is operational since 2008 [1], [2], [3]. T2L2 relies on the propagation of laser pulses that permit to enhance the performance of time transfer by one or two order of magnitudes as compared to existing microwave techniques such as GPS and Two-Way Satellite Time and Frequency Transfer (TWSTFT).

It provides the capability to compare today's most stable frequency standards with unprecedented stability and accuracy [4]. Ultimate expected T2L2 performances are in the 100 ps range for accuracy, with a time stability of about 1 ps over 1,000 s and 10 ps over one day [5].

T2L2 ground time transfer can be performed in a common view configuration when the distance between the stations are lower than roughly 5000 km or in a non common view mode when the distance is greater. In that case, some additional noises must be considered to take into account the time stability of both the on-board oscillator (provided by the space equipment DORIS) and the ground clocks to synchronize over the time interval between data acquisition. In order to evaluate the T2L2 performances in those 2 modes, we have realized and planned several dedicated campaigns:

- a special campaign between Tahiti and France for both common view and non common operations (May – Oct. 2011),
- a collocation campaign at OCA for time transfer accuracy involving RF link, direct comparison and T2L2 (April 2012),
- a long term time stability with a common clock and two laser station (June – Aug. 2012).
-

These experiments imply some accurate comparisons between some techniques which are radically different: RF link, optical link, direct comparison. It is crucial to define a unique reference points in the laboratories and to refer these different time transfer techniques to this point.

Firstly, this paper presents the technological deployment and highlights the complexity of time transfer techniques comparisons during the Tahiti campaign. In the next part, we focus on the collocation campaign at OCA for time transfer accuracy. We will present the hardly obtained results. Then we will described the next campaign that will begin next month in OCA. To finish we will gives an overview of the T2L2 web site and conclude with the description of the our futur work and progress.

II. TAHITI TIME TRANSFER CAMPAIGN

This campaign was done during 6 months at the French University of Polynesia (UPF) from May to October 2011 (Fig. 1).

Figure 1 French University of Polynesia; Moblas 8 station in the centre, FTLRS on the left

The experimental putting in places includes (Fig. 2) the Moblas 8 and FTLRS Laser Stations, an Hydrogen Maser, a GPS time transfer unit, a DORIS system and the T2L2 Calibration station (event timer, time distribution). The H-Maser (MH 23), the FTLRS station and the calibration station was installed at UPF especially for that experiment; the Moblas 8 station and the DORIS equipment are installed on the UPF site definitively. The Hydrogen Maser (MH23) is the nominal low noise time reference for the FTLRS station and for the T2L2 calibration equipment (Fig. 2). The central equipment of the time and frequency reference of the whole setting-up is the T2L2 calibration station.

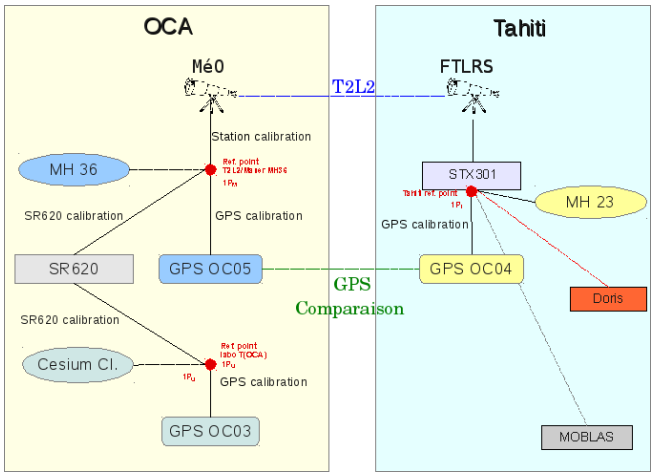

Figure 2. Time delays definition during the Tahiti time transfer campaign

Time delays have been defined to compare absolute T2L2 time transfer and other time transfer technique. Due to several issues with both GPS receivers (Septentrio PolarX2 OC05 and Dicom GTR50 OC04), we have also data from other time devices in OCA (Dicom GTR50 OC03, Stanford SR620) to take into account. Fig. 2 shows time delays defined to highlight time transfer link between various techniques.

The objectives of that campaign were 5 folds:

- collocation at Tahiti between FTLRS and Moblas8
- Adaptation of Moblas 8 in order to perform a T2L2 time transfer with a station which is not designed for that purpose (laser start time in the picosecond domain)
- T2L2 comparison between Moblas8 and FTLRS
- DORIS monitoring
- Non common view time transfer with a site in the pacific which has never been observed in term of optical time transfer

118 passes was acquired during the 6 months mission with FTLRS. The Moblas 8 station was not operational at the beginning of the mission (telescope problems). Common passes with both FTLRS and Moblas 8 were only acquired from the beginning of September.

Data acquired during this campaign will now be processed by the T2L2 Scientific Mission Center. As mentioned before, the on-board clock noise and drift will introduce a significant degradation of the performance of the time transfer if they are not corrected. That implies some important works in order to minimize this noise and to define a synthetic on-board time scale, work which is still under going. A dedicated paper will be proposed in few weeks to present results.

III. CO-LOCATION CAMPAIGN AT OCA

A. *Experiment setting-up*

The aim of the campaign is to carry on a ground to ground time transfer in a collocation mode between two distinct clocks linked to 2 distinct laser stations. This campaign was done in March and April 2012 at OCA with the fix MéO station and the mobile FTLRS stations.

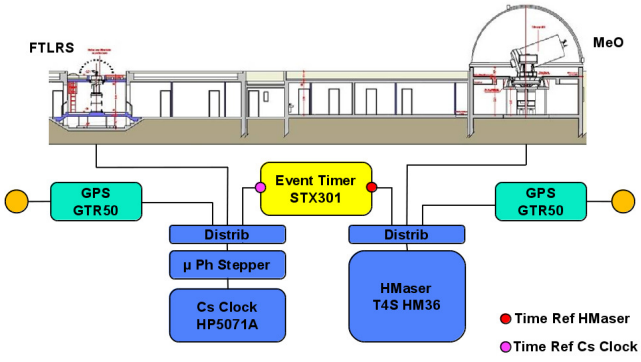

Figure 3. The MéO – FTLRS co-location in Grasse: simplified experimental setup

The mobile station FTLRS was link to a primary Cesium clock and the MéO station to a H-Maser MH36 clock (Fig. 3).

B. *Time transfer techniques links*

We measured time delays to have each laser station calibrated thanks to the time reference points of each clock. We used the dedicated calibration station described in Fig. 4.

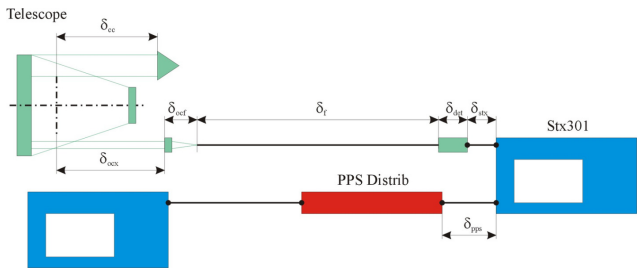

Figure 4: calibration setup for a given laser station. MéO and FTLRS were calibrated with the same equipment and 2 distinct optical fibres.

In order to inter-compare different time transfer techniques, we have defined and measured time delays to connect all the measuring instruments to reference points. The first reference point is the laboratory point outcome-based on our primary cesium clock (hereafter 1Pu). The second one (hereafter $1P_M$) come from our H-maser clock (MH36). Fig. 5 shows the link between the time transfer techniques. STX301 event timer [6] and a Stanford SR620 instrument were settled to perform direct measurement. We used two independent GPS receivers (Dicom GTR50) to inter-compare T2L2 results with GPS.

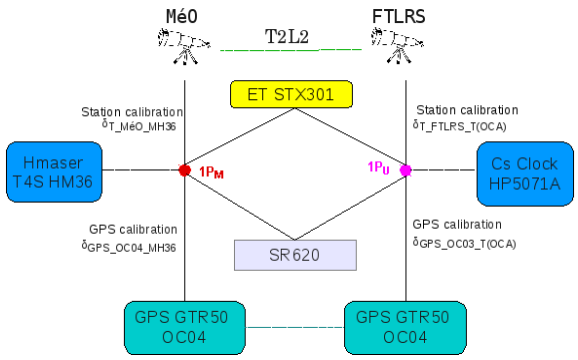

Figure 5. Time delays definition during the Grasse MéO-FTLRS co-location campaign

Time equation that permits to accurately time-stamped laser pulses (station calibration) is given by:

$\delta_T = \delta_{cal} + \delta_{prg}$, where δ_{cal} is the difference between absolute measurement (calibration) and station measurement and δ_{prg} the global propagation between cross axes and the PPS unit.

The difference between the stations are given by :

$\delta_{TFtlrs} - \delta_{TMeo} = \delta_{calFtlrs} - \delta_{calMeo} - (\delta_{ocxFtlrs} - \delta_{ocxMeo}) - (\delta_{fFtlrs} - \delta_{fMeo})$

where δ_{ocx} represent the propagation between the spatial reference of the telescope and δ_f the propagation in the fibres used to transport the laser pulses from the station to the T2L2 calibration station.

The GPS receiver OC04 was calibrated with the traveller reference receiver OPM4 (from Observatoire de Paris OP) in February 2010 using P3 technique. The principle is to determine the delay on P1 and P2 of the local receiver with the two receivers in common clock. The traveller receiver has been calibrated first with the reference OPMT receiver and after the campaign to ensure the measurement continuity. Delays P1 and P2 are general delays including delay antenna, the antenna cable delay, the receiver and the 1PPS delay to the reference point. The combined uncertainty for the common views GPS P3 given by this calibration campaign is 4.82 ns.

A measurement campaign between the two OCA GPS receivers OC04 and OC03 was conducted in December 2010 to calibrate the receiver OC03 compared to OC04.

C. *Results and conclusion*

Fig. 6 represents for a given pass of the satellite the phase difference between T2L2 and the direct comparison measured by STX301.

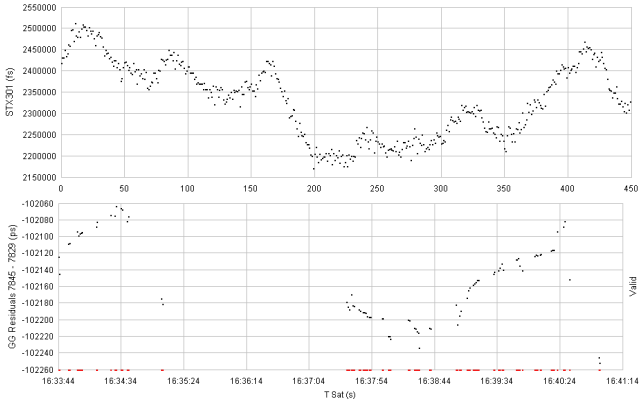

Figure 6. H-Maser – Cesium difference observed by STX301 event timer (above) and T2L2 (below).

If we take into account all the time delay coming from the calibration, the optical fibre the geometry of the telescopes we have:

- from **T2L2**: $\delta_{TFtlrs} - \delta_{TMeo} = \delta_{T2L2} =$ 95910 ps (uncertainty < 200 ps)
- from **STX301** (direct measurement): δ_{STX301} = 96076 ps (uncertainty < 10 ps)
- from **SR620** (direct measurement): δ_{SR620} = 95787 ps (uncertainty < 1000 ps)
- from **GPS** comparison: $\delta_{OC04} - \delta_{OC03} = \delta_{GPS}$ = 89818 ps (uncertainty < 5000 ps)

The difference between T2L2 and the direct comparison δ_{T2L2} - δ_{STX301} is 166 ps which gives a good agreement as compared to the global uncertainty of the whole setup which is evaluated to 200 ps. In the same order the direct measurement with the SR620 gives a good agreement (difference of 123 ps) compare to the device uncertainty.

The difference between GPS l3p and T2L2 is around 6 ns. This result seems slightly removed from results expected. We will do new calibration and measurement to understand it.

IV. LONG TERM TIME STABILITY COLLOCATION COMPARISONS

The objective of that comparison is to evaluate the performance of the T2L2 link in term of long term time stability at the level of the picosecond. The experiment is done with 2 distinct laser stations linked to a unique clock. This permits to eliminate the noise that would have been introduced by two independent clocks. To get a time transfer at the picosecond level it is crucial to have an ultra stable time distribution between the reference clock and the laser stations.

If one considers a typical distance between the stations of 100 m, a thermal sensitivity of the cable used to propagate the time reference of 100 fs/m °C and a long term thermal variation in the range 20°, the total delay variation can reach 200 ps which is far away to picosecond objective. To solve this difficulty we designed an ultra stable time signal generator including an event timer able to monitor the absolute time delay variation in the propagation of the signals (Fig. 7). This monitoring is made through a double propagation of the signal emitted by the distributor and repeated by the user (laser station).

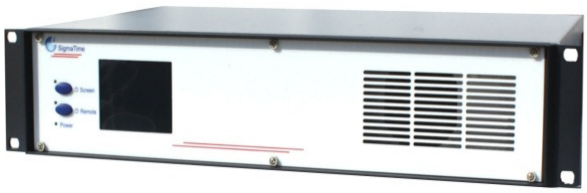

Figure 7 : Ultra stable time signal generator including a sub-picosecond event timer able to measure the time propagation of the signals.

The repeatability error of the instrument is better than 1 ps rms for the PPS distribution and better than 800 fs rms for the time delay measurement made by the event timer.

The experiment is planned to begin in June 2012 during 3 months campaign. It will be installed at OCA between MéO and FTLRS stations connected to the H-Maser HM36 (Fig. 8).

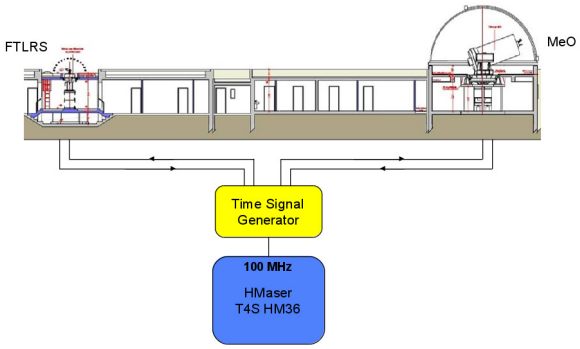

Figure 8. T2L2 long term stability with MéO and FTLRS in co-location in Grasse: simplified experimental setup

V. T2L2 WEB SITE

A T2L2 web site is now available at: https://t2l2.oca.eu
The user can found information about:

- Laser station acquisition
- Number of event acquired on-board or DORIS oscillator monitoring
- Laser energy received
- Ground to space residuals and time Stability

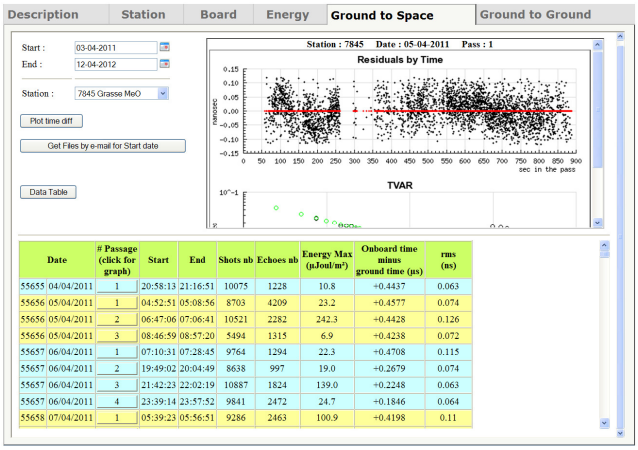

Figure 9 : T2L2 web site at https://t2l2.oca.eu

VI. FUTURE WORKS AND PROGRESS

The space instrument is running since June 2008. All the characteristics on-board are still nominal: there is no sign of weakness. The T2L2 experiment was initially designed for 2 years missions. A first extension of the mission was given by CNES in 2010 and another extension is going to be asked to CNES for 2013-2014.

This paper gives an overview of the T2L2 activities. We have given a description of the Tahiti campaign. We will provide soon a dedicated paper resuming data analysis and conclusion. The OCA campaigns need also extended works to finalise the inter-comparison between time transfer techniques.

The important next steps are:

- Ground to ground time transfer in a non common view configuration. It implies some important works in order to minimize the noise that could be introduce by the on-board oscillator (synthetic on-board time scale)
- International Calibration campaigns including laser station calibration and microwave time transfer calibration (GPS TWSTFT)

ACKNOWLEDGMENT

The authors wish to thanks the Moblas 8 teams from the UPF for operating the laser station at Tahiti.

REFERENCES

[1] P. Fridelance, E. Samain and C. Veillet, "*T2L2 - Time transfer by Laser link : A New Optical Time Transfer Generation*", Experimental Astronomy Vol.7 Num.3 Sept.97

[2] Ph. Guillemot, E. Samain, P. Vrancken, P. Exertier, S. Leon, "Time transfer by laser link - T2L2 : An Opportunity to Calibrate RF Links", Proceedings of the PTTI 2008, pp 95-106

[3] P. Exertier, E. Samain, P. Bonnefond, and P. Guillemot, 2010, "*Status of the T2L2/Jason2 Experiment,*" Journal Advances in Space Research, Doris Special Issue, 46, 1559-1565, doi:10.10.16/j.asr.2010.06.028

[4] P. Vrancken, "Characterization of T2L2 (Time Transfer by Laser Link) on the Jason 2 Ocean Altimetry Satellite and Micrometric Laser Ranging", Thesis, Université de Nice - Sophia Antipolis, 2008.

[5] Ph. Guillemot, P. Exertier, E. Samain, F. Pierron, J.-M. Torre, S. Leon, "Time Transfer by Laser Link - T2L2 : Results of the First Year of Operation", Proceedings of the PTTI 2009, pp 67-79

[6] E. Samain, P. Fridelance, Ph. Guillemot, "An Ultra Stable Event Timer Designed for T2L2", Proceedings of the EFTF/IFCS 2010

Analysis of the Motional Capacitance of the Electric Equivalent Circuit of Quartz-Crystal Tuning Fork Using L-Shaped Bar Model with Torsion Spring and in Consideration of Electric Field Distribution

Takahiro Ishikawa
Shinshu University
Faculty of Engineering
Nagano, Japan
efica@live.jp

Hideaki Itoh
Shinshu University
Faculty of Engineering
Nagano, Japan
rokuro1@shinshu-u.ac.jp

***Abstract*- We derived the motional capacitance of quartz-crystal tuning fork using L-shaped bar model with torsion spring and in consideration of both electric field distribution and the width of electrodes. If the width and the length of electrodes are taken into consideration, the calculated values of motional capacitance of the tuning fork with 100μm in thickness are good agreement with the measured ones under three boundary conditions; free-free bar, clamped-free bar, and L-shaped bar models.**

I. INTRODUCTION

The quartz-crystal tuning fork is miniaturized in progress and nowadays the tuning fork with 100μm in thickness is mainly used as a standard clock in wrist watch application.

To date, there are some methods of calculating motional capacitance of the electrical equivalent circuit of the quartz-crystal tuning fork at resonance. In the bimorph flexure model [1] [2], the calculated value of motional capacitance coincides with the measured one for the tuning fork with 750 μm in thickness. However if the thickness is thinner than 750 μm, the calculated value doesn't coincide with measured one. In the electric field distribution model [3] [4], the calculated value of motional capacitance becomes from 1.3 to 1.9 times the measured one for the tuning fork with 100 μm in thickness and the accuracy is still not satisfactory. So we analyze the motional capacitance among two electrical equivalent capacitances to establish the analytical accuracy method using L-shaped bar model in consideration of electric field distribution, the width of electrodes, and a torsion spring at the joint of the arm and the base. The introduction of both torsion spring and the base into the analysis also serves as the preparation for applying this technique to the analysis of the motional capacitance of quartz-crystal tuning fork tactile sensor [1] [2].

We derived the motional capacitance of quartz-crystal tuning fork using L-shaped bar model with torsion spring and in consideration of both electric field distribution and the width of electrodes. We verified whether the calculated value of the motional capacitance for the tuning fork with 100 μm in thickness coincided with the measured one or not and also investigated how the width of electrodes and the base affected the motional capacitance.

II. ANALYSYS

In order to analyze the tuning fork easily, the right half of the quartz-crystal tuning fork and the coordinate system as shown in Fig. 1 are adopted. The width of electrodes in the x-direction is w_m, and the width of electrodes in the z-direction is equal to the thickness t_0 of the tuning fork. Moreover, the electrode does not cover the base.

The dynamic electromechanical coupling factor k_m is expressed using the motional capacitance C_a and static capacitance C_0 of the electric equivalent circuit of the quartz-crystal tuning fork at resonance by [5]

$$\frac{C_a}{C_0} = {k_m}^2 + O\left({k_m}^4\right) \cong {k_m}^2 . \qquad (1)$$

If we derive the dynamic electromechanical coupling coefficient in (1), then we can derive the motional capacitance. Therefore, firstly, we derive the displacement u_2 (Refer to Fig. 2) of the beam B.

In order to analyze the right half of the quartz-crystal tuning fork as shown in Fig. 1, we introduce the L-shaped bar model and a torsion spring as shown in Fig. 2. L-shaped bar model consists of the beam A of the base having the bending displacement u_1 and the beam B of the arm having the bending displacement u_2. The base is joined to the arm using a torsion spring and Sezawa's approximation.

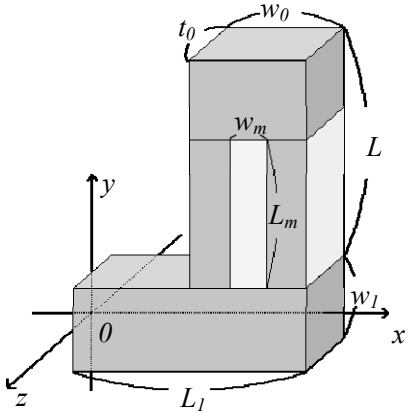

Figure 1. Electrode configurations and the coordinate system of L-shaped bar model for analysis

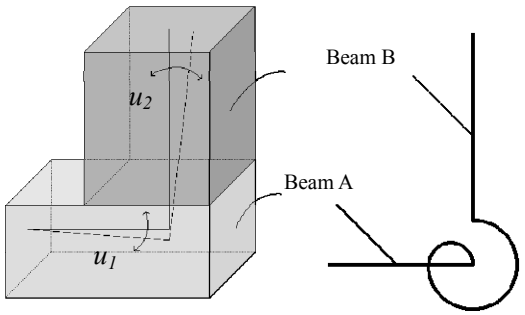

Figure 2.The vibration of L-shaped bar model and a torsion spring

Since the displacement of the base and the rotation angle are set to be *0* from the boundary conditions of the fixed end of beam A at $x= 0$ in Fig.2, we have

$$u_1 = 0\,, \tag{2}$$

$$\frac{\partial u_1}{\partial x} = 0\,. \tag{3}$$

The bending moment M_1 is given by

$$M_1 = -E_1 I_1 \frac{\partial^2 u_1}{\partial x^2}\,, \tag{4}$$

where E_1 is the Young's modulus of the base, and $I_1=w_1{}^3 t_0/12$.

From the Sezawa's approximation [6] which is made the shear force S_1 of beam A equal to the inertia force of beam B at the joint of beams A and B at $x=L_1$, S_1 is given by

$$S_1 = -E_1 I_1 \frac{\partial^3 u_1}{\partial x^3} = -\rho A_2 L \frac{\partial^2 u_1}{\partial t^2} = \rho A_2 L p^2 u_1\,, \tag{5}$$

where S_1 is the shear force of the beam A, ρ is the mass density of quartz crystal, $A_2=w_0 t_0$, and $p=2\pi f$ (f is the resonance frequency).

Since the longitudinal displacement at the joint of beams A and B is disregarded from Sezawa's approximation, we have

$$at \;\; y = 0, \qquad u_2 = 0\,. \tag{6}$$

From the torsion spring model at the joint of beams A and B at $x=L_1$ and $y=0$, the two boundary conditions are given by

$$\frac{\partial u_1}{\partial x} = \frac{\partial u_2}{\partial y}\,, \tag{7}$$

$$M_2 = -E_2 I_2 \frac{\partial^2 u_2}{\partial y^2}\,, \tag{8}$$

$$M_1 - M_2 + R\frac{\partial u_2}{\partial y} = 0\,, \tag{9}$$

where E_2 is the Young's modulus of beam B, $I_2=w_0{}^3 t_0/12$, and R is the rotational Winkler coefficient [7].

Since the top end of beam B at $y=L$ is the free end, we have

$$M_2 = 0\,, \tag{10}$$

$$S_2 = -E_2 I_2 \frac{\partial^3 u_2}{\partial y^3} = 0\,. \tag{11}$$

The equations of motion of the beams A and B are given by

$$A : \rho\frac{\partial^2 u_1}{\partial t^2} + \frac{E_1 I_1}{A_1}\frac{\partial^4 u_1}{\partial x^4} = 0, \tag{12}$$

$$B : \rho\frac{\partial^2 u_2}{\partial t^2} + \frac{E_2 I_2}{A_2}\frac{\partial^4 u_2}{\partial y^4} = 0, \tag{13}$$

where $A_1=w_1 t_0$.

By assuming $u_1 = U_1 e^{jpt}$, the characteristic equation of (12) is given by

$$\frac{E_1 I_1}{A_1}\lambda_1{}^4 - p^2\rho = 0,$$

$$\therefore \pm\lambda_1 = \pm\sqrt[4]{\frac{\rho A_1 p^2}{E_1 I_1}} \tag{14}$$

.

The characteristic one of (13) is similarly given by

$$\pm\lambda_2 = \pm\sqrt[4]{\frac{\rho A_2 p^2}{E_2 I_2}} \tag{15}$$

.

Therefore, u_1 and u_2 are denoted by

$$u_1 = C_1\cos\lambda_1 x + C_2\sin\lambda_1 x + C_3\cosh\lambda_1 x + C_4\sinh\lambda_1 x, \tag{16}$$

$$u_2 = C_5\cos\lambda_2 y + C_6\sin\lambda_2 y + C_7\cosh\lambda_2 y + C_8\sinh\lambda_2 y, \tag{17}$$

where C_1~C_8 are constants.

Substituting (2) and (3) into (16), u_1 is given by

$$u_1 = C_1(\cos\lambda_1 x - \cosh\lambda_1 x) + C_2(\sin\lambda_1 x - \sinh\lambda_1 x)\,. \tag{18}$$

Substituting (18) into (5), (5) is rearranged by

$$C_1\{(\sin\alpha - \sinh\alpha) + \gamma(\cos\alpha - \cosh\alpha)\}$$

$$+ C_2\{\gamma(\sin\alpha - \sinh\alpha) - (\cos\alpha + \cosh\alpha)\} = 0, \tag{19}$$

where $\gamma=\rho A_2 L p^2/E_1 I_1 \lambda_1{}^3$, and $\alpha=\lambda_1 L_1$.

From (6) and (17), we have

$$u_2 = C_5(\cos\lambda_2 y - \cosh\lambda_2 y) + C_6\sin\lambda_2 y + C_8\sinh\lambda_2 y. \tag{20}$$

Substituting (10) and (11) into (20) using $\lambda_2 L=\beta$, we have

$$C_5(\cos\beta + \cosh\beta) + C_6\sin\beta - C_8\sinh\beta = 0, \tag{21}$$

$$C_5(\sin\beta - \sinh\beta) - C_6\cos\beta + C_8\cosh\beta = 0. \tag{22}$$

From (7), (18), and (20), we have

$$C_1(\sin\alpha + \sinh\alpha) - C_2(\cos\alpha - \cosh\alpha) + \xi(C_6 + C_8) = 0, \tag{23}$$

where $\xi=\lambda_2/\lambda_1$.

From (9), we have

$$C_1(\cos\alpha + \cosh\alpha) + C_2(\sin\alpha + \sinh\alpha)$$

$$+ \lambda_2\delta(C_6 + C_8) - 2\eta C_5 = 0, \tag{24}$$

where $\delta=R/E_1 I_1 \lambda_1{}^2$, and $\eta=E_2 I_2 \lambda_2{}^2/E_1 I_1 \lambda_1{}^2$.

Next, a set of linear algebraic equations (19), (23), (21), (22), and (24) is expressed by matrices, it becomes

$$\begin{bmatrix} X & Y & 0 & 0 & 0 \\ \sin\alpha+\sinh\alpha & -(\cos\alpha-\cosh\alpha) & 0 & \xi & \xi \\ 0 & 0 & \cos\beta+\cosh\beta & \sin\beta & -\sinh\beta \\ 0 & 0 & \sin\beta-\sinh\beta & -\cos\beta & \cosh\beta \\ \cos\alpha+\cosh\alpha & \sin\alpha+\sinh\alpha & -2\eta & \delta\lambda_2 & \delta\lambda_2 \end{bmatrix} \begin{bmatrix} C_1 \\ C_2 \\ C_5 \\ C_6 \\ C_8 \end{bmatrix} = 0, \tag{25}$$

where X=(sin α-sinh α)+γ(cos α-cosh α),

and $Y=\gamma(\sin\alpha-\sinh\alpha)-(\cos\alpha+\cosh\alpha)$.

From the first and second rows of (25), we have

$$\begin{bmatrix} C_1 \\ C_2 \end{bmatrix} = -\frac{1}{\Delta}\begin{bmatrix} 0 & -\xi Y & -\xi Y \\ 0 & \xi X & \xi X \end{bmatrix}\begin{bmatrix} C_5 \\ C_6 \\ C_8 \end{bmatrix}, \quad (26)$$

where $\Delta=-X(\cos\alpha-\cosh\alpha)-Y(\sin\alpha+\sinh\alpha)$.

Substituting the fifth row of (25) into (26), we have

$$\begin{bmatrix} -2\eta & Z+\delta\lambda_2 & Z+\delta\lambda_2 \end{bmatrix}\begin{bmatrix} C_5 \\ C_6 \\ C_8 \end{bmatrix} = 0, \quad (27)$$

where

$$Z = \frac{\xi}{\Delta}\left[Y(\cos\alpha+\cosh\alpha)-X(\sin\alpha+\sinh\alpha)\right].$$

When (27) and the third and fourth rows of (25) are combined, we have

$$\begin{bmatrix} -2\eta & Z+\delta\lambda_2 & Z+\delta\lambda_2 \\ \cos\beta+\cosh\beta & \sin\beta & -\sinh\beta \\ \sin\beta-\sinh\beta & -\cos\beta & \cosh\beta \end{bmatrix}\begin{bmatrix} C_5 \\ C_6 \\ C_8 \end{bmatrix} = 0. \quad (28)$$

From (28), eigenvalue equation can be obtained as

$$\eta(\sin\beta\cosh\beta-\cos\beta\sinh\beta) + (Z+\delta\lambda_2)(1+\cos\beta\cosh\beta) = 0. \quad (29)$$

Therefore, the resonance frequency is given by

$$f = \frac{\beta^2}{2\pi L^2}\sqrt{\frac{E_2 I_2}{\rho A_2}}. \quad (30)$$

After the eigenvalue equation is rearranged, the rotational Winkler coefficient R is rewritten as

$$R = E_1\frac{I_1}{L_1}\frac{\alpha}{\xi}\left\{\eta\frac{\cosh\beta\sin\beta-\sinh\beta\cos\beta}{1+\cos\beta\cosh\beta}-Z\right\}. \quad (31)$$

Next, we must derive u_2. From (28), we have

$$\frac{C_6}{C_8} = \frac{2\eta\sinh\beta-(Z+\delta\lambda_2)(\cos\beta+\cosh\beta)}{2\eta\sin\beta+(Z+\delta\lambda_2)(\cos\beta+\cosh\beta)} = \frac{2\eta\cosh\beta+(Z+\delta\lambda_2)(\sin\beta-\sinh\beta)}{2\eta\cos\beta-(Z+\delta\lambda_2)(\sin\beta-\sinh\beta)} = \frac{1}{g}, \quad (32)$$

$$\frac{C_5}{C_6} = \frac{(Z+\delta\lambda_2)(1+g)}{2\eta} = \frac{g\sinh\beta-\sin\beta}{\cos\beta+\cosh\beta} = \frac{\cos\beta-g\cosh\beta}{\sin\beta-\sinh\beta} = G. \quad (33)$$

Therefore, from (20) and (33) using $C_6=C$, we have

$$u_2 = C\{G(\cos\lambda_2 y-\cosh\lambda_2 y)+\sin\lambda_2 y+g\sinh\lambda_2 y\}. \quad (34)$$

If we make the width w_1 of the base infinite, the displacement u_2 and the eigenvalue equation of L-shaped bar change into that of the clamped-free bar.

First, about η and $(Z+\delta\lambda_2)$, we have

$$\lim_{w_1\to\infty}\eta = \lim_{I_1\to\infty}\frac{E_2 I_2\lambda_2{}^2}{E_1 I_1\lambda_1{}^2} = 0, \quad (35)$$

$$\lim_{w_1\to\infty}(Z+\delta\lambda_2) = \lim_{I_1\to\infty}\left(Z+\frac{R}{E_1 I_1\lambda_1{}^2}\lambda_2\right) = Z. \quad (36)$$

Substituting (35) and (36) into (32) and (33), we have

$$\lim_{w_1\to\infty} g = \frac{Z(\cos\beta+\cosh\beta)}{-Z(\cos\beta+\cosh\beta)} = -1, \quad (37)$$

$$\lim_{w_1\to\infty} G = \lim_{g\to-1}\frac{\cos\beta-g\cosh\beta}{\sin\beta-\sinh\beta} = \frac{\cos\beta+\cosh\beta}{\sin\beta-\sinh\beta}. \quad (38)$$

Therefore, u_2 and eigenvalue equation in a limiting case are given by

$$\lim_{w_1\to\infty} u_2 = C\left\{\frac{\cos\beta+\cosh\beta}{\sin\beta-\sinh\beta}(\cos\lambda_2 y-\cosh\lambda_2 y) + (\sin\lambda_2 y-\sinh\lambda_2 y)\right\} = C'\left\{(\cos\beta+\cosh\beta)(\cos\lambda_2 y-\cosh\lambda_2 y) + (\sin\beta-\sinh\beta)(\sin\lambda_2 y-\sinh\lambda_2 y)\right\}, \quad (39)$$

$$\lim_{w_1\to\infty}\left\{\eta(\sin\beta\cosh\beta-\cos\beta\sinh\beta) + (Z+\delta\lambda_2)(1+\cos\beta\cosh\beta)\right\} = Z(1+\cos\beta\cosh\beta) \qquad \therefore \beta\cong 1.875. \quad (40)$$

From (39), if we make the width w_1 of the base infinite, the displacement u_2 changes into the equation of the clamped-free bar model [4]. Moreover, since the term of the Winkler coefficient has disappeared out of (40), the influence of the torsion spring disappears out of the eigenvalue equation and the eigenvalue equation changes into the equation of the clamped-free bar model. So the formulas of the displacement u_2 and eigenvalue β are not contradictory to the vibration behavior of L-shaped bar model.

From (34), the stress T_2 can be shown by

$$T_2 = \frac{x}{S_{22}^E}C\lambda_2{}^2\left\{G(\cos\lambda_2 y+\cosh\lambda_2 y) + \sin\lambda_2 y-g\sinh\lambda_2 y\right\}, \quad (41)$$

where S_{22}^E is compliance of the quartz for the beam B.

Using the dynamic elastic energy density u_m, the dynamic electric energy density u_e, and the piezo-electric energy density u_p, the dynamic electromechanical coupling factor k_m is defined by

$$k_m{}^2 = \frac{u_p'{}^2}{u_m' u_e'}. \quad (42)$$

In order to calculate each energy density, the domain of integration is determined in consideration of the width and length of the electrodes covered over the arms of the tuning fork.

At this time, for piezoelectric energy density, we assume that a whole surface of the tuning fork is covered with electrodes by considering that the effect of width of electrodes on piezoelectric energy density is very small.

$$u_m' = \frac{1}{2w_0 t_0 L}\int_0^L\int_{-\frac{t_0}{2}}^{\frac{t_0}{2}}\int_{-\frac{w_0}{2}}^{\frac{w_0}{2}} S_{22}^E T_2{}^2\,dxdzdy \quad (43)$$

$$u_e' = \int_0^L \frac{1}{w_m t_0 L_m}\frac{d}{dy}\left(\frac{1}{2}C_0\Phi_0{}^2\right)dy \quad (44)$$

$$u_p' = -\frac{1}{2w_0 t_0 L_m}\int_0^{L_m}\int_{-\frac{t_0}{2}}^{\frac{t_0}{2}}\int_{-\frac{w_0}{2}}^{\frac{w_0}{2}} d_{32}\frac{\partial \Phi}{\partial x}T_2\,dxdzdy \quad (45)$$

If an applied voltage is set to be V, potentials $\overline{\Phi}$ and Φ_0 are defined as follow [3];

$$\overline{\Phi} = \overline{\Phi}_s - \frac{\overline{\Phi}_{\lambda 1} + \overline{\Phi}_{\lambda 2}}{2}, \quad (46)$$

$$\overline{\Phi}_s = \frac{1}{w_0 t_0}\iint_s \Phi(x,z)dxdz, \quad (47)$$

$$\overline{\Phi}_{\lambda 1} = \frac{1}{t_0}\int_{-\frac{t_0}{2}}^{\frac{t_0}{2}} \Phi\left(-\frac{w_0}{2}, z\right)dz, \quad (48)$$

$$\overline{\Phi}_{\lambda 2} = \frac{1}{t_0}\int_{-\frac{t_0}{2}}^{\frac{t_0}{2}} \Phi\left(\frac{w_0}{2}, z\right)dz, \quad (49)$$

$$\Phi_0 = V - 0 = V. \quad (50)$$

In order to analyze the potential Φ(x, z) using Fourier series in Cartesian coordinate system [8] for the right half section of the beam B, the coordinate transformation is carried out as shown in Fig. 3.

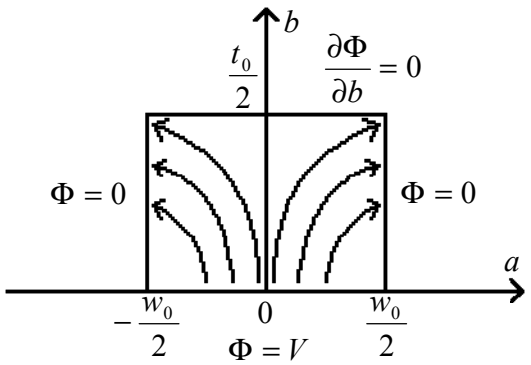

Figure 3. Boundary conditions for Φ(*X, Y*) in the right half section of the tuning fork

The coordinate transformation adopted here is as follows:

$$a = x, \quad (51)$$

$$b = \frac{t_0}{2} - z. \quad (52)$$

The potential Φ(*a, b*) should be subjected to the following equations as

$$\Phi(a,b) = A(a)B(b), \quad (53)$$

$$\frac{\partial^2 \Phi}{\partial a^2} + \frac{\partial^2 \Phi}{\partial b^2} = 0. \quad (54)$$

Substituting (53) into (54), we have

$$A(a) = A_1 \sin na + A_2 \cos na, \quad (55)$$

$$B(b) = A_3 \sinh nb + A_4 \cosh nb, \quad (56)$$

where A_1, A_2, A_3, and A_4 are integral constants and n is the coefficient.

From the boundary conditions as shown in Fig.3,

$$A\left(-\frac{w_0}{2}\right) = A\left(\frac{w_0}{2}\right) = 0 \quad (57)$$

.

From (55) and (57), we have

$$A_1 = 0 \quad (58)$$

$$A_2 \cos n\left(\frac{w_0}{2}\right) = 0 \quad (59)$$

From (59), the following results are obtained as

$$n = \frac{2q-1}{w_0}\pi \qquad (q = 0, \pm 1, \pm 2, \pm 3, \cdots). \quad (60)$$

Moreover, the norm of Fourier cosine transform is given by

$$N_A = \int_{-\frac{w_0}{2}}^{\frac{w_0}{2}} \cos^2\left(\frac{2q-1}{w_0}\pi a\right)da = \frac{w_0}{2}. \quad (61)$$

From a boundary condition at the upper surface $b=t_0/2$ in Fig.3,

$$\frac{\partial \Phi}{\partial b} = nA\left(A_3 \sinh nb + A_4 \cosh nb\right) = 0, \quad (62)$$

$$\Leftrightarrow \frac{A_4}{A_3} = -\tanh n\frac{t_0}{2}. \quad (63)$$

Thus, Φ(*a*, *b*) can be shown by

$$\Phi(a,b) = \sum_{q=1}^{\infty} I_q \cos\left(\frac{2q-1}{w_0}\pi a\right)\frac{\cosh\left(\frac{2q-1}{2}\pi\frac{t_0 - 2b}{w_0}\right)}{\cosh\left(\frac{2q-1}{2}\pi\frac{t_0}{w_0}\right)}, \quad (64)$$

where I_q is an arbitrary constant.

From (64) and the fact that $\Phi=V$ at $b=0$, we have

$$\Phi(a,0) = \sum_{q=1}^{\infty} I_q \cos\left(\frac{2q-1}{w_0}\pi a\right) = V. \quad (65)$$

From (61) and (65), I_q is determined as

$$I_q = \frac{1}{N_A}\int_{-\frac{w_0}{2}}^{\frac{w_0}{2}} \cos\left(\frac{2q-1}{w_0}\pi a\right)da = \frac{4V(-1)^{q+1}}{(2q-1)\pi}. \quad (66)$$

Therefore, the potential Φ(x, z) can be rewritten as

$$\Phi(x,z) = \sum_{q=1}^{\infty}\frac{4V(-1)^{q+1}}{(2q-1)\pi}\cos\left(\frac{2q-1}{2}\pi x\right)\frac{\cosh\left(\frac{2q-1}{2}\pi\frac{2z}{w_0}\right)}{\cosh\left(\frac{2q-1}{2}\pi\frac{t_0}{w_0}\right)}. \quad (67)$$

Therefore, (47), (48), and (49) can be written as

$$\overline{\Phi}_s = \frac{16}{\pi^3}\frac{w_0}{t_0}V\sum_{q=1}^{\infty}\frac{\tanh\left(\frac{2q-1}{2}\pi\frac{t_0}{w_0}\right)}{(2q-1)^3}, \quad (68)$$

$$\Phi_{\lambda 1} = 0. \quad (69)$$

$$\Phi_{\lambda 2} = 0. \quad (70)$$

$\overline{\Phi}$ can then be written as

$$\overline{\Phi} = \frac{16}{\pi^3}\frac{w_0}{t_0}V\sum_{q=1}^{\infty}\frac{\tanh\left(\frac{2q-1}{2}\pi\frac{t_0}{w_0}\right)}{(2q-1)^3}. \quad (71)$$

From the results described above, (43), (44), and (45) can be rewritten as

$$u'_m = \frac{1}{48}\frac{{w_0}^2}{L}\frac{C^2{\lambda_2}^3}{S_{22}^E}K_1, \tag{72}$$

$$u'_e = \frac{L}{2w_m t_0 L_m}{\Phi_0}^2\frac{dC_0}{dy}, \tag{73}$$

$$u'_p = \frac{1}{2L_m}\frac{d_{32}}{S_{22}^E}C\lambda_2\overline{\Phi}K_2, \tag{74}$$

where

$$K_1 = G^2\begin{pmatrix}\sin\beta\cos\beta+\sinh\beta\cosh\beta\\ +2\sin\beta\cosh\beta+2\sinh\beta\cos\beta+2\beta\end{pmatrix}$$

$$+2G\begin{Bmatrix}\sin^2\beta-g\sinh^2\beta+(\sin\beta\sinh\beta-\cos\beta\cosh\beta)\\ -g(\sin\beta\sinh\beta+\cos\beta\cosh\beta)+1+g\end{Bmatrix}$$

$$-\sin\beta\cos\beta+g^2\sinh\beta\cosh\beta$$

$$-2g(\sin\beta\cosh\beta-\cos\beta\sinh\beta)+(1-g^2)\beta,$$

$$K_2 = G(\sin\upsilon\beta+\sinh\upsilon\beta)-(\cos\upsilon\beta+g\cosh\upsilon\beta)+1+g,$$

and $\upsilon = L_m/L$.

From (42), the dynamic electromechanical coupling factor is obtained as

$$k_m^2 = 12\mu\frac{{d_{32}}^2}{S_{22}^E}\frac{w_m t_0}{{w_0}^2}\frac{\left(\frac{\overline{\Phi}}{\Phi_0}\right)^2}{\frac{dC_0}{dy}}, \tag{75}$$

$$\mu = \frac{2}{\upsilon\beta}\frac{{K_2}^2}{K_1}, \tag{76}$$

where μ is the efficiency of vibration.

Since the analysis is fulfilled for a right half of the arm, the motional capacitance is two times (75) as,

$$C_a \cong 2{k_m}^2 C_0 = 24\mu L_m\frac{{d_{32}}^2}{S_{22}^E}\frac{w_m t_0}{{w_0}^2}\left(\frac{\overline{\Phi}}{\Phi_0}\right)^2 \tag{77}$$

Next, we consider approximating a torsion spring to a plate spring. We must derive an inclination angle φ from the model as shown in Fig. 4, in order to investigate the validity of this approximation.

The moment M_1, the force P in the tangential direction to the length direction of the spring, and the force R in the normal direction to the length direction of the spring are working at the point A' which is located at the position of the radius r of the spring from origin and the point A shows the position of the equilibrium state. In Fig, 4, an angle φ is shown by $\angle AOA'$.

The point O is origin of the coordinate and also a fixed point. It is assumed that the rotation moment M_0 is acting on the spring.

A rotation moment M_0 can be denoted by the following equation as

$$M_0 = P\times r + M_1, \tag{78}$$

The bending moment M at an arbitrary point (x, y) is

$$M = P(r+y)+M_1 - Rx. \tag{79}$$

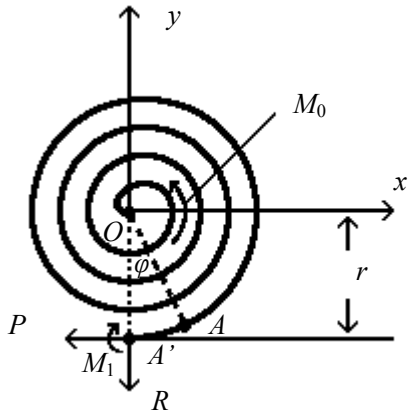

Figure 4. A swirl type spring having the same action as a torsion spring

Substituting (78) into (79), we have

$$M = M_0\left(1+\frac{y}{r}\right)-M_1\frac{y}{r}-Rx. \tag{80}$$

The energy U accumulated in the spring is given by

$$U = \int_0^l \frac{M^2}{2EI}dl, \tag{81}$$

where E is Young's modulus, I is the geometrical moment of inertia, l is the full length of the spring, and dl is the infinitesimal length of the spring.

From the *Castigliano*'s theorem [9], M_1 does not act on the inclination of the spring, so we have

$$\frac{\partial U}{\partial M_1} = \int_0^l \frac{M}{EI}\frac{\partial M}{\partial M_1}dl$$

$$= -\frac{1}{EI}\int_0^l\left\{M_0\left(1+\frac{y}{r}\right)-M_1\frac{y}{r}-Rx\right\}\frac{y}{r}dl = 0. \tag{82}$$

From the *Castigliano*'s theorem, the following formula of the inclination angle φ is similarly given by

$$\varphi = \frac{\partial U}{\partial M_0} = \int_0^l \frac{M}{EI}\frac{\partial M}{\partial M_0}dl$$

$$= \frac{1}{EI}\int_0^l\left\{M_0\left(1+\frac{y}{r}\right)-M_1\frac{y}{r}-Rx\right\}\left(1+\frac{y}{r}\right)dl. \tag{83}$$

As for the force R, we have similarly

$$\frac{\partial U}{\partial R} =$$

$$-\frac{1}{EI}\int_0^l\left\{M_0\left(1+\frac{y}{r}\right)-M_1\frac{y}{r}-Rx\right\}xdl = 0. \tag{84}$$

For the spring, the equations may be established as follows:

$$\int_0^l xdl \cong 0,\ \int_0^l ydl \cong 0,\ \int_0^l xydl \cong 0. \tag{85}$$

R=0 can be shown by (84) and (85).

Substituting (82) into R=0, we have

$$\int_0^l (M_0 - M_1)\frac{y^2}{r^2}dl = 0 \tag{86}$$

$$\therefore M_0 = M_1$$

After substituting the result of (86) into (78), we can easily show the result being P=0.

Substituting these results into (83), the inclination angle φ is given by

$$\varphi = \frac{M_0 l}{EI}. \tag{87}$$

Since φ in (87) holds the same form as the inclination angle θ of a plate spring mentioned later, the validity of approximating the torsion spring to the plate spring is guaranteed.

Figure 5 (b) shows the deformation of the beam (the plate spring) when the moment M is applied to the tip of the beam.

The one end A of the plate spring AB is fixed, the length of AB (the width of the base of the tuning fork) is w_1, and the thickness of AB is t_0. When the moment M is added to the other end B of AB, the displacement at the tip B is x, the inclination angle is θ, and the flexural rigidity of the plate spring is E_1I.

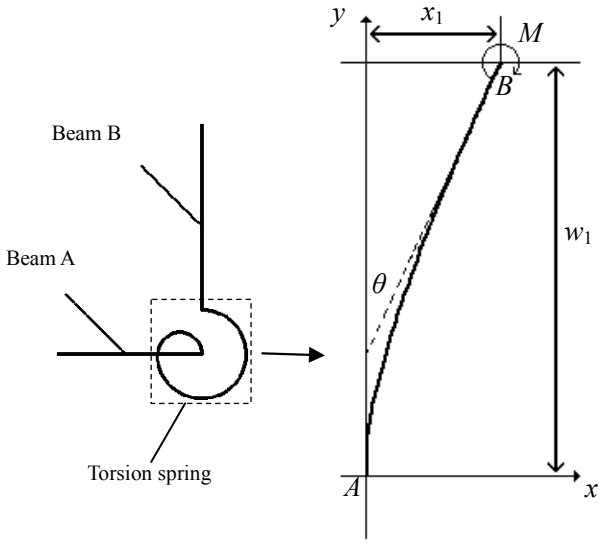

(a) Torsion spring (b) Plate spring

Figure 5. A plate spring is approximation of a torsion spring

The boundary conditions are given for the plate spring by

$at\ \ y = 0,$

$$x = 0, \tag{88}$$

$$\frac{dx}{dy} = 0, \tag{89}$$

$at\ \ y = w_1,$

$$E_1 I \frac{d^2 x}{dy^2} = -M, \tag{90}$$

$$E_1 I \frac{d^3 x}{dy^3} = 0. \tag{91}$$

From (88), (89), (90), and (91), the bending displacement x_1 and inclination angle θ at y=w_1 is shown by

$$x_1 = \frac{M w_1^{\,2}}{2E_1 I}, \tag{92}$$

$$\theta = \frac{M w_1}{E_1 I}. \tag{93}$$

When the plate spring inclines only by θ, the moment M can be shown using the rotational Winkler coefficient R by

$$M = R\theta. \tag{94}$$

Therefore, from (93), a righting moment is equal to

$$M = \frac{E_1 I}{w_1}\theta. \tag{95}$$

Since (95) is intrinsically equivalent to (87) for a torsion spring, the rotational Winkler coefficient can be denoted by

$$R = \frac{E_1 I}{w_1} = \frac{E_1}{w_1}\frac{w^3 t_0}{12} \geq 0, \tag{96}$$

where w is the width of the plate spring.

From (31) and (96), when L-shaped bar is in resonance, w can be denoted by

$$w = w_1 \sqrt[3]{12\frac{w_1}{L_1}\frac{\alpha}{\xi}\left\{\eta\frac{\cos\beta\sinh\beta - \sin\beta\cosh\beta}{1+\cos\beta\cosh\beta} - Z\right\}}. \tag{97}$$

If the value of the cubic root of (97) is almost constant, we can regard that the width w of the plate spring is approximately proportional to the width w_1 of the base.

III. Comparison Of Mesured And Calculated Values

We could obtain the calculated values of the motional capacitance for five quartz-crystal tuning forks. The impedance analyzer's measured points by one span are 801 points, its delay time is 1000 ms, its bandwidth is 5, its frequency span is 100 Hz, and OSC level is 100 mV. We measured the parameters of the electric equivalent circuit of the tuning fork at resonance with impedance analyzer and measured the sizes of electrodes covered over the tuning fork and its sizes with a surface texture measuring instrument.

One of five quartz-crystal tuning forks is 250 μm in thickness and is only made by the mechanical process, and others with 100 μm in thickness are made by the etching process.

Figure 6 shows the ratio of the calculated values to the measured ones of the motional capacitance for six analytical models: that is, (77), free-free and clamped-free bar models [4], and bimorph flexure model [1], and free-free bar and clamped-free bar models in consideration of the width of electrodes.

Figure 6 also shows that the calculated values of the motional capacitance are in greatly agreement with the measurement values under the boundary conditions of L-shaped bar and free-free bar and clamped free bar models in consideration of the width of electrodes. We can especially calculate the value of motional capacitance with errors less than 6% of the measured one using L-shaped bar model in consideration of the width of electrodes. The calculated values by bimorph flexure model are 0.3~0.5 times the measured values, and the calculated values under the boundary conditions of free-free bar and clamped-free bar models in no consideration of the width of electrodes are 1.3~1.9 times the measured values. Therefore, we can

calculate the motional capacitance of the quartz-crystal tuning fork with errors less than 6% of the measured one suing L-shaped bar model by taking the electric field distribution and the width of electrodes into consideration. The large shift of the calculated values from measured ones of the motional capacitance near 2.5 fF was observed because of the large deviation of the design of the tuning fork from the analytical model's design.

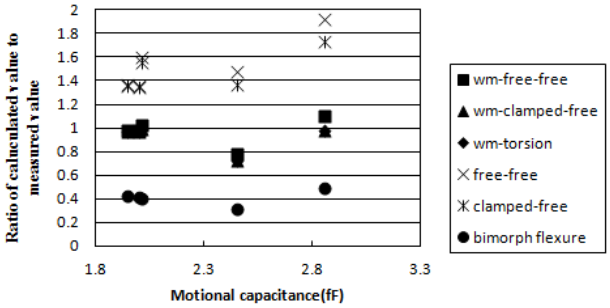

Figure 6. Ratio of the calculated values to the measured value against motional capacitance

Next, the relationship between the length ratio υ of the electrode to the full length of the bar and the efficiency of vibration μ is shown in Fig.7. μ indicates the efficiency of vibration whose maximum value takes at about υ=0.6 for free-free bar model and takes at about υ=0.5 for clamped-free bar and L-shaped bar models. The values of μ for L-shaped bar model have overlapped with that of μ for clamped-free bar completely.

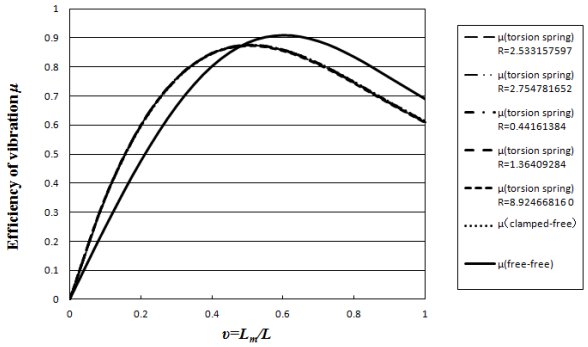

Figure 7. Efficiency of the vibration μ against the length ratio of electrodes υ

The enlargement of the graph near at υ= 0.51 in Fig.7 is shown in Fig.8. Figure 8 shows the relationship between μ and υ when the rotational Winkler coefficient R for L-shaped bar model is changed. Although the μ-υ curve for L-shaped bar model is very close to that for clamped-free bar model, the maximum μ-υ curve for the L-shaped bar model is always less than that for clamped-free bar model. Decrease in efficiency of vibration μ is induced by the vibration of the base. If the value of μ has correlation with quality factor (Q-value), the results in Fig. 8 show that R also affects Q-value. Since L-shaped bar model describes the vibration behavior of the tuning fork structure, it is necessary to derive the theoretical formula showing the relationship between Q-value of the tuning fork and μ, and to verify whether the calculated Q-value for clamped-free bar or free-free bar models is nearer to the measured Q-value of a quartz-crystal tuning fork.

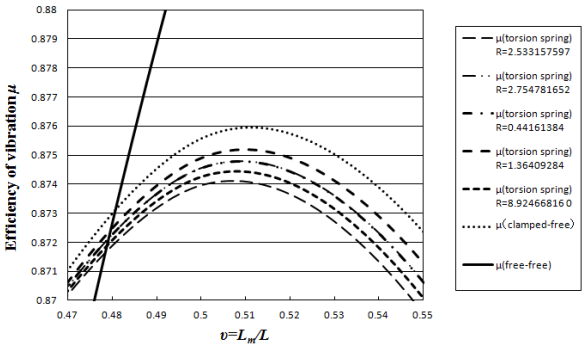

Figure 8. Efficiency of the vibration μ against the length ratio of electrodes υ
(Near the peak of clamped-free bar model in Fig.7)

We investigate the change in both motional capacitance and the rotational Winkler coefficient when the magnification of the thickness t_0 of the tuning fork decreases. Figure 9 shows the relationship between the motional capacitance and the rotational Winkler coefficient against the magnification of thickness of the tuning fork. The rotational Winkler coefficient decreases as the magnification of the thickness t_0 becomes small according to (31). At this time, the motional capacitance also decreases as shown in Fig. 9 since the electric field distribution changes according to (71) and (77) as t_0 decreases.

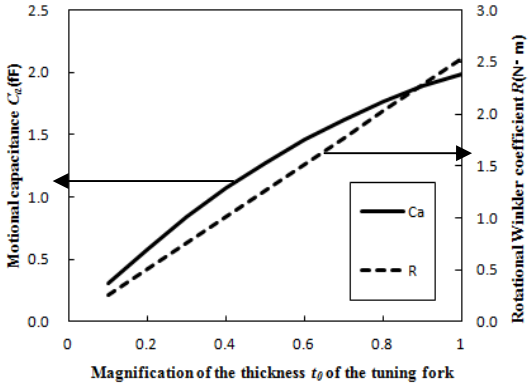

Figure 9. The motional capacitance and the rotational Winkler coefficient against the magnification of thickness of the tuning fork

In order to apply L-shaped bar model to the quartz-crystal tuning fork tactile sensor [1][2], what is necessary is to introduce the reaction force ku_1 and the axial force P_1 from an acrylic resin case which clamp the base of the tuning fork to the equation of motion of beam A when beam A in Fig. 2 gets into contact with an object, to derive the theoretical formula of the motional capacitance, and just to investigate the change in reciprocal motional capacitance by Winkler coefficient k (being equal to Young's modulus) of an object.

IV. CONCLUSION

If the electric field distribution, the width and the length of electrodes are taken into consideration, we can calculate the value of motional capacitance with errors less than 6% of the measured one using L-shaped bar model. Although the influence on the value of the motional capacitance

under three boundary conditions; free-free bar, clamped-free bar, and L-shaped bar models, is very small, the width and the length of electrodes affects the value of motional capacitance greatly. From a viewpoint of the efficiency of vibration μ, it becomes clear that the rotation Winkler coefficient R for L-shaped bar model affects the efficiency of vibration μ.

ACKNOWLEDGMENT

This work was partly supported by Grant-in-Aid for Scientific Research (c) in Japan.

REFERENCES

[1] H. Itoh and N. Hatakeyama, "Proposal of novel method to measure Young's modulus of materials using change in motional capacitance of the electrical equivalent circuit of quartz-crystal tuning-fork tactile sensor at resonance," *Jpn. J. Appl. Phys.* vol.49, pp. 07HC03-1-07HC03-5, 2010.

[2] H. Itoh and N. Hatakeyama, "Analysis of change in motional capacitance of the electrical equivalent circuit of quartz-crystal tuning-fork tactile sensor at resonance by combining analytical models for elastic foundation and L-shaped bar with torsion spring," *Jpn. J. Appl. Phys.* vol.49, pp. 126702-1-126702-9, 2010.

[3] J. Herman, "Determination of the electromechanical coupling factor of quartz bars vibrating in flexure or length—extension", *Pro.29th annual FCS*, 1975, pp.26-34.

[4] T. Ishikawa and H. Itoh, "Analysis of the capacitances of the electrical equivalent circuit of quartz-crystal tuning fork in consideration of electric field distribution by conformal mapping method," The 40th Electromechanical Symposium, pp.57-64, 2011.(In Japanese)

[5] R. Holland and E. P. EerNisse, "Design of Resonant Piezoelectric Devices," Cambridge: M.I.T. Press, 1969, p.28.

[6] K. Sezawa and K. Kanai, J. Earthquake Inst. **10** (1932) 767.

[7] Karl F.Graff, "Wave Motion in Elastic Solids," New York: Dover pub.,1975, p.154.

[8] E. Weber, Electromagnetic Theory Static Fields and Their Mapping. New York: Dover Pub., 1965, pp.387-390.

[9] S.Timoshenko, "Strength of Materials Part 1 Elementary Theory and Problems," Princeton: D. Van Nostrand, 1955, p.328.

Modeling of BVA Resonator for Collective Fabrication

A. Clairet[1], T. Laroche[2], L. Couteleau[1], and J.J. Boy[3]

[1]*RAKON FRANCE, 2 rue Robert Keller, 10150 Pont-Sainte-Marie, FRANCE*
[2]*FEMTO-ST, UMR 6174, Frequency & Time Dept, 26 chemin de l'Epitaphe, 25000 Besançon, FRANCE*
[3]*ENSMM/FEMTO-ST, Frequency & Time Dept, 26 chemin de l'Epitaphe, 25000 Besançon, FRANCE*

***Abstract*— In this paper, we report on the use of Finite Elements Software to model and simulate new resonator designs, working at about 9 MHz. We aim to review the concept of BVA resonator by reducing the size. The miniaturization of the whole resonator will allow us to use collective processes and therefore reduce the cost of manufacturing. To achieve this result, we investigated to replace the radius of curvature, necessary for a good trapping of the vibrating energy at this frequency, by several mesas.**

I. Introduction

High quality resonators are only made by unitary way. In order to allow a better integration in electronic system but also and especially a lower cost of manufacturing by performing collective processes [1], we investigated a way to reduce the size of these resonators while maintaining at least the same performances. Therefore, we tried to discretize the radius of curvature and replace it by a series of steps (cf. Fig. 1).

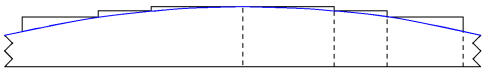

Fig. 1. Example of discretization

We focus our study on SC-cut quartz resonator for which its C-mode 3^{rd} overtone is vibrating at about 10 MHz. Computations have been done with COMSOL Multiphysics® on the "Mesocentre de calcul de Franche-Comté machine".

II. Resonator with radius of curvature

The resonator has a diameter of 14 mm and a thickness of 600 μm. We apply an electrical potential by using gold electrodes with a diameter of 7 mm and a thickness of 200 nm. With this configuration, we seek the radius of curvature which gives the best quality factor. The results obtained with various radii are summarized in the table I and displacements obtained for some of them are ploted in the Fig. 2 along the projection in the plane of the x-axis.

Even if the quality factor evolves according to the different designs, it remains around 1.5 million (the Q.f product is equal to 1.36e13).

The acoustic loss is evaluated by introducing the tensor of viscosity constants measured by Lamb and Richter [2]. For each modeling, the quality factor is deduced from the motional parameters of the equivalent electrical circuit. The higher Q and the best displacements are obtained when Rc is equal to 300 mm with Lm = 1.46 H and Rm = 55.2 Ω. We will use these data to compare the performances of the new designs.

TABLE I
Frequency and quality factor for various radius of curvature

Rc [mm]	f [MHz]	Q
100	9.078	1 498 000
200	9.049	1 499 000
240	9.043	1 494 000
250	9.041	1 495 000
260	9.040	1 501 000
300	9.036	1 504 000
400	9.028	1 501 000

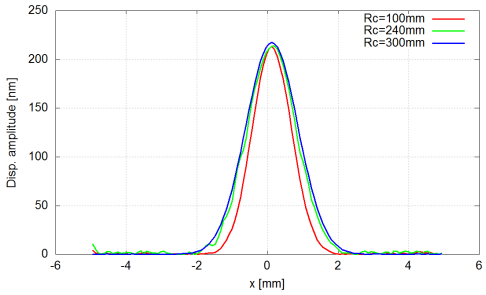

Fig. 2. Displacements within the resonator for 3 radii

III. Multi Mesa Resonator

We tested various configurations with several number and height of steps by ensuring that the discretization perfectly follows the chosen curvature as shown below.

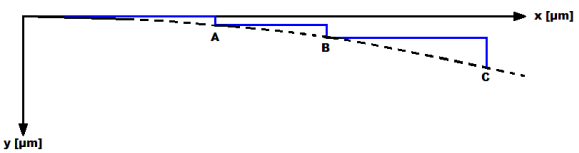

Fig. 3. Discretization of the curvature

The radius of curvature is represented in the figure 3 by the dotted line. The dimensions and the quality factor of new designs are summarized in the table II.

TABLE II

DIMENSIONS OF THE DIFFERENT DESIGNS IN MICROMETERS

Design	A(x,y)	B(x,y)	C(x,y)	D(x,y)	Q
1	(2500,10)	(3500,20)	(4500,33)	No	1 561 000
2	(2500,10)	(3500,20)	(4500,33)	(5500,50)	1 664 000
3	(3000,15)	(4000,27)	(5000,42)	No	1 586 000
4	(2500,10)	(3500,24)	(4500,72)	No	1 601 000
5	(2500,10)	(3500,24)	(4500,40)	(5500,72)	1 581 000
6	(3500,20)	(4500,33)	(5500,50)	No	1 524 000

As we can see in this table, in spite of a poor trapping of the vibrating energy (cf. Fig. 4 and 5), the quality factors are higher than those determined on a resonator owning a spherical surface.

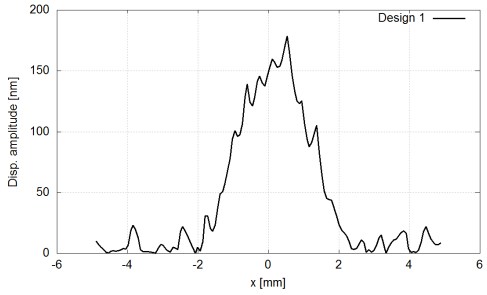

Fig. 4. Amplitude of displacements for design 1

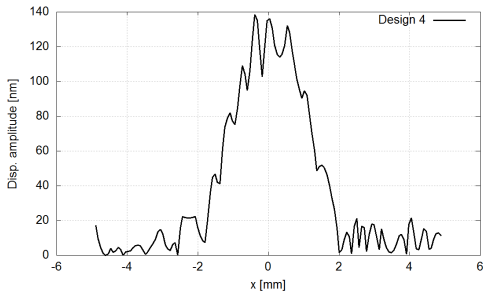

Fig. 5. Amplitude of displacements for design 4

Contrarily to the Fig. 2, the shape of the displacement curves is not perfect. We observe a lot of peaks which disturb the good trapping of the vibrating energy.

IV. PROGRESSIVE MESH

The thickness of the steps (and the elements within the mesas) is very small compared to the main part of the resonator. So, we have created a progressive mesh in order to avoid a possible discontinuity of mesh between the second mesa and the bulk which can be translated by a discrepancy on the final result. The height of the elements in the resonator will increase gradually to the opposite electrode.

This new mesh is created with COMSOL® by using the following algorithm [3] :

$$\sum_{i=1}^{e} \frac{i * r}{e * l} = L \tag{1}$$

where L is the total thickness of the resonator, e the number of elements, r the evolution ratio and l the length of the first layer. The equation (1) gives the value of l then we can determine the height of each element with :

$$h = \frac{i * r}{e * l} \tag{2}$$

By choosing the good ratio, the element near the last step will have the same thickness than those in the mesas. Various configurations have been tested with different ratio and number of elements in the bulk and steps. The results of the simulations are summarized in the table III. The dimensions of the resonator are identical to those of the design 1.

TABLE III

QUALITY FACTORS OBTAINED WITH PROGRESSIVE MESH

Design	Q	Lm [H]	Rm [H]
1.1	1 661 000	2.17	74.80
1.2	1 610 000	1.35	47.41
1.3	1 548 000	1.18	43.12
1.4	1 600 000	1.87	66.00
1.5	1 588 000	1.26	44.79
1.6	1 532 000	1.07	39.39
1.7	1 548 000	1.25	45.45
1.8	1 530 000	1.06	39.00

After testing several geometrical progressions, we succeed to improve the quality of the energy trapping (cf. Fig. 6 and 7). The displacement curves obtained with these two meshes are almost identical. The presence of peaks disturbing the trapping is less important than the design 1 (cf. Fig. 4).

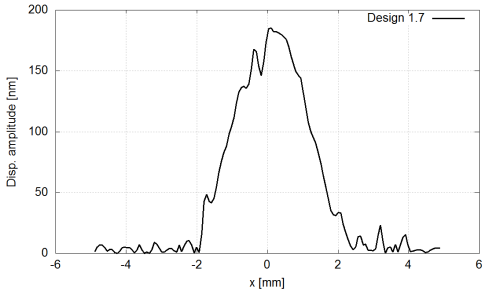

Fig. 6. Amplitude of displacements for design 1.7

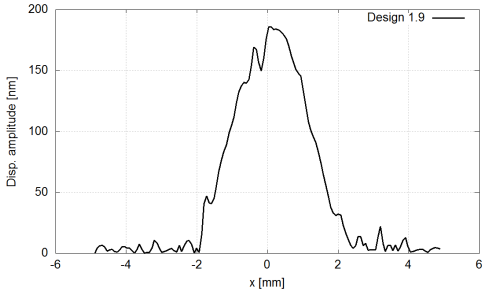

Fig. 7. Amplitude of displacements for design 1.9

But, despite a better trapping of the energy, the calculated quality factors are always too high compared to the "classical" resonator. By comparing the results determined with a radius of curvature with an internal software, we note that the value of the motional resistance is different between both whereas the inductance and the capacitance are very close. The quality factor being calculated with the motional parameters, the Q is not reliable to determine the best resonator design. So, we decided to refer only to the motional inductance (which translate the mechanical inertia) to select the optimal dimensions of the new resonator. As a reminder, the value of the inductance for a resonator with a radius of curvature of 300 mm is equal to 1.46 H (highest value that we choose as reference).

V. One step resonators

Modeling has been performed in order to study the behavior of resonators when the discretization is restricted to one step. For these simulations, the diameter of the mesa is equal to or bigger than the upper electrode. So, the electrical potential is only applied on one level in contrary to the previous computations.

TABLE IV
RESULTS OBTAINED FOR 1-STEP RESONATORS

Design	A(x,y)	Lm [H]
1	(3500,20)	0.84
2	(4500,34)	0.63
3	(5500,50)	0.62

For each design, the discretization still follows the radius of curvature choosen in the section II.

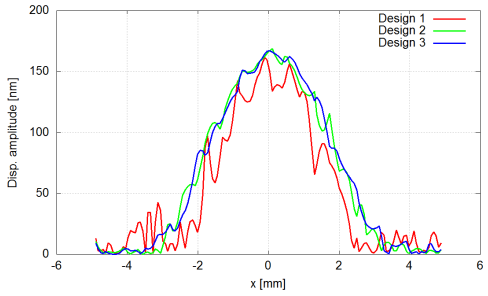

Fig. 8. Amplitude of displacements

By using only 1 mesa to discretize the radius of curvature, the value of the motional inductance decreases. Compared to the previous simulation, it is divided by 2 and it seems that the system has the same behavior as a plano-plano resonator and not as a plano-convex one. We also observe an improvement of the displacement curves when the diameter of the step is big. So, a high number of mesas would damage the trapping of the energy under the electrodes.

VI. Modeling of prototype

Following the previous results, we decided to realize a prototype for which the radius is discretize by two steps. The diameter of the smallest one should not be greater than the electrodes. The quality of these designs is evaluated only with the motional inductance and compared to the best value : 1.46 H (cf. Table I). The results of computations are summarized in the table V.

TABLE V
FREQUENCY AND INDUCTANCE FOR 2-STEP PROTOTYPES

	$\emptyset$ step 1	h step 1	$\emptyset$ step 2	h step 2	f [MHz]	Lm [H]
1	5 mm	10 μm	7 mm	10 μm	8.976	1.55
2	3 mm	4 μm	7 mm	16 μm	8.990	1.57
3	6 mm	15 μm	8 mm	12 μm	8.971	1.00
4	5 mm	10 μm	9 mm	24 μm	8.975	1.04
5	6 mm	15 μm	7 mm	5 μm	8.972	1.14
6	4 mm	7 μm	6 mm	8 μm	8.984	1.56
7	5 mm	10 μm	11 mm	40 μm	8.974	1.17
8	4 mm	7 μm	7 mm	13 μm	8.983	1.45
9	5 mm	10 μm	7 mm	15 μm	8.976	1.88
10	5 mm	10 μm	7 mm	5 μm	8.977	1.37
11	3 mm	4 μm	7 mm	20 μm	8.989	1.28
12	3 mm	4 μm	7 mm	10 μm	8.990	1.24
13	5 mm	5 μm	7 mm	10 μm	8.974	0.98

We note that the design 8 gives the closest value to our reference while the prototype 13 is the most different (Lm = 0.98 H). The displacements obtained for these configurations are ploted in the figure 9.

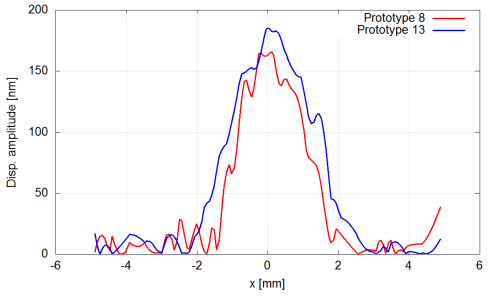

Fig. 9. Amplitude of displacements for the prototypes 8 and 13

For both, we did an eigenvalue analysis to search the position of some anharmonic spurious modes of the C-mode 3^{rd} overtone. The frequency of these several modes is summarized in the table VI.

TABLE VI
FREQUENCIES OF SPURIOUS MODES

	Frequency [MHz]		
Mode	With curvature	Prototype 8	Prototype 13
C300	9.036	8.983	8.974
C320	9.144	---	---
C302	9.155	9.083	9.049
C340	9.254	9.157	9.133
C322	9.264	9.170	---
C304	9.276	9.175	9.149

Some of these anharmonic modes are not "visible", maybe due to the sparse mesh (used to decrease the computation time) or due to the choosen geometry. By calculating the shift between the main mode C300 and the spurious ones, we note that it is smaller for the prototype 13 than the 8. For example, there is a shift of 174 kHz between C300 and C340 while it is 159 kHz for the 13 (cf. Table VII).

TABLE VII

SHIFT BETWEEN THE MAIN MODE AND THE ANHARMONIC MODES

	Frequency shift [kHz]		
Mode	With curvature	Prototype 8	Prototype 13
C320	108	---	---
C302	118	100	75
C340	218	174	159
C322	228	187	---
C304	240	192	175

Compared to the resonator with radius of curvature, the evolution of the shift between C300 and the spurious modes is different for the prototype 8. It evolves from 218 kHz to 240 kHz for the high frequency modes (C340 and more) of the system with spherical surface while it is between 174 kHz and 192 kHz for the discretized resonator. We see with this table that the diameter of the smallest mesa has an effect on the position of these modes. If the diameter increases (e.g. prototype 13), the anharmonic modes get closer to the main one. So, the diameter of the first step of prototype 8 is maybe to big if we observe the frequency shift between this new design and the resonator with curvature.

VII. CONCLUSION

Though the trapping of the vibrating energy is not perfect, our first simulations gave high quality factors. So, in the goal of solving our problem, we have modified the mesh of the resonators in order to avoid the discontinuity of mesh between the second mesa (the largest) and the bulk. We succeed to improve the quality of the trapping but the Q is still too high compared to the "classical" resonator. Then, we note that the calculation of the motional resistance (which is used to determine the quality factor) is probably biased. Nevertheless, we selected an optimum configuration with two steps for the new resonator by only refering to the motional inductance. Prototypes will be manufactured according to the dimensions determined by modeling (with radius of curvature and steps). Measurements on these prototypes will allow us to check our assumptions.

ACKNOWLEDGMENT

This work was funded by the "Agence Nationale de la Recherche" in the framework of a french research project entitled "FREQUENCE2009".

REFERENCES

[1] J. Boy, H. Tavernier, X. Vacheret, T. Laroche, and A. Clairet, "Collective fabrication of 20 mhz resonators by deep reactive ion etching on 3" quartz wafers," in *Joint Conference of the IEEE International Frequency Control and the European Frequency and Time Forum*, San Francisco, 2011.

[2] J. Lamb and J. Richter, "Anisotropic acoustic attenuation with new measurements for quartz at room temperatures," *Proceedings of the Royal Society of London. Series A. Mathematical and Physical Sciences*, vol. 293, no. 1435, pp. 479–492, 1966.

[3] COMSOL® Support.

Growth of $Li_2B_4O_7$ Films on $LiNbO_3$ and $LiTaO_3$ Substrates

Takehiko Uno and Seiji Mutoh
Dept. Electrical & Electronic Engineering, Kanagawa Institute of Technology
Atsugi-shi, Kanagawa 243-0292, Japan
Email: tk_u-no@ele.kanagawa-it.ac.jp

***Abstract*—Lithium niobate ($LiNbO_3$: LN) and lithium tantalate ($LiTaO_3$: LT) are widely used for bulk and surface acoustic wave devices because of their excellent piezoelectricity and high mechanical Q-factors. However, the frequency temperature coefficients (TCF) of these crystals are relatively large. On the contrary, lithium tetraborate ($Li_2B_4O_7$: LBO) has high piezoelectricity and a positive TCF. We investigated a method of growing LBO single crystal films on LN and-/or LT substrates in order to achieve piezoelectric substrates with high electromechanical coupling and low TCF.**

I. Introduction

Lithium tantalate (LT) and lithium niobate (LN) crystals are very useful materials for piezoelectric frequency control devices because of their high piezoelectricity and low mechanical friction. However, the temperature coefficients of frequency (TCFs) of these materials are relatively large. On the contrary, lithium tetraborate (LBO) crystal has a large positive TCF with high electromechanical coupling for the c-axis longitudinal wave. Therefore, a composite substrate of LBO on LT and/or LBO on LN may be suitable for very low or zero TCF piezoelectric resonators with a high mechanical coupling constant.

Relatively thick LBO film must be deposited on the LT or LN substrate in order to obtain a piezoelectric composite substrate with low TCF. This makes conventional deposition techniques such as sputtering, chemical vapor deposition (CVD), and molecular beam epitaxy (MBE) unsuitable for due to their slow deposition rates. We present a simple method of fabricating thick LBO films on LN and/or LT substrates in order to achieve piezoelectric substrates with high electromechanical coupling and low TCF.

II. Calculation of TCF and Electromechanical Coupling Factor

First, we present the frequency temperature characteristics and electromechanical coupling factors for composite substrates of LBO on LT and/or LBO on LN. Table 1 lists the material constants of LT, LN, and LBO crystals[1-4]. The values in the table lead us to predict that zero TCF may be achieved with structures consisting of LBO on LT and/or LBO on LN. We estimated the resonant characteristics of the thickness extensional mode for c-axis oriented composite substrates using Mason's equivalent circuit. The first-order TCF and frequency constant of the LBO on LT structure are plotted in Fig. 1. The horizontal axis, R_H, is the thickness ratio of LBO to LT, and the left- and right-side vertical axes respectively correspond to the first-order TCF, α_f, and the effective frequency constant for fundamental resonance. In the calculation, we assumed that the c-axes of LBO and LT were in the same orientation as shown in the figure. This figure indicates that zero TCF will be obtained around $R_H \approx 0.33$, and the frequency constant for the condition is about 3,400 $\mathrm{Hz \cdot m}$. Fig. 2 plots the dependence of the effective electromechanical constant, k_{eff}, on R_H. The value at around $R_H = 0.33$ is about 0.24, which is about 27% larger than of a c-cut LT plate. The frequency width, Δf, between resonant and anti-resonant frequencies is proportional to the square of k_{eff}, and therefore, Δf for the zero TCF condition will be over 60% larger than that of a c-cut LT plate.

The calculated results for an LBO on LN structure are shown in Figs. 3 and 4. In this structure, zero α_f will be realized at around $R_H = 0.37$, and the value of k_{eff} will be 0.27.

TABLE 1. Constants of LBO, LT and LN crystals

Material	$LiTaO_3$	$LiNbO_3$	$Li_2B_4O_7$
Crystal system point group	Trigonal 3m	Trigonal 3m	Tetragonal 4mm
Lattice const. (nm)	a: 0.5145 c: 1.3783	0.5148 1.3863	0.9479 1.028
Mass density(kg/m^3)	7450	4647	2450
Melting point (˚C)	1,650	1,250	917
Curie temp. (˚C)	610	1,140	-
EM coupling const. k_{33}	0.186	0.164	0.461
TCF(c-axs longitudinal,ppm/K)	-38	-65	+160

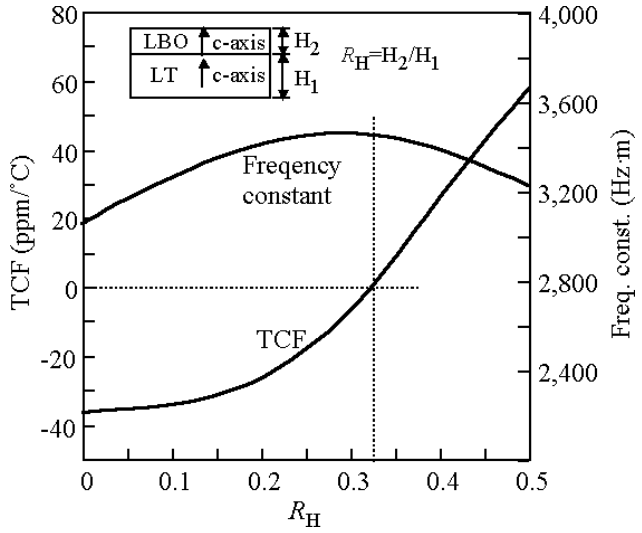

Fig. 1. Calculated results of first-order TCF and frequency constant of LBO on LT structure.

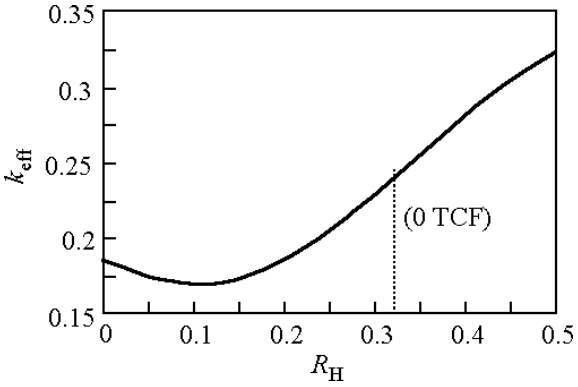

Fig. 2. Effective electromechanical coupling constant of LBO on LT structure.

In both the LBO on LT and LBO on LN structures, the zero TCF conditions exist at $R_H > 0.3$, and thus, a very thick LBO film is necessary. Commonly used film fabrication processes are not suitable for this purpose, and therefore, we investigated a simple method described in the following sections.

III. Fabrication Process and Characterization of Films

A. Fabrication process

As described above, very thick LBO films need to be fabricated on c-cut plates of LT and/or LN with the same orientation. Furthermore, single crystal LBO films should be grown in order to achieve high quality resonators. We examined for that purpose a simple process, as shown in Fig. 5, where a small LBO chip was put on a c-cut LN or LT substrate in an oven. The chip is heated at around the melting point, T_M, of LBO (917˚C). Consequently, the LBO chip melts while the substrate does not, and the melted LBO extends all over the substrate surface. Then the sample is

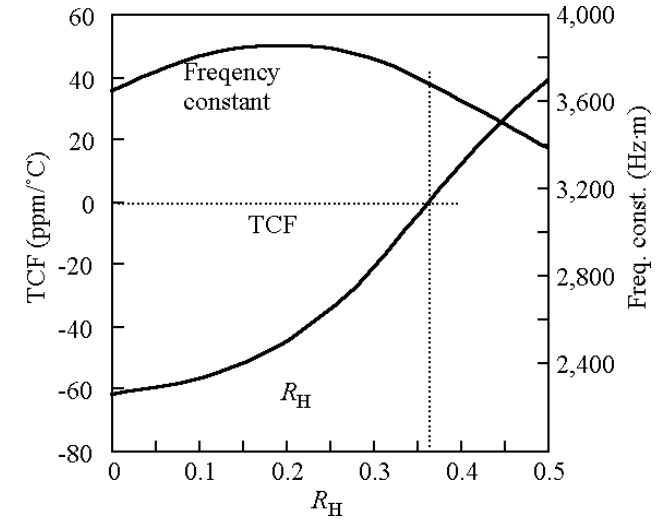

Fig. 3. Calculated results of first-order TCF and frequency constant of LBO on LN structure.

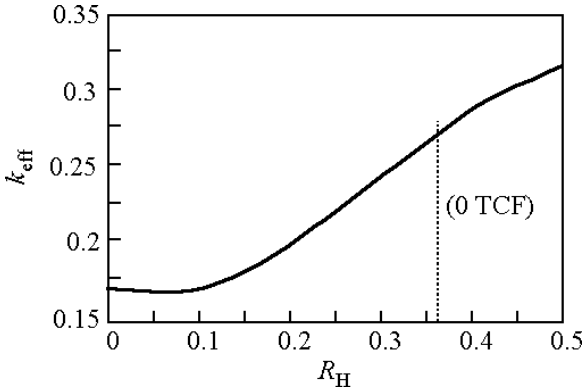

Fig. 4. Effective electromechanical coupling constant of LBO on LN structure.

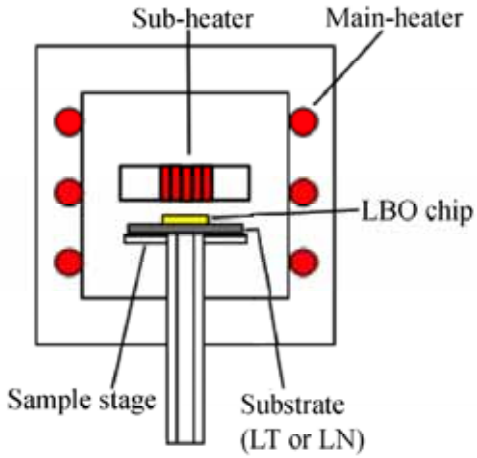

Fig. 5. Schematic diagram of fabrication setup.

cooled down very slowly to crystallize the LBO. If the lattice-misfit between the LBO and the substrate is minimal, epitaxial growth of LBO is expected.

Table 1 indicates that the lattice constant $a(=b)$ of LBO is about twice that of LT and LN, so if we estimate the misfit by

$$m = a_{\mathrm{LBO}} / 2a_{\mathrm{LT\ or\ LN}} - 1, \quad (1)$$

we find that the misfit between LBO and LT and/or LN of about 7.9%. Although this value is rather large for epitaxial growth, epitaxy is still possible. In contrast, the misfit of lattice constant c is about 25%, which is a rather large value.

Fig. 6 shows an example of the fabrication process of LBO on LN, where (a) is the temperature profile of the process, and (b) shows how the samples appear.

We used a resistance heater for sample heating, and the process was carried out in atmospheric pressure to avoid evaporation of the components. At about 850˚C, no change was observed from room temperature (Fig. 6(b)-1). At about 885˚C, the LBO chip began to melt (Fig. 6(b)-2)), and at 890˚C the whole LBO chip melted and extended over the substrate surface (Fig. 6(b)-3). Then the sample was cooled slowly at a rate of -0.1˚C/min to crystallize the LBO. As shown in this figure, the LBO chip melted at a considerably lower temperature than the T_{M} of LBO, 917˚C, and this melting-point depression was repeatedly observed. We confirmed that the temperature difference between the sample and the temperature sensor was less than 1˚C. Thus, the LBO on LN substrate was melted at a temperature more than 30˚C lower than the T_{M} of LBO. This suggests that some kind of reaction such as a eutectic reaction occurs between LBO and LN at high temperatures. Furthermore, the melted LBO wrapped around the bottom surface of the LN substrate, and we could not obtain a thick LBO film.

On the contrary, only a slight reduction in temperature occurred when the LBO was melted on LT. The LBO chip began to melt at about 909˚C. Furthermore, the LBO did not wrap around the bottom surface as much, so we were able to fabricate relatively thick LBO films on LT substrates.

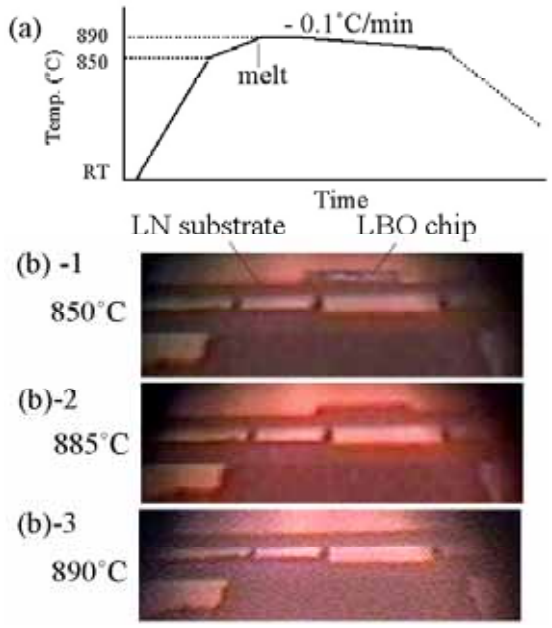

Fig. 6. Temperature profile and sample photographs near melting point.

B. *Characterization of films*

We applied electron back scattering diffraction (EBSD) to characterize the films. The principle of EBSD is shown in Fig. 7. Irradiated electrons on the sample are scattered by the crystal lattice, and both elastic and inelastic scattering occur, and a stripe pattern corresponding to the crystal lattice appears on a fluorescent screen (Kikuchi pattern). The use of a narrow scanning electron beam makes it easy to observe the distribution of crystalline in the film.

Fig. 8(a) shows an EBSD pattern by an LBO film on a z-cut LT substrate. A clear diffraction was observed, and the same patterns were observed by scanning the irradiation point. Fig. 8(b) shows the orientation distribution of the film. The displayed pattern had a single colored corresponding to the c-axis except some defects or dusts on the surface. This suggests that a uniform c-axis oriented LBO film was obtained.

The process temperature was much higher than the Curie point of LT, and this caused the polarization of the substrate to disappear. Nevertheless, a piezoelectric response was observed, as shown in Fig. 9. Because the inverse response voltage was observed in comparison with the reference (x-cut quartz plate), the film normal was negative along the on the c-axis, as illustrated in the figure.

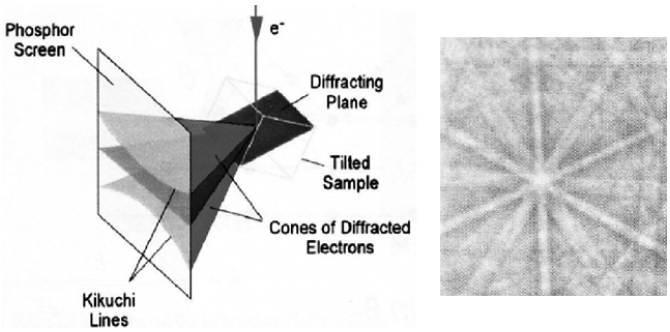

Fig. 7. Depiction of EBSD method.

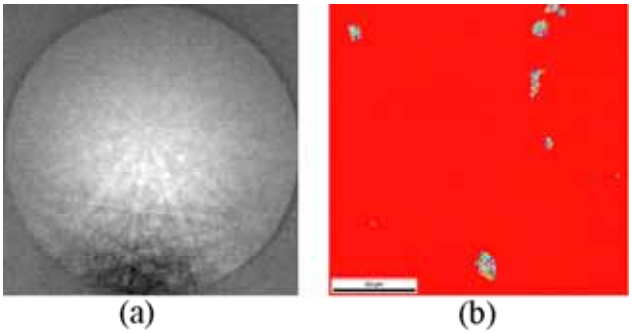

Fig. 8. EBSD pattern and orientation distribution figure made by a LBO film on LT-z substrate.

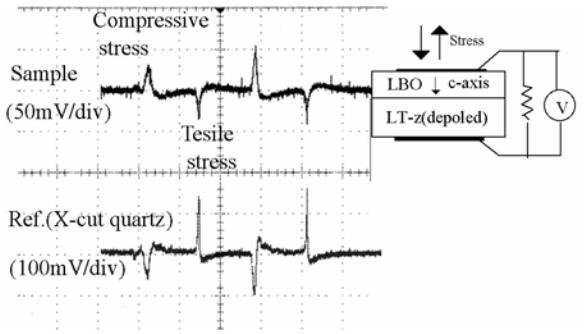

Fig. 9 Piezoelectric response by LBO on LT before poling treatment.

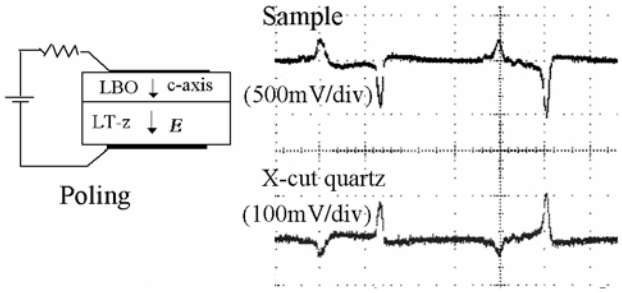

Fig. 10. Poling of LT substrate and piezoelectric response.

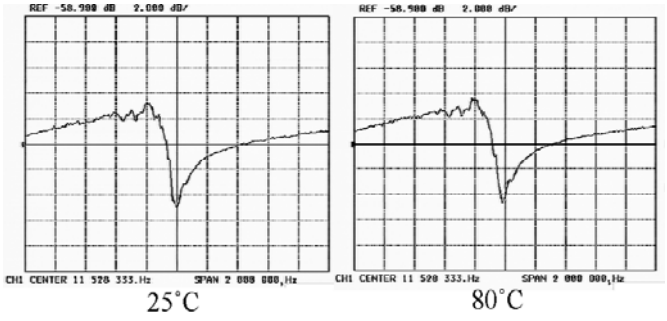

Fig. 11. Resonance curves at 25˚C and 80˚C.

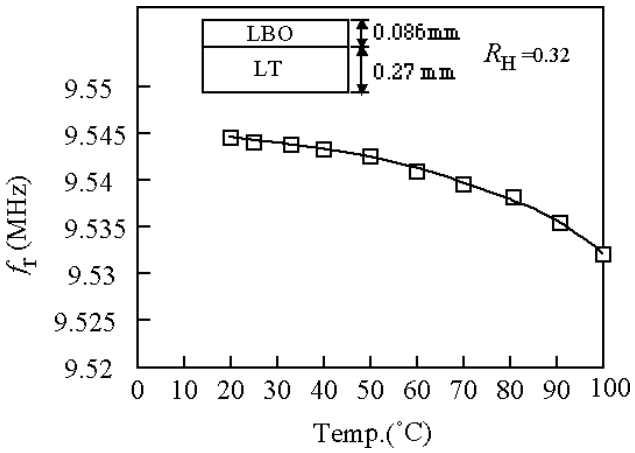

Fig. 12. Temperature dependence of resonant frequency.

IV. Resonance Properties

Poling of the LT substrate is necessary in order to utilize the composite substrate of LBO on LT-z for a piezoelectric resonator. Fig. 10 shows the poling method and piezoelectric response after the process. Because the c-axis of the LBO film was directed downward of the surface, a poling field directed downward was applied to the LT substrate. The piezoelectric response after poling is shown on the right side of Fig. 10. This response is of the same order as the poled LT crystal.

We fabricated a thickness extensional mode resonator with R_H=0.32. Fig. 11 plots the resonance characteristics for 25˚C and 80˚C. The flatness of the surface was not very good, and therefore, spurious responses were observed. However, only a small change in resonance characteristics was observed in the temperature range above 60˚C. Fig. 12 plots the experimental results of the resonant frequency dependence on temperature for R_H=0.32. The first-order TCF is about -3ppm/˚C, which fits fairly well with the calculated values in Fig. 1. In contrast the second-order TCF is about $-0.16\times10^{-7}/(°C)^2$, which may arise from the second-order temperature characteristics of LN. We found that the experimental k_{eff} values almost agreed with the calculated values.

V. LN Films on LT Substrates

Because the lattice misfits between LN and LT are very small and the T_M of LN is lower than that of LT, we examined the epitaxial growth of LN film on LT substrates.

Fig. 13 shows the appearance of LN just below and at T_M(=1250˚C). The LN chip on the LT substrate melted at 1250˚C, and the drop in melting point that was observed in

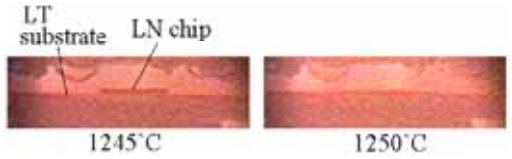

Fig. 13 Photographs of LN on LT around melting point.

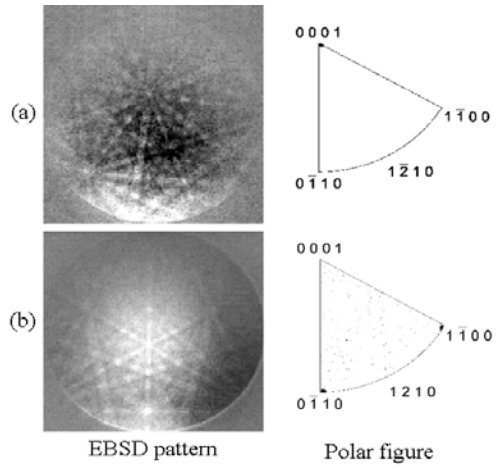

Fig. 14. EBSD patterns and polar figures of LN films on LT. (a) on z-cut substrate, (b) on y-cut substrate.

LBO on LN did not occur. The EBSD patterns and polar figures for epitaxial grown films on c-cut and b-cut LT substrates are shown in Fig. 14. These results show that LN epitaxial growth of LN is possible on LT substrates. Because TCF values for both LN and LT are negative, there are not so many advantages in using them in piezoelectric applications. However, applications for optical devices such as acousto-optic and electro-optic devices are promising. The LN film in these devices functions as an optical guide layer because the refractive index of LN is slightly larger than that of LT.

VI. Conclusions

We have examined a simple method of fabricating composite piezoelectric substrates using the melting point difference between the film and substrate materials. Lithium tetraborate films were obtained on lithium tantalate substrates, and thickness extensional mode resonators were fabricated with very low frequency temperature coefficients and relatively large electromechanical coupling constants.

We used the same process to obtain epitaxial growth of lithium niobate films on lithium tantalate substrates. The composite substrate of LN on LT may be useful for acousto-optic and electro-optic devices.

The process presented in this paper is very simple and is suitable for fabricating relatively thick films, although more research is needed to find ways to improve the flatness and adjust the thickness. One possible solution is to use some kind of spinner for high temperature operation.

References

[1] N. M. Shorrocks, R. W. Whatmore, F. W. Ainger and I. M. Young, "Lithium tetraborate-A new temperature compensated piezoelectric substrate material for surface acoustic wave devices", *Proc. Ultrasonics Symp.* IEEE *1981* Oct., pp. 337-340.

[2] M. Adachi, T. Shisaki, H. Kobayashi, O. Ohnishi and A. Kawabata, "Temperature compensated piezoelectric lithium tetraborate crystal for high frequency surface scoustic wave and bulk wave device applications" , *Proc. Ultrasonics Symp.* IEEE *1985* Oct., pp. 228-232.

[3] A.W.Warner, M. Onoe and G. A. Coquin, " Determination of elastic and piezoelectric constants for crystals in class(3m)", *J. Acoust. Soc. Am.,* vol.42 No.6, pp.1223-1231, 1967.

[4] R.T.Smith and F. S. Welsh, "Temperature dependence of the elastic, piezoelectric, and dielectric constants of lithium tantalate and lithium niobate", *J. Appl. Phys.,* Vol.42 No. 6, pp.2219-2230, 1

Collective Fabrication of BAW Resonators on 4'' SC-cut Quartz Wafers

A. Zarzycki[1], X. Vacheret[1], O. Bel[2], D. Picchedda[3], JJ Boy[1]
[1]ENSMM / FEMTO-ST, Freq & Time Dept, 26 chemin de l'Epitaphe – 25000 BESANCON - FRANCE
[2]RAKON France, 2 rue R. Keller – 10150 Pont-Ste-Marie - FRANCE
[3]GEMMA, 4 rue du Radar – 74008 ANNECY – France

Abstract - **In this paper we report new results on collective fabrication of resonators, designed to work at about ten MHz, on 4'' SC-cut quartz wafer. In this frame, their spherical curvature has been changed into discretized shape composed on two (or three) steps. For fabrication of the proposed design, two independent methods were investigated:**

- **deep reactive ion dry etching (DRIE) and**
- **wet chemical etching in two different etchants.**

For DRIE we applied inductively coupled plasma RIE (ICP RIE). This method allows quartz etching of 40 µm depth with an etch rate of about 0.7 µm/min. The homogeneity of the depth obtained over the entire 4" wafer is better than ± 5%. Moreover, the fabricated structures present very small roughness (less than a few nm) and nearly vertical walls.

Wet chemical etching was done with two different etchants: NaOH and NH_4F-HF.

The first one is used at about 180°C and allows a very good roughness when we start from polished surface (from 5 to 10 nm after 20 to 30 µm removed). The removal material rate (RMR) is ranged between 2.6 to 5.8 µm per hour, different on the 2 surfaces due to the anisotropy of the SC-cut.

In contrary, the 2^d etchant (acid) which allows a strong anisotropy etching, can be used to remove more material during one hour with a temperature close to 65°C (5.2 to 10 µm/h). But, unfortunately, the obtained roughness is not so good (45 nm instead of 11 nm with NaOH in the same time). Furthermore, after a strong etching, we have problem of adhesion of the mask and etch channels can appear. Generally, the mask is made by sputtered gold deposition.

The homogeneity of the wet etching process is also discussed. We show that it is strongly linked to the homogeneity of the fluid flow in the bath.

I. INTRODUCTION

High quality resonators for spatial and military applications are still fabricated by unitary way. Although techniques of deep directional dry etching allow collective fabrication, it is still insufficiently developed to be introduced in the industry.

In the framework of a french research project entitled "FREQUENCE", we aim to review the concept of high quality resonators in reducing the size and the cost while maintaining the best performances.

So, our main task for collectively made resonators working at a frequency lower than 20 MHz is to discretize their radius of curvature and replace it by a series of steps as described below and for which the dimensions have been defined by finite elements modelling. As shown in this conference, the best design for resonators working at 10 MHz has to follow a radius of curvature equal to 300 mm.

The different zones defining the resonator with 2 mesas are called: Vcs (in the center, under the central mesa), Vss (under the intermediate step) and Vls which is the volume limited by the larger step, far from the vibrating area.

Our study focused on SC-cut quartz resonator for which its 3rd overtone is vibrating at about 10 MHz. And finally, the heights of the 2 steps are: 7 µm for the first one (with a diameter of 4 mm) and 13 µm for the second whose the diameter is of 7 mm).

Fig. 1: design of a discretized shape of a resonator (with the 3 zones: Vcs, Vss and Vls)

II. 4'' SC-CUT QUARTZ WAFERS QUALITY

Before considering the collective fabrication of SC-cut resonators on the whole surface of 3 or 4'' diameter quartz wafers, we have to define the specifications of such oriented wafers in order to obtain a frequency vs temperature curve (TFC) with its first turnover point (TOP) positionned at around 80°C for USO applications.

The entire cutting, lapping and polishing process has been defined and realized by the manufacturer **KRYSTALY**,

located in Czech Republic. To control the homogeneity of the geometrical dimensions and after measuring the global crystallographic orientation, we cut the wafer into small squared blanks in which we have realized circular plano-plano resonators. We have to note that the resonators crossed by the seed do not work correctly.

After measuring the crystallographic θ, φ angles of each blank, we mount few resonators for which their orientations are defined as:

$$\theta = \theta_0 \text{ +/- } 1'30'' \text{ and } \varphi = \varphi_0 \text{ +/- } 2'$$

The figure below shows 2 examples of TFC with TOP (black plot) and without TOP (red one). And we observe that the difference between them corresponds to a change of **2 or 3' on the crystallographic angles**.

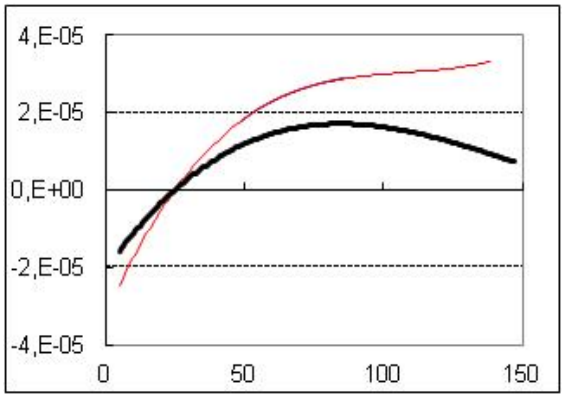

Fig. 2: TFC of 2 resonators with different orientations

III. DEEP REACTIVE IONS ETCHING

In order to define the best possible process using dry etching we have tested various configurations of resoantors with different number and height of steps [1, 2]. Also, some resonators were fabricated with bridges. The goal of bridges is to separate active part of the resonator from its handling part.

The process flow for fabrication of two mesas is presented in Fig. 3. It can be devided onto two identical stages, one stage per mesa. Each stage is composed of the seven following items:

1. Cr/Cu deposition (marked in yellow),
2. photoresist deposition and photolithography (marked in red),
3. Ni electrodeposition (in green),
4. Photoresist stripping
5. Cr/Cu dry etching } illustrated by I.b and II.b
6. Quartz deep etching
7. at least wafer cleaning – final shapes shown in I.c and II.c

In the same way, we can fabricate any number of mesas and bridges, the first stage concerning the largest pattern. A SEM photo of a finished wafer with resonators with two steps and bridges is presented in Fig. 4.

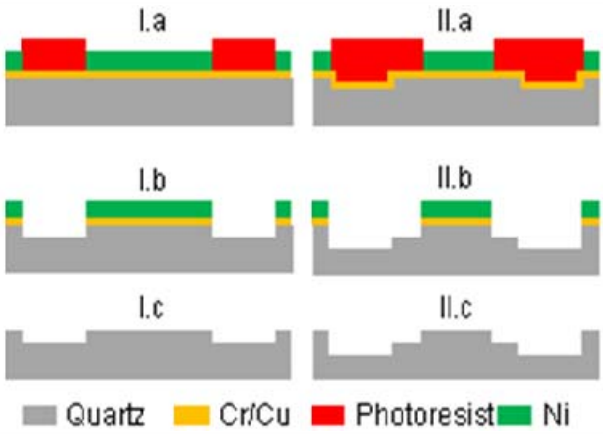

Fig. 3: sequences of the 2 steps of dry deep etching

An inductively coupled plasma reactive ion etching (ICP RIE) has been applied to both Cr/Cu seed layer etching and deep etching of quartz. However, we use pure Ar for Cr/Cu etching and C_4F_8/O_2 gas mixture for quartz etching.

Developed in our laboratory, the procedure of Cr/Cu layer etching in Ar plasma has two great advantages:

- first, it removes metallic layer very well and
- second, it does not attack quartz.

These two factors induce a clean and free of defects open quartz surface and if the initial surface is well prepared, we conserve its high quality after etching.

ICP RIE using C_4F_8/O_2 gas mixture allows etching of quartz with etch rate of about 0.67µm/min and high selectivity to Ni mask (~30). The etched surface is very smooth (see Tab. 1) even after very deep etching (up to 40 µm).

TABLE 1: roughness after dry etching on the different surfaces

Roughness	Vcc	Vss	Vls
Depth etched (µm)	0	10	20
Ra (nm)	0.8	1	1
Rp (nm)	2.2	3.2	3.8

Etching a few substrates let us conclude that the etch rate of quartz gives the highest value at the center of the substrate and decreases of about 5% at the edge of the wafer. The dispersion of the etch rate between wafers does not exceed ±3%.

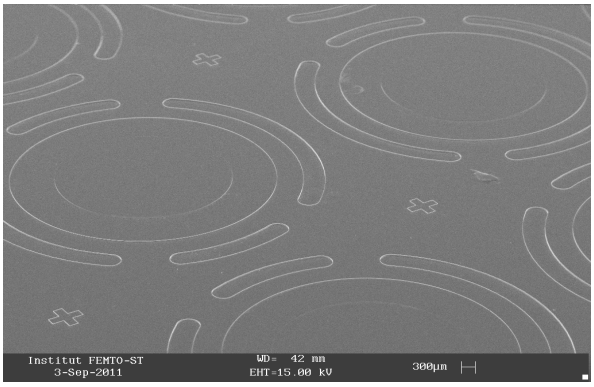

Fig. 4: details of the surface of the wafer after dry etching

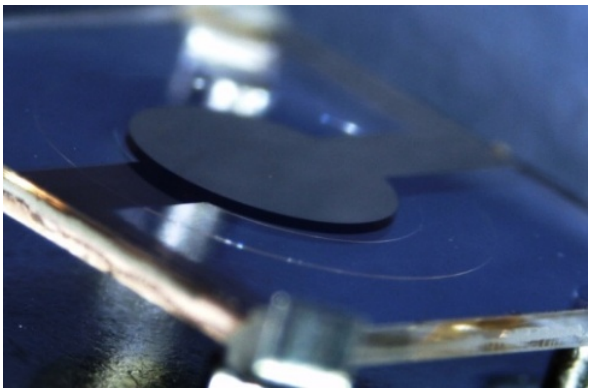

Fig. 5 : 2-mesa resonator after metallization

IV. WET ETCHING (NaOH AND NH_4F-HF)

The collective realization of resonators by wet etching has been planned with 2 etchants. For the first process we use acid NH_4F-HF (at 80°C) and for the second one, etching is realized at 180°C with NaOH, a basic solvent. Our aim is to use the advantages of each solvent:

- NH_4F-HF allows a quite fast etching (i.e. 10µm/h) with depths up to 80 microns,
- while NaOH has been used to achieve the etching process in the areas under the electrodes (i.e. on the surfaces of Vcs and Vss).

Almost previous works have been achieved to obtain a polished surface from a surface whose the roughness is obtained by a grinding process. So, from a roughness with Ra = 170 nm, authors presented final state for which the Ra is about 75 nm after 60 µm depth with NH_4F-HF [3] or about 80 nm with NaOH after removing 100 µm [4]. Of course, beyond the influence of the etchant, the final roughness is first function of the initial state.

If these results from the literature are interesting, the final states are not good enough for our application. Furthermore, we prefer to dissociate looking for a good roughness independently to a deep etching, up to 100 µm.

Our study has been realized with small samples and 3 or 4'' wafers (SC-cut oriented). The roughness of their surfaces is characterized by a Ra of about 1 nm (polish state) and we aim to maintain it as far as possible. Our works consisted so to reduce the deterioration caused by chemical etching by adjusting the parameters of the process:

Etchant type, bath temperature, fluid circulation, concentration, orientation of the wafer in the bath…

Finally, by monitoring the Ra factor, we show that we have reduced the deterioration of the surface roughness by a factor 5 with NH_4F-HF and 3 with NaOH as indicated in the figures 5a and 5b.

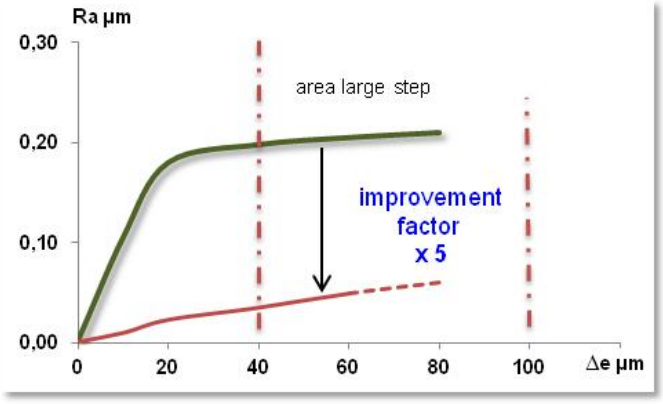

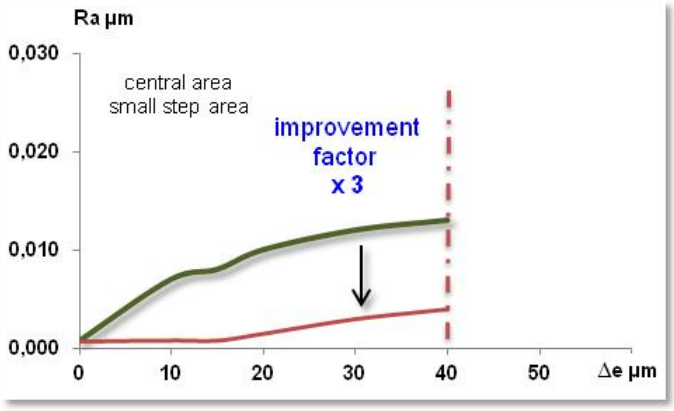

Fig. 5a and Fig. 5b: adjustment of the parameters to improve the process with 2 different etchants

We know that the composition of the etchant is also an important parameter for chemical etching. The adding of surfactant [5], the concentration, the mixing of solvents (NaOH and KOH for instance) [6] are previously studied and have shown their important influence. But, here, we prefer to limit our study to avoid the use of a "fractional factorial designs" tool, too time consuming.

And finally, we obtain roughness as presented in the following table:

TABLE 2: roughness after wet etching

Roughness	Vcs	Vss	Vls
Depth etched (µm)	0	15	+40
Ra (nm)	0.7	1	35
Rp (nm)	2.5	3.5	160

V. CONCLUSION

From high quality big quartz blocks grown by GEMMA, the cutting, lapping and polishing process used to fabricate 4'' SC-cut quartz wafers are achieved with a tolerance of +/- 2' on the crystallographic orientation, the direct consequence being an uncertainty of +/-5°C on the TOP...

The deep RIE process is very promissing for collective fabrication of BAW resonators. In SC-cut quartz wafers, it allows fast etching, high precision and acceptable dispertion. Furthermore, the roughness of the etched surface, which is an important key factor, remains at a very high level.

Unfortunately, during DRIE, a sort of wall (few µm high) appears on the edge of the first realized step (the largest) (see Fig.7a and 7b). We suppose it can be caused by too high passivation during etching. This sort of wall perturbates the continuity of the deposited electrodes and it turns the whole resonator failure. Therefore, before realizing the electrodes, it is necessary to remove this contamination.... surely by wet etching.

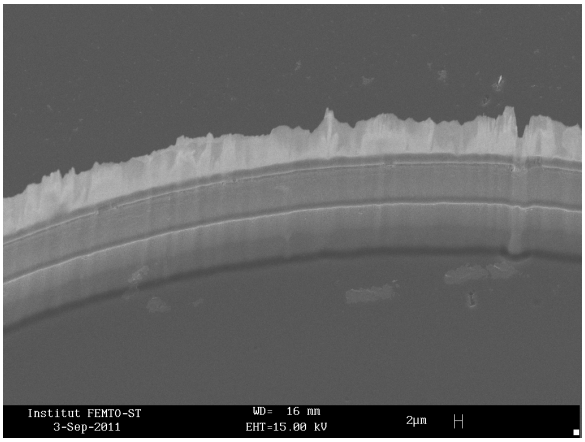

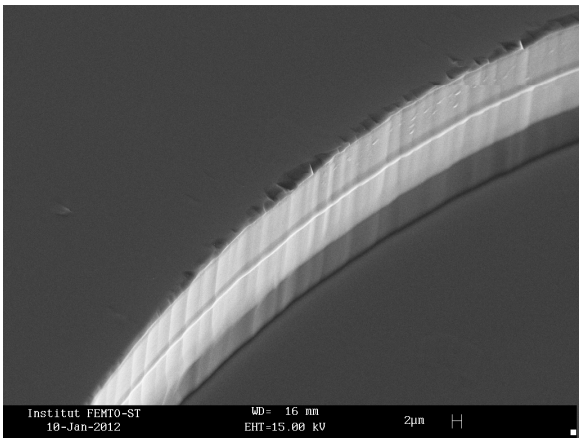

Fig. 7a and 7b: sort of wall…before and after etching by NaOH during 20 min

At least, we achieve very important improvements in the wet chemical etching which allows an acceptable roughness. Indeed, the preliminary results are very close to the needed roughness to obtain high quality of the resonant frequency of the resonator. We have sure today that the final process will include the use of few etchants for which we continue to optimize the parameters.

ACKNOWLEDGMENT

This work was funded by the "Agence Nationale de la Recherche" in the framework of a french research project named "FREQUENCE"

REFERENCES

[1] J. Boy, S. Queste: "deep reactive ion etching of quartz crystal for frequency metrology" – Proc EUSPEN 09

[2] J.J. Boy et al., "Collective fabrication of 20 MHz resonators by deep reactive ions etching on 3'' quartz wafers", IFCS-IEEE and EFTF, 2011, pp. 832, 836.

[3] J. Vig, J. Lebus, "Chemically polished quartz", 31st Annual Frequency Control Symposium, 1977, pp 131-143.

[4] M. Deleuze, M. Goiffon, "Controlled crystal dissolution applied to quartz", Journal of materials science 29, 1994, pp 5390-5398.

[5] R.J. Brandmayr, J. Vig, "Chemical polishing in etching solutions that contain surfactants", 39th Annual Fréquency Control Symposium, 1985, pp 276-281.

[6] M. Deleuze, "Dissolution controlée du quartz en milieu basique", Thèse Université de Montpellier I, 1994, pp 194-202.

Properties of Sapphire Crystals Elaborated with Different Grow Technics for Microwave Ultra-stable Oscillator Applications

Vincent Giordano, Mohamad Mrad, Jean-Louis Masson
Pierre-Yves Bourgeois, Yann Kersalé

FEMTO-ST Institute - Time and Frequency Dept.
UMR 6174, CNRS - U. Franche-Comté - ENSMM
32 Av. de l'Observatoire
25044 Besançon cedex, France
Email: giordano@femto-st.fr

Serge Grop and Benoît Dubois

ULISS® Business Unit
32 Av. de l'Observatoire
25044 Besançon cedex, France

***Abstract*—State-of-the-art microwave ultra-stable oscillators are currently based on sapphire resonator operated in whispering gallery modes in the range $5 - 12$ GHz. Indeed the best near carrier phase noise is achieved with commercial systems incorporating a room temperature sapphire reference associated with a sophisticated electronics degenerating the noise of the sustaining oscillator stage [1]. On the other part, relative frequency instabilities better than few 1×10^{-15} are achieved with laboratory Cryogenic Sapphire Oscillator (CSO) in which the sapphire crystal is cooled into a large liquid Helium dewar and maintained at its turnover temperature (between 5-8 K) [2] . More reccenlty, we demonstrated an original and reliable technology incorporating a pulse-tube cooler instead of a bath cryostat thus eliminating the need for regular supplies and manual transferring of liquid helium [3]. The advent of reliable and cryocooled (CSO) open the possibility to implement such an ultra-stable reference not only in metrological laboratories with liquid helium facilities but also in remote sites like base stations for space navigation, VBLI antenna sites, ... This technology is today available through a newly created business unit: ULISS® [4].**

To get such a type of high performances, the heart of the system, i.e. the Sapphire resonator, is made from a high purity monocrystal elaborated with a sophisticated grow method able to produce large sapphire boule exempt of structural defect. Nevertheless presence of paramagnetic impurities in small concentration (1 ppm or less typically) is required to obtain a turnover temperature near the liquid helium temperature.

In this paper we present the comparison of sapphire resonators machined from monocrystal elaborated with two different grow methods. For each crystal, Q-factor and thermal sensitivity have been measured at low temperature for some whispering galery modes.

I. Introduction

In the field of Ultra-Stable Oscilators (USO) needed for time and frequency metrology, space navigation, radioastronomy or for fundamental physical experiments, the most stable frequency source is the Cryogenic Sapphie Oscillator (CSO). The CSO achieves in an autonomous and reliable version a frequency stability better than 2×10^{-15} at short term and can be as good as 4×10^{-15} over one day [5], [6], [7]. An Hydrogen Maser or a stabilized laser can present better frequency stabilty but only on some restricted integration time ranges.

Today the CSO technology is mature enough to be proposed as a commercial product [4]. The heart of a CSO is a microwave cylindrical resonator machined in a high quality sapphire monocrystal. The low defect or impurities concentrations existing in these high quality monocrystals are generally difficult to evaluate with a great accuracy due to the limited resolution of the classical material characterisation equipment. Nevertheless, these crystal imperfections even at a low concentration level (below 1 ppm) can impact on the system performances. Any new information on the material quality and its impurities concentration will reinforce our capability to produce robust systems limiting the risk coming from the repetability of the crystal production.

II. Sapphire resonator specifications

Our goal is to provide an ultra-stable oscillator (USO) that meet the most stringent short term frequency stability specifications as those for the Deep Space Network for satellites and space vehicles navigation. The frequency stability of our CSO is specified as:

- Short term: $\sigma_y(\tau) \leq 3 \times 10^{-15}$ for 1 s$\leq \tau \leq 1000$ s.
- Long term: drift $< 5 \times 10^{-14}$/day.

These performances mainly depend on the USO frequency reference characteristics with as a prime relevant parameters: the resonator Q-factor and its sensitivity to environmental perturbations.

A. Short term frequency instability: The Line Splitting Factor

Noise in the oscillator's electronic components is the main source of short-term frequency instabilities; how exactly this

noise affects the frequency stability depends on the resonator configuration and on Q_L its loaded Q-factor. Without characterizing the exact nature of the oscillator's individual noise sources, one would like a rough estimate of what the resonator's bandwidth should be to achieve a given frequency stability. It is generally admitted that the attainable frequency stability $\sigma_y(1s)$ at a given time interval (e.g. 1s) cannot be lower than a given fraction of the resonator bandwidth [8]. We thus define an empirical figure of merit, namely the "line splitting factor", or LSF, as the ratio of the frequency fluctuations $\Delta\nu$ of the generated signal over the resonator's bandwidth $\Delta\nu_R$:

$$LSF = \frac{\Delta\nu}{\Delta\nu_R} = Q_L \times \frac{\Delta\nu}{\nu_0} = Q_L \times \sigma_y(1s) \qquad (1)$$

The LSF provides a way of quantifying the overall effect of the noise associated with the oscillator's electronics. Considering the best experimental results obtained to date, one can state that a good $LSF \geq 1 \times 10^{-6}$. Thus, to get a frequency stability of 3×10^{-15}, the minimum resonator loaded Q-factor should be at least:

$$Q_L = \frac{LSF}{\sigma_y(1\mathrm{s})} \geq 330 \times 10^6 \qquad (2)$$

The CSO frequency reference is a cylindrical sapphire resonator in which high order whispering gallery modes can be excited. These modes are characterized by a high energy confinement in the dielectric due the total reflection at the vacuum-dielectric interface. The different resonators we designed operate on quasi-transverse magnetic whispering galery modes as $WGH_{m,0,0}$ where m is the number of wavelength in resonator along the azimuthal direction φ. To get useful resonance in the range 8-12 GHz, the resonator diameter and thickness are $\Phi =$ 30-50 mm and $H =$ 20-30 mm respectively. Due to the sapphire low dielectric losses, a Q factor as high as 1×10^9 can be obtained at the liquid-He temperature providing m sufficiently high ($m \geq 13$ typically).

B. Long term frequency limitation

The resonator frequency is determined by its geometry and by the wave velocity inside the resonator medium. These physical characteristics are in turn affected by the resonator's temperature and the power of electromagnetic signals applied to its coupling ports. The resonator's sensitivity to these environmental parameters limits the oscillator's long-term frequency stability. Random-walk fluctuations in any of these parameters will lead to a frequency stability (Allan deviation) varying as $\tau^{1/2}$. Beyond pure fluctuations, the properties of the resonator, or an environmental parameter, may *drift* with time. For example, a mechanical stress induced during the resonator's assembly might relax with a long time constant. Should the change in such a stress causes a corresponding change in the wave velocity of the resonator's medium, the oscillator's frequency will drift with time. Such phenomena will cause a degradation in the oscillator's frequency stability over the longer term. This "aging" is generally characterized in the time domain by an Allan standard deviation increasing proportionally with the integration time τ. For our purposes, the two relevant parameters are the resonator sensitivities to temperature and to the injected power.

1) Thermal sensitivity: let's assume that the resonator's temperature is controlled to ± 1 mK. Such a resolution can be easily obtained with commercially available thermal sensors and controllers. To attain our stated frequency-stability objective, i.e. $\sigma_y \leq 3 \times 10^{-15}$, the residual resonator's thermal sensitivity must be:

$$\frac{1}{\Delta T}\frac{\Delta\nu_0}{\nu_0} \leq 3 \times 10^{-12}\mathrm{K}^{-1}. \qquad (3)$$

The pure sapphire resonator has not the frequency-vs-temperature turning point otherwise found in most piezoelectric resonators after appropriate design. Although the mode frequency thermal sensitivity decreases significantly at low temperature, it never goes low enough for the target stability to be achieved with state-of-the-art temperature control. Fortunately, it turns out that high-purity sapphire crystals always contain a small concentration of paramagnetic impurities, as Cr^{3+}, Fe^{3+} or Mo^{3+}. These ions induce a small magnetic permeability whose temperature dependence compensates for the natural sapphire resonator thermal sensitivity. It is then result that the actual resonator frequency dependence on the temperature is quadratic. The resonator frequency reaches a maximal value at a specific temperature T_0. This turnover temperature T_0 depends on the mode and on the impurity concentration.

2) Power sensitivity: microwave resonators are also sensitive to the injected power. Assuming fractional power control at the 10^{-5} level (i.e. $\frac{\Delta P}{P} = 10^{-5}$), the resonator's power sensitivity is required to be

$$\frac{1}{\Delta P}\frac{\Delta\nu_0}{\nu_0} \leq 3 \times 10^{-10}\ \mathrm{W}^{-1}. \qquad (4)$$

In the case of the cryogenic whispering gallery mode resonator, the sensitivity to the injected power results mainly from the thermal effect and from ther radiation pressure, which becomes noticeable when the Q-factor is so high. However, the power sensitivity can also be affected by the paramagnetic impurities for modes laying nearby or in the ESR bandwidth.

C. Sapphire samples

Since our preliminary works more than 15 years ago, we tested different crystals and geometries. Those that have been used for this comparison are listed in the table I.

TABLE I

Crystal Type - Year of delivery	$\Phi \times H$ (mm × mm)	Features
HEMEX-1995	50 x 20	Opened cavity
HEMEX-2007	54 x 30	Optimized for 9.99 GHz CSO
HEMEX-2012	54 x 30	Optimized for 9.99 GHz CSO
CZ-2012	54 x 30	Optimized for 9.99 GHz CSO

III. Q-FACTOR

For high azimutal numbers, the unloaded Q-factor is ultimately limited by the resonator material dielectric losses. However, at low temperatures, it can be affected by some other detrimental effects as:

- Cavity wall losses due to non-optimized geometry
- Residual contamination of the resonator surface
- Extra-losses induced by nearby spurious modes
- Extra-losses due to the coupling probes
- Structural resonator defects (dislocations, inclusions, paramagnetic impurities,...)

The figure 2 shows the unloaded Q-factors as measured at 4 K for two resonator geometries and for two types of sapphire crystals.

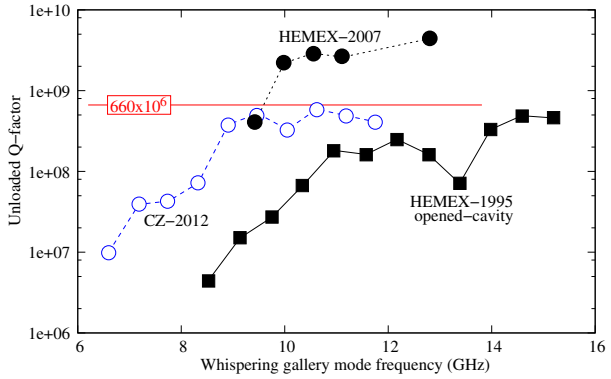

Fig. 1. Whispering gallery mode unloaded Q-factor. Network Analyzer output power: -10 dBm

In the opened cavity [9], the cavity cylindrical walls are replaced by a microwave absorber which limits the low order WG modes Q-factor. However for $m > 13$ this limitation is not longer relevant, and the unloaded Q-factor is of the order of 5×10^8, a value relatively lower than those expected for an HEMEX grad resonator. Firstly the resonator shape factor 5/2 is not optimum for a X-band operation. Secondly in the case of the opened cavity, the resonator cleaning can be an issue as it is not protected by the cavity walls. In some experiments we observed clearly the effect of residual particules or gas condensation on the resonator surfaces during the cooling affecting the Q-factor. Even with a great caution during the resonator mounting, this effect can not be totally eliminated.

The two other resonators operate in a closed cavity and have been optimized for the $WGH_{15,0,0}$ mode at 9.99 GHz [3]. HEMEX grad resonator shows superior performances than CZ crystal attaining 2 billions for the operating mode. The CZ resonator can achieve 5×10^8 unloaded Q-factor just under our spectification. Nevertheless, it can get a relative frequency stability still in the 10^{-15} range.

IV. THERMAL SENSITIVITY

A. Background [10]

At low temperature, residual paramagnetic impurities induce a magnetic susceptibility χ which is temperature dependent. In that case, the resonator frequency thermal dependance can be written as:

$$\frac{\nu(T) - \nu_{0K}}{\nu_{0K}} = AT^4 + \frac{\eta\chi'(\nu, T)}{2} \tag{5}$$

where, ν_{0K} would be the mode frequency at 0 K if no paramagnetic impurities were present and χ' the real part of the susceptobility

The first term in equation 5 is always negative. It combines the temperature dependance of the dielectric constant and the thermal expansion. We assume in a first approximation that A is not mode dependant and is of about -3×10^{-12} K^{-4} for high azimutal number WGH modes.

The second term is the contribution of the paramagnetic impurities contained in the sapphire. η is the mode filling factor representing for given mode how the a-c magnetic field couples to the susceptibility. For a high azimutal number WGH mode, $\eta \approx 1$. Considering only one paramagnetic specy characterised by its electron spin resonance (ESR) at ν_j such as $\nu_j \ll k_B T/h$, with a linewidth $\Delta\nu_j$, χ' is:

$$\chi'(\nu, T) = \frac{C(\nu)}{T} = \frac{g^2\mu_B^2 J(J+1)}{3k_B T} N \frac{\nu_j}{\Delta\nu_j} \frac{\left(\frac{\nu - \nu_j}{\Delta\nu_j}\right)}{1 + \left(\frac{\nu - \nu_j}{\Delta\nu_j}\right)^2} \tag{6}$$

where N is the paramagnetic ions density, g is the spectroscopic splitting factor, μ_B is the Bohr magneton and J the total angular momentum of the ground state of the ion.

A thermal compensation can occur if the derivative of equation 5 nulls, which imposes $\chi' < 0$, and thus $\nu < \nu_j$, i.e the signal frequency is below the ESR. In that case, the temperature T_0 at which the resonator thermal sensitivity nulls is:

$$T_0 = \left(\frac{C}{4A}\right)^{1/5} \tag{7}$$

The ESR frequencies of ions commonly found in sapphire is given in the following table:

TABLE II
PARAMAGNETIC IONS IN SAPPHIRE CRYSTAL

Paramagnic Ion	ESR frequency (GHz)	g	J
Cr^{3+}	11.4	2	1/2
Fe^{3+}	12.0	2	5/2
Mo^{3+}	165	2	1

The following figures show typical frequency-vs-temperature curves for different crystals and mode orders.

The Fig. 3 summarizes the different results showing observed turnover temperature as a function of the mode frequency.

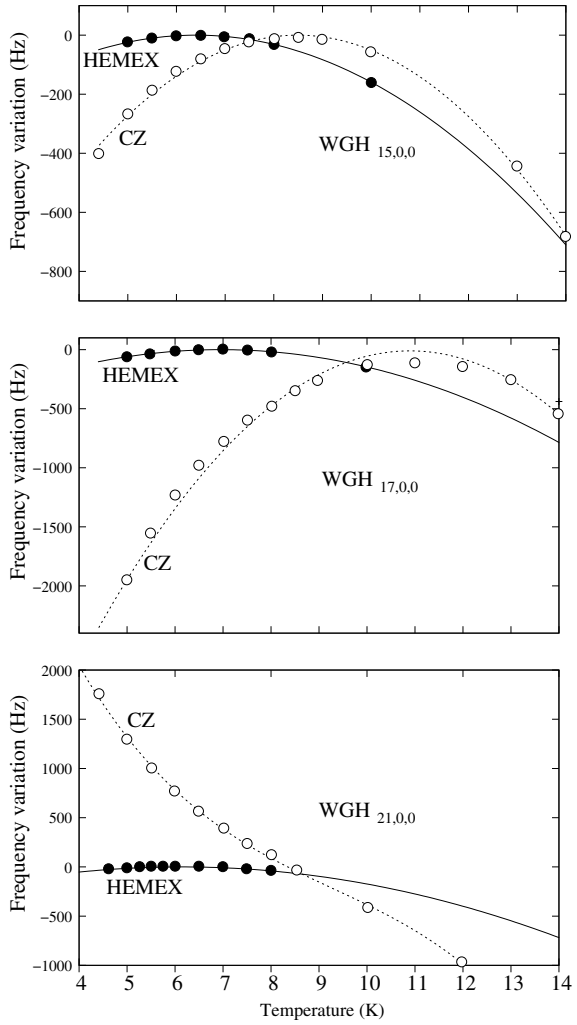

Fig. 2. Whispering gallery mode unloaded Q-factor. Network Analyzer output power: -10 dBm

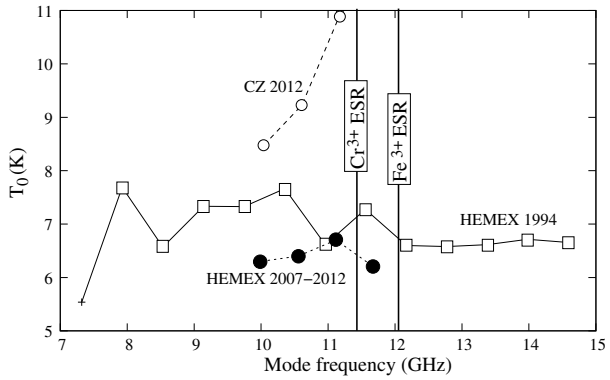

Fig. 3. Whispering gallery mode unloaded Q-factor. Network Analyzer output power: -10 dBm

In old samples provided in the 90s (HEMEX-1995), all whispering gallery modes in a large frequency range present a turnover temperature almost independent of the mode order. Luiten [10] demonstrated that it is due to the predominance of the Mo^{3+} ion, whose ESR frequency is 165 GHz. The spread in turnover temperatures observed for low frequency modes ($\nu < 12$ GHz) could result from Cr^{3+} or/and Fe^{3+} residuals. The concentration of these residuals should be very low as the turnover temperature imposed by the Mo^{3+} ions is not greatly affected.

In most recent HEMEX crystals, it appears that the relative concentrations of Cr^{3+} and Fe^{3+} are higher. Starting from the lower frequencies, the turnover temperature increases as the mode frequency approaches the Cr^{3+} ESR frequency. Modes staying between the ESR frequencies of Cr^{3+} and Fe^{3+} are strongly power dependant and, generally show no turnover temperature. WG modes recover a turnover temperature for $\nu \geq 13$ GHz.

The Czochralski crystal shows turnover temperature only for the WG mode below the Cr^{3+} ESR, indicating that this ion is the predominant paramagnetic impurity.

ACKNOWLEDGMENT

The ULISS team wish to express acknowledgements to the *Fond Européen de développement Régional* (FEDER), *le Conseil Général de Franche-Comté* and OSEO for their support.

REFERENCES

[1] `http://www.psi.com.au/`.
[2] C. R. Locke, E. N. Ivanov, J. G. Hartnett, P. L. Stanwix, and M. E. Tobar, "Invited article: Design techniques and noise properties of ultrastable cryogenically cooled sapphire-dielectric resonator oscillators," *Review of Scientific Instruments*, vol. 79, pp. 051301–1–12, 2008.
[3] S. Grop, P.-Y. Bourgeois, N. Bazin, Y. Kersalé, E. Rubiola, C. Langham, M. Oxborrow, D. Clapton, S. Walker, J. D. Vicente, and V. Giordano, "A crycooled 10 GHz oscillator with 10^{-15} frequency stability," *Review of Scientific Instruments*, vol. 81, pp. 025102–1–7, 2010.
[4] `http://www.uliss-st.com/`.
[5] S. Grop, P. Y. Bourgeois, R. Boudot, Y. Kersalé, E. Rubiola, and V. Giordano, "10 GHz cryocooled sapphire oscillator with extremely low phase noise," *Electronics Letters*, vol. 46, pp. 420–422, 18th March 2010.
[6] S. Grop, P.-Y. Bourgeois, E. Rubiola, W. Schäfer, J. De Vicente, Y. Kersalé, and V. Giordano, "Frequency synthesis chain for the ESA deep space network," *Electronics Letters*, vol. 47, pp. 386–388, Mar. 17, 2011.
[7] S. Grop, W. Schafer, P.-Y. Bourgeois, Y. Kersalé, M. Oxborrow, E. Rubiola, and V. Giordano, "Unprecedented high long term frequency stability with a microwave resonator oscillator," *IEEE Transactions on Ultrasonics, Ferroelectrics and Frequency Control*, vol. 58, May 24, 2011.
[8] M. E. Tobar, J. G. Hartnett, E. N. Ivanov, D. Cros, P. Blondy, and P. Guillon, "Cryogenically cooled sapphire–rutile dielectric resonators for ultrahigh–frequency stable oscillators for terrestrial ans space applications," *IEEE Transactions on Microwave Theory and Techniques*, vol. 48, pp. 1265–1268, July 2000.
[9] P. Y. Bourgeois, Y. Kersalé, N. Bazin, M. Chaubet, and V. Giordano., "A cryogenic open-cavity sapphire reference oscillator with low spurious mode density.," *IEEE Transactions on Ultrasonics, Ferroelectrics and Frequency Control*, vol. 51, Oct. 2004.
[10] A. N. Luiten, A. Mann, and D. Blair, "Paramagnetic susceptibility and permittivity measurements at microwave frequencies in cryogenic sapphire resonators," *J. Phys. D: Appl. Phys.*, vol. 29, pp. 2082–2090, 1996.

Using Quartz Resonators for Maximizing Wake-up Range in Wireless Wake-up Receivers

Gerd Ulrich Gamm, Tolgay Ungan and Leonhard Michael Reindl
Laboratory for Electrical Instrumentation
Department of Microsystems Engineering - IMTEK
Georges-Koehler-Allee 106, 79110 University of Freiburg, Germany
Email: Gerd.Ulrich.Gamm@imtek.uni-freiburg.de

***Abstract*— Separate wake-up receiver circuits for wireless sensor nodes combine the advantage of permanent accessibility with a very low current consumption, enabling nodes to work for several years. In a sleeping node incoming signals are passively demodulated and low-pass filtered. Till now we used an R-C circuit for filtering. In this work a quartz resonator is used between its parallel and serial resonance as an inductance with high Q-factor. This way higher voltages after demodulation compared to the R-C circuit could be reached. Since a higher voltage results in an increased wake-up signal detection, the wake-up range of the node can be extended.**

I. Introduction

Wireless sensor nodes with a separate wake-up receiver combine the advantage of a low current consumption and therefore long operating times with a real time behavior. The separate wake-up receiver circuit listens in sleep mode to incoming wake-up signals. In case a correct wake-up signal is detected, the node is triggered from sleep to active mode. In active mode the nodes main radio is used to establish a standard communication link. First prototypes of wake-up receivers can be found in [1]. An overview about commercially available wake-up receivers and their technology can be found in [2]. A node with included wake-up receiver was presented by the author of this paper in [3]. The there presented node consumes 2.8 µA in sleep mode while still being able to react to incoming wake-up signals. Wake-up range was measured to 50 meters in an free field environment. The low current consumption is achieved by using a low frequency receiver circuit working at 125 kHz. In the sending node the 125 kHz wake-up signal is modulated on the 868 MHz carrier of the main radio using OOK-modulation (On Off Keying). The 125 kHz signal is additionally modulated with a 16 bit address information to wake up selected nodes. A block diagram of the node can be seen in figure 1.

In sleep mode all incoming signals are routed to the upper path of the node. After impedance matching and lowpass filtering only the 125 kHz envelope signal remains and is fed to the AS3932 wake-up receiver chip from Austriamicrosystems. If a correct wake-up sequence is detected the AS3932 chip interrupts the microcontroller from it's sleep mode. The controller then toggles the antenna switch and starts a communication using the CC1101 transceiver from

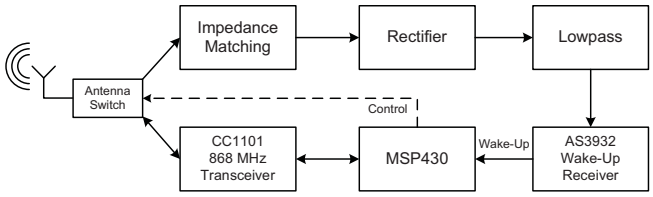

Fig. 1. Block diagram of the sensor node. In sleep mode all incoming signals are routed to the upper path. After demodulation and low pass filtering the signal is fed to the 125 kHz wake-up receiver IC.

Texas Instruments. In figure 2 a schematic of the passive demodulation circuit can be seen.

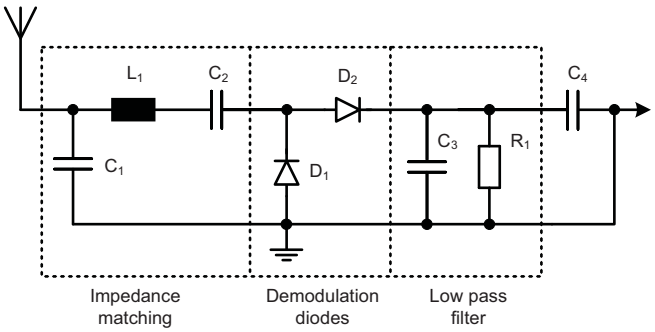

Fig. 2. Schematic of the passive demodulation circuit. The lowpass filter is realized by a shunt RC.

The lowpass filtering in this circuit is realized by an R and C in parallel. In this work we want to replace the R-C part of the demodulation circuit by an LC lowpass. To avoid loses in the inductance we want to use a quartz resonator as an inductance with a high quality factor. A quartz resonator between it's serial and parallel resonance frequency behaves like an inductance with high quality factor. Figure 3 visualizes the inductive frequency range. The concept was proofed in [4] by Ungan et. al at a frequency of 24 MHz. There it is shown that with a rising quality factor of the resonator a higher impedance is achievable. And since the quality factor is anti proportional to the frequency of the resonator we expect that at a frequency of 125 kHz a high impedance is possible. A higher voltage level at the input of the 125 kHz wake-up receiver IC

then results in a longer wake-up range and therefore extends the range of applications that are possible with the nodes.

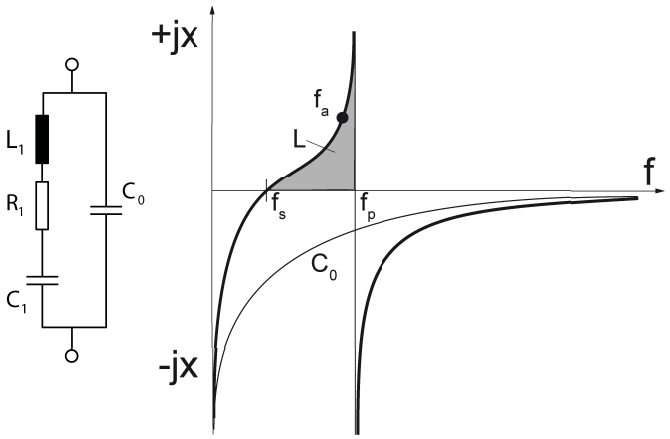

Fig. 3. A quartz between it's serial and parallel resonance behaves like an inductance with a high quality factor. [Source: Tolgay Ungan]

II. Measurement Setup

For testing the performance of the quartz resonator two circuits were designed. In the first circuit the quartz is connected in series to the antenna. A capacitance in parallel completes the LC lowpass circuit. The schematic drawing of the first circuit can be seen in figure 4. The SMA jack of the antenna is connected directly to a 125 kHz frequency generator. At the output the resulting signal is measured with an oscilloscope.

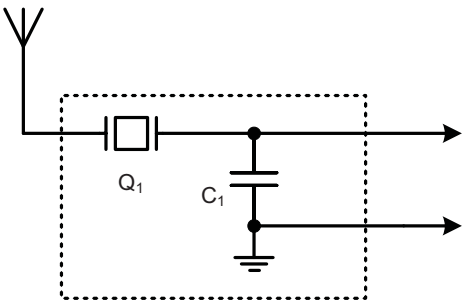

Fig. 4. Schematic diagram of the first circuit. It is just to test the quartz together with an shunt C as an lowpass filter at 125 kHz.

The second circuit is very similar to the original demodulation circuit. The only change that has been done is the replacement of the parallel R and C with an serial 125 kHz quartz and a shunt capacitor. This circuit includes the demodulation diodes and is meant to work at 868 MHz. At the SMA antenna jack a frequency generator is connected. The generator is configured to deliver an 868 MHz sinusoidal signal with an 125 kHz square signal amplitude modulated on it. After the demodulation diodes only the 125 kHz envelope signal remains. At the output an oscilloscope is connected to visualize the signals. The schematic of the circuit can be seen in figure 5

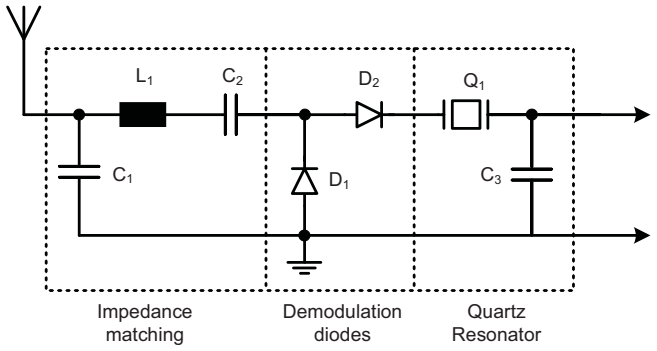

Fig. 5. Schematic diagram of the second test circuit. The input signal is an 868 MHz carrier with an 125 kHz square wave signal modulated on it.

In picture 6 a photo of the manufactured test board can be seen. It was build on an 1 mm FR4 substrate. For the upper circuit a 125 kHz quartz together with an 1 pF capacitor in parallel was used. For the lower circuit the values of the standard demodulation circuit were used but the RC combination was replaced by a serial 125 kHz quartz and a parallel 1 pF capacitor.

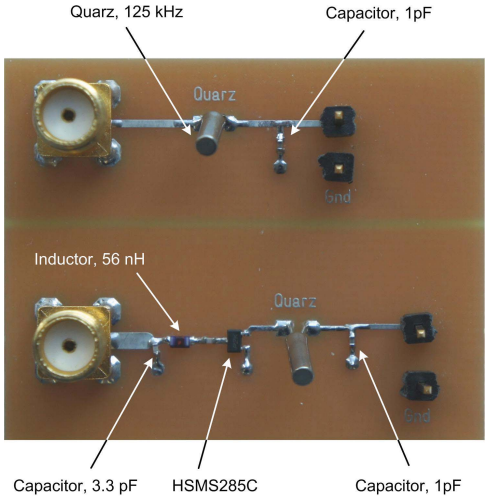

Fig. 6. Picture of the manufactured test board. The upper circuit is for testing the quartz lowpass. The lower circuit is for testing the whole demodulation circuit.

III. Measurement Results

To judge whether the quartz circuit delivers a higher voltage at it's end a reference circuit is needed. For the first measurement a second test board was used where all the components were bridged so that the incoming signal at the SMA Jack was fed directly to the output. For the second measurement the quartz capacitor combination was replaced by the original RC combination as can be seen in fig. 2.

Figure 7 shows the measurement results of the first test circuit as shown in 4. The red curve is the direct 125 kHz sinus signal from the signal generator *Rhode & Schwarz SMA 100*. The blue curve is the output signal after the serial 125 kHz quartz and parallel 1 pF capacitor. It was measured using a *Tektronix MSO4140 Mixed Signal Oscilloscope*. As can be seen the voltage after the quartz is about 3 times higher.

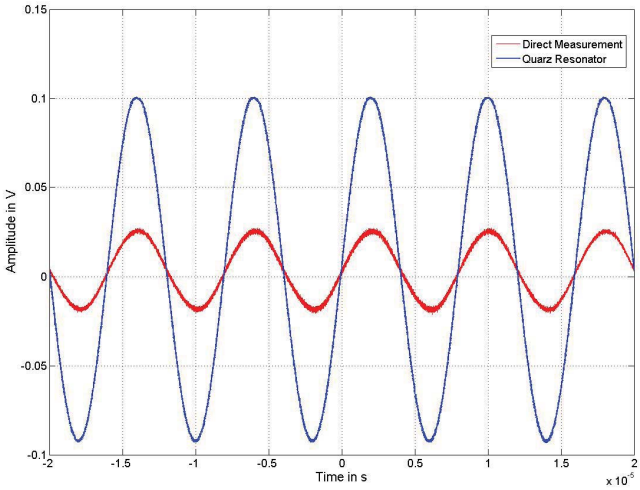

Fig. 7. Measurement of the first circuit. The red curve represents a pure 125 kHz signal. The blue curve represents the same signal measured after the quartz and capacitor circuit. Input was an 125 kHz sinus signal.

The second test circuit is closer to the real intended application. That is to use the quartz in the demodulation circuit with the goal to maximize the output voltage. For this measurement the signal generator was programmed to deliver an 868 MHz carrier with an OOK modulated 125 kHz square signal. The red curve represents the state of the art demodulation circuit with the RC combination. The blue curve represents the voltage using the quartz and the capacitor as shown in 5. As can be seen in the measurement figure 8 the resulting voltage at the output of the circuit is about 25 % higher compared to the original circuit.

IV. Conclusion and Outlook

Using a 125 kHz quartz as an inductance with a high quality factor provides some promising results for use in a demodulation circuit for wireless wake-up receivers. Due to the high quality factor the quartz has a significant post-pulse oscillation which means that after excitation of the quartz the voltage at the output does not disappear immediately. It takes some time till the voltage level reaches zero again. For the wake-up of selective nodes the 125 kHz signal is modulated with an 16 bit address information. If the fade out of the quartz takes more time than the duration of one bit problems might occur. Then the quartz has to be damped with an additional resistor which will also lower the possible output voltage.

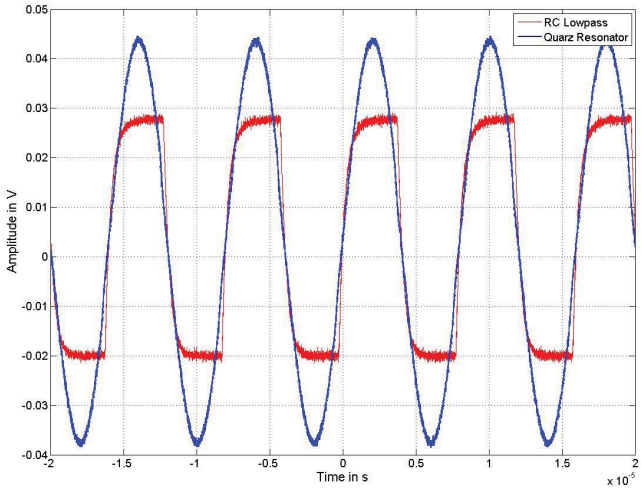

Fig. 8. Measurement results of the second test circuit. The red curve represents the original demodulation circuit. The blue curve represents the circuit with serial quartz and parallel C. Input was an 868 MHz carrier with 125 kHz square signal modulation.

Acknowledgment

This work has partly been supported by the German Research Foundation (DFG) within the Research Training Group 1103 (Embedded Microsystems).

References

[1] K. W. van der Doorn, B. and K. Langendoen, "A prototype low-cost wakeup radio for the 868 mhz band," *Int. J. Sensor Networks*, vol. 5, no. 1, pp. 22–32, 2009.

[2] I. Demirkol, C. Ersoy, and E. Onur, "Wake-up receivers for wireless sensor networks: benefits and challenges," *Wireless Communications, IEEE*, vol. 16, no. 4, pp. 88 –96, aug. 2009.

[3] G. U. Gamm, M. Kostic, M. Sippel, and L. M. Reindl, "Low-power sensor node with addressable wake-up on-demand capability," *Int. J. Sensor Networks*, vol. 11, no. 1, pp. 48–56, 2012.

[4] T. Ungan, X. Le Polozec, W. Walker, and L. Reindl, "Rf energy harvesting design using high q resonators," in *Wireless Sensing, Local Positioning, and RFID, 2009. IMWS 2009. IEEE MTT-S International Microwave Workshop on*, sept. 2009, pp. 1 –4.

Recently result on passive hydrogen maser of SHAO by single frequency modulation

LIU TieXin, Xu wen, CHEN W.X, DAI J.Y,
ZHANG Y, XIE Y.H, LIN C.F
Time & frequency research
Shanghai Astronomical Observatory, CAS
Shanghai, China
tiexinl@shao.ac.cn

Xu wen
Graduate University,
CAS,
Beijing, China

***Abstract*—This paper introduces recently result on passive hydrogen maser of shanghai Astronomical Observatory by single frequency modulation. Digital servo system and analog servo system have been experimented. DDS is used to generate frequency modulation in the RF interrogation chain in both systems. The algorithm separating two errors is used in digital system. The traditional integrator and digital phase shift are used in analog system. An Allan standard deviation of two systems has been tested based on same physical part. Both of them have achieved at $\sigma_y(\tau) < 1\times10^{-12}\tau^{-1/2}$ ($1s\le\tau\le10000s$) and σ_y (day) $<2\times10^{-14}$.**

I. INTRODUCTION

Conventional active hydrogen masers are developed in Shanghai Astronomical Observatory for a long time, which are limited in some applications for their size and weight. Miniature passive hydrogen maser has been researched in recently years [1, 2]. The electronic design of single frequency modulation has been experimented since 2008.This paper describes the designs and recently results of passive hydrogen maser by this method.

II. DESIGN

The passive hydrogen maser is subdivided into two principal functional packages. The physics package is used as a very narrow-band amplifier and frequency discriminator. The electronics package comprises two frequency lock-loops: 10MHz crystal oscillator frequency is locked to the hydrogen emission line and the resonant cavity frequency is locked to the crystal oscillator frequency.

physics package

The conventional active hydrogen maser has the cylindrical TE011-mode resonant cavity. The key to miniaturization of the active hydrogen maser is to use a smaller microwave cavity. But the quality factor of the cavity is reduced as it becomes smaller. So the atomic resonance needs to be interrogated with an externally generated microwave signal in the passive hydrogen maser.

A solid-state hydride storage container is used to supply the molecular hydrogen gas, which is purified by the Pd tube. After discharged, hydrogen atoms pass through a four-pole state selector. The hydrogen flux is controlled by Pd tube temperature. This physics package has one high vacuum enclosure for storage bulb. The cavity is made of aluminum. There are two layers ovens to keep the cavity temperature. Four layers magnetic shields are used for physics package.

The gain of physics package is about 2.8dB and the H line-width is about 3~4Hz at -80dBm microwave signal input.

Electronic package

The main units of electronic package are detailed in fig1, which comprises two frequency lock-loops: 10MHz VCXO is locked to the hydrogen emission line and the resonant cavity frequency is locked to the VCXO frequency.

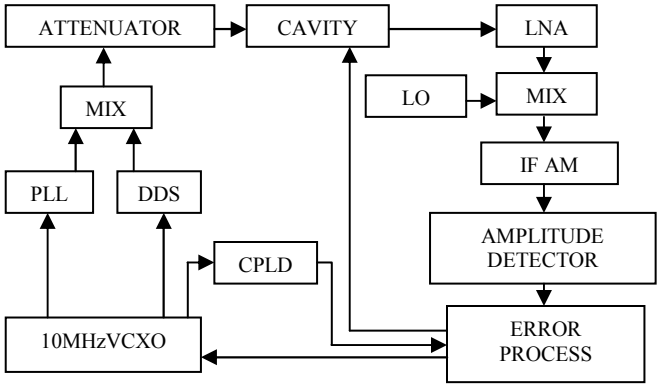

Fig 1.The functional block diagram of the electronic package

The 10MHz of the VCXO is multiplied to 1.4GHz by PLL. Direct digital frequency synthesizer AD9854 is used to produce square frequency modulation signal. The modulation frequency is 12.5KHz. It is convenient to change modulation frequency and modulation factor by controlling software for DDS.

This work was supported by National Natural Science Foundation of China (10778704 &11178023)

The out signal is amplified and mixed with the 1.44GHz LO. LNA (NF<1dB) is used. The IF single is 19.6MHz. 12.5KHz error signal is gotten by the amplitude detector.

Two 12.5KHz square waves are provided by CPLD as synchronic signal. For single frequency modulation the phase of this signal is very important. The phases of two signals need to be decided carefully for good frequency stability. The digital phase shift is realized by CPLD. It is easy to change the phase by software.

The error signal is processed with the two synchronic signals to produce two proper control voltages for VCXO (Voltage Control Crystal Oscillator) and ACT (Automatic Cavity Turning) varactor diode. Both digital algorithm and analog integrator are experimented in error process system.

Digital servo

The main hardware structures of the digital servo system are showed in fig2.The AD samples the 12.5KHz error signal. The DA produces control voltage. The algorithm is developed in our lab to separate the error single by two 12.5KHz square signals according to the single frequency modulation principle. The PID control is used in both loops.

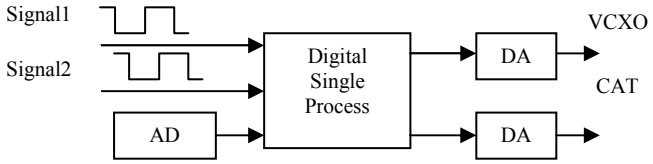

Fig2. Block diagram of digital servo system

At first the DSP is used for its user friendly interface. The S curves are easy to observe. Then the FPGA is used for its real-time processing [3].

Analog servo

The analog servo system is showed in fig3. The traditional synchronic detector and integrator are used in two loops.

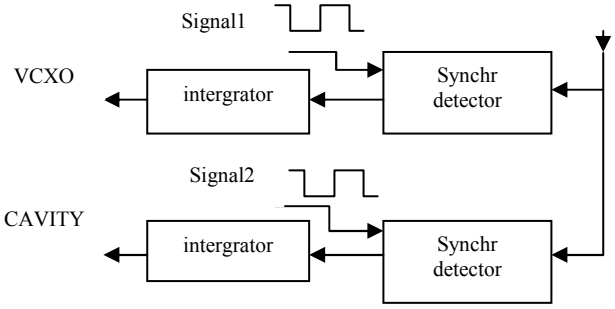

Fig3.Block diagram of analog servo system

The error signal is separated by the two synchronic square waves to control VCXO and varactor diode of ACT according to the single frequency modulation principle too. The parameters of the integrator and the phase of the synchronic signal are very important to get good frequency stability.

III. EXPERIMENTAL RESULTS

The frequency stability of the passive hydrogen maser is tested by the Picotime (from SpectraTime of Switzerland). The active hydrogen maser VCH-1003 provides the reference signal.

The passive hydrogen maser is put in the simply controlling temperature room by a commercial air conditioner. The temperature sensitivity is tested in the room with the temperature transitions between +18℃and +26℃.The result is provided in fig4. The measured temperature coefficient is below $2\times10^{-14}/℃$.

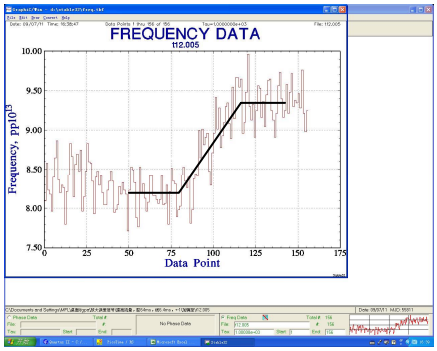

Fig4. Output frequency VS temperature transition

The molecular hydrogen gas is purified by the Pd tube. The hydrogen flux is changed by controlling Pd tube temperature. So the atomic gain variation is simulated by controlling the Pd tube temperature. Fig5 shows the results of the output frequency when 1dB atomic gain variation. The measured sensitivity is below 2×10^{-13}/1dB. The conventional hydrogen flux tuning is difficult to realize by single frequency modulation. How to reduce the atomic gain variation is important.

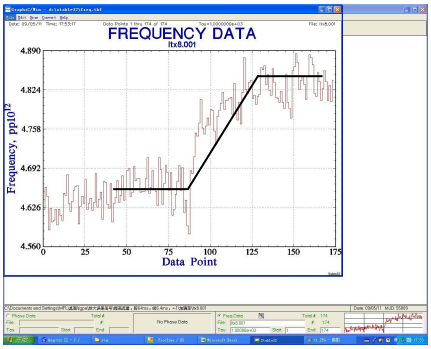

Fig5.Output frequency VS the atomic gain variation

Measurement of frequency stability has been performed. Allan standard deviations of the digital servo and analog servo have been tested based on the same physical part. Both of them have achieved at $\sigma_y(\tau) < 1\times10^{-12}\tau^{-1/2}$ ($1s\le\tau\le10000s$) and σ_y (day) $<2\times10^{-14}$. The long time frequency stability is σ_y (day) $<1\times10^{-14}$ when the drift is removed. Fig6 shows the result of the Hadamard Deviation of the analog servo design.

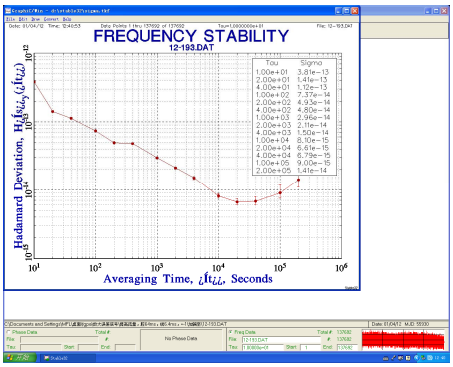

Fig6.frequency stability of the passive hydrogen maser

IV. CONCLUSIONS

We have reported the recently result of passive hydrogen maser of SHAO by single frequency modulation. Digital modulation and digital phase shift are used in electronic design. Both digital servo and analog servo have the similar result. The frequency drift of this passive hydrogen maser is needed to analyze in the future.

REFERENCES

[1] Chuanfu lin,Tiexin Liu,Zaicheng Zhai etc,"MINITURE PASSIVE HYDROGEN MASER AT SHANGHAI OBSERVATORY,"2001 IEEEInternational Frequency Control Symposium and PDA Exhibition

[2] Xie Yonghui,Dai Jiayu,etc."Development of passive hydrogen maser in Shanghai Astronimical Observatory,"24th European Frequency and Time Forum,2010

[3] YuYingLI， TiexinLIU， ChuanfuLIN etc. "A Digital Servo with Single Frequency Modulation for Passive Hydrogen Maser"2012 JOINT CONFERENCE OF THE IEEE INTERNATIONAL FREQUENCY CONTROL SYMPOSIUM &EUROPEAN FREQUENCY AND TIME FORUM

Orientation Light Shift Suppression in Alkali Atom Microwave Standards with Laser Pumping

Alexey Baranov, Sergey Ermak, Vladimir Semenov
Department of Quantum Electronics
St. Petersburg State Polytechnical University
St. Petersburg, Russia
lexusbar@gmail.com

***Abstract* - This work presents analytical studies of the orientation and light frequency shifts in microwave standards with regard to tensor component. It was shown that modulation technique application not only allows eliminating light shift but also provides significant reduction of the frequency errors introduced by external magnetic field orientation fluctuations while pumping alkali atoms with either D1 or D2 line.**

I. INTRODUCTION

In applications of optical-microwave double resonance spectroscopy one of the most negative roles plays so-called light shift associated with the Stark effect. Energy sublevels of the atoms shift under the influence of the electromagnetic field of the pump source that leads to the precision limit of such quantum devices as quantum magnetometers and frequency standards [1]. As shown in [2], when lamp source is used to pump atoms, significant dependence of the frequency shift on the orientation of the working magnetic field with respect to the direction of the optical axis takes place. This dependence is determined by the tensor component of the light shift associated with the effect of alignment of the atoms in ground state. This effect depends on the degree of resolution of the excited state energy structures of the alkali atoms [3].

When changing lamp source to a laser in order to improve overall parameters of quantum devices, in [4] a technique of the laser spectrum frequency modulation was presented. This procedure can drastically reduce the dependence of the light shift on the frequency detuning of the laser source from the atomic transition frequency. However, tensor component, which in the case of pumping D2-line is much smaller than its contribution to the scalar component hadn't been taken into account. This paper presents the results of the calculation of the light and orientation frequency shift of microwave resonance in a variety of alkali atoms, taking into account the tensor component. We show that the modulation technique not only reduces the light shift, but also makes it possible to suppress the orientation shift of the resonance frequency.

II. MAIN RESULTS

For our study we selected isotopes of rubidium, potassium and cesium, the most commonly used in the practice of radio-optical resonance. Calculations were carried out similarly to the way it had been done in [3]. Laser spectrum was approximated by Doppler functions with weighting factors proportional to the square of the Bessel function. We made calculations for different pumping regimes, "tuning" laser to D_1 and D_2-lines with the hyperfine structure of the ground-state atoms with total angular momenta F and F+1 and utilizing different modulation frequencies and indices. Fig. 1 and 2 show the orientation and light frequency shifts of the frequency vs. laser detuning from the ground state transition of alkali atoms with total angular momenta F and F +1 of unmodulated pump source.

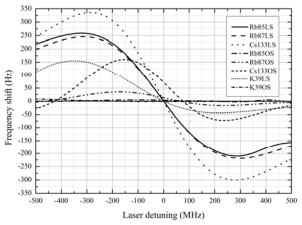

Figure 1. Orientation and light shift curves for D_2 line F transition

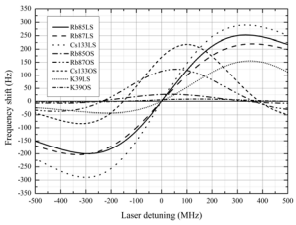

Figure 2. Orientation and light shift curves for D_2 line F+1 transition

The suppression effect of light and orientation shifts is illustrated in Fig. 3 and 4, which show the corresponding dependence for Rb^{87} atoms in a laser pump lines D_1 and D_2 with the hyperfine structure of the ground-state atoms with total angular momentum F = 2.

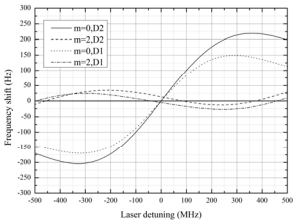

Figure 3. Light shift suppression effect demonstration for Rb^{87} isotope, F=2

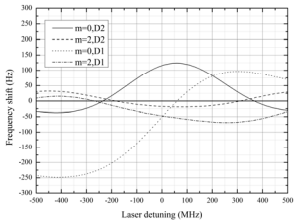

Figure 4. Orientation shift suppression effect demonstration for Rb^{87} isotope, F=2

Examples of the orientation shift for Rb^{85} isotope for various modulation frequencies and indices of the laser source tuned to D_1 and D_2 lines are shown in Fig. 5 and 6.

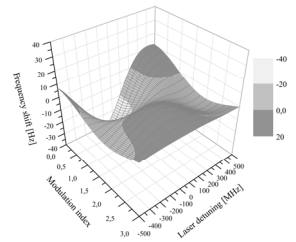

Figure 5. 3d visualization of the orientation shift behavior for D_1-line of Rb^{85} isotope

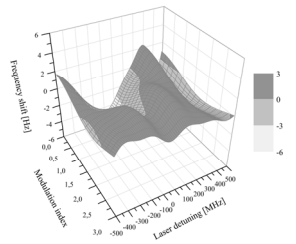

Figure 6. 3d visualization of the orientation shift behavior for D_2-line of Rb^{85} isotope

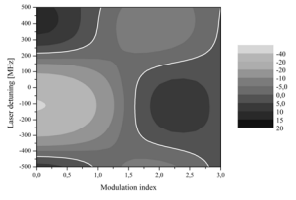

Figure 7. Top view of the figure 5 plot. White line represents zero frequency shift

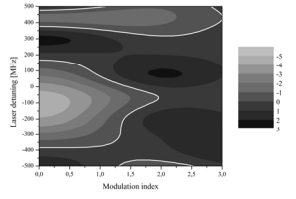

Figure 8. Top view of the figure 6 plot. White line represents zero frequency shift

Analysis of the results leads to the following conclusions. First of all, for equal integral intensities of a laser tuned to D_2-line hyperfine sublevel with total angular momentum F, absolute values of the light shift and its steepness increases with the increase of the nuclear spin of an alkali isotope. In this case, orientation correction depends on the resolution of the excited state energy structures: for cesium atoms (with the splitting of the excited state ~ 600 MHz), this correction is maximum, for the isotopes Rb^{87} and K^{39}, where the splitting of the excited state are respectively 213 and 72 MHz [5], orientation correction is an order of magnitude smaller. Despite the relatively low operating frequencies in these isotopes (462 MHz for K^{39} and 3036 MHz for Rb^{87} [5]), a relatively small orientation correction to the frequency of the quantum discriminator makes such devices competitive for moving and rotating applications. This assertion remains valid in the case of laser optical pumping of alkali atoms with the D_2-line hyperfine sublevel with total angular momentum of the atom F +1: the only difference is in the sign of the slope of the dependences, and (slightly) in the absolute values of light and orientation shifts.

Secondly, if laser is tuned to D_1-line where tensor component of the light shift is much higher than in D_2, orientation correction to the frequency for all of the alkali atoms is approximately an order of magnitude higher in comparison to D_2-line pumping.

Thirdly, applying frequency modulation to the pumping laser it is possible to reduce both the magnitude and steepness of the dependence of the light and the orientation changes as a function of frequency detuning of the laser due to modification of its spectrum.

At the same modulation index light and orientation shift suppression effect appears in varying degrees and depends on the size of the numeric value of the alkali atom nuclear spin, the value of its total angular momentum in the ground state and the choice of a spectral line of the pumping spectrum. In the case of an appropriate modulation index the regime of coincidence of frequency detuning of the laser, when both the light and the orientation frequency shifts reach zero can be realized

The analysis of the light shift effect shows that the variation of the laser linewidth as well as the modulation frequency does not lead to qualitative changes in the results. We expect to receive the suppression of the orientation and light frequency shifts for a wide range of laser pump sources used in quantum discriminators.

REFERENCES

[1] Fritz Riehle, “Frequency standards. Basics and applications”, WILEY-VCH Verlag GmbH Co. KGaA, 2005, p.526.

[2] A. Baranov, S. Ermak, V. Semenov, “The orientation dependence of the SHF radio-optical resonance frequency light shift in rubidium vapors”, IFCS-EFTF 2011 Conference Proceedings, 2011.

[3] V.V. Semenov, “About the contribution of the radio-optical resonance tensor component light shift in rubidium vapors”, Izvestia Vuzov, Physics, №2, 1999, pp. 86-90.

[4] C. Affolderbach, C.Andreeva, S.Cartaleva, [et al.] “Light-shift suppression in laser optically pumped vapor-cell atomic frequency standards”, Appl.Phys. B., Vol. 8.,№7.,2005, pp. 1–8.

[5] A.A.Radcig, B.M.Smirnov, “Parametry atomov I atomnih ionov”, M.: Energoatomizdat, 1986, p. 344

Cell-related effects in the Pulsed Optically Pumped frequency standard

S. Micalizio, C. E. Calosso, A. Godone, and F. Levi
Optics Division
Istituto Nazionale di Ricerca Metrologica, INRIM
Torino, Italy
s.micalizio@inrim.it

***Abstract*—In this paper we describe two phenomena that may affect the medium-long term stability performance of the pulsed vapor cell Rb clock we implemented at INRIM. The first effect is an anomalously large temperature sensitivity of the clock frequency. This effect is related to the presence of large stems in the cell and the order of magnitude of the observed phenomenon may be explained in terms of a model based on the ideal gas law.**

The second phenomenon is related to losses in the microwave cavity induced by the presence of the dielectric material (the cell) in the cavity and by the deposition of metallic Rb on the inner walls of the clock cell.

I. Introduction

In a previous work [], we presented the implementation and the performances of the pulsed optically pumped (POP) Rb clock. Specifically, the prototype we implemented at INRIM exhibits a frequency stability expressed in terms of Allan deviation of $1.7\times10^{-13}\,\tau^{-1/2}$, remaining in the 10^{-15} range for integration times τ up to 10^5 s. Moreover, the observed frequency drift is of few units of 10^{-15}/day. These results represent a record achievement for a vapor-cell frequency standard and make the POP clock potentially very attractive for a variety of applications, including telecommunication and space radio-navigation.

In this work, we discuss two phenomena related to the clock cell that should be controlled if we want the above performances to be repeatable.

The first one is the observation of an enhanced temperature sensitivity of the clock frequency. Specifically, despite we used in our cell a temperature compensated mixture of buffer gases, the observed temperature sensitivity is $\approx 1\times10^{-10}$/°C, more than one order of magnitude larger than the expected value. Yet, this phenomenon cannot be ascribed to cavity pulling and/or to spin exchange that are in fact negligible in our setup.

We explained this unexpected effect in terms of a simple model based on the ideal gas law. In particular, our cell is composed of a main body that is housed in the microwave cavity and two relatively large stems that are outside the cavity. We demonstrated that a temperature fluctuation in the stems produces a change of the buffer gas pressure in all the cell. This pressure variation induces a shift of the clock resonance and is responsible of the observed temperature sensitivity of the clock frequency. This effect is proportional to the ratio between the volumes of the stems and of the main body, then it can be reduced manufacturing the cell with a stem, if required, much smaller than the cell main body.

The second one is the effect of the cell on the cavity parameters, such as resonance frequency and quality factor Q. The cavity behavior is described in terms of a lumped equivalent circuit in which the input coupling loop and the dielectric cell containing ^{87}Rb atoms are taken into account. In particular, the effect of the cell on the cavity resonance frequency is evaluated via a first-order perturbation approach. Moreover, we report two critical behaviors of the cavity Q: the cavity Q versus the temperature and versus time at a fixed temperature. The observed degradation of the cavity Q may be related to the deposition of Rb atoms on the inner cell surface.

II. The POP Rb Clock with Optical Detection

The prototype is based on a pulsed approach in which the clock transition is detected by observing Ramsey fringes on a laser absorption signal.

The experimental set-up is represented in Fig. 1.

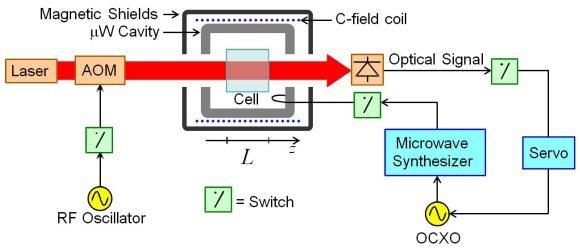

Fig. 1. Experimental setup of the POP clock.

This work was supported by ESA (contract 21504/08/NL/GLC)

It is composed of three main parts:

1) physics package;

2) optics;

3) electronics.

The physics package is layer structure and several components can be identified (Fig. 2).

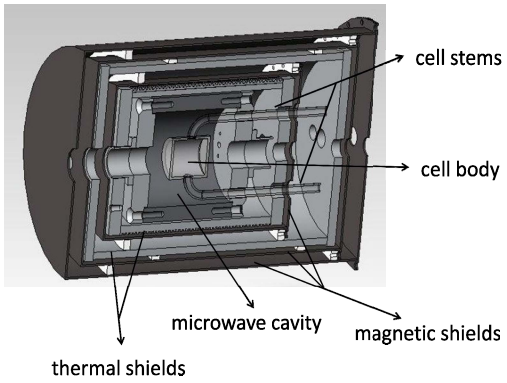

Fig. 2. Physics package of the POP clock.

The quartz cell contains the ^{87}Rb atoms and a buffer gas mixture N_2+Ar, at the total pressure P_s = 25 Torr. As shown in Fig. 2, the cell exhibits two large stems required to have a cold point in the cell; in this way, the condensation of Rb atoms inside the main body of the cell is in principle avoided.

The cell is placed in a Mo cavity resonating at 6.834 GHz. A quantization magnetic field along the cavity axis is applied (B_0 = 1.5 μT). Moreover, three mu-metal magnetic shields the physics package for an overall shielding factor of 1000.

Two thermal oven working at different temperatures were implemented. The internal one works at 65.5 °C and is devoted the cell body-cavity system and the external one at 63.5 °C for the stems. The thermal stability for both the oven is of the order 1 mK for integration times up to 10000 s.

All the physics package is placed in vacuum structure in order to isolate the system from environmental fluctuations.

The optics is composed of a DFB laser at 780 nm (D_2 line) and delivers a full power of 15 mW. An AOM is used to switch on and off the laser during the pulsed operation.

The electronics is composed of a low phase noise synthesis chain delivering a signal at 6.834 GHz starting from a 10 MHz OCXO. The synthesis chain is based on non-linear transmission lines [2]. A digital electronics was also implemented on FPGA to drive all the clock operation phases.

The clock operation is based on a pulsed optical pumping, followed by a microwave Ramsey interaction, as represented in Fig. 3

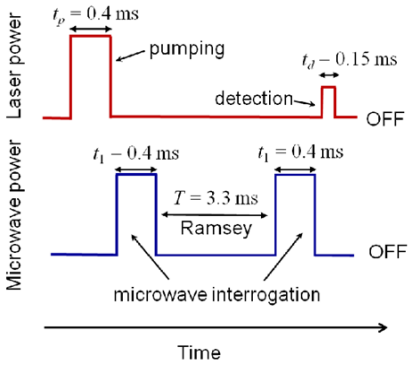

III. ANOMALOUYSLY LARGE TEMPERATURE SENSITY OF THE CLOCK FREQUENCY

It is well established that the unperturbed ground state hyperfine frequency ν_0 of alkali-metal atoms is shifted by the interaction with buffer gas atoms/molecules [3, 4]. This shift versus the cell temperature is a parabola: working around the maximum of the parabola it is in principle possible to reduce the temperature sensitivity of the clock frequency vs temperature (Fig. 4). Referring the coefficients of the curve to the inversion temperature T_i and fitting the experimental points with a parabola, the clock frequency can be written as:

$$\nu(T) = \nu_0 + P_s\left[\beta'_i + \gamma'_i(T - T_i)^2\right] \quad (1)$$

where $\beta'_i = 174\ \mathrm{Hz/Torr}$ and $\gamma'_i = -0.00071\,\frac{\mathrm{Hz}}{\mathrm{K}^2}\mathrm{Torr}$.

Supposing to work at a temperature T so that $|T–T_i|$<0.2 K, the temperature stability of the clock frequency is expected to be 4×10^{-12}/K.

However, a high sensitivity of the clock frequency vs temperature is observed despite the use in the cell of a compensated mixture of buffer gases and the cell working temperature is set on the maximum of the parabola.

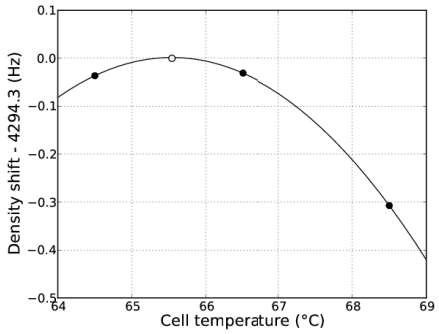

Fig. 4. Clock frequency shift versus temperature.

In particular, the measured coefficient is of the order of 1×10^{-10}/K. To understand the origin of this phenomenon, we consider that a high unexpected correlation between the clock frequency and the stem temperature is observed (Fig. 5).

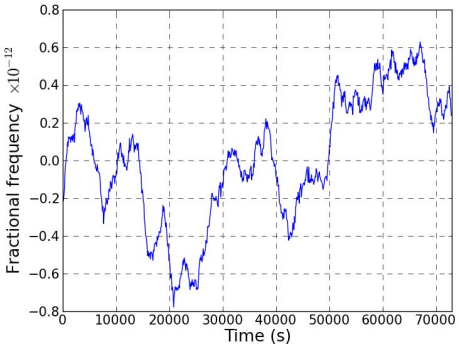

(a)

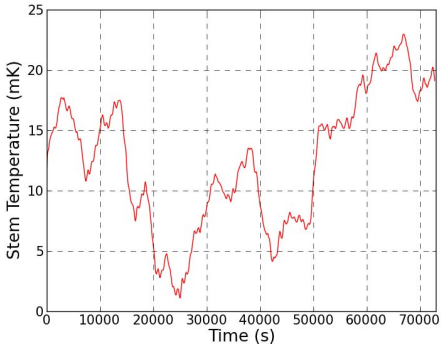

(b)

temp … the stem … l on the idea … *A*. … cell is divi… ock cell plac… upled to the … ined by the two stems (volume V_b) that are outside the microwave cavity; they are thermally coupled to the external oven at the temperature T_b.

It is easy to see that thanks to the ideal gas law, the atomic density n_a of buffer gas particles taking part to the interaction is given by:

$$n_a \approx n_s\left(1-\frac{T_a-T_b}{T_b}\mathrm{v}_b\right) \tag{2}$$

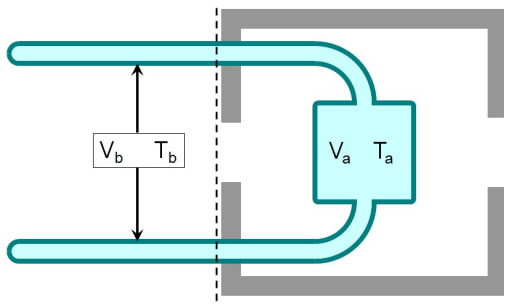

Fig. 6. Model used to explain the observed large temperature sensitivity.

where n_s is the buffer gas density in the entire cell and $\mathrm{v}_b = V_b/(V_a+V_b)$.

From Eq. (2) it is easy to see the density of buffer gas atoms really involved in the interaction with Rb atoms depends on T_a and T_b, and for consequence may fluctuate due to variations of T_a and T_b. Conversely, ns is fixed at the cell sealing time and is related to P_s by the ideal gas law (in our case $n_s \approx 8\times10^{17}$ cm^{-3}.

In form totally equivalent to (1), the buffer gas shift can be written in terms of n_a:

$$\nu(T_a,T_b)=\nu_0+n_a\left[a'_{0i}+a'_{2i}(T_a-T_i)^2\right]\approx \nu_0+n_s\left(1-\frac{T_a-T_b}{T_b}\mathrm{v}_b\right)\left[a'_{0i}+a'_{2i}(T_a-T_i)^2\right] \tag{3}$$

with $a'_{0i} \approx 5.5\times10^{-15}$ Hz cm^{-3}, $a'_{2i} \approx -2.2\times10^{-20}$ Hz K^2 cm^{-3}. Deriving Eq. (3) with respect to and T_b (T_a) keeping constant T_a (T_b) we have:

$$\left.\frac{\partial\nu}{\partial T_b}\right|_{T_a=const} \approx n_s\,a'_{0i}\frac{\mathrm{v}_b}{T_b} \Rightarrow \frac{\partial\nu/\nu_0}{\partial T_b}\approx\frac{P_s\,\beta'_i\,\mathrm{v}_b}{\nu_0 T_b}=1.4\times10^{-10}/\mathrm{K} \tag{4}$$

that is of the same order of magnitude of the observed effect.

Similarly, we have:

$$\left.\frac{\partial\nu}{\partial T_a}\right|_{T_b=const} \approx n_s\,a'_{0i}\left[-\frac{\mathrm{v}_b}{T_b}+2\frac{a'_{2i}}{a'_{0i}}(T_a-T_i)\right] \tag{5}$$

From (5) it turns out that a new point where the clock frequency is insensitive to temperature fluctuations of the cell is found. In fact, (5) is null when:

$$T_a = T_i+\frac{a'_{0i}}{2a'_{2i}}\frac{\mathrm{v}_b}{T_b} \tag{6}$$

On the other hand, from (4) and (5) it is observed that $\left.\frac{\partial\nu}{\partial T_b}\right|_{T_a=const} = -\left.\frac{\partial\nu}{\partial T_a}\right|_{T_b=const}$ when the cell temperature is set to the inversion temperature T_i. This means that designing the physics package so that T_a and T_b are correlated the two temperature coefficients compensate each other.

According to previous equations, several solutions can be applied to reduce this anomalously large temperature sensitivity of the clock frequency:

- make the cell with v_b negligible;
- good control of the temperature not only of the cell but also of the stems;

- adopt a mixture of three buffer gas to reduce not only the linear term but also the pressure coefficient β_i'.

In our system we used essentially the second technique, implementing an active temperature control devoted to the stems only. Moreover, to limit thermal bridges from the environment to the physics package, the vacuum structure was wrapped with highly insulating material.

In this way, the clock frequency stability in the medium long term remains at the level of 1×10^{-14} or better for integration times of the order of 1 day (Fig. 7).

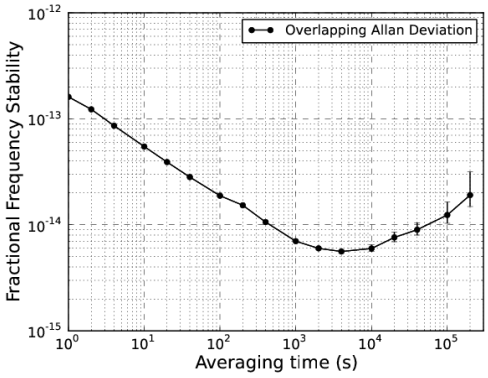

IV. DIELECTRIC AND ALKALI-METAL DEPOSITION EFFECT

It is well known that the cavity behavior is described with a lumped equivalent circuit where the input coupling loop, the cell and the eventual presence of PIN and varactor diodes for tuning or *Q*-control are considered [5].

In the frame of this model, the losses in the dielectric medium (quartz cell) can be described by the corresponding *Q* factor:

$$Q_d = \frac{\omega_0 W}{P_\varepsilon} = \frac{\varepsilon}{\varepsilon_i}\frac{\int_{V_C}|\mathbf{E}|dv}{\int_{V_d}|\mathbf{E}|dv} \tag{6}$$

where ω_0 is the cavity frequency, W the energy stored in the cavity, **E** the electric field and P the power dissipated in the dielectric. Moreover, $\tilde{\varepsilon} = \varepsilon - j\varepsilon_i$ is the complex dielectric constant and $\varepsilon_r = \varepsilon/\varepsilon_0$, $\varepsilon_{ir} = \varepsilon_i/\varepsilon_0$, being ε_0 the vacuum permittivity; V_C and V_d are the cavity and the cell volumes respectively.

If the cell thickness t is small compared to cell size the mode is only slightly perturbed and a first-order approximation in t may be found for the evaluation of the denominator []. It turns out that:

$$Q_d = \frac{1}{2\varepsilon_{ir}\zeta t} \tag{7}$$

where ζ is a geometrical factor. Similarly, the cavity resonant frequency is shifted due to the presence of the dielectric by an amount given by:

$$\frac{\Delta\nu_C}{\nu_0} = -(\varepsilon_r - 1)\zeta t \tag{8}$$

The geometrical factor ζ is represented in Fig. 8 for the case of a cylindrical cavity.

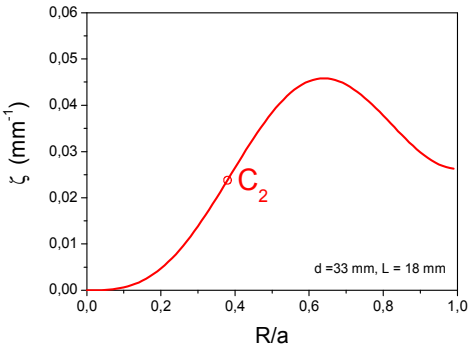

Fig. 8. Geometrical factor in (7) and (8). The point C_2 represents the value of ζ for our cell-cavity system.

Concerning other losses mechanisms, it is known that 6-7 monolayers of liquid Rb may be absorbed by the cell surface. Their thickness is much smaller than penetration depth of Rb and significant losses are not expected. However, during cell fabrication and filling, impurities may be introduced acting as trapping centers of metallic Rb leading to dramatic power losses in the cavity. Even if not well understood, these effects may be accounted for introducing an impedance Z_a and a related figure of merit Q_a:

$$Q_a = \frac{\omega_0 L}{\mathrm{Re}\, Z_a} \tag{9}$$

Medium-long term clock stability is limited by the time stability of Q_a. A critical behavior of Q_a was experimentally observed (Fig. 9).

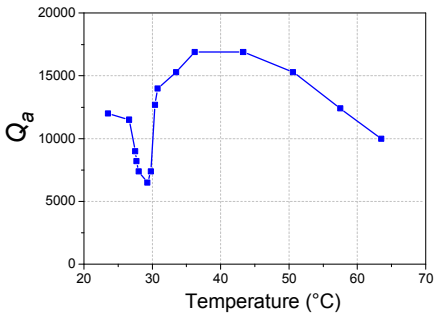

Fig. 9. Behavior of the cavity quality factor vs temperature.

In particular, the temperature "resonance" around 30 °C is rarely reported in literature and may be due to the formation of RbOH, while the decreasing behavior after 40 °C is probably due to the Rb liquid phase.

REFERENCES

[1] S. Micalizio, C. E. Calosso, A. Godone, and F. Levi, "Metrological characterization of the pulsed Rb clock with optical detection," Metrologia, vol. 49, May 2012.

[2] R. Boudot, S. Guerandel, and E. De Clercq, , "Simple-Design Low-Noise NLTL-Based Frequency Synthesizers for a CPT Cs Clock" IEEE Trans. Instrum. Meas. vol. 58, pp. 3659-3665, 2009.

[3] J. Vanier, R. Kunski, N. Cyr, J. Y. Savard, and M. Tetu, "On hyperfine frequency shifts caused by buffer gas: Application to the optically pumped passive rubidium frequency standard," J. Appl. Phys. vol. 53, pp. 5387-5391, 1982.

[4] O. Kozlova, S. Guerandel, and E. De Clercq, "Temperature and pressure shift of the Cs clock transition in presence of buffer gases: Ne, N_2, Ar," Phys. Rev A vol. 83, 062714 (1-9), 2011.

[5] A. Godone, S. Micalizio, F. Levi, and C. Calosso, "Microwave cavities for vapor cell frequency standards", Rev. Sci. Instrumnts Vol. 82, 074703 (1-15), 2011.

Characterization of compact CPT Clocks based on a Cs-Ne microcell

R. Boudot[1], X. Liu[1], E. Kroemer[1], P. Abbé[1], N. Passilly[1], S. Galliou[1], R. K. Chutani[1], V. Giordano[1], C. Gorecki[1], A. Al-Samaneh[2], D. Wahl[2] and R. Michalzik[2]

***Résumé*—This paper reports the characterization of compact Cs CPT clocks based on a single buffer gas Cs-Ne microcell. Two different experimental set-ups are tested. The first set-up uses an externally-modulated 895 nm Distributed Feedback (DFB) laser source while the second one uses a directly-modulated custom-designed 895 nm Vertical Cavity Surface Emitting Laser (VCSEL) source. Using the DFB set-up, through reduction of the temperature-dependent collisional frequency shift and an active light shift suppression technique, a clock frequency stability of 3.8×10^{-11} at 1 s and greatly better than 10^{-11} at 60000 s is demonstrated. This proves the potential of single buffer gas Cs-Ne microfabricated cells for the development of miniature atomic clocks. Preliminar characterization of CPT resonances are reported with the VCSEL-based setup. It is expected that similar clock stability performances are achievable in this case.**

I. Introduction

The combination of Coherent Population Trapping (CPT) physics [1] and micro electro-mechanical systems (MEMS) allows the development of chip scale atomic clocks (CSAC) [2] exhibiting a volume of a few cm^3, a power consumption of about 100 mW and a fractional frequency stability better than 10^{-11} at 1 hour and 1 day integration time [3]. Such frequency references, outperforming crystal quartz oscillators over long time scales, are intended to provide excellent base timing for numerous battery-operated applications such as telecommunication networks synchronization, navigation, military systems or even power distribution and underwater sensoring.

The heart of a miniature atomic clock is a microfabricated cell containing the alkali vapor and a buffer gas atmosphere to operate in the Dicke regime [4]. Pioneering cell fabrication and filling techniques are reported in [5], [6], [7]. Recently, we proposed an original method where the Cs vapor is generated after complete sealing of the cell by local heating of a side-cavity Cs metallic dispenser with a high-power infrared laser source [8], [9]. The presence of buffer gas in the cell induces a temperature-dependent frequency shift of the clock transition. Currently, the dependence on temperature of the clock transition is cancelled at the first order around a so-called inversion temperature by filling the cell with a buffer gas mixture [10], [11]. This technique is widely used in Rb standards. We recently reported the first direct observation of quadratic dependence on temperature of the Cs clock transition around a so-called inversion temperature T_{inv} of about 80°C in presence of a single Ne buffer gas [12]. In such a case, the inversion temperature was measured to be not dependent on the buffer gas pressure [13]. These results were confirmed by O. Kozlova et al. reporting in a delicate and metrological study the temperature and pressure shift the Cs clock transition in presence of several buffer gases [14]. Cs-Ne cells are then potential simple-configuration efficient candidates to be used at the heart of chip scale atomic clocks.

We report in this article the metrological characterization of CPT-based vapor cell clocks based on a Cs-Ne microfabricated cell. These cylindrical cells present a diameter of 2 mm and a length of 1.4 mm. Two different experimental set-up are implemented. The first one uses a DFB laser source at 894.6 nm on the Cs D_1 line and an external pigtailed electro-optic modulator for the generation of CPT sidebands. Additive advanced noise reduction techniques are developed in this set-up to improve greatly mid and long-term frequency stability performances. The second set-up uses a directly-modulated custom-designed VCSEL prototype at 894.6 nm developed in the frame of the MAC-TFC project [15] by Ulm University. Preliminar key parameters of the clock as well as an estimation of its short-term frequency stability are reported for this setup.

II. DFB set-up

A. Experimental set-up

Fig. 1 shows a simplified scheme of the set-up 1.

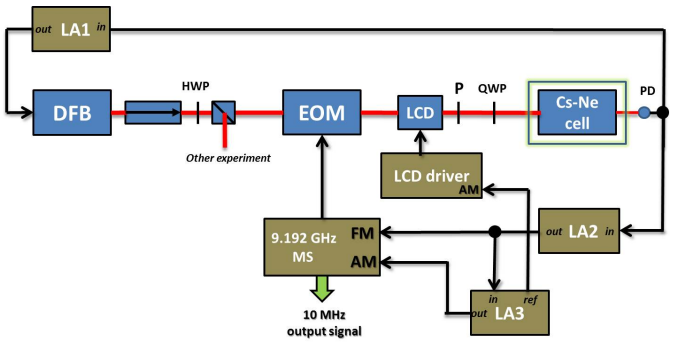

FIGURE 1. Schematic of the Cs-Ne microcell based CPT clock with a DFB laser resonant at 894.6 nm. MS : 10 MHz quartz-oscillator based microwave synthesizer, EOM : electro-optic modulator, LCD : voltage-controlled liquid crystal plate attenuator, P : polarizer, HWP : half-wave plate, QWP : quarter-wave plate, LA1 : lockin amplifier-based servo for laser frequency stabilization through modulation at 60 kHz of the laser bias current, LA2 : lockin amplifier-based servo for locking the local oscillator frequency to the CPT resonance transition, LA3 : lockin amplifier-based servo for light shift correction (LSC).

The laser source is a commercially-available GaAs semiconductor DFB laser diode emitting at 894.6 nm on the Cs D_1 line.

[1] The authors are with FEMTO-ST, CNRS, 26 chemin. de l'Epitaphe, Besancon, France. [2] The authors are with Ulm University, Institute of Optoelectronics, Ulm, Germany. e-mail: {rodolphe.boudot}@femto-st.fr

A Faraday optical isolator is placed at the output of the DFB laser in order to avoid optical feedback. Optical sidebands are generated by driving an external pigtailed phase electro-optic modulator (EOM) at 9.192 GHz using a microwave frequency synthesizer inspired from [16]. No phase noise degradation was observed between the microwave frequency synthesizer output and the 9.192 GHz optically carried signal. The collimated laser beam is circularly polarized using a quarter-wave plate and sent through the atomic cell. The cell temperature T_{cell} is stabilized close to 80°C. Temperature fluctuations of the microcell are below the mK level. A static magnetic field of a few μT parallel to the laser beam propagation is applied to split the hyperfine ground-state Zeeman transitions. The ensemble is surrounded by a two-layers mu-metal magnetic shield. The CPT resonance is monitored by detecting the laser power transmitted through the cell using a low-noise photodiode. The laser is frequency-stabilized near the center of the homogeneously broadened absorption line by modulating the DFB laser current at 60 kHz and demodulating it with the lock-in amplifier LA1. The atomic clock closed-loop operation is achieved by conventional synchronous modulation-demodulation technique ($\sim$ 1 kHz frequency) applied to the local oscillator frequency through the lockin amplifier LA2. Light shift is continuously minimized using a method inspired from [17]. For this purpose, the laser power is slowly modulated at 15 Hz (12 % depth) using a voltage-controlled liquid crystal display (LCD) attenuator. This laser power modulation is converted across the cell through the light shift effect into a slight clock frequency modulation that can be easily detected at the error signal output of the lockin amplifier LA2 used to stabilize the LO frequency. This modulation signal is found to be vanished close to a so-called RF power zero-light-point driving the EOM [18], [19]. An additional servo loop based on the lockin amplifier LA3 is eventually added to lock the RF power point where no light shift is present.

B. Experimental results

Fig. 2 shows both the CPT resonance contrast and the clock frequency shift versus the cell temperature. The CPT contrast is maximized in the 74-81°C temperature range. In this temperature range, it is clearly observed that the Cs clock frequency temperature-dependence is cancelled at the first order around 79-80°C. This measurement is in good agreement with [21]. Using coefficients published in [14], a fit of experimental points gives a Ne cell pressure of 79 Torr. This cell allows to make coincide a zero-sensitivity of the clock frequency to temperature variations and a maximum of CPT contrast close to 80°C. This will lead to mutual improvements of the clock long-term and short-term frequency stability.

Fig. 3 reports the frequency stability (Allan deviation) of the CPT clock based on a Cs-Ne microcell. It is measured at 10 MHz by comparison with a reference hydrogen maser. The short-term frequency stability is measured to be 3.8×10^{-11} at 1 s. The Allan deviation curve decreases well with a $\tau^{-1/2}$ slope until 1000 s. After 1000 s, the Allan deviation increases again. The frequency stability is greatly lower than 10^{-11} at 60 000 s. These results prove the potential of the Cs-Ne microcell solution to develop high-performance chip-scale atomic clocks.

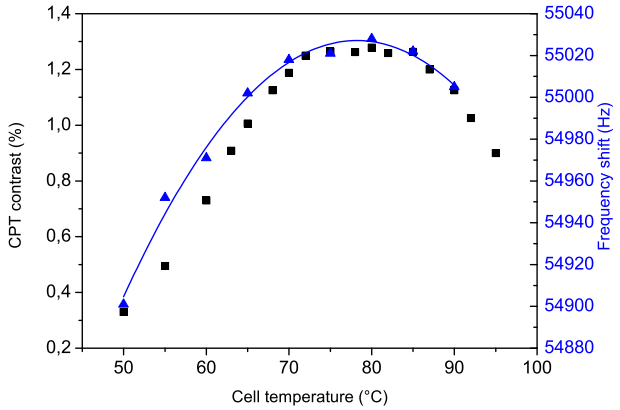

FIGURE 2. CPT resonance contrast (squares) and clock frequency shift (triangles) versus the cell temperature. The solid line is a second order polynomial function fit to the frequency data. For a given temperature, data results from interpolation at zero intensity of light-shift curves. The CPT contrast is found to be optimized close to the clock frequency inversion temperature.

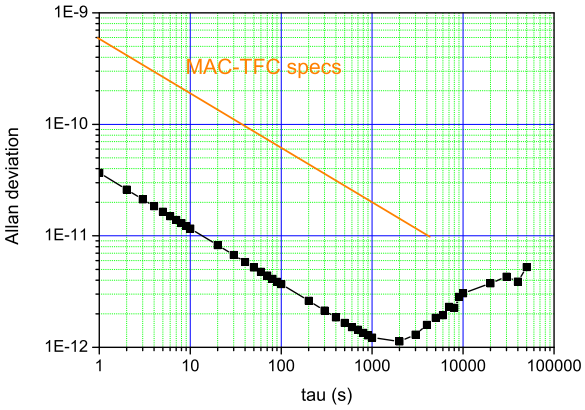

FIGURE 3. Allan deviation of the DFB-based Cs CPT clock. Specifications of the MAC-TFC project are reported for information.

III. VCSEL SET-UP

A. Experimental set-up

Fig. 4 shows a simplified scheme of the set-up 2.

The laser source is a custom-designed VCSEL resonant at 894.6 nm developed by Ulm University [20]. The laser dc current-temperature couple is biased to 1.3 mA - 30°C to be resonant with Cs atom transition D_1 line. The output beam of the laser is collimated into a 2-mm diameter beam and sent across a linear polarizer. The laser power incident to the cell is about 22 μW. The injection current of the laser is directly modulated at 4.596 GHz with a commercial frequency synthesizer in order to generate two phase-coherent optical sidebands frequency-separated by 9.192 GHz for CPT

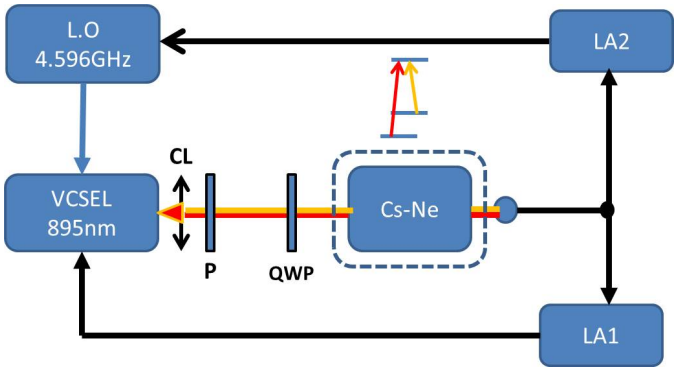

FIGURE 4. Schematic of the Cs-Ne microcell based CPT clock with the custom-designed 894 nm VCSEL. LA1 : lockin amplifier-based servo for laser frequency stabilization through modulation at 60 kHz of the laser bias current, LA2 : lockin amplifier-based servo for locking the local oscillator frequency to the CPT resonance transition. L.O : local oscillator, 10 MHz quartz oscillator multiplied to 4.596 GHz. P : linear polarizer. QWP : quarter-wave plate.

interaction. The RF power incident on the VCSEL is in the -6 - 0 dBm range. The Cs cell is filled with 75 Torr of Ne. It is temperature-stabilized, surrounded by a static magnetic field of several μT and placed in a single-layer mu-metal magnetic shield. The laser power is detected at the output of the cell with a photodiode. From this detector is extracted two servo loops. The first one aims to stabilize the laser frequency while the second one is used to stabilize the local oscillator frequency to the atomic hyperfine transition frequency. Up to date, active light shift correction technique has not been implemented in this set-up yet.

B. Preliminary experimental results

Fig. 5 shows the CPT frequency discriminator error signal in the VCSEL-based set-up for a cell temperature of 80°C.

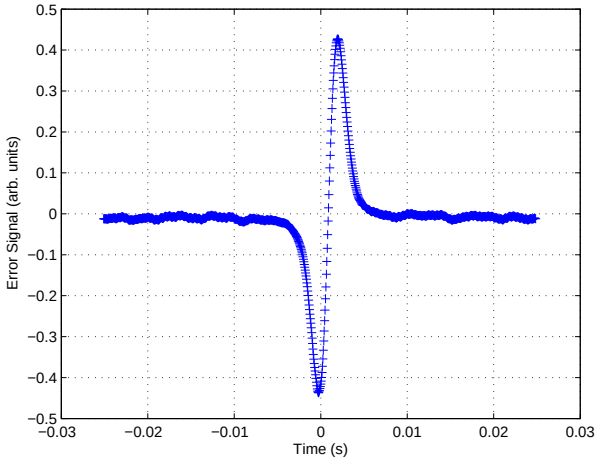

FIGURE 5. CPT frequency discriminator error signal. The slope is 0.9 10^{-6} V/Hz. The cell temperature is 80°C. The RF power is $-$ 2dBm.

The CPT linewidth is measured to be about 1.05 kHz at 80°C and does not vary significantly in the 70-90°C range. The contrast, defined as the ratio between the CPT signal and the background, is maximized at about 0.95 % at 80°C. The detection noise N in a 1 Hz bandwidth at the LO modulation frequency is 1.7×10^{-7} V/$\sqrt{Hz}$. The CPT clock frequency discriminator slope D is typically 0.9×10^{-6} V/Hz. The expected short-term stability of the clock is then expected to be $\sigma_y(\tau)=\frac{N}{\sqrt{2}\nu_0 D}=2.9\times10^{-11}$ at 1 s averaging time at T= 80°C. Frequency stability measurements will be led in a near future.

Fig. 6 reports the CPT contrast versus the 4.6 GHz RF power. The contrast is found to be maximized in the -2 - -3 dBm range.

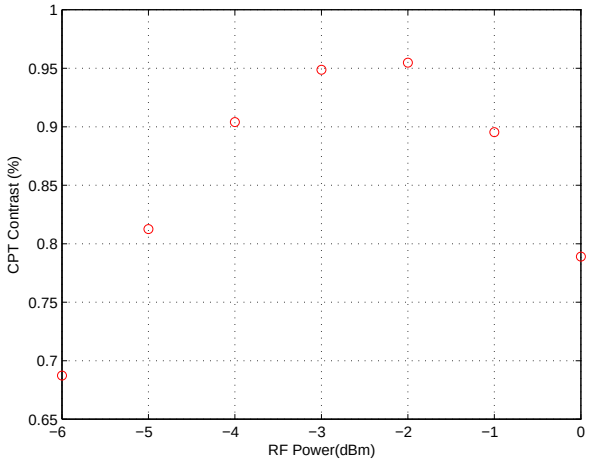

FIGURE 6. CPT resonance contrast versus the 4.6 GHz RF power. The cell temperature is 80°C.

IV. CONCLUSIONS

We developed compact Cs CPT clocks based on a Cs-Ne microfabricated cell. A first clock set-up, using an externally-modulated 894 nm DFB laser, exhibits a typical relative frequency stability of 3.8×10^{-11} and lower than 7×10^{-12} at 60 000 s. Light shift cancellation techniques were implemented to improve the mid and long term frequency stability. We presented also a compact demonstrator combining a novel custom-designed 895 nm VCSEL and a Cs-Ne microcell. A typical short-term frequency stability of 2.9×10^{-11} at 1 s is expected with correct adjustment of experimental parameters. Further studies are in progress to evaluate the mid and long term stability performances of the VCSEL-based clock.

RÉFÉRENCES

[1] J. Vanier, Appl. Phys. B Lasers Opt. **81,** 421 (2005).
[2] S. Knappe, V. Shah, P. D. D. Schwindt, L. Hollberg, J. Kitching, L. A. Liew and J. Moreland, Appl. Phys. Lett., **85,** 1460 (2004).
[3] R. Lutwak et al., Proc. of the 7th Symp. Freq. Standards and Metrology, edited by Lute Maleki (World scientific), 454, (2008).
[4] R. H. Dicke, Phys. Rev. **89,** 472 (1953).
[5] J. Kitching, S. Knappe, L. Hollberg, Appl. Phys. Lett., **81,** 553 (2002).
[6] L. A. Liew, S. Knappe, J. Moreland, H. Robinson, L. Hollberg and J. Kitching, Appl. Phys. Lett., **84,** 2694 (2004).
[7] S. Knappe, V. Gerginov, P. D. D. Schwindt, V. Shah, H. Robinson, L. Hollberg and J. Kitching, Opt. Lett., **30,** 2351 (2005).

[8] A. Douahi, L. Nieradko, J. C. Beugnot, J. Dziuban, H. Maillotte, S. Guérandel, M. Moraja, C. Gorecki and V. Giordano, Elec. Lett., **43,** 279 (2007).

[9] M. Hasegawa, R. K. Chutani, C. Gorecki, R. Boudot, P. Dziuban, V. Giordano, S. Clatot, L. Mauri, Sensors Actuat. A : Phys, **167,** 594 (2011).

[10] M. Arditi and T. R. Carver, Phys. Rev. **124,** 800 (1961).

[11] J. Vanier, R. Kunski, N. Cyr and J. Y. Savard and M. Tetu, Journ. Appl. Phys., **53,** 5387 (1982).

[12] D. Miletic, P. Dziuban, R. Boudot, M. Hasegawa, R. K. Chutani, G. Mileti, V. Giordano and C. Gorecki, Elec. Lett., **46,** 1069 (2010).

[13] R. Boudot, P. Dziuban, M. Hasegawa, R. K. Chutani, S. Galliou, V. Giordano and C. Gorecki, Journ. Appl. Phys., **109,** 014912 (2011).

[14] O. Kozlova, S. Guérandel and E. De Clercq, Phys. Rev. A **83,** 062714 (2011).

[15] http ://www.mac-tfc.eu

[16] R. Boudot, S. Guérandel and E. De Clercq, IEEE Trans. Instr. Meas., **58,** 3659 (2009).

[17] V. Shah, V. Gerginov, P. D. D. Schwindt, S. Knappe, L. Hollberg and J. Kitching, Appl. Phys. Lett., **89,** 151124 (2006).

[18] M. Zhu and L. S. Cutler, Proc. 32^{th} Annual Precise Time and Time Interval (PTTI) Meeting, Reston, VA, USA, 311 (2000).

[19] E. E. Mikhailov, T. Horrom, N. Belcher, I. Novikova, Journ. Opt. Soc. Am. B, **27,** 417 (2010).

[20] A. Al-Samaneh, M. Bou Sanayeh, S. Renz, D. Wahl, and R. Michalzik, IEEE Phot. Tech. Lett., **23,** 1049 (2011).

[21] O. Kozlova, R. Boudot, S. Guérandel and E. De Clercq, IEEE Trans. Instr. Meas., **60,** 2262 (2011).

[22] S. Knappe, V. Shah, V. Gerginov, A. Brannon, L. Hollberg and J. Kitching, Proc. 38^{th} Annual Precise Time and Time Interval (PTTI) Meeting, Reston, VA, USA, 241, (2008).

[23] B. H. McGuyer, Y. Y. Jau and W. Happer, Appl. Phys. Lett., **94,** 251110 (2009).

[24] S. Knappe, J. Kitching, L. Hollberg and R. Wynands, Appl. Phys. B, **74,** 217 (2002).

[25] N. Castagna, R. Boudot, S. Guérandel, E. De Clercq, N. Dimarcq and A. Clairon, IEEE Ultrason. Ferroelec. Freq. Contr., **56,** 246 (2009)

Recent Progress on Cryogenic MASER Oscillator

M. Mrad, Y. Kersalé and P.-Y. Bourgeois
FEMTO-ST Institute, UMR 6174 CNRS
Time & Frequency dpt.
Université de Franche-Comté
Besançon, France
Email: pyb2@femto-st.fr

V. Giordano and S. Grop
ULISS-ST® Business Unit
FEMTO-ST/UFC
Besançon, France

K. Benmessaï
and M.-E. Tobar
The University of Western Australia
Perth, Australia

***Abstract*—This paper reports on the comparison of a Cryocooled Sapphire Oscillator with our Cryocooled MASER Oscillator thanks to a home-made synthesis chain. The MASER oscillator demonstrates for the first time a fractional frequency deviation below $6 \cdot 10^{-15}$ over 4 s sampling time which is comparable to the conventional CSRO but achieved in a free running environment.**

I. Introduction

THE whispering gallery mode MASER oscillator is a highly stable secondary frequency standard involving paramagnetic ions of the Fe^{3+} type within Al_2O_3 matrix at cryogenic temperature and has been described in detail in previous publications [1]–[6].

Numerous scientific and technical applications require the use of highly stable references where the cryogenic sapphire resonator oscillator (CSRO) generates the lowest short-term frequency instability [7], [8]. They have been employed as local oscillator for atomic fountains clocks [9] or for modern physics tests [10]. Space segment for radar, doppler-tracking or VLBI would also benefit of such instruments as well as industry for certification purposes.

In this work, we present for the fisrt time the ability of our MASER oscillator to compete with CSRO, in a free running environment and tuned in a simple setup as opposed to the highly complex structure of the CSRO.

We also report on the design of a microwave synthesis chain that is mandatory to compare the MASER to a CSRO in the process of the frequency instability determination.

II. MASER Design

Unlike the conventional CSRO whose operational frequency has to be tuned outside electron spin resonances (ESR) of paramagnetic impurities contained within the sapphire crystal, the MASER operational frequency must fit the microwave ESR linewidth of the Fe^{3+} ions. It is also required that the pump mode frequency should fit the ESR line at 31 GHz. This last point is not as crucial as there exists a density of modes at those frequencies. One may then need to determine the resonator dimensions by using finite elements analysis or mode matching technique. The whispering gallery (WG) modes are more affected by a change of the resonator radius than height. Using simulation techniques requires the knowledge at 4 K of the sapphire permittivity tensor which is defined by matching

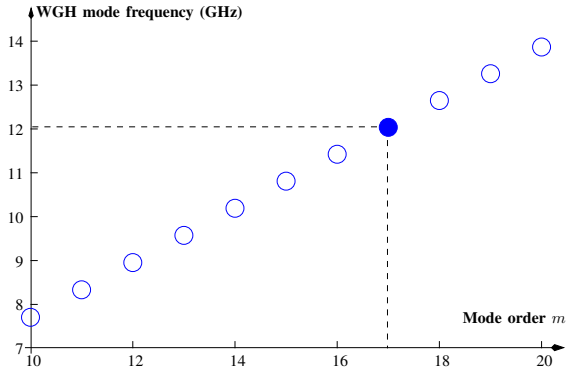

Fig. 1. Simulated and measured resonator mode frequencies, for $\Phi = 50.026$ mm and $h = 30.047$ mm, at 4 K. The filled circle represents the chosen resonant mode $m = 17$ at 12.04 GHz.

experimental data to simulations. The WG mode is chosen to be sufficiently high ($m > 15$) to limit the radiation losses and sufficiently low ($m < 20$) to avoid a too strong confinment of the electromagnetic energy within the crystal making harder the coupling setup. Numerous modes are appearing making the isolation of the main resonance harder.

TABLE I
CALCULATED AND MEASURED WGH FREQUENCIES AT 4 K.

m	ν_0 (calculated)	ν_0 (measured)
10	7.7075	7.711
11	8.3321	8.331
12	8.9543	8.950
13	9.5743	9.5685
14	10.1923	10.1854
15	10.8086	10.8007
16	11.4232	11.4144
17	12.0363	12.041
18	12.6480	12.6375
19	13.2584	13.247
20	13.8676	13.856

Table I indicates the validity of our model thanks to good agreement between the measured and calculated WGH frequencies at 4 K.

III. The cryogenic MASER operation

A. Setup

Fig. 2. Picture of the cryostat

The resonator is placed in the center of a gold-plated oxygen free copper cavity. The pump signal is provided by an external signal generator placed at room temperature. It feeds the cavity through a semi rigid low loss microwave cable. The output MASER signal is caught by a small magnetic loop and travels along another microwave cable to the room temperature plate.

The cavity is anchored to the second stage of a pulse tube cooler specially designed to ensure a thermal instability of $\pm$ 1 mK and a low level of mechanical vibrations with an axial displacement below ± 2 μm at the 1 Hz pulse cycle.

The MASER oscillates on the main resonant mode $WGH_{17,0,0}$ at 12.04 GHz at 4 K when applying a 10 dBm 31.340 GHz pump. It is well known that the mode degeneracy is common to any cylindrical ring resonant structure because of geometrical imperfections or crystal defects [11], [12].

Table II indicates this doublets characteristics.

TABLE II
$WGH_{17,0,0}$ doublets characteristics at 4 K (Frequency, Insertion Losses, Loaded Q-factor). MASER operates on the lowest frequency.

	Frequency (GHz)	IL (dB)	Q_L (10^6)
ν^-	12.040,623,700	-23	800
ν^+	12.040,633,094	-27	450

B. Turnovers

In order to minimize the frequency-temperature dependence of the oscillator, the MASER is stabilized around a turnover point reported on figure 3. This turning point has been measured for a fixed pump frequency of 31.340,949,620 GHz with 10 dBm of power. A polynomial estimate gives the temperature stabilisation point $T_0 \sim 7.042$ K.

It is interesting to note that the MASER frequency depends also of the pump frequency like reported on figure

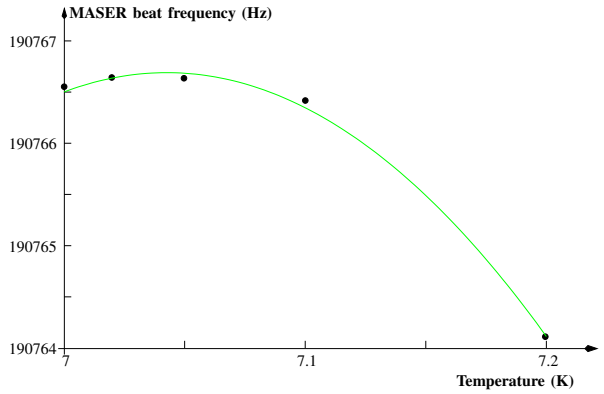

Fig. 3. MASER turnover for a pump frequency of 31,340 949 620 GHz with $P_p = 10$ dBm

4. The MASER frequency - pump frequency dependance is annuled at first order at 7.042 K for a pump frequency of 31.340,949,646,683 GHz with a power of 10 dBm. Though both effects are interrelated, this last dependence undergo small changes.

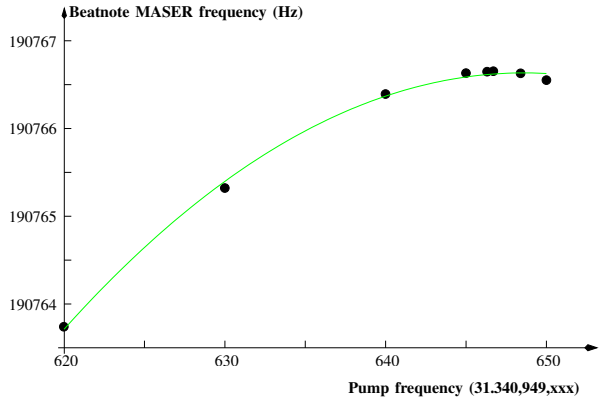

Fig. 4. MASER frequency as a function of pump frequency, $T = 7{,}042$ K and $P_p = 10$ dBm

IV. MASER validation

In order to characterize the frequency stability of our MASER oscillator it was necessary to build a microwave synthesis chain to be able to compare the MASER to a CSO because the oscillators frequency difference is to high to feed correctly a high resolution counter.

A. Synthesis chain design

We have used a different setup from [13]. The dedicated CSRO synthesis enables to transfer the frequency stability of the Elisa CSRO of about $3 \cdot 10^{-15}$ at 100 MHz and 10 MHz. The 100 MHz synthesis output is used to generate a microwave frequency close to the operational MASER frequency. This signal amplified and fixed at a 20 dBm level drives a non linear transmission line (NLTL) that generates a frequency comb. The 120$^{\text{th}}$ hamonic is selected with the help of a microwave cavity filter. The first mixing stage compares this

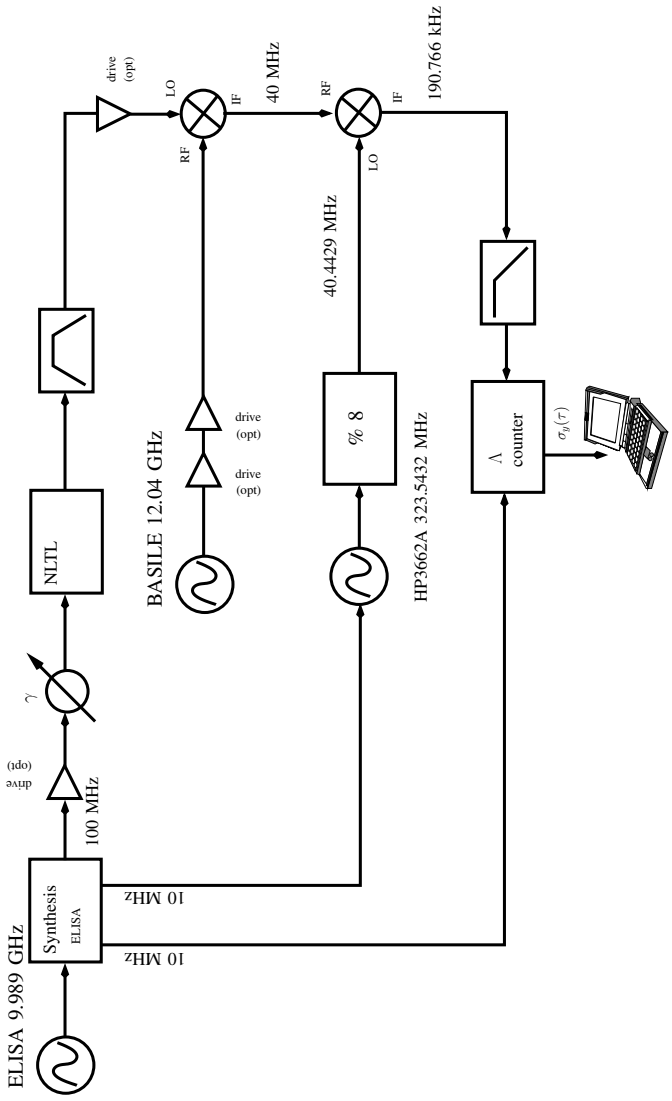

Fig. 5. Synthesis chain design for the measurement of frequency instability by comparing a CSO to the MASER

filtered harmonic to the MASER frequency to obtain a 40 MHz signal. It is needed to lower its frequency down to 200 kHz to maximise the counter resolution. This is done through a second mixing stage with a 40.4429 MHz signal generated from an external low noise rf synthesiser divided by 8 and referenced to the 10 MHz from the CSRO synthesis. This division is needed to get the lowest noise operation of the rf synthesizer. The resulting signal is then low pass filtered and feeds a Λ-reciprocal 1 s gated counter.

B. MASER frequency instability

The measured frequency instability of the system MASER-synthesis is shown on figure 6.

No isolators and no active control except for temperature have been used for this preliminary version. By stabilising the MASER temperature at 7.042 K and for a pump frequency of 31.340,949,620 GHz, 10 dBm, a minimum deviation of $5.3{\cdot}10^{-15}$ was obtained for 4 s integration times, followed

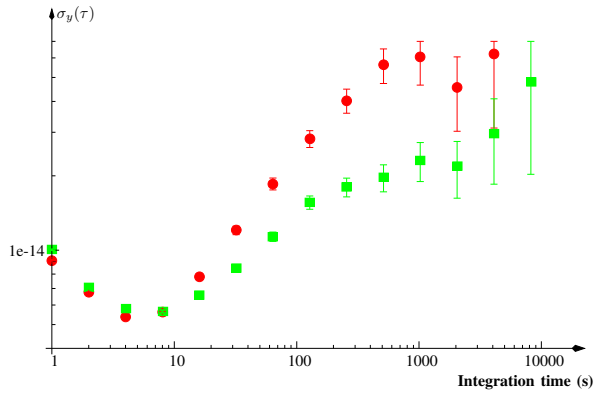

Fig. 6. Curve with red circles is measured at MASER turnover 7.042 K for ν_p =31.340,949,620 GHz, 10 dBm, T=7.042 K. Green squares curve is measured at Pump frequency turn ν_p =31.340,949,646,68 GHz, 10 dBm.

by a random walk process possibly indicating the absence of power control or the lack of isolation. By placing the pump frequency to its turn 31.340,949,646,68 GHz we eventually get the same result except for a less important drift.

V. Conclusion

We have shown for the first time a MASER operation presenting performances similar to those obtained with a CSRO in the short term area but in a really simple setup compared to the highly complex structure of the CSRO, and in free running. The frequency instability at 4 s was below $6 \cdot 10^{-15}$ with no removed data point nor frequency drift removal nor -3 dB "technique" applied, although it was necessary to build a high performance microwave synthesis chain.

References

[1] P. Bourgeois, N. Bazin, Y. Kersalé, V. Giordano, M. Tobar, and M. Oxborrow, "Maser oscillation in a whispering-gallery-mode microwave resonator," *Applied Physics Letters*, vol. 87, no. 22, pp. 224 104–224 104, 2005.

[2] P. Bourgeois, M. Oxborrow, M. Tobar, N. Bazin, Y. Kersalé, and V. Giordano, "Maser oscillation from electronic spin resonance in a cryogenic sapphire frequency standard," *International Journal of Modern Physics B*, vol. 20, no. 11-13, pp. 1606–1612, 2006.

[3] K. Benmessai, D. L. Creedon, M. E. Tobar, P.-Y. Bourgeois, Y. Kersalé, and V. Giordano, "Measurement of the fundamental thermal noise limit in a cryogenic sapphire frequency standard using bimodal maser oscillations," *Phys. Rev. Lett.*, vol. 100, p. 233901, Jun 2008. [Online]. Available: http://link.aps.org/doi/10.1103/PhysRevLett.100.233901

[4] K. Benmessai, P. Bourgeois, M. Tobar, N. Bazin, Y. Kersalé, and V. Giordano, "Amplification process in a high-Q cryogenic whispering gallery mode sapphire Fe^{3+} maser," *Measurement Science and Technology*, vol. 21, p. 025902, 2010.

[5] K. Benmessaï, M. Mrad, D. Creedon, J. Lefloch, M. Tobar, P.-Y. Bourgeois, Y. Kersalé, and V. Giordano, "Study of Fe^{3+}-Sapphire Maser above 4K," in *Proceedings of the 2011 IEEE IFCS-EFTF*, San Francisco, US, Sep. 2011, pp. 901–905.

[6] D. Creedon, K. Benmessai, M. Tobar, J. Hartnett, P. Bourgeois, Y. Kersale, J. Le Floch, and V. Giordano, "High-power solid-state sapphire whispering gallery mode maser," *Ultrasonics, Ferroelectrics and Frequency Control, IEEE Transactions on*, vol. 57, no. 3, pp. 641–646, 2010.

[7] S. Grop, W. Schafer, P.-Y. Bourgeois, Y. Kersalé, M. Oxborrow, E. Rubiola, and V. Giordano, "Unprecedented High Long Term Frequency Stability with a Microwave Resonator Oscillator," *IEEE Transactions on Ultrasonics, Ferroelectrics and Frequency Control*, vol. 58, no. 8, pp. 1694 – 1697, Aug. 2011. [Online]. Available: http://hal.archives-ouvertes.fr/hal-00624334

[8] J. Hartnett, C. Locke, E. Ivanov, M. Tobar, and P. Stanwix, "Cryogenic sapphire oscillator with exceptionally high long-term frequency stability," in *Frequency Control Symposium, 2007 Joint with the 21st European Frequency and Time Forum. IEEE International*. IEEE, 2007, pp. 1028–1031.

[9] G. Santarelli, P. Laurent, P. Lemonde, A. Clairon, A. Mann, S. Chang, A. Luiten, and C. Salomon, "Quantum projection noise in an atomic fountain: A high stability cesium frequency standard," *Physical review letters*, vol. 82, no. 23, pp. 4619–4622, 1999.

[10] P. Wolf, S. Bize, A. Clairon, A. Luiten, G. Santarelli, and M. Tobar, "Tests of lorentz invariance using a microwave resonator," *Physical review letters*, vol. 90, no. 6, p. 60402, 2003.

[11] D. Smith, H. Chang, and K. Fuller, "Whispering-gallery mode splitting in coupled microresonators," *JOSA B*, vol. 20, no. 9, pp. 1967–1974, 2003.

[12] P. Bourgeois and V. Giordano, "Simple model for the mode-splitting effect in whispering-gallery-mode resonators," *Microwave Theory and Techniques, IEEE Transactions on*, vol. 53, no. 10, pp. 3185–3190, 2005.

[13] K. Benmessai, P. Bourgeois, Y. Kersale, N. Bazin, M. Tobar, J. Hartnett, M. Oxborrow, and V. Giordano, "Frequency instability measurement system of cryogenic maser oscillator," *Electronics Letters*, vol. 43, no. 25, pp. 1436–1437, 2007.

Wall-coated cells for Rb atomic clocks: Study of the ripening process by double-resonance spectroscopy

M. Pellaton, C. Affolderbach, G. Mileti
Laboratoire Temps-Fréquence (LTF)
Institut de Physique, Université de Neuchâtel
Neuchâtel, Switzerland
matthieu.pellaton@unine.ch

R. Straessle, D. Briand, N. F. de Rooij
The Sensors, Actuators and Microsystems Laboratory (SAMLAB)
Ecole Polytechnique Fédérale de Lausanne (EPFL)
Neuchâtel, Switzerland

***Abstract*—We present a study of our in-house made tetracontane wall-coated ^{87}Rb vapour cells for rubidium atomic clock applications. Evolution of the double-resonance (DR) signal during the so-called ripening process of these cells is measured and interpreted. Intrinsic properties of the coated cells post ripening are presented. Intrinsic linewidths below 70 Hz, and moderate temperature coefficients (1.5 x 10^{-10} /K) are promising cell properties in view of highly compact and miniature atomic clocks.**

I. INTRODUCTION

Antirelaxation surface coatings in alkali vapour cells have already been proposed in the early 50's by Robinson et al. [1] for clock applications. They have then been extensively studied as an alternative to the buffer gas technology to understand the mechanism involved in the preservation of the alkali spin polarization. These coatings are known to be of poor quality right after the production phase, and need to go through a so-called ripening process in order to show efficient antirelaxation properties and stable clock signal. This process is usually mentioned as a required step in the production phase but it has not been reported in details and is not fully understood.

In this paper, we present a study of the double resonance clock signal obtained from our in-house made tetracontane coated cells (Fig. 1) during this ripening process. A qualitative interpretation of the evolution of the signal's characteristic properties is also given. Intrinsic properties of the coating for the five produced cells are presented as well, showing an excellent agreement with previously published results. Finally, the possibility to obtain a strong and narrow clock signal from a cell with an internal volume < 1.4 cm^3 is demonstrated.

II. EXPERIMENTAL SETUP

Figure 1 In-house made tetracontane coated cells.

A. Cell description

The cells are made of borosilicate glass. The inner (outer) dimensions are diameter D = 12 (14) mm and height H = 12 (14) mm. Purified tetracontane is applied on the inner walls by vapour deposition. Enriched ^{87}Rb is distilled to a reservoir attached on the side one of the optical window. Purpose of the reservoir is to keep the metallic rubidium away from the coated surfaces.

B. Spectroscopic setup

A schematic of the experimental setup for the spectroscopic studies is shown on Fig. 2. The laser head [2] consists of a distributed feedback (DFB) laser with a linewidth < 3 MHz, and an integrated saturated absorption spectroscopy setup including an evacuated (uncoated) reference cell containing enriched ^{87}Rb. This laser head allows the generation of a laser beam frequency-stabilized to any optical transition or crossover of the ^{87}Rb D2 line. Neutral density filters and a polarizer are used to control the light intensity and polarization sent to the clock cell.

The physics package (PP) surrounding the in-house made clock cell consists of a magnetron-type cavity [3] allowing an excellent control on the field geometry (TE011-like mode) and phase. The magnetron, surrounded by a coil generating the DC quantization magnetic field parallel to the light beam, is driven by a commercial synthesizer referenced to a hydrogen maser. Two μ-metal shields enclose the PP to isolate the system from external magnetic perturbations. The excellent control on the magnetic fields seen by the Rb atoms allows the generation of microwave DR spectra without pedestal, nor sigma transitions. Temperatures of the cell body and its stem are independently controlled; the stem temperature is maintained lower than the cell itself in order to avoid any condensation of metallic Rb on the coating. The transmitted light power, i.e. the transmission of the cell, is recorded using a photodiode while the RF frequency is swept around 6'834'682'611 Hz. The resulting microwave DR spectrum, or clock signal (we restrict the span of the microwave to the clock transition: $|F_g = 1; m_F = 0\rangle \rightarrow |F_g = 2; m_F = 0\rangle$) is then fitted with a lorentzian curve and relevant parameters, such as line center frequency, amplitude, linewidth and background are extracted.

This work was supported by the Swiss National Science Foundation and the European Space Agency (ESA).

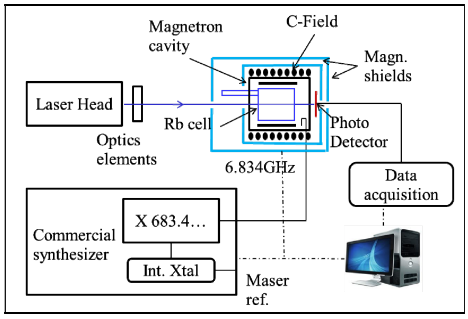

Figure 2 Block diagram of the experimental setup.

Since the synthesizer and data acquisition are computer-controlled the measurement system is fully automatized and can acquire and analyze one DR spectrum every minute.

III. EXPERIMENTAL RESULTS

A. DR signal evolution during ripening process

Immediately after the cells were sealed off the production setup, they have been placed inside the magnetron cavity and heated at 70°C. Double resonance signal of the clock transition have been continuously recorded during the whole ripening process. The laser frequency was locked to the $F_g = 2 \rightarrow F_e = 2, 3$ cross over, and a 7 mm diameter beam was sent through the cell. The light intensity and RF power have been chosen sufficiently small to not induce any significant line broadenings.

All the produced cells showed a similar evolution of the clock signal throughout the ripening process as shown on the Fig. 3-6: a slight reduction of the total frequency shift, a strong improvement of the linewidth and amplitude and an increase of the background level. The relatively large scattering in the shifts and linewidths measured at the early times of the ripening process are related to the difficulty to extract the lineshape parameters from data with extremely small signal to noise ratio.

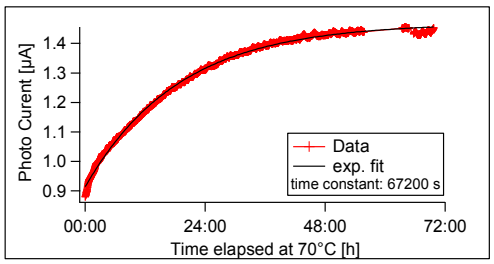

Figure 3 Evolution of the clock signal background.

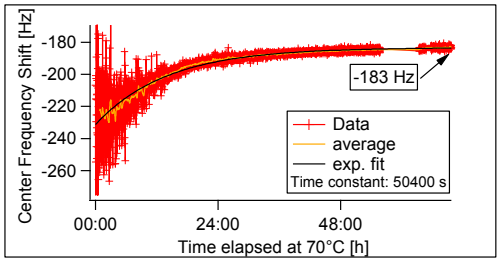

Figure 4 Evolution of the clock signal frequency shift.

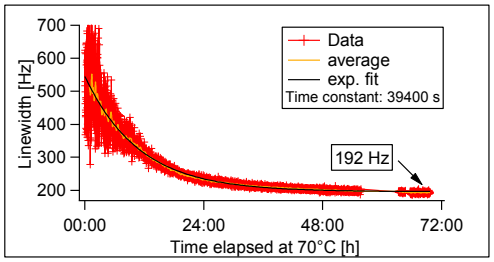

Figure 5 Evolution of the clock signal linewidth.

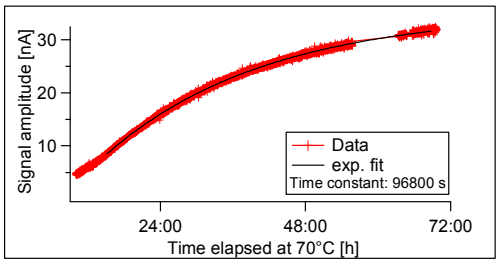

Figure 6 Evolution of the clock signal amplitude.

B. Interpretation

A qualitative interpretation of this evolution can be made using a basic three-level system, as schematized on Fig. 7.

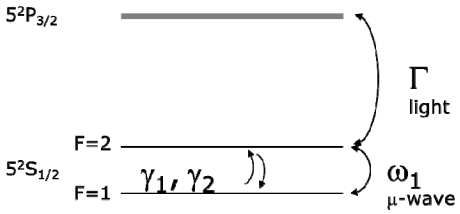

Figure 7 Three level system. Γ corresponds to the optical pumping rate, ω_1 to the microwave transition rate and γ_1, γ_2 to the longitudinal, and coherence relaxation rates, respectively.

The steady state solution for a constant atomic density is given by the following formula [4]:

$$\Delta I \propto \frac{\Gamma}{2\gamma_{\parallel}} - \frac{\Gamma}{2\gamma_{\parallel}} \frac{\Omega^2}{(\omega - \omega_{Rb})^2 + \gamma_{\perp}^2 + \Omega^2} \quad (1)$$

Where $\gamma_{//} = \gamma_1 + \Gamma/2$ and $\gamma_{\perp} = \gamma_2 + \Gamma/2$ are the global relaxation rates, and $\Omega^2 = 4\omega_l^2 \gamma_{\perp}/\gamma_{//}$. In absence of a microwave field only the first member of the equation (1) remains, corresponding to the background level. The increase of the background on Fig. 3 is thus a direct expression of the reduction in longitudinal relaxation rate that develops during ripening.

The second member of equation (1) is the clock signal itself. Its linewidth, in Hz, for small microwave power is approximated by $\gamma_{\perp}/\pi$. Thus, Fig. 5 shows the evolution of the coherence relaxation rate. The total coherence relaxation rate is the sum of several known mechanisms: spin-exchange (γ_{se}), adiabatic (γ_{ad}) and "strong" (γ_{er}) collisions on coated walls [5], or losses of polarization (γ_{loss}). These losses can be of three different but experimentally undistinguishable origins:

- Polarized atoms can enter the reservoir and being replaced by "new" unpolarized atoms from the reservoir (hole effect), this contribution can be estimated using Eq. (5).
- Atoms from the vapour can be adsorbed for a sufficiently long time on the coating, being as well replaced by new unpolarized atoms from the reservoir, or re-emitted from the coating (adsorption losses).
- Collisions with uncoated glass surfaces (covering factor losses).

One can reasonably assume that the ripening process affects only the coherence relaxation rates related to the collisions of the alkali-metal atoms with the wall coating and the losses due to the adsorption process (chemical reaction have been rejected by Seltzer et al.[6]) and the covering factor. The spin-exchange losses and the losses through the reservoir hole will not evolve during the ripening process since the temperature of the cell is constant.

One can estimate the adiabatic relaxation rate induced by the average phase shift ϕ experienced by the atoms at each collision with the coating [5]:

$$\gamma_{ad} = 2\phi^2 \nu_{coll} \tag{2}$$

ν_{coll} being the average collision rate between the atoms and the walls of the cell:

$$\nu_{coll} = \frac{v_{avg}}{l} \tag{3}$$

where v_{avg} is the average thermal velocity and l the mean distance between two collisions. l depends on the geometry of the cell; in our case, l is given by 2D/3 [7]. Finally ϕ is given by:

$$\phi = \frac{2\pi\delta\nu}{\nu_{coll}} \tag{4}$$

where $\delta\nu$ is the clock signal frequency shift.

From Eq. (2)-(4), the calculated value of the adiabatic relaxation rate is below 60 s^{-1} during the whole ripening process and cannot explain the huge reduction of the total coherence relaxation rate observed in terms of linewidth in Fig. 5. We thus conclude that this improvement is dominated by a substantial reduction of the polarization losses.

C. *Intrinsic coating properties post ripening*

Intrinsic linewidths were extracted by extrapolation of the measured linewidths to zero light and microwave power. Rather than being an intrinsic property of the coating, the intrinsic linewidth obtained, 63 ± 5 Hz, are mainly a contribution of the reservoir (or hole) effect. Indeed, the linewidth contribution of a hole, in our case the channel from the reservoir to the cell cavity, is given by [8]:

$$\bar{v}\frac{a}{\pi V} \tag{5}$$

where a is the surface of the hole and V the volume of the cell cavity. For our cells, a 1 ± 0.1 mm diameter hole contributes at a level of 58 ± 6 Hz in the total linewidth.

Intrinsic shifts, extracted by extrapolation of the measured total shifts to zero light and microwave power, are presented in Fig. 8. An average shift of -180 ± 10 Hz is obtained over the whole production batch, corresponding to an average wall shift of -0.28 ± 2 mrad/coll., which is slightly smaller than previously published values (see Table 1).

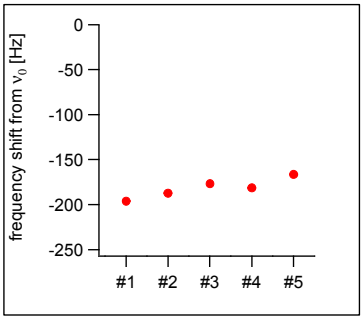

Figure 8 Intrinsic shifts of the produced cells.

These intrinsic shifts were measured for different cell body temperatures between 45°C and 75°C maintaining the stem temperature constant. A linear behavior is observed with a slope of 1 ± 0.05 Hz/K. The corresponding calculated adsorption energies [5] are also in very good agreement with the results found in the literature.

Table 1 Paraffin properties in literature for ^{87}Rb and hyper-fine transitions.

Author	Coating	Inter.	Φ [mrad/coll]	TC [Hz/K]	E_a [eV]
Risley [9]	paraffin	DR	-49	~2	0.06
Robinson [10]	tetracontane	DR	-58	n.c.[a]	n.c.[a]
Budker [5]	tetracontane	DR	-43 – -36	n.c.[a]	0.06
Bandi [11]	tetracontane	DR	-59	1.4	n.c.[a]
Breschi [12]	tetracontane	CPT	n.c.[a]	1.4	n.c.[a]
This study	tetracontane	DR	-28 ± 2	1	0.053

[a]n.c. not-communicated.

D. *Optimized clock signal*

An optimized clock signal was measured using one of our in-house produced wall coated cell (laser frequency stabilized to the $F_g = 2 \rightarrow F_e = 2, 3$ transition cross over). It has a full-width at half-maximum (FWHM) of 679 Hz and a contrast (amplitude over background level) > 30 %. The corresponding error signal has a discriminator slope of $D = 0.65$ nA/Hz leading to a shot-noise limit for the short-term clock instability $\sigma_{shot\text{-}noise}(\tau) = 1 \times 10^{-13}\,\tau^{-1/2}$.

IV. CONCLUSIONS

We put in evidence the different evolutions of the two main relaxation rates of relevance for the clock transition during the ripening process of rubidium cells with tetracontane as wall coating. The dominant improvement of the linewidth is due to a reduction of the polarization losses. After ripening, the produced tetracontane coated cells have excellent intrinsic properties comparable to the ones found in the literature. The

clock signals obtained give a shot-noise clock instability limit of $\sigma_{\text{shot-noise}}(\tau) = 1 \times 10^{-13}\, \tau^{-1/2}$, which is an excellent value for a cell volume < 1.4 cm^3.

ACKNOWLEDGMENT

We thank P. Scherler, F. Gruet, M. Dürrenberger for their contributions.

REFERENCES

[1] H. G. Robinson, E. S. Ensberg, and H. G. Dehmelt, "Preservation of spin state in free atom-inert surface collisions," *Bull. Am. Phys. Soc*, vol. 3, p. 9, 1958.

[2] S. Micalizio et al., "Pulsed Optically Pumped Rb Clock with Optical detection: First Results," in *24th European Frequency and Time Forum*, 2010.

[3] C. Affolderbach, F. Droz, and G. Mileti, "Experimental demonstration of a compact and high-performance laser-pumped rubidium gas cell atomic frequency standard," *IEEE Trans. Instrum. Meas.*, vol. 55, no. 2, pp. 429-35, April 2006.

[4] G. Mileti, "Etude du pompage optique par laser et par lampe spectrale dans les horloges à vapeur de rubidium," Ph.D. dissertation, Université de Neuchâtel-Faculté des Sciences, 1995.

[5] D. Budker, L. Hollberg, D. F. Kimball, J. Kitching, S. Pustelny, and V. V. Yashchuk, "Microwave transitions and nonlinear magneto-optical rotation in anti-relaxation-coated cells," *Phys. Rev. A*, vol. 71, p. 012903, Jan 2005.

[6] S. J. Seltzer et al., "Investigation of antirelaxation coatings for alkali-metal vapor cells using surface science techniques," *The Journal of Chemical Physics*, vol. 133, no. 14, p. 144703, 2010.

[7] J. Vanier and C. Audoin, *The Quantum Physics of Atomic Frequency Standards*, I. of Physics Publishing, Ed. Adam Hilger, 1989.

[8] H. G. Robinson, ""Evacuated, Wall-coated, Sealed, Alkali Atom Cell for an Atomic Frequency Standard"," U.S. Pat. 4596962, June, 1986.

[9] A. Risley, S. Jarvis, and J. Vanier, "The Dependence of Frequency Upon Microwave Power of Wall-coated and Buffer-gas-filled Gas Cell Rb87 Frequency Standards", *J. Appl. Phys.*, vol. 51, no. 9, pp. 4571–6, 1980.

[10] H. Robinson and C. Johnson, "Narrow ^{87}Rb hyperfine-structure resonances in an evacuated wall-coated cell", *Appl. Phys. Lett.*, vol. 40, no. 9, pp. 771–3, May 1982.

[11] T. Bandi, C. Affolderbach, and G. Mileti, "Study of Rb 0-0 hyperfine double-resonance transition in a wall-coated cell," in *24th European Frequency and Time Forum*, April 2010.

[12] E. Breschi et al., "Light effects in the atomic-motion-induced Ramsey narrowing of dark resonances in wall-coated cells," *Phys. Rev. A*, vol. 82, p. 063810, December 2010.

Recent progress on the pulsed CPT Cs clock at SYRTE

J-M. Danet, O. Kozlova*, S. Guérandel, E. de Clercq
LNE-SYRTE
Observatoire de Paris CNRS-UMR 8630, UPMC
61 avenue de l'Observatoire, 75014 Paris, France
* present adress, LCM, LNE-CNAM, 61 rue du Landy, 93210 La Plaine-St-Denis, France
jean-marie.danet@obspm.fr

***Abstract*— Recent progress are reported on a compact cesium cell atomic frequency standard based on pulsed Coherent Population Trapping interaction in the Dicke regime. Main short term and long term limiting parameters have been identified. Last improvements have permitted to reach a stability of $7x10^{-13}$ at 1sec and $2x10^{-14}$ at 2000 s. The noise characterization process is presented in this article.**

I. INTRODUCTION

Compact and stable frequency standards are needed in many applications such as GPS or Galileo, the European GNSS. Double resonance (microwave and optical) alkali-metal vapor-cell atomic clocks are currently used for this purpose. The next generation of space clocks could be based on the coherent population trapping (CPT) phenomenon [1]. In such clocks the microwave interrogation and the microwave cavity are suppressed. The atomic vapor in the cell is pumped and probed, in the same time, by two laser beams which frequencies are separated by the microwave clock frequency. Because of their scheme simplicity and potential higher performances, CPT clocks are promising candidates for on-board applications.

To build a high stability clock, the CPT signal amplitude is enhanced with crossed linear polarization lasers realizing the so-called double-lambda scheme. Confined with a correct mixture of buffer gases, the cesium atoms are in a Dicke regime that drastically reduces the effects of the atomic velocity distribution. Compared to conventional CPT clocks, the pulsed interaction provides a Raman-Ramsey signal which combines the advantages of a good frequency discriminator [2], whose slope is limited by the atomic relaxation in the cell (a few milliseconds), and the high rejection of the light effects during the clock interrogation [3]. Part II will present the experimental setup.

A recent frequency comparison to a local hydrogen maser as reference gave a short term stability lower than 10^{-12} at 1 sec, mainly limited by microwave phase noise and laser intensity fluctuations in the mid term. Part III will present how it has been possible to significantly improve this performance, by identifying and reducing those critical sources of fluctuations. The long term stability has also been investigated thanks to two studies presented in part IV. The first is a study of the collisional shift [4,5] and the second presents the evaluation of the optical power effects. Finally the stability and the noise budget will be presented in part V.

II. EXPERIMENTAL SET-UP

As shown on the Fig. 1, the superimposed beams of two phase-locked extended cavity diode lasers (ECDL), 9 GHz apart, are switched by an acousto-optic modulator (AOM) before crossing the Cs-buffer gas cell. The cell is enclosed in magnetic shields and temperature regulated. The transmitted laser intensity is measured by the photodiode PD1, linked to the computer (PC), which drives the time sequence of the AOM and lock the frequency synthesizer on resonance. The clock frequency is measured versus an H maser of the laboratory. The lasers are tuned to the Cs-D_1 line at 895 nm, the inset shows a scheme of the involved energy levels

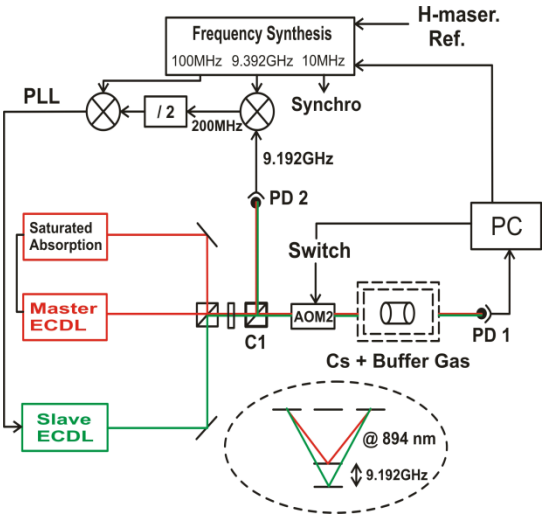

Figure 1. Experimental setup. Red: Master extended cavity diode laser (ECDL). Green: Slave ECDL, locked at 9GHz from the master frequency using a phase locked loop (PLL). Clock evaluation is made by comparison with an H-maser. Inset: D1 Cs energy levels, red: master laser, green: slave laser. Cell : Ar/N2 mixture, P=21torr, P_{Ar}/P_{N2}=0.6

III. NOISE CARACTERISATION FOR SHORT TERM STABILITY

If the shot noise was assumed as the noise limiting parameter and the clock signal remained unchanged, this clock would reach a stability of $1x10^{-14}$ at 1sec. As the measured limit was 10^{-12}, a noise characterisation process have been undertaken in order to identify and reduce the main noise sources.

A. Master laser frequency noise

The master laser (ML) frequency noise contribution to the short term stability is evaluated by measuring the clock frequency sensitivity to the ML frequency, which is $2.62.10^{-2}$ Hz/MHz. The measured master laser frequency noise level is 1 kHz.Hz$^{-1/2}$ at 1 Hz, see Fig. 2. It can be converted to clock noise using the sensitivity, giving a contribution of 2.10^{-15}Hz at 1 sec, which is far below the limitation level.

B. Master laser intensity noise

Among the different microwave (MW) frequency noises generated by the ML intensity noise, the first is the power fluctuation of the laser directly transmitted on the detector's output voltage and interpreted by the computer as frequency noise. The second is the AM→FM_{MW} noise converted by the atoms, notably because of the light shift.

In Fig. 2, the power spectral densities (PSD) of the intensity signal and of the frequency lock error signal are plotted for two cases: narrow band frequency lock ON (red and blue) and OFF (black). One can notice that when this lock is turned on, the intensity noise is degraded because of the ML frequency lock, which is peaking around 500 Hz for the narrow band lock (PZT) and around 8 kHz for the high band lock (laser diode current).

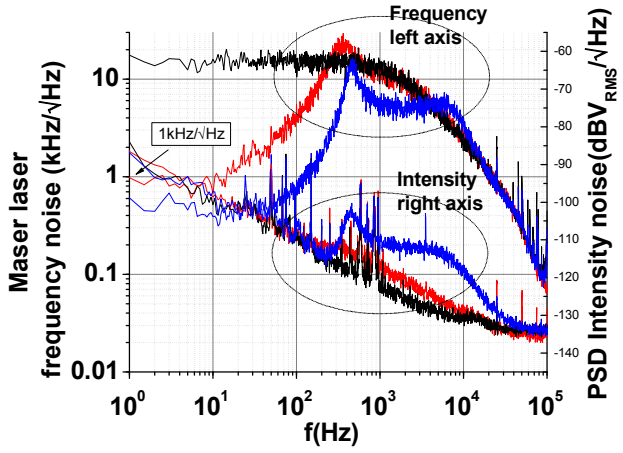

Figure 2. Master laser intensity noise degradation with narrow-band frequency lock. Left axis: PSD of the master frequency lock error signal, for hard (blue), smooth (red) and OFF (black) narrow band frequency lock. Right axis: PSD of intensity noise for hard (blue), smooth (red) and OFF (black) frequency lock. Boxed value gives the frequency value used for master laser frequency noise contribution to short term stability.

Thus, there is a transfer of frequency noise into intensity noise creating an intensity perturbation between 300 Hz and 10 kHz. However, as far as the master laser frequency noise is not limiting the clock short term stability, it can be a slightly degraded (up-red) so that the intensity noise is improved (bottom red). The best compromise found after optimisation is shown on Fig. 2(red).

The Figure 3 is presenting the impact of this intensity noise optimization process on the clock stability. One can see that the clock noise continuously decreases with the intensity noise, indicating that up to now there is no noise margin on this parameter. As the intensity noise level changed only in the 300 Hz – 10 kHz region, the 8 kHz PSD level is taken as typical and is plotted on Fig. 4 on the horizontal axis.

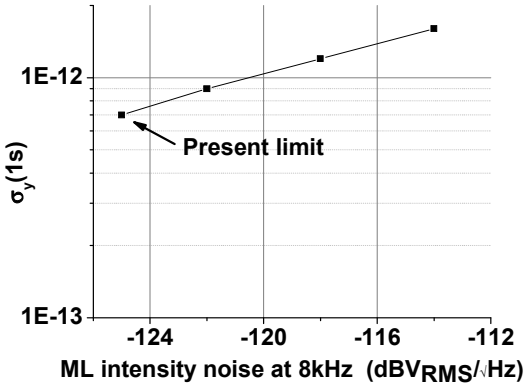

Figure 3. Short term stability as a function of the PSD master laser intensity noise level at 8 kHz, which is a typical point of the PSD behaviour in the 300 to 10 kHz region, see Fig. 2.

C. Microwave phase noise

The dependence of the clock stability to microwave phase noise is observed by adding white phase noise to the 9.192GHz reference signal, see Fig. 4. As this reference is used to lock the slave laser using a fast and a slow actuator, this white phase noise can be converted to slave laser intensity noise or laser phase noise. For this study, the conversion of microwave frequency noise to slave laser intensity noise has been neglected.

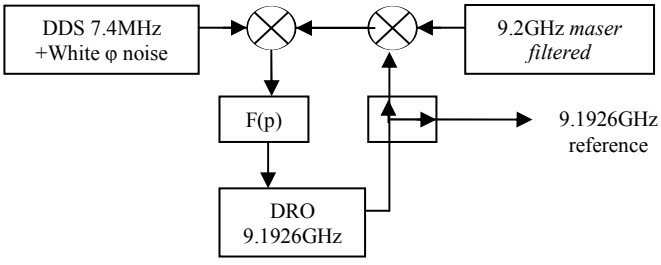

Figure 4. Setup for noisy 9.192GHz generation. White phase noise is added on a 7.4MHz signal generated by a direct digital synthesis (DDS). A beatnote between the 9.2GHz maser filtered and a dielectric resonator oscillator is then mixed with the 7.4MHz to create the error signal of the PI loop.

The figure 5 shows the clock noise as a function of the white phase noise level. A linear part and a floor are observable, showing that under a certain level, the added noise does not degrade the clock. By extrapolating the linear fit to our clean white phase noise level, we can say that the upper limit for a phase noise limitation is around 5.5×10^{-13} at 1 sec. This is an upper limit because the clock noise is a quadratic sum of all noise contributions. If another noise, like intensity noise for example, decreases, the linear part will be down-shifted, giving a lower limit.

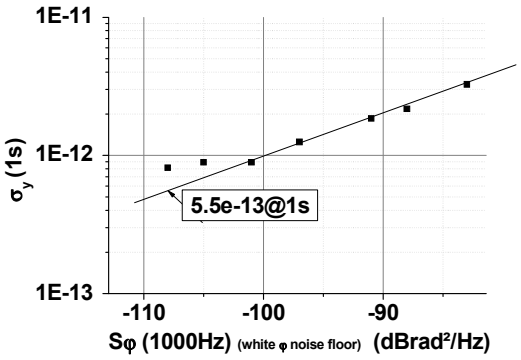

Figure 5. Short term stability versus white phase noise level. Dots: experimental data. Solid line: linear fit of the data without the two first points.

IV. LONG TERM STABILITY

The long term stability is affected by phenomena different from those affecting the short term stability. Temperature effects and long term laser intensity variation effects and their consequences are dominant.

A. Optical power effects

The dependence of the clock frequency to total laser intensity, so called light shift, is one of the major effects with the buffer gas pressure shift which can limit the long-term stability of alkali vapour cell clocks [1]. We have measured the light shift in cells with different buffer gases as a function of the laser intensity and the cell temperature (Fig 6). We have noticed that the light shift is sensitive to the cell temperature [6, 7]: the slope of the light shift versus laser intensity changes value and even changes sign (Fig. 6). So for a given temperature of the cell it is possible to have a zero slope and to cancel the light shift.

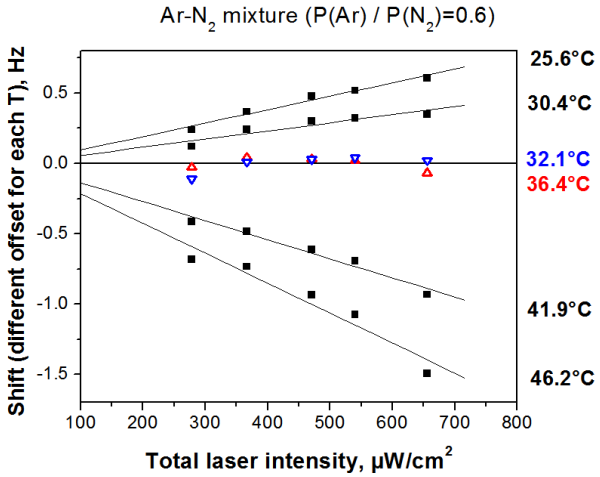

Figure 6. Light shift for different temperatures. For better visibility a different offset is applied for each temperature. Ramsey mode (T_R=4ms) interrogation. Cell with Ar-N2 mixture, pressure ratio r (P_{Ar}/P_{N2}) = 0.595.

Two effects are involved. One is the temperature dependence of the optical transitions detuning. Indeed, the light shift varies with the detuning of the optical resonance [8], and the frequency shift of the optical resonance induced by the buffer gas is temperature dependent. In these experiments the laser frequency was locked on the saturated absorption spectrum, it was then fixed independently of the temperature of the clock buffer gas cell. The other one is the temperature dependence of the differential absorption of the two laser beams [6].

The effect of the laser intensity ratio on the light shift has also been measured, see Fig.7. The investigation on this behaviour is in progress.

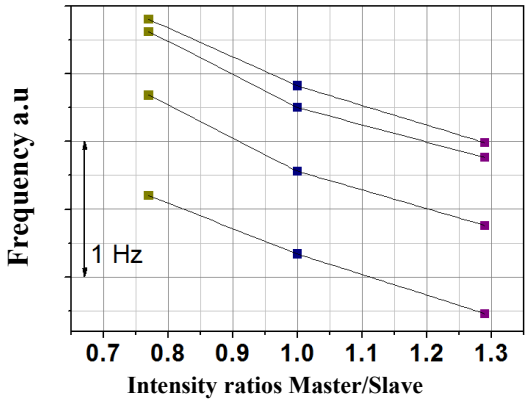

Figure 7. Frequency shift versus intensity ratio. From the top to bottom, total lasers intensities:1600, 1000, 400, 200μW/cm²

The sensitivity and contribution of all those effects are summarized in the section C.

B. Collisional effects

In order to reduce the Doppler width, a buffer gas is added to the Cs vapour. However, collisions between alkali-metal atoms and buffer gas can shift the frequency of the clock transition by several kHz per torr, and this shift is temperature

dependent. This effect can limit the long-term frequency stability of cell clocks.

A study of the temperature dependence of the shift in presence of Ne, N_2, and Ar [5] has enabled the manufacturing of a cell with temperature dependence cancelled at 29°C, see Fig. 8, our maximum signal and working point. The cell is a Ar/N2 mixture, P=21 torr, P_{Ar}/P_{N2}=0.6

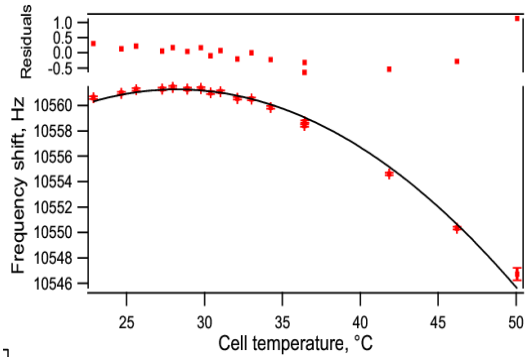

Figure 8. Temperature dependence of the clock frequency in Ar-N2 Cs cells with r = 0.595. Experimental points are fitted with N2 pressure and the ratio *r* as free parameters, the pressure coefficients and temperature coefficients for both gases as fixed.

C. *Evaluation of long term noise budget*

The contribution to the long term stability of the previously described effects has been evaluated and is presented in Table I. Regarding the temperature fluctuation, for a cell filled with a mixture N_2-Ar of buffer gases, (P=21 torr, P_{Ar}/P_{N2}=0.6) at the optimised temperature, a 10 mK variation will cause a 3.10^{-16} fractional frequency shift induced by the pressure shift, see Table 1, and a 8.10^{-14} frequency shift caused by the temperature dependence of the light shift (in our experimental condition the intensity is 500 µW/cm²). The dependence of the light shift on the intensity ratio of two lasers has been evaluated for an intensity ratio variation of 0.01% and will cause a 3.10^{-14} frequency shift.

The contributions of the optical detuning and of the total laser intensity variation have also been evaluated to be lower than a $1x10^{-14}$.

TABLE I. SENSITIVITY, TYPICAL VARIATION AND CONTRIBUTIONS TO LONG TERM STABILITY OF MAIN PARAMETERS

Effect or Frequency shift	Sensitivity	Typical var.	Fluctuation at 10^4 s $\Delta\nu / \nu$
Intensity ratio M/S	0.03 Hz / 1 % var.	< 0.01%	< 3 · 10 -14
LS temperature dependence	$1.5 \cdot 10^{-4}$ Hz / mK	< 2 mK	< 3 · 10 -14
2nd order Zeeman shift	427.45Hz/G²	1.7.10-6G	2.4 x 10-14
Colisional shift	0.46.10-4Hz/mK	10mK	3.0 x 10-16

V. STABILITY AND NOISE BUDGET

The noise characterization process has been studied separately for short term and long term measurements. The Allan deviation plotted in Fig. 9 shows that a 7.10^{-13} $t^{-1/2}$ relative stability has been achieved for the short term and 2.10^{-14} for the long term (2000s).

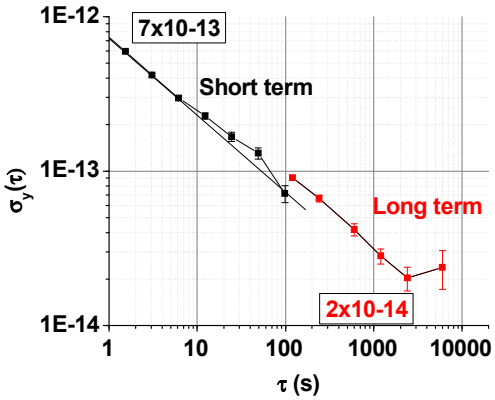

Figure 9. Short term (black squares) and long term (red squares) stability

The main limiting parameter for the short term is the laser intensity noise, limiting at a value of 7.10^{-13}, see Table II. The estimation of the long term noise contributions led to point out three effects as definitely limiting the frequency stability at the 2.10^{-14} level: laser intensity ratio, light shift temperature dependence and 2nd order Zeeman shift, see Table. III.

TABLE II. MAIN NOISE SOURCES LIMITING THE SHORT-TERM STABILITY

Noise source	σ_y (1 s)
Laser intensity noise (AM-AM)	<7 x 10^{-13}
Microwave chain phase noise	<5 x 10^{-13}

TABLE III. MAIN NOISE SOURCES LIMITING THE LONG-TERM STABILITY

Noise source	σ_y (10^4 s)
Intensity ratios M/S	<3 x 10^{-14}
LS temperature dependent	<3 x 10^{-14}
2nd order Zeeman shift	2.4 x 10^{-14}

VI. CONCLUSION

We have reported here recent progress on the characterization of short and long term noise sources on a Raman Ramsey CPT Cs clock. Main noise sources contributing to the short term stability have been investigated and laser intensity fluctuations presently are identified as our main limiting parameter. If the noise budget was dominated by the microwave chain, the clock frequency stability would be better than $5.5.10^{-13}$ at 1s.

Most probable systematic frequency shift that are currently limiting the long term stability of the clock have been identified as intensity ratios, 2nd order Zeeman shifts and light shift temperature dependence, for which an optimal temperature was reported.

ACKNOWLEDGMENT

We are pleased to acknowledge Pierre Bonnay and Annie Gérard for very careful manufacturing of Cs cells. We are grateful to Michel Lours and the SYRTE electronic team for their help.

REFERENCES

[1] J. Vanier, "Atomic clocks based on coherent population trapping: a review", Appl. Phys. B, vol. 81, pp. 421-442, 2005

[2] T. Zanon, S. Guérandel, E. de Clercq, D. Holleville, N. Dimarcq, and A. Clairon, "High contrast Ramsey fringes with coherent-populationtrapping pulses in a double lambda atomic system," Phys. Rev. Lett. vol. 94, no. 19, p. 193 002, May 2005.

[3] N. Castagna, R.Boudot, S.Gu´erandel, E. de Clercq,N.Dimarcq, and A. Clairon, IEEE Trans. Ultrason. Ferroelectr. Freq. Control 56, 246, 2009.

[4] J. Vanier & C. Audoin, The Quantum Physics of Atomic Frequency Standards, IOP Publishing, Bristol and Philadelphia, 1989.

[5] O. Kozlova, S. Guérandel, E. De Clercq, "Temperature and pressure shift of the Cs clock transition in presence of buffer gases Ne, N_2 Ar", *Phys. Rev. A*, 83, 062714, 2011

[6] O. Kozlova, J.M. Danet, S. Guérandel, E. De Clercq: "Temperature dependence of a Cs vapor cell clock: pressure shift, signal amplitude, light shift.", in *Proc. of the joint meeting EFTF-IFCS*, San Franscisco, USA,. p 607-611, 2011

[7] D. Miletic, C. Affolderbach, G. Mileti, M. Hasegawa, C. Goreki: "Light Shift in CPT Based Cs Miniature Atomic Clocks", in *Proc. of the joint meeting EFTF-IFCS*, San Franscisco, USA,. p200-203, 2011

[8] J. Vanier, A. Godone, and F. Levi, "Coherent population trapping in cesium:Dark lines and coherent microwave emission", *Phys. Rev. A*, 58,2345,1998.

Development of NPL Rb fountain frequency standard

Yuri B. Ovchinnikov
National Physical Laboratory
Teddington, Middlesex, TW11 0LW, UK
E-mail: yuri.ovchinnikov@npl.co.uk

***Abstract* — The first characterization of the distributed cavity phase frequency shift of the NPL Rb fountain frequency standard is reported. It is shown how the symmetric part of the distributed cavity phase shift can be used to set up the vertical angle of the fountain. The estimated uncertainty of the distributed cavity phase frequency shift of 1.25×10^{-16} reduces the total type B uncertainty of the Rb fountain down to 2.4×10^{-16}.**

I. INTRODUCTION

The NPL Rb fountain frequency standard [1-3] is designed to have both high frequency stability and accuracy. The main advantage of Rb atoms is their low collision cross section at the low temperatures used in atomic fountains. It has been proved both theoretically [4] and experimentally [5,6] that the collision cross section of Rb atoms is about 30 times smaller than Cs atoms. This makes it possible to reduce the systematic frequency shift related to collisions between the Rb atoms. It also allows us to operate the Rb fountain with a larger number of atoms, which reduces the quantum projection noise of the standard.

One of the distinctive features of the NPL Rb fountain is the use of a Ramsey microwave cavity, with a loaded quality factor 28500, which is very close to the quality factor 32100 of an ideal copper cavity of the same size. This is intended to suppress the corresponding distributed cavity phase (DCP) frequency shifts [7-11].

In this paper we provide the results of the first characterization of the DCP frequency shift of the NPL Rb fountain frequency standard.

II. DISTRIBUTED CAVITY PHASE SHIFT

A. General

The DCP frequency shift [7-11] arises from the presence of phase gradients in the microwave field inside the Ramsey cavity. The atom trajectory, which is not exactly vertical, passes the Ramsey cavity in different places. The resulting frequency shift is proportional to the phase difference of the interrogation field, experienced by the atoms on their way up and down.

In the theoretical work [7] it was proposed that the transverse phase distribution of the microwave field inside a TE011 cavity could be described as a Fourier series of $\cos(m\phi)$, where $m = 0,1,2\ldots$ and ϕ is the azimuthal angle. The $m = 0$ term corresponds to the azimuthally symmetric phase distribution, the $m = 1$ term is related to the linear transverse gradient of the phase, and the $m = 2$ term corresponds to the quadrupolar phase variation. The higher terms are claimed to be much smaller and were neglected in the existing characterizations [9-11] of the DCP frequency shift and its power dependencies.

B. Setting the fountain vertically

Setting the fountain vertically makes it possible to eliminate the asymmetric component of the DCP frequency shift, which provides the largest uncertainty of the DCP frequency shift in the most accurate fountains [11, 12].

The simplest way to set up the fountain vertically is to maximize the number of atoms returned to the detection region of the fountain after their launching. Possible directions of propagation of atoms in the fountain are restricted by several apertures, the smallest of which is formed by the cut-off tubes of the Ramsey cavity with inner diameter 1.6 cm. The lower cut-off tube limits the transverse velocity of the atoms reaching the detection region to a maximum value of 1 cm/s, which corresponds to an initial full divergence of the atomic cloud ~ 4.6 mrad and an average transverse kinetic energy of 0.5 μK. The atoms are initially launched vertically along the axis of the fountain with vertical velocity of 4.32 m/s. Taking into account such a large initial divergence of the atomic cloud, the precise alignment of its vertical angle is a challenging problem.

Fig. 1 and Fig. 2 show the amplitude of the detection signal at normal operation of the fountain as a function of its angle. The figures correspond to the tilting of the fountain perpendicular to or along the feeds of the Ramsey cavity (and direction of propagation of the detection laser beams).

The relative angles presented in the graphs are measured at the test platform, which is rigidly attached to the bottom of the

Pathfinder Programme of the National Measurement Office

fountain. These measurements give us the vertical angles of the fountain of $\alpha_{\parallel} = 7.7$ mrad and $\alpha_{\perp} = 1.8$ mrad.

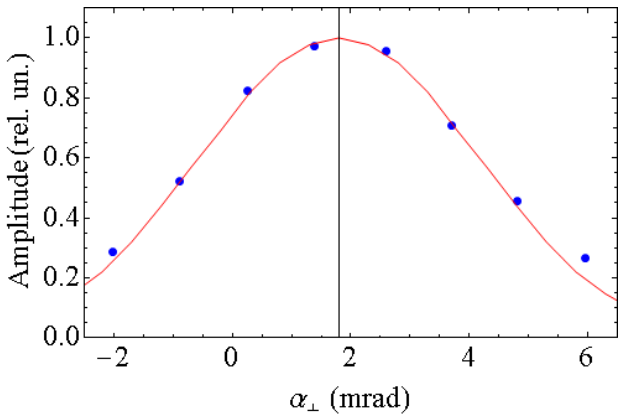

Figure 1. Amplitude of the detection signal as a function of the angle of the fountain, changed perpendicularly to the feeds of the Ramsey cavity. The fit line is the calculated dependence of the number of atoms reaching the detection region in the presence of the cut-off tubes of the Ramsey cavity for an atomic cloud with a temperature of 0.5 μK.

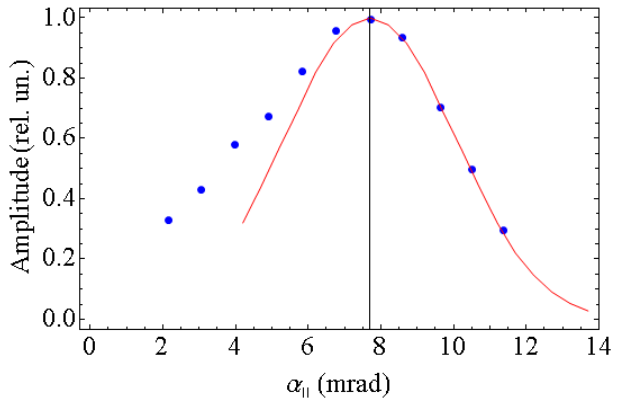

Figure 2. Amplitude of the detection signal as a function of the angle of the fountain, changed along the feeds of the Ramsey cavity. The fit line is the same as in the previous figure. The asymmetry of the experimental profile explained by the light pressure acceleration of atoms along the detection laser beam, which is directed along the feeds.

A more accurate measurement of the verticality of the fountain can be performed by measurement of the asymmetric component of the DCP frequency shift of the fountain. Here, by asymmetric DCP shift we mean the part of the shift that is not symmetric with respect to the symmetry axis of the cylindrical cavity. The main component of this shift is the m=1 term [7, 8]. In the work [9] the $\alpha_{\parallel}$ of the Cs fountain was set to zero with an uncertainty of 0.1 mrad. To achieve this, the Ramsey cavity of the tilted fountain was fed alternately from one side or the other, and the differential m=1 DCP frequency shift was measured as a function of the fountain's angle at several different amplitudes of the microwave field inside the cavity.

In our case, to set up the vertical direction of the fountain in the parallel plane, we measured the angular dependence of the asymmetric DCP frequency shift for two amplitudes of the microwave field inside the cavity, which were set near its $3\pi/2$ and $5\pi/2$ Ramsey resonances, while the cavity was excited from one side only. These microwave amplitudes were chosen because the symmetric component of the DCP frequency shift at these powers is essentially suppressed. It is important also that the cavity pulling frequency shift at these elevated powers is about 10 times smaller than at the optimal amplitude, which corresponds to the $\pi/2$ Ramsey resonance. Note, that due to the small collision cross section of the Rb atoms, its dependence on the microwave power can be completely neglected. The corresponding dependencies are presented in Fig. 3. From the independent measurements of the symmetric DCP frequency shifts (Fig. 7) and their angular dependencies in the perpendicular plane, it is concluded that their possible input to the measured relative frequency DCP shift of the fountain at these amplitudes of the field is below 10^{-15}.

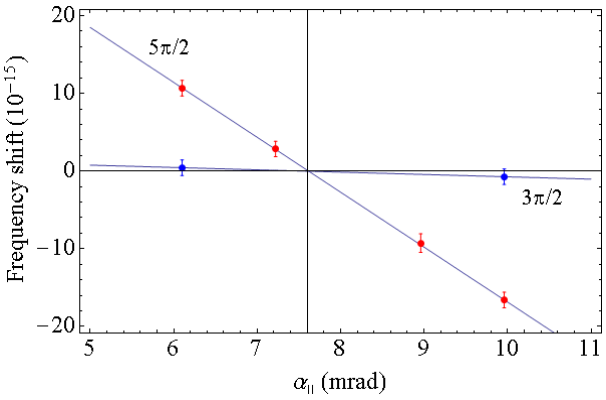

Figure 3. Angular dependence of the asymmetric DCP frequency shift for amplitudes of the microwave field inside the Ramsey cavity at $3\pi/2$ and $5\pi/2$ Ramsey resonances.

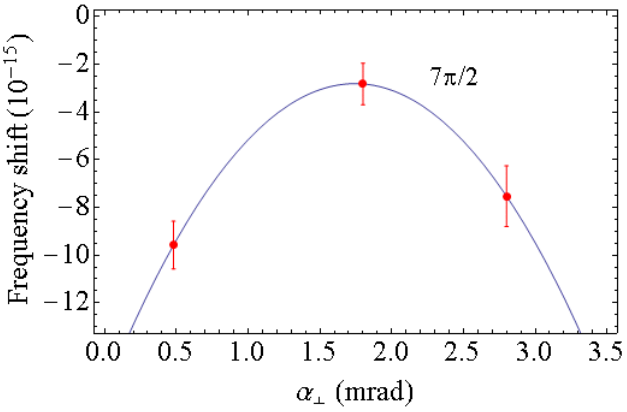

Figure 4. Angular dependence of the symmetric DCP frequency shift for the $7\pi/2$ Ramsey resonance of the microwave field.

The determination of the vertical direction of the fountain in the plane perpendicular to the feeds of the cavity cannot be done by measuring the angular dependence of the asymmetric DCP frequency shift, because in this direction it is either absent or very small. On the other hand, the symmetric DCP shift can be used to solve this problem.

We have found that the angular dependence of the symmetric DCP shift is essentially enhanced at the $7\pi/2$ and $9\pi/2$ amplitudes of the microwave field inside the Ramsey cavity. The parabolic fit of the angular dependence of the transverse symmetric DCP frequency shift on Fig. 4 gives the vertical angle of the fountain $\alpha_{\perp} = 1.74 \pm 0.2$ mrad.

Summarizing the results, both methods of determination of the vertical direction of the fountain give about the same resulting angles of $\alpha_{\parallel} = 7.6 \pm 0.2$ mrad and $\alpha_{\perp} = 1.74 \pm 0.2$ mrad.

C. *Measurement of the asymmetric DCP-shift uncertainty*

The measurement of the uncertainty related to the asymmetric DCP frequency shift was done after carefully balancing the powers of the two feeds to the Ramsey cavity at the amplitude of the microwave field corresponding to a $\pi/2$ Ramsey resonance. The corresponding data on the angular dependence of this shift in the two orthogonal directions are presented in Fig. 5 and Fig. 6.

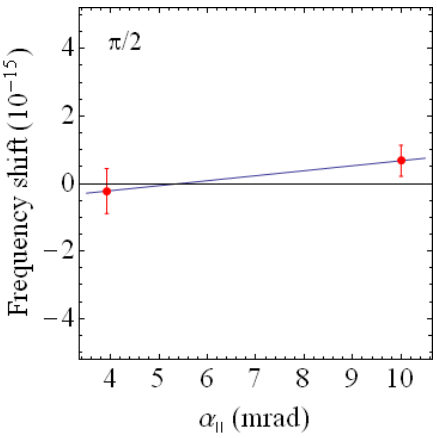

Figure 5. Dependence of the asymmetric DCP frequency on the relative angle of the fountain tilted away from vertical in the plane parallel to the feeds of the Ramsey cavity. The feeds of the cavity are balanced and correspond to a $\pi/2$ Ramsey resonance of the microwave field.

The resulting angular sensitivity of the fractional frequency of the Rb fountain frequency standard in the plane parallel to the feeds of the Ramsey cavity is equal to

$$\frac{1}{\nu}\frac{d\nu}{d\alpha_{\parallel}} = 1.4 \pm 1.3 \ (10^{-16}/\text{mrad}).$$

The corresponding angular sensitivity in the plane perpendicular to the feeds is equal to

$$\frac{1}{\nu}\frac{d\nu}{d\alpha_{\perp}} = 0.0 \pm 2.0 \ (10^{-16}/\text{mrad}).$$

The fit line in Fig. 6 is taken to have no slope, which corresponds to an absence of phase gradient in that direction.

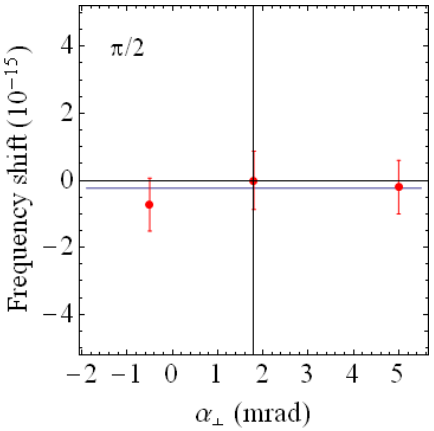

Figure 6. Dependence of the asymmetric DCP frequency on the relative angle of the fountain tilted away from vertical in the plane perpendicular to the feeds of the Ramsey cavity. The feeds of the cavity are balanced and correspond to a $\pi/2$ Ramsey resonance of the microwave field.

For an uncertainty in the vertical angle of the fountain of 0.2 mrad, the corresponding uncertainty in the asymmetric part (mainly the $m = 1$ term) of the DCP fractional frequency shift is 0.55×10^{-16} for the tilt of the fountain in the parallel plane and 0.4×10^{-16} for its tilt in the perpendicular plane.

D. *Estimate of the symmetric DCP-shift contributions*

The symmetric DCP frequency shift consists mainly of the $m = 0$ and $m = 2$ terms, which are too small ($< 10^{-16}$) to be measured directly. The estimates of these shifts were based on mathematical modeling [9-12]. In our case we rely on the calculations [12] for the LNE-SYRTE Rb fountain, the Ramsey cavity of which has the same aspect ratio and size as our cavity. The only difference is that our cavity has a larger diameter of the cut-off tubes (16 mm instead of 12 mm) and a much higher quality factor (28500 instead of 6000).

The $m = 0$ contribution of the DCP frequency shift of the LNE-SYRTE Rb fountain [12] is estimated to be as small as $-0.2(5)\times10^{-17}$. Therefore, it is absolutely safe in our case to take the uncertainty of the $m = 0$ DCP frequency shift to be equal to 0.3×10^{-16}.

The estimate of the $m = 2$ DCP shift for the LNE-SYRTE Rb fountain, which includes the spatial inhomogeneity of the detection and a possible 2 mm transverse offset of the launched atoms, gives a total shift of $0.5(3) \times 10^{-16}$. Since the size of our initial atomic cloud (with radius of 3 mm at the 1/e density level) and the transverse inhomogeneity of the detection beam are very close to the LNE-SYRTE fountain, we take the uncertainty of the $m = 2$ frequency shift to be equal to 1.0×10^{-16}. In future we plan to turn the detection beams to be at 45° with respect to the feeds of the Ramsey cavity, as is done in the LNE-SYRTE Cs fountain FO1, to essentially suppress the $m = 2$ component of the DCP shift.

The total uncertainty budget for the DCP frequency shift of the NPL Rb fountain frequency standard is presented in Tab. I.

TABLE I. DCP-SHIFT UNCERTAINTY BUDGET

Type of DCP shift	**Uncertainty (10^{-16})**
$m = 1$ (parallel)	0.55
$m = 1$ (perpendicular)	0.4
$m = 0$	0.3
$m = 2$	1.0
Total	**1.25**

III. MEASUREMENT OF ALL POWER DEPENDENT SHIFTS

Finally we have performed more detailed measurements of the dependence of the fountain frequency on the amplitude of the microwave field inside the Ramsey cavity. This time the measurements were done for the fountain precisely aligned vertically and after proper balancing of the feeds of the cavity, which minimizes the asymmetric DCP frequency shift.

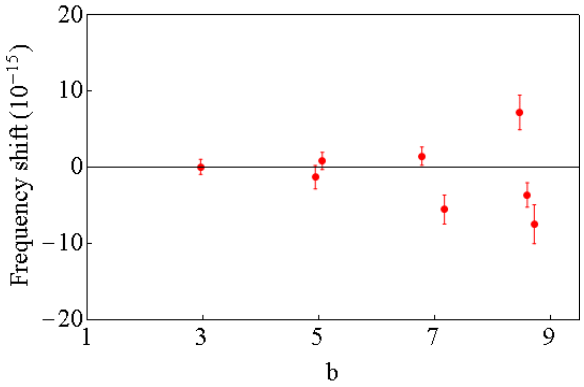

Figure 7. Dependence of the frequency shift of the fountain on the amplitude of the microwave field inside the Ramsey cavity, which is taken for a vertically aligned fountain and balanced feeds of the cavity.

This measurement was performed relative to the frequency shift at the optimal power (b=1). The results of these measurements are presented in Fig. 7.

This dependence includes all power dependent frequency shifts of the Rb fountain, the main contributions of which are the symmetric DCP shift and possible microwave leakage shift.

One can see that the frequency shifts turn to zero around all the Ramsey resonances of higher order (b=3, 5, 7, 9). Therefore, the general character of the observed dependence agrees well with the typical power dependence of the symmetric DCP frequency shift and indirectly confirms the smallness of the microwave leakage shift.

IV. SUMMARY

The DCP frequency shift of the NPL Rb fountain has been characterized and its total uncertainty is equal to 1.25×10^{-16}. The corresponding total type B uncertainty of the Rb fountain (Tab. 1) is reduced down to 2.4×10^{-16}.

TABLE II. TYPE B UNCERTAINTY BUDGET

Effect	**Frequency shift (10^{-16})**	**Uncertainty (10-16)**
Second order Zeeman	857.6	1.0
Blackbody radiation	-133.5	0.6
Distributed cavity phase	0	1.25
Collisions with residual gas	<0.7	0.7
Microwave lensing	-0.9	0.5
Microwave leakage	0	1.0
Gravity	12.6	0.3
Other	0	1.0
Total		**2.4**

Based on this improved accuracy of the NPL Rb fountain frequency standard we will perform a new absolute measurement of the Rb ground state hyperfine splitting.

ACKNOWLEDGMENT

I would like to thank Krzysztof Szymaniec and Rachel Godun for useful discussions of the results presented in this paper.

REFERENCES

[1] Y. Ovchinnikov and G. Marra, "Accurate rubidium atomic fountain frequency standard," Metrologia, vol. 48, no. 3, pp. 87-100, 2011.

[2] R. Li and K. Gibble, “Comment on ’accurate rubidium atomic fountain frequency standard’,” Metrologia, vol. 48, no. 5, pp. 446-447, 2011.

[3] Y. Ovchinnikov and G. Marra, “Reply to comment on ’accurate rubidium atomic fountain frequency standard’,” Metrologia, vol. 48, no. 5, pp. 448-449, 2011.

[4] S. Kokkelmans, B. Verhaar, K. Gibble and D. Heinzen, "Predictions for Laser-Cooled Rb Clocks," Phys. Rev. A, vol. 56, R4389, 1997.

[5] C. Fertig and K. Gibble, "Measurement and cancellation of the cold collision shift in an ^{87}Rb fountain clock," Phys. Rev. Lett., vol. 85, pp. 1622–1625, 2000.

[6] Y. Sortais, S. Bize, C. Nicolsa, A. Clairon, C. Salomon and C. Williams, “Cold collision frequency shifts in a ^{87}Rb atomic fountain ,” Phys. Rev. Lett., vol. 85, pp. 3117-3120, 2011.

[7] R. Li and K. Gibble, “Phase variations in microwave cavities for atomic clocks,” Metrologia, vol. 41, no. 6, pp. 376–386, 2004.

[8] R. Li and K. Gibble, “Evaluating and minimizing distributed cavity phase errors in atomic clocks,” Metrologia, vol. 47, no. 5, pp. 534-551, 2010.

[9] J. Gu´ena, R. Li, K. Gibble, S. Bize, and A. Clairon, “Evaluation of Doppler shifts to improve the accuracy of primary atomic fountain clocks,” Phys. Rev. Lett., vol. 106, no. 13, p. 130801, 2011.

[10] R. Li, K. Gibble, and K. Szymaniec, “Improved accuracy of the NPL-CsF2 primary frequency standard: evaluation of distributed cavity phase and microwave lensing frequency shifts,” Metrologia, vol. 48, no. 5, pp. 283-289, 2011.

[11] S. Weyers, V. Gerginov, N. Nemitz, R. Li, and K. Gibble, “Distributed cavity phase frequency shifts of the caesium fountain ptb-csf2,” Metrologia, vol. 49, no. 1, pp. 82-87, 2012.

[12] J. Guéna, M. Abgrall, D. Rovera, P. Laurent, B. Chupin, M. Lorus, G. Santarelli, P. Rosenbusch, M. E. Tobar, R. Li, k. Gibble, “Progress in atomic fountains at LNE-SYRTE,” IEEE T Ultrason. Ferr., vol. 59, no. 3, pp. 391-410, 2012.

Hyperfine coherence and population lifetime in Cs vapor cells

Jean-Marie Danet, Olga Kozlova*, Stéphane Guérandel and Emeric de Clercq
LNE-SYRTE
Observatoire de Paris CNRS-UMR 8630, UPMC
* present adresse LNE-CNAM
Paris, France
jean-marie.danet@obspm.fr

***Abstract*—Within the frame of a Raman-Ramsey CPT clock optimisation, we present our investigations on the coherence and population lifetime measurements in Cs vapour cells. To guarantee the reliability of the coherence lifetime measurements, three different methods are compared. Very good agreement is found between two of them and results are discussed for the third. In order to increase the coherence lifetime, two techniques are tested: Firstly a buffer gas can be added in the Cs vapour cell and secondly cell walls can be coated to reduce the destructive collisions against the walls. Buffer gas is tested first and then combined to a coating. First results are presented.**

I. INTRODUCTION

Thanks to compactness, reliability and good short term frequency stability, vapor cell clocks can be used in many applications such as navigation and defence systems or telecommunications. Short term stability can be improved by increasing the atomic coherence and population lifetime which leads to spectral line narrowing and then more accurate frequency discriminator. In the case of our pulsed coherent population trapping (CPT) [1] clock, described in Part II, longer Ramsey time will be accessible sharpening even more this discriminator.

In part III we present a comparison of three different methods: Franzen method of relaxation in the dark, Ramsey method, based on the amplitude decay of the Ramsey fringes, and a continuous interrogation method which consists of the extrapolation of the CPT resonance width to the zero laser intensity. As the goal of this comparison is to guarantee the reliability of a measurement, attention has been paid to measure also the width of the $\Delta m_F=2$ transitions between hyperfine Zeeman sublevels, allowed by the double lambda scheme.

To increase the coherence lifetime, two different techniques have been used. The first consists in an addition of buffer gas which also suppresses the Doppler broadening of the hyperfine transition by Dicke effect. The second technique consists in coating the cell walls with an anti-relaxing layer [2], avoiding destruction of the atomic coherence during the collision with the walls. A study of coatings and buffer-gas techniques is presented in part VI, buffer gas is firstly tested alone and then a combination buffer gas and coating. The influence of relevant parameters (pressure of buffer gas, beam diameter) on the relaxation time has been investigated.

II. EXPERIMENTAL SETUP

In this Raman Ramsey CPT clock [3], the dark state is produced by a double lambda scheme, using two linear and orthogonally polarised laser beams. This scheme gives high S/N on the 0-0 transition but allow also $\Delta m_F=2$ transitions [4] (dashed grey in Fig. 1). Given that those transitions are close to the 0-0 one (220Hz at 0.2G), they influence the clock signals, thus their coherence lifetime will be also measured.

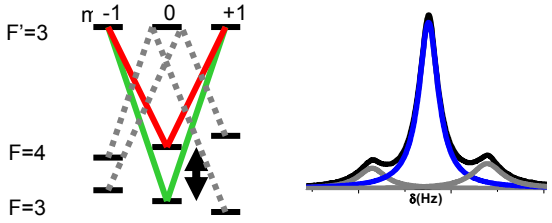

Figure 1. Left figure: double lambda scheme , red line: Master laser, green line: Slave laser, dashed grey line: $\Delta m_F=2$ transition, Right figure: black line: observed CPT signal when the slave laser frequency is swept around the zero detuning, solid blue line: 0-0 transition, grey line: $\Delta m_F=2$ transitions. Blue and grey line results from a fit of the experimental signal by three lorentzian profiles.

The setup, presented in Fig.2 allows to observe CPT different transitions ($\Delta m_F=0,2$) depending on the chosen L plate. In order to select only the 0-0 transition, one has to build a pure σ+ or σ- by transforming L into a polarizer and a λ/4 plate. The $\Delta m_F=2$ transitions which needs one σ+ polarized laser and the second one in σ-, will be cancelled. To select only the $\Delta m_F=2$ transition L has to be a λ/4 plate and to have the double lambda scheme, no L is needed.

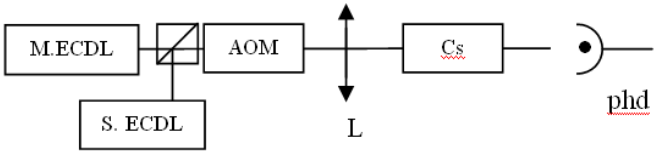

Figure 2. Setup. M ECDL is an extended cavity diode laser used as master laser. S ECDL is the slave laser phase locked on the master laser. The acousto–optic modulator (AOM) is used in pulsed mode to switch ON/OFF the beams. PHD is the photo-diode. L is a polarisor or plate, see text.

III. METHODS COMPARISON

T_1 will refer to the population lifetime and T_2 to the hyperfine coherence lifetime.

A. *Linewidth versus Power method*

In continuous wave mode, the intensity linearly broadens the linewidth because of the saturation effect [5]. The T_2 value is given by the linewidth extrapolation to zero intensity according to (1).

$$\Delta\upsilon = \frac{1}{T_2\pi} + \frac{\Omega^2}{2*\Gamma\pi} \qquad (1)$$

where T_2 is the hyperfine coherence lifetime, Ω^2 is the sum of the squared master laser and slave laser Rabi frequencies, Γ is the relaxation rate of the excited level. To take into account $\Delta m_F=2$ transitions, a three lorentzian peak fit was used to measure the linewidths, as shown in Fig. 1.

B. *Franzen method of relaxation in the dark*

The Franzen's sequence [6], presented in Fig. 3, is applied to the atoms. A first pulse pumps the atoms in the dark state, and a probe pulse is sent after a free evolution time in the dark. The frequency is fixed at the zero Raman detuning so the detected level corresponds to the top of the Ramsey fringe. The lifetime is extracted from an exponential fit of the detection level decay with the free evolution time. A dead time is inserted, to ensure total relaxation between the two sequences. Population and coherence lifetimes (T_1&T_2) can be measured.

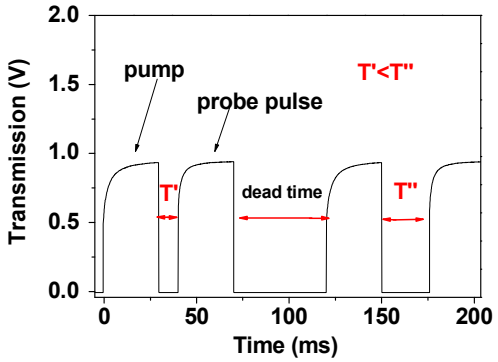

Figure 3. Pulse sequence for Franzen's method

However, if a double lambda scheme is used, a modulation rises up on the exponential decay, as shown on the Fig. 4. Its linear frequency dependence with the magnetic field of 1.1kHz/G and its suppression by using a σ+ scheme (Fig. 4 right) have shown that this modulation came from the $\Delta m_F=2$ transitions. Indeed, as the Ramsey time changes during the T_2 measurement, the width of $\Delta m_F=2$ fringes changes and modulates the 0-0 fringe amplitude. Thus, in order to keep a good accuracy, 0-0 T_2 measurement have been realised in σ+ scheme.

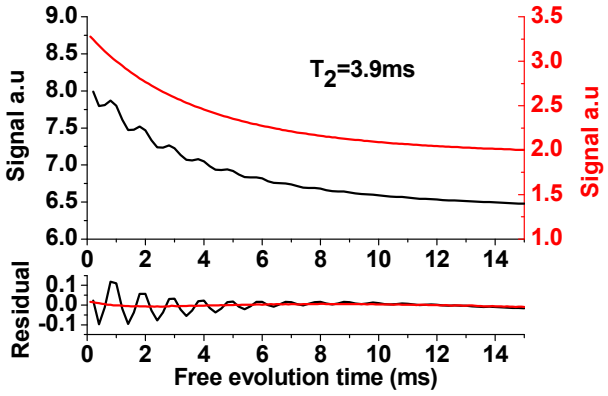

Figure 4. Signal level versus the free evolution time. Black curves: double lambda scheme, red curves : circular polarised beams. Up: Raw signals, Bottom: Residual calculation after first order exponential fit of experimental data.The modulating signal is cancelled on the red curves.The cell used is 5cm long, filled with a Ar-N_2 buffer gas mixture with $P_{N2}/P_{Ar}=0.6$, T=29°C, beam diameter 1cm.

C. *Amplitude of Ramsey fringes*

In a pulsed mode, the Ramsey fringes amplitude evolves over the free evolution time as an exponential decay. As in Franzen's method, a σ+ scheme has been used to measure the 0-0 T_2, which is also extracted from an exponential fit. The $\Delta m_F=2$ transition T_2 has been measured using a σ+σ- scheme.

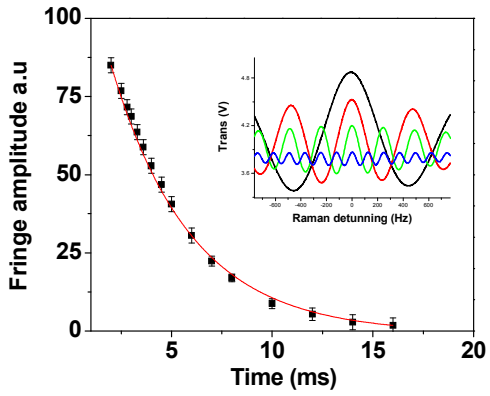

Figure 5. Fringes amplitude decay versus free evolution time. The laser beams are circulary polarised. Black dots: experimental data. Solid red curve: fit by an exponential function. Inset: Ramsey CPT signal for different free evolution time.

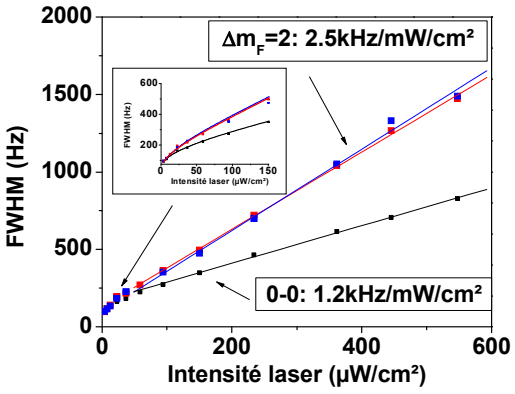

Figure 6. Linewidth broadening with intensity, for 0-0 (black) & $\Delta m_F=2$ (blue and red) transitions. Inset: Zoom on the low intensity domain and fit using Javan's formula.

D. *Results*

The hyperfine coherence lifetime measurements are coherent for the two pulsed method: Ramsey & Franzen, and is in the range of 4ms, see Table 1. The T_2 of the $\Delta m_F=2$ transitions is similar to the 0-0 one. Regarding the continuous method, the classical linear extrapolation to zero intensity, see Fig. 6, gives shorter coherence lifetime than the other methods for 0-0 and $\Delta m_F=2$ transitions (column $\Delta\nu_{CW}$ LIN in Table 1). The cell used is a buffer gas compensated cell with $P_{N2}/P_{Ar}=0.6$, T=29°C, beam diameter 1cm.

TABLE I. T_2 MEASUREMENTS

Transition	T_2 (ms)			
	Ramsey	*Franzen*	*$\Delta\nu_{CW}$ LIN*	*$\Delta\nu_{CW}$ JAVAN*
0-0	3.9 ±0.1	4.0± 0.2	1.8±0.2	4.1±0.4
$\Delta m_F=2$	4.0± 0.2	4.8 ±0.3	2.9±0.2	4.6±04

However, we noticed that fitting with a linear + square root function (inset in Fig. 6), show coherent results with Ramsey and Franzen methods (column $\Delta\nu_{CW}$ JAVAN in Table 1), despite the fact that the calculus hypothesis corresponds to a pure Cs cell without buffer gas broadening [7].

A broadening with intensity twice bigger for $\Delta m_F=2$ than 0-0 transition have been observed, see Fig. 6.

IV. BUFFER GAS & COATINGS

A. *Buffer Gas*

Buffer gases allow working in the Dicke regime, cancelling the hyperfine Doppler broadening. On Fig. 7, T_2 is plotted as a function of pressure. On the left side of the optimum, the increase of T_2 corresponds to the diminution of the wall collision when pressure increases. On the right side of the optimum, T_2 decreases because the broadening by Cs-buffer gas collision becomes predominant. Impact of pressure has been measured and compared with a theoretical model and a qualitative agreement is noticed.

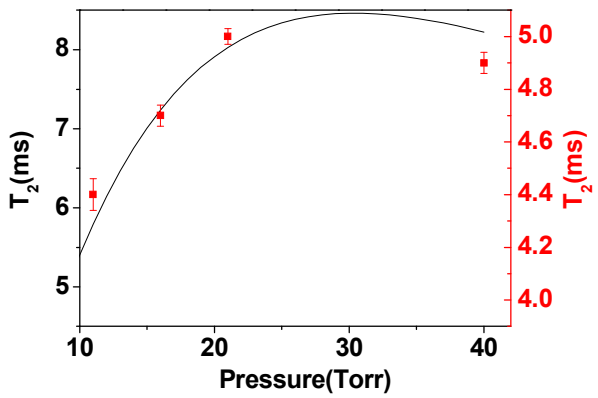

Figure 7. Coherence lifetime versus buffer gas pressure. Black curve is the calculated data, red curve, experimental data.

B. *Combinaison of buffer gas and coatings*

A cell combining buffer gas and paraffin coating was built and compared to a cell with the same buffer gas pressure, P=21 torr. The paraffin used is an hexatricontane D74 CIL 365°C. The first measurements show that the population life time is greatly increased by the paraffin. For a laser beam

diameter approaching the cell diameter, the life time is three times bigger, see Fig. 8.

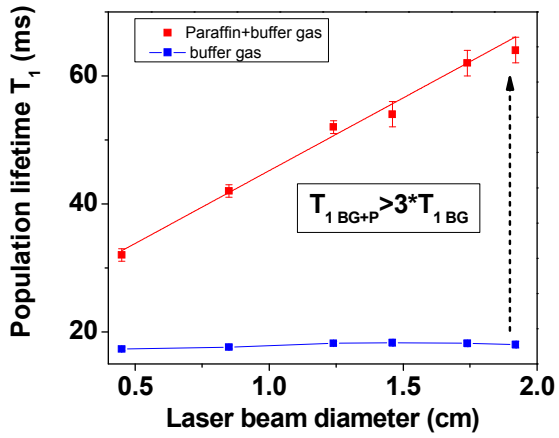

Figure 8. Population lifetime measurements versus laser beam diameter for buffer gas (blue) & buffer gas + paraffin (red) cells

V. Conclusion

Our method comparison has shown a good agreement between Franzen method of relaxation in the dark, and amplitude of Ramsey fringes method. The coherence lifetime of the $\Delta m_F=2$ transitions have been measured and are similar to the clock transition one. However, their broadening by saturation effect is twice bigger than the 0-0 transition one.

Further studies have to be carried regarding the linewidth versus power method because the linear extrapolation to zero gives a different value than the pulsed methods.

Finally, promising results have been obtained on the association of buffer gas and paraffin. The population lifetime is increased by a factor three. Next step will be the metrology of the clock using that coating.

Acknowledgment

We are pleased to acknowledge Pierre Bonnay and Annie Gérard for very careful manufacturing of Cs cells. We are grateful to Michel Lours and the SYRTE electronic team for their help.

References

[1] J. Vanier, "Atomic clocks based on coherent population trapping: a review", Appl. Phys. B, vol. 81, pp. 421-442, 2005

[2] M. A. Bouchiat and J. Brossel, "Relaxation of optically pumped Rb atoms on paraffin-coated walls," Phys. Rev., vol. 147, no. 1, pp. 41–54, Jul. 1966.

[3] T. Zanon, S. Guérandel, E. de Clercq, D. Holleville, N. Dimarcq, and A. Clairon, "High contrast Ramsey fringes with coherent-populationtrapping pulses in a double lambda atomic system," Phys. Rev. Lett. vol. 94, no. 19, p. 193 002, May 2005.

[4] R. Boudot, S. Guerandel, E. De Clercq, N. Dimarcq et A.Clairon, "Current status of a pulsed CPT Cs cell clock" , IEEE Trans. Instr. Meas., 58, 2009, 1217

[5] J. Vanier & C. Audoin, The Quantum Physics of Atomic Frequency Standards, IOP Publishing, Bristol and Philadelphia, 1989.

[6] W. Franzen, "Spin relaxation of optically aligned rubidium vapor," Phys. Rev., vol. 115, no. 4, pp. 850–856, Aug. 1959.

[7] A. Javan, O. Kocharovskaya, H. Lee and M.O. Scully, Phys.Rev. A 66, 013805 (2002)

Towards First Active Clock Based on Mode-Locked InGaN VECSEL with Rubidium Vapor Cell Saturable Absorber

Xi Zeng and Dmitri L. Boiko
Centre Suisse d'Électronique et de Microtechnique (CSEM)
Neuchâtel, Switzerland
xi.zeng@csem.ch, dmitri.boiko@csem.ch

***Abstract*— We report the first detailed theoretical study of mode-locking dynamics in an active atomic clock based on a 420 nm wavelength, III-nitride vertical external cavity surface emitting laser with a ^{85}Rb vapor cell as the intracavity saturable absorber.**

I. INTRODUCTION

Self-mode-locked lasers employing alkali vapor cell as the saturable absorber hold promise for a new class of active atomic clocks that are vastly simpler than traditional microwave clocks. So far, only a mode-locked laser of the cavity length 325 mm (repetition frequency of 462 MHz) based on GaAs edge-emitting semiconductor diode laser and potassium vapor cell absorber was attempted [1]. Here, we report the first detailed theoretical study of mode-locking dynamics in such active atomic clock with a 420 nm wavelength, III-nitride vertical external cavity surface emitting laser (VECSEL) and a ^{85}Rb vapor cell as the intracavity saturable absorber. The laser cavity length of 49.3 mm and pulse repetition rate are matched to the 3.04 GHz F=3-F=2 hyperfine splitting in ^{85}Rb atoms such that the modes are phase locked via the Λ transition $5^2S_{1/2}$-$6^2P_{3/2}$ in ^{85}Rb atoms.

II. MODEL OF THE LASER SYSTEM

A. Mode-Locking Model

The theoretical modeling of the mode-locked Rb-GaN VECSEL used here is based on the Haus-New master equation for a laser with a saturable absorber [2-3]. Its general analytical solution [4] enables one to study the impact of the Rb vapor cell on mode-locking dynamics of GaN VECSEL, provided a suitable description of the saturated absorption in atomic vapor is available. The model here accounts for the structure of the VECSEL cavity and thermodynamic description of Rb vapor. The model parameters for the optical gain in InGaN/GaN quantum wells (QWs), ^{85}Rb absorption cross-section, and fluorescence quenching as a function of the buffer gas pressure and temperature were obtained from literature and are currently under experimental verification.

The Haus-New master equation and its analytical solution [4] assume essentially a two-level absorber system. The rubidium line of interest, however, is a three-level system with one upper energy state and two hyperfine ground states. Special attention has been given to adapt this mode-locking model to that particular case.

The stable self-sustaining mode-locking regime requires (i) positive saturated net cavity gain at the peak of the lasing pulse and (ii) negative net gain before and after the mode-locked pulse, which can be achieved if the recovery time of absorber is comparable to the typical carrier lifetime in the InGaN/GaN QWs (~1 ns). However, in the absence of a buffer gas, the excited $6^2P_{3/2}$ state of ^{85}Rb atoms has a long lifetime (>>1 ns). He and N_2 are considered to be suitable buffer gas candidates due to their efficient quenching of fluorescence in Rb atoms, and the parameters of ^{85}Rb atomic vapor cell absorber are analyzed as a function of the buffer gas pressure and cell temperature.

For the gain section of the VECSEL cavity consisting of InGaN/GaN QWs, the major parameters of the model such as differential gain, intrinsic loss, transparency carrier density, and carrier recombination lifetimes are taken from literature, and they allows us to calculate important secondary parameters used in the model (e.g. saturation energy of the gain). For simplicity, the gain spectrum linewidth is assumed to be independent of the injected carrier density. All QWs are assumed to be pumped at an equal rate, although this assumption might not be fulfilled in optically pumped QWs as different amount of optical power density can reach each QW. Finally, due to fast intraband carrier relaxation (~ 100 fs), the optical gain line can be assumed to be homogeneously broadened (a requirement for the Haus-New model to be valid) at the time scale considered here, which is set by the width of generated mode-locked pulses (~4 ps).

B. Modeling the ^{85}Rb Saturable Absorber

The most critical parameters of the model are those of the alkali vapor cell, mainly the absorption cross-section,

linewidth, and lifetime of excited state in Rb atoms. All these parameters depend on the cell temperature, buffer gas composition, and buffer gas pressure.

The linewidth of the $5^2S_{1/2}$-$6^2P_{3/2}$ transition in ^{85}Rb atoms as a function of He buffer gas pressure is available from [5]. No similar data has been reported for N_2 buffer gas in the $5^2S_{1/2}$-$6^2P_{3/2}$ transition. For N_2 buffer gas, the linewidth was evaluated using comparative measurements with helium and nitrogen buffer gases reported for the conventional $5^2S_{1/2}$-$5^2P_{3/2}$ transition [6]. The temperature dependence of the linewidth broadening is accounted for by introducing a factor $\sqrt{T/T_{ref}}$ with T_{ref} being the reference temperature [7]. For the temperature ranges utilized here, the collisional self-broadening of Rb atomic vapor is negligible compared to the impact of the buffer gas [8]. As an example, the calculated linewidth vs. temperature for a ^{85}Rb cell with 6 torr N_2 buffer gas is shown in Figure 1.

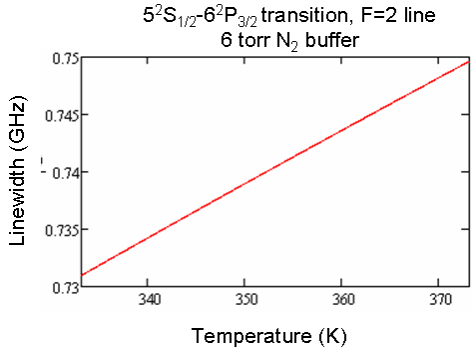

Figure 1. Calculated linewidth vs. temperature for a ^{85}Rb cell with 6 torr N_2 buffer gas. Temperature range is 333 to 373 K (60° to 100° C).

The impact of collisions with the buffer gas atoms (molecules) on fluorescence lifetime quenching in Rb atoms has been incorporated into the model. The excited state $6^2P_{3/2}$ of isolated ^{85}Rb atom has a lifetime of 112 ns [9]. The collisional quenching of fluorescence lifetime is defined by the mean time between collisions with the buffer gas atoms (molecules) and collisional cross-section σ_{buffer} [10], given by:

$$\tau_{collision} = \frac{1}{v_T \cdot \sigma_{buffer}} \cdot \left(\frac{k_B T}{P_{buffer}}\right) \qquad (1)$$

where k_B is the Boltzmann constant; T and P_{buffer} are the temperature and pressure of the buffer gas, $v_T = \sqrt{8RT/(\pi M)}$ is the thermal velocity of Rb atoms, R is the ideal gas constant, and M is the molar mass of ^{85}Rb. The overall lifetime of the Rb absorber for the ^{85}Rb $5^2S_{1/2}$-$6^2P_{3/2}$ line is then:

$$\tau_{absorber} = \frac{1}{\frac{1}{112ns} + \frac{1}{\tau_{collision}}} \qquad (2)$$

As an example, the calculated absorber lifetime for a ^{85}Rb cell with 200 torr N_2 buffer gas is shown in Figure 2. By varying the cell temperature and buffer gas pressure, the recovery time of ^{85}Rb cell absorber can be made shorter than the carrier lifetime in the GaN QWs (~1 ns), the optical gain medium. This is a prerequisite condition for achieving the stable regime in passive mode-locking operation.

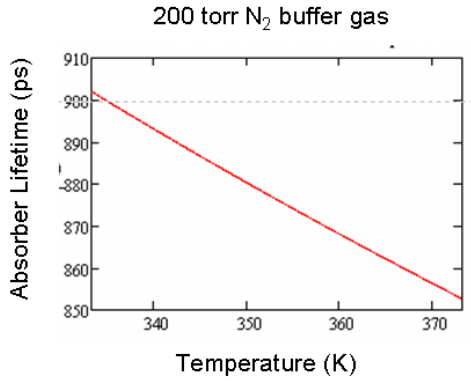

Figure 2. Calculated absorber lifetime for a ^{85}Rb cell with 200 torr N_2 buffer gas. Temperature range is 333 to 373 K (60° to 100° C).

Finally the effective absorption cross-section describing two hyperfine transitions was estimated from Einstein's spontaneous emission coefficients A_{21}, using the expression:

$$\sigma_{eff} = (1-\rho)\frac{N_2}{N_1} A_{21} \frac{\lambda^2}{8\pi n^2}\left[\frac{2}{\pi}\frac{1}{\Delta\nu_1} + \frac{2}{\pi}\frac{1}{\Delta\nu_2}\right] \qquad (3)$$

where N_2 is the degeneracy of the upper energy state, N_1 is the degeneracy of the lower energy state, λ is the wavelength, n is the refractive index of the absorbing medium, and $2/\pi\Delta\nu_{1,2} = g_{1,2}(f_0)$ is the peak value of the Lorentzian spectral line shape function of the two hyperfine transitions.

In this model, N_2 is 1, N_1 is 2 (two hyperfine levels). A_{21} for the $5^2S_{1/2}$-$6^2P_{3/2}$ line is taken to be 0.018×10^{-8} s^{-1} [11]. λ is 420.2 nm. The refractive index n is 1.

The coefficient ρ accounts for the fact that that absorber only absorbs on two relatively narrow bands of the optical spectrum overlapping with the two adjacent modes of the frequency comb generated by the VECSEL in mode-locking lasing regime. Conceptually, this is demonstrated in Figure 3. Thus, even if the absorber completely absorbs the two cavity modes with which it interacts, the overall pulse amplitude (and shape) will only change partially.

When the absorber interacts with two modes of the laser cavity, the other modes will be affected and phase-locking will result because the gain medium is homogeneously broadened. As discussed earlier, this assumption is valid at the time scale considered here.

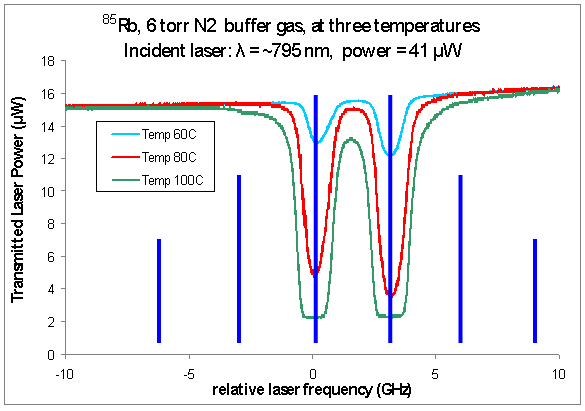

Figure 3. An example optical frequency comb constituting a mode-locked pulse is overlaid with measured absorption profile to illustrate the limited interaction between the absorber and the lasing modes.

An iterative approach is implemented to calculate ρ and mode-locked pulse parameters self-consistently. At each iterative step, the spectral width of the pulse is estimated from the pulse widths in the time domain obtained from the previous iteration using the well known time-bandwidth product equation for a hyperbolic secant pulse:

$$\Delta\nu = \frac{0.315}{\tau_{FWHM}} \tag{4}$$

Calculating $\Delta\nu$/3.04GHz (3.04 GHz is the Fabry-Perot cavity mode separation; also hyperfine frequency in ^{85}Rb atoms) yields the number of modes, N_{mode}, in the comb constituting the optical pulse train.

The σ_{eff} from the previous iteration is used to calculate the attenuation that will be applied to the two center cavity modes of the optical pulse train as illustrated qualitatively in Figure 4. From the calculated N_{mode}, one can use Fourier series analysis to reconstruct the optical pulse in the time domain (as seen in Figure 5) and calculate the portion (or percentage) of the total optical pulse energy that transmits through the absorber. This number is the ρ for the next iteration of calculations.

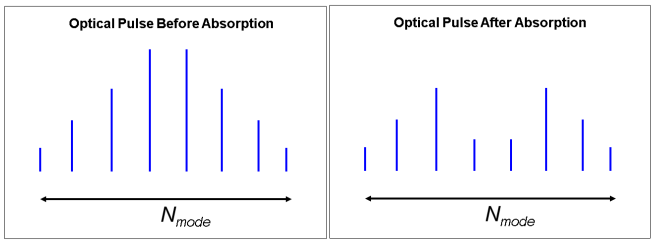

Figure 4. In frequency domain, the optical comb constituting the optical pulse train is illustrated before and after interaction with the absorber.

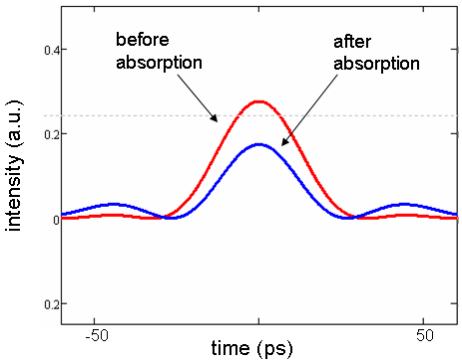

Figure 5. Fourier series analysis is used to reconstruct the optical pulse in the time domain before and after interaction with the absorber. Example here is an optical pulse consisting of 5 modes.

III. Preliminary Results

Some preliminary results have been obtained. Figure 6 shows the predicted domain of stable mode-locking regime as a function of the Rb cell temperature and driving current of the VECSEL QW gain structure with a ^{85}Rb cell containing 2 torr of N_2 buffer gas. Here, the cavity net gain is negative at the leading and trailing edges of the mode-locked pulse, ensuring the stability with respect to spontaneous emission noise. At the same time, the saturated net cavity gain is positive at the peak of the lasing pulse. As an example of the typical pulse parameters, at an injection current of 6.45 kA/cm^2 and Rb vapor cell temperature of 80° C, the calculated optical pulse width is ~4 ps and intracavity peak power is ~70 W. This corresponds to the output peak power of the mode-locked pulses of 350 mW and average power of 4 mW (0.5% output coupling mirror losses are used in the model).

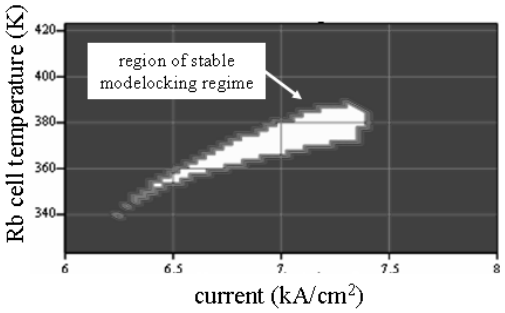

Figure 6. Region of the InGaN/GaN QW VECSEL pump current densities and ^{85}Rb absorber cell temperatures that yields stable mode-locking regime in active Rb clock.

Interestingly, the mode-locking regime in such laser with an alkali vapor cell absorber is predicted to be not self-starting, meaning that the cold cavity net gain is negative and that some initial perturbation will be required to start the mode-locked lasing. This is in agreement with reported experimental results for the potassium clock [1].

Acknowledgment

The authors would like to thank the Swiss National Science Foundation (FNS) for funding this research.

REFERENCES

[1] Y.-Y. Jau and W. Happer, “Push-Pull Laser-Atomic Oscillator,” Physical Review Letters, vol. 99, pp. 223001-1 – 223001-4, 2007.

[2] H. Haus, "Theory of mode locking with a slow saturable absorber," IEEE Journal of Quantum Electronics, vol. 11, pp. 736-746, 1975.

[3] G. New, "Pulse evolution in mode-locked quasi-continuous lasers," IEEE Journal of Quantum Electronics, vol. 10, pp. 115-124, 1974.

[4] I. V. Smetanin, P. P. Vasil’ev, and D. L. Boiko, "Theory of the ultrafast mode-locked GaN lasers in a large-signal regime," Optics Express, vol. 19, pp. 17114-17120, 2011.

[5] D. Aumiler, T. Ban, and G. Pichler, "High-resolution measurements of the pressure broadening and shift of the rubidium $5^2S_{1/2}$ - $6^2P_{3/2}$ line by argon and helium," Physical Review A, vol. 70, pp. 032723-1 - 032723-5, 2004.

[6] M. D. Rotondaro and G. P. Perram, "Collisional broadening and shift of the rubidium D_1 and D_2 lines ($5^2S_{1/2}$ --> $5^2P_{1/2}$, $5^2P_{3/2}$) by rare gases, H_2, D_2, N_2, CH_4 and CF_4," Journal of Quantitative Spectroscopy and Radiative Transfer, vol. 57, pp. 497-507, 1997.

[7] R. J. Beach, W. F. Krupke, V. K. Kanz, and S. A. Payne, "End-pumped continuous-wave alkali vapor lasers: experiment, model, and power scaling," Journal of the Optical Society of America B, vol. 21, pp. 2151-2163, 2004.

[8] T. Varzhapetyan, A. Nersisyan, V. Babushkin, D. Sarkisyan, S. Vdovic, and G. Pichler, "Study of atomic transition self-broadening and shift with the help of a nano-cell," Journal of Physics B: Atomic, Molecular and Optical Physics, vol. 41, pp. 185004-1 - 185004-6, 2008.

[9] T. Meijer, J. D. White, B. Smeets, M. Jeppesen, and R. E. Scholten, "Blue five-level frequency-upconversion system in rubidium," Optics Letters, vol. 31, pp. 1002-1004, 2006.

[10] E. S. Hrycyshyn and L. Krause, "Inelastic collisions between excited alkali atoms and molecules. VII. Sensitized fluorescence and quenching in mixtures of rubidium with H_2, HD, D_2, N_2, CH_4, CD_4, C_2H_4, and C_2H_6," Canadian Journal of Physics, vol. 48, pp. 2761-2768, 1970.

[11] *Persistent Lines of Neutral Rubidium (Rb I)* [Online]. Available: http://physics.nist.gov/PhysRefData/Handbook/Tables/rubidiumtable3.htm

The Error Model and the method analysis of TWSSTT for a low-rate dynamic object

Xuejun Chen, Zongwen Wu, Wenhua Zhao
China Satellite Maritime Tracking and Control Department
CSMTC
Jiangyin, Jiangsu, 214431, P.R. China
Wzw8723@tom.com

***Abstract*—The method aimed at enhancing precision of the two-way satellite time transfer for a low-speed dynamic object is presented in this paper. Calculous and vector algebra are used to analysis the precision of two way satellite time transfer when one of the station is a low-rate dynamic object, such as one satellite-communication station on a vessel. Mathematic model of the precision is hence obtained. Experimental results show that the main factors which affect the precision of the two-way satellite time transfer mainly includes a velocity and a course of the vessel, an elevation of the antenna, measure periods, a rise-fall range and period, a measure starting time and a initialization phase.**

I. INTRODUCTION

Measure system using wireless determines rate and location of a goal by measuring time delay and frequency transfer between a transmit wave and a reflected wave from the object. Hence, the precision of the time-frequency signal determines the precision of time delay and frequency transfer, and accordingly decides the precision of the rate and the location measured.

Two-way satellite time transfer (TWSTT) is a time transfer method derived from 1962, when the precision can arrived at 0.1~20us level. After that, TWSTT developed quickly as a time transfer method between fixed stations with high precision. As yet, precision of TWSTT between a fixed earth station can reach 0.3ns[1], one level higher than GPS method and three level higher than the long-wave method. But in real application, time authorization center sometimes authorized time to a shift object, while hardly any paper reports the precision of TWSTT in this case.

In this paper, we proposed a method aimed at enhancing precision of TWSTT between shore and a vessel. We use calculous and vector algebra to analysis precision of the authorized time resulted from movement of low-rate dynamic object, such as satellite-communication station on vessel. And hence, the mathematic model of factors effecting TWSTT precision is obtained. Numerical calculation of the factors is simulated by the model.

The outline of the rest of this paper is as follows. Section 2 introduces the error model of TWSTT between shore and a vessel. Section 3 describes the numerical calculation and simulation results. Some discussions about methods of TWSTT between shore and a vessel are given in section 4. Section 5 concludes this paper.

II. PRECISION ANALYSIS

Precision of TWSTT between fixed earth stations was meticulously analyzed in some papers[1-3]. The main conclusions still has application value when time authorized station is a low-rate dynamic object. To achieve high precision, TWSTT should possess two conditions[1]: (1) precision of time measurement is high enough; (2) transmission path is symmetrical in bidirection. To satisfy the first condition, correlative characteristic of pseudo random code can be used to two-way impulse time measurement. The second condition can be easily satisfied when the two stations are fixed. But for the low-rate dynamic object, the error of time transfer is inevitably produced, because transmission path is dissymmetrical in one measure period (about 0.27s when the dynamic object is satellite-communication station on vessel). The rest of this chapter deduces the change of transmission path affected by movement of the low-rate dynamic object.

Synchronous satellite is immobile relative to the earth coordinate when ignoring excursion of synchronous satellite itself. The servo system of satellite-communication station on a vessel can overcome swag of vessel, ensuring the earth-orientation of the antenna changeless. When the vessel is immobile, the error of the servo system overcoming swag of vessel just affects the signal-to-noise ratio of the received signal, and don't change the radial distance between satellite-communication station and synchronous satellite. Hence, main factors affecting radial distance between a satellite-communication station and a synchronous satellite are geography locations and heights of the vessel.

We establish a right-angle reference frame and its corresponding sphere reference frame, in which XOY plane in right-angle reference is a sea level, OZ vertical at XOY. X, Y, Z axes' unit vectors are $\vec{e}_x$、$\vec{e}_y$、$\vec{e}_Z$ respectively. A sphere reference frame is established according to right-angle reference, and its unit vectors are $\vec{e}_r$、$\vec{e}_\theta$、$\vec{e}_\varphi$ respectively.

For convenience, using relativity of movement, a vessel is supposed immobile, while synchronous satellite is mobile with velocity V_x、V_y、V_z in each weight of the right-angle reference frame. Well then:

$$\overrightarrow{V} = v_x\overrightarrow{e_x} + v_y\overrightarrow{e_y} + v_z\overrightarrow{e_z} \tag{1}$$

Projection of velocity $\overrightarrow{V}$ in the sphere reference frame is as follow:

$$\begin{aligned}\vec{V} &= v_x \sin\theta\cos\varphi\vec{e}_r + v_x\cos\theta\cos\varphi\vec{e}_\theta - v_x\sin\varphi\vec{e}_\varphi \\ &+ v_y\sin\theta\sin\varphi\vec{e}_r + v_y\cos\theta\sin\varphi\vec{e}_\theta + v_y\cos\varphi\vec{e}_\varphi + v_z\cos\theta\vec{e}_r - v_z\sin\theta\vec{e}_\theta\end{aligned} \tag{2}$$

$$\begin{aligned}\vec{V} &= (v_x\sin\theta\cos\varphi + v_y\sin\theta\sin\varphi + v_z\cos\theta)\vec{e}_r \\ &+ (v_x\cos\theta\cos\varphi + v_y\cos\theta\sin\varphi - v_z\sin\theta)\vec{e}_\theta + (v_y\cos\varphi - v_x\sin\varphi)\vec{e}_\varphi\end{aligned} \tag{3}$$

That's to say, movement of V_x、V_y、V_z in the right-angle reference results in changes in direction $\vec{e}_r$、$\vec{e}_\theta$、$\vec{e}_\varphi$ as follows:

$$V_r = v_x\sin\theta\cos\varphi + v_y\sin\theta\sin\varphi + v_z\cos\theta \tag{4}$$

$$rV_\theta = v_x\cos\theta\cos\varphi + v_y\cos\theta\sin\varphi - v_z\sin\theta \tag{5}$$

$$r\sin\theta V_\varphi = v_y\cos\varphi - v_x\sin\varphi \tag{6}$$

For the reason that radial distance of the vessel is much bigger than the horizontal displacement and the vertical displacement (about 10^{-7} times) in time $\Delta\vec{r}$ (0.27s), projection of the vector change $\Delta\vec{r}$ which is caused by movement and rise-fall of the vessel in direction $\vec{e}_r$、$\vec{e}_\theta$、$\vec{e}_\varphi$ is differential minuteness. Accordingly,

$$\Delta r = \int_{T_0}^{T_0+\Delta\tau} v_x\sin\theta\cos\varphi dt + \int_{T_0}^{T_0+\Delta\tau} v_y\sin\theta\sin\varphi dt + \int_{T_0}^{T_0+\Delta\tau} v_z\cos\theta dt \tag{7}$$

$$r\Delta\theta = \int_{T_0}^{T_0+\Delta\tau} v_x\cos\theta\cos\varphi dt + \int_{T_0}^{T_0+\Delta\tau} v_y\cos\theta\sin\varphi dt - \int_{T_0}^{T_0+\Delta\tau} v_z\sin\theta dt \tag{8}$$

$$r\sin\theta\Delta\varphi = \int_{T_0}^{T_0+\Delta\tau} v_y\cos\varphi dt - \int_{T_0}^{T_0+\Delta\tau} v_x\sin\varphi dt \tag{9}$$

Suppose that the angle between $\Delta\vec{r}$ and $\vec{r}$ is ψ, see Fig 1., then:

$$\left|\Delta\vec{r}\right| = \sqrt{(\Delta r)^2 + (r\Delta\theta)^2 + (r\sin\theta\Delta\varphi)^2} \tag{10}$$

$$\psi = \tan^{-1}\frac{\sqrt{(r\Delta\theta)^2 + (r\sin\Delta\varphi)^2}}{\Delta r} \tag{11}$$

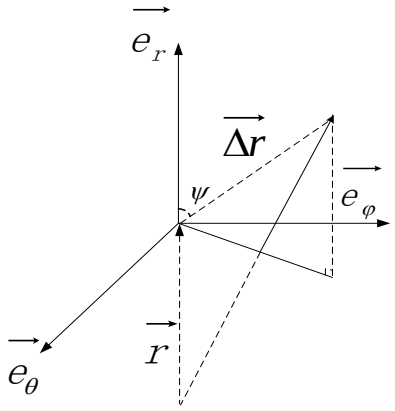

Fig 1. Location change of the vector space.

Module of the radius vector $\Delta\vec{r}'$ caused by $\Delta\vec{r}$ is as follow:

$$\Delta\vec{r}' = \sqrt{r^2 + \left|\Delta r\right|^2 + 2r\left|\Delta r\right|\cos\psi} \tag{12}$$

Sum all, the radial change of the satellite-communication antenna cased by movement and rise-fall of the vessel can expressed as follow:

$$\Delta L = \left|\Delta\vec{r}'\right| - \left|r\right| \tag{13}$$

Formulas (7) ~ (13) represent the error model of TWSTT between shore and the vessel. Using the model, main factors that affect the precision of TWSTT between shore and the vessel can be analyzed, errors of time transfer can be estimated, and methods that reduce or eliminate the error may be proposed.

III. NUMERICAL CALCULATION AND SIMULATION

In order to be convenient for analyzing our results more clearly, we can define the axis X of center-of-mass coordinates is the center line of a vessel from stem to stern, speed of a vessel is unchangeable in a measure period of two-way time transfer, deck azimuth angle of an earth station is represented by φ_0, speed is represented by V_c, geodetic azimuth angle of an earth station by α, geodetic elevation angle of an earth station by β, amplitude of swinging by A, swinging period by T, character of rising and falling for a vessel corresponds to that of a sine wave, its initial phase by ϕ_0. Meanwhile, the distance between a satellite and a vessel, which is represented by d, is far longer than that of the movement for a vessel in a horizontal plane, which is represented by L. In the condition of V_c =9m/s and A=±5, L is about 3 meters. According to the reference, $d \geq 35786.4km$. We can consider α and β are constant, then

$$V_x = -V_c \tag{14}$$

$$V_z = -A\sin(\omega t + \phi_0) \tag{15}$$

$$\varphi = \varphi_0 \tag{16}$$

$$\theta = \frac{\pi}{2} - \beta \tag{17}$$

Instead of the parameters in formula (7), (8), (9), we can acquire formulae as follows:

$$\Delta r = -V_c \cos\beta \cos\varphi_0 \Delta\tau + \frac{A\sin\beta}{\omega}\{\cos[\omega(T_0 + \Delta\tau) + \phi_0] - \cos(\omega T_0 + \phi_0)\} \tag{18}$$

$$r\Delta\theta = -V_c \sin\beta \cos\varphi_0 \Delta\tau - \frac{A\cos\beta}{\omega}\{\cos[\omega(T_0 + \Delta\tau) + \phi_0] - \cos(\omega T_0 + \phi_0)\} \tag{19}$$

$$r\sin\theta\Delta\varphi = V_c \sin\varphi_0 \Delta\tau \tag{20}$$

Assume T_0=0, then

$$\Delta r = -V_c \cos\beta\cos(A_d - \alpha)\Delta\tau + \frac{A\sin\beta}{\omega}[\cos(\omega\Delta\tau + \phi_0) - \cos\phi_0] \tag{21}$$

$$r\Delta\theta = -V_c \sin\beta\cos(A_d - \alpha)\Delta\tau - \frac{A\cos\beta}{\omega}[\cos(\omega\Delta\tau + \phi_0) - \cos\phi_0] \tag{22}$$

$$r\sin\theta\Delta\varphi = V_c \sin(A_d - \alpha)\Delta\tau \tag{23}$$

The parameters in the formulaes above are defined as follows [5-6]:

$$\alpha = 180° + \sin^{-1}\frac{\sin\gamma}{\sqrt{1-(\cos\gamma\cos\chi)^2}} \tag{24}$$

$$\beta = \tan^{-1}[\frac{\cos\gamma\cos\chi - 0.151}{\sqrt{1-(\cos\gamma\cos\chi)^2}}] \tag{25}$$

$$d = 42164.56\sqrt{1.023 - 0.302\cos\gamma\cos\chi} \tag{26}$$

$$\alpha = A_d - \varphi_0 \tag{27}$$

A_d corresponds to the course angle of a vessel, γ represents the latitude of an earth station. χ represents the margin for the longitude of an earth station and that of a synchronous satellite.

For example, the position of a vessel is 95.3°E, 27.5°S. The synchronous satellite locates in 64°E. The parameters are as follows:

T=12s, A=±5, V_c =9m/s, $\Delta\tau$ =0.27s, $\omega = \pi/6$.

We can calculate results as follows by these parameters:

$$\alpha = 236.89°$$

$$\beta = 39.71°$$

$$r = 37816117m$$

Therefore, the formulaes can be described as follows:

$$\Delta r = -2.43\cos\beta\cos(A_d - \alpha) + 9.55\sin\beta[\cos(\phi_0 + 8.1) - \cos\phi_0] \tag{28}$$

$$r\Delta\theta = -2.43\sin\beta\cos(A_d - \alpha) - 9.55\cos\beta[\cos(\phi_0 + 8.1) - \cos\phi_0] \tag{29}$$

$$r\sin\theta\Delta\varphi = 2.43\sin(A_d - \alpha) \tag{30}$$

We can calculate the change of the transmission path in a measure period through the formula (13) by the formulae (10), (11), (12). The simulation results are as show in Fig 2(a)~(d).

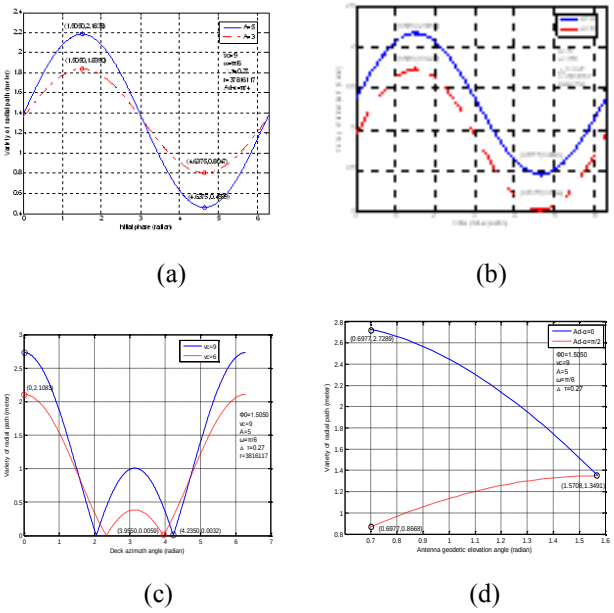

(a) (b) (c) (d)

Fig 2. Simulation results on variety of radial path: (a) different swing, (b) different speed, (c) different azimuth angle, (d) different antenna geodetic elevation angle

IV. METHOD ANALYSIS

We can draw conclusions from what we analyze above that main factors influencing the precision of two-way time transfer in a dynamic condition include vessel speed, sailing course, antenna elevation angle, measure period, amplitude and phase of rising and falling for a vessel, initial phase of measure, etc.

The impact of sailing circumstance can be reflected by A and T, the bigger A and the smaller T, the worse the circumstance. ϕ_0 embodies varieties of different measure points. V_c corresponds to a sailing speed. $A_d - \alpha$ expresses the influence of a change of a deck azimuth angle. From Fig 2. we can come to conclusions as follows:

(1) For a low speed object, factors of affecting measure precision comprise of a vessel horizontal movement and a variety of rise-fall of a vessel. On condition that A=±5, V_c =9m/s, $\varphi_0 = \pi/4$, the maximal error arrives at 7.28ns, the minimal 1.53ns; on condition that A=±3, the maximal error

arrives at 6.13ns,the minimal 2.68ns; on condition that $A=\pm 5$, V_c =6m/s, $\varphi_0 = \pi/4$, the maximal 5.81ns, the minimal 0.064ns.

(2)When a vessel sails along the direction of a geodetic azimuth angle of an earth station, the error is maximal. On condition that $A=\pm 5$, V_c =9m/s, $\varphi_0 = 0$, $\phi_0 = \pi/4$, the maximal error arrives at 9.10ns; On condition that V_c =6m/s, the maximal 7.28ns.

(3)On condition that $A= \pm 5$, V_c=9m/s, $\varphi_0 = 0$, $\phi_0 = \pi/4$, the error, brought about by a horizontal movement of a vessel which sails towards the satellite that locates in 64°E, falls gradually. The maximal 9.10ns, the minimal 4.50ns; On condition that $\phi_0 = \pi/2$, the error brought about completely by rising and falling of a vessel is increasing bit by bit, the maximal 4.5ns, the minimal 2.89ns.

Therefore, we can reach conclusions based on the thesis discussing above:

(1) The main error of two-way time transfer for a low speed object comes from a horizontal movement and rise-fall of a vessel , which is related nearly to sailing circumstance, speed, direction of sailing, a geodetic azimuth angle, a geodetic elevation angle, etc.

(2) When a vessel approaches a satellite, the error which is induced by a horizontal movement gets declining, meanwhile, and becomes increasing owing to rising and falling. If the deck azimuth angle of an earth station φ_0 is equivalent to 90° , the change of a transfer path brought about by horizontal motion is null.

(3) For the change of a transfer path brought about by rise-fall of a vessel， the precision of two-way time transfer is related to an initial phase of a sine wave. The error is pretty great through a single measure, as it is showed in Fig 2(a), the maximal error arrives at 7.28ns. An effective way to decline the error is to deal with the error data by mathematic method.

(4) The analysis above is based on the thesis that the rise-fall character corresponds to a sine wave. In practice, the situation is rather complicated. Amplitude A and initial phase φ_0 are the function of time. If we can acquire real data of rise-fall samplings, we can apply the data to the error model and obtain a high timing precision.

V. CONCLUSIONS

Two-way time transfer is the highest precision method to achieve an exact time standard. For a low speed object, movement makes a strong impact on precision, especially when we need win precision within 10ns. However, from the paper above, we can see that if we can design a reasonable working circumstance, and adopt an effective method to deal with the data, we are hopeful to arrive at our aim.

ACKNOWLEDGMENT

In this paper, engineer Jianjun Cai from China Satellite Maritime Tracking and Control Department gives many constructive suggestions. His openness is gratefully acknowledged.

REFERENCES

[1] Li Liu, and Chunhao Han (2004). "Two way satellite time transfer and its error analysis (in Chinese)". *Progress in Astronomy,* Vol. 22, No. 3, pp. 219-226.

[2] Hongwei Sun, Zhigang Li, Huanxin Li, and Shuangyou Liang (2001). "Error estimation in two-way satellite time transfer (in Chinese)". *Journal of astronautic metrology and measurement*, Vol. 21, No. 2, pp. 55-58.

[3] F.G. Ascarrunz, S.R. Jefferts, and Thomas E.Parker (1996). "Earth station errors in two-way time transfer", *IEEE International Frequency Control Symposium,* Vol. 2762, pp. 1169-1172.

[4] Yulan Huang. *Technology of Electromagnetic field and Microwave (in Chinese),* People Post and Telegraph Publisher, Beijing China, 2007, pp.264.

[5] Minyi Shen, and Zhenyuan Cai. *Antenna for Satellite Communication (in Chinese),* People Post and Telegraph Publisher, Beijing China, 1993, pp.276.

[6] Xudong Liu. *Technology of Satellite Communication (in Chinese),* National Defence Industry Publisher, Beijing China, 2002, pp.1-36.

Experiment Research of Europe-Asia TWSTFT Link

Zhiqiang Yang, Aimin Zhang, Yuan Gao, Kun Liang,
Xiaoxun Gao
National Institute of Metrology
Beijing, China
Email:yangzq@nim.ac.cn

Abstract—TWSTFT is one of the most precise technique of time and frequency transfer, NIM established TWSTFT system in the year 2008 and participated the Europe-Asia TWSTFT link. We analyze the TWSTFT comparative results of NIM and PTB, TL, NICT. It is shown that Europe-Asia TWSTFT link is stable. The frequency stability(1day) is better than 5×10^{-15}. The comparative result of TWSTFT system coincides with GPS system.

I. INTRODUCTION

Two-way satellite time and frequency transfer (TWSTFT) is one of the most precise technique of time and frequency transfer[1,2], it has been developed into a widely used technique of time and frequency transfer between laboratories that contribute, with their atomic clocks and, in some cases, with their primary frequency standards, to the realization of International Atomic Time[3]. At present, TWSTFT is performed operationally in at least two laboratories in the United States, twelve in Europe, and seven in the Asia Pacific region. The cooperation is organized by the CCTF Working Group on TWSTFT.

The NIM01 TWSTFT earth station was established in year 2008. National Institute of Metrology (NIM) and Physikalisch-Technische Bundesanstalt (PTB) have signed the cooperation agreement of TWSTFT in year 2009. After May of year 2009, NIM participated the Europe-Asia TWSTFT link which is organized by National Institute of Information and Communications Technology(NICT), the geostationary satellite is IS-4, and the participant laboratory include PTB, NICT, NMIJ, KRISS, NIM, NTSC, TL, OP. But the IS-4 satellite has equipment failure which is irreparable in 2010 February. In order to continue the Europe-Asia TWSTFT link, the satellite was changed to AM2 which belongs to RUSSIA Intersputnik. After the communication experiment in 2010 August, NIM restarts the TWSTFT work. At present, the participant laboratories of Europe-Asia TWSTFT link include PTB, TL, NICT, NIM, NTSC, SU and NPLI. The results of laboratories should be processed to a specified format which follows the agreement of ITU-R SG4 [4,5,6], and be reported to BIPM.

In this paper, we will introduce the establishment and operation of NIM TWSTFT system, and analyze the recent experimental result; it is shown that the NIM TWSTFT system operates stably, the frequency stability (1 day) reach to 10^{-15} level.

II. THE OPERATION OF NIM TWSTFT SYSTEM

TWSTFT is based on the exchange of timing signals through geostationary telecommunication satellites. It involves the transmission and reception of radio frequency (RF) signals carrying binary phase-shift keying (BPSK) modulations containing pseudorandom noise (PRN) codes. Modems generate the modulation at the intermediate frequency (IF) level which are then transmitted after up-conversion to the RF band (Ku-band or X-band are currently used). The received RF-signal is down-converted and the modem detects the modulation at the IF level. The phase modulation is synchronized with the local clock, and the modem generates a one-pulse-per-second (1PPS) output, synchronous with the BPSK sequence and named 1PPSTX. This signal represents the realization of a time scale. Each station uses a dedicated PRN code for the BPSK sequence in its transmitted signal. The receiving equipment generates the BPSK sequence of the remote station and reconstitutes a 1PPS tick from the received signal, named 1PPSRX. The difference between PPSTX and PPSRX (in general plus a constant) is measured by a time-interval counter (TIC). Following a pre-arranged schedule, a pair of stations lock on the code of the corresponding remote station for a specified period, called a session, measure the signal's time of arrival, and store the results. After exchanging the data records the difference between the two clocks can be computed.

The difference of the time scale between the laboratories is determined as follows:

$$\begin{aligned} TS(1)-TS(2) = &+0.5[TI(1)] \\ &-0.5[TI(2)] \\ &+0.5[SPT(1)-SPT(2)] \\ &-0.5[SCD(1)-SCU(1)] \\ &+0.5[SCD(2)-SCU(2)] \\ &+0.5[SPU(1)-SPD(1)] \\ &-0.5[SPU(2)-SPD(2)] \\ &+0.5[TX(1)-RX(1)] \\ &-0.5[TX(2)-RX(2)] \end{aligned} \tag{1}$$

Where,

TS(i) is Local time scale

TI(i) is Time interval reading

SPT(i) is Satellite path delay through the transponder

SCD(i) is Sagnac delay for a signal propagating from the GEO satellite to station i

SCU(i) is Sagnac delay for a signal propagating from station i to the GEO satellite

SPD(i) is Signal path downlink delay

SPU(i) is Signal path uplink delay

TX(i) is Signal delay in the transmit path of the TWSTFT station i

RX(i) is Signal delay in the receive path of TWSTFT station i

NIM earth station uses the SATRE modem which is made by Timetech Company; it has 1 transmission channel and 2 receiver channel. The diameter of antenna is 1.8 meter. The power of signal transceiver is 8W.

There are many parameters that influence the stability of two-way time transfer system must be considered, such as transmission frequency, power level, carrier-to-noise density, and so on. For Europe-Asia TWSTFT link, NIM earth station need to arrange the transmission power close to PTB station, so that we can get a better RMS for data. The BPSK code rate of Europe-Asia TWSTFT link is 2.5Mch/s, the carrier-to-noise density reach to 55dBHz, 1pps jitter is lower than 500ps. Figure 1 shows the relationship between the carrier-to-noise density and 1pps jitter of SATRE modem.

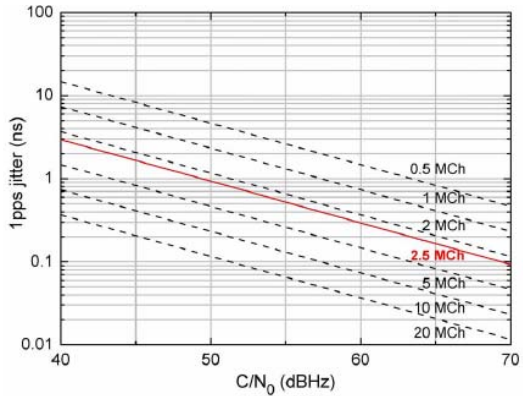

Figure 1. the relationship between the carrier-to-noise density and 1pps jitter of SATRE modem

At present, according to the pre-determined schedule, the laboratories of Europe-Asia TWSTFT link communicate once per-hour, and work 10 hours everyday. When the communicate work finish, we will process the raw data, recorded by modem, to a quadratic fit results and report to BIPM. The purpose of this format is to reduce the amount of data to be exchanged and to be able to report in one data file session results of one laboratory involving different partner stations and different satellite links. Data from more than one day may be reported in a single file. Such files allow clock differences to be calculated in an easy way.

III. EXPERIMENTAL RESULTS

The frequency reference of the NIM earth station is a controlled hydrogen atomic clock. According to the schedule, the Europe-Asia TWSTFT link works from 12:30 to 22:59(UTC time) everyday. At first, from 12:30 to 12:40, the clean carrier will be transmitted, and after that, the time modulation signal will be transmitted. Every laboratory will communicate with each other once per-hour, the length of the period is 5 minute.

UTC(NIM1) running for test is the local reference of the NIM TWSTFT system which locates at the new campus where we will move to in Changping Dist., Beijing. UTC(NIM) reported to BIMP now is still running in old campus. Figure2 to Figure4 is the TWSTFT experimental results and frequency stability of NIM and PTB, NIM and TL, NIM and NICT, respectively. The experiment date is from MJD55740 to MJD56000. It is shown that Europe-Asia TWSTFT link is stable.

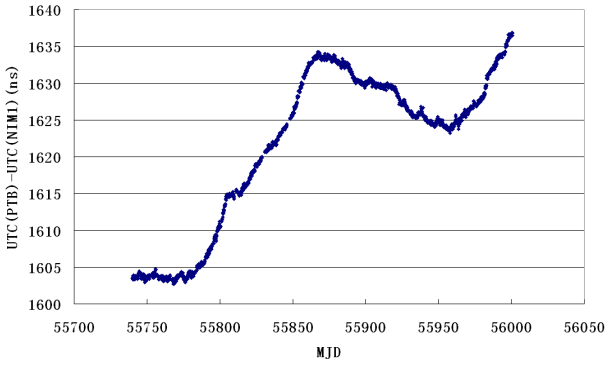

(a) Time difference

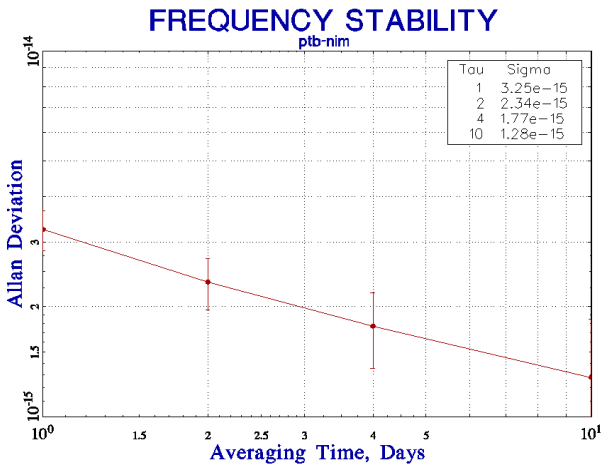

(b) ADEV

Figure 2. Time difference and ADEV of NIM and PTB by TWSTFT

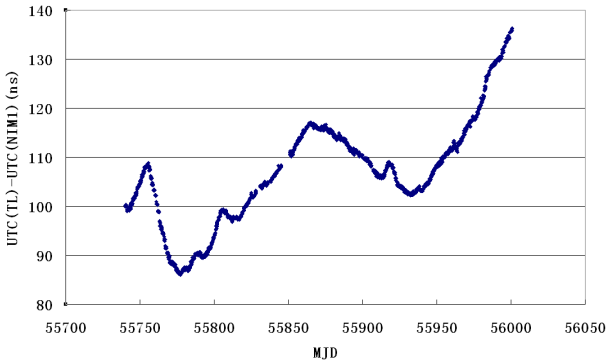

(a) Time difference

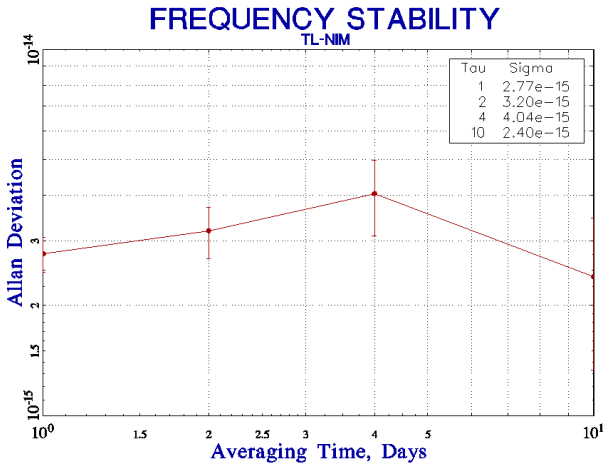

(b) ADEV

Figure 3. Time difference and ADEV of NIM and TL by TWSTFT

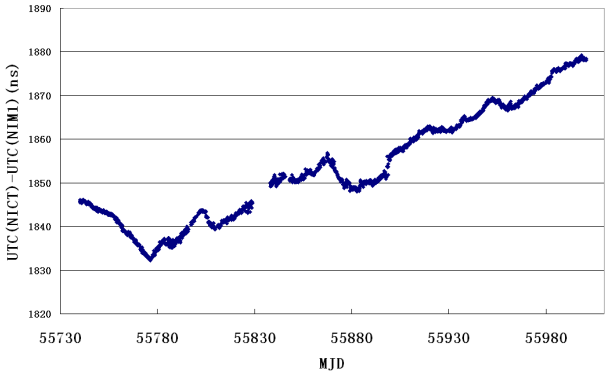

(a) Time difference

Table Ⅰ summarizes the frequency stability of NIM and PTB, NIM and TL, NIM and NICT; it is shown that the one day frequency stability is better than 5×10^{-15}.

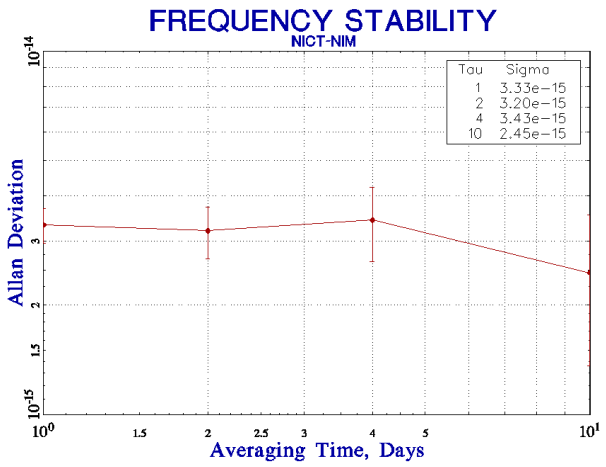

(b) ADEV

Figure 4. Time difference and ADEV of NIM and NICT by TWSTFT

TABLE I. FREQUENCY STABILITY OF EUROPE-ASIA TWSTFT LINK

	days			
link	1	2	4	10
PTB-NIM	3.25E-15	2.34E-15	1.77E-15	1.28E-15
TL-NIM	2.77E-15	3.20E-15	4.04E-15	2.40E-15
NICT-NIM	3.33E-15	3.20E-15	3.43E-15	2.45E-15

Figure5 is TWSTFT and GPS time transfer experimental result of PTB and NIM, include GPS P3, GPS PPP and TWSTFT techniques. It is shown that the three time transfer techniques results are consistent.

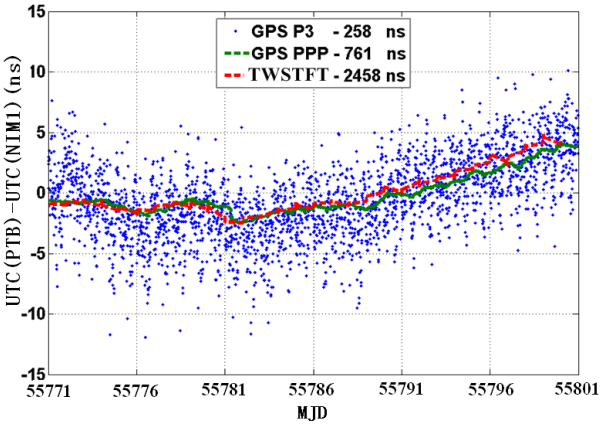

Figure 5. TWSTFT and GPS experimental result of PTB and NIM

IV. CONCLUSIONS

The NIM01 TWSTFT earth station was established in year 2008, and participate the Europe-Asia TWSTFT link which is organized by National Institute of Information and Communications Technology (NICT). We introduced the establishment and operation of NIM TWSTFT system, and analyze the recent experimental result; it is shown that the NIM TWSTFT system operates stably, the frequency stability

(1 day) reach to 10-15 level. The comparative result of TWSTFT system coincides with GPS system.

REFERENCES

[1] Kirchner D 1991 Two-Way Time Transfer Via Communication Satellites Proc. of the IEEE 79 983-989

[2] D. W. Hanson, Fundamentals of Two-Way Time Transfer by Satellite, 43rd Annual Frequency Control Symposium, pp. 174-178, 1989

[3] Guinot B and Arias E F 2005 Atomic time-keeping from 1955 to the present Metrologia 42 S20-S30

[4] ITU Radiocommunication Sector 2003 The operational use of two-way satellite time and frequency transfer employing PN codes Recommendation ITU-R TF.1153-2 (Geneva, Switzerland)

[5] ITU Radiocommunication Sector 2002 ITU Handbook on Satellite Communications (3rd edition, Geneva, 2002) Section 2.3, Chapter 2 and Section AN2.1, Annex 2

[6] ITU Radiocommunication Sector, Recommendations ITU-R 524, ITU-R S.580, ITU-R S.725, ITU-R S.726, ITU-R S.728, and ITU-R S.729

Short-term stability of GNSS on-board clocks using the polynomial method

Jérôme Delporte, Cyrille Boulanger, Flavien Mercier
CNES – French Space Agency
Toulouse, France
jerome.delporte@cnes.fr

***Abstract*— The stability of on-board clocks is an essential issue in the performance of Global Navigation Satellite Systems (GNSS). We developed a straightforward method (the polynomial method) that allows to determine the short term stability of a GNSS on-board clock for a pass over a ground station driven by a clock, the characteristics of which are better than the space clock we want to characterize. In previous papers [1,2], we validated the method on GPS on-board clocks using IGS clock products as reference. In this paper, we continue this work with GLONASS, Galileo, COMPASS/Beidou and QZSS on-board clocks.**

I. INTRODUCTION

The stability of on-board clocks is an essential issue in the performance of Global Navigation Satellite Systems (GNSS). For relatively short integration times (about 100 s), it impacts the required sampling or update interval for clocks solutions in floating Precise Point Positioning (PPP) ; while, at longer integration times (about 1 day), it impacts the update rate of clock coefficients performed by the GNSS ground control segment. The estimation of GNSS on-board clocks behaviour is generally a complex task requiring a large ground infrastructure (a global network of ground stations) and an intense computation (the so-called ODTS, Orbit Determination and Time Synchronization).

We proposed [1,2] two alternative methods that allow to estimate the short term stability of GNSS on-board clocks with respect to a given ground station on a pass. The first method, which simply consists in applying a high-order polynomial fitting to the observation data, is particularly straightforward. It has the definitive advantage to require only a GNSS receiver connected to a ground clock, the performances of which are better than the space clock.

Here, we extend the analysis previously performed on GPS to GLONASS, Galileo, COMPASS/Beidou and QZSS on-board clocks. The aim is to provide a generic comparison of the short-term stability of all GNSS on-board clocks.

It shall be added that the timing signal observed through the Signal in Space (SIS) may not be fully representative of the GNSS on-board clock itself since some degradations might be present (e.g. temperature sensitivity of the GNSS payload). Therefore the on-board clock as observed through the SIS is often referred to as apparent clock.

II. THE POLYNOMIAL METHOD

Basically the GNSS measurements represent the clock difference between the transmitter and the receiver. The idea is to exploit that feature in a very simple way. The raw phase measurements and their iono-free combination for a given satellite pass over a ground station are merely adjusted by a polynomial of high order (typically 24). Thus we keep the high-frequency part of the measurement that is expected to be representative of the clock difference. We then compute the Allan deviation excluding end segments that are generally noisier.

We proved [1,2] by comparison with IGS clock products [3] for GPS on-board clocks that this method provides a correct estimation of the short term stability of the on-board clock up to about 1000 seconds. Of course, this upper limit may vary according to the pass duration and to the on-board clock performance. We also showed [1,2] that the raw phase observables are better suited to estimate very short term stabilities (up to about 100 s) but might be affected by ionosphere effects. Therefore for integration times between 100 and 1000 s, it is better to use the iono-free combination.

III. RESULTS FOR GLONASS CLOCKS

GLONASS on-board clocks are Caesium beam clocks with magnetic deflection. We can compare our results to IGS clock products for validation purposes. For instance, the ESA Analysis Center produces GLONASS clock products with a sampling rate of 30 s [3].

Fig. 1 is a typical example of a short term stability of a GLONASS on-board clock computed with the polynomial method (in black for L1C, in blue for L2C and in red for the L1C/L2C iono-free combination) for a PRN2 satellite pass compared to the ESA clock product computed on the very same period (light blue). The station used is at CNES : the receiver is a Septentrio PolaRx4 driven by an active Hydrogen Maser.

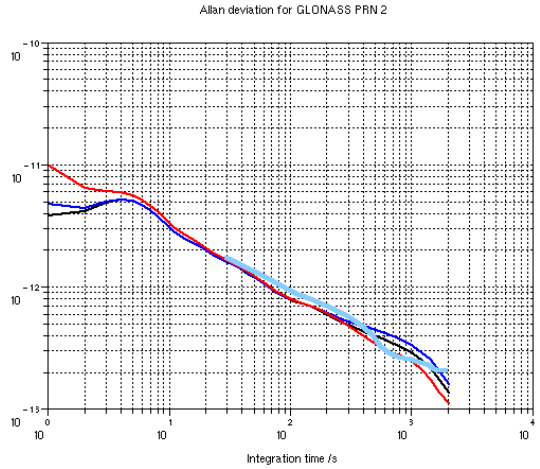

Figure 1. Short term stability of GLONASS PRN 2 on-board clock using the polynomial method on L1C (black), L2C (blue), L1C/L2C iono-free combination (red) and compared to ESA clock product (light blue)

We observe an excellent agreement between the polynomial method results and the IGS clock product between 30 and at least 1000 seconds.

Fig. 2 shows the short term stability of all GLONASS on-board clocks computed with the polynomial method on the L1C/L2C iono-free combination. Most recent launches are in black (PRN 3, 4, 7 and 17), they exhibit the best performances in the constellation.

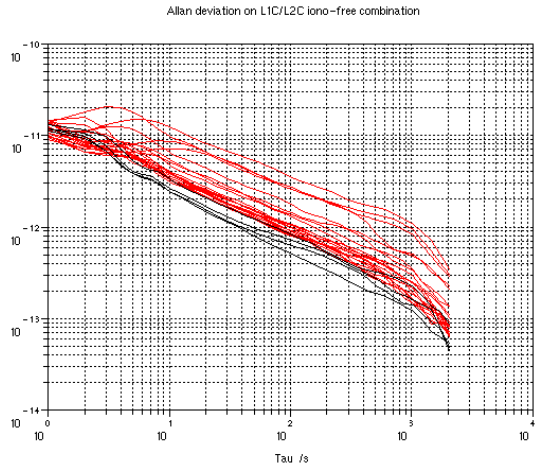

Figure 2. Short term stability of all GLONASS on-board clocks using the polynomial method on the L1C/L2C iono-free combination

We can deduce from Fig. 2 that GLONASS on-board clocks have a frequency stability between 5 and $50.10^{-12}.\tau^{-1/2}$.

Of course more interesting cases are GNSS for which no clock products are publicly available. This is the case of Galileo, COMPASS/Beidou and QZSS, which are discussed herefafter.

IV. RESULTS FOR GALILEO CLOCKS

At the time of writing, the GALILEO constellation is composed of 2 experimental satellites (GIOVE-A and B) and the first 2 operational satellites (IOV-1 and 2). GIOVE-A embarks only 2 RAFS (Rubidium Atomic Frequency Standard), while GIOVE-B embarks 2 RAFS and 1 PHM (Passive Hydrogen Maser). Each of the 2 IOV satellites embark 2 RAFS and 2 PHM.

Measurements were collected at CNES Toulouse in February and March 2012 using a Septentrio PolaRx4 receiver driven by an active Hydrogen Maser. Results are presented in Fig. 3 to 6. For GIOVE-B and both IOV satellites, the type of clock (RAFS or PHM) that drives the payload at a given period is a priori unknown. However our analysis allows to indicate presumably the type of clock that drives the payload.

A. *GIOVE-A RAFS*

Fig. 3 presents the short term stability of the GIOVE-A apparent clock obtained with the polynomial method for a GIOVE-A pass.

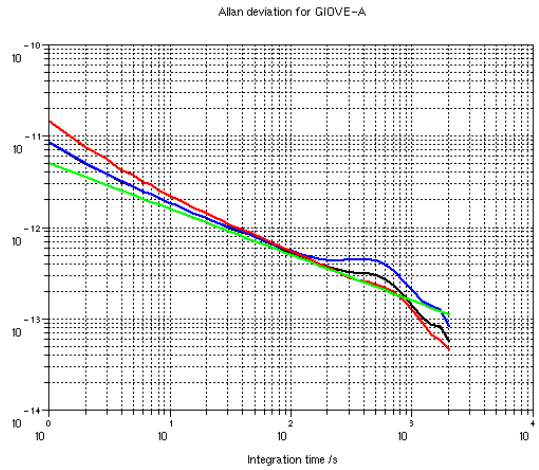

Figure 3. Short term stability of GIOVE-A on-board clock using the polynomial method on L1C (black), L5Q (blue) and L1C/L5Q iono-free combination (red). A WFM of 5e-12/sqrt(tau) has been added in green.

Fig. 3 shows that the GIOVE-A RAFS that drove the payload at that time has an apparent stability of $5.10^{-12}.\tau^{-1/2}$, which is fully in line with the RAFS specifications [4]. As also mentioned in [1,2], the stability obtained with the polynomial method above 1000 seconds might be slightly too optimistic.

B. *GIOVE-B RAFS*

Fig. 4 presents the short term stability obtained with the polynomial method for the apparent clock of GIOVE-B.

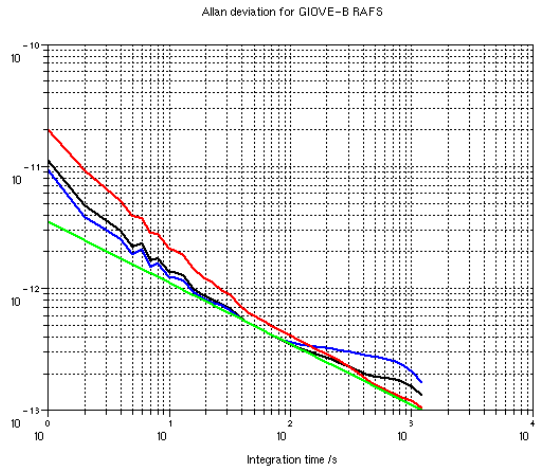

Figure 4. Short term stability of GIOVE-B on-board clock using the polynomial method on L1C (black), L5Q (blue) and L1C/L5Q iono-free combination (red). A WFM of 3.5e-12/sqrt(tau) has been added in green.

Fig. 4 shows that the GIOVE-B on-board clock that drove the payload at that time was presumably a RAFS with an apparent stability of $3{,}5.10^{-12}.\tau^{-1/2}$.

C. IOV-1 and IOV-2 RAFS

Fig. 5 presents the short term stability obtained with the polynomial method on the IOV-1 and IOV-2 measurements on a period, the results of which lead us to think that both payloads were driven by a RAFS.

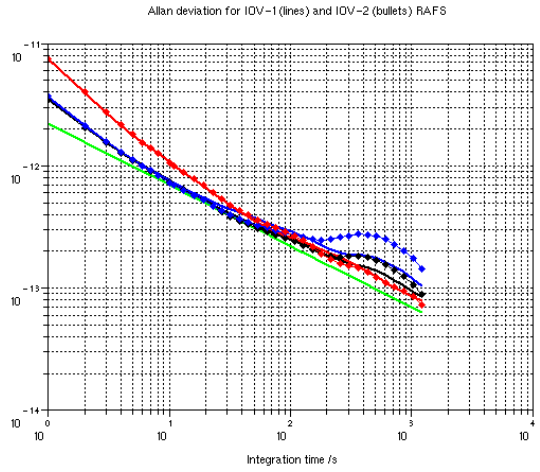

Figure 5. Short term stability of GALILEO IOV-1 (solid lines) and 2 (lines with bullets) on-board clock using the polynomial method on L1C (black), L5Q (blue) and L1C/L5Q iono-free combination (red). A WFM of 2,2e-12/sqrt(tau) has been added in green.

Fig. 5 shows that the apparent stability of both IOV RAFS is in the range of $2{,}2.10^{-12}.\tau^{-1/2}$.

D. IOV-1 and IOV-2 PHM

Fig. 6 presents the short term stability obtained with the polynomial method on the IOV-1 and IOV-2 measurements on a period, the results of which lead us to think that both payloads were driven by a PHM.

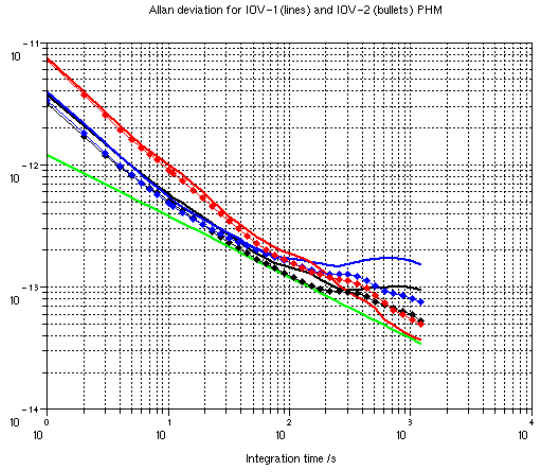

Figure 6. Short term stability of GALILEO IOV-1 (solid lines) and 2 (lines with bullets) on-board clock using the polynomial method on L1C (black), L5Q (blue) and L1C/L5Q iono-free combination (red). A WFM of 1,3e-12/sqrt(tau) has been added in green.

Fig. 6 shows that the apparent stability of both IOV PHM is in the range of $1{,}3.10^{-12}.\tau^{-1/2}$. This result is rather consistent with GIOVE-B PHM performance estimation [4,5].

V. RESULTS FOR BEIDOU/COMPASS CLOCKS

Beidou/Compass is China's satellite positioning system. Upon completion foreseen in 2020, it shall be composed of 5 geostationary (GEO) satellites, 5 inclined geosynchronous orbit (IGSO) satellites and 27 Medium Earth orbit (MEO) satellites. A first step of this programme is to provide operational signals over the Asia-Pacific region. China released a "test version" Interface Control Document (ICD) for Compass (Beidou-2) in December 2011 [6]. This ICD covers the open B1 civil signal centered at 1561.098 MHz but is not complete.

At the time of writing, Compass has 11 Beidou-2 satellites operating in its constellation, 5 of them are in GEO, 5 in IGSO and 1 in MEO. The MEO satellite, called Compass M-1, is an experimental satellite and has been launched in April 2007 and embarks Rubidium-cell clocks [7]. Some of the Beidou on-board clocks were Rb-cell clocks purchased from SpectraTime in Switzerland. However the delivery of these SpectraTime atomic clocks started mid 2007. Therefore, the COMPASS M-1 on-board clock(s) has(have) probably been produced in China.

In [9], the Compass M-1 orbit is computed using laser ranging measurements and then the on-board clock is computed using two ground stations equipped with multi-GNSS receivers.

Compass measurements were collected in mid November 2011 using a Septentrio PolaRx4 receiver that allowed to collect C2I and L2I (E2 data), C7I and L7I (E5b data). Doppler spikes are observed, similarly as in [8,9]. It shall be noted that ionosphere and widelane are correct, which means that code and phase observables are consistent with one another. The observed phase jumps are not integral number of

cycles. Fig. 7 shows the clock as a function of time for a part of the pass over our receiver.

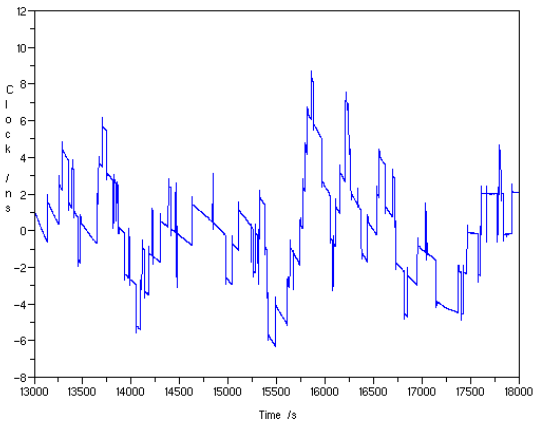

Figure 7. COMPASS M-1on-board clock using the polynomial method on L2I

If we consider a segment of regular data (i.e. without any phase jumps), we get the stability displayed on Fig. 8.

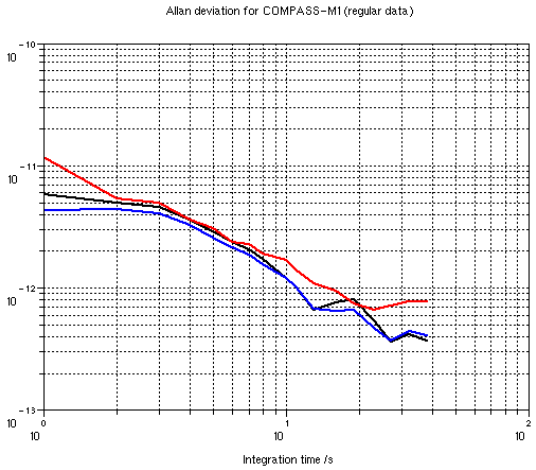

Figure 8. Short term stability of COMPASS M-1 on-board clock using the polynomial method on L2I (black), L7I (blue) and L2I/L7I iono-free combination (red)

VI. RESULTS FOR QZSS CLOCKS

QZSS (Quasi-Zenith Satellite System) is a regional Satellite Based Augmentation System for GPS that will cover the Asia-Pacific region. The total number of satellites is 4 to 7 including quasi-zenith orbit and GEO satellites [10]. The first satellite called QZS-1 or Michibiki was launched in September 2010. Full operational status is expected by 2013.

The pattern of the QZSS observables is very different from the usual observables of MEO satellite due to the quasi-zenith orbit. Fig. 9 shows a typical pass of Michibiki (observable L1X). We applied here the polynomial method using an odd order.

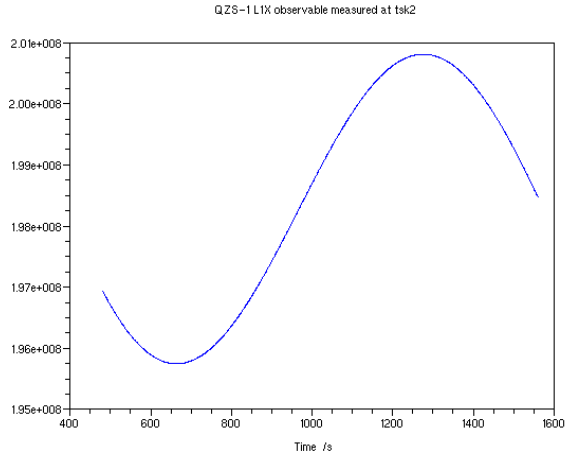

Figure 9. Michibiki L1X observable (pass over TSK2)

Measurements were collected on the IGS ftp site, within the Multi GNSS Experiment (MGEX). We used the IGS station TSK2 (Tsukuba) that is unfortunately driven by a Caesium clock. If we apply the polynomial method to the QZS-1 measurements, we would observe the short term stability of the ground Cs clock. Therefore we carried out a frequency transfer between TSK2 and IGS station USUD (Usuda Deep Space Tracking Station) located close to TSK2 and driven by a H Maser. We performed a PPP computation on each station and then we differentiated the PPP clock solutions. This time offset was then subtracted to the polynomial result on TSK2 measurements.

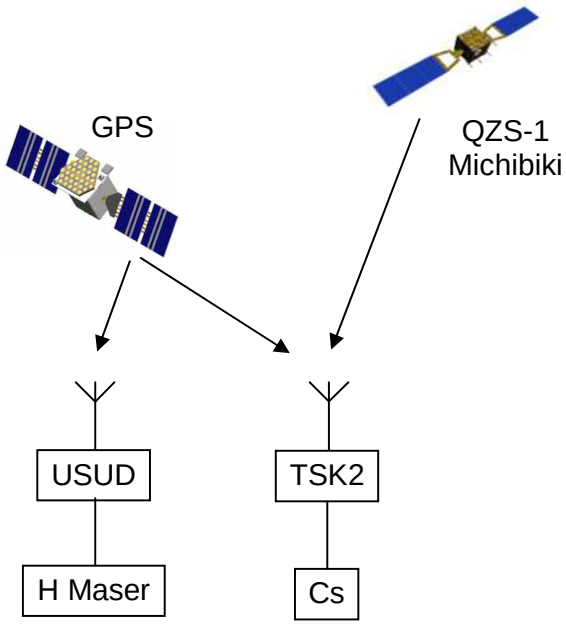

Figure 10. Estimation of QZS-1 on-board clock stability using a GPS time transfer between TSK2 and USUD

Fig. 11 displays the short term stability obtained, this result is rather consistent with [11] that was obtained with a complete orbitography and synchronization of QZS-1.

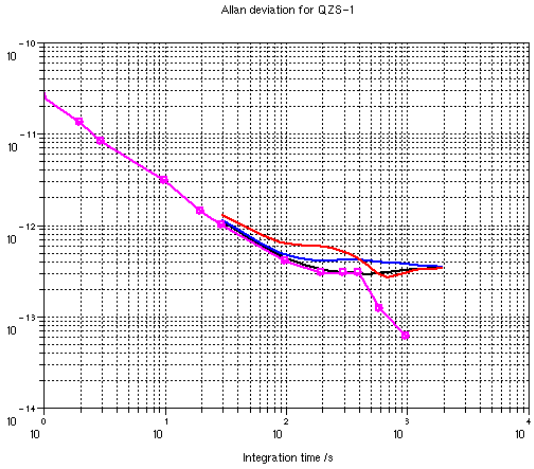

Figure 11. Short term stability of QZS-1 on-board clock using the polynomial method on L1C (black), L2X (blue) and L1C/L2X iono-free combination (red), after GPS PPP with IGS station USUD. The stability obtained in [11] has been added in magenta.

CONCLUSIONS

The method used here allows to determine the short term stability of GNSS on-board clocks without any other information than RINEX observation data. This allows to easily compare the short-term stability of various recent GNSS on-board clocks. Table 1 summarizes the stability at 100 seconds of all the GNSS on-board clocks using [1-2] for GPS and the present results for the others. Compass M1 results have been discarded because no segment of regular data allowed to compute an Allan deviation up to 100 seconds.

TABLE I. OVERVIEW OF GNSS ON-BOARD CLOCKS SHORT-TERM STABILITY

Constellation	Type of clock	Allan deviation at 100 s
GPS IIF	Rb-cell	$1\text{-}2.10^{-13}$
GLONASS	Cs beam	5 to 50.10^{-13}
GALILEO	Rb-cell	$2\text{-}3.10^{-13}$
	PHM	$1\text{-}2.10^{-13}$
QZS-1	Rb-cell	$4\text{-}5.10^{-13}$

REFERENCES

[1] J. Delporte, C. Boulanger, F. Mercier, “Straightforward estimations of GNSS on-board clocks”, Proc. of EFTF 2011.

[2] J. Delporte, C. Boulanger, F. Mercier, “Simple methods for the estimation of the short term stability of GNSS on-board clocks”, Proc. of PTTI 2010.

[3] J.M. Dow, R.E. Neilan, C. Rizos, “The International GNSS Service in a changing landscape of Global Navigation Satellite Systems”, Journal of Geodesy (2009) 83:191–198, DOI: 10.1007/s00190-008-0300-3.

[4] P. Waller et al., “In-orbit Performance Assessment of GIOVE clocks”, Proc. of PTTI 2008.

[5] O. Montenbruck et al., “Flight Characterization of New Generation GNSS Satellite Clocks”, Proc. of ION GNSS 2011.

[6] China Satellite Navigation Office, “BeiDou Navigation Satellite System - Signal In Space Interface Control Document (Test Version)” December 2011, available on http://www.beidou.gov.cn.

[7] L. Mallette, J. White, P. Rochat, “Space Qualified Frequency Sources (Clocks) for Current and Future GNSS Applications”, Proc. of IEEE/ION PLANS conference 2010.

[8] Inside GNSS News, “Septentrio Reports Frequency Spikes in Compass M1 Satellite Signals”, April 25, 2010.

[9] A. Hauschild, O. Montenbruck, J-M Sleewaegen, L. Huisman. P. J. G. Teunissen, “Characterization of Compass M-1 signals”, GPS Solut., DOI 10.1007/s10291-011-0210-3, February 2011.

[10] S. Fujirawa, “QZSS and MSAS”, Presentation at ICG-6, Sept. 2011, available on http://www.unoosa.org/oosa/SAP/gnss/icg/meetings.html.

[11] P. Steigenberger, C. Rodriguez-Solano, U. Hugentobler, A. Hauschild, O. Montenbruck, “Orbit and clock determination of QZS-1 based on the CONGO network”, Proc. of Ion International Technical Meeting, 2012.

Research on the Uncertainty Evaluation of Network Time Service System

Kejia Zhao/ Aimin Zhang/ Kun Liang
Time and Frequency Metrology Center
National Institute of Metrology
Beijing, P.R. China
zhaokj@nim.ac.cn

***Abstract*—Network time service system is constructed in NIM based on network time protocol (NTP). The synchronization software programm based on NTP is run at the client side. The mathematical uncertainty model of time offset is established. The uncertainty is analyzed and evaluated. The uncertainty of time server and client are evaluated particularly by the synchronizing experiments using a time and frequency solutions TimeAcc-007. The data processing algorithms are proposed for improving synchronization precision based on the result of uncertainty evaluation.**

I. INTRODUCTION

The network time synchronization based on network time protocol (NTP) is applied extensively. But the uncertainty of network time service system is rarely researched in detail. If the uncertainty of time server and client can be analyzed and evaluated, it will be useful for researching the algorithms to improve synchronization precision.

Network time service system is constructed in NIM based on network time protocol (NTP). The 1PPS and 10MHz signals from UTC (NIM) serve as reference sources of time server. The synchronization software programm based on NTP is run at the client side. A time and frequency solutions TimeAcc-007 is used to measure the data of time offset during synchronizing experiments. The uncertainty of network time service system will be analyzed and evaluated by common reference source experiments.

II. THEORY OF TIME SYNCHRONIZATION

Figure 1 shows the theory of time synchronization about NTP [1] [2]. The client A sends the time stamp information package at T_1 to NTP server B to asks for time synchronizing service. B receives the package from A at T_2. Then B continues to send the package to A at T_3. Finally A receives the package at T_4. δ_1 is the network delay of sending package from A to B. δ_2 is the network delay of sending package from B to A. θ is the time offset between A and B.

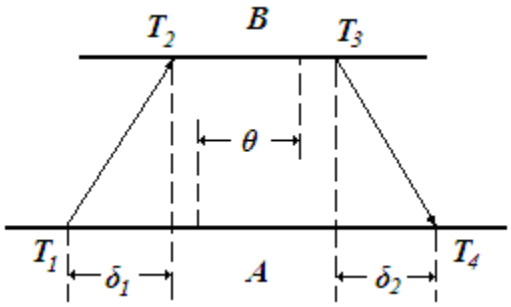

Figure 1. *Theory of time synchronization*

Suppose the total network delay is called δ, then

$$\begin{cases} T_2 = T_1 + \theta + \delta_1 \\ T_4 = T_3 - \theta + \delta_2 \\ \delta = \delta_1 + \delta_2 \end{cases} \tag{1}$$

Suppose the network delay between from A to B and from B to A are absolutely the same, $\delta_1=\delta_2$, then

$$\begin{cases} \theta = \dfrac{(T_2 - T_1) - (T_4 - T_3)}{2} \\ \delta = (T_4 - T_1) - (T_3 - T_2) \end{cases} \tag{2}$$

In general, the round-trip route is not symmetrical, the offset θ will be calculated by formula (1), instead of (2). So the single-trip route of network delay must be evaluated. Suppose the single network delay is called δ_S, the equality between δ_S and δ can be expressed

$$\delta_s = k\delta \qquad (0 < k < 1) \tag{3}$$

Therefore, if k can be controlled to close to 0.5 or δ_S can be measured accurately, the offset θ can be calculated accurately, the precision of time synchronization will be improved.

On Internet, the network condition is quite complex, the uncertainty of symmetry for round-trip route is large under

network jam condition [3]. To analyze and evaluate the uncertainty of NTP server and client accurately, the following synchronization experiments has been performed under LAN condition.

III. EXPERIMENTS OF TIME SYNCHRONIZATION

The NTP server in Network Time Service System of NIM is S250 made by Symmetricom, whose reference source is GPS signal in common reference source experiments. The client is a notebook PC, the type is Thinkpad X60 made by IBM. The operation system on client is windows XP. The software of time synchronization is NIMTime developed by NIM, which is programmed based on NTP version (3). A time and frequency solutions TimeAcc-007 which is calibrated by NPL is used to measure the data of time offset. The GPS signal serves as the reference source of TimeAcc-007. The equipments are connected directly by an Ethernet cable in synchronization experiments.

A. Experiment A: NTP Server and PC

NTP server and PC are connected by Ethernet cable as shown in Figure 2. The GPS signal serves as the reference source of NTP server. NIMTime is run on PC to calculate the time offset between server and client.

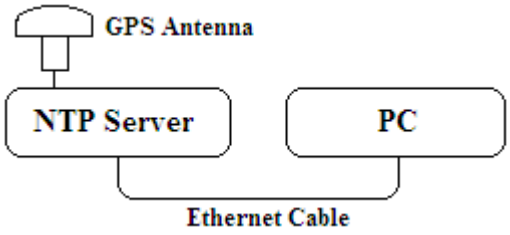

Figure 2. *Synchronizing between NTP server and PC*

B. Experiment B: PC and TimeAcc-007

PC and TimeAcc-007 are connected by Ethernet cable as shown in Figure 3. The GPS signal serves as the reference source of TimeAcc-007. NIMTime is run to set PC as NTP server. TimeAcc-007 serves as the client to measure the time offset between PC and TimeAcc-007.

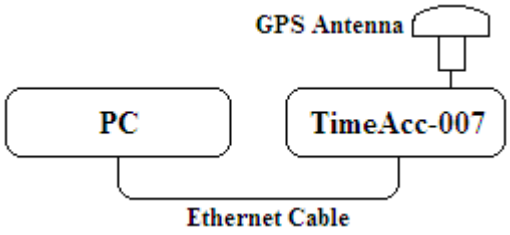

Figure 3. *Synchronizing between PC and TimeAcc-007*

C. Experiment C: NTP Server and TimeAcc-007

NTP server and TimeAcc-007 are connected by Ethernet cable as shown in Figure 4. The GPS signal serves as the reference source of NTP server and TimeAcc-007. TimeAcc-007 serves as the client to measure the time offset between NTP server and TimeAcc-007.

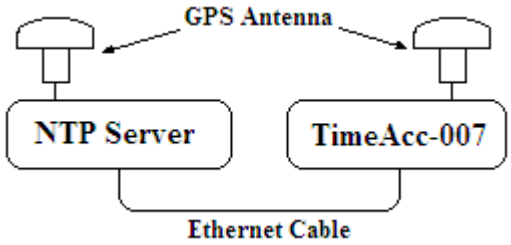

Figure 4. *Synchronizing between NTP server and TimeAcc-007*

IV. ANALYZING DATA OF TIME OFFSET

A. Time Offset of Client

The experiment A and B are performed in turn repeatedly 20 times. Figure 5 shows the data of time offset in TimeAcc-007 for one time. The blue curve shows the time offset between PC and TimeAcc-007, one offset datum is measured every second. The red line shows the mean of time offset between PC and TimeAcc-007 for 100 points. Because the precision of time stamp for NTP server and TimeAcc-007 are better than PC at least 10 times, NTP server and TimeAcc-007 use common reference source, and the network delay can be ignored, the mean value can be considered as the error of time offset imported by PC after PC is synchronized by NTP server.

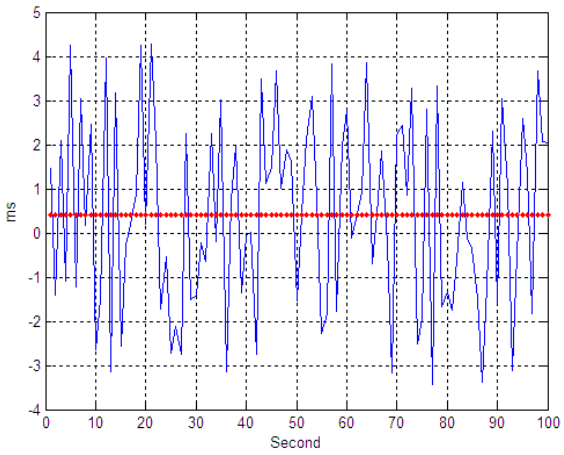

Figure 5. *Time offset of client*

B. Time Offset of NTP Server

Figure 6 shows the data of time offset in TimeAcc-007 for experiment C. The blue curve shows the time offset between NTP server and TimeAcc-007, one offset datum is measured every second. The red line shows the mean value of time offset between NTP server and TimeAcc-007 for 100 points. Because the precision of time stamp for TimeAcc-007 is better than NTP server at least 10 times, NTP server and TimeAcc-007 use common reference source, and the network delay can be ignored, the mean value can be considered as the error of time offset imported by the hardware time stamp of NTP server.

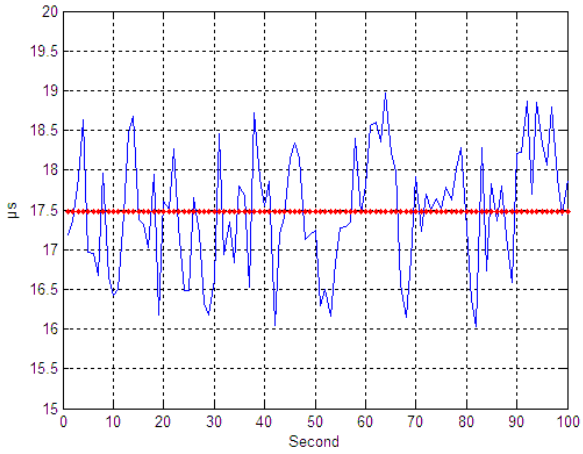

Figure 6. *Time offset of NTP server*

V. EVALUATING UNCERTAINTY

A. Mathematical Model

By analyzing procedures and results of above experiments, we can get the conclusion that the uncertainty components include the repeatability of measurements results, the reference source of NTP server, the time offset error of NTP server, the time offset error of client and the round-trip delay of network. The mathematical uncertainty model of time offset can be established as shown in formula (4), in which t is the offset between client time and

$$t = t_0 + \delta t_{ref} + \delta t_{server} + \delta t_{client} + \delta t_{net} \quad (4)$$

standard time after synchronizing, t_0 is the mean error which is calculated with a group of time offset error imported by PC in the experiment B, δt_{ref} is the error imported by reference source, δt_{server} is the error imported by hardware time stamp of NTP server, δt_{client} is the error imported by software time stamp of client, δt_{net} is the error imported by network delay.

B. Uncertainty Components

1) Repeatability of Measurements Results: The mean error t_0 can be calculated by averaging 20 errors of time offset imported by PC, equals to 0.4ms. The standard deviation of 20 errors of time offset imported by PC is calculated, equals to 1.2ms. Therefore, the standard uncertainty of repeatability of measurements results u_{t0} is 1.2ms.

2) Reference Source of NTP Server: GPS signal serves as the reference source. Its time uncertainty is in ns magnitude. Therefore, the standard uncertainty of reference source u_{ref} can be ignored.

3) Time Offset Error of NTP Server: According to the result of experiment C, there is a fixed error of time offset imported by the hardware time stamp of NTP server, the mean value is 17.5μs. It can be served as a correction for the time offset θ calculated by formula (2). But the correction is less than the time offset at least 10 times, it can be ignored. The standard deviation of experiment C result is calculated, equals to 1.1μs. Therefore, the standard uncertainty of time offset error of NTP server u_{server} can be ignored.

4) Time Offset Error of Client: According to the result of experiment B, the standard deviation of blue curve is resulted from the software time stamp of client, which equals 2.5ms. Therefore, the standard uncertainty of error of time offset of client u_{client} is 2.5ms.

5) Round-trip Delay of Network: In the course of experiments, just an Ethernet cable is used to organize the LAN. There is not any Switch or Router in the route of network. Therefore, the symmetry of round-trip is ideal. The standard uncertainty of round-trip delay of network u_{net} can be ignored.

Table1 lists all of the standard uncertainty components.

TABLE I. SUMMARY OF STANDARD UNCERTAINTY COMPONENTS

Standard Uncertainty Components	Source of Uncertainty	Type of Uncertainty	Value of Standard Uncertainty
u_{t0}	Repeatability of Measurements Results	A	1.2ms
u_{ref}	Reference Source of NTP Server	B	Ignored
u_{server}	Time Offset Error of NTP Server	B	Ignored
u_{client}	Time Offset Error of Client	B	2.5ms
u_{net}	Round-trip Delay of Network	B	Ignored

C. Final Result

All of the standard uncertainty components are combined as shown in formula (5).

$$u_c = \sqrt{u_{t0}^2 + u_{ref}^2 + u_{server}^2 + u_{client}^2 + u_{net}^2} = 2.8\text{ms} \quad (5)$$

Suppose the coverage factor k=2, and hence the expanded uncertainty $U=ku_c$=5.6ms. The final result can be stated as:

$t = (0.4 \pm 5.6)$ ms, k=2

VI. CONCLUSIONS

According to the analyzing and evaluating procedures in this paper, the precision of network time service system is less than 10ms under LAN condition. For Internet, the round-trip delay can result in dozens of millisecond time offset error. The precision usually may be less than 100ms under Internet condition.

The uncertainty imported by software time stamp of client is the largest among the uncertainty components under LAN condition. The mean algorithm can decrease it effectively, but you have to take more system time to accumulate data and distinguish gross errors. Under Internet condition, Kalman filter algorithm can improve the accuracy of the estimated delay [4], and then improve the precision of synchronization.

REFERENCES

[1] Mills D L, “Internet Time Synchronization: the Network Time Protocol,” IEEE Trans. Communications 39, pp. 1482-1493, October 1991.

[2] Mills D L, “Network Time Protocol (version 3) Specification, Implementation and Analysis,” Network Working Group Report RFC - 1305, University of Delaware, 1992.

[3] Wenwei Li, Dafang Zhang, Gaogang Xie, and Jinmin Yang, “A High Precision Approach of Networ Delay Measurement Based on General PC,” *Journal of Software*, vol. 17, No. 2, pp. 275-284, February 2006.

[4] Xing Kailiang, Ying Yirong, Huang Yonghua, and Gao Yong, “Network time transfer accuracy improvement with Kalman filter method,” *Chinese Journal of Scientific Instrument*, vol. 32, No. 4, pp. 949–954, April 2011.

[5] Kejia Zhao, Aimin Zhang, and Dayu Ning, “Implementation of Network Time Server System Based on NTP,” *Electronic Test*, vol. 7, pp. 13-16, July 2008.

Inter-comparison of the UTC time transfer links

Z. Jiang
Time Department
Bureau International des Poids et Mesures (BIPM)
Pavillon de Breteuil F-92312, SÈVRES CEDEX, France
zjiang@bipm.org

W. Lewandowski
Time Department
Bureau International des Poids et Mesures (BIPM)
Pavillon de Breteuil F-92312, SÈVRES CEDEX, France

***Abstract*—** We present the new side-product of the monthly UTC computation: the long-term time links which is monthly published since Jan. 2010 and available on the BIPM ftp site: ftp://tai.bipm.org/TimeLink/LkC/LongTerm/. The techniques used for UTC generation are now TW, GPS and GLN. If they are considered independent, we can apply them in the investigations of the measurement uncertainties and the relative long-term variation in the link calibrations. 26 months' data have been collected and analyzed in this paper. For the short term measurement instability, we have similar conclusion as presently given in the section 6 of the BIPM Circular T. It seems however, for some baselines, exist long-term variations in the link calibrations. Limited by the knowledge of the raw data, we cannot explain the causes of this instability. Except for the extreme cases, most of the annual variations are within 2 ns. This is the limit of the uncertainty of the nowadays instrumentation and calibration and should not affect the UTC generations beyond its total uncertainty.

Key words: UTC, time transfer, GPS, GLONASS (GLN), TWSTFT (TW), calibration

I. INTRODUCTION *(HEADING 1)*

UTC time transfer is based on two basic spatial techniques: TWSTFT (Two Way Satellite Time and Frequency Transfer, TW for short) and GNSS (Global Navigation Satellite Systems). In practice, depending on the two systems, types of the receivers and observations, as well as the data processing methods, different accurate time links are used in UTC generation. They are, at present, TW, GPSPPP, GPS P3 code, GPS C/A code and GLONASS L1C code (GLN), combination of TW and GPSPPP, combination of GPS and GLN. For the GNSS code links, there are two time transfer techniques applied: Common View (CV) and All in View.

In this paper we compared the results of different time links over the same baselines. Advantage of the common clock comparison is that the clock noise is cancelled and we can then study the uncertainty in the time link measurements and the calibration instability which is not limited to the internal reference of the time link receivers as traditionally defined. The equipment involved in a time link is not only the receivers but also the whole system such as the antennas and the cables at both laboratories of a baseline. However, in this study, we will not separate the impacts of each individual part but consider the total effect of the receiver-system in the frame of the UTC time links.

We are interested in short-term and long-term stabilities. The dominant part of the short-term comes mainly from the measurement noise and the random effects up to 30 days. That of the long-term comes mainly from the equipment-system's instability up to years. The data analyzed in this study are collected from the time link and time link comparisons monthly updated in the BIPM web site ftp://tai.bipm.org/TimeLink/LkC/LongTerm/. Laboratories are encouraged to make independent analysis using these data.

The main purpose of this paper is, as the document introducing the BIPM time link comparison products [1], to present this new product and what can we do with these data. Limited by the knowledge of the raw data, the hardware setup in the UTC laboratories, we are not able to discuss in details the causes of the instability in the calibrations. The calibrations, either TW or GNSS, are of the total delay of the receiver, antennas, cables and related equipment etc. To perform a rigorous investigation in the calibration variations, we should fully aware of the hardware setup in the related UTC laboratories and this is obviously beyond the task and the capacity of the BIPM. What we can do in the point of view of the BIPM is to monitor the calibration and once anomalies observed, we inform the laboratory(s) on question. There are successful examples, such as given below in the discussion in section 3.3.

On the other side, more frequent calibrations should be organized through the standard BIPM calibrations tours and the coordination with the MRA facility. More study should be carried out in an easy, precise and robust calibration method. Through more and accurate calibrations, we can better monitor the changes or variations in the calibration with an order of nanosecond level.

II. THE LONG-TERM TIME LINK PRODUCTS AVAILABLE ON THE BIPM FTP SITE

Required by the UTC contributing laboratories, an automatic procedure in the frame of the monthly UTC computation has been developed and installed in the Software package Tsoft since the beginning of the year 2011.

Long term time link data since January 2010 are available and updated every month just after the publication of the Circular T on the BIPM ftp site: ftp://tai.bipm.org/TimeLink/LkC/LongTerm/. A notice of this new product is given in the Read-Me file ftp://tai.bipm.org/TimeLink/LkC/LongTerm/TM187_ReadMe-LongTerm-Link_V01.doc.

The long-term link data is interpolated on the epochs of integer hours, i.e. there are 24 points per day. The holes or the missing data larger than two times of the nominated intervals will not be interpolated but filled up by 888888.888.

Each link file is given in a unique name that will not be changed monthly. The size of the file is increased every month. Started from the 1st Jan. 2011, all the new link data are added monthly. They are published always in the same ftp site with the same names. The type of the time link data are those computed for not only the official but also the additional links: GPS MC, P3, PPP, GLN MC and TW as well as the combined links of GPS+GLN (GPSGLN) and PPP+TW (TWPPP). In addition to the time links, there are also the results of the so called 'zero-link', i.e. the UTC(k)-GPS TIME (or GLN TIME), as what given in the column REFGPS in the CCTF CGGTTS file.

The data are listed in two columns, MJD and the link or 'zero-link' data in nanosecond. For example, the zero-link PPP solution of the AUS is as follows (AU3AU3.Y3i):

```
MJD                Ref-IGST  Lab1 Lab2  code  method     GNSS DataType     σ/Vdk    yymm
55194.0000         1806.306  AU3 - AU3  54_54 MjdInterpl/GPS Y3i For F2   0.779 TAI1001
55194.0417         1806.487
55194.0833         1806.677
… …
55224.0000         1955.838  AU3 -AU3   54_54 MjdInterpl/GPS Y3i For F2   0.804 TAI1002
55224.0417         1956.213
55224.0833         1956.580
… …
… …
55924.0000         -766.015  AU3 -AU3   54_54 MjdInterpl/GPS Y3i For F2   0.795 TAI1201
55924.0417         -766.033
55924.0833         -766.058
```

In the first line of each UTC month, there are comments giving the most important information about the data in the related file, as given above. Here is another example: the first line of the data file SUPTB.Y3i is:

```
55194.0000                320.094   SU$ -PTB$ 38_ 5
MjdInterpl/GPS Y3i For F2    1.260 Tai1001
```

First by the name of the file, we know it is of GLN. The information given by the comment tells us, it is a GLN time link (if it was SU$-SU$ and 38-38, it would be a 0-link) between SU and PTB. Their UTC codes are 10038 and 10005 respectively. The hourly listed data are given on fixed Mjd epochs and can be used directly for the Tsoft sub-menus Z4 (for link comparison) and F2 (for the link triangle closures computation). The raw data noise vs. Vondrak smoothing is 1.260 ns. They belong to the monthly data set TAI1001 (Jan. 2010). This comment is only for the month 1001 and the indicated baseline and technique used.

III. USES OF THE LONG-TERM DATA TO ESTIMATE THE MEASUREMENT UNCERTAINTY AND CALIBRATION VARIATION

So far, the BIPM long-term data are collected from Jan. 2010 to Feb. 2012 or 1001-1202 in the term of yymm. In total there are 26 months of link data from MJD 55194 to 55984. These data are the base of the numerical analysis in this report.

In the following discussion, we estimate the measurement uncertainty (the type A uncertainty) and analyze the relative calibration variation using the method of the inter-comparison between different types of time link data (GPS MC, P3, PPP, GLN MC, TW, GPSGLN and TWPPP) over the UTC comment clock baselines. Because the three types of measurements TW, GPS and GLN are independently measured with different equipment, therefore if one of three has same variation vs. the other two, we can judge it is most probably this link changes.

It should be pointed out that, we cannot exclude the changes of the setups, changes of the cables and antennas or even the receivers, which may also produce the calibration variations. We set a tolerance of 2 ns per year which is the limit of the accuracy of the present instrumentation technology and the total delay of the link calibration. If the calibration variation is within 2.5 ns for 2 years, no further investigation is necessary otherwise the regarded laboratory should be contact to find the solution. This is the case of ROA-PTB, see section 3.3 below.

A. The UTC baseline AOS-PTB

Fig. 1 is the comparison between the time links of GPS PPP and GLN MC on the UTC baseline AOS-PTB. The left plot is the two time links and the right plot is the difference of the two links. The sigma is the standard deviation of the differences (σ). It is seen by the discontinuities that the calibrations changed three times, most likely due to the setup changes. By removing the huge calibration changes, we obtain the Fig. 2. The σ is 1.128 ns that is within the normal measurement uncertainty. However, by a close look, we can see a significant relative calibration variation with a peak to peak difference of about 2.5 ns, as shown by the blue lines. In the figures, the red lines are the mean values of the differences. Although we do not know if it was the GPS PPP or the GLN MC link or both of them changed. A third reference is required to indicate this.

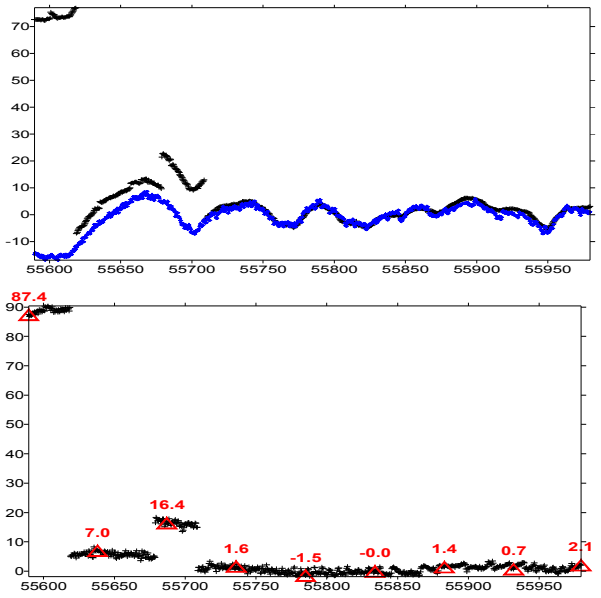

Figure 1. Comparison between the time links of GPS PPP and GLN MC on the UTC baseline AOS-PTB. The left plot is the time links and the right plot is the difference of the links. All the data are in nanosecond. The x-axis is MJD and y-axis is the time links or the difference of the time links. The sigma is the standard deviation of the differences (σ). The same is as the figures below.

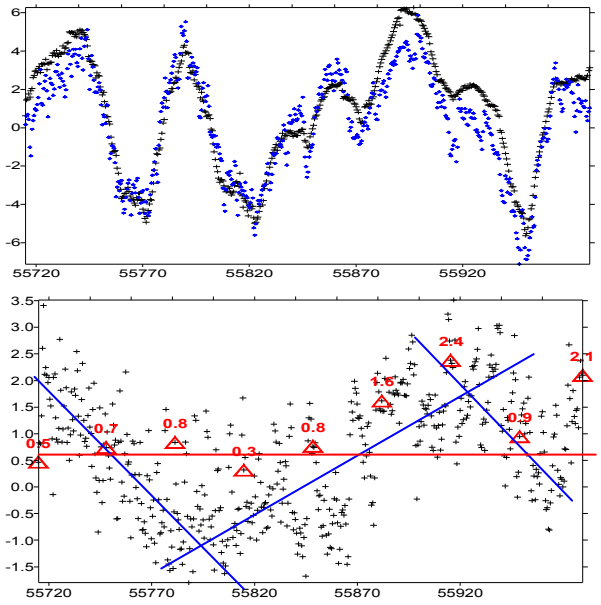

Figure 2. Comparison between the time links of GPS PPP and GLN MC on the UTC baseline AOS-PTB. This figure uses the same data as in Fig. 1 with the discontinued data before MJD 55720 removed. The red line marks the mean values of the differences. The blue lines demonstrate the tendency of the calibration variation with Mean±σ = 0.633±1.128 ns. The same is as in the figures below. The peak to peak variation is about 2.5 ns

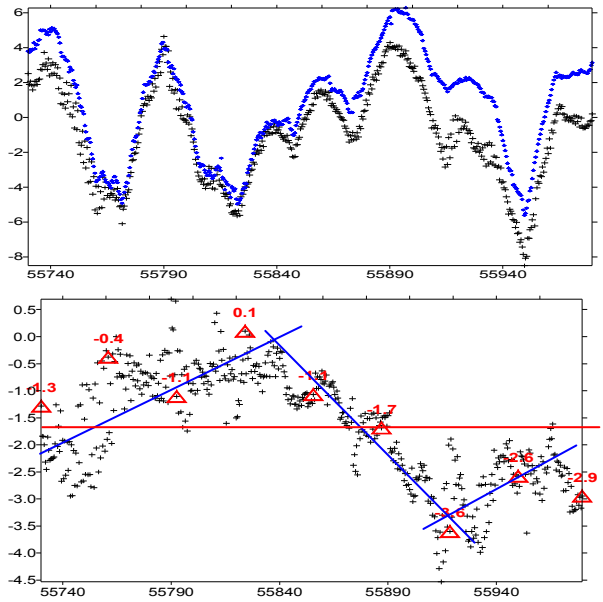

Figure 3. Comparison between the time links of TW and GPS PPP on the UTC baseline AOS-PTB. The peak to peak variation is about 2.5 with Mean±σ = -1.699±1.009 ns

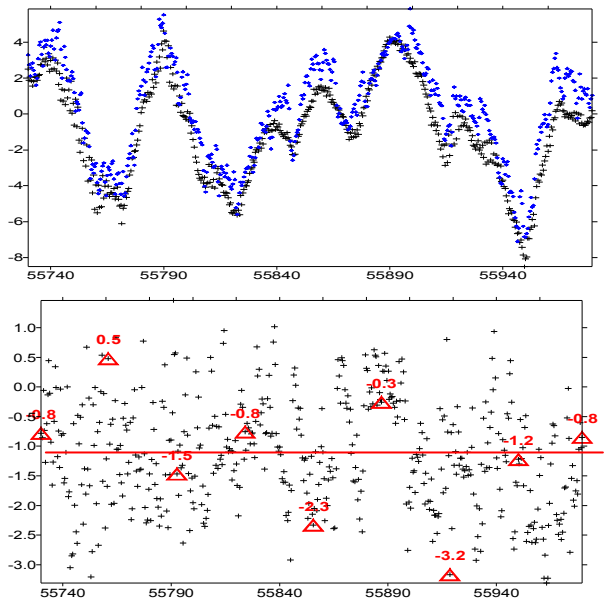

Figure 4. Comparison between the time links of TW and GLN on the UTC baseline AOS-PTB with Mean±σ = -1.120±0.913 ns

Fig. 3 is the comparison between the time links of TW and GPS PPP over the UTC baseline AOS-PTB. The blue lines demonstrate the calibration variation. The peak to peak variation is about 2.5 ns. Fig. 4 is the comparison between the time links of TW and GLN on the same baseline. The red line goes through the center of the differences suggests that the calibrations of TW and GLN were kept no change during this period of two years. By comparing the figures 2, 3 and 4, the TW and GLN agree with other. It is therefore the calibration of the GPSPPP varied about 2.5 ns during the monitoring period.

B. *The UTC baseline NIST-PTB*

Fig. 5 is the comparison between the time links of TW and GPS PPP over the UTC baseline NIST-PTB. The blue lines demonstrate the calibration variation over a period of a little longer than 2 year. The peak to peak variation is about 2 ns. The mean value of the difference is -2.054 ns and the σ is only 0.661 ns which, if taken into account of the calibration variations, means the measurement noise in both measurements of GPS PPP and TW is very small, in an order of two or three hundred picoseconds, caused mainly from the diurnals in the TW measurements and discontinuities in the PPP solution.

Fig. 6 is the comparison between the time links of TW and the combination of TWPPP over the UTC baseline NIST-PTB. The blue lines demonstrate the convergence of the measurement noise reduced from ± 0.6 ns to ± 0.3 ns. It suggests that the measurement noise is reduced gradually during the last two years. Because the GPS PPP has no significant improvement, the gain in precision should come mainly from the TW link thanks to the efforts in the frequency adjustments. This figure shows also that the calibration of the combined link is piloted by the TW link.

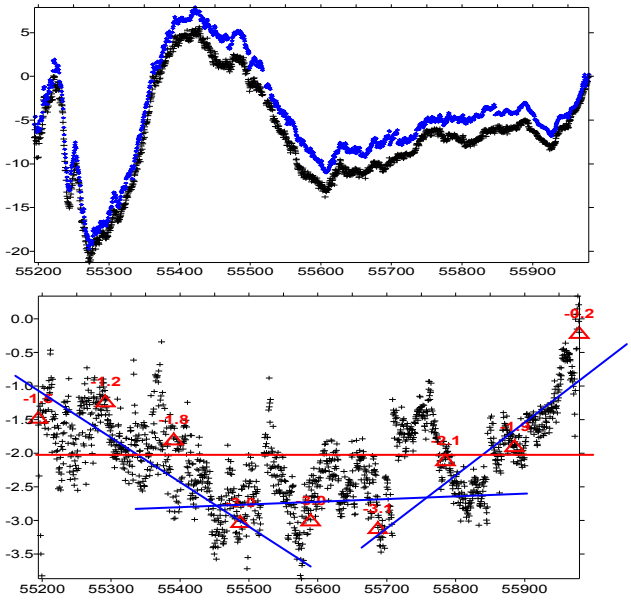

Figure 5. Comparison between the time links of TW and GPS PPP on the UTC baseline NIST-PTB. It is seen that there is a down-flat-up variation. The peak to peak variation is about 2 ns with Mean±σ = -2.054±0.661 ns

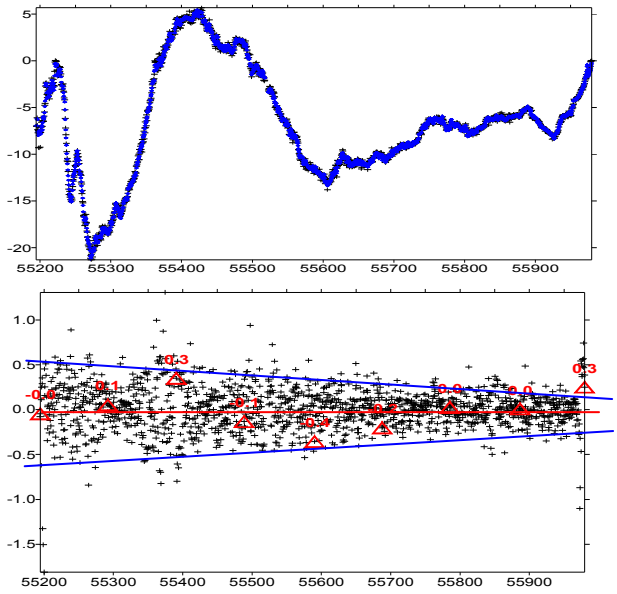

Figure 6. Comparison between the time links of TW and the combination of TWPPP on the UTC baseline NIST-PTB. The blue lines demonstrate the convergence of the measurement noise reduced from ± 0.6 ns to ± 0.3 ns. The Mean±σ = 0.012±0.242 ns

C. *The UTC baseline ROA-PTB*

Fig. 7 is the comparison between the time links of TW and GPS P3 over the UTC baseline ROA-PTB. The blue lines demonstrate the calibration variation. The peak to peak variation is about 12 ns during about 2 years. Informed by BIPM about the calibration variation, the ROA changed their master GPS receiver on about 55890 as can be seen in the figure, the variation starts to change in the opposite direction.

Figures 8 and 9 are the comparisons between TW to GPS PPP and to GPS MC C/A codes respectively. The phenomena of the calibration variations are seen in Fig. 8 appear again. About 5 ns variation per year is too big to be negligible for the UTC time transfer. This shows the importance of monitoring the long-term comparisons because 0.5 ns variation per month is not observable in the monthly comparison which is now a part of the standard procedure of the monthly UTC computation.

An up-down variation with even a peak to peak variation up to 2 or 3 ns, probably due to the environmental temperature variation and characterized more or less periodic, is not a dramatic problem in the UTC generation because it is within the limit of the state-of-the-art of the instrumentation. However a slope-down and slope-up change like in this baseline is rather dangerous.

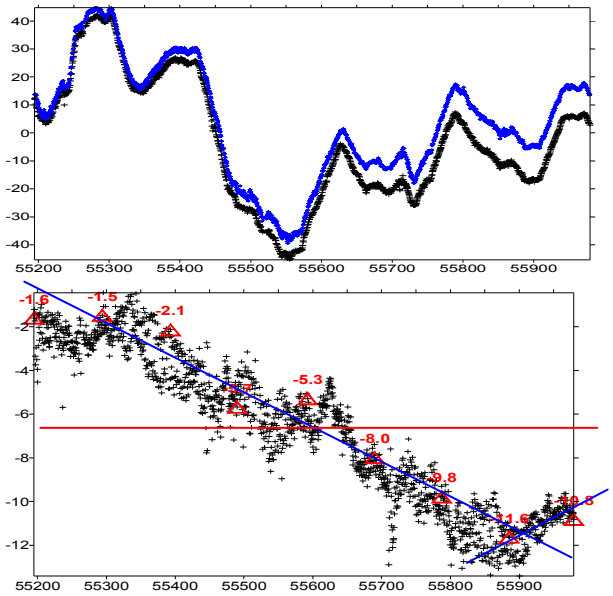

Figure 7. Comparison between the time links of TW and GPS P3 on the UTC baseline ROA-PTB. It is seen a one-way-down variation of about 12 ns in total during about 2 years with Mean±σ = −6.768±3.464 ns

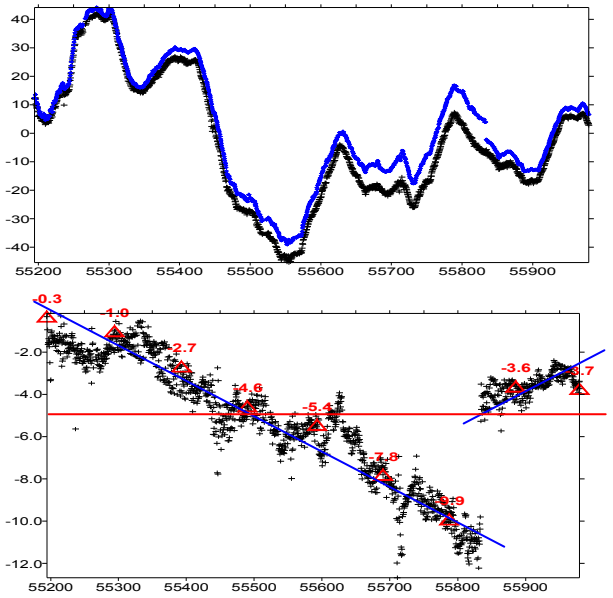

Figure 8. Comparison between the time links of TW and GPS PPP on the UTC baseline ROA-PTB. It is seen a one-way-down variation of about 12 ns in total during about 2 years with Mean±σ = −4.979±2.755 ns

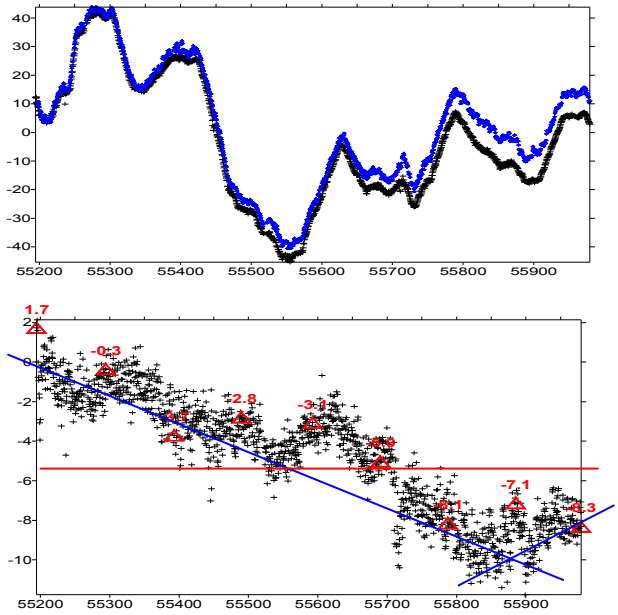

Figure 9. Comparison between the time links of TW and GPS MC C/A on the UTC baseline ROA-PTB. It is seen a one-way-down variation of about 12 ns in total during about 2 years with Mean±σ = −4.750±2.990 ns

D. The UTC baseline OP-PTB

The case of the baseline OP-PTB is rather complex. It seems there are two kinds of variations. The first, as shown in the Figures 10, 11 and 12, is an up-down tendency (identical with down-up. The sign depends on the order of the subtraction when making the differences) and the second, as shown in the Figures 12 and 13 is a down-up-down tendency. The peak to peak variations are about 2 ns.

Fig. 10 is the comparison between GPS PPP and GPS MC C/A. Fig. 11 is between GPS PPP and GLN MC L1C. Fig. 12 is between GPS PPP and TW. Comparing the three figures, the GPS PPP solution has the similar changes vs. all the other three and seems to be responsible for the up-down variations. On the other side, the σ is respectively 1.1 ns, 1.2 ns and 1.0 ns. The all are within the normal limit of the uncertainty u_A. Taking into account of the calibration variations, the measurement noise should be much smaller.

Fig. 13 is the comparison between TW and GPS MC C/A. Fig. 14 is between TW and GLN MC L1C. If the TW, GPS and GLN links are completely independent, TW should be responsible for the down-up-down variations. But again, the amplitude of the variations of 2 ns is acceptable compared with the limit of the instrument stability for the UTC generation. We cannot exclude the calibration changes caused by the changes of the setups, the cables, the antennas and even the receivers. However, by the values of the peak to peak variations, we conclude that annual variations within 2 ns are acceptable for the UTC generation. We do not need to make deeper study to find the true causes.

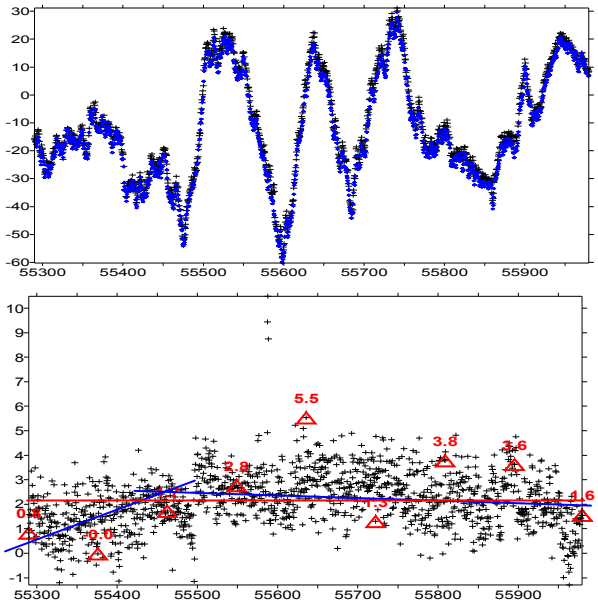

Figure 10. Comparison between the time links of GPS PPP and GPS MC C/A on the UTC baseline OP-PTB. A quick-up and slow-down variations can be seen. The peak to peak variation is about 2 ns with Mean±σ = 2.155±1.148 ns

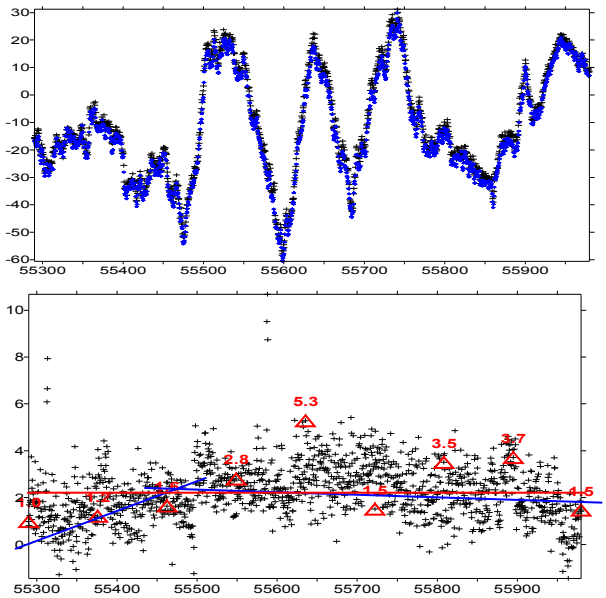

Figure 11. Comparison between the time links of GPS PPP and GLN MC L1C on the UTC baseline OP-PTB. A quick-up and slow-down variation can be seen. The peak to peak variation is about 2 ns with Mean±σ = 2.220±1.204 ns

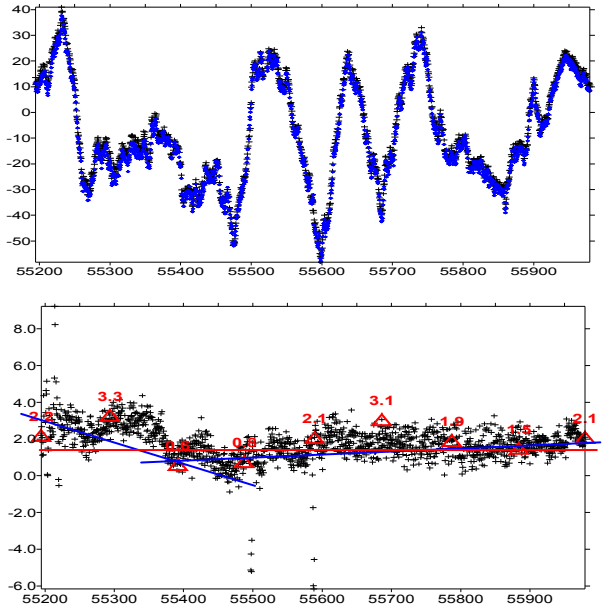

Figure 12. Comparison between the time links of GPS PPP and TW on the UTC baseline OP-PTB. A quick-down and slow-up variation can be seen. The peak to peak variation is about 2 ns with Mean±σ = 1.786±0.995 ns

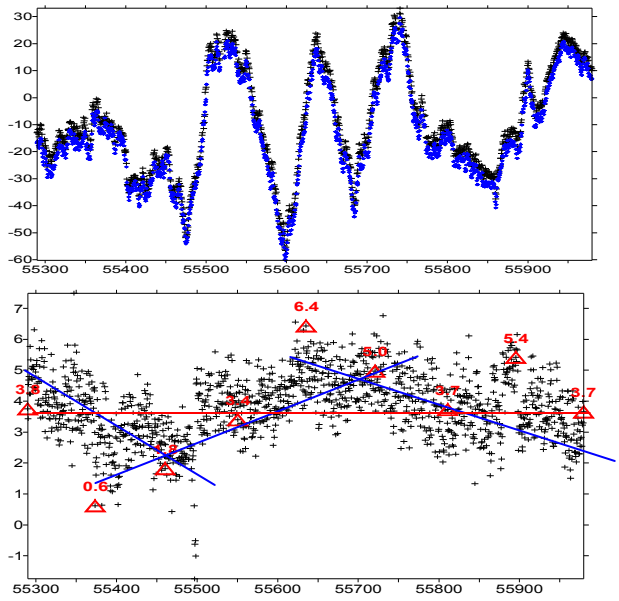

Figure 13. Comparison between the time links of GPS MC C/A and TW on the UTC baseline OP-PTB. A down-up-down variation can be seen. The peak to peak variation is about 2 ns with Mean±σ = 3.813±1.067 ns

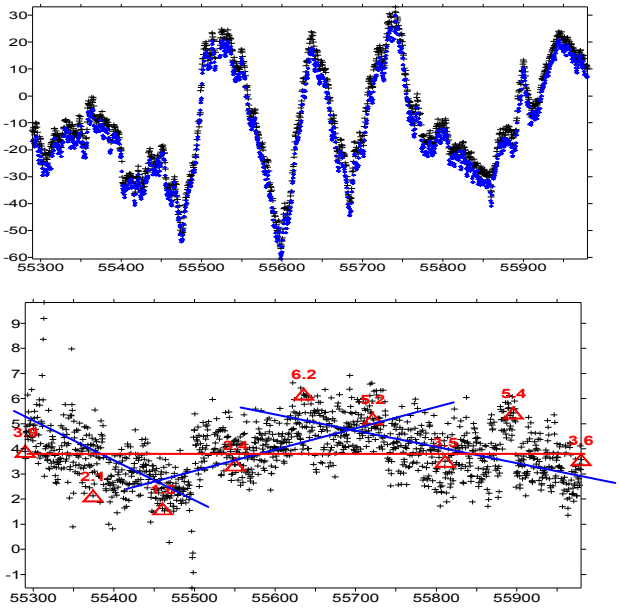

Figure 14. Comparison between the time links of GLN MC L1C and TW over the UTC baseline OP-PTB. A down-up-down variation can be seen. The peak to peak variation is about 2 ns with Mean±σ = 3.882±1.125 ns

IV. SUMMARY

Table I summarizes the statistic characters of the long-term versions in the differences of the different types of the UTC links. Except for the baseline ROA-PTB, the standard deviation (σ) of the link differences (0.242 ns to 1.204 ns) and the calibration variations (< 2.5 ns) are in the reasonable limits. ROA-PTB is a special case. Reported by ROA, the slope-down calibration changes of about 12 ns during two years were mainly caused by the master GPS receiver-antenna system. In consequence, the σ of the link differences are up to 3.5 ns which is much higher than the usually measurement noise. The duration after replacing the master receiver by a new one is too short to estimate the tendency of the calibration variation of the new receiver-system.

In this report, we present the new side-product of the monthly UTC computation: the long-term time links of TW, GPS and GLN. They are available on the BIPM ftp site since the Jan. 2010. If they are considered as the independent measurements, we can apply them in the investigations of the measurement uncertainties and in the relative long-term variation of the TW and GNSS calibrations. 26 months' data have been analyzed in this document. For the short term measurement instability, we have similar conclusion as before. It seems however, for some baselines, exist the long-term calibration variations. Limited by the understanding of the raw data, we cannot explain the causes of this instability. However, except for the extreme cases, most of the annual variations are within 2 ns. This is the limit of the uncertainty of the nowadays' instrumentation and calibration and should not affect the UTC generations beyond its total uncertainty given in the section 1 of the BIPM Circular T. More study should be made, in particular, the BIPM calibration should be performed regularly.

TABLE I. **Table 4.1** Result of the link comparisons during Mjd 55194 and 55984 or 26 months (TWPPP is the combination of TW+GPSPPP; GPSCA and GLNCA are the GPS/GLN C codes)

Baseline	Link types	Calibration variation / ns	σ of link differences / ns
AOS-PTB	PPP-GLN	2.5	1.128
	TW-PPP	2.5	1.009
	TW-GLNCA	0.0	0.913
NIST-PTB	TW-PPP	2.0	0.661
	TW-TWPPP	0.0	0.242
ROA-PTB	TW-P3	12	3.462
	TW-PPP	11	2.755
	TW-GPSCA	11	2.990
OP-PTB	PPP-GPSCA	2.0	1.148
	PPP-GLNCA	2.0	1.204
	TW-PPP	2.0	0.995
	TW-GPSMC	2.5	1.067
	TW-GLNCA	2.0	1.125

V. **Reference**

[1] Arias F., Z. Jiang, G. Petit, W. Lewandowski, *BIPM Comparison of Time Transfer Techniques*, Proc. FCS/PTTI 2005

INRIM Tool for Satellite Clock Characterization in GNSS

Alice Cernigliaro, Ilaria Sesia
Optical Division
National Institute of Metrological Research (INRIM)
Turin, Italy
a.cernigliaro@inrim.it, i.sesia@inrim.it

***Abstract*— In Global Navigation Satellite Systems (GNSS) the role of atomic clocks is essential for the determination of the user position and due to their excellent stability they are fundamental to ensure the adequate performances required in the positioning service.**

Since a degradation of the clock stability would immediately impact the navigation performances, the on board clock behaviour has to be continuously monitored. In this work, we illustrate a software tool developed at INRIM, optimized for GNSS clock characterization and monitoring. Although some commercial software are available for clock characterization, special attention has to be paid when dealing with space clocks. In fact, the space clock behaviour analysis may be complicated by different aspects: data from satellite clocks often present gaps and outliers as well as periodic fluctuations . On the contrary, data from timing laboratories are equally spaced and usually not affected by many outliers. Hence, often, the typical methods for clock characterization currently used in timing laboratories are not sufficient for space applications: new approaches, more suitable for GNSS applications, are required. To overcome these limitations, we developed the Clock Analysis Tool: a software, developed in Matlab, for clock characterization to be used either in metrological laboratories or for space applications. To fulfill GNSS needs, the software has been enhanced and extended, including new routines and functionalities of particular interest when characterizing the space clock behaviour, such as the dynamic stability analysis, as well as the addition of the uncertainty evaluation in the clock parameter estimation, or the inclusion of the system noise estimate in the frequency stability analysis. Moreover, the algorithms commonly used for clock characterization, such as the Allan Deviation computation and the frequency drift estimation, have been adapted to deal with space clock features, namely data gaps and outliers, treating missing data with the best possible procedure to allow the estimate of the stability over long observation intervals. In addition, the software has been provided with a graphical user interface, allowing an easy handling of satellite clock data and permitting a quick estimate and graphic representation of the clock key parameters.

I. INTRODUCTION

Atomic clocks on board satellites are one of the most critical technologies for Global Navigation Satellite Systems (GNSS) developers. Different clock technologies are employed: Cesium clocks and Rubidium Atomic Frequency Standard (RAFS) are used in GPS, while the European satellite navigation system Galileo will fly Rubidium Atomic Frequency Standard and Passive Hydrogen Masers (PHM). As expected, each clock technology is different from the others and, most importantly, the clock behavior observed in space is different from the one observed on the same type of clock in timing laboratories. This is certainly due to the clock technology itself, which is differently designed to work on ground or in space, but also to the different operational environment and the complex space-to-ground measurement system. Indeed, space clock data present some particular features which make unsuitable the typical methods and techniques currently in use in timing laboratories for clock characterization. In fact, it is very common that space clocks present missing data and outliers [1], as well as periodic fluctuations [2]. These aspects complicate the analysis since typically clock data from timing laboratories, regularly used by INRIM, are equally spaced and usually do not present outliers. The strict requirements of reliability and integrity needed in navigation systems, require the development of new approaches and algorithms, more suitable for GNSS applications. With this aim, INRIM developed the *Clock Analysis Tool* [3], a software tool for clock characterization optimized to deal with atomic clocks for space applications. For this purpose, an existing software used for clock characterization in INRIM laboratories has been adapted to fulfill GNSS needs: it has been enhanced and extended including new routines for the monitoring such as the Dynamic Allan Deviation (DADEV) and Dynamic Hadamard Deviation (DHDEV), commonly used for GNSS satellite clock characterization [4].

This paper illustrates the methodology applied at INRIM for satellite clock characterization, and the tool realized to

analyze atomic clocks and time scales, optimized for space clocks.

II. METHODOLOGY

The main objectives of the clock characterization performed at INRIM are:

- The check on data regularity
- The check on clock deterministic behaviour
- The check on clock stochastic behaviour
- The check on the non-stationarity of noise
- The possible clock sensitivity to environmental parameters (temperature, radiation)

The *Clock Analysis Tool* presented in this paper has been realized with the aim of covering the first four of the five steps listed above: the study of clock sensitivity to environment is performed by means of another tool specifically developed at INRIM, not described here.

III. THE CLOCK ANALYSIS TOOL

The *Clock Analysis Tool* has been developed in MATLAB® language and it has been provided with a Graphical User Interface (GUI), as illustrate in Fig. 1, to ease the procedure of analysis. The results were checked with respect to those generated by other commercial software and complete agreement was found. Main products for the clock characterization tool are ASCII files and plots generated in an automatic way; such figures allow to monitor easily the clock key parameters and to perform an accurate clock analysis.
The results of all the analysis performed by the Clock Analysis tool are automatically saved as ASCII files and images in an output folder purposely created during the tool execution. The user can also observe the graphics while they are generated so that one can have an immediate idea of the general clock behaviour; moreover one can analyze the saved plots in order to deepen the analysis focusing on certain periods of data or on particular features. The analysis can be reset and repeated in any moment with different configuration parameters or input files.

A. Input Data Pre-Processing

Clock data extracted from standard files used in GNSS (RINEX for clock) are firstly pre-processed in order to identify and properly manage any potential data gap and outlier. In fact, often space clock data may be unavailable

due to ground stations problems in data collection or satellite maintenance or faults: clock estimates need to be regularized for stability analysis. Data regularization is performed inserting neutral values called *Not A Number* (NaN) where data gaps are identified. In addition, frequently space clock data present outliers, which have to be identified and removed to allow a representative analysis of clock performances. The method adopted to identify and remove outliers is a Median Absolute Deviation filter. The filter selectiveness and the data sampling are set by the user through the proper panel on the graphical user interface.

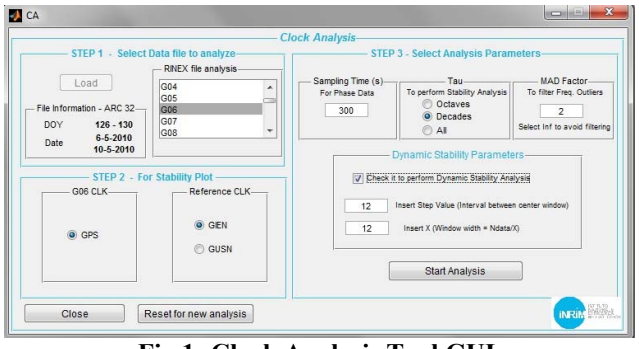

Fig 1: Clock Analysis Tool GUI

B. Deterministic Behaviour Analysis

The clock frequency offset is obtained from the clock time offset extracted from RINEX for clock data through a time derivative, and its evolution is showed. Then, the main deterministic effect, the frequency drift, is evaluated. The objective is to monitor its evolution over time and to remove such deterministic contribution from the clock estimates when the aim is to observe only the clock stochastic behaviour. The tool has been implemented to evaluate the clock frequency drift estimating the coefficients of a quadratic least squares fit on time offset data. The frequency drift is then removed from both time and frequency offset data by subtracting to the original data sets the estimated quadratic and linear fit respectively, as illustrated in Fig. 2 and Fig. 3.

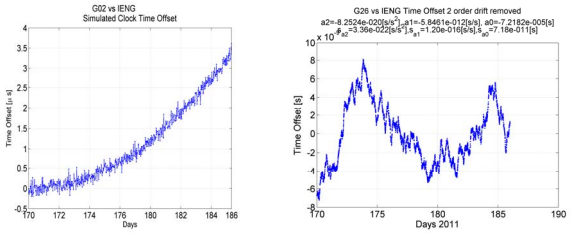

Fig 2: Typical satellite time offset data, before and after quadratic drift removal

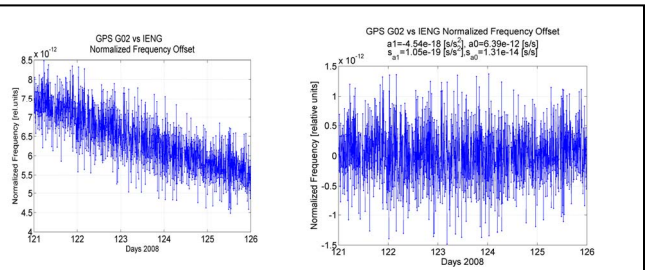

Fig 3: Typical satellite frequency offset data, before and after linear drift removal

The values of the statistical dispersion of the polynomial coefficients of the fitted curve are reported on the graphics of

both phase and frequency clock data: this permits to have direct evidence of the frequency drift entity together with the level of accuracy of the estimate.

C. *Stochastic Behaviour Analysis*

Two independent statistics are used to estimate the clock frequency stability: first the Allan Deviation (ADEV) is computed on the averaged frequency estimates, then the Hadamard Deviation is also determined. Both statistics are evaluated for different observation intervals τ.

The Clock Analysis Tool has been designed to extend the approaches commonly used for the study of frequency stability, to deal with the peculiar aspects of satellite clocks: missing data and outliers. In fact, usually the stability analysis is based on the assumption of using equispaced samples. Since data from space vehicles are not always available, very often space clock data present long periods of missing values. In the presented tool NaN values are inserted in case of missing data. In addition, only complete triplets of data are considered [1]. Besides, triplets are dynamically filtered for each interval τ.

The number of different observation intervals for frequency stability computation can be set by the user at the beginning of the analysis, through the proper panel on the graphical user interface.

An estimate of the system noise is also evaluated and displayed in the frequency stability figures. The system noise is estimated as the difference between the time offset of two ground stations connected to an active hydrogen maser.

As an option, the clock specifications can be displayed together with the apparent clock stability estimate.

D. *Dynamic Stability*

Optionally, the Dynamic Allan Variance (DAVAR) and the Dynamic Hadamard Variance can be estimated. The DAVAR is a sliding version of the Allan Variance. When, for a given epoch t, all the time offset triplets are incomplete for a given observation interval τ, the DAVAR at epoch t is completely missing, generating 'canyons', as illustrated in Fig. 4:

IV. CONCLUSION

The Clock Analysis Tool has been expressly developed by INRIM the perform the analysis of the atomic clocks used in metrological laboratories and it has been optimized for space clocks to be used in GNSS. The optimization for space clocks has been necessary due to the intrinsic differences of satellite clock data with respect to the ones of ground clocks (due to the clock technology, to the complex measurement system, the spatial environment…), making inappropriate the typical algorithms and techniques already in use in metrological laboratories. The presented tool has been used by the INRIM staff, in the frame of the experimental phase of the Galileo Project named GIOVE Mission, to characterize the clocks employed on board the first experimental Galileo satellites, namely GIOVE-A and GIOVE-B. Besides, the tool has been used as prototype for the characterization of the first satellites of the Galileo system.

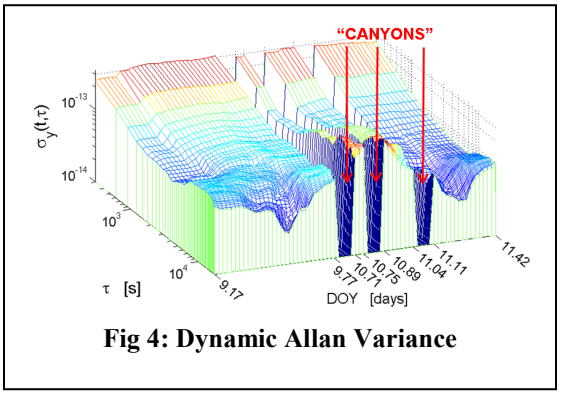

Fig 4: Dynamic Allan Variance

REFERENCES

[1] I.Sesia, P.Tavella, "Estimating the Allan variance in the presence of long periods of missing data and outliers ", Metrologia, 45, December 2008, pp.S134-S142.

[2] F.Gonzalez, A.Cernigliaro, P.Tavella, J.P Boyero, "Clock Strategy Experimentation with GIOVE Clocks", in Proc. of the 24th European Frequency and Time Forum (EFTF), April 13th-16th 2010, ESTEC; Noordwijk, The Nederland.

[3] A.Cernigliaro, I.Sesia, "Satellite Clocks Characterization and Monitoring for Global Navigation Satellite Systems", in Proc of the XXX URSI General Assembly and Scientific Symposium of International Union of Radio Science, August 13th-20th 2011, Istanbul, Turkey.

[4] I. Sesia, L. Galleani, P. Tavella, "Application of the Dynamic Allan Variance for the Characterization of Space Clock Behavior", IEEE Transactions on Aerospace and Electronic Systems, Volume 47, issue 2, April 2011, pp. 884-895.

SIDGET: A first Composite Clock Prototype

Olivier Pajot and François Vernotte
UTINAM
Observatory THETA of Franche-Comté
University of Franche-Comté/CNRS
41 bis avenue de l'observatoire - B.P. 1615
25010 Besançon Cedex - France
Email: francois.vernotte@obs-besancon.fr

***Abstract*—This paper presents the working prototype of a composite clock. This apparatus combines the stability of several references clocks for different duration. A voltage-controlled quartz oscillator is driven by a hydrogen maser clock for mid-term stability and by a cesium atomic clock for long-term stability. The best clock stability at a given averaging time is transfered to the VCO by a special control system using two comands.**

I. Introduction

The composite clock is composed of a voltage-controlled oscillator (VCO) controlled by both an hydrogen Maser and a cesium clock. The core of this apparatus is the Dual Mixer Time Difference system used for estimating frequency offsets and the double commands algorithm used for servoing the VCO. In this paper, we will describe both the components used and the locked-loop algorithm as well as the enhancements developped and the final results using differents master clocks.

II. Frequency Measurement System

A. Hardware

As shown in Figure 1, the master clocks frequency are risen to 100MHz with frequency multipliers (mostly PLL), then go through a Dual Mixer Time Difference (DMTD) [1] [2]. A secondary oscillator with a slightly different frequency have his signal multiplied with each source. The output combines their frequencies as followed.

$$V_o(t) = V_0 \left\{ \cos\left[2\pi(\nu_1 + \nu_2)t\right] + \cos\left[2\pi(\nu_1 - \nu_2)t\right] \right\}. \quad (1)$$

Outputs are the addition and the subtraction of the inputs' frequencies, meaning both output signals have the same frequency variations as their sources, but a smaller output frequency will rise the maximum system stability (Eq. 2).

The stability of the output signal (σ_{yo}), at the frequency ν_o is linked to the stability of the input signal (σ_{yi}), at the frequency ν_i by the following formula.

$$\sigma_{yo}(\tau) = \frac{\nu_o}{\nu_i}\sigma_{yi}(\tau) \quad (2)$$

For our application, the input signal stability is 125,000 times greater than the output. We only have to ensure a stability better than 10^{-9} for a given integration time to reach a stability of 10^{-14} for the input signal.

The following zero crossing detectors (ZCD) [5] [6] filter the $\nu_1 + \nu_2$ component of the DMTD and transform the sine signal into a square one. Five levels of high-gain amplification are used to ensure a sharp slope and a minimal noise. The biggest concern about the ZCD is its temperature sensibility. It needs to be maintained at a constant temperature using either heaters or air conditionning.

An FPGA is then used for the acquisition and processing of the three signals. A counter measures the time difference between two rising edges, the corresponding frequency offsets are calculated and a C language program takes care of the servoing as well as communication with the DAC.

The feedback loop go through a 20 bits DAC which generates $2^{20} = 1,048,576$ steps between 0V and 10V, meaning we can pilot the VCO with 9.53 µV steps or 0.27 µHz steps for the chosen oscillator.

B. Estimator

We use a counter running at 400 MHz for measuring the period with an accuracy of ± 1.25 ns. This means that if we collect the information during 1s (800 periods), we can detect a variation of ± 1µHz. But the signal still have many variations due to the ambient noise. Consequently, an estimator is used to smooth the counter results.

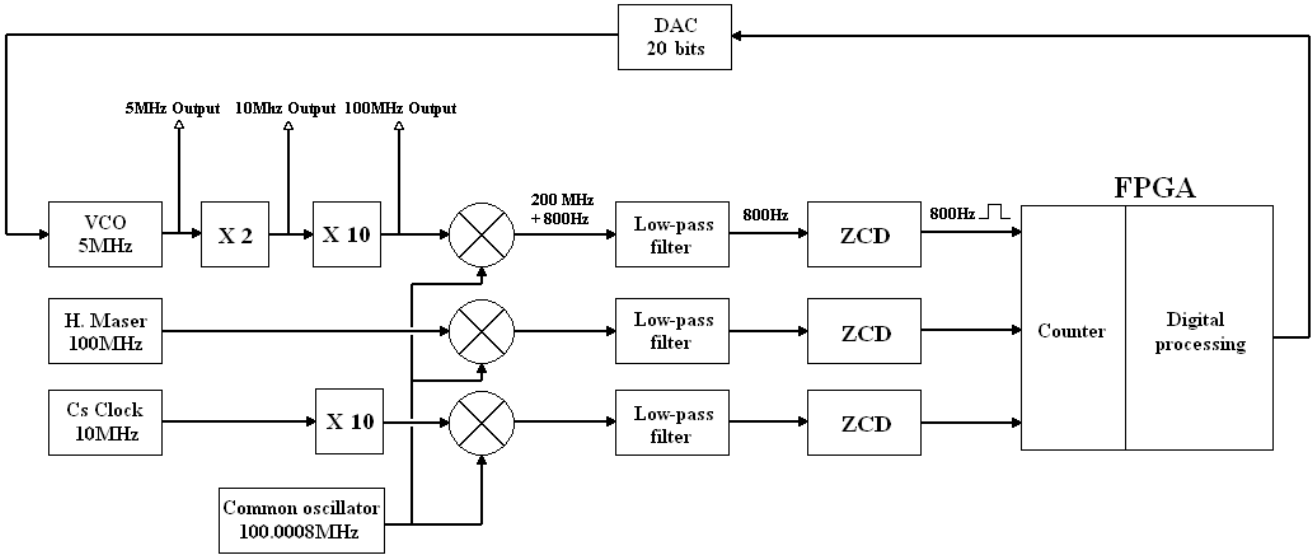

Fig. 1. Composite clock layout

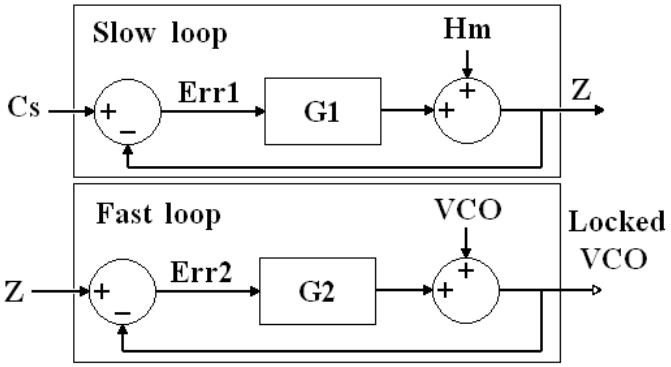

Fig. 2. Digital processing

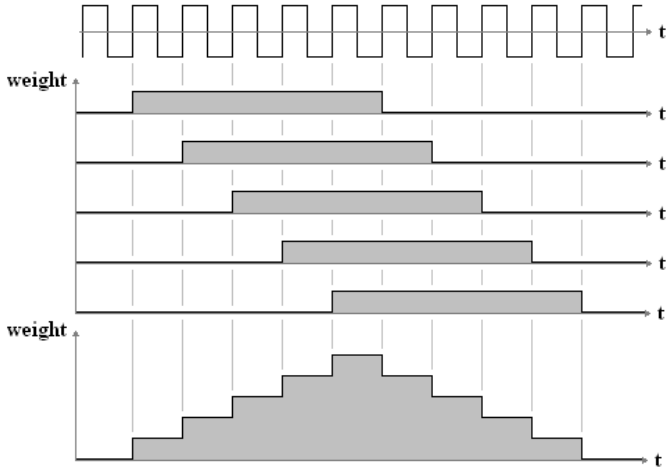

Fig. 3. Triangular averaging estimator

The estimator role is crucial to obtain the required stability. Tests made on the ZCD output signal reveals that the white noise is overriding. Consequently, a triangular filter was chosen to reduce its influence [3]. To make the calculations easier, we measure the beat frequency with a 1 s gate time then we shift this gate every 1 ms (Fig. 3). Then we average the value of the frequency offset in 800 gates to obtain a triangular estimator. From the first value, we only need to substract the influence of the first gate and add the next one to calculate the following value (only 2 operations per ms).

III. Digital Locked Loop

The control algorithm is divided into two parts : A slow loop which compare the frequency offset of the hydrogen maser and the cesium clock to produce an "artificial" frequency offset Z ; and a fast loop which compare this result with the VCO to generate the command (Fig. 2). We use it to generate an output signal for locking the VCO which depends on the free VCO, the Hygrogen maser (Hm) and the cesium (Cs) without modifying the maser nor the cesium.

$$VCO_L = VCO_F \frac{1+G1}{(1+G1)(1+G2)} + Hm \frac{G2}{(1+G1)(1+G2)} + Cs \frac{G1G2}{(1+G1)(1+G2)} \quad (3)$$

Both loops compares two frequency offset but with

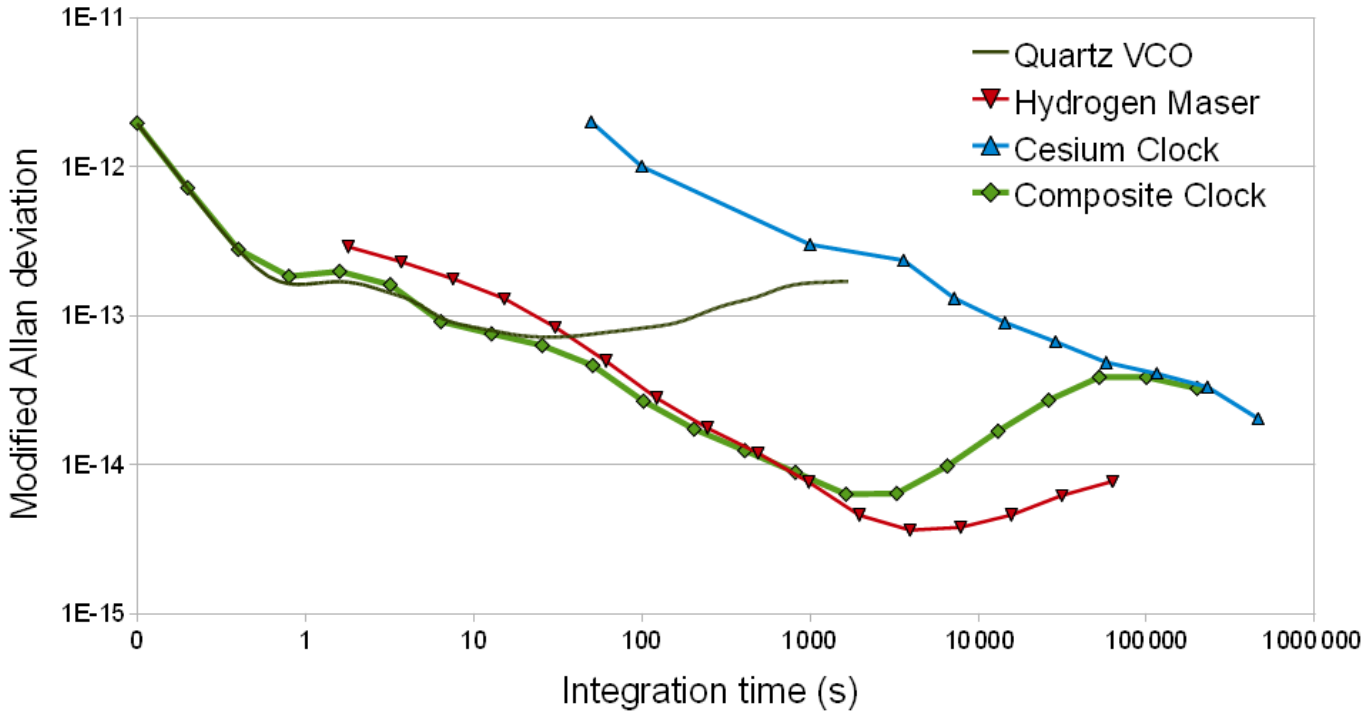

Fig. 4. Allan deviation of the composite clock

different integration times. The transfer functions G1 and G2 are based on the same model (4) : a double integrator to eliminate the VCO and maser long-term drift and a phase ahead filter for increasing stability, but their time constants are differents.

$$G(z) = \frac{b_0 z^{-1} + b_1 z^{-2}}{(1 - z^{-1})^2} \tag{4}$$

In the slow loop, the hydrogen maser and cesium clock are both free from any control. It aims at generating the "artificial" frequency offset Z ; an image that keeps the maser short-term stability and the cesium long-term stability. In fact, Z follow the maser variations with an offset which is corrected by the cesium clock. It is not a locked-loop since the resulting command has no inluence on either inputs. But we chose to use a transfer function to make the calculations easier. Still, we used this fact to modify Z as we see fit since there won't be repercussions on its future values.

The fast loop is a standard PID frequency-locked loop. The VCO is corrected every second in order to follow the virtual signal Z.

The very long term stability would need several months of measures, but we can be sure that a drift induced by the slow algorithm exists (mainly due to mismeasurements and number rounding). A simple way to ensure long term stability is to add a phase-locked loop between the VCO and the maser. We only use a proportional controller with a low parameter for not disturbing the main algorithm.

IV. Results

For the first prototype, we used a 5MHz BVA (SN 102) as a quartz oscillator ; a passive Hydrogen maser (OSA 3705) ; and a Cesium atomic clock (OSA 3210). As we can see (Fig. 4), the composite clock have the same stability as the Quartz oscillator until 20s of integration time then follow the maser stability. The maser/cesium transition is chosen in order to minimize the peak. However, we have to keep the maser best stability interval disturbed. The behavior of the composite clock is close to the one expected by previously ran simultations [3] [7] [4] except for the capacities of the VCO and the Hydrogen maser which were overrated compared to the real clocks used. Still, we were able to follow the lead of two differents master clocks using a frequency-locked loop control on a VCO.

V. Conclusion

The composite clock is able to follow the stability of 3 reference clocks. The transition between the first clock (VCO) and the second (Hydrogen maser) occurs without stability loss. The transition with the third (Cesium

clock) induces a loss of stability due to the chosen integration time but can be corrected with enough time.

REFERENCES

[1] G. Brida, "The dual mixer time difference at ien," in *Proc. Precision Electromagnetic Measurements*, 2000, pp. 52–53.

[2] L. Sojdr, J. Cermak, and G. Brida, "Comparison of high precision frequency stability measurements systems," in *Proc. Frequency Control Symp. PDA Exhibition*, 2003, pp. 317–325.

[3] C. Plantard, "Conception et réalisation d'une horloge de référence à oscillateurs multiples," PhD thesis, Université de Franche-Comté, Observatoire de Besançon, November 2010.

[4] C. Plantard, P. Mbaye, and F. Vernotte, "Composite clock including a Cs clock, a H-maser clock, and a VCO," *Transactions on Ultrasonics, Ferroelectrics, and Frequency Control*, vol. 57, no. 3, pp. 707–713, 2010.

[5] R. L. Sydnor, G. J. Dick, and P. F. Kuhnle, "Zero crossing detector with sub-microsecond jitter on crosstalk," in *Proc. Precise Time and Time Interval*, 1994, pp. 269–282.

[6] R. Barillet, "Thermal effects in high performance frequency synthesizers," in *Proc. Frequency Control Symp.*, 1997, pp. 980–984.

[7] P. M. Mbaye, "Réalisation d'une horloge composite pour une application physique d'échelle de temps : nouvel algorithme d'asservissement développé," PhD thesis, Université de Franche-Comté, Observatoire de Besançon, July 2011.

Environment Effect on Two Way Satellite Time and Frequency Transfer

Hong ZHANG, Huanxin LI
National Time Service Center, Lintong, China, zhong@ntsc.ac.cn

***Abstract*—Two-way time and frequency transfer (TWSTFT) is a high precision time transfer because TWSTFT via the GEO satellite can eliminate path delay mostly. Many factors affect the time transfer precision, such as: the modem time delay, the uplink and downlink path delay, a satellite transponder delay and delay of Sagnac effect etc.. These effects can be measured or calculated. However, Temperature and humidity will reduce the performance of time transfer[1]. Besides, it can not be measured and calculated. In this text, we analyzed several years' TWSTFT data including the temperature and humidity value between NTSC (National Time Service Center) earth station and international earth stations and discussed the correlation between the external environment and TWSTFT comparison result. On the other hand, we did the experiment using satellite simulation, measured the earth stations equipment time delay and recorded the temperature and humidity. In the last, we drew the conclusion with the external environment and TWSTFT comparison result and had the advice to compensate for it.**

I INTRODUCTION

Two-way satellite time and frequency transfer via geostationary satellite is potentially one of the most accurate ways to compare clocks. The high accuracy is obtained by the users simultaneously exchanging signals via a communications satellite. If the paths between the clocks are reciprocal or very nearly so, the delays cancel. The difference between the clocks is then half the difference in time interval counter readings. That is the principle of two way time transfer[2]. But in fact, many factors affected the performance of the time transfer include: the non-reciprocal path delay, the different equipment time delay between earth stations, the satellite transponder delay , Sagnac delay, the effect by temperature and humidity around the equipment. Mostly effects usually can be measured or computed while environment effects can not be gained directly. That environment as weather and temperature is not be controlled. It will reduce the performance of the time transfer and change the equipment time delay. In this paper, we did the experiment and analyzed the two way data and discussed the environment effect on time transfer. The aim of the work is to obtain more accurate time difference in two time scales.

In NIST(USA) some researchers did such a experiment, the results are that temperature coefficient of the receive delay was -150±30ps/℃ and transmit delay was -50±10ps/℃.The overall temperature coefficient for the station was -100±30ps/℃[3].From these, we may say the temperature change can lead to a large error. But the error can be reduced by temperature control or temperature compensation of the data.

II DATA OF THE WEATHER ANALYSIS EFFECTS ON THE TWO WAY TIME AND FREQUENCY TRANSFER

NTSC (National Time Service Center, China) carried the TWSTFT twice a week and 15 minutes each time with NICT (National Information and Communication Technology Institute) from 1998[4,5]. In the early time, two stations only record the weather and the time difference of two clocks. The performance of the time transfer between NTSC and NICT is good. The average of the root mean square (RMS) value of five minutes raw data fitting is about 0.3ns, some times it is big than 0.6ns. Following we analyze the weather data and drew the conclusion why the RMS is not smooth. Table1 shows the two stations weather data during this period.

As is demonstrated in table 1: column 1 'weather' means what is the weather when the NTSC and NICT earth stations carried on the TWSTFT; Column 2 'total day' means how much day when in the column 1 case during the period from MJD 51740 to 54640; Column 3 'RMS>0.6 day' means how much day when in the column 1 case and RMS value bigger than 0.6 nanosecond; Column 4 means the proportion of the RMS value bigger than 0.6 nanosecond to total day. Generally, RMS value is smaller and the time transfer is more stable. So seen from

the table 1, when both the stations are cloudy, rainy or snowy, the proportion of the RMS>0.6 day to total day is about 6%, is smaller than others. That is to say, this time the time transfer is more stable. So we can say the weather will affect the performance of the time transfer.

III Temperature influence on the TWSTFT

After May 2005, using the multi-channel modem NTSC carried on TWSTFT with five time and frequency laboratory every day. At that time, NTSC record the temperature value around the outdoor equipment. With the constant changes in outside temperature, the time difference between two time scales is changing. The following figure 1-3 show the relationship of the temperature value and the time difference.

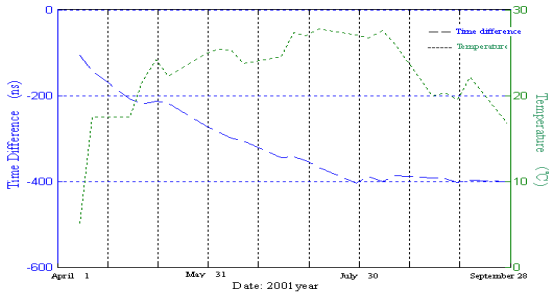

Figure 1 2001 the relationship of the time difference and temperature

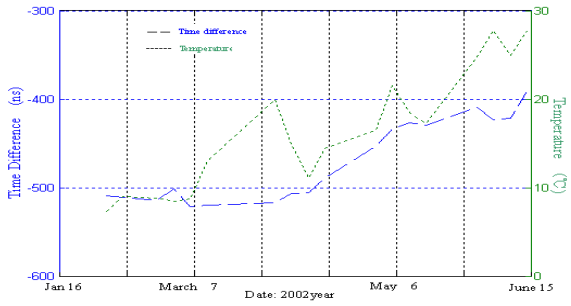

Figure 2 From Feb to June 2002, the relationship of the time difference and temperature

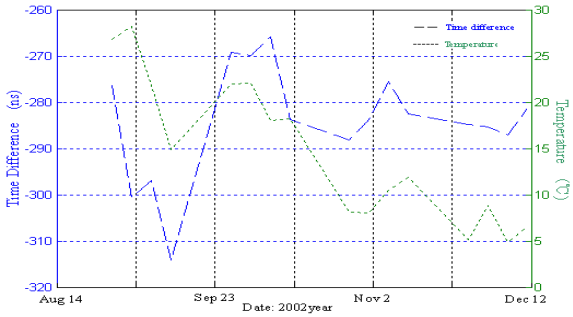

Figure 3 From August to December 2002, the relationship of the time difference and temperature

As show in the figures, the blue dots line seems to correlate with green dots line. The blue dots line represents the time difference between two scales without calibration while the green dots line represents the temperature value during the time transfer period. Seen from above the figure 2-4, when the temperature high than 12 degree, the correlation coefficient is bigger than that as the temperature less than 12 degree, the correlation coefficient shows as table 2.

IV Equipment time delay measurement experiment

In order to measure the influence of the equipment time delay with the temperature change, we used the satellite simulate transponder instead of GEO satellite in the two way time transfer. Figure 4 shows the device system connected. When the time transfer running on, we change and record the temperature around the equipment. Continuous measurement the equipment time delay at the temperature range from 3 degree Celsius to 30 degree Celsius started from December 2nd to the December 6th, 2009. Figure 5a to 5e below show the measured results, the blue lines represent the equipment time delay, the green lines represent the temperature value; the correlativity in red letter represents the correlation coefficient of the equipment time delay with temperature, for example in figure 5a: X axis unit is minute, this figure shows the total time is about 1200 minute that equal to 20 hours; Y axis unit is nanosecond, this figure shows the total time delay is about 4 ns; The front part for the temperature is 13 to 15 degree, at that time the correlation coefficient of the equipment time delay with temperature is about 0.7 while the back part for the temperature is 6 to 13 degree, at that time the correlation coefficient is about -0.2. In the figure 5b, the temperature from 6 to 13 degree, the correlation coefficient is about -0.008, very close to zero, in other words, the equipment time delay is hard to correlate with temperature. From the other figures, we also can draw the same conclusion.

Seen from the above experimental results, two-way satellite time and frequency transfer equipment time delay correlate with temperature changes. For DT4513 down converter and UT4514 up converter, during the temperature range from 6 degree Celsius to 13 degree Celsius, the converter time delay is relative stable. Maybe for the different type converter, the relative stable temperature range is not same.

As has been mentioned above, the weather and temperature have influence on time transfer. So most international time laboratory use the air condition to keep the temperature in a small range about 1-2 degree. The following we will introduce the international time laboratory device

configuration.

V. THE STATUS OF TWSTFT DEVICE CONFIGURATION AND CONCLUSION

Currently, International time laboratory's device configurations are following situations:

1. Few laboratories' TWSTFT equipment used the outdoor unit, which combines the up, down converter, power amplifier and the low noise amplifier. All of them are not be controlled by air-condition. Then the equipment time delay will effected by season temperature change.
2. The other case is that: Up and Down converter put in the room which controlled by temperature while the power amplifier and low-noise amplifier put in outdoor which not controlled by temperature. NTSC current equipment configurations belong to this situation.
3. Only the power amplifier is not controlled by air condition. Others equipment are all put in the room which controlled by temperature and humidity.
4 All the equipment including the Up and Down converter, power amplifier and low noise amplifier are all controlled by air condition.

The fourth case of the device configuration is the best choice for the time transfer. It can maximize eliminate the impact of the temperature and the humidity, so TWSTFT is more accurate and more stable. More and more international two way time laboratory agree that the temperature changes directly affect the equipment time delay and start to use the controlled system.

To sum up, temperature and humidity will affect the performance of the time transfer. The equipment can be put in the room which controlled by the temperature and humidity. The best temperature range is 6 to 13 degree Celsius. Or using the data compensate for the error caused by temperature and humidity.

REFERENCES

[1] T.E.Parker, V.S.Zhang. Investigation of Instabilities in Two-Way Time Transfer[J].34thAnnual Precise Time and Time Interval(PTTI) Meeting:381-388.

[2]. Michito Imae etc. Two-Way Satellite Time and Transfer Network in Pacific Rim Region[J].IEEE Transactions on Instrumentation and Measurement,Vol.50,NO.2,April 2001,559-562.

[3]. Franklin G. Ascarrunz etc. Earth Station Errors in two-way Time and Frequency Transfer[J].IEEE Transactions on Instrumentation and Measurement,Vol.46,NO.2,April 1997,205-208.

[4] W. Lewandowski, "Report of the 8th Meeting of the BIPM Working Group on Two-Way Satellite Time and Frequency Transfer", Proc. 32nd PTTI, 2000, pp. 229-234

[5] M. Imae, Li Huanxin et al: Two way Satellite Time and Frequency Transfer Networks in Pacific Rim Region, IEEE Transactions on Instrumentation and Measurement April 2001, Volume 50. No.2

Table1 shows the two stations weather data from MJD 51740 to 54640

weather	Total day	RMS>0.6ns day	The proportion of the RMS>0.6ns to total
Two stations are sunny day	75	9	12%
One of the stations is sunny	172	17	10%
Both stations cloudy or rainy or snowy weather	33	2	6%
Total number of the days	280	28	10%

Table 2 The correlation coefficient of time difference line and temperature profile

	date	The correlation coefficient of time difference and temperature	
		Temperature less than 12 degree	More than 12 degree
Figure 1	2001.4.10～2001.9.28		-0.545
Figure 2	2002.2.8～2002.6.15	-0.499	0.754
Figure 3	2002.8.20~2002.12.20	0.137	0.496

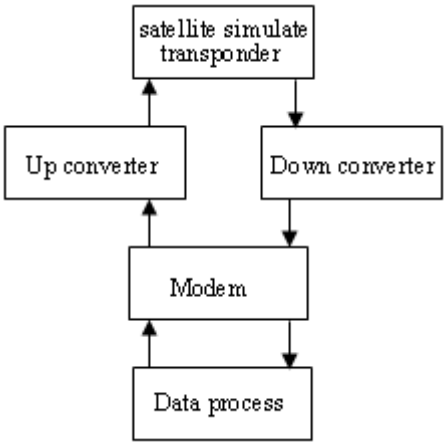

Figure 4 The equipment delay measurement system

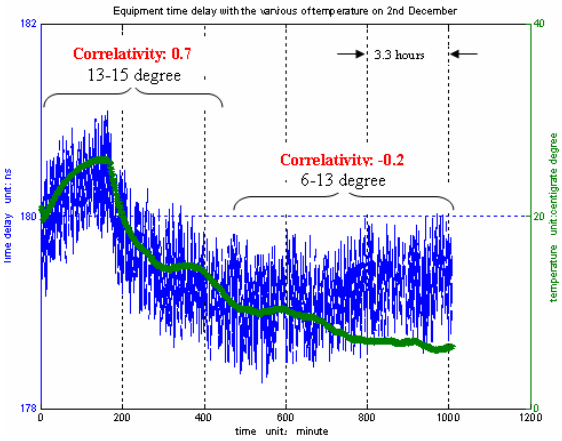

Figure 5a

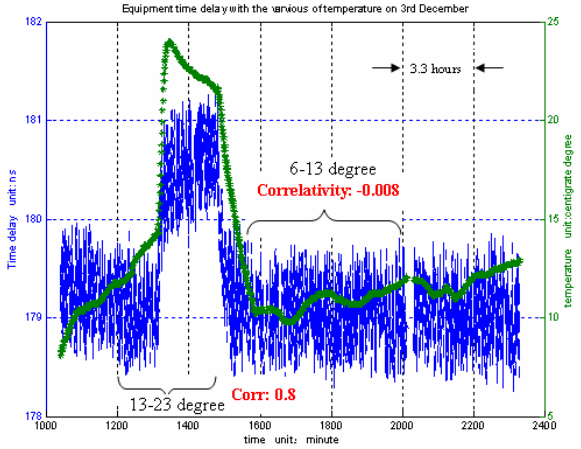

Figure 5b

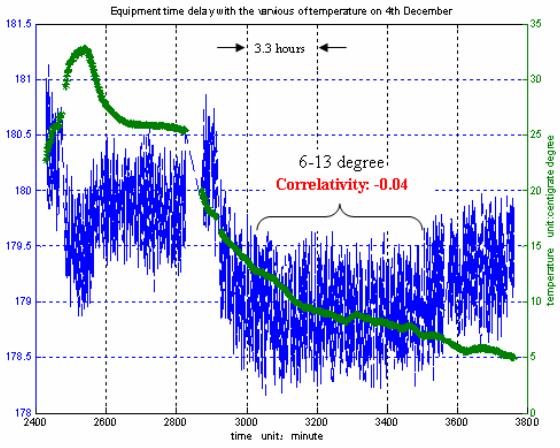

Figure 5c

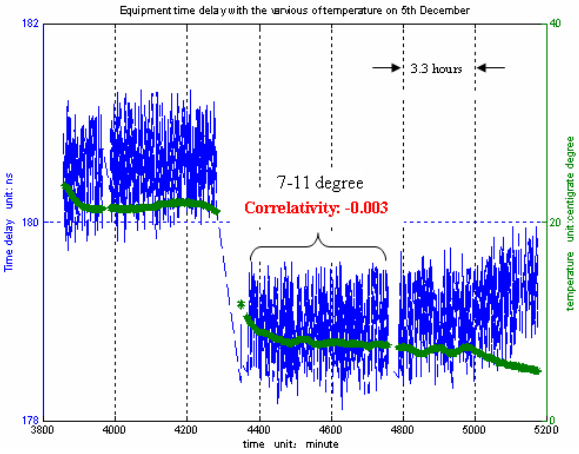

Figure 5d

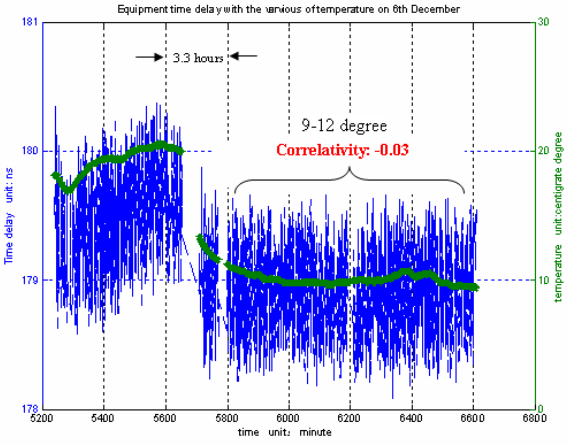

Figure 5e

Progress at the State Time and Frequency Standard of Russia

Blinov I., Domnin Yu., Donchenko S.,
Koshelyaevsky N., Kostromin V.
The Main Metrology Center of the State Time and Frequency Service
FGUP "VNIIFTRI"
Mendeleevo, Moscow region, Russia
nkoshelyaevsky@vniiftri.ru

***Abstract*— The paper presents results of development programs just finished in VNIIFTRI. Some of them, such as CS fountain standard, ensemble of new H-masers and TWSTFT station, directly improved the State Time and Frequency Standard of Russia, the influence of other are expected in closest future.**

I. INTRODUCTION

A few development programs have been just finished in VNIIFTRI. First of all new prototype of primary CS fountain standard with uncertainty $\leq 5\times10^{-16}$ runs more than three months. During November and December 2011 this have been compared across Paris Observatory CS fountain type SYRTE-FO2 (stated uncertainty $u_B \leq 2.8\times10^{-16}$). Their frequencies coincided within $\leq 5\times10^{-16}$. The metrology investigations are still continues and new results will be reported. The National time scale UTC(SU) generation based on ensemble of VNIIFTRI H-masers have been continued with RMS difference against UTC about 7-8 ns. New time algorithm for TA(SU) which is under test in VNIIFTRI is based on regular calibration H-masers frequency and frequency drift relative to primary CS standards. Basing on these data we produce clock frequency prediction for next step. The algorithm was first successfully tested basing on simulated data. Operational time transfer equipment consists of set GNSS receivers of TTS3 and TTS4 type. Time transfer link resolution between SU and USNO have been estimated and demonstrated u_A frequency comparison uncertainty consi-derably less than 1×10^{-15} for sample time more than 10 days. The other very important output is TWSTFT experimental sessions with PTB and NICT via AM2 satellite. Till now this link is not calibrated and can't be used to the full extend to contribute to TAI. This is the most urgent need especially keeping in mind much more better u_A uncertainty for TWSTFT link compare to GNSS one. The Master Clock for real time realization of UTC(SU) have been developed and yielded RMS difference UTC(SU)-MC(SU) $\leq$ 1 ns. A new laser ranging instrument have been just installed in VNIIFTRI and the other one is expected to be installed in secondary state time and frequency laboratory in Irkutsk in closest future. These instruments open the door to join to T2L2 time transfer.

A few investigation programs are also in progress. These are frequency standard on ^{87}Sr neutral atoms in an optical lattice, T&F transfer over optical fiber.

The paper will deliver more detailed information on particular projects and stated current status of State Time and Frequency Standard of Russia.

II. CS FOUNTAIN STANDARDS

At the moment we have two operational CS fountains – CS 103 and CS 105, Fig.1.

The estimated uncertainties u_B of them are $\leq 5\times10^{-16}$ and $\leq 3\times10^{-15}$ correspondingly. Results of CS - H maser frequency

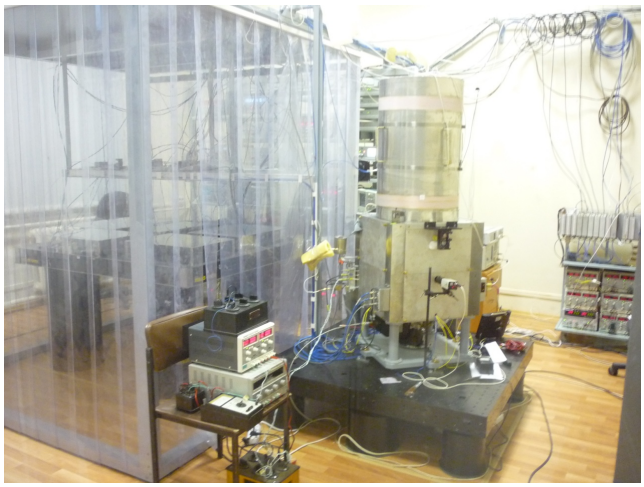

Fig.1 CS 103 general view

comparison shows white frequency noises of $2\times10^{-15}/\sqrt{\tau}$ and $3\times10^{-15}/\sqrt{\tau}$ with τ in days, Fig.2. During November and December 2011 CS 103 have been compared across Paris Observatory CS fountain type SYRTE-FO2 ($u_B \leq 2.8\times10^{-16}$). Their frequencies coincided within $\leq 5\times10^{-16}$. The metrology investigations are still continues and in closest future we expect to deliver official protocols to the BIPM.

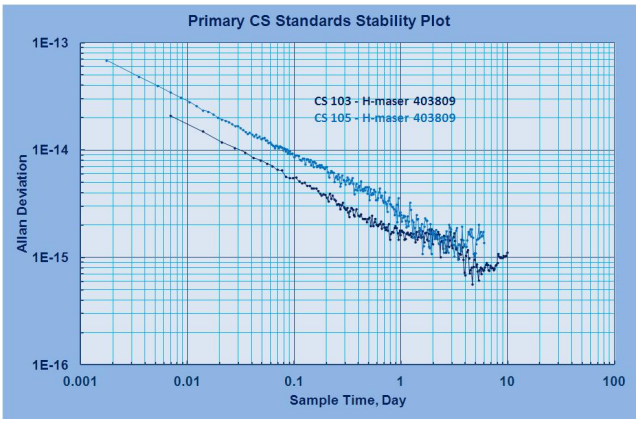

Fig.2 CS 103 and CS105 stability plot relative to H-maser

III. H-MASERS ENSEMBLE AND NEW TIME ALGORITHM

Two operational ensembles each of four H-masers locate in environmentally controlled chambers. Frequency stability of the H-masers varies within $4\text{-}6\times10^{-16}$ for sample times 1 – 10 days. Frequency drift of the H-masers $1\text{-}4\times10^{-16}$/day. Currently time algorithm to generate independent atomic time scale TA(SU) is based purely on the ensemble of H-masers. As consequence TA(SU) manifests residual frequency drift inevitable for H-masers. TA(SU) forms a reference frame for National time scale UTC(SU) and steering corrections introduced to UTC(SU) basing on it's comparison relative to UTC produced RMS difference (UTC – UTC(SU)) ≤ 10 ns.

A new time algorithm for TA(SU) which is under test in VNIIFTRI is based on regular calibration H-masers frequency and frequency drift relative to primary CS standards. Basing on these data we produce clock frequency prediction for next step. The algorithm was first successfully tested basing on simulated data. For this purpose frequency difference of CS standard with measured white frequency noises of $2\times10^{-15}/\sqrt{\tau}$ with τ in days relative to abstract ideal reference (REF) and artificially limited by flicker floor at the level about 3×10^{-16} have been simulated, Fig.3. Apart from

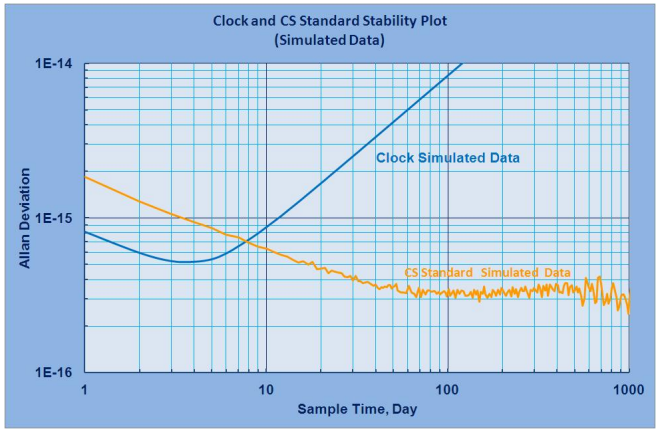

Fig.3 CS fountain and H-maser simulated data stability plot relative to REF

this 6 H-maser's readings relative to the same reference also have been simulated. Clock frequency stability, drift and drift variation of simulated data were in conformity with actual clock performances.

Then was calculated frequency difference of master clock relative to CS standard for interval 1 month and other clock differences relative to master clock. These set of data were source for frequency prediction of H-masers to the next month. As a first step we generated atomic time scale TA(SU) with time unit matched to that of CS 103.

Consequently we got time scale with time unit which coincided to CS within 3×10^{-17} and RMS difference ≤ 3.3 ns, Fig.4.

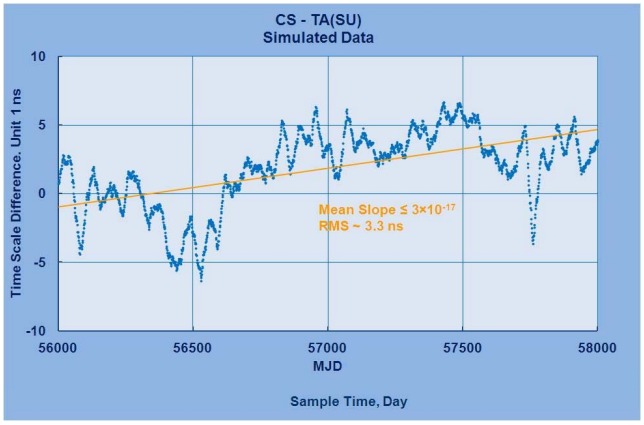

Fig.4 Time scale difference CS 103-TA(SU) (simulated data)

Stability estimations of the simulated TA(SU) across CS standard, Fig.5, manifests bump about 3 dB at 30 days, which is typical for control system, and then stability improvement which in turn exceeded original CS standard stability relative to REF. This means only that TA(SU) followed carefully any changes in CS standard. On other hand TA(SU) stability across REF manifested considerable improvement for sample time from 1 day to 10 days in conformity with statistical av-

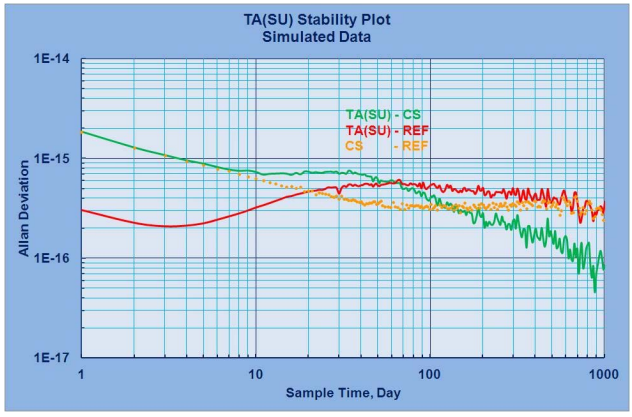

Fig.5 TA(SU) stability plot (simulated data)

eraging (proportional $\sim1/N^{1/2}$) and obvious clock frequency

drift suppression due to regular clock frequency calibration across CS standard, then the same bump at 30 days. For bigger sample time stability coincided with that of CS standard in conformity with fundamentals of control theory.

The next step was UTC(SU) generation based on TA(SU) and steered to UTC. For this purpose we first of all stimulated REF – UTC sequence. Here we proceeded from the following assumptions:

- UTC based on TAI, which by turn on EAL [1];
- current EAL stability is defined in Circular T [2];
- for sample times bigger than 30 days TAI stability exceeded that of EAL due to steering corrections and manifested stability level about $(1\text{-}2)\times10^{-16}$;
- UTC(SU) link uncertainty u_A to UTC is currently limited by 1 ns, and in future in case of TWSTFT link by ~0.3 ns [2].

Basing on these assumption we simulated REF – UTC data and then generated UTC(SU) basing on time differences between these time scales. At first step (1 month according to current UTC time lag) a role of UTC played TA(SU). Then steering frequency corrections have been applied every month to produce UTC(SU), Fig.6.

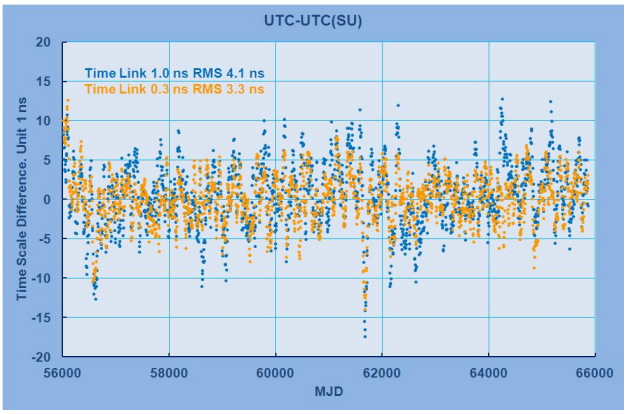

Fig.6 UTC – UTC(SU) scale differences
for various link uncertainty

So the main goal was reached. Basing on the new primary CS fountain standard, ensemble of H-masers, and new time algorithm we have shown, at least at simulation level, feasibility to generate atomic time scale TA(SU) with time unit matched to that of primary CS standard within 1×10^{-16} and stability level $\leq 5\times10^{-16}$. Coordinated UTC(SU) have steered to UTC with RMS difference < 5 ns.

Our next task will be demonstrate such a level basing on real CS standard and clock readings.

IV. Time Transfer Links

Operational time transfer equipment consists of set GNSS receivers of TTS3 and TTS4 type. Basing on last year data we have estimated u_A uncertainty for long range time link between our laboratory SU and USNO. This estimation have been done basing on readings SU TTS3#26 receiver (GPS C/A and P3) and USNO AOS SRC TTS-2 #014 (GPS C/A) and ASHTECH Z-XII3T #RT920012203 (GPS P3). Then we calculate second difference

$$\{[\text{UTC(SU)-GPSST]-UTC(USNO)-GPSST]}\}_{C/A} - \{[\text{UTC(SU)-GPSST]-UTC(USNO)-GPSST]}\}_{P3}$$

In this way we've eliminated influence of UTC(SU) – UTC(USNO) for big sample time. The obvious manifestation of this limitation is coincidence of C/A and P3 link resolution (green and blue curve) for sample time more than 10 days, Fig.7. The rest difference contains only noises in both time-

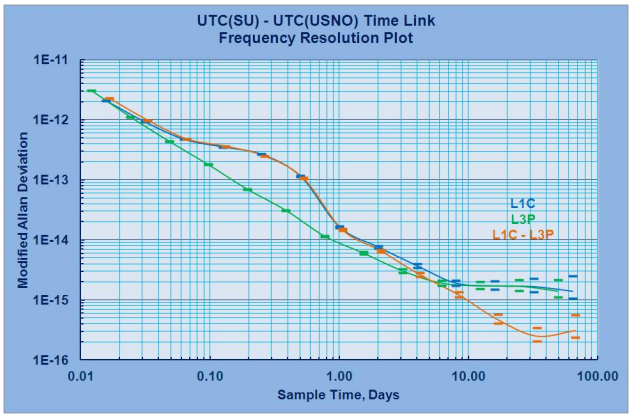

Fig.7 UTC(SU) – UTC(USNO)
time link frequency resolution plot

links. C/A – P3 difference demonstrate u_A frequency comparison uncertainty considerably less than 1×10^{-15} at least for sample time more than 10 days. Such a resolution level open the door for frequency comparisons with remote CS primary standards.

The other very important output is TWSTFT experimental sessions with PTB and NICT via AM2 satellite. Due to AM2 limitations only about ten sessions per day is now available. Till now this link is not calibrated and can't be used for accurate estimation of time scale difference. Nevertheless this doesn't prevent to contribute to TAI, because of in this case only time scale differences is necessary and keeping in mind much more better u_A uncertainty for TWSTFT link compare to GNSS one, Fig.7.

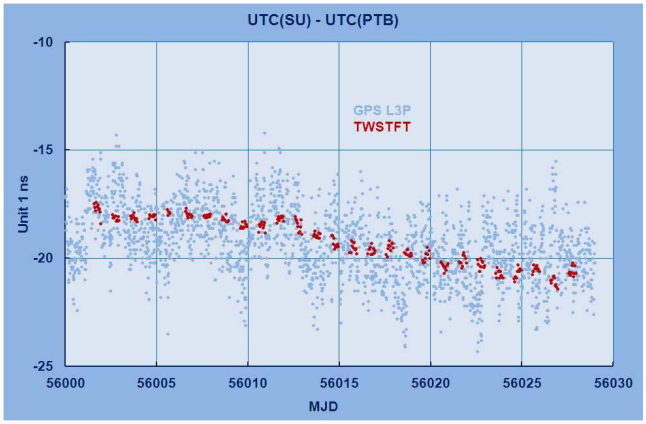

Fig.7 UTC(SU)-UTC(PTB) via GPS L3P and TWSTFT

V. UTC(SU) REAL TIME MASTER CLOCK

Basing on existing ensemble of H-masers and phase and frequency offset generator HROG-5 Master Clock for real time realization of UTC(SU) have been developed. Master Clock operates reliably and accurately for half a year and yields RMS difference UTC(SU)-MC(SU) ≤ 1 ns.

VI. A NEW LASER RANGING INSTRUMENT

A new laser ranging instrument have been replaced old one in Mendeleevo, Fig 8.

Fig.8 A new laser ranging instrument in VNIIFTRI

Main features of the instrument:

- wavelength 532 nm
- pulse energy 2 mJ
- pulse width 200 ps
- repetition rate 300 Hz
- u_A 1 cm
- u_B 1 cm

Despite this instrument is mainly designated for the Earth orientation parameters determination we are going to utilize it for remote time scale comparison within T2L2 technology.

VII. INVESTIGATION PROJECTS

An accurate transfer method using bi-directional signal transmission along a 50 km fiber have been developed. Our results show that the optical transmission fibers over several tens kilometers have the capability for time synchronization accuracy better than 1 ns.

We continue our development [3] of an optical lattice clock on Sr atoms. As a first step for realization of the project Sr atoms have been effectively cooled and traped in a blue magnetic-optical trap employing a Zeeman slower. The first stage MOT aws operated on $^1S_0$-$^3P_1$ transition at 461 nm. The Sr-MOT is operative and the first observation of the cold atom cloud in the blue MOT was reported.

ACKNOWLEDGMENT

O. Sokolova – gratefully acknowledges for her contribution to new time algorithm code creation and software testing.

REFERENCES

[1] B.Guinot, C.Thomas, “Establishment of International Atomic Time”, Annual Report of the BIPM Time Section, Volume 1, 1988, Part D, Scientific Contribution, D1-D22, Bureau International des Poids et Mesures, Pavillon de Breteuil, F-92312 Sevres Cedex.

[2] Circular T 288, 2012 January11, 10h UTC, Bureau International des Poids et Mesures, Organization intergouvernementale de la Convention du Metre, Pavillon de Breteuil, F-92312 Sevres Cedex.

[3] S.Slusarev et al., “The Design Consideration for a ^{87}Sr Optical Clock in VNIIFTRI”, Proceedings of the Joint Conference of the IEEE International Frequency Control Symposium & European Frequency and Time Forum, pp. 736-738, May 1-5, 2011, San Francisco, California, USA.

Ongoing Renewal of the ROB PTF

Wim Aerts and Pascale Defraigne
Royal Observatory of Belgium
Ringlaan 3, B-1180 Ukkel, Belgium
Telephone: +32 (0)2 373–0283
Email: wim.aerts@oma.be

***Abstract*—In order to increase the reliability of the PTF at ROB and hence the reliability of UTC(ORB), the time was high for replacement of some major equipment. Obviously this was the ideal opportunity to give the PTF an upgrade and to solve some problems and issues. First the "old" PTF architecture was studied to pinpoint its shortcomings and possible improvements. Then a "new" PTF layout was defined and is gradually being implemented. This new PTF setup focuses on automatic (health) status monitoring, as well as on automatic control, of all operational devices. This should allow early detection of problems and prepares the PTF for future implementation of steering algorithms, such as a clock ensemble.**

***Index Terms*—time keeping, time dissemination**

I. Introduction

As is the case at many Observatories world wide, at Royal Observatory of Belgium (ROB) (or Observatoire Royal de Belgique (ORB)) too, time keeping has been one of the major activities, already since its start in 1832.

Since then, many upgrades and adaptations were applied to our Precise Timing Facility (PTF). In 1968 the first atomic clock was installed, that later on served for a ROB implementation (and approximation) of Universal Time Coordinated (UTC), called UTC(ORB). But the most recent considerable renewal of the PTF already dates back more than ten years ago.

Hence the devices started suffering from old ages aches. Our old CH1-75 maser fell out with an error on the cavity auto tuning Printed Circuit Board (PCB) after 18 years of service. The HP5071A Cesium Beam atomic clock, bought at about the same time, ran out of cesium. The contacts of our RACAL-DANA 1250 universal switch controller were worn, introducing oscillations when closing. And our RACAL-DANA 1992 Time Interval Counter (TIC) introduced jumps of 50 ns.

In short, the time was high for a complete renewal. This article reports on this work in progress. First the specifications were defined (see Sect. II), then the old layout was reviewed to pinpoint its shortcomings (see Sect. III-A), suggest improvements (see Sect. III-B), and draw a new layout (see Sect. III-C). Currently, the new layout is being implemented (see Sect. IV).

II. Specifications

Without doubt, the major end product of the PTF is the real time implementation UTC(ORB).

This UTC(ORB) has to stay within 100 ns from the (a posteriori) calculated UTC, as requested by the Bureau International de Poids et Mesures (BIPM). Hence it should be deduced from atomic clocks with a decent stability, and be steerable, to correct or avoid large deviations.

An accuracy of 100 ns is definitely enough for dissemination to the public via e.g. a Network Time Protocol (NTP) service, due to the (unpredictable) jitter on the Internet that reduces the accuracy at the end users node to roughly a few (tens of) ms, see e.g. [1]. But also for Precision Time Protocol (IEEE-1588) (PTP), promising µs accuracy, which will go operational at the ROB PTF in the near future, this should do.

For Internet time services, such as NTP or PTP, hence robustness and uptime are of greater concern than stability. So multiple NTP servers should be installed, which have a backup timing input, like NAVSTAR Global Positioning System (GPS) or DCF77.

But besides generating UTC(ORB), the clocks at our PTF also contribute to Temps Atomique International / International Atomic Time (TAI) as managed by the BIPM. This means that if UTC(ORB) is generated by a master clock (as opposed to an oscillator steered with a clock ensemble) the output of this master clock should be externally steered (not using the synthesizer in the output circuitry of the clock) so that the master clock itself is free running and hence can contribute to TAI.

Moreover, to guarantee input data for the TAI of a decent quality, the (health) status of the clocks should be monitored so that in case of (hardware) degradation, the clock data is no longer considered for submission to the BIPM.

For the TAI, the clocks should be operating continuously. Down time should be reduced as much as possible. Consequently, all clocks installed are connected to a direct current (dc) backup power supply.

Yet another end product of the PTF are the 5, 10 and 20 MHz reference sine waves. They are currently only used for Local Oscillator (LO) generation in Global Navigation Satellite System (GNSS) reference station receivers for scientific applications, such as ionosphere modeling. But they might come in handy in future for measuring stability of oscillators.

This however does not impose requirements on stability or uptime other than those that were already discussed.

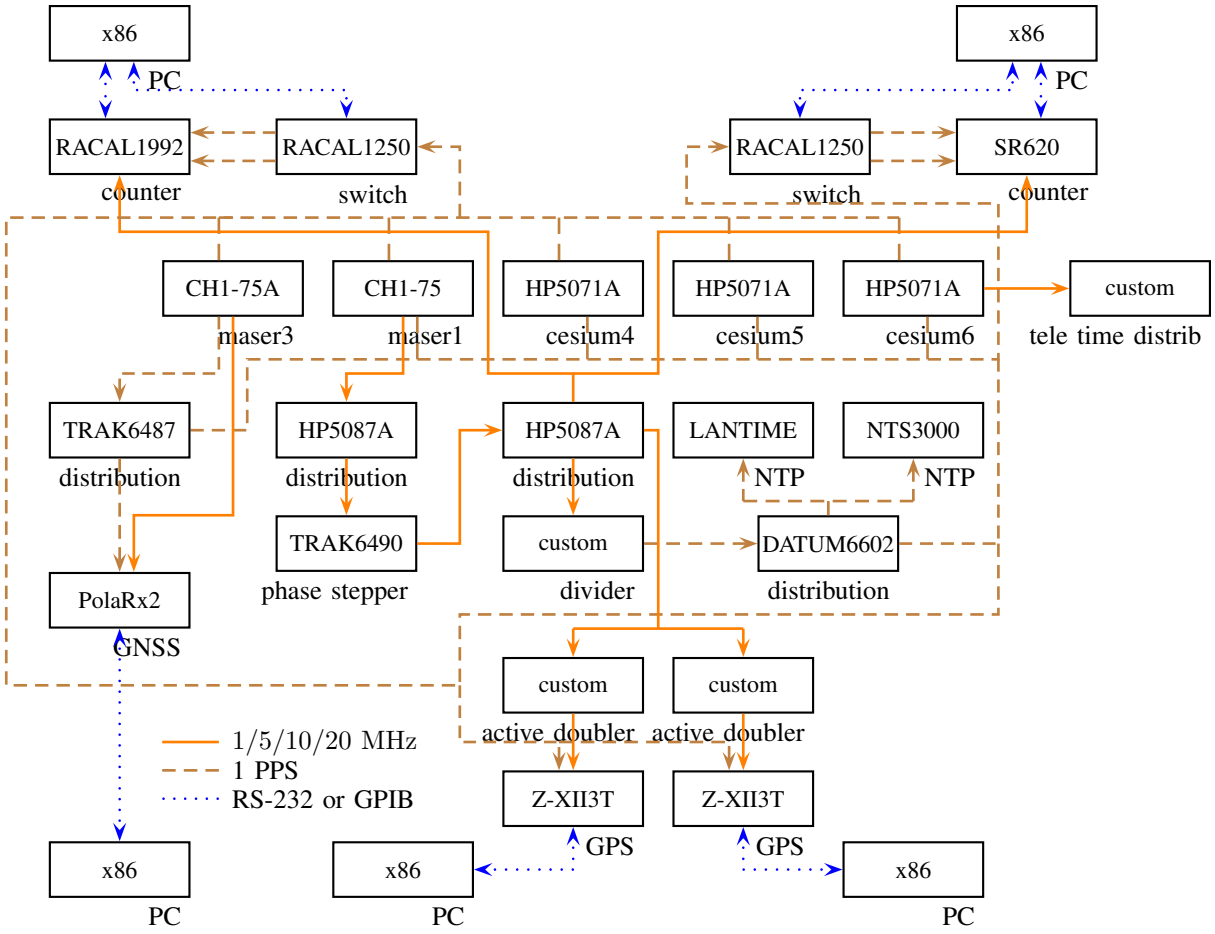

Fig. 1: The "previous" (2009) layout of the ROB PTF.

III. Design

Based on the specifications and their implications as given in Sect. II, the previous (or "old") PTF layout was reviewed, and transformed into a new layout, that is easier to manage and maintain.

A. Review of the "old" layout

The old (2009) layout, depicted in Fig. 1, actually served as a good reference (or starting point) for the design of the new layout.

The main shortcomings in this 2009 layout were:

- quality checks were only done on the output, not at intermediate points of the signal chain. This may not necessarily be a problem for guarantee of end product quality, but prevents fast and accurate determination of the source of a problem.
- except for measuring the clock outputs, all monitoring and maintenance, including UTC steering, was to be manually performed.

B. Improvements

1) Health and status monitoring: Any device in the new layout should be continuously monitored for Service ReQuest (SRQ) or alarms, and regularly queried for status variables. In case of anomalies, an e-mail and Short Message Service (SMS) alert should be issued.

2) Automatic steering of output: The phase stepper in the new PTF layout, used to steer the output of the (master) clock, should be computer controllable. This allows remote or automatic control and is a first step in implementing a clock ensemble, steering the phase stepper based on measurement of all clocks in the PTF, which is indeed also foreseen in the "new" PTF layout.

3) Simplified signal chain: As amplification should be avoided, due to the temperature dependent output phase of (most) amplifiers and the added noise, active frequency doublers should be replaced by passive ones and distribution amplifiers by power splitters whenever required power levels allow to do so.

Furthermore, because in the TIC used for clock comparison, the UTC pulse serves as the reference for *all* measurements, there is no use in passing this UTC pulse through a switch matrix. It would make more sense to directly connect the UTC pulse to the TIC. Selection of a clock to measure can simply be obtained using a Single Pole Multi Throw (SPMT) switch.

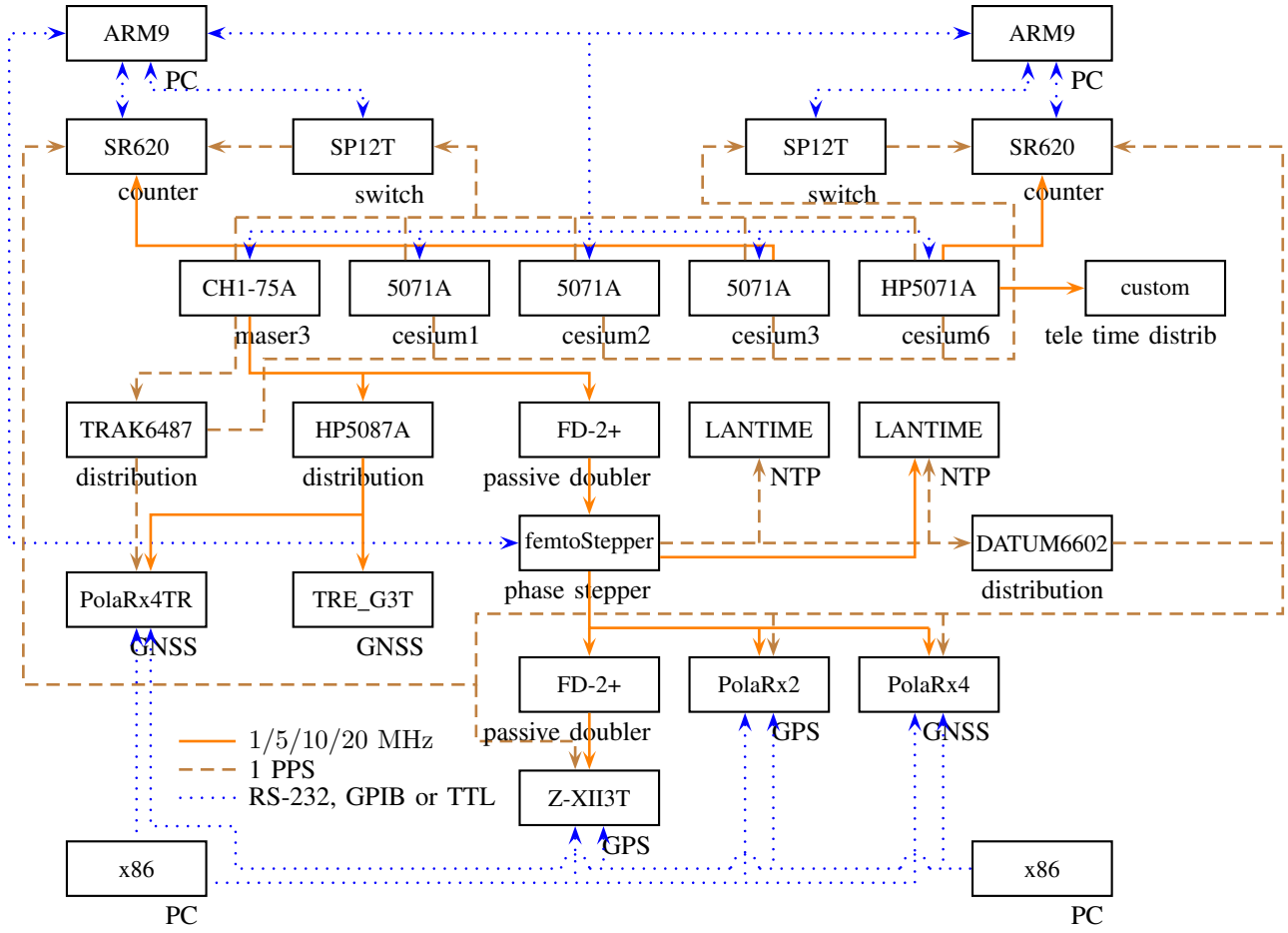

Fig. 2: The "new" (2013) layout of the ROB PTF.

C. The "new" layout

Starting from the "old" layout in Fig. 1 and applying all improvements detailed in Sect. III-B, one gets the "new" layout as depicted in Fig. 2.

IV. Implementation Details

1) Health and status monitoring: In order to monitor the status of the clocks, computers query the clocks regularly for their most important control variables and status information. In case of errors or abnormal values, the operator is alerted by e-mail and SMS.

The KVARZ CH1-75A maser is connected to a computer over General Purpose Interface Bus (GPIB) with an Agilent 82357B Universal Serial Bus (USB)-to-GPIB adaptor. The Digital to Analog Converter (DAC) value of the cavity auto tuning system is recorded every hour and the error codes of the maser are checked to be `ppp`. This results in log lines like the one below:

```
#timestamp   TIME   SYNTH    DAC    ERR
1330036201 223001 37175 2551341 pp2
```

For the HP/Agilent/Symmetricom 5071A Cesium Beam Tube (CBT) clocks a lot more variables are monitored. Their values are recorded four times a day. Tab. I lists intervals for the internal variables. They are based on [2] but differ slightly as each device is unique and moreover [2] does not deal with high performance cesium beam tubes. Once outside the interval of Tab. I, an alert is issued and close inspection of the device is mandatory. No monitoring of the changes of the variables is performed yet, although this will signal device failure much more timely, according to [2].

As can clearly be seen on the detailed layout in Fig. 2, the 5071A clocks are monitored by a "master" and a "backup" computer. But the device only houses a single (3 wire Tx, Rx and GND) serial RS-232 port. Hence the circuit in Fig. 3 was implemented to allow (non simultaneous) serial communication with the clock from multiple computers.

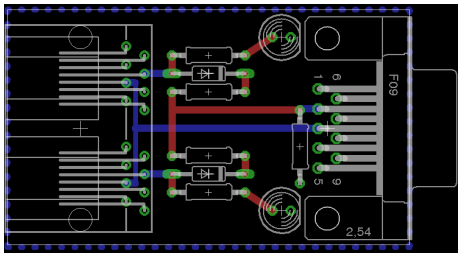

Fig. 3: PCB for connection of 2 computers to a single 5071A.

TABLE I: Intervals for 5071A variables.

variable	unit	interval from manual	interval from [2]	interval used
Beam current	μA	-	-	0.1
C-field current	mA	10.00 to 14.05	12.1 to 12.2	12.1 to 12.2
Ion Pump current	μA	0 to 40	0 to 0.5	0 to 11.5
Signal gain	%	14.4 to 58	14.4	14.4
RF Attenuators	%	0 to 100	15 to 35	15 to 35
Temperature	°C	-	30 to 50	30 to 50
Oven voltage	V	0 to 10	7 to 9	5 to 9
Electron Multiplier voltage	*volt*	1000 to 2553	0 to 2552	1000 to 2000
Hot Wire Ionizer voltage	V	-	0.9 to 1.1	0.9 to 1.1
Mass Spectrometer voltage	V	-	10 to 14	10 to 14
DRO tuning	V	-	5 to 7	2 to 7
SAW tuning	V	-	-2.5 to 2.5	-2.5 to 2.5
87 MHz PLL	V	-	1.0 to 3.5	0.5 to 3.5
9 MHz PLL	V	-	2.5 to 3.5	1.5 to 3.5
Oscillator Oven voltage	V	-10 to -5	-9 to -8.5	-9 to -8.5
+5V power supply	V	-	5.0 to 6.0	5.0 to 6.0
+12V power supply	V	-	12.0 to 12.5	12.0 to 12.5
−12V power supply	V	-	-13 to -12	-13 to -12
Oscillator Control voltage	%	-95 to 95	-20 to 45	-30 to 45

2) Automatic steering of output: The new phase stepper, a SpectraTime femtoStepper, is connected to the same "master" and "backup" computers as the clocks. A binary, written in `C` allows automatic control. A `bash` script wraps the binary and provides the operator with an easy to use interface, depicted in Fig. 4.

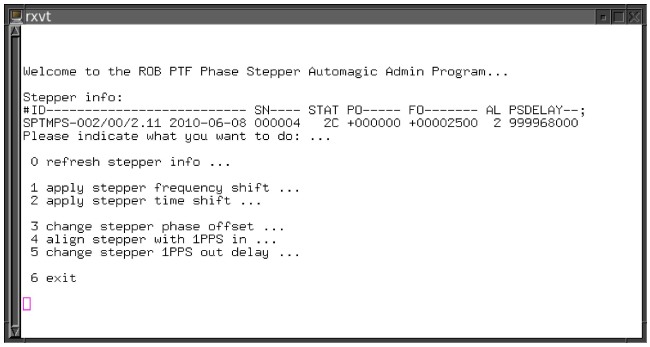

Fig. 4: Screen dump of the phase stepper control tool.

Another advantage of the new phase stepper is that it contains an oscillator inside that is locked to the input signal. This will certainly add noise and degrade the short term stability of the time and frequency signals as put out by the device. But, on the other hand this adds robustness: whenever the input fails, the device will still continue on its internal oscillator, and hence still be capable of feeding the downstream devices.

The other choice for providing robustness is installing a device that automatically switches over to a second frequency standard in case the master input fails.

This would however inevitably result in a (small) interruption of the frequency output signal (of 5 ms as measured on the Pendulum DA-34 with option 16). This would stop all connected GNSS receivers. Hence it was opted for the "flywheel" option of using an external oscillator locked to the master clock and offset steered.

3) Simplified signal chain: In the "new" layout, the HP5087A amplifiers are no longer used for frequency doubling. Instead is opted for the Minicircuits FD-2+.

The replacement of the RACAL-DANA 1250 switch boxes by CEI SP12T-210520 RF switches is still ongoing. These new RF SPMT switches are controlled with Transistor-Transistor Logic (TTL) signals from an Artila Matrix-520 ARM9 embedded computer. Due to technical problems with these devices, however, the authors would not recommend this type above other devices from other vendors available on the market.

The replacement of pulse and frequency distribution amplifiers by power dividers is still investigated.

V. Conclusion

In this work, we reported on the ongoing renewal of the PTF at ROB. Besides replacing old devices with new ones, also the entire PTF layout was reviewed and changed where advantageous.

The major improvements in the new layout with respect to the old layout, are automatic monitoring and control of all equipment and signal chain simplification whenever possible.

References

[1] D. L. Mills, "On the accuracy and stability of clocks synchronized by the network time protocol in the internet system," *ACM Computer Communication Review*, vol. 20, no. 1, pp. 65–75, 1990.

[2] H. Chadsey, "An automated alarm program for HP5071A frequency standars," in *31st Annual Precise Time and Time Interval (PTTI) Meeting*, 1999.

Development of a Kalman filter based GPS satellite clock time-offset prediction algorithm"

John Davis
National Physical Laboratory
Teddington, TW11 0LW, UK
john.davis@npl.co.uk

Santosh Bhattarai and Marek Ziebart
Space Geodesy and Navigation Laboratory
University College London
WC1E 6BT, London, UK

***Abstract*— An enhanced deterministic model along with a stochastic model for describing clock noise is used to compute predictions of the time-offset of individual GPS satellites from the IGS rapid timescale. These are determined with significantly lower prediction uncertainties than may currently be obtained using the IGS ultra-rapid predictions. At prediction length of one day IGS prediction errors are commonly of the order of several ns for all GPS satellite clocks. In comparison the new techniques offers to limit prediction errors at the order of 1 ns for prediction lengths of one day in the newer generation Block IIR and IIF satellites. The factors contributing to the uncertainties in the IGS predictions are discussed. The application of a Kalman filter based prediction algorithm is shown to produce close to optimal predictions.**

I. INTRODUCTION

Accuracy of individual GPS satellite clock time-offset estimates from GPS system time is fundamental to the use of GPS technology for positioning, navigation and timing applications. Estimates of time differences between pairs of GPS satellite clocks are also valuable.

Clock prediction techniques for precise oscillators typically combine a model of deterministic properties such as time-offset, normalized frequency offset and linear frequency drift with a model describing the stochastic processes driving the phase and frequency of the oscillator [1]. Such a technique, commonly used for ground-based precise clocks, is applied here to space-borne clocks with some differences. For example, in the case of GPS satellite clocks, it has been shown in [2] that signals with periods of 6 and 12 hours must be modeled explicitly into a GPS space clock predictor to produce results suitable for high accuracy applications. One such method to account for periodic signals in a GPS satellite clock is presented in [3]. Real-time estimation of GPS satellite clocks has been investigated in [4, 5, 6]. Kalman filter based techniques for clock prediction have been adopted successfully [7].

In this paper a Kalman filter based method is described that has been developed to produce predictions of individual GPS satellite clock time-offsets relative to the IGS rapid timescale and predictions of the time differences between individual pairs of GPS clocks. We examine the predictability of individual GPS satellite clocks and also of the time differences between them. Section II describes features of the IGS clock predictions that could be limiting their quality. In section III the new prediction algorithm is discussed. Section IV and V show results of the technique in predicting individual clocks and the time difference between pairs of clocks respectively. Section VI discusses the potential impact of improved satellite clock predictions for position computation using the precise point positioning (PPP) strategy. Section VII concludes with a discussion.

II. CHARACTERISTICS OF THE IGS PREDICTIONS

The International GNSS Service (IGS) [8] provides GPS users with individual GPS satellite clock time-offset predictions with prediction lengths varying from 15 minutes to 1 day. These prediction sets are provided once every 6 hours as part of the IGS ultra-rapid clock products. A detailed performance analysis of this product has been carried out and an alternative method has been developed and shown here that aims to improve satellite clock prediction performance.

The study of the IGS satellite clock predictions during the period July 2011 to February 2012 revealed several characteristics:

- IGS prediction files are released every 6 hours with each new file providing satellite clock time-offset predictions relative to a new IGS ultra-rapid timescale and belonging to a new prediction run with its unique set of initial time-offset and normalized frequency offsets.
- Signals with periods of 12, 6, 4 and 3 hours are observed in many of the GPS satellite clocks.
- There is significant linear frequency drift in the rubidium satellite clocks.
- Large discrete changes in clock frequency occur in many satellite clocks. These are usually unique events, however these do occur with regularity in a few satellite clocks.

Some of these observed characteristics are shown in this paper for GPS PRN 16 which, in the time period considered in the analysis, corresponds to GPS satellite vehicle number (SVN) 56, a Block IIR satellite with a rubidium as the active onboard frequency standard. At the time of writing on 1 May 2012, there are 19 Block IIR satellites with active rubidium clocks out of 32 total GPS satellites in orbit.

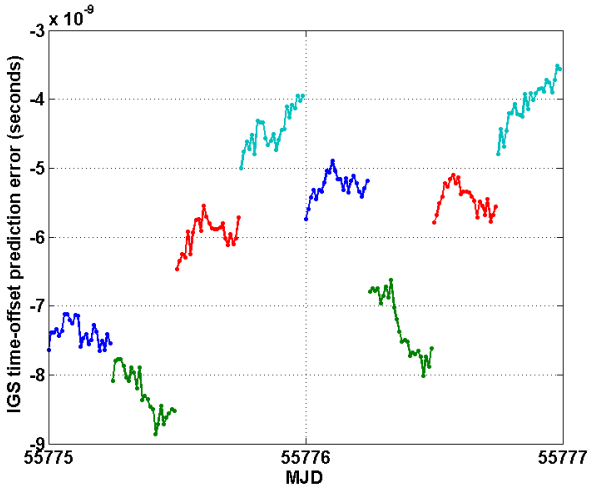

Figure 1 IGS prediction data sets.

Figure 1 shows the IGS ultra-rapid predictions of the clock on satellite PRN 16 using the first six hours of successive IGS ultra-rapid prediction sets. Large discrete changes in the prediction values occur at the boundary of each six-hour data block. This is due in part to a new ultra rapid timescale being used for each block, and in part to the discrete change of the start time of the prediction.

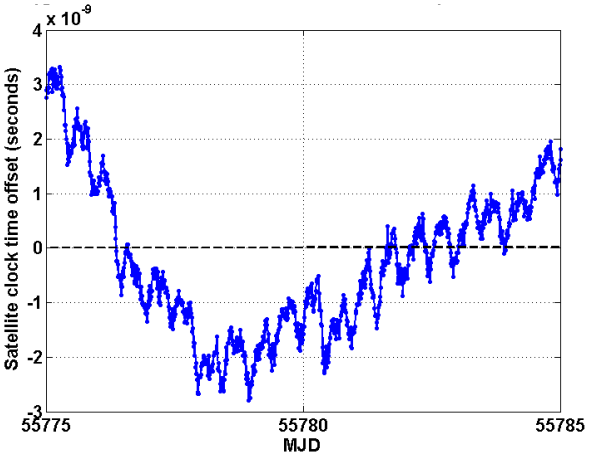

Figure 2 Time-offset from the IGS rapid timescale of GPS satellite PRN 16.

Figure 2 shows periodic signals with periods of multiples of half a sidereal day along with a significant linear frequency drift.

III. THE NEW PREDICTION ALGORITHM

A GPS satellite clock prediction algorithm has been developed. This uses both rapid (IGR) and ultra-rapid (IGU-O) IGS estimated clock data as inputs to a Kalman filter. The algorithm operates five times per day, four times on receipt of new IGU-O data sets and once on receipt of a new IGR clock data set. The stages in the algorithm processing are shown in figure 3.

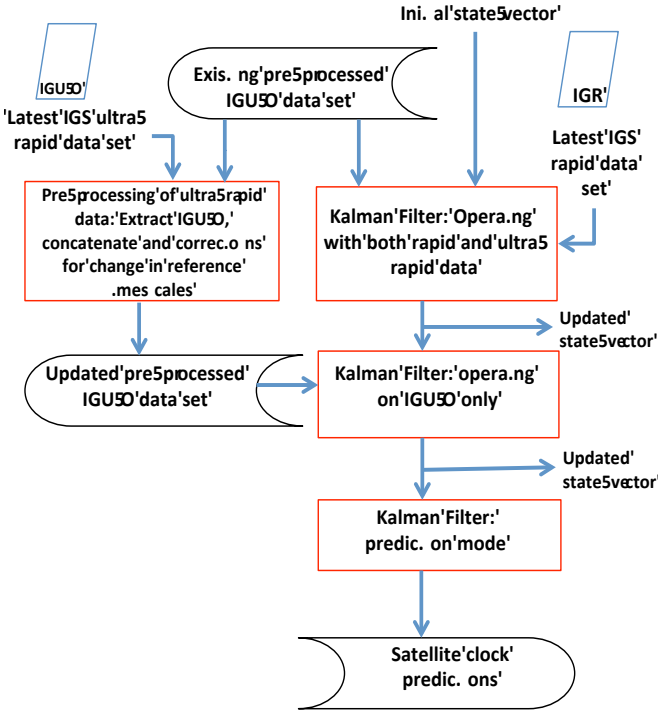

Figure 3 Overview of the new clock prediction algorithm

The ultra-rapid clock data is pre-processed, using data from all available satellites to correct for the resetting of both the time-offset and normalized frequency offset that occurs with each new ultra-rapid data block.

Standard Kalman filter equations [9] are used in this algorithm, with both IGR and IGU-O clock data being input at each epoch. Currently 15 minutes data spacing is used. At epochs where only ultra-rapid clock data is available the algorithm will input only this data set. The algorithm is designed so that estimates made at the most recent epochs will have made use of all available IGR and IGU-O clock data. Satellite clock predictions are obtained by extrapolating the state vector propagation equation and the parameter covariance matrix propagation equation in the absence of any input data.

The state vector, x, consists of the following components

$$x = (R_x, R_y, R_z, U_x, U_y, x_{p1} \ldots x_{p2n}, x_{m1} \ldots x_{mr}) \qquad (1)$$

where R_x, R_y and R_z are the time-offset, normalized frequency offset and linear frequency drift of the satellite clock from the IGS rapid timescale. U_x and U_y are the time

and normalized frequency offsets between the rapid and the pre-processed ultra-rapid estimates of the satellite clock offsets. These are caused by errors accumulating in the ultra-rapid pre-processing technique. $x_{p1}\ldots x_{p2n}$ model n periodic clock signals, there are two state vector components per signal. $x_{m1}\ldots x_{mr}$ consists of r state vector components that model noise memory processes in the clock noise using either Markov or integrated Markov processes [7].

To obtain close to optimal performance, the values of the associated clock noise parameters, and initial values of the Kalman filter state vector and parameter covariance matrix, must be carefully determined. This may be achieved using a significant length of historical data. Up to one month of historical data has been used in this study.

The new prediction technique has the potential to offer the following performance improvements in comparison with the predictions of the IGS:

- Ability to cope with the realignment of the IGS ultra-rapid timescales with the release of each new IGU-O set.
- Effective identification and prediction of periodic features.
- Unbiased predictions in the presence of linear frequency drift.
- Improved predictions of individual GPS satellite clocks (in an RMS time-offset prediction error sense).
- Improved predictions of clock differences.

For White Frequency Modulation (WFM), that is the dominant short-term noise, the Prediction Error Deviation (PED) and ADEV are related by PED = ADEV*τ where τ is again both the prediction length and the averaging time. The two curves agree reasonably well at some averaging times. At averaging times of $3x10^4$ s, $6x10^4$ s and $3x10^5$ s the PED/τ values are significantly higher. This is due both to signals of period half a day as well as the clock linear frequency drift being correctly predicted but still contributing to the clock ADEV.

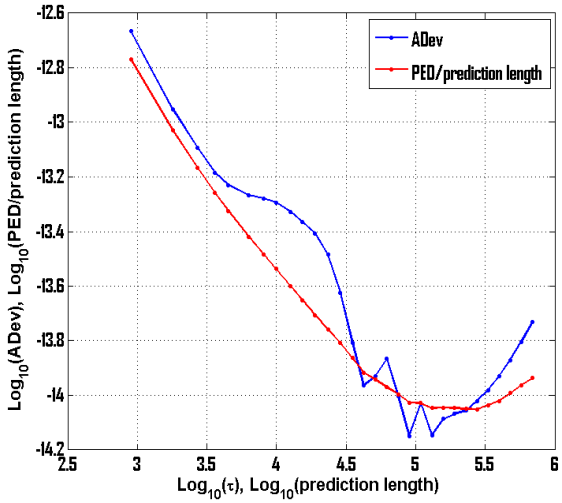

Figure 4 ADEV and prediction error plots for satellite PRN 16

Figure 4 shows plots of Log_{10}(ADEV), and Log_{10}(PED/τ) against $Log_{10}(\tau)$, where τ is both the prediction length and the averaging time.

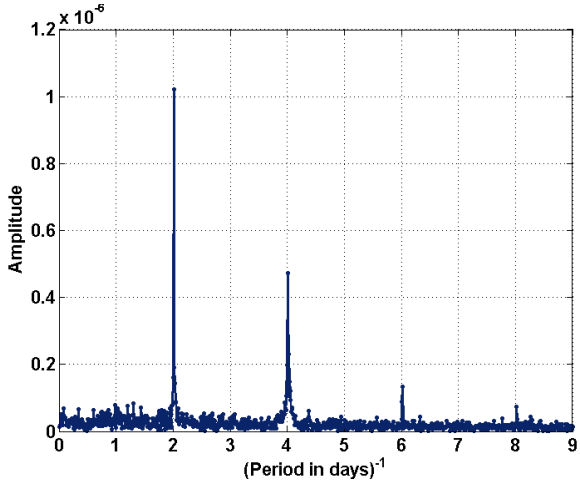

Figure 5 Results of applying a FFT to the Kalman filter residuals

The result of applying a Fast Fourier Transform (FFT) to the Kalman filter residuals is shown in figure 5, in the case where the filter contains no active periodic states. Signals with periods ½, ¼, 1/6, and 1/8 of a sidereal day are very clearly identified. This information is used then to include suitable state vector components in the clock model.

IV. PREDICTION OF INDIVIDUAL SATELLITE CLOCKS

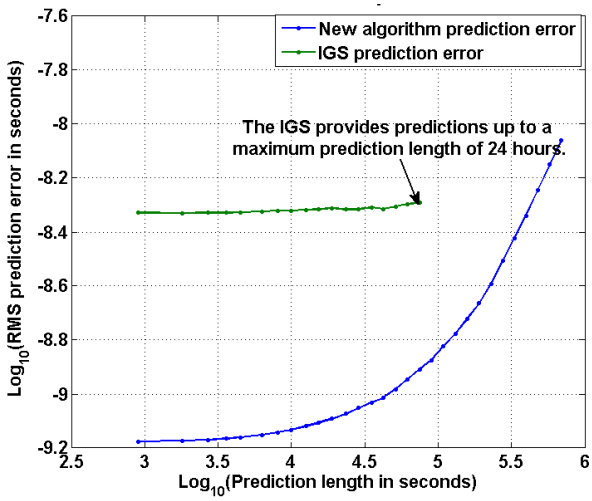

Figure 6 RMS prediction errors obtained using IGS ultra-rapid predictions and the new prediction techniques.

Figure 6 shows the prediction errors resulting from the IGS ultra-rapid predictions and from the new prediction technique on the PRN 16 clock. These results are typical of those obtained from most GPS satellite clocks. The IGS prediction errors are much larger than obtained using the new technique, and are not strongly dependent upon prediction length. In contrast, the new prediction technique produces prediction errors that are strongly dependent upon prediction length. There results are due primarily to the resetting of the IGS ultra-rapid timescale at each new computation of the IGS ultra-rapid predictions.

V. PREDICTION OF DIFFERENCES BETWEEN PAIRS OF CLOCKS

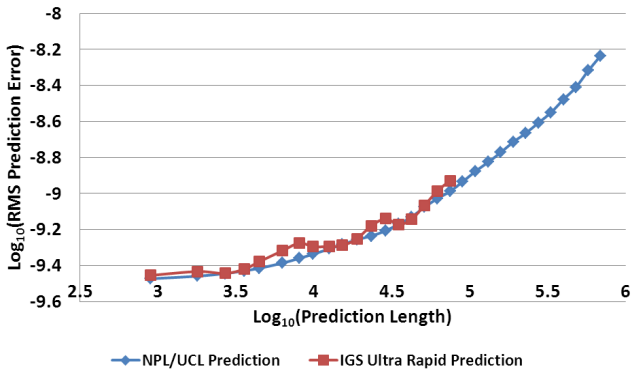

Figure 7 Prediction errors of (PRN16 – PRN15) clock differences

Figure 7 shows plots of RMS prediction error against prediction length on a log-log scale, obtained from (PRN16 – PRN15) clock differences. Results obtained from the new prediction technique and those obtained from the IGS predictions are much more similar to each other than in the case of individual clock predictions. The new prediction technique is noticeably better at prediction lengths of 8×10^3 s, and 3×10^4 s, the latter of these may be due to signals of period 1/2 day being better predicted. At prediction length of 1 day the new prediction technique is producing a small but significant improvement. Careful tuning of the Kalman filter, so that the clock models match closely the actual clock noise is required in order to achieve these results.

VI. PPP COMPUTATION USING CLOCK PREDICTIONS

One of the aims of the new satellite clock time-offset prediction algorithm is improved positioning performance. Figure 8 shows the results of a position domain analysis using the precise point positioning (PPP) strategy, as implemented in UCL's PPP software, to illustrate the impact of the predicted satellite clocks on positioning. The IGS station, Herstmonceux (HERT) was considered on 17 August 2011. The position solution using the GPS satellite clock predictions of the IGS product, igu16492_00.sp3, gives standard deviations of 0.590, 0.670 and 0.992 m in easting, northing and height, respectively.

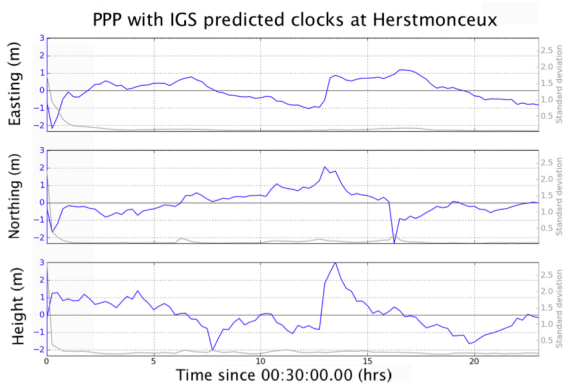

Figure 8 Coordinate time series from PPP with IGS predicted clocks.

Centimetre-level positioning is achieved with the IGS rapid and IGS final clock products (see figure 9). The aim of the this

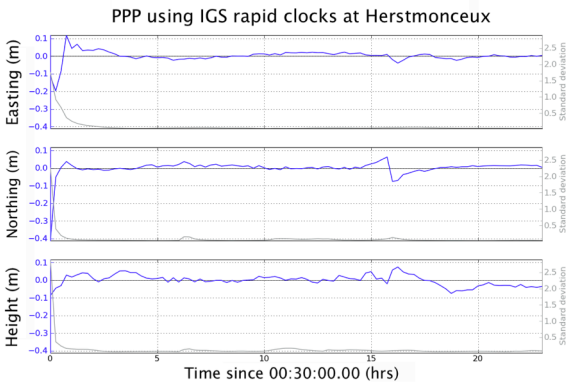

Figure 9 Coordinate time series from PPP with IGS rapid clocks.

new satellite clock prediction algorithm is to bridge the gap

between the IGS rapid and the IGS predicted clock product to assist in real-time centimeter level precise point positioning. Figures 8 and 9 show significant differences in the positioning precision. This is at the centimeter level when using the post-processed IGR product, in comparison with decimeter level precision achieved using the clock predictions provided in the IGS predicted product.

VII. DISCUSSION

Typically, satellite clock predictions are computed by a simple linear (or polynomial) extrapolation using previous satellite clock solutions. A new clock prediction technique has been developed in this paper. The resulting enhanced deterministic model (accounting for periodic signals) combined with a stochastic model has been shown to significantly improve individual satellite clock prediction performance. This prediction improvement occurs at all prediction lengths, in comparison to predictions published by the IGS. The plot of prediction error against prediction length for PRN 16 shown in figure 6 is typical for all GPS satellite clocks. This shows prediction errors at the sub nano-second level, up to predictions length greater than $5x10^4$ seconds, whereas the IGS prediction errors are substantially greater at the level of a few nanoseconds.

Future work involves further development of the prediction algorithm to ensure that instances of missing data, outliers and abrupt changes can be dealt with. Development is also ongoing to enable the output of the prediction algorithm to plug in to the UCL PPP software.

ACKNOWLEDGMENTS

Santosh Bhattarai's PhD research at the Space Geodesy and Navigation Laboratory, UCL is funded by the Engineering and Physical Sciences Research Council (EPSRC) as part of the UK-wide collaborative research project 'Innovative navigation using new GNSS signals with hybridised technologies' (iNsight).

The work at NPL is supported by the UK Department for Business, Innovation, and Skills, as part of the NMS Physical Metrology Programme.

REFERENCES

[1] Allan DW (1987) Time and frequency (time-domain) characterization, estimation and prediction of precision clocks and oscillators. IEEE Transactions on Ultrasonics, Ferroelectrics and Frequency Control. Vol UFFC-34, No 6.

[2] Senior K, Ray JR, Beard RL (2008) Characterization of periodic variations in the GPS satellite clocks. GPS Solutions 12(3): 211-225.

[3] Heo YJ, Cho J, Heo MB (2010) Improving prediction accuracy of GPS satellite clocks with periodic variation behaviour. Meas. Sci. Technol. 21 073001.

[4] Bock H, Dach R, Jäggi A, Beutler G (2009) High-rate GPS clock corrections from CODE: support of 1 Hz applications. J Geodesy 83(11): 1083-1094.

[5] Hauschild A, Montenbruck O (2009) Kalman-filter-based GPS clock estimation for near real-time positioning. GPS Solutions 13:173-182.

[6] Zhang X, Li X, Guo F (2010) Satellite clock estimation at 1 Hz for realtime kinematic PPP applications. GPS Solutions 15: 315-324.

[7] Davis JA, Greenhall CA, Boudjemaa R (2005) The development of a Kalman Filter clock predictor. 19th European Frequency and Time Forum.

[8] Dow JM, Neilan RE, Rizos C (2009) The international GNSS service in a changing landscape of global navigation satellite systems. J Geodesy 83(3-4): 191-198.

[9] Brown RG, Hwang PYC (2012) Introduction to random signals and applied Kalman filtering 4th edition. John Wiley & Sons, Inc.

Improved GPS receiver clock modeling for kinematic orbit determination of the GRACE satellites

Ulrich Weinbach and Steffen Schön
Centre for Quantum Engineering and Space Time Research (QUEST)
Institut für Erdmessung, Leibniz Universität Hannover
Hannover, Germany
Email: weinbach@ife.uni-hannover.de

***Abstract*— Kinematic orbit positions of Low Earth Orbiting satellites (LEOs) derived from GPS observations are frequently used for single satellite gravity field recovery. Unfortunately, the precision of the kinematic coordinates is compromised by the estimation of the receiver clock synchronization offset in addition to the three kinematic coordinates for every observation epoch. In this paper the potential of receiver clock modeling to improve the precision of the kinematic orbit determination is investigated. The formation flying twin satellites of the Gravity Recovery And Climate Experiment (GRACE) mission are considered as a case study. A unique feature of these satellites is the combination of a dual frequency GPS receiver with an Ultra Stable Oscillator (USO), that provides the required frequency stability for the proposed clock modeling approach. Based on a piece-wise linear clock parametrization with 60 s intervals, a significant reduction of the high-frequency radial orbit differences with respect to a reduced-dynamic orbit is shown.**

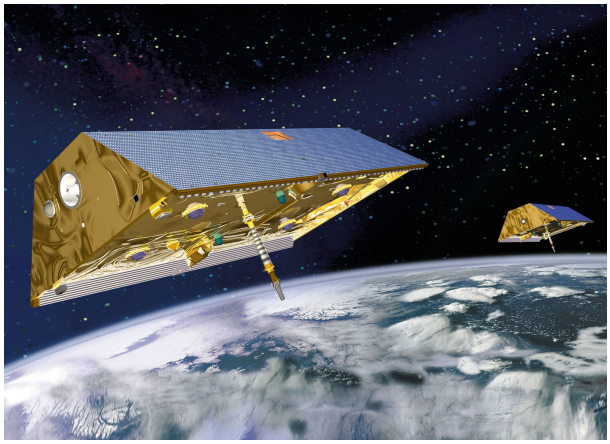

Fig. 1. The formation flying GRACE satellites ©Astrium

I. Introduction

In recent years, precise kinematic positioning of Low Earth Orbiters equipped with GPS receivers has been succesfully applied in single satellite gravity field determination [1], [2]. The main advantage of kinematic orbits can be seen in the fact that no a priori information concerning the Earth's gravity field and the non-gravitational forces acting on the satellite are introduced. However, kinematic orbit determination is much more sensitive to systematic errors in the observation data and requires a good observation geometry. In particular, tracking of at least 4 GPS satellites at any time is necessary to compute a kinematic position. This requirement causes sometimes gaps in the computed orbit. If the GPS receiver onboard the LEO is connected to a highly stable oscillator and the GPS satellite clock corrections are referenced to a stable time scale (e.g. IGST/IGRT), modeling of the receiver clock has the potential to significantly strengthen the observation geometry, resulting in an improved precision of the kinematic LEO positions and a reduction of outliers and gaps caused by poor GPS satellite geometry. The kinematic LEO orbit determination procedure analyzed in this study is based on the Precise Point Positioning (PPP) approach [3].

II. The GRACE mission

The Gravity Recovery And Climate Experiment (GRACE) mission consists of two identical satellites in a near polar orbit at an altitude of approximately 500 km with an along track distance of approximately 200 km. The primary observable for gravity field determination is the highly precise inter-satellite K-band microwave link that allows to measure the distance between the two spacecrafts with μm accuracy. Furthermore, both spacecrafts are equipped with a dual frequency BlackJack GPS receiver built by JPL. This receiver type behaves like a classical semicodeless geodetic receiver [4]. In addition to tracking the GPS satellites, the BlackJack receivers are also used to measure the K-band signal transmitted by the other GRACE spacecraft. The highly accurate determination of the inter-satellite distance is achieved through the dual one-way operation of the K-band link. This measurement configuration relies on an Ultra Stable Oscillator that provides the required short term frequency stability and a relative receiver synchronisation of better than 150 ps [5]. Since both the K-Band Ranging system (KBR) and the GPS receiver share the same oscillator, the GPS data can be used for this synchronisation during postprocessing.

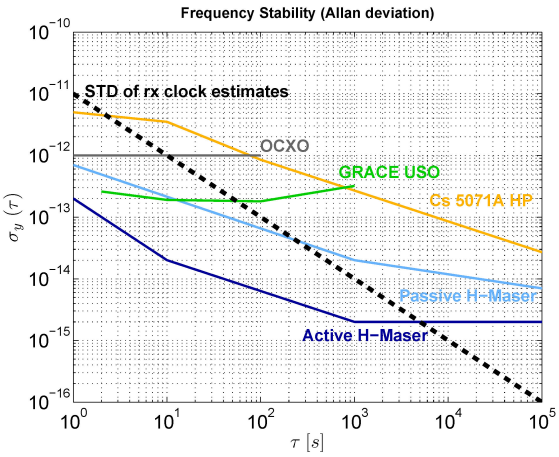

Fig. 2. Frequency stabilities of various precision oscillators including the GRACE USOs, dashed line: L3 receiver clock observation noise

III. Performance of the GRACE Ultra Stable Oscillators

The frequency stability of the GRACE Ultra Stable Oscilators is specified with $\sigma_y(\tau) = 1 - 3 \times 10^{-13}$ for averaging times τ between 1 and 1000 seconds [6]. In figure 2 the Allan deviation for a number of high-performance frequency standards including the GRACE USOs is shown. For reference, the observation noise of the epochwise PPP receiver clock estimates (σ_{clk}=3 mm) based on GPS L3 carrier phase observations has been added. This approximate value holds for a good observation geometry and can be much larger, when only few GPS satellite are tracked. As a rule of thumb, modeling of the receiver clock by a linear function is reasonable for intervals where the Allan deviation of the oscillator is below the Allan deviation of the observation noise. According to figure 2 linear modeling of the Ultra Stable Oscillators onboard the GRACE satellites should be feasible theoretically for intervals up to 60 s.

IV. Adjustment and Correction Models

The GRACE kinematic orbits have been determined in a least squares adjustment based on undifferenced ionosphere-free code and phase observations at 30 s intervals using the PPP approach. The precision of ionosphere-free pseudorange and carrier phase observations is assumed to be 60 cm and 2 mm, respectively. Precise ephemeris and satellite clock corrections of the Center for Orbit Determination in Europe (CODE) are fixed in the solution. At LEO altitudes tropospheric delays can be savely neglected, thus only kinematic coordinates, carrier phase ambiguities and receiver clock offsets need to be estimated. Receiver antenna phase center variations are corrected with phase residual maps kindly provided by Adrian Jäggi of the Astronomical Institute University of Berne (AIUB). The receiver clock is either estimated on an epoch-by-epoch basis or modeled by a sequence of piece-wise linear parameters.

TABLE I

RMS of high-pass filtered PPP position residuals with and w/o clock modeling for a simulated GRACE A data set

	PPP	PPP 60 s clk	Improvement
Radial RMS	9.8 mm	4.5 mm	**54** %
Along-track RMS	4.0 mm	3.6 mm	**10** %
Cross-track RMS	3.4 mm	3.4 mm	**0** %

Based on comparisons with reduced-dynamic orbits, we found that a 60 s piece-wise linear parametrization showed the smallest radial position RMS. Due to this short interval, only very few observations contribute to the linear drift in each linear segment. Therefore, the drift estimates in consecutive segments were constrained with $\sigma_{rel} = 0.8\,\mathrm{ns/h}$ relative to each other. Note, that no relativistic clock corrections have been applied to the LEO oscillator, because these are already removed in the Level 1B GPS observation data used for this work (W. Bertiger, personal communication).

V. Simulation Results

In a preliminary study, the potential improvements of kinematic LEO orbit determination through clock modeling were analyzed using simulated GRACE observation data. Synthetic observations were generated at 30 s intervals based on the trajectory of GRACE A on day 4 in 2008 and only for those satellites that were actually observed by the onboard receiver. White noise with a standard deviation of 0.1 m and 1 mm was added to the L1 and L2 pseudorange and carrier phase observations, respectively. In order to closely reproduce the real GRACE observation data, the pseudorange noise was multiplied by the elevation-dependent factor $1/sin(e)$. The receiver clock offset was assumed to be zero. The main advantages of using simulated observations are the independence of the data quality and the availability of a "true" reference trajectory, which facilitates the statistical interpretation of the results.

The differences of the solutions with and without clock modeling with respect to the values used in the simulation are shown in figure 3. Due to the estimation of a large number of float carrier phase ambiguities, both solutions are affected by systematic variations. In order to get rid of these variations and to asses only the high frequency noise of the time series a 5 epoch moving average has been removed before computing the RMS of the time series. The results are summarized in table I. According to this analysis, clock modeling can reduce the RMS of the kinematic positions in the radial direction by approximately 50 %, while the improvement of the along-track positions is only 10 % and the cross-track orbit positions are unaffectd. This behavior can be explained by the fact that GPS satellites are only observed in the hemisphere above the receiver, which results in a high degree of correlation between receiver clock and radial position estimates. The same effect can be observed for the height estimates of terrestrial GPS receivers [7].

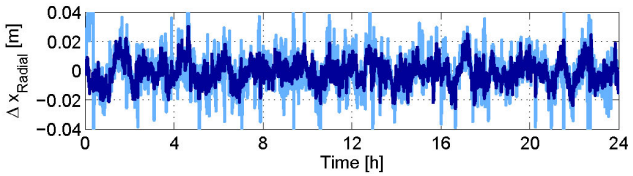

(a) Radial position residuals

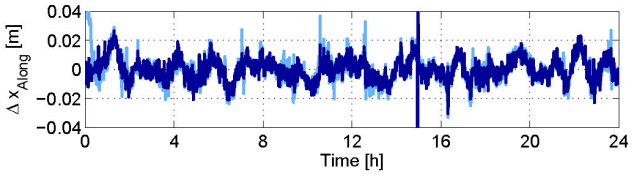

(b) Along-track position residuals

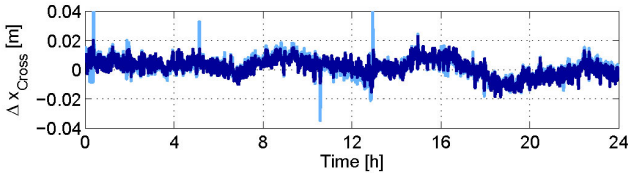

(c) Cross-track position residuals

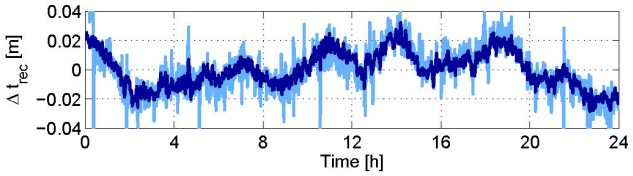

(d) Clock residuals from a straight line fit

Fig. 3. PPP position and clock residuals based on simulated data for epoch-wise independent (light blue) and 60 s piece-wise linear (dark blue) receiver clock estimation (GRACE A on January 4, 2008)

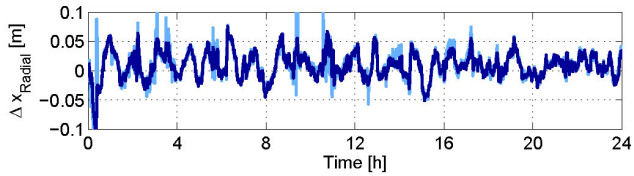

(a) Radial position residuals

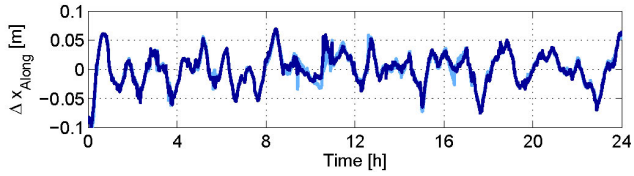

(b) Along-track position residuals

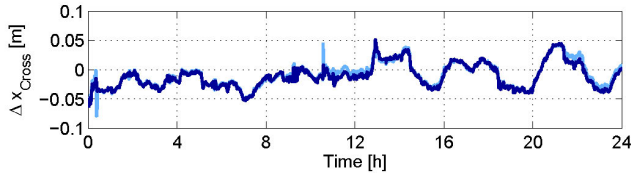

(c) Cross-track position residuals

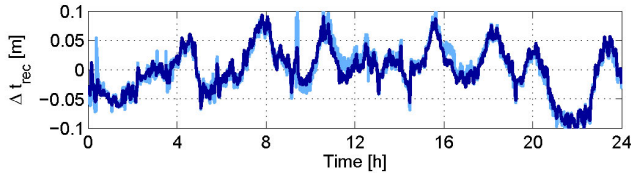

(d) Clock residuals from a straight line fit

Fig. 4. PPP position and clock residuals with respect to the reduced-dynamic GRACE Level 1B orbit for epoch-wise independent (light blue) and 60 s piece-wise linear (dark blue) receiver clock estimation (GRACE A on January 4, 2008)

VI. Real Data Results

The real GRACE observation data were first processed using the conventional PPP algorithm with epoch-wise independent receiver clock estimation. In a second run the receiver clock was modeled as a piece-wise linear function with 60 s intervals. The differences of the two solutions with respect to the reduced-dynamic reference orbit are shown in figure 4. Compared to the solutions for the simulated data set, the position residuals exhibit even stronger systematic variations, that are either caused by modeling deficiencies in the PPP software, the reduced-dynamic reference orbit or both. In fact, the accuracy of the computed kinematic orbit is at the same level as the reference orbit. Nevertheless, the reduced-dynamic orbit can serve as a reference for the analysis of high-frequency errors of the kinematic trajectory because it is smooth like the true LEO orbit. This can be confirmed, e.g. by comparing the inter satellite distance from the reduced-dynamic orbits with the highly-precise observations of the GRACE K-band link, which results in smoothly time varying residual time series. Applying the same high-pass filter as in section V, the standard deviations of the high frequency noise in table II are obtained. An improvement of the radial component can again be noted, but it is substantially smaller, than in the simulation. However, the numbers in table II have to be interpreted with care since the RMS values depend on the chosen outlier rejection threshold, which was 3 cm here.

Instead of high-pass filtering the residual time series, the Allan deviation of the position residuals can be analyzed. In figure 4 the modified Allan deviation of the kinematic radial position residuals is shown. For short averaging times the noise of the kinematic radial position estimates is in fact reduced, whereas for longer averaging times the impact of systematic errors is dominating. At 60 s averaging time, which is the sampling rate of the reduced-dynamic reference orbit, the difference between the modified Allan deviations amounts to 35 %, i.e. the improvement is significantly larger than what is obtained by comparing the filtered position time series. The results obtained for GRACE B are very similar.

VII. Conclusion

It has been shown that receiver clock modeling can significantly improve kinematic (PPP) LEO orbit determination. A piece-wise linear clock parametrization with 60 s intervals has been successfully employed to model the USOs onboard the two GRACE satellites. Based on simulated data, an improvement of almost 50 % for the radial components

TABLE II

RMS OF HIGH-PASS FILTERED PPP POSITION RESIDUALS WITH RESPECT TO A REDUCED-DYNAMIC REFERENCE ORBIT FOR A REAL GRACE A DATA SET

	PPP	PPP 60 s clk	Improvement
Radial RMS	6.4 mm	5.1 mm	**20** %
Along-track RMS	2.4 mm	2.4 mm	**0** %
Cross-track RMS	1.9 mm	1.9 mm	**0** %

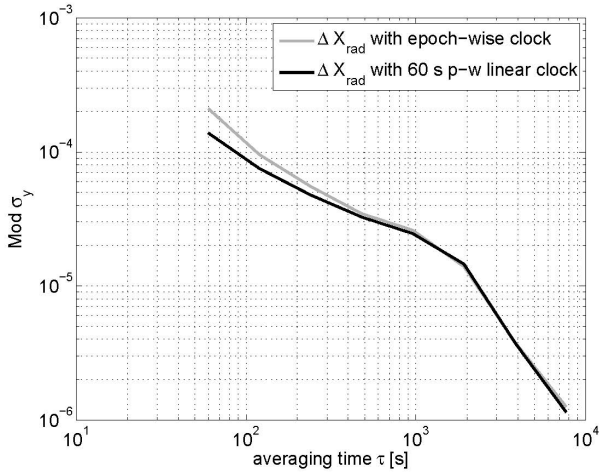

Fig. 5. Modified Allan deviation of the kinematic radial orbit residuals with respect to the GRACE Level 1B orbits based on epoch-wise (grey) and 60 s piece-wise linear (black) receiver clock modeling (GRACE A on January 4, 2008)

can be expected. For real data, however, the effect is more difficult to assess since no suitable reference orbit is available. The differences between the kinematic orbit and the reduced-dynamic GRACE Level 1B orbits is dominated by systematic variations. Nevertheless, the Allan deviation of the kinematic position residuals with respect to the smooth reduced-dynamic orbit, indicates a significant reduction of the high-frequency noise in the radial direction by approximately 35 %.

ACKNOWLEDGMENT

The authors would like to thank the GRACE science team for making their data publicly available and Adrian Jäggi of AIUB for providing phase center correction maps and helpful advice.

This work has been funded by the Deutsche Forschungsgemeinschaft (DFG) in collaboration with the centre for QUantum Engineering and Space Time research (QUEST), Hannover.

REFERENCES

[1] Gerlach, C., Földvary, L., Svehla, D., Gruber, T., Wermuth, M., Sneeuw, N., Frommknecht, B., Oberndorfer, H., Peters, T., Rothacher, M., Rummel, R., und Steigenberger, P. (2003). A CHAMP-only gravity field model from kinematic orbits using the energy integral. *Geophys. Res. Lett.*, 30 (20):2037.

[2] Jäggi, A., Bock, H., Prange, L., Meyer, U., und Beutler, G. (2011). GPS-only gravity field recovery with GOCE, CHAMP and GRACE. *Advances in Space Research*, 47(6):1020 – 1028.

[3] Zumberge, J. F., Heflin, M. B., Jefferson, D. C., Watkins, M. M., und Webb, F. H. (1997). Precise point positioning for the efficient and robust analysis of GPS data from large networks. *Journal of Geophysical Research*, 102(B3):5005–5017.

[4] Montenbruck, O. und Kroes, R. (2003). In-flight performance analysis of the CHAMP BlackJack GPS receiver. *GPS Solutions*, 7:74–86.

[5] Bertiger, W., Dunn, C., Harris, I., Kruizinga, G., Romans, L., Watkins, M., und Wu, S. (2003). Relative time and frequency alignment between two low earth orbiters, GRACE. In *Frequency Control Symposium and PDA Exhibition Jointly with the 17th European Frequency and Time Forum, 2003. Proceedings of the 2003 IEEE International*, pages 273 – 279.

[6] Dunn, C., Bertiger, W., Bar-Sever, Y. E., Desai, S., Haines, B., Kuang, D., Franklin, G., Harris, I., Kruizinga, G., Meehan, T., Nandi, S., Nguyen, D., Rogstad, T., Thomas, J., Tien, J., Romans, L., Watkins, M., Wu, S., Bettadpur, S., und Kim, J. (2003). Instrument of GRACE. *GPS World*, 14(2):17–28.

[7] Weinbach, U. und Schön, S. (2010). GNSS receiver clock modeling when using high-precision oscillators and its impact on PPP. *Advances in Space Research*, 47(2):229 – 238.

Measuring the relative synchronization error of frequency counters with sub-µs accuracy via a phase-stabilized fiber link

S. M. F. Raupach, H. Schnatz, and G. Grosche
Physikalisch-Technische Bundesanstalt (PTB)
Bundesallee 100, 38116 Braunschweig, Germany
sebastian.raupach@ptb.de

S. Droste
Max-Planck-Institut für Quantenoptik (MPQ)
Hans-Kopfermann-Str. 1, 85748 Garching, Germany

***Abstract*—When comparing independent simultaneous measurements of the same, non-constant frequency, synchronization errors between the frequency counter's gate time intervals lead to an apparent frequency deviation between the measurements. Here we present a technique that allows for a remote measurement of the counters' synchronization offset with sub-microsecond accuracy using a phase-stabilized fiber link.**

I. INTRODUCTION

Phase-stabilized fibre links are intended mainly for comparing the frequencies of optical atomic clocks with an accuracy of 10^{-18} or better; this will allow for measuring differences in the gravitational potential at distant locations [1]. Here, the optical frequency transmitted over a glass fiber link can either be a laser locked to the fixed frequency of one of the clock lasers [2], or it can be a drifting laser frequency, measured against the clocks.

Ideally, at any instant the difference between beat frequencies measured locally and at the remote site of a stabilized two-point-link are, apart from residual noise [3], the difference of the clock laser frequencies. However, if the transferred frequency is not constant, any synchronisation mismatch Δt between the measurements, in the presence of a frequency drift D_ν, leads to an apparent additional frequency offset $\delta\omega$ of:

$$\delta\omega = D_\nu \, \Delta t \qquad (1)$$

In the case of e.g. a linear frequency drift of 100 mHz/s at 194 THz, the synchronization offset would have to be smaller than 200 µs to ensure that the impact on the accuracy of the measurement remains below 10^{-19}.

Figure 1 shows an example of a drift, that is not constant [4]. Here, not only the accuracy but also the stability of the frequency transfer is affected.

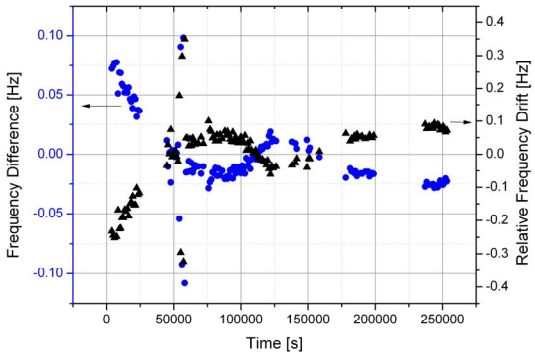

Figure 1. Difference between "simultaneous" frequency measurements at opposite ends of a 920 km phase-stabilized fiber link (blue circles) and laser frequency drift (black triangles). All data points are averaged over 1000 s, the frequency data was taken with Λ-type counters (1 s gate). The observed frequency offset shows a strong correlation to the observed frequency drift.

Here we present a technique [5], that allows for measuring the synchronization mismatch between remote frequency counters with high accuracy. Once measured, the determined synchronization mismatch in connection with the observed frequency drift can be used to correct the frequency data for the apparent frequency offsets.

II. DESCRIPTION

To measure the synchronization mismatch, we apply a strong triangular frequency modulation to the optical frequency transferred via the phase-stabilized fiber link.

After first measurements of the synchronization mismatch over a 920 km link to correct the data shown in figure 1, we set up a laboratory link experiment with 50 km of spooled

fiber and an artificially limited control bandwidth of 70 Hz. Here we ramped the frequency with a slope of about 100 kHz/s. In this loop-experiment, we measured the transferred optical frequency at the starting and the end point of the loop against the same optical reference frequency, using two unsynchronized Λ-type counters for the "local" and the "remote" beat frequency. To measure the "true" synchronization mismatch, we directly counted the swept radiofrequency that modulates the laser, without transfer over the fiber link, and calculated the mismatch Δt from eq. 1.

III. RESULTS

The "true" synchronization mismatch is determined by directly counting the rf sweep on both counters, yielding Δt = 226.05934771 ms +/- 70 ps.

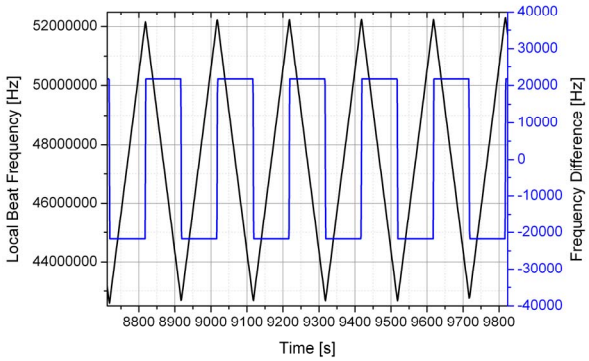

Figure 2. Measurement over a looped 50 km link: "local" beat frequency during modulation (black curve) and observed frequency offset between the "simultaneous" frequency measurements at both ends of the looped link.

Figure 2 displays the variation of the beat frequency under modulation of the transfer laser, and the observed apparent frequency offset between the beat frequency measurements at the "local" and the "remote" end of the stabilized looped fiber link. As the sign of the slope changes, the sign of the apparent frequency offset changes as well, as is expected from eq. 1.

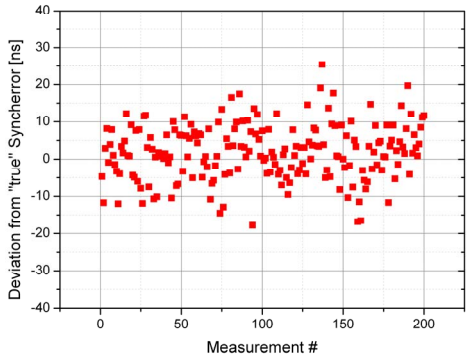

Figure 3. Deviation of the synchronisation mismatch between the frequency counters measured via a phase stabilized 50 km fiber link from the "true" synchronisation mismatch (see text for details; preliminary data).

From that we determine the synchronization mismatch over the fiber link in every point (excluding the regions around the extrema of the beat frequency) using eq. 1. We then average over a period of 40 s for each slope and calculate the mean of pairs of consecutive averages, i.e. always taking one 40 s average from a period with positive and one from a period with a negative slope. Figure 3 displays the deviation of these mean values from the "true" synchronization mismatch. Each values comprises 80 s of data and is corrected for known systematic offsets of around 10 ns (preliminary data). Most measurements of the synchronization mismatch over the fiber link can be seen to be within +/- 10 ns of the "true" value.

Once the synchronisation error is known, the measurement can be corrected for it.

For the data shown in fig. 1, an according correction was performed, with an early implementation of the scheme and a conservative estimate of the uncertainty of the synchronisation error's measurement of 100 µs. There, the correction yielded an improvement in statistical uncertainty by more than one order of magnitude to better than 10^{-18} [4].

REFERENCES

[1] C. W. Chou, D. B. Hume, T. Rosenband, and D. J. Wineland, "Optical Clocks and Relativity," Science, vol. 329, pp. 1630-1633, 2010.

[2] A. Yamaguchi, M. Fujieda, M. Kumagai, H. Hachisu, S. Nagano, Y. Li, T. Ido, T Takano, M. Takamoto, and H. Katori, "Direct comparison of distant optical lattice clocks at the 10^{-16} uncertainty," Appl. Phys. Exp., vol. 4, 082203, 2011.

[3] P. A. Williams, W. C. Swann, and N. R. Newbury, "High-stability transfer of an optical frequency over long fiber-optic links," J. Opt. Soc. Am. B, Vol. 25, pp. 1284-1293, 2008.

[4] K. Predehl, G. Grosche, S. M. F. Raupach, S. Droste, O. Terra, J. Alnis, Th. Legero, T. W. Hänsch, Th. Udem, R. Holzwarth, and H. Schnatz, "A 920-kilometer optical fiber link for frequency metrology at the 19th decimal place," Science, vol. 336, pp. 441-444, 2012.

[5] S. M. F. Raupach et al., unpublished.

VLBI Frequency Transfer using CONT11

Carsten Rieck[1,2], Rüdiger Haas[2], Per Jarlemark[1] and Kenneth Jaldehag[1]

[1]Measurement Technology
SP Technical Research Institute of Sweden
Box 857, SE-50115 Borås, Sweden

[2] Chalmers University of Technology
Department of Earth and Space Sciences, Onsala Space Observatory

Email: carsten.rieck@sp.se

***Abstract*— Geodetic VLBI is an independent technique, which does not rely on third parties. This makes it a viable future alternative for time- and frequency transfer over long baselines. Frequency link instabilities in the order of 1.5e-15 for time periods of one day are comparable to those achievable with methods using GNSS carrier-phase observations. Data of the continuous VLBI campaign CONT11 were analyzed and compared to results from GPS PPP analysis on collocated/common clock stations.**

I. INTRODUCTION

The continuous Very Long Baseline Interferometry (VLBI) campaign CONT11 was observed during September 15-29, 2011, involving 13 IVS (International VLBI service for Geodesy and Astrometry) stations. CONT11 is a continuation of the series of very successful continuous VLBI campaigns that were conducted since 1994. The CONT11 campaign was to acquire state-of-the-art VLBI data in order to demonstrate the highest accuracy of which the current VLBI system is capable of. The collected data set supports high resolution Earth rotation studies, investigations of reference frame stability, investigations of daily to sub-daily site motions, estimation of ultra-rapid dUT1 and the study of time- and frequency transfer techniques [1].

A Previous study of CONT08 campaign data [2] has shown that the frequency transfer capability of geodetic VLBI is comparable to that obtainable using GNSS (Global Navigation Satellite System) carrier phase analysis. During CONT08 both techniques performed frequency link instabilities in the order of 1e-15 for time periods of one day comparing H-maser clocks. Though VLBI is technically complicated and heavy headed, it is an independent technique, which does not rely on third parties. This could make VLBI a viable future alternative for time- and frequency transfer over long baselines. In this paper we present further comparisons using the data set of CONT11.

A requirement for a meaningful comparison of the performance of the two techniques is that VLBI and GNSS

Figure 1. VLBI stations during CONT11. Station WARK12M had to cancel participation due to technical problems. A total of 13 stations successfully collected data. Image taken from [1].

instrumentation is co-located and connected to the same frequency standard, i.e. the same H-maser. The continuous VLBI campaigns provide perfect test beds to compare and evaluate the performance of the two techniques. These campaigns last a few weeks and involve several internationally well distributed co-location stations with the potential to use the same frequency standard for the techniques. During CONT11 eleven out of the thirteen participating stations used the same frequency standard for VLBI and GNSS, with four of the stations also being UTC(k) nodes, providing clock data to the BIPM for contribution to TAI/UTC. Table I presents an overview of the IVS and IGS stations involved during CONT11, Fig. 1 shows the geographical distribution of the stations involved.

II. METHOD

The analyzing methods used for CONT11 are similar to those presented in [2] for the CONT08.

VLBI data were analyzed with the VLBI data analysis software Calc/Solve [3]. The setup was a standard network solution using the 15 days of the CONT campaign. Radio source coordinates were fixed to ICRF2, while station

coordinates were kept fixed on VTRF2008a values. However the station coordinates of Tigo Concepcion and Tsukuba were estimated on a daily basis since these two stations were affected by earthquakes in early 2010 and early 2011, respectively. Earth rotation and orientation parameters were estimated on a daily basis. Atmospheric parameters were estimated as piece-wise linear offsets for zenith wet delays every 20 minutes and horizontal gradients one a day. As constraints we used 50 ps/hour for the zenith wet delays and 0.5 mm for the gradient offset and 2 mm/day for the gradient rate. One station clock, Wettzell, was used as reference clock and clock parameters for all other stations were estimated as daily second order polynomials together with additional continuous spline corrections every 20 minutes. The clock constraints were set to 5e-14.

The GNSS data analysis was performed with the NRCAN-PPP software [4]. GPS data were analyzed for each station using the precise point positioning strategy in a continuous mode for the entire 15 day period, i.e. avoiding 24 hour batches and thus day boundary jumps due to code uncertainties. During the processing final IGS products were used. Zenith wet delays and horizontal gradients were estimated as random walk parameters. Clock parameters were estimated as white noise parameters with 60 s updates. These clock parameters are relative phase differences to the IGS-timescale, which is common to all individual solutions. In order to gain comparable time series with VLBI, all solutions were differenced with the WTZZ solution.

Whereas the PPP clock differences estimates are forced to be continuous over the entire 15 days period[1], the VLBI derived time series are not and may experience day boundaries. This is due to the fact that correlation and analysis is done in 24h batches and that geodetic applications can handle constant clock offsets during the duration of a batch. In order to gain a continuous time series, daily solutions were fitted together with the help of overlapping Solve estimates.

TABLE I. VLBI STATIONS AND IGS COLOCATION DURING CONT11

IVS	*IGS*	*CC*[a]	*CLOCK*
HARTRAO	HRAO	YES	EFOS-C 28
KOKEE	KOKB	YES	Sigma Tau
NYALES20	NYAL	YES	APL No 2
ONSALA60	ONSA	YES	CH1-75A
WESTFORD	WES2	YES	APL No 4
WETTZELL[b]	WTZZ/WTZR	YES	EFOS 18
TIGOCONC	CONZ/CONT	YES	EFOS 20
TSUKUB32	TSKB	YES	Anritsu SA0D05A
ZELENCHK	ZELE	YES	VCH-1003A/CH1-80M
BADARY	BADG	YES	CH1-80
FORTLEZA	BRFT	NO	Sigma Tau (VLBI)
HOBART12	HOBA	NO	VCH-1005A
YEBES40M	YEBE	YES	EFOS 66

a. Common Clock for both IVS and IGS.

b. Reference, IGS WTZZ was used for PPP reference, WTZR performed similarly

Link instability analysis uses the fact that the inherent maser-instability is better then most link instabilities for averaging times shorter than approximately one day. Ideally, maser frequency drift is considered to be constant during the duration of the experiment. Thus, individual quadratic clock models were fitted and removed from all time series. The resulting residuals were analyzed using Overlapping Allan Deviation.

The phases of VLBI and PPP clock estimates for each baseline to WETTZELL were also differenced in order to compare the two techniques. A line was estimated, where the trend parameters describes the difference in frequency estimate between the two methods.

III. RESULTS

Table II summarizes the results of the study. As for CONT08, also during CONT11 the WETTZELL-ONSALA baseline performs best, both the PPP and the VLBI comparisons reach frequency link instability levels of about 1.2e-15 (overlapping ADEV) for time periods of one day[2]. Both PPP and VLBI derived frequency estimates differ insignificantly from each other, line residuals have a RMS deviation of about 90 ps. Fig. 2 shows the VLBI results and a comparison to the PPP solution for this baseline.

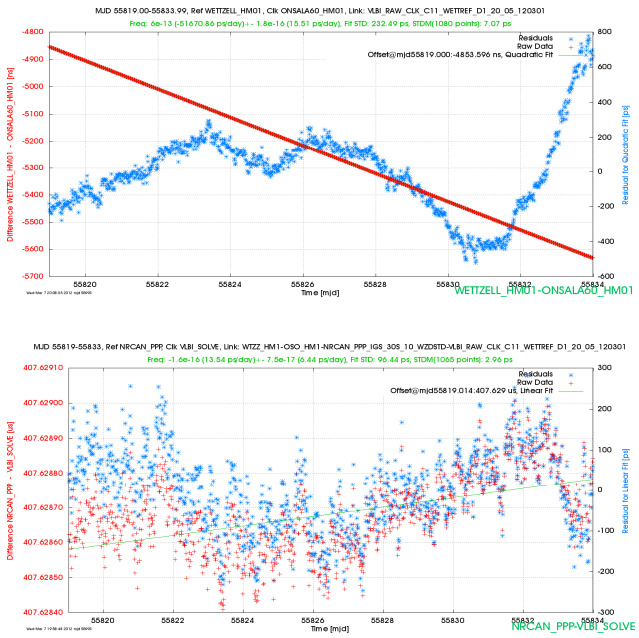

Figure 2. Baseline WETTZELL-ONSALA, MJD 55819-55833. The upper graph shows the VLBI solution, in red the raw phase of the clock difference, blue the residuals to a quadratic model. There is a rapid frequency change MJD55831 due to change in the Onsala clock. The lower graph shows the phase difference between the PPP and the VLBI solutions with a sampling of 1200 s. Both techniques virtually estimate the same relative clock phase with less then 100ps difference in a RMS sense.

[1] This is only partly true: loss of phase at the receiver due to e.g. loss of signal or receiver reset, forces PPP to estimate a new clock parameter with help of the code phase, which is noisy in nature and introduces uncertainties of about 1ns to the clock solution.

[2] Best case is based on a reduced data set MJD 55819-55830, Onsala clock has an apparent frequency change on MJD 55831 which violates the assumption of a constant frequency drift of the maser pair. Both, VLBI and PPP estimate the same phase pattern.

TABLE II. CONT11 15 DAYS, MJD 55819-55833, VLBI AND PPP

Station	*VLBI*		*GPSPPP*		*GPSPPP-VLBI*	
	oADEV@1200s []	*oADEV@1d []*	*oADEV@1200s []*	*oADEV@1d []*	*Δf []*	*RMS [ps]*
HARTRAO	3.12e-14	3.7e-15	3.94e-14	3.6e-15	-6.0e-16 ±8.7e-17	112
KOKEE	2.58e-14	1.7e-15	4.44e-14	1.9e-15	-1.1e-15 ±1.1e-16	143
NY ÅLESUND [a]	2.10e-14	8.5e-15	6.91e-13	1.3e-14	-3.8e-16 ±5.2e-16	628
ONSALA	2.81e-14	1.5e15	3.67e-14	1.4e-15	-1.6e-16 ±7.5e-17	96
ONSALA [b]	**2.82e-14**	**1.1e-15**	**3.69e-14**	**1.2e-15**	**-7.9e-17 ±8.7e-17**	**90**
WESTFORD	3.05e-14	9.3e-15	4.08e-14	9.1e-15	1.1e-16 ±1.1e-16	142
CONCEPCIóN [c]	2.25e-14	1.9e-15	4.60e-14	1.7e-15	-6.4e-15 ±1.0e-16	134
CONCEPCIóN [d]			3.84e-14	1.8e-15	7.2e-16 ±1.1e-16	140
TSUKUBA [e]	2.38e-14	1.8e-15	3.78e-14	2.6e-15	7.4e-16 ±2.2e-16	153
ZELENCHUKSKAYA [f]	2.33e-14	2.1e-15	3.53e-14	2.3e-15	-3.3e-16 ±1.8e-16	151
BADARY [g]	2.18e-14	1.1e-14	3.76e-14	1.8e-15	1.7e-15 ±5.3e-16	135
FORTALEZA [h]	3.71e-14	1.1e-14	3.49e-12	5.1e-14	no common clock	
HOBART [i]	4.65e-14	3.1e-15	4.41e-14	7.3e-15	no common clock	
YEBES [j]	9.08e-14	5.0e-15	5.26e-14	4.1e-15	1.0e-15 ±4.2-16	291
WETTZELL [k]	Reference		3.67e-14	7.7e-16	Reference	
WETTZELL [l]			2.89e-14	8.3e-16		

a. PPP CA phase break removed.

b. MJD 55819-55830, due to a frequency change of Onsala Maser at MJD 55831

c. IGS CONT

d. IGS CONZ

e. MJD 55826-55826, VLBI clock frequency change at 55825

f. MJ55824-55833, bad VLBI clock prior to 55824

g. MJD 55824-55833, bad VLBI clock prior to 55824, PPP phase break removed

h. no GPS data post to 55825.7, no common clock

i. MJD 55826-55833, VLBI clock frequency change at 55825, no common clock

j. MJD 55819-55826, VLBI clock frequency change at 55827

k. WTZR, short baseline with WTZZ, common clock

l. WTZS, short baseline with WTZZ, common clock

Trend estimates for many of the PPP-VLBI differences in Table II can be considered insignificant. Fig. 3 summarizes the instability measures for the VLBI baselines calculated.

IV. CONCLUSIONS, FUTURE WORK

VLBI derived relative clock differences for CONT11 have confirmed results from CONT08. Frequency link instabilities are comparable to GPS Carrier Phase processing reaching the 1e-15@1d level. Considering the size and complexity of today's VLBI stations these are excellent figures. It can be anticipated that the next VLBI generation, VLBI2010, will improve VLBI's timing capabilities by providing higher sensitivities, a 24/7 operation and possible real-time capabilties.

The development of tailored analysis methods is an important step to make VLBI acceptable for metrological use. We propose a Kalman-filter based VLBI filter software for continuous clock difference estimation and correct ambiguity resolution. Further, the calibration of VLBI systems would be necessary in order to be useful for time comparisons.

ACKNOWLEDGMENT

We thank the International VLBI Service for Geodesy and Astrometry and their individuals for organizing and observing CONT11. We thank in particular the VLBI group at the Bundesamt für Kartographie und Geodäsie for their support with the CONT11 data analysis. We acknowledge the National Resources Canada for the NRCAN GPS PPP software.

REFERENCES

[1] http://ivs.nict.go.jp/mirror/program/cont11/

[2] Rieck et al. "VLBI Time-Transfer using CONT08 Data", EFTF2010

[3] Ma C, Sauber JM, Bell LJ, Clark TA, Gordon D, Himwich WE, Ryan JW (1990) Measurement of horizontal motions in Alaska using Very Long Baseline Interferometry. Journal of Geophysical Research, 95(B13), 21991-22011.

[4] Orgiazzi D, Tavella P, Lahaye F (2005) Experimental Assessment of the Time Transfer Capability of Precise Point Positioning (PPP). In: Proc. of the Joint IEEE Intl. FCS and the PTTI, 337-345.

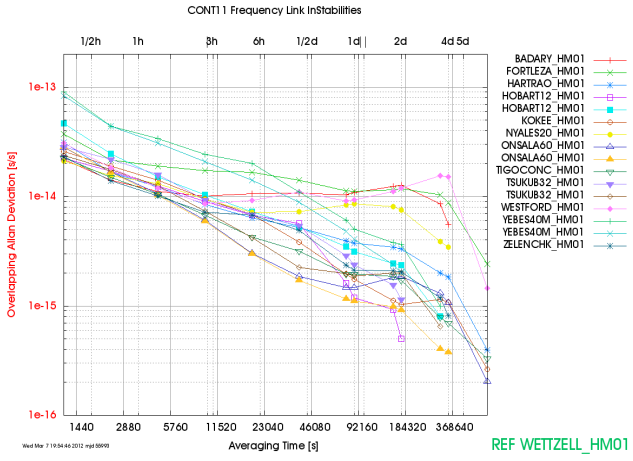

Figure 3. CONT11 Frequency link instabilities, overlapping ADEV.
For some stations more results are shown than those reported in Table II.
Hobart 1:(MJD 55819-55824), 2:(MJD 55826-55833),
Tsukuba 1:(MJD 55819-55824), 2:(MJD 55826-55833),
Yebes 1:(MJD 55819-55826), 2:(MJD 55828-55833),
Onsala 1:(MJD 55819-55833), 2:(MJD 55819-55830).

Absolute frequencies of ^{133}Cs $6S_{1/2}$-$8S_{1/2}$ two-photon transition stabilized diode lasers

Chien-Ming Wu, Tze-Wei Liu, You-Huan Chen and Wang-Yau Cheng
Department of Physics, National Central University
Taoyuan, Taiwan
wycheng@ncu.edu.tw

Shinn-Yan Lin
Telecommunication Laboratories,
Chunghwa Telecom
Taoyuan, Taiwan
sylin@cht.com.tw

***Abstract*—We report on our measured frequencies of cesium 6S-8S two-photon transitions. We also point out our finding on the influence of different cesium cells from different producer to the measured values of absolute frequency.**

I. INTRODUCTION

Two-photon transition of Alkali atoms possesses good features for laser stabilization, such as high spectral contrast and narrow spectral linewidth [1, 2, 3]. Therefore, Rubidium 5s-5d two-photon stabilized laser was recommended as a secondary frequency standard at 778-nm wavelength [1]. In recent years, we found that cesium 6s-8s two-photon transitions possess even more good features and give a great potential to serve as the other frequency standard at 822-nm due to the following facts [2]:

1. No linear Zeeman shift. We had once examined the influence of magnetic field on the transition frequency by unveiling the μ-metal shielding or putting an inhomogenous magnetic base nearby μ-metal-housed cesium cell, no frequency shift was observed within 5 kHz measurement precision.
2. The nearby hyperfine transition of Cesium $6S_{1/2}$ → $8S_{1/2}$ transition is 4-GHz far away, that is, the spectral line is very isolated.
3. Cesium atom has only one natural occurring isotope. Therefore, no isotope impurity problem has to be concerned.
4. A hand-size version of cesium two-photon stabilized diode laser (CTSDL) had been successfully demonstrated [3]. The versatility for installing in various systems will speed up the applications once this transition was recommended as one of the optical frequency standards.
5. Absolute frequency of Cesium $6S_{1/2}$ → $8S_{1/2}$ hyperfine transitions had been measured by direct frequency comb spectroscopy [4], within 15 kHz accuracy, and C. Y. Cheng et al. had showed 3 kHz reproducibility [2].
6. The absolute frequency of the second harmonic of CTSDL (411 nm) could be directly calibrated by ytterbium ion clock at 411 nm.

The significant application in our previous experiment was that we incorporated the aforementioned hand-sized cesium two-photon stabilized diode laser (CTSDL) into our mode locked lasers to monitor the absolute frequency of two Ti:sapphire lasers that are the most popular and wideband laser among the optical wavelength region of 700 nm to 900 nm. If our ultrafast Ti:sapphire laser was frequency locked to the CTSDL, it was referred to as "optical frequency comb laser" of which the feasibility was shown in reference [5]. However, frequency discrepancies from different cesium cells that were easily ignored [4] were recently found in our experimental system. In other words, different cesium cells of different producing sources yielded different values of transition frequency that might be the reason of the discrepancies of the previous two experimental results [4, 6].

II. EXPERIMENTAL SETUP

The experimental setup for investigating the absolute frequency of CTSDL, with various cesium cells, is illustrated in Fig. 1. A home-built diode laser described in reference [2], together with a tapered amplifier that boosted up the laser power to 250 mW, was used to provide three individual tasks for the finial purpose of spectral lineshape detection: The region that highlighted by solid line is for locking laser frequency to the two-photon transition center (sub-Doppler). However, due to the limited frequency bandwidth of PMT (photomultiplier tube), the high-frequency laser jitter had to be

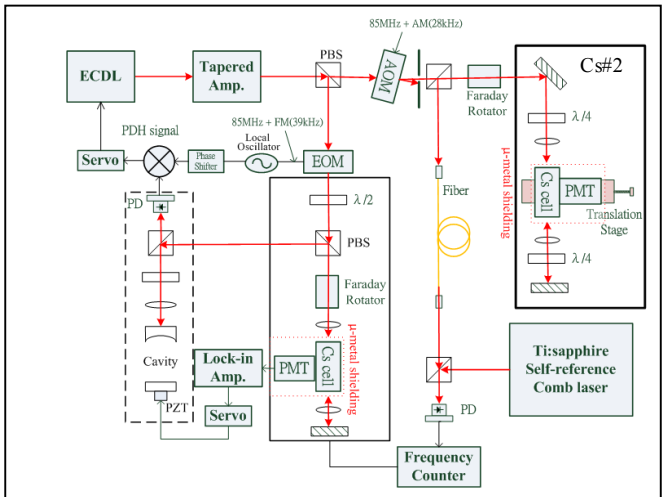

Fig. 1: Block diagram of our experimental setup that comprised three regions of dashed line: reference cavity system; solid line: laser stabilization system and solid bold line: spectral lineshape scanning system, see text.

further reduced by using a high-Q cavity system that is highlighted by the dashed line of Fig. 1. The other region of Fig. 1 that is highlighted by solid bold line comprises of one cesium cell is for the kernel task of this experimental setup, that is, for obtaining the spectral lineshape. Our unique approach on the optical frequency measurement is described in the following: we first reducing the laser frequency jitter with the assistant of a high-Q cavity (dashed-line part) where a Pound-Drever Hall signal could be obtained. By tuning the cavity length while laser frequency locking was engaged and after an electro-optical modulator (EOM), the +1 order laser frequency (85-MHz driving frequency) could reach the resonance frequency of the aforementioned cesium transitions (solid line part). We dither the 85-MHz EOM frequency from 84.5 MHz to 85.5 MHz with a 39-kHz dither frequency for

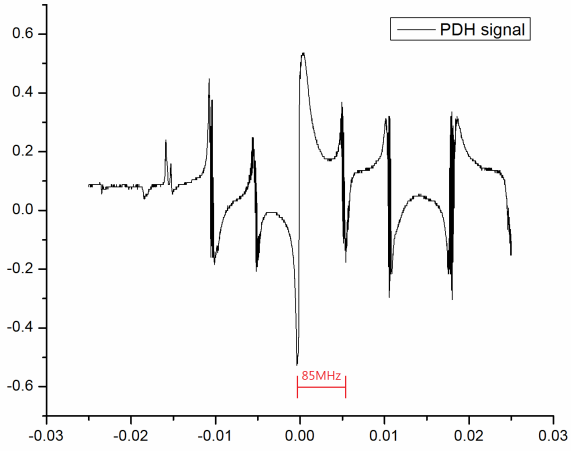

Fig. 2: The position of central zero of Pound-Drever Hall signal remained the same as that when EOM driving frequency was not dithered. Note that, the other zeros corresponding to the other sidebands were seriously dithered that they could not be used for laser stabilization.

obtaining the first-derivative like transition signal and for locking the +1 order laser frequency to the transitions center. Note that the dither on the EOM driving frequency would not influence the aforementioned cavity frequency locking since the center of Pound-Drever Hall signal was remained, as shown in Fig. 2. The laser carrier frequency would not be on resonance with cesium atoms in cesium cell #2 unless the laser frequency was shifted back, We used an AOM, shown in Fig. 1, to shift back the laser frequency to cesium resonance frequency and we tuned EOM driving frequency to scan the profile of the room-temperature cesium transitions. Transition profile (lineshape) was achieved by tuning the EOM drive frequency step by step (100 kHz/step) than in turn varied the optical carrier frequency step by step, and then we were able to scan the whole spectral profile for determining the transition center. During the EOM scanning, the laser frequency is constantly calibrated by a self-reference optical frequency comb laser in which the repetition rate was locked against a radio-frequency synthesizer where the time base was locked to a high performance cesium clock (Symmetricom 5071a). High-accuracy cesium clock is vital in this experiment since the mode number is around 10^6. That is, even 0.5 mHz repetition rate instability over 100 MHz repetition rate could yield 500 Hz optical frequency instability. Since the Symmetricom 5071a was calibrated by the National Time and Frequency Standard Laboratory of Taiwan, Telecommunication Laboratories (TL), using flying clock method and the uncertainty of frequency offset was less than 10^{-13}, the absolute frequency measurement could be controlled to have smaller than 1 kHz uncertainty.

III. RESULTS AND DISCUSSIONS

Fig. 3 shows a typical scan of cesium 6S-8S two-photon transitions. The estimated accuracy of the determined frequency was 10 kHz, obtained through a serial of routine measurements for two months. We list our obtained values in Table 1. To assure the frequency reproducibility, we also tried various cesium cells of different producers while kept all the optical and electronic setup the same for each measurement.

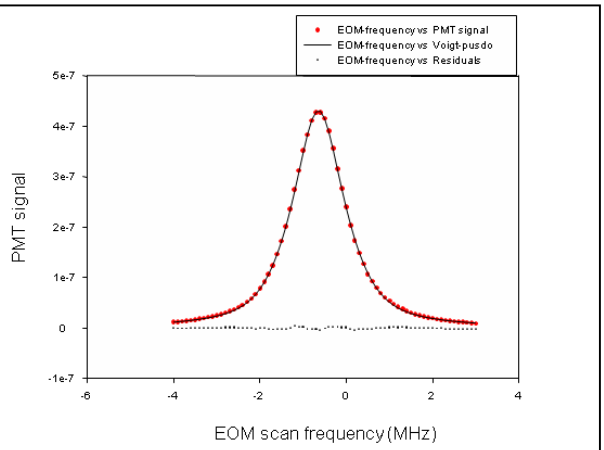

Fig. 3: The lineshape of F'=3 to F=3 hyperfine component of the 6s-8s transition fitted to Pseudo-Voigt profile. The transverse axis frequency is equal to $f_{laser}+AOM_f-EOM$ where f_{laser} was frequency stabilized and monitored by self- reference frequency comb laser.

We were aware that, however, different cesium cells presented different frequency measurement results that could deviate from each other for even 74 kHz. The reason is not clear though.

Table 1 Comparing absolute frequency measurement of F'=3 to F=3 transition

Reports	***frequencies (relative to [5])***	***measurement uncertainity***	***Linewidth***	***cell material***
Ref. [5]	0	15 kHz	1.2 MHz	N. A.
Ref. [6]	-97 kHz	100 kHz	1.9 MHz	N. A.
This work Thorlabs cell	-42 kHz	10 kHz	1.2 MHz	Pyrex
This work Opthos cell	- 57 kHz	10 kHz	1.3 MHz	Pyrex
This work Toptica cell	+17 kHz	10 kHz	1.3 MHz	Pyrex

ACKNOWLEDGMENT

This author is grateful for the financial support by National Science Council: NSC100-2112-M008-015.

REFERENCES

[1] Edwards, C.S., Barwood, G.P., Margolis, H.S., Gill, P., Rowley, W.R.C., Development and absolute frequency measurement of a pair of 778 nm two-photon rubidium standards, Metrologia vol. 42, pp. 464-467, 2005, and reference therein.

[2] C. -Y Cheng, C, -M Wu, G. -B Liao and W. -Y Cheng, "Cesium 6S1/2 → 8S1/2 two-photon transition stabilized 822.5 nm diode laser", Opt. Lett. vol. 32, pp. 563-565, March, 2007

[3] Y.-H. Chen, T. –W Liu, C. M. Wu, C. –C. Lee, C. K. Lee and W. –Y. Cheng, "High-resolution 133Cs 6S-8S, 6S-6D two-photon spectroscopy using an intracavity scheme", Opt. Lett. vol. 36, pp. 76-78, Janurary, 2011

[4] P. Fendel. D. Bergeson, Th. Udem, and T. W. Hansch, "Two-photon frequency comb spectroscopy of the 6s-8s transition in ceisum" Opt. Lett. vol. 32, pp. 701-703, March, 2007.

[5] W.-Y. Cheng, T.H. Wu, S.W. Huang, S.Y. Lin, and C.M. Wu, "Stabilizing the frequency of femtosecond Ti:sapphire comb laser by a novel scheme", Appl. Phys. B, vol. 92, 13-18, April, 2008.

[6] G. Hagel, C. Nesi, L. Jozefowski, C. Schwob, F. Nez and F. Biraben, "Accurate measurement of the frequency of the 6S-8S two-photon transition in cesium", opt. comm. vol. 160, 1-4, Feburary, 1999.

Active Disturbance Rejection Control: Application to the Temperature Stabilization of Ultra-Stable Cavities

Marco Pizzocaro*, Davide Calonico†, Claudio Calosso†, Cecilia Clivati*,
Giovanni Antonio Costanzo*, Filippo Levi† and Alberto Mura†
* Politecnico di Torino, Torino, Italy
†Istituto Nazionale di Ricerca Metrologica (INRIM), Torino, Italy
Email: m.pizzocaro@inrim.it

***Abstract*—The examples of controls in a high-precision scientific laboratory are countless and most scientific applications rely on controls of the powerful proportional-integral-derivative (PID), first introduced by Minorsky in 1922. In recent years a novel Active Disturbance Rejection Control (ADRC) has been proposed. The ADRC is a linear, simple, intuitive, and inherently robust form of control. It is based on a linear extended state observer (LESO) that estimates and compensates the disturbance of the system in real time with a certain bandwidth. The bandwidths of the control and of the observer are the only parameters needed for tuning. The design of the ADRC is model independent and requires only some approximate knowledge of the fast frequency response of the system. We applied the ADRC to the stabilization of the temperature of optical ultra-stable cavities. Such cavities are used for laser frequency stabilization for high-resolution spectroscopy and in optical clocks. In our case a $578\,\mathrm{nm}$ yellow laser is locked to the cavities and it will be used for the spectroscopy of ytterbium atoms. The temperature of the cavities has to be stabilized to prevent drift in their length and thus in the frequency of the laser. We will present the details of the ADRC and show the performance of the temperature stabilization. The ADRC shows attractive features that motivates our choice: it is easy to design and to implement digitally, insensitive to environmental changes, and avoids typical problems encountered with PID like overshoots and integral windup.**

I. Introduction

The examples of controls in a high-precision scientific laboratory are many and varied: for example controlled current sources for diode lasers, stable voltage references, stabilization of the frequency and the amplitude of lasers, precise controlling of length through piezoelectric elements, etc. Most scientific applications rely on controls of the powerful proportional-integral-derivative (PID), first introduced by Minorsky in 1922 [1]. PID controls need to be tuned through experience, intuition or even look-up tables.

We report here an application of a novel Active Disturbance Rejection Control (ADRC): a linear, simple, easy, intuitive, and inherently robust form of control [2], [3]. ADRC can be used effectively instead of a PID.

We applied the ADRC to the stabilization of the temperature of two optical ultrastable cavities used in a forthcoming optical clock experiment [4], [5]. Ultra-stable lasers with narrow linewidth are a critical technology for high-resolution spectroscopy, optical atomics clocks, tests on fundamental constants or frequency transfers via optical link. The stabilization of the laser source is typically accomplished with a locking to high-finesse cavities. The cavity should be insulated from vibration and temperature variation. In particular the temperature of the cavity has to be stabilized to prevent drifts in the frequency of the laser. Cavities are usually made in Corning Ultra Low Expansion glass (ULE), characterized by a quadratic thermal expansion and thus by a zero in the coefficient of thermal expansion (usually around room temperature) [6].

In our case a $578\,\mathrm{nm}$ yellow laser is locked to a fringe of one of the two cavities and it will be used for the spectroscopy of ytterbium atoms [7], [8]. We will show that the ADRC is a feasible technology, readily applied to problems related to the realization of clock lasers.

This work is funded by: Regione Piemonte, YTRO contract.

II. Active Disturbance Rejection Control

Let say we want to control a second order system, also known as plant, governed by the equation

$$\ddot{y} = bu + f(y, \dot{y}, u, \nu, t, \dots), \tag{1}$$

where y is the output, u is the command (input), and b is a constant of the plant, at least approximately known. The function $f(y, \dot{y}, u, \nu, t, \dots)$, or simply f, is called the generic disturbance and can depend on the variable y and its derivatives, the command, the time t or external noise ν. It accounts for internal dynamics of the plant, friction, noise, hysteresis, non-linearity, time dependencies, and it is generally unknown. Basically, the generic disturbance f accounts for any *uncertainty* in the system dynamics while, for controlling the plant, we only need to know that the plant responds to the command u approximately through the coefficient b.

For example, consider the equation of a simple harmonic oscillator of frequency ω_0 and width k, where y is the position and u the force (Newton's law):

$$\ddot{y} = b_0 u - k\dot{y} - \omega_0^2 y$$

Here b_0 is the inverse of the mass. Then we could write it as

$$\ddot{y} = bu + \underbrace{(b_0 - b)u - k\dot{y} - \omega_0^2 y}_{f}, \tag{2}$$

where uncertainty in the value of b is absorbed into f too. Since we assume only b known (both k and ω_0 could be unknown or time-varying), we shall show that we need only to know the mass of the mechanical system to control it.

Equation (1) describes also a second order thermal system where y is the temperature we want to control, u is the power applied, and b parametrizes the fast frequency limit of the thermal transfer function.

The basic idea behind ADRC is that f can be estimated in real time and then it can be canceled in the command reducing the dynamics of the system to the simple, ideal, double integrator part ($\ddot{y} \approx bu$).

A. State equation and the linear extended state observer

We can rewrite the equation of our system $\ddot{y} = bu + f$ in a state equation for the vector

$$x = \begin{bmatrix} y \\ \dot{y} \\ f \end{bmatrix},$$

where the state x is augmented by the presence of f. Then (1) becomes the matrix equation

$$\begin{aligned} \dot{x} &= Ax + Bu + Eh \\ y &= Cx \end{aligned} \tag{3}$$

where

$$A = \begin{bmatrix} 0 & 1 & 0 \\ 0 & 0 & 1 \\ 0 & 0 & 0 \end{bmatrix} \quad B = \begin{bmatrix} 0 \\ b \\ 0 \end{bmatrix} \quad E = \begin{bmatrix} 0 \\ 0 \\ 1 \end{bmatrix}$$

$$C = \begin{bmatrix} 1 & 0 & 0 \end{bmatrix}$$

and $h = \dot{f}$ is responsible for the unknown dynamics.

From this equation we construct a state observer for the variable

$$z = \begin{bmatrix} \hat{y} \\ \hat{\dot{y}} \\ \hat{f} \end{bmatrix},$$

where $\hat{y}$, $\hat{\dot{y}}$ and $\hat{f}$ are the estimates of y, $\dot{y}$, and f respectively, that is

$$\begin{aligned} \dot{z} &= Az + Bu + L(y - \hat{y}) \\ \hat{y} &= Cz \end{aligned} \tag{4}$$

where the unknown dynamic in (3) is replaced by the observer gain vector $L = [l_1, l_2, l_3]^\mathsf{T}$. Equation (4) describes the linear extended state observer (LESO) (see Figure 1). When properly implemented, the state of the LESO z will track the state of the plant x [2], [3].

As shown in [2], we can parametrize the LESO choosing the three gains in L so that all the observer eigenvalues are set to $-\omega_\mathrm{o}$. That is imposing $\det[sI - (A - LC)] = (s + \omega_\mathrm{o})^3$ we get

$$L = \begin{bmatrix} 3\omega_\mathrm{o} \\ 3\omega_\mathrm{o}^2 \\ \omega_\mathrm{o}^3 \end{bmatrix}. \tag{5}$$

In this way, the LESO is simply characterized only by the parameter b and by the observer bandwidth ω_o. The parameter b is known from the plant or can be measured from the open loop response. The bandwidth ω_o can be tuned looking for a compromise between performances and noise sensitivity.

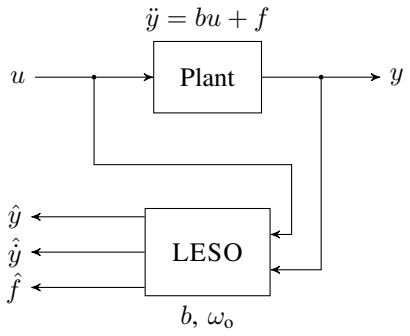

Figure 1. Schematic diagram of the physical system under control (plant) and of the linear extended state observer (LESO). Taking as input the output of the plant y and the command u, the LESO gives as output the estimates of the plant output $\hat{y}$, of its derivative $\hat{\dot{y}}$ and of the generic disturbance $\hat{f}$.

B. The controller

Once the LESO is set up it is easy to design a controller for the plant. We write the control law as

$$u = u_0 - \hat{f}/b, \tag{6}$$

so that (1) becomes

$$\ddot{y} = bu + f = bu_0 - \hat{f} + f \approx bu_0. \tag{7}$$

We used $\hat{f}$ to cancel out the contribution from f thus reducing the system dynamics to approximately a double integral plant (7). This can be easily controlled by a proportional-derivative (PD) controller of the form

$$bu_0 = k_\mathrm{p}(r - \hat{y}) - k_\mathrm{d}\hat{\dot{y}}, \tag{8}$$

where r is the desired set point (see Figure 2). Since eq. (7) has a simple form, we can impose the gains

$$k_\mathrm{p} = \omega_\mathrm{c}^2, \quad k_\mathrm{d} = 2\omega_\mathrm{c}, \tag{9}$$

so that the closed loop poles of (7) lay at the control bandwidth ω_c. In fact, substituting (8) in (7) and assuming z tracking x we can write the closed loop transfer function between r and y in the frequency domain ($s = j\omega$)

$$G(s) = \frac{k_\mathrm{p}}{s^2 + k_\mathrm{d}s + k_\mathrm{p}} = \frac{\omega_\mathrm{c}^2}{(s + \omega_\mathrm{c})^2}. \tag{10}$$

Note that this PD control is always, at least approximately, critically damped.

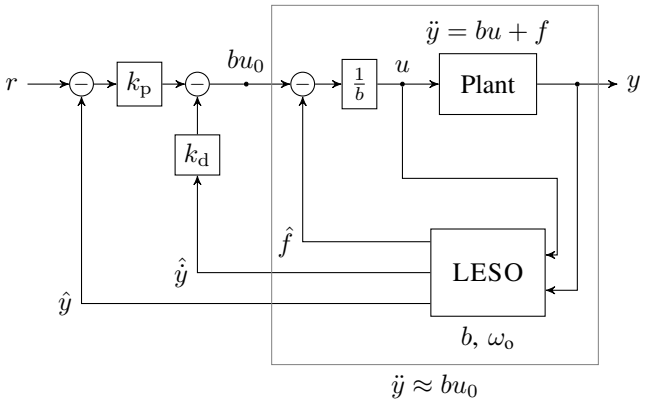

Figure 2. Schematic diagram of the ADRC scheme.

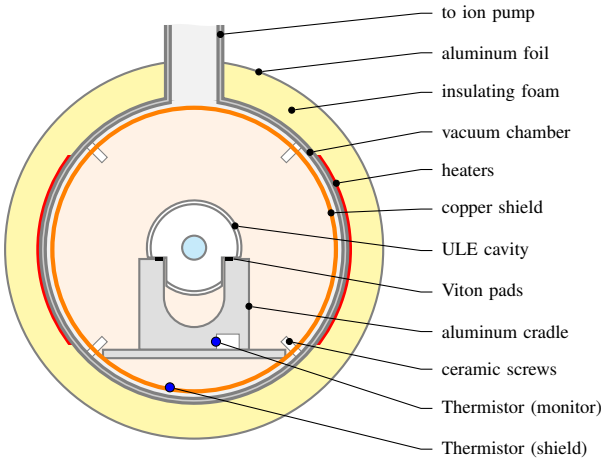

Figure 3. Schematic diagram of the vacuum chamber, showing the thermal isolation of the ULE cavity. The vacuum chamber is kept on a seismic-isolation platform and inside an acoustic-isolation enclosure.

C. Properties of the ADRC

The estimate of $\hat{f}$ is the central part of ADRC. Instead of integrating the error signal, like in a traditional PID, the ADRC integrates the difference between the measured output of the plant and the ideal response of the LESO

$$\hat{f} = \omega_\mathrm{o}^3 \int (y - \hat{y})\mathrm{d}t. \tag{11}$$

This achieves zero steady-state error but avoids typical problems encounter with integral controls like overshoot and integral windup.

The estimate $\hat{f}$ is a low-pass filtered version of the real f, with bandwidth ω_o; that is, in the frequency domain [9]:

$$\hat{f}(s) = f(s)\frac{\omega_\mathrm{o}^3}{(s+\omega_\mathrm{o})^3}. \tag{12}$$

This feature makes the ADRC robust against (slow) changes in the system dynamics.

III. Experiment

Our two ULE cavities are 10 cm long and will be used for the stabilization of the local oscillator in a future ytterbium optical clock. A yellow laser at 578 nm is locked to the fringes of the two cavities [8]. The two cavities are independent and build with a similar design.

The cavity is held in a stainless steel vacuum chamber where an ion pump keeps the pressure below 1×10^{-4} Pa (see Figure 3). The cavity is supported by 4 Viton pads on an aluminum structure. A radiation shield made in copper surrounds the cavity and it is held in place by 4 ceramic and 4 nylon screws. Two flexible heaters are applied externally on the vacuum chamber. For the laser stabilization purpose the vacuum chamber is held on a vibration-isolation platform inside an acoustic-isolation chamber.

The ADRC is used to stabilize the temperature of the copper shield. In the vacuum chamber there are two thermistors. The first is thermally contacted on the copper shield and it is the sensor in the control loop. The second thermistor is used as a monitor and is placed on a piece of glass below the cavity. No thermistor is placed on the cavity itself preserving the good mechanical property of the ULE glass. Since the cavity is well insulated (time constant > 40 000 s) on the short term we are relying on the passive thermal property of the system to stabilize the cavity temperature.

The control of the temperature of the copper shield is performed digitally with a software program (written in Python) running on a personal computer. A multimeter reads the resistance value of the thermistor. The software gets the instrument measurements through a GPIB interface every 2 s and performs an ADRC in discrete time, using a zero order hold, current estimator approximation (see [10] for details). The calculated commands are then converted to analog signals used to drive the heaters around the vacuum chamber. The sampling time of 2 s is chosen to minimize the dead time in the measurement of the two thermistors.

IV. ADRC in practice

A. Tuning of the control

Tuning of the ADRC involve an approximate knowledge of the fast frequency response parameter b. In our case it can be estimated from a simple thermal equivalent circuit of the system (Figure 4), where we considered the thermal capacity of the vacuum chamber C_c, the thermal resistance of the foam insulation R_i, the thermal capacity of the copper shield C_s, and the resistance between the shield and the vacuum chamber, where half the contribution comes from the conduction through the support screws (R_c) and the other half from thermal black body radiation (R_t). From this circuit, a second order equation rewritable in the form of eq. (1) can be obtained where

$$b = \frac{1}{C_\mathrm{c}C_\mathrm{s}}\left(\frac{1}{R_\mathrm{c}} + \frac{1}{R_\mathrm{t}}\right). \tag{13}$$

Alternatively we measured the value of b from the thermal transfer function of both systems Figure 5. We applied sinusoidal signals at different frequencies to the power sent

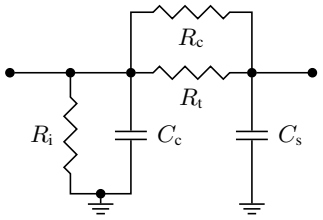

Figure 4. Equivalent circuit of the thermal properties of the system.

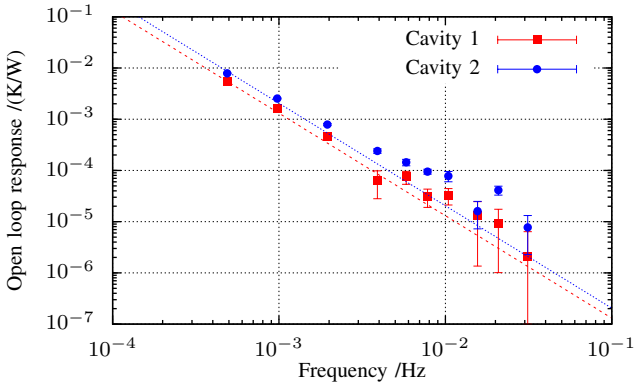

Figure 5. Transfer function of the two cavities. The dots represent measurement of the response of the shield temperatures (in kelvin) to sinusoidal signal in the command (in watts) at different frequencies. The lines show fits for the fast frequency response $b/(2\pi\nu)^2$, where ν is the frequency.

to the heaters of each cavity monitoring at the same time the temperature of the thermistor. A computer program allows us to extract the in-phase and out-of-phase responses of the temperature for each frequency and, sorting out transient behaviors, to reconstruct the transfer function. In Figure 5 the data are fitted with the function $b/(2\pi\nu)^2$ where ν is the Fourier frequency.

Table I shows the measures of b resulting from the fit and the final values of the parameters used in our control. Tuning the ADRC is a simple matter of making the control more of less aggressive looking for a compromise: increasing ω_o increases the disturbance rejection at the expense of a greater sensitivity to noise; increasing ω_c allows the control to follow the set point faster but increasing sensitivity to noise and noise in the command. We chose the bandwidths preferring a low noise command over fast time response.

A maximum command of 8 W is imposed by the control to limit the current in the heaters. With these limits, we can set the temperature between room temperature (24 °C) up to about 45 °C.

Table I
FINAL PARAMETERS FOR THE CONTROLS OF THE TWO CAVITIES.

	Cavity 1	Cavity 2
b	5.2×10^{-8} K/(W s^2)	8.1×10^{-8} K/(W s^2)
ω_o	8×10^{-3} rad/s	6×10^{-3} rad/s
ω_c	15×10^{-3} rad/s	15×10^{-3} rad/s

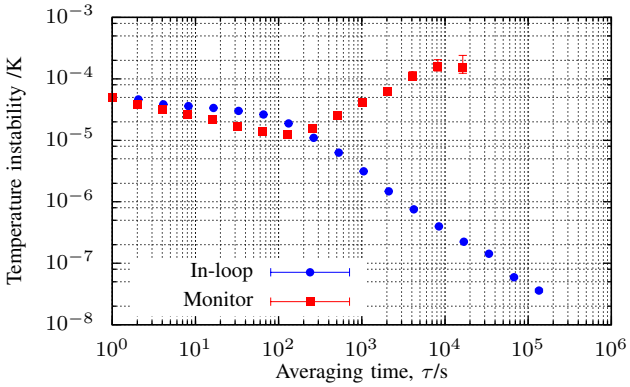

Figure 6. Overlapping Allan deviation of the temperature of the thermal shield (in-loop measurement) and of the monitor thermistor of one of our cavities.

B. Some results

The ADRC works well when applied to the real system. In general the temperature of the shield follows closely the set point with little overshoot after changes.

Figure 6 shows the instability of the temperature of the shield (measured in loop) of one of our cavities, expressed as overlapping Allan deviation [11]–[13]. The cavity were held at 25.5 °C during the measurement, in quiet environment. The total measurement time was 11 days; data were recorded every 2 s by the computer program that performs the control. At averaging time $\tau = 2$ s the instability value is limited by the noise of the multimeter used in the control. The control starts working between $\tau = 100$ s and $\tau = 200$ s (that is approximately $1/\omega_o$) and then the noise decreases with averaging time.

The same figure shows the instability of the monitor temperature. This temperature usually varies less than 0.5 mK on a day by day basis. It has been measured for 100 h every 4 s. The overlapping Allan deviation shows an instability of 150 µK at one day of integration time.

V. CONCLUSIONS

The ADRC shows attractive features that motivate our choice: it is easy to design and to implement digitally, insensitive to environmental changes, and avoids typical problems encountered with PID like overshoots and integral windups.

- ADRC is simple and intuitive.
- It is inherently robust to changes in the system.
- The design is model independent. The only parameter needed is the approximate value of b.
- ADRC is very easy to tune (only two parameters involved ω_o, ω_c, both with the simple physical meaning of a bandwidth).
- Zero steady state error is achieved without the disadvantages of the integrator term in PID.
- It outputs smooth command signals.
- It is easy to implement in digital form.
- It is easy to extend to multiple-inputs/multiple-outputs systems.

Compared to PID, the ADRC main advantage lays on the easiness of design and tuning since no special effort should be done to achieve a critically damped control. ADRC is also intrinsically robust to changes in the system and it is less sensitive to noise (for example, there is no need to close the bandwidth at high frequency). The digital implementation of the ADRC does not require much more effort than that of a digital PID.

The ADRC works well in practice, as we have shown in the case of the stabilization of the temperature of two ultrastable cavities.

REFERENCES

[1] N. Minorsky, "Directional stability of automatically steered bodies," *Journal of the American Society for Naval Engineers*, vol. 34, no. 2, pp. 280–309, 1922.

[2] Z. Gao, "Scaling and bandwidth-parameterization based controller tuning," in *American Control Conference, 2003. Proceedings of the 2003*, vol. 6, 2003, pp. 4989–4996.

[3] ——, "Active disturbance rejection control: a paradigm shift in feedback control system design," in *American Control Conference, 2006*, 2006, p. 7.

[4] D. Calonico, F. Levi, L. Lorini, G. A. Costanzo, M. Zoppi, M. Pizzocaro, A. Mura, E. K. Bertacco, and A. Godone, "Yb optical lattice clock at INRIM," in *Proceedings of the 24th European Frequency and Time forum*, 2010.

[5] N. D. Lemke, A. D. Ludlow, Z. W. Barber, T. M. Fortier, S. A. Diddams, Y. Jiang, S. R. Jefferts, T. P. Heavner, T. E. Parker, and C. W. Oates, "Spin-$1/2$ optical lattice clock," *Phys. Rev. Lett.*, vol. 103, p. 063001, Aug 2009.

[6] T. Legero, T. Kessler, and U. Sterr, "Tuning the thermal expansion properties of optical reference cavities with fused silica mirrors," *J. Opt. Soc. Am. B*, vol. 27, no. 5, pp. 914–919, May 2010.

[7] C. Oates, Z. Barber, J. Stalnaker, C. Hoyt, T. Fortier, S. Diddams, and L. Hollberg, "Stable laser system for probing the clock transition at 578 nm in neutral ytterbium," in *Frequency Control Symposium, 2007 Joint with the 21st European Frequency and Time Forum. IEEE International*, 29 2007-june 1 2007, pp. 1274–1277.

[8] M. Pizzocaro, G. Costanzo, A. Godone, F. Levi, A. Mura, M. Zoppi, and D. Calonico, "Realization of an ultrastable 578-nm laser for an yb lattice clock," *IEEE Trans. Ultrason., Ferroelect., Freq. Cont.*, vol. 59, no. 3, pp. 426 –431, march 2012.

[9] R. Miklosovic and Z. Gao, "A robust two-degree-of-freedom control design technique and its practical application," in *Industry Applications Conference, 2004. 39th IAS Annual Meeting. Conference Record of the 2004 IEEE*, vol. 3, 2004, pp. 1495–1502.

[10] R. Miklosovic, A. Radke, and Z. Gao, "Discrete implementation and generalization of the extended state observer," in *American Control Conference, 2006*, 2006.

[11] D. W. Allan, "Statistics of atomic frequency standards," *Proc. IEEE*, vol. 54, no. 2, pp. 221–230, Feb. 1966.

[12] J. Rutman, "Characterization of phase and frequency instabilities in precision frequency sources: Fifteen years of progress," *Proc. IEEE*, vol. 66, no. 9, pp. 1048–1075, Sep. 1978.

[13] D. A. Howe, D. W. Allan, and J. A. Barnes, "Properties of signal sources and measurement methods," in *Thirty Fifth Annual Frequency Control Symposium. 1981*, 1981, pp. 669–716.

Compact Hz-level linewidth laser system

Erwin Portuondo-Campa, Stefan Kundermann, Steve Lecomte
CSEM, Centre Suisse d'Electronique et de Microtechnique
Jaquet-Droz 1, 2002 Neuchâtel, Switzerland
steve.lecomte@csem.ch

Abstract— **Increasing the compactness and robustness of laser stabilization systems is a critical need for the development of industrial applications of ultra-narrow linewidth lasers. In this aim, a compact optical setup based on the Pound-Drever-Hall scheme with a high finesse cavity was built with overall dimensions of L x W x H = 45 x 35 x 13 cm^3. An external cavity diode laser (PLANEX™, RIO Inc.) as well as a distributed-feedback fiber laser (Koheras Adjustik, NKT photonics) were stabilized using this system. The frequency stability was evaluated using a similar setup as reference. The combined relative stability of the systems reached 7·10^{-15} at 1s.**

I. INTRODUCTION

In recent years, significant progress has been made in the stabilization of narrow linewidth cw-lasers. State of the art frequency stabilities reach already the order of 10^{-16} [1][2]. So far, the main driver for these developments has been academic research in fundamental physics (e.g. gravitational wave detectors) and time and frequency metrology. There are, on the other hand, many possible applications of ultra-narrow linewidth lasers in industrial fields such as fiber optics sensors, analytical chemistry, security systems and general-purpose frequency references. In order to unfold the full industrial potential of this technology, it is mandatory to develop more affordable systems, with special emphasis on their compactness, robustness, flexibility and ease of operation. With this aim, we have built a compact laser stabilization system based on the Pound-Drever-Hall locking scheme with a high-finesse reference cavity [3]. The whole optical setup fits in a 45 x 35 cm^2 breadboard and allowed reaching stability values in the order of $7{\cdot}10^{-15}$ on a time scale of 1 s, which constitutes a very good compromise of size and performance.

This paper presents the main elements of the design of the stabilization setup. The results obtained for the stabilization of two different types of cw-lasers are discussed.

II. DESCRIPTION OF THE SETUP

A. Design of the optical cavity module

A Fabry-Perot reference cavity was built for the compact stabilization system. The spacer was a 4 cm long hollow cylinder of ultralow expansion (ULE) glass to which the mirrors were optically contacted. The mirrors were made of fused silica to reduce the thermal noise of the substrates [4]. ULE rings were optically connected to the external side of each mirror to hinder bending effects resulting from the different coefficients of thermal expansion (CTE) of the fused silica mirrors and the ULE spacer [4]. The nominal finesse of the cavity is superior to 120'000, for a maximum linewidth of 31 kHz. The free spectral range is 3.75 GHz.

A module consisting of a vacuum chamber with temperature control was designed and built to host the optical cavity. The optical cavity is held by four steel pins in horizontal position inside a copper cylinder [5]. An ion pump maintains a vacuum of 3·10-7 mbar in the enclosure. The system is heated with externally mounted flexible resistors to keep a constant temperature of 29°C, close to the expected zero-CTE of the composite cavity. For improved thermal stability, the whole module is wrapped with IR-reflecting plastic film. The temperature fluctuations of the cavity are expected (no measurement) to be well below 1 mK over 1 second.

The optical setup was mounted on a breadboard with overall dimensions of L x W x H = 45 x 35 x 13 cm^3. For sound and vibrations isolation the breadboard was mounted on an anti-vibration table (minus K®) and the setup was enclosed in a heavy-wood box, with its interior coated with 1 cm thick noise isolation wraps. The box provides the additional advantage of hindering air flow around the setup, which affects the temperature stability of the cavity module and other optical components.

B. Pound-Drever-Hall locking scheme

A diagram of the PDH setup is represented in Figure 1. The laser is coupled to the setup through a fiber. The light is sent through an acousto-optic modulator (AOM) enabling a frequency modulation bandwidth of several hundred kHz. In order to minimize the steering effects of the free space beams due to the AOM modulation, a double pass configuration was adopted. The optical beam is sent twice across the AOM through a cat's eye retroreflector [6] as shown in Figure 2. Frequency modulation occurs twice at the AOM and the returning beam follows exactly the same path as the incident beam, regardless of the applied frequency modulation. Beam separation at the exit is achieved with a circulator scheme.

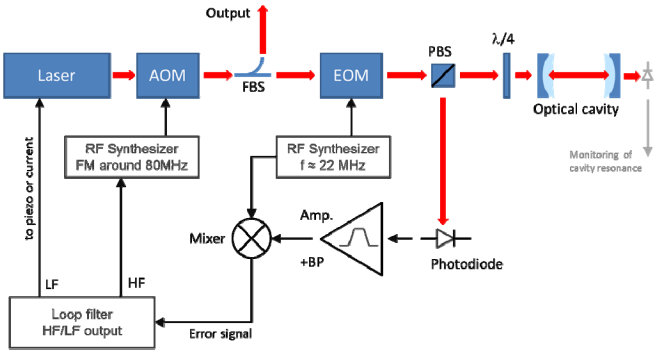

Figure 1. Diagram of the PDH setup. Red arrows represent light and black arrows represent electronic signals.

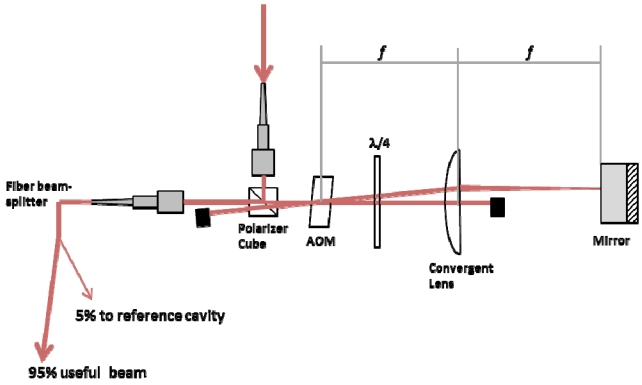

Figure 2. Configuration of the double-pass AOM scheme

Following the double pass AOM, the light is coupled into a fiber beam splitter (FBS) which splits 95% of the optical power as output for the user. The remaining 5% of the light is directed into the electro-optic modulator (EOM) that modulates the phase of the optical beam with a frequency of 22 MHz. After the EOM, the beam passes through an arrangement of lenses to adjust its diameter and divergence to the cavity mode. A polarizing beam splitter (PBS) and a λ/4 wave-plate at the entrance of the cavity allow separating the light reflected from the cavity, which is directed onto a fast photodiode for the detection of the error signal. The signal from the fast photodiode is demodulated by mixing with the oscillator signal driving the EOM. The low frequency component of the error signal is conditioned by a servo loop and the corresponding correction signal is sent to the laser. Depending on the laser type this actuation can be done through the current of a diode laser or through an intracavity piezo actuator. Faster fluctuations of the laser frequency are corrected through the high frequency loop which modulates the frequency of the AOM through a voltage controlled oscillator (VCO).

C. *Reference system*

For the measurements of frequency stability, another narrow linewidth laser stabilized on a cavity was used as reference. The cavity of the reference setup was 10 cm long and has a finesse of 180'000, for a resonance width of 8.3 kHz. The cavity enclosure was in this case bulkier and had a double stage temperature control with peltier elements to cool the cavity to a temperature of 5°C (±1 mK). The vacuum in the enclosure was kept at $4 \cdot 10^{-8}$ mbar with an ion pump. The PDH scheme for the stabilization of the reference laser followed on every aspect the design of the compact system discussed above.

D. *Characteristics of the cw-lasers*

Two different types of cw-lasers were locked using the compact and reference stabilization units: a narrow-linewidth external cavity diode laser (PLANEX™, RIO Inc.) and a distributed-feedback fiber laser (Koheras Adjustik™, NKT photonics). In the following, we refer to these lasers as the ECL (for External Cavity Laser) and the DFB (for Distributed Feedback) laser. The main technical characteristics of these lasers are resumed in Table 1.

Laser	**ECL**	**DFB**
Wavelength	1560 nm	1560 nm
Wavelength tunability range	0.03 nm (Temp. control)	0.6 nm (Temp. control)
Fast frequency tunability range	200 MHz (diode current)	2.5 GHz (intracavity PZT)
Free running linewidth	3 kHz @ 250 µs	1 kHz @ 120 µs
Dimmensions (LxWxH)	9x9x3 cm^3 (standard butterfly 14-pin mount, no electronics)	10x45x38 cm^3 (19 inch housing, with electronics)

Table 1. Technical characteristics of the two cw-lasers tested with the stabilization setup

III. RESULTS AND DISCUSSION

A. *Frequency noise spectra of the stabilized lasers*

The RF spectra of the PDH detectors of the stabilized ECL and DFB lasers are shown in Figure 3. The frequency axis has been shifted to center both plots on the respective modulation frequencies, which were 22 MHz and 18 MHz for the compact and reference stabilization setups, respectively. In these measurements the DFB laser was locked to the compact stabilization unit and the ECL to the reference. It is worth mentioning, however, that the features of the spectra in Figure 3 depend only on the laser and on the servo loop parameters that were applied. The stabilization units, being essentially equivalent, could be exchanged without influencing the frequency noise spectra of the stabilized lasers.

The central peaks in both spectra correspond mostly to RF pick-up of the modulation signals. This can be checked by blocking the light on the photodiode and seeing that the peak is almost not affected. An unavoidable component of amplitude modulation by the EOM also produces a contribution at the modulation frequency. The bumps at the sides of the central peak for the stabilized ECL correspond to the bandwidth limit of the servo loop (around 450 kHz). Close to the central peak there is barely any signal since the system suppresses frequency fluctuations very efficiently in the kHz bandwidth. The strongest noise component around 450 kHz is only 9 dB above the detection floor of the analyzer.

In the case of the DFB laser, the spectrum is dominated by a series of peaks starting around 50 kHz that probably correspond to mechanical resonances of the PZT in the laser cavity. In order to attenuate this high-frequency noise, a low-pass filter with cut-off frequency at 50 Hz was introduced at the input of the laser-PZT channel. This permitted a reduction of ca. 25 dB in the noise peaks amplitudes.

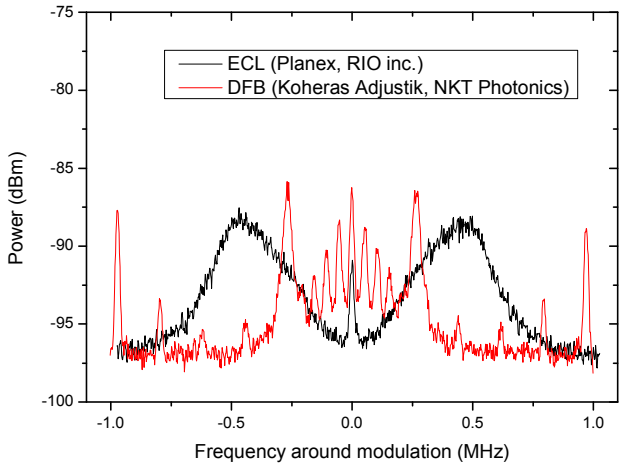

Figure 3. RF spectrum of the PDH photo-detector's signal for the ECL and DFB lasers (frequency axis shifted to center both plots on the respective modulation frequencies). Resolution Bandwidth of the microwave spectrum analyzer: 18 kHz.

B. Frequency stability analysis

For assessing the combined optical frequency stability both lasers were tuned to similar wavelengths around 1560 nm, in a range of ± 0.01 nm and locked to the reference cavities. The beat note of the two stabilized sources was detected with a fast highly linear photodiode and analyzed with a Universal Counter (53132, Agilent) and home-made data log software. The spectrum of the beat-note signal was also recorded in the RF spectrum analyzer (N9010A, Agilent).

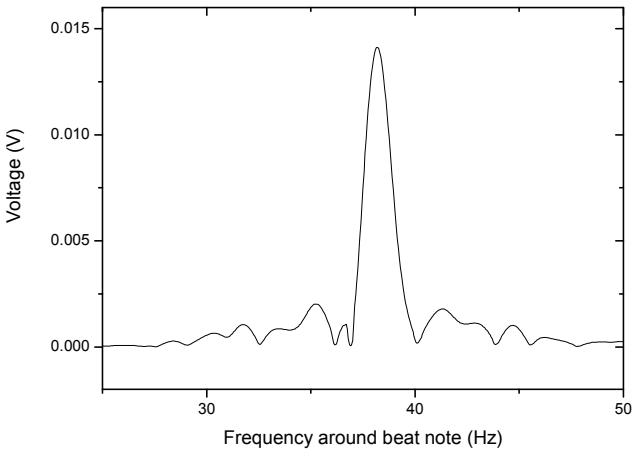

Figure 4. RF spectrum of beat note signal (frequency axis centered on the beatnote frequency of 1.4 GHz). Resolution bandwidth of the measurement: 1 Hz

Figure 4 presents the spectrum of the beat note signal obtained with an acquisition time of 1.8 s. The FWHM of the peak is 1.8 Hz, which corresponds to a relative frequency stability of $7 \cdot 10^{-15}$. This spectral width corresponds to the cross-correlation of the two laser spectra. Considering that both systems have similar stabilities, the spectral width of each locked laser would be approximately 1 Hz. In terms of cavity length stability, this represents a cumulated cavity length change of approximately 0.3 fm on a timescale of 1.8 s for the compact 4 cm long cavity.

Figure 5 presents a typical overlapping Allan deviation of the optical frequency for an acquisition period of 25 min, 10 ms integration time and 100 ms time step. Best stability, in the order of $6.7 \cdot 10^{-15}$ is achieved in the 1.5 s timescale. This corresponds to frequency fluctuations in the order of 1.2 Hz over 1 s; which is in good agreement with the width of the RF spectrum of the beat note signal. A linear drift of the beat note frequency, typically in the range of 1 – 3 Hz/s was removed from the data for the frequency stability analysis. This drift is the result of residual temperature drifts of the cavities (the cavities were not operated at their zero crossing temperatures of thermal expansion).

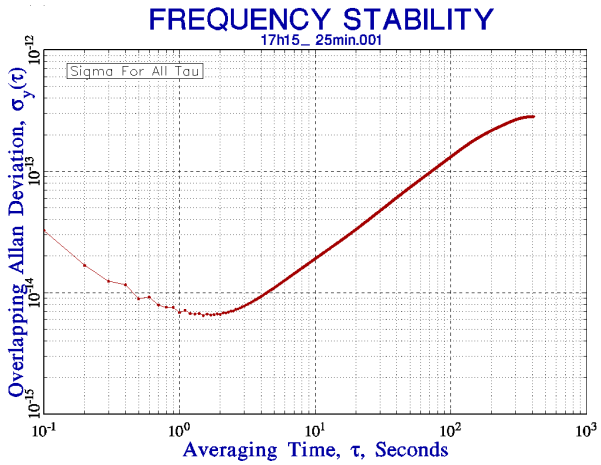

Figure 5. Overlapping Allan deviation of the beat note frequency (linear drift of 2.5 Hz/s removed)

IV. CONCLUSION AND FUTURE DEVELOPMENTS

This work aims at the development of miniaturized turn-key laser stabilization systems for industrial applications. Our efforts were mainly focused on the design of the optical part of the setup, which is the most critical to the robustness and performance of the system. For this goal, a PDH stabilization unit was built with overall dimensions of 45 x 35 x 13 cm^3. The frequency stability of the system was measured in combination with a similar setup and reached relative values of $7 \cdot 10^{-15}$ for integration times of 1 s. This result is close to the state of the art and remarkable for a system of such compact dimensions.

Further developments will include reducing the dimensions and improving the mechanical robustness of the system. The design of custom electronics and vibration isolation will be the last step in the development of a compact turn-key system.

ACKNOWLEDGMENT

The authors would like to thank Jonathan Bennès, Marianne Toimil, Gérald Perruchoud and Jean-François Léchenne for their contributions to the realization of this work This work has been supported by the Swiss Innovation Promotion Agency with the CTI contract Nr. 10500.2 PFNM-NM.

REFERENCES

[1] Y.Y. Jiang, A.D. Ludlow, N.D. Lemke, R.W. Fox, J.A. Sherman, L.S. Ma, C.W. Oates, "Making optical atomic clocks more stable with 10^{-16} level laser stabilization", *Nature Photonics* 5, 158-161 (2011)

[2] T. Kessler, C. Hagemann, C. Grebing, T. Legero, U. Sterr, F. Riehle, M.J. Martin, L. Chen, J. Ye, "A sub-40 mHz linewidth laser based on a silicon single-crystal optical cavity", http://arxiv.org/abs/1112.3854v2

[3] R.W.P. Drever, J.L. Hall, F.V. Kowalski, J. Hough, G.M. Ford, A.J. Munley, H. Ward, "Laser phase and frequency stabilization using an optical resonator", *Appl. Phys. B* 31, 97-105 (1983)

[4] T. Legero, T. Kessler, U. Sterr, "Tuning the thermal expansion properties of optical reference cavities with fused silica mirrors", *J. Opt. Soc. Am. B*, Vol. 27, No. 5/May (2010)

[5] T. Nazarova, F. Riehle, U. Sterr, "Vibration insensitive reference cavity for an ultra-narrow-linewidth laser", *Appl. Phys.B* 83, 531-536 (2006)

[6] E.A.Donley, T.P. Heavner, F. Levi, M.O. Tataw, S.R. Jefferts, "Double-pass acousto-optic modulator system", *Review of Scientific Instruments* 76, 063112 (2005)

Mass-Ratio Sensitivity of rovibrational Transitions

Florin Lucian Constantin
Laboratoire de Physique des Lasers, Atomes, Molécules
CNRS UMR 7523
Villeneuve d'Ascq, France

***Abstract*—The measurement of the frequency difference of rovibrational transitions from two different molecules is suggested to test the variation of the electron-to-proton mass-ratio μ. The frequency of rovibrational transitions is sensitive to μ. Small frequency splittings reached between the transitions from two isotopomers allow an enhancement relative to the variation of μ.**

I. INTRODUCTION

Experimental data from precision spectroscopy and astronomical observations allow addressing the question of time variation of fundamental constants [1]. The comparison between atomic frequency standards put tight constraints on the temporal variation of the fine structure constant at an unprecedented level with the exceptional accuracy of the single ion clocks [2]. The comparison between a molecular transition and the primary frequency standard [3] allowed a direct and model-free test of the temporal variation of the proton-to electron mass-ratio. An interest is growing up for exploiting the rich structure of energy levels of the molecules that are sensitive to the fundamental constants. Recent advances focus on probing the gap between two closely-spaced narrow molecular energy levels of different nature that allows an enhancement of the sensitivity to the variation of the fundamental constants. The vibrational energy levels are sensitive mainly to electron-to-proton mass-ratio variation. Homonuclear dimers [4,5] display pairs of closely-spaced vibrational levels that enhance the sensitivity to the mass-ratio variation by the depth of the vibrational potential.

An alternative approach is proposed by using the difference between molecular transitions. Instead of probing a gap between two closely-spaced energy levels, the strategy is to measure the frequency difference of two near-resonant molecular transitions. Rovibrational transitions probed in the same electronic state are sensitive to $\mu=m_e/m_p$, where m_e is the electron mass, m_p is the proton mass, and their frequency splitting allows an enhancement relative to the variation of μ. The sensitivity of this approach arises from the comparison of the entire structure of the molecular rovibrational spectrum. Highly sensitive near-resonant transitions arise in a molecule with many vibrational levels or in pairs of different molecules from the cancellation between the differences of the vibrational intervals and the rotational intervals.

II. CLOSELY-SPACED ROVIBRATIONAL TRANSITIONS WITH AN ENHANCED MASS-RATIO SENSITIVITY

A few key elements should be taken in account to discuss the sensitivity of this approach.

First is the change of the frequency splitting $X=f_{rv1}-f_{rv2}$ between two closely-spaced molecular rovibrational transitions (f_{rv1},f_{rv2}) with the fractional change of μ: $dX/d(ln\mu)$. In addition, the statistic uncertainties in the measurement of the rovibrational frequencies are governed by the transition linewidths $\Gamma_{1,2}$ and the signal to noise ratios $SNR_{1,2}$ $\delta f_{rv1,2}=\Gamma_{1,2}/SNR_{1,2}$ that add to yield the uncertainty of the frequency splitting δX. If both molecular transitions are measured with the same linewidth Γ, the fractional statistic uncertainty of mass-ratio constant measurement δμ/μ is governed by the factor δX/Γ.

Testing the temporal stability of μ via the measurement of the frequency difference between closely-spaced molecular transitions has the advantage to reduce the contribution of some systematic frequency shifts as the second-order Doppler effect. In addition, as the molecular frequencies are measured against a reference clock, the fractional frequency uncertainty of the frequency difference is ultimately limited by the fractional uncertainty of the reference clock. The frequency of the clock is subject to a possible drift due, for example, to the temporal variation of other fundamental constants. In this case, the quantity that is the frequency ratio between the frequency splitting and the absolute frequency of one rovibrational transition keep an enhanced sensitivity to the variation of the mass-ratio, while it is insensitive to the temporal drift of the reference clock.

The diatomic molecules in the Born-Oppenheimer approximation allow discussing the enhancement. Molecules in the $^1\Sigma$ electronic ground state are considered at the lowest level of approximation when the molecular rotation is modelled with a rigid rotor and the vibration is accounted with a harmonic oscillator. The rovibrational frequencies are expressed as a sum $f_{rv1,2}=f_{r1,2}+f_{v1,2}$ of the rotational terms ($f_{r1,2}$) and the vibrational terms ($f_{v1,2}$):

$$f_{v1,2}=\omega_{e1,2}\times(v_{1,2}+½). \quad (1)$$

with the vibrational frequency $\omega_{e1,2}$ and the vibrational quantum number $v_{1,2}$, and:

$$f_{r1,2}=2B_{1,2} \times m(J_{1,2}). \quad (2)$$

with the rotational constant $B_{1,2}$ and the integer m depending on the rotational quantum number $J_{1,2}$ in the lower vibrational state (m=-$J_{1,2}$ for P branch J'= $J_{1,2}$-1 ← J''= $J_{1,2}$ rovibrational transitions, respectively m=$J_{1,2}$+1 for the R branch J'= $J_{1,2}$+1 ← J''= $J_{1,2}$ transitions).
The vibrational frequency increases as the square root of $\mu=m_e/m_p$ and the rotational constant increases linearly with μ. This lead to the expression of the mass-ratio dependence of the frequency splitting between closely-spaced rovibrational transitions:

$$dX/d(\ln\mu) = ½ \times (1+(f_{r1}-f_{r2})/X) \times X. \quad (3)$$

The relative variation of μ yields an enhanced variation of the frequency splitting by $\sim ½ \times (f_{r1}-f_{r2})/X$. A typical rovibrational spectrum for two molecules is shown in Fig. 1. The strength of the transitions is estimated following the thermal distribution over the rotational levels [6]. For a given temperature, near-resonant transitions are visible. The enhancement of the sensitivity to the mass-ratio variation increases as the frequency difference between the vibrational bands origins and the inverse of the splitting of the near-resonant transitions from the two molecules.

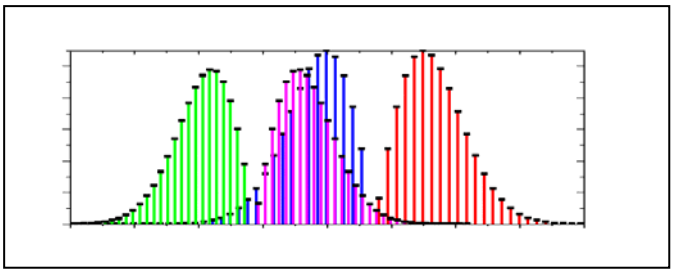

Figure 1. Simulation of the rovibrational spectrum (transition strength vs. frequency, in arbitrary units) for two diatomic molecules.

III. ROVIBRATIONAL SPECTRUM OF ACETYLENE ISOTOPOMERS

Acetylene is a linear symmetric molecule with $^1\Sigma$ electronic ground state that has a dense rovibrational spectrum. The isotope shift for acetylene is used in this work to define the pairs of molecules with close-lying transitions. The isotopic molecules have the same electronic structure, therefore the forces under that the nuclei are oscillating are the same at a high order of approximation.

The approximations used previously to discuss the mass-ratio sensitivity of the splitting between the close-lying transitions are not generally applicable. Anharmonicity contributes to the classical vibrational energy with supplementary terms:

$$2T = \sum_i m_i \dot{u}_i^2 + \sum_{i,j} k_{ij} u_i u_j + \\ + \sum_{i,j,k} f_{ijk} u_i u_j u_k + \sum_{i,j,k,l} g_{ijkl} u_i u_j u_k u_l . \quad (4)$$

where u_i are the Cartesian coordinates of the nuclei oscillating in the molecule-fixed reference frame (i=1,12), m_i are the masses of the nuclei (the mass $m_1=m_2=m_3$ of the first nuclei, $m_4=m_5=m_6$ of the second nuclei…) and quadratic k_{ij}, cubic f_{ijk}, quartic g_{ijkl} terms are the force constants. A linear transformation is applied to the Cartesian coordinates to get the adimensional normal coordinates for which the motion of the nuclei for a single frequency vibration mode (normal mode) corresponds to a harmonic oscillator. The vibrational energy is expressed in function of the normal coordinates q_k and their conjugate momenta p_k (k=1,7) as:

$$2H_V = \sum_k \omega_k (p_k^2 / \hbar^2 + q_k^2) + \\ + \sum_{i,j,k} \beta_{ijk} q_i q_j q_k + \sum_{i,j,k,l} \gamma_{ijkl} q_i q_j q_k q_l . \quad (5)$$

where ω_k are the normal mode frequencies, and the cubic β_{ijk} and the quartic γ_{ijkl} are the potential constants. The mass-ratio dependences of these terms are:

$$d\beta_{ijk}/d(\ln\mu)=3\beta_{ijk}/4 \; ; \; d\gamma_{ijkl}/d(\ln\mu)=\gamma_{ijkl}. \quad (6)$$

The quantum-mechanical rovibrational Hamiltonian [7] is derived with the method of Wilson and Howard. A perturbation treatment at the second order of approximation yields the expression of the total energy as a sum $E=h(G_v+F_r)$. The vibrational term is:

$$G_V = G_0 + \sum_s \omega_s (v_s + g_s / 2) + \\ + \sum_{s \le s'} x_{ss'} (v_s + g_s / 2)(v_{s'} + g_{s'} / 2) + \sum_{s \le s'} g_{ss'} l_s l_{s'} . \quad (7)$$

where G_0 is a constant for the lowest vibrational level, v_s is the vibrational quantum number associated to the normal frequency ω_s and g_s the degree of degeneracy of the same mode ($g_1=g_2=g_3=1$, $g_4=g_5=2$); $x_{ss'}$ is the first-order anharmonicity; $g_{ss'}$ is a contribution from the twofold degenerate vibrations 4 and 5 to the vibrational term, l_s is the vibrational angular momentum quantum number for the degenerate vibrations: $l_s= \pm v_s, \pm(v_s-2), \pm(v_s-4),\ldots$, 1 or 0. The rotational term is:

$$F_r = B[v][J(J+1)-l^2] - D[v][J(J+1)-l^2]^2 . \quad (8)$$

where J is the total angular momentum quantum number, $J \ge |l_4+l_5|$, B[v] is the rotational constant, D[v] is the centrifugal distortion constant. Vibration-rotation coupling in the

hamiltonian lead to a dependence of the rotational constants on the vibrational level, that is expressed at the first order of approximation as:

$$B[v] = B_e - \sum_s \alpha_s (v_s + g_s / 2). \quad (9)$$

where B_e is the equilibrium value of the rotational constant and a_s are the vibration-rotation constants. These constants depend on masses of the nuclei and the potential constants [7] that lead to the following mass-ratio dependences:

$$\begin{aligned} &d\omega_i / d(\ln \mu) = \omega_i / 2; dx_{ss'} / d(\ln \mu) = x_{ss'}; \\ &dg_{ss'} / d(\ln \mu) = g_{ss'}; dB_e / d(\ln \mu) = B_e; \\ &d\alpha_s / d(\ln \mu) = 3a_s / 2; dD / d(\ln \mu) = 2D. \end{aligned} \quad (10)$$

IV. Frequency Metrology with Acetylene Isotopomers at 1.5 μM

Doppler-free acetylene rovibrational lines have been used as frequency references in the near-infrared [8]. CIPM adopted the frequency of $^{13}C_2H_2$ P(16) rovibrational transition of v_1+v_3 combination vibration band as secondary frequency standard at 1.5 μm [9]. Vibration-rotation interactions and extensive anharmonic couplings between the combination vibrational levels lead to a specific mass-ratio dependence of each rovibrational transition. The molecular constants for acetylene isotopomers available in the literature [10] are determined from a global adjustment of rovibrational transitions frequencies. Note that the numerical values of the constants are obtained with a reduced expression in Equation 7 (term J(J+1) is used instead of $[J(J+1)-(l_4+l_5)^2]$) and in Equation 8 (term v_k is used instead of $(v_k+g_k/2)$).

Here is discussed the mass-ratio sensitivity of the transitions from the lowest vibrational level to a combination level that is coupled to another with a specific interaction. The $^{13}C_2H_2$ isotopomer displays a Fermi resonance between v_1+v_3 and $v_1+v_2+v_4+v_5$ combination vibration levels that splits the excited states energy levels and enhances the line strengths in the $v_1+v_2+v_4+v_5$ band. The vibrational energy levels, with energies E_{i0} of v_1+v_3 level and E_{n0} of $v_1+v_2+v_4+v_5$ level, are coupled by an off-diagonal term expressed as $W_{ni}=K_{3,245}/4$. Couplings to other close-lying vibrational levels are neglected. The interaction constant $K_{3,245}$ is expressed in terms of the previously defined cubic potential constants, normal mode frequencies and a Coriolis term [11] that lead to the following mass-ratio dependence:

$$dK_{3,245}/d(\ln\mu) = K_{3,245}. \quad (11)$$

Diagonalisation of the Hamiltonian of the coupled vibrational levels leads to:
- vibrational energy levels shift:

$$E_{1,2} = E_0 \pm \frac{1}{2}\sqrt{4W_{ni}^2 + \delta^2}. \quad (12)$$

where E_0 is the mean and δ is the difference of the energies of the vibrational levels;
- vibrational wavefunctions mix:

$$\begin{aligned} &\psi_n = a\psi_{n,0} + b\psi_{i,0}; \\ &\psi_i = b\psi_{n,0} + a\psi_{i,0}; \\ &a^2 = \frac{1}{2}\left(1 + \frac{\delta}{\sqrt{4W_{ni}^2 + \delta^2}}\right); \\ &b^2 = \frac{1}{2}\left(1 - \frac{\delta}{\sqrt{4W_{ni}^2 + \delta^2}}\right). \end{aligned} \quad (13)$$

where a, b are the mixing coefficients and Ψ_n, Ψ_i the perturbed and Ψ_{n0}, Ψ_{i0} the unperturbed vibrational wavefunctions;
- effective vibrational constants change in each vibrational level:

$$\begin{aligned} B_1 &= a^2 B_{n,0} + b^2 B_{i,0} \\ B_2 &= b^2 B_{n,0} + a^2 B_{i,0}. \end{aligned} \quad (14)$$

where B_n, B_i are the perturbed and $B_{n,0}$, $B_{i,0}$ are the unperturbed rotational constants.
The mass-ratio dependences of the previously introduced parameters are:

$$\begin{aligned} &dE_{1,2} / d\ln\mu = E_{1,2} / 2 \pm \varepsilon(\delta + 4W_{ni}^2 / \delta) + \\ &+ (A_h + \delta A_h \sqrt{1 + 4W_{ni}^2 / \delta^2} / 2) / 2; \\ &dB_{1,2} / d\ln\mu = B_{1,2} \pm \varepsilon(B_{i,0} - B_{n,0}) - \\ &- (a^2, b^2) / 2 \sum_k \alpha_{k,n}(v_{k,n} + g_{k,n} / 2) - \\ &- (b^2, a^2) / 2 \sum_k \alpha_{k,i}(v_{k,i} + g_{k,i} / 2). \end{aligned} \quad (15)$$

where $db^2/d(\ln\mu)=\varepsilon$, A_h is the mean anharmonicity (difference between the vibrational term in Equation 7 and the pure normal mode harmonic oscillator energies) of the vibrational levels, δA_h is the difference between the anharmonicities in the vibrational levels. In the last expression (a, b) coefficients go with (+,-) signs.

An experimental setup for frequency measurements of acetylene lines [12] is based on the frequency modulation spectroscopy approach. Radiation from a diode laser is frequency-modulated with an electro-optic modulator and coupled to a high finesse Fabry-Perot cavity. Radiation reflected by the input mirror of the cavity is used to lock the laser frequency to the cavity resonance using the Pound-Drever-Hall technique. The cavity is filled with a sample of high purity isotopic acetylene. The enhanced optical power

allows saturating rovibrational transitions. Each mirror of the cavity is mounted on a PZT. Modulation of the cavity length yields an additional frequency modulation of the laser that is used to probe molecular resonances. Acetylene line is recorded using a 3*f* phase-sensitive technique in the transmission of the cavity. This signal is applied on the second PZT to servo the cavity length and lock the laser frequency to the acetylene saturated absorption line. Metrological performances are the laser linewidth ~50 kHz, the fractional frequency stability $\sim 1.6\times10^{-12}\ \tau^{-1/2}$ and the long term reproductibility of ~0.4 kHz. Subsequent work with frequency combs provided absolute frequency measurement of $^{13}C_2H_2$ P(16) line with a fractional frequency uncertainty of 5×10^{-11} [12]. In addition, accurate frequency measurements of many Doppler-free lines have been performed on $^{13}C_2H_2$ [12] and $^{12}C_2H_2$ [13] isotopomers. The examination of these results allows identifying the following closely-spaced rovibrational transitions:

1) R(25) of $\nu_1+\nu_3$ band of $^{13}C_2H_2$ and R(6) line of $\nu_1+\nu_3$ band of $^{12}C_2H_2$, splitting X_1,

2) P(20) of $\nu_1+\nu_3$ band of $^{12}C_2H_2$ and P(13) line of $\nu_1+\nu_2+\nu_4+\nu_5$ band of $^{13}C_2H_2$, splitting X_2.

Mass-ratio dependences of the values of the energies of the rovibrational levels involved in the $^{12}C_2H_2$ transitions are determined with the reduced expression for Equations 7, 8 and the numerical values of the molecular constants from [10]. Mass-ratio dependences of the values of the energies of the rovibrational levels involved in the $^{13}C_2H_2$ transitions are determined with Equations 12-15 and the numerical values of the molecular constants from [10]. The enhancement factor to the mass-ratio variation, estimated as $d(\ln X_{1,2})/d(\ln\mu)$, is 503 for the first pair of closely-spaced transitions and 4501 for the second one. The metrological performances of the frequency modulation spectroscopy setup lead to a projection of a mass-ratio stability measurement at $3.2\times10^{-15}\ \tau^{-1/2}$, respectively at $3.6\times10^{-16}\ \tau^{-1/2}$ level.

V. Conclusion

This research point out the enhancement of the sensitivity of the frequency splitting of closely-spaced rovibrational transitions to the mass-ratio variation. This work establishes an approach to calculate the sensitivity of the rovibrational transitions to the ratio of electron to proton masses. A frequency modulation spectroscopy setup with acetylene isotopomers at 1.5 µm allows a projection to constrain the stability of the mass-ratio temporal variation in the $10^{-15}\ \tau^{-1/2}$ range. In addition, the rich rovibrational spectrum of the acetylene allows extending this approach to other spectral domains, where the acetylene, as a primordial astrophysical molecule, has a key role in the astronomical observations.

Acknowledgment

The author acknowledges financial support for this work from CNRS.

References

[1] see for example the special topic volume Eur. Phys. J. Special Topics vol. 163, pp. 1, October 2008.

[2] T. Rosenband, D. B. Hume, P. O. Schmidt, C. W. Chou, et al., "Frequency Ratio of Al^+ and Hg^+ Single-Ion Optical Clocks; Metrology at the 17 Decimal Place," Science, vol. 319, pp. 1808–1812, March 2008.

[3] A. Shelkovnikov, R. J. Butcher, C. Chardonnet, and A. Amy-Klein, "Stability of the Proton-to-Electron Mass Ratio," Phys. Rev. Lett., vol. 100, pp. 150801-1 – 150801-4, April 2008.

[4] D. DeMille, S. Sainis, J. Sage, T. Bergeman, et al., "Enhanced Sensitivity to Variation of m_e/m_p in Molecular Spectra," Phys. Rev. Lett., vol. 100, pp. 043202-1 – 043202-4, February 2008.

[5] T. Zelevinsky, S. Kotochigova, and Jun Ye, "Precision Test of Mass-Ratio Variations with Lattice-Confined Ultracold Molecules," Phys. Rev. Lett., vol. 100, pp. 043201-1 – 043201-4, February 2008.

[6] G. Herzberg, Molecular Spectra and Molecular Structure. I. Spectra of Diatomic Molecules, 2nd ed., vol. 1. New-York: Van Nostrand, 1950.

[7] W. H. Shaffer and A. H. Nielsen, "The Near-Infrared Spectra of Y_2X_2 Molecules," J. Chem. Phys., vol. 9, pp. 847–852, December 1941.

[8] M. de Labachelerie, K. Nakagawa, and M. Ohtsu, "Ultranarrow $^{13}C_2H_2$ Saturated-Absorption Lines at 1.5 µm," Opt. Lett., vol. 19, pp. 840–842, June 1994.

[9] T. J. Quinn, "Practical Realization of the Definition of the Metre, Including Recommended Radiations of Other Optical Frequency Standards (2001)," Metrologia, vol. 40, pp. 103–133, April 2003.

[10] M. Hermann, A. Campargue, M. I. El Idrissi, and J. Wander Auwera, "Vibrational Spectroscopic Database on Acetylene $X^{\sim}\ ^1\Sigma_g^+$ ($^{12}C_2H_2$, $^{12}C_2D_2$, $^{13}C_2H_2$)," J. Phys. Chem. Ref. Data, vol. 32, pp. 921–1361, March 2003.

[11] A. F. Borro, I. M. Mills, and E. Venuti, "Quartic Anharmonic Resonances in Acetylenes and Haloacetylenes," J. Chem. Phys., vol. 102, pp. 3938–3944, March 1995.

[12] C.S. Edwards, H.S. Margolis, G.P. Barwood, S. Lea, et al., "High-accuracy Frequency Atlas of $^{13}C_2H_2$ in the 1.5 µm Region," Appl. Phys. B, vol. 80, pp. 977–983, June 2005.

[13] C.S. Edwards, G.P. Barwood, H.S. Margolis, P. Gill, et al., "High-precision frequency measurements of the $\nu_1+\nu_3$ combination band of $^{12}C_2H_2$ in the 1.5 µm region," Jounal of Molecular Spectroscopy, vol. 234, pp. 143–148, November 2005.

Design of an Optical Reference Cavity with Flexible Thermal Expansion Tuning Properties

Yingxin Luo, Jie Zhang*, Bing Ouyang, Ke Deng, Zehuang Lu, Jun Luo
MOE Key Laboratory of Fundamental Quantities Measurement
School of Physics, Huazhong University of Science and Technology
Wuhan, 430074, China
*Email: jie.zhang@mail.hust.edu.cn

***Abstract*— An ultra-stable optical cavity is designed as the frequency reference of a clock laser for an Al^+ optical clock by finite element analysis (FEA). The cavity has a structure with fused silica (FS) mirrors contacted to FS rings and re-entrant inside the ULE spacer. This design yields a low thermal noise limit and a flexible tuning range of the total coefficient of thermal expansion (CTE) which is suitable for applications with ULE materials that have various zero-crossing temperatures of CTE from 5 °C to 35 °C, and for applications for cavities with various dimensions and configurations.**

I. Introduction

Ultra-stable lasers with narrow linewidth are essential in optical frequency standards [1] [2], tests of fundamental physics [3] and gravitational wave detections [4]. Free running lasers are typically servo locked to a high-finesse optical cavity to achieve this stability. Within the servo bandwidth the frequency stability of lasers depends on the optical path-length of the cavity, which may be disturbed by the environmental temperature fluctuations [5] and seismic noises [6]. Besides, the inevitable thermal noise which is mainly due to the Brownian motions of materials fundamentally limits the achievable stability of the reference cavity [7]. According to the theoretical studies in [7], contributions from mirror substrates and coatings dominate the total thermal noise level of cavities. Materials with higher Q factors and thus less mechanical dissipations such as fused silica (FS) as the mirror substrates are preferred. Additionally, longer cavity can also benefit the suppression of thermal noise by reducing the relative contributions of mirror noise to the optical path-length of cavity.

Here we present a newly designed cavity which will be used as a reference cavity of a clock laser for an Al^+ optical clock. In order to lower the thermal noise limit, we apply the ultra-low expansion material (ULE) as the spacer and the high Q factor material of FS as the mirror substrates to a cavity with 30 cm length and 15 cm diameter. Usually the cavity system will be thermally stabilized at a critical temperature where the coefficient of thermal expansion (CTE) of ULE spacer crosses zero to eliminate the influence of temperature fluctuations to the cavity length. This critical temperature, written as $T_0(ULE)$, of the ULE is usually at around the room temperature. However, by replacing the ULE mirrors with FS, mismatch of the CTE between ULE and FS occurs because FS has a CTE of more than an order of magnitude larger than that of ULE [5]. Deformations caused by this CTE mismatch will change the effective CTE, α_{eff}, and thus the effective zero-crossing temperature, $T_0(eff)$, of the composite cavity down to a few 10 degrees lower than 0 °C, which is not convenient for thermal stabilization, and may introduce extra problems, like water condensation on cavity housing, etc. Strategies like sandwich structures with ULE rings attached on the back of FS mirrors [8] and re-entrant structures with FS mirrors placed inside the central bore of the ULE spacer [9] were proposed and reported to be effective in tuning the zero-crossing temperature of cavity's CTE back to room temperature in some kinds of cavity structures. However, we found limitations of these approaches when applying them to a longer cavity with a larger diameter. New design of the mirror configuration of cavity is proposed, analyzed and compared with the other approaches in this paper. This design has a more flexible tuning capability for various cavity sizes and applicable for ULE materials with $T_0(ULE)$ from 5 °C to 35 °C.

II. Thermal Compensation

For more convenient temperature stabilization of the whole optical system, it is preferred to stabilize the system temperature at slightly higher than room temperature (25 °C ∼ 28 °C). Normal ULE materials have their zero-crossing temperature, $T_0(ULE)$, differs from batches to batches, and is usually in the range between 5 °C and 35 °C [5]. As a consequence, we need an effective approach which has the capability to tune the zero-crossing temperature of the cavity, $T_0(eff)$, by a large range so that:

$$T_0(eff) - T_0(ULE) = \Delta T = -10^oC \sim 23^oC. \quad (1)$$

Sandwich structure, re-entrant structure as well as the modified new structure we proposed in this paper, are applied and simulated by both Comsol multiphysics and ANSYS finite element analysis (FEA) packages.

A. Sandwich Structure

Approach that applying ULE rings attached on the back of FS mirrors to form a sandwich structure is examined in our case of the 30 cm long cavity with 15 cm diameter. Numerical analysis indicates that this method is not effective in the case

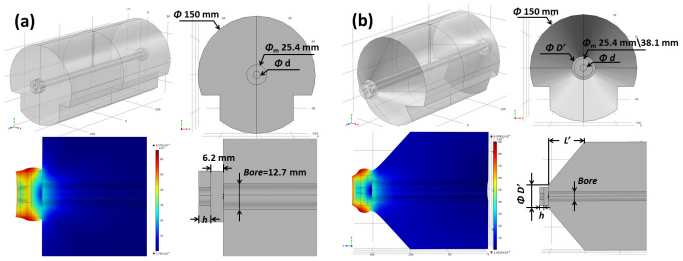

Fig. 1. Geometries of sandwich cavities and FEA results mirror deformations caused by the CTE mismatch when temperature is increased by 1 °C. (a) cavity with a cylindrical spacer. (b) cavity with a tapered spacer. Color scale represents the axial displacement. d and h are the inner diameter and thickness of the ULE rings, respectively.

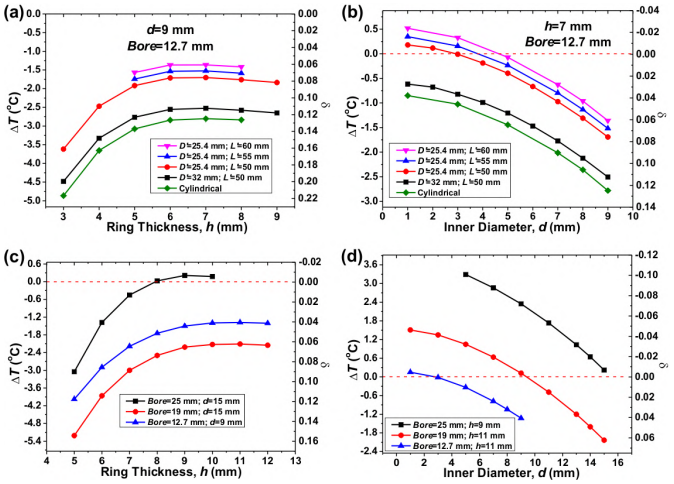

Fig. 2. Simulations of the CTE zero crossing temperature tuning capabilities of sandwich cavities with different dimensions and configurations, including cylindrical and tapered structures (upper panel) as well as that of 1.5 inch mirrors (lower panel). Geometry parameters are defined in Fig. 1, and the right vertical axis shows the coupling coefficient δ defined in [8].

of cavities with larger spacer diameter. The tuning capability of the temperature difference ΔT is found to be only slightly higher than zero, even the introduction of a tapered structure to reduce the areas of the ends of spacer, or adoption of larger mirrors (1.5 inch diameter) can not enhance the tuning effect. However, larger diameter is crucial for a long cavity to increase the symmetry which is essential to suppress the sensitivity to environmental vibrations in our case and many other cases [10] [11] [12]. Cavity geometries and FEA analysis results are shown in Fig. 1 and Fig. 2, respectively. In the simulations, structure parameters including the thickness h and inner diameter d of the rings, central bore diameter of the spacer $Bore$, tapered depth L' and the diameter of end surfaces of tapered spacer D' *et al.*, are changed to tune the effective CTE of the composite cavities. As shown in Fig. 2, the temperature difference ΔT of cavities with simple cylindrical structures can not be tuned to greater than zero. For tapered cavities, an upper limit of 3 °C of ΔT in the case of 1.5 inch mirrors structure can be achieved. For some cases where the ULE spacer has a $T_0(ULE)$ near or higher than room temperature, this result might be enough. However, it is not applicable for ULE with $T_0(ULE)$ lower than 20 °C, thus not flexible enough because it is normally difficult and highly cost to choose the very batch of material with the characteristics you want. It should be noticed that although smaller inner diameter of the ULE ring d can further increase the range of ΔT, it should not be smaller than a practical limit otherwise the entrance of the laser beam will be affected, and the scattered light caused by laser diffraction at small hole will introduce unwanted noise.

B. Re-entrant Structure

The re-entrant approach with the FS mirrors placed within the bore of cavity spacer to generate compensation of opposite thermal expansions between spacer and mirrors inside is also examined in our case of 30 cm long and 15 cm diameter cavity. In this structure, the FS mirrors are optically contacted to ULE rings with the outer and inner diameters of d_2 and d_1 respectively and the thickness of h, these rings then are optically contacted to the ends of ULE spacer in turn. Configurations and geometries are illustrated in Fig. 3, and the FEA simulation results are shown in Fig. 4. In contrast with that

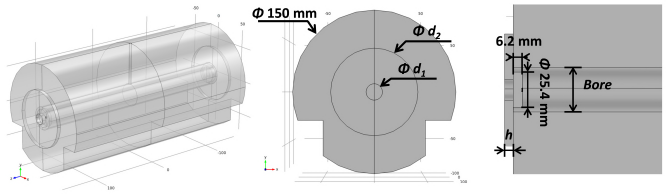

Fig. 3. Configurations and dimensions of cavity with re-entrant FS mirrors optically contacted to ULE rings. h, d_1 and d_2 are the thickness, the inner and outer diameter of rings, respectively.

of the sandwich structure, the temperature difference between $T_0(eff)$ and $T_0(ULE)$ can be as large as 30 °C. However, it is difficult to tune the $T_0(eff)$ lower, the tuning range of ΔT is about 20 °C $\sim$ 30 °C. Consequently, this design is only suitable for cases when ULE materials have a $T_0(ULE)$ lower than 5 °C for 30 cm long cavities. Moreover, for shorter or medium length cavities (less than 30 cm) ΔT is much too large and this approach is not applicable anymore, which will be further discussed in the next subsection. Again, this strategy is not flexible enough in our case and other cases that may need a more compact and miniature cavity for the transportable [11] [12] or space applications [13]. A new design is necessary to accomplish these flexibility requirements.

C. Modified Re-entrant Structure

One of the reasons for such high ΔT of CTE tuning of the re-entrant structure cavities discussed above is due to the huge difference of CTE between FS and ULE. At room temperature, FS has the CTE of more than an order of magnitude larger than that of the ULE, which means the ULE spacer has to be longer than the thickness of FS mirrors by a factor of more than twenty to compensate the thermal expansions of two mirrors on both sides of spacer. Furthermore, the deformation of mirrors caused by CTE mismatch is another reason and

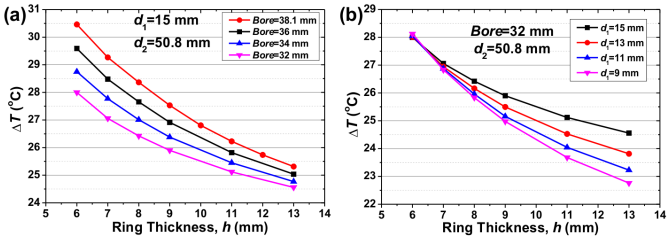

Fig. 4. Simulation results of the CTE zero crossing temperature tuning capabilities of re-entrant cavities with FS mirrors contacted to ULE rings with different structure parameters.

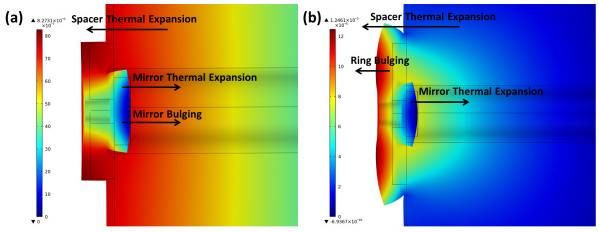

Fig. 5. Mirror deformations caused by CTE mismatch of the re-entrant cavities calculated with FEA analysis; (a) deformation between FS mirror and ULE ring introduces the mirror bulging in the same direction as its thermal expansion; (b) deformation between FS ring and ULE spacer introduces the ring bulging in the opposite direction as the mirror thermal expansion. Color scale shows the axial displacements.

seems to be more important. As illustrated in Fig. 5(a), the deformation makes the FS mirrors bulge in the same direction of its thermal expansion direction, requiring the spacer to be even longer, and leading to a consequence that only the cavities with their lengths longer than 30 cm are suitable for this design. The numerical calculation results are shown in Fig. 7(a), in which the re-entrant cavities with different length are compared. It can be seen that the zero-crossing temperature tuning ranges are narrow and only of about 5 °C. Furthermore, to obtain a moderate temperature tuning (less than 25 °C), the cavity length must be longer than 30 cm with this re-entrant design.

To obtain a more flexible tuning range of ΔT with a moderate cavity length, a modified design of re-entrant cavity is proposed here, in which the FS mirrors are optically contacted to FS rings rather than ULE rings. In this configuration, the deformation of CTE mismatch is between the FS rings and the ULE spacer, causing the FS rings bulge in the opposite direction as that of the mirror thermal expansion, and thus relax the stringent requirement of the spacer's length, as shown in Fig. 5(b). FEA simulations of cavities with this modified structure are shown in Fig. 6. According to the simulations, the modified re-entrant structure introduces a larger tuning range of ΔT from -7 °C to 25 °C by simply varying the thickness h of FS rings, and this range can be further adjusted by altering the outer diameter d_2, according to the corresponding ULE batches that are used and the conditions of thermal control system. The flexibility requirement of (1) is easily achieved. Practically, FS rings with relatively smaller outer diameter d_2 are more preferred because of the less area of optical contact as well as the compatibility with vibration immunity design which will introduce notch structures to the bottom of spacer.

Comparison of the zero-crossing temperature tuning capabilities of modified re-entrant cavities with different lengths are simulated and shown in Fig. 7(b). Compared with the original re-entrant structure (Fig. 7(a)), the modified structure can introduce a large and moderate temperature tuning range of cavities with various spacer lengths from 10 cm to any longer. It indicates that the modified design proposed here is much more flexible and applicable for various cavity sizes and for ULE materials with various zero-crossing temperatures of CTE from 5 °C to 35 °C. In addition, mirror deformations caused by CTE mismatch of different cavity designs are analyzed

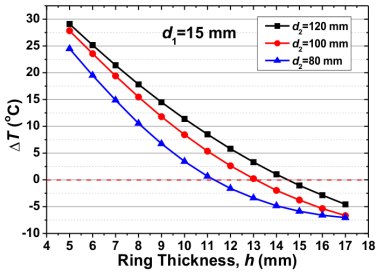

Fig. 6. Tuning range of the $T_0(eff)$ of modified re-entrant cavities with FS mirrors optically contacted to outer FS rings instead of ULE rings. The dimensional parameters are defined the same as those in Fig. 3.

and compared, as shown in Fig. 8. Mirrors of both sandwich design (Fig. 8(a)) and re-entrant designs (Fig. 8(b)) deform in a convex shape at the mirror centers under 1 °C of temperature increase, and the additional radius of curvature (written as R_x and R_y in both orthogonal directions on the mirror surface) has a magnitude of approximately 10^4 m to 10^5 m, corresponding to curvatures of about 10^{-4} m^{-1} to 10^{-5} m^{-1} which are 4 to 5 orders of magnitude smaller than those of the cavity mirrors (normally 1 m^{-1} or 2 m^{-1}), and thus have negligible contribution. It should be noticed that, as seen from the figure, sandwich structure causes more abrupt distortions within the mirror, which may degrade the performance of mirrors in long term applications.

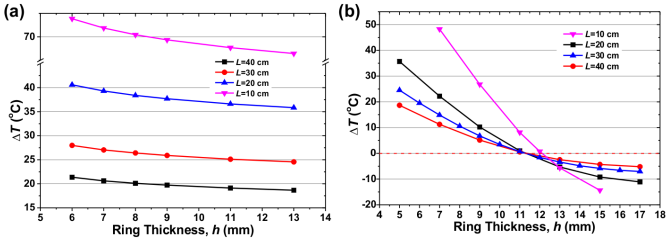

Fig. 7. Comparison of the zero-crossing temperature tuning capabilities with different cavity lengths between the original re-entrant cavity (a) and the modified cavity with FS rings (b). The inner diameters of the rings d_1 are 15 mm for both cases, and the outer diameter d_2 of FS rings in (b) is 80 mm.

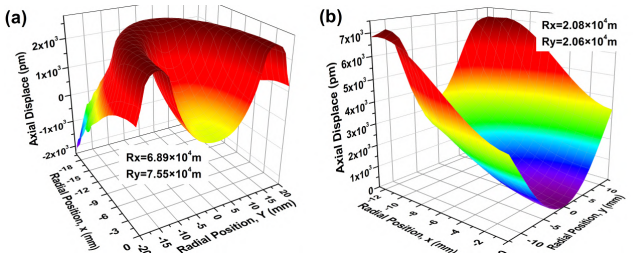

Fig. 8. Mirror deformations due to CTE mismatch under 1 °C of temperature increase of sandwich design (a) and re-entrant designs (b), respectively.

III. Conclusion

In conclusion, we have proposed a new design of ultra-stable optical cavity with ULE spacer, re-entrant FS mirrors and FS rings based on FEA simulations for different cavity structures. The designed cavity has an ultra-low thermal noise limit at the levels of 1×10^{-16}. The zero crossing temperature of the effective CTE of the designed cavity can be easily tuned to above room temperature with any ULE spacer materials, as long as the CTE zero crossing temperature of the selected ULE spacer is measured beforehand. Currently the CTE zero crossing temperature of ULE can be measured with an accuracy of ± 1 °C at reasonable cost (Stable Laser Systems). This accuracy level is more than enough for our design purpose. No matter what the zero crossing temperature of the selected ULE spacer is measured to be, one can always design a cavity with compatible FS rings thickness such that the zero crossing temperature of the effective CTE is above room temperature. The design is applicable for cavities with different lengths.

Ultra-low thermal noise limit reference cavities play a key role in realizing ultra-narrow linewidth lasers especially in the applications as the clock lasers for ionic or atomic optical clock. Reference cavities based on ULE and FS materials are still very popular choices for lab-based or transportable ultra-narrow linewidth lasers. To further reduce the thermal noise limit to below 1×10^{-16}, ULE based reference cavities are no longer adequate. To this end, there are currently strong interests in the developments of cryogenic cavities based on single crystal silicon [14] or sapphire [15]. We hope the technique discussed in this paper can also stimulate ideas in the design of these cryogenic cavities.

References

[1] S. A. Diddams, Th. Udem, J. C. Bergquist, E. A. Curtis, R. E. Drullinger, L. Hollberg, W. M. Itano, W. D. Lee, C. W. Oates, K. R. Vogel and D. J. Wineland, "An optical clock based on a single trapped $^{199}Hg^{+}$ ion," *Science*, vol. 293, pages 825–828, 2001.

[2] H. S. Margolis, G. P. Barwood, G. Huang, H. A. Klein, S. N. Lea, K. Szymaniec, and P. Gill, "Hertz-level measurement of the optical clock frequency in a single $^{88}Sr^{+}$ ion," *Science*, vol. 306, pages 1355–1358, 2004.

[3] T. Rosenband, D. B. Hume, P. O. Schmidt, C. W. Chou, A. Brusch, L. Lorini, W. H. Oskay, R. E. Drullinger, T. M. Fortier, J. E. Stalnaker, S. A. Diddams, W. C. Swann, N. R. Newbury, W. M. Itano, D. J. Wineland, and J. C. Bergquist, "Frequency ratio of Al^{+} and Hg^{+} single-ion optical clocks; metrology at the 17th decimal place," *Science*, vol. 319, pages 1808–1812, 2008.

[4] B. Willke, K. Danzmann, M. Frede, P. King, D. Kracht, P. Kwee, O. Puncken, R. L. Savage, B. Schulz, F. Seifert, C. Veltkamp, S. Wagner, P. Weβels, and L. Winkelmann, "Stabilized lasers for advanced gravitational wave detectors," *Class. Quant. Grav.*, vol. 25, pages 114040, 2008.

[5] R. W. Fox, "Temperature analysis of low-expansion Fabry-Perot cavities," *Opt. Express*, vol. 17, pages 15023–15031, 2009.

[6] S. A. Webster, M. Oxborrow, and P. Gill, "Vibration insensitive optical cavity," *Phys. Rev. A*, vol. 75, pages 011801, 2007.

[7] K. Numata, A. Kemery, and J. Camp, "Thermal-noise limit in the frequency stabilization of lasers with rigid cavities," *Phys. Rev. Lett*, vol. 93, pages 250602, 2004.

[8] T. Legero, T. Kessler, and U. Sterr, "Tuning the thermal expansion properties of optical reference cavities with fused silica mirrors," *J. Opt. Soc. Am. B*, vol. 27, pages 914–919, 2010.

[9] S. Webster and P. Gill, "Low-thermal-noise optical cavity," *Proc. 2010 IEEE Int. Freq. Control Symp.*, pages 470–473, 2010.

[10] J. Millo, D. V. Magalhães, C. Mandache, Y. Le Coq, E. M. L. English, P. G. Westergaard, J. Lodewyck, S. Bize, P. Lemonde, and G. Santarelli, "Ultrastable lasers based on vibration insensitive cavities," *Phys. Rev. A*, vol. 79, pages 053829, 2009.

[11] D. R. Leibrandt, M. J. Thorpe, M. Notcutt, R. E. Drullinger, T. Rosenband and J. C. Bergquist, "Spherical reference cavities for frequency stabilization of lasers in non-laboratory environments," *Opt. Express*, vol. 19, pages 3471–3482, 2011.

[12] S. Webster and P. Gill, "Force-insensitive optical cavity," *Opt. Lett.*, vol. 36, pages 3572–3574, 2011.

[13] W. M. Folkner, G. deVine, W. M. Klipstein, K. McKenzie, R. Spero, R. Thompson and N. Yu, "Laser frequency stabilization for GRACE-2," *http://esto.nasa.gov/conferences/estf2011/papers/Folkner_ESTF2011.pdf*, available online.

[14] T. Kessler, C. Hagemann, C. Grebing, T. Legero, U. Sterr, F. Riehle, M. J. Martin, L. Chen, and J. Ye, "A sub-40 mHz linewidth laser based on a silicon single-crystal optical cavity," *arXiv:1112.3854v1*, 2011.

[15] M. Nagel and A. Peters, "Towards an ultra-stable optical sapphire cavity system for testing Lorentz invariance," *arXiv:1112.3623v1*, 2011.

Simulation of finite acoustic resonators from Finite Element Analysis based on mixed Boundary Element Method/Perfectly Matched Layer.

T. Laroche, S. Ballandras,
W. Daniau, J. Garcia, K. Dbich,
FEMTO-ST, UMR CNRS 6174
Time & Frequency Dept.
Besançon, France
Email: thierry.laroche@femto-st.fr

M. Mayer, X. Perois, K. Wagner
TDK
Sophia Antipolis France
& München Germany

***Abstract*—The simulation of finite length Surface Acoustic Wave (SAW) resonators is addressed here. Both the electro-mechanical coupling and the acoustic wave propagation in inhomogeneous space are considered through a Finite Element Analysis (FEA). The homogeneous parts of the space are treated using a Boundary Element Method (BEM) whereas the side edges of the transducer are completed by Perfectly Matched Layer (PML) method. By combining these two boundary methods BEM and PML, we are able to decrease the contributions of the losses due to the diffraction of SAW into Bulk Acoustic Waves (BAW). Thus, we can simulate the effects of real boundary filters (dual mode) on SAW resonators behavior as well as infinite passivation layer laid aver acoustic resonators.**

I. Introduction

The Finite Element Analysis (FEA) is commonly used to characterize the behavior of acoustic resonators such as Surface Acoustic Wave (SAW) or Bulk Acoustic Wave (BAW) devices [Ballandras, 2009]. Some developments requires the improvement of the numerical methods, e.g. the finite phononic devices [Zhao, 2007] or SAW and BAW dual mode filters [Wang, 2006]. The first approach was to develop a FEA code considering the radiation by a Green's function method [Laroche, 2011]. However, the side edges effects cannot be neglected so we are unable to simulate an infinite or very huge passivation layer on a finite device. To consider these effects, the Perfectly Matched Layer (PML) method is of interest [Tajic,2010]. This way enables us to study the behavior of a finite resonator in a very large surrounding medium for instance. So the combining of these two boundary conditions (i.e. BEM and PML) leads to a complete numerical method to characterize finite SAW or BAW devices.

In this work, we first give the basis of the FEA used for both periodic and non-periodic devices. Next, we demonstrate the two methods of boundary conditions (i.e. BEM and PML). At last, we present some results highlighting the efficiency of this boundary conditions method.

II. FEA fundamental equations

The Finite Element model allows to simulate the behavior of acoustic devices against many parameters such as coated medium, electrodes apodization... This method was first initiated by Tiersten [Tiersten, 1967]. The principle consists in the equilibrium of the potential and kinetic energy in the volume with the electrical and mechanical excitation applied on the edges. Thus we obtained the variational formulation from the equilibrium point of the Lagrangian functional [Courant, Hibert, 1953] :

$$\iiint_\Omega \left(\frac{\partial \delta u_i}{\partial x_j} C_{ijkl} \frac{\partial u_l}{\partial x_k} + \frac{\partial \delta u_i}{\partial x_j} e_{kij} \frac{\partial \phi}{\partial x_k} + \frac{\partial \delta \phi}{\partial x_i} e_{ijk} \frac{\partial u_j}{\partial x_k} - \frac{\partial \delta \phi}{\partial x_j} \varepsilon_{jk} \frac{\partial \phi}{\partial x_k} - \rho \omega^2 u_i \delta u_i\right) dV = \iiint_\Omega F_i \delta u_i dV + \iint_\Gamma \delta u_i T_{ij} n_j dS + \iint_\Gamma \delta \phi D_j n_j dS \tag{1}$$

u_i and ϕ are respectively the displacement and the potential unknowns, C_{ijkl} the elastic constants, e_{ijk} the piezoelectric ones, ρ the density, ω the angular frequency and ε_{ij} the dielectric coefficients. F_i, T_{ij} and D_i are respectively the forces the stress and the displacement vector. Ω and Γ are respectively the studied domain and its frontier with the outer space (See Fig. 1). The solution of such an equation is not trivial. The scheme of FEA allows to find a global solution from an exact one computed at local points. The global solution is obtained by polynomial interpolation in finite elements. The sum of each elements give the Ω domain. The

variational equation (1) is given for the FEA scheme:

$$\sum_{e=1}^{E} \iiint_{\Omega^{(e)}} \left(\frac{\partial \delta u_i^{(e)}}{\partial x_j} C_{ijkl}^{(e)} \frac{\partial u_l^{(e)}}{\partial x_k} + \frac{\partial \delta u_i^{(e)}}{\partial x_j} e_{kij}^{(e)} \frac{\partial \phi^{(e)}}{\partial x_k} + \frac{\partial \delta \phi^{(e)}}{\partial x_i} e_{ijk}^{(e)} \frac{\partial u_j^{(e)}}{\partial x_k} - \frac{\partial \delta \phi^{(e)}}{\partial x_j} \varepsilon_{jk}^{(e)} \frac{\partial \phi^{(e)}}{\partial x_k} - \rho \omega^2 u_i^{(e)} \delta u_i^{(e)} \right) dV = \iiint_{\Omega^{(e)}} F_i^{(e)} \delta u_i^{(e)} dV + \iint_{\Gamma^{(e)}} \delta u_i^{(e)} T_{ij}^{(e)} n_j^{(e)} dS + \iint_{\Gamma^{(e)}} \delta \phi^{(e)} D_j^{(e)} n_j^{(e)} dS \tag{2}$$

where e defines the e^{th} element and E the total number of elements. In equation (2), all the unknowns (δu, u...) should be written using polynomial interpolation for each element [Zienkiewicz, 2005]. Each quantities $\Delta^{(e)}(x_i)$ is written according to the following interpolation in one element:

$$\Delta^{(e)}(x_i) = \sum_{n=1}^{N_e} \Delta^{(e,n)} P^{(e,n)}(x_i), \tag{3}$$

where x_i is one space direction, N_e the number of nodes in the e^{th} element, $\Delta^{(e,n)}$ the value of the quantity Δ at the nth node of the eth element and $P^{(e,n)}(x_i)$ is the Lagrangian interpolation polynomial for the same node. For the sake of clarity, only the elastic part is written below according to the FEA formulation for a dimensional device (for instance along x_1 in Fig. 1) with all the mechanical contributions:

$$\sum_{e=1}^{E} \sum_{n=1}^{N_e} \sum_{\mu=1}^{N_e} \left(\iiint_{\Omega^{(e)}} \frac{\partial P^{(e,n)}(x_1)}{\partial x_1} C_{i11l}^{(e)} \frac{\partial P^{(e,\mu)}(x_1)}{\partial x_1} dV - \rho \omega^2 \iiint_{\Omega^{(e)}} P^{(e,n)}(x_1) P^{(e,\mu)}(x_1) dV \right) u_i^{(e,\mu)} \delta u_i^{(e,n)} = 0. \tag{4}$$

In the nodal expression (4), the right hand is zero. The boundary is actually not considered in this trivial model.

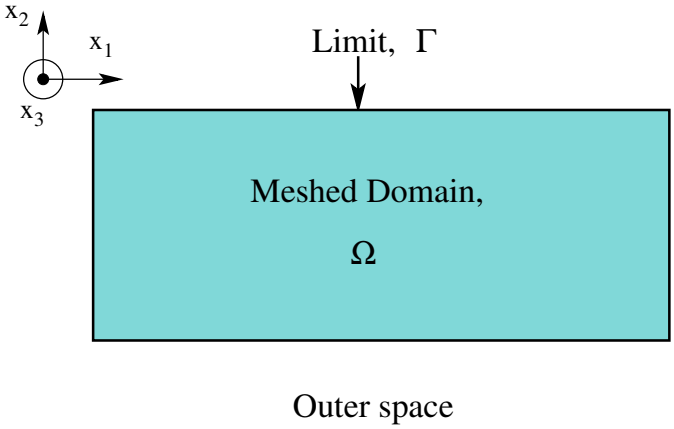

Fig. 1. Splitting of space for a FEA. Ω is the inhomogeneous space under simulation. This is the meshed domain in which the FEA is applied. Γ is the boundary of Ω with the remaining space. The latest is either simulated using boundary conditions or considered as vacuum.

The right hands of equations (1) and (2) show several boundary conditions. They are represented by the integration on the limit Γ. This domain is also discretized in all its elements. The boundary conditions can be applied on each element considering a condition on the stress as well as on the displacement or the potential. These parts are for example the beginning of the radiating conditions. We define below this condition and how consider it in the variational equation.

III. Boundary Element method for finite acoustic resonators

A radiating surface in an non periodic acoustic problem can be included to the FEA formalism in the right hand side of the general variational equation (1).

The right hand of equation (1) limited to the stress part stands for the radiation part. It can thus be treated by using Green's function based relation [Ventura, 1998],

$$T_{ij} n_j = Gi_{ijk}(\omega, S) n_j * u_k, \tag{5}$$

where $*$ denotes the convolution between the displacements u and Gi, the inverse Green tensor relating the stress T to the displacement. Knowing the Green tensor, one can just insert equation (5) in equation (1) to solve the problem with radiation boundaries conditions without any restriction. We developed a first approach of this method for isotropic radiation medium in further work [Wilm, 2004]. However, we can't apply straight this method for anisotropic medium. Indeed, the spectral Green function $\hat{Gi}(\omega, s)$ (where s is the slowness) is not holomorphe and so its inverse Fourier Transform (iFT) can't be computed directly for the general case (anisotropic medium). So to avoid this problem we use the reciprocal form of equation (5),

$$u_k = G_{ijk}(\omega, S) * T_{ij} n_j, \tag{6}$$

in which the direct green function G relates the displacements to the stress [Ventura, 1998]. This function is defined from its iFT in the slowness space,

$$G_{ijk}(\omega, x_1) = \frac{\omega}{2\pi} \int_{-\infty}^{+\infty} \hat{G}_{ijk}(\omega, s_1) \exp(j\omega s_1 x_1) ds_1, \tag{7}$$

where $\hat{}$ defines the Fourier Transform. s_1 is the slowness along the direction x_1. To avoid the problem of loading or time calculation, we use the canonical Green function $\hat{H}(s_1)$ [Hode, 1999] which is frequency independent. This function is related to the Green function as following

$$\hat{G}_{ijk}(\omega, s_1) = \frac{\hat{H}_{ijk}(s_1)}{\omega}. \tag{8}$$

Thus we are able to compute the canonical function before the FEA once and for all assuming the radiation medium is semi-infinite [Boyer, 1994]. The actual Green function is obtained by including the equation (8) in equation (7),

$$G_{i2k}(\omega, x_1) = \frac{1}{2\pi} \int_{-\infty}^{+\infty} \hat{H}_{i2k}(s_1) \exp(j\omega s_1 x_1) ds_1. \tag{9}$$

(Here the notation takes into account the propagation and radiation assumptions of this work i.e., $j = 2$). However, the

spectral canonical Green function $\hat{H}(s_1)$ gives rise to some singularities. So, we must to divide up this function into three parts [Ribbe, 2002]

$$\hat{H}_{i2k}(s_1) = \hat{H}^{(res)}_{i2k}(s_1) + \hat{H}^{\infty}_{i2k}(s_1) + \hat{H}^{(0)}_{i2k}(s_1) + \hat{H}^{R}_{i2k}, \quad (10)$$

where $\hat{H}^{(0)}_{i2k}(s_1)$ is the contribution for the slowness $s_1 = 0$, $\hat{H}^{\infty}_{i2k}(s_1)$ is the asymptotic one and $\hat{H}^{R}_{i2k}$ stands for the acoustic poles contribution. Thus, we can define $\hat{H}^{(res)}_{i2k}(s_1)$ as the residual Green function part without singularities. The computation in the spectral domain as well as in the spatial one always takes into account separately these four parts. The residual part can be numerically computed whereas the others need to be considered analytically [Ribbe, 2002].

Once, the Green function numerically and/or analytically defined, one can express the variational form of equation (6),

$$\int_{x_1=-\infty}^{x_1=+\infty} \delta u_k^* u_k(x_1) dx_1 = \int_{x_1=-\infty}^{x_1=+\infty} \delta u_i^* \int_{x_1'=-\infty}^{x_1'=+\infty} G_{i2k}(\omega, x_1 - x_1') T_{i2}(x_1') dx_1' dx_1, \quad (11)$$

in order to develop the Finite Element scheme for the radiation conditions,

$$\sum_{e=1}^{N_e}\sum_{m=1}^{\eta_e} \delta {u_k}^{*(em)} \sum_{\mu=1}^{\eta_e} u_k^{(e\mu)} \int_{\Gamma_e} P^{(em)}(x_1^e) P^{(e\mu)}(x_1^e) dx_1 = \sum_{e=1}^{N_e}\sum_{m=1}^{\eta_e} \delta {u_k}^{*(em)} \sum_{\epsilon=1}^{N_e}\sum_{\mu=1}^{\eta_e} T_{i2}^{(\epsilon\mu)} \int_{\Gamma_e} P^{(em)}(x_1^e) \int_{\Gamma_\epsilon} P^{(\epsilon\mu)}(x_1^\epsilon) G_{i2k}(\omega, (x_1^e - x_1^\epsilon)) dx_1^\epsilon dx_1^e, \quad (12)$$

where N_e is the number of elements on Γ_2 and η_e the number of nodes by element. $P^{(em)}$ are the FEA interpolation polynomials (first or second degree). The integrations from $-\infty$ to $+\infty$ are bound to the Γ_2 length. Indeed, anywhere else that the activated domain the Green function is null. Note also that the nodal displacement, variational unknown and stress are outside the convolution and the integrals on the elements.

So to match the FEA algorithm, we must write equation (12) in a nodal matrix relation,

$$< \delta u > (\Psi) \{u\} =< \delta u > (G) \{T\}, \quad (13)$$

where (Ψ) is the nodal matrix relating the nodal vectors of the variational unknown and displacements. In the same way, (G) is the nodal Green matrix relating the nodal vectors of the variational unknown and stress. Equation (13) is right whatever the variational unknown. So, on can write the reciprocal relation relating the stress to the displacement,

$$\{T\} = (G)^{-1}(\Psi) \{u\}, \quad (14)$$

where $(G)^{-1}$ is the inverse of the nodal Green matrix defined in equation (12,13). The general variational equation (1) must be also written in a matrix formulation (Only the elastic part is considered without losses of generality)

$$< \delta u > \left[K - M\omega^2\right] \{u\} =< \delta u > (\Psi) \{T\}, \quad (15)$$

where K, M are respectively the nodal stiffness and mass matrices. Thus the final FEA/BEM system is obtained by including equation (14) in equation (15),

$$\left[K - M\omega^2 - (\Psi)(G)^{-1}(\Psi)\right] \{u\} = 0. \quad (16)$$

the global FEA/BEM system is similar to the ideal case with an additional correction which doesn't change the scheme to solve the problem.

IV. Perfectly Matched Layer method

The PML method was first developped in electromagnetism [Berenger, 1996] and well adapted to the Finite Difference in Time Domain (FDTD) method [Laroche, 2005]. More recently, some works demonstrated the implementation of this approach for acoustic simulations based on FEA [Mayer,2007] [Tajic,2010]. The basic idea consists in rigorously simulating an exponential decrease of the acoustic field along at least one space direction. To clear the approach, let us consider the following incident plane wave

$$u = Aexp^{-j(k_x x - \omega)} = Aexp^{-j\omega(s_x x - t)} \quad (17)$$

We then consider that in the absorbing area, one can apply a geometrical transform in the complex plane to introduce the exponential decay. Since it must not modify the propagation phase, this transform can be written

$$\tilde{x} = x - jf(x) \quad (18)$$

where $f(x)$ growths from the origin of the absorbing area to its end along a defined rate. However, since this transform must be efficient for any frequency (we represent the problem in the spectral domain), it is wise to define this function as follow :

$$f(x_i) = \frac{1}{\omega} \int_0^{x_i} d(x) \mathrm{dx}, \quad (19)$$

$$d(x_i) = d_{max} \left(1 - \frac{(abs(x_i) - x_p)^2}{(x_a - x_p)^2}\right)^n, \quad (20)$$

which allows for an easy definition of the transform Jacobian linking the considered coordinate systems. This reads

$$\frac{1}{\partial\tilde{x}} = \frac{j\omega}{j\omega + d(x)} \frac{1}{\partial x} \rightarrow \frac{1}{\partial x} = \left(1 + \frac{d(x)}{j\omega}\right) \frac{1}{\partial\tilde{x}} = \alpha_x \frac{1}{\partial\tilde{x}} \quad (21)$$

Replacing x by $\tilde{x}$ in (17) provides the wanted exponential decay if $f(x)$ unconditionally growths, imposing $d(x)$ even and positive to fulfil the absorbing condition for any x (we assume the problem centred around $x = 0$). Since the absorbing function $d(x)$ is not frequency dependent, its efficiency should be constant along ω. Conformably to Zheng and Huang [Zheng, 2002], we develop a formulation based on the usual piezoelectricity equations, yielding significant modifications of

the elastic, piezoelectric and dielectric constants to account for the absorption.

We now rewrite the elasticity equations in the absorbing region turning x to $\tilde{x}$, using then (5) to express the result in the initial coordinates. As in [Zheng, 2002], the absorbing effect is assumed along the three space directions for the sake of generality. The equilibrium equation then reads

$$-\rho\omega^2 u_i = \frac{\partial T_{ij}}{\partial \tilde{x}_j} = \frac{1}{\alpha_j}\frac{\partial T_{ij}}{\partial x_j} \tag{22}$$

where α_j is characterized by its specific function $d_j(x_j)$. T_{ij} and u_i respectively represent the dynamic stresses and displacements, and ϱ is the mass density. We introduce a non symmetrical stress tensor, expressed in the transformed axis

$$\tilde{T}_{ij} = \frac{\alpha_1\alpha_2\alpha_3}{\alpha_j} C_{ijkl}\frac{\partial u_l}{\partial \tilde{x}_k} = \frac{\alpha_1\alpha_2\alpha_3}{\alpha_j\alpha_k} C_{ijkl}\frac{\partial u_l}{\partial x_k} = \tilde{C}_{ijkl}\frac{\partial u_l}{\partial x_k} \tag{23}$$

where $\tilde{C}_{ijkl}$ is the transformed elastic constant tensor relative to the absorption area. We multiply (22) by $\alpha_1\alpha_2\alpha_3$, thus yielding Newton relation for PMLs in the real coordinates

$$-\tilde{\rho}\omega^2 u_i = \frac{\partial \tilde{T}_{ij}}{\partial x_j} \tag{24}$$

where $\tilde{\rho} = \rho\alpha_1\alpha_2\alpha_3$ is the mass density relative to the transformed domain. Since the obtained form of the equilibrium equation complies with the classical expression for usual solids, it is liable to exploit the standard FEA formulation for PML as well, accounting for the frequency dependence of the transformed physical tensors. These developments of course can be extended to piezoelectricity by rewriting Poisson's equation and taking into account the piezoelectric coupling in the stress definition as follows

$$\begin{array}{c}\tilde{T}_{ij} = \frac{\alpha_1\alpha_2\alpha_3}{\alpha_j}\left(C_{ijkl}\frac{\partial u_l}{\partial \tilde{x}_k} + e_{kij}\frac{\partial \varphi}{\partial \tilde{x}_k}\right) = \\ C_{ijkl}\frac{\partial u_l}{\partial x_k} + \tilde{e}_{kij}\frac{\partial \varphi}{\partial x_k}\end{array} \tag{25}$$

Poisson's equation expressed in the transformed system of axes reads

$$\frac{\partial D_i}{\partial \tilde{x}_i} = 0 \Rightarrow \frac{1}{\alpha_i}\frac{\partial D_i}{\partial x_i} = 0 \tag{26}$$

with D_i the electrical displacement vector. To provide an homogeneous formulation, we proceed as for the stress definition (23), multiplying the electrical displacement by $\alpha_1\alpha_2\alpha_3$, yielding

$$\tilde{D}_i = \frac{\alpha_1\alpha_2\alpha_3}{\alpha_i} D_i \tag{27}$$

As for the propagation equation (22), the Poisson's condition is written accounting for these changes as

$$\frac{\partial \tilde{D}_i}{\partial x_i} = 0 \tag{28}$$

Conformably to the stress tensor transformation, we introduce modified piezoelectric and dielectric constants defined as follows

$$\begin{array}{c}\tilde{D}_i = \frac{\alpha_1\alpha_2\alpha_3}{\alpha_i}\left(e_{ikl}\frac{\partial u_l}{\partial \tilde{x}_k} - \varepsilon_{ik}\frac{\partial \varphi}{\partial \tilde{x}_k}\right) = \\ \tilde{e}_{ikl}\frac{\partial u_l}{\partial x_k} - \tilde{\varepsilon}_{ik}\frac{\partial \varphi}{\partial x_k}\end{array} \tag{29}$$

We now are able to establish a FEA formulation exploiting these developments without fundamental changes of the existing code. Thus, equation (1) becomes

$$\begin{array}{l}\iiint_{\Omega_{PML}}\left(\frac{\partial \delta u_i}{\partial x_j}\tilde{C}_{ijkl}\frac{\partial u_l}{\partial x_k} + \frac{\partial \delta u_i}{\partial x_j}\tilde{e}_{kij}\frac{\partial \phi}{\partial x_k} + \frac{\partial \delta\phi}{\partial x_i}\tilde{e}_{ijk}\frac{\partial u_j}{\partial x_k}\right. \\ \left. -\frac{\partial \delta\phi}{\partial x_j}\tilde{\varepsilon}_{jk}\frac{\partial \phi}{\partial x_k} - \rho\omega^2 u_i\delta u_i\right) dV = \\ \iint_{\Gamma_{PML}}\left(\delta u_i\tilde{T}_{ij}n_j + \delta\phi\tilde{D}_j n_j\right) dS\end{array} \tag{30}$$

where Ω_{PML} and Γ_{PML} are respectively the PML domain and its boundary.

We must note here that all the parameters of the absorbing polynomial (Eqs. (19) and (20)) are empirically defined. Indeed, the polynomial $d(x)$ must increase from zero to the maximum value $dmax$ by a progressive slope. The value of $d(x)$ must be zero at the beginning of the PML to verify the impedance match. Moreover, the derivative of $d(x)$ must be null too to avoid any singularities. However, the absorbing polynomial must increase as quick as possible to minimize the number of PML finite elements with respect to the better smoothy shape. Therefore one can choose the degree of polynomial $d(x)$ equal to 3. The depth of the PML domain $(x_p - x_a)$ is also defined according the absorbed waves. So, we defined that this length must be approximately equal to one wavelength.

V. The mixed BEM/PML approach results

In the last part of the results exhibiting, the complete mixed BEM/PML approach is highlighted. This is done considering the general SAW configuration and adding PML area. This configuration is depicted in figure 2. A finite SAW resonator is characterized considering both the PML and the BEM as boundary conditions. The piezoelectric medium is a YXl/36 quartz. Its thickness can increase from zero to a non null value. It's excited by two non massive electrodes. The width of each electrodes is equal to $2.5\mu m$ and the length of the resonator is $10\mu m$. The excitation is symmetric and $V_1 = -V_2 = 0.5V$. The number of finite elements by length unit is equal to $1.6e6$ $elements/m$ along x direction and $6e5$ $elements/m$ along y. The PML domains have the same FEA properties except for the absorbing conditions. The absorbing coefficient $dmax$ is equal to $1e-6$ and the order of the polynomial is set to $n = 3$. The BEM stands for the bottom radiation on Γ_β and simulates the propagation to the infinite in the same medium as the piezoelectric one. It's important to note that the BEM introduces an infinite slab in the x direction under the piezoelectric medium. So if the thickness of the piezoelectric is zero, the two electrodes are placed on an infinite layer of YXl/36 quartz.

We first focused on the effects of the thickness of the piezoelectric medium on the response of the resonator to an electric excitation. The excitation and the geometric configuration are depicted in figure 2. This response is exhibited in figure 3. We depict the logarithm of the conductance expressed in micro

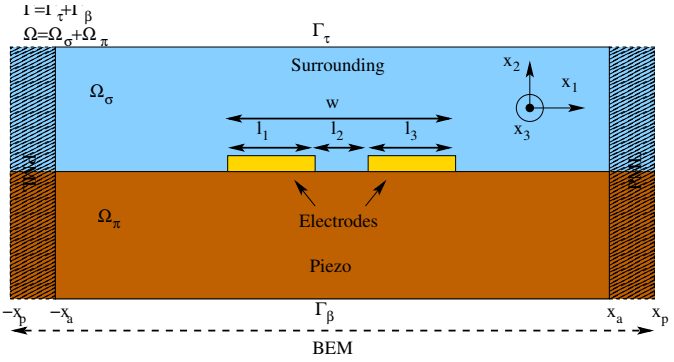

Fig. 2. Characteristic configuration for finite SAW resonators considering the mixed BEM/PML approach. Two non massive electrodes are activated ($V_1 = 0.5V$, $V_2 = -0.5V$). The width of electrodes is equal to $2.5\mu m$ and the period of the resonator is set to $10\mu m$. The piezoelectric medium is quartz YXl/36. Its thickness vary from zero. Only the radiation on Γ_β is active and the radiating medium is the same as the piezoelectric one. The surrounding medium is vacuum so there is no radiation on Γ_α. On the left and right parts of the scheme, two PML domain are added.

Siemens against the frequency for different thicknesses of the piezoelectric medium. The depth of the piezoelectric medium increases from zero for the red solid line to 2 microns for the red stars. It can be noted that when the thickness decreases the conductance converges to the result of the infinite slab, i.e. when the thickness is zero. This evolution can be explained by the diffraction at the end of the resonator when the depth is non zero. So even is the behavior is nearly the same whatever the thickness of the piezoelectric, the influence of this parameter is actually important.

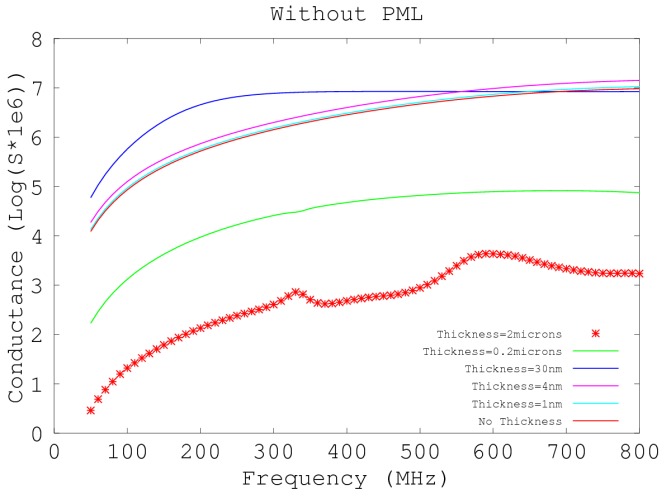

Fig. 3. The logarithm of the conductance in μS against the frequency for different thicknesses of the piezoelectric medium when the PML is switch off. The radiation in the substrate is simulated with BEM. The width of the transducer is finite and equal to $10\mu m$ and the PML domains vanish. The electrodes are non massive. The number of finite elements by length unit is equal to $1.6e6$ $elements/m$ along x direction and $6e5$ $elements/m$ along y.

So to highlight the PML efficiency, we compare the results of the thickness equal to zero in figure 3 to the non-zero ones

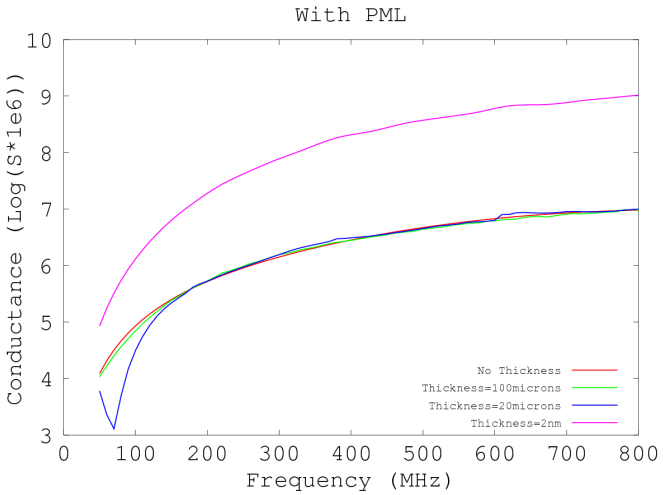

Fig. 4. The logarithm of the conductance in μS against the frequency for different thickness of the piezoelectric medium when the PML is switch on. Except for PML domains, the configuration is the same as in the figure 3. The width of PML Domains is equal to $30\mu m$ for the both right and the left part. The number of finite elements by length unit is the same as outside PML domains. The absorbing coefficient is set to $dmax = 1e6$ and the polynomial order is equal to $n = 3$.

when the PML are activated. The same configuration as in figure 3 is used for the non PML area, we only add two PML on the right and the left parts. The depth of the PML domains is equal to $x_p - x_a = 3\mu m$. The absorbing coefficients are defined above. Again, the variation of the conductance against the frequency is depicted for different thickness of piezoelectric when PML is switch on in figure 4. We can notice again that the conductance converges to the result for a zero thickness when the piezoelectric depth increases. That means there is a non zero interaction between PML and BEM giving rise to undesirable effects for low thickness. So, It's again important to notice that the mixed of the two boundary conditions PML and BEM must be used in a drastic validity domain. One must consider a sufficient thickness of piezoelectric medium or used a zero thickness without PML. The last way can be used if no surrounding medium is taken into account. However, the PML must be used for an infinite passivation layer and we must check if the simulation is in the validity domain.

The last part of the results on mixed PML/BEM approach shows the effects of the boundary conditions on the x-displacement in the sagittal plane (XY). The distortion is depicted in figure 5. This is due to the electric excitation of the piezoelectric medium located in references 1 and 2. This result is obtained for a fixed frequency equal to 170MHz for the previous geometrical configuration of figure 4 for a $20\mu m$ thickness. The PML areas are denoted by the white dashed line and the conservative part (or the physical one) is under the electrodes. First, we can notice that the x-displacement is absorbed in the PML domains with a $1e4$ factor. Indeed, we really pay attention to the validity domain and thus the PML

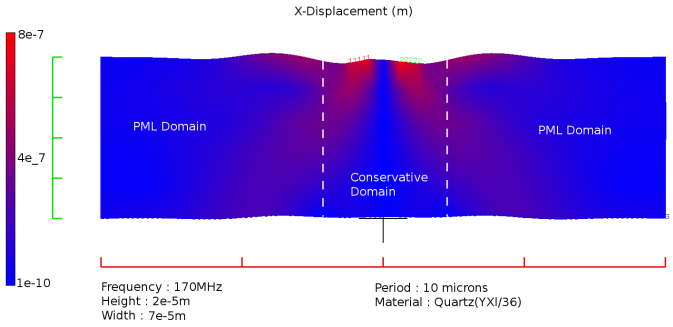

Fig. 5. The map of x-displacement in the XY plane for the fixed frequency $170MHz$. The configuration is the one depicted in figure 2. The height of the piezoelectric medium is set to $2e5m$. The electrodes are denoted by the references 1 and 2. The PML domain are delimited by the white dashed line. The BEM is set at the bottom of the meshed domain also in PML area.

actually acts as a propagation towards the infinity in the same material that initially. Secondly, we can also note the presence of lobes on the left and the right parts of the resonator due to its finite lateral dimension. We already signified the lateral absorbed ones in the PML. However, there are two other which propagate in the y-direction. They are not only absorbed by PML too but also not reflected at the BEM interface indicating thus that the Green radiation conditions work well too. These results show the possibility of combining these two boundary conditions.

VI. Conclusion

We demonstrate in this work a new approach to simulate the behavior of a finite acoustic resonator considering both radiation in a substrate and side edges effects. It is based on the combining of the PML method and the BEM. we demonstrate here both of these boundary conditions methods.

We also show the efficiency of this method allowing the simulation of complex and finite acoustic configurations. However, we define a domain of validity for this method. Indeed, there is an unwanted interaction between the two boundary conditions method. So we must take into account this spurious effect in the modeling. But whatever the domain of validity, this method opens up new fields of numerical investigation.

References

[Ballandras, 2009] Ballandras, S., Lardat, R., Wilm, M., Pastureaud, Th., Reinhardt, A., Champavert, N., Steichen, W., Daniau, W., Laude, V., Armati, R., Martin, G.: A mixed finite element/boundary element approach to simulate complex guided elastic wave periodic transducers, Journal of Applied Physics 105(1), JAN 1 2009

[Zhao, 2007] Zhao, DG.,Liu, ZY.,Qiu, CH., He, ZH., Cai, FE., Ke, MA., Surface acoustic waves in two-dimensional phononic crystals: Dispersion relation and the eigenfield distribution of surface modes, Phys. Rev. B, 76, 144301-1-6, 2007

[Wang, 2006] Wang, WB., Zhang, XD., Shui, YG., Wu, HD., Zhang, D., Plessky, V.P., Minimizing the bulk-wave scattering loss in dual-mode SAW devices, IEEE Transactions on Ultrasonics Ferroelectrics and Frequency Control 53(1), 193-198, JAN 2006

[Laroche, 2011] Laroche, T., Mayer, M., Perois, X., Daniau, W., Garcia, J., Ballandras, S., Wagner, K., Simulation of complex 2D transducer structures using finite element analysis combined with a canonical Green's function based boundary element method, IUS 2011 proceeding

[Tajic, 2010] Tajic, A., Volatier, A., Aigner, R., Solal, M., Simulation of Solidly Mounted BAW Resonators using FEM combined with BEM and/or PML, 2010 IEEE International Ultrasonics Symposium Proceedings

[Tiersten, 1967] Tiersten, H.F., Hamilton's principle for linear piezoelectric media, Proc. of the IEEE, Vol. 55, pp. 1523- 1524, 1967.

[Courant, Hibert, 1953] Courant, R., Hilbert, D.: Methods of Mathematical Physics, Interscience Publishers, Inc., 1953

[Zienkiewicz, 2005] Zienkiewicz, O. C., Taylor, R. L., Zhu, J. Z.: The finite element method: its basis and fundamentals, Butterworth-Heinemann, 2005

[Ventura, 1998] Ventura, P.,Hodé, J.M., Solal, M., Desbois, J. Ribbe, J., Numerical methods for SAW propagation characterization, Proc. of the IEEE Ultrasonics Symposium, pp175-186, 1998.

[Wilm, 2004] Wilm, M., Ballandras, S., Laude, V.: Non periodic acoustic devices radiating in semi-infinite solids simulated by a combination of finite element analysis and a boundary element method, 2004 IEEE Ultrasonics Symposium, Vols 1-3, 1620-1623, Eds: Yuhas, MP, 2004, IEEE Ultrasonics Symposium, Montreal, CANADA, AUG 23-27, 2004

[Hode, 1999] Hodé, J.M., Desbois, J., Original basic properties of the Green's functions of a semi-infinite piezoelectric substrate, Proc. of the IEEE Ultrasonics Symposium, pp131-136, 1999.

[Boyer, 1994] Boyer, L., Étude des phénomènes de réflexion/réfraction dóndes planes acoustiques dans les milieux piézoélectriques, Thèse de lÚniversité de Paris VII an Acoustique Physique, Paris, 1994

[Ribbe, 2002] Ribbe, J., On the coupling of integral equations and finite element/Fourier modes for the simulation of piezoelectric surface wave component, Phd Thesis, École Polytechnique, 2002.

[Berenger, 1996] Berenger, J.P., Three-dimensional perfectly matched layer for the absorption of electromagnetic waves, J. Comp. Phy. 127, 36379, 1996

[Laroche, 2005] Laroche, T., Baida, F.I., Van Labeke, D., Three -dimensional finite-difference time domain study of enhanced second-harmonic generation at the end of a apertureless scanning near-field optical microscope metal tip, josab 22, 10451051, 2005

[Mayer,2007] Mayer, M., Zaglmayr, S., Wagner, K.,Schöberl, J., Perfectly Matched Layer Finite Element Simulation of Parasitic Acoustic Wave Radiation in Microacoustic Devices, 2007 IEEE Ultrasonics Symposium Proceedings

[Tajic,2010] Tajic, A., Volatier, A., Aigner, R., Solal, M., Simulation of Solidly Mounted BAW Resonators using FEM combined with BEM and/or PML, 2010 IEEE International Ultrasonics Symposium Proceedings

[Zheng, 2002] Zheng, Y., Huang, X., Anisotropic Perfectly Matched Layers for Elastic Waves in Cartesian and Curvilinear Coordinates, 2002 MIT Earth Resources Laboratory Industry Consortium Report

Loosely coupled transformer based wireless sensing of open loop micro coils

A.Yousaf,F.Hoeflinger and Prof.L.Reindl
Institute of Microsystem Engineering IMTEK
Laboratory for Electrical Instrumentation
University of Freiburg, Germany
adnan.yousaf@imtek.uni-freiburg.de

***Abstract*—This work explains loosely coupled transformer based wireless sensing of open loop micro coils. Different approaches like multi turn air core helical and planar coils are used to wirelessly measure and extract the resonance frequency, Q factor and inductance of the open loop test micro coil. The coupled system is analytically modeled and simulated in COMSOL Multiphyscics.**

Keywords: Micro coils, Q factor, loosely coupled transformer

I. Introduction

Mitigation of electronics components broadened the potential use of micro coils in different electronics applications. This device miniaturization made the process of testing micro coils a challenging task for the manufacturers since making proper ohmic contact(as shown in figure 1) not only requires more concentration for the operating person but also in certain cases deform the micro coil structure. Further contacting probes also

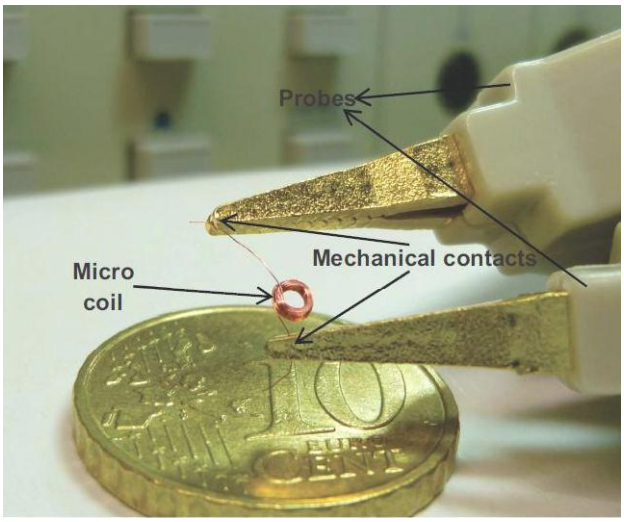

Fig. 1. Mechanical contact based micro coil measurement [1], [2]

influences the micro coil parameters which get difficult to eliminate from the actual desired parameters. This leads to the requirement of investigating new wireless test methods which can be integrated in the manufacturing industry.

II. Related Work

Several passive read out systems using inductive and capacitive coupling approaches have been reported frequently.[2] reports a wireless measurement system for extracting open loop micro inductors inductively coupled to an electrically small magnetic loop antenna having a constant current and inconsistent magnetic field around the loop antenna. Fluid based wireless characterization of micro coil parameters was reported was also reported in [1].In [3] a wireless passive pressure sensors for measuring intraocular pressure where the sensor device consists of a capacitor array and a coil inductor, which form a series LC type resonator.The concept of inductively coupled wireless LC sensor where the stimulus or the applied pressure, strain or torque signal changes the capacitance of an LC circuit, hence shifting the resonance frequency are presented in [4], [5], [6], [7], [8].We present here an approach to wirelessly characterize the micro coil parameters using multi turn air core helical and planar coils as excitation coils.

III. Concept of open loop micro coil wireless measurement

Concept of open loop micro coil wireless measurement is shown in figure 2 where two different wireless measurements on an open and closed loop micro coil were performed. Wireless impedance signal was measured by inductively coupling (in near electromagnetic field) the micro coil to an electrically small loop antenna (as discussed in [2]).In case of open loop micro coil a frequency peak f_0 close to the wired self resonance frequency of tested micro coil was observed. The same test micro coil when wirelessly measured by shorting its terminals had no frequency peak. The frequency peak f_0 observed during the open loop micro coil measurement is due to the coupling capacitance effect between the excitation and micro coil hence giving the frequency peak. In contrast to the open loop ,close loop micro coil behaves like a closed loop circuit having no current flowing through it as shown by the equivalent circuit realization in 2.

IV. Micro coil Structure

In the presented work the micro coils tested wirelessly were all multilayer coils which is constructed by piling layers of single layer coils and connecting these layers in series. Figure 3 and 4 depicts 3D and 2D cross section of the multi layer coil. Further the coil wire is insulated using coatings of Polyurethane and Polyamide. TableI contains the geometrical

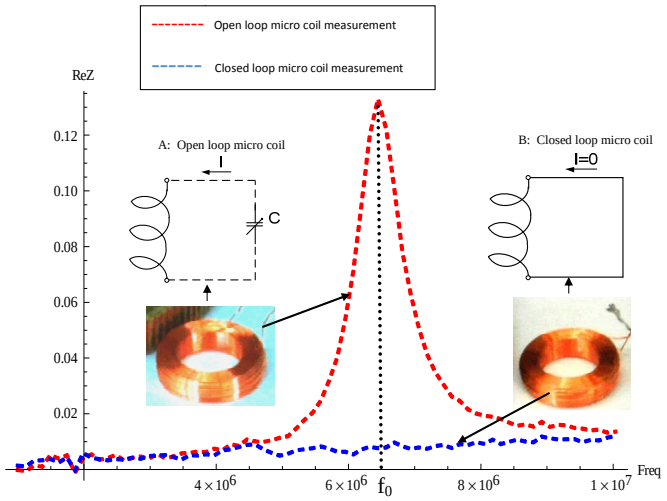

Fig. 2. Concept of open loop micro coil wireless measurement

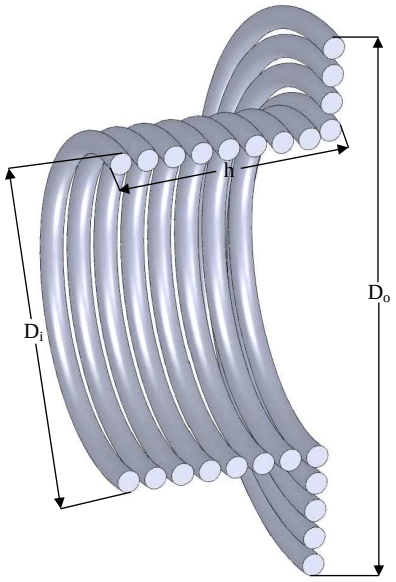

Fig. 3. 3D Multi layer coil stricture

data of the micro coils wirelessly characterized in this study.

V. Analytical Model

In this work two approaches were used to wirelessly characterize open loop micro coils as shown in figure 5. Both approaches were based on the transformer based magnetically coupled coils. Figure 6 shows the equivalent electrical circuit modeling both measurement approaches. To analytically model the magnetically coupled systems a transformer based impedance model is developed using standard coil impedance model given in [9] and defined in equation1.

$$Z(f) = R_1 + j2\pi f L_1 + \frac{(2\pi f M)^2}{\frac{1}{R_2}\left[1 + jQ_0\left\{\frac{f}{f_0} - \frac{f_0}{f}\right\}\right] + \frac{1}{2\pi f C_x}} \quad (1)$$

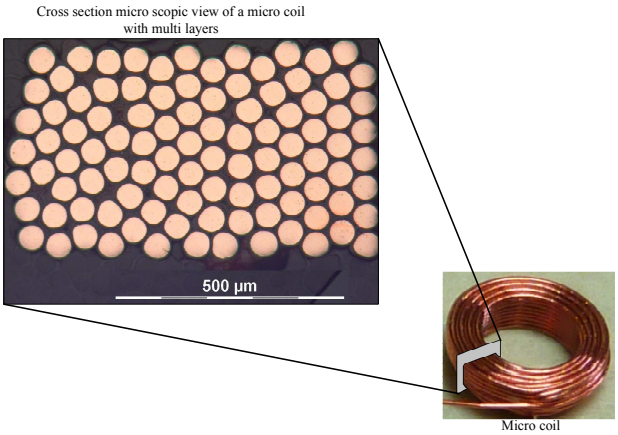

Fig. 4. 2D cross section microscopic view of a micro coil

TABLE I
Micro coils geometrical data Fa. Hopt GmbH

Coil	Turns	Layers	h[mm]	D_i[mm]	D_o[mm]	W_d[μm]
1	30	5	0.43	3.4	4.8	71
2	60	8	0.6	1.23	1.95	50
3	100	7	0.5	1.36	3.6	50
4	200	10	1.18	3.3	5.5	71
5	300	11	1	2	4.6	50
6	500	15	2	2.5	4.7	50

Where Z(f) represents the complex wirelessly measured impedance signal with R_1 and L_1 being the resistance and inductance of the excitation coils i.e.(Helical and Planar coils).C_x and R_2 represents the test micro coil inductance and resistance. Where Q_0 is the quality factor of the test micro coil which is calculated using the half power bandwidth approach (as given in [1]) as follows:

$$Q_0 = \frac{f_0}{\Delta f} \quad (2)$$

M is the mutual inductance between the magnetically coupled coils and defined as follows:

$$M = k\sqrt{L \cdot L_1} \quad (3)$$

Where k is the coupling coefficient having its value between 0 to 1.The developed frequency dependent impedance model in equation1 has 3 degree of freedom with three unknown micro coil parameters i.e. inductance *L*,distributed capacitance C_x and resistance R_2.The resonance frequency is determined from the real part of wirelessly measured impedance signal Re(Z).Analytically the impedance model in equation 1 is split in its real and imaginary parts, subsequently maximum of impedance real part with respect to frequency f_{max} is evaluated as given below:

$$f_{max} = \frac{2Q_0}{\sqrt{4{Q_0}^2 - 1}} f_0 \quad (4)$$

For values of $Q_0 \geq 3$, maximum of real part of impedance equals the frequency peak f_0 as given below:

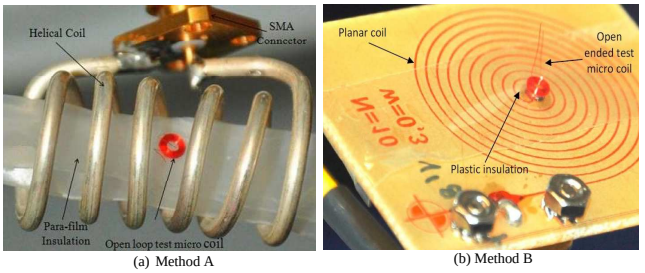

(a) Method A (b) Method B

Fig. 5. Transformer based wireless characterization approaches (a) Air core helical coil (b) Planar coil

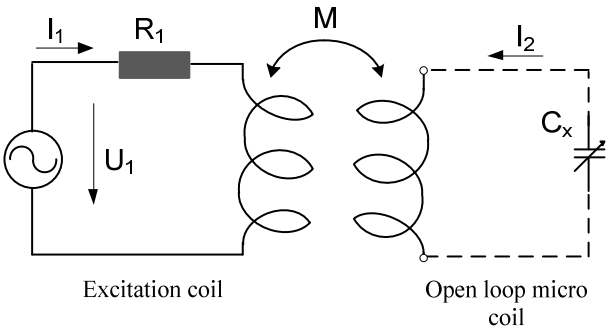

Fig. 6. Equivalent electrical model of the system

$$f_{max} \approx f_0$$

VI. Results

A. Measurement Results

Micro coils were tested wirelessly using Network analyzer. A frequency sweep from 1-100MHz is performed since the micro coils tested in this study (as given in table I) had the maximum wired self resonance frequency of 68.5MHz.The excitation coils i.e. planar and helical coils used in wireless measurement systems (as shown in 5) were designed having their self resonance frequencies well above the wireless frequency of operation.Table II and III contains the specifications of the designed Planar and Helical coils. The AC current *I* in both the excitation coil is measured between 1-100MHz using the reflected voltage and impedance magnitude signal and depicted in figure 7. In case of helical coil highly non uniform of AC current flows through as compared with the planar coil. Figure 8 shows the wirelessly measured impedance real part Re(Z) of a test micro coil for both of the measurement approaches.

TABLE II
Planar coil specifications

Turns N	Q_p	L_p [μ H]	f_r[GHz]
10	0.016	1.84	1.743

TABLE III
Helical coil specifications

Turns N	Q_h	L_h [μ H]	f_r[GHz]
6	0.086	0.012	1.35

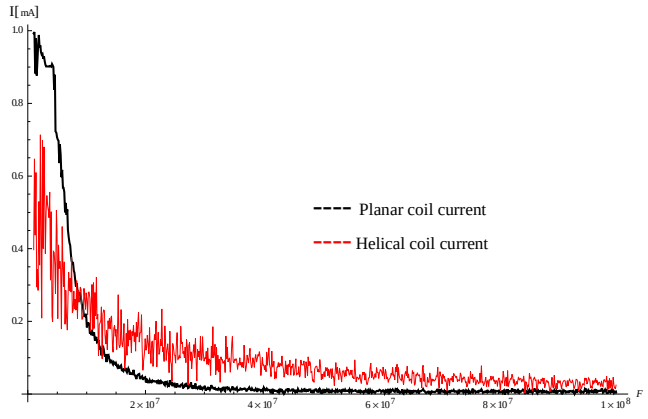

Fig. 7. AC currents through the excitation coils

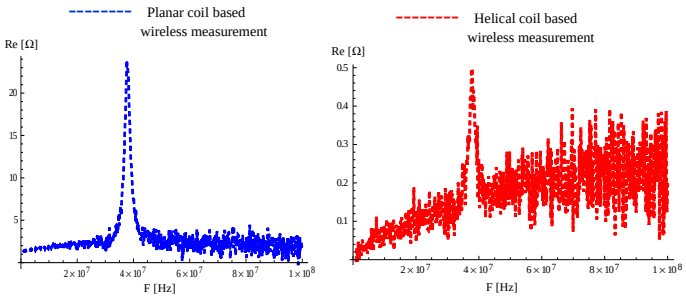

Fig. 8. Wirelessly measured impedances of an open loop test micro coil

Table IV contains the wirelessly measured and extracted parameters of a test micro coil with 30 turns (specifications given in table I).Further the comparison between both the measurement methods with each other(%Difference) and the reference wired measurements are given in tableIV as below:

TABLE IV
Measured and extracted parameters of an open loop test micro coil using Planar and Helical coils

Parameter	Method A	Method B	Difference%	Wired Ref.
f_0(MHz)	41.4	39.2	5.31	40.1
Q Factor Q_0	8.97	8.81	1.78	9.03
Inductance L(μH)	5.8	6.3	7.93	6.6
Resistance R(Ω)	168	176	4.54	184

The test micro coil inductance L and resistance R were extracted from the real part of the wirelessly measured impedance signal.From tableIV clearly shows that Method B for wirelessly measuring and extracting open loop test micro coil parameters has improved results as compared with Method A.

B. Simulation Results

To visualize the magnetic field behavior and numerically compute the micro coil parameters, COMSOL Multiphyscics

is used. As mentioned in section IV, the tested coils were multi layer having coil wire coated with polyurethane (base coating) and (top coating) of polyamide hence making difficult to construct a 3D geometry of the coupled system. To overcome the geometrical complexities a simplified geometry in 2D axial asymmetrical is constructed. Figure 9 and 10 shows the 2D geometries of the both the method used in this study.

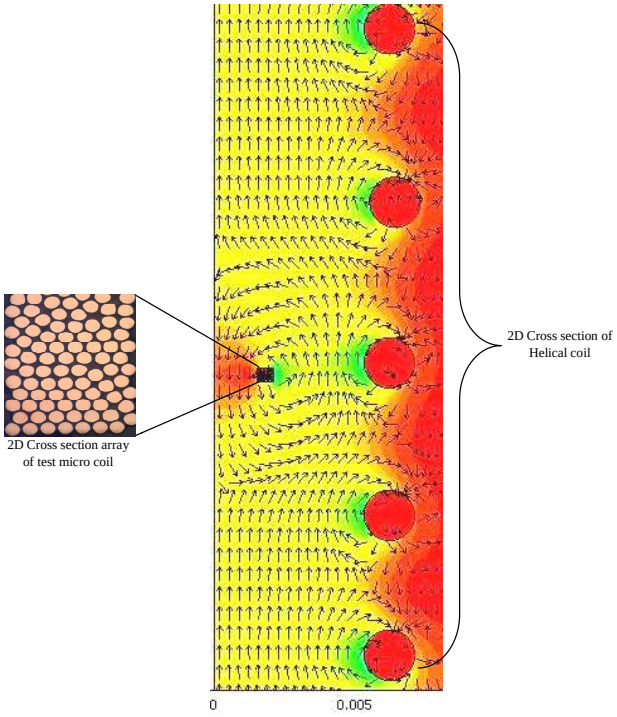

Fig. 9. 2D simulation geometry of helical coil based coupled system

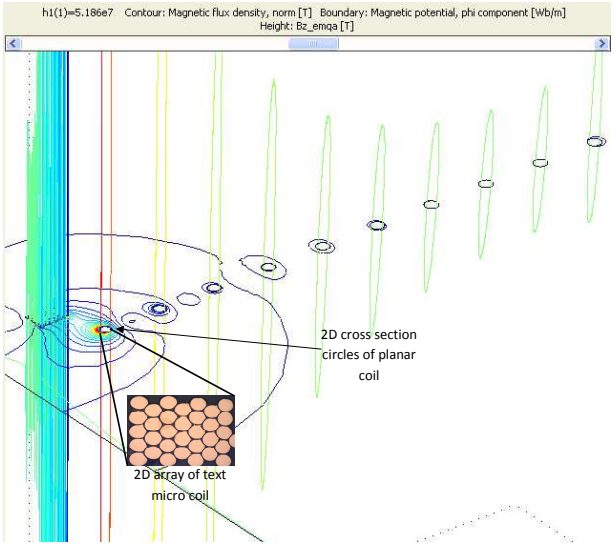

Fig. 10. 2D simulation geometry of planar coil based coupled system

To numerically calculate the micro coil parameters, the weak magnetic flux ϕ_s of the test micro coil at the constructed 2D coil array boundary and the total induced current I_{Total} through the planar and helical coil circular cross sections are calculated as given in equation 5.

$$L_s = \frac{\phi_s}{I_{Total}} * n^2 \tag{5}$$

Where n is the number of turns of the test micro coil. Table V contains the numerically calculated inductance, resonance frequency and Q factor.

TABLE V
NUMERICALLY COMPUTED PARAMETERS OF AN OPEN LOOP TEST MICRO COIL USING PLANAR AND HELICAL COILS

Parameter	Method A	Method B	Difference%
f_s(MHz)	42	40.8	2.85
Q Factor Q_s	8.2	8.58	4.42
Inductance $L_s(\mu H)$	6.1	6.33	3.63

VII. Conclusion

We report here wireless characterization of open loop micro coil inductance, resistance, Q factor and resonance frequency using two different approaches based on transformer coupling. A wireless analytical model is developed for these inductively coupled systems. It was found here that planar coil is better approach as compared to helical coil which has non uniform current at high frequencies. Further FEM analysis is performed by constructing 2D simplified geometry using COMSOL multiphyscics.

Acknowledgment

The authors would like to thanks German Federation of Industrial Research Associations AIF,for supporting this project.

References

[1] Adnan Yousaf F. A Khan and L.M Reindl, 2012. Passive Wireless Sensing of Micro coil parameters in fluidic environments,Sensors and Actuators A: Physical doi:10.1016/j.sna.2012.01.032.

[2] Adnan Yousaf Thomas Jeager and L.M Reindl, 2011. Wireless Measurement System for Extracting Open Loop Micro Coil Parameters,FREQUENZ, Journal of RF/Microwave Engineering, Photonics and Communications, Special Issue GeMiC2011.

[3] Haibo Cao, R.J. Weber, and N.G. Hamouche. A passive intraocular pressure sensor and a wireless sensing technique using an intermediate lc resonator. In *Life Science Systems and Applications Workshop (LiSSA), 2011 IEEE/NIH*, pages 5 –8, april 2011.

[4] Michel Nowak, Nicolas Delorme, Eric Colinet, Gilles Jacquemod, and Francois Conseil. A readout circuit for remote interrogation of capacitance transducers. *Integration Issues of Miniaturized Systems - MOMS, MOEMS, ICS and Electronic Components (SSI), 2008 2nd European Conference Exhibition on*, pages 1 –8, april 2008.

[5] M.A. Fonseca, J.M. English, M. von Arx, and M.G. Allen. Wireless micromachined ceramic pressure sensor for high-temperature applications. *Microelectromechanical Systems, Journal of*, 11(4):337 – 343, aug 2002.

[6] A. Baldi, W. Choi, and B. Ziaie. A self-resonant frequency-modulated micromachined passive pressure transensor. *Sensors Journal, IEEE*, 3(6):728 – 733, dec. 2003.

[7] M. Nowak, E. Colinet, N. Delorme, F. Conseil, and G. Jacquemod. A wireless sensing platform for battery-free sensors. In *Circuits and Systems, 2008. ISCAS 2008. IEEE International Symposium on*, pages 2122 –2125, may 2008.

[8] Sajeeda and T.J. Kaiser. Passive telemetric readout system. *Sensors Journal, IEEE*, 6(5):1340 –1345, oct. 2006.

[9] K. Naishadham. Closed-form design formulas for the equivalent circuit characterization of ferrite inductors. *Electromagnetic Compatibility, IEEE Transactions on*, 53(4):923 –932, nov. 2011.

Phononic Crystal Sensors

Ralf Lucklum
Otto-von-Guericke-University
Institute of Micro and Sensor Systems
Magdeburg, Germany
ralf.lucklum@ovgu.de

***Abstract*— A phononic crystal device is investigated as a sensor platform combining band gap engineering with resonant transmission. A slit cavity perpendicular to the propagation direction of ultrasound and placed in the middle of a phononic crystal causes a peak in the transmission spectrum with the peak frequency strongly dependent on the speed of sound of the liquid filling the slit. A resonant transmission peak through a plate regularly perforated by holes arranged in square lattice can also be found in case of normal incidence of sound. In this arrangement the peak frequency is strongly dependent on speed of sound of the liquid surrounding the plate and filling the holes. These findings are the basis of two resonant liquid sensor platforms based on phononic crystals.**

I. INTRODUCTION

Ultrasonic sensors and acoustic (resonant) microsensors are well accepted devices in many application fields. In both principles the value of interest perturbs wave propagation in a distinct manner. Ultrasonic sensors determine the time of flight of an ultrasonic burst traveling through the object of interest with high accuracy. Here speed of sound can act as a material-dependent value providing information, e.g. on the composition of a liquid mixture. The sensing capabilities of resonant microsensors result from the high *Q*-factor of the resonator and precise determination of the resonance frequency. In the most basic application as liquid sensor (often called QCM although not being a mass balance) the resonance frequency shift is proportional to the square root of the density-viscosity product ($\rho\eta$) of a liquid facing the resonator. To avoid radiation of acoustic waves into the liquid, thereby limiting losses of the resonator and keeping its *Q*-factor high, a thickness shear mode is applied. In consequence, only the properties of a thin layer will be probed, its thickness is defined by the penetration depth of the acoustic wave $\delta = \sqrt{2\eta/(\omega\rho)}$. The sensitivity of the sensor, S_f can be defined as follows:

$$S_f = \frac{\Delta f}{\Delta x} \qquad (1),$$

where Δf is the frequency shift and Δx the change of the input parameter to be measured.

When considering scaling with the probing frequency, f_0, and taking the peak half value full band width, f_{HBW}, as a measure of experimental frequency resolution into account, a reduced sensitivity, S_{fr}, can be defined which gives much better insights to the sensor capabilities:

$$S_f = \frac{\Delta f}{\Delta x \, f_{HBW}} \qquad (2).$$

Phononic crystals are periodic composite materials with spatial modulation of acoustically relevant parameters like elasticity, mass density and longitudinal and transverse velocities of elastic waves. When applied as sensor, the material of interest constitutes one component of the phononic crystal. A favorable design of such a sensor is a solid matrix and a periodic arrangement of holes as schematically shown in Fig. 1. The holes act as scatters from the acoustic wave propagation point of view. A band gap appears when destructive interference of waves happens in a given direction. The holes may act as liquid containers as well. Since longitudinal waves up to MHz frequencies can propagate through a (simple) liquid without significant losses, the liquid-filled hole must be considered also as cavity resonator. In contrast to QCM, where the quartz crystal (or any other device) acts as resonator and where its resonance frequency shifts due to changes in the boundary conditions of the resonator and where consequently the sensor measures interfacial properties [1], the frequency of a cavity mode is determined by the bulk properties of the liquid (assuming fixed geometry).

Similar to QCM and many other chemical sensors principles, chemical sensitivity can be gained by immobilizing a chemically sensitive film onto the surface of the holes. In this application of phononic crystals as (bio-) chemical sensor a cavity mode as applied here would not be appropriate. Similar to e.g. photonic crystal sensors a mode extending into the sensitive film with its 'evanescent tail' should be selected.

Our recent work concentrates on the determination of the concentration of one component in a liquid mixture in a small volume where classical ultrasonic techniques are not appropriate anymore. For the purpose of a well separated transmission peak in the spectrum a defect in an otherwise regular design of a phononic crystal has been introduced. A slit perpendicular to the propagation of sound exactly serves the need of a sufficiently large output span, i.e., a frequency region without disturbing other transmission peaks, mode crossing e.t.c. The slit furthermore acts as microchannel. In our experimental realization the slit has a characteristic dimension (width) in the mm-range, however, there is no indication that the characteristic dimensions cannot be scaled down to the dimensions of microfluidic and nanofluidic devices, thereby moving the characteristic features of the transmission spectrum to higher frequencies.

We recently have demonstrated, that the transmission coefficient measurement of ultrasonic waves through a phononic crystal is appropriate to localize a characteristic sensitive mode within the spectrum and that the respective frequency of maximum/minimum transmission is a measure of speed of sound of the liquid mixture [2, 3]. The concentration measurement scheme therefore relies on a beneficial relation between speed of sound, c, of the mixture and concentration of the component of interest, x_i (molar ratio in this paper). A high sensitivity where Δx represents Δc with respect to eq. 1 does not necessarily means a high sensitivity to Δx_i. As typical for many similar sensors, although the transfer function of the sensor device is known those sensors must be calibrated in terms of the frequency dependence of maximum transmission on the concentration of the component of interest in the mixture of interest. Those numbers are usually not available. We therefore have chosen a rather simple demonstrator, a binary mixture of water and 1-propanol. Different liquid properties are obtained by gradually changing the liquid in the holes, the slit and the surrounding from pure DI-water to pure 1-propanol via a series of liquid mixture with different molar ratios, x_2, of 1-propanol. Density and sound velocity have been taken from [4]. One of the advantageous features of this mixture is that density decreases monotone with molar ratio of 1-propanol from 998 kg m^{-3} for pure DI-water to 804 kg m^{-3} (about 20 %) whereas speed of sound increases from 1483 m s^{-1} to a maximum of 1588 m s^{-1} at x_2 = 0.056 (7 %) and decreases to 1220 m s^{-1} (for pure 1-propanol (-25 %; with respect to water). With respect to the sensitivity of the acoustic principle is also worth to mention that the refractive index of this mixture increases monotone from 1.3330 to 1.3852 (3.9%; with respect to water). Optical sensors, famous for their high sensitivity, face a drawback by the nature of the material properties.

Basically the above applies to the normal incidence setup as well [5-7], where we concentrate on the most apparent feature, the so-called extraordinary acoustic transmission phenomenon (EAT) [for references see 6]. We keep the name phononic crystal sensor although the physics behind this phenomenon significantly differs from the physics behind the band gap crystals. The common aspect is a resonance effect whereas the band structure has been found being less relevant for extraordinary transmission.

II. SIMULATION

Several methods have been developed to investigate propagation of elastic waves in phononic crystals and to calculate the transmission and/or reflection coefficient. We have applied the layer multi scattering theory (LMST) for 2D phononic crystals and the finite difference time domain (FDTD) method for 3D phononic crystals. The LMST method interprets the phononic crystal as a stack of layers of cylindrical scatters. Scatters in a monolayer are located periodically along the x-axis. Identical monolayers are stacked one by one along the y-axis. The LMST considers the acoustic waves scattering by three steps. It firstly deduces the displacement distribution of the central cylinder, and once the externally incident wave is presented for a given central scatter, the wave scattered by all the scatters in the monolayer can be determined. Next scattering matrices of the monolayer and also the matrices for one scattering plane are derived. By using of the matrices for one scattering plane, one can easily obtain the matrices of a slab with two scattering planes. The procedure can be repeated to obtain the matrices for a slab with 2n scattering planes. The FDTD method has been applied to calculate the transmission spectrum through the plate. One obtains the relation equations of stress and the velocity by using discretization of the equations in both space and time domains. The faces of the computational cell normal to x and y axes are chosen to have Bloch boundary conditions, while the faces normal to z axis (the top and bottom ones) have Mur's absorbing boundary conditions. For transmission spectrum calculations, a broad band wave packet is launched with both in-plane and normal incidence, respectively. The transmitted signal is recorded as a function of time. The frequency dependence of the field at a particular point can be obtained by fast Fourier transforming the time results. COMSOL™ simulations have been performed to gain further insights. We especially have been concentrating on the EAT phenomenon. Coupled elements, i.e. liquid confined in the holes, regular set of portions of the plate surrounded by the holes and regular set of holes with adjacent portions of the plate have been found being the key to EAT. Each of these elements has its own set of modes and each of these modes can support either transmission or reflection. Eigenfrequencies of each of these elements depend on bulk properties, which have been used for our sensor development, and boundary conditions, which pave the road to other secondary values, including rheological properties of the liquid, which may lead to sensing schemes not considered so far.

Since all these numerical procedures can be very time consuming, investigations on the sensor performance of the phononic crystal sensor featuring the slit defect have been performed using a one-dimensional approximation based on the 1D transmission line model as used in [2]. The two 4-row pieces of the phononic crystal sensor and the cavity slit have been modeled in a 17-layer arrangement. Each of the two semi-PnC's have been replaced by a 4 x 2 layers, where one layer is steel, the other a metamaterial having a density and speed of sound averaged from the steel and liquid values based on the volumetric contributions to this layer. The slit is presented by a layer having the thickness equivalent to the slit width. In this way one avoids any free parameter to fit the data. The results agree very well with the experiments [3].

III. EXPERIMENTAL

The transmission curves have been obtained using a network analyzer (Agilent 4395A) together with an S-parameter test set (Agilent 87511A, both not shown). Transmission S_{21} has been measured with and without sample in place, respectively. The transmission amplitude is obtained by normalizing with the amplitude of the equivalent setup without the sample.

Several stages have been used to fix and align the sample parallel between two piezoelectric transducers (V153, Olympus, central frequency of 1.0 MHz, half bandwidth of 1 MHz, Fig. 2a, Panametrics V302-SU, central frequency 860 kHz, -6 dB bandwidth 68 %, Fig. 2b). Although the signal amplitude reduces considerably off the resonance, the amplitude is still sufficiently above the noise floor.

DI-water (< 0.1 µS cm^{-1}) has been made in-house, 1-propanol has been obtained from Roth (Germany, p.a. grade). The sensor has been carefully cleaned before filling in the new liquid mixture. Temperature control has been performed via room temperature maintenance.

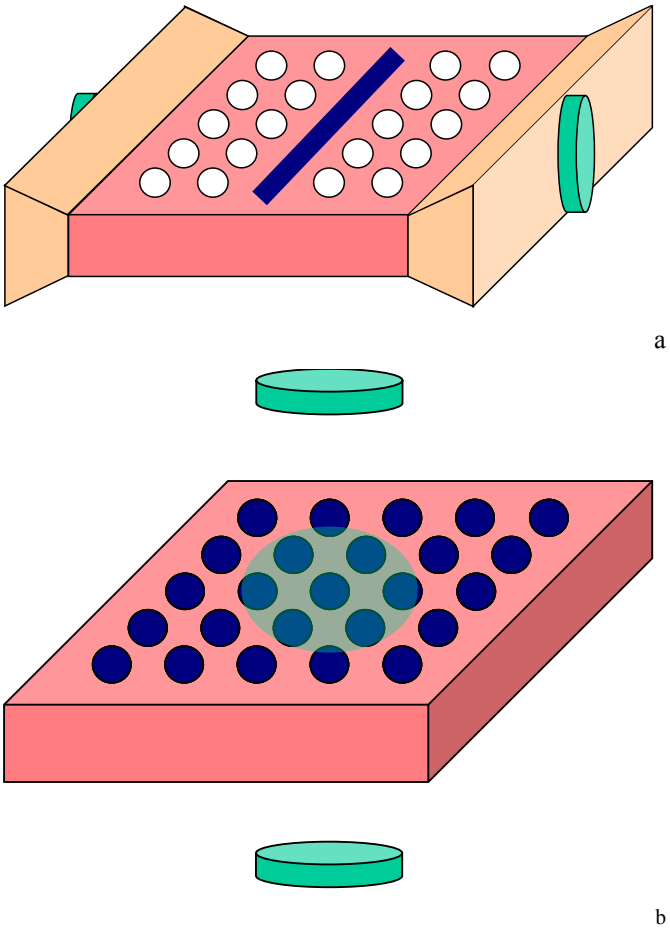

Figure 1. Scheme of the sensor arrangements. a..phononic crystal with slit and in-plane incidence of sound, b..regular phononic crystal with normal incidence of sound.US transducer..green, holes..white, matrix..red, liquid..blue

IV. RESULTS

We observed both in simulation and in experiment that the frequency of resonant transmission peak significantly changes with the molar ratio of 1-propanol in the liquid mixture for both arrangements, Fig. 3. The shift of the maximum transmission peak frequency reflects the difference in speed of sound. The highest resonance frequency appears at a molar ratio x_2 = 0.056, corresponding to the maximum acoustic velocity of the mixture. The sensitivity $\Delta f/\Delta x_2$ in the concentration range between x_2 = 0–0.035 is about 1.34 MHz for the slit geometry and 1.43 MHz for the normal incidence case. The theoretical reduced sensitivity, eq. 2, is about 0.4 and 0.03. The 2D phononic crystal sensor with the slit cavity has theoretically the highest sensing capability. We however have to consider that the peak half bandwidth is about 5 times larger in experiment. We have therefore taken a conservative estimate of the frequency resolution of 1 kHz from experiment for the estimation of the limit of detection (LOD), x_{2min}, of the phononic crystal sensor which is better than 0.001 (55 mmol l^{-1}) [7].

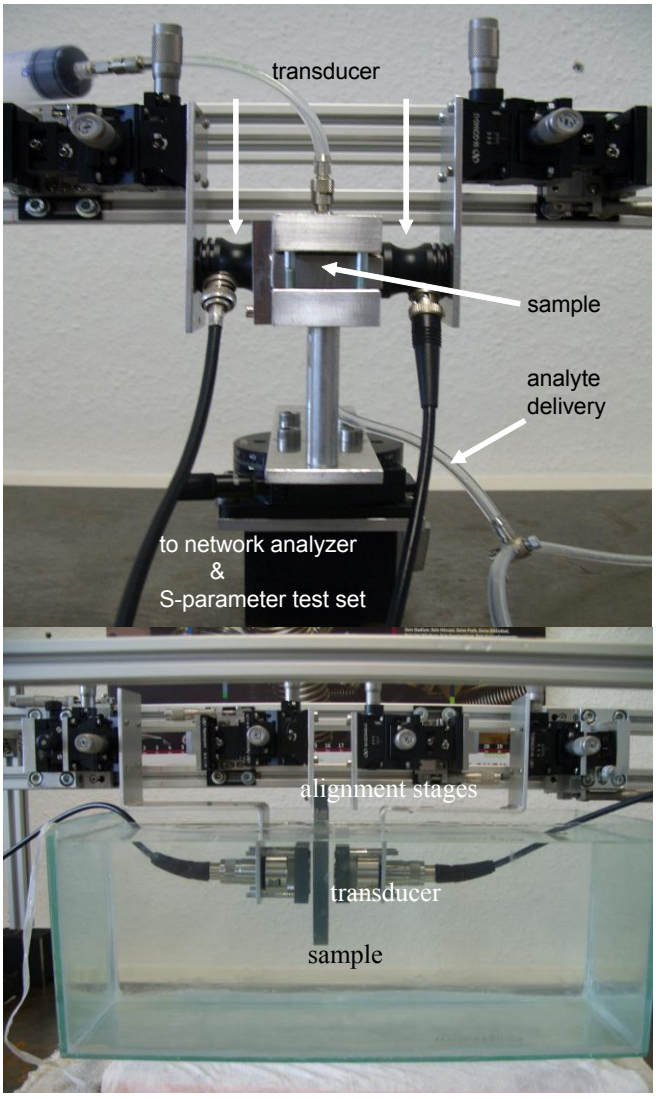

Figure 2. Photos of the experimental setup realizing the sensor schemes shown in Fig. 1

The major contribution to the decline of the reduced sensitivity at normal incidence is the 8 times larger half band width of the extraordinary transmission peak. Fig. 3 exhibits also a systematic frequency difference between simulation and experiment here. We have found that the peak position is more sensitive to a difference in the lattice constant between the fabricated sample and the design whereas the peak frequency is much less sensitive to similar deviations in the hole diameter as well as in the acoustic velocity of steel. However, precise measurements disclose, that the real deviations cannot entirely explain the systematic difference. One can conclude that the FDTD model does not describe the effect of extraordinary transmission completely.

COMSOL simulations, the Schlieren method and Laser vibrometer measurements have been further used for visualization of ultrasound wave propagation (for experimental details see 7, 8]. They provide more details about internal mechanisms involved in extraordinary transmission. As an example Fig. 4 shows the color visualization of the out-of-plane displacement of the phononic crystal plate at normal incidence of sound having a frequency close to the peak of extraordinary transmission. The most important finding is that the white nodal lines do not coincide with the circumference of the holes. We conclude that interactions between propagating ultrasonic pressure waves and the periodically perforated plate are better described by acoustic wave-structure interaction. Plate vibrations are fundamentally associated with EAT and probably determine the phenomenon. The EAT picture, which has been developed upon a base of ideally stiff solids that do not account for structural vibrations and solid-liquid interactions on the interface, seems to provide incomplete description of the problem and could be the reason for the discrepancy between the FDTD model predictions and the experimental findings.

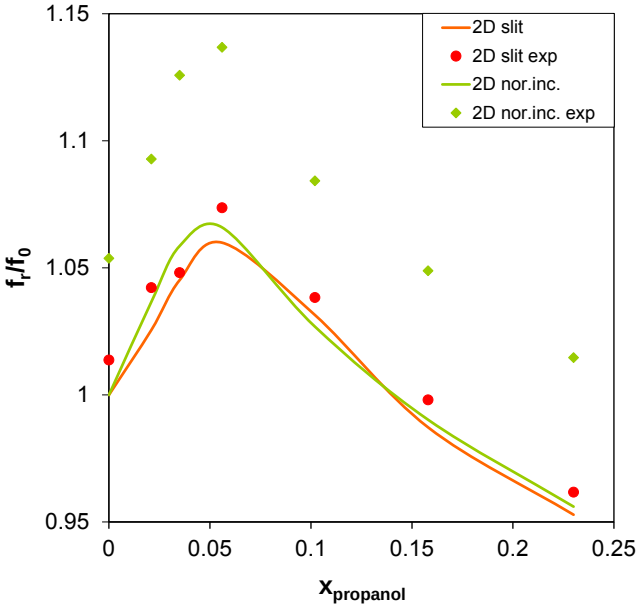

Figure 3. Summary of the theoretical and experimental data fur the two setups, see inset

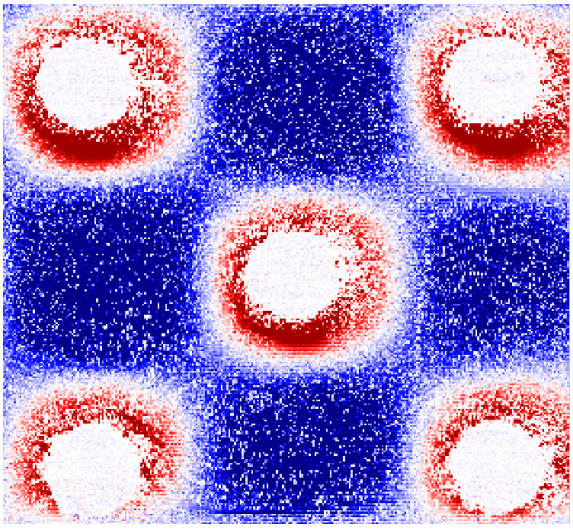

Figure 4. Out-of-plane displacement of the solid matrix surface at normal incidence of sound close to the frequency of extraordinary transmission of sound through an array of sub-wavelenth holes. The white circles do not coinceed with the circumference of the holes which appear as filled white circles due to the absence of scattered laser light.

V. CONCLUSIONS

Phononic crystals either using an analyte-filled defect to create a well isolated peak in the transmission spectrum or exploiting the EAT phenomenon in an arrangement with normal incidence of sound can be used as sensor platform to measure speed of sound of a liquid. This value can be used to determine secondary values like the concentration of a component in a mixture with sensitivities comparable to ultrasonic and microacoustic sensors.

ACKNOWLEDGMENT

The work has been supported by a grant of the German Research Foundation (Lu 606/12-1) and the European Commission Seventh Framework Program (233883, TAILPHOX) which is gratefully acknowledged.

REFERENCES

[1] R. Lucklum, P. Hauptmann, " Acoustic microsensors—the challenge behind microgravimetry," Anal. Bioanal. Chem. 384, pp. 667-682, (2006).

[2] R. Lucklum J. Li, "Phononic crystals for liquid sensor applications", Meas. Sci. Technol., 20, pp. 124014, 2009.

[3] R. Lucklum, M. Ke, M. Zubtsov: Two-dimensional Phononic Crystal Sensor based on a Cavity Mode, Sensors and Actuators B (2012), in press, online available.

[4] R. Kuhnkies, W. Schaaffs, Acustica 13, 407, (1963).

[5] M. Ke, M. Zubtzov, R. Lucklum,"Sub-wavelength phononic crystal liquid sensor," J. Appl. Phys. 110, pp. 026101, (2011).

[6] R. Lucklum, M. Zubtsov, M. Ke, "Liquid Sensor Utilizing a Regular Phononic Crystal With Normal Incidence of Sound," Transact. Ultrason., Ferroel., Freq. Contr. 59, pp. 463-471, (2012).

[7] M. Zubtsov, R. Lucklum, M. Ke, A. Oseev, R. Grundmann, B. Henning, U. Hempel, "2D Phononic Crystal Sensor with Normal Incidence of Sound, " Sensors and Actuators A (2012), in press, online available.

[8] A. Oseev, R. Lucklum, M. Ke, M. Zubtsov, R. Grundmann, " Phononic crystal sensor for liquid property determination," Proc. SPIE Smart Structures/NDT, San Diego, (2012), in press.

An Optimal 2D and 3D Modelling of Finite SAW and BAW Devices Based on Perfectly Matched Layer Method

K. Dbich, T. Laroche, S. Ballandras
FEMTO-ST, UMR CNRS 6174
Time & Frequency Dept.
Besançon, France
Email: karim.dbich@femto-st.fr

M. Mayer, X. Perois, K. Wagner
TDK
Sophia Antipolis France
& München Germany

***Abstract*—The characterization of finite length Surface Acoustic Wave (SAW) and Bulk acoustic Wave (BAW) resonators is addressed here. The Finite Element Analysis (FEA) induces artificial wave reflections at the edges of the mesh. In fact, these ones do not contribute in practice to the corresponding experimental response. The Perfectly Matched Layer (PML) method, allows to suppress the boundary reflections. In this work, we first demonstrate the basis of PML adapted to FEA formalism. Next, the results of such a method is depicted allowing a discussion on the behavior of finite acoustic resonators.**

I. Introduction

The behavior of Surface Acoustic Wave (SAW) and Bulk Acoustic Wave (BAW) resonators is an well known area of numerical and theoretical investigation in recent decades [Zhang, 1993]. One of the most common numerical technique used to simulate such devices is the Finite Element Analysis (FEA) [Ballandras, 2009]. One of the biggest challenges in FEA is to address the problem of boundary conditions. Indeed, the FEA is done on a meshed domain depicting an inhomogeneous part of space and limited by a frontier. However the last one acts like a perfect mirror. So, one must apply Absorbing boundary conditions on it to avoid spurious reflections [Engquist, 1997]. Up to now, FEA is commonly used to simulate periodic geometries. This numerical method coupled with Boundary Elements Method (BEM) allows the understanding of most of SAW and some BAW [Wilm, 2003]. Indeed, the spurious reflections at the bottom and top edges are replaced by a radiating condition (BEM) while a periodic condition is set on the side ones.

Some advancements in this domain require to go further in the development of numerical methods, e.g. the finite phononic devices [Zhao, 2007] or SAW and BAW dual mode filters [Wang, 2006]. Indeed, such configurations need consideration of effects due to the finite size of the resonator. A recent work demonstrates a numerical method to consider the influence of the lateral size of an acoustic device [Laroche, 2011]. This method is based on a mixed FEA/BEM approach. However, the side edges effect are not taken into account and it cannot be applied to simulated the radiation in a passivation layer for instance. One of the best way to consider such an influence is the Perfectly Matched Layer (PML) method. It was first developed in electromagnetism [Berenger, 1996] and well adapted to the Finite Difference in Time Domain (FDTD) method [Laroche, 2005]. More recently, some works demonstrated the implementation of this approach for acoustic simulations based on FEA [Mayer,2007] [Tajic,2010]

In this paper, the fundamentals of FEA are first illustrated. Next, the theoretical approach of PML is introduced for the simple case of a plane wave and expressed for the general case. At last, the 2D-results on a finite SAW resonator are depicted for a piezo electric medium YXl/36 quartz. 3D-results are also shown on one hand to corroborate the 2D-ones and on the other hand to introduce the lateral effects in SAW resonator considering buses and lateral leaky mode influences.

II. Theoretical basis of FEA

The finite elements method was first initiated by Tiersten more than forty years ago [Tiersten, 1967]. The principle consists in the equilibrium of the potential and kinetic energy in the volume with the electrical and/or mechanical excitations applied on the edges. The usual starting point is the antisymmetric formulation giving rise to the Lagrangian. It is thus written under the variational formulation from the equilibrium point of the first functional [Courant, Hibert, 1953] :

$$\iiint_{\Omega}\left(\frac{\partial\delta u_i}{\partial x_j}C_{ijkl}\frac{\partial u_l}{\partial x_k}+\frac{\partial\delta u_i}{\partial x_j}e_{kij}\frac{\partial\phi}{\partial x_k}+\frac{\partial\delta\phi}{\partial x_i}e_{ijk}\frac{\partial u_j}{\partial x_k}-\frac{\partial\delta\phi}{\partial x_j}\varepsilon_{jk}\frac{\partial\phi}{\partial x_k}-\rho\omega^2u_i\delta u_i\right)dV=\iiint_{\Omega}F_i\delta u_i dV+\iint_{\Gamma}\delta u_iT_{ij}n_jdS+\iint_{\Gamma}\delta\phi D_jn_jdS \tag{1}$$

u_i and ϕ are respectively the displacement and the potential unknowns, C_{ijkl} the elastic constants, e_{ijk} the piezoelectric ones, ρ the density, ω the angular frequency and ε_{ij} the dielectric coefficients. F_i, T_{ij} and D_i are respectively the forces the stress and the displacement vector. Ω and Γ are respectively the studied domain and its frontier with the

outer space (See Fig. 1). The solution of such an equation is not trivial. The scheme of FEA allows to find a global solution from an exact one computed at local points. The global solution is obtained by polynomial interpolation in finite elements. The sum of each elements give the Ω domain. The variational equation (1) is given for the FEA scheme:

$$\sum_{e=1}^{E} \iiint_{\Omega^{(e)}} \left(\frac{\partial \delta u_i^{(e)}}{\partial x_j} C_{ijkl}^{(e)} \frac{\partial u_l^{(e)}}{\partial x_k} + \frac{\partial \delta u_i^{(e)}}{\partial x_j} e_{kij}^{(e)} \frac{\partial \phi^{(e)}}{\partial x_k} + \frac{\partial \delta \phi^{(e)}}{\partial x_i} e_{ijk}^{(e)} \frac{\partial u_j^{(e)}}{\partial x_k} - \frac{\partial \delta \phi^{(e)}}{\partial x_j} \varepsilon_{jk}^{(e)} \frac{\partial \phi^{(e)}}{\partial x_k} - \rho \omega^2 u_i^{(e)} \delta u_i^{(e)} \right) dV = \iiint_{\Omega^{(e)}} F_i^{(e)} \delta u_i^{(e)} dV + \iint_{\Gamma^{(e)}} \delta u_i^{(e)} T_{ij}^{(e)} n_j^{(e)} dS + \iint_{\Gamma^{(e)}} \delta \phi^{(e)} D_j^{(e)} n_j^{(e)} dS \tag{2}$$

where e defines the e^{th} element and E the total number of elements. In equation (2), all the unknowns (δu, u...) should be written using polynomial interpolation for each element [Zienkiewicz, 2005]. Each quantities $\Delta^{(e)}(x_i)$ is written according to the following interpolation in one element:

$$\Delta^{(e)}(x_i) = \sum_{n=1}^{N_e} \Delta^{(e,n)} P^{(e,n)}(x_i), \tag{3}$$

where x_i is one space direction, N_e the number of nodes in the e^{th} element, $\Delta^{(e,n)}$ the value of the quantity Δ at the nth node of the eth element and $P^{(e,n)}(x_i)$ is the Lagrangian interpolation polynomial for the same node. For the sake of clarity, only the elastic part is written below according to the FEA formulation for a dimensional device (for instance along x_1 in Fig. 1) with all the mechanical contributions:

$$\sum_{e=1}^{E} \sum_{n=1}^{N_e} \sum_{\mu=1}^{N_e} \left(\iiint_{\Omega^{(e)}} \frac{\partial P^{(e,n)}(x_1)}{\partial x_1} C_{i11l}^{(e)} \frac{\partial P^{(e,\mu)}(x_1)}{\partial x_1} dV - \rho \omega^2 \iiint_{\Omega^{(e)}} P^{(e,n)}(x_1) P^{(e,\mu)}(x_1) dV \right) u_i^{(e,\mu)} \delta u_i^{(e,n)} = 0. \tag{4}$$

In the nodal expression (4), the right hand is zero. The boundary is actually not considered in this trivial model.

The right hands of equations (1) and (2) show several boundary conditions. They are represented by the integration on the limit Γ. This domain is also discretized in all its elements. The boundary conditions can be applied on each element considering a condition on the stress as well as on the displacement or the potential. These parts are for example the beginning of the radiating conditions. We define below this condition and how consider it in the variational equation.

III. Perfectly Matched Layer method

The PML is a theoretical artifact to simulate the propagation of a monochromatic wave or a wave packet from an interface to the infinite. The basic idea consists in rigorously simulating an exponential decrease of the acoustic field along at least one space direction. To clear the approach, let us consider the following incident plane wave

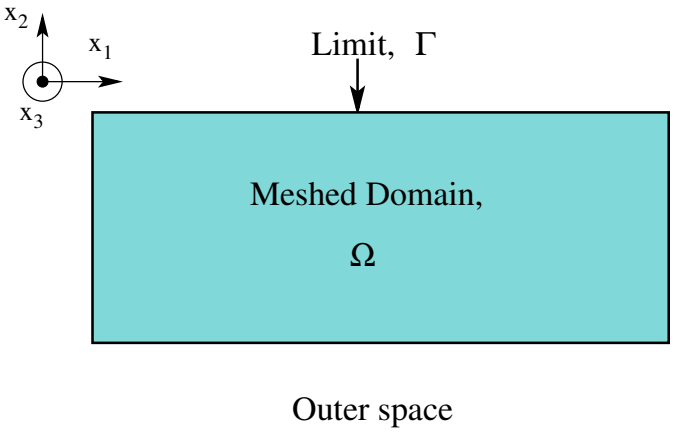

Fig. 1. Splitting of space for a FEA. Ω is the inhomogeneous space under simulation. This is the meshed domain in which the FEA is applied. Γ is the boundary of Ω with the remaining space. The latest is either simulated using boundary conditions or considered as vacuum.

$$u = Aexp^{-j(k_x x - \omega)} = Aexp^{-j\omega(s_x x - t)} \tag{5}$$

We then consider that in the absorbing area, one can apply a geometrical transform in the complex plane to introduce the exponential decay. Since it must not modify the propagation phase, this transform can be written

$$\tilde{x} = x - jf(x) \tag{6}$$

where $f(x)$ growths from the origin of the absorbing area to its end along a defined rate. However, since this transform must be efficient for any frequency (we represent the problem in the spectral domain), it is wise to define this function as follow :

$$f(x_i) = \frac{1}{\omega} \int_0^{x_i} d(x) \mathrm{dx}, \tag{7}$$

$$d(x_i) = d_{max} \left(1 - \frac{(abs(x_i) - x_p)^2}{(x_a - x_p)^2} \right)^n, \tag{8}$$

which allows for an easy definition of the transform Jacobian linking the considered coordinate systems. This reads

$$\frac{1}{\partial \tilde{x}} = \frac{j\omega}{j\omega + d(x)} \frac{1}{\partial x} \rightarrow \frac{1}{\partial x} = \left(1 + \frac{d(x)}{j\omega} \right) \frac{1}{\partial \tilde{x}} = \alpha_x \frac{1}{\partial \tilde{x}} \tag{9}$$

Replacing x by $\tilde{x}$ in (5) provides the wanted exponential decay if $f(x)$ unconditionally growths, imposing $d(x)$ even and positive to fulfil the absorbing condition for any x (we assume the problem centred around $x = 0$). Since the absorbing function $d(x)$ is not frequency dependent, its efficiency should be constant along ω. Conformably to Zheng and Huang [Zheng, 2002], we develop a formulation based on the usual piezoelectricity equations, yielding significant modifications of the elastic, piezoelectric and dielectric constants to account for the absorption.

We now rewrite the elasticity equations in the absorbing region turning x to $\tilde{x}$, using then (5) to express the result in the initial coordinates. As in [Zheng, 2002], the absorbing effect is assumed along the three space directions for the sake of generality. The equilibrium equation then reads

$$-\rho\omega^2 u_i = \frac{\partial T_{ij}}{\partial \tilde{x}_j} = \frac{1}{\alpha_j}\frac{\partial T_{ij}}{\partial x_j} \tag{10}$$

where α_j is characterized by its specific function $d_j(x_j)$. T_{ij} and u_i respectively represent the dynamic stresses and displacements, and ϱ is the mass density. We introduce a non symmetrical stress tensor, expressed in the transformed axis

$$\tilde{T}_{ij} = \frac{\alpha_1\alpha_2\alpha_3}{\alpha_j} C_{ijkl}\frac{\partial u_l}{\partial \tilde{x}_k} = \frac{\alpha_1\alpha_2\alpha_3}{\alpha_j\alpha_k} C_{ijkl}\frac{\partial u_l}{\partial x_k} = \tilde{C}_{ijkl}\frac{\partial u_l}{\partial x_k} \tag{11}$$

where $\tilde{C}_{ijkl}$ is the transformed elastic constant tensor relative to the absorption area. We multiply (10) by $\alpha_1\alpha_2\alpha_3$, thus yielding Newton relation for PMLs in the real coordinates

$$-\tilde{\rho}\omega^2 u_i = \frac{\partial \tilde{T}_{ij}}{\partial x_j} \tag{12}$$

where $\tilde{\rho} = \rho\alpha_1\alpha_2\alpha_3$ is the mass density relative to the transformed domain. Since the obtained form of the equilibrium equation complies with the classical expression for usual solids, it is liable to exploit the standard FEA formulation for PML as well, accounting for the frequency dependence of the transformed physical tensors. These developments of course can be extended to piezoelectricity by rewriting Poisson's equation and taking into account the piezoelectric coupling in the stress definition as follows

$$\begin{gathered}\tilde{T}_{ij} = \frac{\alpha_1\alpha_2\alpha_3}{\alpha_j}\left(C_{ijkl}\frac{\partial u_l}{\partial \tilde{x}_k} + e_{kij}\frac{\partial \varphi}{\partial \tilde{x}_k}\right) = \\ C_{ijkl}\frac{\partial u_l}{\partial x_k} + \tilde{e}_{kij}\frac{\partial \varphi}{\partial x_k}\end{gathered} \tag{13}$$

Poisson's equation expressed in the transformed system of axes reads

$$\frac{\partial D_i}{\partial \tilde{x}_i} = 0 \Rightarrow \frac{1}{\alpha_i}\frac{\partial D_i}{\partial x_i} = 0 \tag{14}$$

with D_i the electrical displacement vector. To provide an homogeneous formulation, we proceed as for the stress definition (11), multiplying the electrical displacement by $\alpha_1\alpha_2\alpha_3$, yielding

$$\tilde{D}_i = \frac{\alpha_1\alpha_2\alpha_3}{\alpha_i} D_i \tag{15}$$

As for the propagation equation (10), the Poisson's condition is written accounting for these changes as

$$\frac{\partial \tilde{D}_i}{\partial x_i} = 0 \tag{16}$$

Conformably to the stress tensor transformation, we introduce modified piezoelectric and dielectric constants defined as follows

$$\begin{gathered}\tilde{D}_i = \frac{\alpha_1\alpha_2\alpha_3}{\alpha_i}\left(e_{ikl}\frac{\partial u_l}{\partial \tilde{x}_k} - \varepsilon_{ik}\frac{\partial \varphi}{\partial \tilde{x}_k}\right) = \\ \tilde{e}_{ikl}\frac{\partial u_l}{\partial x_k} - \tilde{\varepsilon}_{ik}\frac{\partial \varphi}{\partial x_k}\end{gathered} \tag{17}$$

We now are able to establish a FEA formulation exploiting these developments without fundamental changes of the existing code. Thus, equation (1) becomes

$$\begin{gathered}\iiint_{\Omega_{PML}}\left(\frac{\partial \delta u_i}{\partial x_j}\tilde{C}_{ijkl}\frac{\partial u_l}{\partial x_k} + \frac{\partial \delta u_i}{\partial x_j}\tilde{e}_{kij}\frac{\partial \phi}{\partial x_k} + \frac{\partial \delta\phi}{\partial x_i}\tilde{e}_{ijk}\frac{\partial u_j}{\partial x_k}\right. \\ \left. -\frac{\partial \delta\phi}{\partial x_j}\tilde{\varepsilon}_{jk}\frac{\partial \phi}{\partial x_k} - \rho\omega^2 u_i\delta u_i\right) dV = \\ \iint_{\Gamma_{PML}}\left(\delta u_i\tilde{T}_{ij}n_j + \delta\phi\tilde{D}_j n_j\right) dS\end{gathered} \tag{18}$$

where Ω_{PML} and Γ_{PML} are respectively the PML domain and its boundary.

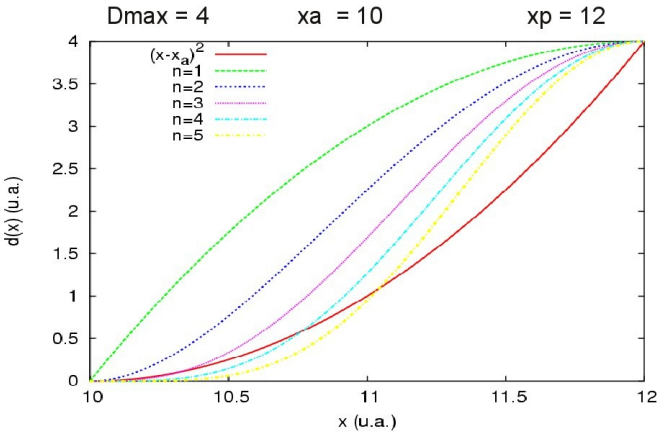

Fig. 2. Plotting of the absorbing polynomial for different order n. The parabolic reference is drawn with red solid line. The $dmax$ parameter is arbitrary fixed to 4 and the PML area varied from $x_a = 10\mu m$ to $x_p = 12\mu m$.

We must note here that all the parameters of the absorbing polynomial (Eqs. (7) and (8)) are empirically defined. Indeed, the polynomial $d(x)$ must increase from zero to the maximum value $dmax$ by a progressive slope. The value of $d(x)$ must be zero at the beginning of the PML to verify the impedance match. Moreover, the derivative of $d(x)$ must be null too to avoid any singularities. However, the absorbing polynomial must increase as quick as possible to minimize the number of PML finite elements with respect to the better smoothy shape. In figure 2, different orders of the absorbing polynomial are depicted against the distance in the PML. The reference polynomial $(x-x_a)^2$ is also drawn with the red solid line. All polynomials match the first conditions of zero at the beginning of the PML. However, while those with an order higher or equal to two have a zero derivative at $x = x_a$, the one for $n = 1$ has a non zero one and give rise to numerical singularities. The same comment can be done for the reference polynomial at $x = x_p$. Even if the risks of singularities are lower than for $n = 1$, it is better to eliminate these two of them. Moreover, when the order is too high, the polynomials increase slowly at the beginning of the PML and very sharply in the middle part for instance for order higher than three. This would also lead to numerical problems. Therefore one can choose the degree

of polynomial $d(x)$ equal to 3. The depth of the PML domain $(x_p - x_a)$ is also defined according the absorbed waves. So, we defined that this length must be approximately equal to one wavelength. At last, the parameter $dmax$ is chosen to be in the interval 10^6 to 10^7 but it can slightly vary outside of this range.

IV. Numerical results & discussions

The efficiency of the PML implemented in FEA is depicted in three parts. First, a 2D-case is investigated showing the absorbing due to the PML domain and the effects of the effects of the finite lateral size on the behavior of a SAW resonator. Next, the same study is repeated but in a 3D configuration in order to validate the general PML approach. At last, a realistic SAW problem is addressed by considering the aperture of the resonator and absorbing the lateral leaky modes.

First, A 2D SAW resonator problem is addressed. The geometrical configuration is depicted in figure 3. A piezoelectric medium (quartz YXl/36) is driven by 4 pairs of electrodes. The electrodes are non massive and alternatively activated with $V = 1V$ and $V = 0V$. The period is $10\mu m$. The depth of PML on both sides is $35\mu m$. The eight of the mesh is $75\mu m$. The absorbing parameters are set to $dmax = 10^6$ and $n = 3$. The

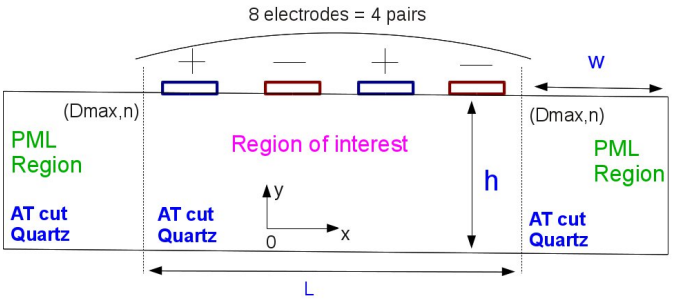

Fig. 3. Characteristic configuration for finite SAW resonators considering the mixed PML/FEA approach. Eight non massive electrodes are activated alternatively ($V_1 = 1V$, $V_2 = 0V$). The width of electrodes is equal to $2.5\mu m$ and the period of the resonator is set to $10\mu m$. The piezoelectric medium is quartz YXl/36. Its thickness vary from zero. On the left and right parts of the scheme, two PML domains are set. No boundary conditions are defined neither at the top nor at the bottom. Th depth of the piezoelectric h is chosen to avoid any interaction with the penetrating bulk wave at the bottom interface. $dmax = 10^6$ and $n = 3$.

result of this simulation is shown in figure 4. We depicted the vibrations for the x-displacements in the XY plane. The vibrations in both the right and left PML domains are strongly reduced as and as they enter into. The decreasing factor is around 10^{-5}. We also hardly observed the phenomena of diffraction due to the finite lateral size of the resonator. Indeed, weak lobes appears at the both lateral end of the grating and give rise to bulk wave and so losses in the medium.

Next, we repeat the same simulation as the one depicted in figure 3 but for a 3D geometry. The configuration is drawn in figure 5. The piezoelectric is once more quartz YXl/36. The same set of non massive electrodes is still powered in the same way. The absorbing conditions are also the same. The x-displacement obtained by FEA/PML is shown

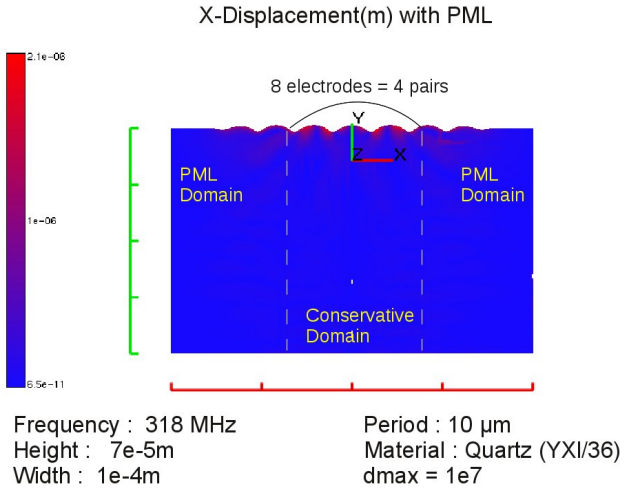

Fig. 4. The vibrations for x-displacement in the XY plane for the 2-D problem depicted in figure 3. The piezoelectric medium is quartz YXl/36 activated by eight electrodes alternatively powered by $V = 1V$ and $V = 0V$. The PML domains are delimited by the white dashed line at the let and right sides. The frequency is $318MHz$. $h = 7e-5m$, $dmax = 10^6$ and $n = 3$.

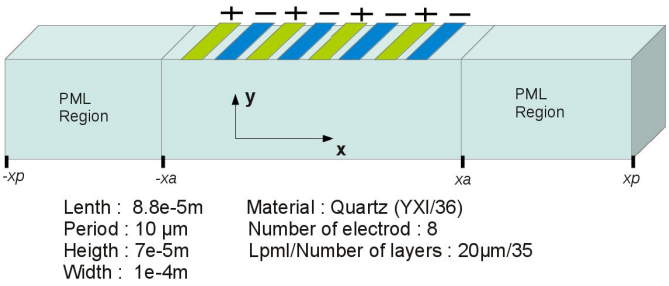

Fig. 5. Same configuration as in figure 3 but in 3D-case. The z-direction is periodically infinite. So the electrodes are infinitly long in the z-direction. Eight non massive electrodes are activated alternatively ($V_1 = 1V$, $V_2 = 0V$).$h = 7e-5m$, $dmax = 10^6$ and $n = 3$.

in the perspective figure 6. It is clearly demonstrated that the vibration have the same absorption as in the 2D-case even if the absorbing factor is slightly worse. One more time, the losses in the medium can also be observed at the end of the resonator. We notice that there is no relection at the end of the mesh for both side edges and bottom boundaries.

The last configuration highlight a new point to design SAW resonator. Indeed, up to now, the devices modelings were most often considered as 2D systems infinitely periodic in the direction of propagation and infinite in the perpendicular one. We just demonstrate that it is now possible to take into account the effects due to finite dimension along the direction of propagation. In this part, we depict the way to address the problem of real aperture of a SAW resonator. In other words, we consider a finite dimension in the perpendicular direction of the propagation. In this study, the number of electrodes is infinite. The geometrical configuration is depicted in figure 7. The materials properties, excitation and dimensions of the grating are still the same as previously in figure 5.

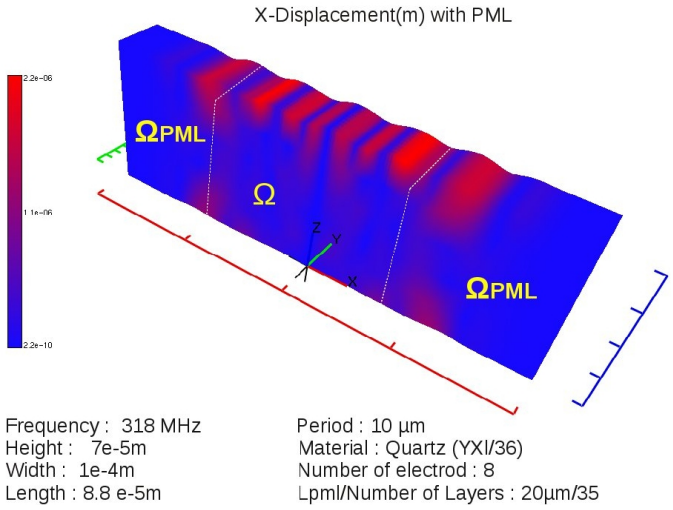

Fig. 6. The vibrations for x-displacement for the 3-D problem depicted in figure 5. The piezoelectric medium is quartz YXl/36 activated by eight electrodes alternatively excited by $V = 1V$ and $V = 0V$. The PML domains are delimited by the white dashed line at the let and right sides. The frequency is $318MHz$. $h = 7e-5m$, $dmax = 10^6$ and $n = 3$.

We now consider a length of the electrodes equal to $54\mu m$ for a period in the direction of propagation equal to $10\mu m$. The buses on the both right and left gratings are infinite along the propagation and $20\mu m$ wide. We also assume that the piezoelectric medium continue towards the infinity on the both sides of the resonator. The PML method allows this assumption. Once again, we show the vibration for the

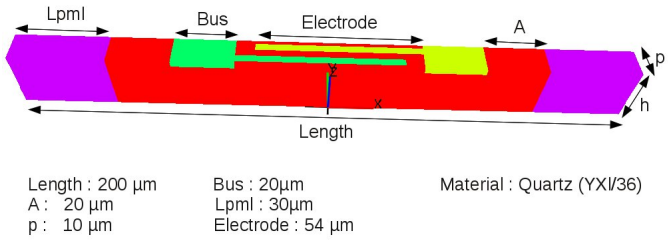

Fig. 7. Configuration of an infinitely periodic SAW resonator in the propagation direction but with finite lateral dimension. The z-direction is infinitely periodic and the non massive electrodes are alternatively excited with $V_1 = 1V$ and $V_2 = 0V$. The piezoelectric medium is quartz YXl/36. The length of electrodes is $54\mu m$ while the period is $10\mu m$. $h = 30\mu m$, $dmax = 1e-6$ and $n = 3$.

x-displacement in the perspective figure 8. The factor of absorption is still very high even if we notice a slight decrease. The Ω domain stands for the physical space in which the SAW is generated. We observe the Rayleigh wave in the middle of Ω. On each side of this vibration, the presence of th buses is denoted by two maxima of displacement. This displacements give rise to a lateral mode which is reflected on the side edges if there is no activated PML. But, in figure 8, all PML are turned on. So, the lateral modes can be detected at the very end of the Ω area, just before the PML domains. However, due to the presence of the PML, this mode do not reflect on the side edges and moreover its amplitude decreases at the time it progress in the PML from the beginning to the end where it almost vanishes by then.

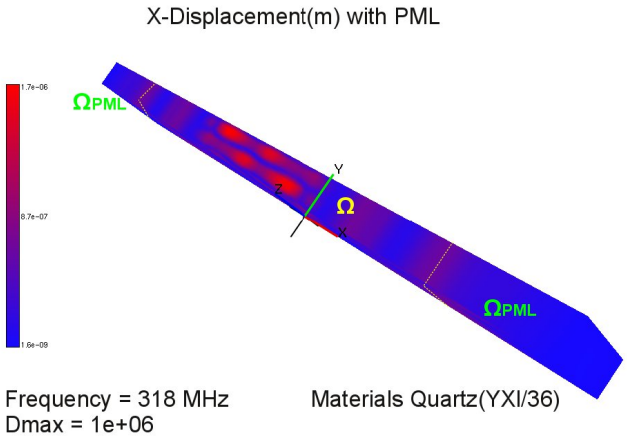

Fig. 8. The vibrations for x-displacement for the 3-D problem depicted in figure 7. The piezoelectric medium is quartz YXl/36 activated by eight electrodes alternatively excited by $V = 1V$ and $V = 0V$. The PML domains are delimited by the white dashed line at the let and right sides. The frequency is $318MHz$. $h = 7e-5m$, $dmax = 10^6$ and $n = 3$.

These three results show the efficiency of the combining of PML and FEA to simulate the effects due to the consideration of the real length or width of a SAW resonator. Thus, using this kind of method, we are able to simulate realistic effects in SAW. This method can also be applied to other kind of resonator.

V. Conclusion

In this work, we demonstrated a PML method well adapted to the FEA. The ability to absorb the outgoing wave from a resonator has been highlighted for different configurations. First, a 2D-system of SAW resonator was address and we noticed that all the waves going into the PML are absorbed. The lobes of diffraction due to the ends of the grating were also observed. Next, the comparison between the 2D-results and 3D-ones in the same configuration allow us to validate complete PML approach. At last, we displayed the influence of the lateral modes for a real model of SAW resonator considering the length of the electrodes as well as the buses.

We must also note that this absorbing method could be coupled with the BEM to consider most configurations for any kinds of acoustics devices

References

[Zhang, 1993] Zhang, Y., Desbois, J., Boyer, L., Characteristic parameters of surface acoustic waves in a periodic metal grating on a piezoelectric substrate, IEEE Trans. UFFC, vol. 40, pp. 183192, May 1993.

[Ballandras, 2009] Ballandras, S., Lardat, R., Wilm, M., Pastureaud, Th., Reinhardt, A., Champavert, N., Steichen, W., Daniau, W., Laude, V., Armati, R., Martin, G.: A mixed finite element/boundary element approach to simulate complex guided elastic wave periodic transducers, Journal of Applied Physics 105(1), JAN 1 2009

[Engquist, 1997] Engquist, B., Majda, A., Absorbing boundary conditions for the numerical simulation of waves, Mathematics of Computation, vol. 31, pp. 629651, 1977.

[Wilm, 2003] Wilm, M., Ballandras, S., Reinhardt, A., Laude, V., Lardat, R., Armati, R., Daniau, W., Lanteri, F., Gelly, J.F., Burat, O.: 3-D mixed finite-element/boundary-element model for the simulation of periodic ultrasound transducers radiating in layered media, 2003 IEEE Ultrasonics Symposium Proceedings, VOLS 1 and 2, 1654-1657

[Zhao, 2007] Zhao, DG.,Liu, ZY.,Qiu, CH., He, ZH., Cai, FE., Ke, MA., Surface acoustic waves in two-dimensional phononic crystals: Dispersion relation and the eigeneld distribution of surface modes, Phys. Rev. B, 76, 144301-1-6, 2007

[Wang, 2006] Wang, WB., Zhang, XD., Shui, YG., Wu, HD., Zhang, D., Plessky, V.P., Minimizing the bulk-wave scattering loss in dual-mode SAW devices, IEEE Transactions on Ultrasonics Ferroelectrics and Frequency Control 53(1), 193-198, JAN 2006

[Laroche, 2011] Laroche, T., Mayer, M., Perois, X., Daniau, W., Garcia, J., Ballandras, S., Wagner, K., Simulation of complex 2D transducer structures using finite element analysis combined with a canonical Green's function based boundary element method, IUS 2011 proceeding

[Berenger, 1996] Berenger, J.P., Three-dimensional perfectly matched layer for the absorption of electromagnetic waves, J. Comp. Phy. 127, 36379, 1996

[Laroche, 2005] Laroche, T., Baida, F.I., Van Labeke, D., Three -dimensional finite-difference time domain study of enhanced second-harmonic generation at the end of a apertureless scanning near-field optical microscope metal tip, josab 22, 10451051, 2005

[Mayer,2007] Mayer, M., Zaglmayr, S., Wagner, K.,Schöberl, J., Perfectly Matched Layer Finite Element Simulation of Parasitic Acoustic Wave Radiation in Microacoustic Devices, 2007 IEEE Ultrasonics Symposium Proceedings

[Tajic,2010] Tajic, A., Volatier, A., Aigner, R., Solal, M., Simulation of Solidly Mounted BAW Resonators using FEM combined with BEM and/or PML, 2010 IEEE International Ultrasonics Symposium Proceedings

[Tiersten, 1967] Tiersten, H.F., Hamilton's principle for linear piezoelectric media, Proc. of the IEEE, Vol. 55, pp. 1523- 1524, 1967.

[Courant, Hibert, 1953] Courant, R., Hilbert, D.: Methods of Mathematical Physics, Interscience Publishers, Inc., 1953

[Zienkiewicz, 2005] Zienkiewicz, O. C., Taylor, R. L., Zhu, J. Z.: The finite element method: its basis and fundamentals, Butterworth-Heinemann, 2005

[Zheng, 2002] Zheng, Y., Huang, X., Anisotropic Perfectly Matched Layers for Elastic Waves in Cartesian and Curvilinear Coordinates, 2002 MIT Earth Resources Laboratory Industry Consortium Report

Real-time Phase Stable One-way Frequency Transfer Over Optical Fiber

Sven-Christian Ebenhag*, Claes Wingqvist, and Per Olof Hedekvist*
Measurement Technology, Communications Lab
SP Technical Research Institute of Sweden
Borås, Sweden
*also with Chalmers University of Technology
Göteborg, Sweden

***Abstract*— The fundamental and most straightforward method for high performance time and frequency transfer is the two-way technique, which is suitable when the user has access to the whole system, and when both transmission paths are equal or with a known and predictable asymmetry. Furthermore it is most practical when the numbers of users are limited and when no security concerns limit the bidirectional connectivity.**
An alternative technique for fiber based time and frequency transfer, utilizing a one-way co-propagation of two light waves, has been demonstrated previously. The technique utilizes dual wavelengths and measures the difference in group velocity to estimate the delay variation of the timing signal in one of the wavelength channels.
This paper presents experimental data in a real-time delay compensated one-way frequency transfer and an investigation of the noise that is introduced in the receiver.

I. INTRODUCTION

The need for frequency and time transfer has during the last decade increased and is still increasing both for low-end and high-end users. High-end users are investigating using optical fibers for these purposes since the accuracy of GNSS (Global Navigation Satellite Systems) based methods seems to have reached their limits. Recent work of in the field of optical frequency transfer shows promising results and accuracy below 10^{-17}, which can be used for comparisons of optical clocks of varying types [1-2]. Most of these optical frequency transfers focus on two way frequency transfer whether it uses the optical phase, intensity modulation, dark fiber or wavelength division multiplexing channels [1-15]. When two-way transfer is used there is a presumption that both directions are symmetrical in transfer delay, which in most of the cases using two different transmission paths includes an error. Solutions using bidirectional signals in a single fiber results in a close to perfect match, but other limitations do occur [12]. A solution with single direction frequency transfer is therefore beneficial if the delay variations can be sufficiently compensated. At present there are two different directions of the known research groups working with this technique, one focus at transmitting a higher modulation frequency in a fiber network where the fiber type and manufacturing brand and year are known and can therefore compensates for variations along the path [16]. The other research group focuses in transmitting their intensity modulated signals in WDM-channels in already existing optical communication networks with unknown and varying properties which must be characterized for each system [17].
This paper presents a technique for one-way dual wavelength time transfer utilizing the difference of group velocity to estimate the delay variation of the timing signal in one of the wavelength channels. The first proof-of-concept was presented in 2009 [18], using modulated lasers at 1310nm and 1550nm and wavelengths at 1535 and 1553nm [19]. Those results showed that it is possible to perform a one-way time and frequency transfer with two wavelengths and by evaluate these two against each other, create a correction signal for compensation for influences along the transmission path.
This evaluation is performed with two wavelengths 8nm apart and focused to develop a real-time compensation algorithm and evaluating different kind of error source in the receiver after propagating signals along the 160km long fiber link that included Erbium doped fiber amplifiers (EDFAs).

II. BACKGROUND

The possibility to transfer a phase stable frequency over a one-way fiber optic connection relies on the unambiguous correlation between the dispersion and the group velocity in optical fiber, such that a variation in dispersion, which is detectable at the receiver, can be transformed to a corresponding change in delay through the fiber. This has been investigated previously [16-24] resulting in a scale factor inversely proportional to the wavelength separation, estimated to approximately 300 when the wavelengths are 23

nm apart [16]. The wavelengths are preferably chosen in the standardized channel of wavelength division multiplexed (WDM) systems. Since the scale factor is at the order of 100 – 1000, any variations in arrival time of the two signals must be detected at 2-3 orders of magnitude more precise than the resolution necessary for the delay compensation. To achieve sub-ns correction, a detection system in the ps-range is necessary. Until now, an analogue solution based on a double-balanced mixer has been used both in setups using feedback pre-compensation [16] or a digital post-compensation [21]. This removes any influence of digitalization of the time difference, but sets high requirements on noise. In the latter case, linearity of the output will also be important.

III. PHASE DETECTION THEORY

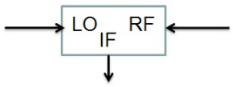

Figure 1. Schematics of a single RF mixer

The analogue phase detection in the experiment is based on a double balanced mixer, where the two transmitted signals are connected to the RF and LO inputs, as shown in fig.1. At the output (IF) port the signal can be described as

$$V_{IF}(t)=((A_{RF}A_{LO})/2)(\cos(2\pi(f_{RF}-f_{LO})t+\varphi_{RF}-\varphi_{LO}) + \cos(2\pi(f_{RF}-f_{LO})t+\varphi_{RF}-\varphi_{LO})) \quad (1)$$

where A_{RF} and A_{LO} are the amplitudes of the two inputs, f_{RF} and f_{LO} are the modulation frequencies and ϕ_{RF} and ϕ_{LO} are the phases of each input. With a system based on $f_{RF} = f_{LO}$, and the low-pass filter achieved by connecting the output to a DC voltmeter, the signal to detect is:

$$V_{IF}(t)=((A_{RF}A_{LO})/2)(\cos(\varphi_{RF}-\varphi_{LO})) \quad (2)$$

.

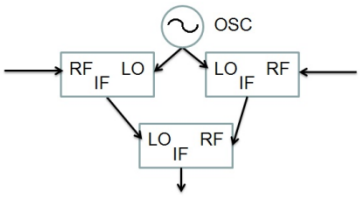

Figure 2. Schematics of three single double balanced mixers connected to a local oscillator.

While the first results using this setup emitted rather poor results [18], an improvement was expected with the addition of a local oscillator and three mixers, as shown in Fig. 2. Each input is thereby individually compared with the local oscillator, and the two outputs are then combined in the final mixer. This solution will in theory enable a higher output voltage, due to the multiplication of the amplitude of the local oscillator. The signal can be described by

$$V_{IF}(t)=((A_{RF1}A_{RF2}A^2_{LO})/8)(\cos(\varphi_{RF}-\varphi_{LO})) \quad (3)$$

assuming that the two transmitted frequencies are equal, and that all sum-frequencies are removed through low-pass filters From previous experiments it is apparent that there is additional noise introduced. In order to evaluate the magnitude of the noise from the mixing, the phase comparison using different connections was analyzed thoroughly. Three different sets of phase comparators assembled from connectorized mixers were evaluated. In all evaluations, a stable 10 MHz oscillator was connected to the two inputs of the comparator, with approx. 90 degree phase offset. The result will correspond to the limit of the phase variation measurement using each setup. In Fig. 3 is the mixer from the first demonstration used [18], a Mini-Circuit ZX05-5-S+, and with the settings of the experiment it outputs 4 mV/° in phase difference. Measurements resulted in a standard deviation of 0.013° (3,6ns).

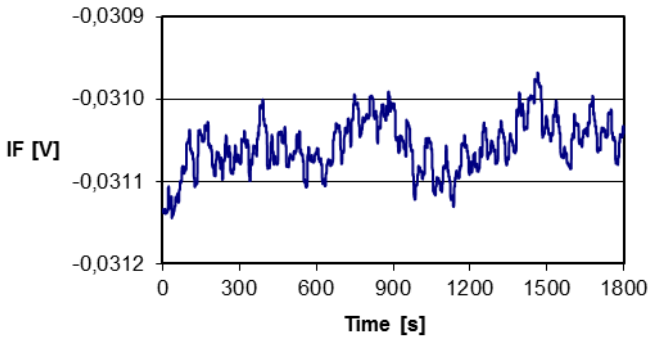

Figure 3. The figure presents the results of a 10 MHz oscillator connected to both RF and LO inputs of a single double balanced mixer. The IF output is measured with a voltmeter and the the standard deviation is 0.013 ° (3,6 ns).

The graph in Fig 4 shows the result when three mixers (Mini-Circuit ZX05-5-S+,) was connected as shown in Fig. 2, with a 10 MHz local oscillator (Agilent 33220A). The sensitivity of the IF was 1,8 mV/° which is in contrast to the expected increased sensitivity from eq.(3) The standard deviation for in the output signal is 0.029° (8ns) while the structure of the output signal is similar to the graph in Fig 3. When the same setup was used, however with the 10 MHz oscillator used for RF inputs synchronized to an H-maser connected through a commercial fiber distribution link an extensive noise was added in the link. The graph in Fig.5 shows that the output is dominated by fast variations. Nevertheless the sensitivity and standard deviation of the output remains at almost the same level. The analysis resulted in 1,8 mV/°, and standard deviation 0.026° (7,2ns).

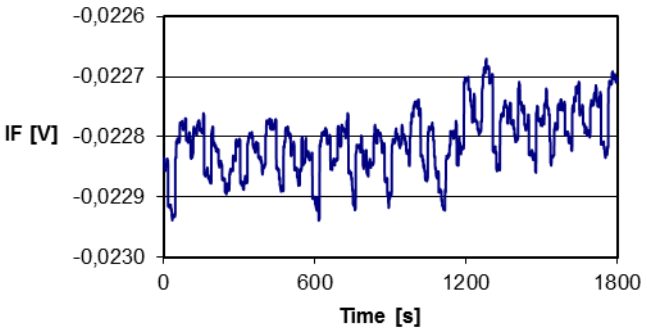

Figure 4. The output of a 10 MHz oscillator connected to both RF inputs of a three mixer setup as presented in Figure 2. The LO is a 10 MHz free running oscillator and the output IF is measured with a voltmeter and the the standard deviation is 0.029 ° (8 ns).

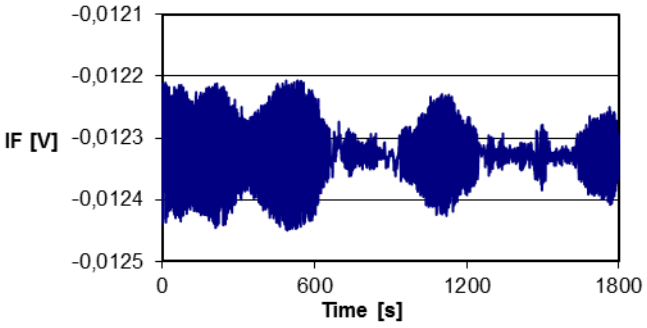

Figure 5. The output of a 10 MHz oscillator steerd to another oscillator at a remote location connected to both RF inputs of a three mixer setup as presented in Figure 2. The LO is a 10 MHz free running oscillator and the output IF is measured with a voltmeter and the the standard deviation is 0.026 ° (7,2 ns).

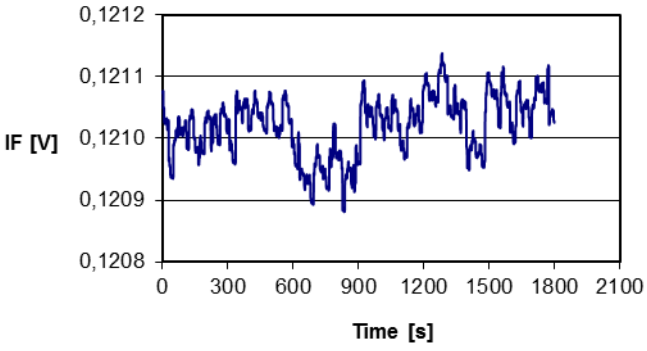

Figure 6. The output of a low frequency phase comparator optimized for equal input amplitudes and labelled phase comparator. A 10 MHz oscillator was connected to both RF and LO inputs and the IF output is measured with a voltmeter and the the standard deviation is 0.003 ° (0,9 ns).

Finally, a single phase comparator (Mini-Cicuit ZRPD-1+) was analyzed. Using this component, the IF sensitivity was 15 mV/° and measurements showed a standard deviation of 0.003° (0,9ns) with an IF output shown in Fig.6.

IV. Experimental and Reference Setup

The experimental setup is presented by the schematics in Fig. 7. Two tunable lasers emitting light at different wavelengths 8nm apart (1550nm and 1558nm) are individually modulated by a 10MHz sinusoidal signal. The modulated light is combined in a WDM multiplexer and launched into two sequential sections of 80km fiber each, both with an optical pre-amplification ensuring that the input to each section is +12dBm. At the receiver is the light split in a WDM demultiplexer and connected to APDs (avalanche photodiodes) for conversion to an electrical signal. To enhance the signal to noise ratio, the electrical signals are amplified before being combined in the phase comparison sub-system. The output voltage of this will be determined by the input phase difference of the two signals, and the slave oscillator is used to further enhance the signal. Finally, the splitters in the signal paths enable reference measurements at different positions. During the evaluations, the two oscillators in Fig. 7 are synchronized.

Even though the theory predicts that the output voltage depends on the cosine of the phase difference, as shown in eq.(3) the algorithm for post-delay uses a linear approximation, which is presumed acceptable while the output is much smaller than the amplitude. A separate analysis when changing the phase a full circle verifies that the amplitude of the output is 175mV, and thereby a voltage variation below 10% will be considered tolerable [21]. Furthermore, as shown in Fig. 7, the phase comparison is performed with three double balanced mixers and a 10 MHz local oscillator, corresponding to the setup in Fig. 2. The detailed analysis in Fig 4 and 5 revealed the additional noise using this technique, explaining the poor performance.

In addition to the analysis of the variation of arrival time for the two wavelengths, the experimental setup includes a digital delay unit, as shown in Fig.7. The voltage measured by the voltmeter is sampled once every 15s, in conjunction with the detector currents of the two APDs, which are used to verify that no amplitude variations in the signals will be misinterpreted as phase variation, as seen in eq. 2 and 3. The voltmeter reading is entered into a 240 value running average process and a constant scale factor to create a desired delay addition. The delay is entered into the digital delay unit, and both TICs are monitored to create a log for stability evaluation.

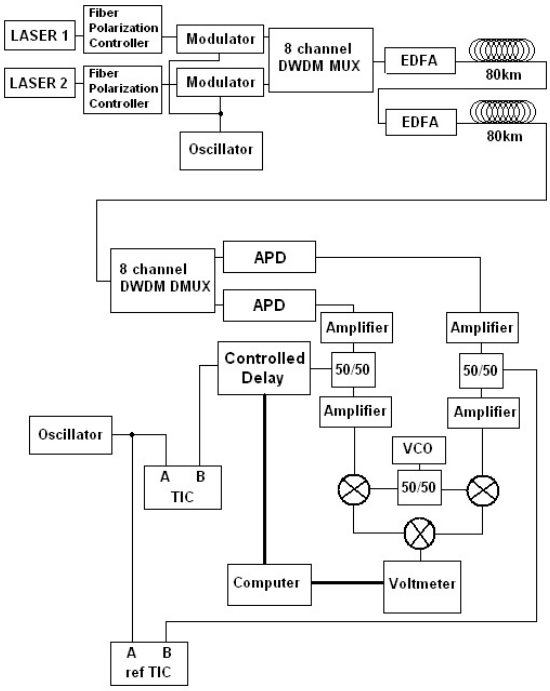

Figure 7. Experimental setup. Amplifiers are electrical amplifiers and TICs are time-interval counters

Following the noisy results of the output signal, and the lack of improvement using a local oscillator, a detailed evaluation of the phase detection was performed. The graphs in Fig. 3–6 show the output during identical circumstances. It is apparent that the noise addition when using the local oscillator will dominate the output, eliminating any improvement from the added amplitude.

V. RESULTS

The conducted experiment will present the results from an actual electrical delay compensation being steered in real-time by an algorithm created by measurements from the phase comparator assembly and photocurrent from the APDs in the receiver.

A. Real-time delay compensation

At the receiver in Fig. 7, the electrical real-time delay compensation is introduced and in this section it is steered from a software algorithm created from measuring the output voltage of the phase comparator, and the photocurrents as presented in the previous section. The post-delay is proportional to the average of the 240 last voltage samples and the scale factor is chosen by empirical evaluation of suppression of daily variations.

The real-time compensation of time transfer is evaluated during more than 30 days, and continuously compared with the uncompensated transfer in the link. It is apparent that some variations in the uncompensated, blue, curve is compensated in the red, however not to a satisfiable extent.

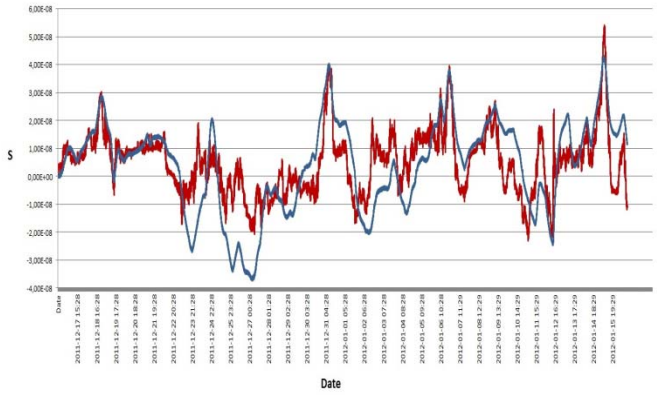

Figure 8. The red graph presents one month of continious data using a post compensating delay that is steered by a simple algorithm proportional to detected voltage. The blue figure presents the uncompensated reference for the same time frame.

VI. CONCLUSION

The aim of this study was to improve the steering algorithm to the real-time post-delay. However, the need for a thorough noise addition analysis was required. Focus was set on the noise addition of the phase comparison, and the results showed that the theoretically enhanced setup worsened the standard deviation of the measurement data from 4 to 8 ns. Finally, it was apparent that sub-ns were achievable. Nevertheless this can still be considered too high.

In addition to the variation introduced in the phase comparators, additional variations due to polarization effects in the optical fiber have been observed in complementary studies.

In conclusion, the need for a high performance phase comparison is paramount for the proposed technique, and overshadows the optimization of post-delay algorithms.

REFERENCE

[1] [C. Cliviati, D. Colonico, C.E. Calosso, G.A. Costanzo, F. Levi, A. Mura and A. Godone 2012, "Time transfer on optical fiber development at INRIM", 26th European Frequency and Time Forum, , Gothenburg, Sweden, 24-26 April 2012.

[2] O. Lopez, A. Amy-Klein, C. Daussy, Ch. Chardonnet, F. Narbonneau, M. Lours, and G. Santarelli, "86-km optical link with a resolution of 2×10-18 for RF frequency transfer", Eur. Phys. J. D 48, 35-41 2008.

[3] S.R. Jefferts, M. Weiss, J. Levine, S. Dilla, and T. E Parker, "Two-Way Time Transfer through SDH and Sonet Systems", European Frequency and Time Forum EFTF'96, 5-7 March, 1996.

[4] M. Kihara, A. Imaoka, M. Imae, K. Imamura, "Two-Way Time Transfer through 2.4 Gb/s Optical SDH Systems", IEEE Trans. Instr. Meas., vol. 50, pp. 709-715, 2001.

[5] F. Narbonneau, M. Lours, S. Bize, A. Clairon, G. Santarelli, O. Lopez, C. Daussy, A. Amy-Klein, C. Chardonnet, "High resolution frequency standard dissemination via optical fiber metropolitan network", Rev. Sci. Instrum. 77, 064701, 2006.

[6] H. Jiang, F. Kéfélian, S. Crane, O. Lopez, M. Lours, J. Millo, D. Holleville, P. Lemonde, A. Amy-Klein, Ch. Chardonnet, G. Santarelli, "Progress to a full optical link on a telecom network," Proceedings of the the 22nd European Frequency and Time Forum, Toulouse, France, 23-25 April 2008.

[7] R. Newbury, P. A. Williams, W. C. Swann, "Coherent transfer of an optical carrier over 251 km", Opt. Lett. 32, 3056-3058, 2007.

[8] P.A. Williams, W.C Swann, and N.R. Newbury, "High-stability transfer of an optical frequency over long fiber-optic links", J. Opt. Soc. Am. B 25, 1284-1293, 2008.

[9] G. Grosche, B. Lipphardt, H. Schnatz, G. Santarelli, P. Lemonde, S. Bize, M. Lours, F. Narbonneau, A. Clairon, O. Lopez, A. Amy-Klein, Ch. Chardonnet , "Transmission of an Optical Carrier Frequency over a Telecommunication Fiber Link", in Conference on Lasers and Electro-Optics/Quantum Electronics and Laser Science Conference and Photonic Applications Systems Technologies, OSA Technical Digest (CD) (Optical Society of America, 2008), paper CMKK1, 2008.

[10] O. Terra, G. Grosche, K. Predehl, R. Holzwarth, T. Legero, U. Sterr, B. Lipphardt, H. Schnatz,, "Phasecoherent comparison of two optical frequency standards over 146 km using a telecommunication fiber link", Applied Physics B, Laser and Optics, vol. 97, pp. 541551, 2009

[11] O. Terra,G. Grosche, G. and H. Schnatz, "Brillouin amplification in phase coherent transfer of optical frequencies over 480 km fiber".Opt. Express 18, 16102-16111, 2010.

[12] A. Imaoka and M. Kihara, "Accurate time/frequency transfer methodusing bidirectional WDM transmission," IEEE trans. On Instrumentation and Measurement, Vol.47,No.2, pp.537-542, April 1998.

[13] F. Kéfélian, H. Jiang, P. Lemonde and G. Santarelli, "Ultralow-frequency-noise stabilization of a laser by locking to an optical fiber-delay line", Optics Letters ,Vol 34, No 7, April 1, 2009.

[14] R. Emardson, P.O. Hedekvist, M. Nilsson, S.C. Ebenhag, K. Jaldehag, P. Jarlemark, C. Rieck, J. Johansson, L. Pendrill, P. Löthberg and H. Nilsson, 2008, "Time Transfer by Passive Listening over a 10 Gb/s Optical Fiber," IEEE Trans. Instr. Meas., Vol. 57, pp. 2495-2501.

[15] S.C. Ebenhag, P.O. Hedekvist, C. Rieck, H. Skoogh, P.Jarlemark, and K. Jaldehag, 2009, "A fiber based frequency distribution system with enhanced output phase stability", 23rd European Frequency and Time Forum, EFTF'09, 20-24 April 2009, Besançon, France, pp. 1061-1064.

[16] J. Hanssen, S. Crane, and C. Ekstrom, 2011, "One-Way Temperature Compensated Fiber Link," 25th European Frequency and Time Forum, EFTF'11, San Francisco, California, Paper 7273, 1-5 May 2011

[17] S.C. Ebenhag, P.O. Hedekvist and K. Jaldehag, 2011, "Active Detection of Propagation Delay Variations in Single Way Time Transfer Utilizing Dual Wavelengths in an Optical Fiber Network," 25th European Freq. and Time Forum, EFTF'11 , San Francisco, California, Paper 7084. 1-5 May 2011.

[18] S.C. Ebenhag, P.O. Hedekvist, and K. Jaldehag,, "Fiber based frequency distribution based on long haul communication lasers", Paper 7, 41st Precise Time and Time Interval (PTTI) Systems and Applications Meeting, Santa Ana Pueblo. NM, 2009.

[19] S.C. Ebenhag, P.O. Hedekvist, J. Johansson, "Fiber based one-way time transfer with enhanced accuracy", Proc. of the 24th European Frequency and Time Forum, Space Research and Technology Centre of the European Space Agency (ESA/ESTEC) Noordwijk, The Netherlands, April 13-16, 2010

[20] S.C. Ebenhag, P.O. Hedekvist, and K. Jaldehag, "Single way fiber based time transfer with active detection of time transfer variations", Paper 32, 42nd Precise Time and Time Interval (PTTI) Systems and Applications Meeting, Reston, Virginia, 2010.

[21] S.-C. Ebenhag, P.O. Hedekvist, and K. jaldehag, "One Way Time Transfer Utilizing Active Detection of Propagation Delay Variations of Dual Wavelengths in an Optical Fiber Network", 43rd Topical Meeting on Time and Time Interval, PTTI 2011, Long Beach, California, 2011.

[22] W. Sellmeier, "Zur Erklärung der abnormen Farbenfolge im Spectrum einiger Substanzen,", Ann. der Phys. und Chem., Vol. 219, pp. 272-282, 1871

[23] G. Ghosh, M. Endo and T. Iwasaki, "Temperature-Dependent Sellmeier Coefficients and Chromatic Dispersions for Some Optical Fiber Glasses,", J. Lightwave Technol., Vol. 12, pp. 1338-1342, 1994.

[24] P.O. Hedekvist and S.C. Ebenhag, 2011,"Time and frequency transfer in optical fibers," Optical Fibers / Book 3, ISBN 979-953-307-652-1, InTech Open Access Publishing., 2011.

Microwave Frequency Transfer with Optical Stabilisation

Sascha Schediwy and Andre Luiten
School of Physics,
University of Western Australia
Perth, Australia
sascha.schediwy@uwa.edu.au

Kenneth Baldwin
Research School of Physics and Engineering
Australian National University
Canberra, Australia

Guido Aben
Australian Academic and Research Network
Perth, Australia

Yabai He and Brian Orr
Department of Physics and Astronomy
Macquarie University
Sydney, Australia

Bruce Warrington
National Measurement Institute
Sydney, Australia

***Abstract*—In this paper we present a novel frequency dissemination technique which uses an all-optical interferometer to sense length fluctuations with high precision, and then utilises this information to simultaneously stabilise a transmitted optical and signal and a microwave signal.**

I. Introduction

A. Time and Frequency Dissemination

The stability of atomic clocks has improved to the extent [1] that the traditional method of transmitting time and frequency information (using dedicated two-way microwave-frequency[1] satellite links) is no longer sufficiently stable to convey the full precision of the atomic clocks [2]. Newly developed techniques based on dissemination of time and frequency via optical fibre networks can offer substantially improved performance over satellite transfers. However, it is necessary to actively stabilise the length of the fibre link to achieve the highest precision time and frequency dissemination. The two most common stabilisation schemes involve either the direct detection of optical phase using an all-optical interferometer, or the sensing of the phase of some microwave modulation imposed on the optical carrier [3].

Given the higher frequency of optical- as compared to microwave-frequencies, optical stabilisation schemes [4] can offer intrinsically better frequency transfer in the short-term and also operate over longer links [5] when compared to microwave transfer schemes [6]. However, standard all-optical systems can only disseminate optical frequency information. Therefore, an ideal 'hybrid' system is one that utilises optical stabilisation to achieve the maximum frequency precision and link length, but also contains a stabilised microwave frequency signal, which delivers the capacity for immediate use in electronic systems. In addition, the technique does not require a dedicated dark fibre link. In this paper we demonstrate, for the first time, this hybrid technique.

B. Disseminating Two Optical Signals Separated by a Microwave Frequency

In our technique, we use a telecommunications-grade modulator to generate a microwave signal; however, unlike [7], we simply sense the phase fluctuation of the optical carrier frequency. In this way, our technique is identical to other standard optical stabilisation schemes. The first key innovation of our technique is that we do not actuate on the microwave signal; we simply rely on a strong correlation between the noise experienced by the microwave and optical signals. The stabilisation of the optical signal therefore also stabilises the microwave signal (similar to the optical frequency comb transfer described in [8]).

The second innovation is that we transmit only two optical frequencies. In our technique, we configure a dual-drive Mach-Zehnder modulator (an intensity modulator that has an electro-optic phase modulating birefringent crystal in both arms) to generate single-sideband modulation, thereby effectively resulting in two optical signals separated by a microwave frequency. This avoids the destructively of the microwave signal from the upper- and lower -sideband products when standard amplitude modulation is used. This occurs relative phase of the two sideband due to chromatic

[1] In this paper we use the term 'microwave frequency' to collectively refer to all frequencies in the radio, microwave, and millimeter frequency bands; specifically10 MHz to 300 GHz.

This research was supported under Australian Research Council's *Linkage Projects* funding scheme (project number LP110100270).

dispersion of optical fibre. A similar technique that also transmits two optical frequencies [9] was proposed (but not implemented) as a local oscillator distribution system[2] for the ALMA telescope [10]. However, the modulation state required in their proposed technique suppresses much of the optical power and so additional optical amplification is required. This system is therefore more expensive and complex to implement, and not suitable for large-scale time and frequency networks.

II. Method

Figure 2 shows the schematic diagram of our experimental setup. A single frequency synthesiser is used to provide the 10 GHz driving signal for both arms of the modulator. The signal is split into two parts, with one going through a variable delay line component to adjust the relative phase, before each signal is applied to the microwave input on the modulator.

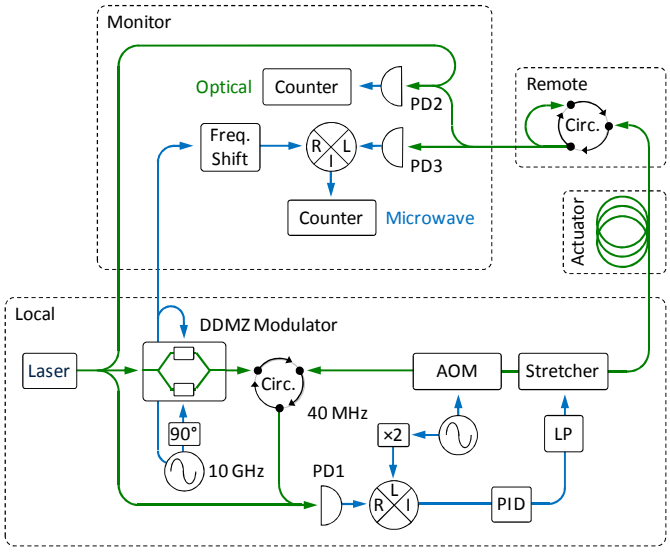

Figure 1. Schematic representation of the experimental layout. Optical signals are shown in green and electronic signals are shown in blue. All signal synthesisers are connected to a common 10 MHz frequency reference. R-radio frequency port of mixer, I-intermediate frequency port, L-local oscillator port, Circ.-optical circulator, DDMZ Modulator-telecommunications grade dual-drive Mach-Zehnder modulator, DP-photodetector, ×2-frequency doubler, LP-low-pass filter, PID-proportional-integral-derivative controller.

We use an optical interferometer to sense the phase fluctuations induced in the optical link as shown in Figure 1. For this experiment, both the local and remote sites are situated within the same laboratory to enable the stability of the transfer scheme to be measured. The frequency stability of the transmitted microwave signal was always measured synchronously with the optical frequency stability. In order to count the signal away from DC, we introduce a frequency shift between the reference signal and the remote signal. A mechanical actuator was inserted into the fibre loop to increase the total noise impacting on the optical fibre link. This actuator consisted of a 20 m length of fibre wound around a mechanical displacement device.

III. Results

The actuator was used to apply white-noise to the optical fibre link. These data were converted to fractional frequencies for a range of integration times to produce the Allan deviation curves shown in Figure 2 (dotted lines). With no stabilisation, the actuation system was able to induce fluctuations in both the microwave and optical signals at a level of around 1×10^{-14} at 1 s.

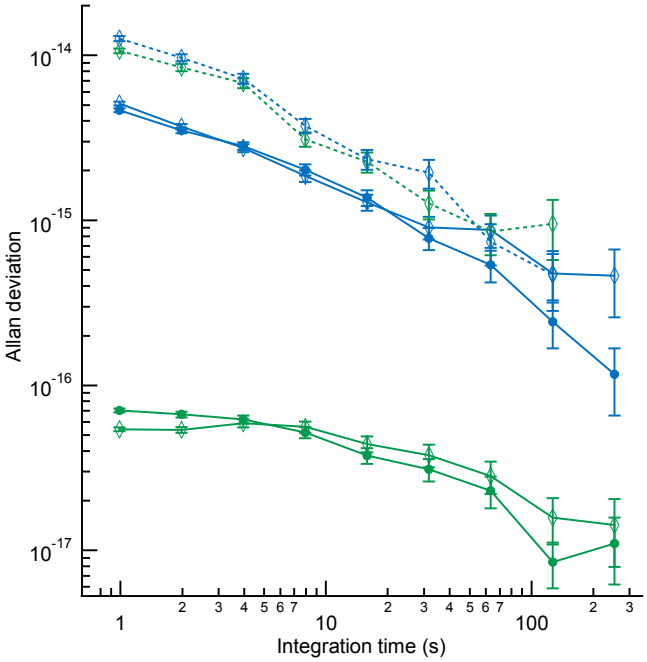

Figure 2. Allan deviation plot of measured optical and microwave frequency counts. Green-optical signals; blue-microwave signals; solid line-closed-loop measurements; dotted line-free-running measurements; open diamonds-white-noise fibre actuation; filled circles-no actuation.

We closed the feed-back loop using the fibre stretcher as the loop-actuator. The resultant frequency fluctuation data are shown in Figure 2 as the solid lines with diamond-shaped markers. Here we see that both the optical and microwave signals are stabilised down to their individual measurement system noise floors (the noise floors are shown as solid lines with circular-shaped markers).

IV. Discussion

Our results demonstrate that our hybrid stabilisation technique is able to suppress microwave frequency fluctuations to a level at least as low as 4.6×10^{-15} at 1 s. As we are currently limited by the noise floor of the microwave measurement system, this value is therefore an upper limit for the stability. The actual microwave stability could be significantly better, with the potential limit being set by the stability of the optical signal (6.8×10^{-17} at 1 s). The value will be determined by the degree of correlation between the optical

[2] The local oscillator distribution system adopted by the ALMA telescope uses a tuneable laser phase-locked to fixed master laser with a variable microwave frequency offset [10]. As the link noise sensing is done in the microwave frequency domain, the stability is not as good as optical stabilisation. A tests with 700 m of buried fibre and 14 km of spooled fibre resulted in stability of only 8×10^{-16} at 10 s [11].

and microwave signals to noise in the optical fibre, which has not yet been determined. That is, the value depends on how differently a specific source of noise impacts the optical carrier (at 193 THz) as compared to the sideband (at 193 THz ± 10 GHz)

V. Conclusion

We have demonstrated a novel frequency dissemination technique which senses noise fluctuations in a fibre link with the precision of an all-optical interferometer, and which applies this to simultaneously stabilise the transmitted optical and microwave signals. Our scheme utilises a dual drive Mach-Zehnder modulator to generate two optical signals which are separated by the driving frequency of the modulator. Our scheme can be implemented on optical links of arbitrary length because it does not suffer from the issue of microwave signal interference resulting from the chromatic dispersion in the fibre, which is the case with techniques that generate the microwave signal using standard amplitude modulation. The dissemination technique outlined in this paper is ideally suited to be implemented on long-distance links which require ultra-stable optical phase, as well as stabilised microwave signals.

Acknowledgement

The authors wish to thank John Hartnett for frequency shifter idea, and Eugene Ivanov for lending us the appropriate component. Thanks also extend to Phil Light for access to his data acquisition software, and James Anstie for help with the loop lock.

References

[1] C. W. Chou *et al.*, Physical Review Letters **104** (2010).

[2] T. E. Parker, and V. Zhang, in *Proceedings of the 2005 Joint IEEE International Frequency Control Symposium and Precise Time and Time Interval Systems and Applications Meeting*Vancouver, Canada, 2005), pp. 745.

[3] P. A. Williams, W. C. Swann, and N. R. Newbury, J. Opt. Soc. Am. B **25** (2008).

[4] O. Lopez *et al.*, Opt. Express **18** (2010).

[5] K. Predehl *et al.*, Science **336** (2012).

[6] O. Lopez *et al.*, Applied Physics B: Lasers and Optics **98** (2010).

[7] R. Wilcox *et al.*, Opt. Lett. **34** (2009).

[8] G. Marra, H. S. Margolis, and D. J. Richardson, Opt. Express **20** (2012).

[9] H. Kiuchi, Microwave Theory and Techniques, IEEE Transactions on **56** (2008).

[10] A. Wootten, and A. R. Thompson, Proceedings of the IEEE **97** (2009).

[11] B. Shillue, in *Frequency Control Symposium (FCS), 2010 IEEE International*2010), pp. 569.

The Fairy World of Quartz Vibrating MEMS

O. Le Traon, D. Janiaud, J. Guerard, R. Levy,
S. Masson, O. Ducloux, M. Pernice, R. Taïbi
ONERA – The French Aerospace Lab
Palaiseau, France
olivier.le_traon@onera.fr

***Abstract*—Quartz crystal has been an essential material for time and frequency and radio-frequency applications during the 20th century. Quartz is always an unmatched material at the beginning of the 21st century, and hold 80 % of oscillators & RF market which represent today 17 billions € market with a 10 % growth per year. This paper describes other more confidential applications – the vibrating inertial MEMS - where the quartz crystal plays also a major role. Clearly, quartz crystal has still a future in these high added value applications, and for a long time.**

I. INTRODUCTION

The invention of the electronic watch [1] in the 1960's was certainly the starting point -the seed- of Quartz Micro Electro Mechanical System (Quartz MEMS) development. This revolutionary invention, based at this time on an electromagnetic tuning fork resonator, imposed the major world watch industries to react: CEH in Switzerland and Seiko in Japan then engaged the development of electronic wristwatches based on a quartz tuning fork, leading to the Beta prototype for CEH and the Astron for Seiko in 1967. In the 1970's, J.S Staudte [2] proposed and patented a compact and inexpensive quartz tuning fork resonator and its collective micromachining process by photolithographic technique particularly suited to low cost and mass production. Seiko and Micro Crystal acquired the rights and engaged the production of quartz wristwatches. Today, several billion of quartz resonators are manufactured per year, still in Switzerland and Japan, but also in China and India.

The watch quartz technology paved the way for further quartz MEMS developments, particularly in the field of vibrating inertial sensors, i.e Coriolis Vibrating Gyro (CVG) and Vibrating Beam Accelerometer (VBA), based on a resonator as sensitive element. J. S. Staudte was the first to re-imagine the concept of tuning fork CVG proposed by the Sperry Gyroscope Company [3] in 1943: he patented an original quartz resonator made of a double tuning-fork [4] dedicated for a solid-state vibrating gyro. In 1986, the Systron Donner Company acquired an exclusive worldwide license, developing the famous QRS gyro for military and aerospace applications as well as accurate quartz IMUs [5]. More recently, the QRS concept has been declined fore automotive market and over 25 million of quartz gyros have been producing since the 2008's crisis.

Vibrating Beam Accelerometer (VBA), based on the change in the resonance frequency of a vibrating beam when subjected to acceleration, is also an old idea [6], and famous industrial development has been done in the field of the 1970's lunar program, leading to lunar gravity measurement [7]. In the end of 1980's, Onera was one of the first laboratories to propose monolithic quartz vibrating beam accelerometer. An original concept [8], called VIA (or DIVA in its differential configuration), based on a simple beam as resonator and a dedicated insulating system, has been proposed, as well as a collective micromachining process, close to that of watch resonators, but able to obtain a pseudo 3D structure from a initial planar structure. This vibrating beam accelerometer is today one of the most accurate MEMS accelerometer. Onera has also been involved in quartz CVG [9][10] and is currently developing a 1°/h class quartz gyro for military and aerospace applications.

The choice of quartz crystal instead of silicon was made because of its piezoelectricity allowing very accurate sensing and driving systems by simple electrodes deposited on the resonator, and also because of its well-known high stability, including low temperature dependency.

This paper provides an overview of past and current developments performed at Onera in the field of inertial quartz MEMS, e.g. VBA and CVG, as well as more recent research on quartz resonator for fundamental physics. Trends will be also given, mainly focused on high added value applications but also on new technological challenges of quartz 3D integration, under vacuum wafer level packaging and new micromachining techniques by Deep Reactive Ion Etching for dielectric materials.

II. QUARTZ VIBRATING BEAM ACCELEROMETERS

The VIA concept (fig. 1), was proposed in 1995. Made of a single vibrating beam instead of a double-ended tuning fork, the main originality of this monolithic structure consists of the insulating system (the frame and the two links) connecting the active part to the mounting areas. As explained in [11][12], this insulating system allows a very efficient insulation of the beam -vibration and thermal stresses – given an excellent frequency stability (bias stability) and an excellent temperature behavior (low hysteresis with temperature). The beam vibrates in the plan of the structure and the sensitive axis is quasi perpendicular to the plan. The beam frequency is 60 kHz, its quality factor 15 000 (limited by intrinsic thermoelastic damping [13][14]) and the scale factor is 12 Hz/g.

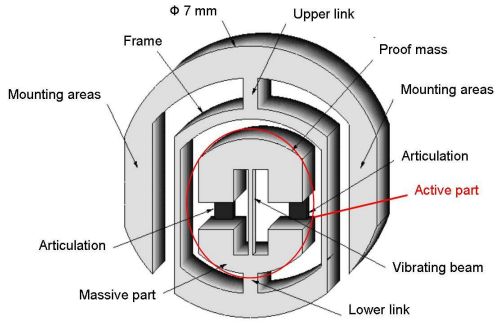

Figure 1. VIA concept

The VIA manufacturing process by chemical etching of quartz (fig. 2) is very similar to that used in watch industry, the difference being that the depth etching is used to define a third dimension in the thickness of the quartz wafer. The etching duration is thus well controlled to etch the thickness of the wafer minus the wanted thickness of the beam and the articulations (~30 µm). The roughness of the etched surface, defining one face of the beam, must be well controlled and minimized, because it impacts on the beam frequency, the scale factor and the beam temperature behavior. A dedicated chemical etching process, based on a mixture of fluoridric acid (HF) and ammonium fluorure (NH_4F), has been optimized in order to obtain a roughness of the etching surface compatible with the accelerometer accuracy.

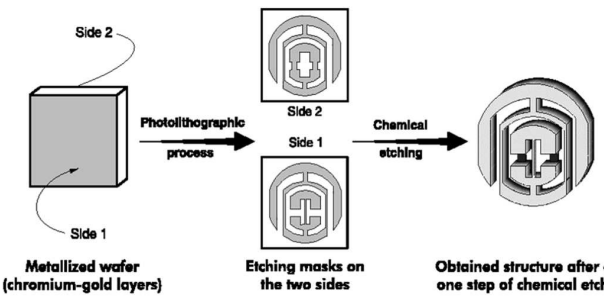

Figure 2. VIA manufacturing process by only one step of chemical etching

The VIA accelerometer (fig. 3) includes 2 identical VIA transducers in a push-pull configuration in order to reduce all common parasitic sensitivities e.g. temperature, pressure, aging. A vacuum better than 0.1 mbar (over the sensor lifetime) is required for preserving the quality factor of the beams. Two oscillator circuits maintain continually the 2 beams at their resonance frequencies and the opposite variations of the two frequencies provide directly the applied acceleration. The whole Onera's prototype volume was at that time 10 cm^3 with a consumption lower than 0.1 W.

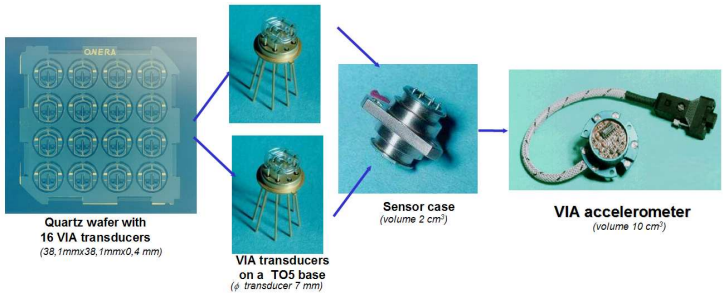

Figure 3. VIA Accelerometer

Table 1 synthesized typical performances of the VIA accelerometer [15], characterized by an excellent scale factor behavior (one of the main feature of Vibrating Beam Accelerometer), but also an excellent thermal behavior and long term stability of the bias, obtained thanks to the VIA concept and, of course, quartz crystal. This accelerometer is now transferred to the major French companies specialist of inertial systems.

TABLE I. TYPICAL PERFORMACES OF THE VIA ACCELEROMETER

Measurement Range	±100 g
Bandwidth	> 1000 Hz
S/N ratio	5 µg @ 1 Hz
Scale Factor K1 K2 K3 Thermal residual (-40°C,90 °C) Repeatability (3 years)	 24 Hz/g 2 µg/g^2 0,02 µg/g^3 <10 ppm (1 σ) <15 ppm (1 σ)
BIAS Thermal residual (-40°C,90 °C) Repeatability (3 years)	 80 µg (1 σ) <90 µg (1 σ)

In the 2000s, a full quartz monolithic differential vibrating beam accelerometer, called DIVA, has been proposed. The DIVA configuration is shown on fig. 2. This monolithic configuration is obviously more suitable to miniaturization than the VIA and simplifies the assembly process.

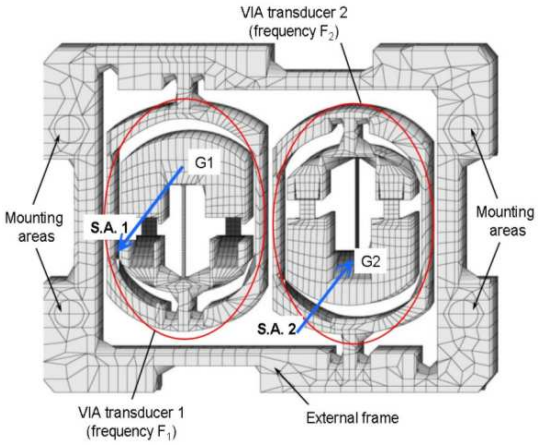

Figure 4. DIVA Concept

The DIVA is made up of two VIA transducers in a planar push-pull configuration and linked together by an external frame [16]. The major problem to solve with monolithic differential VBA is called "lock-in". The lock-in phenomena is due to the mechanical coupling between the two beams and is characterized, close to the frequency crossing, by a lock between the two frequencies, with no frequency variations in spite of the applied acceleration. That leads to a blind zone of measurement which degrades the VBA accuracy. The role of the frame as insulating system between the two beams is explained in [17] and provides a very small lock-in zone, less than 500 µg.

The whole DIVA prototype made at Onera is shown on fig. 5. The manufacturing process is exactly the same as that used for the VIA. In addition, note that the specific arrangement of the DIVA taken into account the quartz crystal symmetry provides two nominally identical VIA transducers by chemical etching of quartz, given an efficient differential effect. The performance of the DIVA accelerometer are given in [18] and are very similar to the VIA accelerometer.

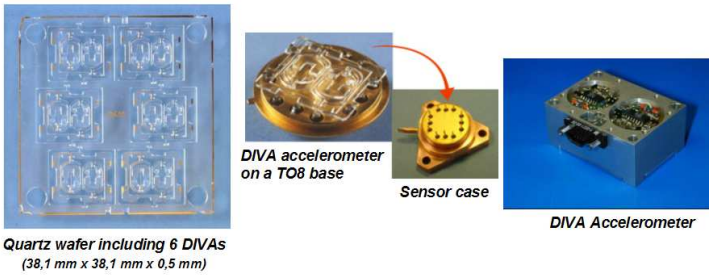

Figure 5. DIVA Accelerometer

More recently, two new quartz VBA developments have been started (fig. 6):

- the first one concerns a navigation grade quartz VBA where a bias stability better than 50 µg for a measurement range of ±50 g, including harsh environment, is targeted. For that, a new manufacturing process based on two chemical etching steps has been implemented in order to obtain a more larger structure (needed for the accuracy improvement) , but above all, a more compact device allowing a high natural frequency of the device despite the increase in size. Indeed, a high natural frequency is necessary to ensure the robustness of the device and also to reduce vibration rectification errors in harsh environment ;
- the second one targets an extremely low noise quartz VBA: a 50 nanog noise (with a reduced measurement range at ±5g) is expected for a centimeter-size device, always compatible with collective chemical etching micromachining. Precise thrust measurement of satellite for a better attitude and orbit control is a targeted application of this accelerometer, as well as all low dynamic applications needed by accurate acceleration measurement.

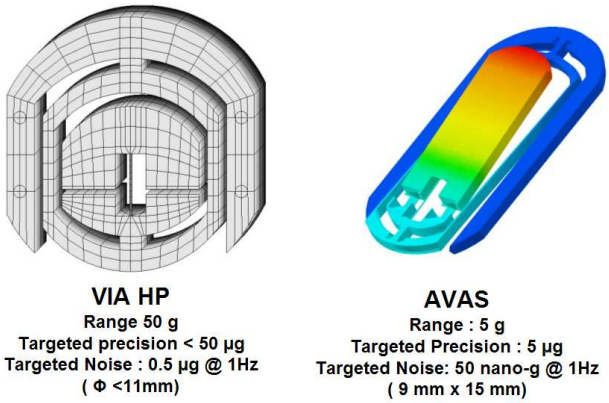

Figure 6. Under development Onera's VBAs

Other original works on the vibrating beam also deserve to be addressed:

- Fig. 7 (left) shows an optimized quartz vibrating beam having a central portion with reduced thickness. This dedicated geometry optimizes the compromise between the quality factor, limited by thermoelastic losses, and the force sensitivity of the beam [19]. An improvement by a factor 2 of the long terme stability of the VIA or DIVA accelerometers has been obtained thanks to this arrangement.
- Fig. 7 (right) represents a dual mode vibrating beam composed of an accelerometric mode (flexural mode) and a thermometric mode made of a torsional mode located at the center of the vibrating beam. This

arrangement has been designed in order to obtain a "true" measurement of the beam temperature and its gradient. The use of a torsional mode, insensitive to acceleration but sensitive to the temperature gives a very accrutate temperature measurement (10^{-4} °C @ 1s expected). By the means of a "true" measurement of each beam temperature and gradient, an efficient thermal compensation is thus expected, allowing a simpler and cheaper packaging. Indeed, the differential effect in a VBA is even more effective than the two beams see exactly the same temperature and temperature gradient, which is very demanding for the packaging. With a "true" temperature measurement of each beam, it is now possible to compense directly the effect of temperature on each beam, thus simplifying the packaging.

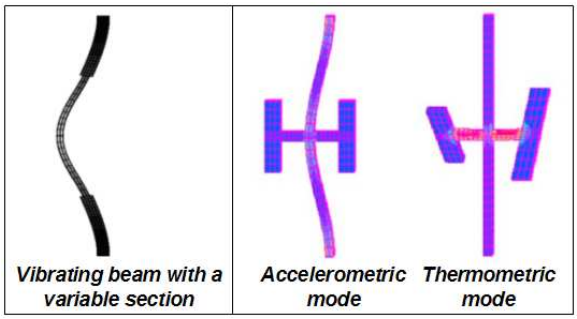

Figure 7. Optimized vibrating beam (left). Dual mode vibrating beam(right)

III. QUARTZ CORIOLIS VIBRATING GYRO

In the 2000's, taken advantage of experience gained in monolithic quartz resonator, study on Coriolis Vibrating Gyro (CVG) has been engaged. The VIG structure has been proposed [9], based on a tuning fork as sensitive element and an insulating system (our trademark) composed of massive parts and flexible arms connected to the mounting areas (fig. 8).

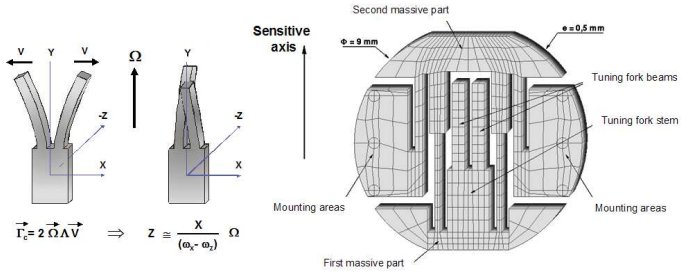

Figure 8. VIG CVG concept

Thanks to this monolithic structure, high quality factors, in the order of 150 000, are obtained for the driving (tuning fork mode) and the sensing mode (out of plane mode), showing the quality of the vibrating structure. The driving and the sensing modes frequencies were at this time around 30 kHz.

The VIG gyro takes advantage of the quartz piezoelectricity since the excitation of the driving mode and the detection of the sensing mode are realized by dedicated electrodes. The manufacturing process is closed to the one developed for VIA & DIVA accelerometers, with only one step of chemical etching, but without a third dimension defined by the etched depth (all the grooves are etched on the total wafer thickness). In addition, the chromium-gold mask used for the chemical etching very easily provides the excitation electrodes of the driving mode and the detection electrodes of the sensing mode (fig. 9).

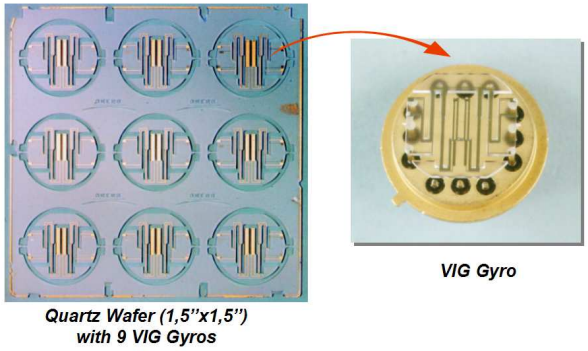

Figure 9. Quartz wafer including 9VIGs obtained by chemical etching

First VIG prototypes highlighted two major problems limiting the performance of the gyro: the quadrature coupling, due to mechanical coupling between the sensing and driving modes, and the phase coupling due to capacitive coupling between the driving and sensing electrodes, inducing unwanted signals on the sensing electrodes (quadrature and phase signals mean respectively quadrature and phase with the Coriolis signal). Quadrature coupling can be cancelled by the demodulation stage, but high level of coupling requires a high stable phase control to be efficient.

Phase coupling gives directly an output bias and must be reduced or cancelled in order to avoid a saturation of the sensing electronics. In the first generation of VIG gyro, the phase coupling (bias) was around 10,000 °/s, which could be reduce by passive compensation, but of course at the expense of stability (long term and versus temperature).

The mechanical coupling (fig. 10) is mainly due to the oblique facets generated during the chemical etching of quartz and located at the built-in ends of the tuning fork. This mechanical coupling has been divided by a factor 100 thanks to a change in the geometry of the built-in ends of the beams [17] but is always today very important: for a difference frequency of 500 Hz between the driving and the sensing modes, the quadrature coupling is around 10 000 °/s, required a phase control of 10^{-7} rd to remove by synchronous demodulation the mechanical coupling for a few °/h stability.

Highly stable CGV requires of course a drastic reduction of phase and quadrature couplings.

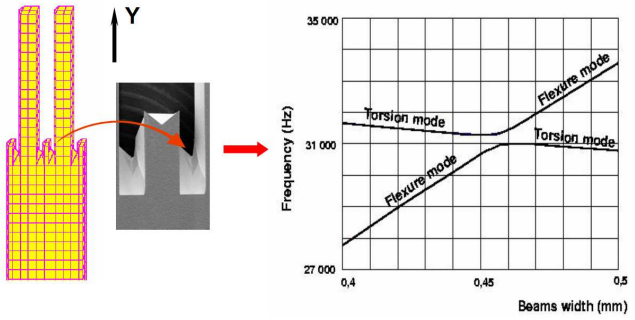

Figure 10. Mechanical coupling between the driving and sensing modes

The phase coupling due to the capacitive coupling between the sensing and the driving electrodes has been cancelled thanks to an original electrode scheme [23] allowig a double step of insulting, first obtained by a symmetrical excitation voltage (±V driving voltage) and, above all, by the virtual ground plane given by detection electrodes of the driving mode connected to a charge amplifier (fig. 11).

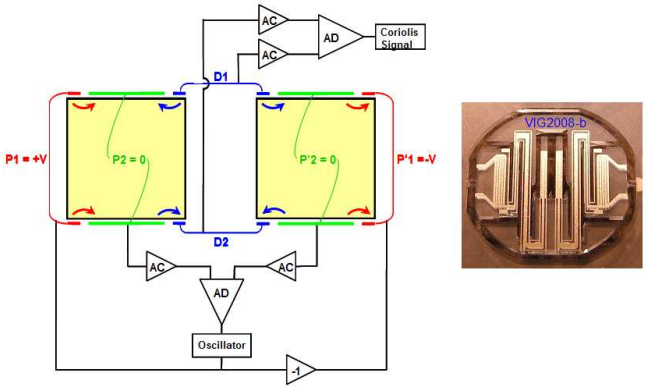

Figure 11. Electrode scheme for the driving and sensing modes

Concerning the quadrature coupling, the choice was made to avoid individual trimming at the quartz structure level. So electronic compensation with accurate synchronous demodulation stage have been developed.

A first step was obtained [22], based on passive charge injection to compensate for the quadrature coupling, and an accurate phase control at 1. 10^{-3} rd, given a stability of 100 °/h RMS including thermal cycles.

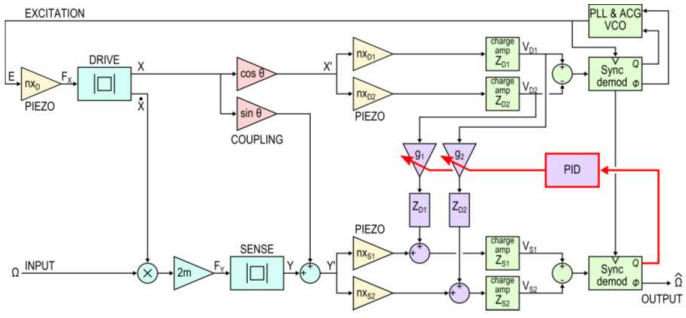

Figure 12. VIG electronic architecture including an active re-injection of quadrature coupling.

In a second step, a closed-loop compensation of the quadrature coupling has been implemented (fig. 12). 20 °/h RMS stability has been obtained [24], and the minimum of the Allan variance, shown on Fig. 13 (VIG 2010; green curve), is 1.3°/h and the angular random walk (ARW) is 0.2 °/√h.

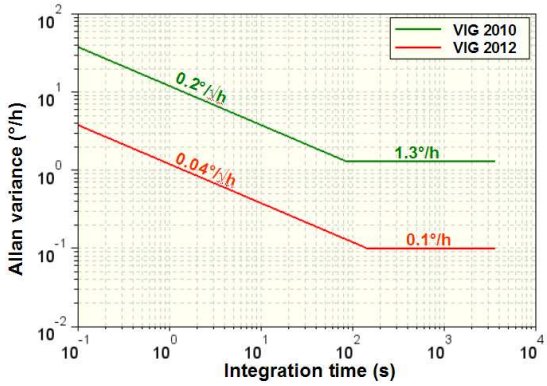

Figure 13. Mechanical coupling between the driving and sensing modes

Recent improvements, both on the quartz structure and on a new digital electronic architecture allowing a phase control at 3.10^{-4} rd, give excellent results: a minimum of the Allan variance of 0.1 °/h has been obtained as well as an ARW of 0.2 °/√h (fig. 13, VIG 2012; red curve). A bias stability of a few °/h is expected and long term evaluations are underway.

These recent results place the piezoelectric VIG gyro at a better level of present MEMS gyro, at this time made in silicon [25]. Nevertheless, in contrast to current accurate closed-loop silicon MEMS gyro, the VIG is based on an open loop scheme and is far from its ultimate performance. This open loop choice is due to the high mechanical coupling which prohibits closed-loop operation. It is the reason why a new configuration of quartz gyro have been studied [26] in order to nominally cancel the mechanical coupling, in spite of chemical etching facets. Taken into account the quartz crystal symetry, a new orientation and a new design based on a torsional mode as driving mode and a tuning fork like sensing mode, is proposed (fig. 14), called VIGTor.

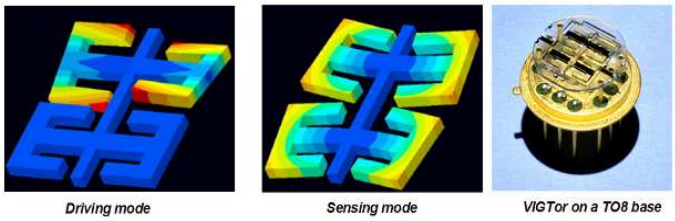

Figure 14. VIGTor Gyro. Mechanical coupling between the driving and sensing modes

First experimental evaluations of the VIGTor show an excellent behavior of the vibrating structure with quality factors higher than 250 000 for the two modes (@ ~30 kHz). A huge reduction of the mechanical coupling between the two modes has also been observed, confirming the theoritical prediction. An even more stable gyro, and above all, a closed-loop configuration can be quietly envisaged. The VIGTor

should allow an improvement by one or two order of magnitude the present 2012 VIG performance, opening the way of an inertial class gyro at the MEMS scale.

IV. RESONTOR FOR FUNDAMENTAL PHYSICS

Recently, a dedicated resonator for the observation of its quantum ground state has been studied [27]. A high frequency, small mass and high quality factor resonator is sought [28], implemented in a high-finesse Fabry-Perot cavity, taken advantage of the unique sensitivity of optical interferometer (state of the art: 10^{-38} m^2/Hz).

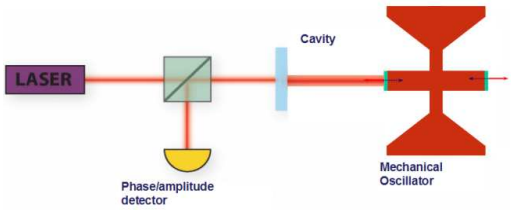

Figure 15. Quantum ground state experiment: a resonator in a Fabry-Perot cavity for the dection of its fundamental fluctuations

A length extension mode was chosen because of its perfect implementation in a Fabry-Perot cavity (fig. 15) - the length cavity is directly linked to the resonator fluctuations - but also because of the highly reflective mirror deposited on the resonator has a quasi null strain, leading to a high quality factor.

The choice of quartz crystal has been done to benefit from its high intrinsic quality factor, as it is well known in time and frequency applications, such as for ultra-stable oscillators.

The basic resonator structure consists in a micro-pillar maintained at its center by a thin membrane. In order to compensate the huge Poisson effect, an original concept has been proposed [29], based on a complementary ring around the pillar and an external membrane for the clamping of the resonator (fig. 16).

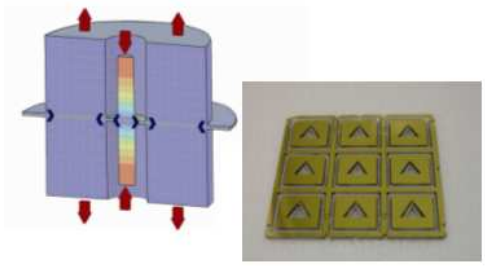

Figure 16. Quartz high Q length extension resonator obtained by collective chemical etching. F =3.87 MHz, Q= 1.9510^6, M=25 µg

A detailed description of the resonator is given in [30]. Very interesting preliminary measurements have been obtained on a 3.9 MHz, 25 µg resonator, given a 1.95 million quality factor, at room temperature and under a 5 10^{-2} mbar vacuum: This resonator reached the first step to the observation of its quantum ground state. Next steps will be the coating of a highly reflective mirror on the top of the resonator, and its implementation in the Fabry-Perot cavity at cryogenic temperatures.

Nevertheless, by its planar configuration compatible with collective etching process, this resonator should also find interesting opportunities in the time and frequency domain, in particular for new generation of miniature ultrastable oscillator (USO). Work has been undertaken in this way, looking for a temperature compensated cut and an efficient piezoelectric excitation/detection of the vibration. Manufacturing process is also under consideration, including manufacturing process by Deep Reactive Ion Etching now available at Onera, and under vacuum wafer level packaging.

V. CONCLUSION

ONERA has been a pioneer in Quartz MEMS Vibrating Beam Accelerometer and is today widely engaged for the development of accurate inertial quartz MEMS (CVG, VBA) and quartz IMU.

We are deeply convinced that quartz, combined with innovative concepts including electronic architecture and suited technologies, will be able to fulfill high added value applications as inertial navigation. We are working towards that goal.

Concerning oscillators & RF market which represent today 17 billions € market with a 10 % growth per year, quartz hold 80 % of the market, and continuous innovation in the field of quartz technologies [31][32], allowing miniaturization at equal performance, will be able to conserve the quartz advantage for a long time.

New quartz technologies are also under development for high added value applications like Ultra Stable Oscillator (USO) [33]. Quartz Deep Reactive Ion Etching [34][35][36], under vacuum wafer level packaging, 4" quartz wafers, 3D integration are some quartz key technologies that should be developed in near future.

Quartz crystal has been an essential material for time and frequency and radio-frequency applications during the 20th century. Quartz is always an unmatched material at the beginning of the 21st century, and clearly has still a future, at least for vibrating inertial MEMS, and for a long time.

REFERENCES

[1] M. Hetzel, “Electric Timepiece”, US patent n° 2,929,196, issued Mars 22 1960.

[2] J. S. Staudte “Microresonator of Tuning Fork Configuration”, US patent n° 3,683,213 filed March 9 1971.

[3] J. Lyman & Al. “Rate and Attitude Indicating Instrument”, US patent n° 2,309,853 filed April 10, 1943

[4] J.S. Staudte & Al. “Vibratory Angular Rate Sensor System”, US patent n° 4,524,619 filed Jan. 23, 1984

[5] R. Jaffe & Al. “Advances in Ruggedized Quartz MEMS Inertial Measurement Units”, IEEE PLANS 2006.

[6] H. C. Hayes, “Method and Apparatus for Determining the Force of Gravity”, US patent n° 1,995,305 filed oct. 1928

[7] G. Mamon, “A Traverse Gravimeter for the Lunar Surface”, IEEE Transactions on Geoscience Electronics, Vol.. GE-10, n° 1, January 1972.

[8] O. Le Traon, D. Janiaud, S. Muller “Monolithic Accelerometric Transducer” US patent 5,962,786, Priority Data, Sep. 26 1995.

[9] D. Janiaud, O. Le Traon, B. Le Corre, S. Muller “Monolithic vibrating rate gyro structure” US patent 6,414,416 Filed Jul 26, 2001

[10] O. Le Traon & al. “The DIVA Accelerometer and VIG Gyro: Two Quartz Inertial MEMS for Guidance and Navigation Applications” IEEE NTM Institute Of Navigation (ION), Jan 22, 2007

[11] O. Le Traon & al. “The VIA Vibrating Beam Accelerometer: Concept and Performances”, Proceedings of the Position, Location and Navigation Symposium, Palm springs, April 1998.

[12] O. Le Traon & al. “The VIA vibrating beam accelerometer: a new quartz micromachined sensor”, Proceedings of the European Frequency and Time Forum and the IEEE International Frequency Control Symposium, April 1999.

[13] C. Zener, “Internal friction in solids”, Physical review 52, (August, 1937), 230-235.

[14] S. Lepage, O. Le Traon, JC Golinval, I. Klapka, S. Masson, “Thermoelastic Damping in Vibrating Beam Accelerometer: A new thermoelastic finite element approach”, CANEUS 2006, Toulouse, August 27 - September 1.

[15] P. Bouniol; D. Janiaud, O. Le Traon, S. Muller “Performance evaluation of the VIA accelerometer” Proceedings of ION National Technical Meeting, january 1998.

[16] O. Le Traon, M. Pernice, D. Janiaud, B. Lecorre, S. Muller “Mechanical decoupling device for monolithic differential vibrating sensor” US patent n° 7448268 - Filed Apr 21, 2005

[17] O. Le Traon, D. Janaiud, B. Lecorre, M. Pernice, S. Muller, J-Y Tridera, “Monolithic Differential Vibrating Beam Accelerometer within an Isolating System between the two Resonators” IEEE Sensors Conference, Irvine, October 2005.

[18] O. Le Traon, D. Janiaud, M. Pernice, S. Masson, S. Muller, J-T. Tridera “A New Quartz Monolithic Differential Vibrating Beam Accelerometer”, Proceedings of the Position, Location and Navigation Symposium, San Diego, april 2006.

[19] O. Le Traon, D. Janiaud, B. Lecorre, S. Muller “Force transducer having a central portion of reduced thickness” US patent n° 6807872 – filed Aug 14, 2002.

[20] O. Le Traon, C. Chartier, V. Gaudineau, J. Guérard, D. Janiaud, R. Levy “Dispositif de mesure de la température d’une poutre vibrante et application à l’amélioration de la précision de mesure d’un capteur à poutre vibrante” French patent n° FR 1100196, filed Jan 24, 2011.

[21] D. Janiaud, O. Le Traon, B. Lecorre, R. Levy, S. Muller, M. Pernice “The VIG vibrating gyrometer : a new quartz micromachined sensor” Symposium Gyro Technology 2004, Stuttgart, Germany.

[22] J. Guérard, M. Descharles, D. Janiaud, O. Le Traon , “Digital/Analog Electronic Architecture for Coriolis Vibrating Gyro” Proceedings of the Gyro Technology Symposium, Karlsruhe, septembre 2009

[23] O. Le Traon, S. Masson, J. Guérard, R. Levy, C. Chartier, D. Janiaud “Electrodes and associated electronic circuits for a piezoelectric vibrating gyroscope”, PCT Patent 2010/000854, filed Dec. 20, 2010

[24] M. Descharles, J. Guérard, H. Kokabi, O. Le Traon “Closed-loop compensation of the cross-coupling error in a quartz Coriolis Vibrating Gyro”, Sensors & Actuators: A. Physical, to be published

[25] B. Chaumet, B. Leverrier, C. Rougeot, S. Bouyat, “A New Silicon Tuning Fork Gyroscope for Aerospace Applications”, Proceedings of the Gyro Technology Symposium, Karlsruhe, septembre 2009.

[26] D. Janiaud, O. Le Traon, C. Chartier, S. Masson, J. Guérard, R. Levy, “Element vibrating in two uncoupled modes, and use in vibrating rate gyroscope” - PCT Patent 2010/112594 filed Apr. 1, 2010

[27] M. Bahriz, O. Ducloux, S. Masson ,D. Janiaud, O. Le Traon , A. Kuhn, C. Molinelli, T. Briant, P-F Cohadon, A. Heidmann, C. Michel, L. Pinard, R. Flaminio “A micromechanical resonator to reach the quantum regime”, IEEE Sensors Conference, Waikoloa, Nov. 2010.

[28] A Kuhn, M. Bahriz, O. Ducloux, C. Chartier, O. Le Traon, T. Briant, A. Heidmann, C. Michel, L. Pinard, R. Flaminio “A micropillar for cavity optomechanics” Applied Physics Letters 99, 121103 (2011)

[29] M. Bahriz, O. Le Traon “Module for the mechanical uncoupling of a resonator having a high quality factor” Patent n° FR2011/000389 filed July 04, 2011

[30] O. Le Traon, M. Bahriz, O. Ducloux, S. Masson ,D. Janiaud, A. Kuhn, T. Briant, P-F Cohadon, A. Heidmann, C. Michel, L. Pinard, R. Flaminio “A Micro-Resonator for Fundamental Physics Experiments and its Possible Interest for Time and Frequency Applications”, Frequency Control and the European Frequency and Time Forum, San Francisco, May 2011

[31] S. Lam “A review of the recent development of MEMS and crystal oscillators and their impacts on the frequency control products industry”, IEEE Ultrasonics Symposium, 2008

[32] M. Takana “An Overview of Quartz MEMS Devices” IEEE IFCS june 2010

[33] J-J. Boy & Al. “Collective Fabrication of 20 MHz Resonators by DRIE on 3” Quartz Wafers”, IFCS-EFTF 2011

[34] David T. Chang & Al. "Optimized DRIE Etching of Ultra-Small Quartz Resonators" Frequency Control Symposium and PDA Exhibition Jointly with the 17th European Frequency and Time Forum, 2003

[35] Hyoung-Kyoon Jung & Al. “Silicon/quartz bonding and quartz deep RIE for the fabrication of quartz resonator structures” 3rd IEEE International Conference on NEMS, Jan. 2008

[36] T. Abe & Al. “Dry etching method using double-layered etching mask for modulating shape of deep-etched quartz surface” Transducers, June 2011

New Electrostatically–Excited Single Crystal Silicon Resonator vibrating in a Thickness–Extensional Mode

Mihaela Ivan, Bernard Dulmet, Gilles Martin and Sylvain Ballandras
Time and Frequency Dpt., FEMTO-ST Institute, Besançon France
Email: bernard.dulmet@ens2m.fr

***Abstract*— This paper presents a new patent-pending structure of BAW resonator built on standard silicon wafer and driven by electrostatic force. Thickness-Extensional (TE) modes are exploited, yielding a fundamental frequency near 10 MHz with a 400μm-thick Si wafer. The device is based on a one-port design featuring a 1μm gap submitted to a superimposition of a DC voltage bias and a lesser–amplitude AC excitation. In contrast with conventional bar and plate MEMS resonators relying on structural resonances, our resonators are designed to use an energy–trapping of the TE waves to optimize the Q factor.**

The structure essentially consists of a single (100) Silicon plate, p-doped and bonded onto a Corning glass substrate by standard anodic bonding. The thin gap required for the electrostatic excitation is machined in the glass layer by Reactive Ion Etching. Extensive electrical and mechanical characterisations were performed. They match rather well the behavior predicted by the theoretical analysis. A compensation of the large static capacitance is needed to give a better access to the motional parameters. Q factors near 9000 have been observed on the fundamental TE-mode, with a sufficient coupling for frequency source applications. The stabilization of a RF oscillator using the resonators is still under development.

I. Introduction

Here–presented research is part of a project lead by the CoSyMA (Components and Systems for Micro-ACoustics) group to develop oscillators relying on Single Crystal Silicon (SCS) resonators built using a rather standard MEMS technology, while taking advantge of acoustics concepts largely proven in the field of high-performance BAW/SAW piezoelectric resonators. The target of the research in the middle term is to provide MEMS oscillators exhibiting a good short term stability at low production cost. The association of MEMS technology with a resonator design favouring high-Q actually relies on a combination of electrostatic excitation with the concept of energy–trapping of quasi-plane waves, in order to minimize the losses in and outside the structure. This combination is currently investigated for the two following reasons:

- electrostatic coupling makes possible to using pure monocrystalline silicon while virtually eliminating the need for layers of other material, at the difference of composite structures with grown, deposited or assembled thin piezoelectric layers [1], [2].
- by using the stop band properties granted by theory of guided wave propagation in thin plates [3] one can localize the vibration [4], [5] to get good Q-factors in a more efficient manner than by using a technique of fine tuning the structure suspension which is required and more largely used in most resonant MEMS literature-centered on structural resonances rather than quasi–plane waves resonances [6], [7].

In particular, we want to promote a concept of reduced dimensionality in MEMS resonators, since the frequency of a localized vibration depends on a minimal number of dimensions, *e.g.* essentially the tickness of plate in here–presented work. Conversely, structural resonances such as flexure or contour modes used in most MEMS control the frequency through several dimensions, and generate more acoustic losses towards the clamping structures with a much higher dependence with respect to the tolerances of a dedicated suspension scheme.

Although its versatile technology [6] provides a strong leverage on the development of MEMS resonators research, it is a fact that silicon is not the best material to deliver superior acoustic performances. For this reason, here–presented resonators are designed on the so–called "Full-Wafer technology", which consists in transferring most machinings onto the drive–electrode supporting layer instead of the silicon wafer itself. Two advantages are expected from this approach:

- by minimizing the amount of micro-machining steps on the substrate itself, it will facilitate future developments based on other types of resonant substrates,
- simplicity of machining and minimization of the treatments performed on the resonant substrate are essential requirements for further co–integration of regular MOS technology with the acoustic resonator.

II. Electrostatic driving of TE- modes

A few earlier works on MEMS resonators used longitudinal waves in bars or rectangular plates [8], [9], [10]. Nevertheless, we had to build the specific model for thickness–extensional modes driven by electrostatic force. In order to reduce the risk of failure arising from too many process stages and to leave a free access to a vibrating surface for optical measurements of the out–of–plane displacement, single–side excitation was clearly a more reasonable choice than double–side one. In addition, we chose p–type doped highly–conductive wafers to simplify the application of the driving voltage to the required thin enclosed gap. Then, according to the conventions defined

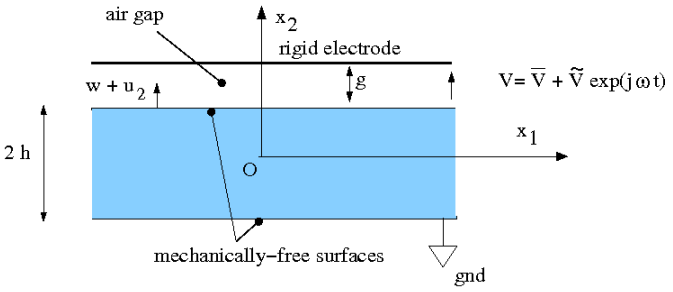

Fig. 1. single–side electrostatic excitation with perfectly-conductive substrate (doped silicon)

by Fig. 1, single–side driving leads to the following set of asymmetric boundary conditions after linearization of the net electrostatic surface–force around the DC polarisation point:

$$\tilde{T}_2(+h) = f_e, \quad c_{22}\tilde{u}_{2,2}(+h) \approx \frac{\varepsilon_0 \bar{V}\tilde{V}\cos\omega t}{(g-\bar{w}(r))^2} + \frac{\varepsilon_0 {V_0}^2 \tilde{u}_2(h,t)}{(g-\bar{w}(r))^3}$$
$$\tilde{T}_2(-h) = 0, \quad c_{22}\tilde{u}_{2,2}(-h) = 0. \tag{1}$$

where f_e is the electrostatic surface–force, $2h$ denotes the thickness of the plate and we introduce the notation

$${V_0}^2 = \bar{V}^2 + \frac{\tilde{V}^2}{2}$$

to lighten the expressions. Beside standard notations for stress, elastic constants and permittivity, we use g for the initially undeformed gap, $\bar{w}$ for the static out–of–plane displacement arising from the polarisation voltage $\bar{V}$, and $\tilde{u}_2$ stands for the thickness–extensional dynamic displacement.

A single–side excitation with circular electrode on top of (001) Si substrate generates an axisymmetric distribution of electrostatic force, and our gap cavity is circular, so that the static deflection is axisymmetric, r denoting the distance from the axis of symmetry to the local point. Due to energy–trapping, we can simplify the analysis by retaining the value of the static displacement on that symmetry axis, $r = 0$. The cornerstone of the model is a variable change:

$$\tilde{u}_2(x_2) = \hat{u}_2(x_2) + K{x_2}^2 + 2Khx_2,$$

where K is a constant whose value is determined in terms of V_0, $\bar{w}$, ε_0, g, h, c_{22}, so that the system of non homogenous boundary conditions and the one–dimensionnal homogenous partial derivative equation of elasticity

$$c_{22}\frac{\partial^2 \tilde{u}_2}{\partial x^2} + \rho\omega^2\tilde{u}_2 = 0$$

is turned into a more tractable system of homogeneous boundary conditions and non homogeneous PDE:

$$c_{22}\hat{u}_{2,2}(+h) - \frac{\varepsilon_0 {V_0}^2}{{g_1}^3}\hat{u}_2(+h) = 0, \qquad \hat{u}_{2,2}(-h) = 0$$
$$c_{22}\frac{\partial \hat{u}_{2,22}}{\partial x^2} + \rho\omega^2\hat{u}_2 = -(2c_{22} + \rho\omega^2{x_2}^2 + 2\rho\omega^2 h x_2)K \tag{2}$$

This new system gives an easy access to the mechanical response of the resonator as a sum of orthogonal solutions of the free homogeneous system obtained without the right–hand member of the PDE:

$$\hat{u}_2 = \sum_n H_n \hat{u}_2^n \text{ with } \begin{cases} c_{22}\hat{u}^n_{2,2}(h) - \frac{\varepsilon_0 {V_0}^2}{{g_1}^3}\hat{u}^n_2(h) = 0 \\ \hat{u}^n_{2,2}(-h) = 0 \\ c_{22}\frac{\partial \hat{u}^n_{2,22}}{\partial x^2} + \rho{\omega_n}^2\hat{u}^n_2 = 0. \end{cases}$$

The free–standing solutions $\hat{u}_2^n$ should take the form:

$$\hat{u}_2^n = A\sin\eta_n x_2 + B\cos\eta_n x_2, \quad \text{with } \eta_n = \omega_n\sqrt{\frac{\rho}{c_{22}}},$$

which leads to an approximate expression of the eigenfrequencies as roots of the determinant of the boundary conditions system:

$$\omega_n \approx \frac{n\pi}{2h}\left(1 - \frac{2\varepsilon_0 h {V_0}^2}{n^2\pi^2 c_{22}{g_1}^3}\right)\sqrt{\frac{c_{22}}{\rho}}, \tag{3}$$

where $g_1 = g - \bar{w}$ and n is simply the overtone number, restricted to 1 in the present paper. This formula shows that the resonant frequency depends on the polarization. It is the electrostatic–excitation equivalent of the well–known formula for the eigenfrequency of a thickness-shear quartz resonator, for instance:

$$\omega_n \approx \frac{n\pi}{2h}\left(1 - \frac{4{k_{26}}^2}{n^2\pi^2 c_{66}}\right)\sqrt{\frac{\bar{c}_{66}}{\rho}}. \tag{4}$$

Comparing above formulas, one immediately obtains the coupling factor of the TE–mode resonator with single–sided electrostatic excitation:

$$k^2 \approx \frac{\varepsilon_0 h {V_0}^2}{2{g_1}^3 c_{22}}. \tag{5}$$

In the case of double–sided symmetric excitation, the factor 2 disappears from the denominator, but, conversely, the statically–deformed gap is larger since symmetric traction conditions cancel out any static bending of the plate.

A. Frequency tunability

Frequency tuning is a major issue of acoustic resonators for oscillator applications [11], [12], especially for MEMS structures built on substrates without turn–over point of the frequency–temperature characteristic, since it can be used for an automatic temperature–compensation by adjustment of the polarisation. Eq. 3 predicts a polarization–induced relative frequency shift equal to $-4k^2$, but this shift is actually limited by either the polarisation–induced pull-in effect or the breakdown electric field, whatever comes first. Let us denote by E_t the practical limiting value of electric field in the cavity. Whatever is the stiffness of plate, the pull–in effect will preclude g_1 to be lower than $2g/3$, so that the limit value of the relative frequency shift of TE–fundamental mode is

$$\frac{\delta\omega_n}{\omega_n} = \frac{\omega_n(V_0^{max}) - \omega_n(0)}{\omega_n(0)} \approx -\frac{3\varepsilon_0}{\pi^2 c_{22}}\frac{h}{g}{E_t}^2. \tag{6}$$

Assuming a practical treshold field near $100\,MV/m$, the largest relative frequency shift arising from the polarisation of here–presented TE MEMS resonators operating near 10.3MHz is $\delta\omega_n/\omega_n \approx -40ppm$. Thus, although the so–called "electrostatic spring softening" well–known in flexural mode MEMS still exists in TE–modes resonators, it stays rather limited since the dynamic stiffness of the structure is only slightly reduced at static pull–in treshold. This feature precludes the use of electrostatic spring softening to compensate the temperature drift of TE-MEMS, but may be an advantage for their use in higher stability frequency–sources since the relative frequency unstability arising from a jitter of the DC polarization will be several order of magnitude lower than in flexural MEMS.

B. Calculation of motional capacitance

The calculation of the motional capacitance of here–studied TE–mode single–side driven resonator is quite straightforward. Aster substituting the above–mentionned series into the PDE with restored second member, one easily obtain the coefficients H_n with help of the orthogonality of the free solutions:

$$H_n = \frac{K\displaystyle\int_{-h}^{+h}(2c_{22}+\rho\omega^2{x_2}^2+2\rho\omega^2 h x_2)u_2^n(x_2)dx_2}{\rho\left({\omega_n}^2-\omega^2\right)\displaystyle\int_{-h}^{+h}\left[\hat{u}_2^n(x_2)\right]^2 dx_2}$$

which leads to the closed–from expression

$$H_n \approx (-1)^{\frac{n-1}{2}}\frac{16h}{n^2\pi^2}\frac{\varepsilon_0\bar{V}\tilde{V}}{{g_1}^2\left(4c_{22}-3\dfrac{\varepsilon_0{V_0}^2h}{{g_1}^3}\right)}\frac{\omega^2}{{\omega_n}^2-\omega^2}$$

This procedure is altogether similar to the standard procedure encountered in the analysis of BAW piezoelectric resonators [4], [5] and provides with a complete determination of the mechanical response. The electrical response is derived next by applying Gauss theorem on the driven surface of the wafer:

$$\sigma = \varepsilon_0 E_2 \quad \Rightarrow \quad I = \varepsilon_0\int_S \frac{\partial}{\partial t}\left(\frac{V(t)}{g_1(V_0)-\tilde{u}_2(h,t)}\right)dS$$

where σ is the charge density, E_2 the normal electrical field in the gap cavity and I the current. The harmonic admittance is obtained by linearization of the integrand with respect to the small dynamic displacement and substitution of the series. It takes the following form :

$$Y(\omega) = \frac{j\omega C_0 8k^2}{n^2\pi^2}\sum_n\frac{\omega^2}{{\omega_n}^2-\omega^2} \tag{7}$$

where C_0 is the static (parallel) capacitance of the air–gap:

$$C_0 \approx \frac{\varepsilon_0 S_e}{g_1},$$

and S_e is the area of the driving electrode. Eventually, a bare identification of the admittance with the classical equivalent circuit encountered in BAW piezoelectric resonators provides with the value of the motional (series) capacitance:

$$C_1^s = \frac{8k^2}{n^2\pi^2}C_0 \tag{8}$$

Similar calculations performed for double–side excitation permit a comparison between the predicted motional capacitances in both cases:

$$\frac{C_1^s}{C_1^d} = \frac{{g_2}^2\left[c_{22}-\frac{\varepsilon_0{V_0}^2}{{g_2}^3}h\right]}{2{g_1}^2\left[c_{22}-\frac{3\varepsilon_0{V_0}^2h}{4{g_1}^3}\right]} \tag{9}$$

where g_2 is the actual value of the gap when the same polarization voltage is symmetrically applied on both sides of the resonator.

The value of the motional capacitance C_1 can be very significant even with modest values of k^2, due to the large value of C_0 (a few hundred of pF, depending on tolerances and on the bending effect of single–side polarisation voltage). Thus the devices can be used for frequency sources applications at the expense of compensating the large current flowing through C_0 that shadows the series resonance of the motional current.

III. Energy–trapping issues

The procedure of deriving the dispersion curves for guided waves in acoustics problems is well–known [3]. It consists of finding the combinations of elementary guided solutions of the PDE equations, so–called partial waves, that satisfy the boundary conditions. In here–studied case, because u_3 is not coupled with u_1, u_2 within the two–dimensionnal elasticity equations for waves propagating in the (x_1Ox_2) cross–section of a cubic plate, the equations take the following form:

$$\begin{aligned} c_{11}u_{1,11}+(c_{12}+c_{44})\,u_{2,12}+c_{44}u_{1,22} &= \rho\ddot{u}_1,\\ c_{44}u_{2,11}+(c_{12}+c_{44})\,u_{1,12}+c_{11}u_{2,22} &= \rho\ddot{u}_2. \end{aligned} \tag{10}$$

The associated mechanical boundary conditions for free standing modes without driving force are the following:

$$\begin{aligned} T_{21}(\pm h) &= c_{44}\,(u_{1,2}+u_{2,1})|_{\pm h} = 0\\ T_{22}(\pm h) &= c_{12}u_{1,1}+c_{11}u_{2,2}|_{\pm h} = 0. \end{aligned} \tag{11}$$

In this case, the determination of the dispersion curve is particularly easy, since only two partial waves should be combined to obey the boundary conditions on the free surfaces:

$$\begin{aligned} u_1 &= \left(\beta_1^1\cos\eta_1 x_2+\beta_1^2\cos\eta_2 x_2\right)\sin\xi x_1\\ u_2 &= \left(\beta_2^1\sin\eta_1 x_2+\beta_2^2\sin\eta_2 x_2\right)\cos\xi x_1 \end{aligned} \tag{12}$$

where the two vertical wavenumbers η_α and the vertical to horizontal amplitude ratios of each partial wave $\beta_2^\alpha/\beta_1^\alpha$ are separate solutions of the PDEs system, closed–form functions of ω and ξ. Then, the roots of the determinant of the boundary conditions give the dispersion curves of Fig. 2, drawn in terms of the dimensionless angular frequency Ω and lateral wavenumber γ defined as follows:

$$\omega = \Omega\sqrt{\frac{c_{44}}{\rho}}\frac{\pi}{2h} \quad \text{and} \quad \gamma = \frac{2h\xi}{\pi} \tag{13}$$

The angular frequency and lateral wavenumber of the guided waves are respectively normalized by the angular frequency and the vertical wave number of the pure–thickness shear, *i.e.* the slowest mode that can propagates vertically in the

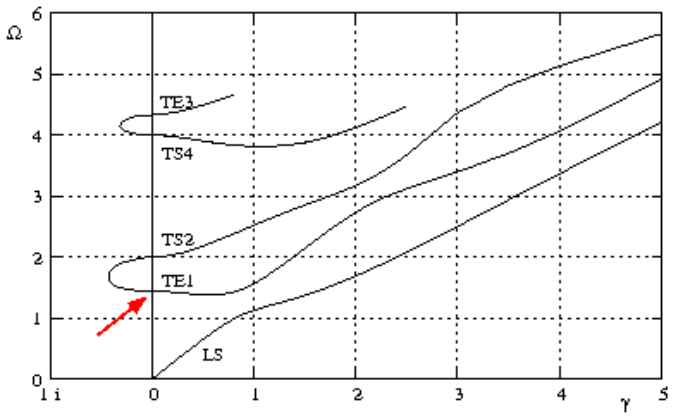

Fig. 2. dispersion curves for si (100) substrate. Left side of Ω axis : imaginary values of lateral wavenumber γ ; right side : real values of γ.

structure. Following Tiersten's well–known approach [4], [5] one easily derives the asymptotic expansion of the essentially thickness–extensional branches in the vicinity of Ω axis:

$$\Omega \simeq n\sqrt{\frac{c_{11}}{c_{44}}} + \frac{M_n}{2n\sqrt{c_{11}c_{44}}}\gamma^2, \qquad |\gamma| \ll 1,$$

$$M_n = c_{11} + \frac{(c_{12}+c_{44})^2}{c_{44}-c_{11}} - \frac{4c_{44}}{\kappa n\pi}\left(\frac{c_{12}+c_{11}}{c_{11}-c_{44}}\right)^2 \tan\frac{n\pi}{2\kappa}. \tag{14}$$

This asymptotic expansion holds when the small wavenumber γ is either imaginary or real. $M_n \simeq -98.2\ GPa$ for the TE–fundamental mode in (100) Si. Negative dispersion constants require inverse–mesa structure to confine the vibration through matching real wavenumbers in the central region with imaginary wavenumbers *i.e.* damped waves in the outer region [4]. Fig. 2 shows that the curvature of the dispersion TE-1 branch remains rather small in a large region near Ω axis, so that the efficiency of energy trapping will stay limited, unless the resonators are built with a very large aspect ratio, which puts severe requirements on the technical realization of the gap.

IV. Design and technology of TE–MEMS resonators

Various series of micro-machined Si resonators conforming to above–analyzed configuration were fabricated and tested with help of the MIMENTO technological center of FEMTO-ST institute. Essential features of the resonators are summarized below (See also Fig. 3):

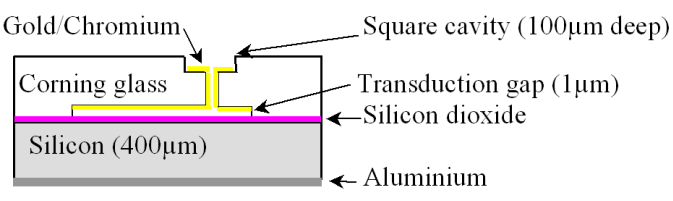

Fig. 3. $\phi_{cavity} = 10\,mm, \quad f_F \approx 10.3\ MHz.$

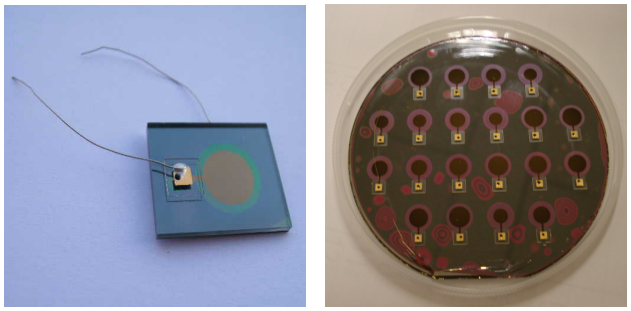

Fig. 4. A resonator sample and a wafer holding 20 resonators.

- The resonant layers consist of standard 4" highly–conductive p–doped Si wafers, $400\mu m$–thick and passivated with a thin PECVD-SiO2 film, a few hundreds of nm. Passivating the surface drastically reduced electric breakdowns during the tests, especially when the polarisation voltage exceeded 100 V_{DC}.
- The electrostatic gap, typically $1\mu m$ thick, was etched by RIE in a $1mm$–thick Corning glass wafer.
- The Si and glass wafers are assembled by anodic bonding under high voltage (900 V) and pressure near 350°C. Driving electrodes of various diameters have been tested. The electrode is deposited in the cavity and is electrically connected to the outer surface of the glass through a via realized by ultrasonic machinig. The connecting pad on the top surface is located in a recessed cavity to avoid the breakdown of the electrostatic gap upon applying the high voltage needed by the bonding process.
- Energy–trapping is controlled by patterning a thin aluminum layer deposited on the free surface of the Si wafer and used as ground electrode. The effective diameter of the resonators is taken as the diameter of the electrostatic air–gap cavity, namely 10 mm.

Figs. 4 show a resonator sample and a processed wafer holding 20 components before dying with a micro–saw. Fig. 5 shows a cross–cut of a sample. The trash on the close-up was actually made by the micro–saw. The technology has been validated for electrostatic gaps close $1\mu m$ or less, over surfaces of $75mm^2$, much larger than frequently–encountered sacrificial gaps made from the buried oxyde layer of SOI wafers, although the latter ones would allow for smaller gaps.

V. Compensation of parallel capacitance

Two kinds of compensations [13] of C_0 have been investigated: a basic compensation by LC_0 parallel resonance circuit, and a more elaborate compensation with help of a middle–point transformer circuit (*cf.* Fig. 6). In the first case, the compensation requires a precise tuning of the self L at the antiresonance condition $LC_0{\omega_n}^2 = 1$, while the capacitance C on Fig. 6–a avoids the short–cut of the polarization voltage by the DC conductivity of self. The second compensation technique (Fig. 6-b) cancels out the current flowing through

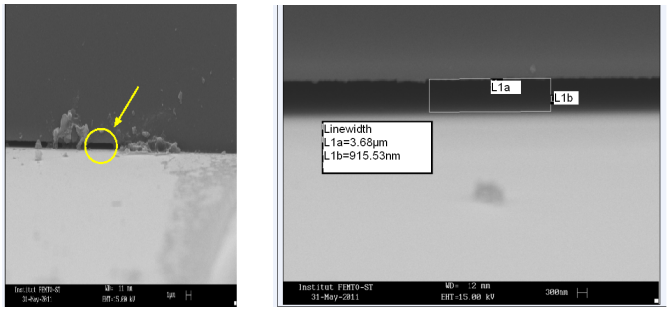

Fig. 5. SEM images of the small internal gap. Cross-section cut view..

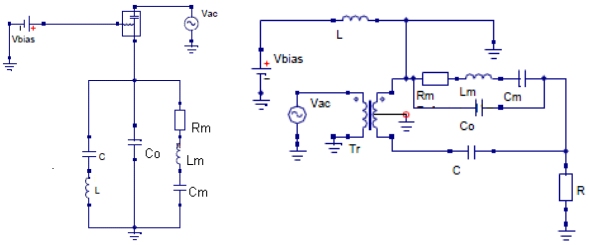

Fig. 6. compensations : a) LC parallel circuit ; b) middle–point transformer

C_0 by a current with same amplitude but opposite phase flowing through a tuned parallel capacitance $C \approx C_0$. The compensation circuit stays tuned when ω_n varies, as far as C_0 stays constant. This scheme is efficient for passive measurements of the devices with help of a network analyzer.

VI. Characterization of Samples

The mechanical response of the produced devices has been analyzed with help of a BMI heterodyne optical gauge. The plots of Fig. 7) show that both the maximum displacement and the mechanical Q–factor increase with the polarisation voltage.

The electrical response was measured both with and without compensation of the parallel capacitance. The compensation permits to overcome the large bias courant in C_0 and get precise measurements of the motional parameters. Fig. 8–b) shows spurious peaks of admittance located below the main resonance. Obtained with compensation, these measurements validate the negative value of the dispersion constant M_n.

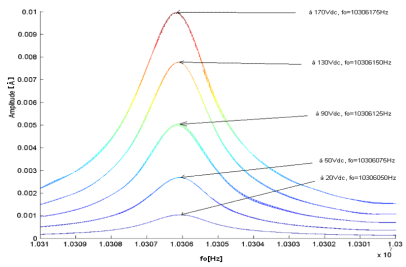

Fig. 7. Acoustic response measured with BMI heterodyne gauge

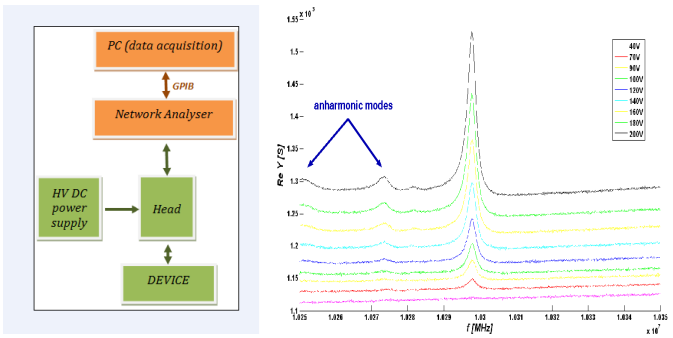

Fig. 8. Electrical setup and evidence of negative dispersion constant

Fig. 8–b) also shows a strong dependence of the measured Q–factor *vs.* the polarization voltage. The observed increase of bias current with $\bar{V}$ clearly shows that the compensation is not total on the investigated sample. The measurement plot of the static capacitance *vs.* $\bar{V}$ produced on Fig. 9–a) indicates that the gap is significantly reduced at higher values of the polarisation voltage. We have setup a model of the characteristic $\bar{w}(r, \bar{V})$ with help of a Green's function analysis of a flexural axisymmetric clamped cicular disc submitted to the electrostatic force arising from a rigid driving electrode under constant potential. This analysis will be published in details shortly after the present conference. The measurement plot of k^2 on Fig. 9–b) indicates a rather linear behavior in terms of the polarization voltage instead of the parabolic behavior predicted by Eq. 5. A more refined stress analysis of the effects of the polarization voltage will be necessary to further address the limits of the various modelling stages developped for here–presented devices.

A significant number of 20–samples wafers were processed, so that the fair amount of experimental data were not yet entirely analyzed at the time of conference. Q–factors close to 10,000 have been obtained at 10.3 MHz, while the compensation techniques were found mandatory for an accurate characterization of the devices. Nevertheless, a specific difficulty appeared on the set of Nyquist admittance plots of Figs. 10.

The typical plots on the left side of the Fig. are experimental plots of DUT without (top) and with (bottom) compensation of the parallel capacitance, while the plots on the right side are simulated after extraction of the motional parameters with

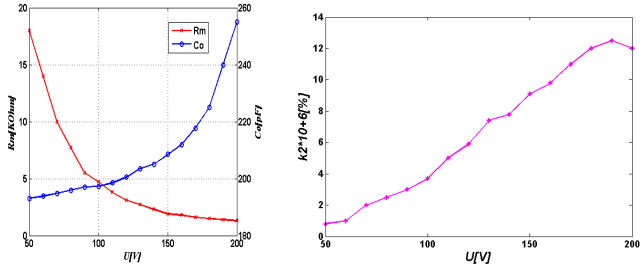

Fig. 9. Typical sensitivity of parameters *vs.* polarisation voltage

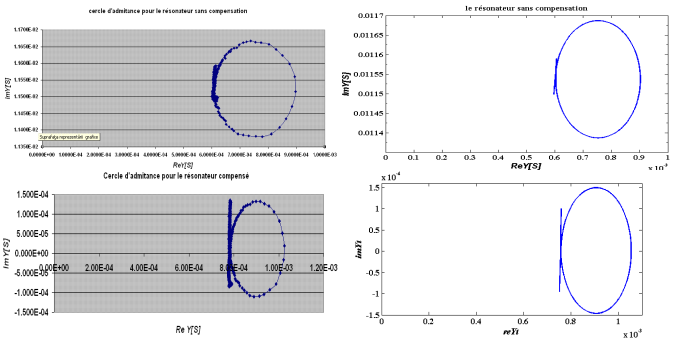

Fig. 10. Identification of compensated and uncompensated admittance plots through matlab program: left = measurement ; right = identification.

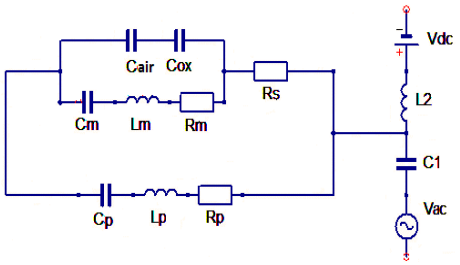

Fig. 11. Improved equivalent circuit with series resistance of the via R_s.

help of a simple Matlab program. These plots show that the compensation move down the admittance circle as expected. Nevertheless, the admittance circles are shifted toward the right of the real axis, indicating the existence of a conductance close to $0.8mS$, in parallel to the series/parallel equivalent circuit. Since no shortcut was observed or physically explainable upon close inspection of the devices, it was found from Matlab simulations that this anomaly of the admittance plots actually arises from the resistance of the via, namely R_s on the equivalent circuit of Fig. 11. For instance, a value of R_s as small as 4.7Ω generates a parallel conductance close to $0.6mS$ on the compensated admittance plots. This unwanted conductance severely decreases the phase shift in the vicinity of the resonance and induces an elliptic deformation of the admittance circle after applying the C_0 compensation. Rather small values of R_s suffice to defeat the efficiency of the inductive compensation which has to be connected at the far ends of the equivalent circuit, as shown on Fig. 11. Due to the high conductivity of the substrate, it is actually difficult to deposit a thick layer of gold in the via since any overthickness will shortcut the gap cavity. An ongoing development is targeting this specific issue. Finally, the resonators were temperature–tested in air between 0°C and 100°C and the TCF of TE fundamental was measured as $-28\,ppm/°\mathrm{C}$

VII. Conclusion and perspectives

Up to now, here–presented development came through the following points:

- setup of a reliable technology for $1\,\mu m$ gap over $75\,mm^2$, with relatively standard clean–rom equipments (classical UV lithography, glass RIE and DRIE, RF sputtering, anodic bonding) and micromechanical ones (micro–saw and ultrasonic machining),
- validation of the rule of thumb: *moderate* k^2 + *large* C_0 = *significant* C_1,
- mesa–inverse structures trap TE–fundamental in (100) Si,
- Q-factor close to 10,000 were attained at 10.3 MHz.

The moderate values of Q–factor are not yet sufficient to assert the competitiveness of the devices w.r.t. high–end quartz resonators. The relatively weak trapping attributed to the dispersion constant is a limiting factor whereas the intrinsic losses of doped silicon could be reduced by using a better material. The impedance of via will have to be reduced or neutralized to permit the development of oscillators based on here–presented MEMS principle.

Acknowledgments

The authors wish to thank the Région of Franche-Comté for its support of this research through C/N 2009C–07760. Here–presented structures are covered by the french patent application $n°11\,56250$, submitted July 8-th 2011.

References

[1] Piazza G., Stephanou P.J., Pisano A.P., *One and Two Port Piezoelectric Contour–Mode MEMS Resonators for Frequency Synthesis*, ESSDERC (2006).

[2] Rinaldi M., Zuniga C., Zuo C., Piazza G., *Super–high–frequency two–port AlN contour-mode resonators for RF applications*, IEEE Trans. Ultrason, Ferroelec. and Freq. Contr., vol.57, no.1, pp. 38–45, Jan. (2010).

[3] Kaul R.K., Mindlin R.D., *Frequency Spectrum of a Monoclinic Crystal Plate*, J. Acoust. Soc. Am. Volume 34, Issue 12, pp. 1902-1910 (1962).

[4] Tiersten, H.F., *Linear Piezoelectric Plate Vibrations*, Plenum Press (1969).

[5] Stevens D.S. and Tiersten H.F., *An analysis of doubly rotated quartz resonators utilizing essentially thickness modes with transverse variation*, J. Acoust. Soc. Am. Volume 79, Issue 6, pp. 1811-1826 (1986).

[6] Nguyen C., *MEMS Technology for Timing and Frequency Control*, IEEE Trans. Ultrason., Ferroelect.and Freq. Contr., vol. 54, no. 2, pp. 251–270, Feb. (2007).

[7] Nguyen C., Kathei L.P.B. and Rebeiz G., *Micromachined Devices for Wireless Communications*, Proceedings of the IEEE, Vol. 86, No. 8, pp. 1756-1768, Aug. (1998).

[8] Mattila T., Jaakkola O., Kiihamaki J., Karttunen J., Lamminmaki T., Rantakari P., Oja A., Seppa H., Kattelus H., Tittonen I., *14 MHz micromechanical oscillator*, Sensors and Actuators A 97–98, pp. 497–502, 2002.

[9] Kaajakari V., Mattila T., Oja A., Kiihamaki J., Kattelus H., Koskenvuori M., Rantakari P., *Square-Extensional Mode Single-Crystal Silicon Micromechanical RF-resonator*, The 12th International Conference on Solid State Sensors, Actuators and Microsystems (2003).

[10] Koskenvuori M., Mattila T., Haara, Kiihamaki J.,Tittonen I., Oja A., Seppa H., *Long Term Stability of single–crystal microresonators*, Sensors and Actuators A 115 (2004).

[11] Smart K.J., Olsson R. H. III, Ho D., Heine D.R., and Fleming J.G., *Frequency Agile Radios Using MEMS Resonators*, Govt. Microcircuit App. and Critical Tech. Conf., pp. 409-412, Mar. (2007).

[12] Hsu W.T., *Vibrating RF MEMS for clock and frequency reference applications*, Technical Digest, International Microwave Symposium 2006, San Francisco, June 10-15 (2006).

[13] Arcamon J., Colinet E., Niel A., Ollier E., *Enhanced Capacitive Detection of Bulk-Mode MEMS Resonators by active cancellation of Feedthrough Capacitance*, IEEE Intl. Freq.Ctrl. Symp. (2010).

Investigation of Drive Level Dependencies of Higher Overtones in SC Quartz Resonators

Vladimír Štofanik[*, +]
[+] Department of Thermophysics
Institute of Physics, Slovak Academy of Sciences
Bratislava, Slovak Republic
vladimir.stofanik@savba.sk

Zdenko Brezovič[*], Marián Minárik[*]
[*]Institute of Electronics and Photonics
Faculty of Electrical Engineering and Information Technology, Slovak University of Technology
Bratislava, Slovak Republic

***Abstract* - In this paper we illustrate our experimental investigations of drive level dependencies of two higher overtones (the 5th and the 7th ones), as well as of the main mode (the 3rd overtone) of several different stress compensated (SC) quartz resonators. The drive level dependencies of basic parameters in the simple Butterworth-Van Dyke one-port equivalent circuit of the particular mode were derived from the impedance vs. frequency responses measured in the vicinity of the particular modes, while temperature of the investigated resonator was maintained approximately at the lower turnover point temperature of the main mode.**

In the 3rd overtone 10-MHz SC quartz resonators, for example, the 5th overtone or the 7th overtone (the c-modes, i.e. the slow thickness-shear modes of vibration) can be exited simultaneously along with the main c-mode, with assistance of an appropriate dual-mode or multi-mode crystal oscillator (DMXO or MMXO); and the resonator self-temperature-sensing can be reliably implemented [1], [2], [3]. Level of amplitudes of particular modes, which are simultaneously excited in DMXO or MMXO, has impact on short-term, as well as on long-term frequency instabilities of generated signals; hence drive levels of individual c-modes have to be set-up properly in the oscillator circuit.

I. INTRODUCTION

Conventional methods for sensing resonator's temperature in temperature compensated crystal oscillators, for example, utilize temperature-sensing elements (e.g. thermistors), placed in close proximity to the resonator. These methods suffer from inaccuracies due to thermal lag stemming from differences in time constants and thermal gradients between the resonator and the external temperature-sensing element, as well as the sensing element aging. Simultaneous excitation of two modes of vibration in a piezoelectric resonator enables to realize self-temperature-sensing of the resonator, which eliminates temperature offset and lag effects, since no external temperature-sensing element is used. A range of different applications related to the dual-mode excitation has been reviewed in [4], [5].

This work was supported by the Ministry of Education of Slovak Republic under the grants No. 3/7411/09 and No. 1/0055/10 and by the Slovak Research and Development Agency under the contract No. APVV-0641-10.

Self-temperature-sensing of quartz resonator utilizing simultaneous excitation of fundamental slow thickness-shear mode (i.e. c-mode) together with the 3rd overtone c-mode in the resonator has been introduced in [6]. This method has been successfully employed in Microcomputer Compensated Crystal Oscillator (MCXO) [7]. Since the MCXO was primary intended for military applications, it has to operate reliably in the wide temperature range between -55°C and +85°C. Optimal quartz resonators (modified SC resonators) with the lower turnover temperature of the 3rd overtone frequency close to +20°C have been developed especially for the MCXO [8]. However, the differences between agings of the two exited mode frequencies in the resonator cause an offset with a tilt in the MCXO output frequency over the operating temperature range; it limits the accuracy of the correction process implemented in the MCXO [9]. Full recalibration of MCXO is time-consuming process and usually can be carried out only in a lab.

Simultaneous excitation of the three modes of vibrations in the volume of the resonator enables to enhance the self-temperature-sensing [3]. For example, we designed a three-mode crystal oscillator especially for simultaneous excitation of three overtones (c-modes) in a typical 10-MHz 3rd overtone SC-cut resonator: the 3rd overtone, the 5th overtone and the 7th overtone. Each excited mode in the SC-cut resonator has its own frequency vs. temperature characteristic that can be measured and approximated as well. With assistance of the three mode excitation, in addition to compensation for frequency shifts due to variations of the resonator's temperature, frequency shifts caused by different aging of the particular excited modes can be identified autonomously as well [3]. Level of amplitudes of particular modes, which are simultaneously excited in the MMXO, has impact on short-term, as well as on long-term frequency instabilities of generated signals; hence drive levels of individual modes have to be set-up properly in the oscillator circuit.

II. IMPLEMENTATION OF ENHANCED SC-CUT RESONATOR SELF-TEMPERATURE-SENSING

We developed an MMXO, which consists of three crystal oscillators (XOs) with similar structure shown in Fig.1. Each of the XOs comprises of a sustaining amplifier to provide regeneration for the respective mode of the SC-cut and an isolation amplifier based on dual-gate MOS-FET to provide sufficient isolation and to minimize the effect of loading impedance. Appropriate oscillator frequency is fine-tuned by connection of several surface mounted capacitors in parallel, since compact fixed-value inductors are used. Corresponding mode in the particular oscillator is selected by inductor L1 and two parallel combinations of capacitors: C11 || C12 || C13 and C21 || C22 || C23. The resistor R3 forms negative voltage feedback of the sustaining amplifier with bipolar junction transistor Q1. The value of resistance R3 is selected according to required driving level of the appropriate mode in the SC-cut. Realized prototype of the MMXO is illustrated in the Fig. 2. Block diagram of the enhanced SC-cut self-temperature-sensing implementation is shown in Fig. 3.

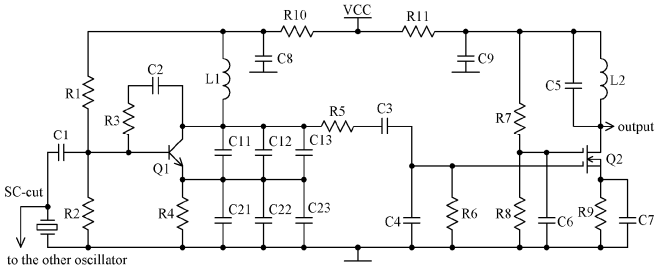

Figure 1. Schematic diagram of the bridge-type crystal oscillator (XO) with isolation amplifier; the three similar structures form the MMXO.

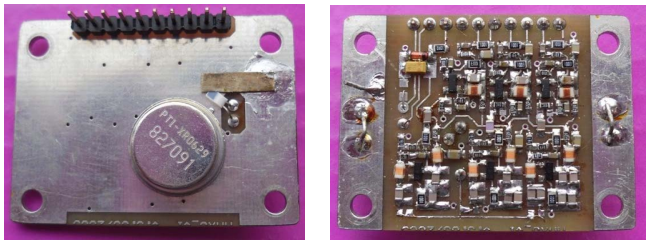

Figure 2. Photographs showing prototype of the three-mode crystal oscillator (MMXO).

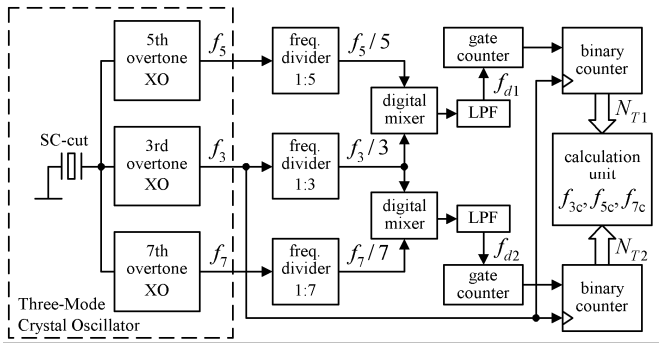

Figure 3. Block diagram of the enhanced SC-cut resonator self-temperature-sensing implementation.

The 5th overtone (the 7th overtone) oscillator frequency divided by five (seven) is subtracted from the 3rd overtone oscillator frequency divided by three, with assistance of the digital mixers and low pass filters (LPF). The difference frequencies f_{d1} and f_{d2} at the output of the low pass filters can be expressed as follows:

$$f_{d1}(\vartheta) = \frac{f_3(\vartheta)}{3} - \frac{f_5(\vartheta)}{5} \tag{1a}$$

$$f_{d2}(\vartheta) = \frac{f_3(\vartheta)}{3} - \frac{f_7(\vartheta)}{7} \tag{1b}$$

Figure 4 a) shows the measured frequency vs. temperature dependencies of the three simultaneously excited overtones.

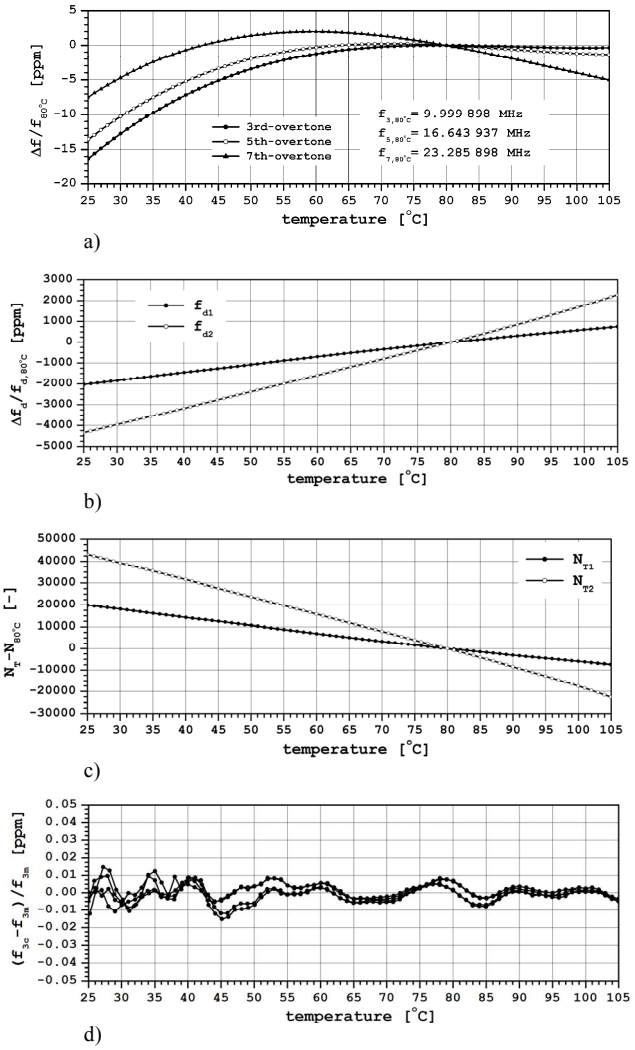

Figure 4. a) Frequency vs. temperature dependencies of the three overtones measured at the output of the three-mode crystal oscillator; b) difference frequencies f_{d1} and f_{d2} vs. temperature; c) number of clock pulses accumulated in the two binary counters during the time interval $4460 / f_{d1}$ and interval $6700 / f_{d2}$ vs. temperature; d) residuals vs. temperature in the case of 3rd overtone XO, data from calibration-run were fit to the 9th order polynomial (3b).

Figure 4 b) illustrates that the both difference frequencies are almost linear functions of the SC-cut resonator's temperature. The difference frequency f_{d1} is close to 4.5 kHz and its relative value increases with temperature approximately by +38 ppm / ^{o}C. The difference frequency f_{d2} is close to 6.7 kHz and its relative value increases with temperature approximately by +75 ppm / ^{o}C. The sensitivity of f_{d2} to temperature changes of the SC-cut is approximately two times higher than the sensitivity of f_{d1}. The gate counters, shown in Fig. 3, produce approximately one-second time intervals, during which the binary counters accumulate clock pulses with frequency f_3 (i.e. frequency of the 3rd overtone XO). At the end of each measuring cycle (time intervals formed by the gate counters), the contents of both binary counters N_{T1} and N_{T2}, shown in Fig. 3, represent an actual temperature of the SC-cut resonator in the DMXO. After the clock pulses accumulation, the contents of the binary counters can be expressed as follows:

$$N_{T1}(\vartheta) = \mathrm{int}\left(\frac{f_3(\vartheta)}{f_3(\vartheta)/3 - f_5(\vartheta)/5} 4460 \right) \quad (2a)$$

$$N_{T2}(\vartheta) = \mathrm{int}\left(\frac{f_3(\vartheta)}{f_3(\vartheta)/3 - f_7(\vartheta)/7} 6700 \right) \quad (2b)$$

The contents of the binary counters N_{T1} and N_{T2} are used to form two independent variables, which represent actual temperature of the SC resonator. Figure 4 c) illustrates that both independent variables are almost linear functions of temperature with the negative slopes of -38 ppm / ^{o}C and -75 ppm / ^{o}C, respectively.

The calculation unit (in Fig. 3) computes actual frequencies of particular oscillators according to actual values of the independent variables, with assistance of appropriate approximating polynomials. For example, in the case of 3rd overtone XO frequency as follows:

$$f_{3c,1}(\vartheta) = \sum_{k=0}^{9} a_k \cdot N^k \text{ , where } N = N_{T1}(\vartheta) - N_{T1,80\,^{\circ}\mathrm{C}} \quad (3a)$$

$$f_{3c,2}(\vartheta) = \sum_{k=0}^{9} b_k \cdot N^k \text{ , where } N = N_{T2}(\vartheta) - N_{T2,80\,^{\circ}\mathrm{C}} \quad (3b)$$

The integers $N_{1,80°C}$ and $N_{2,80°C}$ represent the content of the two binary counters, at selected temperature of the resonator (e.g. at 80^{o}C, which is approximately the lower turnover point temperature of the 3rd overtone). The coefficients a_k, b_k in the polynomials (3a) and (3b), have to be determined according to collected data obtained from the calibration run. The calibration process usually requires a personal computer (PC), controllable temperature chamber, three precise counters and frequency reference. During the calibration run, the temperature of MMXO, which is inside the temperature chamber, is set to the required value. When the temperature of MMXO is stabilized, the frequencies of all three modes are measured simultaneously, with assistance of precise counters. PC controls required temperature profiles in the chamber, controls the measurements and collects all the measured data as well.

Immediately after performing the MMXO calibration, the actual frequency calculated according the polynomial (3a) as well as according to the (3b) has to be approximately the same; i.e. the differences between both calculated values have to be within some specified tolerance. Figure 4 d) illustrates relative differences between calculated frequency of 3rd overtone XO using approximating polynomial (3b) and measured frequency of the signal generated at the 3rd overtone XO output.

However, later, the calculated frequencies can start to differ, due to different aging rates of resonant frequencies of particular modes simultaneously excited in the SC-cut. When the calculated values, according the polynomial (3a) and according to the (3b), differ too much (i.e. the difference between the two calculated values is outside of the defined tolerance), then it indicates that the aging rates of particular modes differ too much as well. In this case, the system with the MMXO has to be recalibrated. Autonomous compensations for long-term frequency shifts can be implemented as well; however, only if the aging rates of the particular excited modes in the used resonator are known or if the aging rates can be predicted accurately.

III. Used Method of the Drive Level Dependencies Measurements

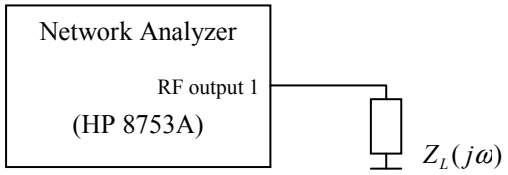

Figure 5. One-port reflection method of unknown impedance/admittance vs. frequency measurements with assistance of a network analyzer.

Network Analyzer shown in Fig. 5 evaluates complex scattering reflection coefficient on the RF port 1, which is related to the loading impedance (or admittance) connected between output of the RF port and the ground as follows

$$S_{11}(j\omega) = \frac{Z_L(j\omega) - R_{syst}}{Z_L(j\omega) + R_{syst}} = \frac{G_{syst} - Y_L(j\omega)}{G_{syst} + Y_L(j\omega)} \text{ , } \quad (4)$$

where R_{syst} represents characteristic impedance of measuriring system (network analyzer) (e.g. 50 Ω) and Y_{syst} represents characteristic admittance of the system (e.g. 0.02 S);

$Z_L(j\omega)$ and $Y_L(j\omega)$ represents unknown complex loading impedance and admittance respectively, and $\omega = 2 \cdot \pi \cdot f$ is the angular frequency.

From (4) one can easily derive following formula for the loading impedance

$$Z_L(j\omega) = R_L(\omega) + j \cdot X_L(\omega) = \frac{1 + S_{11}(j\omega)}{1 - S_{11}(j\omega)} \cdot R_{syst} \text{ , } \quad (5)$$

as well as for the loading admittance

$$Y_L(j\omega) = G_L(\omega) + j \cdot B_L(\omega) = \frac{1 - S_{11}(j\omega)}{1 + S_{11}(j\omega)} \cdot G_{syst} \text{ . } \quad (6)$$

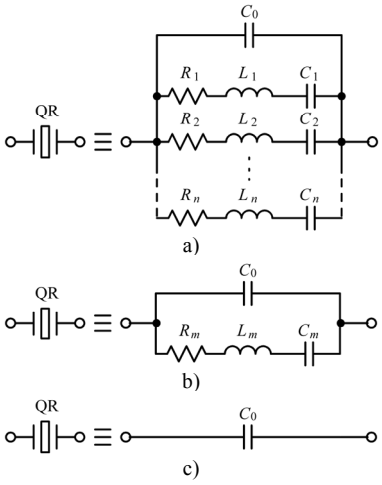

Figure 6. Butterworth - Van Dyke equivalent linear circuits (model) of the quartz resonator: a) in whole (or wide) frequency range, b) near to the selected mode "m", c) in frequency range far away any mode of vibration.

For the complex impedance and admittance of quartz resonator (QR) in the vicinity of the mode "m" can be, according to Fig 4 b), written

$$Z_{QR}(j\omega)=\frac{\left(R_m+j\omega L_m+\frac{1}{j\omega C_m}\right)\cdot\frac{1}{j\omega C_0}}{R_m+j\omega L_m+\frac{1}{j\omega C_m}+\frac{1}{j\omega C_0}} \tag{7}$$

$$Y_{QR}(j\omega)=\frac{R_m+j\omega L_m+\frac{1}{j\omega C_m}+\frac{1}{j\omega C_0}}{\left(R_m+j\omega L_m+\frac{1}{j\omega C_m}\right)\cdot\frac{1}{j\omega C_0}} \tag{8}$$

One-port reflection method of measurements of quartz resonators requires direct connection of the resonator between the RF output port and the ground, i.e. the resonator represents the loading impedance or admittance.

Once the data set, representing frequency response of complex reflection coefficient at discrete frequencies, is collected, we can calculate the values of elements in the equivalent electrical circuit of the quartz resonator.

A characteristic resonance frequency of the particular mode "m" $f_{m,res}$ corresponds to the frequency of the local maximum of real part of the loading admittance; which can be calculated according to (6) from the measured data-set representing complex scattering parameter $S_{11}(j\omega)$; it can be written as follows

$$G_L(\omega_{m,res})=G_{QR}(\omega_{m,res})=\max\left[G_L(\omega)\right], \tag{9}$$

where $\omega_{m,res}=2\cdot\pi\cdot f_{m,res}$ is the angular series resonance frequency.

Since measured data set represents complex scattering parameter $S_{11}(j\omega)$ response at discrete frequencies only, an approximating function can improve accuracy of determination of the resonant frequency. Second order polynomial approximation, for example, applied to the several data points measured at discrete frequencies below, as well as above the discrete frequency, where $G_L(\omega)$ calculated from the data set was maximum, usually gives good results. It is simple to calculate the resonant frequency, where derivative of approximating polynomial should be zero. From the approximating polynomial can be calculated $G_{QR}(\omega_{m,res})$ as well.

Next step is determination of the motional inductance, which is used as initial value for the least squares method of fitting parameters of the Butterworth - Van Dyke equivalent model of the resonator (appropriate mode). It can be determined from the linear approximation of the imaginary part of the impedance (5), applied again to the several data points measured at frequencies below, as well as above the discrete frequency where the $G_L(\omega)$ was maximum. It can be written as follows

$$L_{m,init}=\left[X_L(\omega_{m,res}+\Delta\omega)-X_L(\omega_{m,res}-\Delta\omega)\right]/2\Delta\omega \tag{10}$$

Initial value of motional resistance for the fitting algorithm can be calculated as follows

$$R_{m,init}=1/G_L(\omega_{m,res}) \tag{11}$$

Initial value of the static capacitance C_0 for the fitting algorithm can be calculated according to (6) from the measured scattering reflection coefficient at the frequency far from the resonance. For example, first point in the data set (at the lowest discrete angular frequency $\omega_{i=1}$) can be used, then for the initial value of the static capacitance can be written

$$C_{0,init}=1/B_L(\omega_{i=1}) \tag{11}$$

According to the Thomson equation, with respect to the series resonance frequency (characteristic resonance frequency) and the motional inductance, the motional capacitance is

$$C_m=\frac{1}{L_m}\cdot\omega_{m,res}^2 \tag{12}$$

Motional capacitance in (7) can be replaced with (12) and then for the complex impedance of the resonator for the frequencies near the particular mode "m" can be written

$$Z_{QR,m}(j\omega)=\frac{\left(R_m+j\omega L_m-j\frac{L_m\cdot\omega_{m,res}^2}{\omega}\right)\cdot\frac{-j}{\omega C_0}}{R_m+j\omega L_m-j\frac{L_m\cdot\omega_{m,res}^2}{\omega}-j\frac{1}{\omega C_0}} \tag{13}$$

Theoretical frequency response of reflection scattering coefficient then can be calculated from the complex impedance (13) as follows

$$S_{11,m}(j\omega)=\frac{Z_{QR,m}(j\omega)-R_{syst}}{Z_{QR,m}(j\omega)+R_{syst}} \tag{14}$$

The optimum fit of element values in the Butterworth - Van Dyke equivalent model of the resonator (appropriate mode), based on the least squares method, has to reach the minimum value of the *error* according to following relation

$$error = \sum_{i=1}^{N} \left[\mathrm{Re}\{S_{11,m}(j\omega_i)\} - \mathrm{Re}\{S_{11,meas}(j\omega_i)\} \right]^2 + \\ + \sum_{i=1}^{N} \left[\mathrm{Im}\{S_{11,m}(j\omega_i)\} - \mathrm{Im}\{S_{11,meas}(j\omega_i)\} \right]^2 \quad (15)$$

In our case, to fit the optimum of element values in the model, we used the standard function *fminsearch* in the MATLAB.

IV. Measured Characteristics

We investigated eight 10-MHz 3rd overtone SC quartz resonators in HC37/U holders. Five resonators, from two different series (XR0629 and XR064D), were provided by MTRON/PTI; and three resonators from the same group were provided by NOFECH.

During measurements, the temperature of measured resonator was precisely controlled inside the temperature chamber, wherein the resonator's temperature was maintained at the lower turnover temperature of the main mode (the 3rd overtone c mode).

Following graphs, as examples, shown in Fig. 7, Fig. 8 and Fig. 9, illustrate only a method of measurements of drive level dependency of the main mode (the 3rd overtone) as well as of two higher overtones (the 5th and the 7th ones) belonging to one selected SC quartz resonator (SN169903, NOFECH), using one-port reflection method.

All graphs were derived from collected data sets representing the complex reflection coefficient S_{11} frequency responses obtained from measurements with assistance of the HP 8753A network analyzer. Each response is represented by 1601 complex data points. The frequency sweeping was set to 50 Hz in the case of measurement of 3rd overtone c-mode, and to 200 Hz in case of measurement of 5th overtone c-mode as well as 7th overtone c mode.

V. Conclusions

To implement the resonator self-temperature-sensing, at least two modes of vibrations are necessary to be excited simultaneously in the resonator. However, simultaneous excitation of three modes of vibrations in the volume of the resonator enables to enhance the self-temperature-sensing. In addition to compensation for frequency shifts due to variations of the resonator's temperature, also frequency shifts caused by different aging rates of the particular modes can be identified autonomously (without necessity for any external frequency reference). Moreover, autonomous compensations for long-term frequency shifts can be implemented as well; however, only if the aging rates of the particular excited modes in the used resonator are known or if the aging rates can be predicted accurately.

An impact of drive level (the amplitude of vibration) on the basic parameters of three different c-modes in several SC-cut resonators has been investigated.

For all the investigated c-modes (3rd, 5th and 7th overtone) the nonlinear effects has been evident usually when the driving power is higher than approximately 0.5 mW. For very low driving powers, below 1 μW the dependency of parameters is negligible.

Level of amplitudes (drive levels) of particular modes, which are simultaneously excited in a dual-mode or multi-mode crystal oscillator, has impact on short-term, as well as on long-term frequency instabilities of generated signals; hence drive levels of individual modes have to be set-up properly in the oscillator circuit.

References

[1] V. Stofanik, I. Balaz, and M. Minarik, "Dual-Mode Crystal Oscillator with Simultaneous Excitation of Two Overtones in a Stress Compensated Quartz Resonator," Proc. of the 2007 Joint European Frequency and Time Forum and the 2007 IEEE Frequency Control Symposium, 2007, pp. 227-229.

[2] V. Stofanik, I. Balaz, M. Minarik, and E. Cocherova, "Investigation of Self-Temperature-Sensing of SC-Cut with Simultaneous Excitation of Two Higher Overtones in Dual-Mode Crystal Oscillator," Proc. of the 2008 IEEE International Frequency Control Symposium, 2008, pp. 170-173.

[3] V. Stofanik, I. Balaz, M. Minarik, and S. Kozinka, "Multi-Mode Crystal Oscillator for Simultaneous Excitation of Three Thickness-Shear Modes in Stress Compensated Resonator," Proc. of the Joint 2009 European Frequency and Time Forum and the 2009 IEEE Frequency Control Symposium, 2009, pp. 516-519.

[4] J. R. Vig, "Dual-mode Oscillators for Clocks and Sensors," Proc. of the 1999 IEEE Ultrasonics Symposium, 1999, pp. 859-868.

[5] J. R. Vig, "Temperature-Insensitive Dual-Mode Resonant Sensors - A Review," IEEE Sensors Journal, Vol. 1, No. 1, June 2001, pp. 62-68.

[6] S. S. Schodowski, "Resonator Self-Temperature-Sensing using a Dual-Harmonic-Mode Oscillator," Proc. of the 43rd Annual Symposium on Frequency Control, 1989, pp. 2-7.

[7] A. Benjaminson and S. C. Stallings, "A Microcomputer Compensated Crystal Oscillator using a Dual-Mode Resonator," Proc. of the 43rd Annual Symposium on Frequency Control, 1989, pp. 20-26.

[8] R. L. Filler and J. R. Vig, "Resonators for the Microcomputer Compensated Crystal Oscillator," Proc. of the 43rd Annual Symposium on Frequency Control, 1989, pp. 8-15.

[9] Y. Kim, "Aging of Dual Mode Resonator for Microcomputer Compensated Crystal Oscillator," Proc. of the 2005 Joint IEEE International Frequency Control Symposium and Precise Time and Time Interval Systems and Applications Meeting, 2005, pp. 171-175.

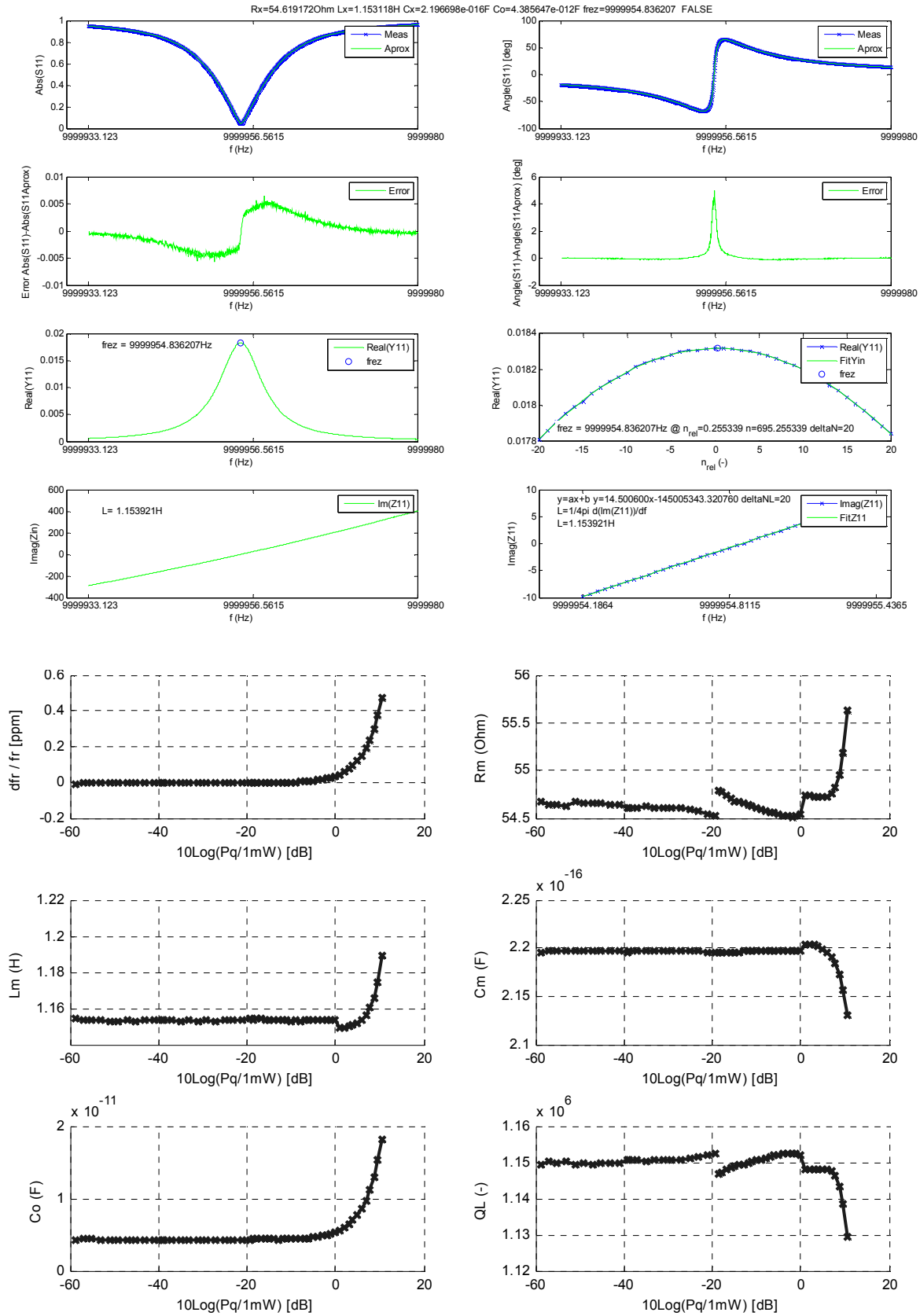

Figure 7. Measured and calculated frequency responses, and basic value of elements in Butterworth - Van Dyke equivalent model of the SC resonator SN169903 vs. driving power, in the case of the 3rd overtone c mode.

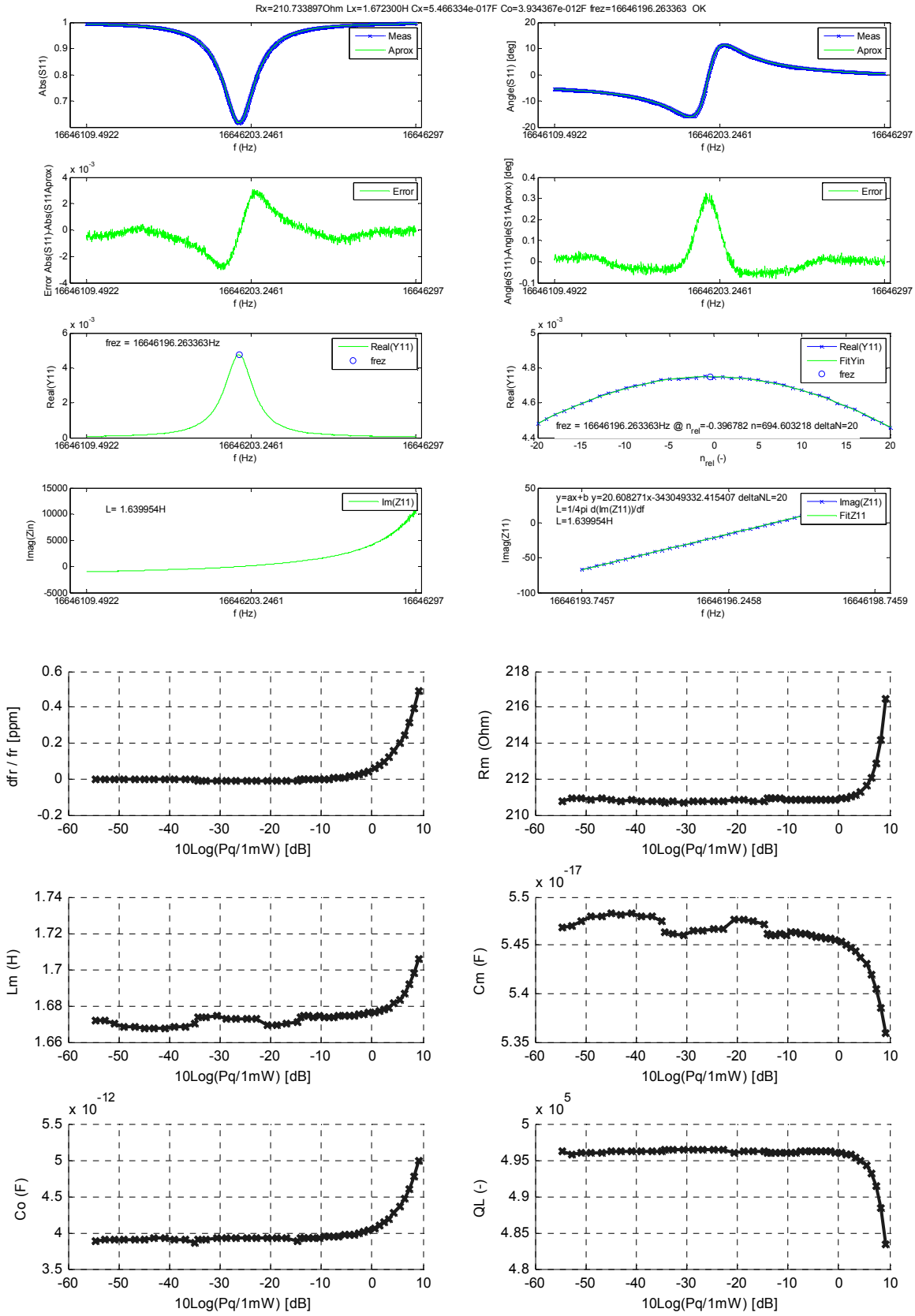

Figure 8. Measured and calculated frequency responses, and basic value of elements in Butterworth - Van Dyke equivalent model of the SC resonator SN169903 vs. driving power, in the case of the 5th overtone c mode.

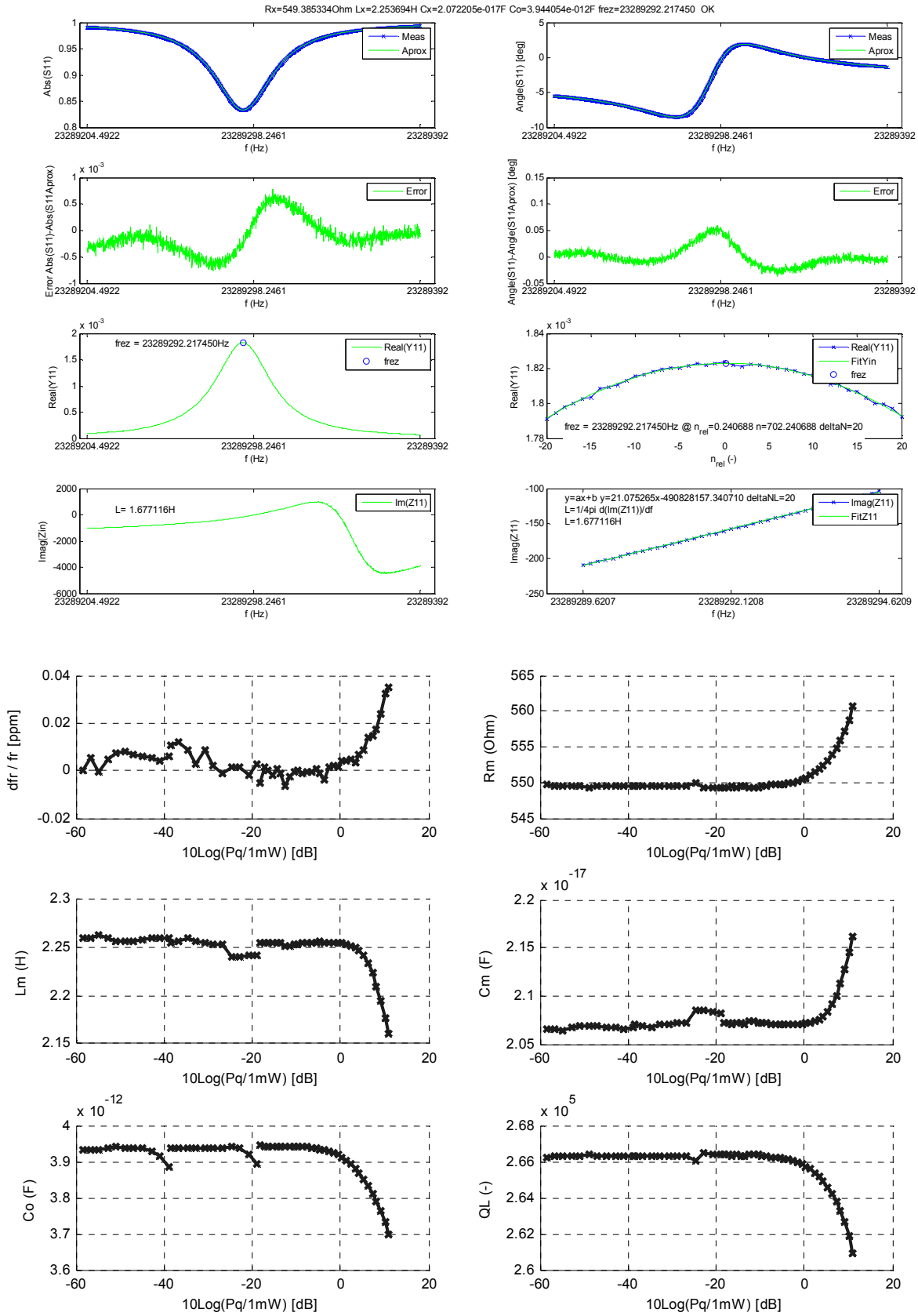

Figure 9. Measured and calculated frequency responses, and basic value of elements in Butterworth - Van Dyke equivalent model of the SC resonator SN169903 vs. driving power, in the case of the 7th overtone c mode.

Direct Frequency Metrology Up To PHz Frequencies

T.J. Pinkert, J. Morgenweg, I. Barmes, D.Z. Kandula*,
Ch. Gohle**, K.S.E. Eikema
LaserLaB Amsterdam
VU University
Amsterdam, The Netherlands
k.s.e.eikema@vu.nl

*Present address: Max-Born-Institute
Berlin, Germany
**Present address: Physics Department
Ludwig-Maximilians-University
Munich, Germany

Abstract—**The capability of frequency-comb (FC) lasers to precisely measure optical frequencies has been extended to the to the extreme ultraviolet (XUV, wavelengths shorter than 100 nm), corresponding to frequencies of multiple PHz. We demonstrate "broad frequency comb generation" for a wavelength range of 51-85 nm. Our method is based on amplification and coherent up-conversion of a pair of pulses originating from a near-infrared femtosecond FC laser. Excitation of argon, neon, and helium with these upconverted laser pulses in the XUV lead to Ramsey-like signals with up to 61% contrast. From these signals an accuracy of 6 MHz has been achieved in the determination of the ground state ionization energy of helium at 51 nm. Further improvement to a kHz-level accuracy is expected based on a new pump laser for the employed parametric amplification system.**

I. INTRODUCTION

Frequency comb (FC) lasers [1,2] have greatly advanced fields such as precision spectroscopy, optical atomic clocks, and attosecond science. FC lasers provide a phase-coherent link between optical frequencies of several hundred THz, which cannot be measured directly, and radio frequencies that can readily be counted and compared to frequency standards.

A FC effectively acts as a gearbox between these two frequency domains, so that optical frequencies can be counted electronically. This is possible because all the emitted modes (easily up to a million) of a comb laser are equidistant in frequency, and can be described by only two numbers, f_{CEO} (the carrier-envelope offset frequency) and the repetition frequency f_{rep}, both in the RF domain. In the frequency domain a comb-like spectrum is seen, where the m^{th} mode has a frequency equal to:

$$f_m = f_{CEO} + m f_{rep} \quad (1)$$

Viewed in the time domain, the laser emits an infinite train of pulses at the repetition rate f_{rep}, with a phase slip between subsequent pulses (as measured between the optical carrier and the pulse envelope) of $\Delta\phi = 2\pi f_{CEO}/f_{rep}$.

This work is supported by the Dutch FOM organization through its IPP-program 'Metrology with frequency comb lasers', by NWO via a VICI grant, by the EU via the JRA ALADIN, and 'Atlas' network, and by the Humboldt Foundation.

We demonstrate that the remarkable precision and structure of frequency combs can be transferred to extreme ultraviolet (XUV) wavelengths by parametric amplification and high-harmonic generation (HHG) of two subsequent comb laser pulses (see Fig. 1b). In effect a pair of phase-locked extreme ultraviolet pulses is generated, which can be used directly for precision spectroscopy without the need for an additional spectroscopy laser. Viewed in the frequency domain, the spectrum of the upconverted pulse sequence in the XUV resembles again a frequency comb, but now in the form of a cosine-modulated spectrum (see Fig. 1a). From a time-domain perspective, excitation with phase-locked pulses is a form of Ramsey excitation (see e.g. [3,4]).

II. EXPERIMENTAL METHODS

The setup (Fig. 1b) consists of a Ti:Sapphire FC laser which is referenced to a GPS-controlled rubidium frequency standard. From this source of phase controlled pulses, a center wavelength and bandwidth of phase-controlled pulses is selected with a slit placed in the stretcher that is part of the parametric amplifier system. The resulting 'clipped' comb laser pulses can be tuned from 745 nm to 805 nm. A dedicated non-collinear chirped pulse parametric amplifier (NOPCPA) is used to amplify two subsequent (and spectrally clipped) pulses from the comb laser to 5 mJ per pulse. After compression 1-2 mJ per pulse is available for HHG. The phase distortion by the amplification process (typically on the order of 100 mrad) is measured by spectral interferometry and is taken into account [5]. The XUV comb is then produced by HHG of the two pulses in a noble gas jet. By selecting different harmonics (the 9^{th} to 13^{th} harmonic made in xenon, the 15^{th} made in krypton) and the center wavelength from the FC, XUV comb generation is made possible over a range of 85 nm down to 51 nm. The bandwidth in the IR of the comb pulses is set between 3 and 6 nm to ensure that the harmonics produced after amplification and HHG are narrow enough to excite only one transition at the time.

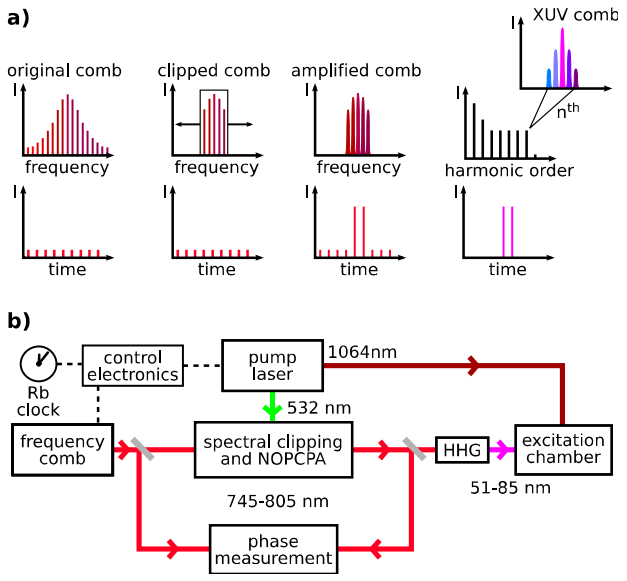

Figure. 1. (a) Spectral and temporal structure of the different stages of XUV comb generation and spectroscopy (left to right): continuous coherent pulse train from the FC laser, the clipped FC spectrum in the stretcher, the cosine-modulated spectrum of a pair of amplified pulses, and odd harmonics of the amplified FC laser pulses, each containing a cosine-modulated XUV comb corresponding to the XUV pulse pair. (b) Schematic of the experimental setup; NOPCPA: non-collinear parametric chirped pulse amplifier, HHG: high-harmonic generation.

The coherence of the generated XUV light has been verified by exciting one-photon transitions in argon, neon and helium. For this purpose the XUV beam is crossed perpendicularly with a low divergence (< 4 mrad) atomic beam.

After excitation with the two XUV pulses, the excited state atoms are ionized with an infrared laser pulse at 1064 nm and detected in a time-of-flight spectrometer. By changing the delay between the XUV pulses (i.e. the repetition rate of the frequency comb laser) in approximately one-attosecond steps, the cosine-shaped comb spectrum is scanned over the transition. The recorded signals are binned in 20 equidistant groups over a Ramsey period, which is equal to the mode spacing, and therefore the repetition rate of the frequency comb laser. In Fig. 2 a typical resulting signal is shown for argon excited at 82.53 nm from the ground state to the $3s^2\ 3p^5(^2P_{1/2})6s[1/2]_1$ excited state. The XUV comb was generated in this case by the 9th harmonic in xenon. The argon signal shows a high contrast of 61% for a repetition rate of the FC of 148 MHz. Similar spectra have been recorded for neon near 60 nm (13th harmonic) and for helium (15th harmonic in krypton) near 51 nm.

III. RESULTS

In the case of helium, recordings were made of 4 different transitions ($1s^2\ ^1S_0$ - $1snp\ ^1P_1$ with n = 4-7). The signals for n=4,5 were used to obtain an improved value for the ground state ionization energy, by measuring the ion signal together with the parameters of the frequency comb laser, the phase shift between the amplified pulses, and the energy of the IR and XUV pulses. Fig. 3 shows a typical He ion signal as a function of pulse delay for f_{rep}=185 MHz. From the fit of the recorded signals precise transition frequencies can be deduced. Because the spectroscopy signal is periodic with f_{rep} the measured transition frequency can only be determined up to an integer multiple of the repetition frequency. To resolve this ambiguity, the measurements in helium were repeated for different repetition rates of the laser between 100 MHz and 185 MHz. The correct 'comb mode' is located where the possible transition energies for all repetition frequencies coincide. Furthermore, a careful analysis of systematic effects was performed. Differential spatial and temporal pulse deformation of the amplified IR double pulse were monitored and controlled using the aforementioned spectral interferometric measurement technique [5], with an accuracy better than a 200th of an optical cycle. Many other systematic effects have been investigated as well, such as effects of ionization and adiabatic phase shifts during the HHG process, self-phase modulation in optics, and Doppler shifts. Using the precisely known 4p and 5p excited state energies, we find the ground state energy (ionization potential) of helium at 5945204212(6) MHz [6]. This is in good agreement with the most recent theoretical calculations [7,8]. The obtained accuracy is nearly an order of magnitude better than previous experiments where the ionization potential of helium was determined using single nanosecond-duration laser pulses [9,10], which clearly demonstrates the power of XUV frequency comb excitation.

The contrast of the signals in helium have been analyzed using a model that includes the effects of the lifetime of the excited state, Doppler broadening, XUV pulse energy ratio, direct ionization background, and the time delay between the pulses. From this analysis it is found that the XUV comb at

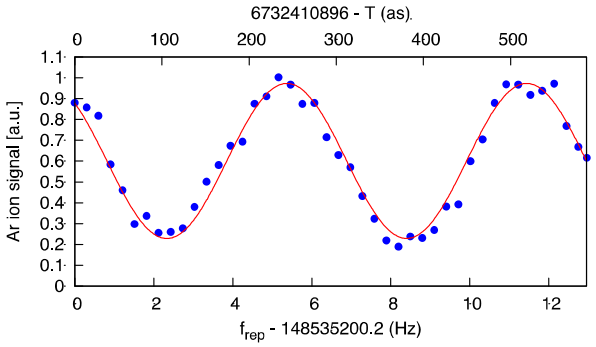

Figure 2. Measured excitation probability (circles) of argon at 82.53 nm from the ground state to $3s^2\ 3p^5(^2P_{1/2})6s[1/2]_1$ excited state, normalized by the XUV pulse energy, as a function of the repetition rate f_{rep} of the frequency comb laser. A pure argon beam is used, and the red line represents a sinusoidal fit to the data. The upper scale shows the time delay between the pulses in attoseconds.

51 nm has a 50 attosecond rms excess timing jitter which can be attributed to the HHG process. A possible cause of this

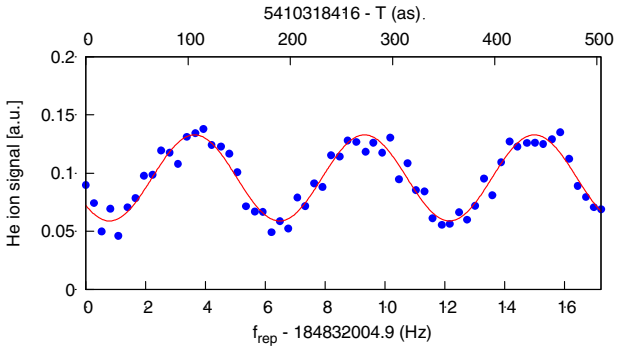

Figure 3. Measured excitation probability (circles) of helium at 51.5 nm on the $1s^2\ ^1S_0 - 1s5p\ ^1P_1$ transition, normalized by the XUV pulse energy, as a function of the repetition rate f_{rep} of the frequency comb laser. In this example f_{CEO} is locked at 46.21 MHz, and a 1:5 He:Ne mixture is used for the atomic beam. The red line represents a sinusoidal a fit to the data. The upper scale shows the time delay between the pulses in attoseconds.

jitter is intensity fluctuations of the IR pulses (~ 5%), and fluctuations in density and level of ionization in the HHG gas jet.

For the results presented here, the two pump pulses for the parametric amplifier were generated using beam splitters and an optical delay line in the pump laser. This presents a significant limitation, also because the system does not operate in a steady-state situation, in contrast to full-repetition rate XUV comb generation with enhancement resonators (see e.g. [12]). However, the accuracy of our method improves for larger pulse delays, as the phase errors introduced in the amplification and upconversion process represent a smaller frequency deviation. Moreover, for delays larger than about 200 ns, for each pulse harmonic generation takes place in a 'fresh' sample of gas from the jet, so that the phase shift from ionization is circumvented. Up to now, the largest delay between the pump pulses (and therefore the amplified FC pulses) was 10 ns. Extending the optical delay line in the pump laser to larger delays is rather impractical. We have therefore started the development of a new pump-laser frontend allowing delays extending well into the microsecond range. In the new system both the pump laser and the FC operate at the same repetition rate, so that selection of the appropriate pump laser pulses automatically amplifies FC pulses with the same delay.

The pump laser system under development [13] consists of a Nd:YVO_4 modelocked laser (operating near 125 MHz) followed by a combination of a fast AOM and EOM. With these modulators, two pulses can be selected with a time delay that is a multiple of 8 ns. After this selection the pulses are amplified in a so called 'bounce' amplifier based on a Nd:YVO_4 crystal, and pumped from a single side at 880 nm by a QCW laser diode. Amplification of two pulses normally leads to a reduction of the energy in the second pulse due to gain depletion. However, with the EOM it is possible to tailor the input energy to the bounce amplifier such that equal 0.1 mJ pulses at 1064 nm are obtained with pulse delays up to several microseconds. Further amplification to the level of 100 mJ, required for the parametric amplifier, is in progress.

IV. Conclusions

XUV frequency comb generation has been demonstrated from 85 nm to 51 nm based on amplification and upconversion of two FC laser pulses. With this comb, the first absolute frequency measurement was performed in the XUV, resulting in an 8-fold increase in the accuracy of the helium ground state ionization energy. Improvements to the laser setup are in progress based on bounce-amplifier technology, extending the pulse delay between two upconverted FC pulses by several orders of magnitude to the microsecond range. It is expected that this system will allow XUV-FC metrology at a kHz-level accuracy in the near future.

References

[1] R. Holzwarth et al., "Optical frequency synthesizer for precision spectroscopy", *Phys. Rev. Lett.* **85**, pp. 2264-2267 (2000).

[2] S.A. Diddams et al., "Direct link between microwave and optical frequencies with a 300 THz femtosecond laser comb", *Phys. Rev. Lett.* **84**, pp. 5102-5105 (2000).

[3] S. Witte et. al., "Deep-ultraviolet quantum interference metrology with ultrashort laser pulses", *Science* **307**, pp. 400-403 (2005).

[4] S. Cavalieri et. al., "Ramsey-type spectroscopy with high-order harmonics", *Phys. Rev. Lett.* **89**, 133002 (2002).

[5] D.Z. Kandula et. al., "Ultrafast double-pulse parametric amplification for precision Ramsey metrology", *Opt. Expr.* **16**, pp. 7071-7082 (2008).

[6] D.Z. Kandula et al., "Extreme ultraviolet frequency comb metrology", *Phys. Rev. Lett.* **105**, 063001 (2010)

[7] G.W.F. Drake and Z.C. Yan, "High-precision spectroscopy as a test of quantum electrodynamics in light atomic systems", *Can. J. Phys.* **86**, 45 (2008).

[8] K. Pachucki, "α^4R corrections to singlet states of helium", *Phys. Rev. A* **74**, 022512 (2006).

[9] K.S.E Eikema et al., "Lamb shift measurement in the 1 ^{1}S ground state of helium", *Phys. Rev. A* **55**, pp. 1866-1883 (1997).

[10] S.D. Bergeson et al., "Measurement of the He ground state Lamb shift via the two-photon 1 ^{1}S-2 ^{1}S transition", *Phys. Rev. Lett.* **80**, pp. 3475-3478 (1998).

[11] V. A. Yerokhin and K. Pachucki, "Theoretical energies of low-lying states of light helium-like ions", *Phys. Rev. A* **81**, 022507 (2010).

[12] A. Cingöz, D. C. Yost, T. K. Allison, A. Ruehl, M. E. Fermann, I. Hartl, J. Ye, "Direct frequency comb spectroscopy in the extreme ultraviolet", Nature **482**, 68-71 (2012).

[13] J. Morgenweg and K. S. E. Eikema, "Tailored pulse sequences from an 880 nm pumped Nd:YVO_4 bounce amplifier, Opt. Lett. **37**, 208-201 (2012).

Investigation of an optical frequency comb with intra-cavity EOM and optimization of microwave generation

Y. Le Coq, W. Zhang, G. Santarelli
LNE-SYRTE,
Observatoire de Paris, CNRS, UPMC
75014, Paris, France
yann.lecoq@obspm.fr

M. Fischer, R. Holzwarth
MenloSystems GmBH
D-82152, Martinsried, Germany

***Abstract*—We present here a detailed investigation of a commercial-core Erbium-doped fiber-based femtosecond laser optical frequency comb equipped with an intra-cavity Electro-Optics modulator. This device allows rapid feed-back on the laser's repetition rate, enabling reaching the narrow-linewidth regime when locked to a ultra-high spectral purity optical continuous wave reference. Our study makes use of transfer functions analysis to characterize the laser dynamic response and the residual unavoidable cross talks. In a second part, we also present some results which show how to combine the signals from two photodetector to obtain a very low amplitude-phase conversion detection of the repetition rate, which is very useful in the context of low phase noise microwave generation with optical frequency combs.**

I. INTRODUCTION

Low-phase-noise and stable microwave signals are of prime importance in a variety of scientific and technological fields, such as, for example, atomic frequency standards, radar and remote sensing, and very long baseline interferometry [1-4]. The combination of ultra-stable lasers and low noise optical frequency division by use of a femtosecond laser presents a possibility of realizing extremely low phase noise microwave sources with reliable and operational-level technology. We have previously reported phase noise levels at -120 dBc/Hz at 1 Hz from a 12 GHz carrier [5-7], with a white phase noise plateau below -160 dBc/Hz [8].

We present our investigation of a commercial-core optical frequency comb based on an Erbium-doped fiber-based femtosecond laser equipped with an intra-cavity Electro-Optic Modulator (EOM) [9-11]. The EOM is configured as a voltage-controlled group delay actuator and allows high bandwidth (>500 kHz) servo-locking of the repetition rate of the laser. By using a thorough analysis based on transfer functions, we were able to characterize the dynamical effect of the various available actuators (pump power/current supply, cavity length piezo actuator, and EOM control voltage) on the 3 global parameters governing the laser (average amplitude, repetition rate and carrier-envelop offset) [12]. This study allows our system to reach the narrow linewidth regime, when locked to an ultra-high spectral purity optical continuous wave (cw) laser. In this regime, each tooth of the comb is as narrow-linewidth as that of the optical reference it is locked to.

In our context of low phase noise microwave generation by photodetection of the pulse train of the laser, this approach allows optimization of the performance and identification of the technical bottlenecks which require further improvement. Most particularly, the photodetector's amplitude-phase conversion process (AMPM) results in a strong effect of the relative intensity noise (RIN) of the laser on the microwave phase-noise performance [13]. Decreasing the RIN therefore requires particular care, even when the amplitude-phase conversion is kept low by adequate working conditions.

Along this line, we also present our work on combining two photodetector to realize a device which exhibits a particularly low amplitude phase conversion factor, on a wide range of working conditions. Compared to our previous studies on low AMPM conversion detectors [13], this realization considerably increases the ease-of-use of such techniques as, in this case, neither careful calibration nor fine tuning is necessary to obtain low AMPM.

II. FIBER-BASED OPTICAL FREQUENCY COMB WITH INTRA-CAVITY ELECTRO-OPTIC MODULATOR

Our study of fiber-based optical frequency comb with intra-cavity EOM is detailed in the reference [12]. We use the formalism of transfer functions to characterize the dynamic effect of our three available actuators on the frequency comb (piezo-actuating mirror in the laser cavity, pump diode current and EOM voltage) on the three global parameters governing the state of the frequency comb (repetition rate f_{rep}, carrier-envelop offset frequency f_0 and output optical power A). The complete results can be expressed in a 3 by 3 transfer matrix whose each term exhibits a dependence with the Fourier frequency (*i.e.* it is a transfer function), as expressed in the following mathematical relation.

Part of this work has been carried out within the European Metrology Research Program (EMRP) IND14 project, which is jointly funded by the EMRP participating countries within European Association of National Metrology Institutes (EURAMET) and the European Union

$$\begin{pmatrix} A(j\omega) \\ f_{rep}(j\omega) \\ f_0(j\omega) \end{pmatrix} = \begin{bmatrix} H_{I_{pump},A}(j\omega) & H_{V_{PZT},A}(j\omega) & H_{V_{EOM},A}(j\omega) \\ H_{I_{pump},f_{rep}}(j\omega) & H_{V_{PZT},f_{rep}}(j\omega) & H_{V_{EOM},f_{rep}}(j\omega) \\ H_{I_{pump},f_0}(j\omega) & H_{V_{PZT},f_0}(j\omega) & H_{V_{EOM},f_0}(j\omega) \end{bmatrix} \begin{pmatrix} I_{pump}(j\omega) \\ V_{PZT}(j\omega) \\ V_{EOM}(j\omega) \end{pmatrix}$$

In Figure 1, we present typical transfer functions obtained for the EOM actuator. The first important point to notice is that the dephasing of the transfer function from this actuator to the intended target (frep) is not reaching a pi phase-shift before about 1MHz of Fourier frequency. This allows very fast feed-back in servo-locking the comb to an optical reference and enables reaching the narrow-linewidth regime, where each tooth of the comb exhibits a spectral purity identical to that of the optical reference the comb is locked to (which linewidth is typically <1Hz for modern ultra-stable Fabry-Perot cavity references lasers).

A second important feature to notice is the fact that the dynamics response of the intended target (f_{rep}) and those of the unavoidable cross-talks (f_0 and A) are not identical (the cross talks start behaving differently than at low Fourier frequencies much before the intended target f_{rep}). This demonstrates the limits of the well-known rubber-band model and must be taken into account, especially when the cross talks are large.

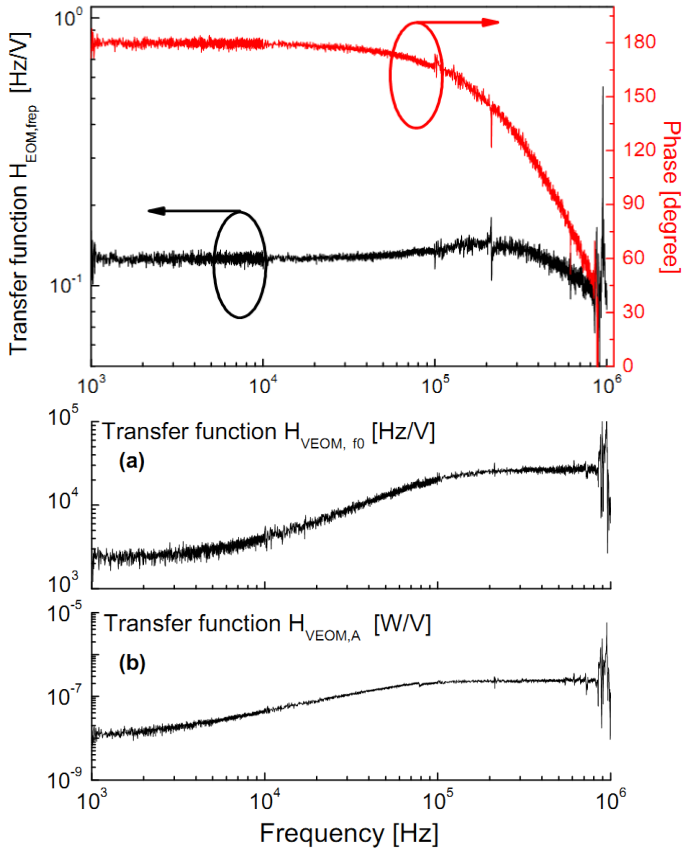

Figure 1. The three transfer functions pertaining to the intra-cavity Electro-Optic Modulator actuator, whose intended target is to act primarily on the repetition rate of the laser.

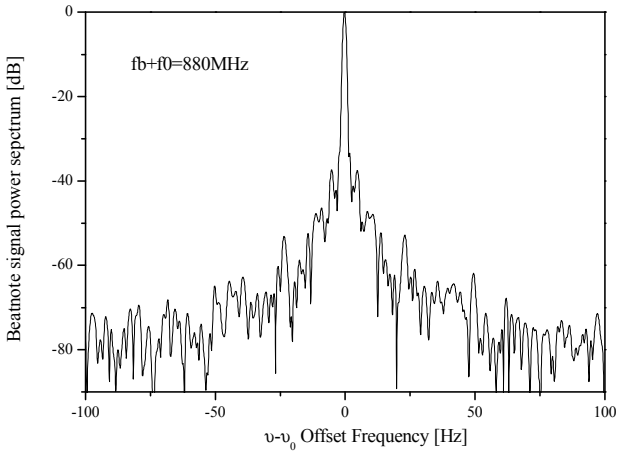

Figure 2. Beatnote between a tooth of the optical frequency comb near 1 µm wavelength and an ultra-stable Fabry-Perot cavity stabilized laser at the same wavelength. The optical frequency comb is independently locked on a separate ultra-stable cavity referenced laser at 1.5 µm wavelenght using the EOM actuator by the method described in [12].

The large feedback bandwidth available via the EOM actuator allows us to reach the narrow linewidth regime when we lock the comb to an ultra-stable optical reference at 1.5µm wavelength. To demonstrate this, we have realized the optical beatnote between the 1.5 µm stabilized frequency comb and a separate ultra-stable laser operating at a wavelength near 1 µm [14,15]. The spectrum of the result is shown in figure 2, and demonstrates the narrow-linewidth that is limited by that of the two cw references (at 1.5 µm and 1 µm) and not by the residual noise of the optical frequency comb. The narrow linewidth regime allowed us to conveniently measure the ratio of the optical frequencies of the laser at 1 µm and the laser at 1.5 µm with a residual noise below 10^{-16} at 1s averaging time (as measured by comparing the results obtained from two independent EOM-equipped fiber frequency combs realizing synchronously the same measurement).

An exemple of the use of the transfer function measurement obtained for the other actuators is presented in Figure 3. The Relative intensity noise (RIN) of the optical frequency comb is measured and compared to that of the constant current electrical source driving the pump diode lasers of the fiber-based femtosecond laser. The transfer function from pump diode current to laser amplitude allows us to predict the laser RIN that is arising solely from the noise of the current power supply. Our measurement shows that the original power supply was the limiting factor of the RIN performance of the laser. A substantially lower noise power supply was subsequently used and is shown not to be a RIN limitation anymore. We have further inquired the sources of noise producing the residual RIN. Although further studies need to be carried on, it appears that the intrinsic RIN of the pump diode (independent of the noise of its power supply) is itself a limiting factor, at least for some Fourier frequencies, and that choosing low RIN pump diodes could improve even more the RIN performance of the femtosecond laser which is the core of the optical frequency comb.

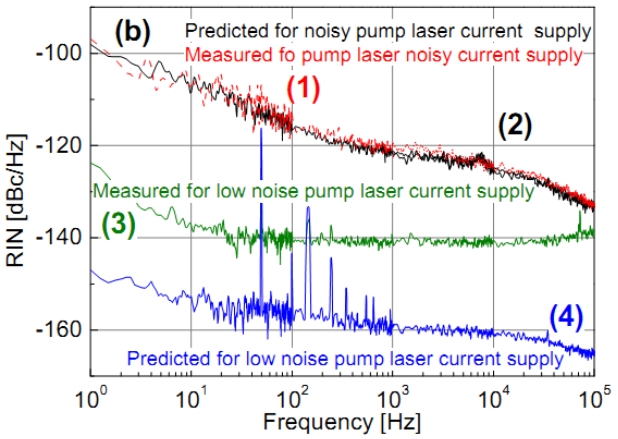

Figure 3. Relative Intensity Noise (RIN) of the fiber-based femtosecond laser which produces the optical frequency comb. (1) and (2) are respectively the measured and predicted RINS for the original (noisy) power supply. (3) and (4) are measured and predicted for an improved (low noise) power supply.

As a further exemple, we have also used the transfer functions analysis to calculate the extra-RIN of the femtosecond laser that arises when it is locked to an ultra-stable reference cw laser with the EOM, due to the cross talk action of the EOM to the laser amplitude A. This effect effectively couples the free-running frequency noise of the laser into amplitude extra noise when the servo-loop is activated via the $H_{VEOM,A}(j\omega)$ cross-talk transfer function. Our calculation shows that this extra-RIN is still about more than 10dB lower than the "intrinsic" RIN of the laser, but may have to be taken into account should further improvement lead to even lower RIN than currently demonstrated.

III. Combined Photodetectors for Low Amplitude-Phase Conversion

The study of the RIN of the laser is particularly important in the context of low phase noise microwave signal generation by photodetection of the pulse train when the optical frequency comb is locked to a high spectral purity cw optical reference. As a matter of facts, amplitude phase conversion in the detection process is turning laser RIN into extra-phase-noise of the produced microwave which is usually a substantial limitation of such a technique.

In our previous work [12], as well as other groups working on the same topic [16,17], we have shown that, due to saturation effect that arise in the photodetector illuminated by fs-regime light pulses, the AMPM conversion factor exhibits alternatively positive and negative values with increasing total energy per optical pulse, with special "magic" points in between where it vanishes. Furthermore, these vanishing points are strongly dependent on the bias of the photodetector and the exact energy per pulse at which they appear can be easily tuned by this parameter. Even though we have shown that it was possible to use these AMPM vanishing points to generate microwave signals devoid of RIN-induced extra phase noise, the steep slope around such points make the requirement in laser and photodetector stability quite stringent.

We have successfully combined the signal from two photodetector illuminated by the same femtosecond laser where one of the photodetectors operates in positive AMPM while the other operates in negative AMPM regime to produce a combined device that is largely immune to AMPM conversion on a large range of impinging optical power. Our dual photodetector system relies on our cascaded Mach-Zender architecture pulse repetition rate multiplication device, previously reported in [8]. This device was originally designed to increase the repetition rate of a femtosecond laser, so as to increase the signal to noise of the photodetection of harmonics of the repetition rate, which substantially improved the white phase-noise floor achievable with such systems. A collateral benefit of these device is that they exhibit two optical ouput which can conveniently be used to drive two independent photodetectors. Coherent addition (with controlled amplitude and phase) of the signals from these photodetector allows realizing the low AMPM photodetection process.

We chose to operate both photodetectors near one of their AMPM vanishing point, although with opposite slopes of AMPM with reference to optical energy per pulse. This corresponds to using one photodetector at its first AMPM vanishing point and the second photodetector at its second AMPM vanishing point (as shown in figure 4). In this way, we realized a combined photodetection process with very low AMPM on a large range of illuminating optical power. The advantage of this technique is that very low level of tuning and stability is required to guaranty low AMPM induced extra phase noise in the produced microwave signal.

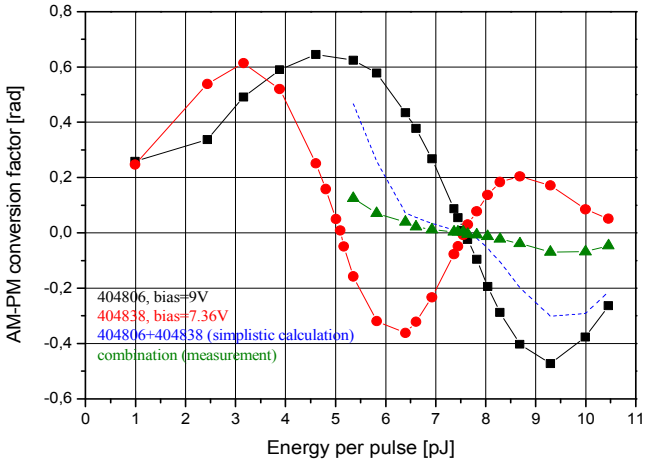

Figure 4. Amplitude phase conversion of photodetectors illuminated by femtosecond regime laser pulses for microwave generation at 12 GHz. The squares (black) curve is obtained at 9V bias for one of the photodetector. The circles (red) curve is obtained at 7.36V bias for another photodetector. Coherent addition of the two microwave signals from these two photodetectors produces the triangle (green) curve which exhibits low AMPM on a large range of impinging optical energy per pulse.

ACKNOWLEDGMENT

YLC thanks S. Seidelin for providing the phaselock that allowed timely completion of this contribution.

REFERENCES

[1] T. M. Fortier, M. S. Kirchner, F. Quinlan, J. Taylor, J. C. Bergquist, T. Rosenband, N. Lemke, A. Ludlow, Y. Jiang, C. W. Oates and S. A. Diddams, Nature Photonics 5, 425 (2011).

[2] J. Kim and F. X. Kärtner, Optics Letters 35, 2022 (2010).

[3] B. Lipphardt, G. Grosche, U. Sterr, C. Tamm, S. Weyers and H. Schnatz, IEEE Transaction on Instrumentation and Measurement 58, 1258 (2009).

[4] J. Millo, M. Abgrall, M. Lours, E. M. L. English, H. Jiang, J. Guéna, A. Clairon, M. E. Tobar, S. Bize, Y. Le Coq and G. Santarelli, Applied Physics Letters 94, 141105 (2009).

[5] J. Millo, R. Boudot, M. Lours, P. Y. Bourgeois, A. N. Luiten, Y. Le Coq, Y. Kersalé, G. Santarelli, Optics Letters 34, 3707 (2009).

[6] W. Zhang, Z. Xu, M. Lours, R. Boudot, Y. Kersalé, G. Santarelli, Y. Le Coq, Applied Physics Letters 96, 211105 (2010)

[7] W. Zhang, Z. Xu, M. Lours, R. Boudot, Y. Kersalé, A. N. Luiten, Y. Le Coq, G. Santarelli, IEEE Transaction on Ultrasonic Ferromagnetic and Frequency Control, 58, 886 (2011).

[8] A. Haboucha, W. Zhang, T. Li, M Lours, A. N. Luiten, Y. Le Coq and G. Santarelli, Optics Letters 36, 3654 (2011).

[9] D. D. Hudson, K. W. Holman, R. J. Jones, S. T. Cundiff, J. Ye, and D. J. Jones, Optics Letters 30, 2948-2950 (2005).

[10] Y. Nakajima, H. Inaba, K. Hosaka, K. Minoshima, A. Onae, M. Yasuda, T. Kohno, S. Kawato, T. Kobayashi, T. Katsuyama, and F. Hong, Optics Express 18, 1667 (2010).

[11] F. Quinlan T. M. Fortier, S. Kirchner, J. A. Taylor, M. J. Thorpe, N. Lemke, A. D. Ludlow, Y. Jiang, C. W. Oates and S. A. Diddams, Optics Letters 36, 3260 (2011).

[12] W. Zhang, M. Lours, M. Fischer, R. Holzwarth, G. Santarelli and Y. Le Coq, IEEE Transactions on Ultrasonic, Ferromagnetic and Frequency Control 59, 432 (2012).

[13] W. Zhang, T. Li, M. Lours, S. Seidelin, G. Santarelli and Y. Le Coq, Applied Physics B 106, 301 (2012).

[14] J. Millo, D. V. Magalhaes, C. Mandache, Y. Le Coq, E. M. English, P. G. Westergaard, J. Lodewyck, S. Bize, P. Lemonde and G. Santarelli, Physical Review A 79, 053829 (2009).

[15] S. T. Dawkins, R. Chicireanu, M. Petersen, J. Millo, D. Magalhaes, C. Mandache, Y. Le Coq, S. Bize Applied Physics B: Lasers and Optics, 99, 41-46 (2010).

[16] J. Taylor, S. Datta, A. Hati, C. Nelson, F. Quinlan, A. Joshi, and S. Diddams, IEEE Photonics Journal, 140, 2011.

[17] K. Wu, , P. P. Shum, S. Aditya, C. Ouyang, J. H. Wong, H. Q. Lam, K. E. K. Lee, Journal of Lightwave Technology, 29 (2011)

The new prediction algorithm for UTC: application and results

(Invited Paper)

Gianna Panfilo
International Bureau of Weights and Measures (BIPM)
Pavillon de Breteuil 92312 Sevres France
Email: gpanfilo@bipm.org

***Abstract*— A new quadratic prediction algorithm is used in UTC calculation starting from August 2011. The positive effects in term of long-term stability are already evident. The results obtained after the implementation of the new algorithm are presented and discussed.**

I. Introduction

The algorithm used for the calculation of the time scales at the BIPM is an iterative process that starts by producing a free atomic scale (EAL) from which the International Atomic Time (TAI) and the Coordinated Universal Time (UTC) are derived. Research into time-scale algorithms continues with the aim of improving the long-term stability of EAL and the accuracy of TAI. Recently, a new clock frequency prediction algorithm for EAL has been studied, validated and implemented for the monthly calculation of UTC. The new model takes into account the frequency drift or long-term aging affecting most of the participating atomic clocks. The frequency drift of each contributing clock is estimated with respect to the Terrestrial Time (TT), a time scale computed at the BIPM as an optimized frequency reference. Several tests performed using past data have shown that the new prediction model reduces the EAL frequency drift. As a consequence, an important improvement in the long-term stability of EAL is expected. The new frequency prediction algorithm has been implemented in the UTC calculation routine starting from September 2011. After few months, an improvement in the long-term performance of EAL is already clear. After the revision of the prediction algorithm, an improvement of the weighting routine seems necessary and is under study to better exploit the H-maser performances in the calculation of UTC. As the EAL goal is the calculation of a weighted average which shows long-term stability better than any of the contributing elements, its algorithm should provide higher weight to the clocks with better long-term stability. In the present EAL algorithm, the weight assigned to a clock is the reciprocal of the individual classical variance computed from the frequencies of the clock, with respect to EAL, on one year long time series. A maximum weight is set to avoid clocks take a predominant role. At the moment the weighting procedure does not take into account the prediction terms that is suitable to better weight the atomic clocks. In Sec. II the algorithms used to calculate UTC will be briefly reported, in Sec. III the new prediction algorithm will be described and presented. Sec. V presents the results and effects of the new prediction algorithm on the long-term stability of EAL, on TAI and on the weights distribution. Sec. VI reports a discussion on a possible new algorithm for the weighting routine.

II. Algorithms for UTC generation

The various time laboratories achieve a stable local time scale using individual atomic clocks or a clock ensemble. These clock readings are then combined at the BIPM through an algorithm designed to optimize the frequency stability and accuracy, and the reliability of the time scale beyond the level of performance that can be realized by any individual clock in the ensemble. An efficient algorithm is necessary for the statistical generation of the world reference time scale. The algorithm ALGOS [1]–[4] is used by the BIPM Time Department to generate the international reference UTC each month. The calculation of UTC using ALGOS is carried out in three steps:

- The free atomic time scale EAL is computed as a weighted average of about 400 free-running atomic clocks distributed world-wide. A clock weighting procedure has been designed to optimize the long-term frequency stability of the scale.
- The frequency of EAL is steered to maintain agreement with the definition of the SI second, and the resulting time scale is TAI. The steering correction is determined by comparing the EAL frequency with that of the primary frequency standards (PFS).
- Leap seconds are inserted to maintain agreement with the time derived from the rotation of the Earth. The resulting time scale is UTC.

Different algorithms can be considered depending on the requirements of the scale; for an international reference such as UTC, the requirement is extreme reliability and long-term frequency stability. UTC therefore relies on the largest possible number of atomic clocks of different types, located in different parts of the world and connected via a network, coordinated by the BIPM, that allows precise time comparisons between remote sites. Each month the differences between the international time scale UTC and the local time scales UTC(k) maintained at the contributing time laboratories are reported at 5-day intervals in an official document called BIPM *Circular T* [5]. ALGOS used until now in the BIPM Time Department

is under revision. The first accomplished step is the new prediction algorithm the second will be the revision of the weighting procedure.

III. Prediction Algorithm

In the generation of a time scale, prediction of atomic clock behaviour plays an important role and it is inserted in all time scale algorithms. In the establishment of the international time references UTC and TAI, the prediction algorithm is useful to avoid or minimize the frequency jumps of the time scale when a clock is added or removed from the ensemble or when its weight changes. By using the prediction we can remove or minimize the deterministic signatures (like frequency drift or aging) affecting the atomic clocks. Until July 2011 the linear prediction [2], [3], [6] had been used to describe the clock behaviour. This simple approach does not take into account the frequency drift (or the aging) affecting the atomic clock and the clock frequency is taken as being constant over a month interval for all types of clocks. As a consequence of this, EAL showed a significant frequency drift of about $-1.3\times 10^{-17}/day$ [9] with respect to TT(BIPM) the Terrestrial Time realized by the BIPM [7], [8]. This is due to the fact that UTC is calculated with data from about 400 clocks of which more than 270 are Caesium clocks 5071 (high performance tube) and more than 50 are H-masers from Symmetricom or Sigma Tau. Clocks of the same type come from the same manufacter and the deterministic signatures (frequency drift or aging) do not average out.

A. The new prediction algorithm

Starting from August 2011 (MJD 55774) a quadratic model is used to describe the atomic clock behaviour [9], [10]. The model takes into account the frequency drift affecting the H-masers and the long-term drift of caesium clocks. When considering two successive intervals of TAI calculation $I_{k-1}(t_{k-1}, t_k)$ and $I_k(t_k, t_{k+1})$ we impose several conditions on the prediction term $h_i'(t)$ at time t_k to avoid or minimize time and frequency jumps in the resulting time scale. The algorithm operates in a post-processing mode, treating as a whole, measurements taken over a basic period of T=30 or 35 days. For each one-month period, the results are the quantities $x_i(t_k + nT/6)$ (or $x_i(t_k + nT/7)$) with $n = 0, ..., 6$ (or $n = 0, ..., 7$) for each clock H_i. The correction term $h_i'(t)$ for clock H_i is the sum of three terms:

$$h_i'(t) = a_{i,I_k}(t_k) + B_{ip,I_k}(t)(t-t_k) + \frac{1}{2}C_{ip,I_k}(t)(t-t_k)^2 \quad (1)$$

The term index i identifies the clocks and the term index p corresponds to the values of the parameters "predicted" from the previous interval. To evaluate the parameters in (1) we assume that at time t_k the following conditions exist on h_i':

1) no time steps, by imposing the continuity to EAL;
2) no frequency steps, by imposing the continuity to the first derivative of EAL;
3) no change in frequency drift, by imposing the continuity to the second derivative of EAL.

We obtain a system of three equations with three unknowns and by solving this system we find that the relation (1) can be expressed as:

$$\widehat{h}_i'(t) = \widehat{a}_{i,I_k}(t_k) + \widehat{B}_{ip,I_k}(t-t_k) + \frac{1}{2}\widehat{C}_{i,I_{k-1}}(t_k - t_{k-1})(t-t_k) + \frac{1}{2}\widehat{C}_{ip,I_k}(t-t_k)^2 \quad (2)$$

The physical meanings of the terms present in (2) are:

- $\widehat{a}_{i,I_k}$ is the estimation of the time correction relative to EAL of clock H_i at date t_k
- $\widehat{B}_{ip,I_k}$ is the estimation of the frequency of clock H_i, relative to EAL, predicted for the period $[t_k, t]$
- $\widehat{C}_{ip,I_k}$ is the estimation of the frequency drift of the clock H_i, relative to TT(BIPM), predicted for the period $[t_k, t]$
- $\widehat{C}_{i,I_{k-1}}$ is the estimation of the frequency drift of the clock H_i, relative to TT(BIPM), for the period $[t_{k-1}, t_k]$.

Considering that $\widehat{C}_{i,I_{k-1}}$ is equal to $\widehat{C}_{ip,I_k}$ the prediction takes a more simple form:

$$\widehat{h}_i'(t) = \widehat{a}_{i,I_k}(t_k) + \widehat{B}_{ip,I_k}(t-t_k) + \frac{1}{2}\widehat{C}_{ip,I_k}(t_k - t_{k-1})(t-t_k) + \frac{1}{2}\widehat{C}_{ip,I_k}(t-t_k)^2 \quad (3)$$

Two very important aspects should be considered in this relation; first, the drift is constant during the calculation interval; and second, differently from the linear prediction model, the frequency does not remain constant during the interval. The relationship (3) describing the correction applied to the atomic clocks includes three parameters, the phase, the frequency and the frequency drift. A major issue is the estimation of the frequency drift. It was decided, based on past studies [9], to use TT(BIPM) as reference for the frequency drift estimation and to fix the length of the evaluation period equal to 4 months. More details about the parameter estimation can be found in [9]. The current weighting algorithm keeps the H-masers at the very low weight; the estimation of the drift could be refined whit a weighting procedure optimized for H-masers weight.

IV. Simulations results: the prediction algorithm applied to the past data

Tests have been performed on two data samples from 2006 and 2008 until 2010 to validate the new prediction algorithm. Fig.1 shows the different EALs calculated with data since 2006 and 2008 [9] (the corresponding MJDs at the beginning of 2006 and 2008 are 53734 and 54464) as well as those calculated by the linear method. The results obtained are very satisfactory, the frequency drift of EAL is almost completely removed in both cases and the results are independent of the starting date. After the application of the new prediction algorithm the improvement on the EAL long-term stability is evident. More details about the simulation results can be found in [9].

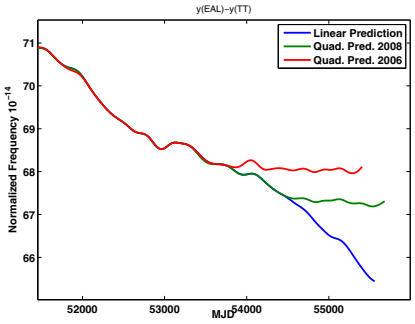

Fig. 1. $y(EAL) - y(TT)$ calculated by applying the linear prediction (blue line), the quadratic predictions starting in 2008 (green line) (MJD equal to 54464) and in 2006 (red line) (MJD equal to 53734).

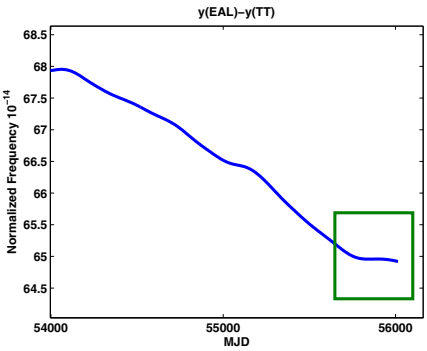

Fig. 2. The difference between $y(EAL)$ and $y(TT)$.

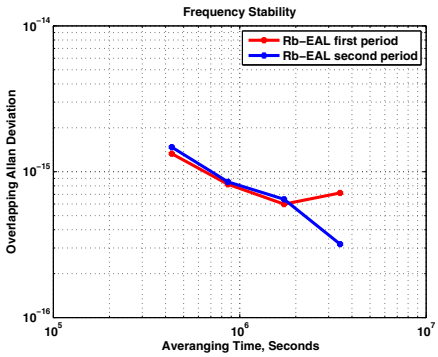

Fig. 3. Allan deviation of EAL with respect to the USNO rubidium fountain.

V. Application and Results of the New Prediction Algorithm on UTC Calculation

In this section the results obtained by applying the quadratic model to describe the atomic clock behaviour for UTC calculation are reported. Special consideration will be given to the effects of the new algorithm on the EAL long-term stability, on TAI and on the weight distribution. Since the starting of the routine calculation of UTC with the new frequency prediction model (8 month of data from September 2011) a clear effect stopping the drift is observed.

A. Effect on the EAL long-term stability

To evaluate the effect of the new prediction algorithm on EAL we need a very stable reference. For this reason two different results will be presented; first the frequency of EAL will be compared to the frequency of TT(BIPM), a time scale optimized for frequency accuracy; and second, data coming from the most stable of the USNO (United States Naval Observatory) Rubidium fountains [11] are used to evaluate EAL long-term stability. The USNO Rubidium fountains are reported to the BIPM as clocks and are considered a good reference to estimate the improvement of EAL with the introduction of the new prediction algorithm. The choice of an external reference as the USNO Rubidium fountain is due to the fact that EAL and TT(BIPM) are strictly correlated at short-term (until 1 month). By analyzing EAL with respect to TT(BIPM) we can observe the absence of the frequency drift but we can't have information on the long-term stability of EAL due to the correlation. In Fig. 2 the difference between the frequency of EAL and TT(BIPM) ($y(EAL) - y(TT)$) is reported. In the green square the results obtained from the application of the quadratic prediction (MJD equal to 55774) are highlighted. A positive effect on EAL behaviour is already evident even if only 8 months of data are available. The frequency drift affecting EAL, after the application of the new prediction algorithm is almost completely removed. Considering the results obtained by the simulations and reported in Fig. 1 the behaviour of EAL should remain the same with some noise. Considering the data coming from the USNO Rubidium fountains as clocks data at 5 day interval, the difference between EAL and these data can be obtained. The stability results reported in Fig. 3 are obtained by splitting the data in two parts. In the first part (MJD from 55634 to 55769) EAL is calculated with the linear prediction, in the second part (MJD from 55774 to 55984) EAL is calculated with the quadratic prediction. The results are reported in Fig. 3 with red and blue lines respectively. The improvement in the long-term stability of EAL is already clear; the value of the Allan deviation at 40 days is 3.2×10^{-16} from the application of the new prediction prediction model, whilst with the old model it was 7.2×10^{-16}. The short-term value at 5 days is dominated in both cases by the time transfer noise.

B. Effect of TAI accuracy

TAI is a realization of coordinate time TT. Section 4 of *Circular T* [5] reports the fractional deviation d of the scale interval of TAI from that of TT based on all available primary frequency standard (PFS) measurements; Fig. 4 shows the values of d as published in *Circular T*. The frequency of EAL has been steered monthly by applying a correction at a maximum value of 0.7×10^{-15} until two months before the application of the new prediction algorithm. Since MJD 55739 a correction of 0.5×10^{-15} is applied. The green square highlights the results obtained from the application of the new prediction model. The value of d is approaching zero with some noise. Considering the results obtained by the simulations and published in [9] this value should approach

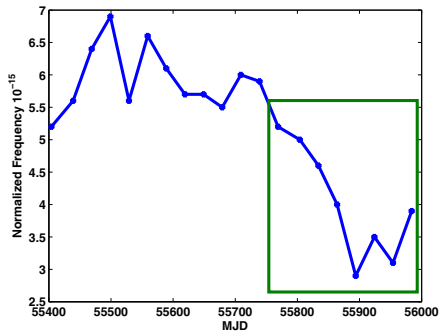

Fig. 4. The values of d as published in *Circular T*

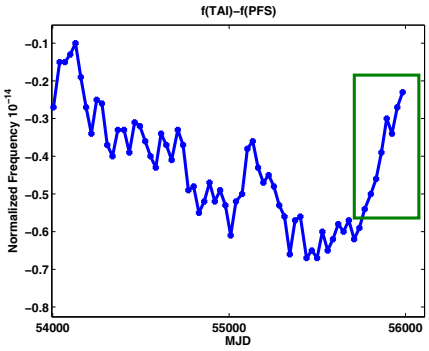

Fig. 5. The difference between $y(TAI)$ and $y(PFS)$

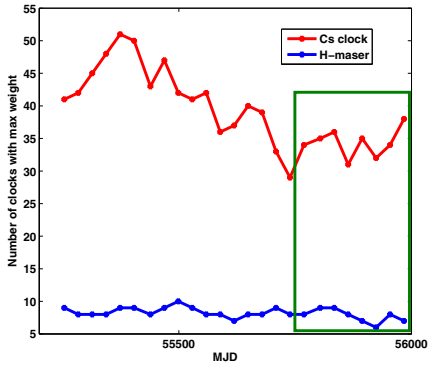

Fig. 6. Number of the clocks (H-masers and caesium clocks) with the maximum weight.

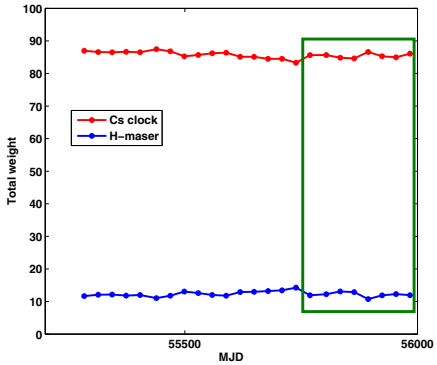

Fig. 7. Total weight in percentage term for the H-masers (blue line) and caesium clocks (red line).

zero in the term of few months and should remain close to zero with some noise. When the frequency drift of the EAL was dominant the noise affecting this value was not clearly characterized. It will be of interest to perform a statistical analysis of the noise after the elimination of EAL frequency drift, when the zero value will be approached.

To conclude the analysis also the difference between $y(TAI)$ and $y(PFS)$ is analyzed and reported in Fig. 5. This difference should be close to zero, and it was not the case before the application of the new prediction algorithm. In the green square in Fig. 5 the values obtained from the application of the new prediction algorithm are highlighted. After 8 months of application of the new prediction algorithm the behaviour of the frequency of TAI has changed. The difference between $y(TAI)$ and $y(PFS)$ was about -6×10^{-15} with an increasing trend; with the new algorithm is become -2×10^{-15} and approaches zero with some noise as expected. In the term of few months this value should be close to zero and remain there.

C. Effect on the weight distribution

To complete the analysis of the effect of the new algorithm on UTC we studied the impact of the new frequency prediction on the weight of the clocks. We concentrated on the case of caesium and H-maser clocks at the maximum weight. Fig.6 plots with red and blue lines the number of caesium clocks and H-masers at maximum weight respectively. Fig. 7 shows the total weight (in percentage) of the same clocks. In both figures the green square highlights the results obtained since the application of the new prediction algorithm. From these results, we conclude that the use of the new frequency prediction has a negligible effect on the clock weights justified by the way they are calculated in ALGOS. Data used to evaluate the weights are the differences between EAL and the readings of the clock H_i; the prediction is not taken into account at this stage in the algorithm.

VI. A POSSIBLE NEW DEVELOPMENT FOR THE WEIGHTING ALGORITHM

In time-scale algorithms, clock weights are generally chosen as the reciprocals of a statistical quantity which characterizes their frequency stability, such as a frequency variance (classical variance, Allan variance, etc.) [12], [13]. If strictly applied, this gives a time scale which is more stable than any contributing element. In the EAL computation, the weight attributed to a clock is the reciprocal of the individual classical variance computed from the frequencies of the clock, relative to EAL, estimated over the current 30 day interval and over the past eleven consecutive 30 day intervals (12 consecutive 30 day intervals are considered). The weight determination thus

uses clock measurements covering a full year. This reduces the weight of clocks that are both highly sensitive to seasonal changes and that show a large frequency drift as hydrogen masers. It thus helps to improve the long-term stability of EAL. A maximum weight is fixed to avoid a clock having a predominant role. In the current weighting algorithm the weight attributed to a clock reflects its long-term stability. The clocks with deterministic signatures like frequency drift or aging are de-weighted and considered "bad" clocks. The H-masers have a small weight due to frequency drift affecting their behaviour. The current weighting algorithm does not take into account the prediction term used in the time scale ensemble; the difference between EAL and the clock H_i not affected by the clock prediction is used to evaluate the weight. The BIPM Time Department is studying a possible new weighting strategy to take into account the prediction used in EAL calculation. The main idea is to consider that a good clock is a predictable clock [14]. By using the prediction the deterministic signatures affecting the atomic clocks, like the frequency drift or aging, are eliminated or minimized. The H-masers are characterized by a very important frequency drift that usually can be predicted with a very low uncertainty. By taking into account the prediction the H-masers will contribute to the time scale ensemble with an important weight without degrading the long-term stability of EAL. A possible way to do that is by analyzing the difference between the readings of the clocks H_i and their prediction h_i' instead of the difference between EAL and the readings of the clock H_i. Many attention should be put in avoiding the frequency drift of the H-masers degrading the EAL long-term stability of EAL.

VII. Conclusion

Starting from August 2011 (MJD 55774) a new prediction algorithm has been officially used for UTC calculation. The mathematical model embedded in the algorithm takes into account the correct treatment of the frequency drift. By the moment no change in the weighting strategy has been implemented. After 8 months of application of the new algorithm the positive effects are observed in term of EAL long-term stability; in fact the frequency drift of EAL is almost completely removed. It was observed that the new prediction algorithm has no impact on the weights; a revision of the weighting algorithm is under study and a new procedure should increase the impact of the H-masers in the time scale ensemble. In the framework of the Rapid UTC pilot project [15] data clock and time transfer data are available at 1 day interval. At 1 day interval the dominant noise is given by the time transfer system provided that the H-masers are correctly used. In this situation it could be interesting to implement a new weighting algorithm to observe the short term contribution of the H-masers to the ensemble.

Acknowledgment

The author would like to thank the BIPM Time Department for the helpful discussions and collaborations.

References

[1] Panfilo G and Arias E-F 2010 Algorithms for TAI *UFFC* **57** (1) 140-150.
[2] Thomas C Wolf P and Tavella P 1994 Time Scales, *BIPM Monographie 94/1*.
[3] Guinot B and Thomas C 1988 Establishment of international atomic time *Annual Report of the BIPM Time Section* **1**.
[4] Tavella P and Thomas C 1991 Comparative study of time scale algorithms *Metrologia* **28** (2) 57-63.
[5] Circular T: http://www.bipm.org/jsp/en/TimeFtp.jsp?TypePub=publication
[6] Guinot B 1987 Some properties of Algorithms for atomic time scales *Metrologia* **24** 195-198.
[7] Azoubib J, Graveaud M., Guinot B. 1977 Estimation of the scale unit duration of time scales *Metrologia* **13** 87-93.
[8] Petit G 2003 A new realization of Terrestrial Time *Proc. 35th Precise Time and Time Interval (PTTI) meeting*, pp. 307-316.
[9] Panfilo G, Harmegnies A, Tisserand L. A new prediction algorithm for the generation of International Atomic Time. Metrologia, 2012, 49, n. 1, pp. 49-56.
[10] Panfilo G and Arias E-F 2010 Studies and possible improvements on EAL algorithm *UFFC* **57** (1) 154-160.
[11] Peil S, Crane S, Hanssen J, Swanson T-B and Ekstrom C-R 2011 Measurements with multiple operational fountain clocks. *Proc. FCS-IEEE*, San Fransisco, CA (USA).
[12] Thomas C and Azoubib J 1996 TAI computation: study of an alternative choice for implementing an upper limit of clock weights *Metrologia* **33** 227-240.
[13] Azoubib J 2000 A revised way of fixing an upper limit to clock weights in TAI computation *Proc. 32nd Annual Precise Time and Time Interval (PTTI) Meeting, Reston (USA)*, pp. 195-210.
[14] Levine J 1999 Introduction to time and frequency metrology *Review of Scientific Instruments*, Vol. 70, No. 6, pp.2567-2596.
[15] Petit G, Arias E-F, Harmegnies A, Jiang Z, Konat H, Lewandowski W, Panfilo G, Tisserand T 2012 UTCr: a rapid realization of UTC. *Proc. EFTF, (Gothenburg(Sweden))*.

Real-Time Assessment of Dynamic Allan Deviation and Dynamic Time Deviation

Andrzej Dobrogowski, Michal Kasznia
Chair of Telecommunication Systems and Optoelectronics
Poznan University of Technology
Poznan, Poland
dobrog@et.put.poznan.pl, mkasznia@et.put.poznan.pl

***Abstract*— In this paper the methods enabling real-time assessment of dynamic Allan deviation and dynamic time deviation are presented. The idea of real-time analysis of timing signals using dynamic approach is described first. Then the algorithms of real-time computation of dynamic parameters are presented. The results of experimental tests of the methods proposed for different conditions are presented and discussed.**

I. INTRODUCTION

Allan deviation ADEV and time deviation TDEV are commonly used for describing the quality of synchronization signals in the telecommunication network [1, 2, 3]. The parameters allow the variations of time interval provided by the synchronization signal to be assessed and the type of phase noise affecting the signal to be recognized. The characterization of the timing signal using dynamic parameter (dynamic Allan deviation, DADEV) [4, 5] allows to recognize the variations of the phase noise affecting the analyzed signal. This approach was extended by the authors of this paper. The dynamic time deviation (DTDEV) was introduced and the time effective methods of calculation of the dynamic parameters were proposed [6, 7].

The estimates of the parameters are computed for a series of observation intervals using the sequence of time error samples previously measured at some network interface. The evaluation of the synchronization signal is commonly a two-stage process. The measurement of the sequence of time error samples is followed then by the calculation of the parameter's estimate. Application of the methods of real-time computation enables to simplify the evaluation process [10, 11]. Real-time tracking of the parameter value of the signal delivers timely information about behavior of the signal source and may result in a suitable activity, for example some reaction of the network maintenance team (as network reconfiguration could be the cause of the parameter variations).

In the paper the methods of the real-time computation of the dynamic parameters are proposed. These methods allow to compute the estimates of dynamic Allan deviation and dynamic time deviation (which characterizes of more complex estimator's formula) in the real time, during the time error measurement process, simultaneously for a set of observation intervals.

The computation of the dynamic parameters requires a specific arrangement of data. We can consider overlapping and non-overlapping segments of data used for calculation in order to obtain a set of curves presented in the form of 3D plot. The arrangement of the segments depends on the number of segments, their length and the length of the whole data sequence. This arrangement (overlapping or non-overlapping segments) influences the method of data organization applied for the real-time computation.

In the paper the results of experimental tests of the methods proposed for different conditions are presented. Different arrangements of the data segments simultaneously analyzed were considered.

II. IDEA OF DYNAMIC PARAMETERS

The idea of dynamic parameters is quite simple. Instead of one curve representing the values of ADEV or TDEV as a function of observation interval τ, the set of the curves plotted in the form of three-dimensional graph as a function of observation interval τ and time t is considered. As a result we can recognize the changes of the type of phase noise affecting analyzed timing signal. The changes of the slope of the parameter's curve indicate the changes of the noise type [4, 5].

In order to obtain such form of graph, the following computation procedure must be performed. First, the data sequence (time series of time error measured at some network interface) is divided into equal segments (slices) with the length of T_s. We can consider overlapping data segments (Fig. 1) and non-overlapping data segments (Fig. 2). Then the calculation of the parameter's value for a required range of observation intervals for each data segment is done. The results of calculation are plotted in a form of three-dimensional graph (Fig. 3).

This work was supported by the National Science Centre in the frame of the project N N517 470540.

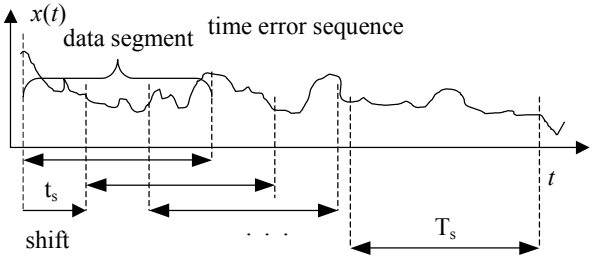

Figure 1. Overlapping segments of time error sequence

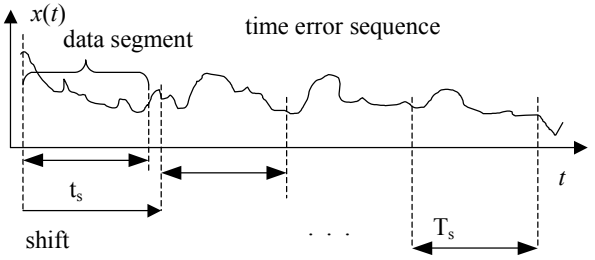

Figure 2. Non-overlapping segments of time error sequence

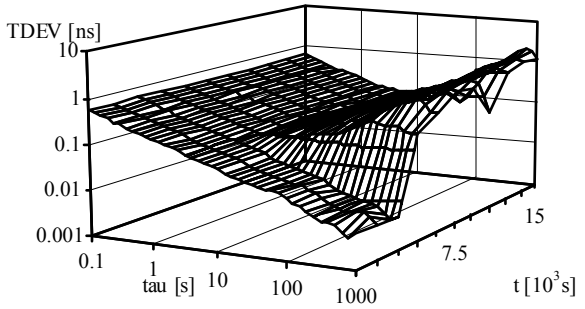

Figure 3. Example plot of dynamic time deviation

The procedure of dynamic ADEV and dynamic TDEV calculation depends on the set of quantities. These are: length of the whole data series T, length of the data segments created within the whole data series T_s, time shift between the initial points of the data segments t_s, and range of observation intervals ($\tau_{min} - \tau_{max}$).

The relation between the whole data series length, segments' lengths and the time shift t_s determines the number of segments and the arrangement of the segments (overlapping or non-overlapping). We must also take into consideration the relation between T_s and the maximum observation interval τ_{max}. In practice, the value of the parameter's estimate can be calculated, when the length of data series (in this situation: segment's length) is two times longer for ADEV and three times longer for TDEV. According to the telecommunication standards and recommendations, the length of data sequence used for ADEV or TDEV calculation must be 12 to 15 times longer than the maximum observation interval τ_{max} [1, 2, 3]. The minimum observation interval τ_{min} is determined by the sampling interval τ_0: τ_{min} must be three times longer than τ_0.

III. Real-Time Computation of ADEV and TDEV

Allan deviation and time deviation are computed based on the averaging of second differences of the phase process $x(t)$ of the analyzed timing signal. We can assume for the telecommunication applications, in the case of negligible influence of frequency drift, that ADEV and TDEV are estimated based on the time error function measured between the analyzed timing signal and the reference one [8].

The formulae for the estimators of Allan deviation ADEV and the time deviation TDEV take the form:

$$\hat{ADEV}(\tau) = \sqrt{\frac{1}{2n^2\tau_0^2(N-2n)}\sum_{i=1}^{N-2n}(x_{i+2n} - 2x_{i+n} + x_i)^2} \quad (1)$$

$$\hat{TDEV}(\tau) = \sqrt{\frac{1}{6n^2(N-3n+1)}\sum_{j=1}^{N-3n+1}\left[\sum_{i=j}^{j+n-1}(x_{i+2n} - 2x_{i+n} + x_i)\right]^2} \quad (2)$$

where $\{x_i\}$ is a sequence of N samples of time error function $x(t)$ taken with interval τ_0; $\tau = n\tau_0$ is an observation interval. For TDEV computation the estimator formula (2) is changed in order to simplify the summing [8, 9] and takes the form:

$$\hat{TDEV}(n\tau_0) = \sqrt{\frac{1}{6}\cdot\frac{1}{N-3n+1}\cdot\frac{1}{n^2}\sum_{j=1}^{N-3n+1}S_j^2(n)} \quad (3)$$

where

$$S_j(n) = S_{j-1}(n) - x_{j-1} + 3x_{j+n-1} - 3x_{j+2n-1} + x_{j+3n-1} \quad (4)$$

$$S_1(n) = \sum_{i=1}^{n}(x_{i+2n} - 2x_{i+n} + x_i) \quad (5)$$

When computing in the real time, we do not have access to the time error samples indexed by $i+n$ or $i+2n$ for the current time instant described by index i, because these samples have not been measured yet. We have access to the sample currently measured (for the current sampling instant i) and the samples measured earlier (with indexes smaller than i) and saved in the memory of the measurement equipment. Therefore, the indexes in formulae for ADEV and TDEV estimators should be changed in the case of real-time calculation.

The rearrangement of indexes for both estimators was performed in [10]. As a result we have obtained the ADEV estimator's formula for a current instant i in the form depending on the sum of squares of second differences computed for the instant $i-1$

$$A\hat{D}EV_i(n\tau_0)=\sqrt{\frac{1}{2n^2\tau_0^2(i-2n)}\left(A_{i-1}(n)+(x_i-2x_{i-n}+x_{i-2n})^2\right)} \quad (6)$$

were $A_i(n)$ is the sum of squares of second differences of time error samples

$$A_i(n)=\sum_{j=2n+1}^{i}\left(x_j-2x_{j-n}+x_{j-2n}\right)^2, i>2n \quad (7)$$

The rearrangement of time deviation estimator is a little more complex than for Allan deviation [10]. After changing the indexes with the use of the simplified formula (3-5), we have obtained:

$$T\hat{D}EV_i(n\tau_0)=\sqrt{\frac{1}{6}\cdot\frac{1}{i-3n+1}\cdot\frac{1}{n^2}S_{ov,i}(n)} \quad (8)$$

where $S_{ov,i}(n)$ is the overall sum updated for each sample i, given in the form:

$$S_{ov,i}(n)=S_{ov,i-1}(n)+S_i^2(n) \quad (9)$$

where

$$S_i(n)=S_{i-1}(n)-x_{i-3n}+3x_{i+2n}-3x_{i+n}+x_i, i>3n \quad (10)$$

$$S_{3n}(n)=\sum_{j=2n+1}^{3n}\left(x_j-2x_{j-n}+x_{j-2n}\right), j>2n \quad (11)$$

Finally, the operations of TDEV computation for i-th sampling interval are performed using the formula (12) [10]. As a result of the rearrangement of the parameters' formulae, in order to compute ADEV and TDEV for a current sampling instant i and given observation interval $\tau=n\tau_0$, we need the values of appropriate sum $A_{i-1}(n)$, $S_{ov,i-1}(n)$, and $S_{i-1}(n)$, currently measured sample x_i and the samples x_{i-n}, x_{i-2n}, and x_{i-3n} previously measured and stored in the memory.

The formulae of the parameters given in the forms presented above allow us to perform the computation in the real time, during the time error measurement process. The calculation can be performed jointly for both parameters considered, as well as for single parameter [11]. The course of operations is as follows:

1. Measure a new time error sample and store it in a data file.
2. Compute the appropriated differences for a given n (observation interval $\tau=n\tau_0$) using the current sample, and the samples measured n, $2n$, or $3n$ sampling intervals earlier.
3. Update the appropriated sums.
4. Compute current averages and their square roots.
5. Execute Steps 2-4 for successive larger observation intervals (larger n).
6. Return to Step 1 (measure a new sample).
7. When the measurement is finished, the values of the parameter's estimate for the observation intervals considered are known.

The computations of ADEV and TDEV start when the sample no. $2n$+1 has been measured. The first value of ADEV estimate can be computed at this instant. However, for the TDEV the computation of the internal sum $S_i(n)$ only just starts. The first value of TDEV can be computed after the sample no. $3n$+1 has been measured. The example of the joint real-time computation process is presented in Fig. 4 [11].

$$T\hat{D}EV_i(n\tau_0)=\sqrt{\frac{1}{6}\cdot\frac{1}{i-3n+1}\cdot\frac{1}{n^2}\left[S_{ov,i-1}(n)+(S_{i-1}(n)-x_{i-3n}+3x_{i-2n}-3x_{i-n}+x_i)^2\right]} \quad (12)$$

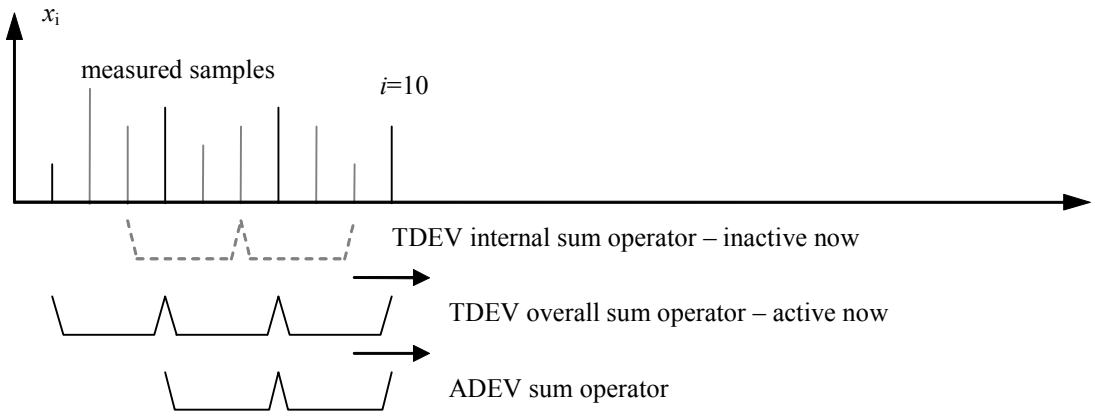

Figure 4. Real-time TDEV and ADEV computation for observation interval $3\tau_0$, sample no. 10 have been measured, ADEV sum operator is active, TDEV internal sum operator is inactive, TDEV overall sum operator is active

IV. REAL-TIME COMPUTATION OF DYNAMIC PARAMETERS

The computation methods presented in the previous section can be useful for the real-time assessment of dynamic parameters. The final result of computation of dynamic ADEV or dynamic TDEV contains the results of computation of parameter performed for particular data segments. In the case of *off-line* computation (performed after the measurement of time error series), we can consider the analysis of each data segment independently regardless of whether we are dealing with overlapping or non-overlapping data segments. When computing in the real time simultaneously for several observation intervals and several data segments, all necessary operations related with the time error sample just measured should be performed in the time period between two sampling instants, i.e. during the sampling interval τ_0. Therefore the computations for non-overlapping and overlapping data sequences will be considered separately.

A. Computation for non-overlapping data segments

We consider non-overlapping data segments when the time shift t_s between the initial points of successive segments is equal to or greater than the length of the segments T_s. In this case each segment can be analyzed independently during the real-time computation process of dynamic parameters. This process will run in the same way as the real-time computation process of usual Allan deviation or time deviation regarding that for each segment a new line of the three-dimensional graph is obtained. Only one set of observation intervals is analyzed for one sampling instant. The scheme of the real-time computation is presented in Fig. 5. The data segments (grey boxes) are successively analyzed. The operators of ADEV and TDEV sums (black and white lines) run along the incrementing data sequence within analyzed data segment (dark grey box).

B. Computation for overlapping data segments

The arrangement with overlapping data segments appears when the time shift t_s between the initial points of successive segments is shorter than the length of the segments T_s. In this case more than one set of observation intervals have to be analyzed for one sampling instant – each set is related with different data segment. The necessary operations performed within one sampling interval can be executed in different ways. First method can be described as "data segment first". The computations are performed for all observation intervals within one data segment. Then the next overlapping data segments are considered independently. The configuration of this order of computation is presented in Fig. 6. Detailed procedure for this method will be as follows:

1. Read TE sample from the TE meter and store it in the data file.
2. Read TE samples measured n, $2n$ or $3n$ sampling intervals earlier from data file.
3. Compute parameters' values according to (6) and (12) for first data segment.
4. Execute Steps 2 and 3 for successive longer observation intervals (greater n).
5. Execute Steps 2-4 for successive overlapping data segments.

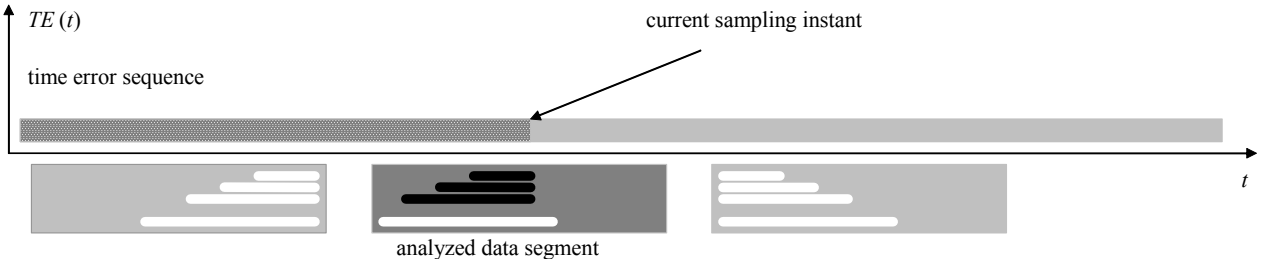

Figure 5. Real-time computation for non-overlapping data segments; dark grey box – analyzed data segment, black and white lines – ADEV and TDEV sum operators (active – black line, inactive – white line)

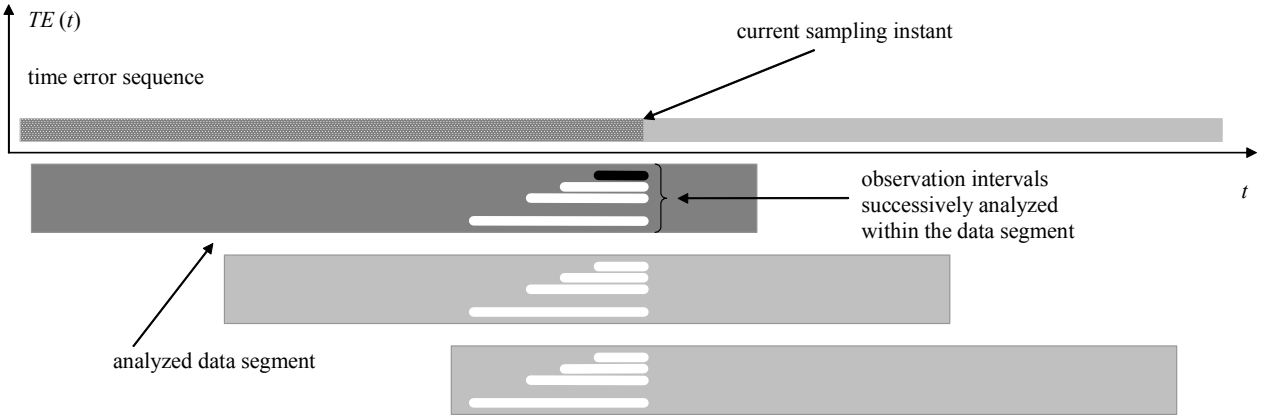

Figure 6. Real-time computation for overlapping data segments according to the rule "segment first"; dark grey box – analyzed data segment, black and white lines – ADEV and TDEV sum operators (analyzed operator – black line, waiting for analysis – white line)

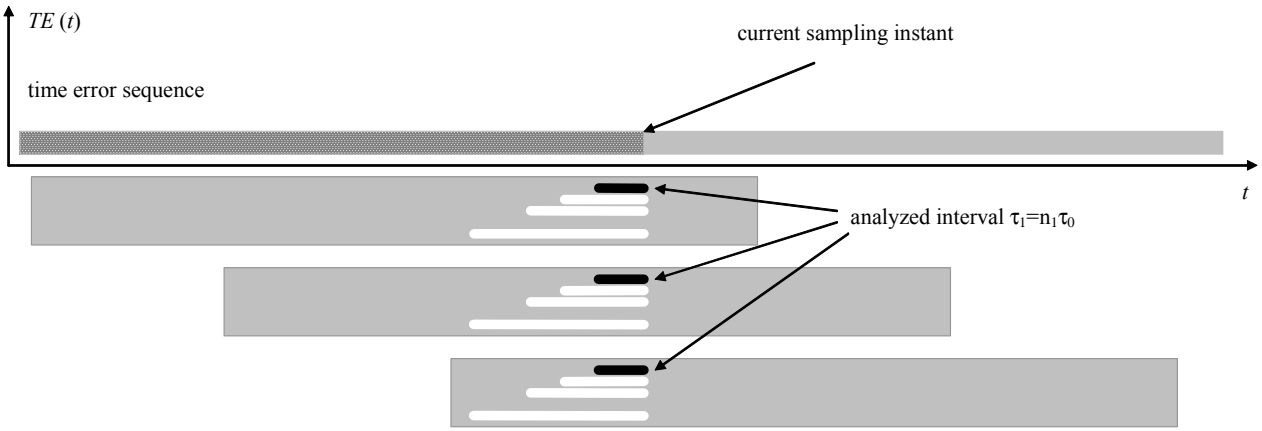

Figure 7. Real-time computation for overlapping data segments according to the rule "observation interval first"; black and white lines – ADEV and TDEV sum operators (analyzed operator – black line, waiting for analysis – white line)

Second method can be described as "observation interval first". The computations for the shortest observation interval τ_{min} for all segments (overlapping for this sampling instant) are performed first. Then successive longer observation intervals (for a greater n) are analyzed. The configuration of this order of computation is presented in Fig. 7. Detailed procedure for this method will be as follows:

1. Read TE sample from the TE meter and store it in the data file
2. Read TE samples measured n, $2n$ or $3n$ sampling intervals earlier from the data file.
3. Compute parameters' values according to (6) and (12) successively for each overlapping data segment for current n.
4. Execute Steps 2 and 3 for successively longer observation intervals (greater n).

The analysis of the observation interval $\tau=n\tau_0$ for a current sampling instant i according to the formula (6) and (12) requires the time error samples just measured and the samples measured n, $2n$, and $3n$ sampling instants earlier and stored in the equipment memory. If a personal computer is used to control of measurement process, the time error samples are stored in the form of data file on the hard drive. The time used for the data access is the critical issue in the real-time computation process. The second method of computation (interval first) gives us an advantage, because it allows to use the same samples (read using one procedure for a given n) for many overlapping data segments. Another solution, that effectively saves the time of data access, is creation of a buffer in the memory in order to store recently measured time error samples. All computational operations according to (6) and (12) will be performed on the samples stored in this buffer, which will reduce the time of data access. The buffer should have the length of $3n_{max}$ (where $\tau_{max}=n_{max}\tau_0$ is the maximum observation interval considered), in order to store all samples necessary to computation.

V. Results of Experiment

The methods of real-time computation of dynamic Allan deviation and dynamic time deviation were tested in the experiment. The experiment was realized similarly as the tests of real-time ADEV and TDEV computation methods presented in [10, 11]. The calculations were performed *off-line* with the imitation of *on-line* work. The data sequence contains time error samples taken with the sampling interval $\tau_0=1/30$ s during the time of 20000 s.

The calculations were performed for 41 observation intervals (10 intervals per decade), arranged in the logarithmic scale in a range between $\tau_{min}=0.1$ s (n=3) and $\tau_{max}=1000$ s (n=30000).

Three arrangements of overlapping data segments were considered:

A. 21 segments having the length $T_s=4000$ s with the shift 800 s (maximum 5 overlapping segments analyzed simultaneously);
B. 21 segments having the length $T_s=8000$ s with the shift 600 s (maximum 12 overlapping segments analyzed simultaneously);
C. 21 segments having the length $T_s=10000$ s with the shift 500 s (maximum 20 overlapping segments analyzed simultaneously).

Three personal computers with Intel Pentium IV 3.0 GHz, Intel Core 2 Quad 2.83 GHz, and Intel Core i7 3.2 GHz microprocessors were used in the experimental tests. The maximum time used for calculation within one sampling interval was the observed quantity. We have assumed that this time cannot exceed the length of sampling interval $\tau_0=1/30$ s = 33.3… ms.

The computations were performed using the rules "segment first" and "observation interval first", as well as the method with buffering of time error samples. The results of experimental tests are presented in the Table I. The best results (the shortest computation time) were obtained using the method with buffering of the time error samples. The method "observation interval first" have proved their advantage over the method "segment first". However, the time results were satisfactory for all cases considered. The maximum time spent for computation within one sampling interval does not exceed the length of considered sampling interval 1/30 s.

TABLE I. MAXIMUM TIME OF COMPUTATION FOR ONE SAMPLING INSTANT (IN MILLISECONDS)

Segments arrangement	Type of computer								
	Pentium IV			Core2 Quad			Core I7		
	segment first	*interval first*	*buffering*	*segment first*	*interval first*	*buffering*	*segment first*	*interval first*	*buffering*
A	2.39	0.65	0.06	0.99	0.28	0.04	0.96	0.27	0.03
B	6.83	0.70	0.11	2.79	0.31	0.07	2.77	0.30	0.06
C	10.06	0.72	0.15	4.17	0.32	0.09	4.14	0.31	0.07

The time results obtained in the experiment show that there is some reserve of computational power of the tested equipment. One can expect good results (maximum time not exceeding the length of sampling interval) for wider range and greater number of observation intervals, as well as for greater number of overlapping data segments than the quantities considered in the experiment.

VI. CONCLUSIONS

The results of the experimental tests have proved the ability of joint real-time computation of the dynamic Allan deviation and dynamic time deviation.

The real-time computation of the dynamic parameters can be performed jointly simultaneously for numerous series and wide range of observation intervals for different arrangements of data segments: for non-overlapping as well as for overlapping data segments.

The methods of real-time computation of the dynamic Allan deviation and dynamic time deviation can be very useful tools for analysis of the behavior of synchronization signals.

REFERENCES

[1] ETSI EN 300 462, "Generic requirements for synchronization networks" (1998).

[2] ITU-T Rec. G.810, "Considerations on timing and synchronization issues" (08/96).

[3] ANSI T1.101-1999, Synchronization interface standard.

[4] L. Galleani, P. Tavella, "The characterization of clock behavior with the dynamic Allan variance," Proc. of the 2003 IEEE International Frequency Control Symposium and 17th European Frequency and Time Forum, pp. 239-244, Tampa, USA, 5-8 May 2003.

[5] L. Galleani, P. Tavella, "The dynamic Allan variance," IEEE Trans. on Ultrasonics, Ferroelectrics, and Frequency Control, vol. 53, pp. 450-464, No. 3, 2009.

[6] A. Dobrogowski, M. Kasznia, "Time effective methods of calculation of dynamic parameters of synchronization signal," Proc. of the 18th European Frequency and Time Forum, Guildford, UK, 5-7 April 2004.

[7] A. Dobrogowski, M. Kasznia, „Dynamic parameters of synchronization signals for non-overlapping and overlapping data segments", Proceedings of the 19th European Frequency and Time Forum, pp. 509-514, Besancon, France, 21-24 March 2005.

[8] S. Bregni, Synchronization of Digital Telecommunications Networks, J. Wiley & Sons, 2002.

[9] M. Kasznia, "Some approach to computation of ADEV, TDEV and MTIE," Proc. of the 11th European Frequency and Time Forum, pp. 544-548, Neuchatel, 4-6 March 1997.

[10] A. Dobrogowski, M. Kasznia, "Real-time assessment of Allan deviation and time deviation," Proc. of the 2007 IEEE International Frequency Control Symposium Jointly with the 21st European Frequency and Time Forum, pp. 887-882, Geneva, 29 May – 01 June 2007.

[11] A. Dobrogowski, M. Kasznia, "Joint real-time assessment of Allan deviation and time deviation," Proc. of 22nd European Frequency and Time Forum, Toulouse, France, 22-25 April 2008.

Cramer-Rao-Bounds for Cross-Spectrum Measurements of Oscillator Phase Noise

Michael Nebel, Berthold Lankl
University of the Federal Armed Forces
Institute for Communications Engineering
Munich, Germany
Email: michael.nebel@unibw.de

***Abstract*—The cross-spectrum method is one of the best ways to measure the phase noise of an oscillator. Basically, the phase noise of a device-under-test oscillator is measured using two identical measurement circuits each with a reference oscillator which are synchronized by a phase-locked loop. In this paper, the exact Cramer-Rao-Bounds for the estimation of the oscillator phase noise power spectral density are given and efficient estimators are determined using the maximum-likelihood approach. Furthermore, our measurement system is presented where we discuss crucial points in the practical implementation. Finally, several measured results are shown where we also present a possibility to use an a-priori measurement of the system's background noise to improve the measurement precision or to reduce the measurement time.**

I. Introduction

Oscillator phase noise is a crucial factor in lots of communication systems. For example, it can lead to problems during the start-up synchronization of a GPS receiver [1] or it can directly degrade the bit error rate (BER) of an OFDM system [2]. Thus, it is desirable to develop oscillators with very low phase noise. There are a lot of different strategies to do so using heuristic approaches but also methods based on fundamental theories. However, in the end it is inevitable to be able to measure the actual phase noise level of the designed oscillator. Several well-known possibilities exist for this purpose as for example described in [3]. Moreover, there are also newer approaches such as the shifter-less delay line method published in [4]. However, the most precise method is the so-called cross-correlation measurement [5]. Here, two identical measurement branches are used and a cross-correlation is carried out to eliminate the noise coming from the measurement circuits. Using this technique, it is possible to measure the phase noise originating from a device-under-test (DUT) even if it is much lower than that being added by the measurement setup. Of course, this big advantage comes with high effort during the development of the measurement layout and during the calibration of the system. In this paper, some fundamental aspects of the phase noise estimation are discussed. Furthermore, we present our measurement setup and we give some exemplary measurements to receive an impression of the system's performance. Thus, the paper is organized as follows: first, some basics concerning the theory of phase noise in oscillators and the principal relationships and equations of cross-correlation measurement are briefly discussed in section II. Furthermore, in section III we derive the Cramer-Rao-bounds (CRB) as a lower bound for the estimation of the desired quantities (i.e. the power spectral densities of the DUT's phase noise and of the background noise). Moreover, the corresponding efficient estimators are derived using the maximum-likelihood approach. Our measurement setup is then discussed in section IV where we also explain some practical points which turned out to be important during the realization of the system. Finally, several measured results are presented in section V where different correlation times were used. In the end, we also show the benefit of using a-priori knowledge of the system's background noise during the estimation of the DUT's phase noise characteristic.

II. Basics

First of all, some basics concerning the theory of phase noise in oscillators and its measurement by the cross-correlation method are to be briefly recapitulated in the following section.

A. Theory of phase noise in oscillators

Several theories for describing phase noise in oscillators are available. Especially the theoretical framework published by Demir [6] allows to compute the connection between the noise sources within an oscillator's circuit and the stochastic characteristics of its output signal. This theory is perhaps the most comprehensive work as it is directly based on the stochastic differential equations modeling the physical behavior of an oscillatory system. However, for this paper we restrict ourselves on the most popular distinction of the noise in an amplitude and a phase component described in the following.

In the best case, the output of an oscillator should be a periodic signal with period T_0 thus consisting of a fundamental wave with $f_0 = 1/T_0$ and an infinite number of harmonics with frequency $\nu \cdot f_0,\ \nu \geq 2$. Restricting our considerations to the oscillator's fundamental wave, the oscillator output is written as

$$s(t) = A_0 \left(1 + \alpha(t)\right) \cdot \cos\left(2\pi f_0 t + \varphi(t)\right) \tag{1}$$

where A_0 is the signal's magnitude. The fluctuations in the signal's amplitude and in its phase are described by two uncorrelated stochastic processes with zero mean, $\alpha(t)$ and

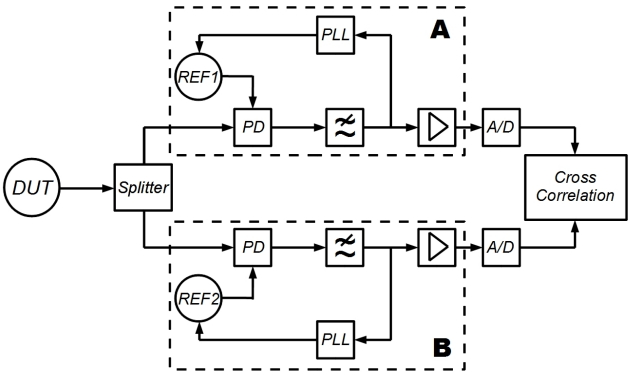

Fig. 1. Principal system structure of cross-correlation measurement

$\varphi(t)$, respectively. The variance of the amplitude noise is constant whereas the variance of the phase fluctuations grows linearly with time and thus without any bound.

B. Phase noise measurement by cross-correlation

The phase noise of an oscillator can be determined most accurately by a cross-correlation. The principal system structure for the measurement of the phase noise of a device-under-test (DUT) is shown in figure 1.

The system consists of two identical measurement branches A and B. In each of them, the signal of the oscillator under test is converted down to baseband where two reference oscillators $REF1$ and $REF2$ are used. Both DUT and reference oscillator have the same frequency and a phase-locked-loop (PLL) ensures that their phase difference is $\pi/2$. Thus, in the phase detector, the amplitude noise component of both the DUT and the reference oscillator is suppressed.

For this reason, the output signal should consist only of the phase noise of the DUT $\varphi_c(t)$ and of the reference oscillators $\varphi_a(t)$ and $\varphi_b(t)$. Thus, the output signal is $x(t) = \varphi_c(t) + \varphi_a(t)$ and $y(t) = \varphi_c(t) + \varphi_b(t)$ in the measurement branches A and B, respectively. After amplification, the signal is A/D-converted and can subsequently be processed in a computer.

For the sake of notational clarity, in the following the phase noise components $\varphi_a(t)$, $\varphi_b(t)$ and $\varphi_c(t)$ are denoted as $a(t)$, $b(t)$ and $c(t)$, respectively. Thus, the measured quantities $x(t)$ and $y(t)$ in the branches A and B and their spectra $X(f)$ and $Y(f)$ are written as

$$x(t) = c(t) + a(t) \qquad X(f) = C(f) + A(f) \quad (2)$$

$$y(t) = c(t) + b(t) \qquad Y(f) = C(f) + B(f) \quad (3)$$

The goal of the measurement system is the estimation of the power spectral density $S_{cc}(f)$ of the DUT's phase noise. This is done by calculating the so-called cross-spectrum $S_{xy}(f)$ [5]:

$$\begin{aligned} S_{xy} &= \frac{1}{T}\mathbb{E}\left(XY^*\right) = \\ &= \frac{1}{T}\left[\mathbb{E}\left(AB^*\right) + \mathbb{E}\left(AC^*\right) + \mathbb{E}\left(BC^*\right) + \mathbb{E}\left(CC^*\right)\right] \end{aligned} \quad (4)$$

Here, T denotes the block length of the signals. If the measurement branches A and B are completely uncorrelated, it is $\mathbb{E}\left(AB^*\right) = \mathbb{E}\left(AC^*\right) = \mathbb{E}\left(BC^*\right) = 0$ and thus, the result is the desired quantity $S_{cc}(f)$. However, it is to mention that possible imperfections (f.ex. no perfect isolation between the measurement branches) have to be considered in practice which is discussed in section IV.

The expectation in equation 4 is estimated by averaging a number of m spectra of the sampled signals $x_T(t)$ and $y_T(t)$ each of time length T:

$$\hat{S}_{xy} = \frac{1}{T}\langle XY^*\rangle_m = S_{cc} + \mathcal{O}\left(1/\sqrt{m}\right) \quad (5)$$

The error term consists of the cross-spectra AB^*, AC^* and BC^* and can be shown to decrease with the square root of m.

III. Cramer-Rao-Bounds and estimators

In this section, different possibilities for the estimation of the phase noise power spectral density of the DUT are discussed. First, the Cramer-Rao-Bound (CRB) is calculated in section III-A as the lower bound for the variance of any unbiased estimator. Then, the ML-estimation approach is presented in section III-B and several estimators are discussed in section III-C.

With both branches assumed to be equal, we can define

$$\begin{aligned} \mathrm{var}(A_{Re}(f)) = \mathrm{var}(A_{Im}(f)) &= \frac{\alpha^2(f)}{2} \\ \mathrm{var}(B_{Re}(f)) = \mathrm{var}(B_{Im}(f)) &= \frac{\alpha^2(f)}{2} \end{aligned} \quad (6)$$

where f.ex. $A_{Re} = \mathbb{R}\{A\}$ and where $\mathrm{var}(.)$ denotes the variance which is of course a function of f. However, as the spectral bins of the noise signals are mutual independent, the following discussion holds true for any arbitrary frequency and we write α instead of $\alpha(f)$. Furthermore, for the DUT spectrum it is

$$\mathrm{var}(C_{Re}(f)) = \mathrm{var}(C_{Im}(f)) = \frac{\gamma^2(f)}{2}. \quad (7)$$

It thus follows that $S_{cc}(f) = \frac{1}{T}E(C(f)C^*(f)) = \frac{1}{T}\gamma^2(f)$.

A. Cramer-Rao-Bound for cross-correlation-measurement

The Cramer-Rao-Bound (CRB) is a lower bound for any possible unbiased estimator of a parameter θ if a vector $Z \in \mathbb{R}^n$ is observed. In the case of the phase noise measurement described above, the observables (at a certain frequency) are X and Y, i.e.

$$Z = \begin{pmatrix} X_{Re} \\ Y_{Re} \\ X_{Im} \\ Y_{Im} \end{pmatrix} \tag{8}$$

Furthermore, Z follows a multivariate normal distribution, i.e. $Z \sim \mathcal{N}(\mu, \Sigma)$ and the density is

$$f_Z(z) = \frac{1}{4\pi^2} (\det \Sigma)^{-1/2} \exp\left(-\frac{1}{2}(z-\mu)^T \Sigma^{-1} (z-\mu)\right) \tag{9}$$

where the expectation $\mu = E(Z) = (0\ 0\ 0\ 0)^T$ and where the covariance matrix $\Sigma = \mathrm{Cov}(Z)$ with its entries $\Sigma_{ij} = \mathrm{Cov}(Z_i, Z_j), 1 \leq i, j \leq 4$ is given by

$$\Sigma = \frac{1}{2} \begin{pmatrix} \alpha^2+\gamma^2 & \gamma^2 & 0 & 0 \\ \gamma^2 & \alpha^2+\gamma^2 & 0 & 0 \\ 0 & 0 & \alpha^2+\gamma^2 & \gamma^2 \\ 0 & 0 & \gamma^2 & \alpha^2+\gamma^2 \end{pmatrix}. \tag{10}$$

Furthermore, the determinant $\det \Sigma$ and the inverse matrix Σ^{-1} can be computed as

$$\det \Sigma = \frac{1}{4}\left(\frac{1}{4}\alpha^8 + \alpha^6\gamma^2 + \alpha^4\gamma^4\right) \tag{11}$$

and

$$\Sigma^{-1} = \frac{2}{\alpha^4 + 2\alpha^2\gamma^2} \cdot \begin{pmatrix} \alpha^2+\gamma^2 & -\gamma^2 & 0 & 0 \\ -\gamma^2 & \alpha^2+\gamma^2 & 0 & 0 \\ 0 & 0 & \alpha^2+\gamma^2 & -\gamma^2 \\ 0 & 0 & -\gamma^2 & \alpha^2+\gamma^2 \end{pmatrix}. \tag{12}$$

For N observations $z_1 \dots z_N$ of Z and with the known expectation $\mu = 0$, the likelihood function $\mathfrak{L}(\gamma^2, \alpha^2 | z_1 \dots z_N)$ and the log-likelihood function $\mathfrak{l}(\gamma^2, \alpha^2 | z_1 \dots z_N)$ can be written as

$$\begin{aligned} &\mathfrak{L}(\gamma^2, \alpha^2 | z_1 \dots z_N) = \\ &= \prod_{i=1}^{N} f_Z(z_i | \Sigma) = \\ &= \frac{1}{(4\pi^2)^N} (\det \Sigma)^{-N/2} \prod_{i=1}^{N} \exp\left(-\frac{1}{2} z_i^T \Sigma^{-1} z_i\right) \end{aligned} \tag{13}$$

and

$$\begin{aligned} &\mathfrak{l}(\gamma^2, \alpha^2 | z_i) = \\ &= \ln \mathfrak{L}(\gamma^2, \alpha^2 | z_1 \dots z_N) = \\ &= \ln\left(\frac{1}{(4\pi^2)^N} \prod_{i=1}^{N} (\det \Sigma)^{-1/2} \exp\left(-\frac{1}{2} z_i^T \Sigma^{-1} z_i\right)\right) = \\ &= N \cdot \ln\left(\frac{1}{4\pi^2\sqrt{\det \Sigma}}\right) + \sum_{i=1}^{N} -\frac{1}{2} z_i^T \Sigma^{-1} z_i, \end{aligned} \tag{14}$$

respectively.

1) Estimation of γ^2 with knowledge of α^2: The second derivative of the log-likelihood function with respect to γ^2 is given as

$$\begin{aligned} \frac{d^2 \mathfrak{l}(\gamma^2 | z_i)}{d(\gamma^2)^2} &= \frac{4N}{(\alpha^2 + 2\gamma^2)^2} \\ &\quad - \sum_{i=1}^{N} \frac{4}{(\alpha^2+2\gamma^2)^3} z_i^T \begin{pmatrix} 1 & 1 & 0 & 0 \\ 1 & 1 & 0 & 0 \\ 0 & 0 & 1 & 1 \\ 0 & 0 & 1 & 1 \end{pmatrix} z_i \end{aligned} \tag{15}$$

In case of the estimation of a single parameter, the Fisher information is just the expected value of the second derivative with respect to the desired parameter to estimate. Thus, for the estimation of γ^2 under the assumption that α^2 is known, this yields

$$\begin{aligned} &I(\gamma^2 | \alpha^2) = -E\left(\frac{d^2 \mathfrak{l}(\gamma^2 | z_i)}{d(\gamma^2)^2}\right) = \\ &= -\frac{4N}{(\alpha^2+2\gamma^2)^2} + \frac{16N}{(\alpha^2+2\gamma^2)^3}\left(\frac{\alpha^2+\gamma^2}{2} + \frac{\gamma^2}{2}\right) = \\ &= \frac{4N}{\alpha^4 + 4\alpha^2\gamma^2 + 4\gamma^4}. \end{aligned} \tag{16}$$

Finally, the respective Cramer-Rao Bound is given as

$$CRB(\gamma^2 | \alpha^2) = \frac{1}{I(\gamma^2 | \alpha^2)} = \frac{\alpha^4 + 4\alpha^2\gamma^2 + 4\gamma^4}{4N} \tag{17}$$

2) Estimation of γ^2 without knowledge of α^2: If both parameters are unknown, the Fisher information of the vector of parameters $\left[\alpha^2\ \gamma^2\right]^T$ is a matrix which is computed as follows:

$$I\left(\left[\alpha^2\ \gamma^2\right]^T\right) = \begin{pmatrix} \frac{d^2\mathfrak{l}\left(\alpha^2,\gamma^2|z_i\right)}{d(\alpha^2)^2} & \frac{d^2\mathfrak{l}\left(\alpha^2,\gamma^2|z_i\right)}{d\alpha^2\gamma^2} \\ \frac{d^2\mathfrak{l}\left(\alpha^2,\gamma^2|z_i\right)}{d\gamma^2\alpha^2} & \frac{d^2\mathfrak{l}\left(\alpha^2,\gamma^2|z_i\right)}{d(\gamma^2)^2} \end{pmatrix} = \\ = \begin{pmatrix} \frac{N}{\alpha^4} + \frac{N}{\alpha^4+4\alpha^2\gamma^2+4\gamma^4} & \frac{2N}{\alpha^4+4\alpha^2\gamma^2+4\gamma^4} \\ \frac{2N}{\alpha^4+4\alpha^2\gamma^2+4\gamma^4} & \frac{4N}{\alpha^4+4\alpha^2\gamma^2+4\gamma^4} \end{pmatrix} \tag{18}$$

The inverse of the Fisher information matrix can be computed to be

$$I\left(\left[\alpha^2\ \gamma^2\right]^T\right)^{-1} = \begin{pmatrix} \frac{\alpha^4}{N} & -\frac{\alpha^4}{2N} \\ -\frac{\alpha^4}{2N} & \frac{2\alpha^4+4\alpha^4\gamma^2+4\gamma^4}{4N} \end{pmatrix} \tag{19}$$

Thus, the CRB for the estimation of γ^2 without any knowledge of α^2 is given as

$$CRB\left(\gamma^2\right) = \frac{2\alpha^4 + 4\alpha^4\gamma^2 + 4\gamma^4}{4N}. \tag{20}$$

As could be expected, it is $CRB\left(\gamma^2\right) \geq CRB\left(\gamma^2|\alpha^2\right)$. Furthermore, for the case of a DUT with very low phase noise compared to the reference oscillators (i.e. $\gamma^2 \ll \alpha^2$), it is $CRB\left(\gamma^2\right) = 2 \cdot CRB\left(\gamma^2|\alpha^2\right)$.

3) Estimation of α^2: For the estimation of the *background noise* α^2 produced by the reference oscillators and the phase-locked loops, the respective Cramer-Rao-Bound can also be taken from the inverse of the Fisher information matrix given in equation 19:

$$CRB\left(\alpha^2\right) = \frac{\alpha^4}{N} \tag{21}$$

B. Maximum-likelihood approach

In the following, the maximum-likelihood estimators for α^2 and for γ^2 with and without knowledge of the reference oscillator's phase noise PSD is to be derived.

1) ML-estimation of γ^2 with knowledge of α^2: In a first step, the derivation of the log-likelihood function with respect to γ^2 is set to zero which yields

$$\hat{\gamma}^2_{ML|\alpha} = -\frac{\alpha^2}{2} + \frac{1}{4N}\sum_{i=1}^{N} X^i_{Re}X^i_{Re} + Y^i_{Re}Y^i_{Re} + X^i_{Im}X^i_{Im} + Y^i_{Im}Y^i_{Im} + 2X^i_{Re}Y^i_{Re} + 2X^i_{Im}Y^i_{Im} \tag{22}$$

for the ML-estimator where the index $ML|\alpha$ means that the value of α^2 is known in advance. This is also obvious as $\hat{\gamma}^2_{ML|\alpha}$ is a function of α^2.

The expectation and the variance of the estimator $\hat{\gamma}^2_{ML|\alpha}$ can be calculated to be

$$E\left(\hat{\gamma}^2_{ML|\alpha}\right) = \gamma^2 \tag{23}$$

$$\mathrm{var}\left(\hat{\gamma}^2_{ML|\alpha}\right) = \frac{\alpha^4 + 4\alpha^2\gamma^2 + 4\gamma^4}{4N} \tag{24}$$

and hence it can be stated that the estimation is unbiased. Furthermore, it is $\mathrm{var}\left(\hat{\gamma}^2_{ML|\alpha}\right) = CRB\left(\gamma^2|\alpha^2\right)$ which means that the ML-estimator is efficient.

2) ML-estimation of γ^2 without knowledge of α^2: Moreover, without the knowledge of α^2, the ML-estimator of the DUT's phase noise power spectral density $\frac{1}{T}\gamma^2$ is obtained by setting the derivation of the log-likelihood function with respect to α^2 to zero and substituting the result into equation 22. The resulting ML-estimator is given as

$$\hat{\gamma}^2_{ML} = \frac{1}{N}\sum_{i=1}^{N} X^i_{Re}Y^i_{Re} + X^i_{Im}Y^i_{Im}. \tag{25}$$

Obviously, using the ML-estimator just means to take the real part of the cross-correlation $\frac{1}{T}\Re\left\{\langle XY^*\rangle_m\right\}$ as an estimate for the DUT's phase noise PSD. The estimator can be shown to be unbiased and its variance is

$$\mathrm{var}\left(\hat{\gamma}^2_{ML}\right) = \frac{2\alpha^4 + 4\alpha^2\gamma^2 + 4\gamma^4}{4N} = CRB\left(\gamma^2\right) \tag{26}$$

which means that it is also efficient.

3) ML-estimation of α^2: The so-called *background noise* coming from the reference oscillators is evaluated by estimating the reference oscillator's phase PSD $\frac{1}{T}\alpha^2$. Using the likelihood function and its derivatives, it can be shown that the ML-estimator $\hat{\alpha}^2_{ML}$ is given as

$$\hat{\alpha}^2_{ML} = \frac{1}{N}\sum_{i=1}^{N} X^i_{Re}X^i_{Re} + Y^i_{Re}Y^i_{Re} + X^i_{Im}X^i_{Im} + Y^i_{Im}Y^i_{Im} - 2X^i_{Re}Y^i_{Re} - 2X^i_{Im}Y^i_{Im}. \tag{27}$$

C. Discussion of different estimators

1) Common absolute value estimator: Perhaps the most obvious and most frequently used estimator of the PSD of the DUT's phase noise is taking the absolute value of the measured cross-spectrum which is

$$\left|\langle S_{xy}\rangle_N\right| = \frac{1}{T}\sqrt{\Re\left\{\langle XY^*\rangle_N\right\}^2 + \Im\left\{\langle XY^*\rangle_N\right\}^2} \tag{28}$$

Choosing this estimator seems very natural and the result is always a positive number which makes it always possible to plot it in logarithmic scale. However, the estimator is obviously not unbiased. In contrast to the ML-estimator $\hat{\gamma}^2_{ML}$, it takes into account the imaginary part $\Im\{\langle XY^*\rangle_m\}$ which only contains the phase noise of the reference oscillators. For these two reasons, it is advisable not to use this estimator.

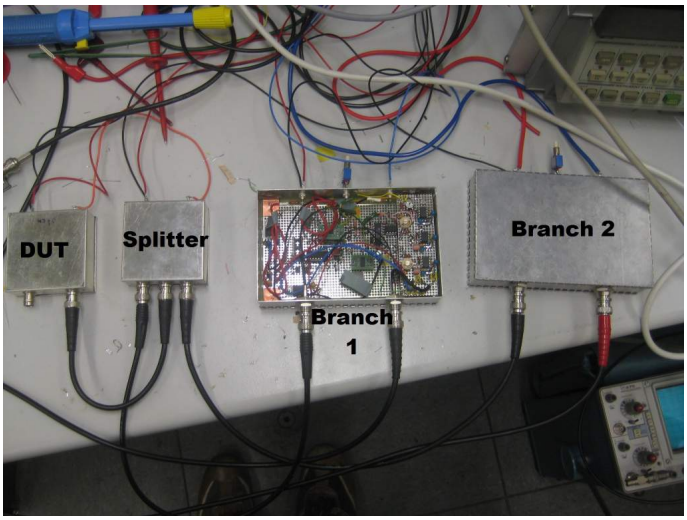

Fig. 2. Cross-correlation measurement system

2) Other estimators: In [5], several other positive-valued estimators were suggested. These are directly suitable for a logarithmic plot. However, for this reason they are also biased although their variance is much less than that of the absolute value estimator. Of course, with an increasing number of averages N in a real measurement, the bias diminishes. Thus, these estimators are a good trade-off between statistical consistency and the needs of a possible logarithmic plot.

3) Estimation in our measurements: In our measurement setup we use the ML-estimators presented above in section III-B. This is the most useful choice when it comes to comparison of measurement results with the CRB discussed in section V. Of course, if we plot the measurement results in logarithmic scale, we have to leave out those frequency bins where the result is negative. However, with increasing number of averages N and thus decreasing standard deviation but constant (and positive) expectation, more and more results become positive.

4) Estimate improvement with a-priori knowledge: The variance of the estimator $\hat{\gamma}^2_{ML}$ without knowledge of α^2 and of the estimator $\hat{\gamma}^2_{ML|\alpha}$ is given in equation 26 and in equation 24, respectively. Obviously, it is $\mathrm{var}\left(\hat{\gamma}^2_{ML}\right) > \mathrm{var}\left(\hat{\gamma}^2_{ML|\alpha^2}\right)$. For the measurement of a DUT with very low phase noise compared to the reference oscillators, it is $\gamma^2 \ll \alpha^2$ and thus $\mathrm{var}\left(\hat{\gamma}^2_{ML}\right) \approx 2 \cdot \mathrm{var}\left(\hat{\gamma}^2_{ML|\alpha^2}\right)$ which is the maximum gain if the knowledge of α^2 is used during the estimation.

IV. Measurement setup

In this section, our implementation of the cross-correlation principle for the measurement of oscillator phase noise is presented. After describing our system in section IV-A, some important aspects of the realization are discussed in section IV-B.

A. Description

The measurement system is basically structured as shown in figure 1 and explained in section II-B. Our practical implementation is shown in figure 2. Here, the oscillator to be measured is within the box titled *DUT*. The oscillator signal is the input to the box denoted as *Splitter* in the middle. Here, the signal is split into two branches where it is very important that the two outputs are decoupled. In our system, the attenuation between the two output ports of the splitter is about 90 dB. These two output signals are then fed to *Branch 1* and to *Branch 2* on the right part of figure 2. The measurement circuit itself can be seen within the open box of branch 1. We use a double-balanced mixer as phase detector and a VCXO as reference oscillator. The bandwidth of the PLL is very low (about 15 Hertz) and the push-button on the top of the box allows a fast charging of the very large capacity during the start-up phase of the PLL. The signal after the downconversion is filtered with a low-pass. As it has a very small amplitude, it is important to amplify it where we use to amplification stages each with amplification factor 10. Finally, the output signal is digitalized with a 12-bit-A/D converter card. If possible, the quantization range of the ADC should be chosen such that the quantization noise is minimized. Finally, after digitalization, the results can be processed in a PC.

B. Practical points

In the following, some points of the practical realization of the cross-correlation measurement system are discussed which turned out to be crucial for good and exact results.

1) Isolation of the branches: The components of the measurement system are to be separated and decoupled. Therefore, we put the DUT, the splitter and the two measurement circuits in separate boxes and designed the splitter to provide sufficient decoupling between both of them. In fact, the remaining coupling induces a cross-correlation between both branches which finally determines a lower bound for the measurement of the DUT's phase noise.

2) Noise figures of circuit components: In a first attempt, standard circuit elements were used but the resulting measurements were not satisfying. However, after replacing some components with low noise counterparts, such as low-noise OpAmps, the variance of the measurement results decreased considerably. This entails that the measurement time can be reduced or that an oscillator with lower phase noise can be measured within the same measurement time.

3) Power Supply: The importance of decoupling also requires to pay attention to the system's power supply. For our measurement system, separate power supplies for each system component turned out to be the best solution. More precisely, we used a buffered voltage transformer within each box to decouple the inner circuits. With this measure, some mutual interference could be removed and it turned out to be sufficient to use a single power supply unit for all boxes.

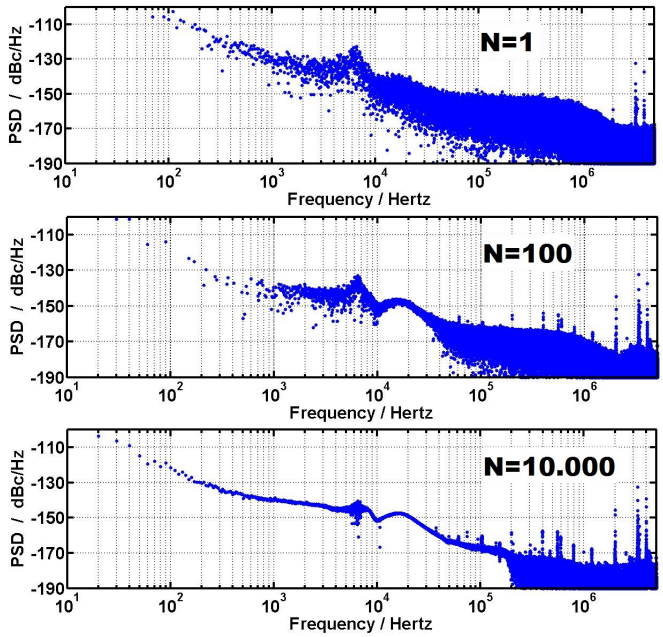

Fig. 3. PSD of the HOSONIC HO-12C @ 16.384 MHz measured with our system for different lengths of the correlation time (0.1 s, 10 s and 1000 s)

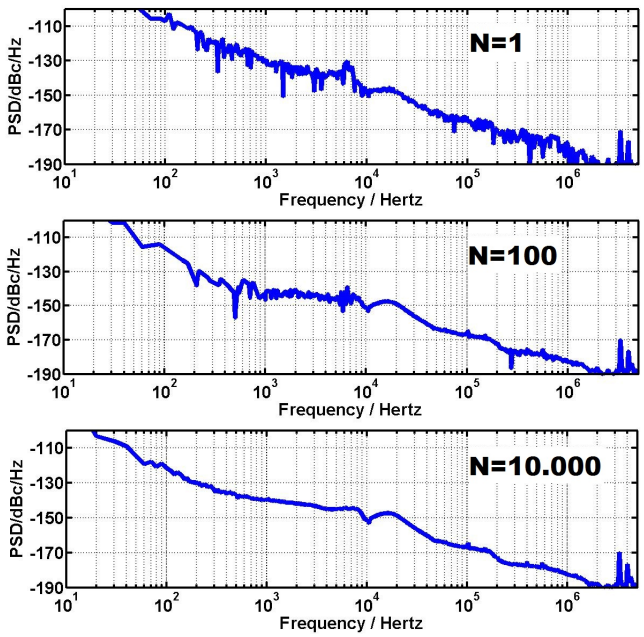

Fig. 4. PSD of the HOSONIC HO-12C @ 16.384 MHz measured with our system for different lengths of the correlation time (0.1 s, 10 s and 1000 s) with additional averaging in the frequency domain

V. Measurement results

In the following, measurement results for different lengths of correlation time are shown in section V-A. In section V-B, our measurement results are compared to those obtained with a commercial phase noise analyzer. Finally, the improvement of the results obtained by using a-priori knowledge of the background noise is discussed in section V-C.

A. Measurement results for different correlation times

In figure 3, some exemplary measurement results are shown for different lengths of the correlation time. Here, the ML-estimator $\hat{\gamma}^2_{ML}$ as derived in section III-B2 was applied. The frequency axis is again scaled logarithmically and the results are given in dBc/Hz. Note that all plots show a spectral resolution of 10 Hertz corresponding to a part of the signal with a time length of 100 ms. However, a different number of signal parts were averaged: whereas for the plot on the top of figure 3 only one signal part was used (thus without averaging), the plots in the middle and at the bottom show the average of 100 and 10000 signal parts, respectively. It can be easily seen that the variance of the estimated PSD decreases by about 10 dB as the number of averaged signal parts is hundredfold. This is consistent with equation 26 predicting a $1/N$-dependency of the variance of the estimator. Note that for some parts of the frequency axis, the estimation already converges when the number of averaged signal parts is increased from 100 to 10000 as shown in the middle and on the bottom of figure 3.

However, a big disadvantage of the simple logarithmic plot is that the results for higher values of frequency cannot be shown in sufficient resolution. Therefore, an additional averaging of estimation results for a number of frequency bins within a certain interval of the frequency axis can be carried out. For example, the plots in figure 4 show the same measurements as in figure 3 but with additional averaging within the frequency domain where each decade of frequency is divided into 100 intervals each equally large in logarithmic scaling. Thus, there is in fact no averaging in the first two decades as there are not even 100 results there. In contrast, for higher frequency areas a large number of results are averaged. For example, between 100 kHz and 1 MHz, 90000 results of the original estimation are merged into 100 points in the plots in figure 4. This results in an improved precision of the estimation which can be easily understood if the figures 3 and 4 are compared.

B. Comparison to commercial spectrum analyzer

To verify the results obtained with our measurement system, we compared it to a commercial phase noise tester where the *Rohde&Schwarz FSUP50 Signal Source Analyzer* was used. For this verification, the *HOSONIC HO-12C 16.384 MHz* quartz oscillator was used. A measurement result obtained with our system is shown at the top of figure 5. Here, the power spectral density of the DUT's phase noise in dBc/Hz is shown as a function of the offset to the oscillator's frequency. Note that the frequency axis is also scaled logarithmically. For comparison, a measurement result obtained with the commercial device is at the bottom of figure 5 where the frequency range shown is nearly identical with that in our plot (note that it starts at 1 Hertz instead of 10 Hertz). Obviously, both results correspond with each other very well, both qualitatively and quantitatively. Thus, we state that our system is calibrated

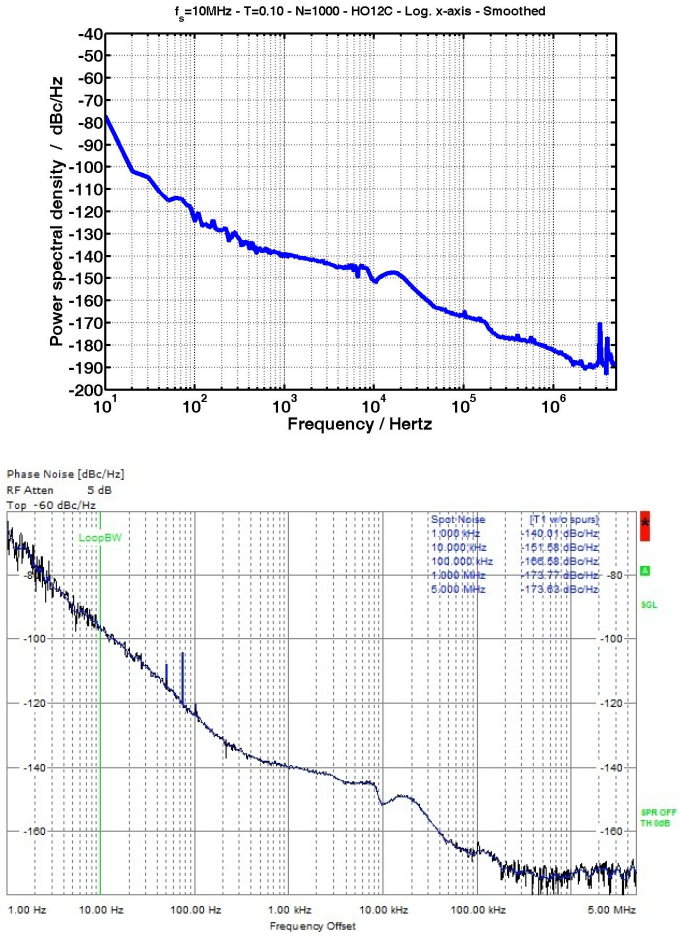

Fig. 5. PSD of the HOSONIC HO-12C @ 16.384 MHz. Top: Measured with our system. Bottom: Measured with R&S FSUP50.

correctly and works properly.

C. Improvement by knowledge of background noise α^2

In section III-C4 we discussed the potential advantage of using the ML-estimator for the DUT's phase noise PSD $\frac{1}{T}\gamma^2(f)$ with a-priori knowledge of the background noise α^2 as described in section III-B1. Therefore, the PSD of the phase of the reference oscillators $\frac{1}{T}\alpha^2(f)$ has to be estimated in advance where the ML-estimator $\hat{\alpha^2_{ML}}$ (see section III-B3) is the best choice. Then, the estimation results can be improved as shown in figure 6 where the number of averaged signal parts is chosen to be $N = 100$. Here, the green dashed line shows the estimation result without knowledge of the background noise, thus using the estimator $\hat{\gamma^2_{ML}}$ with additional averaging in the frequency domain afterwards. Furthermore, the blue solid line shows the result using $\hat{\gamma^2_{ML|\alpha}}$ with usage of a-priori knowledge of α^2. Therefore, the background noise had to be estimated in advance using the ML-approach $\hat{\alpha^2_{ML}}$. Obviously, there is a slight improvement of the results, at least in some regions of the frequency axis.

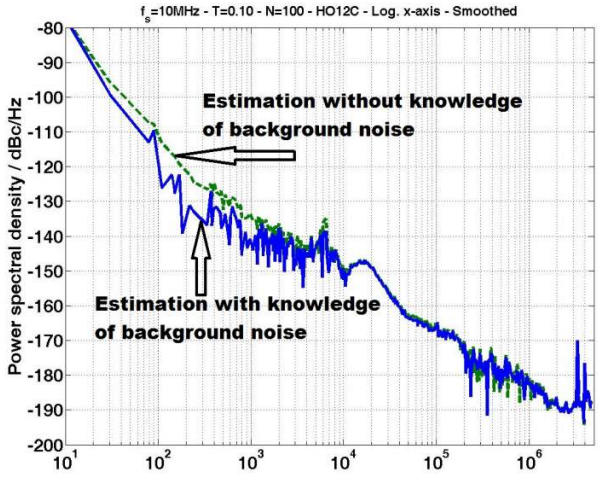

Fig. 6. PSD of the HOSONIC HO-12C @ 16.384 MHz. Number of averaged signal parts is $N = 100$. Green dashed line: estimation without knowledge of background noise α^2. Blue solid line: estimation with a-priori knowledge of α^2.

VI. Conclusion

In section III, we derived analytical expressions of the Cramer-Rao-Bound for the estimation of the power spectral density of an oscillator's phase noise when it is measured using the cross-correlation method. Moreover, we showed that the maximum-likelihood estimators are efficient and thus very well suited for estimating the desired quantities. Furthermore, in section IV we presented our implementation and showed some results in section V. Here, it became obvious that the results are consistent with the predictions from theory. Finally, we presented measured results of an estimator using a-priori knowledge of the background noise of the system to improve the measurement results. However, the practical benefit of this approach has to be further studied. In our future work, we plan to examine some additional aspects of our system, such as the reliable suppression of amplitude noise in the phase detector and the impact of the bandwidth of the phase-locked loop on the measurement results.

References

[1] M. Nebel, B. Lankl, *Oscillator Phase Noise as a Limiting Factor in Stand-Alone GPS-Indoor Navigation*, 5th ESA Workshop on Satellite Navigation Technologies and European Workshop on GNSS Signals and Signal Processing (NAVITEC), 2010.

[2] D. Petrovic, W. Rave, G. Fettweis, *Phase Noise Influence on Bit Error Rate, Cut-off Rate and Capacity of M-QAM OFDM Signaling*, International OFDM Workshop (InOWo), 2002.

[3] W. Walls, *Practical Problems Involving Phase Noise Measurements*, 33rd Annual Precise Time and Time Interval (PTTI) Meeting, 2001.

[4] H. Gheidi, A. Banai, *A New Phase Shifter-less Delay Line Method for Phase Noise Measurement of Microwave Oscillators*, Proceedings of the 38th European Microwave Conference, 2008.

[5] E. Rubiola, F. Vernotte, *The cross-spectrum experimental method*, CNRS/UFC, http://rubiola.org, 2010.

[6] A. Demir, A. Mehrotra and J. Roychowdhury, *Phase Noise in Oscillators: A Unifying Theory and Numerical Methods for Characterization*, IEEE Transactions on Circuits and Systems - I: Fundamental Theory and Applications, Vol. 47, No. 5, 2000, pp. 655-674.

Iridium-Next Master Clock

M. Bloch, J. Ho, O. Mancini, T. McClelland

Frequency Electronics, Inc.,
Uniondale, NY/USA
Email: tomm@freqelec.com

***Abstract*— A high resolution, digitally tuned quartz oscillator with excellent phase noise and temperature stability has been developed for space applications and is being utilized in the Iridium NEXT constellation, the largest commercial satellite constellation in the world. Significant effort has been expanded to optimize the quartz resonator design, the double oven circuitry and the digital tuning scheme. The oscillator is implemented using readily available space qualified parts.**

The best results have been achieved with 5 MHz, third overtone, SC cut resonators multiplied by a factor of two to provide the Iridium NEXT frequency of 10 MHz. A temperature coefficient of 5E-12/10^{O}C-interval has been realized, and single sideband phase noise of -115 dBC/Hz at offset of 1 Hz. has been achieved on the 10 MHz output. Allan deviation performance of 5E-13 for averaging times of 1 to 100 seconds has also been demonstrated.

Digital tuning from the ground is accomplished by commanding a custom 16 bit DAC, implemented in a space qualified FPGA. The DAC architecture provides for high resolution (< 1E-11) tuning, with spurious outputs below -125 dBC.

Unique features of resonator design, and oscillator circuitry are discussed, and data are presented.

I. INTRODUCTION

A second generation Iridium satellite constellation, known as "Iridium-Next" is currently in development [1]. It will consist of 66 new operational satellites; 6 on-orbit spares, and 9 ground spares. This next-generation Iridium system is designed to be backward compatible with the currently operational system, but with enhanced data capabilities as well as the addition of various sensor payloads. Satellite launches are currently scheduled to begin in 2015.

Frequency Electronics, Inc. (FEI) is currently under contract to provide the Master Frequency Generation Unit (MFGU) for the Iridium-Next satellites. Each Iridium-Next satellite will include a redundant MFGU in order to provide a stable, tunable frequency reference for all onboard systems.

A functional block diagram of the MFGU is shown in Figure 1. A 5 MHz quartz oscillator provides the stable frequency reference for the MFGU. The 5 MHz frequency is doubled, and conditioned in order to provide multiple (ten) 10 MHz outputs for the system. In addition, 1545 MHz is synthesized from the 5 MHz reference, with 10 outputs available to the system. An outline drawing of the MFGU is shown in Figure 2.

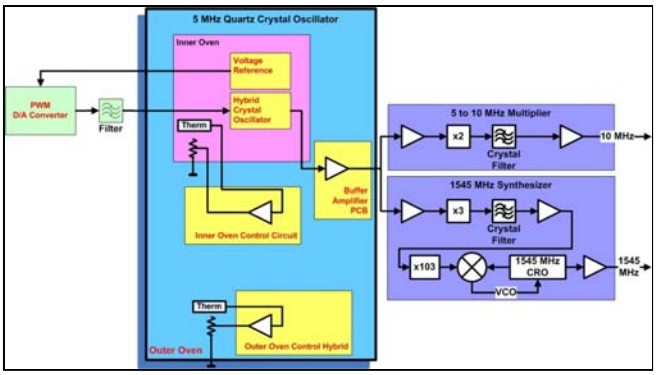

Figure 1. Functional Block diagram of Master Frequency Generation Unit (MFGU). Actual MFGU consists of two of the units shown above in order to provide redundancy.

This paper describes the design of the 5 MHz quartz oscillator used as the frequency reference for the MFGU. The oscillator must provide the demanding frequency stability required for proper system operation , but must also meet the cost constraints of a commercial satellite system, and be manufacturable in relatively large quantities (162).

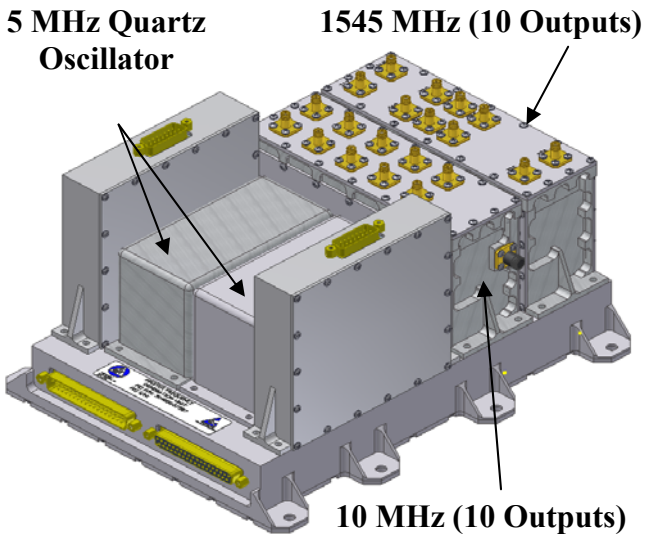

Figure 2. Outline Drawing of MFGU, showing redundant 5 MHz oscillators, 10 MHz and 1545 MHz output modules.

II. 5 MHz Quartz Oscillator Design Highlights

The MFGU frequency outputs must meet stringent stability requirements. Frequency drift, frequency variation with temperature and radiation, and phase noise requirements together necessitate near state-of-the-art quartz oscillator performance. The quartz oscillator therefore utilizes a 5 MHz, third overtone, SC-cut quartz resonator in order to provide the required frequency stability performance. Each resonator is fabricated from premium-Q, swept quartz material, and is pre-conditioned by exposure to gamma radiation, in order to provide improved immunity to natural radiation occurring in the space environment. The resonator is maintained inside a double oven enclosure in order to keep its temperature stable. An outline drawing of the oscillator is shown in Figure 3.

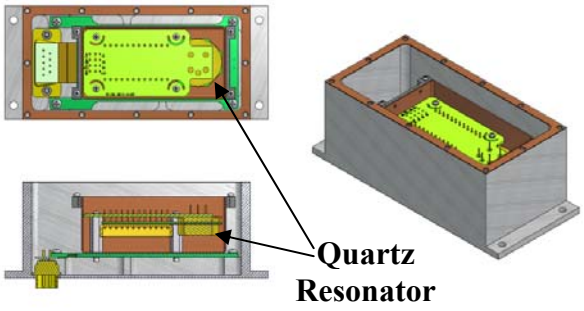

Figure 3. Outline of the 5 MHz quartz oscillator

The 5 MHz output of the quartz oscillator is doubled in order to provide the required 10 MHz outputs, and a crystal filter is employed at 10 MHz in order to provide an improved phase noise floor at offset frequencies greater than 10 kHz.

The oscillator frequency is tuned by command from the ground. Within the MFGU, ground control commands are processed, then converted to an analog voltage which is used to adjust the frequency of the quartz oscillator. A 16 bit digital to analog converter is implemented in a space qualified FPGA. The pulse width modulated output from the FPGA is filtered such that frequency tuning with a resolution of 1×10^{-11} is possible.

III. 5 MHz Quartz Oscillator Performance

A. *Frequency Stability*

Frequency stability over an extended period of time is shown in Figure 4 for two different oscillators.

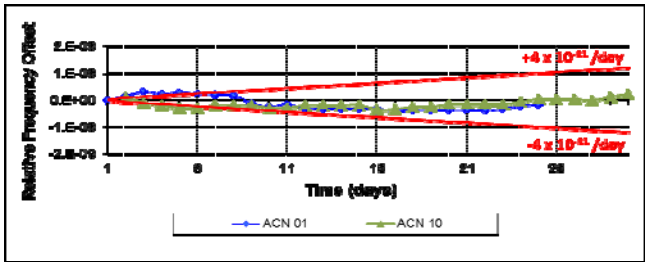

Figure 4. Frequency drift at constant temperature. Performance is shown for two oscillators over a one month period of time.

Allan deviation performance for a single oscillator is shown in Figure 5. From this figure it is seen that

$$\sigma_y(\tau = 1 \text{ second}) < 2 \times 10^{-13}$$

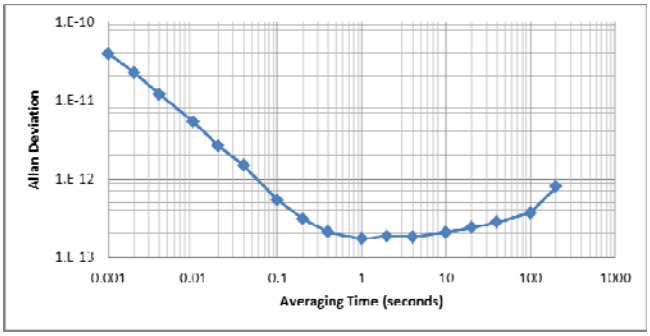

Figure 5. Allan Deviation

B. *Phase Noise*

The single sideband phase noise performance has been measured at 10 MHz in order to include the effect of the crystal filter on the noise floor. Typical results are shown in Figure 6.

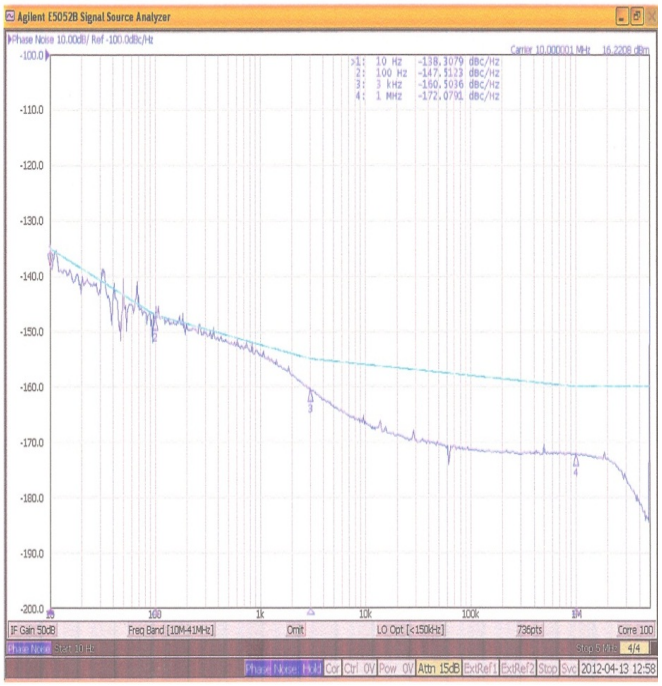

Figure 6. Single sideband phase noise measured at 10 MHz

C. *Frequency Variation with Temperature*

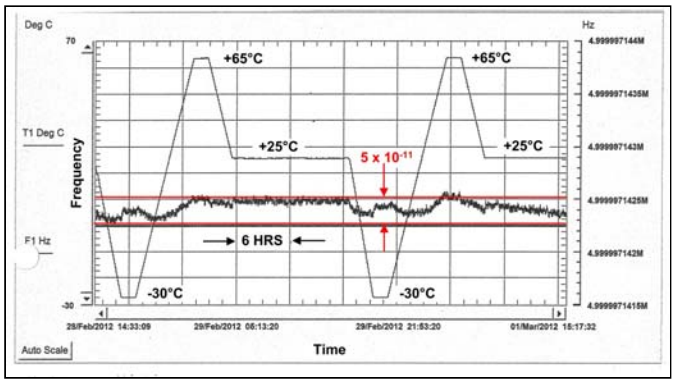

Figure 7. Frequency variation with temperature. Horizontal axis is time. Plot shows two temperature cycles in which the temperature was varied linearly over a six hour period of time from -30 to +65°C. Total frequency variation over this temperature range is seen to be < 5 x 10^{-11}

REFERENCES

[1] Gupta, Om P., "Global augmentation of ADS-B using Iridium-NEXT hosted payloads," Integrated Communications, Navigation, and Surveilance Conference (ICNS), May, 2011

Advantageous GPS disciplining of the OSA BVA oscillator

Clive Green
Atomic Clock Development, Quartzlock
Quartzlock
Devon England
Email sales@quartzlock.com

Abstract*— This paper provides evidence of Quartzlock's work in advantageously GPS disciplining an (OSA) BVA oscillator. Such disciplining by GPS of an (OSA) BVA quartz oscillator is a demanding task because the exceptional short term stability (8E-14/3…30s) and low phase noise (-130dBc/Hz at 1Hz) of the BVA OCXO must not be disturbed whilst at same time the natural drift (timescales of a day or more) of an OCXO must be corrected. This has been successfully achieved by Quartzlock by using multiple parameter controls in a modern DPLL (within the limits of GPS accuracy per day).Introduction *(Heading 1)

I. INTRODUCTION

GPS Disciplined Oscillators (GPSDOs) are now used throughout the world as time and frequency standards. The advantages of GPSDOs is that they combine the long term stability of the timing signals available from GPS with the short term and medium term frequency stability available from the quartz or rubidium oscillator. GPSDOs offer many advantages over other time and frequency standards. The global nature of the GPS enables GPSDOs to be used anywhere in the world. The quality of the timing signals results in an improved accuracy over frequency standards disciplined by terrestrial standard frequency transmissions. GPSDOs do not require periodic recalibrations, they are not excessively expensive. GPSDOs have many applications world-wide, in particular within the telecommunications.

The GPS BVA is fully programmed to operate without adjustment anywhere in the world. The GPS receiver is held in reset until the BVA reference has warmed up and stabilised around 30 minutes. During this time the GPS LEDs (green and amber) will be off. After about 5 minutes the GPS receiver will start looking for satellites. It will take about 1 minute to obtain a fix from a cold start with unknown location. The receiver then does a "site survey" for about 15 minutes, averaging the positions obtained. After the site survey is complete, the receiver switches to position hold mode, and uses all the satellites available to improve the accuracy of the time calculation. At this point the unit will start to lock its internal BVA reference oscillator to the GPS signal. This will take up to 30 minutes. When the PLL locks the red "lock" LED should go out, but may flash (flash of 0.1seconds) for a further 10 minutes as the PLL settles. The normal operating condition is with the red "lock" LED off.

The status of the satellite tracking is shown by the green and amber LEDs. The normal situation is that the green LED shows a long flash, followed by a number of short flashes. The number of short flashes shows the number of satellites being tracked, and included in the time solution. The amber LED may also flash. This shows the number of satellites being tracked, but not included in the timing solution.

If the red "lock" LED should start to flash (flash of 0.1seconds) at about 1Hz rate, this indicates that the phase error between the GPS signal and the reference oscillator is greater than a pre-programmed threshold. This does not indicate that the 10MHz output is unlocked.

During normal operation the GPS receiver estimates the accuracy of the timing solution using the "TRAIM" algorithm (Time Receiver Autonomous Integrity Monitoring) developed for the Motorola Oncore receiver. If the predicted timing error is greater than the programmed limit, the receiver will switch into holdover mode, and the red lock LED will start to flash at a 2Hz rate with equal mark space ratio, i.e. on for 1 second, off for 1 second. The 10MHz output and 1pps output will then drift according to the ambient temperature and aging of the BVA oscillator. When the GPS receiver comes out of standby, the 1PPS output will immediately revert to full accuracy. The 10MHz output may require a period to settle.

The unit should never go into holdover during normal operation. The most likely reason for doing so is a poor antenna location.

II. TECHNICAL DESCRIPTION

This GPS module is based on our active noise filter technology and is designed to overcome the disadvantages of narrow band width analogue phase lock loops used to lock relatively stable oscillators together, or to generate arbitrary frequencies from a 10MHz reference with good phase noise,

freedom from non harmonically related spurii, and good short term stability.

When locking a low noise BVA to a GPS reference, for example, the ideal PLL bandwidth will be very much less than 1Hz, probably in the region of 10 to 100mHz. An analogue loop will have a very long time constant integrator, leading to thermal drift, capacitor dielectric absorption, and operational amplifier offset drift. In addition, acquisition time of the loop will be very long, and if there is any frequency error, acquisition may not occur at all. There is also a problem of providing an effective "in lock" indicator to the user, or for use with associated equipment.

The digital loop overcomes all these problems. The long time constant integrator is replaced by a digital integrator that does not drift at all. A combination of an analogue phase detector for low noise and an extended range phase/frequency detector for certain acquisition can be used. The loop bandwidth can be set to maximum for acquisition, followed by glitch free reduction to the working bandwidth when the phase error becomes small. In addition performance measures related to the phase error in the loop, and the frequency error can easily be derived and used to indicate lock and bandwidth control.

As an additional benefit a hold over mode that keeps the controlled oscillator tuning voltage constant if there should be a reference failure can be easily provided.

A. Technical details of design

The design uses mixer type phase detectors operating at frequencies between 1.8MHz and 10MHz. A dual phase detector is used with quadrature square wave inputs from the controlled oscillator. The main input, which is split between the quadrature phase detectors, is a sine wave input at a level between 0 and 13dBm.

The sine wave signal from the controlled oscillator is converted to a square wave using a fast comparator. The output from the dividers forms the "Q" reference signal to the Q phase detector. A quadrature "I" reference is generated by passing the Q signal through a programmable delay line, which may be set to delays from 10ns to 137ns, in steps of 0.5ns. This enables quadrature references to be generated for phase detector frequencies between 1.8MHz and 25MHz. The outputs from the phase detectors are filtered and amplified by DC amplifiers with gain control using digital potentiometers. The gain is controlled by a software AGC system which tries to keep the input to the ADCs at optimum levels. The phase detector outputs are sampled by two channels of the 10bit A to D convertor internal to the PIC microcontroller. All other functions of the PLL are carried out by software. The control of the BVA uses a precision tuning voltage derived from D to A convertors. Two 16 bit DACs are used, with the output of the fine tune DAC divided by 256 and added to the output of the coarse tune DAC. This gives effectively 24 bit resolution with an overlap between the coarse and fine tune DACs. A software normalisation process ensures that the fine tune DAC is used for tuning most of the time. Only when the controlled oscillator has drifted out of range of the fine tune DAC would the coarse tune DAC need adjusting, with the chance of a very small glitch in the tuning voltage. A precision, low noise, voltage reference is used to supply the DACs. The microcontroller is provided with an RS232 interface. A simple set of control codes enable monitoring and set up of the digital PLL parameters to accommodate a wide range of controlled oscillators. A Windows front end program will use the control codes to enable the operation of the PLL to be monitored with real time graphs of performance measures.

III. SOFTWARE DESIGN

The input to the software is the sampled I and Q signals from the phase detectors. These are sampled at a 1kHz rate. As the final bandwidth of the PLL will be less than 1Hz, this oversampling enables pre-filtering to be used which extends the resolution and reduces noise in the 10bit A to D convertor internal to the microcontroller. Single pole digital filters are used on both the I and Q channels. These are implemented as exponential filters which have a 3dB band width which is a function of the "order" of the filter. Filter orders between 0 (no filter) and 15 are provided. This gives bandwidths between 114Hz for order 1, and 4.8mHz for order 15. The filter order is varied as the user selected PLL bandwidth is varied. After pre-filtering, the I and Q channels, now at 16 bit resolution, are sub-sampled at a rate between 15.625 s/s, and 1.953 s/s depending on the user bandwidth and lock state of the PLL. The "Q" sample is now divided by the "I" sample (after checking that I>Q) to give a binary fraction. This is used to look up the phase value in a TAN-1 look up table. The look up table is used to synthesise two types of phase detector:

- A phase detector with 16 bit resolution between Pi/2 and -Pi/2.
- A phase/ frequency detector with 16 bit resolution between 2Pi and -2Pi. This phase detector is equivalent to the well known digital phase/frequency detector. This rolls over between 2Pi and 0 for positive cycle slips, and between -2Pi and 0 for negative cycle slips, and will always provide reliable lock if there is a initial frequency error.

The output of the selected phase detector now has digital gain applied, selectable between 1/256 and 128. After digital gain, the phase value is added into the integrator, which is 32 bits wide. In order to make the loop stable, by providing a phase lead, the phase value has proportional term gain applied, also selectable between 1/256 and 128. This value is added to the upper 3 bytes of the integrator to give the tuning voltage (24 bits). The tuning voltage is divided between the coarse and fine tune DACs as follows: When normalisation is performed, the fine tune DAC most significant 8 bits are set to mid point (80h). The least significant 8 bits of the fine tune DAC are set to the least significant 8 bits of the tuning word. The coarse tune DAC is then set to provide the final tuning voltage. During all subsequent tuning, only the fine tune DAC is used over its 16 bit range. If the range is exceeded, the normalisation procedure is repeated. A state machine provides control of locking. After reset the last value of the integrator, which has been stored in EEPROM on a regular basis, is restored. This will retune the controlled oscillator to very

nearly the correct frequency. The loop is then opened and the software waits for the following all to occur

(state 0):

- GPS site survey completed and switched to position hold.
- OCXO supply current to drop below a threshold showing the OCXO has warmed up
- c) A measure |I|+|Q| which is an approximate measure of the signal level at the phase detector to rise above a threshold.

When these conditions are fulfilled, the software attempts to lock the loop (state 1) by selecting the phase frequency detector, maximum bandwidth, and maximum subsample rate. It then closes the loop and waits for another measure, which is |phaseresult|, to drop below a threshold. The measure |phaseresult| is the modulus of each phase calculation filtered in an 8th order exponential filter, the bandwidth of which, for the 15.625 s/s subsample rate, equals 9.7mHz. Once the lock threshold for |phaseresult| is reached, the lock state (state 2) is entered. The bandwidth is switched to the users selected bandwidth, which has been maintained in EEPROM, and the phase detector is switched over to the narrow band phase detector (Pi/2 to -Pi/2). All the time during normal operation, |phaseresult| is being compared to a lower threshold than the lock threshold. If it exceeds this threshold, state 3 is entered which provides a brief flash of the lock LED to warn the user that the selected bandwidth may be too narrow for the PLL to track the drift of the controlled oscillator fast enough. This low threshold is currently set at 480ps maximum phase error.

In extreme cases the lock threshold (4.8ns phase error) may be exceeded, in which case the software assumes lock is lost and re-enters state 1. A further performance measure is calculated, which is available over the interface. This is the first difference of the phase error, filtered in an 8th order exponential filter. It is corrected for subsample rate, and has a constant sensitivity of 5.8x10-15 per bit (at 10MHz phase detector frequency). This performance measure gives the mean fractional frequency difference between the controlled oscillator and the reference, and is useful for setting up the optimum bandwidth of the PLL. The band width and damping of the PLL is controlled by 4 parameters, integrator digital gain, proportional digital gain, pre-filter order, and subsample rate. These are preset for 8 values of user selected bandwidth, and can only be changed by modifying the software. It is possible to temporarily adjust the four individual parameters as part of a test procedure carried out over the RS232 interface. The selection of the 4 parameters has been optimized using a mathematical model of the PLL modelled as a MATHCAD spreadsheet.

IV. TESTING

The E8000 BVA has a much lower tuning constant of the BVA compared to a standard OCXO. The gain table was originally optimised using MCAD for an OCXO with a tuning constant of 20.2 r/Vs, this is 3.215 Hz/V, or 3.2E-7/V at 10MHz. The BVA tuning rate is 1.2E-8/V, or 0.377 r/Vs. This meant that the loop was under damped for all the values of the user gain parameter. Running the spreadsheet for the BVA using the original values in the gain table (Note the OCXO divider is 2 as the BVA is 5MHz, the VCO tuning rate is 0.377, and the VCO modulation pole is 10Hz) the graphs are showing more than 10dB of peaking. This shows under damping.

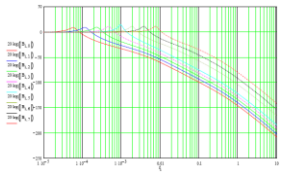

Figure 1. Transfer function (output phase to reference phase)

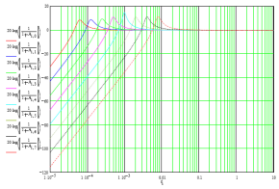

Figure 2. VCO phase noise reduction by loop

With the gain table re-optimised specifically for the BVA the damping has been significantly improved.

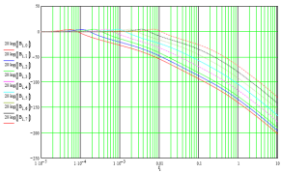

Figure 3. Transfer function (output phase to reference phase)

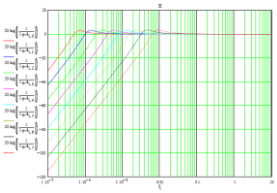

Figure 4. VCO phase noise reduction by loop

When the loop is locking, special values are used instead of the gain table. The objective when locking is to get the widest possible loop bandwidth. The loop can be under damped provided it is stable. These special values are values are different for rubidium, OCXO and BVA.

The gain tables all have the same pattern. For a step of 1 in the user gain parameter, the digital gain must change by 2. A change of subsample rate of 2x is equivalent to a change of 1 in the digital gain. Hence the digital gain changes 2, 4, 5, 6, 8, 9, B, D. The proportional gain changes by 1 each step to keep the same damping. In order to increase the damping, 1 may be added to all the values of the proportional gain.

The pre-filter does not really affect the loop results, unless its cut off frequency is too close to the loop bandwidth when the additional phase shift will reduce the damping.

The slew rate limiter is only important when locking. By observing the tuning voltage when locking, you should see the limiter working when the tuning voltage changes linearly, not sinusoidal. If the GPS receiver loses lock, then the slew rate limit should be decreased.

It is a good idea to test the loop damping with the complete system working. This may be done as follows:

Using a reasonably fast loop wait until the loop is stable with the oscillator well warmed up. Inhibit state control. Monitor the frequency with the A7 signal stability analyser. Now introduce a frequency step by writing a new value to the loop integrator. This must be quite small, around a 1/20 of the maximum pulling range of the oscillator. The output frequency will change quickly, and then slowly recover to its previous value there should be a small amount of overshoot.

V. CONCLUSION

The GPS BVA has a number of significant advantages over the current primary standards such as caesium and hydrogen maser.

- Excellent short term stability of the BVA combined with the long term of GPS
- No drift due to GPS disciplining
- Low phase noise
- Reduced cost of ownership and initial purchase costs savings of some 50%

Our current development has shown significant improvements on performance, however we have had initial problems with environmental factors such as laboratory noise and component manufacturers' reluctance to specify the noise performance of their products as can be seen from the chart in figure 5 the optimum performance that we are currently achieving (red line) however the performance of the BVA can be dramatically affected by the op amps noise in the tuning line (purple line) the difference between the optimum and actual is the variation in performance of the op amp in the tuning line (same manufacturer, part number and batch).

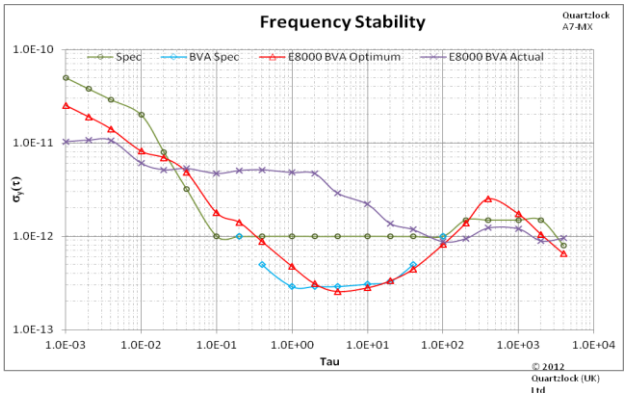

Figure 5. BVA Frequency stability comparison chart

- Having measured the GPS BVA with
- the DPLL loop opened
- The BVA adjust input disconnected from tuning line and biasing the adjust input to Vref/2.

There is now clear evidence that the tuning source in the GPS BVA which consists of voltage reference, DAC, and output amplifier, is generating sufficient noise below 10Hz to degrade the phase noise of the GPS BVA. With the tuning line connected, the noise is -132dBc/Hz at 10Hz and -97 at 1Hz. With the BVA disconnected the noise is -138 at 10Hz and -108 at 1Hz.

In this design we have replaced the original op amp with an Analogue Devices op amp. This is a lower noise op amp, also in a smaller package. The DACs, which may be the main source of the noise, are still the Maxim devices. These are used in the A6-CPS, and all the GPS products. We have investigated the possibility of using the analogue devices dual DAC, which may have lower noise. Unfortunately DACs are very badly specified as to low frequency noise. For example the Maxim DAC shows a noise of 600nV/rtHz at 100Hz, and rising rapidly at lower frequencies. The Analogue Devices DAC claims 64nV/rtHz at 1kHz, with no specification at lower frequencies.

Another possible source of noise is the Maxim digital potentiometer. Because the digital potentiometer is only available in 50kohm versions, the feedback resistors which set the amplifier gain are higher value than is desirable from the point of view of noise

All these changes will make an improvement. In order to try them we need a new GPS board. There would also be firmware modifications as the programming of the Analogue Devices is different.

We are looking into the possibility to make a small test board consisting of the voltage reference, DAC and output amplifier, using the new parts. This could be attached to a GPS board with wires to the clock, data and chipselect to try the new parts without the cost of making and building a complete board. If the new tuning circuit was sucessful, then all the products which use the current arrangement would be updated.

Direct comparison of two Cryocooled Sapphire Oscillators presenting relative frequency instability at 10^{-15}

S. Grop[†], B. Dubois[†], J.-L. Masson[*], P.-Y. Bourgeois[*], Y. Kersalé[*], E. Rubiola[*], G. Haye[*†] and V. Giordano[*†]
[*]FEMTO-ST Institute, Time and Frequency Dpt., 32 av. de L'Observatoire, 25044 Besançon Cedex, France
[†]ULISS–ST, SAIC Université de Franche-Comté, Témis Sciences, 25000 Besançon Cedex, France

***Abstract*— In this paper we present the direct comparison of two microwave Cryocooled Sapphire Oscillators demonstrating a relative frequency stability better than 2×10^{-15} at short term and of the order of 1×10^{-14} over one day integration. We also report the frequency stability evaluation of a microwave signal generated from a planar waveguide external cavity laser (PW-ECL) referenced to a Fabry-Perot cavity through optical-to-microwave frequency division with a commercial Er:fiber optical frequency comb owned by the "laboratoire temps-fréquence" (LTF) of the university of Neuchâtel, Switzerland, and the phase noise measurement of the engineering model of the Pharao clock frequency synthesis owned by the "Centre National d'Etudes Spatiales" (CNES) at Toulouse, France. These lastest results were obtained by moving one of our Cryogenic Sapphire Oscillator (CSO) from the FEMTO-ST Institute to these two metrological sites.**

I. Introduction

We recently developped a Cryogenic Sapphire Oscillator (CSO) named Elisa presenting a short term frequency stability better than 3×10^{-15} for 1 s $\leq \tau \leq$ 1000 s and achieving 4.5×10^{-15} for one day integration [1], [2]. This CSO was designed and built in the framework of a research contract funded by the European Space Agency (ESA). It incorporates a pulse-tube cryocooler instead of a bath cryostat, thus eliminating the need for regular supplies and manual refilling of liquid helium. The advent of reliable and cryocooled CSO open the possibility to implement such an ultra-stable reference not only in metrological laboratories with liquid helium facilities but also in remote sites like base stations for space navigation, VBLI antenna sites, ... [3], [4]

In our project ULISS (Ultra Low Instability Signal Source), funded by Regional and European Institutions, we built a new cryocooled oscillator named ULISS specially designed to be transportable. The ULISS oscillator was already used to qualify with success a high stability frequency source located at Neuchâtel, Switzerland, and the PHARAO frequency synthesis Toulouse, France. ULISS was specially moved from FEMTO-ST for the measurement compaigns.

In this paper we present the frequency stability characterization of the newly built CSO demonstrating the reproductibility of our technology and we summarize the main results obtained at the LTF and CNES.

A. Schematic architecture of the Cryocooled Sapphire Oscillator Instruments

The architecture of a Cryocooled Sapphire Oscillator Instrument is represented in the figure 1.

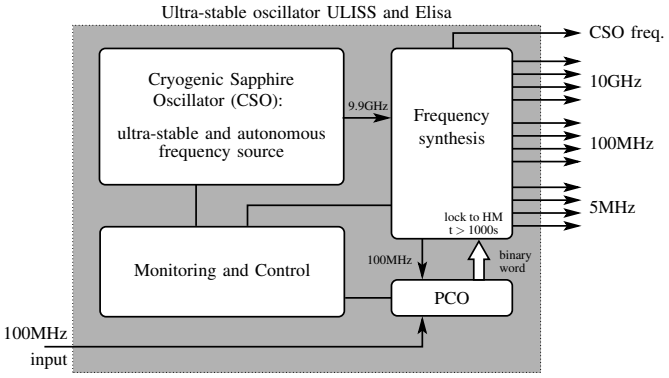

Fig. 1. Schematic architecture of a Cryocooled Sapphire Oscillator Instrument

The CSO design and its characterization were already described in the references [1], [2], [5]–[7].

II. ULISS frequency stability characterization

ULISS unit is a copy of the first unit Elisa and was finalized the 11th November 2011. The two CSO outputs were mixed to generate a beatnote at 750kHz. This beatnote was directly counted on an Agilent 53132A Λ-counter parametrized with a gate time $\tau = 1$ s [8], [9]. After approximately 4 days of acquisition, the relative frequency deviation $\sigma_\Lambda(\tau)$ was calculated for the different integration times τ by grouping the 1 s data. The first significant result was measured the 12th December 2011, the time to tune the different servo control loops. The result is given in the figure 2. No data post-processing has been done: no abnormal point suppression nor drift removing.

We measured a relative frequency stability $\sigma_\Lambda(\tau)$ better than 2×10^{-15} for integration times 1 s $\leq \tau \leq$ 200 s. For longer integration times, we observed a hump around 2000 s, that we still have to determined the source, and a drift of 1×10^{-14}/day. The second curve of the figure 2 is the relative frequency deviation calculated from a quiet selected time period of about

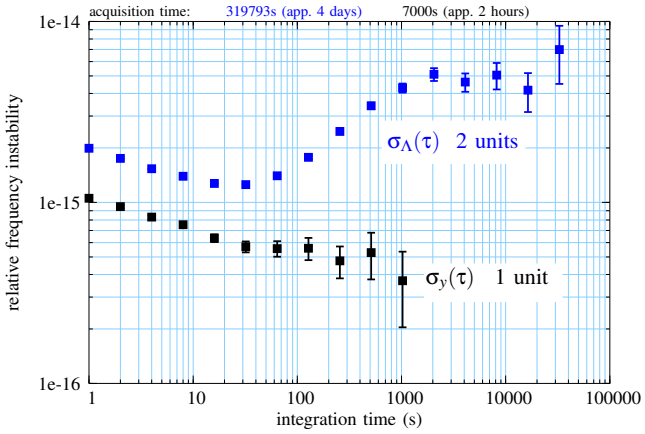

Fig. 2. Relative frequency stability of the 9.99 GHz CSO outputs

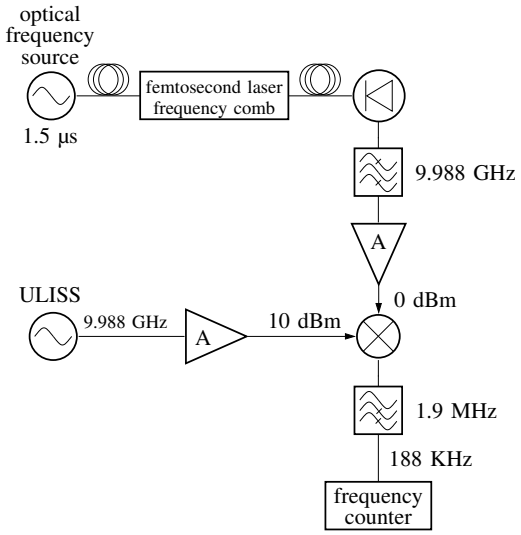

Fig. 3. Comparison set-up

7000 s extracted from the complete set of data. The calculated standard deviation corresponds to a flicker floor, i.e. its value does not depends on τ. This flicker floor comes from the USO internal noise sources. As the two CSOs operate at a different frequency, we assume that these noise sources are decorrelated. In that case and if the two CSOs are assumed identical, it is justified to divide the result by $\sqrt{2}$ to obtain the frequency stability of one unit. Moreover the reference [9] gives the correspondance between $\sigma_\Lambda(\tau)$ and the true Allan deviation $\sigma_y(\tau)$. For white frequency of flicker frequency noise: $\sigma_\Lambda(\tau) \approx 1.3 \times \sigma_y(\tau)$. The open squares in the figure 2 represent $\sigma_y(\tau)$ evaluated taking into account these two corrections. The flicker floor of one unit is thus:

$$\sigma_y(\tau) = 4 \times 10^{-16} \text{ for } 30 \text{ s} \leq \tau \leq 500 \text{ s} \qquad (1)$$

Although the following procedure has reasonable assumption and is often used to present USO characterization. It represents an optimistic evaluation. Remainder aware of this uncertainty, the flicker floor given in the equation 1, can be considered as the best stability achievable by a well adjusted CSO in stable environmental conditions. The upper curve is the typical frequency stability achievable with our CSO in standard laboratory conditions.

III. ULISS's odyssey

A. Test of an all-optical microwave signal generation

The ULISS's odyssey started the 15th February 2012 at the LTF of Neuchâtel. ULISS was operational three days later and was used as frequency reference to evaluate the frequency stability of a microwave signal generated from an optical frequency reference.

The optical frequency reference consists in a compact and low-cost planar waveguide external cavity laser (PW-ECL) stabilized on a high finesse Fabry-Perot ULE optical cavity. The frequency stability of this optical reference is transfered to microwave domain through optical-to-microwave frequency division with an femtosecond laser frequency comb. The comparison set-up is given in the figure 3.

The beam of the stabilized femtosecond laser was sent to a large bandwidth photodiode. The output signal of the photodiode is filtered to keep the 40th harmonic of the femtosecond laser repetition rate, amplified and mixed with the amplified 9.988 GHz ultra-stable signal generated by ULISS. The resulting beatnote at 188 kHz was counted to evaluate the frequency stability. The measurement result is shown in the figure 4.

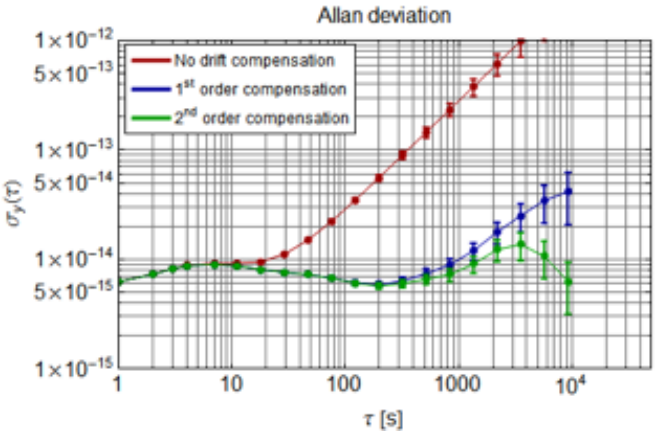

Fig. 4. Relative frequency stability of the 9.99 GHz microwave signal generated with the femtosecond laser and ultra-stable laser

ULISS allowed to evaluate the frequency stability of an all-optical microwave signal generator without the need of a second equivalent unit.

B. Test of an USO X-tal

During the measurement compaign at the LTF, a quartz oscillator prototype from the Oscilloquartz company was characterized in term of frequency stability. The set-up measurement scheme is presented on figure 6.

To ensure a sufficient resolution of the measurement instrumentation, the quartz signal frequency was multiplied by

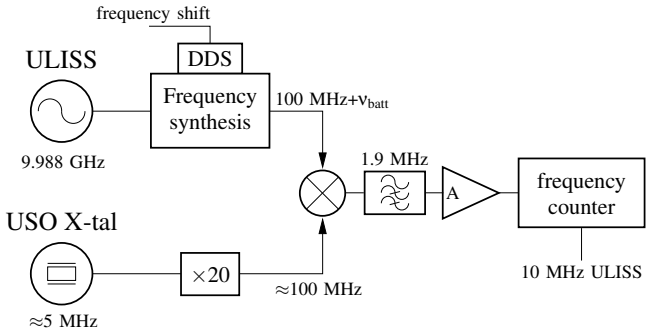

Fig. 5. Quartz oscillator frequency stability measurement set-up

20 and compared to the 100 MHz coming from the ULISS frequency synthesis. The best result is shown on figure 6.

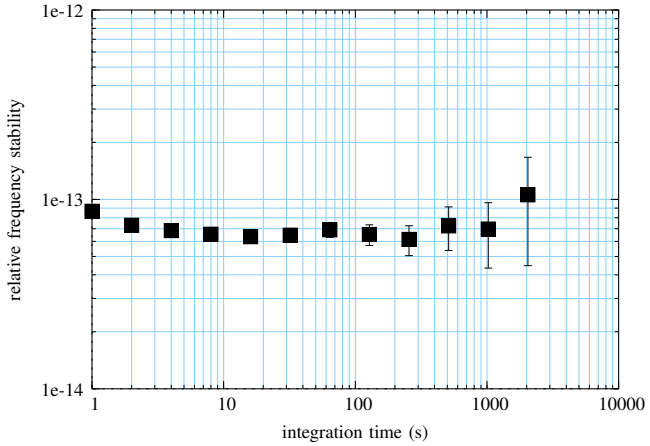

Fig. 6. Relative frequency stability of the best quartz oscillator

This is the second time that such a performance was observed unambiguously for a quartz crystal USO [10]. The frequency stability measured at the FEMTO-ST Institute in 2010 and at the LTF are identicals. It demonstrates the potentiality of ULISS to be used to qualify high-performances industrial products.

The 5th May, ULISS returned back to the FEMTO-ST Institute and was tested against Elisa to checked if any malfunctions appeared due to the trip. The 9th May, the same frequency stability as our first measurement compain was measured (figure 7).

This result is enough to prove the robustness and reliability of our ultra-stable frequency source.

C. Test of an ultra-low noise microwave frequency synthesis

The PHARAO project aimed to operate a cold-atoms caesium clock in microgravity in the International Space Station (ISS). The performances of this cold-atoms clock will be combined with those of an active Hydrogen Maser (HM) to generate an onboard timescale using the excellent short-term stability of the HM and the long-term stability and accuracy of the cesium clock PHARAO. This assembly constitutes the core of the ACES (Atomic Clock Ensemble in Space) instrument.

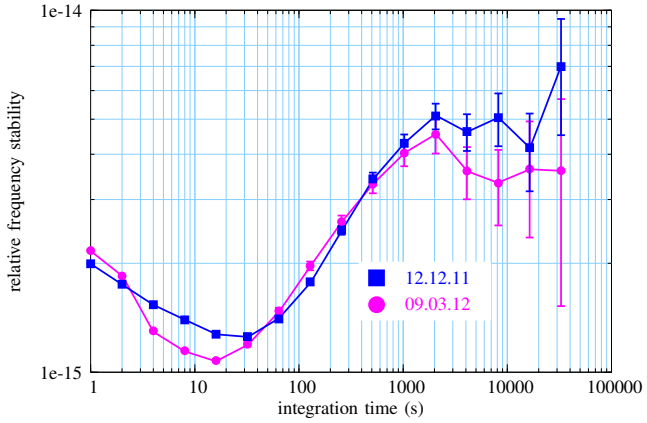

Fig. 7. Relative frequency stability of the 9.99 GHz CSO output before and after the trip to the LTF at Neuchâtel

Today, the PHARAO instrument is completing its qualification. ULISS was thus be used to qualify the flying model of the PHARAO 9.192GHz local oscillator. The signal that will probe the cold atoms is generated from a frequency synthesis referenced on a state-of-the-art quartz oscillator. Apart from the 9.192GHz signal, the PHARAO's frequency synthesis delivers a high frequency stable 100 MHz signal to compare PHARAO to the HM. Drastic phase noise specification has been imposed on these two outputs. The use of ULISS as a frequency reference greatly simplfied the validation of the PHARAO's frequency synthesis. The figure 8 represents the phase noise measurement set-up used to characterize the 9.192 GHz output signal.

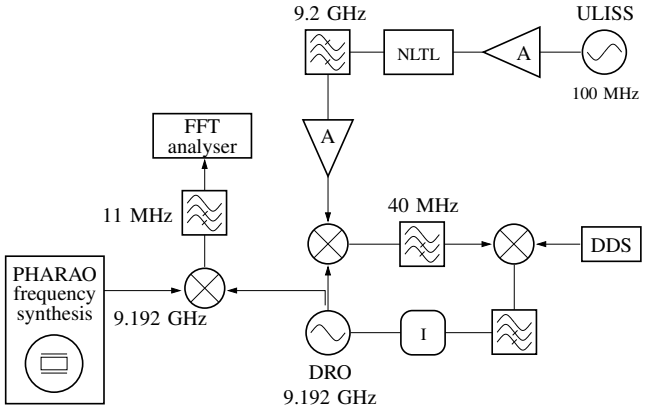

Fig. 8. Set-up of the 9.192 GHz signal generation and phase noise measurement

A nonlinear transmission line (NLTL) generates some harmonics of the incoming amplified 100 MHz generated from ULISS. After filtering, the 9.2 GHz signal is amplified and compared to the signal of a 9.192 GHz Dielectric Resonator Oscillator (DRO). A Direct Digital Synthesizer locked on ULISS output signal compensates the frequency difference and is used to phase lock the DRO. The result is shown in the figure 9 and was obtained two days after our arrival at CNES site.

The 100 MHz phase noise measurement set-up is far sim-

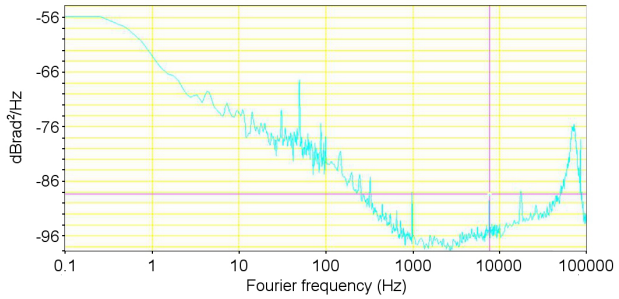

Fig. 9. Phase noise of the PHARAO frequency synthesis at 9.192GHz

pler. The 100 MHz output of ULISS is adjusted, by shifting the frequency output of the ULISS's frequency synthesis DDS, to perfectly fit to the 100 MHz output of the PHARAO's frequency synthesis, with the use of a industrial phase comparator produced by the company Timetech Gmbh. The result is shown in the figure 10.

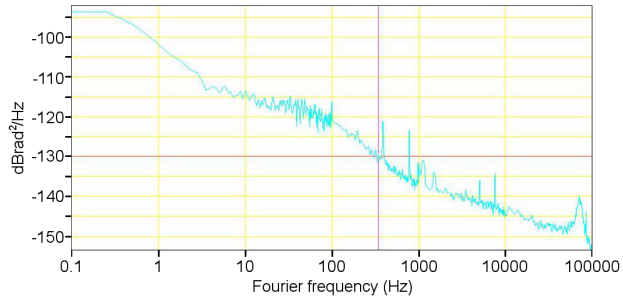

Fig. 10. Phase noise of the PHARAO frequency synthesis at 100Hz

The results fit to the phase noise measurement results made few years ago at CNES except the modulation observed at 80 KHz Fourier frequency. The modulation is justified by a malfunction of the ULISS's frequency synthesis DRO.
Despite the modulation, the results are convincing and show the utility of such kind of state-of-the-art frequency source for the characterization of low phase noise frequency source.

IV. Conclusion

The results shown on this paper demonstrate the technology maturity and reliability of our CSOs. We reached our objective to develop a transportable version of the state-of-the-art crycooled sapphire oscillator Elisa with equivalent performances and we already visited two scientific institutes which led to interesting collaboration and results.

Acknowledgment

The authors wish to acknowledge to the Fond Européen de développement Régional (FEDER), le Conseil Général de Franche-Comté and OSEO for their support and also Jacques CHAUVIN from OSA to provide USO X-tal during the test compain at the LTF, Gianni DI DOMENICO, Stéphane SCHILT, Vladimir DOLGOVSKIY and Nikola BUCALOVIC from the LTF to provide their results and Claude ESCANDE, David VALAT and Sébastien TELLIER from CNES to provide the phase noise curves of the engineering model of the PHARAO frequency synthesizer.

References

[1] S. Grop, P.-Y. Bourgeois, N. Bazin, Y. Kersalé, E. Rubiola, C. Langham, M. Oxborrow, D. Clapton, S. Walker, J. DeVicente and V. Giordano, Elisa: a cryocooled sapphire oscillator with 1.10-15 frequency stability, Revue of Scientific Instruments, 81, 2010.

[2] S. Grop, W. Schafer, P.-Y. Bourgeois, Y. Kersalé, M. Oxborrow, E. Rubiola and V. Giordano, Unprecedented High Long Term Frequency Stability with a Microwave Resonator Oscillator, IEEE Transactions on Ultrasonics, Ferroelectrics and Frequency Control, 58, 8, 1694-1697, 2011.

[3] V. Giordano, S. Grop, P.-Y. Bourgeois, Y. Kersalé, E. Rubiola, M. Mrad, C. Langham, M. Oxborrow and W. Schafer, Cryogenic sapphire microwave oscillators for space, metrology and scientific applications, General Assembly and Scientific Symposium, URSI, Istanbul, Turkey, 2011.

[4] J. G. Hartnett, N. R. Nand, Ultra-low vibration pulse-tube cryocooler stabilized cryogenic sapphire oscillator with 10-16 fractional frequency stability, IEEE Trans. on MTT, 58, 3580-3586, 2010.

[5] S. Grop, P.-Y. Bourgeois, R. Boudot, Y. Kersalé, E. Rubiola and V. Giordano, 10 GHz cryocooled sapphire oscillator with extremely low phase noise, Electronics Letters, 46, 6, 420-422, 2010.

[6] S. Grop, W. Schafer, P.-Y. Bourgeois, Y. Kersalé, M. Oxborrow, E. Rubiola and V. Giordano, Unprecedented High Long Term Frequency Stability with a Microwave Resonator Oscillator, IEEE Transactions on Ultrasonics, Ferroelectrics and Frequency Control, 58, 8, 1694-1697, 2011.

[7] S. Grop, P.-Y. Bourgeois, E. Rubiola, W. Schafer, J. DeVicente, Y. Kersalé and V. Giordano, Frequency Synthesis Chain For The ESA Deep Space Network, Electronics Letters, 47, 6, 386-388, 2011.

[8] E. Rubiola, On the measurement of frequency and of its sample variance with high-resolution counters, Revue of Scientific Instruments, 76, 5, 2005.

[9] S. T. Dawkins, J. J. McFerran and A. N. Luiten, Considerations on the measurement of the stability of oscillators with frequency counters, IEEE Transactions on Ultrasonics, Ferroelectrics and Frequency Control, 54, 5, 918-925, 2007.

[10] S. Grop, B. Dubois, P.-Y. Bourgeois, Y. Kersalé, E. Rubiola, G. Haye and V. Giordano, ULISS: A Mobile Cryogenic U ltra- Stable Oscillator, Joint conference of the 2011 IEEE IFCS-EFTF, San Francisco, US, 2011.

OCXO Ensemble As Improved Local Oscillator For Atomic Fountains

C. E. Calosso, E. K. Bertacco, S. Micalizio, A. Godone, D. Calonico
Divisione di Ottica
INRIM
Torino, Italy

G. A. Costanzo
Dipartimento di Elettronica e Telecomunicazioni
Politecnico di Torino
Torino, Italy

***Abstract*—In this paper we present a technique to improve the phase noise capabilities of local oscillators for atomic fountains. Specifically, the local oscillator is a combined system composed of two independent BVA oscillators. In this way, the measurement time reduces of a factor of two in comparison to the more usual local oscillator realized by one single BVA.**

I. INTRODUCTION

In atomic fountains the phase noise of the local oscillator is responsible of the short-term stability degradation related to the Dick effect. Ultra stable cryogenic oscillators or other ultra-low noise sources are used to avoid this effect, however these solutions are quite expensive and not always completely reliable on long measurement times.

On the other hand, BVA oscillators [1] have a low exercise cost, but the associated phase noise may lead to a significant increase in the measurement time, considering that the latter scales as the square of the short-term stability. A nominal improvement in the measurement time of a factor of two can be reached by combining two independent BVA. In this case, extreme care has to be paid to avoid injection-locking of the two oscillators, in order to maintain them uncorrelated, as required by the scheme. For this purpose, besides a high isolation between the two, it is useful to have them at different frequencies. A high resolution real-time phase-meter able to manage that frequency difference is then necessary.

II. ONE BVA SYSTEM

In principle, the more usual scheme adopting one BVA oscillator is shown in Fig. 1.

BVA is used as a cleaning filter for the relatively high phase noise of the Hydrogen Maser in the range of the Fourier frequency involved in the Dick effect (1-100 Hz). This is shown in Fig. 2.

At INRIM, this is currently done in the simplest way, by phase locking a BVA (option 08) on the 5 MHz output of the Maser with a classical analog PLL with a bandwidth of about 0.3 Hz. The PLL is followed by a X20 frequency multiplier to obtain 100 MHz, an intermediate frequency of the synthesis chain (see Fig. 1) [2].

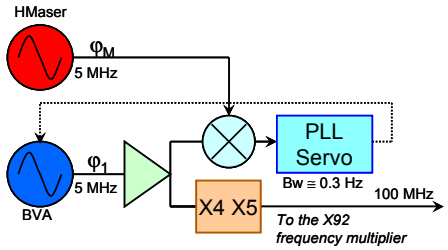

Figure 1. Scheme of the usual local oscillator system.

In this manner, in the ideal case, only the noise of the BVA contributes to the Dick effect and represents the ultimate limit for it. Even using the best BVA available, this limit remains significant, of the order of 10^{-13}, leading to averaging time of 10^6 to reach the 10^{-16} level.

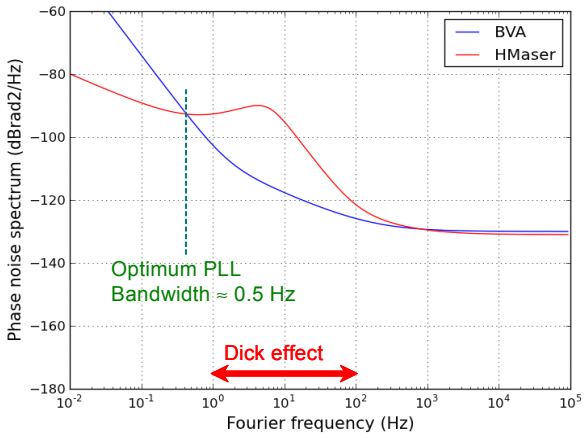

Figure 2. Phase noise of the local oscillator in the case of a single BVA oscillator. Carrier at 100 MHz.

III. THE COMBINATION OF TWO INDEPENDENT BVA

To improve the ultimate limit without employing cryogenic oscillators or ultra-stable lasers plus optical comb, it

is possible to use two or more nominally identical BVA oscillators. In fact, we suppose that the two oscillator are affected by phase noises $\varphi_1(t)$ and $\varphi_2(t)$ that are uncorrelated, and moreover that they have the same variance:

$$E\{\varphi_1(t)\varphi_2(t)\}=0 \tag{1}$$

$$E\left\{\varphi_1(t)^2\right\}=E\left\{\varphi_2(t)^2\right\}=\sigma_\varphi^2 . \tag{2}$$

Defining $<\varphi>$ as the average of the two process it is easy to see that:

$$\sigma_{\langle\varphi\rangle}^2=\frac{1}{2}\sigma_\varphi^2 \Rightarrow \sigma_{\langle\varphi\rangle}=\frac{1}{\sqrt{2}}\sigma_\varphi \tag{3}$$

Therefore, the variance of the average of the two signals improves of 3 dB and consequently the integration times halves. Previous relations can be generalized to a number N of signals.

Here we present the case of two BVA locked to one H-maser, but the scheme can be extended to an arbitrary number of BVA and Masers.

IV. THE PROPOSED SCHEME

The phases of the Maser and of two BVA are measured respect the 100 MHz Ultra Low Noise local oscillator (ULN) by means three high resolution phase meters and then processed by the clock ensemble algorithm to calculate the correction to the ULN (see Fig. 3).

The phase meters provide the phase error of the ULN with respect to the 100 MHz output of the Maser (φ_M - φ_0) and to the two 5 MHz BVA ($20\varphi_1$ - φ_0, $20\varphi_2$ - φ_0). The averaging of the BVA noises is done for Fourier frequencies f below Bw_1 by the first Digital PLL that locks the ULN to the average of the BVA phases reported at 100 MHz [$20(\varphi_1 + \varphi_2)/2$]. For f below Bw_2, the second DPLL intervenes applying a correction φ_C in order to lock φ_0 to φ_M (see Fig. 4).

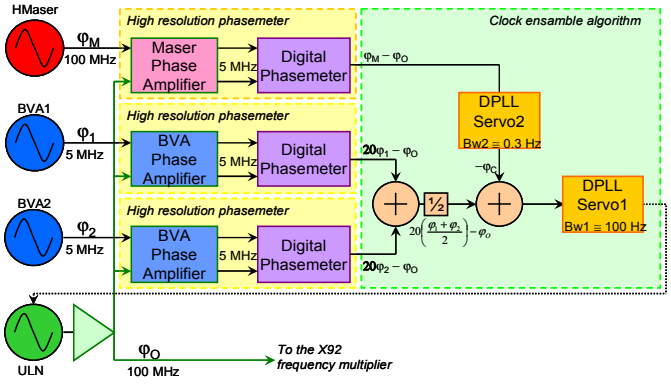

Figure 3. The proposed scheme.

In this manner, we have:

$$\begin{aligned} &\varphi_0 \approx \varphi_{0\text{-OL}} && f > Bw_1 \approx 100\ \text{Hz} \\ &\varphi_0 \approx 20(\varphi_1+\varphi_2)/2 && Bw_2 < f < Bw_1 \\ &\varphi_0 \approx \varphi_M && f < Bw_2 \approx 0.3\ \text{Hz} \end{aligned} \tag{4}$$

The phase noise improvement is reported by the dashed line in Fig. 4.

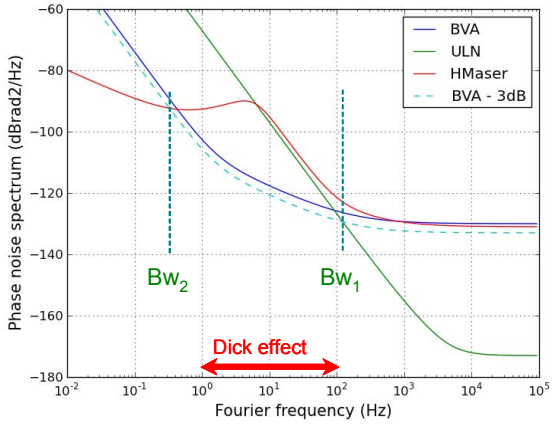

Figure 4. Phase noise improvement with respect to Fig. 2.

V. THE HIGH RESOLUTION PHASE METER

The high resolution phase meter gives great flexibility to this scheme, but, on the other hand it is a critical point, because its noise is directly added to the oscillators one. In particular, due to the low pass filtering nature of the PLL, the BVA phase meter has to be better than the BVA for $Bw_2 < f < Bw_1$ and the Maser phase meter has to be better than the Maser for $f < Bw_2$. For this reason, the digital phase meter is preceded by a phase amplifier that improves the resolution and the noise by a factor 20.

A. BVA phase amplifier

The BVA phase amplifier down-converts φ_0 from 100 to 10 MHz and from 10 to 5 MHz, by using two signals derived from the BVA: a 90 MHz obtained by direct multiplication and the distributed 5 MHz. With this scheme, at the output of the digital phase meter we have:

$$20\varphi_{1(2)} - \varphi_0 + \varphi_{PM} \tag{5}$$

where the digital phasemeter noise φ_{PM} clearly gains a factor 20 with respect to the BVA. It also gains a factor 20 with respect to φ_0, because of the ratio between the carrier frequencies (see Fig. 5).

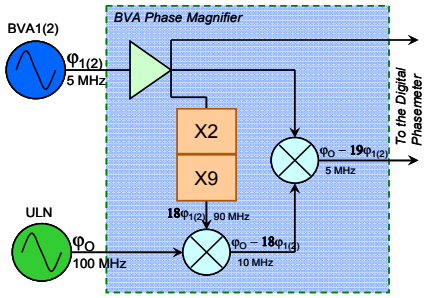

Figure 5. Scheme of the BVA phase amplifier.

B. *Maser phase amplifier*

Also the BVA phase amplifier down-converts φ_0 from 100 to 5 MHz, taking advantage of the 100/5 MHz ratio. In this case, the H-maser is already at 100 MHz, so we obtain a 95 MHz signal by using a by 20 frequency divider and a Single Side Band (SSB) mixer (see Fig. 6). With this scheme, at the output of the digital phase meter we have:

$$\varphi_M - \varphi_0 + \varphi_{PM} \tag{6}$$

Strictly speaking, this is a time amplifier, because at its output we have the same phase noise but that is referred to an amplified period (200 ns instead of 10 ns).

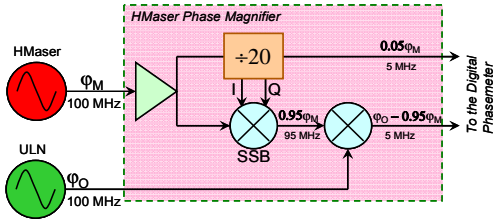

Figure 6. Scheme of the maser phase amplifier.

VI. DIGITAL PHASE METER

The digital phase meter shown in Fig. 7 is one of the key points of this work. With respect to a mixer it is much more complex and noisier, but, on the other hand, it allows to have the inputs at different frequencies, overcoming the main limitation of the mixer: the limited input phase range. Being free running, the VCO input of the BVA is unconnected, reducing the possibility of injection locking. The latter is also reduced thanks to the possibility to run the BVA at different frequencies.

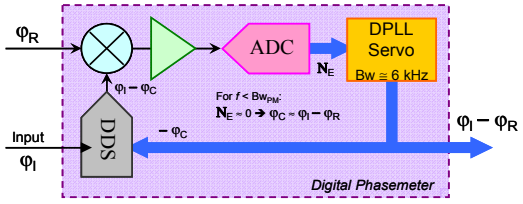

Figure 7. Scheme of the digital phase meter

The phase meter is based on a Direct Digital Synthesizer (DDS) [3] clocked by the input frequency and that digitally tracks the reference. The correction, the digital phase to the DDS, is the measure. This quantity is used by the FPGA that implements the clock ensemble algorithm.

In open loop condition with φ_C = cost, the output of the DDS is in fixed phase relation with the input (φ_I - φ_C). It is compared with the reference and the error signal obtained [(φ_I - φ_C)- φ_R] is amplified and acquired by the Analog to Digital Converter (ADC) that feeds the Digital PLL servo. By closing the phase loop, for $f < Bw_{PM}$ the error signal approaches zero, forcing

$$\varphi_C = \varphi_I - \varphi_R \tag{7}$$

VII. RESULTS

The phase noise of the digital phase meter (Fig. 8) in the Dick effect region is 10 dB lower than the BVA noise, leading to a degradation of the overall performance of about 0.3 dB. The noise bump at 10 kHz is due to the quantization of the DDS phase, few ps and is filtered out by the Digital PLL at 100 Hz.

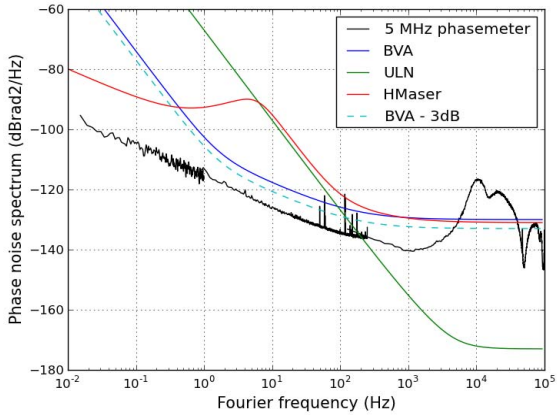

Figure 8. Comparison of the different phase noises.

The relative frequency stability of the digital phasemeter is 1.9×10^{-13} at 1 s and is improved by the phase amplifier to 1×10^{-14} at 1 s (see Fig. 9). In this manner it is negligible with respect to the frequency stability of the H-maser and of the BVA.

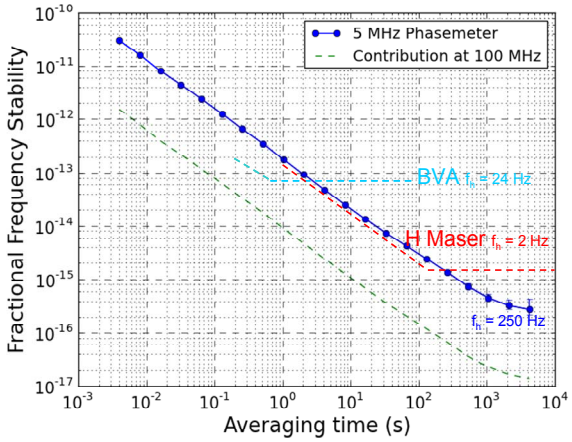

Figure 9. Frequency stability of the digital phasemeter.

VIII. CONCLUSIONS

In conclusion, we have proposed a scheme that implements two BVAs working at different frequencies, avoiding the injection locking problem. The digital phase meter, the core of the system, has been implemented and characterized, showing a negligible residual phase noise.

This scheme has several advantages: each BVA works in open loop condition and can be used by other experiments; the digital nature of the scheme can support more advanced algorithm (Kalman filters, Active Disturbance Rejection Control, …); the PC download of the internal signals provides the monitoring of the external oscillators, being the latter free running and this is done at zero cost.

The same architecture can be used for other applications, i.e. the generation of a real time ensemble time scale if, instead of OCXO, atomic clocks are used.

IX. ACKNOWLEDGEMENTS

The authors would like to thank E. Rubiola for useful and stimulating discussions.

[1] E. Rubiola, “Phase noise and frequency stability in oscillators”, Cambridge University Press, November 2008

[2] S.R. Jefferts, E.A. Donley, T.E. Parker, F. Levi, “A new microwave synthesis chain for the primary frequency standard NIST-F1” Proceedings of the 2005 IEEE International, pp. 308 - 311, 29-31 Aug. 2005.

[3] V. Kroupa, “Direct Digital Frequency Synthesizers”, Wiley-IEEE Press

System for evaluation of long-term stability of precision quartz crystal oscillators and results of its use.

Nikonov A.G, Ivanov Y.A.
Morion, Inc, Saint-Petersburg/Russian Federation
E-Mail: morion@morion.com.ru
www.morion.com.ru

Abstract - **Long-term stability (aging) is one of the key parameters of quartz crystal oscillator. Approximation and time series prediction methods are used to evaluate it. An improved mathematical model which allows to evaluate quartz crystal oscillators from the point of long-term stability (aging) has been developed. Evaluation of the stabilization of aging process is used as the basis for the model's algorithm. Basing on such model a software system has been developed. In process of it's development different approximation functions were considered, including procedure of selection of suitable functions as well as their applicability, forecast accuracy and reliability. Also accuracy of forecast vs. duration of aging testing was studied. In this way the developed software system allowed to reach forecast of 5xE-9 accuracy for long-term stability per year. Also, what is practically important, the developed mathematical model allows to minimize possible human errors in evaluation of subject long-term stability of precision oscillators.**

INTRODUCTION.

Long-term stability (aging) is a quartz crystal oscillator frequency change during a certain long time span. Its value depends on continuous changes occurring in a quartz crystal unit, and other elements of the oscillator circuit. Long-term stability is expressed as an average frequency relative change for a given period of time. The methods of forecasting, allowing to quite accurately represent an oscillator drift in a required period of time (including the whole lifespan) from a certain initial sector (usually not exceeding 30 days), are applied to evaluate it. Extrapolation based on approximation of data obtained through measurements is used for the most accurate forecasting. Oscillator aging is most commonly behaves logarithmically, i.e. being the strongest within the first weeks and gradually decreasing thereafter. The main function of approximation applied is determined by the following expression [1]:

$$df/f_0 = A+B*Ln(Ct+1), \qquad (1)$$

where *A, B u C* - approximation coefficients, and *t* – time passed from the first measurement

The task of long-term extrapolation (1-10 years) from data taken for a short initial sector (15-30 days) is hard to present algorithmically. Non-ideal behavior of a quartz crystal unit in the process of measurements also complicates it; therefore, a subjective method (i.e. results evaluation by an experienced specialist) is often used for evaluation of fidelity of data obtained through calculations. At that, the specialist's evaluation includes data quality, approximation thereof, and long-term oscillator stability reliability. Problems inherent in all subjective methods, namely:

- Low stability of evaluation due to a subjective factor effect.
- Increased laboriousness.

The main problem of automation of quartz crystal oscillator aging evaluation involves data processing, as frequency graphs often show jumps, drops etc.; at that, a decision is needed as to whether they are an error of measurements or actually caused by oscillator operation. In addition, the initial sector's oscillator aging has very steep; therefore a more accurate forecast requires removing it from the consideration. It should also be noted that approximation built to formula 2 does not fit well to all oscillators; hence,

the automation problem is added with the problem of approximation function selection.

An algorithm, permitting automatic evaluation of precision quartz crystal oscillators aging, thus solving all the above named problems, has been developed by Morion, Inc. Aging of quartz crystal oscillators can be forecasted with high precision and minimum span time due to this algorithm and the algorithm-based software.

METHOD DESCRIPTION

The method the developed aging forecasting algorithm is based on, involves transformation of a univariate time series, resulting from quartz crystal oscillator frequency measurements, into components, being parts of the initial series. At that, the least square method is applied for calculating coefficients of the approximation functions. The ratio of annual aging forecast for a current component of the series to this component position in the initial series is calculated in the process of transformation. Accordingly, the description of the process of aging forecast in time is obtained, allowing to visualize the aging progress within the span of oscillator long-term stability measurement. Automatic selection of the start point of analysis, enabling removing the oscillator aging initial stage of a high steepness from the consideration, is also performed based on the deviations. The aggregate value of the forecast is calculated as the difference between the approximation curve ends values of the forecast interval multiplied by a certain error coefficient, considering oscillator behavior during forecasting. (These error coefficients were added when experimenting with the method accuracy determination and allowed to increase it considerably).

Software, allowing pre-processing of data to improve the forecast accuracy in the course of forecasting long-term oscillator stability, has been developed based on the algorithm considered. At that, the program automatically decides on whether to apply certain filters or not to maintain automatic operation.

Therefore, a part of jumps and drops not connected with behavior of a quartz crystal unit is processed automatically and does not distort the forecast results. All the above permits to conclude on accuracy of the forecast obtained in the course of calculations. It should also be noted that data, from which building the forecast by the program is impossible, are marked for subjective evaluation by the specialist that follows.

ACHIEVED RESULTS

In order to test the developed model, selected were data of ageing measurement of quartz crystal oscillators that have been measured for a long period of time (from half a year to two years). The sampling includes oscillators with 10 MHz/SC-cut quartz crystal units in HC43 and HC37 cases, as well as 5MHz quartz crystal units in HC37 and HC40 cases. Each type of oscillators was separately evaluated. In order to forecast aging, the set of approximation functions was added with the following ones:

- Logarithmic:
  - $A+B*Ln(t/C+1)$ (2)
  - $A+B*Ln(t/30+1) + C/t$ (3)
- Linear:
  - $A+B*t$ (4)
- Exponential:
  - $A+B*Exp(-C/t)$ (5)

Function 2 described in MIL-O-55310[1] is mainly used at forecasting aging as most suitable for description of quartz crystal oscillators aging. Function 3 allows description of data, showing more than one inflection on the data graph. Function 4 provides for description of a frequency linear change in the course of aging. Function 5 can be used for forecasting and was experimentally added to the analysis. The coefficients of these functions were calculated by means of the least square method. Aging was calculated for each oscillator, followed with the forecast to the above mentioned method made from a certain initial interval. The actual-to-forecasted value ratio of oscillator aging was used as the criterion of evaluation. The approximation function was

automatically selected by the program based on the value of total deviations of the curve from actual data. The initial sector boundary, downstream which the forecast was made, was also determined automatically. This sector is of high aging steepness and has a negative effect on the forecast results.

By results of this data array processing, we can arrive to the following conclusions:

1) The program automatically selected approximation function 2 for most oscillators (more than 80%). Function 5 has most poor convergence of series and thus is inapplicable for processing in the boundaries of this model. The linear function was selected for 13% of oscillators, function 3 was selected for other cases.

2) In order to increase accuracy of forecasting, error coefficients, considering oscillator behavior during running, were added to the method. Thus, the following data was obtained based on resulting evaluation of long-term stability of precision quartz crystal oscillators:

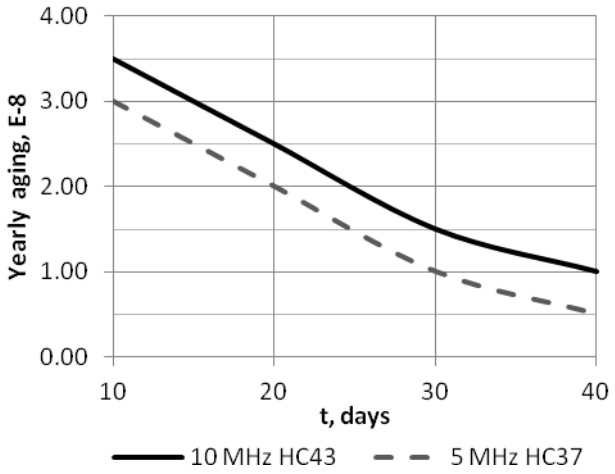

Fig.1.The ratio of the year aging rates, enabling forecasting with a probability of 95%, to the measurements period.

The values of the standard rates of year aging in relation to the period of measurements for oscillators with quartz crystal units in various types of cases are given in Fig.1. According to the analysis, an evaluation period of oscillators of less than 10 days is inadvisable for year aging forecasting, as forecasting confidence sharply decreased thereat. It should be noted that the given rates do not limit forecasting confidence, since the evaluation of forecast accuracy improves with data accumulation, thus making it possible to evaluate oscillators to tighter standards.

3) Aging of oscillators, which frequency is fixed more rapidly, is evaluated most accurately. Certain old data in the archives had a higher discretization and were counted with a difference of approximately 24 hours. Forecast of this data in the framework of this method is difficult as useful information is lost for the most part. However, modern equipment of the company enables fixing readings every 15 min, making most accurate evaluation of aging possible.

4) The program failed to evaluate 2% of data.

The experiment was carried out multiply for several groups of oscillators and has proved the method functionality, approximation coefficients selection accuracy, and practical validity of this method. As of now, the method has been used in production for evaluation of long-term stability of precision quartz crystal oscillations, permitting reliable forecasting of year aging of oscillators to $1…2\times10^{-8}$ rates.

CONCLUSIONS

Algorithm, permitting automatic evaluation of long-term stability of precision quartz crystal oscillators, was considered in this article. The application of the considered algorithm allowed to improve confidence and decrease complexity of evaluation of quartz crystal oscillators aging. Confidence of aging forecasting with use of the developed method was evaluated; in such a manner 5MHz oscillators can be evaluated to the rate of 5E-9/year at a 40 day period of measurements.

REFERENCES

[1] MIL-O-55310, Military specification, General specification for crystal oscillators.

[2] B. Neubig, “Comparsion of passive and active of SC-cut and AT-cut crystals”, 50th IEEE FCS (1996), p.316-322.

[3] J. Vanier, J.J. Cagnepain, W.J. Riley. M. Granveaud, “Aging, Warm-up time and retrace: important characteristics of standard frequency generators”, 46th IEEE FCS (1992), p.807-815.

[4] J. Vig, “Quartz crystal resonators and oscillators for frequency control and timing applications a tutorial”, U.S. Army Communications - Electronics Command, 2000.

Recent achievements in performance of low profile ultra precision single oven quartz oscillators

Nikonov A.G., KotyukovA.V., Kamochkin A.S., Dyakonova N.I.
Morion Inc.
KIMa ave., 13a/St. Petersburg/Russian Federation
E-mail: morion@morion.com.ru
www.morion.com.ru

The article gives a description of single oven-controlled quartz oscillators (OCXO), which frequency stability comparable with double oven-controlled quartz oscillators (DOCXO), and are considerably lower in weight, consume less power, and are smaller in sizes (up to a height thereof to 10 mm).

I. FINDINGS

Double oven-control solves in evident way problem of precision oven-control of quartz crystal units and most thermal responsive elements. In this case the immediate ideology of such design imposes serious restrictions for the height of oscillator.

Temperature stability of single oven-controlled quartz oscillators is much more responsive to the design and features thereof. Capabilities of modern programs for temperature processes calculation and accumulated experience, permitted manufacturing of a small-size single stage oven-controlled oscillators of high frequency stability versus temperature within a wide range. It was achieved due to ensuring of low temperature gradients in a zone occupied by a quartz crystal unit and most thermo sensitive elements.

Additional improvement of frequency stability versus temperature is provided owing to the compensation circuits of oscillator drift caused by temperature changes that are adjusted with the help of elements having the adjustable parameters.

Capability to attain an approximately 5^{o} C higher operation temperature is another important advantage of a single-stage thermostats.

An extremely urgent task is to miniaturize components of modern telecommunication equipment while keeping parameters thereof unchanged. Obtaining frequency stability versus temperature of up to $\pm 2*10^{-10}$ with help of quartz oscillators of a smaller sizes became most important for new generation (in LTE standard) base stations of cellular communication.

DOCXOs have been used for a long time in the applications requiring stabilities in degree of 10^{-10}, as OCXOs were unable to ensure the required frequency stability. (See Table 1).

Table 1.

Parameter	OCXO	DOCXO
Frequency stability versus temperature p-p -20…+70 ^{o}C, 10^{-9}	1…3	0.2…0.8
Frequency stability versus voltage supply change ±5%, 10^{-10}	<5	<1.5

As the requirements placed to the quartz oscillators overall dimensions became much more tighten, the task was to decrease quartz oscillators overall dimensions considerably while keeping the parameters thereof unchanged. To meet this requirements, new family of OC-

XOs (MV200, MV197, MV199) has been developed. The different oscillator's models parameters are given in Table 2.

Table 2

Parameter	MV216 (DOCXO)	MV180 (DOCXO)	MV200 (OCXO)	MV197 (OCXO)	MV199 (OCXO)
Dimensions, mm	51×51×40	51×51×19	51×51×12.7 (10)	36×27×12.7 (10)	20×20×12.7
Volume, cm^3	104	49.5	33	12.5	5.1
Weight, g	130	80	60	35	15
Power consumption per -20°C, W	14.5	9	5.5	3.5	2.5
Supply voltage, V	12	12	12 or 5	12 or 5	12 or 5
Frequency stability versus temperature - 20…+70 °C, $\pm 10^{-9}$	±0.05…0.2	±0.1…0.4	±0.15…0.4	±0.2…0.5	±1…2
Frequency stability versus temperature - 40…+85 °C, $\pm 10^{-9}$	-	-	±0.2…0.5	±0.3…0.6	±1.5…2.5
Frequency stability versus voltage supply change ±5%, 10^{-10}	<1.5	<1.5	<2	<2	<5

As shown in Table 2, OCXO have almost the same frequency stabilities as DOCXO and they are much smaller in size, weight, and in power consumption.

II. FREQUENCY VERSUS TEMPERATURE STABILITY

To minimize frequency unstability versus temperature the thermal model of the oscillator design should be optimized. Present-day the level of digital modeling development for physical phenomena provides wide opportunities for optimization of the oscillator thermal model. Thermal modeling of a future design is one of the main development stages. The finite element method is used for temperature modeling .

Fig. 1 shows a thermal model of OCXO.

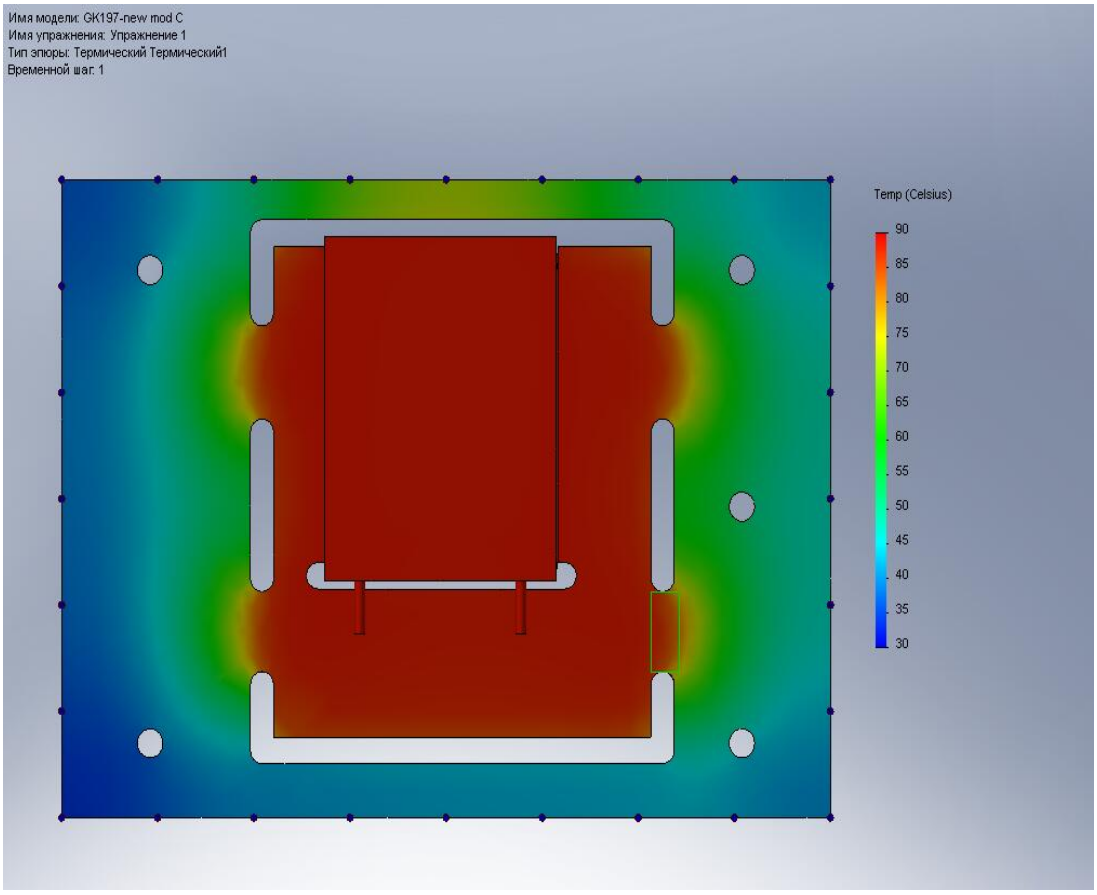

Figure 1. Thermal model of OCXO

A considerable improvement of frequency stability versus temperature for OCXO is attained through optimization of the design by results of the thermal model evaluation and additional thermal isolation of the “hot zone” (Fig.2).

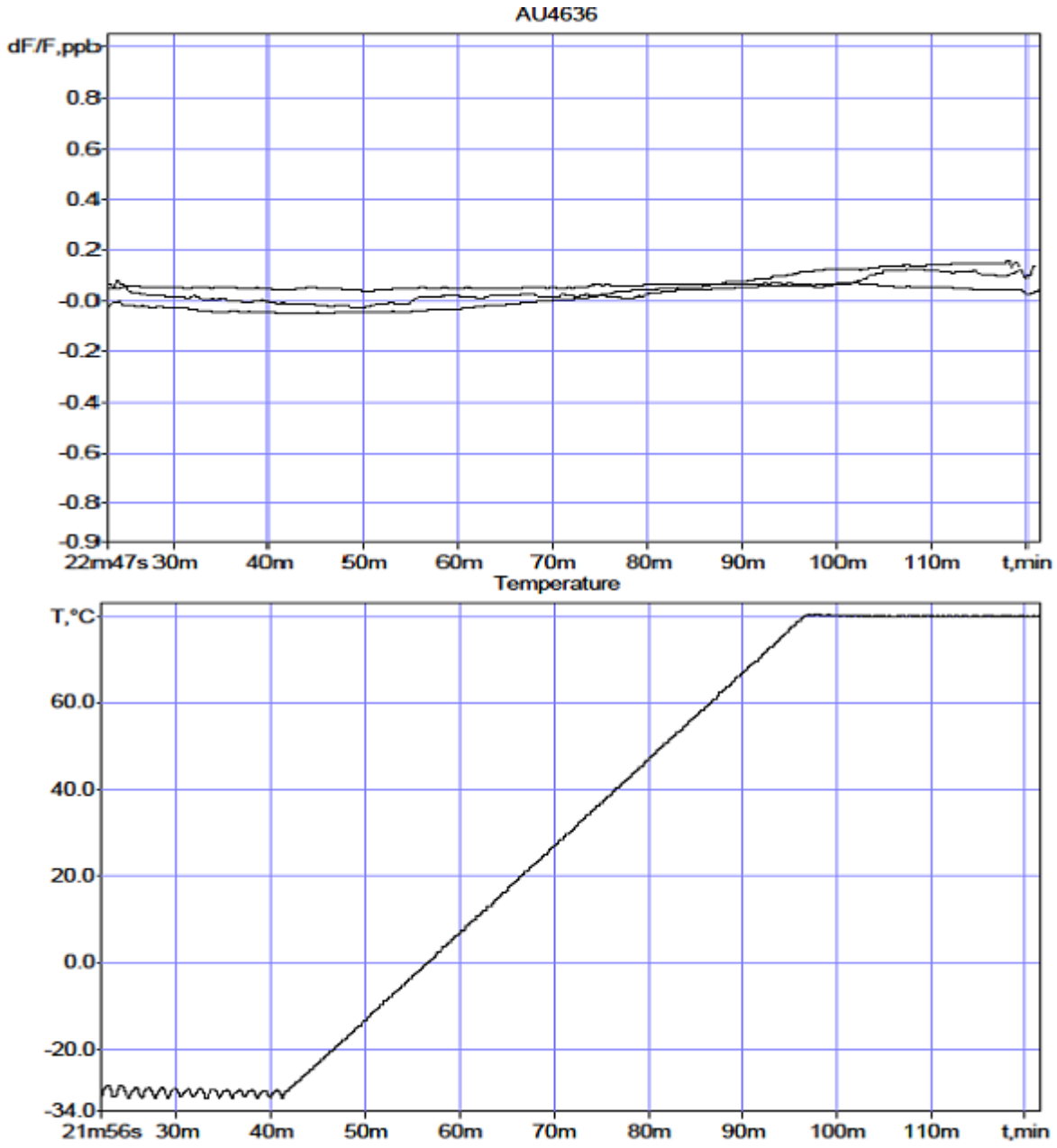

Figure 2. Frequency stability versus temperature of OCXO at various control voltages

However, a thermal error that remains after optimizing the design does not allow to obtain temperature stability of $\pm 2*10^{-10}$ within the temperature range. Specialized correction of frequency stability versus temperature which permits improvement in 2…3 times is used for it.

The one of the main point at using OCXOs instead of DOCXOs is the changing of oscillator frequency at sharp ambient temperature changes (for instance, for 20 ^{o} C in less than a minute). It has been possible to bring this parameter to a level that is competitive with same parameter of DOCXOs, as Fig. 3 shows.

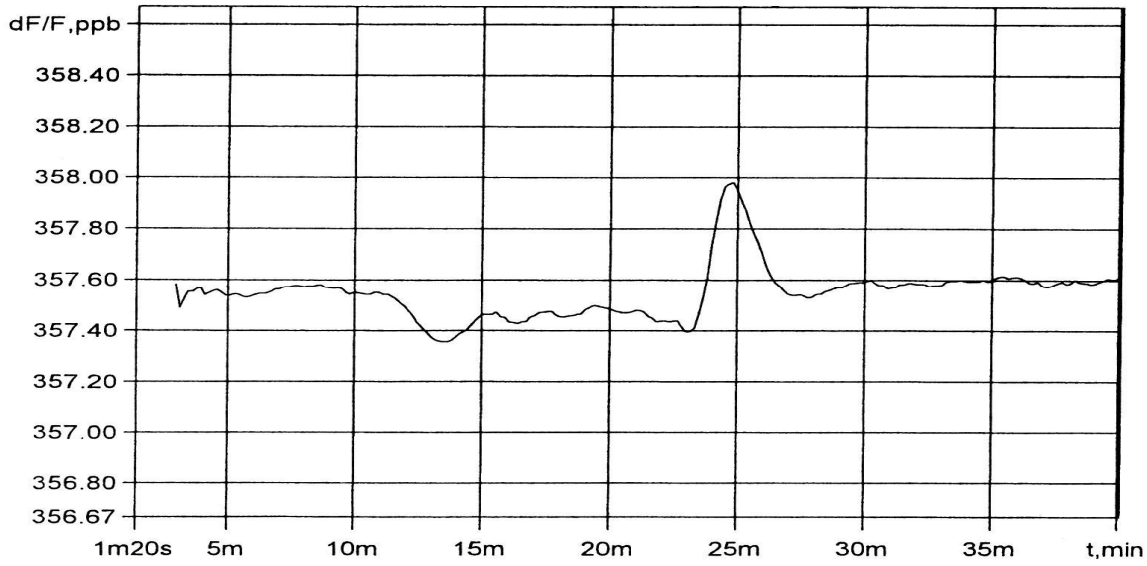

Figure 3-A. Response to a thermal shock for DOCXO

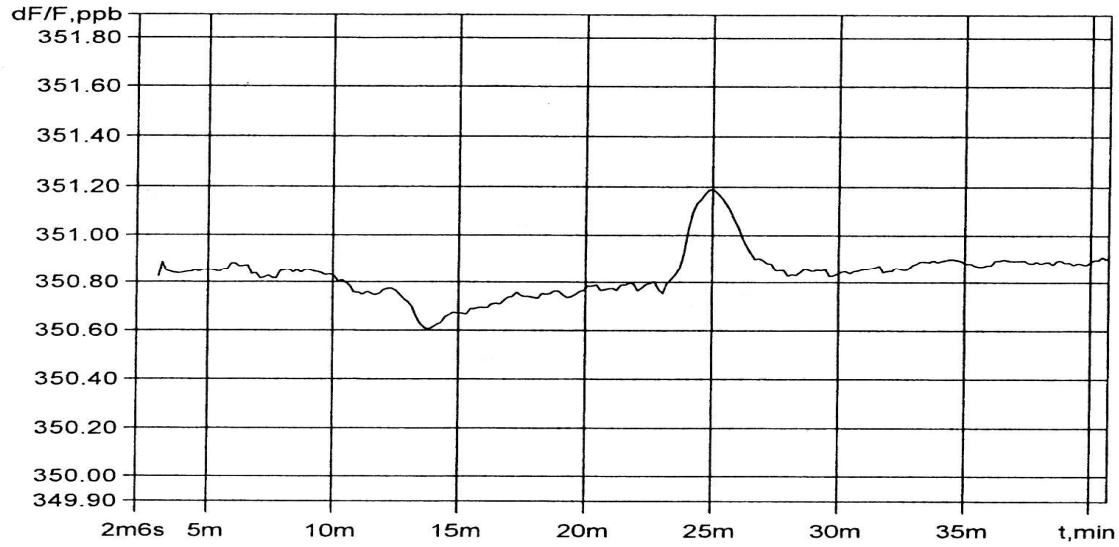

Figure 3-B. Response to a thermal shock for OCXO.

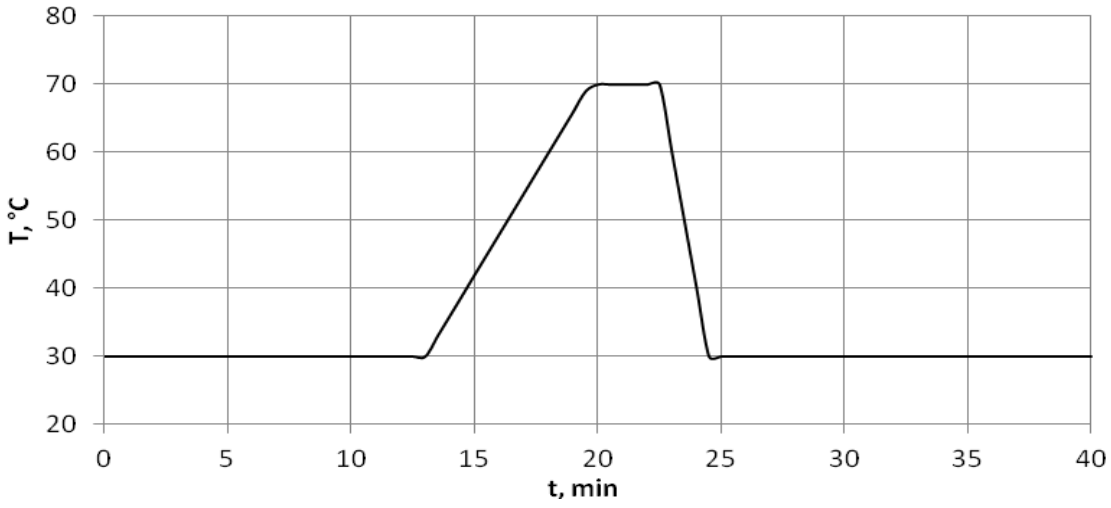

Figure 3-C. Temperature characteristic

5

III. RELIABILITY AND LONG TERM STABILITY

A top operation temperature of +85 ^{o}C was a serious problem for development. It has been known that the higher is an operation temperature of a product, the lower is its reliability. Taking this statement into consideration an element base allowing to ensure high reliability of the product operation at an elevated temperature of the thermostat, was used within product development. This oscillators are as good as the oscillators with a lower thermostat temperature in terms of reliability.

The tests have revealed that transfer to a higher operation temperature of the thermostat does not deteriorate the value of oscillator long-term frequency stability (Fig. 4), owing to the improved technology of quartz crystal units manufacture.

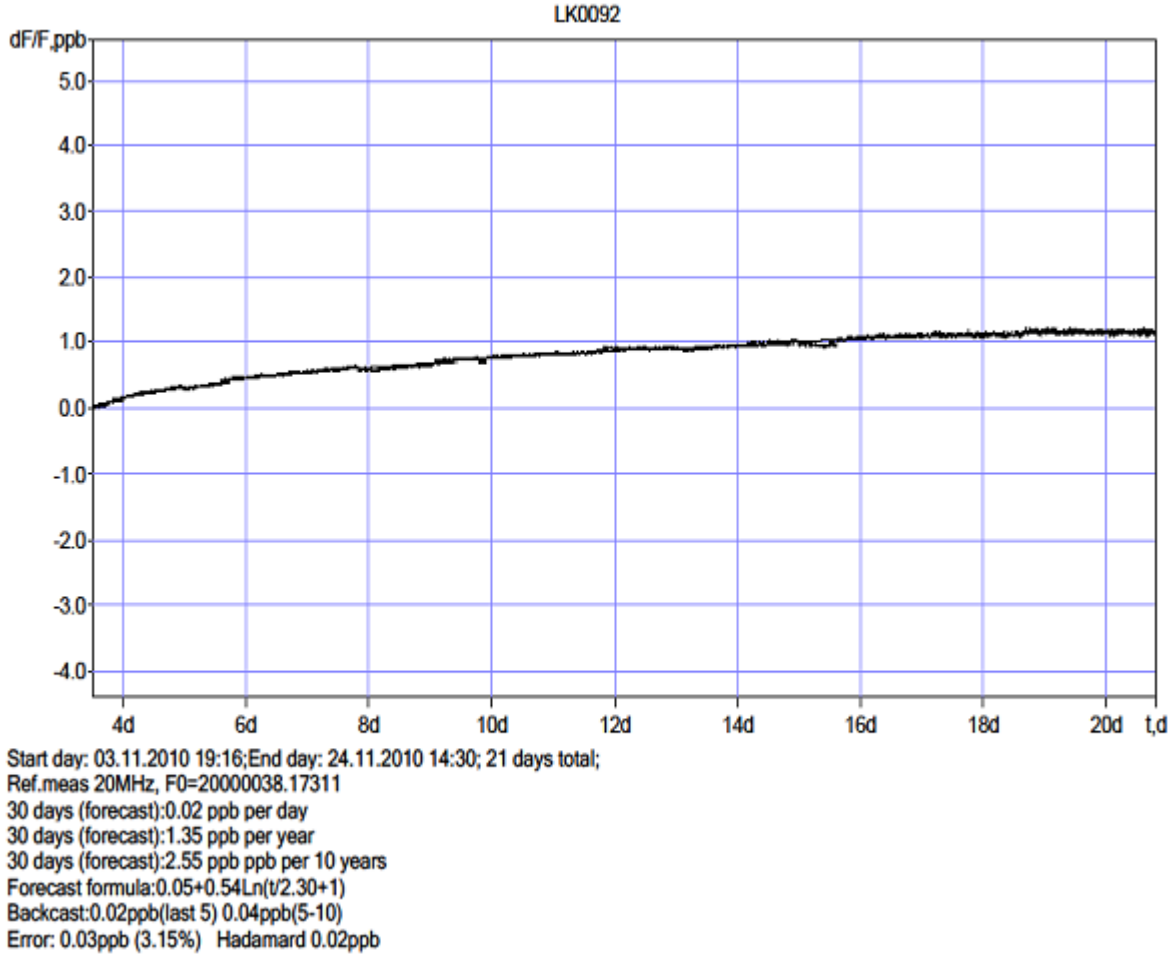

Figure 4. Standard long term frequency stability of OCXO

IV. PHASE NOISE AND SHORT TERM STABILITY

Standard phase noises and short term frequency stability are represented in Figs. 5 and 6, accordingly.

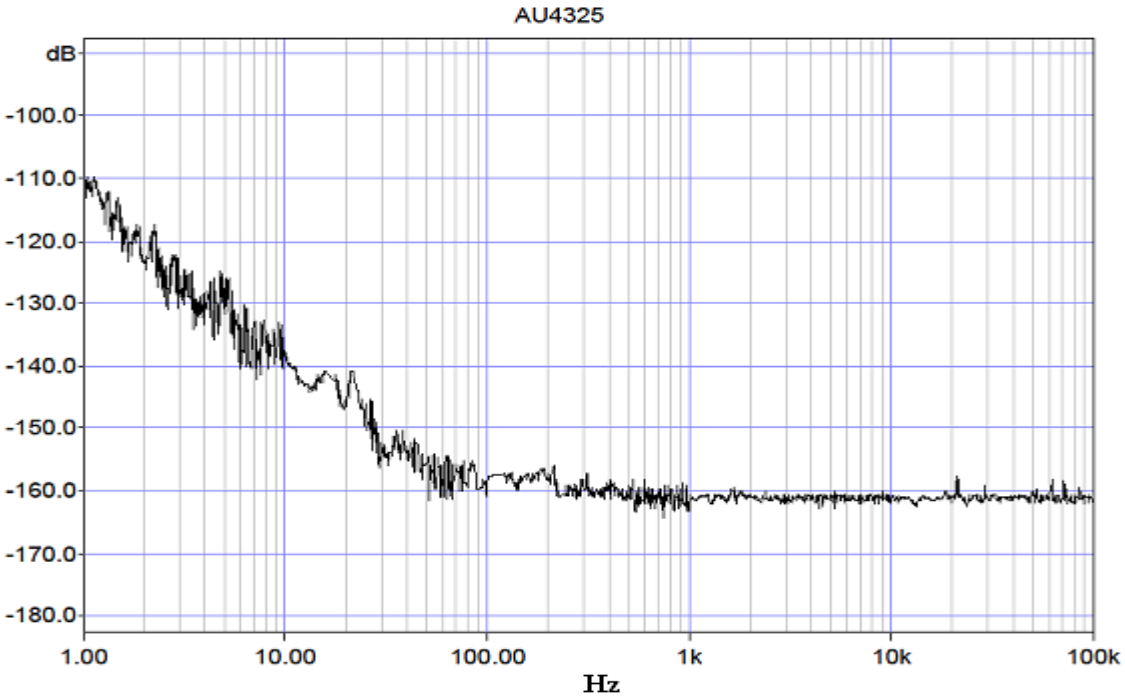

Figure 5. Standard phase noises for OCXO

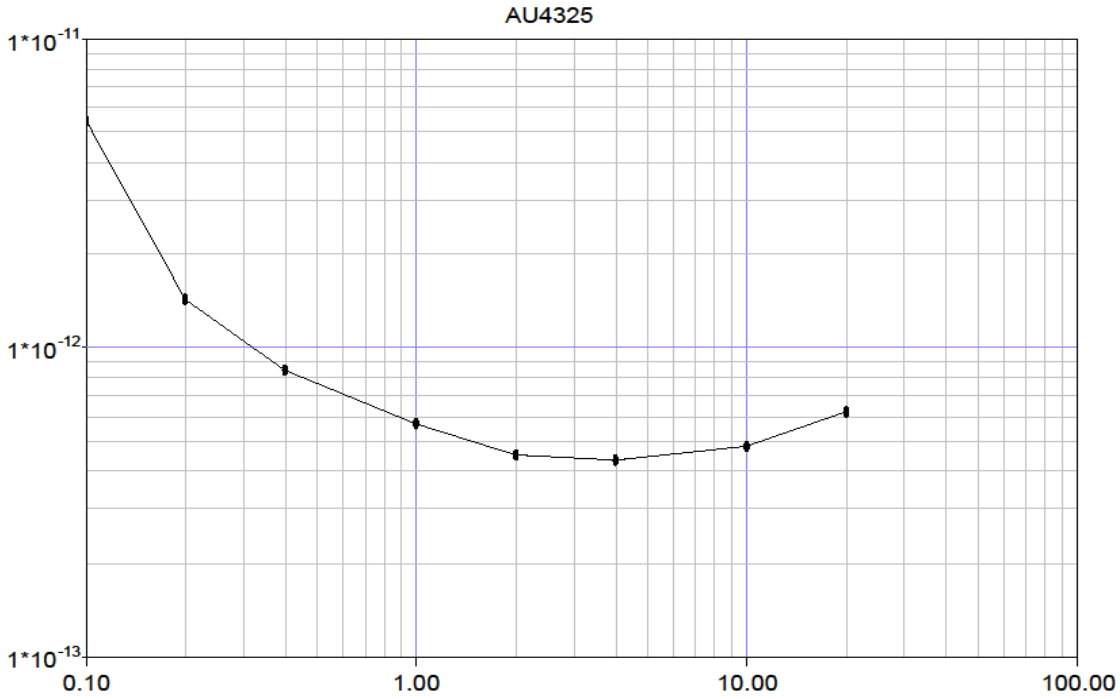

Figure 6. Standard short term frequency stability for OCXO

It should be noted additionally, that MV200-based oscillator MV220 has been developed to have similar temperature stability and considerably better noise floor.

V. CONCLUSION

The represented data shows that OCXOs can successfully replace DOCXOs in multiple applications.

Time-to-Digit Converter Based on Radiation-Tolerant FPGA

Marek Peca*, Michael Vacek, Vojtěch Michálek
Výzkumný a zkušební letecký ústav, a. s., Beranových 130, Praha – Letňany, Czech Republic
České vysoké učení technické v Praze, Břehová 7, 115 19 Praha 1, Czech Republic
*e-mail: peca@vzlu.cz

***Abstract*— Architecture of a time-to-digit converter (TDC) is presented. TDC is an electronic device which measures time of arrival of discrete electronic pulses, with respect to reference time base. Our work on TDC is motivated by its applications in field of long-range laser distance measurement and time synchronization. Unlike earlier time interpolation methods, we have chosen all-digital approach based on pulse propagation through tapped delay line. We do not expect it could outperform recent invention of time interpolation using narrow-band filter excitation [1], [2]. However, our approach relies on a standard digital circuitry only. With space applications in mind, we are implementing the TDC into a space qualified, radiation-tolerant field-programmable gate array (FPGA). On top of related works [4] and [5] on all-digital TDCs, delay line, we try to gather more complete information about the sampled pulse. It is done by sampling of whole bit vector, corresponding to all of the delay line taps. A calibration method based on random pulse source is discussed, including preliminary results. Impact of physical FPGA cell placement on resulting time measurement granularity is observed. Actually measured jitter distribution is compared to normal distribution function, giving an insight of absolute accuracy limit of our approach within the given FPGA platform.**

I. Introduction

General principle of time-to-digit conversion is as follows. Ticks of a high stable and low noise reference clock is counted by a digital counter. In this manner, time can be measured in chunks of reference clock period, which is, however, insufficient if precision higher than clock period is required. For this reason, time interpolation is employed while measuring times with resolution higher than clock period.

The digital approach employs tapped delay line on which the incoming pulse propagates. Each part of the line is sampled regularly by reference clock and the pulse position determines time elapsed since previous clock tick. The delay line can be either active or passive. Active line is formed by chain of active elements with defined delay such as buffers, latches, multiplexers, or gates [3].

The passive delay is formed purely by a ”slow” wire structure without any active element [5]. Thereby the jitter of delay elements is eliminated and only jitter of sampling elements remains. Less significant aging and temperature influence on TDC performance is expected, too. Moreover, each part of the delay line could have much lower delay (thus finer resolution) than any active component. The goal is to reach such a resolution that the limiting factor will be the jitter of the sampling elements. In order to obtain relevant data, it is necessary to ensure that the clock signal will propagate much faster than incoming pulse signal traveling through passive delay line to data inputs of sampling elements.

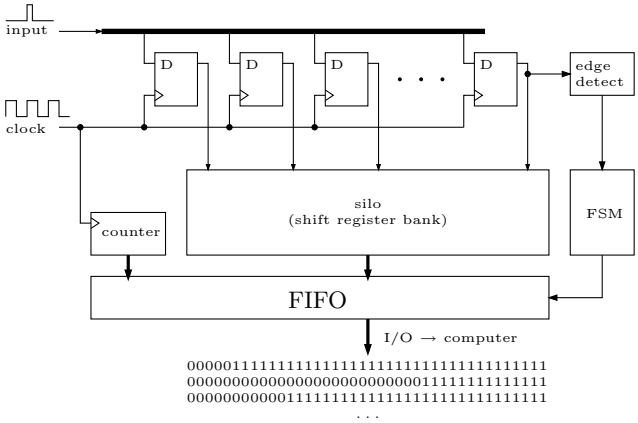

Fig. 1. TDC block diagram

II. Design

The TDC concept being presented (Fig. 1) employs passive delay line naturally offering the best possible line granularity thus theoretically the ultimate TDC resolution in a given FPGA technology. The pulse to be measured propagates from an input through the passive line which is connected to a number of D-type flip-flop inputs sampling (snapshotting) the line on clock edge. The position, spacing, and number of flip-flops are crucial aspects affecting the TDC precision and linearity. The outputs of the snapshotting flip-flops are connected to bank of parallel shift registers, called ”silo”. In other words, there is a cascade of flip-flops where bit information from a top level flip-flop (directly connected to the delay line) propagates through multiple levels of silos to the bottom flip-flops to be serialized into FIFO memory. Alternatively, the outputs of the snapshotting flip-flops are summed to get the total number of flip-flop ”ones” thus not preserving the whole bit vector. The advantages of the adopted principles are pure digital approach (standard FPGA/CMOS), scalability (the more flip-flops the better precision), implementation in a single principal component, and availability of radiation-tolerant FPGA for space applications.

III. Calibration

A calibration is necessary in the case of TDC using passive delay line implemented within FPGA. Since there is little control over FPGA net routing, there is no prior knowledge of actual tap delays. The non-linearity issue may be overcome by employing a random pulse source as a base for stochastic calibration. It is beneficial compared to deterministic calibration since it provides in-situ (on-board) stability check and long-term recalibration (drift, aging). Provided the reference clock is accurate, a huge amount of pulses arriving at random times is able to provide sufficient data for calibration by histogram. The non-linearity compensation uncertainty after N_{RE} random events (negligible jitter assumed [1]) is defined as

$$\sigma_t = \frac{T_0}{2\sqrt{N_{RE}}} \tag{1}$$

where T_0 is the total delay of the line. The calibration by histogram is based on following assumptions: the frequency of reference clock is defined and stable, incoming pulses have known probability distribution in time, and the sample set of pulses is sufficiently large and representative. The most likely and simplest assumption is that pulse event time within one clock period follows uniform probability distribution ($t \sim \mathcal{U}(0, T_0)$), where T_0 is reference clock period and t is pulse arrival time modulo T_0.

After collecting huge amount of data, a histogram is created. Each pulse yields a bit vector of length M, corresponding to M taps of delay line. The sum of all bit vectors gives the histogram of M bins.

A. Random Pulse Sources

Simple and efficient realization of the random pulse source is made by using oscillator with large phase-noise ($t \sim \mathcal{U}(0, T_0)$), which is unrelated in frequency and not coupled by any means to the reference clock oscillator. The reference clock used was a crystal oscillator, while the random pulse source has been an RC astable generator formed around NE555 chip. The care was taken to isolate NE555 from the FPGA and crystal oscillator. Independent power supplies have been used. The configuration is depicted in Fig. 2.

Alternatively, a single photon avalanche diode (SPAD) may be adopted as a random pulse source. There are two modes of operation in case of SPADs. Either it generates uniformly distributed pulses ($t \sim \mathcal{U}(0, T_0)$) in non-gated mode, or the SPAD is coherently gated with clock exhibits exponential-like distribution having origin in background thermal or photoelectric events.

IV. Performance

There are two main uncertainty factors determining the TDC precision. The major factor is the maximum inter-tap delay, i.e. a delay line granularity. It may be reduced by increasing the number of line taps (N); thus, it decreases as $\frac{1}{N}$. The second perturbation phenomenon comes out from the flip-flop jitter including metastability. This factor is reduced as $\frac{1}{\sqrt{N}}$. Currently, our design is still limited by the inter-tap delay.

[1]The presence of jitter tends to smooth histogram by occurrences of "leap" bit vectors, such as ...00010111..., ...000100111... etc. which cause systematic error in histogram. Calibration jitter estimation and compensation methods are under development.

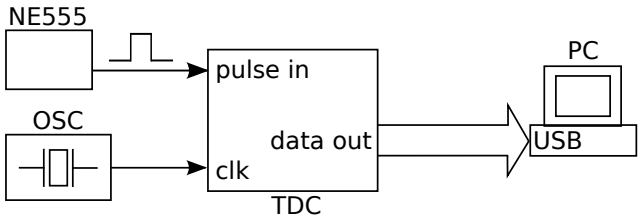

Fig. 2. TDC calibration setup

The worst-case deterministic error may be expressed as follows

$$\Delta t_{max} = \frac{1}{2} \max_k \Delta t_k, \tag{2}$$

where Δt_k is delay of k-th tap element. Root mean square (RMS) deterministic error is calculated under the assumption of uniformly distributed pulse epochs ($t \sim \mathcal{U}(0, T_0)$) as follows

$$\Delta t_{RMS}^2 = \frac{1}{12 T_0} \sum_{k=1}^{N} \Delta t_k^3 \tag{3}$$

A. Topology (FPGA floor-plan) impact on inter-tap delay

The first delay line topology was formed as a horizontal straight line across the FPGA floor-plan. Besides it is constituted from relatively small number of flip-flops (320), it suffers from the fact that the tapped line crosses structural boundary of the FPGA floor-plan giving about an order of magnitude times higher propagation delay in the case of the boundary taps compare to the same net between an adjacent flip-flops. These non-uniform inter-tap delays result in the strong regions of non-linearity depicted in Fig. 3. The worst-case deterministic error of the 320-tap topology is $\Delta t_{max} = 87.6\,\text{ps}$ and $\Delta t_{RMS} = 24.8\,\text{ps}$.

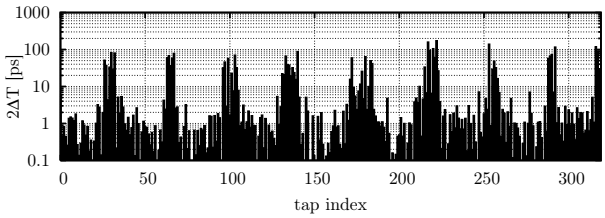

Fig. 3. TDC delay line topology consisting of 320 taps

Consequently, an optimized tapped delay line design was proposed where 2700 flip-flops are nearly equidistantly distributed around the FPGA floor-plan giving $\Delta t_{max} = 20.7\,\text{ps}$ and $\Delta t_{RMS} = 3.03\,\text{ps}$, respectively.

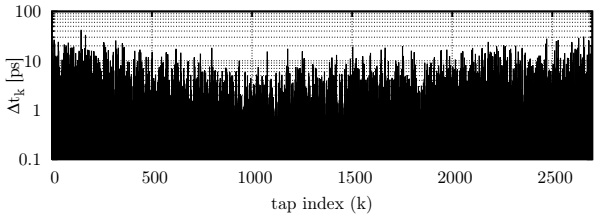

Fig. 4. TDC delay line topology consisting of 2700 taps

V. Results

There has been performed several experiments testing the performance of the device. Block diagram of configuration in which a delay generator has been employed is shown in Fig. 5.

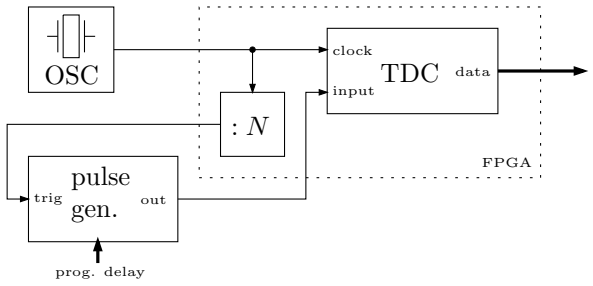

Fig. 5. Test measurement using delay generator

The delay generator was triggered by reference clock and produced several programmed delays with respect to the sampling clock; thus, arbitrary part of the TDC delay line could be verified. For each preset delay on pulse generator, a set of impulses was recorded and a histogram calculated. Each data set is plotted with respect to absolute time axis as bin numbers was already calibrated. Normalized cumulative histograms (NCH) for each data set are plotted in Fig. 6. Each NCH is an approximation of cumulative distribution function (CDF) of pulse arrival time, as measured by calibrated TDC.

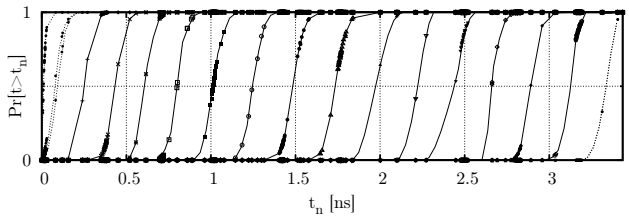

Fig. 6. Normalized cumulative histograms approaching pulse delay CDF

In ideal case of zero jitter, the CDFs would be straight vertical $0 \rightarrow 1$ steps residing at measured time delay. The S-shaped slope of measured CDFs is caused by jitter. The uneven spacing of "sampling points", i.e., histogram bins, is of no surprise, since it consists of peaks and valleys (Fig. 3). Mean observed time delay should lie in the center of CDF curve. Variation then corresponds to its slope. Due to sparsity of data points, we have assumed normal model of probability distribution and fitted each CDF with an error-function. After rejection of five data sets suffering from delay line boundary conditions, the agreement in fitted standard deviation σ among all NCH was better than 10%.

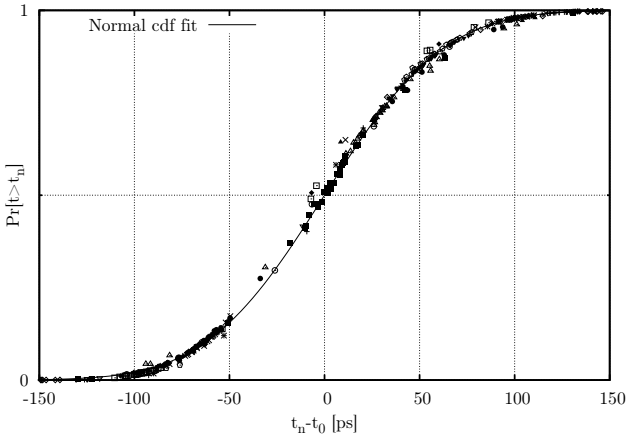

Fig. 7. CDF fit with measured data

Finally, the CDFs have been compared to the normal CDF model after subtraction of mean values, see Fig. 7 . Solid line represents true normal CDF with points of all NCHs superimposed. The overall agreement of fitted model and NHCs data points is 3 ps RMS. Standard deviation of the model is 49 ps RMS, which match the pulse generator specification being 50 ps.

Other experiment configurations has shown that the second largest jitter contributor (after pulse generator itself) is on-chip PLL. Additionally, jitter added by FPGA circuitry to a signal simply passing through the chip without any intended interaction was determined to be 2 ps RMS. Considering this facts, another configuration, omitting both main jitter contributors, was employed during tests.

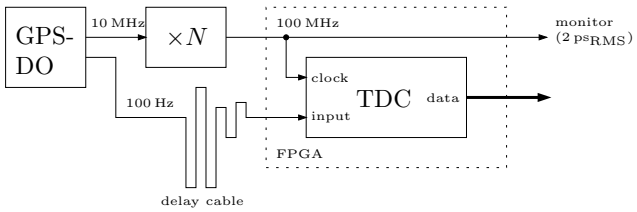

Fig. 8. Test measurement using delay cable and signal distributor

The block diagram in Fig. 8 shows experiment setup where delay generator is substituted by a delay cable. Moreover, a 100 MHz signal directly from coherent multiplier serves as system clock thus the on-chip PLL was not utilized. The 10 MHz signal from GPS Disciplined Oscillator (TM-4) was divided by a signal distributor giving 100 Hz pulses synchronous with system/sampling clock. Employing delay cables with various lengths, various points of the delay line could be checked. Measured histogram of such a point can be seen in Fig. 9 which shows that the jitter in design without on-chip

PLL has been significantly reduced. Random jitter measured at one point of tapped line was $\sigma_j = 4.93\,\mathrm{ps}$, evaluated by standard RMS formula and line calibration method described above.

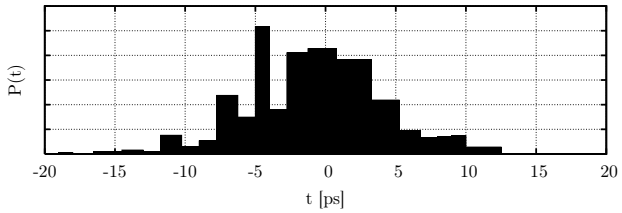

Fig. 9. Histogram data from a single point

VI. Conclusion

We have implemented several designs of TDC in single A3PE1500 FPGA by Actel/MicroSemi company, which has its radiation tolerant equivalent. The experiments show that the jitter of the TDC elements obeys normal distribution quite accurately (3 ps). The latest design exhibits worst-case deterministic error $\Delta t_{max} = 20.7\,\mathrm{ps}$, RMS deterministic $\Delta t_{RMS} = 3.03\,\mathrm{ps}$, and measured random jitter $\sigma_j = 4.93\,\mathrm{ps}$. The intended future experiments will focus on measuring the temperature and long term stability. The efforts in theoretical part will be concentrated mainly on evaluating impact of flip-flop metastability and also jitter self-estimation from whole bit vector data to improve histogram calibration.

References

[1] P. Panek, I. Prochazka. Time interval measurement device based on SAW filter excitation, IEEE Review of Scientific Instruments, 2004
[2] P. Panek, Time-Interval Measurement Based on SAW Filter Excitation. IEEE Transactions on Instrumentation and Measurement, 2008
[3] W. Becker. Advanced Time-Correlated Single Photon Counting Techniques: Springer-Verlag, 2005
[4] Y. Zhang, P. Huang, R. Zhu. Upgrading of integration of time to digit converter on a single FPGA. Proc. 15th Int. Laser Ranging Workshop
[5] R. Salomon, R. Joost. BOUNCE: A New High-Resolution Time-Interval Measurement Architecture. IEEE Embedded Systems Letters, 2009

Development of an active hydrogen maser in Belgium-first results

Cipriana Mandache, Thierry Bastin
University of Liège, Institut de Physique Nucléaire, Atomique et de Spectroscopie
Sart Tilman Bât.B15
Liege, Belgium
e-mail:cipriana.mandache@ulg.ac.be

Jean Nizet, Daniel Leonard
Gillam-Fei
Mont Saint-Martin 58
Liege, Belgium

Abstract—**A Hydrogen Maser has been developed by GILLAM-FEI and IPNAS University of Liège (Belgium) under Plan Marshall - SKYWIN-TELECOM. The construction of the maser is the first effort in a program of development of atomic clocks based on hydrogen maser technology initiated in Region Wallonne de Belgique.**
A first evaluation of the Belgium Atomic Hydrogen Maser (Wally One) was performed between October 2011-March 2012. For the initial settings of the maser parameters a full determination of the maser characteristics was initiated.

I. INTRODUCTION

The research work concerning the hydrogen maser was concentrated on:
1) the development of the physical part of the maser, including design and realization of all mechanical part(at IPNAS - ULG);
2) the development of electronic control of the maser (at Gillam-FEi).
The maser view is show in Figure 1.

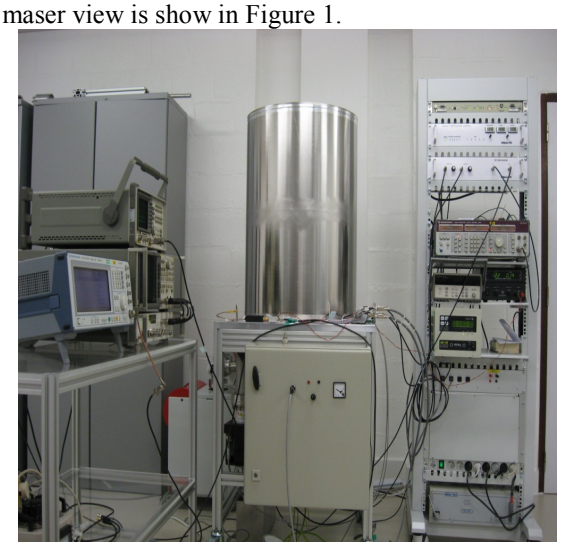

Figure 1. View of Belgium hydrogen maser

A. The maser

The maser, as shown in Figure 1, can be described as follows. The atomic hydrogen source is formed by a Hydrogen Storage System (HB-SC-0050-Q), a Palladium Leak, and a discharge tube. The molecular hydrogen is obtained from a silver-palladium leak. Palladium has the property of being permeable to hydrogen, depending on its temperature. An electronic system controls the pressure in the atomic hydrogen source in order to control the atomic beam intensity. Atomic hydrogen is dissociated in a bulb of Pyrex by means of a rf field which produces a plasma. The power required is of the order of 10 W at a frequency of about 150 MHz. At the exit of the source, the beam enters the bore of a hexapole magnet which acts as a spatial state selector. The focusing six-pole lens has a length of 77 mm, and the gap between poles of 3 mm. The field at the top of pole is 0.75 T. After its exit from the magnet, the beam, drifts towards the cavity and enters the storage bulb. The cavity, operating in the TE_{011} mode, is made in aluminium**,** silver plated**.** The storage bulb is made of clear fused silica and the inner surface of the bulb is coated with a thin film of Teflon (FEP 120). The arrangement, aluminium cavity plus quartz bulb, has an unloaded quality factor of the order of 60.000. The measured loaded Q for the silver plated cavity was 38.500. On the top cover of the cavity is located a piston in order to coarse adjust the resonant frequency of the cavity. A diode varactor is used for the fine tuning of the cavity. The cavity is provided also with two coupling loops. One of these loops couples maser oscillation power to a signal detection system, the other loop is used to couple an external exciting signal into the maser cavity.
The temperature of the cavity must be regulated in the range 10^{-3} - 10^{-4} °C. The thermal control is provided by five ovens. The non-magnetic thermistors are used as temperature sensors (Figure 2).
The vacuum tank is made in aluminium. In order to reduce the effect of environmental fluctuations, 4 concentric magnetic shields, made in Mumetal, with a thickness of 1

mm, surround the maser cavity. The thermal isolation between vacuum tank, magnetic shields and resonant cavity is provided by 19 mm AF/Armaflex foil (Figure 3). The maser use two Ion pump VacIon Plus 75.

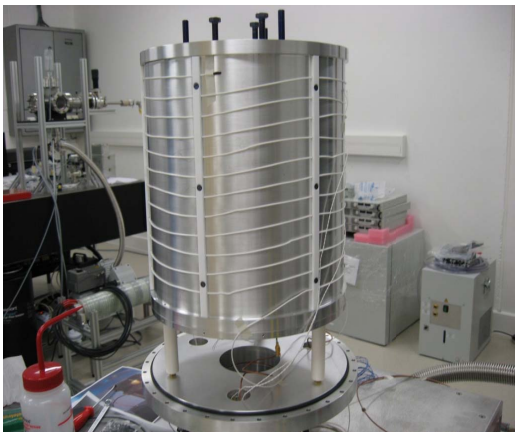

Figure 2. Heating system for the cavity

Figure 3. One of thermal isolation

B. The Maser Electronic Controls

The maser electronic controls consist essentially of five major parts (Figure 4):

- Radio frequency H_2 dissociator. A RF field produces a plasma in the discharge tube. The frequency is around 150 MHz and the power lies between 5 and 10 W.
- The temperature control is provided by 5 ovens with a temperature stability of 10^{-4} K.
- Magnetic field control with 10^{-4} stability of current.
- The maser receiver. The traditional diagrams use many changes of frequency accompanied by pass-band filters; that involves a strong sensitivity of the assembly to the temperature and requires a thermal regulation of all the circuits of the receiver. Our new diagram limits the number of changes of frequency and filters what makes it possible to remove the thermal regulation of RF circuits.

Figure 4. Electronic system

- A new and more precise ACT system than the systems used in the past.

II. FIRST RESULTS

A. Basic characteristics of the maser

The Belgian maser was constructed with a TE_{011} aluminum silver plated cavity containing two coupling loops and a varactor diode. The maser is also equipped with external positive feedback A low noise amplifier and attenuator provided variable feedback gain allowing a variation of the cavity Q over a broad range of values, from less than 35 000 to 100 000. The maser could thus be operated at various values of the maser oscillation parameter. The minimum and maximum fluxes of operation could thus be determined at any values of the cavity Q within that range. The relative atomic beam flux intensity was determined by the pressure of molecular hydrogen at the exit of the palladium purifier in the source.

Using the basic theory of the maser [1], starting from the power output P of the atomic ensemble

$$\frac{P}{P_c} = -2q^2\left(\frac{I}{I_{\text{th}}}\right)^2 + (1-3q)\frac{I}{I_{\text{th}}} - 1 \qquad (1)$$

we can write the expression for minimum and maximum flux intensities for maser oscillation :

$$I^{\pm} = I_{th}\,\frac{(1-3q) \pm \sqrt{(1-3q)^2 - 8q^2}}{4\,q^2} \qquad (2)$$

where q is the quality factor of the maser and

$$P_c = \frac{\omega \mu_0 V_c h^2}{2 Q_c \eta\, \mu_B^2}(\gamma_b + \gamma_p)^2 \qquad (3)$$

The experimental parameters are:

-cavity volume V_c

-cavity loaded quality factor Q_c

-bulb volume V_b

-filling factor, η, determined by the shape and size of the storage bulb relative to the volume of the cavity
- ω the maser angular frequency
-(I_{tot}/I), the ratio of the total atomic flux to the flux in state F=1, m_F=0; this ratio is equal to 2 for a good state selector.
-γ_b, the relaxation rate or escape rate of atoms through the hole at the entrance of the storage bulb, usually set around 2 s^{-1}
-γ_w, the relaxation rate of atoms on the internal wall of the storage bulb
A calculation, assuming a cavity Q of 39 000 and maser parameters such as to make q = 0.172 sets the threshold of oscillation according to the graph. It is then straightforward to calculate minimum and maximum flux intensities for maser oscillation from Equation 2. The results are shown as a continuous line in Figure 5.

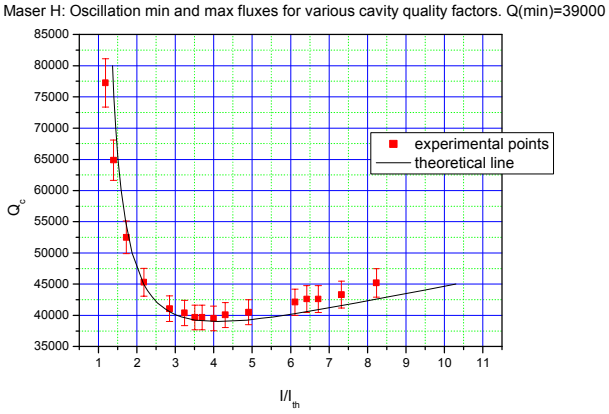

Figure 5.Determination of the minimum and maximum flux intensities for oscillation in a hydrogen maser as determined by means of the variable cavity Q technique described in the text. The points are experimental and the continuous line is theoretical.

B. Variation of the maser level of the current in the palladium

We performed the measurement concerning the level at the exit of the maser as a function of the pressure in the palladium purifier. The output level is constant with the pressure in a large interval (between 0.49 Torr and 1 Torr at the exit of palladium).

C. Gradient of magnetic field.

The hydrogen maser operates normally in a magnetic field of the order of 10^{-7}T. The maser frequency is related to the magnetic field through the relation [1]:

$$\upsilon - \upsilon_0 = 2750\, H^2 \qquad (3)$$

and to hold the fractional frequency shift to one part in 10^{13} requires that a field of 10^{-3} gauss be held constant to 3%. The variation of the frequency of the maser signal according to the current in the C- coil is given in Figure 6.

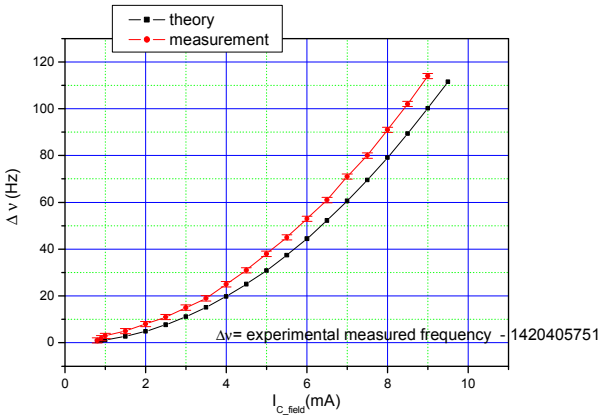

Figure 6. Frequency as a function of C-field current

III. EVALUATION OF THE WALLY ONE PHYSISCS PACKAGE

A. Microwave cavity

The measured loaded quality factor of the cavity is Q_c= 38.500.

B. Atomic quality factor

The operating atomic quality factor is Q_a = 1.1 10^9 and the corresponding q factor of the maser is ~ 0.12. The nominal atomic signal power is -107.8 dBm.

C. Total relaxation rate

The total relaxation rate γ_2 is given by: $Q_a = \frac{\omega}{2\gamma_2}$. For our maser we obtain $\gamma_2 = 3.94$ sec^{-1}.

D. Storage time

The time constant of the storage bulb is given by $T_b = \frac{1}{K}\frac{4V_b}{v_m A}$

Using v_m=2585 m/s as average velocity of atomic hydrogen at 44°C and measured values of V_b , the volume of the bulb, A the cross-section of the collimator and K is the Clausing factor, we obtain T_b= 0.57 s.

E. Thermal control

The cavity temperature is stable within 1mK upon a base plate temperature variation of 1.5°K.
The thermal sensitivity was obtained as $\Delta\nu/\nu = 2\ 10^{-10}$/ degree Kelvin.

F. Frequency Shift

- Second order Doppler Effect. The second-order Doppler effect produces a frequency shift of the hyperfine transition proportional to the temperature. The value of this shift at 44°C is:

$\Delta\nu_D = -0.062$ Hz

- Wall relaxation plays an important role in the operation of the maser. The theoretical wall shift for the FEP 120 surface at 44° C for our storage bulb is evaluated to be :

$\Delta\nu_W = -20.57$ mHz

IV. CONCLUSION

The evaluation of "Wally One" physics package reported in this paper is still in progress but most of the important conclusions have been drawn already. Most of the design parameters have been measured and analyzed and have been shown to be compliant with the specifications. In particular the maser physics parameters, i.e. atomic quality factor and the threshold flux have been verified.

On the other hand, the breadboard electronics package is still in development and does not reach yet all the performance goals set by the instrument specifications. A new iteration of the breadboard ACT is in preparation and is expected to comply with the thermal sensitivity and frequency stability requirements.

ACKNOWLEDGMENT

The authors thank the Region Wallonne de Belgique for financial support through Plan Marshall SKYWIN-TELECOM convention no.5545.

REFERENCES

[1] D. Kleppner, H.C. Berg, S.B. Crampton, N.F. Ramsey, R.F.C. Vessot, J. Vanier, "Hydrogen maser principles and techniques", Phys. Rev. 138, A972-983 (1965).

[2] C. Mandache " Étude des phénomènes de relaxation dans le maser à hydrogène", PhThesis, Bucarest (1982)

[3] J. Vanier, C. Audoin, "The Quantum Physics of Atomic Frequency Standards" Adam Higler, IOP Publishing, (1989).

[4] C.Mandache, D.Leonard, T.Bastin "Development of an active hydrogen maser: first results" Euramet Time and Frequency Meeting Brussels (2009)

[5] C.Mandache, D.Leonard, T.Bastin "Development of an active H maser" European Space Technology Harmonisation ESTEC- Noordwijk 2011 (2011)

[6] Claude Audoin, "Le maser à hydrogene en regime transitoire", Revue de Physique Appliquée, tome 2, p.309,1967.

[7] R. Vessot, "State of the Art and Future Directions for the Atomic Hydrogen Maser", 22nd Annual Precise Time and Time Interval (PTTI) Applications and Planning Meeting, Vienna, Dec 1990

[8] C.Mandache, J. Nizet, D.Leonard, T.Bastin, "On the Hydrogen Maser Oscillation Threshold", Applied Physics B – Lasers and Optics (DOI: 10.1007/s00340-012-5008-7) (accepted for publication)

The Electronic Improvement of The Hydrogen Maser for Time Keeping Application

Yong Cai Yan Xie Weiqun Zhang Zaocheng Zhai
Shanghai Astronomical Observatory
Chinese Academy of Science
Shanghai, China
yxie@shao.ac.cn

***Abstract*— The hydrogen maser for time keeping must have excellent performances with long term frequency stability, low frequency drift and high reliability for long term working. Based on the research experiences on hydrogen masers of Shanghai Observatory, the key technical improvements for time keeping hydrogen masers are described in this paper. The mainly electronic improvements include : analysis on the principle of the cavity auto-tuning technique and improving the modulation system, the development of phase-lock receiver.The primary test result reaches the expert performance as follows: the frequency stability reaches 1.5E-15/day, frequency drift rate is 8.6E-16/day ,and temperature sensitivity is 8.1E-15/℃.**

I. INTRODUCTION

With the deepening of the ongoing deep-space explosions and satellite navigation systems, atomic clocks are playing a crucial role as the assurance of navigation accuracy in recent years. Started from Oct 30th of the year 1969, Shanghai Astronomical Observatory (SHAO), successfully developed the first experimental hydrogen maser of China in 1972, has manufactured nearly 90 masers up to the present which are applied in very long baseline interferometry (VLBI), time and frequency comparisons, the establishment of atomic time scale, and other academic fields. The maser is a time and frequency standard which is stable, transportable and integrated. As a project-based maser, it has been proved to be stable in structure and high-quality in performances after gone through rigorous experimental testing. During these years, the maser is integrated into a cabinet of 54cm wide by 73cm deep by 110cm high, with 150kg overall weight and 200W power consumption, which is more convenient for transportation. The appearance of the maser is shown in Figure 1. Experiences learned from world-wide studies on frequency standards could convey that specifications of the maser, been perfect in physical part design, rely mainly on the design of electronic circuits. Consequently, better circuit design, including digitization, is vital to the better performance of the maser.

The hydrogen maser for time keeping must have excellent performances with long-term frequency stability, low frequency drift and high reliability for long term working. Although the maser made by SHAO has been improved in its performances and reliability to some extent, it is necessary to make technical breakthrough to satisfy needs for atomic time keeping. Thus the project aims to improve the existing technique on long-term characteristics and reliability. Some key techniques would be in-depth studied in this paper including: developments on the cavity auto-tuning unit and phase-locked receiver.

Figure 1. Appearance of SOHM-4 maser

II. BASIC PRINCIPLES OF THE HYDROGEN MASER

The active hydrogen maser is a self-excited atomic oscillator whose sustained energy comes from atomic hydrogen itself. It operates at a frequency of approximately 1420.405MHz determined by the transition between the two

ground-state hyperfine levels of atomic hydrogen. Figure 2 is the schematic diagram of the hydrogen maser [1].

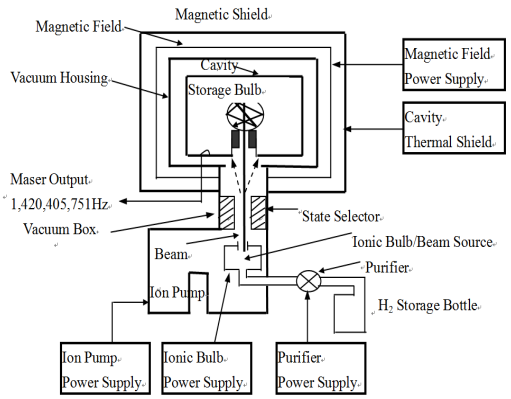

Figure 2. Schematic diagram of the hydrogen maser

Molecular hydrogen from a storage bottle is dissociated into atomic hydrogen by effect of radiofrequency electric field and is formed into an atomic beam which passes through a state-selecting magnet. Atoms in the ground-state hyperfine levels of $[F=1,m_F=0]$ and $[F=1,m_F=1]$ are focused into a Teflon coated storage bulb, located in the center of a resonant cavity tuned at the transition frequency between the hyperfine levels of $[F=1,m_F=0]$ and $[F=0,m_F=0]$. Atoms entering the bulb collides with the bulb wall for approximately 10^5 times before escaping, remaining for 1s on the average, and interact with the magnetic field of the cavity to release energy. When the intensity of the atomic beam is enough to compensate for the loss of the resonant cavity, the maser oscillations take place. Energy generated by the oscillating couples from a pick-up loop and is connected to a phase-locked loop [1][2].

Thermal noise and additional phase noise within bandwidth of the receiver contributes to the frequency stability limitations of the maser, which could be described using Vessot-Culter-Searle Equation[3].

$$\frac{\Delta f}{f}=\sqrt{\frac{kT}{2}\left(\frac{1}{Q_l^2 P_b \tau}+\frac{FB}{2\pi^2 f_0^2 P_0 \tau^2}\right)} \qquad (1)$$

Here

f is the oscillating frequency of the maser.

k is the Boltzmann constant.

T is the Kelvin temperature of the cavity.

$Q_l=\pi f_0 T_2$ represents the quality factor of the atomic line, where f_0 is the transmission frequency of the atomic hydrogen and T_2 is the time constant of phase coherence by atoms in storage bulb.

P_b is the power delivered by the beam to the loaded cavity.

τ is the sample time.

F is the noise figure of the receiver.

B is the effective noise bandwidth of the receiver, which is often determined by the low pass filter, for the output signal of the maser is heterodyned to lower frequencies.

P_0 is the input power of the receiver.

Generally, for $\tau < 10\ 000$s the frequency fluctuation is mainly due to the thermal noise dominate, especially related to the output power of the oscillator, the value of line Q and both the noise figure and the structure of the receiver, while for $\tau > 10\ 000$ s, this is dominated by the systematic effects such as changes of cavity resonant frequency, external magnetic field and etc. Among all the systematic effects, the temperature effect of the resonant cavity is considered to be the predominant; hence the solution for time-keeping maser is focused on the control of the resonant frequency of the cavity.

III. RESEARCHES AND IMPROVEMENTS ON KEY TECHNIQUES

A. Principles and discussion of cavity auto-tuning

With high cavity Q and low expansion coefficient, the loaded cavity would change its resonant frequency by time accumulation and environmental conditions. By acts of pulling effect[3], there is:

$$\Delta f=\Delta f_c(Q_c/Q_l) \qquad (2)$$

Where f_c is the resonant frequency, Q_c is the quality factor of the cavity which is usually around 40000, Q_l is the quality factor of the atomic line and is typically around 2×10^9.

This formula shows that if the cavity frequency has changed for 1Hz, it would bring frequency variation of the maser to the absolute value of 2×10^{-5}Hz and the relative value of

$$\Delta f/f=(2\times10^{-5})/1420405751=1.41\times10^{-14} \qquad (3)$$

In this case, to get the frequency stability to the level of 10^{-15}/day, frequency variation of the cavity should be strictly limited within 0.7Hz. Thus, the cavity auto-tuning system is essential to long-term frequency stability of the maser.

Principles of the cavity auto-tuning is shown by Figure 3[4], where f_0 is the reference tuning frequency approximately equal to the atomic transmission frequency, f_t is the injected microwave signal given by:

$$f_t=f_0+f_m g(t) \qquad (4)$$

Here f_m is the frequency modulation depth which is *15kHz* and $g(t)$ is a function with period T as:

$$\begin{cases} g(t)=1 & 0<t<T/2 \\ g(t)=-1 & T/2<t<T \end{cases} \qquad (5)$$

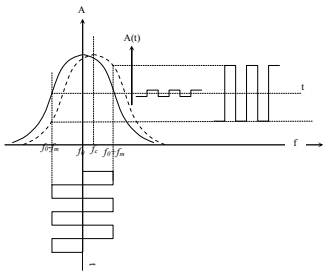

Figure 3. Principles of cavity auto-tuning

Actually, f_t contains two frequencies, (f_0+f_m) and (f_0-f_m), modulated by a square-wave with period T and injected into the resonant cavity alternatively. In amplitude response of the cavity view, the two injected frequencies, (f_0+f_m) and (f_0-f_m), are upper and lower half-power frequency of the cavity response with the center frequency f_0, respectively. Figure 3 shows the response curve of the cavity. In case that center frequency of the cavity is exactly at f_0, as described by the solid line in Figure 3, the two frequencies coupling from resonant cavity should be equal in amplitude, with no error signal. However, if the cavity frequency has drifted to f_c, as described by the dash line in Figure 3, the two frequencies coupling from resonant cavity would be unequal in amplitude, with amplitude-modulated error signal A.

After amplified, detected and multiplied by $g(t)$ in the synchronous detector, the effective low-frequency signal is extracted by the amplitude-modulated error signal A，given by[3]

$$d = k(f_0 - f_c)\frac{\partial A}{\partial f}\bigg|_{f_0+f_m} \qquad (6)$$

Where k is the gain link of the amplifier, the detector and the synchronous detector.

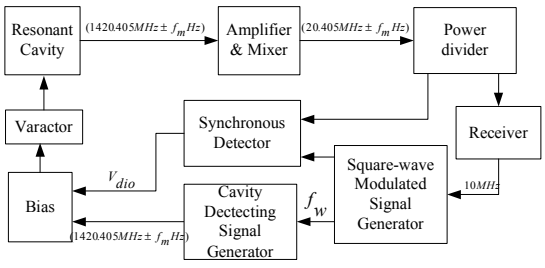

Figure 4 Block diagram of cavity auto-tuning

As shown in Figure 4, by passing through the bias and the varactor, the cavity detecting signal is injected into the resonant cavity. The output microwave signal of the resonant cavity, including detecting signal and oscillating signal of the maser, is down-converted and amplified, and then would enter an equal-split two-way power divider, where one output port is connected to the phase-locked loop locking the VCO source and another output port is connected to the synchronous detector. By the synchronous detector, the cavity detecting signal is extracted into the cavity error signal which is applied to the varactor in the form of a DC feedback voltage after integrated and amplified, pushing the cavity response curve(shown by the dash line in Figure 3) to its operating frequency(shown by the solid line in Figure 3).

The period of the square-wave modulation signal, whose value was 1s in the previous design, should be far greater than the time constant of the resonant cavity τ_c ($\tau_c \approx 10\ \mu s$). Specifically, the cavity injected signal ($1420.405MHz \pm 15kHz$) is modulated by the frequency $f_w=1Hz$, at $\pm 15kHz$ offset from center frequency which is exactly the emission frequency of atomic hydrogen. According to the theory of FSK, in frequency domain, the magnitude A of n-order harmonic component is

$$A_n = A_{-n} = (2m/\pi)\left|(\sin(n+m)\pi/2)/(n^2-m^2)\right| \qquad (7)$$

Where $m = \dfrac{2f_m}{f_w}$ and f_m is $15kHz$. From eq.(7),we can conclude that magnitudes of n-order harmonics of the modulation signal attenuate with an interval of $2f_w$, as shown in Figure 5 and Figure 6.

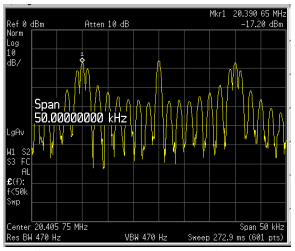

Figure 5. Spectrum of FSK (fw=1kHz)

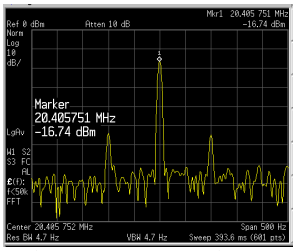

Figure 6. Spectrum of FSK (fw=100Hz)

As shown in Figure 5 and Figure 6, the spectrum is centered at the oscillating frequency of hydrogen maser. To avoid the oscillating signal of the maser being interrupted by n-order harmonics, the modulation signal must conform to the principle of $m/2=(f_m/f_w)=odd$. Thus, to choose $f_w=1kHz$ is infeasible ($m/2=15$). In addition, in the case of $f_w=7.5kHz$, although its spectrum could be far enough from the oscillating signal to lower the nearby frequency interference, the signal-to-noise ratio of the oscillating signal would be degraded because the low-order harmonic makes it attenuate smaller near the oscillating frequency. However, in the previous design, setting $f_w=1Hz$ to get higher signal-to-noise ratio would not a proper option, either. Thus, there is a contradiction between lower nearby frequency interference and higher signal-to-noise ratio, and a breakthrough to cavity auto-tuning is to pursue a solution to this contradiction. For practical measurements are mainly focus on time intervals which are greater than or equal to 10ms in time-domain, we choose $f_w=100Hz$ to minimize interference brought by the

modulation signal to practical frequency stability. Test results of final frequency stability of the maser are shown in Figure 7 and Figure 8.

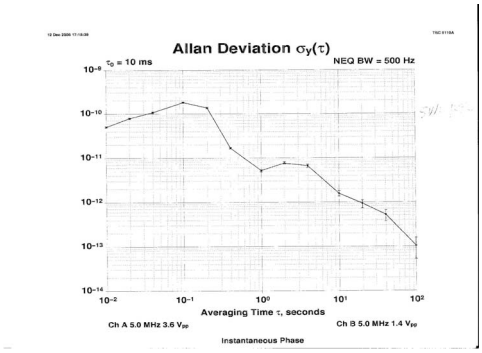

Figure 7. Curve of frequency stability(fw＝1kHz)

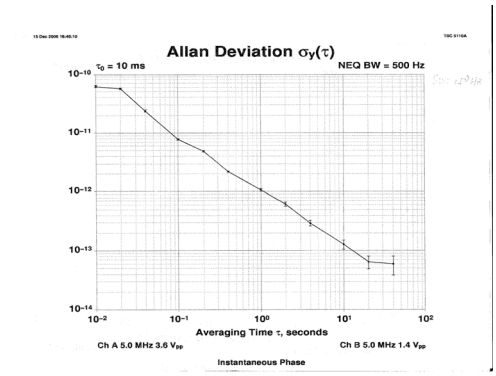

Figure 8. Curve of frequency stability(fw＝100Hz)

The input control voltage of the varactor in resonant cavity ranges from 0V to 9V, and the cavity frequency changes about 2kHz accordingly, so we can get its voltage control sensitivity, which is 222Hz/V. In this case, to achieve the frequency stability of the maser to the level of 10^{-15}/day, the precision of the varactor control voltage must be limited within 3.1mV. Therefore, high sensitivity cavity detecting circuits and low temperature drift devices should be taken into consideration. In the new cavity auto-tuning circuits, lower value resistances and capacitors with lower temperature drift are applied in filter circuits instead of large value ones in previous circuits, for the modulation frequency is higher. Besides, the use of analog devices with ultra low temperature drift and digitalize delay circuits can also lower the temperature drift of entire circuits. Experiments shows that the frequency stability of the maser could reach the level of 10^{-15}/day in operational environment without constant temperature system, whose diurnal temperature variation exceeds 6℃.

Furthermore, the new circuits widen the operating range of the varactor from 0~9V to 0~20V, extending the control range of the cavity frequency more than double to greater than 4kHz, which would benefit to the environmental compatibility and reliability of time-keep masers.

B. Improvements on phase-locked receiver

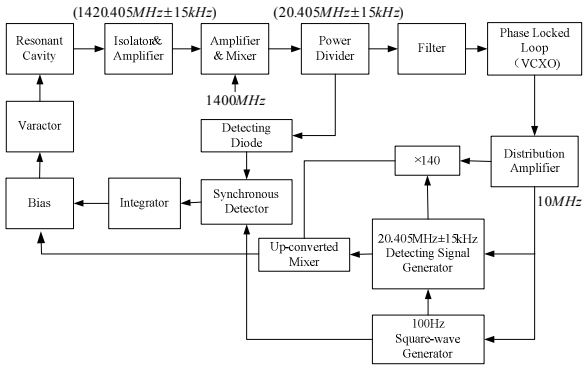

Figure 9. Block diagram of main electronic system of the maser

Figure 9 shows a complete block diagram of cavity auto-tuning and phase-locked receiver system. Mixed by an FSK signal at *(20.405MHz ±15kHz)* generated by a detecting signal generator and a microwave signal at 1.4GHz, the detecting signal is injected into the resonant cavity. The output signal from the resonant cavity, including both the detecting signal and the oscillating signal, isolated and amplified in the first stage, and then down-converted mixed, is divided into two output signals by a power divider: one is used to correct the cavity frequency variation by amplitude-demodulating in the synchronous detector, the other is used to lock the VCXO after extracted the oscillating signal by a bandpass filter with the bandwidth of 4kHz and then down-converted to the frequency of 405kHz.

Improvements on the receiver are mainly as follows:

a) Isolation and amplification circuits in the first stage:

In previous circuits, the noise figure of the amplifier is small(NF ≈ 1dB), however, tests found that the input impedance of the amplifier at operating frequency was not 50 Ω , mismatching with the cavity. Besides, the mismatching between the amplifier and the cavity leads the amplifier can not be connected to the output of the maser directly; otherwise it would cause the maser stop oscillating. Therefore, changes of the input impedance of the amplifier, such as changes caused by temperature variation, would make the maser not stable. Moreover, coupling between the external circuits and the cavity reveals that impedance matching of an isolator is not better, or even worse, than that of an amplifier. For the isolator is a resonance ferrite device whose operating frequency is the function of its internal magnetic intensity which might change with temperature or lower over time, the changing of the input impedance of the isolator would influence the frequency of the maser. Instead of the previous circuits, the new generation of the amplifier with ultra-low noise figure and good matching of input impedance is directly connected to the maser, with the post

isolator. By this way, the operating stability of the maser is improved with NF=0.6dB.

b) Frequency multiplier at 1.4GHz:

As the local oscillator of the maser, the frequency multiplier at 1.4GHz would influence the specifications of the output signal of the maser. The former frequency multiplier was consisted of lumped elements, which was large in volume and high power consumption. And the internal local oscillating source in phase-locked frequency multiplier took a common LC oscillator for option, having higher phase noise, as shown in Figure 10. Instead, we use a dielectric oscillator with high Q as internal local oscillator and a voltage-controlled phase detection module using modern VLSI technology, leaving only 1/4 of its original volume and lowering the output phase noise, as shown in Figure 11.

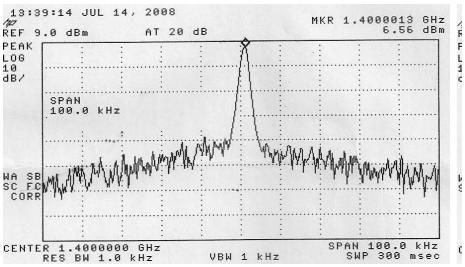

Figure 10. Output spectrum of 1.4GHz frequency multiplier (former)

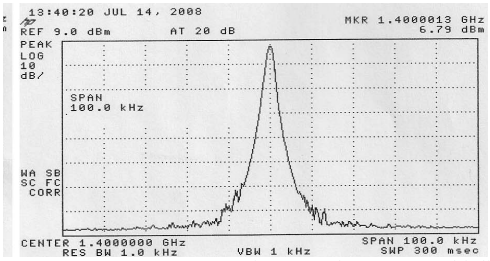

Figure 11. Output Spectrum of 1.4GHz frequency multiplier (present)

Figure 10 and Figure 11 show that at least an improving signal-to-noise ratio of 30dB is realized. Besides, the frequency stability under the time interval of 10s is 2~3 times as low as the former one.

c) Phase-locked circuits:

A special method for the PLL circuit was applied in former circuits, having a mixer and an integrator, which is complex and using longer time for locking. Instead, we choose AD9956 with a 48-bit DDS and a Phase-frequency-detector circuit, integrating the PLL circuit into a single chip. The new circuits are simple and fast to locking. The locking time could be limited within the level of ms, compared with the former circuits which would cost at least 10s to lock and a voltage re-searching circle of 0~5V if unlocked. Apparently, the new circuits can improve the reliability of the system for time-keeping without influence its practical frequency stability.

IV. PRELIMINARY TESTS ON SPECIFICATIONS OF THE MASER

The high-precision masers for time-keeping should primarily take long-term frequency stability, such as the one-day frequency stability or even more than five-day frequency stability, into consideration. Two masers developed for national time service center by SHAO have been put into use with two masers from Symmetricom of the U.S. under the same laboratory conditions. Results are shown in Figure 12.

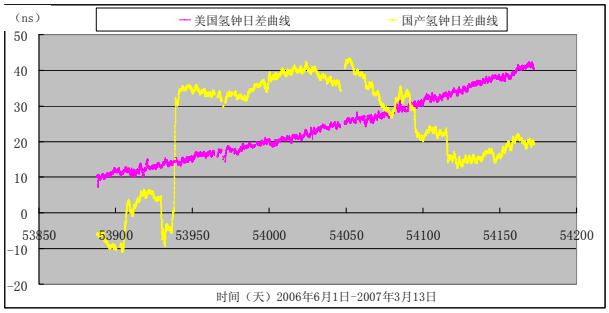

Figure 12. Comparison curves of daily range for time-keeping(curve in yellow shows the data from SHAO and curve in rose shows the data from Symmetricom)

As shown in Figure 12, frequency fluctuations of masers from the U.S. with frequency stability of 1~2E-15/day are apparently lower than masers from SHAO with frequency stability of 5E-15/day. Masers from the U.S. with higher frequency drift have a lower time-keeping weight, however, customers thought masers from SHAO are not competent enough for time-keeping. In addition, tests for time-keeping need at least six-month continuous data, which seems difficult to ensure for masers from SHAO. Therefore, we have taken the improved masers under the test of one-day frequency stability. Results are shown in table 1 and the original data are shown in Figure 13 and Figure 14.

TABLE 1. SPECIFICATIONS OF THE IMPROVED MASER

Expected Specifications	Measured Specifications
Frequency Stability：4×10^{-15}/d	1.5×10^{-15}/d
Frequency Drift：$\leqslant1\times10^{-15}$/d	8.6×10^{-16}/d
Temperature Sensitivity：$\leqslant1\times10^{-14}$/℃	8.1×10^{-15}/℃

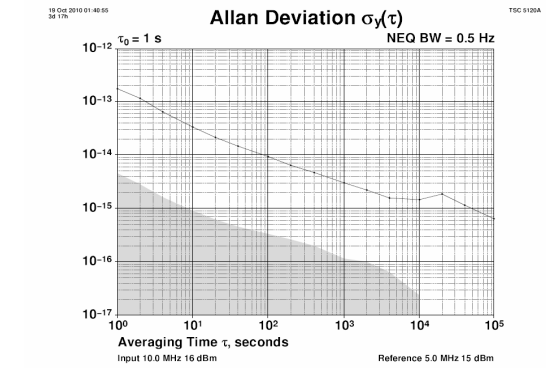

Figure 13. Short-term stability original data of the improved maser

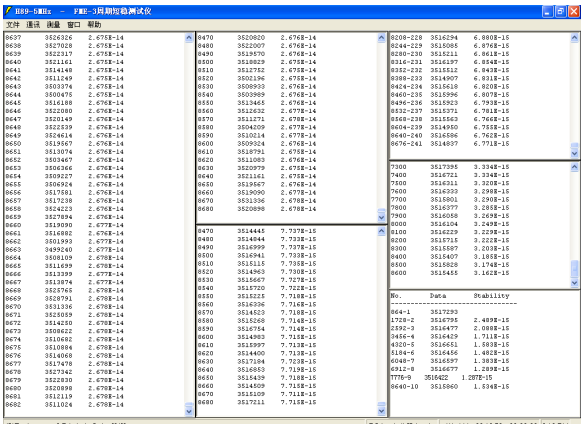

Figure 14. Long-term stability original data of the improved maser

The measured data reveals that specifications of the improved maser have achieved the anticipated targets, approaching to the world-class maser, while the measured time-keeping weight should be proved in further tests and time-keeping applications.

V. CONCLUSION

Experimental results show that improvements on time-keeping masers are effective in practice. Reliability (MTBF to 10 000h) and weights in time-keeping need be proved in further tests. Expectations are taken that the improved masers developed by SHAO could reach the average weight among all the masers served in International Time Bureau. A highlight of further studies would be improving the reliability and lowering the entire temperature sensitivity to improve long-term frequency stability of the maser to the-state-of-art 7 $\times 10^{-16}$/day.

REFERENCES

[1] D. Kelppner, H.C. Berg, S.B. Crampton, N.F. Ramsey, R.F.C. Vessot, H.E. Peters, J. Vanier. Hydrogen-Maser Principles and Techniques. Physical Review, Vol 138(4A), A972-A983.

[2] D. Kelppner, H. Mark Goldenberg, Norman F. Ramsey. Theory of the Hydrogen Maser. Physical Review, Vol 126(2), p603-615.

[3] G.J. Dick, T.K. Tucker. Fast autotuning of a hydrogen maser by cavity Q Modulation. The Telecommunications and Data Acquisition Report(1987), p295-303.

[4] C.Audoin. Fast cavity auto-tuning systems for hydrogen masers [J]. Revue.Phys.Appl.16 (1981), p125-130.

[5] Zhang Yanjun, Wu Yidong, Cai Yong. Improvement of the New Hydrogen Atomic Clock and It's Application in Time Keeping [J] Acta Metrologica Sinica 2009,Vol.30 No.3 p261-266.

[6] Zhai Zaocheng. Frequency-Temperature Effects Analysis on Hydrogen Maser Microwave Cavity [J] Journal of Astronautic Metrology and Measurement, 2006,26(5).

[7] Peng Ke, Zhang Yanjun, Zhang Weiqun. Design Improvement and Performance Expectation of Hydrogen Maser SOHM-4 [J] Journal of Time and Frequency 2004, Vol.27 No.1,p41-47.

Push-pull optical pumping on the Cs D_1-transition

Evelina Breschi and Antoine Weis

Physics Department
University of Fribourg
CH-1700 Fribourg Switzerland
Email: evelina.breschi@unifr.ch

***Abstract*— We report on preliminarily results of push-pull optical pumping (PPOP) on the D_1-transition of cesium. PPOP is based on a coherent population trapping effect prepared with polarization-modulated bichromatic light coupling the two ground-state hyperfine levels, the light polarization being modulated at the microwave frequency. With a suitable choice of polarizations, a single specific coherent superposition (dark state) formed by the two $m_F = 0$ sublevels can be prepared under optimal conditions. This increase the contrast of the clock reference signal without significant line-broadening.**

I. Introduction

Research in microwave-based frequency standards using alkali vapor in sealed cells has received a renewed interest in the last 10 years thanks to the progress in diode lasers and MEMS technologies. Vapor cell atomic clocks (VCACs) are used in applications such as navigation, positioning and telecommunications, where small and stable clocks are required. VCACs can be divided in two groups depending on the approach used to excite the clock resonance: double resonance (DR) and coherent population trapping (CPT) clocks. From a technical point of view, the relevant difference is the fact that in DR-clocks the microwave is applied to the atoms via an AC magnetic field while in CPT-clocks it is applied via amplitude-, phase- or frequency-modulation of the laser beam. The two types of devices have their respective merits and technical challenges. Currently, DR-clocks have a superior performance (short term stability $\sim 10^{-13}$ at 1 s) [1] than the CPT atomic clocks, but they are bulkier. The smallest DR-clock has a volume of about 1 liter while miniature CPT-clocks with a volume of about tens of mm^3 [2] have been demonstrated.

The fundamental performance limiting factor in conventional CPT-clocks, is that the clock reference signal (prepared with circularly polarized laser light) suffers from population by optical pumping to other dark states. Several alternatives to conventional CPT spectroscopy have been proposed [3]-[6], but no satisfactory solution has been found so far. In 2005, the Happer group at Princenton University proposed a novel approach, the so-called push-pull optical pumping (PPOP)technique, based on the excitation of the CPT effect with bichromatic laser light whose polarization is modulated at the microwave frequency [7].

In this communication we report on our realization of a push-pull optical pumping experiment on the Cs D_1-line. We start with a short description of the PPOP interaction scheme, then we introduce the experimental apparatus and finally present first results on PPOP. The advantages and disadvantages of this approach for atomic clock applications are discussed in the conclusions.

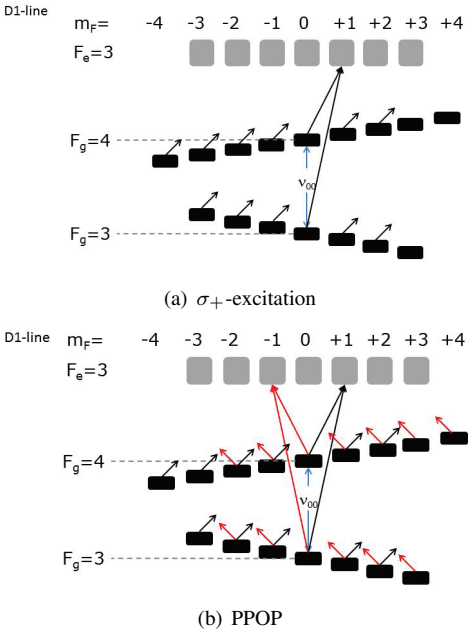

(a) σ_+-excitation

(b) PPOP

Fig. 1. Scheme of the optical transitions in the cesium D_1 (case $F_e = 3$) excited with 1(a) circularly polarized laser light ($\sigma_+\sigma_+$-excitation), and 1(b) PPOP, i.e., $\sigma_+\sigma_+$- and $\sigma_-\sigma_-$-excitation alternating at ν_{00}.

II. Push-pull optical pumping

We consider the Cs D_1-line excited by a bichromatic, phase-coherent electromagnetic field. To achieve CPT, the two frequency components are tuned to resonance with the $|F_g = 3\rangle \rightarrow |F_e = 3\rangle$ and $|F_g = 4\rangle \rightarrow |F_e = 3\rangle$ transitions, respectively. A longitudinal (i.e. parallel to the laser propagation vector) magnetic field is applied to the atoms.

In the conventional CPT clock the two frequency components have identical σ_+ (or σ_-) circular polarization. The clock signal is produced by the coherent superposition of the ground-state Zeeman sub-levels having $m_F = 0$. In Figure 1(a) the interaction scheme and the optical transitions in the case of $\sigma_+\sigma_+$-excitation are represented . During the

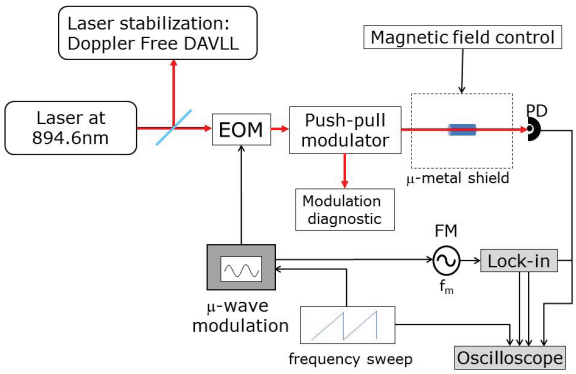

Fig. 2. Block diagram of the experimental apparatus.

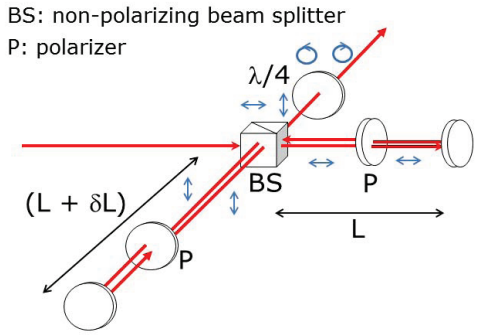

Fig. 3. Push-pull modulator used in the experiments presented here.

interaction with σ_+-polarized light the sublevel populations are partially pumped into the three outermost states which do not interact with the radiation: $|F_g, m_F\rangle = |3,3\rangle$, $|4,3\rangle$, and $|4,4\rangle$. Conversely, $\sigma_-\sigma_-$-excitation will accumulated populations in the sublevels at lower m_F $|3,-3\rangle$, $|4,-3\rangle$, and $|4,-4\rangle$. In both cases atoms trapped in the outermost states will thus not contribute to the clock signal.

The idea of PPOP is to alternate $\sigma_+\sigma_+$-excitation and $\sigma_-\sigma_-$-excitation at the clock transition frequency. In this way the population of the outermost states can be driven efficiently into the $m_F = 0$ levels that form the clock state and trapped there. The interaction scheme of PPOP is shown in Figure 1(b). The probabilities that σ_+ and σ_- light are absorbed by the clock state are proportional to $\sin^2(\omega_{00}t/2)$ and $\cos^2(\omega_{00}t/2)$, respectively. Alternating between the two polarization states at the appropriate rate thus ensures the clock state to be the only dark state in the manifold.

III. Experimental apparatus

We have set up a modular experiment in which different light-atom interaction schemes for CPT-spectroscopy (and related effects) can be tested and compared under similar conditions. A block diagram of the experimental apparatus is shown in Figure 2. A mono-mode distributed feedback laser (Toptica model DL100 DFB) can be frequency stabilized on the transitions of the D_1-line of Cs (at 894.6 nm) via a Doppler-free DAVLL system [8]. The beam is phase-modulated at the frequency ν_μ with an electro-optic modulator (Photline model NIR-MX800-LN-10). We tested different modulation configurations (ν_{00} is the hyperfine splitting of $m_F = 0$ sub-levels, Figure 1):

- $\nu_\mu = \nu_{00} \approx 9.2$ GHz. The carrier and one of the 1^{st} order sideband are resonant with the optical transitions. Thus, the optimal modulation amplitude corresponds to the laser power equally distributed between the carrier and the two first order sidebands. In this way, about 66% of the light power is resonant with the optical transitions. The remaining 33% of the optical power is in the second (non-resonant) first order sideband, which increases the photo-detector background signal and hence the detection noise, and contributes to the light shift of the clock resonance.
- $\nu_\mu = \nu_{00}/2 \approx 4.6$ GHz. The two first order sidebands are resonant with the optical transitions. Thus the optimal modulation amplitude corresponds to the maximum laser power in the two first order sidebands. In this way about 40% of the light power is in the carrier and in the off-resonance higher order sidebands, contributing to the background and to the detection noise. Due to the symmetry of the off-resonant light spectrum, the light-shift contributions of the different side-bands are suppressed [9].

The microwave modulation was characterized by monitoring the amplitude of the beat signal at ν_μ and $2\nu_\mu$, measured by focusing the modulated beam onto a fast photo-diode. Simultaneously we recorded the dark resonance whit no magnetic field applied to the atoms.

Our modulation system is equipped with a feedback loop that can fix the working point of the modulator (to compensate for drifts) and efficiently suppress the carrier frequency. One part of the modulated beam is detected by a photo-diode whose dc signal is injected in the modulator bias controller (Photoline model MBC). MBC generates the bias voltage to polarize the EOM at the zero of the transfer function. We measured a 20 dB carrier suppression, which can nominally be improved up to 39 dB. With the carrier suppression system we can work at $\nu_\mu = \nu_{00}/2$, yielding an almost pure bichromatic field that increases the resonance contrast and reduces the light-shift.

In order to increase the detection sensitivity, ν_μ is modulated at $f_m = 3$ kHz and, the detected signal is demodulated with a commercial lock-in amplifier (Stanford model SR830).

The Cs atoms are contained in a cylindrical cell (diameter 25 mm and length 20 mm) whose internal walls are coated with Paraflint. The cell is produced in the Fribourg cell production-facility [10].

Finally, the polarization of the phase-modulated beam is in turn modulated at ν_{00} via the "push-pull modulator" shown in Figure 3.

The key requirement for PPOP is the generation of a bichromatic light field with identical polarizations that alternate between $\sigma_+\sigma_+$ and $\sigma_-\sigma_-$ at the clock transition frequency. We built a variable delay line with the geometry of a Michelson

interferometer: the input beam is divided in two sub-beams with an non-polarizing beam splitter (BS) cube. The sub-beams are vertically and horizontally polarized with polarizing plates (P). The optical path length difference is $2 \cdot \delta L$. In this scheme only about 25% of the input light power is available at the output. To solve this problem, a second version of the delay line will be mounted in the same geometry by simply replacing the BS by a polarizing beam splitter, and the two polarizers by two quarter-wave plates.

The polarization modulation can be fully described by the calculation of the (unnormalized) Stokes parameters for the superposition of two polarized bichromatic light fields with linear orthogonal polarization:

$$E_1 = \frac{1}{2}\begin{pmatrix}1\\0\end{pmatrix} e^{i(kL-\omega t)}[1 + e^{i(k_{00}L-\omega_{00}t)}] \ ,$$
$$E_2 = \frac{1}{2}\begin{pmatrix}0\\1\end{pmatrix} e^{i[k(L+\delta L)-\omega t]}[1 + e^{i(k_{00}(L+\delta L)-\omega_{00}t)}] \ , \quad (1)$$

where k and ω are the optical wave-vector and angular frequency; $k_{00} = 2\pi/\lambda_{00}$, $\lambda_{00} \approx 32.6$ mm and, $\omega_{00} = 2\pi\nu_{00}$ are the microwave vector, wavelength and angular frequency, respectively; L and $L + \delta L$ are the lengths of the two arms of the delay line.

The unnormalized Stokes parameters are defined by the difference of intensities between pairs of orthogonal polarizations : H/V horizontal and vertical, $\pm$ linear polarization rotated by $\pm 45^\circ$ with respect to H and V, and, σ_+/σ_-.

When $2 \cdot \delta L = \lambda_{00}/2$ ($k_{00} \cdot \delta L = \pi$) the polarization vector of total field ($E_1 + E_2$) oscillates between the horizontal (H) and vertical (V) polarization states at ω_{00} passing through intermediate states of elliptical polarization; the Stokes parameters read:

$$S_{+/-} = \sin(k\delta L)\sin(k_{00}L - \omega_{00}t) \ ,$$
$$S_{\sigma_+/\sigma_-} = -\cos(k\delta L)\sin(k_{00}L - \omega_{00}t) \ ,$$
$$S_{H/V} = \cos(k_{00}L - \omega_{00}t) \ . \quad (2)$$

It is worth to notice that when $k_{00} \cdot \delta L = \pi$ the intensity of the output beam is constant. On the other hand, $k_{00} \cdot \delta L \neq \pi$ the output beam is a complex combination of intensity and polarization modulation.

The direct measurement of the polarization modulation of a bichromatic field at this frequency is a nontrivial tasks, and still an open point. However the effect on the hyperfine CPT is evident (see in the next section).

IV. Dark state spectroscopy

In Figures 4(a) and 4(b) we compare the dark resonance spectra in a longitudinal magnetic field recorded for conventional $\sigma_+\sigma_+$-excitation and PPOP, i.e., alternating $\sigma_+\sigma_+$- and $\sigma_-\sigma_-$-excitation, respectively, in the same experimental conditions.

In Figure 4(a) six dark resonances are observed when the two-photon Raman detuning is varied around the unperturbed value ν_{00}. This spectrum corresponds to the interaction scheme shown in Figure 1(a). The dark resonance spectrum is not symmetric around ν_{00}. As discussed above, the σ_+-excitation populates the Zeeman sub-levels having large m_F quantum numbers, simultaneously depopulating the Zeeman sub-levels having small m_F.

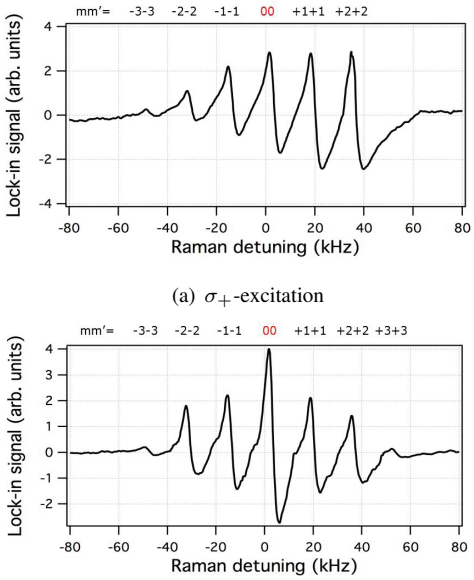

(a) σ_+-excitation

(b) PPOP

Fig. 4. Dark resonance spectra in longitudinal magnetic field prepared with conventional $\sigma_+\sigma_+$-excitation 4(a) and PPOP, i.e., alternating $\sigma_+\sigma_+$- and $\sigma_-\sigma_-$-excitation 4(b), corresponding to the interaction schemes represented in Figure 1(a) and 1(b), respectively.

In Figure 4(b) seven dark resonances are recorded, corresponding to the interaction scheme in Figure 1(b). The dark resonance spectrum is symmetric around the ν_{00}. As anticipated, one can see that PPOP depopulates the outermost Zeeman sub-levels (having large $|m_F|$), while accumulating the populations around the clock resonance.

V. Conclusion

We have presented preliminarily PPOP results in cesium and we have demonstrated the effect of polarization modulation on the dark resonance spectrum: PPOP-excitation accumulates the atomic sublevel populations in states having lower $|m_F|$ quantum numbers. We compared PPOP and conventional $\sigma_+\sigma_+$-excitation under identical experimental conditions: a preliminary enhancement by a factor 2 of the clock resonance strength has been recorded. At the same timevwe observed no significant change of the background (mainly due to the non-resonant laser sidebands) and of the resonance linewidth (essentially dominated by power broadening). Thus, an enhancement by a factor 2 in the short-term stability can be expected. Similar results have been recently obtained in ^{87}Rb atoms [12].

Besides enhancing the clock's short-term stability, PPOP-excitation will reduce the influence of polarization fluctuations on clock performance which have been pointed out to be a critical noise source in CPT-clocks [13].

On the other hand, PPOP requires additional optical elements compared to the conventional $\sigma_+\sigma_+$-excitation, which may be a disadvantage for miniaturized clocks. However, it is worth to note that in the case of Cs atoms ($\lambda_{00} = 32.6$mm) a relatively compact push-pull modulator can be realized using a structure similar to the one built for the micro-saturated absorption spectrometer discussed in [14].

For the time being, our experiments confirms the potential that PPOP has for clock applications. However, a systematic comparison of the final performance at the optimal clock operating conditions for conventional and PPOP CPT-based clocks has not be carried out so far.

ACKNOWLEDGMENT

This work is supported by SNF-Ambizione (grant PZ00P2_131926) and by the Pool de Recherche of the University of Fribourg. We thank our colleagues from the FRAP group for useful discussions, and the machine shop and the electronics pool of the Physics Department for expert technical support.

REFERENCES

[1] S. Micalizio, C. E. Calosso, A. Godone, C. Affolderbach, F. Gruet,F. Levi *Pulsed Optically Pumped Rb Clock with High Frequency Stability Performances* Proceeding 25th EFTF joint with IFCS, 294, 2011

[2] S. Knappe,V. Shah,P. D. D. Schwindt, L. Hollberg, J. Kitching, L.A. Liew and J. Moreland, *A microfabricated atomic clock* App. Phys. Lett. **85**, 9,1460, 2004.

[3] S.V.Kargapoltsev, J. Kitching, L. Hollberg ,A.V. Taichenachev, V.L. Velichansky,and V.I. Yudin, *High-constrast dark resonance in $\sigma_+ - \sigma_-$ optical field* Laser Phys. Lett. **1**, 10 495, 2004.

[4] A.V. Taichenachev, V.I. Yudin, V. L. Velichansky, and S. A. Zibrov, *On the unique possibility to increasee significantly the contrast of dark resonance on D1 line of 87Rb* Pis'ma v ZhETF, **82**, 7 , 449, 2005.

[5] T. Zanon, S. Trémine, S. Guérandel, E. de Clercq, D. Holleville, N. Dimarcq, A. Clairon, *High contrast Ramsey fringes with coherent population trapping pulses in a double lambda atomic system* Phys. Rev. Lett. **94**, 193002, 2005.

[6] M. Rosenbluh, V. Shah,S. Knappe,J. Kitching, *Differentially detected coherent population trapping resonances excited by orthogonally polarized laser field* Opt. Exp. **14**, 15, 6588 (2006)

[7] Y.Y. Jau, E. Miron, and W. Happer, *Push-pull optical pumping of pure superposition states* Phys. Rev. Lett., **93**, 160802, 2004.

[8] T. Petelski, M. Fattori, G. Lamporesi, J. Stuhler, and G. M. Tino, *Doppler-free spectroscopy using magnetically induced dichroism of atomic vapor: a new scheme for laser frequency locking* Eur. Phys. J. D. **22** 279 (2003)

[9] S. A. Zibrov, I. Novikova, D.F. Phillips, R. L. Walsworth, A. S. Zibrov, V. L. Velichansky, A. V. Taichenachev, and V.I. Yudin, *Coherent-population-trapping resonances with linearly polarized light for all-optical miniature atomic clocks* Phys. Rev. A **81** 013833, 2010

[10] N. Castagna, G. Bison, G. Di Domenico, A. Hofer, P. Knowles, C. Macchione, H. Saudan, A. Weis *A large sample study of spin relaxation and magnetometric sensitivity of paraffin-coated Cs vapor cells* Appl. Phys. B **96** 763, 2009.

[11] R. Wynands, A. Nagel, S. Brandt, D. Meschede, and A. Weis, *Selection rules and line strengths of Zeeman-split dark resonances* Phys. Rev. A, **58**,1,196, 1998.

[12] Y. Zhang,S. Qu, and S. Gu, *Spin-polarized dark state free CPT state preparation with co-propagating left and right circularly polarized lasers* Opt. Exp. **20**, 6, 6400, 2011.

[13] J. Camparo, M. Huangn and J. Coffer *Laser Polarization Noise and CPT Atomic Clock Signals* Proc. IEEE 21^{st} EFTF joint with IFCS, 1056, 2007;

[14] S.A. Knappe, H.G. Robinson, and L. Hollberg, *Microfabricated saturated absorption laser spectrometer* Opt. Exp. **15** 10, 2007.

Towards the Detection of High-Contrast Cs CPT Resonances Using a Single Modulated Diode Laser

X. Liu, E. Kroemer, J. M. Merolla, R. Boudot

***Abstract*— This paper reports the key development steps of a Bi-Frequency Bi-Polarization (BiFBiP) laser system that generates from a single externally-modulated Distributed Feedback (DFB) laser source two phase-coherent optical lines resonant on the Cs D_1 line (894.6 nm), frequency-splitted by 9.192 GHz and exhibiting linear crossed polarizations. Two different architectures, based on electro-optic modulators as key components for optical sidebands generation, are presented. Residual frequency stability performances of the DFB laser source are measured to be less than 10^{-11} for integration times up to 200 s. Phase noise performances of the optically carried microwave signal as well as polarization analysis at the output of the BiFBiP system are reported. Using this laser system, Coherent Population Trapping (CPT) resonances with contrast up to 5.8 % in a mm-scale vapor cell and 22 % in a cm-scale cell are preliminary reported.**

I. Introduction

A major drawback of traditional vapor cell clocks based on Coherent Population Trapping (CPT) [1] is the detection of the atomic clock resonance with a poor contrast (about 1 %). This is partly due in standard CPT clocks to the use of a circular polarization excitation scheme leading numerous atoms to be lost in extreme Zeeman sub-levels. Different optimized CPT pumping schemes were proposed to maximize the number of atoms participating to the clock 0-0 transition and consequently increase dramatically the CPT resonance contrast. Y. Jau et al. proposed the so-called push-pull interaction scheme where atoms interact with a D_1 line resonant bi-chromatic optical field that alternates between right and left circular polarization at the Bohr frequency of the state [2]. Contrasts up to 30 % were reported with this method. A method based on the use of a $\sigma_+ - \sigma_-$ configuration of polarized counterpropagating waves resonant with D_1 line of alkali metal atoms in small-size cells was proposed in [3]. Later, the same group proposed the *lin par lin* method and experimentally demonstrated the possibility to increase significantly the contrast of dark resonances on the D_1 line of alkali atoms with nuclear spin $I = 3/2$ using bichromatic linearly polarized light [4]. A prototype atomic clock based on $lin||lin$ coherent population trapping resonances in Rb atomic vapor was developed in [5]. This method was more recently implemented with alkali atoms of large nuclear spin (Cs atom : $I = 7/2$) and demonstrated CPT constrasts of about 10 % [6]. In 2007, V. Shah et al. demonstrated an alternative method to produce very high-contrast CPT resonances by using four-wave mixing in ^{87} Rb atoms [7]. T. Zanon et al. demonstrated the detection of increased CPT resonance contrasts with a so-called *lin per lin* interaction scheme using two linear orthogonally polarized optical lines [8]. CPT contrasts higher than 50 % was obtained using this technique [9]. Nevertheless, this method was demonstrated with two phase-locked lasers. This induces a complex experimental set-up with two laser sources, independent laser electronics, multiple optics components and a low noise optical phase lock-loop. Recently, efforts have been done in different groups and different experimental schemes have been proposed to realize this *lin per lin* interaction scheme with a single laser source [10], [11]. Both of these last articles report research studies based on Rb atom.

The present article aims to report first development steps of a Bi-Frequency Bi-Polarization (BiFBiP) laser system that generates with a single externally-modulated Distributed Feedback (DFB) laser source two phase-coherent optical lines resonant on the Cs D_1 line, frequency-splitted by 9.192 GHz with linear crossed polarizations. This system is constructed in order to allow the detection of high-contrast Cs CPT resonances through the *lin per lin* interaction scheme. Key components used for light field modulation are pigtailed pigtailed $LiNbO_3$ electro-optic modulators (EOMs). Two different architectures are proposed, including one inspired from [10]. Preliminar results report CPT contrasts up to 20 % in Cs vapor cm-scale cells.

II. Frequency-Stabilized Distributed Feedback Laser Source

A frequency-stabilized laser diode is required in the BiFBiP system. Narrow-linewidth extended cavity diode lasers (ECDLs) are usually used for this purpose [12], [13], [14], [15]. Nevertheless, such laser sources require high immunity to ambient vibrations, optical misalignment and accurate control of the cavity length. Nowadays, Distributed Feedback (DFB) lasers represent an efficient and simple alternative when narrow linewidth is desired.

In our BiFBiP system, the laser source is a commercially available GaAs semiconductor distributed feedback laser diode with integrated grating structure emitting in a single-mode at 895 nm. It is housed in a hermetic TO-3 package with thermistance and thermoelectric cooler. It is driven by a low noise current controller inspired from [16]. The DFB laser is frequency-stabilized using standard saturated absorption technique. The feedback correction is applied to the laser current with a servo bandwidth of about 500 Hz. Fig. 1 shows the DFB laser setup. Further details are reported in [17].

Two similar laser systems have been developed to evaluate the laser relative frequency stability. Figure 2 shows the Allan deviation of the beatnote signal frequency between both lasers in free running and locked conditions.

The authors are with FEMTO-ST, CNRS, 26 chemin. de l'Epitaphe, Besancon, France. e-mail: {rodolphe.boudot}@femto-st.fr

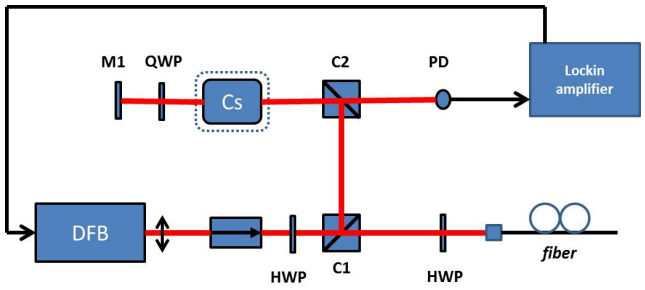

Fig. 1. Distributed Feedback laser diode optical set-up. QWP : quarter-wave plate, HWP : half-wave plate, PD : photodiode, M1 : mirror, C1 and C2 : polarizing cube splitters, Cs : Cs cell.

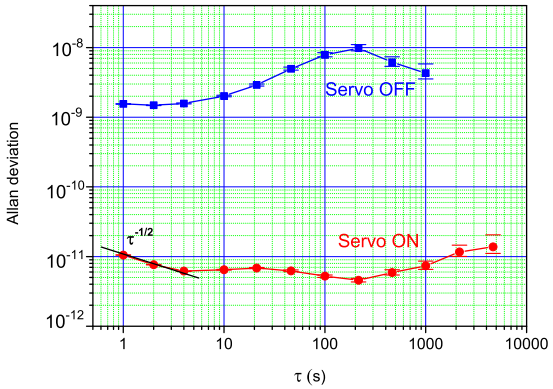

Fig. 2. Allan deviation of the DFB laser beatnote frequency (servo ON or servo OFF).

In the free-running regime, the frequency stability is measured to be 1.5×10^{-9} at 1 s. In the stabilized regime, it is 1×10^{-11} at 1 s. The Allan deviation decrases as a white frequency noise during a few seconds before reaching a wide flicker floor at about 5×10^{-12}. For integration times longer than 200 s, the laser frequency stability is slowly degraded. These results compare favorably with those presented in [18], [19] on Cs D_2 line and are greatly satisfying for a CPT Cs atomic clock.

III. BiFBiP ARCHITECTURES

A. Architecture 1

Fig. 3 shows a simplified scheme of the BiFBiP architecture 1.

The laser output beam is splitted into two parallel arms using a polarizing cube splitter. A half-wave plate is placed before the cube to separate the incident beam into two orthogonal polarization axes with equal power. In the first arm, a pigtailed Mach-Zehnder EOM (MZ EOM) is used to generate two in-phase optical sidebands separated from the carrier by the modulation frequency. The dc electrode bias voltage of the MZ EOM is adjusted in order to obtain three optical lines of equal amplitude. In the other arm, a phase pigtailed EOM allows to generate two optical sidebands around the carrier, each of them with opposite phase. Both arms are then recombined using a polarizing cube combiner.

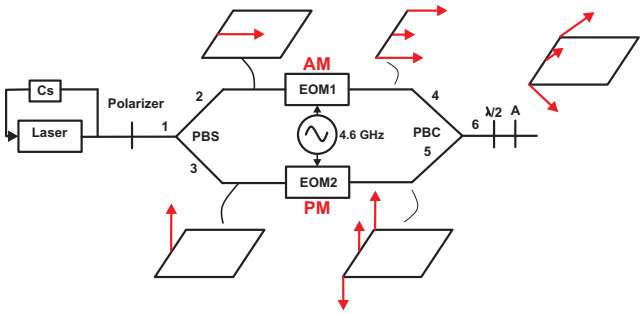

Fig. 3. Architecture 1 : 2 EOMs (a phase EOM and an amplitude MZ EOM) are placed into two parallel arms. The modulation frequency can be 9.192 GHz or 4.596 GHz.

At the BiFBiP output, the carrier is found to be parallel with the first sideband while it is orthogonally polarized to the second optical sideband. In this architecture, the laser can be modulated either at 9.192 GHz or 4.596 GHz. In the first case, CPT interaction will occur thanks to the optical carrier and one sideband. In the second case, CPT interaction is realized using both optical sidebands. Both EOMs, including their fiber input and output, are actively temperature-controlled and placed in a box containing insulating foam. In this architecture, the output spectrum is mainly composed here by three optical lines. Only two of them participate to the CPT interaction. Up to date, no selective optical filter has been placed at the output of the system to suppress the spurious sideband. This will be implemented in a near future.

B. Architecture 2

The second architecture (4) is inspired by and well described in [10].

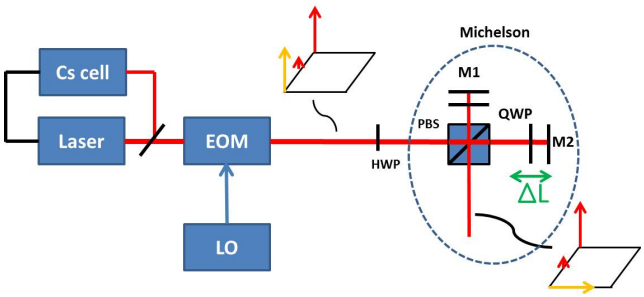

Fig. 4. Architecture 2 : CPT sidebands are generated using a pigtailed MZ EOM driven at 4.596 GHz. The EOM dc electrode bias voltage is tuned to suppress the optical carrier. The best carrier rejection is measured to be 37 dB. Both optical lines are separated and orthogonally polarized using a phase-imbalanced Michelson interferometer.

A MZ EOM, driven at 4.596 GHz, is used to generate two optical sidebands separated of 9.192 GHz from the carrier. The EOM transfer function bias point is stabilized to the so-called dark point where the optical carrier is optimally suppressed using a microwave technique similar to the one described in [20]. A typical carrier rejection of 37 dB is obtained. At the output of the EOM, a Michelson interferometer is placed to separate optical lines and orthogonally polarize them. It is shown that both optical lines of frequency f_1 and f_2 incident

on the cube are orthogonally polarized at the output of the cube if the phase differences satisfy the relations :

$$2k_1\Delta L = 2m\pi \quad (1)$$

$$2k_2\Delta L = 2(n+1)\pi \quad (2)$$

where m and n are integers, $2\Delta L$ is the optical path difference between the two arms and k_1, k_2 are wavevectors for the fields f_1 and f_2 respectively.

It can then be found that the condition required to obtain linear crossed polarizations at the output of the cube is :

$$\Delta L = \frac{c}{4\Delta f} \quad (3)$$

In the case of the Cs atom ($\Delta f = f_2 - f_1$= 9.192 GHz), we obtain ΔL = 8.15 mm.

In such a scheme, changes in the phase difference $\varphi_1 = 2k_1\Delta L$ are caused by changes of f_1 and Δ_L such that $\delta\varphi_1 = \frac{\pi\delta f_1}{\Delta f}$ and $\delta\varphi_1 = \frac{4\pi\delta(\Delta L)}{\lambda_1}$ respectively with λ_1 the field wavelength. For a Rb CPT experiment, authors in [10] report that a delicate control of the experiment such that $\delta f_1 < 190$ MHz et $\delta(\Delta L) < 12$ nm must be achieved to optimize the behavior of the system. The first condition is easily reached with a laser frequency stabilization based on saturated absorption technique. The second condition requires careful temperature control of the Michelson interferometer ensemble. The use of free-space discrete components has been prefered for the Michelson interferometer. Total dimensions are minimized to limit sources of optical length fluctuations.

IV. Technologies and Characterization of the BiFBiP system

A. A low phase noise 9.192 GHz local oscilator

CPT sidebands are achieved in the BiFBiP system by modulating at 9.192 GHz or 4.596 GHz electro-optic modulators. For this purpose, we developed (see Fig. **??**) low phase noise Non-Linear Transmission Line (NLTL)-based 9.192 GHz frequency synthesizers driven by a high-performance 5 MHz quartz-crystal oscillator. The multiplication process from 5 MHz to 9.192 GHz is similar to the one described in [21]. The only slight difference stands for the use of Gali-84+ amplifiers at the output of the 100-200 MHz doublers. These amplifiers are low-power consumption and easy-to-use devices. They can exhibit a 22-25 dBm output power allowing to drive and saturate NLTLs correctly. A low-noise frequency divider by 10 is typically used at the output of the synthesis when a 4.596 GHz signal is required.
Fig. 5 reports the residual phase noise of the frequency synthesizers at 100 MHz and 9.192 GHz. Phase noise performances for two synthesizers at 9.192 GHz are $-$ 75 dBrad^2/Hz, $-$105 dBrad^2/Hz and $-$ 113 dBrad^2/Hz at 1 Hz, 1 kHz and 10 kHz offset frequencies respectively.

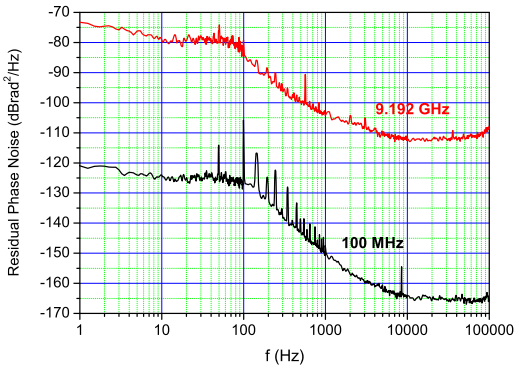

Fig. 5. Residual phase noise of frequency synthesizers at 100 MHz and 9.192 GHz.

B. Phase noise of the optically carried 9.192 GHz signal

Atoms in the cell interact with the optically carried 9.192 GHz signal from the BiFBiP system. It is then required to verify that the microwave signal phase noise is not degraded through optic transfer. For this purpose, the measurement set-up described in 6 was implemented to characterize the residual phase noise at 9.192 GHz of the optically carried signal.

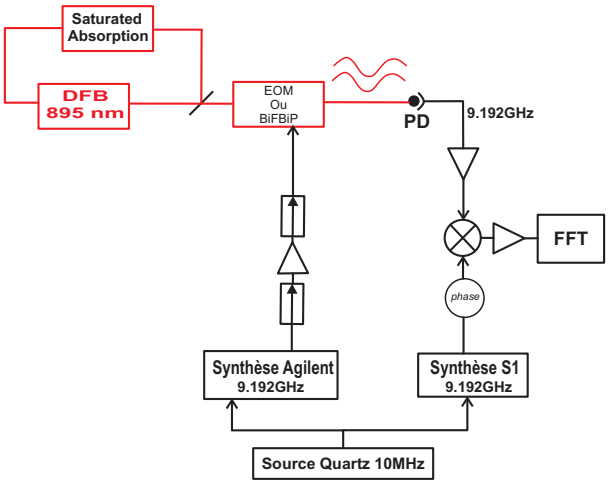

Fig. 6. Residual phase noise measurement set-up to characterize performances of the optically carried 9.192 GHz signal at the output of the BiFBiP system.

A common quartz-oscillator reference is splitted into two arms and drives two microwave synthesizers. The commercial synthesizer is used to drive at 9.192 GHz the EOM in the BiFBiP system. At the output of the BiFBiP system, the 9.192 GHz modulation signal is detected by a fast photodiode, amplified by a low-noise microwave amplifier and bandpass filtered (filter bandwidth $\sim$ 50 MHz) (not visible in the figure). Microwave isolators are inserted to prevent microwave feedback and optimize impedance matching. This signal is phase-compared to the 9.192 GHz signal from the second synthesizer using a saturated microwave mixer. The latter operates as a phase detector. The mixer output voltage is analysed using a FFT analyser.

Fig. 7 reports the residual phase noise performances at 9.192 GHz for the BiFBiP architecture 2. Note that all these measurements are strictly limited by the residual phase noise performances of the Agilent E8254A commercial synthesizer. It is pointed out that there is no phase noise degradation between the direct output of the NLTL-based frequency synthesizer and the output of the complete BiFBiP system.

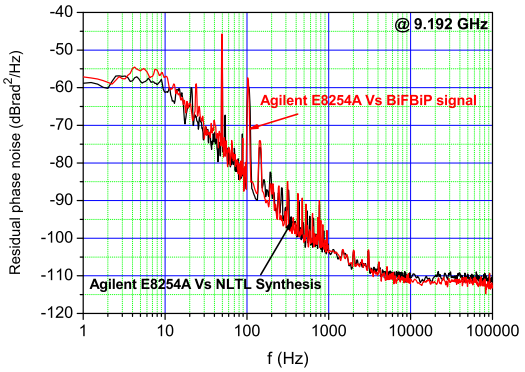

Fig. 7. Residual phase noise at 9.192 GHz of the NLTL-based synthesizer and of the optically carried 9.192 GHz signal at the output of the BiFBiP system (architecture 2).

C. Analysis of polarization

We checked the ability to generate two linearly crossed optical lines at the output of the BiFBiP structure by placing a linear analyser at its output. Fig. 8 reports the evolution of optical power in both optical lines versus the analyser angle (case of BiFBiP architecture 2). It is demonstrated that both optical lines at the output of the system are orthogonally polarized. For both axes, the minimum of transmission is close to be zero. This proves that both fields are really linearly polarized along orthogonal directions. The difference in amplitude is due to the fact that both photodiodes did not present exactly the same transimpedance gain. We confirm that orthogonally polarized optical lines have also been obtained in the case of the BiFBiP architecture 1.

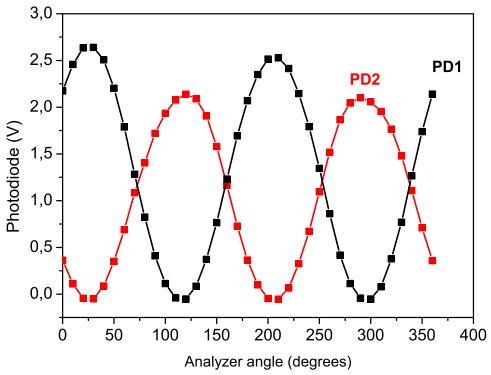

Fig. 8. Voltage at the output of both photodiodes (image of laser power) versus the analyser angle. Case of the BiFBiP architecture 2.

V. Preliminar detection of CPT resonances

This section is devoted to report Coherent Population Trapping resonances detected in Cs vapor cells. Two cells have been tested. Both of them are filled with a buffer gas to operate in the Dicke regime [22]. The first cell is a 2-mm diameter and 1.4 mm-length microfabricated cell realized according to the process described in [23]. This cell is filled with a Ne pressure of 75 Torr. The second cell is a 5-cm long and 2-cm diameter pyrex cell with a N_2-Ar buffer gas mixture. The total pressure is 15 Torr with a pressure ratio $r = P(Ar)/P(N_2)$=0.4. For the dectection of CPT resonances in correct conditions, cells are temperature-controlled, surrounded by a static magnetic field of a few μT and placed in a double layer mu-metal magnetic shield to prevent external electromagnetic perturbations.

A. Architecture 1

Figs 9(a) and 9(b) report a Zeeman spectrum detected in the microcell heated at 80°C for two different CPT excitation schemes.

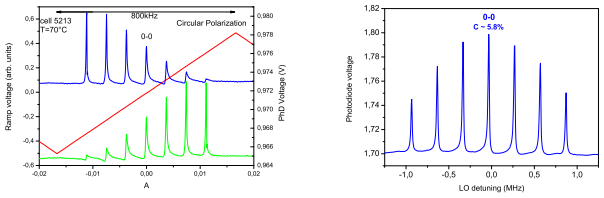

(a) (b)

Fig. 9. Zeeman spectrum obtained in microfabricated cell (Cs-Ne 75 Torr) heated at 80°C. (a) : Circular polarization in σ^+ or σ^- configuration (b) : BiFBiP laser. The modulation frequency is 9.192 GHz.

In the first case, atoms interact with circularly polarized light (standard technique in CPT clocks). Zeeman sublevels with the angular momentum projection $m = \pm 3$ are favored. In the second case, atoms interact with light coming from the BiFBiP laser. The total resonant laser power is about the same in both cases. While extreme Zeeman sublevels are favorably populated in the circular polarization excitation scheme, it is clearly pointed out that the clock 0-0 transition is optimized with the BiFBiP system. The contrast of the 0-0 resonance, defined as the ratio between the CPT signal height and the background, is measured to be 5.8% with the BiFBiP system whereas it is only 1.7% in the classical configuration. This represents a improvement factor of 3.4.

B. Architecture 2

Figs 10(a) and 10(b) show a Zeeman spectrum and a zoom on the clock 0-0 resonance respectively detected in the cm-scale Cs-N_2-Ar. The cell is heated at 33°C. The laser beam incident on the cell is only 6-mm diameter.

It is noted that the Zeeman spectrum presents a clear symmetry. The 0-0 transition contrast is 21.4 %. These results should be improved with an increased laser intensity up to a saturation value, a proper adjustment of the cell temperature [24] or a bigger beam diameter to make participate a maximum

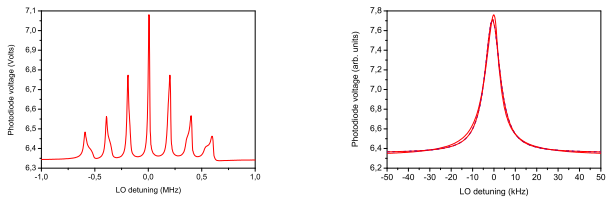

(a) (b)

Fig. 10. (a) Zeeman spectrum. The deformation of Zeeman lines is due to the fact that the static magnetic field is not well homogeneous along the whole length of the cell. The cell was inserted in a physics package devoted to be used with cells of maximum length 2 cm. (b) : Zoom on the 0-0 resonance. The contrast is 21.4 %. The total laser power is 800 μW.

number of atoms to the CPT interaction. Nevertheless, these results remain very encouraging. Detailed characterizations of CPT resonances with BiFBiP architectures versus several experimental parameters will be led in a near future.

VI. Conclusions

We demonstrated the detection of high-contrast CPT resonances in Cs vapor cells using a single modulated laser source that generates at 895 nm two optical lines frequency-separated by 9.192 GHz with linear crossed polarizations. A frequency-stabilized DFB laser source with a relative frequency stability better than 10^{-11} for integration times up to 1000 s was developed. Two different so-called BiFBiP architectures based on electro-optic modulators have been tested. Low phase noise 9.192 frequency synthesizers were developed to drive EOMs. Residual phase noise performances of optically carried 9.192 GHz signal at the output of the BiFBiP system was evaluated. CPT resonance clock (0-0) transition with contrast of 5.8 % was reported in a Cs-Ne mm-scale cell with the architecture 1. In a cm-scale cell, CPT contrasts up to 21 % were reported with the architecture 2.

Acknowledgments

This study was realized in the frame of a contract with Laboratoire National de métrologie et d'Essais (LNE). This work was partly funded by Région de Franche-Comté. X. Liu PhD thesis is supported by Région de Franche-Comté. We thank Philippe Abbé (FEMTO-ST) for technical support in electronics and mechanics design, E. Rubiola and V. Giordano (FEMTO-ST) for their help about the MZ EOM microwave stabilization technique, E. De Clercq (LNE-SYRTE) for fruitful discussions about optimized CPT pumping schemes. The authors wish to express their gratitude to S. Guérandel (LNE-SYRTE) for lending us the Cs-N_2-Ar cm-scale cell.

References

[1] J. Vanier, *Appl. Phys. B*, **81,**pp 421-442 (2005).

[2] Y. Y. Jau, E. Miron, A. B. Post, N. N. Kuzma and W. Happer, *Phys. Rev. Lett.*, **94,** (16), 160802 (2004).

[3] A. V. Taichenachev, V. I. Yudin, V. L. Velichanslky, S. V. Kargapoltsev, R. Wynands, J. Kitching and L. Hollberg, *JETP Lett.*, **80,** (4), 236 (2004).

[4] A. V. Taichenachev, V. I. Yudin, V. L. Velichanslky and S. A. Zibrov, *JETP Lett.*, **82,** (7), 398 (2005).

[5] E. E. Mikhailov, T. Horrom, N. Belcher, and I. Novikova, *J. Opt. Soc. Am. B*, **27,** pp 417-422 (2010).

[6] K. Watabe, T. Ikegami, A. Takamizawa, S. Yanagimachi, S. Ohshima and S. Knappe, *Applied Opt.*, **48,** (6), 1098 (2009).

[7] V. Shah, S. Knappe, L. Hollberg and J. Kitching, *Opt. Lett.*, **32,** (10), 1244 (2007).

[8] T. Zanon, S. Guérandel, E. de Clercq, D. Holleville, N. Dimarcq and A. Clairon, *Phys. Rev. Lett.*, **94,** 193002, (2005).

[9] N. Castagna, R. Boudot, S. Guerandel, E. De Clercq, N. Dimarcq and A. Clairon, *IEEE Trans. Ultrason. Ferroelec. Freq. Contr.*, **56,** (2), pp 246-253 (2009).

[10] S. H. Yim et al., *Rev. Sci. Instr.* 79, 126104 (2008).

[11] P. Yun et al., *Rev. Sci. Instr.* 82, 123104 (2011).

[12] G. D. Rovera, G. Santarelli and A. Clairon, *Rev. Sci. Instrum.* **65**, 5, 1502-1505 (1994).

[13] C. Affolderbach and G. Mileti, *Optics and Lasers in Engineering* **43**, 291-302 (2005).

[14] C. Affolderbach and G. Mileti, *Rev. Sci. Instr.* **76**, 073108 (2005).

[15] X. Baillard, A. Gauguet, S. Bize, P. Lemonde, P. Laurent, A. Clairon and P. Rosenbusch, *Opt. Comm.* **266**, 609-613 (2006).

[16] K. G. Libbrecht and J. L. Hall *Rev. Sci. Instr.* **64**, 8, 2133-2135 (1993).

[17] X. Liu and R. Boudot *IEEE Trans. Instr. Meas.* , to be published (2012).

[18] F. Bertinetto, P. Cordiale, G. Galzerano and E. Bava, *IEEE Trans. Instr. Meas.* **50**, 2, 490-492 (2001).

[19] T. Hori, A. Araya, S. Moriwaki and N. Mio, *Rev. Sci. Instrum.* **78**, 026105 (2007).

[20] B. Onillon, P. Danes, B. Benazet and O. Llopis, *Microwave and Opt. Tech. Lett.*, **49**, 7, 1634 (2007).

[21] R. Boudot, S. Guérandel and E. De Clercq, *IEEE Trans. Instr. Meas.*, **58**, 10, 3659-3665 (2009).

[22] R. H. Dicke, Phys. Rev. **89,** 472 (1953).

[23] M. Hasegawa, R. K. Chutani, C. Gorecki, R. Boudot, P. Dziuban, V. Giordano, S. Clatot, L. Mauri, Sensors Actuat. A : Phys, **167,** 594 (2011).

[24] S. Knappe, R. Wynands, J. Kitching, H. G. Robinson and L. Hollberg *Journ. Opt. Soc. Am. B* **18**, 1545 (2001).

Towards wall-coated microfabricated cells: Alkali vapor-cells using indium thin-film low-temperature bonding

R. Straessle, Y. Pétremand, D. Briand, N.F. de Rooij
The Sensors, Actuators and Microsystems Laboratory (SAMLAB)
Ecole Polytechnique Fédérale de Lausanne (EPFL)
Neuchâtel, Switzerland
rahel.straessle@epfl.ch

M. Pellaton, C. Affolderbach, G. Mileti
Laboratoire Temps-Fréquence (LTF)
Institut de Physique, Université de Neuchâtel (UniNE)
Neuchâtel, Switzerland

***Abstract*—We report on the realization and evaluation of micro-fabricated alkali vapor cells using a thin-film indium bonding technique. Optical and double-resonance spectroscopy performed on the cells demonstrates their suitability for atomic clock applications. Long-term measurements show a stable pressure inside the cells and therefore an excellent hermeticity of the bonding over several months. The low bonding process temperature of ≤ 140°C combined with good bond strength makes this method a promising candidate for realizing micro-fabricated alkali cells with anti-relaxation wall-coatings.**

I. Introduction

While for many years alkali vapor cells for atomic clocks were mainly fabricated using the glass-blowing technique, in recent years the diversity in fabrication techniques increased as the need for micro-scale cells pushed for new solutions. The technique which made it into industrial production is anodic bonding: Pyrex, which is transparent at the required wavelengths, forms optical windows and is bonded to silicon by anodic bonding [1]. The beauty of this technique is that fabrication, cleaning and outgassing, as well as filling and sealing of the pre-forms are relatively simple and can be performed on wafer level. The glass-blowing technique was also combined with micro-fabrication in [2]. Other bonding processes use intermediate layers, such as use of glass frit bonding [3] to encapsulate the alkali metal at a temperature of 400°C. We previously demonstrated a technique for cell sealing with a thick (100 µm) indium ring which, however, suffered from a short lifetime of the cell [4].

As divers the solutions to the problem are, all the reliable fabrication techniques include processing steps with temperatures higher than 250 °C. This starts to be an issue if the effect of wall-coating inside micro-fabricated cells shall be studied. The benefits of anti-relaxation wall-coatings have been mainly investigated in large (cm-scale) glass-blown alkali cells. Next to the use of buffer gases, wall-coatings are an alternative method to enhance the quality factor of the clock signal. As the cell decreases in size, the pressure of the buffer gas has to be increased to successfully suppress spin relaxation due to wall collisions and maintain the clock transition's quality factor. The increased buffer gas pressure, however, leads to increased collisional broadening of the absorption lines which at a critical point cancels out the advantages of having the buffer gas present. At this scale, wall coating might still be an excellent candidate but it has not been studied yet in micro-fabricated cells, due to the restricted temperature range compatible with wall coatings: the antirelaxation coatings which are known to work, like organosilanes [5] or paraffin [6], have melting temperatures well below the highest temperature of the above described bonding techniques.

Based on results of the previously presented technology [4] with thick rings of indium, we developed a technology with thin-film indium rings [7], that allows for improved In purity, better control of geometry, and finally increased life-time of the cell. This thin-film In bonding technique uses a bonding process at temperatures ≤140 °C, and guarantees good hermeticity and bond strengths of the cells.

II. Fabrication of the Alkali Vapor Cell

The first steps in the preform fabrication are carried out at wafer level and are shown in Figure 1. After a Pyrex wafer is bonded to a silicon wafer by anodic bonding, the silicon side is patterned with first a 200 µm-wide adhesion layer and then the actual bonding layer of indium is applied by evaporation

1) Anodic bonding of 390 µm Silicon wafer to 500 µm Pyrex wafer
2) Metallization by evaporation and lift-off
3) DRIE etching of holes and dicing of the wafers into 10 x 10 mm^2 preforms

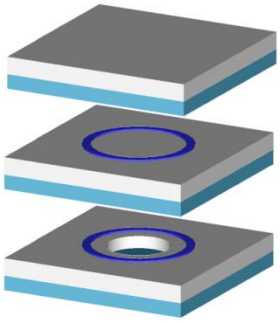

Figure 1: Schematics of preform fabrication.

This work was supported by the Swiss National Science Foundation (Sinergia grant CRSI20-122693/1).

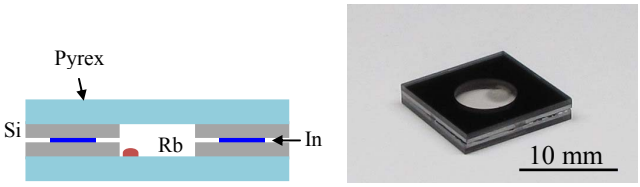

Figure 2: Schematic and photograph of an indium bonded alkali vapor cell with the dimension 10 x 10 x 1.780 mm^3.

and lift-off. Deep reactive ion etching (DRIE)is used to etch the holes forming the cell volume into the silicon. The wafers are then diced into 10x10 mm2 chips. Before bonding two of the pre-forms together to reach a combined cavity height of 780 µm, they are thoroughly cleaned in acetone and isopropanol. As described in [4], the preforms are loaded into a vacuum chamber where dispensing of the alkali metal as well as the bonding is performed. Next to bonding under high vacuum, there is also the possibility of introducing a buffer-gas mixture into the chamber before bonding. In either way, the bonding process consists of heating the preforms to 140 °C and applying a tool pressure of 4 bar (maximum pressure for this machine).

III. Spectroscopic Cell Evaluation

Two different types of thin-film In-bonded Rb cells were studied by spectroscopy: 1) evacuated cells containing Rb vapor but no buffer gas in order to assess the cleanliness of the bonding process, and 2) cells containing both Rb and buffer gas (150 mbar nominal pressure) for demonstration of an atomic clock signal.

A. Optical Spectroscopy

In a first step, both the evacuated and buffer-gas cells were tested by optical absorption spectroscopy on the Rb D2 line (at 780 nm). Both cell types showed the expected absorption features of the Rb D2 lines, indicating proper hermetic enclosure of atomic Rb inside the cells.

Saturated-absorption spectroscopy [8] allows for detection of narrow spectral absorption features with linewidths down to the 10 MHz level, that are superposed to the 550 MHz Doppler-broadened linewidth of one-photon optical

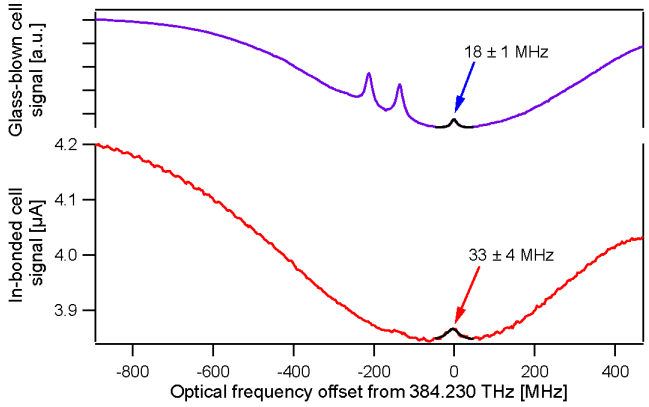

Figure 3: Saturated-absorption signals obtained for the evacuated In-bonded cell (bottom trace) and for a glass-blown reference cell (top trace).

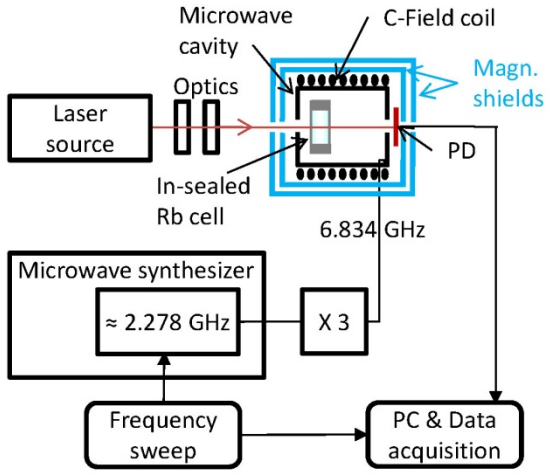

Figure 4: Double-resonance atomic clock setup used for the experiments.

absorption of a thermal Rb vapor. Here we use the width of the saturated-absorption lines to extract information on any potential gas contamination of the In-bonded cells. Figure 3 shows the saturated-absorption spectra for an evacuated In-bonded cell (heated to 60°C) and a conventional glass-blown cell serving as reference, recorded 2 months after sealing of the indium cell, using the same spectroscopic setup. The In-bonded cell shows an additional broadening of 15 ± 4 MHz (i.e. in addition to the linewidth obtained from the glass-blown reference cell). Since He and N2, the most probable contaminants, have broadening coefficients of ≈ 15 MHz/mbar [9], the contamination of the cell results as ≤ 1 mbar. The same measurement was repeated 5 months after fabrication and no further broadening was detected, thus maintaining the same upper limit for a potential contamination.

B. Double-Resonance Spectroscopy

The suitability of the buffer-gas filled In-bonded cell for a CSAC application was evaluated using a laboratory double-resonance (DR) clock setup, shown in Figure 4 [10]. The recorded DR signal of Figure 5 shows a positive shift of the clock frequency by 17.1 kHz (compared to the unperturbed clock transition frequency), which is consistent with the buffer gases used and their partial pressures [11]. The measured

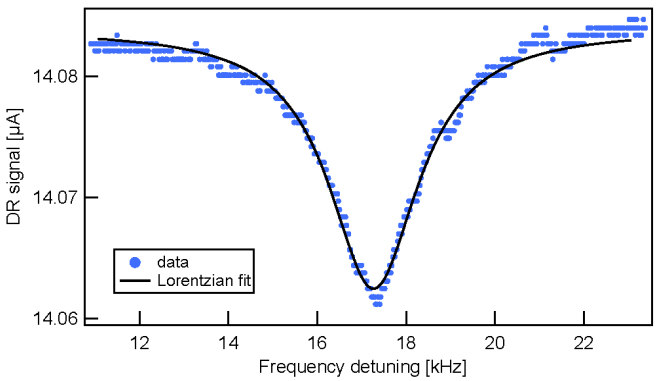

Figure 5: DR signal obtained from an In-bonded cell filled with Rb and buffer gas.

linewidth of 2.45 kHz is only slightly higher than the theoretically predicted intrinsic linewidth of 1.6 kHz for a 780 □m thick cell with the buffer gas pressure used [2], due to power broadening by the optical and microwave fields.

IV. Mechanical Characterization

Tensile tests carried out with samples bonded on chip level at 140 °C and with an applied tool pressure of 4 bar (current maximum of the chip bonder) show tensile strengths of 12 MPa which is comparable to the values achievable with anodic bonding. With samples bonded at wafer level at a temperature as low as 60°C and an increased tool pressure of 8 bar, we can still reach a similar tensile strength, which demonstrates the robustness of the technique.

V. Discussion and Conclusion

We have produced micro-fabricated Rb vapor cells, sealed with a novel thin-film bonding technique that requires very low process temperatures of ≤ 140°C only. Saturated-absorption spectra of an indium-bonded micro-cell without BG showed that a clean and evacuated atmosphere was still present several months after fabrication. A buffer-gas-filled micro-cell was mounted in a laboratory double-resonance setup and a clock signal with 5.4 kHz linewidth was retrieved, demonstrating the suitability of the cell for miniature atomic clocks.

In spite of the low bonding temperatures of our thin-film In-bonding technique, measured tensile strengths of 12 MPa for the cells show that the cells' bond strengths are comparable those obtained by anodic bonding even if the bonding is done at temperatures as low as 60 °C.

In view of their application in atomic clocks, the behavior and aging of the In-bonded cells when operated over extended time at elevated temperature (> 60°C) remains to be studied. Study of the behavior of the bonding at higher temperature is under investigation.

Most anti-relaxation wall-coatings used with alkali atoms are incompatible with the high process temperatures (>300°C) of established techniques for cell sealing. Thanks to its low process temperatures, the demonstrated thin-film In-bonding technique is therefore an ideal candidate for hermetic sealing of micro-fabricated cells with anti-relaxation wall-coatings.

Acknowledgment

The authors thank the CMi EPFL and CSEM Microsystems Division C cleanroom staff for their help and the Sinergia MACQS project partners for useful discussions (http://macqs.epfl.ch).

References

[1] E. Eklund, A. Shkel, S. Knappe, E. Donley, and J. Kitching, "Glass-blown spherical microcells for chip-scale atomic devices," Sensors & Actuators: A. Physical, vol. 143, pp. 175-180, 2008.

[2] J. Kitching, S. Knappe, and L. Hollberg, "Miniature vapor cell atomic-frequency references", Appl. Phys. Lett., 81, pp. 553-5, 2002.

[3] K. Tsujimoto, Y. Hirai, K. Sugano, T. Tsuchiya, and O. Tabata, "Sacrificial microchannel sealing by glass-frit reflow for Chip Scale Atomic Magnetometer," Proc. of MEMS, Cancun, Mexico, January 23-27 2011, pp. 368-371.

[4] Y. Pétremand, C. Schori, R. Strässle, G. Mileti and N. de Rooij et al. "Low Temperature Indium-based Sealing of Microfabricated Alkali Cells for Chip Scale Atomic Clocks", presented at EFTF 2010, Noordwijk, Netherlands, April 13-16, 2010.

[5] H. N. d. Freitas, A. F. A. d. Rocha, M. Chevrollier, and M. Oria, "Radiation trapping and spin relaxation of cesium atoms at cell walls," Applied Physics B: Lasers and Optics, vol. 76, pp. 661-666, 2003.

[6] G. Robinson, and C. E. Johnson, "Narrow 87Rb hyperfine-structure resonances in an evacuated wall-coated cell" Appl. Phys. Lett., vol. 40, pp. 771-3, 1982

[7] R. Straessle, M. Pellaton, Y. Pétremand, C. Affolderbach, D. Briand, G. Mileti, N.F. de Rooij, "Low-temperature Indium hermetic sealing of alkali vapor-cells for chip scale atomic clocks", Proc. of MEMS, Paris, Jan. 29 -Feb. 2 2012, p. 361-364,

[8] S. A. Knappe, H. G. Robinson, and L. Hollberg, "Microfabricated saturated absorption laser spectrometer", Opt. Express 15, pp. 6293-6299, 2007.

[9] M. D. Rotondaro and G. P. Perram, "Collisional broadening and shift of the Rubidium D1 and D2 lines ($5^2S_{1/2} \rightarrow 5^2P_{1/2}$, $5^2P_{3/2}$) by rare gases, H_2, D_2, N_2, CH_4 and CF_4", J. Quant. Spectrosc. Radiat. Transfer 57, pp. 497 –507, 1997.

[10] M. Pellaton, C. Affolderbach, G. Mileti, Y. Pétremand and N. F. de Rooij, "Laser-pumped double-resonance clock using a micro-fabricated cell", Proc. Joint EFTF&FCS (IEEE), San Francisco, May 2011, pp. 604-606.

[11] J. Vanier, R. Kunski, N. Cyr, J. Y. Savard and M. Têtu, "On hyperfine frequency shifts caused by buffer gases: Application to the optically pumped passive rubidium frequency standard", J. Appl. Phys., 53, pp. 5387–91, 1982.

Swiss Miniature Atomic Clock: first prototype and preliminary results

Jacques Haesler, Jonathan Bennès, Thomas Overstolz, Jörg Pierer, Rony Jose James, David Ruffieux, Steve Lecomte
Centre Suisse d'Électronique et de Microtechnique (CSEM) SA
CH-2002 Neuchâtel, Switzerland
jacques.haesler@csem.ch

***Abstract* — The first prototype of an eXtra Small Atomic Resonator (XSAR) was presented by CSEM at the 2009 EFTF conference. This paper describes the progress realized until 2011 towards the realization of a low-power miniature atomic clock. We here present the third generation of the prototype, merging for the first time the physics and electronics packages on a single printed circuit board.**

I. INTRODUCTION

Very accurate local clocks play a fundamental role in modern communication and navigation applications. High precision references enable fast communication data rates, while in navigation they allow longer holdover operation times in absence of synchronization signal, usually provided by the Global Positioning System (GPS). Even if this high accuracy can be achieved with atomic clocks, only the recent developments in photonics and MEMS processes allowed reaching the low power consumptions and small sizes needed for hand-held devices [1], paving the way to the realization of Miniature Atomic Clocks (MAC). However, reaching the target of overall device volumes $< 1\ cm^3$ and power consumptions < 30 mW [2] requires further miniaturization and improved design of all the system aspects, including the RF control electronics, which has to be low-power without affecting the clock performances. State-of-the-art implementations as in [3] and [4] reached impressive low-power consumption performances, but used discrete electronic components which limit the system miniaturization. This work presents the third generation of the prototype, merging for the first time at CSEM the physics and electronics packages on a single battery operated printed circuit board (PCB).

The coherent population trapping (CPT) interrogation [2] consists in modulating the bias current of a wavelength tuned VCSEL at an RF frequency (ν_{RF}) that is half the ground state hyperfine splitting of ^{87}Rb ($\nu_{HF} / 2 = 3.417$ GHz). Figure 1 illustrates the principle. Let's consider that a ramp on the laser diode (LD) bias current sweeps the pumping photon energy (E = hν) producing two peaks of absorption corresponding to transitions between each of the two ground states toward the excited states. When amplitude modulation of the LD is added, the absorption spectrum is composed of each individual laser wavelength (carrier plus sidebands). For $\nu_{RF} = \nu_{HF} / 2$, a transmission peak hundreds of Hertz wide (CPT signal) is observed and this resonance provides the high-Q frequency reference ($> 10^6$) of the MAC. To maintain the system locked around that peak and to provide a highly stable clock, the frequencies of both the RF modulating signal and VCSEL light must be controlled with feedback loops. In particular, locking of the RF frequency onto the atoms is obtained introducing frequency modulation of the RF carrier, which allows to deriving a signed error signal used to form the RF frequency locked loop.

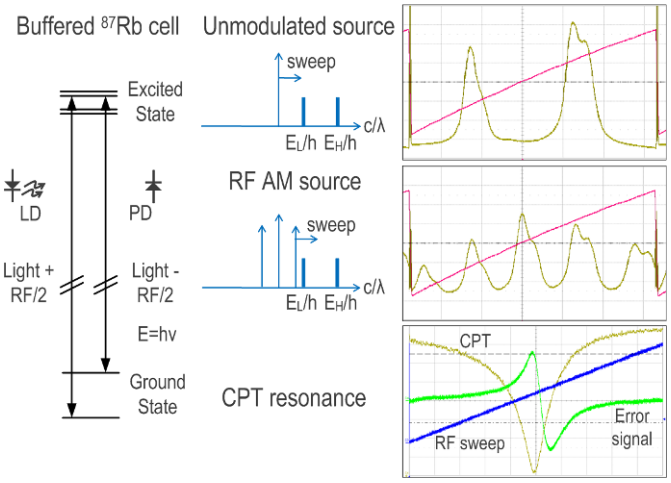

Figure 1 Physical principle of ^{87}Rb CPT interrogation.

II. PREVIOUS MAC PROTOTYPES @ CSEM

The first prototypes (Figure 2) of a miniature atomic clock developed at CSEM have been demonstrated in [5] and [6]. In 2011, a step towards the small size and low-power objective had been tackled by mastering the fabrication of miniature atomic vapor cells using MEMS fabrication techniques. Filling the cells with natural Rubidium had been realized with different techniques (alkali metal dispenser and alkali metal salt) and included controlled partial pressures of the buffer gas mixture.

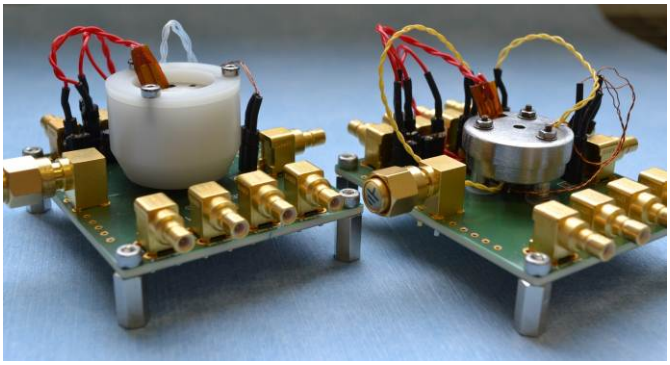

Figure 2 MAC prototypes 2010 (left) and 2011 (right).

Driving the prototype 2011 with laboratory electronics allowed reaching frequency stabilities of 8×10^{-11} @ 1 s.

III. SWISS MINIATURE ATOMIC CLOCK PROTOTYPE

The third generation of the prototype (Swiss Miniature Atomic Clock) is illustrated in Figure 3. It consists of a main PCB with the physics and electronics units and second PCB with the power supply. The dimensions of the main PCB are 100 x 50 x 16 mm^3.

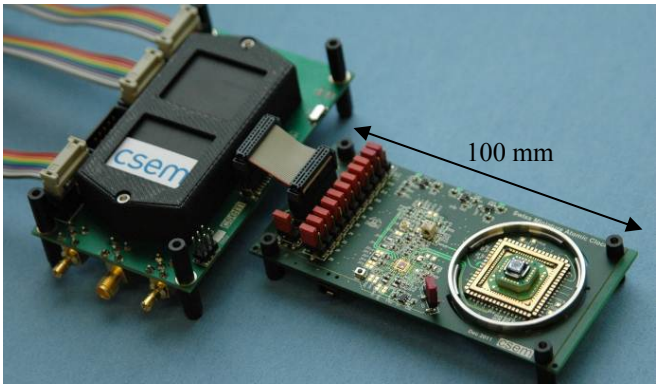

Figure 3 SMAC prototypes: power supply (left) and main PCB (right)

The device can be fully autonomous or driven by external control electronics for debugging and testing purposes. This versatility impacts the overall dimensions of 100 x 50 mm^2 that could easily be further reduced, overall height being 16 mm (with magnetic shielding cap over the physics package). Focus has been settled in the reduction of the electric power consumption of the prototype by integrating new functionalities in the integrated electronics and by designing a physics package with reduced thermal dissipation.

A. *Low-power electronics*

Lowering the overall power consumption of the miniature atomic clock is partially done by integrating most of the electronics in an application-specific integrated circuit (ASIC). Version 3.0 of the RF chip very recently came back from foundry. It integrates the RF frequency and the laser frequency lock loops (v2.0) [6], as well as three additional current sources for heating the laser and the atomic cell and for driving the Helmholtz coils (v3.0). Figure 4 shows a graphical representation of the functionalities integrated in the different versions of the ASIC.

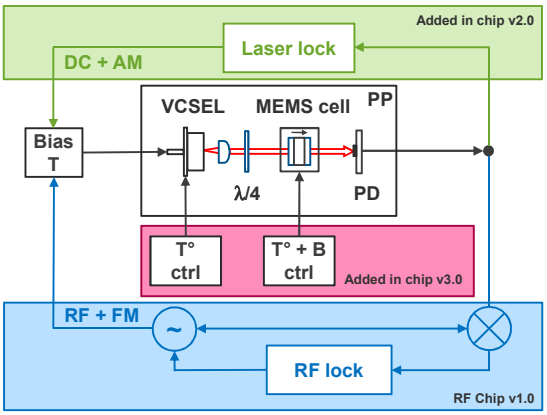

Figure 4 Graphical representation of the 3 different chip versions.

Figure 5 shows the layout and a picture of the chip version 3.0 which has just been integrated into the new prototype: Swiss Miniature Atomic Clock. Full integration is currently on-going although the battery operated chip could already successfully drive a laboratory CPT atomic clock. Deeper characterization of the chip and tests of the new functionalities are ongoing, and interesting results should be communicated in a near future.

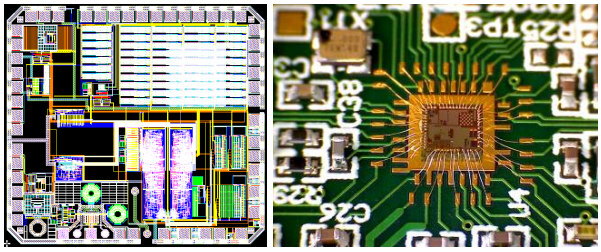

Figure 5 Chip layout (left) and chip bonded on clock PCB (right).

B. *Functionalized MEMS atomic cavities*

Fabricating small leak free atomic cavities with reproducible filling is still challenging. An important effort has been done to develop wafer level fabrication of millimeter size atomic MEMS cells made of silicon and glass by using alkali azide as starting material.

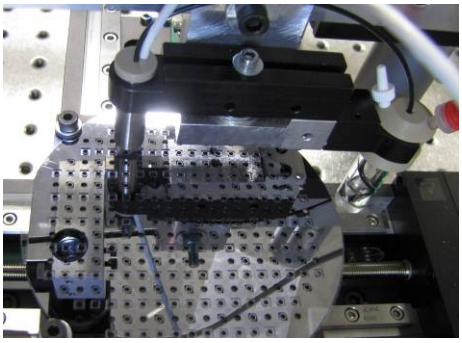

Figure 6 Automatic wafer-level fabrication of atomic MEMS cells.

After full evaporation of the solvent, the cavities are sealed by anodic bonding under controlled atmosphere (Figure 7). Metallic rubidium and nitrogen are obtained by UV decomposition of the crystallized rubidium azide.

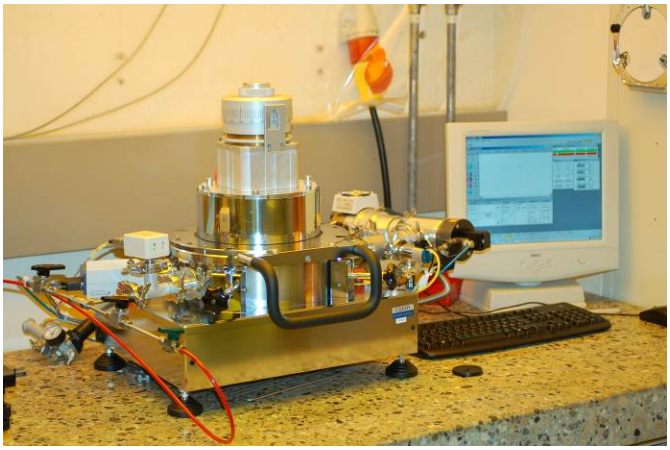

Figure 7 Anodic bonder used for MEMS cells fabrication.

The first cells (10x10 mm^2) fabricated in this way showed promising performances for a CPT miniature atomic clock and optimization of the buffer gas mixture is still on-going.

The cells were miniaturized down to 1x1 mm^2. Much of the work has nevertheless been pursued on 4x4 mm^2 cells in order to add functionalities to the glass windows (Figure 8). Both faces have integrated heaters, temperature sensors and Helmholtz coils.

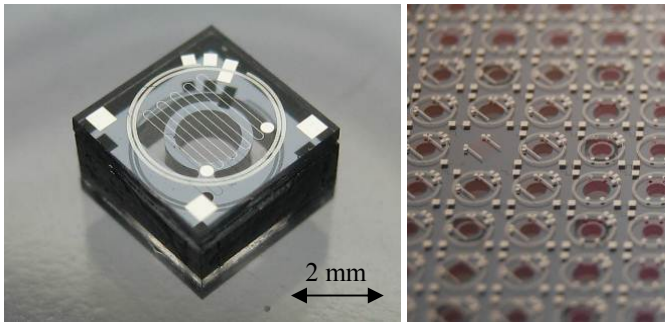

Figure 8 Functionalized 4x4x1.6 mm^3 atomic MEMS cell

The functionalized cells are currently characterized. Heating the cells up to 100°C has been achieved without problems and first 0-0 CPT signal have been measured in a laboratory setup. Integrating the functionalized cells in the prototype is ongoing.

C. Low power dissipation physics package

A close-up on the physics package is shown in Figure 9 with the magnetic shielding caps and the encapsulation cap removed. The use of a commercial ceramic package (24x24 mm^2) for vacuum encapsulation is at cost of the overall size (Ø 42 mm).

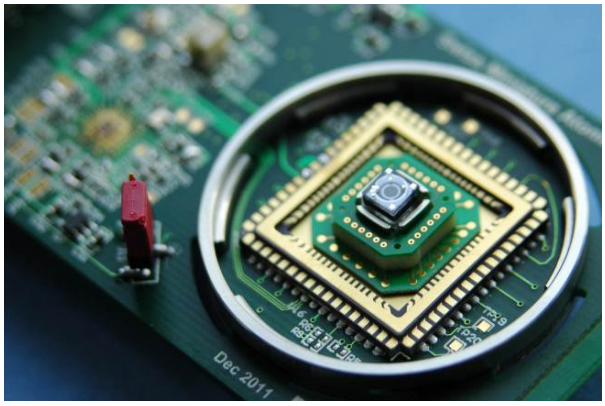

Figure 9 Close-up on the physics package of the Swiss Miniature Atomic Clock.

The physics package is realized by stacking up 6 individual PCB layers (Figure 10). The laser PCB holds the VCSEL and its heater, both of them located on the center of a cross structure to maximize the thermal resistivity. The optical PCB holds the optics and the photodetectors.

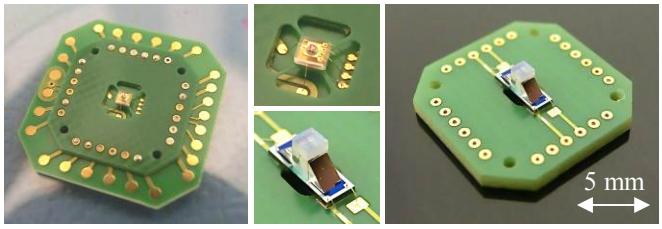

Figure 10 Baseplate and laser PCB layers (left) and optical PCB layer (right).

The atomic cell PCB (Figure 11) is also designed according to a cross structure with thermal bridges. This platform accepts the 4x4 mm^2 functionalized atomic MEMS cell described above. The first magnetic shielding layer surrounds the cell unit only.

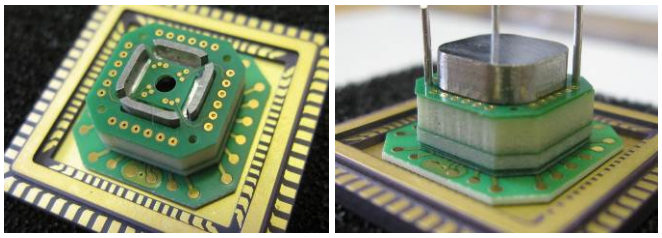

Figure 11 Atomic cell PCB layer (left) and its cell unit magnetic shielding (right).

The full prototype is still in its assembling process stage. The performances of the first fully functional prototype driven by means of a LabVIEW® user interface and an MSP430 microcontroller are expected to be reached very soon. The next steps leading to a fully integrated miniature atomic clock are:

To finalize the assembly of the physics package including the vacuum encapsulation, the programming of the microcontroller, the full integration and the prototype performance tests.

ACKNOWLEDGMENT

This work was made in the frame of CSEM's R&D activity and financed by the SFOTE, the Canton of Neuchâtel, and the Cantons of Central Switzerland. Fruitful discussions and contributions from L. Balet, J.-F. Léchenne, M. Toimil, P. Pilloud, R. Rusconi, T. Le, S. Bitterli and J. Kaufmann are acknowledged.

REFERENCES

[1] J. Kitching, S. Knappe, L. Liew, P. Schwindt, K. Shah, J. Moreland, L. Hollberg, "Microfabricated atomic clocks", IEEE International Conference on Micro Electro Mechanical Systems IEEE, pp. 1-7, February 2005.

[2] R. Lutwak, D. Emmons, W. Riley, R. M Garvey, "The chip-scale atomic clock – coherent population trapping vs. conventional interrogation", 34th Annual Precise Time and Time Interval (PPTI) Meeting, pp. 539-550, December 2002.

[3] R. Lutwak, "The chip-scale atomic clock – recent developments", IEEE International Frequency Control Symposium, pp. 573-577, April 2009.

[4] J.F. DeNatale, R.L. Borwick, C. Tsai, P.A Stupar, Y. Lin, R.A. Newgard, R.W. Berquist, M. Zhu, "Compact, low-power chip-scale atomic clock", IEEE Position, Location and Navigation Symposium, pp. 67-70, May, 2008.

[5] J. Haesler, J. Bennès, S. Lecomte, "Advances in the development of an eXtra Small Atomic Resonator (XSAR)", European Time and Frequency Forum (EFTF), Nordwijk (NL), April 2010.

[6] J. Haesler, T. Overstolz, R. Jose James, J. Pierer, M. Contaldo, D. Ruffieux and S. Lecomte, "Driving an extra small atomic resonator with low-power integrated RF frequency and laser locked loops", IFCS-EFTF, San Francisco (USA), May 2011.

VCSEL-based Raman frequency reference on Rubidium atoms

Laurent Balet, Jacques Haesler, Steve Lecomte
CSEM, Centre Suisse d'Electronique et de Microtechnique
Neuchâtel, Switzerland
laurent.balet@csem.ch

***Abstract*— As an alternative to coherent population trapping (CPT), stimulated Raman scattering in an atomic vapor and implemented in an optoelectronic microwave oscillator can be designed as a compact microwave frequency reference. Due to its simplified architecture and as an active atomic clock, it has the potential to be less energy demanding than CPT. In this paper, we present experimental results on the behavior and frequency stability of a tabletop Raman oscillator.**

I. INTRODUCTION

A portable microwave frequency reference has to be compact and power efficient. To date, the technology of choice is based upon coherent population trapping (CPT) [1] [2] and the first commercial devices are already on the market [3]. As CPT-based clocks are passive, they need an external local oscillator to probe the dark state resonance of an atomic vapor. An active miniature clock however, i.e. where the reference frequency is directly generated by the atoms, has the potential to be less complex and more energy efficient, since it does not need a local oscillator and its associated locking electronics.

A simple architecture, based on optoelectronic microwave oscillators (OEOs) and stimulated Raman scattering (SRS) in an atomic vapor, has been proposed as an alternative to CPT [4]. OEOs are devices that can generate stable and spectrally pure microwave signals (with low phase noise) [5]. Their relatively simple architecture allows integrating them into compact electronic packages for surface mount technology [6].

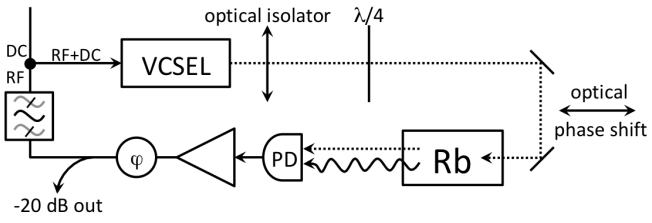

Figure 1. Schematics of the closed-loop Raman oscillator, which includes feedback into the VCSEL injection current through a bias tee.

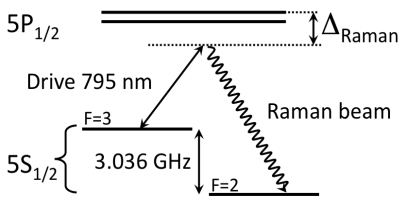

Figure 2. Level diagram for ^{85}Rb showing the relevant energy levels and photon frequencies or wavelengths.

The SRS allows referencing the oscillation frequency to an atomic transition. In this paper, we report on the results obtained on a tabletop Raman oscillator (RO) based on Rubidium 85 (^{85}Rb).

II. DESCRIPTION OF THE RAMAN OSCILLATOR

A. Working principle

Circular polarized light from a 795 nm vertical cavity surface emitting laser (VCSEL) passes through a heated ^{85}Rb vapor cell (Fig. 1). The wavelength is carefully tuned near the D1 transition to produce a Raman beam co-propagating with the laser beam (Fig. 2). The frequency difference between the two beams corresponds to the 3.036 GHz hyperfine energy splitting of the $5S_{1/2}$ level. A fast photodiode detects the beat note and generates the photocurrent, which is then amplified and fed back to the VCSEL. This modulation will create sidebands at 3.036 GHz from the VCSEL drive frequency, one of which is resonant with the Raman beam and will thus induce SRS in the atomic vapor. This extra gain in the OEO allows a steady state oscillation to take place at a frequency of 3.036 GHz.

B. Description of the setup

The VCSEL is mounted in a custom-made mount and is temperature controlled. An optical isolator located after the collimating lens of the VCSEL avoids that any reflected light perturbs its operation. Since its emission is initially linearly polarized, a quarter-wave plate is placed before the atomic cell to produce the required circularly polarized beam for the Raman transition.

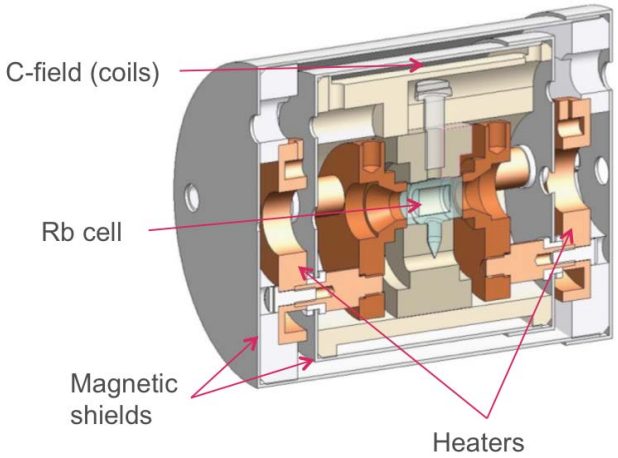

Figure 3. Custom made cell holder: resistive heaters, a coil for the C-field and two layers of magnetic shielding allow to control the thermal and magnetic environment of the cell containing the atomic vapor.

The cell containing the natural mixture of Rb isotopes is made of uncoated glass with optical quality windows. A buffer gas mixture of 58% Ar and 42% N_2 is used to reduce coherence loss through collisions. The external cell dimensions are 4 mm in diameter for a total length of 9 mm and the internal volume is 63 mm^3. A custom-made cell holder (Fig. 3), with two layers of μ-metal magnetic shielding, a coil for the C-field, and resistive heaters, allows to precisely control the temperature and the magnetic environment of the atomic vapor.

After passing through the cell, a portion of the laser beam is extracted by a 5% beam sampler and sent to a slow photodiode to monitor the light absorption by the atoms. The remaining light is focused on a broadband fast GaAs photodiode (bandwidth > 9 GHz) that produces an electrical signal at the 3.036 GHz beating frequency. As the active area of the fast photodiode is of 40 μm^2, care must be taken to ensure a good beam quality and appropriate beam size to keep optimal conversion of photons into photoelectrons. The radiofrequency (RF) beat note signal is then amplified and fed back to the VCSEL through a bias tee. A -20 dB directional coupler picks up a portion of the RF and sends it to a signal analyzer for monitoring, or to a frequency divider and a phase comparator to measure the frequency stability.

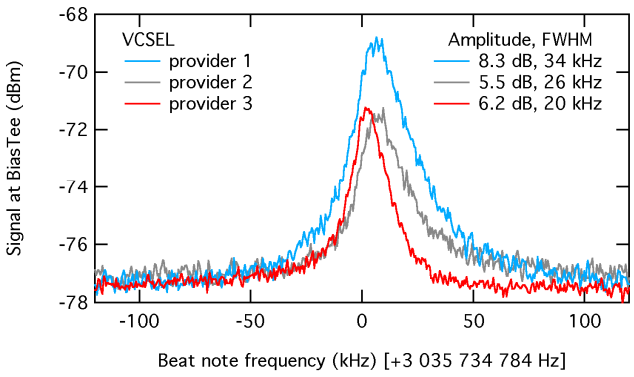

Figure 4. Open loop Raman beat note signal for three VCSELs from different providers. The injection current of the VCSEL has been adjusted to produce a symmetrical spectrum.

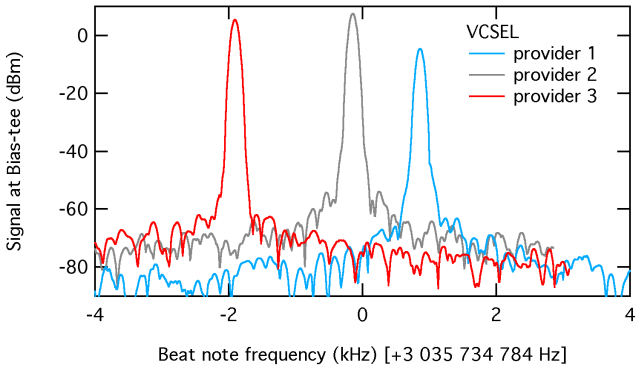

Figure 5. Closed-loop Raman beat note signal for the three VCSELs from different providers.

Since the OEO can sustain several optoelectronic modes, a tunable narrow band filter has been added to the RF line to select only the mode in resonance with the Raman signal. A 10 cm tunable optical delay line and a RF phase shifter were also used to adjust the path length of the OEO and hence the total phase of the oscillator.

III. Open-loop and closed-loop Raman signal

The open loop Raman signal, i.e. the beat note signal measured when the RF signal is not fed back to the VCSEL, provides some information on the quality of the atomic signal for frequency reference. As the laser wavelength is carefully adjusted, either by tuning the VCSEL injection current or its temperature, the Raman signal goes from an asymmetrical to a lorentzian-shaped curve, as shown on Fig. 4 for three VCSELs from different providers. The width and amplitude of the open-loop signal was seen to depend on the beam intensity among other parameters. Typical values are 6 dB above the noise floor and a full-width at half maximum (FWHM) of 25 kHz. Since the Raman scattering can be seen as a narrow band gain medium for the OEO, it is of advantage to have it as narrow as possible: it will act as a narrow band gain to force the OEO oscillation frequency to be on resonance with the atoms.

Once the RF signal is fed back to the VCSEL, and provided that the OEO length is adjusted to sustain oscillation at the Raman beat note frequency, SRS takes place. Fig. 5 shows examples of closed-loop Raman beat note signals for the three types of VCSELs. The amplitude of the signal is now approximately 80 dB above the noise floor and its FWHM is more than 1000 times narrower.

Since the wavelength of the VCSELs is somewhat dependent on the RF amplitude [7], it can be challenging to start the oscillation on the SRS mode.

IV. Selection of the buffer gas pressure

Several glass cells with different buffer gas pressures were measured in the open-loop configuration. The Raman spectra were recorded at 50°C, 75°C and 100°C and their width and amplitude were compared. Since no clear trends were visible on the width of the signal as a function of the pressure or the temperature, we chose to base the selection criteria on the amplitude of the signal only.

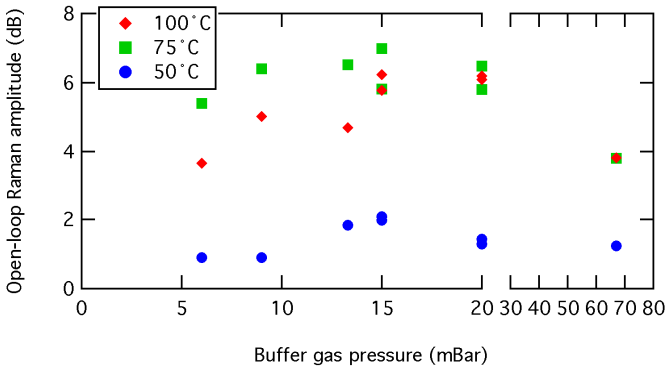

Figure 6. Amplitude of the open-loop Raman signal as a function of the buffer gas pressure and temperature of the atomic cell.

This is also relevant in the case of the OEO, since the Raman signal provides the necessary extra gain to start the oscillation preferably at the Raman frequency. Fig. 6 displays the measured results for 6 cells with pressure ranging from 6 to 67 mbar. A maximum is seen between 15 and 20 mbar for the 3 temperature sets.

V. CONTROL OF THE RESONANCE FREQUENCY

Two key parameters need to be controlled to sustain the closed-loop operation of the Raman oscillator. First, the laser optical wavelength should be resonant with the Raman transition and second, the total phase of the OEO must allow the closed-loop Raman mode to oscillate.

A. Effect of the oscillator total phase

Since the Raman gain is not a delta-function but has some spectral width, it is possible to obtain closed-loop oscillation for a certain range of the OEO total phase. Fig. 7 shows some RF spectra for different total phases of the oscillator. The microwave phase offsets were produced by adjusting the length of the optical delay line. As expected, the oscillation frequency is affected by the total phase of the OEO, but interestingly in a non-linear manner, as depicted by the scale at the top of graph on Fig. 7. The quality of the Raman mode is also degraded for large phase offset, and it should be added that no closed-loop Raman mode could be observed at larger phase offset.

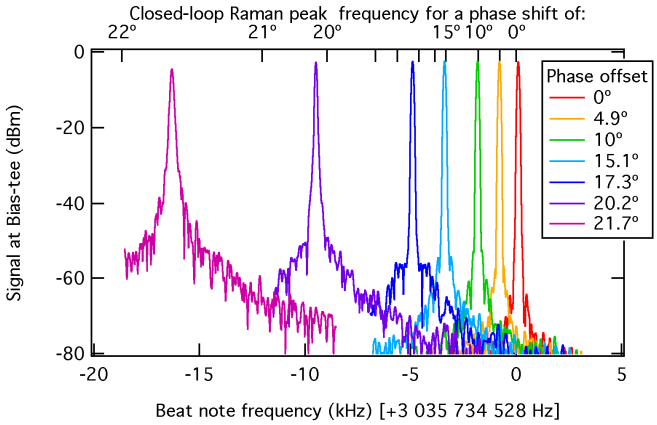

Figure 7. Closed-loop Raman signal dependence on the OEO total phase. The top axis indicates the peak frequency for the given phase shift.

Keeping in mind that the extra gain fed to the OEO comes from the open-loop Raman signal, once the total phase is set to sustain oscillation at frequencies away from its maximum, the amount of gain provided by the SRS will decrease, thus degrading the SNR of the closed-loop Raman mode and hence the oscillator frequency stability.

The total phase of the OEO is sensitive to temperature fluctuations as they can change the total length of the loop or modify the phase of certain components, like for example the narrow band RF filter. To obtain a good frequency stability of the closed-loop Raman mode at averaging times longer than several seconds, it is thus needed to take care of the thermal environment of the setup.

B. Self-control of the VCSEL wavelength

In a first approach, we tried locking the wavelength of the VCSEL to the absorption spectrum of the ^{85}Rb by modulating its injection current. While the technique worked perfectly in the open-loop mode, it was however totally failing once the OEO was set to oscillate on the Raman mode. In fact, in the closed-loop regime, the absorption signal as a function of the VCSEL injection current is flat in the region of interest.

Nonetheless, we noticed that for a certain OEO total phase, the closed-loop Raman signal frequency is relatively robust and insensitive to fluctuations of the VCSEL injection current, as depicted on Fig. 8.

This figure was made by plotting the amplitude (on the left axis) and the frequency (on the bottom axis) of the closed-loop Raman mode as a function of the VCSEL injection current, from 2.269 mA down to 2.228 mA. The right part of the graph correspond to the Raman transition driven from the F=3 state, as depicted on Fig. 2, while the left part is the case when the pumping is made from the F=2 state.

Since the magnitude versus frequency curve is almost vertical, this means that small fluctuations in the VCSEL injection current will have minimal impact on the oscillator frequency. Then, if the current further decreases, saturation occurs which also brings a phase variation, thus shifting the oscillator frequency. This self-control of the VCSEL wavelength in the closed-loop OEO is similar to the self-locked mechanism presented in [7].

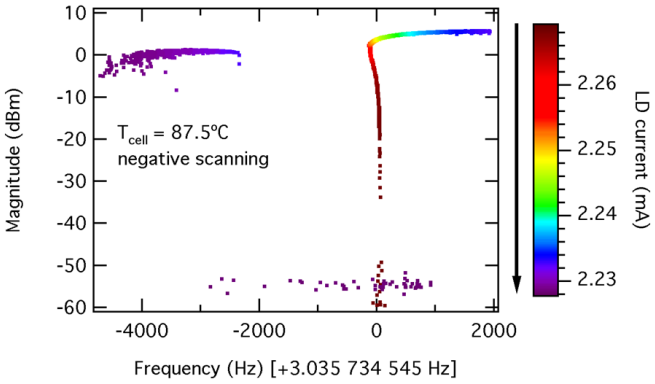

Figure 8. Amplitude (vertical axis) and frequency (horizontal axis) of the closed-loop Raman signal as a function of the VCSEL injection current (color coded).

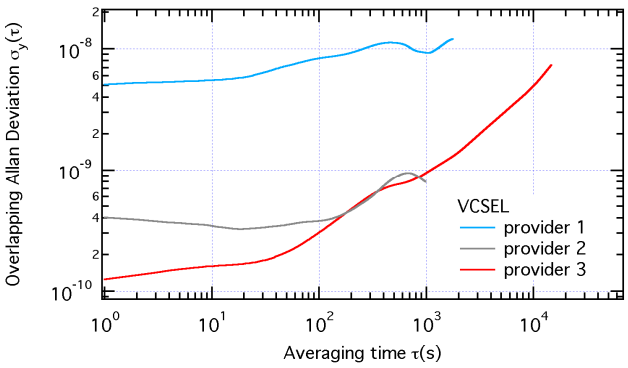

Figure 9. Frequency stability measurements of the Raman OEO for the three VCSELs from different providers.

Fig. 9 shows the frequency stability measurements of the Raman OEO for the three VCSELs. The signal frequency from the -20 dB output coupler was divided by 128 and compared to the 10 MHz reference from an active hydrogen Maser. As expected from the results on Fig. 4 and the corresponding discussion, the VCSEL from provider 3, with the narrowest open-loop Raman signal, shows the best short time stability $<2\cdot10^{-10}$ at 1 s. For longer integration times, a frequency drift is observed. This is believed to be due to temperature fluctuations modifying the length of the oscillator loop. In particular, the slight bump around 300 s corresponds well to the duty cycle of the laboratory air conditioning.

VI. Conclusion and Future Developments

The goal of this study was to demonstrate the feasibility of a simple scheme for a portable microwave frequency reference based on stimulated Raman scattering in an optoelectronic oscillator. The short term frequency stability reached by the tabletop experiment is comparable to values obtained on miniature clocks based on CPT while having the potential to be less power consuming.

The next steps include reducing the physical package dimension by going to MEMS technology for the atomic cell, and building a custom made low-power consumption amplifier (< 10 mW).

Acknowledgment

The authors would like to thank Jonathan Bennès, Marianne Toimil, Jean-François Léchenne and René Maurer for fruitful discussions and sharing their technical know-how for this project.

References

[1] J. Vanier, “Atomic clocks based on coherent population trapping: a review”, Appl. Phys. B, vol. 81, pp. 421-442, July 2005

[2] S. Knappe, “MEMS Atomic Clocks”, Comprehensive Microsystems, vol. 3, pp. 571-612, September 2007

[3] Symmetricom Inc, “New Technology Enables a Chip Scale Atomic Clock” [white paper], January 2011

[4] Nataša Vukičević, Alexander S. Zibrov, Leo Hollberg, Fred L. Walls, John Kitching and Hugh G. Robinson, “Compact Diode-Laser Based Rubidium Frequency Reference”, IEEE transactions on ultrasonics, ferroelectrics and frequency control, vol. 47, pp. 1122-1126, September 2000

[5] X. Steve Yao and Lute Maleki, “Optoelectronic microwave oscillator”, Appl. Phys. B, vol. 13, pp. 1725-1735, August 1996

[6] Lute Maleki, The optoelectronic oscillator, Nature Photonics, vol. 5, pp. 728–730, December 2011

[7] Dmitry Strekalov, Andrey B. Matsko, Nan Yu, Anatoliy A. Savchenkov, Lute Maleki, “Application of vertical cavity surface emitting lasers in self-oscillating atomic clocks”, Journal of Modern Optics, Vol. 53, pp.2469-2484, November 2006

Project of a Satellite Slow Beam Atomic Clock with CPT-Ramsey Registration

Zholnerov V.S
Russian Institute of Radionavigation and Time
St.-Petersburg, Russia
zholnerov@mail.ru

Vershovskiy A.K.
Ioffe Phys.-Tech. Institute of Russian Academy of Science
St.-Petersburg, Russia
antver@mail.ioffe.ru

Rozhdestvenskiy Yu.V.
ITMO University
St.-Petersburg, Russia
rozd-yu@mail.ru

***Abstract*—A scheme of a satellite slow-beam microwave atomic clock is presented. A modified Zeeman slower is used for longitudinal cooling of the atomic beam, and a combined CPT-Ramsey registration technique with space domain separation is used for the signal registration.**

I. INTRODUCTION

The current stage of development of the global positioning systems, such as GPS, GLONASS, Galileo, requires achieving satellite clock stability at the level of $10^{-13}\tau^{-1/2}$ (10^{-15} per day). At the same time, prototypes of cold-atoms and ions optical clock already exist which provide long-term stability at the level of 10^{-16} and even 10^{-17} [1]. These devices can be successfully used as ground-based time standards - as an alternative to microwave standards based both on thermal and cold (e.g. atomic fountain) atomic beams.

However, all the attempts to build a satellite optical clock face certain difficulties; among them – building (1) a compact and reliable source of resonance laser light with the super-narrow (~1 Hz) frequency distribution, based on a stabilized laser locked to high-Q Fabry-Perot cavity, and (2) a scheme for transferring frequency from optical to microwave band based on a femtosecond laser able to emit so-called "super-continuum" – i.e. light, spanning over one octave in the frequency domain. The common drawbacks of all these projects are high power consumption, large dimensions and weight.

Therefore it makes sense to consider thoroughly schemes of microwave clocks based on cold atoms, and investigate the new opportunities – both in laser cooling techniques and in detection techniques, – that can be used for improving their stability to the level of $10^{-13}\tau^{-1/2}$, and in prospect – to the level of $10^{-14}\tau^{-1/2}$.

II. STATEMENT OF THE PROBLEM

In this report we suggest a scheme of a satellite microwave atomic clock that uses a slow pulsed atomic beam (Fig.1). The scheme uses a modified compact Zeeman slower for longitudinal cooling of the atomic beam and the combined CPT-Ramsey registration technique with space domain separation of resonant beams – for the registration of atomic transition frequency.

The main factors impeding the use of Zeeman atomic beam slowers [2] in satellite clock schemes are their dimensions and power consumption. Let us consider a group of atoms that characterize by initial velocity v_0; the distance to the full stop for these atoms is $z_0 = v_0^2/2a$, where $a < 0$ is the atomic beam deceleration. The initial value of the magnetic field is usually chosen in order to provide interaction of the resonance light with atoms with $v_0 \le \bar{v}$, where $\bar{v}$ is the mean velocity of the atomic beam, and therefore effective slowing of the most atoms in the beam is being achieved. The maximal deceleration which atom can acquire by absorbing one photon, is

$$a = \hbar k\gamma / M, \qquad (1)$$

where $k = 2\pi/\lambda$, 2γ is the natural linewidth of the atomic transition, M is the mass of the atom. Consequently, if $v_0 = \bar{v}$, then the minimal stopping distance L_{min} is

$$L_{\min} = \frac{v_0^2}{2a} = \frac{M\bar{v}^2}{2\hbar k\gamma}. \qquad (2)$$

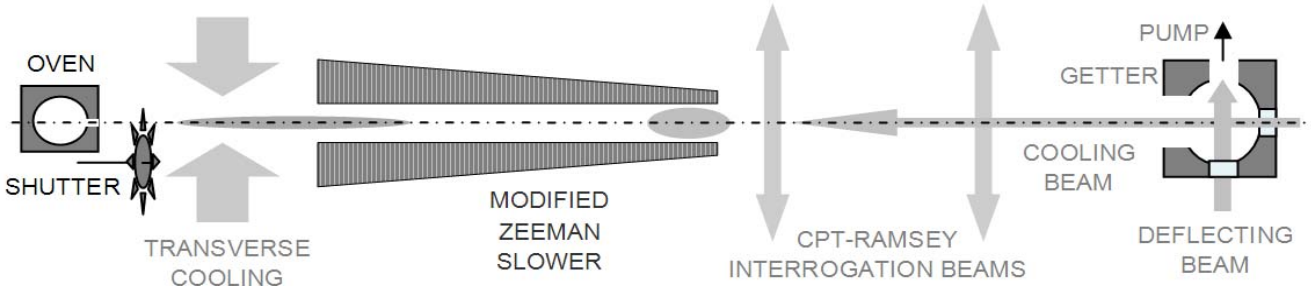

Figure 1. Sheme of the atomic beam preparation/registration unit of the satellite clock.

E.g. for thermal Rb beam with the resonant transition at $\lambda = 780$ nm and the lifetime of the excited state $t_e = 27$ ns, the minimal stopping distance is $L_{min} = 75$cm, and the minimal stopping time is $t_{min} = 3.7$ ms.

III. The Proposed Solution

Below we suggest an essential modification of Zeeman slower, implying that the initial values of the magnetic field and laser frequency are chosen in order to provide an effective slowing of the slowest group of atoms with $v_0 << \bar{v}$ (Fig.2). This change will inevitably lead to the decrease in the number of cooled atoms; thus, at $v_0 = \bar{v}/2$ the number of cooled atoms will consist 2.65% of the total number of the atoms in the thermal beam, and at $v_0 = \bar{v}/4$ – only 0.18%. However, the loss of the atoms will be compensated in metrological aspect by the possibility of their deep cooling to velocities $v < 10$ m/s, and by corresponding narrowing of the atomic resonance line.

This modification allows to decrease considerably dimensions of the Zeeman slower, as well as its power consumption; so, if initial velocity $v_0 = \bar{v}/2$ is chosen, the length of a solenoid of the Zeeman slower will be reduced four times, which is only 18.75 cm in the case of Rb. Moreover, if the value of the magnetic field B_{min} at one ending of the solenoid is close to zero, then (gradient given) the value of the magnetic field B_{max} at its other ending is proportional to the solenoid length: $B_{max} \sim l \sim v_0^2$, and therefore the power consumption is $P \sim l^2 \sim v_0^4$. Consequently, two-fold decrease of v_0 results in 16-fold decrease of the power consumption.

Let us consider the pulsed mode of the Zeeman slower and the registration scheme. This mode allows:

- to prevent heating of the slow ($v \le v_0$) atoms by collisions with the fast ($v > v_0$) atoms;
- to separate the fast atoms, which were not decelerated in the slower, from the slow atoms decelerated down to < 10 m/s, and henceforth register only slow atoms;
- to additionally reduce the power consumption of the slower; we expect that the mean power dissipated on the solenoid, will not exceed 100 W;
- to completely eliminate the influence of the resonance light and the magnetic field on the atomic transition frequency during the registration process.

The working cycle of the proposed device consists of the following stages:

1) At the start of the cycle the shutter opens, letting the atoms out of the oven; the transverse cooling beams, the longitudinal cooling beam, and the magnetic field in the solenoid are switched on.
2) Before the first cold atoms reach the slower output, the shutter closes, and the fast ($v > v_0$) atoms leave the slower. Switching off one of transverse cooling beam would allow to accelerate cutting off the atomic beam.
3) At the moment when the last slow atoms leave the slower, all the cooling beams as well as the magnetic field in the solenoid are switched off.
4) The slow atoms reach the registration zone, where their resonant transition frequencies are being measured by CPT-Ramsey technique in the spatially separated optical fields.

In order to eliminate a possibility of covering the glass window (one which is used for feeding the longitudinal slowing beam into the vacuum chamber) by the atoms deposited from the atomic beam, the atoms after passing through the registration zone may be additionally deflected by the resonant transverse beam which may be switched on before the registration starts (in order to deflect the fast atoms) and after the registration ends (in order to deflect the slow atoms).

Thus, in proposed scheme, all the cooling beams as well as the magnetic field in the solenoid are switched off during the registration process; in this aspect this scheme differs from all existing at the moment cold-beam standards using Zeeman slowers. Reduced solenoid dimensions, and respectively low

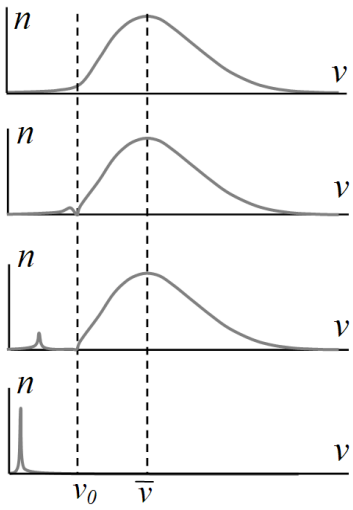

Figure 2. The evolution of the time velocity distribution during the cooling of the slow part of the atoms in the Zeeman slower. The lowest graph corresponds to the moment when the fast atoms have left the slower.

inductivity ensure zeroing of the magnetic field before the start of the registration process.

The proposed scheme does not use the bend of the slow atomic beam, typical for the devices of this type. This bend, or deflection of slow beam before entering the registration zone provides a considerable reduction of the resonant transition light shift, since the light scattered by the atoms can not enter the registration zone. The sharper the bend, the lower the possibility of scattering the light into the registration zone; therefore free of the light shift schemes require large bending angles which leads to the loss of atoms, and to the increase in size and power consumption of the device.

The method of the registration of the atomic resonance in the spatially separated laser light beams, exciting Raman (or CPT - Coherent Population Trapping) resonances, – when low-frequency coherence is being produced by the light fields resonant to the neighboring transitions of a three-level Λ-atom, – in the first time was applied to the thermal atomic beam in [3], but in most of the following works the spatial separation of the inquiring Ramsey beams was replaced with their separation in the time domain; this technique was applied to the cold atoms in MOT [4,5] as well as to the hot atoms in a cell [6].

Here we suggest to return to the scheme with the spatial separation of the registering Ramsey beams. Since the lifetime of low-frequency coherence is determined by various relaxation processes, which are very well suppressed in a cold atomic beam, the Ramsey resonance linewidth is fully determined by a time of flight through the interaction area. The time of flight can be increased up to the parts of a second (comparable to that in atomic fountain) and therefore the resonance linewidth can be reduced to the level of Hz.

The transition to the whole-optical registration and excluding of the microwave cavity from the device scheme will allow to eliminate or reduce considerably many stability deteriorating factors such as pulling the resonance frequency, instability of the phase along the cavity, microwave leaks from the cavity, etc. However, the factors specific for the CPT technique such as a frequency shift by side harmonics of the laser light, must be taken into account.

It is also important to have in mind a gravitational deflection of the atoms from the device axis, when testing device on the Earth surface (and if the axis is not vertical). Nevertheless, the influence of this effect will not be as destructive as in the schemes using the microwave cavity, since the laser registration area may be made as wide as necessary.

IV. Conclusion

According to the simple estimations, at the final beam velocity about 3 m/s and the distance between registering CPT beams about 30 cm (corresponding to the resonance linewidth of 5 Hz) the resonance quality $Q \sim 10^9$ may be achieved, and in order to provide $10^{-13}\tau^{-1/2}$ stability one needs to inquire 10^8 atoms per second. Taking into the consideration that the proposed technique of slowing only small part of the thermal velocity distribution results in reduction of the output beam intensity by $1.5 \div 2$ orders of magnitude, and the mean beam intensity will decrease by approximately one order of magnitude because of the pulsed beam mode – in the thermal beam produced by the oven we will need about $10^{11} \div 10^{12}$ atoms in the solid angle 1/100 of steradian, which seems to be quite realistic.

[1] H.S. Margolis, “Optical frequency standards and clocks”, Contemporary Physics vol. 51, no. 1, pp. 37–58, January–February 2010.

[2] W.D. Phillips, H. Metcalf, “Laser deceleration of an atomic beam”, Phys. Rev. Lett. vol. 48, 1982, pp.596-599.

[3] J.E. Thomas, P.R. Hemmer, S. Ezekiel, C.C. Leiby Jr., R.H. Picard, C.R. Willis. “Observation of Ramsey Fringes Using a Stimulated, Resonance Raman Transition in a Sodium Atomic Beam”, Phys. Rev. Lett. vol. 48, 1982, pp. 867-870.

[4] T. Zanon, S. Guerandel, E. de Clercq, D. Holleville, N. Dimarcq, and A. Clairon, “High Contrast Ramsey Fringes with Coherent-Population-Trapping Pulses in a Double Lambda Atomic System”, Phys. Rev. Lett. vol. 94, 2005, 193002.

[5] C. Xi, Y. Guo-Qing, W. Jin, Z. Ming-Sheng, “Coherent Population Trapping-Ramsey Interference in Cold Atoms” Chin. Phys. Lett. vol.27, 2010, 113201

[6] Chao Guan, Xiaosong Zhu, Qun Zhou, “A Fully Functional Ramsey-CPT Atomic Clock”, EFTF 2011, p.74.

CPT resonances in two frequency pumping and probe beam configuration

Ersoy Sahin[1, 2], Ramiz Hamid[1], Mehmet Çelik[1], Cengiz Birlikseven[1], Gönül Özen[2] and Azad Izmailov[3]

[1] TÜBİTAK, Ulusal Metroloji Enstitüsü (UME), Gebze, Kocaeli, TURKEY
[2]Istanbul Technical University, Faculty of Science and Letters, Engineering Physics Department Maslak, Istanbul, TURKEY
[3]Institute of Physics, Azerbaijan National Academy of Sciences, H. Javid av. 33, Baku, Az-1143, AZERBAIJAN
Email: ersoy.sahin@ume.tubitak.gov.tr

***Abstract*—We have detected and analyzed narrow, high contrast coherent population trapping (CPT) resonances, which appear in transmission of the probe monochromatic light beam under action of the counter propagating two frequency laser radiation, on example of the nonclosed three level Λ-system formed by spectral components of the Doppler broadened D_2 line of cesium atoms. Given resonances may be used in atomic frequency standards, sensitive magnetometers and in ultrahigh resolution laser spectroscopy of atoms and molecules.**

I. INTRODUCTION

At the phenomenon of the coherent population trapping (CPT), a multilevel quantum system subject to decay processes is coherently driven into a superposition state immune from the further excitation, in which the system population is trapped. The CPT is the basis of a number of important applications: ultrahigh resolution spectroscopy, atomic clocks, magnetometry, optical switching, coherent cooling and trapping of atoms and also in some others described, for example in reviews [1-3]. In particular, narrow CPT resonances, detected in absorption of a two-frequency laser radiation (and also in the corresponding induced fluorescence spectrum of a gas medium) on three level atomic Λ-systems, are successfully applied in atomic frequency standards [4] and in high sensitive magnetometers [5]. For these applications, researchers use, mainly, vapors of alkali atoms (in particular Cs or Rb), whose ground quantum term consists of two sublevels of the hyperfine structure [6]. Resonance excitation of atoms on the Λ-system scheme is realized by means of the two-frequency radiation from given sublevels (Fig. 1). Such Λ-systems are not closed because of presence of channels of the radiative decay of the excited state |3> on some Zeeman sublevels of lower levels |1> and |2>, which don't interact with the two-frequency radiation [1-3]. Therefore highly narrow CPT resonances, recorded by known methods on the population of the upper level |3> have a comparatively small contrast on a more wide spectral background of absorption or fluorescence [4]. At the same

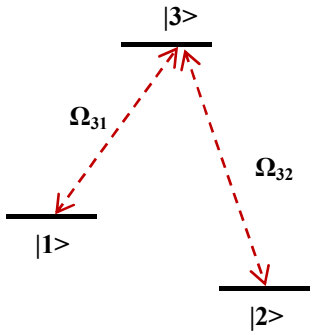

Fig. 1. The Λ-system of optical transitions |1> − |3> and |2> − |3> (with central frequencies Ω_{31} and Ω_{32}) between the excited level |3> and long-lived states |1> and |2>.

time, more contrast CPT resonances may appear in dependences of populations of lower long-lived levels |1> and |2> of a nonclosed Λ-system on the frequency difference ($\omega_2 - \omega_1$) of the bichromatic laser pumping. Indeed, let us consider interaction of such a system with 2 monochromatic laser fields. Frequencies ω_1 and ω_2 of given fields are close to centers Ω_{31} and Ω_{32} of electrodipole transitions |1> - |3> and |2> - |3>, respectively. The population of this nonclosed Λ-system will be exhausted at intensification of the two-frequency laser pumping with the exception of a fraction of atoms, which may remain on lower levels |1> and |2> at the following CPT condition [1-3]:

$$\left| \delta_2 - \delta_1 \right| \leq W \qquad (1)$$

where $\delta_1=(\omega_1 - \Omega_{31})$ and $\delta_2=(\omega_2 - \Omega_{32})$ are detunings of laser frequencies. The width W of the CPT resonance in equation (1) is determined by intensities of laser fields and by relaxation rates

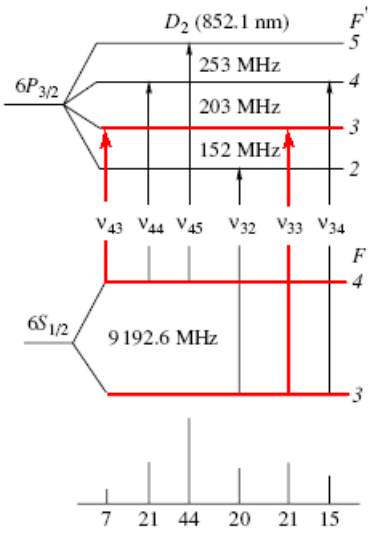

Fig. 2. Energy level scheme of the Cs D_2 line. The relative oscillator strengths of lines, representing hyperfine transitions, are given on the bottom of this figure.

of populations and coherence of quantum states |1> and |2> Under definite conditions, the value W may be much less than homogeneous widths of spectral lines of optical transitions |1> - |3> and |2> - |3>. Given nontrivial CPT resonances may be detected by means of an additional probe radiation resonant to a quantum transition from any lower level |1> or |2>. It is important to note that corresponding nonclosed Λ-systems are characteristic not only for many atoms but also for all molecules, because of possible radiative decay of their excited states on numerous sublevels (vibrational, rotational) of the ground molecular term [7]. Therefore recently theoretical works have appeared on interesting features and possible CPT applications in such atomic (molecular) Λ-systems [8-10]. In this work we have detected and analyzed nontrivial CPT resonances on lower levels of the nonclosed Λ-system on example of spectral components of the D_2 line of Cs atoms (Fig. 2).

II. EXPERIMENTAL METHOD AND SETUP

The experimental configuration is shown in Fig. 3. The laser frequency was stabilized on the transition $6S_{1/2}(F=3)-6P_{3/2}(F'=3)$ (Fig. 2) using reference Cs cell and a saturated absorption spectroscopy (SAS) technique. For obtaining the bichromatic light field (two frequency pumping beam) the output beam of an external cavity diode laser (ECDL) was phase modulated at the ^{133}Cs hyperfine frequency 9.2 GHz by an electro-optical modulator (EOM). The sideband-to-carrier ratio was adjusted up to 50% by changing the radio frequency (RF) power of the frequency synthesizer. To get the higher intensity ratio I_1/I_2 we have used thermo stabilized Fabry-Perot etalon which has a free spectral range of 4 GHz and a bandwidth of 10 MHz (finesse ~ 400). The reflected beam from the etalon consists of first-order sidebands and carrier. By fine tuning the transmission resonance of the etalon via temperature, the bichromatic light

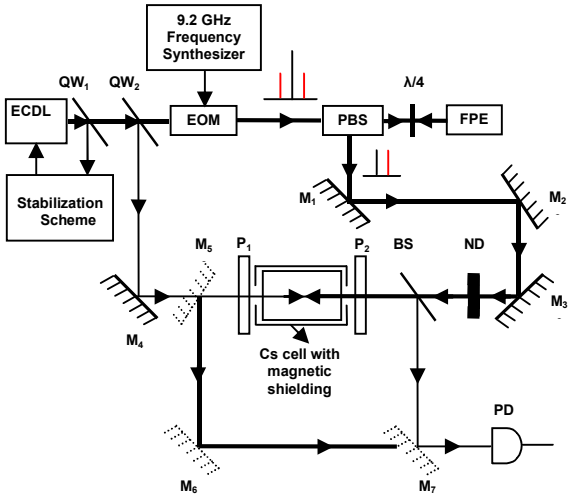

Fig. 3. Scheme of the experimental setup, which includes external cavity diode laser (ECDL), electro-optical modulator (EOM), polarizing beam splitter (PBS), fabry-perot etalon (FPE), quarter waveplate (λ/4), beam splitter (BS), mirrors (M_1, M_2, M_3, M_4), flip flop mirrors (M_5, M_6, M_7), polarizers (P_1, P_2), quartz windows (QW_1, QW_2), neutral density filter (ND), photodiode (PD) and the Cs cell with the magnetic shielding.

beam with equal amplitude components (I_1=I_2) was achieved. The reflected pumping beam was collimated to a diameter of 3 mm and linearly polarized by polarizer (P_2) and then was sent to a rarefied Cs vapor cell. The monochromatic probe laser beam linearly polarized by polarizer (P_1), was sent to the Cs cell in the opposite direction by mirror (M_4). The two frequency pumping and monochromatic probe beams were overlapped in the irradiated Cs cell which had a length of 3 cm and diameter of 2.5 cm. The Cs cell was kept at the temperature of 22 °C and the residual magnetic field inside this cell was less than 10 mG. Transmission of the monochromatic probe and bichromatic pumping laser beams were detected by the photodetector (PD). During the experiment, intensity of bichromatic pumping laser beam was changed while intensity of the monochromatic probe beam with a diameter of 2 mm was kept constant at 0.03 mW/cm^2. To record the CPT resonances, the frequency synthesizer was tuned 10 MHz around the modulation frequency which was 9.2 GHz. To monitor the CPT resonances in the transmission of the probe beam, flip-flop mirrors (M_5, M_6) were folded so that they did not reflect while the flip-flop mirror (M_7) reflected. To record the CPT resonances in the transmission of bichromatic pumping beam, the flip-flop mirror (M_7) was folded not to reflect while the flip-flop mirrors (M_5, M_6) reflected pump beam. CPT resonances for both the probe and the bichromatic pumping beam were detected by the same photodetector.

III. DISCUSSION OF RESULTS

According to the selection rules, in the absence of an external magnetic field and orientation of the quantization axis along the same linear polarization of pumping and probe laser beams for our experimental conditions (Fig. 3), only optical transitions

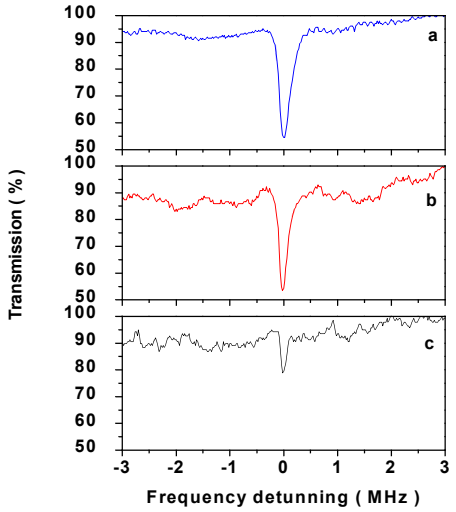

Fig. 4. Detected CPT resonances in transmission of the probe beam at following pumping intensities: (a) 15.83 mW/cm^2 , (b) 10.83 mW/cm^2 and (c) 5.83 mW/cm^2.

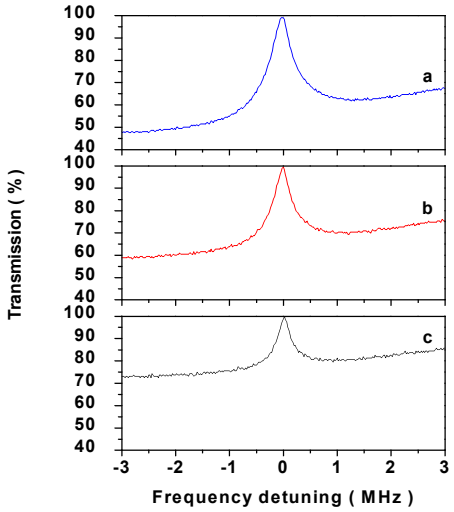

Fig. 5. Detected CPT resonances in transmission of the corresponding two-frequency pumping radiation at following pumping intensities: (a) 15.83 mW/cm^2, (b) 10.83 mW/cm^2 and (c) 5.83 mW/cm^2.

between Zeeman degenerate Cs levels without change of the magnetic quantum number m were induced [11]. Thus we had 6 nonclosed Λ-systems (corresponding to magnetic numbers m=±1, ±2 and ±3) for two resonant adjacent optical transitions: $6S_{1/2}(F=3)-6P_{3/2}(F^{/}=3)$ and $6S_{1/2}(F=4)-6P3_{3/2}(F^{/}=3)$ (Fig. 2), where CPT resonances were formed. Optical repumping of the population of this resultant Zeeman degenerate Λ-system took place on three magnetic sublevels of the ground Cs term $6S_{1/2}(F=4, m=\pm4)$ and $6S_{1/2}(F=3, m=0)$, which did not interact with incident pump and probe radiations. Taking into account given features, further we will analyze obtained results on the basis of the simple model of the nonclosed Λ-system (Fig. 1), where quantum states |1>,|2> and |3> correspond to Cs levels $6S_{1/2}(F=4)$, $6S_{1/2}(F=3)$ and $6P_{3/2}(F^{/}=3)$ (Fig. 2). Fig. 4 presents the narrow CPT deep with the center $\delta_1=\delta_2=0$ in transmission of the probe light beam on the resonant transition |2> - |3> for different pumping intensities. This resonance is caused directly by the trapping of an atomic population fraction of the lower level |2> in the nonclosed Λ-system because of a negligible population of its excited state |3> at the CPT condition (1). Fig. 5 presents well-known CPT peaks in the transmission of the corresponding two-frequency laser pumping. For detected CPT resonances (Fig. 4 and Fig. 5), we have calculated contrasts C (in % with respect to the total recorded background) and widths W (on their half-heights) according to definitions of the paper [12]. Corresponding dependences of these values C and W on the intensity of the pumping radiation are shown in Fig. 6 and Fig. 7. We directly see from given figures, that CPT resonances in the transmission of the probe beam may have not only more contrast but also much less width in comparison with corresponding known CPT resonances in transmission of the two-frequency pumping radiation. This advantage of new CPT resonances is more obvious at the pumping intensity rise. Results of our calculations, carried out on the basis of density matrix equations in the model of nondegenerate quantum levels of the nonclosed Λ-system (Fig. 1), are in good qualitative agreement with corresponding experimental data presented in Figs. 4 - 7. It is necessary to note that, even a small angle (~ a few degrees) between linear polarizations of pumping and probe laser beams or a weak external magnetic field (~1 G) in the Cs cell (Fig. 3) lead to essential decrease of contrasts of given recorded CPT resonances. This is caused by difference of the real system of Zeeman degenerate levels (Fig. 2) from the considered theoretical model of the Λ-system.

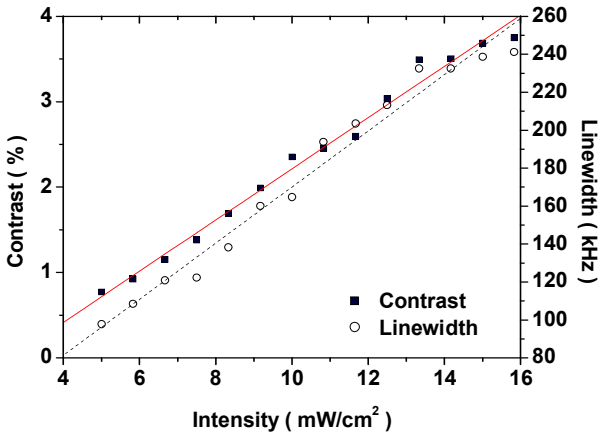

Fig. 6 .The contrast C and linewidth W of the CPT resonance in transmission of the probe beam versus the pumping intensity .

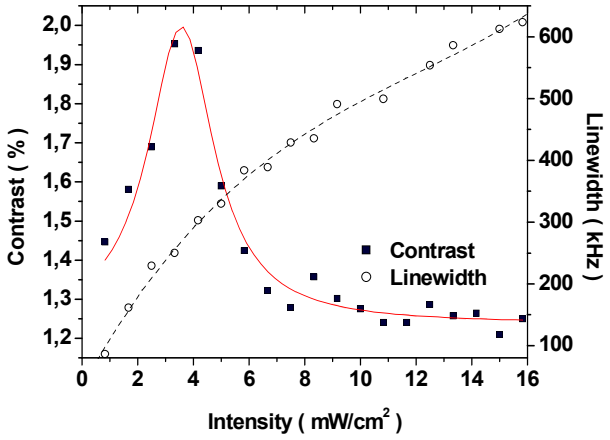

Fig. 7. The contrast C and linewidth W of the CPT resonance in transmission of the corresponding two-frequency pumping radiation versus its intensity.

IV. CONCLUSION

On the basis of the elaborated method, we have detected and analyzed new narrow, high contrast CPT resonances characteristic for a nonclosed atomic (or molecular) three level Λ-system (Fig. 1). These CPT resonances are determined, mainly, by the trapped population on the definite lower level of the Λ-system, from which the resonant optical transition is induced by the weak probe radiation. Given resonances may be used in atomic frequency standards and sensitive magnetometers based on the CPT phenomenon and also in ultrahigh resolution laser spectroscopy of atoms and molecules.

REFERENCES

[1] E. Arimondo, Coherent Population Trapping in Laser Spectroscopy,Progress in Optics, Wolf E. (Ed.), Elsevier 35, 257 (1996).

[2] B.D. Agap'ev, M.B. Gornyi, B.G. Matisov, and Y.V. Rozdestvenskii, Coherent Population Trapping in Quantum Systems,Physics-Uspekhi 36, 763 (1993).

[3] S.E.Harris, "Electromagnetically Induced Transparency," Physics Today, July Issue, 1997, p.36.

[4] J. Vanier, "Atomic Clocks Based on Coherent Population Trapping : a Review," Applied Physics B 81, 421 (2005).

[5] P.D.D. Schwindt, S. Knappe, V. Shah, L. Hollberg, J. Kitching, L. Liew, and J. Moreland, "Chip-scale Atomic Magnetometer," Applied Physics Letters 85, 6409 (2004).

[6] A.A. Radtsig and B.M. Smirnov, Reference Data on Atoms, Molecules and Ions, (Springer, New York, 1985).

[7] H. Haken and H.Ch. Wolf, Molecular Physics and Elements of Quantum Chemistry (Springer, Berlin, 1995).

[8] A.Ch. Izmailov, M. Mahmoudi and H. Tajalli," On the selective photoexcitation of molecules within the homogeneous width of optical lines," Opt. Commun. 176, 137, (2000).

[9] A.Ch. Izmailov, "Coherent Population Trapping in the Λ- System of Zeeman Degenerate Molecular Levels," Laser Physics 15, 1543 (2005).

[10] A.Ch. Izmailov, "Identification of Overlapping Optical Lines in Molecular Spectra by Means of the Coherent Population Trapping of Quantum Levels," Laser Physics. 18, 855 (2008).

[11] W.Demtroder,Laser Spectroscopy Basic Concepts and Instrumentation, (Springer, Berlin, 2003).

[12] J. Vanier, M. W. Levine, D. Janssen, and M. J. Delaney, "On the Use of Intensity Optical Pumping and Coherent Population Trapping Techniques in the Implementation of Atomic Frequency Standarts," IEEE Transactions on Instrumentation and Measurement, 52, 822 (2003).

An Ultra-Miniature Rubidium Atomic Clock Compatible with OCXO

Dr Thomas Cao, Clive Green, Dr Cosmo Little
Atomic Clock Development
Quartzlock (UK) Ltd. Devon, England
Devon, England
Email: sales@quartzlock.com

Abstract: **- This paper shows a traditional Rubidium atomic clock – E10-MRX. The incorporated lamp and ultra-miniature waveguide cavity introduced in the physics package is the main means to reduce the volume of the clock; the electronics consisting of 6.8GHz direct synthesizer and digital servo system is to enhance the automatic functions which ensure large scale production is available with low costs. In all, the clock has the physical dimensions of an oven controlled crystal oscillator (OCXO), measuring 51mm x 51mm (2' x 2') and standing at a mere 25mm (1'). The Allan deviation of 3E-11/s; the temperature coefficient is 3E-10 in the range of -20oC ~ 60oC; the frequency aging is below 5E-12/day. The clock has the same dimension and pin definitions as OCXO's used in telecoms, but higher performance, and will be popular in telecom equipments and base-stations instead of OCXO in future. This paper focuses on the low noise synthesizer development.**

I. INTRODUCTION *(HEADING 1)*

Traditional Rubidium atomic clocks with a combination of high performance and volume have large engineering value and long life until now. Compared with Hydrogen and Caesium clocks, the compact rubidium atomic clock with merits in aspect of low power, small dimension and excellent precession, are one of the most popular atomic clocks, and heavily used in Telecoms, IP-TV, time-keep systems and the Global Navigation Satellite Systems (GNSS), Especially IEEE1588 protocol offering several nanoseconds of web synchronization[1]. In the above area, compact atomic clock will be used instead of OCXOs.

Rubidium clock uses optical pumping by a rubidium spectrum lamp to create a population inversion between the ground state hyperfine energy levels F=2 and F=1 in absorption cell [2]. If the atoms of absorption cell are interrogated with microwave radiation, the change in light transmission through the cell can be checked by optical diode, and a discriminating signal in the light is to lock OCXO in the atomic clock. Employing the two naturally occurring isotopes 85Rb and 87Rb is to enhance the efficiency of the optical pumping by a fortuitous overlap between the two optical absorption lines; and similarly, filling buffer gas (such as N2, NH4) to narrow the line width of the absorption of the clock transition between (F=2, mF=0) and (F=1, mF=0). Therefore, the Rubidium atomic clock has higher Signal-to-Noise ratio and more outstanding short-term ability.

a. Lamp

CLAPP oscillator has a high stability, and can be used as the driving circuit of the spectrum lamp [3]. The frequency of the oscillator is decided by L made up of a coil around the bulb, and by C which is in series with the coil. Because of high frequency scaled 100MHz, the distributing parameters will occur while the circuit is placed in the lamp oven. There is the optimal value of the L and C which need to be tuned in an extent. In order to cancel the temperature coefficient of the circuits, a diode is added in parallel with the b-e loop of transistor in the circuit, which would improve fluctuation and aging of Rubidium clock.

The configuration of assembling the parts to shape the architecture of the spectrum lamp mainly decides the size itself. In general, bulb and exciting circuits are designed separately as two parts. As is known, the temperature coefficient is added by transistor in the circuits. Taking the transistor into the case of lamp can be resolved. The spectrum lamp is called incorporate lamp. In the architecture, the bulb of lamp is held into solenoid and together inserts into a bold which is designed by Teflon which ensure the light density stable. All of these are fixed into a case which is designed by aluminium. The PCB is laid into the case simultaneously. In this way, the electromagnetic radicalization can be shielded effectively. Therefore, the power dissipation can be used to heat up the lamp, and the power of the lamp which is capable of reducing at an extent. In a word, the bottleneck in the aspect of the coefficient, the size and the power dissipation has been resolved in the incorporate lamp. The final appearance of the lamp is shown in Fig. 1.

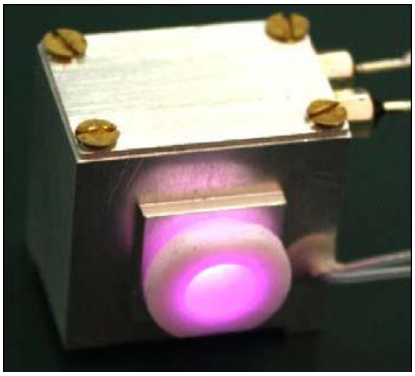

Figure 1. The lamp removed from the clock E10-MRX.

In the process of fabricating lamp, the bulbs are aged with high RF power and high temperature firstly. Secondly, the lamp will be supplied with higher voltage than it being in normal work. All the steps can ensure to fabricate lamp in bulk.

b. Cavity

To reduce the size of cavity in Rubidium atomic clock, there are several types of cavity as below. The first is cylinder cavity of TE111 model, sometimes filled by Al2O3 ceramic [4]. The second is magnetron cavity whose mode is similar to TE011, and has high Q quality. The cavity has been used in Hydrogen clock in advantage. But the complex architecture and difficulty in production by machine hamper its expanding to compact Rubidium clock.

Telecom technology brings digital synthesizer to microwave frequency band, and several synthesizers beyond 7G occur nowadays. The synthesizer has the ability to output the enough power level of 6.8GHz to interrogate atom. So, the cavity has no necessity to be resonant with atomic frequency.

Waveguide port is the avenue for microwave transmitting in a model. One port of the waveguide is enclosed as an emission source, and other port is enclosed excluding a hole at the centre of bottom as the diaphragm the lamp light goes through. Simultaneously, absorption cell insets into the space in the cavity. In this way, one cavity is shaped in the Rubidium clock. Due to the boundary abnormity from absorption cell and the hole, simulation in magnetism is necessary and effective auxiliary tool to calculate the parameters. The simulating is as in Fig. 2.

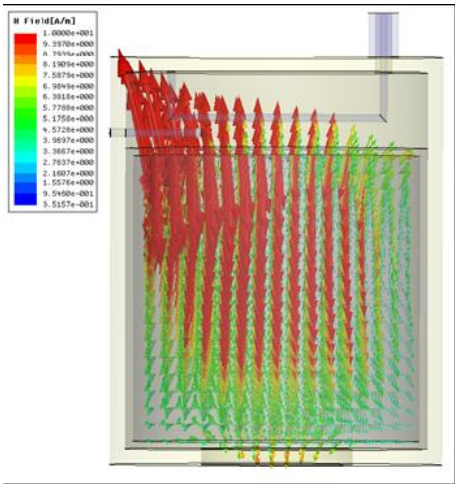

Figure 2. The Cavity of the Rubidium atomic clock E10-MRX.

In Fig. 2, magnetic excitation is from a loop coupling the 6.8GHz microwave. In order to make excitation higher than electricity, there is a special hemicycle soldered with the coupling loop. A bolt made specially is to screw in and out to compensate the boundary abnormity in the cavity after inserting absorption cell. By the design, the tolerance of absorption cell size is bigger than the previous, and the cavity is more available to fabricate in bulk. There is no ceramic in side of the cavity; therefore the lower weight and higher performance in vibration and shock are implemented. In fact, the power level range of -20 to 0 dBm from frequency multiplier is ok to the cavity with screwing the bolt. In addition, the waveguide cavity is made of Permalloy metal so as to reduce frequency shift resulted from magnetism.

II. ELECTRONICS

Electronics in Rubidium clock consists of frequency multiplier which is to multiply 10MHz from OCXO or TCXO to 6.8GHz, and servo which is to synchronously check and output an error to lock VCXO.

a. Frequency Multiplier

Traditional frequency multiplier is designed with step recovery diode (SRD), while SRD has the special property whose capacitance has different quality on the tradition while voltage shifts from positive to negative. 6.8GHz microwave to excite atom is from the high order harmonic wave by SRD. In this way, the resonance cavity must be used as the selective loop to enhance the 6.8GHz microwave, and Rubidium atoms in the absorption cell laid in the resonance cavity will output the enough strength of discrimination signal by transmission of light intensity from lamp to lock VCXO. Owning to the configuration of frequency multiplier in Fig. 3, the above-mentioned cavity can be used in Rubidium atomic clock.

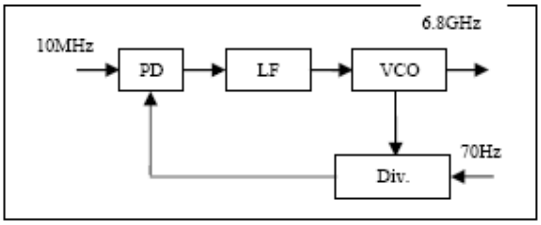

Figure 3. The frequency multiplier scheme block.

In Fig. 3, the 10MHz from OCXO compares with the similar frequency feeding back from VCO in phase detector (PD), and the error voltage of the phase is filtered by Low Filter (LF). Finally, the 6.8GHz is locked in phase with 10MHz and modulated in frequency by 70Hz.

b. Digital Servo System

This part is embedded in a Micro-programmed Control Unit (MCU). The detailed configuration is as below in Fig. 4.

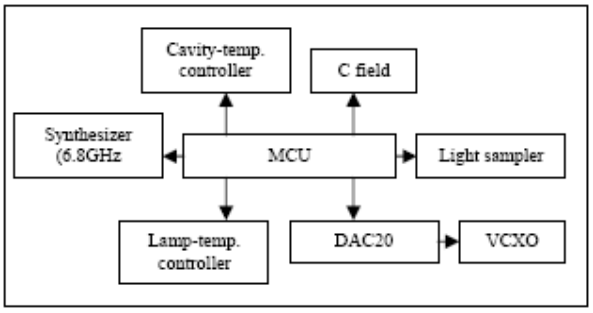

Figure 4. The digital servo system block.

- MCU is the centre controller of the electronics in the Rubidium clock. The first function is to initialize external devices, including synthesizer, DAC20; the second is to sample the light intensity and temperature data and to process digital data to export an error to lock VCXO.
- C field is set by 12 bit DAC which can adjust the accuracy of 10MHz frequency standard signal with high resolution. Therefore, the Rubidium atomic clock can be disciplined by GNSS via tuning this DAC's transiting data, so the long term stability will up to the level of satellite atomic clock.

- DAC20 consists of two 12 bit DAC and is an equivalent 20 bit DAC, which is to lock the VCXO in normal work and to make the VCXO to be in holdover status in abnormal work.
- Light sampler is to gather intensity of the lamp light which contains work status of the lamp and atomic discrimination signal. The first one could assist to check the lamp's off-on statue to shift the voltage from low to high, and the second is to lock VCXO.
- Synthesizer as a frequency multiplier makes the 10MHz from VCXO to 6.834GHz directly and modulates the microwave with a low frequency 70Hz. The synthesizer is made up of a digital phase comparator, digital divider (Div.) and VCO.
- The cavity-temperature controller and lamp-temperature controller are to control the cavity temperature and lamp temperature respectively according to destination value of temperature automatically.

c. Synthesizer

In order to tune the rubidium reference oscillator, normally 10MHz, to exactly nominal frequency, it is desirable that the synthesizer is tunable in very small steps. In addition to very fine resolution, square wave FM at about 80Hz is necessary. This FM is achieved by direct digital modulation of the synthesizer.

The synthesizer is essentially a fixed frequency synthesizer. Variation of the frequency of up to +/- 3kHz is required to compensate for frequency variation of the actual rubidium cell used.

The software is designed to use a timer interrupt at a 2.56kHz rate. Every 16 interrupts, a constant is alternately added or subtracted from the nominal value of the fractional numerator (RF-FN). This changes the frequency of the synthesizer by the constant times the minimum frequency step available. For example, with the programming selected for a 1Hz frequency resolution, and a constant of 100, the FM generated will be at a rate of 80Hz, and a deviation of 100Hz peak. The frequency change will take place within a few microseconds due to the relatively wide loop bandwidth.

The principle of the resolution extension is to vary the fractional numerator nominal value by a few steps either side of nominal according to a pseudo random sequence. The mean value of the sequence will be a fraction which will give a frequency shift which is the same fraction of the minimum step size.

The best method of producing the sequence is a Delta Sigma modulator implemented in software and updated every timer interrupt, ie at a 2.56kHz rate. The resolution extension fractional modulus can be 256, one byte. This will give a resolution extension of up to 1/256 times the basic synthesizer resolution. The output of the software D/S modulator will be a sequence of signed integers, which are added to the 12 lower bits of the synthesizer fractional numerator (RF-FN). The new fractional numerator is output to register R0 at the interrupt rate, ie 2.56kHz.

The sequence will depend upon the order of the software D/S modulator. For a first order modulator, the sequence will include the integers 0, 1 only. Second order the sequence will include –1, 0, 1, 2; 3rd order –3,-2...3, 4; 4th order -7,-6…7, 8.

The test software implements a D/S modulator of up to 4th order. The extra phase noise added to the loop depends upon the order of the modulator. The phase noise is a minimum for very small offset frequencies, and rises to a peak at half the sampling frequency. This would be 1.28kHz offset for our software D/S modulator. The slope of the added phase noise depends upon the order of the modulator. This is fully explained in AN1879.

The basic D/S modulator has a disadvantage that for certain starting values in the accumulators, the sequence can have a short periodicity. This applies to all orders. This will result in discrete spurii at the synthesizer output. The usual method to avoid this is to add the output of a further pseudo random sequence with a long repetition time to the D/S modulator. A maximum length sequence generator can easily be implemented in software with very few instructions, and this has been done for the test software. The shift register is 33 bits long, implemented with feedback to generate a maximum length sequence. The sequence repeat time is 932 hours at an update rate of 2.56kHz. The sequence output may be added to the first accumulator of the D/S modulator. The mean value of the sequence is 0.5, so this results in a fixed frequency offset of 0.5/256 steps. This offset is insignificant in practise.

The theoretical effect of the additional software S/D modulator on the synthesizer phase noise and spurii may be investigated using a simulation. One integer step of the D/S modulator corresponds to low deviation FM of the synthesizer at the 2.56kHz rate. For example, assume the basic step is 1Hz. A first order modulator with a fractional numerator of 128 and a fractional denominator of 256 will generate an output sequence of: 0, 1, 0, 1… . This will produce square wave FM of deviation 0.5Hz peak and rate 1.28kHz. From the theory of low deviation FM, the first pair of sidebands will have a level of 20log(1.25x0.5x0.5/1280) or –72dBc. This is comparable with the synthesizer phase noise floor. A higher order modulator will produce noise like sidebands which may be calculated from a Fourier transform of the sequence. A simulation shows that close in noise should be less than –100dBc/Hz for a third order modulator.

For the purposes of testing, the software D/S modulator may be completely controlled over the RS232 interface using a terminal program. The order of the modulator may be varied between first and fourth. The dither may be switched on and off. The resolution extension fractional numerator may be varied between 0 and FFh. The internal fractional numerator (RF-FN) may be varied between 0 and FFFh. In addition the deviation of the direct digital FM at 80Hz may be adjusted from 0 to FFh steps. The synthesizer output attenuator may also be adjusted, however for all the tests the output was set to maximum.

The first tests were made with RF-R = 4, RF-N = 1366, and RF-FD = 2500000. This gives a basic resolution of 1Hz exactly. RF-FN was 2343750 (23C346h) for the nominal frequency of 3.417343750GHz. The resolution extension was initially disabled to obtain a baseline phase noise measurement of the synthesizer. The internal D/S modulator was set to second order with weak dither.

The resolution extension was then switched on, using a second order modulator with dither. The resolution extension fractional numerator was set to 80h, which is a change of

frequency of 0.5Hz. This shows a 10dB degradation in close in phase noise, which completely disagrees with theory.

In order to check that the phase noise degradation was consistent over a range of programming conditions, the synthesizer was reprogrammed with the following parameters:

RF-R = 4, RF-N = 1366, RF-FD = 2501291. This gives a frequency resolution of 0.99948Hz. RF-FN was 2344960 (23C800h) for a nominal frequency of 3.417343750GHz. The internal D/S modulator was set to 2nd order with weak dither.

The phase noise degradation is only 1.5 dB. This is an improved result, and indicates that the performance depends upon the exact value chosen for the internal S/D modulator RF-FN and RF-FD.

A further test was made on the dependence of the phase noise and spurii on the exact programming conditions. The software D/S modulator was made first order, (without dither) and the resolution extension fractional numerator was set to 80h. This is equivalent to square wave FM at a rate of 1280Hz, and a peak deviation of 0.5Hz. There should be two sidebands with a level of –72dBc. The sidebands are at a level of –45.6dBc, 25 dB worse than theory suggests.

The base value of the fractional numerator (RF-FN) was then changed 2 steps to 23C802h. The level is 10 dB higher!

This shows that there is some unknown interaction between the internal D/S modulator, and the software variation of the fractional numerator (RF-RN) at a constant rate. The internal D/S modulator is updated at the phase detector frequency, several MHz in all the tests made. One would expect the change in fractional modulus to propagate through the internal modulator in a few microseconds only. Thus direct FM at a 1280Hz rate should give a result close to a quasi static consideration of the effect of the FM, an effect that can be exactly predicted by theory.

This method of resolution extension has not been as successful as hoped. Theoretically the method should have had no effect on the phase noise of the synthesizer using the LMX2486. In practice, phase noise degradation of between 1.5 and 10 dB was observed. The amount of degradation was very dependant on the exact settings of the internal D/S modulator. This implied some sort of interaction between the internal modulator, and the variation of the fractional numerator. In particular, the FM sidebands due to low deviation FM at the 1280Hz rate should be completely predictable. However FM modulation of the LMX2486 showed a large deviation from theory, a deviation which again depended greatly on the exact value of the fractional numerator. To confirm the FM modulation theory, an RF signal generator was FM modulated with a 1280Hz square wave with a 1Hz deviation. The level of the 1280 sidebands was at exactly the predicted level.

As we have no details of the internal design of the LMX2486, it is not possible to speculate as to the nature of the interaction. These results have been communicated to National Semiconductor, however as yet they have not suggested an explanation.

The resolution extension method proposed has the advantage of zero cost. The only overhead is a small amount of processor time. If the limitations discussed above can be tolerated, the method may still be useable in the proposed digital rubidium design.

d. Monitor-Control Software

The monitor-control software is installed in the PC which communicates with Rubidium atomic clock with RS232 protocol. Otherwise, the clock's work status including lamp and cavity can be monitored real-timely. Furthermore, the software can also set the parameters including synthesizer's offset and divider coefficient. With the help of the software, the Rubidium clock can be massively produced at a low cost.

e. Architecture Design

The digital electronics and novel physics package are introduced, and the ultra-miniature Rubidium atomic clock can be shaped in a low size scale. Because OCXO with 51mmx51mm dimension is popularly used, as is necessary to design the similar Rubidium clock. Therefore the E10-MRX has completed on this idea. The clock without case is shown in the. Fig.5. It is clear the synthesizer is enclosed in a metal shield, and the 6.8GHz transmits from the synthesizer to cavity by a microwave line with mini SMB connector.

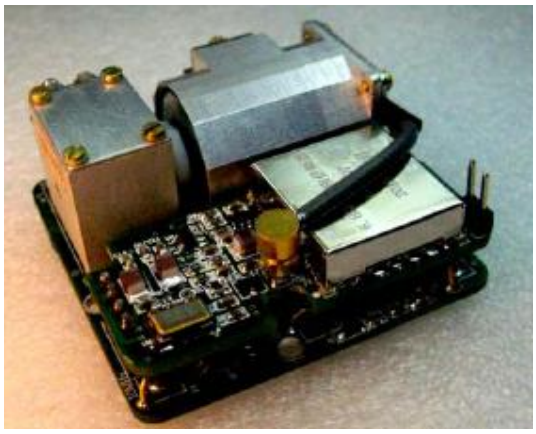

Figure 5. Rubidium atomic clock E10-MRX with the cover removed.

- The two PCBs are overlapped and fixed by 4 sockets. The frequency multiplier is enclosed in a case and directly soldered on the small PCB which is aligned with the cavity and the lamp.
- The case of Rubidium atomic clock is made of Permalloy metal and is to reduce frequency shift resulted from magnetism again. Therefore the magnetic sensitivity will be reduced at large and finally to achieve the 2E-11/G. finally, the dimension is 51mm×51mm×25mm which is compatible with the ordinary OCXO. Especially, the base plate of the clock has 4 screw hole and can be held safely, which makes the clock‘s frequency specifications tolerable on the condition of shock and vibration.

III. TEST

After making the key-technique design, five prototypes of the clock have been fabricated. Firstly, we have tested the five clocks comprehensively. The data and figures of testing are as below.

a. Short-Term Frequency Instability

Short-term frequency instability is relative with noise from synthesizer and physics package and the strength of atomic discrimination. In Fig.6, the short-term frequency instability of the clock E10-MRX is given.

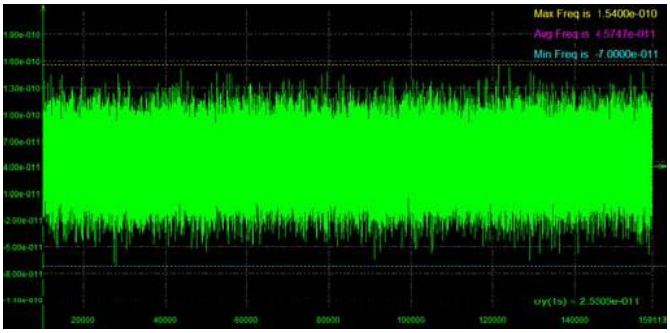

(a)

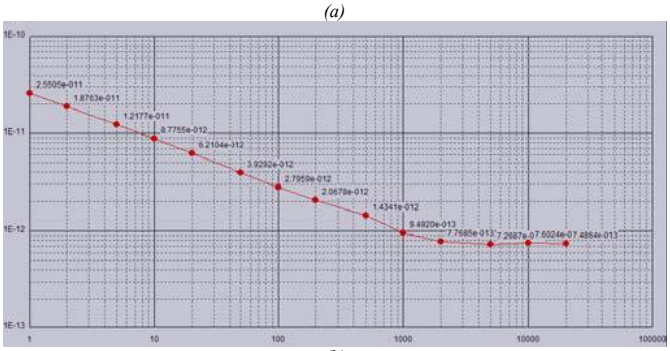

(b)

Figure 6. E10-MRX short-term frequency instability. (a) The typical frequency accuracy of the clock. (b) The typical frequency Allan deviation of the clock.

In Fig.6, the short-term frequency instability is showed. The frequency data are sampled per 1 second in two day, therefore the quality of frequency point is enough to calculate the Allan deviation. From the diagram, the short-term frequency instability is about 2.6E-11/s, 9E-12/10s, 2.8E-12/100s, which is satisfied with root tau in Allan deviation, and is laid in the middle level of compact Rubidium clock.

Obviously, the data is better than ordinary OCXO's, especially in the term of 10s and the time with big scale.

b. Temperature Coefficient

Temperature coefficient is most difficulty in gas cell Rubidium clock while Doppler shift from hot atoms in absorption cell is appended in resonant frequency [5]. In addition, integrating filer technique in compact Rubidium clock is popularly used in order to downsize the clock's volume and brings on bigger coefficient than the scheme of splitting filtering technique. In E10-MRX, the digital electronics is to compensate coefficient by the feeding-back error from the temperature sensor mounted the clock case. In this way, the perfect property of frequency vs. temperature is achieved finally in Fig.7 as below.

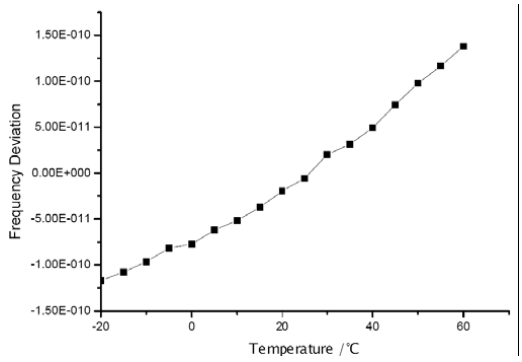

Figure 7. The clock E10-MRX coefficent in the range of -20 to 60°C.

The present temperature coefficient in the range of -20oC to 60oC is within 3E-10. Next step, the range of work temperature will be expanded to fit defence and avionics environment.

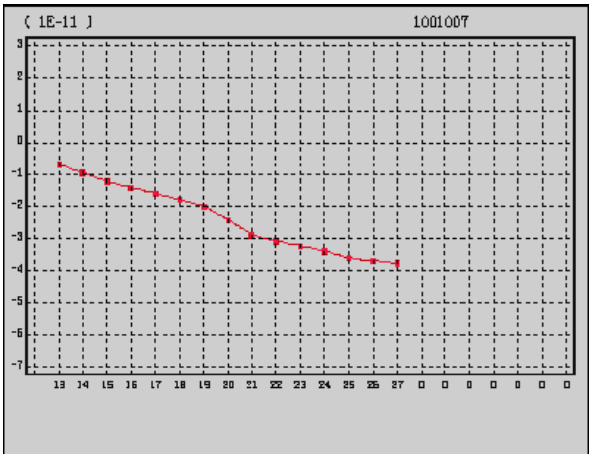

Figure 8. The clock E10-MRX's Long-term aging test diagram.

In Fig.8, the typical data is below 5E-12/day, and better with two or more order of magnitude than ordinary OCXO's.

IV. CONCLUSION

The ultra-miniature Rubidium atomic clock E10-MRX basing on traditional gas cell Rubidium clock scheme is completed now. Furthermore, owning to introduced novel physics package and the digital electronics, the cost, power dissipation and dimension are reduced at large extent. Finally, the shape of the clock is 51mm x 51mm x 25mm (2' x 2' x 1') in the first version of the clock, which is better standing long-term frequency instability than OCXO, but compatible with it. In addition, the clock has better technique maturation than CPT clock occurring several years ago. Consequently, the clock will take on an important application position in future, and will be widely used in aspect of Global Navigation Satellite Systems (GNSS), IEEE1588 web, IP TV, Timing-keep system as frequency standard instead of OCXO with higher frequency performance two or more order of magnitude.

V. REFERENCES

[1] Mills D L. Internet Time Synchronization: the Network Time Protocol. IEEE Trans. Communications, 1991, 39(10): 1482.

[2] Audoin C., Guinot B.: The Measurement of Time, Frequency and Atomic Clock, Cambridge, University Press 2001, pp. 211-215.

[3] Jeff D. Crockett, Fullerton, Calif Lamp Oscillator For Atomic Frequency Standards. United States Patent 5,489,891.

[4] Y. Koyama, et al., "An Ultra-miniature Rubidium Frequency Standard with two-cell scheme," Proc. 49th Annual Symposium on Frequency Control, pp.33-38, 1995.

[5] R. H. Dicke, the effect pf collisions upon the Doppler width of spectral lines physical review volume 89, number 2 January 15, 1953.

Optimization of a Chip-Scale Rb Plasma Discharge Light Source: Effects of RF Drive Frequency and Cell Impedance

Vinu Venkatraman, Herbert Shea
Microsystems for Space Technologies Laboratory (LMTS)
École Polytechnique Fédérale de Lausanne (EPFL)
Neuchâtel, Switzerland
vinu.venkat@epfl.ch

Yves Pétremand, Nico de Rooij
Sensors, Actuators and Microsystems Laboratory (SAMLAB)
École Polytechnique Fédérale de Lausanne (EPFL)
Neuchâtel, Switzerland

Christoph Affolderbach, Gaetano Mileti
Laboratoire Temps-Fréquence (LTF), Institute of Physics
University of Neuchâtel
Neuchâtel, Switzerland

***Abstract*— We report on the performance improvements achieved on our previously demonstrated proof-of-concept chip-scale dielectric barrier discharge (DBD) Rb lamp [1], (1) with change in the plasma regime of operation by changing RF drive frequency and (2) with an improved electrode design, for optical pumping in a chip-scale Double-Resonance (DR) atomic clock. Our realized microfabricated planar DBD Rb lamp now has externally deposited Al electrodes, allowing for efficient power coupling to the discharge volume and was tested at different RF drive frequencies ranging from 2 MHz to 500 MHz. Currently the light source can emit up to 380 µW of optical power on the Rb D2 line depending on input conditions.**

I. INTRODUCTION

The application of the Rubidium double resonance (DR) technique, widely used in compact (100-1000 cm^3) Rb clocks [2] today, has not yet been extended to chip-scale atomic clocks (CSAC) - due to the unsuitable size (several cm^3) and high power consumption (several Watts) of inductively-coupled discharge lamps and the challenging requirement for a miniaturized microwave cavity. To support such development, we aim to realize a chip-scale capacitively coupled Rb plasma discharge lamp and identify the discharge cell parameters and operating conditions that would allow for minimum size and low power consumption for long-term stable operation in a CSAC. We have previously shown a proof of concept chip-scale light source [1]. Here, we report on the performance improvement of a chip-scale dielectric barrier discharge (DBD) Rb lamp achievable: (1) with change in the plasma regime of operation by changing RF drive frequency and (2) with an improved electrode design.

Dielectric barrier discharge lamps have been used in many applications [3] but very rarely used for low-power operation in the MHz drive range. They provide an important advantage of allowing electrodes to be placed outside the lamp-cell discharge gap hence (1) avoiding the limitation of low lamp lifetime from electrode erosion and also (2) avoiding the high Rb diffusion into the metal electrode.

Our realized microfabricated planar DBD Rb lamp (Fig. 1) now has Al electrodes externally deposited onto the cell windows, allowing for efficient power coupling to the discharge volume and a simplified impedance matching circuit. But for such small discharge gaps, a higher buffer gas pressure (up to tens of hPa) is added to maintain a low breakdown potential. As this shifts the plasma regime away from the homogeneous glow-discharge regime, increasing the rf drive frequency and the intrinsic cell capacitance play an important role in determining the power efficiency of the Rb light source and controlling the stability of the optical power emitted on the Rb D lines. We observed a factor of >10 improvement in power efficiency when operating in the 100 MHz range of drive frequency for one of the improved cells (Fig. 2) and a 50% improvement in Rb D lines stability, when compared to previous data [1]. We also report on experiments on sub-mm discharge gaps under varying gas conditions to determine the performance when scaling to smaller cell size.

II. DEVICE DESIGN AND OPTIMIZATION

A. Microfabrication

The micro-fabricated Rb cell (outer dimensions of 1 x 1 x 0.3 cm^3), consists of a stack of three layers: Pyrex (500 µm thick), Silicon (2 mm), Pyrex (500 µm) which enclose a Φ = 5 mm, h = 2 mm cylindrical cavity in which few microliters of Rubidium and low-pressure (< 100 mbar) buffer gas are hermetically sealed by a two-step anodic bonding process (Fig. 2). 200 nm thick layers of Al are deposited on both top and bottom walls of the cell using evaporation technique with

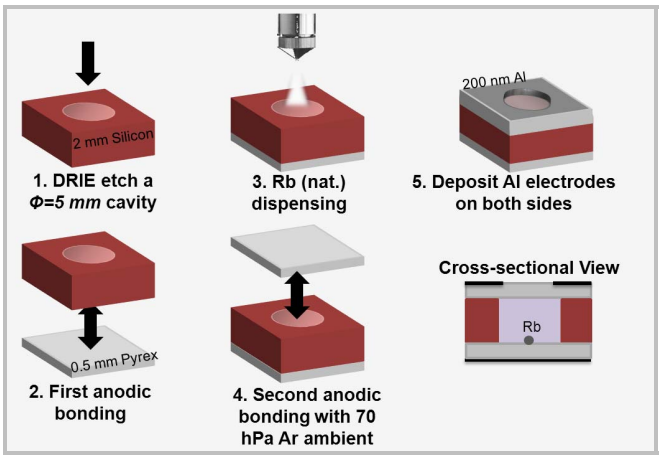

Figure 1. Microfabrication of the light source.

the top layer patterned with a central hole (of diameter 4.5 mm) using a shadow mask.

B. *Electrode Design Optimization*

Several electrode geometries were tested to arrive at the best configuration: blanket 200 nm thick Al for top and bottom electrodes with a 4.5 mm diameter central patterned hole for the top electrode. Fig. 2 shows the experimental results obtained for minimum power consumption from different electrode configurations.

The electrical power consumption of the device is shown in Fig. 3 where it shows a >50% reduction in power consumption (at > tens of MHz) by the new Al electrode configuration when compared to previously used Indium ring electrode configuration. Al electrode with the illustrated geometry, having good surface adhesion properties, allows for low power consumption.

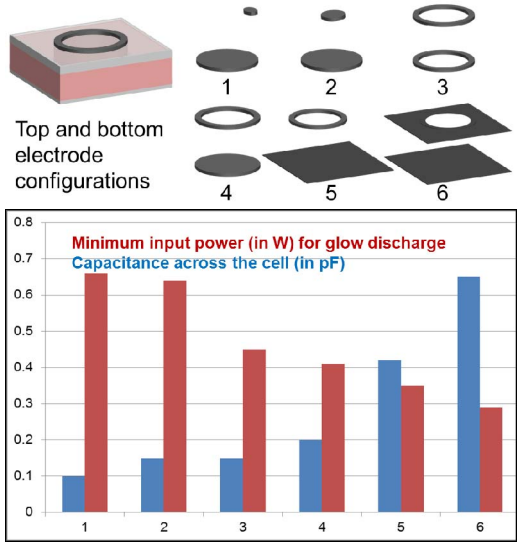

Figure 2. Different electrode configurations showing minimum sustaining power for plasma glow discharge

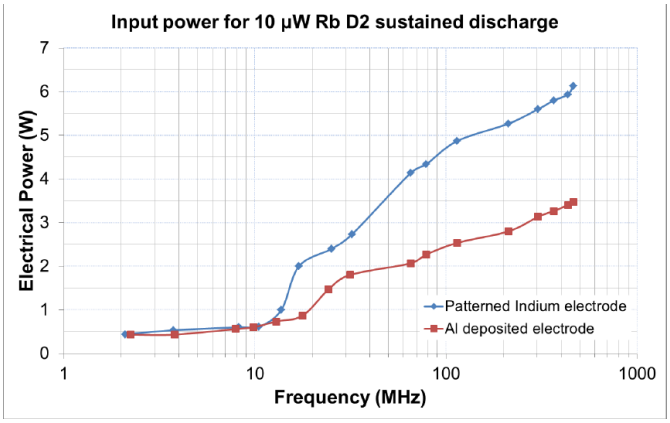

Figure 3. Reduction in power consumption by the device with the Al electrode configuration as compared to an Indium ring electrode

C. *RF Drive frequency*

The cell is driven by a series LC resonant voltage amplifier where the cell is a capacitive load with a series inductor, and it is impedance-matched to the 50 Ω source. Fig. 4 shows the breakdown voltage of the plasma discharge at different frequencies (blue) and the optical power on the Rb D2 line emitted for a constant 700 mW of total input power (red).

The electron oscillation amplitude decreases with higher drive frequency. At values where the discharge gap length (d) is much lower than the electron oscillation amplitude (A), the plasma does not ignite due to very high breakdown voltage. At values A ≈ d, there is some amount of secondary electron emission from the Pyrex to allow breakdown and the breakdown voltage decreases with higher frequency as there are now more electrons adding to the space charge in the discharge gap. At much higher frequencies (>100 MHz here), the maximum kinetic energy effects are seen here, as discussed in [4]. Even though the breakdown voltage decreases with increasing frequency, the power required to achieve a said voltage increases with increasing frequency ($P = C.V^2.f$).

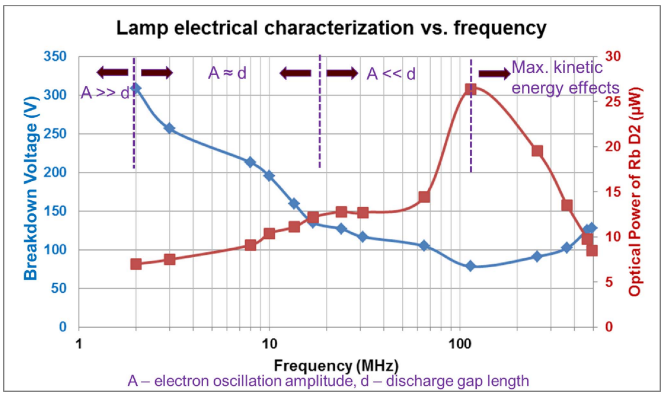

Figure 4. Breakdown voltage of the plasma discharge for a 2 mm gap and 30 hPa Ar added to the Rb cell, at different frequencies and the optical power emitted on the Rb D2 line for 700 mW of input power

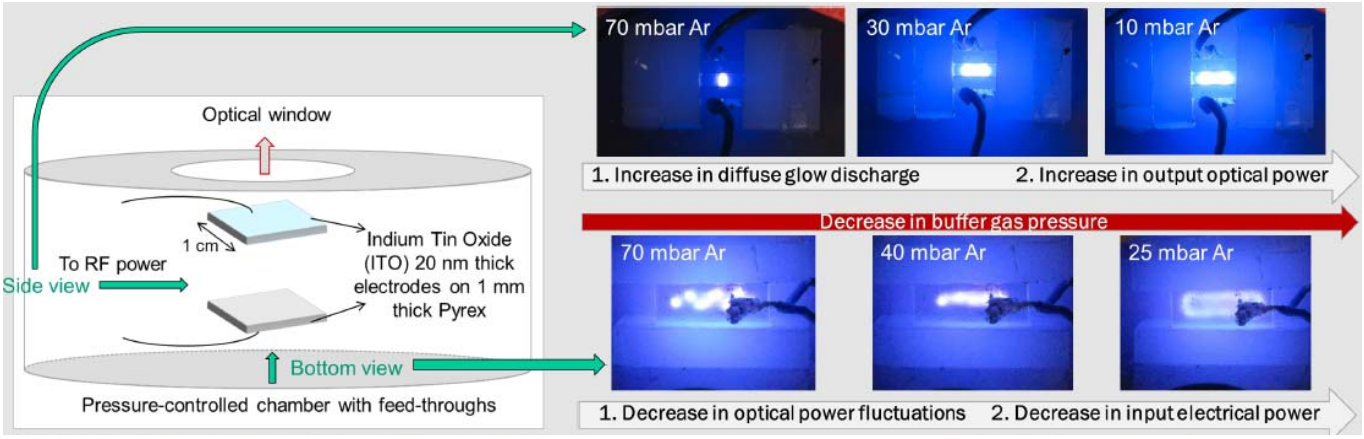

Figure 5. Test setup with ITO-coated borosilicate substrates as cell walls for monitoring the dielectric barrier discharges by varying cell gap conditions. Pictures on the right show the barrier discharges with decrease in buffer gas pressure

III. Towards Cell Design Optimization

To achieve a power-efficient and optically stable Rb light source, the cell parameters including buffer gas and discharge gap length need to be optimized. Fig. 5 shows an experimental setup for these measurements where the optical and electrical powers are measured for different discharge gap conditions. It was observed that the plasma discharge enters the diffuse discharge regime only at lower pressures (values depending on the buffer gas), emitting higher optical power per input electrical power. The stability of the emitted optical power was found to be higher at lower pressures or higher drive frequency where the electron oscillation amplitude becomes smaller than the discharge gap length.

Fig. 6 shows the fluctuations in optical power versus the pressure x distance (p.d) and drive frequency. It can be seen that higher drive frequency or lower (p.d) enables working in the diffuse discharge regime which would be a stable operating region for optical pumping applications. At low drive frequencies (<4 MHz) or high (p.d), there were >0.5% fluctuations in optical power mainly due to the volume discharges [5] formed on the inner dielectric cell surface.

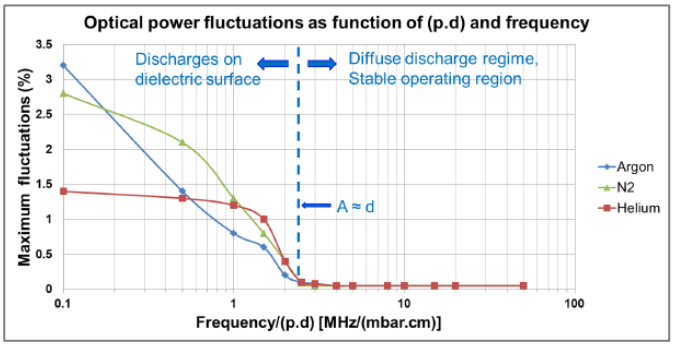

Figure 6. Optical fluctuations versus p.d and frequency

IV. Conclusions

A strong improvement by >50% in the Rb light source power efficiency was achieved with the new Al electrode geometry (at tens of MHz drive range). Currently, the optimal cell conditions have been observed to be around 60 hPa.mm with Argon as buffer gas with a maximum operating frequency around 100 MHz for a 2 mm gap. While at low frequencies (<4 MHz) there is secondary electron emission from Pyrex to allow a low-power breakdown, these discharges give rise to optical fluctuations. Hence a drive frequency of >5 MHz and gas pressures between ~5-40 hPa of buffer gas for mm-scale discharge gaps, would enable operation in the diffuse discharge regime with a stable optical output.

Acknowledgments

We acknowledge support from the SNSF Sinergia grant CRSI20_122693, and the SNSF R'Equip program for the funding of the high-speed data acquisition test bench used in this study. We thank our project group members for their support.

References

[1] V. Venkatraman, Y. Pétremand, C. Affolderbach, G. Mileti, N. de Rooij and H. Shea, "Microfabricated Chip-Scale Rubidium Plasma Light Source for Miniature Atomic Clocks", IEEE Trans. Ultrason. Ferroelectr. Freq. Control, vol. 59. no.3, pp. 448-456, 2012.

[2] J. Camparo, "The rubidium atomic clock and basic research", Phys. Today, vol. 60, pp. 33-39, 2007

[3] U. Kogelschatz, B. Eliasson, and W. Egli, "Dielectric barrier discharges. Principle and applications," J. Phys. IV, vol. 7, no. C4, pp.447–466, 1997.

[4] J. L. Walsh, Y. T. Zhang, F. Iza, and M. G. Kong, "Atmospheric pressure gas breakdown from 2 to 100 MHz," Appl. Phys. Lett., vol. 93, no. 23, art. no. 221505, 2008.

[5] U. Kogelschatz, "Dielectric barrier discharges: Their history, discharge physics, and industrial applications", Plasma Chem. Plasma Process., vol. 23, no.1, p.1-46, 2003.

Use of multi-technique combinations in UTC/TAI time and frequency transfers

Z. Jiang
Time Department
Bureau International des Poids et Mesures (BIPM)
Pavillon de Breteuil F-92312, SÈVRES CEDEX, France
zjiang@bipm.org

W. Lewandowski
Time Department
Bureau International des Poids et Mesures (BIPM)
Pavillon de Breteuil F-92312, SÈVRES CEDEX, France

***Abstract*—** This is a review paper. We revisited the key conceptions of the combined techniques used in the UTC generation: the combination of the GNSS and TWSTFT and that of the GPS and GLONASS code measurements.

I. INTRODUCTION

For decades, the strategy of the UTC time transfer was the primary technique, i.e. for a UTC/TAI baseline only the 'primary' technique was used. The order of the priority was TWSTFT (Two-Way Satellite Time and Frequency Transfer, TW for short), GPS PPP, GPS P3, GPS C/A or GLONASS L1C (GLN).

Since the Circular T 277 in Jan. 2011, multi-technique combinations have been used in UTC generation [1,2]: the GPSGLN, combination of the GPS C/A and GLONASS L1C codes; and the TWPPP, the combination of the TWSTFT and the GPS carrier phase which is derived from the GPSPPP solution. At present there are 16 combined time links which take 1/4 of the total UTC links and the frequency transfer of all the Primary Frequency Standards (Figure 1).

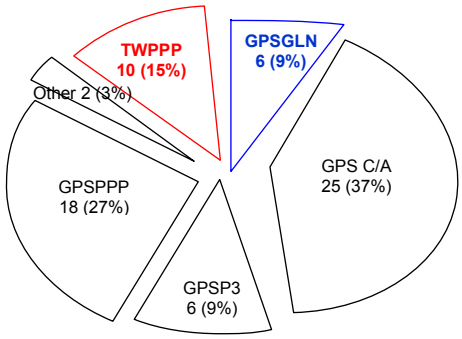

Figure 1. Status the combined links in Nov. 2011 (*Circular T* 287) of the 67 time transfer links used in UTC generation

In this paper, we review the basic conception of the link combinations and its role in UTC/TAI time and frequency transfers. We analyze the uncertainty and the calibration stability etc., using two year's combination data.

II. THE METHOD

A. Mathematic model of GPSGLN code combination

TABLE I. CALIBRATION CONSISTENCY OF GPS C/A VS. GLN L1C LINKS OVER 34 MONTHS (VALUES GIVEN IN THE TABLE ARE THE MONTHLY MEAN OF THE DIFFERENCES BETWEEN GPS AND GLN LINKS. FOR AOS-PTB, THE DATA OF 0905-1002 ARE OF GPS C/A, 1008-1202 GPS P3)

YYMM	AOS-PTB /ns	NIS-PTB /ns	OP-PTB /ns	SU-PTB /ns	UME-PTB /ns
0905	0			0	0
0906	-0,2			-0,3	-0,7
0907	-0,3			-0,7	-0,6
0908	-0,4			-0,4	-0,6
0909	-0,4			-0,4	0
0910	-0,9			-0,3	-0,4
0911	-0,7			-0,4	0
0912	-1			-0,2	-0,4
1001	-1,4	-0,051	-0,256	-0,279	-0,399
1002	-0,6	0,098	-0,081	-0,187	-0,03
1003		0,074		-0,44	-0,027
1004		-0,035	-0,055	-0,488	-0,008
1005		-0,343	-0,011	-0,311	-0,117
1006		-0,416	0,043	-0,445	-0,052
1007		-0,98	-0,679		-0,752
1008	-0,707	-0,176	0,104		-0,063
1009	0,362	-0,078	0,077	-0,524	-0,154
1010	-0,594	0,336	-0,033	-0,3	0,034
1011	1,003	0,52	-0,078	-0,305	-0,189
1012	-0,802	0,903	-0,052	0,036	-0,033
1101	-0,558	0,701	-0,035	0,422	0,172
1102	0,308	0,465	-0,097	0,324	-0,046
1103	-0,211	0,245	-0,078	-0,149	-0,209
1104	-0,342	0,17	-0,155	-0,297	-0,185
1105	-0,382		-0,276	-0,383	-0,168
1106	-0,362	0,029	-0,291	-0,272	-0,117
1107	0,604	0,734	0,117	0,17	0,305
1108	0,575	-0,001	0,042	0,018	-0,354
1109	0,619	0,248	0,026	0,052	-0,251
1110	0,744	0,515	-0,147	0,061	-0,354
1111	0,315	1,008	-0,094	0,108	-0,402
1112	0,817	0,867	0,103	0,084	-0,424
1201	0,964	1,155	0,157	0,113	-0,335
1202	1,023	1,097	0,1	0,146	-0,337
Mean	**-0,087**	**0,283**	**-0,066**	**-0,173**	**-0,212**
σ	**0,662**	**0,519**	**0,177**	**0,268**	**0,239**

One of the prior conditions of the combination GPSGLN is the stability and the agreement of their link calibrations. We

used the results of the BIPM monthly UTC/TAI link comparisons [3] in the following numerical analysis which are all based on the UTC baselines: Lab-PTB.

As given in the Table I and Figure 2, the calibrations of GPS and GLN links agree well with each other and are stable with time. The pick to pick disagreements are within their measurement uncertainties ±1 to ±1.4 ns for all the 5 baselines compared, in particular the two official UTC links: SU-PTB and UME-PTB. The mean values of the disagreements of the calibrations between GPS and GLN and the standard deviations are respectively: 0.087±0.662 ns for AOS-PTB, 0.283±0.519 ns for NIS-PTB, 0.066±0.177 ns for OP-PTB, -0.173±0.268 ns for SU-PTB and -0.212±0.239 ns for UME-PTB

The combination, namely GPSGLN, is of the mean values computed by:

1) The *simple mean values* of data sets of GLN L1C code CV and GPS C/A code AV as: (GPS C/A+GLN L1C)/2;

2) The *weighted mean values,* depending on the measurement quality of GPS and GLN; we compute the weighted mean value combination by the equation: $[n\times(\text{GPS.C/A})+m\times(\text{GLN.L1C})]/(n+m)$. Here n and m are the weights of the GPS and GLN. At present the ratio of the weights is correspondingly 2:1.

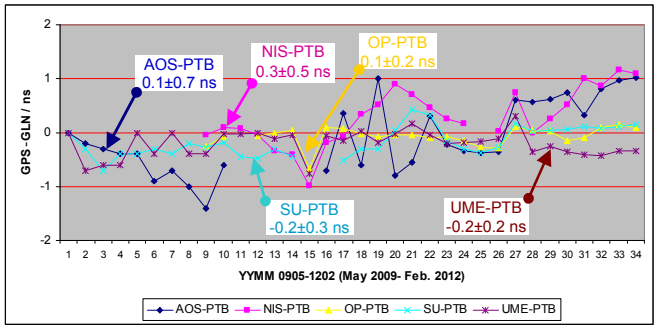

Figure 2. Consistency of UTC links between GPS C/A and GLN L1C (34 months' comparison corresponding to Table 1) The mean values of the disagreements of the calibrations between GPS and GLN and the standard deviations are given in the plots

B. *Mathematic model of TWPPP combination*

In this section, we first summarize the mathematic principles and then in the next sections we evaluate numerically the model proposed.

1) The mathematic principles

We quickly review the principle of the TWPPP combination. Details can be found in [2]. We consider two time series: t_i with i = 1, 2, 3 … and t_j with j = 1, 2, 3 ... The series of TW time transfer observations is $y(t_i)$. As a function of time t_i, its derivative $y'(t_i)$ at epoch t_i can be defined by $[y(t_{i+1})-y(t_i)]/(t_{i+1}-t_i)$. The other series is the PPP observations $Y(t_j)$. Its derivative is $Y'(t_j) = [Y(t_{j+1})-Y(t_j)]/(t_{j+1}-t_j)$. The physical meaning of the two sets of derivatives is the same: the rate of the difference of the two end clocks: $y'(t_i) = Y'(t_j)$ when $t_i = t_j$. Therefore,

$$\int_{\text{MJD1}}^{\text{MJD2}} y'(\text{TW})\,dt = \int_{\text{MJD1}}^{\text{MJD2}} Y'(\text{PPP})\,dt$$

$$\text{TW}_{\text{MJD}\,i+1} = \text{TW}_{\text{MJD}\,i} + \sum_{j=\text{MJD}\,i}^{\text{MJD}\,i+1} \Delta(\text{PPP}_j)$$

i.e.

$$y(\text{MJD 2}) = y(\text{MJD 1}) + \text{Sum}\{Y'(t_j)\Delta t_j\}$$

The interval of the PPP observation (between 30s and 300 s) is much smaller than that of TW (1–2 h). Equation above implies that a TW observation at epoch MJD_{i+1} can be represented by its previous observation value at MJD_i plus the sum of a series of the small increases of PPP during the period, which does not depend on the calibration of PPP. The discrepancy between TW and PPP results is the total observation error during the integrating interval. By minimizing the discrepancy between the two series, we can establish the constraint condition of the combination to determine the smoothed curve. The method we use here to smooth a function with given derivatives is known as Vondrak-Cepek combined smoothing [4], adapted for the combination of TWPPP.

2) The Vondrak-Cepek combined smoothing

We need a tool to combine the two series of the measurements, the function $y(t_i)$ and the derivatives $Y'(t_j)$. This is a typical problem of Vondrak-Cepek combined smoothing. The method is based on the Whittaker-Robinson-Vondrak smoothing that removes the high-frequency noise present in a series of unequally spaced observations. The goal is to find a compromise between the smoothness of the searched curve on the one hand, and the "fidelity" of this curve to the observed values on the other hand. Vondrak-Cepek combined smoothing consists in finding a compromise between three conditions:

- Condition S: smoothness of the searched curve (analytically unknown) as in the original smoothing;
- Condition F: fidelity to the observed function values;
- Condition F': fidelity to the observed first-time derivatives.

III. NUMERICAL EXAMPLES IN UTC COMPUTATIONS

A. *Combination of the GPS and GLN codes*

Table II shows the standard deviations of the GPS-only, the GLN-only and the combination GPSGLN links against TW and GPS PPP. Here σ is the standard deviation of a single technique and $\underline{\sigma}$ is that of the GPSGLN. The gain is computed by the equation $(\sigma-\underline{\sigma})/\sigma$. The standard deviations of the differences of the GPS-only, GLN-only and GPSGLN time

links vs. to TW are 1.240 ns, 1.369 ns and 1.215 ns, respectively. The averaged gain in GPSGLN vs. GLN-only and GPS-only with respect to TW is 6.5 % on average. Similarly, taking PPP as reference, the standard deviations are 1.182 ns, 1.285 ns and 1.149 ns, respectively. The gain with respect to PPP is 7 % on average. The combination thus confirms an average gain of 7 %. Knowing that the measurement uncertainties of TW and of GPS PPP is from 0.3 ns to 0.6 ns and the simplicity of the combination computation, the gain here is hence conservative and the combination operation makes sense.

TABLE II. COMPARISON OF THE STANDARD DEVIATIONS OF THE CLOCK DIFFERENCES FOR THE GPS-ONLY, GLN-ONLY AND GPSGLN LINKS TO THE REFERENCE LINKS PPP AND TW, ON THE BASELINE OP-PTB 1005 (MJD 55313 TO 55346)

Compared to	GPS-only σ / ns	GLN-only σ / ns	(GPSGLN) σ / ns	Gains (σ-σ)/σ
TW	1.240	1.369	1.215	6.5%
PPP	1.182	1.285	1.149	7%

Figures 3a and 3b illustrate the time deviations of the links of GPS-only, GLN-only and the combination GPSGLN on the baselines SU-PTB 1102 and INPL-PTB 1110. The short-term stability of the GPS-only link is slightly better than that of the GLN-only, probably as a result of the advantage of the AV technique against the CV. The stability of the combined solution GPSGLN is better in the short term than that of the GPS-only and the GLN-only. For averaging time beyond 20 hours, the curves of the three time deviation converge.

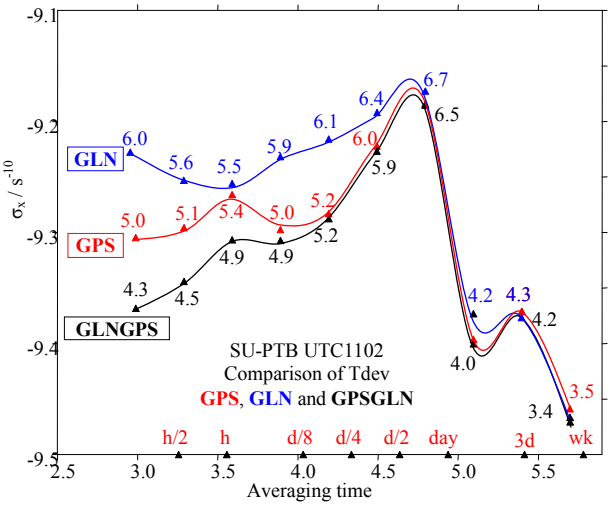

(a)

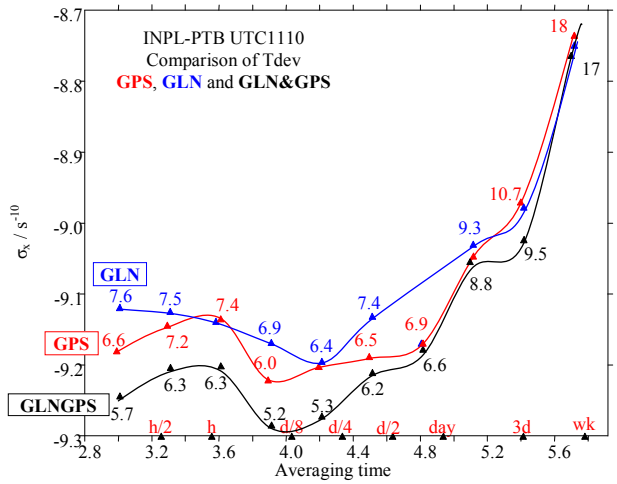

(b)

Figure 3. Fig. 3a is the baseline SU-PTB for the time links of UTC1102 and Fig. 3b is the baseline INPL-PTB for the time links of UTC 1110

Figure 4 shows the (GPSGLN) data for the UTC baseline OP-PTB for the period UTC 1005 (corresponding to MJD 55317 to 55346). It compares the time deviations between the corresponding GPS-only, GLN-only and GPSGLN links. The comparison shows that for averaging times up to half day the combined (GPSGLN) link is much more stable than the data from either of the single techniques: less noisy and less biased.

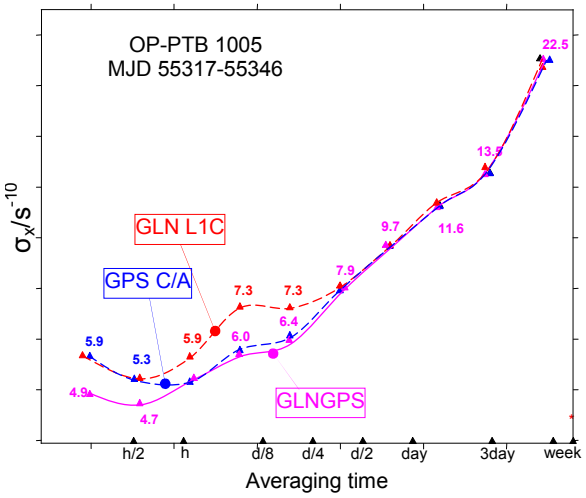

Figure 4. Comparison of the Time Deviations for the GPS-only, GLN-only and combined link GPSGLN for OP-PTB 1005

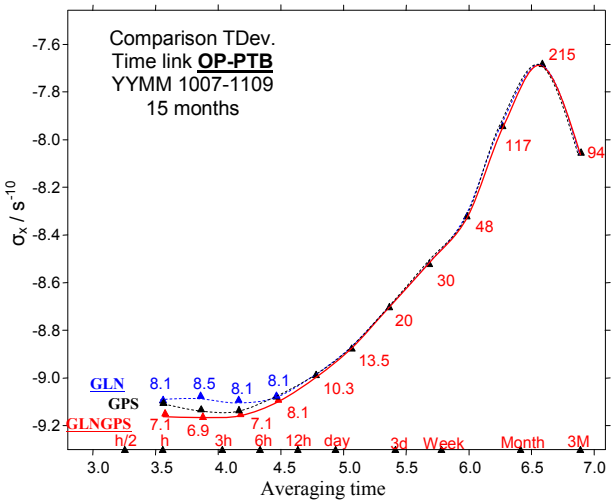

Figure 5. 15 months' long-term comparison of the TDev of GLN/L1C, GPS C/A and GPSGLN on the baseline OP-PTB between 1007-1109. The GPSGLN is the most stable. The TDev of the three links converge up to 1 day

To compare the long-term stabilities, we look at the GPS-only, GLN-only and GPSGLN data over a 15-month period (1007-1109: MJD 55378-55834) on the UTC baseline OP-PTB. Figure 5 shows the comparisons of the corresponding time deviations. After the better averaging based on the increased number of data points, we see here more clearly that the stability of the combined link GPSGLN is much better than the single techniques, at least for averaging times of up to 1 day.

B. Combination of the GPS carrier phase information and the TWSTFT

As numerical examples, we analyzed two UTC baselines NIST-PTB and OP-PTB. As given in the Figures 6, 7 and 8 below, on both of the baselines, we have seen significant improvement in the combined solutions.

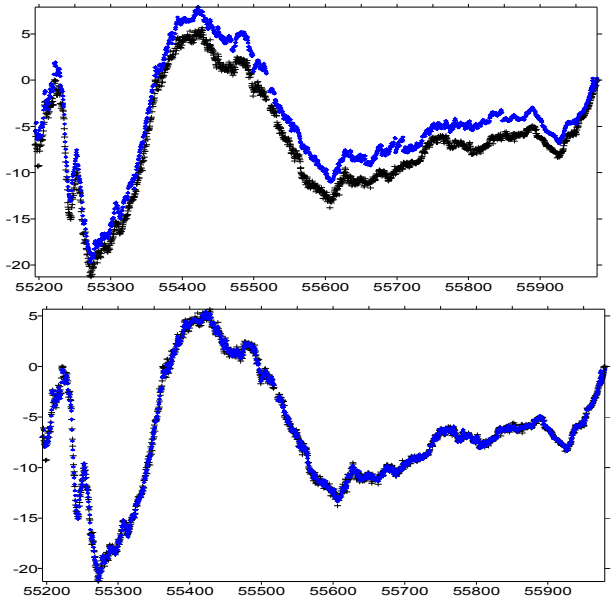

(a)

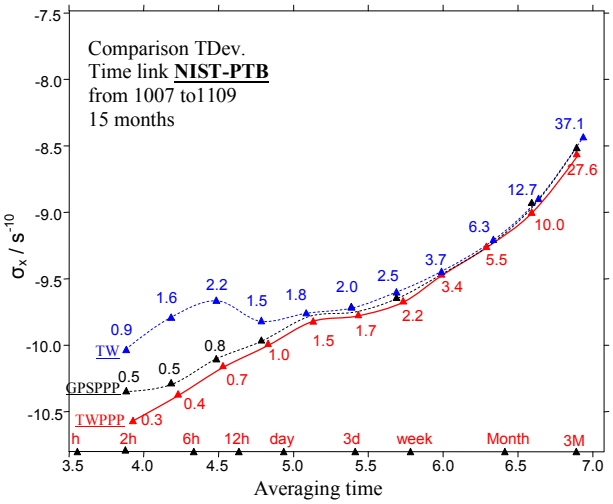

(b)

Figure 6. Comparisons of the three links TW-only and GPSPPP-only (a) and their TDev of the TW-only, the PPP-only and the combination TWPPP (b). The diurnal signals in the TW-only can be seen. The combined link TWPPP is the most stable. From averaging time of a day, the three TDev start to converge

The Table III is the comparisons of the three links over the baseline NIST-PTB during 15 months between 1007 and 1109. It is clear the differences between are all within the concerned measurement uncertainties (u_A the Type A uncertainty). They perfectly agree with eath others with the u_A.

Further examples are given in the Figures 7 and 8 on the baseline OP-PTB.

TABLE III. COMPARISONS OF THE LINKS ON THE BASELINE NIST-PTB DURING 15 MONTHS BETWEEN 1007 AND 1109.

Link1 - Link2	N	Mean /ns	σ /ns
TW - GPSPPP	4815	-2.424	0.580
TW - TWPPP	4815	-0.009	0.281
TWPPP - GPSPPP	4336	-2.437	0.484

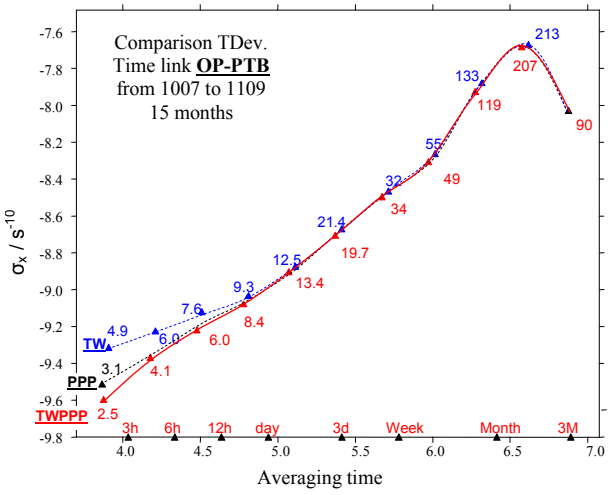

Figure 7. TDev of TW-only, GPSPPP-only and TWPPP on the baseline OP-PTB evaluated during 15 months from 1007 to 1109. The TWPPP is the most stable. The TW link is rather noisy than usual. The TDev of the three links converge from about 16 hours averaging time

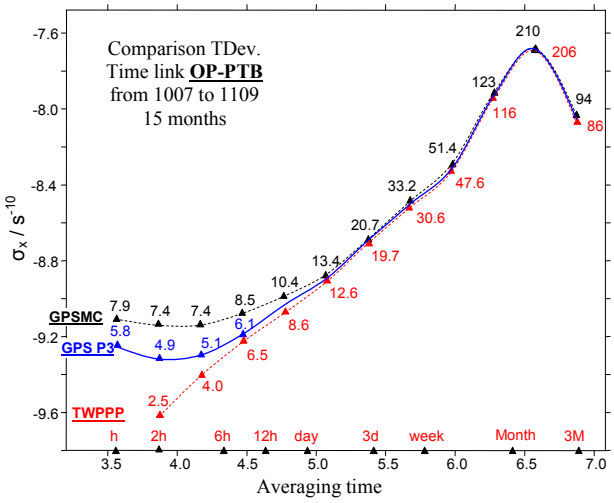

Figure 8. TDev of GPSMC C/A, GPS P3 and TWPPP on the baseline OP-PTB evaluated over 15 months from 1007 to 1109. The P3 link is more stable than the MC but less than the TWPPP. The TDev of the three links converge from about 2 days

IV. SUMMARY

To conclude, we present in the Table 4 the statistical results of different links on the UTC baseline OP-PTB where there are available all the time and frequency transfer techniques including the combinations at present in the BIPM database. Comparisons between these common-clocks' links allow us better understand the advantages of the combinations of the different techniques without the impacts of the clock noise.

- At present, there are 67 official UTC time and frequency transfer links, including 16 combined links;
- High redundancy in the UTC link database: each month about 250 official and backup links are computed for the purpose of the UTC/TAI generations. How to fully use them is a challenge. Since 2005, the BIPM started to make studies in this direction. One of the solutions is the combination of different techniques;
- Combinations of TWPPP and GPSGLN are used for about a quart of the UTC/TAI links;
- Combination increases short-term stability and the robustness of the time and frequency transfers;
- Further study is on going.

TABLE IV. STATISTICS OF ALL LINK TYPES AND THE LINK DIFFERENCES (dL) ON BASELINE OP-PTB (OVER 15 MONTHS BETWEEN 1007 AND 1109. u_A IS THE TYPE A UNCERTAINTY; u_A': STANDARD UNCERTAINTY OF THE LINK DIFFERENCES (dL); Σ: STANDARD DEVIATION OF THE dL; Σ: STANDARD DEVIATION OF THE VONDRAK SMOOTHING RESIDUALS OF A LINK; TDEV/T: TIME DEVIATION CORRESPONDING TO THE AVERAGING TIME T INDICATING THE FLICKER PM SEGMENT)

Lk2 / **Lk1**		**TW** /ns 1	**TWPPP** /ns 2	**GPSGLN** /ns 3	**MC** /ns 4	**P3** /ns 5	**PPP** /ns 6	**GLN** /ns 7
TW u_A σ TDev/τ	1	0.5 0.710 0.40/2h						
TWPPP u_A'/u_A σ/σ TDev/τ	2	0.6 0.664	0.3 0.429 0.25/2h					
GPSGLN u_A'/u_A σ/σ TDev/τ	3	1.3 1.078	1.3 0.852	1.2 1.066 0.81/10h				
MC u_A'/u_A σ/σ TDev/τ	4	1.6 1.253	1.6 1.109	2.0 0.117	1.5 1.154 0.95/10h			
P3 u_A'/u_A σ/σ TDev/τ	5	0.9 0.886	0.8 0.669	1.4 1.077	1.7-2.6 0.605	0.7 0.744 0.7/10h		
PPP u_A'/u_A σ/σ TDev/τ	6	0.7 0.756	0.5 0.705	1.3 1.161	1.6-2.6 1.042	0.8 0.566	0.3 0.176 0.31/2h	
GLN u_A'/u_A σ/σ TDev/τ	7	1.6 1.135	1.6 0.968	2.0 0.186	2.2 0.277	1.7 0.897	1.6 1.027	1.5 1.180 0.94/10h

REFERENCES

[1] Jiang Z and Lewandowski W, 2011, Use of Glonass in UTC time transfer, *Metrologia*, **49**, pp 57-61

[2] Jiang Z and Petit G, 2009, Combination of TWSTFT and GNSS for accurate UTC time transfer, *Metrologia* 46, pp 305-314

[3] Arias F., Z. Jiang, G. Petit, W. Lewandowski, *BIPM Comparison of Time Transfer Techniques*, Proc. FCS/PTTI 2005

[4] Vondrak J and Cepek A 2000 Combined smoothing method and its use in combining Earth orientation parameters measured by space techniques *Astron. Astrophys.* Ser 147 pp 347–59

Analysis of the impact of measurement noise on the TWSTFT stability

Amale Kanj, Joseph Achkar, Daniele Rovera
LNE-SYRTE
Observatoire de Paris
Paris, France
Amale.kanj@obspm.fr

Abstract— **The Two-Way Satellite Time and Frequency Transfer (TWSTFT) is widely used by the time institutes to compare ground atomic clocks and contributes to the production of the Temps Atomique International (TAI) calculated by the BIPM. In the past, TWSTFT links have frequency stability of $1x10^{-15}$ at one day [1], and since the last three years, two-way links became more and more noisy and the frequency stability has been degraded which has motivated the present work. In order to improve the performance of the TWSTFT technique, we focused on the principle parameters that impact the measurements stability and accuracy. In completion to the previous work [2] on the measurement noise in TWSTFT, we analyzed the impact of the changes of reference clock, satellite and satellite transponder on the two-way link instability over the period of the last five years. In addition, we studied the contribution in measurement noise on the two-way links of the following parameters: the chip-rates of the pseudo random noise modulation of the transmitted signal, the power of the transmitted and received signals. We also use the satellite simulator to determine the dependence of the chip rates on the delay difference of the OP ground stations. We completed the work in analyzing the variation of the short term residual noise fluctuations [3] and the carrier to noise ratio of the received signals in function of the previously listed parameters. Different results are presented in this paper and possible issues for improvement of the two-way links are proposed.**

I. INTRODUCTION

TWSTFT is actually the most precise technique for time scales comparisons with a combined uncertainty in time of less than 2 ns (BIPM Circular T publications). At present, the TWSTFT European network includes twelve Time institutes which most of them contribute to the realization of TAI.

Two-way sessions are scheduled every two hours, the earth stations transmit simultaneously a microwave signal and receive the two-way signals from other stations through a geostationary telecommunication satellite, in time slots of 120 s for each pair, in purpose to compare their time scales.

Each two-way station is equipped by a SATRE modem which applies the spread spectrum method over a generated intermediate frequency carrier modulated by a pseudo random noise code sequence at 1 Mchips/s carrying the clock signal. The delay difference between the signal transmission from one site and the reception of the signal transmitted from the other site is measured by the Time Interval Counter (TIC) of each station. Therefore, the phase difference between the two clocks is calculated by the combination of the two measurements made at the two sites in comparison.

II. MOTIVATION

However, the evolution of the performance of the TWSTFT technique shows, in the recent years, a degradation on the link stability, which has motivated this study.

In Fig. 1, we observe the DRMS variation during the last five years of OP ranging signal, a European link (OP-PTB) and a transatlantic link (OP-NIST). The DRMS is the root mean square of the residuals to the quadratic fit of one set of TIC measurements data [4]. It is clearly shown that the DRMS values have increased progressively specially on the European links.

To analyze the cause of this noise elevation, we considered the principle configuration changes that took place during the last five years. Over that period, two satellites have been used, on one satellite, transponder is changed and recently frequency offsets are applied on the transmitted microwave signals.

To observe the impact of each configuration change on the link stability, the frequency stability of OP-PTB link from one side and OP-NIST link from the other side presented by the modified Allan Deviation is shown in Fig. 2 and Fig. 3 respectively. Five different periods corresponding to the five configurations changes are considered. The first one is when the satellite IS-707 was used with 2.5 Mchips/s and a bandwidth (BW) of 3.5 MHz (black). In the second period, we moved to the satellite IS-3R. No change was made to the

allocated bandwidth nor to the chip rate and the link stability on the transatlantic link was improved (red).

We also considered two-way link stability with the current satellite T-11N before the transponder change, the chip rate was reduced to 1 Mchips/s and it was also the case of the BW which was reduced to 2.5 MHz (blue). This configuration caused a clear degradation of the link stability on the European link, which was not the case for the transatlantic link.

In addition, the period after the transponder change of the same satellite is shown in the same figure, we should mention that no frequency offset was applied, the chip rate remained the same but the BW was reduced to 1.7 MHz on the European link and 1.6 MHz on the transatlantic link (green).

As a result of this configuration, an important degradation on the OP-NIST link, appeared.

Finally, we present the frequency stability of two-way links using the same satellite and the new transponder but after the application of a frequency offset on the European and transatlantic links (pink), which is the current configuration.

By comparing all the presented stabilities, we conclude that, at the present, the stability degradation is obvious on both links.

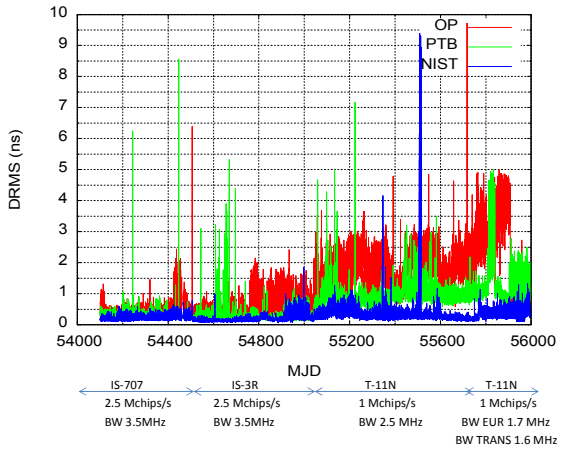

Figure 1. DRMS variation of the OP ranging signal over the last five years.

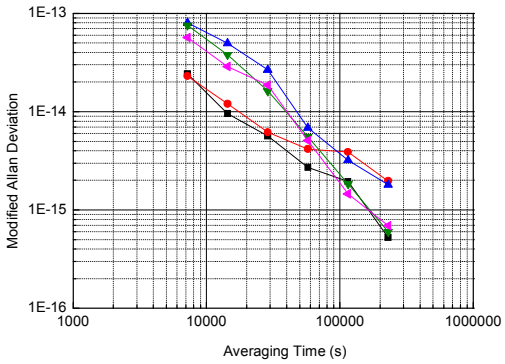

Figure 2. Frequency stability of the OP-PTB link.

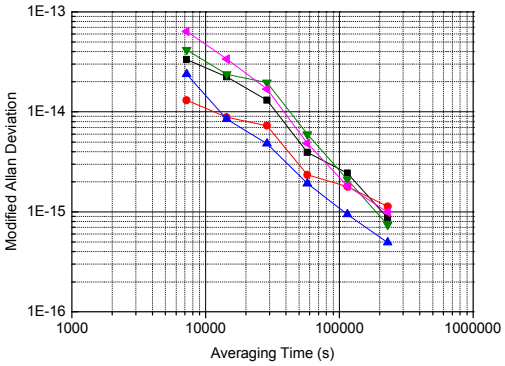

Figure 3. Frequency stability of the OP-NIST link.

In this paper, we focus on the European link and analyze the impact of the principal configuration changes such as: satellite change, code variation, clock change, frequency offset, transmit power, received power, carrier to noise ratio (C/No), link stability and diurnal effect.

III. SATELLITE CHANGE

The CCTF working group on TWSTFT has defined with the satellite provider some fixed satellite services concerning the allocated bandwidth. Actually the satellite T-11N is used by the TWSTFT network for European and transatlantic links. Since 2007, two satellite's changes have occurred, the first one in February 2008 from IS-707 to IS-3R and the second one in July 2009 from IS-3R to T-11N.

According to Fig. 4, the carrier to noise ratio of OP ranging signal remained in the same level after the first satellite change while the received power was decreased by 12 dB. Concerning the second satellite change, Fig. 5 shows that the carrier to noise ratio increased, but the overall performance was not improved because of the reduction of the chip rate and the BW which is confirmed in Fig. 1 and Fig. 2.

In July 2011, after the satellite's transponder change which caused a reduction of the allocated BW, the carrier to noise ratio of OP ranging signal dropped by around 7 dB without changing any parameter of the station, the received power level remained the same (see Fig. 6).

We can conclude that having a better carrier to noise ratio does not necessarily mean the improvement on the link stability, because of other effects.

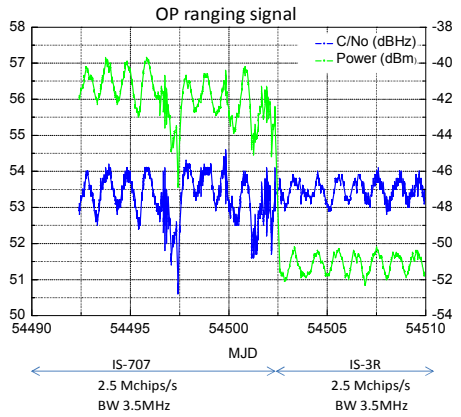

Figure 4. Impact of the satellite change on the carrier to noise ratio and received power of OP ranging signal.

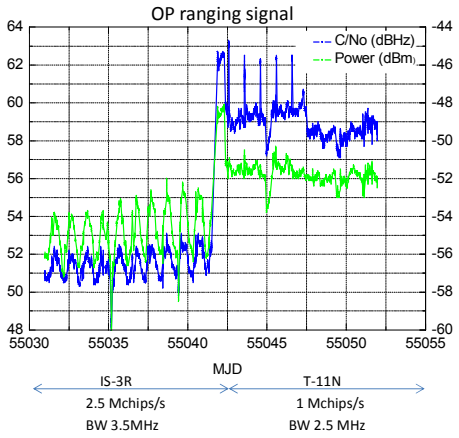

Figure 5. Impact of the satellite, chip rate and BW changes on the carrier to noise ratio and received power of OP ranging signal.

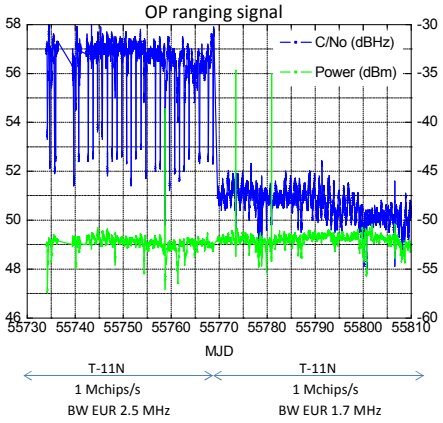

Figure 6. Impact of the satellite transponder and BW changes on the carrier to noise ratio and received power of OP ranging signal.

IV. FREQUENCY OFFSET

During regular two-way sessions, all the stations transmit the same nominal frequency using the Code Division Multiple Access (CDMA) properties of pseudo-noise coded signal. However, the use of SATRE codes at 1 Mchips/s which are not perfectly orthogonal has caused interference between coded signals generating higher DRMS values. Likely, with the recent introduction of offset frequencies in the European network, an obvious improvement of the DRMS values is observed specially for OP signal (code 0) which were reduced by a factor 4 as shown in Fig. 7. As an example, the frequency stability of link OP-IT and OP-ROA is presented in Fig. 8 which shows a slight improvement of the link stability after applying the offset.

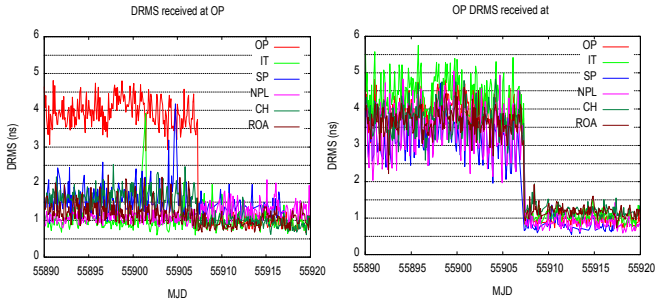

Figure 7. DRMS variation as a function of the frequency offset.

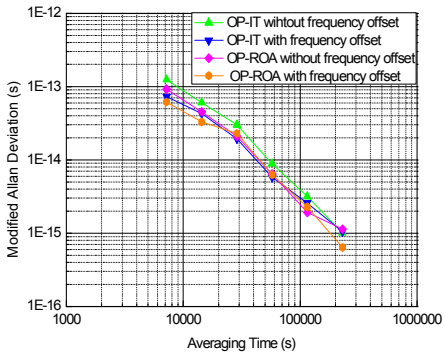

Figure 8. Frequency stability on the two-way links, with and without frequency offsets

V. TRANSMIT POWER

In the current TWSTFT schedule, every even hour, twelve European stations are transmitting and receiving signals through the satellite transponder in order to compare their time scales simultaneously. Thus, the two-way stations contribute to the noise in the received signal which decreases the carrier to noise ratio and increases the DRMS values.

At present, after the application of the frequency offset, we still have high DRMS values and a very bad carrier to noise ratio due to additional noise from outside the network on the European link. We observed also an increasing of the noise instability at one day and diurnal effects which has motivated the investigation to find a possible solution to the problem in order to have a European transponder as good as the transatlantic transponders in use.

The experiment involved OP, PTB and NIST. The test plan consists to use only two European stations during the odd hours with a transatlantic link as a reference in our study.
During each odd-hour slot : five sessions between OP and PTB, one session between PTB and NIST, one session between OP and NIST are scheduled. The sessions between PTB and OP are done with the same parameters as in the even hours except for the incident power at each site (see Table I).

TABLE I. TRANSMIT POWER VARIATION TEST

Links	Transmit power (dBm)
OP21-OP21	-21(nominal power)
OP11-PTB11	-24
OP21-PTB21	-21
OP31-PTB31	-18
OP41-PTB41	-15
OP51-PTB51	-12

Fig.9 reveals a strong dependency between the transmit power and the received power. After 30 days of test, we have adjusted the received power to keep the level than during regular sessions, at the modem input.
The C/No of signals received at OP is shown in Fig. 10. We deduce that higher transmit power increases the carrier to noise ratio. A small degradation of the C/No of PTB signals received at OP during odd hours is observed after the application of the received power adjustment at OP.
Based on the results displayed in Fig. 11, the following observations are made:

- The fluctuations on the DRMS of PTB01 signal received at OP are still high;
- By comparing the links OP21-PTB21 and OP01-PTB01 from one side, and OP21-NIST21 and OP01-NIST01 from the other side, we deduce that the reduction of the DRMS is clearly due to the use of a quiet transponder channel during odd hours;
- There is no significant change in the DRMS of OP signal received at NIST during odd and even hours;
- Higher transmit power leads to lower DRMS;
- No significant change after adjusting the received power except a small degradation of OP signals DRMS received at PTB.

The time deviation (TDEV) shown in Fig. 12 reveals a very good achievement on a European link stability during the test, reaching a value below 40 ps at 1 day (OP31-PTB31 link).
As a conclusion, one principal factor which has leaded to the improvement of the stability of the two-way links and to the reduction of the diurnal effect is the use of a quiet transponder during odd hours with appropriate parameters to apply at two stations in comparison of a selected link.

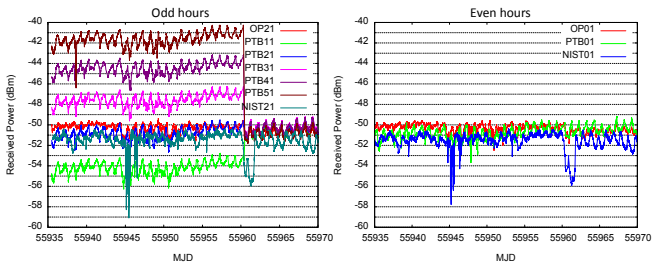

Figure 9. Variation of the received power as a function of the transmit power.

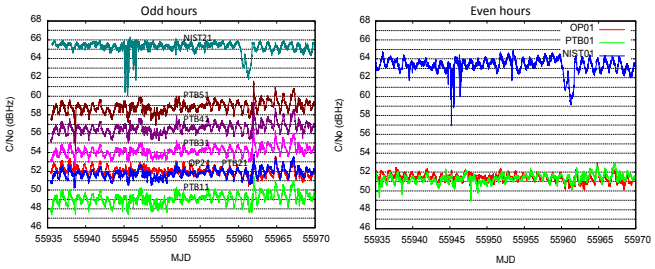

Figure 10. Variation of the carrier to noise ratio of the received signals as a function of the transmit power.

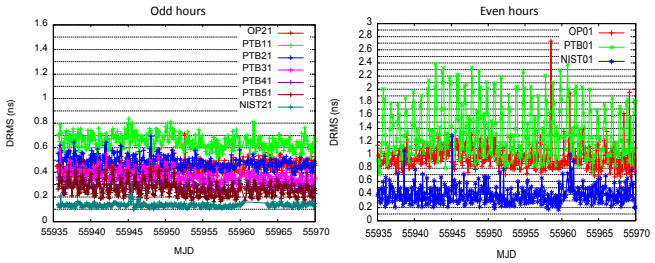

Figure 11. Variation of the DRMS as a function of the transmit power.

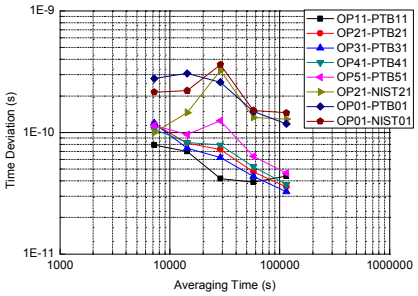

Figure 12. Variation of the time deviation as a function of the transmit power.

VI. CODE IMPACT

The microwave satellite simulator developed at LNE-SYRTE [5], permits to determine the internal delay difference in the TWSTFT earth station. By emitting a signal using the satellite simulator with different chip rates, we measure the signal delay in each configuration. Fig. 13 shows that the residual noise fluctuations at 1 Mchips/s code are higher than for the other codes. In consequence, the noise fluctuations could be decreased by using a higher chip rate. Since we are limited by the use of 1 Mchips/s, other solutions to reduce the measurements noise should be investigated.

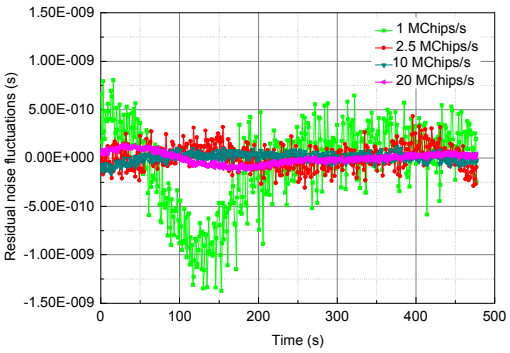

Figure 13. Variation of the residual noise fluctuations as a function of the chip rate.

VII. CLOCK CHANGE

In order to observe the impact of the maser clock change on the stability of the two-way links, the comparison of time deviation presented in Fig. 14 on OP-PTB and OP-NIST links with two different clocks at OP shows that the change of OP maser clock (HM890 → HM889) has clearly improved the links stability in the long term.

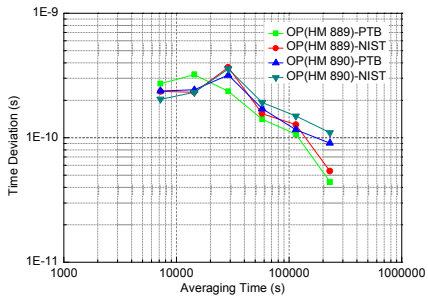

Figure 14. Impact of the used of different OP Maser clocks on the link stability.

VIII. CONCLUSION

After the presented analysis of the contribution of each studied parameter on the two-way measurements noise, we conclude on the following observations:

- The code 0 at 1Mchips/s seems to be more sensitive to interference than the other codes;
- The 1 Mchips/s codes present orthogonality problems which caused interference between two-way signals;
- By applying the frequency offset, the codes interference has been reduced;
- By increasing the transmit power, DRMS and the carrier to noise ratio have been improved;
- The use of a quiet transponder at 1Mchips/s improves the DRMS, measurement noise, diurnal effect and links stability;
- An excellent stability (40 ps at 1 day), using 1 Mchips/s, can be obtained within the European two-way network if all of the above requirements are respected.

And one question: should we modify the two-way schedule to achieve the best performance on the European two-way links?

ACKNOWLEDGMENT

The authors would like to thank the members of the CCTF WG on TWSTFT for their support. A special thank to D.Piester (PTB) and V. Zhang (NIST) for their fruitful contribution to some tests presented in the paper.

REFERENCES

[1] A. Bauch et al., "Comparison between frequency standards in Europe and the USA at the 10^{-15} uncertainty level," Metrologia 43(1), pp. 109-120, 2006.

[2] D. Piester, A. Bauch, J. Becker, E. Staliuniene and C. Schlunegger, "Studies on Measurement Noise in the European TWSTFT Network," Proc. of 2007 Joint IEEE International Frequency Control Symposium (IFCS) and Exposition and the 21st European Frequency and Time Forum (EFTF), pp. 1194-1199, 2007.

[3] P. Merck and J. Achkar, "Typical combined uncertainty evaluation on the Ku band TWSTFT link," 19th European Frequency and Time Forum, Besançon, France, 2005.

[4] "The operational use of two-way satellite time and frequency transfer employing pseudorandom noise codes," Rec. ITU-R TF.1153-3, 2010.

[5] J. Achkar "Design, realization and application of a satellite simulator in a TWSTFT station," 40th European Microwave Conference, pp. 1516-1519, 2010.

Improvement of comparisons between T2L2 & RF Links

Philippe Guillemot
CNES – French Space Agency
Toulouse, France
philippe.guillemot@cnes.fr

Etienne Samain, Pierre Exertier
GeoAzur, Observatoire de la Côte d'Azur
Grasse, France
etienne.samain@oca.eu, pierre.exertier@oca.eu

Philippe Laurent, Joseph Achkar, Daniele Rovera
SYRTE, Observatoire de Paris
Paris, France

Sylvie Leon
CNES – French Space Agency
Paris, France

***Abstract*— The Time Transfer by Laser Link (T2L2) experiment, developed by both CNES and OCA, performs ground to ground time transfer over intercontinental distances. The principle is derived from laser telemetry technology with dedicated space equipment designed to record arrival time of laser pulses at the satellite. Using laser pulses instead of radio frequency signals, T2L2 permits to realize some links between distant clocks with time stability of a few picoseconds and accuracy better than 100 ps.**

The T2L2 space instrument on board the satellite Jason 2 is in operation since June 2008. Several campaigns were done to estimate both the ultimate time accuracy and time stability capabilities. A first comparison between T2L2 and RF links was performed in 2010 from a campaign between the Observatoire de Paris and the Observatoire de la Côte d'Azur. This campaign required the installation of a transportable laser station in Paris and a first calibration of the links between the laser stations in Paris and Grasse and the local time references. It has demonstrated a phase difference between T2L2 and GPS Carrier Phase or TWSTFT lower than 2 ns rms during 2 months.

Since that campaign, T2L2 data processing has been widely improved. This will permit to envision a most extensive comparison between laser and RF techniques. This paper will present some new results of these comparisons in a common view configuration.

I. INTRODUCTION

Optical time transfer is an evolution of RF techniques that takes advantage from optical signals such as higher modulation bandwidth, insensitivity to ionosphere and mono carrier schemes to improve the performances of remote clocks comparisons [1]. T2L2 is a time transfer technique based on laser ranging network at ground and a dedicated space segment. The project, developed by CNES (Centre National d'Etudes Spatiales) and OCA (Observatoire de la Côte d'Azur), has been launched in 2008 on the Jason-2 satellite for a 3 years mission. A first extension until the end of 2012 was decided in June 2010.

T2L2 relies on the propagation of laser pulses between the clocks to be synchronized. It provides the capability to compare today's most stable frequency standards with unprecedented stability and accuracy. Expected T2L2 performances are in the 100 ps range for accuracy, with an ultimate time stability about 1 ps over 1,000 s and 10 ps over one day. A preliminary evaluation of the performances of T2L2 has been done during the validation phase of the mission, in 2008 [2]. Then the experimental program has allowed a first characterization of the stability [3][4] and the accuracy [5] of the time transfer. The objectives of the T2L2 experiment on Jason-2 are threefold:

- Technological validation of optical time transfer, including the validation of the experiment, its time stability and accuracy and of one way laser ranging.
- Characterization of the onboard Doris oscillator for Jason-2 purposes and a contribution to the Jason-2 laser ranging core mission.
- Scientific applications such as time and frequency metrology (comparison of distant clocks, calibration of RF links), fundamental physics (such as anisotropy of the speed of light), earth observation or very long baseline interferometry (VLBI).

Among these objectives, the last T2L2 campaigns were focused on the ground to ground time transfer in common view configuration for the comparison between T2L2 with RF techniques like Two Way Satellite Time and Frequency Transfer (TWSTFT) and GPS Carrier Phase (GPS-CP).

II. PRINCIPLE

The T2L2 elementary block is a space to ground time transfer between the ground clock linked to the laser station and space clock of the satellite. The ground to ground time transfer between several remote clocks at ground is obtained through such individual space to ground time transfers. It can be obtained in a common view mode, when the distance between the laser stations is smaller than 5000 km, or in a non-common view mode when the distance is larger.

The laser station includes a telescope, a pulsed laser, some photo detection devices and two event timers connected to the ground clock, one to time tag the start event, the other for the return. The energy by pulse is between 400 µJ to 200 mJ and the pulse width is in the range of 20 ps up to 200 ps. The laser rate is between 5 Hz to 2 kHz. Laser stations can range the satellite every 2 hours, 5 to 7 times a day when the weather conditions are favorable.

The space instrument (Fig. 1) includes a photo detector and an event timer linked to the space clock and a laser ranging array (provided by the JPL) used to reflect the laser pulse toward the laser station. The space clock is an ultra-stable oscillator (USO) fundamentally used by the Doris equipment.

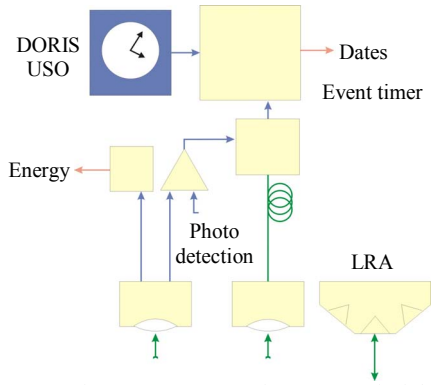

Figure 1. T2L2 Space instrument principle

For a given laser pulse emitted by the laser station one get two dates at ground and one date at the satellite. From these 3 dates (which are called a triplet) we can extract the time delay between the ground clock and the space clock.

T2L2 relies on the laser ranging network which includes 40 international laser stations. Among them, 16 stations provide the full rate data needed for the triplets extraction (start, return and arrival onboard).

III. BACKGROUND

A. *Time transfert by laser link between OP and OCA*

A first comparison between T2L2, GPS and TWSTFT techniques has been performed in 2010 between the Observatoire de Paris (OP) and the Observatoire de la Côte d'Azur (OCA) thanks to a specific campaign of measurements. This campaign relied on the installation at OP of the French Transportable Laser Ranging Station (FTLRS) and at OCA of the Transportable Atomic Fountain (FOM). Thus, the two labs at OP and OCA were equipped with cold atoms atomic fountains, GPS receivers, TWSTFT stations and laser ranging stations, all of them synchronized by an hydrogen maser.

The campaign started in June 2010 and ended in October of the same year. 222 laser passes was acquired in a common view configuration between OP and OCA. To compute laser time transfer, a first prototype of data processing has been developed by the OCA team : From each pass acquired, an equivalent point representing the 'average' value of the time difference and the 'average' value of the date is computed. A low order polynomial is fitted to the pass in order to compute the 'average value' of the time difference from this polynomial at the 'average' date of the data of the pass (Fig. 2).

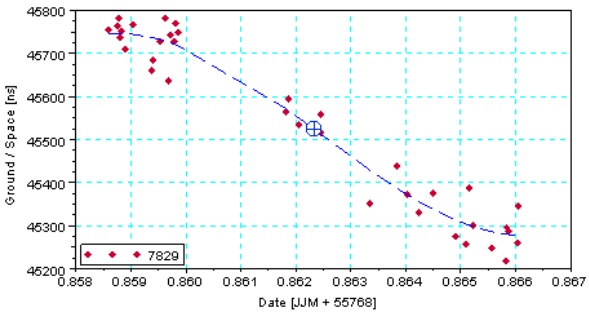

Figure 1. Example of groud to space time transfert processing with one point per pass : raw data (red dots), polynomial fit (blue line) and equivalent point (blue cross)
(FTLRS, Obs. de la Côte d'Azur, 26/07/2011)

B. *First comparaison between T2L2, GPS & TWSTFT*

TWSTFT, GPS-CP and T2L2 data was acquired during several months at both OP and OCA. GPS and TWSTFT were processed by OP with standard software (NRCan software for GPS-CP processing). These results, together with the T2L2 time transfer permitted to compute a first global comparison between all these techniques. Regardless of absolute aspects (the links are not calibrated), the noise between T2L2 and GPS or TWSTFT remains within 2 ns during the 60 days of the campaign, with no relative drift, at least at the nanosecond level [5].

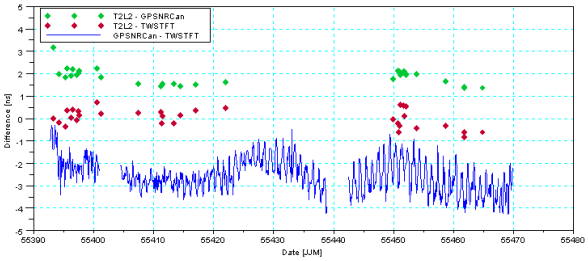

Figure 2. Comparison between T2L2, GPS and Two Ways on the link OP-OCA : T2L2-GPS (green), T2L2-TWSTFT (red) and TWSTFT-GPS (blue)
(The offset between each curve was adjusted to facilitate the graph reading)

These first results are in accordance with the classical long term stability of microwave time transfer systems. They need however to be strengthened by widened comparisons to other links.

IV. IMPROVEMENT OF DATA PROCESSING

In the middle of the year 2011, it was decided to redefine the T2L2 data processing with 3 objectives: improve the performance of the T2L2 time transfer, increase the time resolution in order to be able to analyze the behavior of clocks inside the passes and simplify the process of calculation of the ground to ground time transfers in common view configuration. It led to us to implement two major modifications, one concerning the periodicity of the data and the other concerning the filtering applied to produce them:

- Instead of having a single equivalent point by pass, we now compute a point every round second in the T2L2 local timescale. It allows to have synchronous data, directly usable for a rapid calculation of a ground to ground time transfer by simple difference.
- The filtering of the data was accordingly adapted, by using a process with sliding window. The window allows to isolate a block of elementary data from which we first identify the behavior of the onboard clock, by adjusting a frequency offset and a frequency drift, and then compute the ground to space time transfer. The window is centered around a round second, and moved from one second to the next one. Time transfer is computed only if there is a sufficient number of point in the window. A mechanism to shift the window and to weight the data has been set up to manage the beginning and the end of passes (or of pieces of passes). Obviously, the length of the windows have an impact on the performance of the time transfer, by filtering short term instabilities, and have to be optimized with respect to the performances of onboard and ground clocks. For laser station synchronized by hydrogen masers, this length as been set to 65 s.

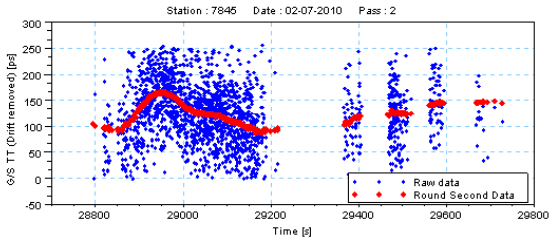

Figure 3. Example of groud to space time transfert processing with one point per pass : raw data (blue dots) and filtered at each round second (red dots) data (MeO, Obs. de la Côte d'Azur, 02/07/2010, on board clock drift removed)

All the data, raw and round seconds ones, are available on the T2L2 web site at https://t2l2.oca.eu/.

V. IMPROVED COMPARAISON OF T2L2 & GPS

A. *Reprocessing of OP-OCA link*

It seemed interesting, before going farther, to validate the performances of the new T2L2 data processing. We thus leaned on the results of the 2010 campaign and on the link OP-OCA to proceed to a new comparison between GPS-CP and T2L2. For this new comparison, we used the software developed by CNES which uses the single difference integer ambiguity method to resolve the ambiguities of phase [6].

One can notice that GPS-CP and T2L2 solutions are not synchronized. GPS-CP solutions are computed every 300s in UTC time scale. T2L2 solution are computed, when we have data, every round second in T2L2 time scale and then T2L2 epochs are transposed into UTC time scale. To synchronize T2L2 and GPS data in order to compute the differences between the 2 methods, we chose to interpolate GPS-CP solutions at T2L2 epochs.

The result of the comparison is given on Fig. 4. What we see first is the differences between T2L2 and GPS-CP solutions which remain within 1 ns peak-to-peak: it is two times better than for the previous comparison. Data on Fig.4 seems also to exhibit a parabolic signature. The comparison of NRCan solution and CNES solution for GPS-CP time transfer (Fig. 5) exhibits nearly the same behavior. It is not possible to be affirmative on that point, but it seems that at least a part of the signature observe on Fig.4 comes from the GPS-CP processing and not from T2L2.

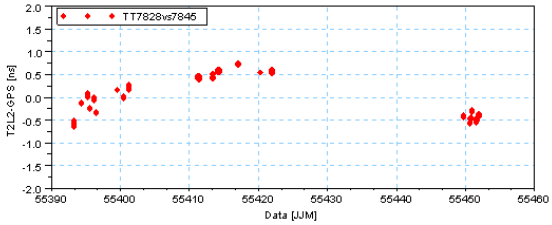

Figure 4. Link OP-OCA : Comparaison between T2L2 and GPS-CP time transfer (uncalibrated data, an offset has been removed)

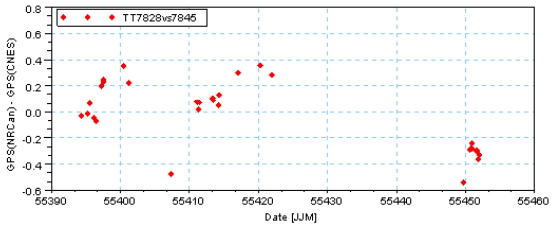

Figure 5. Link OP-OCA : GPS-CP, comparaison between NRCan solution and CNES solution.

B. *Extension of T2L2 vs GPS-CP comparisons to new links*

Among laser stations involved in the 2010 campaign, only two of them were able to gather the 3 following criteria: common view with OP and OCA, synchronized by H-maser and regular laser activity : Herstmonceux (HERL, UK) and Wettzell (WTZL, DEU). It is therefore natural to use these two stations for a first extension of the comparisons between T2L2 and GPS-CP time transfer.

Fig. 6 presents the differences between GPS-CP solutions and T2L2 solutions for the link between OCA and HERS. The differences exhibit a drift of 6 ns per day, which represent the drift of the H-Maser at HERL. This drift is compensated in laser CRD data send by HERL whereas it is not the in RINEX data. This is why it appears as a residual of the comparison between GPS and T2L2. If we removed this drift, the standard

deviation of the residuals is about 5 ns, a little bit higher than the one we observed on the link between OP and OCA.

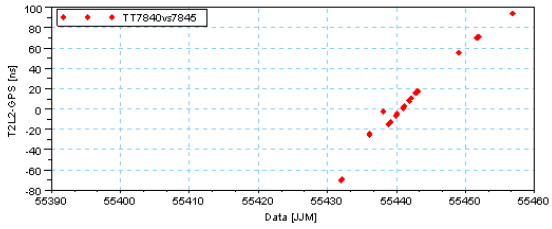

Figure 6. Difference T2L2 – GPS, link OCA – HERL
The drift of 6 ns/day is the one the Maser at HRST
(Data are not calibrated, an offset was removed)

Fig. 7 presents the differences between GPS-CP solutions and T2L2 solutions for the links between WTZL and OP and between WTZL and OCA. The two plots exhibit a drift of about 1 ns per day. If we removed this drift, the standard deviation of the residuals is here also of some nanoseconds.

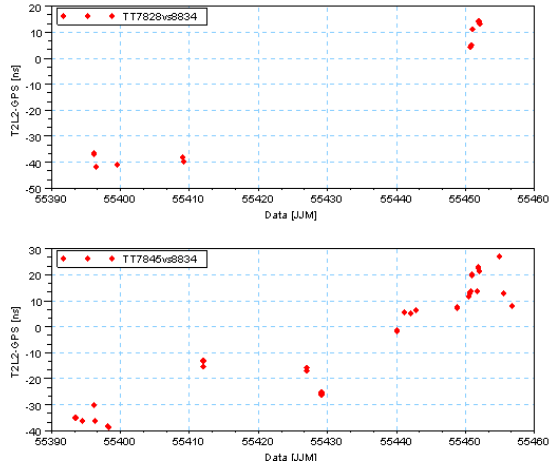

Figure 7. Difference T2L2 – GPS, links OP-WTZL (top) and OCA-WTZL (bottom)
(Data are not calibrated, an offset was removed)

VI. CONCLUSION

T2L2 data processing was improved to produce ground to space time transfer every round second. An optimization of the data filtering allows an improvement of the performance of the T2L2 time transfer of at least a factor 2.

The new comparisons between T2L2 and GPS-CP confirm this : the two system are now consistent at the nanosecond level.

To go farther, we foresee to set up a more systematic comparison of T2L2 with GPS-CP, at least on the links between OCA, WTZL and HERL, maybe with some new stations driven by H-Maser or cesium clocks,.. To make it easier, it could be interesting to produce some T2L2 data synchronized with GPS data. That could be done first by introducing a continuous T2L2 time scale corrected from the drift of the onboard clock (under development) and then by producing laser data in a RINEX like format.

ACKNOWLEDGMENT

The authors wish to thanks the FTLRS and MeO teams from the Observatoire de la Côte d'Azur for operating the SLR stations, SYRTE staff for their welcome and support at the Observatoire de Paris, ILRS and all the stations involved in the T2L2 international campaign for their contribution to the T2L2 project through the availability of SLR data, Wettzell and Herstmonceux teams for their welcome during calibration campaign and for their help to interpret GPS results, and NRCan (NRCan software) and F. Mercier (CNES, GPS PPP software) for their software and support.

REFERENCES

[1] P. Fridelance, E. Samain and C. Veillet, "T2L2 - Time transfer by laser link : A new optical time transfer generation", Experimental Astronomy Vol.7 Num.3 Sept.97

[2] Ph. Guillemot, E. Samain, P. Vrancken, P. Exertier, S. Leon, "*Time transfer by laser link - T2L2 : An Opportunity to Calibrate RF Links*", Proceedings of the PTTI 2008, pp 95-106

[3] E. Samain, P. Exertier, Ph. Guillemot, F. Pierron, D. Albanese, J. Paris, J.-M. Torre, I. Petitbon, S. Leon, "*Time Transfer by Laser Link T2L2 : First Results*", Proceedings of the EFTF/IFCS 2009

[4] Ph. Guillemot, P. Exertier, E. Samain, F. Pierron, J.-M. Torre, S. Leon, "*Time Transfer by Laser Link - T2L2 : Results of the First Year of Operation*", Proceedings of the PTTI 2009, pp 67-79

[5] E. Samain, P. Exertier, Ph. Guillemot, Ph. Laurent, F. Pierron, D. Rovera, J.-M. Torre, M. Abgrall, J. Achkar, D. Albanese, C. Courde, K. Djeroud, M. Laaz-Bourez, S. Leon, H. Mariey, G. Martinot-Lagarde, JL. Oneto, J. Paris, M. Pierron, H. Viot, "*Time transfer by laser link - T2L2: Current status and future experiments*", Proceedings of the IFCS/EFTF 2011

[6] J. Delporte, F. Mercier, D. Laurichesse, O. Galy, "GPS carrier phase time transfer using single-difference integer ambiguities", International Journal of Navigation and Observation, Hindawi Publishing Corporation, Volume 2008, Article ID 273785.

Near real-time comparison of UTC(k)'s through a Precise Point Positioning approach

Pascale Defraigne, Quentin Baire
Royal Observatory of Belgium
Brussels, Belgium
email: p.defraigne@oma.be

François Lahaye
Natural Resources Canada, Geodetic Survey Division
Ottawa, Canada
email: francois.lahaye@nrcan.gc.ca

Giancarlo Cerretto
Optics Division
INRIM (Istituto Nazionale di Ricerca Metrologica)
Torino, Italy
email: g.cerretto@inrim.it

Daniele Rovera
LNE-SYRTE
Observatoire de Paris, LNE,CNRS,UPMC
Paris, France
Email: daniele.rovera@obspm.fr

***Abstract*—The time-transfer technique based on Precise Point Positioning (PPP) allows the comparison of atomic clocks with precisions at the level of hundred picoseconds. This paper presents the results obtained in near real-time using satellite orbit and clock information from IGS real-time streams and from the NRCan Ultra Rapid products (EMU). These results can be considered quite interesting for the National Metrology Institutes, providing a new tool for monitoring their UTC(k)'s. Two different PPP software tools have been used in this study, namely "Atomium" developed and operated at ORB and the NRCan-PPP soon to be operated at INRIM and LNE-SYRTE-OP in near real-time mode. This paper presents a quantification of the degree of equivalence of the results obtained from the analysis conducted using each software as well as the operational web page available at the Royal Observatory of Belgium, providing PPP solutions for the comparison of UTC(k)'s in near real-time.**

I. INTRODUCTION

The time-transfer technique based on Precise Point Positioning (PPP) has proved to be a very effective technique allowing the comparison of atomic clocks with precision at the level of hundred picoseconds, with latency of less than a few days [1,2]. PPP [3,4] is based on the joint analysis of GPS (and possibly GLONASS) dual-frequency code and carrier-phase measurements with a consistent modeling of these observations. It consists in an analysis of the ionosphere-free combinations of codes and carrier phases measured at one station to determine its position and its clock synchronization error at each observation epoch. This technique is widely recognized for its high resolution (1 pt/30 s) and high frequency stability, reaching 10^{-15} at averaging times of one day, thanks to the very low noise level of the carrier phases(see for instance [5,6]), enabling time transfer with a statistical uncertainty of 0.1 ns, when ignoring the uncertainty of the instrumental hardware delays calibration. The use of PPP for time and frequency transfer has been extensively studied and developed in the last years. Usually, Rapid or Final IGS products are used to remove the satellite clock errors from the measurements and to model the satellite positions. As these products are available after a minimum of 18 hours, we propose here to use either the NRCan Ultra Rapid products (EMU) generated hourly with a delay of 90 minutes after the last observation [7], or the IGS real-time products [8], to provide PPP solutions in a near real-time mode (latency down to some minutes). This capability can be considered quite interesting for the National Metrology Institutes, being provided with an additional tool for comparisons of UTC(k)'s or even primary frequency standards to help in the generation of an accurate and reliable national time scale. Two different software tools are used here for this task, namely "Atomium" developed at ORB [2] and the NRCan-PPP [4] soon to be operated at INRIM and LNE-SYRTE-OP in near real-time mode. These two computer software propose different approaches: Atomium is based on a least square analysis over a given data batch, providing one station position for the data batch, one clock solution at each observation epoch and one troposphere path delays with a chosen sampling rate, 2 hours in the present case. NRCan-PPP, on the other hand, performs a sequential least square analysis with noise constraints on the time-varying parameters while generating one station position for the data batch. This paper presents a quantification of the degree of equivalence of the results obtained from the analysis conducted with both software tools, using different sets of products for the satellite clocks and orbits. A web service is furthermore presented, providing a comparison between several UTC(k)'s in near

real-time computed at the Royal Observatory of Belgium using Atomium.

II. SOLUTIONS BASED ON ULTRA RAPID AND REAL-TIME PRODUCTS

We have tested two sets of satellite clocks and orbits which are available with a very short latency. The first set is the IGS real-time clocks and orbits which can be obtained from the streams delivered in real-time by the Ntrip Broadcaster *Products.IGS-IP.Net*. These streams contain corrections with respect to the GPS broadcast ephemerides and clocks. The stream ICG01 was selected; it delivers corrections corresponding to the IGS Ultra-Rapid orbits (IGU) and real-time computed clocks. As the real-time broadcasted orbits are the IGU, we prefer to use directly the IGU SP3 files (standard format for IGS orbits) and use only the real-time clocks broadcasted by the stream, add these corrections to the satellite clocks given in the navigation message and generate RINEX clock files, i.e. the standard format for satellite clock products used by Atomium. The second source of precise satellite orbit and clock are the NRCan Ultra-Rapid products, named EMU, which are available with 1.5 hour latency in the same format as the IGS products, i.e. SP3 and RINEX clock format.

Figure 1 and Figure 2 present clock solutions obtained using Atomium and the different sets of satellite clock and orbits: Rapid IGS products, EMU and IGS real-time. Two time links are proposed here: IENG-PTBB, between Torino (Italy) and Braunschweig (Germany), distant by about 800 km, and USNO-PTBB, distant by about 6000 km. For all the stations involved here the receiver is driven by an active hydrogen maser. The data collected during four weeks were analyzed, from February 20 to March 19, 2012. The solutions have been computed for each day separately, using the data from 0:00 to 23h55, estimating a station clock error every 5 minutes. Only GPS data were used in this study. Due to some imperfections in the clock products used, some outliers appear in the solutions. These outliers were not plotted for visibility, but are indicated as small filled boxes. Empty boxes represent periods where no solution could be computed due missing satellite clocks, e.g. due to some interruption in getting the real-time streams. Figures 1 and 2 also reproduce the differences between the solutions obtained with IGS Rapid (IGR) products and those obtained using the real-time or EMU products. The quality of the solution depends on the station pairs: differences with respect to the solution based on IGR products were observed up to 1 nanosecond for PTBB-USNO and limited to 0.3 ns for IENG-PTBB. This could be explained by the spatial correlation of orbital (positions + clocks) errors which cancels out in the difference of 2 PPP solutions of nearby stations. Further tests will be conducted in the future to confirm this statement. Some epochs with bad orbits/clocks however present large discrepancies, which should be solved by an improved data cleaning within Atomium. Using the EMU products, except for isolated outliers not properly detected/mitigated by Atomium, the differences with the solutions obtained using IGS rapid products is lower than 0.2 ns. For the EMU as well as for the IGS real time products, no significant offset was observed with respect to the solution obtained with IGS Rapid products. The standard deviations of the differences are between 100 and 250 ps for the IGS real-time products, and between 30 and 150 ps for the EMU products as shown in Table 1.

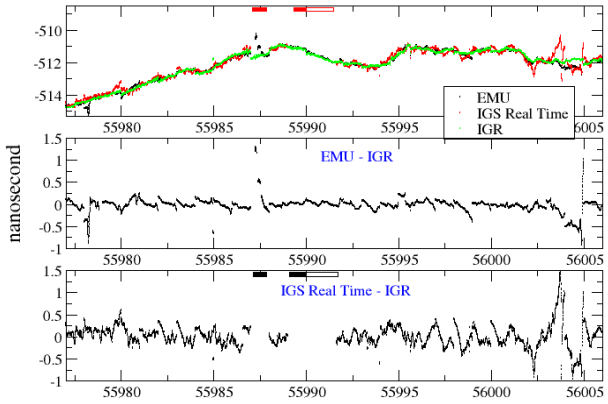

Figure 1. USN3-PTBB comparison between the time transfer solutions obtained with Atomium, using the IGR products, the EMU products and the IGS Real-Time products (IGC01) over one month. The filled boxes in the upper part correspond to outliers and empty boxes correspond to periods where no solution could be computed, e.g. due missing real-time clocks.

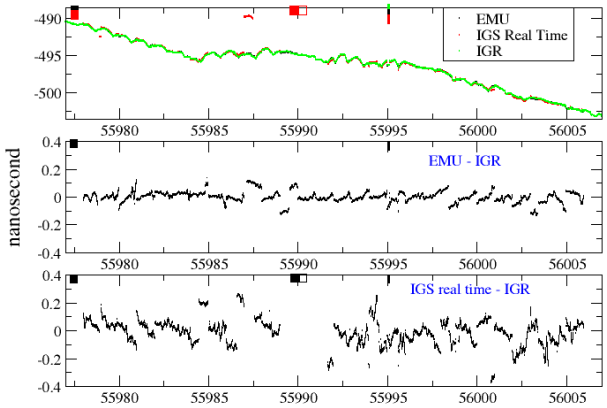

Figure 2. Same as Figure 1 for IENG-PTBB.

Table 1. Averages, standard deviations and maximum (in ps) of the differences between the clock solutions obtained from EMU products or IGS real-time products and the IGR products during one month.

	IGS RT			EMU		
	Av.	σ	max	Av.	σ	max
USN3-PTBB	17	238	1664	-16	149	1282
IENG-PTBB	10	108	978	0	37	138

The results from comparisons between PPP solutions obtained with EMU or IGR orbits are in agreement with the conclusions of [9], i.e. no significant bias and a standard deviation of about 50 to 200 ps. The results obtained with the IGS real-time products show more disagreement with the solutions obtained with IGR products which is an indication of a worse accuracy of the real time satellite clocks with respect to the EMU clocks.

III. DEGREE OF EQUIVALENCE BETWEEN ATOMIUM AND NRCAN PPP RESULT

In order to cross-validate the results obtained in [9] and this study, we computed the differences between the solutions obtained with the two software tools with each of the three satellite products described before. These differences are plotted in Figures 3-5. The averages and standard deviations for the PPP solutions of individual stations and of the links are reported in Table 2. These quantities have been computed after removing the outliers, considering as outliers differences larger than 1.5 ns. From Figures 3-5 it can be seen that more outliers appear in the Atomium solutions than in the NRCan-PPP solutions, which indicates that Atomium could be improved for the detection of data/orbit/clock errors. Apart from these outliers, the average differences reported in Table 2 indicate that no significant offset exists between the two sets of results. Furthermore, the standard deviation of the differences between the solutions obtained with the two software tools is about 50 ps when IGR products are used, and 2 to 3 times larger when EMU or IGS real-time products are used, probably due to the orbit/clock errors in EMU/IGS real-time products affecting processes differently in each software: data editing, noise distribution, etc.

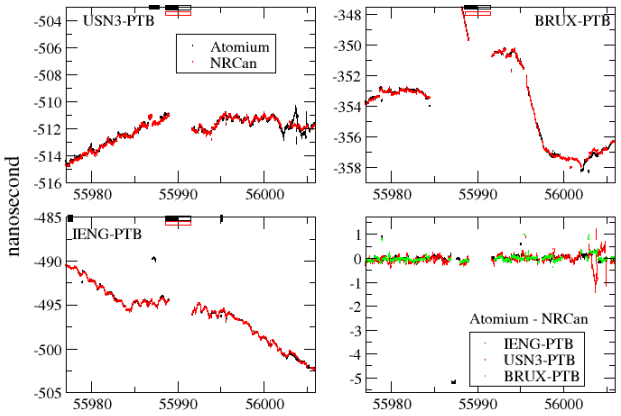

Figure 3. Comparison between the time transfer solutions obtained with Atomium and NRCan-PPP using the IGS real-time products over one month. The filled boxes in the upper part correspond to outliers and empty boxes correspond to periods where no solution could be computed, e.g. due missing satellite clocks. The differences between the two solutions are plotted in the lower right hand side picture for the three links.

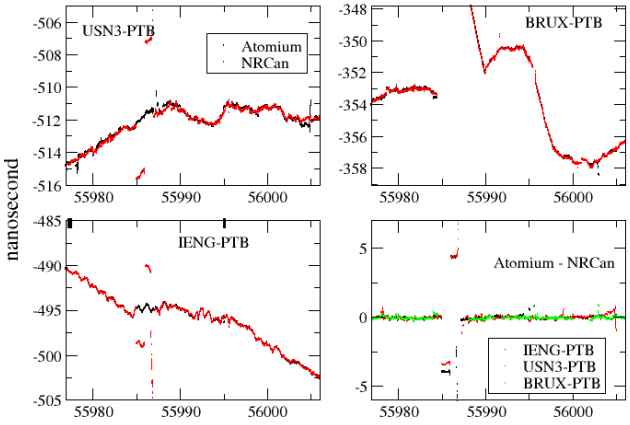

Figure 4. Same as Figure 3 for solutions based on EMU products

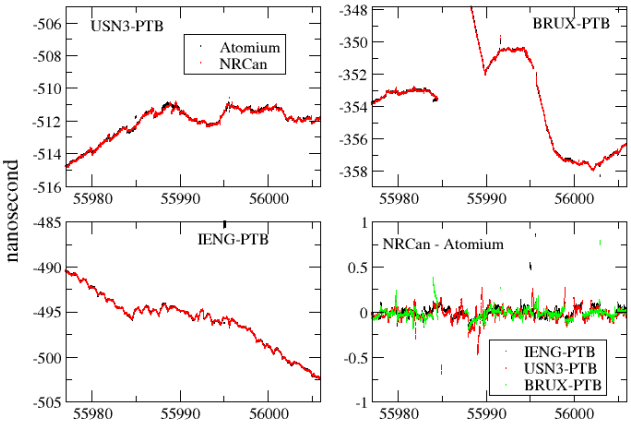

Figure 5. Same as Figure 3 for solutions based on Rapid IGS products.

Table 2. Averages and standard deviations (in ps) of the differences between Atomium and NRCan PPP results.

	Using IGR products		**Using EMU products**		**Using IGS RT clocks and IGU orbits**	
	Av.	σ	Av.	σ	Av.	σ
PTBB	22	50	37	83	14	110
USN3	2	55	5	156	-7	196
IENG	20	40	6	139	23	99
BRUX	10	39	11	85	16	101
USN3-PTBB	-20	75	-30	169	-27	191
IENG-PTBB	-1	60	-8	86	13	116
BRUX-PTBB	-13	67	-25	98	0	131

IV. UTC(K) MONITORING IN NEAR REAL-TIME USING GNSS PPP

An operational computation of near real-time clock solutions has been developed at the ROB, based on Precise Point Positioning (PPP) with the software tool Atomium. Only data from the GPS constellation are used. The solutions are computed each hour (at minute 15) using a 24h data batch built from the hourly RINEX files. The results are then stored in a data bank and a web page proposes pictures based on the last update of the data bank. The computation done with real-time IGS products uses 24h data ending at the current hour. After 2 hours, the solutions in the database (and hence in the pictures) are replaced by new solutions computed with the Ultra-Rapid products (EMU) produced by the NRCan IGS analysis center. This run indeed uses 24h data ending 2h before the current hour. Two days later, the solutions in the data base are replaced by those computed with the Rapid IGS products, and 2 weeks later by the solutions computed with the Final IGS products. The solutions proposed on the website are therefore those obtained using

- Final IGS orbits and clocks for dates prior to two weeks before the present week;
- Rapid IGS orbits and clocks for the two previous weeks and the up to two days before present;
- EMU products for the two previous days and the present day up to the end of current hour –3;
- IGS real-time clocks and IGU orbits for current hour –2 and current hour –1.

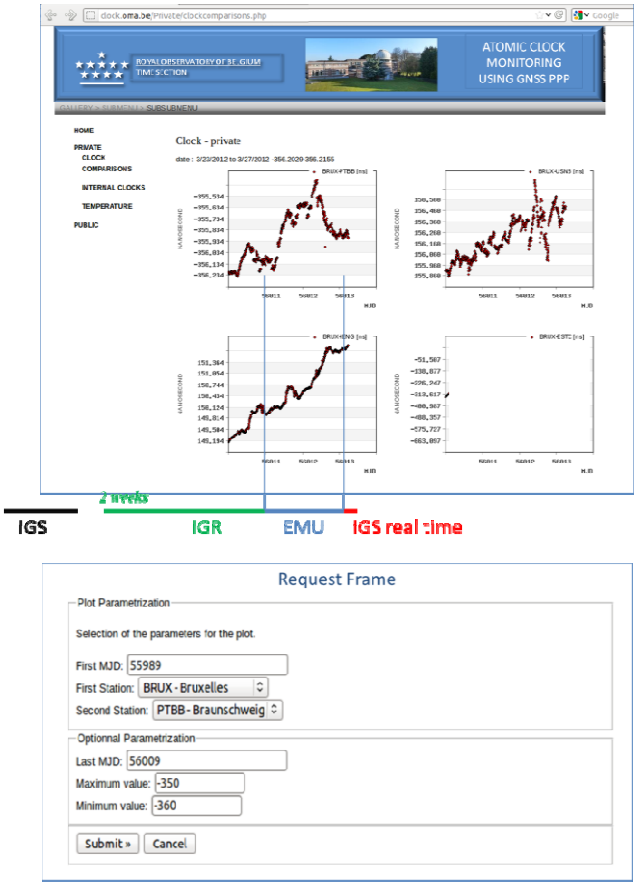

Figure 6. Web page proposed by the ORB for monitoring of UTC(k)'s.

The web page http://clock.oma.be (Figure 6) can be visited on request. By default the solutions are presented for the previous three days plus the present day up to the beginning of the current hour. The plots are updated each hour. A different period of time can also be visualized for a comparison between two stations of the proposed list using the request frame appearing in the bottom of the page. Laboratories willing to be included in the computation may contact the ORB. Only hourly (resp. daily) RINEX files are required for hourly (resp. daily) update of the solution.

V. CONCLUSION

Using Ultra-Rapid or real-time products for satellite orbits and clocks, it is now possible to compute near real-time PPP solutions and hence provide a near real-time clock monitoring. This paper proposed a first study of the quality of PPP solutions obtained using the IGS real-time products (i), and a comparison between these solutions and those which can be obtained with the Ultra-Rapid EMU products (ii) delivered with a 1.5 hour delay by NRCan as well as those obtained with the IGS Rapid products (iii). The results show that the standard deviations of the differences between (i) and (iii) is about two times larger than those of the differences between (ii) and (iii), which indicates a worse quality of the real-time products with respect to the EMU products. However, with a standard deviation of 250 ps on an intercontinental link during one month, we can still consider that a jump of some nanosecond can easily be detected by the near-real time comparisons based on the real-time IGS products. A deeper study should be conducted to determine the minimum size of a frequency shift that can be detected. Two software tools were used and their results compared: Atomium and NRCan-PPP. No significant offset exists between the two sets of results. More outliers appear in the Atomium solutions than in the NRCan-PPP solutions, which indicates that Atomium could be improved for the detection of data/orbit/clock errors. Apart from these outliers, the standard deviation of the differences between the solutions obtained with the two software tools is about 50 ps when Rapid IGS products are used, and 2 to 3 times larger when EMU or IGS real-time products are used, probably due to the orbit/clock errors in EMU/ IGS real-time products affecting processes differently in each software: data editing, noise distribution, etc.

A new service for monitoring atomic clocks connected to GNSS receivers is available at ROB, based on PPP computation using the Atomium software. The clock comparisons are provided with a delay of less than 1 hour using IGS real-time products. After 2 hours, the solutions in the database (and hence in the pictures) are replaced by new

solutions computed with the EMU Ultra-Rapid products produced by the NRCan IGS analysis center. Two days later, the solutions in the data base are replaced by those computed with the Rapid IGS orbits, and 2 weeks later by the solutions computed with the Final IGS orbits.

The ORB webpage therefore provides a near real-time monitoring of atomic clocks that can be used for monitoring of UTC(k)'s. Some jumps that appear in near real-time are however due to an imperfect data cleaning within Atomium and not to the clock. The new version of the software Atomium should solve for these remaining software-related issues.

ACKNOWLEDGMENT

The authors thank the IGS and the NRCan analysis center for the satellite clock and orbit products which allow us to process these near-real time clock comparisons.

REFERENCES

[1] F. Lahaye, D. Orgiazzi, G. Cerretto, "GPS time transfer using Precise Point Positioning for clock comparison", GPS world, November 2006, pp. 44-49.

[2] P. Defraigne, N. Guyennon, and C. Bruyninx, "GPS Time and Frequency Transfer: PPP and Phase-Only Analysis", *Int. J. of Nav. and Obs.*, vol. 2008, Article ID 175468, 7 pages, doi: 10.1155/2008/175468, 2008.

[3] J.F. Zumberge, M.B. Heflin, D.C. Jefferson, M.M. Watkinsand F.H. Webb, "Precise point positioning for the efficient and robust analysis of GPS data from large networks", Journal of Geophysical Research, vol. 102(B3), pp. 5005-5017, 1997.

[4] J. Kouba, and P. Heroux, "GPS Precise Point Positionning using GPS orbit products", GPS solutions, vol. 5, pp. 12-28, 2001.

[5] Th. Schildknecht, G. Beutler and M. Rotacher, "Towards sub-nanosecond GPS time transfer using geodetic processing technique", Proc. of the 4th EF TF, 1990, pp. 335-346.

[6] K.M. Larson, J. Levine, L.M. Nelson, and T. Parker, "Assessment of GPS carrier-phase stability for time-transfer applications". IEEE Trans. Ultrason., Ferroelect., Freq. Contr., vol. 47(2), pp. 484-494, 2000.

[7] Y. Mireault, P. Tétreault, F. Lahaye, P. Héroux, J. Kouba, "Online Precise Point Positioning: a new, timely serice from Natural Resources Canada", GPS World, vol. 19, no. 7, September 2008.

[8] http://www.rtigs.net/

[9] Cerretto, G., P. Tavella, F. Lahaye, Y. Mireault, D. Rovera, "Near real-time comparison and monitoring of time scales with Precise Point Positioning using NRCan Ultra-Rapid Products", IEEE Trans. Ultrason. Ferroelectr. Freq. Control, Vol. 59, No. 3, pp 545-551, 2012.

EURAMET Project 1156, GPSCALEU: Results of two years GPS receiver calibration campaign

Hector Esteban, Juan Palacio, Andreas Bauch*, Dirk Piester*, Giancarlo Cerretto+, Thorsten Feldmann^
Time Department, Real Instituto y Observatorio de la Armada (ROA), San Fernando, Spain
*Physikalisch-Technische Bundesanstalt (PTB), Bundesallee 100, 38116 Braunschweig, Germany
+Time Department, Istituto Nazionale di Ricerca Metrologica (INRIM), Torino, Italy
^TimeTech GmbH, Stuttgart, Germany

***Abstract*— Since 2010 ROA has supported the coordination of the EURAMET Technical Committee for Time and Frequency (TC-TF) Project 1156, GPSCALEU, a reaction from EURAMET TC-TF to Recommendation 2 of CCTF 2009: to study the characterization of GNSS equipment in use for establishing the time links between institutes contributing with their clocks to TAI. Starting that year, it was organized a GPS calibration campaign between three contributing laboratories: ROA (Spain), PTB (Germany) and INRIM (Italy). The time transfer results were achieved by using P3, and also carrier phase PPP comparison techniques. These results were also used to re-calibrate the TWSTFT (Two-Way Satellite Time and Frequency Transfer, TW for short) links between the involved laboratories, with an uncertainty slightly higher than GPS links.**

I. INTRODUCTION

GPS time and frequency transfer using code and phase multichannel GNSS receivers, commonly known as geodetic receivers, is among the most useful tools for remote clock comparisons. It is one of the most precise techniques in this field, in particularly when receiver clocks are compared to IGS-time using Precise Point Positioning software [1]. However, to provide accurate time transfer by means of a GPS link, it is necessary to carry out calibrations periodically to verify the long term stability of the equipment.

In 2011, ROA has repeated its calibration trips performed in 2008 with PTB [2] and in 2010 with PTB and INRIM, to improve the calibration accuracy and to check the reproducibility of the previous measurements of its time transfer links between these laboratories. The last calibration extended in time over several weeks, more than planned, but was still constrained to the summer time period. In this paper we report the calibration results, the long term stabilities of GPS and TW links between visited Labs and some technical issues related with the calibration procedure. It was again shown that link calibrations in the way proposed here can be done with a 1-2 ns uncertainty. On the other hand, intentional and unintentional changes in the receiver set-ups in all stations had to be noted.

II. CALIBRATION PROCEDURE

In the beginning it was considered important to start with the two basic types of calibration, the absolute and the differential, but a third class has been included to clarify all aspects related with a GPS time calibration.

A. Absolute Calibration

This type of calibration is carried out with a GPS signal simulator, and the calibration is focused on internal delays of GPS receivers. In comparison to the differential calibration, relying on a simulator provides the advantage that errors coming from satellite orbit and clock instabilities, signal propagation effects and multipath effect are excluded. Sub-nanosecond calibration uncertainty is feasible once the simulator pseudo-range code have been fixed to the same 1-PPS input used as time reference in GPS receiver.

Nevertheless, for a complete calibration of a GPS time transfer system, as shown in Figure 1, it is necessary to include the calibration of the antenna delay (*ANTDLY*) as well as the antenna cable delay (*CABDLY*). The latter can be measured with a vector network analyzer, but the antenna requires a more complicated system, as presented in [3], where an anechoic chamber was used in concert with a vector network analyzer and a separate radiating antenna [4].

B. Differential Calibration

The differential calibration of geodetic receivers is the traditional method performed by BIPM to calibrate GPS equipment located in time laboratories contributing to TAI. These calibrations are conducted periodically and can be found published in the rapport reports on the BIPM's web pages. Currently several national laboratories are also conducting this type of calibrations, for example PTB, METAS or ROA.

To carry out this calibration the receiver under test is compared with a reference receiver, often, although not necessary, an absolutely calibrated reference receiver. The calculated internal delays can be obtained in a similar way as

the absolute calibration, using a common clock and a zero baseline setup, where the related errors cancel out due to the use of the same antenna.

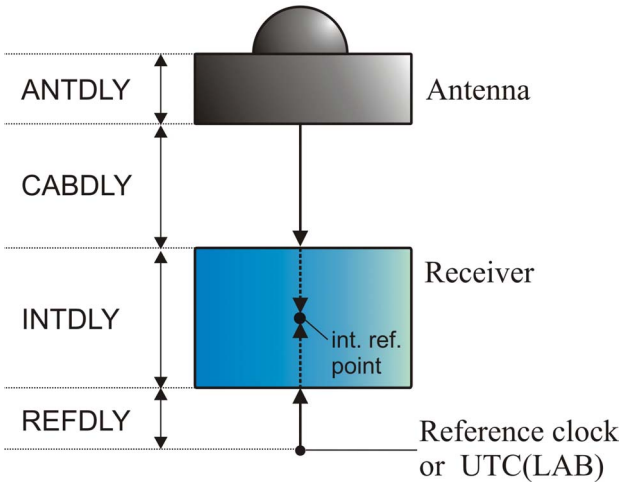

Figure 1. Linked delays to a time and frequency transfer GNSS station.

However the standard and simplest procedure of differential calibration of a complete GPS time station (receiver + antenna + antenna cable) is to calibrate it with respect to a reference equipment or traveling receiver (TR), where the unknown antenna delay is included in the receiver delay, thus:

$$INTDLY(P1/P2) = INTDLY_{Receiver}(P1/P2) + ANTDLY$$

In the differential calibration the local GPS receiver (*LR*) of a Lab is disposed in common clock (*UTC(Lab)*) and near zero baseline set-up together with TR. With this setup, using two different antennas, separated by a few meters, the noise in code signals that appears in addition to pure measurement noise is mainly due to multipath effect. Normally, the antenna cable delay of the local receiver is not determined again, due to the often difficult access to the two ends of a deployed cable, and also to prevent any damage in these rigid cables. However, any error in this measurement is absorbed by internal receiver delays.

The internal calibration values in P1 and P2 GPS code (*INTDLY(P1/P2)*) of a *LR*, are calculated by the common clock differences (*CCD*), which are obtained by simple differences of pseudoranges, only corrected for the geometric effect of receivers' and satellites' positions. This calculation can also be carried out in an easy way, by mean of the common view (*CV*) time transfer technique, using the data collected in the CCTF CGGTTS GPS data files [5]:

$$\gamma = (77/60)^2$$

$$REFGPS(P1)=REFGPS(P3)+ MSIO$$

$$REFGPS(P2)=REFGPS(P3)+ \gamma \times MSIO= REFGPS(P_3) + 1.647 \times MSIO$$

$$\Delta(INTDLY(P1)) = \langle REFGPS(P1)_{TR} - REFGPS(P1)_{LR} \rangle$$

$$\Delta(INTDLY(P2)) = \langle REFGPS(P_2)_{TR} - REFGPS(P_2)_{LR} \rangle$$

since:

$$\rho_{P3}= \gamma/(\gamma-1) \times (\rho_{P1}-INT_{P1}) - 1/(\gamma-1) \times (\rho_{P2}-INT_{P2})$$

$$MSIO=(\rho_{P1} - INTDLY(P1)) - \rho_{P3} - T_{GD} ,$$

where $\rho_{P1,P2,P3}$ are the code pseudoranges for P1, P2, and the P3 ionosphere free combination, *REFGPS(P1,P2,P3)* are the time difference values of respective code between the laboratory reference clock and GPS system time, referred to the midpoint of each 13 min track via a linear fit, *MSIO* are the measured ionospheric delays at the same point, and T_{GD} is the timing group delay. The < > is the average over a certain period, normally one day. The new receiver internal values must be corrected as follows:

$$INTDLY(P1/P2)_{NEW} = INTDLY(P1/P2)_{OLD} - \Delta(INT_{P1/P2}).$$

C. Link Calibration

Link calibration involves at least two receives (*LR1, LR2*) located in different laboratories. To implement this calibration, a traveling receiver is circulated between these two Labs, and after a differential or absolute calibration of these stations (receiver+antenna+cable antenna), the link calibration value is achieved. Nevertheless the latter implies the calculation at least of *REFDLY* (offset between 1 PPS rising edge to the receiver to 1 PPS rising edge at the local reference point) of traveling and local receivers at both Labs, which is not strictly necessary as will be discussed below.

The *REFGPS* measurements are already corrected for the delays outlined in the P3 CGGTTS header, $REFGPS(P3) = REFGPS_0(P3) - P3DLY$, where index 0 refers to uncorrected values, and the total delay correction applied is:

$$P3DLY= \gamma/(\gamma-1) \times INTDLY(P1) - 1/(\gamma-1) \times INTDLY(P2)+ + CABDLY - REFDLY = INTDLY(P3) + CABDLY - - REFDLY.$$

The link calibration value (*GPSCAL*) results from the next equations:

$$CCD1 = \langle REFGPS(P3)_{TR} - REFGPS(P3)_{LR1} \rangle_{LAB1} = = \langle (REFGPS_0 -P3DLY)_{TR} - (REFGPS_0 -P3DLY)_{LR1} \rangle_{LAB1} = = \langle (REFGPS_0 - INTDLY(P3) - CABDLY + REFDLY)_{TR} - -(REFGPS_0 - INTDLY(P3) - CABDLY + REFDLY)_{LR1} \rangle_{LAB1}$$

$$CCD2 = \langle REFGPS(P3)_{TR} - REFGPS(P3)_{LR2} \rangle_{LAB2} = = \langle (REFGPS_0 -P3DLY)_{TR} - (REFGPS_0 - P3DLY)_{LR2} \rangle_{LAB2} = = \langle (REFGPS_0 - INTDLY(P3) - CABDLY + REFDLY)_{TR} - -(REFGPS_0 - INTDLY(P3) - CABDLY + REFDLY)_{LR2} \rangle_{LAB2}$$

$$GPSCAL_{LR1,LR2}=CCD2-CCD1.$$

It is assumed that this calibration value remains valid until any change or event happens in any of the two installations and it can thus be taken into account in calculation of the time scale differences between the pair of laboratories:

$$UTC(LAB1) - UTC(LAB2) = REFGPS(P3)_{LR1} - - REFGPS(P3)_{LR2} - GPSCAL_{LR1,LR2}$$

Ignoring the *REFGPS* measurements, the constant values present in *GPSCAL* equation are:

$$[GPSCAL_{LR1,LR2}]_{CST} = -INTDLY(P3)_{TR} - CABDLY_{TR} + - REFDLY_{TR,LAB2} + INTDLY(P3)_{LR2} + CABDLY_{LR2} - - REFDLY_{LR2} + INTDLY(P3)_{TR} + CABDLY_{TR} - - REFDLY_{TR,LAB1} - INTDLY(P3)_{LR1} - CABDLY_{LR1} + + REFDLY_{LR1}$$

Consequently, any systematic error relative to P3 CGGTTS header values of local receivers cancels out, as well as the internal and antenna cable delays of TR, remaining only the difference of the input time reference delay to traveling receiver at both Labs, the only two values that must be carefully calculated for a GPS link calibration:

$$[REFGPS(P3)_{LR1} - REFGPS(P3)_{LR2}\text{-}GPSCAL_{LR1,LR2}]_{CST} = - REFDLY_{TR,LAB2} + REFDLY_{TR,LAB1}$$

III. EQUIPMENT

The traveling receiver (*TR*) comprises a DICOM GTR50 receiver, its GPS-702-GG NovAtel antenna, and a 48 m low loss H155 antenna cable. This receiver was compared to all available receivers located at each Lab, which are provided in Table 1.

Table 1. GPS receivers involved in calibration.

Laboratory	***Designation***	***Receiver Type***
ROA	RO_5	GTR50
	RO_6	PolaRx3eTR
PTB	PT02	ASHTECH Z-XII3T
	PT06	TTS-3
	PT07	GTR50
INRIM	IT1Z	ASHTECH Z-XII3T
	IT__	GTR50

We started the CCD at ROA. A few days later the TR was shipped to PTB and then it was shipped to INRIM, operating for days and with receivers shown in Figure 2. Finally the equipment was shipped back to ROA, to carry out the closure measurements with the initial set-up.

Table 2 shows the results at ROA stated as mean value and standard deviation (*SD*) of individual values with respect to the mean value over several days. In case of P3 data, individual values are CGGTTS common-view (*CV*) data averaged at each standard epoch and daily. CGGTTS files were generated with Pascale Defraigne software [6] from RINEX observation files, in order to avoid systematic errors induced by imprecise antenna positions, which have been finally calculated utilizing the NRCan PPP v. 1087 software [7]. The CCD has also been established with the PPP technique, by means of the above software and processing at 1-day batch mode.

The closure measurement shows a clear deviation from zero, 1 ns in case of RO_6 and almost 2 ns in the case of RO_5. The results of RO_5 receiver have not been taken into account, because a significant drift was detected during the period of calibration, when comparing CCD data using another local GPS receiver, and also through the TW-GPS link comparison results.

One of the possible causes of the 1-ns offset, which otherwise can be considered totally normal, can be related to the anomalous behaviour observed in the travelling receiver upon its return. It presented many measurement interruptions, related to low signal-to-noise ratio, becoming worse after a few days and making the PPP solution impossible. After the closure measurements, a deeper check was performed and it was found that the antenna cable showed poor performances, and once replaced, the equipment returned to normal operation. This malfunctioning has probably affected the final CCD at ROA, so only the first CCD has been employed in this calibration.

The CCD at PTB and INRIM are summarized in Table 3 and the computation for the P3 code data is illustrated in a detailed example in Figure 3. The individual P3 results are averaged at each standard epoch and daily. In a first step, a 3-σ filter is applied. While the mean value barely changes, the standard deviation drops from about 1 ns after applying the 3-σ filter to 0.1 ns for the daily average values.

The GPS link correction for all participants GPS receivers can be derived from Table 2 and 3, and is summarized in Table 5.

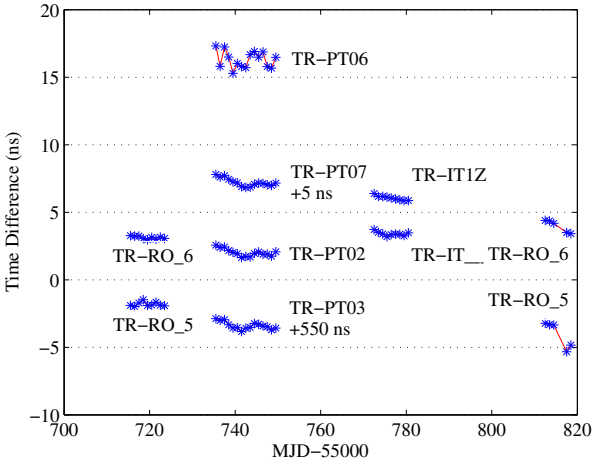

Figure 2. Daily averages of P3 CCD for GPS receivers participating in the calibration.

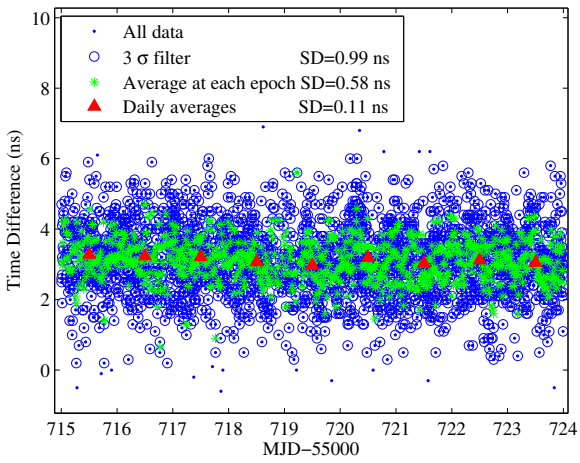

Figure 3. P3 results, showing the difference of TR-RO_6 receivers.

Table 2. Mean and SD values of the CCD measurements recorded at ROA.

CCD	*P3/ns*		*Daily average P3/ns*		*PPP/ns*		*Daily average PPP/ns*		*Number of Data P3/Daily PPP/Daily*
	Mean	*SD*	*Mean*	*SD*	*Mean*	*SD*	*Mean*	*SD*	
TR-RO_6 (Before the trip)	3.12	0.55	3.12	0.11	3.18	0.25	3.18	0.22	755/9 2575/9
TR-RO_5 (Before the trip)	-1.81	1.18	-1.81	0.16	-1.80	0.32	-1.80	0.33	788/9 2570/9
TR-RO_6 (After the trip)	4.12	1.02	4.01	0.44	-	-	-	-	245/5 -
TR-RO_5 (After the trip)	-3.73	2.18	-3.92	0.97	-	-	-	-	284/5 -
Closure Meas. TR-RO_6	+1.00	-	+0.89	-	-	-	-	-	
TR-RO_5	-1.92	-	-2.11	-	-	-	-	-	

Table 3. Mean and SD values of the CCD measurements recorded at PTB and at INRIM.

CCD	*P3/ns*		*Daily average P3/ns*		*PPP/ns*		*Daily average PPP/ns*		*Number of Data P3/D.A. PPP/D.A.*
	Mean	*SD*	*Mean*	*SD*	*Mean*	*SD*	*Mean*	*SD*	
TR – PT02	2.01	0.98	2.01	0.26	1.94	0.46	1.91	0.41	1259/15 3168/13
TR – PT06	16.34	1.48	16.32	0.60	-	-	-	-	1222/15 -
TR – PT07	2.23	1.03	2.23	0.30	2.35	0.37	2.33	0.35	1259/15 3163/13
TR – IT1Z	6.07	0.88	6.07	0.14	6.38	0.33	6.38	0.32	727/9 1974/7
TR – IT__	3.36	0.90	3.38	0.13	3.57	0.53	3.61	0.51	637/9 1999/8

IV. UNCERTAINTY EVALUATION

The overall uncertainty of the calibration value is estimated from the following expression:

$$U_{GPS} = \sqrt{u_{A,1}^2 + u_{A,2}^2 + u_{B,1}^2 + u_{B,2}^2 + u_{B,3}^2 + u_{B,4}^2 + u_{B,5}^2 + u_{B,6}^2}$$

- $u_{A,1}$ reflects the statistical uncertainty of the determination of the CCD at first Lab, and $u_{A,2}$ reflects the statistical uncertainty of the CCD measurements at second Lab. We used the daily average SD of Tables 2 and 3, justified by the fact that white phase noise up to an averaging interval of about one day [8] is prevailing, as illustrated in the slope -3/2 in the log-log plot of Fig. 4.
- $u_{B,1}$ ($u_{B,2}$) represent the uncertainty of the 1PPS delay from the local UTC, connected to each pair of receivers at first Lab (second Lab), and is based on the specifications of the un-calibrated time interval counter (TIC) in use (0.5 ns), the jitter of a TIC measurement (0.05 ns) and an estimation of the instability of the local distribution equipment (0.1 ns).
- $u_{B,3}$ we have included the instability of the receivers and antennae. Environmental effects like humidity and especially temperature have been demonstrated to have a significant impact. We account 0.4 ns for this contribution.
- $u_{B,4}$ we account for signal propagation effects, which mostly cancel in the chosen quasi zero baseline configuration. Only multipath errors might cause a small contribution to the uncertainty (0.3 ns for P3 [9] and 0.1 for PPP).
- $u_{B,5}$ in this uncertainty we account for the closure measurement value.
- $u_{B,6}$ represents the uncertainty of the ambiguity estimation in the PPP processing, which can then be taken as 0.3 ns [10].

The uncertainty results are summarized in Table 5a-c and a detailed example is shown in Table 4. The overall values are slightly higher than 1 ns. If the uncertainty of the TIC could be reduced significantly, for example with the use of calibrated devices or adding a TIC in the TR [11], together with normal closure measurement results, subnanosecond accuracy would become possible.

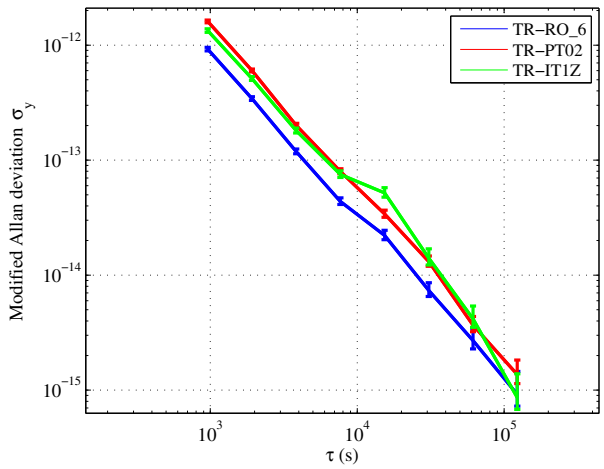

Figure 4. Frequency instability diagrams in terms of Modified Allan Deviation.

Table 4. Uncertainty values in ns estimated for GPS link calibration, involving RO_6 and PT02 receivers.

Method	U_{GPS}	$u_{A,1}$	$u_{A,2}$	$u_{B,1}$	$u_{B,2}$	$u_{B,3}$	$u_{B,4}$	$u_{B,5}$	$u_{B,6}$
P3	**1.28**	0.11	0.26	0.51	0.51	0.4	0.3	0.89	-
PPP	**1.34**	0.22	0.41	0.51	0.51	0.4	0.1	0.89	0.3

Table 5a. Calibration and uncertainty values (GPSCAL ± UGPS) for ROA-PTB GPS links (08 Calibration results for 2008, 10 calibration results for 2010).

GPS LINK	*GPSCAL P3/ns*	*GPSCAL PPP/ns*
RO_5 – PT02[08]	-2.73 ± 0.91	-2.23 ± 0.91
RO_5 – PT06[08]	11.01 ± 0.93	-
RO_5 – PT07[08]	-3.87 ± 0.90	-3.89 ± 0.91
RO_5 – PT02[10]	-2.68 ± 0.95	-1.93 ± 0.99
RO_5 – PT06[10]	11.30 ± 1.02	-
RO_5 – PT07[10]	-5.81 ± 0.96	-5.55 ± 1.01
RO_6 – PT02[10]	-3.94 ± 0.95	-3.01 ± 1.00
RO_6 – PT06[10]	10.04 ± 1.02	-
RO_6 – PT07[10]	-7.07 ± 0.97	-6.66 ± 1.02
RO_5 – PT02	3.82 ± 1.29	3.71 ± 1.37
RO_5 – PT06	18.15 ± 1.40	-
RO_5 – PT07	4.04 ± 1.30	4.13 ± 1.34
RO_6 – PT02	-1.11 ± 1.28	-1.27 ± 1.34
RO_6 – PT06	13.22 ± 1.40	-
RO_6 – PT07	-0.89 ± 1.30	-0.85 ± 1.32

Table 5b. Calibration and uncertainty values ($GPSCAL \pm U_{GPS}$) for INRIM-PTB GPS links ([10] Calibration results for 2010).

GPS LINK	*GPSCAL P3/ns*	*GPSCAL PPP/ns*
IT__ – PT02[10]	-4.49 ± 0.98	4.21 ± 0.99
IT__ – PT06[10]	9.49 ± 1.04	-
IT1Z – PT02[10]	-5.36 ± 0.95	-5.25 ± 0.97
IT1Z – PT06[10]	8.62 ± 1.01	-
IT__ – PT02	-1.37 ± 1.29	-1.70 ± 1.42
IT__ – PT06	12.96 ± 1.40	-
IT__ – PT07	-1.15 ± 1.30	-1.28 ± 1.40
IT1Z – PT02	-4.06 ± 1.29	-4.47 ± 1.36
IT1Z – PT06	10.27 ± 1.40	-
IT1Z – PT07	-3.84 ± 1.30	-4.05 ± 1.34

Table 5c. Calibration and uncertainty values ($GPSCAL \pm U_{GPS}$) for ROA-INRIM GPS links ([10] Calibration results for 2010).

GPS LINK	*GPSCAL P3/ns*	*GPSCAL PPP/ns*
RO_5 – IT__[10]	1.92 ± 0.95	2.28 ± 0.97
RO_5 – IT1Z[10]	2.68 ± 0.92	3.32 ± 0.94
RO_6 – IT__[10]	0.66 ± 0.95	1.20 ± 0.98
RO_6 – IT1Z[10]	1.42 ± 0.92	2.14 ± 0.96
RO_5 – IT__	5.19 ± 1.27	5.41 ± 1.40
RO_5 – IT1Z	7.88 ± 1.27	8.18 ± 1.34
RO_6 – IT__	0.26 ± 1.27	0.43 ± 1.38
RO_6 – IT1Z	2.95 ± 1.27	3.20 ± 1.32

V. TW LINK CALIBRATION

In the next step we use the GPS time transfer results to re-calibrate the TW ROA-PTB and INRIM-PTB links, using a 20-day data set, partly overlapping with the last calibration trip schedule, and once the BIPM has recalibrated the TW links after the satellite frequency change on MJD 55769 (27th July) [12].

We have initially derived the differences between the GPS and TW links (*TWCAL*), as shown in Figure 5. Each data point is the result of the exact difference of a TW value and the interpolation of the adjacent P3 values. In case of PPP the smoothing is not necessary and the RINEX files have been processed at 1-day batch mode. The TWCAL corrections obtained by all participants GPS receivers are summarized in Table 6, and can be calculated by:

$TWCAL = [TW(LAB1) - TW(LAB2)] - \langle REFGPS(R1) - REFGPS(R2) - GPSCAL_{R1R2} \rangle$

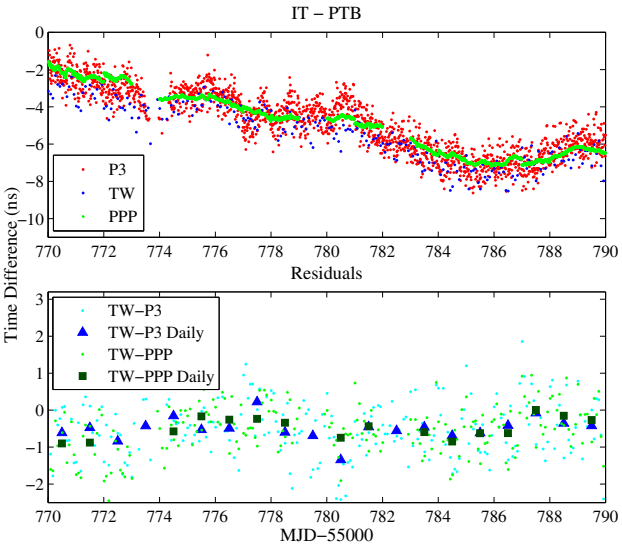

Figure 5. TW ROA-PTB and P3 IT1Z-PT02 results, and its differences.

Table 6. Mean and SD values of the TWCAL daily average values.

GPS LINK	*$TWCAL_{P3}$/ns*		*$TWCAL_{PPP}$/ns*		*Number of Data*
	Mean	*SD*	*Mean*	*SD*	
RO_5 – PT02	~~-5.34~~	~~0.68~~	~~-5.55~~	~~0.47~~	~~240/249~~
RO_5 – PT06	~~-4.91~~	~~0.92~~	~~-~~	~~-~~	~~240/-~~
RO_5 – PT07	~~-5.43~~	~~0.75~~	~~-5.46~~	~~0.51~~	~~240/249~~
RO_6 – PT02	-4.48	0.53	-4.50	0.43	249/217
RO_6 – PT06	-4.26	.82	-		249/-
RO_6 – PT07	-4.50	0.56	-4.39	0.49	249/217
IT__ – PT02	-0.63	0.32	-0.46	0.41	247/226
IT__ – PT06	-0.66	0.82	-		249/-
IT__ – PT07	-0.70	0.40	-0.37	0.38	247/226
IT1Z – PT02	-0.53	0.33	-0.54	0.37	247/207
IT1Z – PT06	-0.67	0.77	-		249/
IT1Z – PT07	-0.50	0.41	-0.44	0.36	249/207
RO_5 – IT__	~~-4.69~~	~~0.74~~	~~-5.13~~	~~0.60~~	~~239/225~~
RO_5 – IT1Z	~~-4.73~~	~~0.68~~	~~-4.98~~	~~0.58~~	~~239/206~~
RO_6 – IT__	-3.84	0.65	-4.10	0.52	236/191
RO_6 – IT1Z	-3.81	0.54	-4.03	0.39	237/181

Afterwards the time scale differences between a pair of Labs have to be corrected according to:

$$UTC(LAB1)-UTC(LAB2)=TW(LAB1)-TW(LAB2)-TWCAL$$

Table 7. Calibration and uncertainty values for TW links ([08] Calibration results for 2008, [10] calibration results for 2010).

LINK	*P3 /ns*		*PPP /ns*	
	TWCAL	σ_{TWCAL}	*TWCAL*	σ_{TWCAL}
ROA – PTB[08]	0.44	0.33	0.74	0.17
ROA – PTB[10]	-4.51	0.15	-4.01	0.15
ROA – PTB	-4.37	0.29	-4.41	0.26
INRIM – PTB[10]	-1.98	0.16	-1.66	0.16
INRIM – PTB	-0.54	0.14	-0.42	0.16
ROA – INRIM[10]	-2.94	0.22	-2.92	0.20
ROA – INRIM	-3.82	0.41	-4.05	0.31

The observed offset between the TWCAL values for the two ROA receivers, was caused by the mentioned drift in RO_5 receiver. Therefore, these results have been eliminated from the calculation of the final TWCAL values of Table 7.

Due to the increasing number of GPS links established between Labs, we have estimated the best TWCAL value by means of the weighted average of respective measurements:

$$TWCAL = \frac{\sum \frac{1}{\sigma_i^2} twcal_i}{\sum \frac{1}{\sigma_i^2}}$$

where σ_i are the SD. The associated uncertainty can be calculated by:

$$\sigma_{TWCAL} = \frac{1}{\sqrt{\sum \frac{1}{\sigma_i^2}}}$$

The uncertainty involved in this calculation is estimated from the following expression:

$$U_{TW} = \sqrt{u_{A,3}^2 + u_{B,7}^2 + u_{B,8}^2}$$

- $u_{A,3}$ reflects the statistical uncertainty of TWCAL values, which are summarized in Table 7.
- $u_{B,7}$ we have estimated the additional overall instability of the involved equipment for the calibration of the TW link: distribution of local UTC signals, the TW station components' instabilities and environmental effects (0.3 ns).

- In $u_{B,8}$ we have included the calculated uncertainty of the GPS link, which is summarized in Table 6, and with values close to 1.4 ns.

The final calibration uncertainty for each TW link is therefore less than:

$$U_{TW} = \sqrt{0.41^2 + 0.3^2 + 1.4^2} \approx 1.5 \text{ ns}$$

We have compared these values to the ones obtained in the previous calibrations. At this time, in contrast to the former calibration, the TW link results are in very good agreement for ROA-PTB link and close to 1 ns for INRIM-PTB link. However the GPS links have changed significantly, especially all related to the RO_5 and PT07 receivers, close to 3 ns for RO_6-PT02, RO_6-PT06, IT__-PT02, IT__-PT06 links, and close to 1 ns for IT1Z-PT02, IT1Z-PT06 links.

VI. CONLUSIONS

In this paper we have summarized the GPS calibration trip experience between ROA, PTB and INRIM, using a portable GTR50 receiver. The uncertainty estimated indicates the possibility of achieving a 1-ns accuracy calibration of GPS links, at least for short/medium periods of time, neglecting possible long term delay changes in GPS equipment, as shown by RO_5 receiver.

The uncertainty estimated for this TW calibration is subject to GPS uncertainty, but was only increased by a tenth of ns. TW links have shown a good long term stability, as has been showed with the last two calibrations results.

Normally, major changes in GPSCAL values are related to equipment changes, which can be due to some PTB receivers, or to a malfunction in one element of the station: receiver, antenna cable and antenna, being the latter the cause of the jump observed in RO_5 receiver, corrected once the antenna was replaced.

We plan to verify these results, by carrying out a calibration campaign again this year, involving also the links to the other EURAMET project partners: ÚFE/IPE (Czech Republic), BEV (Austria), DMDM (Serbia), EXHM/GSCL-EIM (Greece), IPQ (Portugal), JV (Norway), METAS (Switzerland), MIKES (Finland), MIRS (Slovenia), NPL (United Kingdom), SMD (Belgium), SP (Sweden).

ACKNOWLEDGMENT

The authors acknowledge the Geodetic Survey Division, Natural Resources Canada (NRCan), for providing the PPP software.

REFERENCES

[1] J. Kouba and P. Héroux, "Precise Point Positioning Using IGS Orbit and Clock Products," GPS Solutions, vol. 5 no. 2, pp. 12–28, 2001.

[2] H. Esteban, J. Palacio, F. J. Galindo, T. Feldmann, A. Bauch, D. Piester, "Improved GPS-Based Time Link Calibration Involving ROA and PTB," IEEE Trans. UFFC, vol. 57, no. 3, pp. 714–720, 2010.

[3] J. Plumb, K. M. Larson, J. White, E. Powers, "Absolute Calibration of a Geodetic Time Transfer System," IEEE Transactions on Ultrasonics, Ferroelectrics and Frequency Control, no. 52, pp. 1904–1911, 2005.

[4] A. Proia, G. Cibiel, J. White, D. Wilson, K. Senior, "Absolute calibration of GNSS time transfer systems: NRL and CNES techniques comparison," Proc. IFCS / EFTF 2011, pp. 1058–1063.

[5] W. Lewandowski et al., "A Contribution to the Standardization of GPS and GLONASS Time Transfers", Proc. 28th PTTI, pp. 367 - 386.

[6] P. Defraigne and G. Petit, "Time transfer to TAI using geodetic receivers," Metrologia, vol. 40, pp. 184–188, 2003.

[7] J. Kouba, P. Heroux, "Precise Point Positioning using IGS Orbit and clock Products," IEEE Transactions on Ultrasonic, Ferroelectrics and Frequency control, 2002, vol. 46 No. 4.

[8] W. Lewandowski, L. Tisserand, "Determination of the differential time corrections for GPS time equipment located at the OP, PTB, NPL and VSL," Rapport BIPM-2008/01.

[9] W. Lewandowski and C. Thomas, "GPS Time Transfer," Proc. IEEE, vol. 79, no. 7, pp. 991–1000, 1991.

[10] G. Petit, "The TAIPPP pilot experiment," Proc. Joint 23rd European Frequency and Time Forum, and IEEE Frequency Control Symposium, pp. 116–119, 2009.

[11] T. Feldmann, A. Bauch, D. Piester, M. Rost, E. Goldberg, S. Mitchell, and B. Fonville. "Advanced GPS Based Time Link Calibration with PTB's New Calibration Set-Up". Proceedings of the 42th PTTI Systems and Applications Meeting, Reston, VA, USA, 2010.

[12] Z. Jiang, W. Lewandowski, A. Harmegnies, D. Piester and V. Zhang. "Restoration the TWSTFT link calibration using GPSPPP bridging after the satellite change on Mjd 55769/27 July 2011". BIPM TM198, 2011. (ftp://tai.bipm.org/TimeLink/LkC/).

Development of QZSS-mobile station

Hideki NARITA, Jun AMAGAI, Masanori AIDA, Yasuhiro TAKAHASHI, Isao NAKAZAWA, Maho NAKAMURA, Hideki UJIHARA, Shin'ichi HAMA
National Institute of Information and Communications Technology, Koganei, Tokyo, JAPAN
Email: hnarita@nict.go.jp

***Abstract*—As we designed and constructed the QZSS mobile station, we transported it to Okinawa Electromagnetic Technology Center and Kashima Space Technology Center. At each place we carried out time comparison experiments. This paper describes some results of the time comparison experiments.**

I. INTRODUCTION

The 1st Quasi-Zenith Satellite (QZS-1) was successfully launched from JAXA Tanegashima Space Center on September 11, 2010 on inclined geo-synchronous (Quasi Zenith) orbit for the purpose of satellite positioning. As the satellite positioning system using three QZSs, QZS System (QZSS) was developed by Japanese four ministries and their subordinate institutes in 2003. This system adopts the current and more extensive function of the modernized GPS. QZSS greatly extends available area and time for satellite positioning in urban canyon.

QZS-1 carries two on-board atomic clocks connected with a time transfer subsystem (TTS). National Institute of Information and Communications Technology (NICT) developed and has managed the time management system, which consists of on-board TTS and related ground systems such as time management stations (TMS). TMS manages all the clocks for this system. One TMS is set up in Koganei, Tokyo, where UTC(NICT) is generated, and another in Okinawa. For these time comparisons, we adopt the two way time and frequency transfer method. [1]

We developed a QZSS mobile station that can be transported to any places in the cover area of QZS-1; accordingly, we can easily carry out a precise time comparison in those areas. Then QZSS mobile station contributes to performing the time comparison between highly precise atomic clocks in Asian areas.

II. DEVELOPMENT OF MOBILE STATION

We need to track QZS, because QZS is a non-GSO satellite. Table1 shows an automatic tracking function. QZSS mobile station has two kinds of tracking modes. One is a program auto tracking mode, and another is a mono-pulse tracking mode.

For tracking QZS, a program auto tracking mode uses orbital elements (which are) calculated beforehand and a mono-pulse tracking mode uses the telemetry signal of C band transmitted by QZS.

Fig.1 Antenna & Shelter

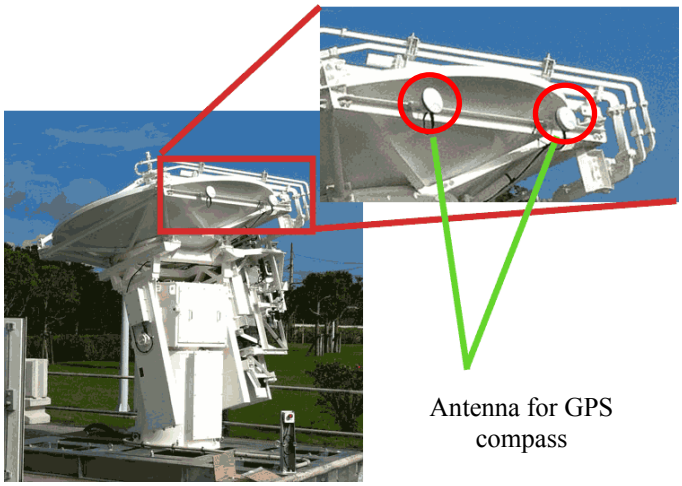

Fig.2 GPS compass

By using GPS compass (Fig.2) equipped in QZSS mobile station, we can calibrate an antenna axis quickly.

Uplink RF signals is 14GHz and Downlink RF is 12GHz.
Polarization is circular polarization.
Table2 shows a specification of signal system.

Table1 Specifications of antenna system

antenna diameter	2.4m	
drive system	Az-El system	
tracking mode	program tracking	0.1° RMS
	mono-pulse tracking	0.2° RMS or less (C/N0=48dBHz)
the maximum drive speed	5deg/s for Az/El	

Table2 Specifications of signal system

tranmission frequency	center freq	14434.53MHz
	bandwidth	49MHz
receiving frequency	center freq	12306.69MHz
	bandwidth	49MHz
EIRP		55.1dBW
G/T		24.0dB/K or more (E1=10deg)
Transmitting beam pattern		ITU-R S.580
Polarization		RHCP

Fig.3 Shelter

Fig.4 Indoor equipment

Fig.3 shows the shelter. A power supply board, an antenna drive unit, a tracking error detection board, etc. are kept in the shelter. We can manually operate an antenna system in this shelter. The antenna and the shelter are located outside. All the transmission and reception of signals between the shelter and the indoor equipment are connected by optical communications.

The last system consists of all the indoor experimental equipment including some PCs and network system (Fig.4). Gross weight of the antenna system is about 5 tons, and the shelter weighs about 1 ton. Maximum electric power consumption is about 10 kVA. QZSS-mobile-station is possible to be transported by a truck.

III. FUNCTION OF MOBILE STATION

QZSS mobile station makes it possible to carry out time comparison with high accuracy by using two-way method.

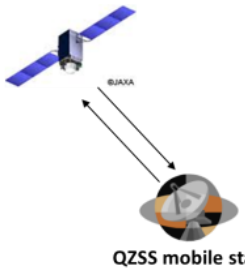

Fig.5 Between an on-board and mobile station

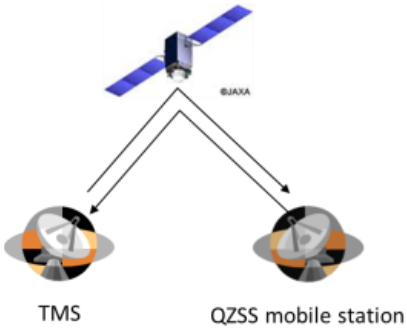

Fig.6 Between other TMS and mobile station using bent-pipe

QZS-1 has two kinds of bent-pipe functions. QZSS mobile station can measure time and frequency difference precisely between an on-board atomic clock (Fig.5) and local atomic clocks using bent-pipe (Fig.6). Moreover this station can also measure time and frequency difference between other time management stations (TMS) and local atomic clocks using bent-pipe. There are two modes: narrow band bent-pipe (NBP) and wide band bent-pipe (WBP).

IV. EXPERIMENT PLAN

At the beginning we planned to perform the experiment in South Korea. But we changed our plan since we could not obtain the radio license in South Korea. So we chose Okinawa Electromagnetic Technology Center and Kashima Space Technology Center as new places. (Fig.7)

In the late November 2011, we transferred the experiment system to Okinawa and we carried out time comparison experiment.

Then we transferred the system to Kashima, and carried out time comparison experiment in the same manner.

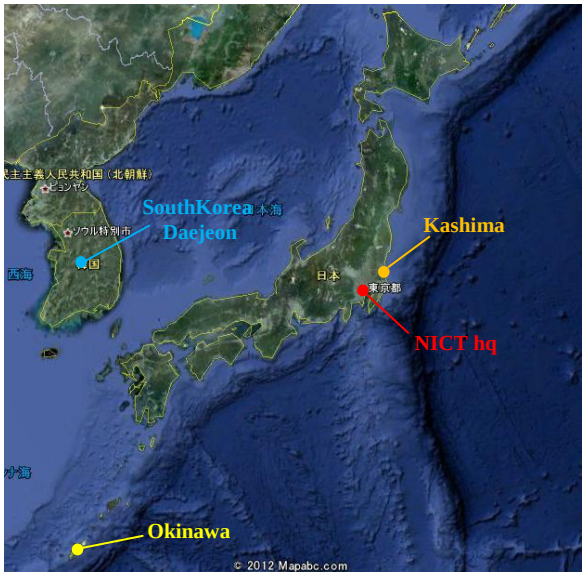

Fig.7 The original working plan and actual implementation

V. RESULTS OF AN EXPERIMENT

i) An experiment between an on-board and mobile station

We carried out a time comparison between an on-board clock and Hydrogen maser set in Okinawa and in Kashima respectively. And at the same time, time comparison between TMS(Okinawa) and TMS(Koganei) is performed in the same manner.

We show the results drawn by the experiment of comparison between QZSS-mobile-station(Okinawa) and TMS(Okinawa) from November 2011 to January 2012.

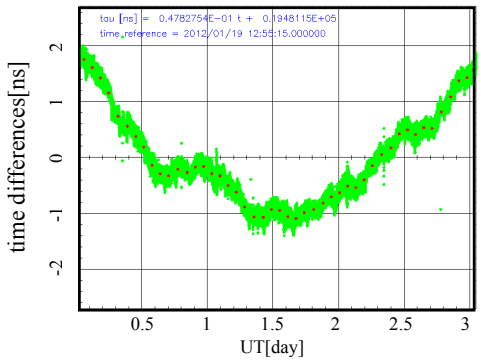

Fig.8 Satellite and QZSS mobile station at Okinawa (2012.1.18)

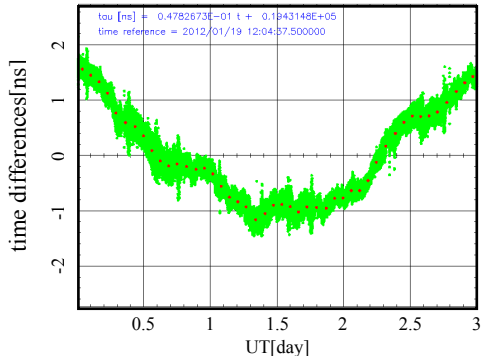

Fig.9 Satellite and QZSS TMS at Okinawa (2012.1.18)

From the above data, we can tell that the time difference between QZS-1 and the mobile station and that between QZS-1 and TMS Okinawa can be measured accurately.

ii) An experiment between other TMS and mobile station using bent-pipe

We carried out this experiment in Okinawa and Kashima as well as we did it between an on-board and QZSS-mobile station.

We show the results of the time comparison experiment between QZSS-mobile-station(Kashima) and other TMS station.

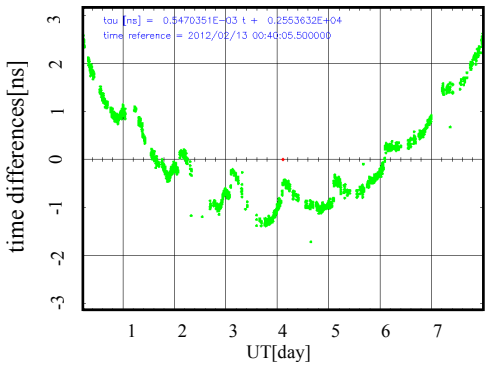

Fig.10 TMS (Koganei) and QZSS mobile station (at Kashima)

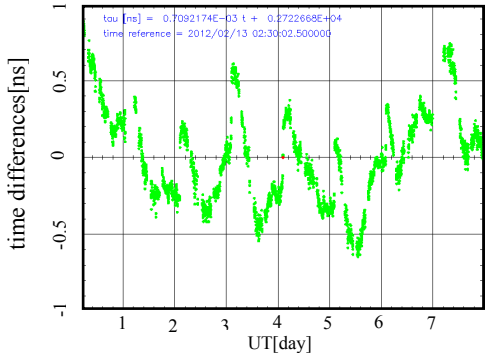

Fig.11 TMS (Okinawa) and QZSS mobile station (at Kashima)

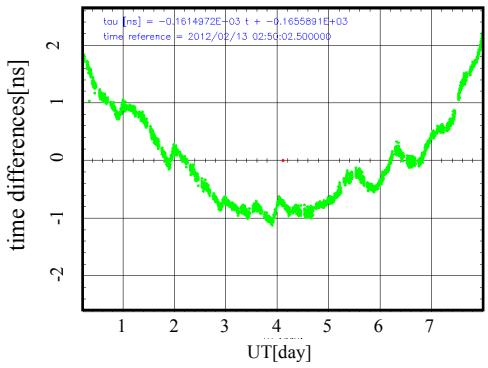

Fig.12 TMS (Koganei) and TMS (Okinawa)

Fig.10, 11 and 12 are the time differences measured at Kashima by using NBP from February to March 2012. After removing the long-term trend, which is the drift of the on-board atomic clock, we achieved the precision better than 1 nsec.

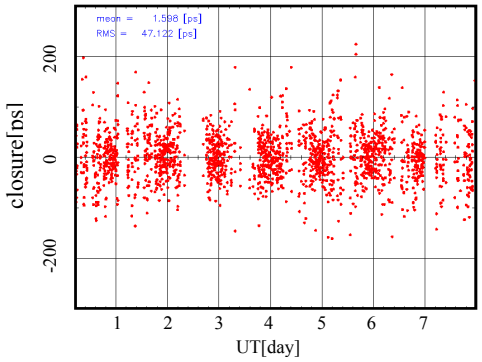

Fig.13 closure resolution (time difference of all station)

Fig. 13 shows the closure delay (QZS-1, TMS Kashima, and the mobile station), whose RMS is 47 ps. It means that the results of this time comparison are consistent.

Ⅵ CONCLUSION

We carried out the time comparison experiment several times between highly precise atomic clocks in Japanese areas.

And these experiments could show QZSS-mobile-station has an expected performance.

Acknowledgment

We appreciate the related engineers from NEC Co. and SED Co. for the technological assistance regarding the above experiment.
This research is sponsored by the Ministry of Internal Affairs and Communications, Japan.

REFERENCES

[1] M. Nakamura, et al., “Initial results of the first QZS(Michibiki)Time Management System,” ION International
Technical Meeting, San Diego, CA, USA, January 2011.

Control Algorithm of UTC(MIKE)

K. Kalliomäki, T. Mansten, I. Iisakka, T. Fordell, and M. Merimaa
Centre for Metrology and Accreditation (MIKES)
P.O. Box 9, 02151 Espoo, Finland
mikko.merimaa@mikes.fi

***Abstract*— The Finnish realization of coordinated universal time, designated UTC(MIKE), is derived from a single active hydrogen maser at the Centre for Metrology and Accreditation (MIKES). The frequency of a hydrogen maser typically drifts with time, leading to an approximately parabolic phase shift. At MIKES, a programmable delay generator is used to negate the phase drift of the maser. An improved control algorithm for the phase compensation has lead to a ten-fold improvement in time stability compared to our previous results. With time-transfer based on precise point positioning, we have been able to keep UTC(MIKE) within ±6 ns of UTC during the past year even though our only link to primary frequency standards is through the CCTF-K001.UTC and Circular T. Moreover, improved predictability has lowered the time deviation (TDEV) of UTC(MIKE) to a level below 500 ps when data from the past 10 months is considered.**

I. Introduction

The Centre for Metrology and Accreditation (MIKES) is the National Metrology Institute (NMI) of Finland and maintains the national time UTC(MIKE), a local representation of coordinated universal time UTC. Many different approaches to local realization of UTC are in use world wide. The standard approach is to take advantage of the stability provided by large clock ensembles that may or may not contain primary frequency standards, and to use sophisticated control algorithms that adjust the frequency and phase of an active hydrogen maser (for a review see [1] and references therein). Contrary to this, the source of UTC(MIKE) is one single active hydrogen maser (AHM2) that is steered only based on the CCTF-K001.UTC and Circular T. The MIKES clock ensemble (Fig. 1) provides redundancy and contributes to EAL.

The phase of a hydrogen maser typically exhibits an approximately parabolic behavior, which can be compensated for using a delay generator and a second degree polynomial model. The problem, then, is to find model parameters that negate the maser drift and produce an optimal estimate of UTC. Since the properties of hydrogen masers slowly vary over time, prediction of the evolution of the model parameters is needed for the best performance. Using the approach described in this article, we have reached a ten-fold improvement in time stability compared to our previous results.

II. Laboratory and Equipment

The laboratory building of MIKES was completed in 2005. It has excellent environmental conditions for the maintenance of different metrological quantities [2]. Air-conditioning machinery first cools or heats the outside air to 9°C, after which the air is humidified to 100%. The cool and humid air is then heated and mixed with circulating air in successive control stages, resulting in a highly stable environment at 23°C and 41% RH. Electrical power to atomic clocks and other critical infrastructure is supplied from a voltage-regulated uninterruptible power supply with diesel generator back-up.

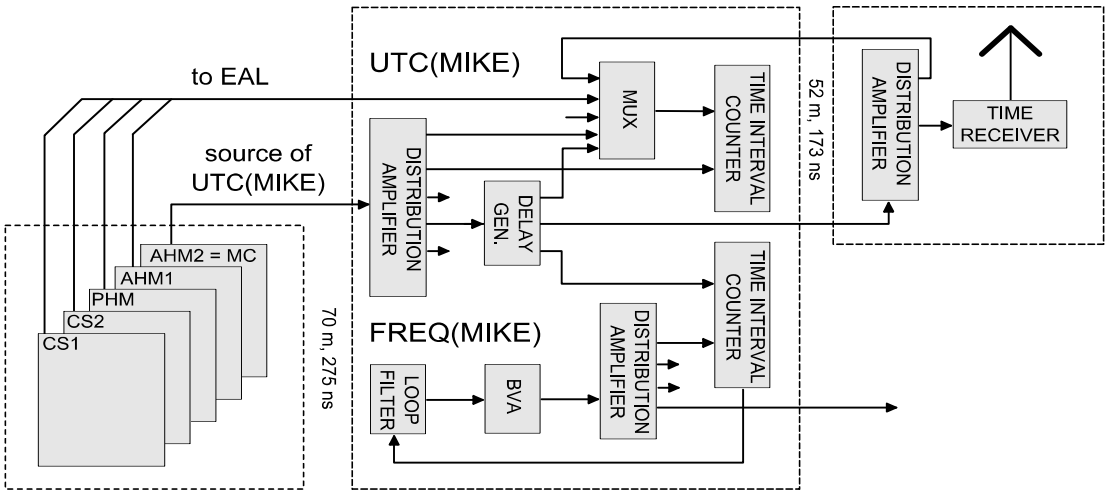

Figure 1. Setup for the generation of UTC(MIKE) and FREQ(MIKE) at MIKES.

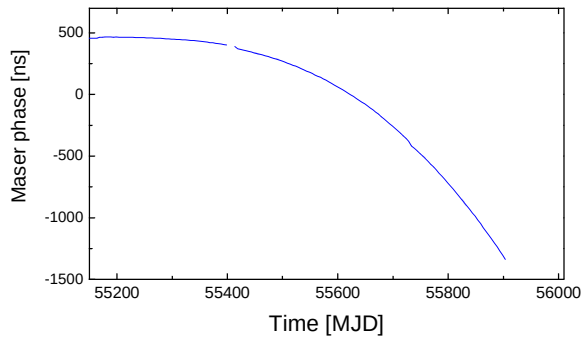

Figure 2. Evolution of the AHM2 phase: UTC-AHM2. Adjustments of the internal frequency synthesizer of the maser and the effect of the delay generator have been removed to show the true phase drift.

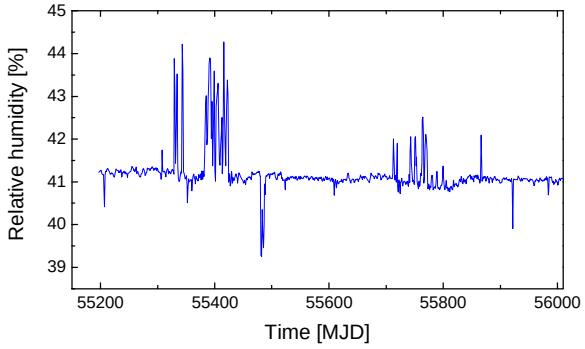

Figure 4. The Relative humidity of air fed to the AHM2 equipment enclosure.

The active hydrogen masers AHM1 and AHM2 [3, 4] (Kvartz CH1-75A) are equipped with computer-controlled delay generators (SRS DG645) that generate a delay according to a model optimized for cancelling the maser phase drift [5]:

$$UTC\text{-}AHM2 = a + bt + ct^2, \quad (1)$$

where t is time and a, b and c are parameters to be determined. Furthermore, a stable 10 MHz reference frequency is synthesized from the delayed time signal using a phase-locked loop where a computer slowly adjusts the frequency of a BVA crystal oscillator.

To improve the predictability of the clocks, all clocks are operated in temperature controlled equipment enclosures with constant air flow. The temperature is stable within ±0.1°C, and no apparent correlation is observed between the remaining temperature fluctuations and clock frequencies (Fig. 3). Relative humidity of the incoming air is kept constant at 41% (Fig. 4). Also in this case, no apparent correlation can be observed. Moreover, the regulated, uninterruptible power supply minimizes variations of the internal heating of the clocks. GPS time link receivers are located in the receiver tower, where ambient conditions are maintained by a separate air conditioning machine. Calibration of the time and frequency receivers at MIKES is traceable to SP (The national metrology institute of Sweden), where a two-way satellite time-transfer link and BIPM calibrated GPS receivers are available [6].

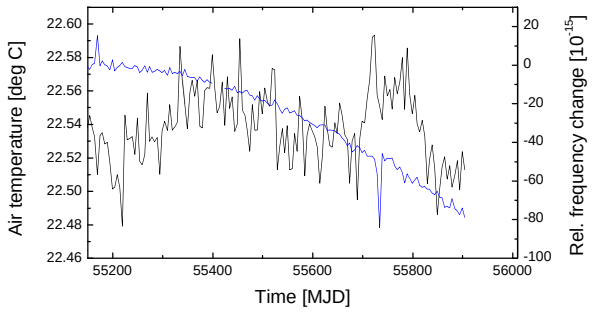

Figure 3. Temperature of air fed to the AHM2 equipment enclosure (black) and AHM2 frequency (blue). No apparent correlations are observed.

III. Control Algorithm of UTC(MIKE)

Following the approach described above, control of UTC(MIKE) reduces to the estimation of the slowly varying parameters of the model in Eq. 1. New estimates are calculated monthly after each Circular T is published and updated to the control system when deemed necessary, typically in 1-4 month intervals. After updating our GPS time link to Precise Point Positioning (PPP), the residual noise of the link reduced to 0.5 ns root-mean-square, allowing reasonable estimates to be calculated using only two months of historical data (u = 0.5 ps/day^2).

The starting point of the new control algorithm is the estimation of parameter c, which equals half the aging of the clock, i.e., the rate of change of the rate deviation. Historical values of c are obtained via parabolic fits to UTC-AHM2 using either two or three months of data. To predict the evolution of parameter c, an exponential model

$$\hat{c}(MJD) = c_0 \cdot \left(1 - e^{-(MJD - MJD_0)/\tau}\right), \quad (2)$$

where c_0, τ and MJD_0 are parameters, is fitted to the historical estimates as shown in Fig. 5. As of MJD=56060, $c_0 \approx$ 15ps/day^2 and $\tau \approx$1000day. MJD_0=55171 is the zero crossing of $\hat{c}$. There is no physical reason to use an exponential model, and other models, depending on aging characteristics of an individual maser, may yield a better fit.

At the moment, we have an aging model of our maser calculated from nearly three years of continuous operation, and by integrating the aging model twice and adding corresponding integration constants (b and a), we obtain a

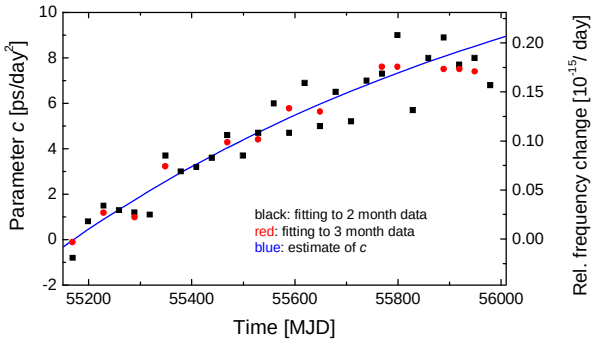

Figure 5. Prediction of parameter *c* for AHM2

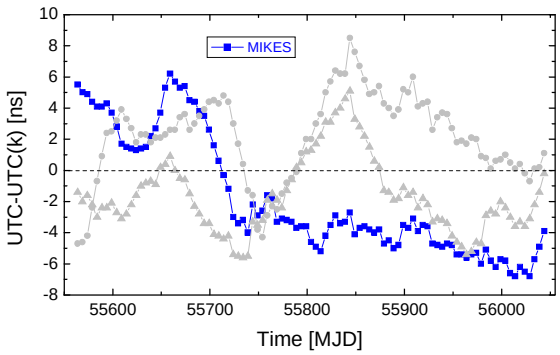

Figure 6. Comparison of the realization of UTC at MIKES and at two other National Metrology Institutes. It should be noted that the reference institutes (semi-)continuously operate primary frequency standards that are used to steer their masers.

model for maser phase performance. The integration constants are determined by a fit to raw UTC-UTC(MIKE) data. The benefit of this method is an improved prediction accuracy, which is approaching 1 ns per month. The model is better than our previous parabolic model, where a second order polynomial was fitted to the last few months of historical data, by about a factor of ten.

.

IV. Results

Aided by the stable environment and a good individual maser, the maser steering approach described above allows us to realize UTC at very low uncertainty. Peak-to-peak variation was ± 6 ns during the past year (Fig. 6), and TDEV is below 500 ps when data from the past 10 months is considered.

V. Conclusions

An excellent realization of UTC can be achieved without direct access to primary frequency standards, if an active hydrogen maser is operated in a tightly controlled environment and the aging of the maser is modeled appropriately. By introducing a separate prediction of the parameter c, instead of simply fitting the parabolic model to UTC-AHM2, we have reached a ten-fold improvement in time stability compared to our previous results. With the PPP time-transfer technique, we have been able to keep UTC(MIKE) within ±6 ns of UTC during the past year even though our only link to primary frequency standards is through the CCTF-K001.UTC and Circular T.

In all likelihood, there are several commercial active hydrogen masers at various national metrology institutes with equal or even superior performance compared to AHM2 of MIKES; however, this performance may be buried under the short term, weighed models used to produce national realizations of UTC. Ambient conditions, including temperature, air flow, relative humidity and power supply voltage are often not stable enough to expose the underlying long term performance of clocks. Therefore, ambient conditions must be carefully controlled. If this is not feasible, conditions should at least be measured and their correlation with the frequency deviations of the standards calculated.

References

[1] P.B. Whibberly, J.A. Davis and S.L. Shemar, Local representations of UTC in national laboratories, Metrologia 48 (2011) S154–S164 doi:10.1088/0026-1394/48/4/S05

[2] A. Lassila, M. Kari, H. Koivula, U. Koivula, J. Kortström, E. Leinonen, J. Manninen, J. Manssila, T. Mansten, T. Meriläinen, J. Muttilainen, J. Nissilä, R. Nyblom, K. Riski, J. Sarilo and H. Isotalo, Design and performance of an advanced metrology building for MIKES, Measurement, doi:10.1016/j.measurement.2010.10.013.

[3] K. Kalliomäki, T. Mansten, Short and long term stability of Kvarz hydrogen masers CH1-76 and CH1-75A, Proceedings of the 19th European Frequency and Time Forum (EFTF'05) (Besançon, France, 21 -24 March, 2005).

[4] K. Kalliomäki, T. Mansten and J. Mannermaa, Short and long term stability of Russian hydrogen masers CH1-76 and CH1-75A, Proceedings of the 22nd European Frequency and Time Forum (EFTF'08), Toulouse, France.

[5] K. Kalliomäki, T. Mansten and I. Iisakka, Maintenance of UTC(MIKE) in Finland by using a delay generator as a micro stepper, Proceedings of the 24th European Frequency and Time Forum (EFTF'10), Noordwijk, The Netherlands

[6] K. Kalliomäki, T. Mansten and I. Iisakka, Time comparison using Cs-clocks, uncertainty evaluation, Proceedings of the 23rd European Frequency and Time Forum (EFTF'09), Besançon, France.

Improving timing capabilities in 3G mobile networks

Rimantas Miškinis, Dmitrij Smirnov, Emilis Urba
Time and Frequency Standard Laboratory
Center for Physical Sciences and Technology
Vilnius, Lithuania
Email: miskinis@pfi.lt

Bronislovas Dzindzelėta
JSC "Omnitel Vilnius"
Vilnius, Lithuania

***Abstract*— Various characteristics of time transfer over 3G mobile telecommunication networks are investigated. The investigation aims at the three typical regimes in which the modem can be operated: 1) UMTS logical CTCH (Common Traffic Channel) operating over the UMTS FACH (Forward Access Channel) physical channel; 2) UMTS data transfer logical DTCH (Dedicated Traffic Channel) operating over the UMTS DCH (Dedicated Channel) physical channel; 3) HSDPA data transfer logical DTCH (Dedicated Traffic Channel) operating over the HS-DSCH (High Speed Shared Data Channel) physical channel. It is found that the most important role in the quality of synchronization and time transfer is played by the network asymmetry, not the absolute delay time.**

I. INTRODUCTION

Emerging technologies of mobile communications allow drastic increase of the data transfer rate over a mobile network. Features of mobile device synchronization and time transfer first of all depends on the data transfer characteristics of mobile network. In our previous works [1, 2], various characteristics of time transfer over mobile telecommunication networks were investigated. The UMTS (Universal Mobile Telecommunications System) and HSDPA (High-Speed Downlink Packet Access) channels revealed the worst results. On the other hand, the UMTS technology is among the most advanced and popular technologies of mobile networks [3, 4, 5]. In the present work, we focus on the possibilities for improvement of timing and synchronization of the UMTS and HSDPA channels.

II. MEASURING TECHNIQUE

We use the same experimental setup as in [1] (see Fig. 1). An Advantech Industrial Computer IPC-610BP running the Linux Ubuntu Server 10.10 operating system, with the LinuxPPS kernel module (PPS API (RFC 2783) implementation) turned on and the Network Time Protocol daemon ntpd (ntp_v4.x package) program implemented is connected to a mobile operator network via a Nokia N95 8 GB modem. The setup makes up a ready-for-use version "3G" of a mobile testing system. The Nokia N95 8 GB modem is connected to the measurement system via an USB interface.

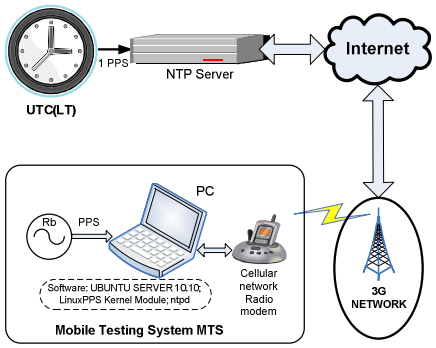

Figure 1. Device setup for investigation of time transfer via the 3G mobile network

The system was used to investigate timing capabilities of the UMTS and HSDPA technologies

III. RESULTS

Here we will review only the results obtained while the mobile terminal operates with the base stations belonging to the same radio network controller (RNC) and the signal level of a base station about -90 dBm. Statistically, switching to another station is rare, however, such a switching usually

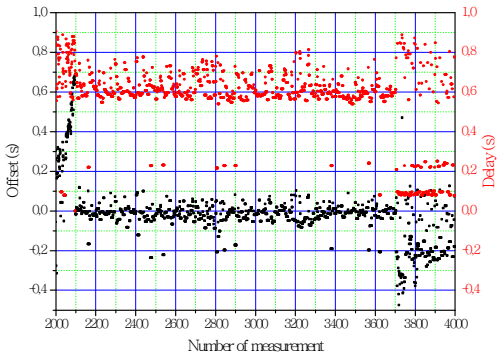

Figure 2. The data from the ntpd statistics file „peerstats". Computer clock is synchronized to the time server by the NTP protocol, by means of the UMTS paging channel technology. Interval between measurements is 16 s

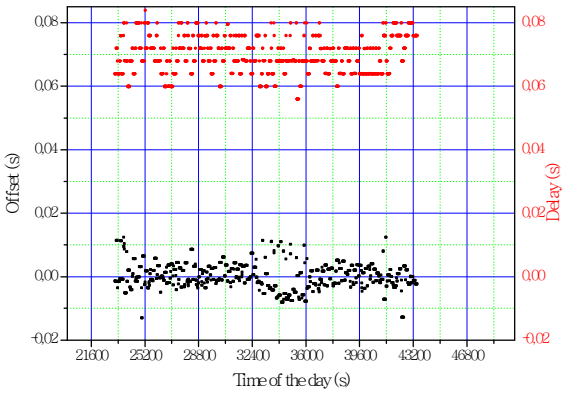

Figure 3. The data from the ntpd statistics file „peerstats“. Computer clock is synchronized the to the time server by the NTP protocol, by means of the HSDPA technology

causes the packet delay of about 3-5 s due to the cell reselection procedure. Sometimes, switching is even longer due to the reselection of a few cells in a row. Yet, the investigation of such phenomena requires separate measurements. We don't account for such phenomena here.

Although synchronization results obtained in the UMTS/HSDPA regime are worse than those obtained in 2G mobile networks, the potential of the UMTS and HSDPA technologies allows achieving better results. Here we will try to find out the reasons which could cause large, non-typical for such networks delays as well as up-and-down transfer asymmetries.

By default, switching between logical channels, selecting the UMTS and HSDPA regimes is controlled by a mobile network. We have noticed that the UMTS technology have several types of logical channels for the data transfer – namely, the Dedicated Control Channel (DCCH) and

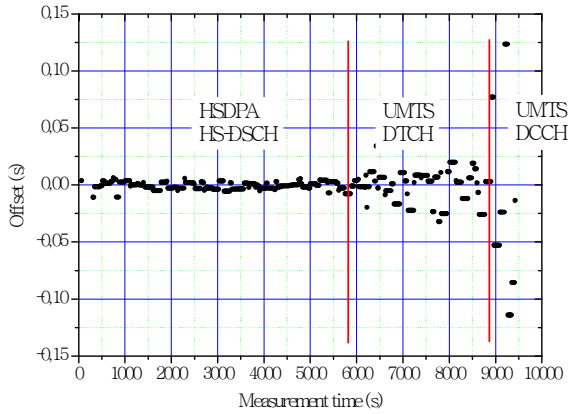

Figure 4. Results of PC clock timing over a 3rd generation network

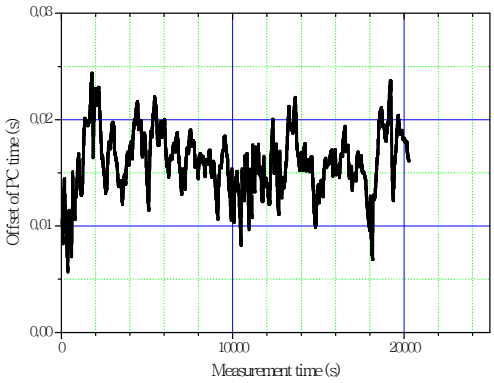

Figure 5. Scattering of the LinuxPPS–formed time marks, while synchronizing the computer clock to the time server by the NTP protocol, by means of the HSDPA technology

dedicated traffic channels (DTCH). The asymmetry of those channels is essentially different. Thus, we investigate three typical operating regimes to which the modem can be switched: UMTS DCCH channel, UMTS DTCH channel, and the HSDPA DCH logical channel over transport channel named High-Speed Downlink Shared Channel (HS-DSCH),

After a repeat investigation of the UMTS DCCH channel, the reason for poor synchronization results in [1] has become clear and can be explained as follows.

ntpd (Network Time Protocol daemon) issues time requests every 16 seconds or even over larger periods; time requests are very short, whereas the mobile communication network is configured so as to minimize the use of the network resources. In our case, UMTS DCCH channel is dedicated for synchronization. Generally, DCCH channel is narrow and has big differences in time delay during data transfer in the down-link and up-link (DL and UL) directions. Main UMTS DTCH data channel is "sleeping" the most of the time due to low traffic. DCCH channel features large delay and asymmetry, while the results of [1] have been obtained with the modem operating in this regime most of the time. In the contrary, the UMTS DTCH channel has lower delay due to higher data transfer rate and less asymmetry.

Fig. 2 shows that the NTP packets are delayed by about 0.6 s, the delay being characteristic of the UMTS DCCH. However, sometimes the delay decreases down to ~80 ms, which implies turning on the HSDPA channel, while the delay of about 200 ms is expected for the UMTS DTCH channel. As far as each channel features different asymmetry and speed, and ntpd is unable to estimate it, we get rather poor synchronization parameters. It is to be emphasized that this regime yields the worst results out of all the operating regimes investigated because of the mixture of different UMTS channels caused by the fact that the network itself commands the phone which channel to use. Fig. 3 reveals the results obtained at each channel separately. We can see that the smallest scattering of the results with the network delay of about 60-70 ms is obtained in the HSDPA regime. UMTS

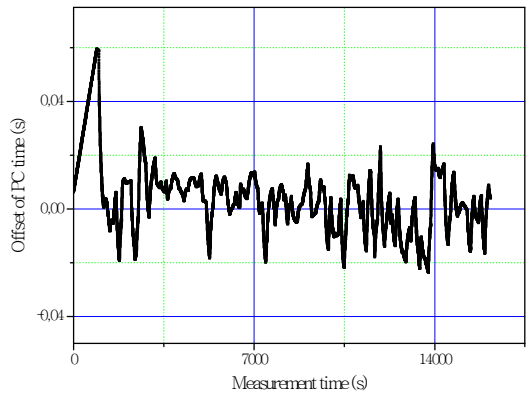

Figure 6. Scattering of the LinuxPPS–formed time marks, while synchronizing the computer clock to the time server by the NTP protocol, by means of the UMTS data channel technology

regime yields intermediate results with the network delay of about 200 ms, while UMTS DCCH regime, with the channel being "waked-up" at every NTP request, features the largest scattering of parameters and delay of about 600 ms.

Consider the peculiarities of the HSDPA technology. The experiment shows that in the case of no data sent the HS-DSCH channel is deactivated after about 8 s. It is why, in order to make the phone operate in the HSDPA regime, we are sending the time server 1008 bits-long ping packets every 7 s. In this way, we ensure the openness of the HSDPA channel and, at the same time, we are sending the NTP requests. Figs. 4 and 5 reveal the results.

From Fig. 4 we see that the asymmetry of the HS-DSCH channel is about 15 ms. Fig. 5 depicts the data from the ntpd peerstats files, which imply that the delay of the NTP packets is about 70 ms, while the scattering of the NTP results is about ±10 ms.

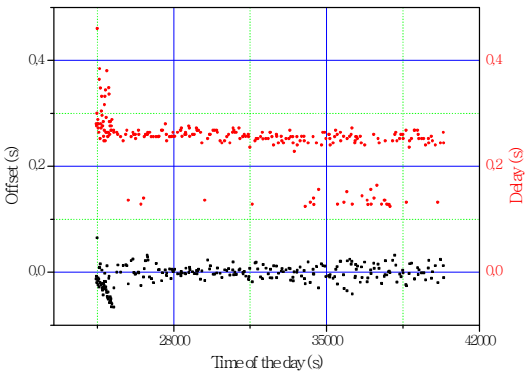

Figure 7. The data from the ntpd statistics file „peerstats". Computer clock is synchronized to the time server by the NTP protocol, by means of the UMTS data channel technology

In order to make the phone operate in the UMTS DTCH regime, we have disabled the HSDPA function in the phone and are sending the time server 16 bits-long ping packets every second. In this way, we ensure that the UMTS DTCH channel is permanently active and, at the same time, we are sending the NTP requests. Figs. 6 and 7 reveal the results.

Fig. 6 implies that the UMTS DTCH data channel features the least asymmetry, which is close to zero, i.e., on average, an NTP packet spends the same time for travelling to the server and returning back. The change in delay from ~180 ms to 250 ms implies switching between the base stations, which are connected in series.

IV. Conclusions

While synchronizing a computer clock over a mobile telecommunication network, the most important role is played by the network asymmetry, not the absolute delay time.

The UMTS DCCH features the largest scattering of the results. Thus, it is the least suitable for such measurements.

The UMTS DTCH reveals moderate scattering and the smallest asymmetry. However, in order to have it open, a data flow of about 168 kB / 24 h is necessary. In a case of continuous synchronization, this would amount to about 4.9 MB per month, which is quite acceptable.

The HSDPA HS-DSCH channel offers the smallest data scattering and rather small asymmetry. In order to have the HSDPA channel open, an additional data flow of about 1.4 MB / 24 h (or about 44 MB per month) is necessary.

V. References

[1] R. Miškinis, D. Smirnov, E. Urba, B. Dzindzelėta, "Timing and synchronization in mobile telecommunication networks," Frequency Control and the European Frequency and Time Forum (FCS), 2011 Joint Conference of the IEEE International, pp. 665-669, San Francisco, CA, 2-5 May 2011.

[2] R. Miškinis, A. Burokas, J. Karuža, V. Simanavičius, D. Smirnov, E. Urba, A. Mašonis, "Timing of GSM audio connections by generating UTC(LT) traceable digital time stamps," Proc. IEEE Int. Freq. Contr. Symp. jointly with the 21th Eur. Freq. Time Forum, pp. 836 – 839, 2007. Available: (www.ieee-uffc.org/main/publications/fcs/proceed/2007/178_7177.pdf)

[3] P. Kovar, K. Molnar, "Precise time synchronization over GPRS and EDGE", IFTP International Federation for Information Processing, Vol. 245. Personal Wireless Communications, B. Simak, R. Bestal, E. Kozowska, Eds. Boston: Springer, 2007, pp. 277-284.

[4] J. Eberspächer, Ch. Bettstetter, H.-J. Vögel, GSM: architecture, protocols and services, 3rd ed. London, UK: John Willey and Sons Ltd., 2009.

[5] **3GPP TS 25.321** Medium Access Control (MAC) protocol specification

Optical Fiber Time and Frequency Transfer inside Urban Telecom Network in Warsaw – Results of Initial Tests

Albin Czubla, Roman Osmyk and Piotr Szterk
Time and Frequency Laboratory, Electricity Department
Central Office of Measures (GUM)
Warsaw, Poland
E-mail: timegum@gum.gov.pl

Waldemar Adamowicz
Orange Lab, Polish Telecom
Warsaw, Poland

Michał Marszalec
Central Chamber for Telecommunications Measurements
National Institute of Telecommunication
Warsaw, Poland

Łukasz Śliwczyński
Department of Electrical Engineering
AGH University of Science and Technology
Krakow, Poland

***Abstract*—In this paper, the initial results of optical fiber time and frequency transfer at the optical distance up to about 40 km inside urban telecom network have been presented. The applied optical methods have been shortly described. The results of optical measurements have been compared with GPS CV method and specifications of compared clocks. In practice, it was obtained a similar effect if compared clocks were standing very close to each other.**

I. INTRODUCTION

Since September 2010 we have been having the opportunity to use some parts of the real urban telecom network in Warsaw for optical fiber time and frequency transfer experiments. Polish Telecom made the fiber connections between Central Office of Measures (GUM), Orange Lab of Polish Telecom (TP) and National Institute of Telecommunication (NIT) available to needs of our experiments (Fig. 1).

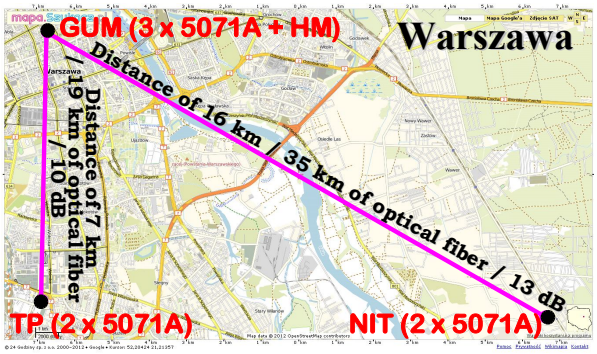

Figure 1. Optical links under test

These laboratories have commercial cesium clocks of 5071A, that are continuously compared with GPS Common-View (GPS CV) method against UTC(PL) and participate in determination of TAI and UTC. So, we are able to verify metrological characteristics of the applied by us optical methods of time and frequency transfer, with the usage of special electronic-optic converters developed by AGH (AGH University of Science and Technology) [1-2], under real urban telecom network conditions for optical links longer than 10 km, whereas our previous experiments were referred to short link of about 3 km of optical fiber [3-5] or to laboratory conditions mainly [2, 6]. The real urban telecom network is more exposed to vibration and the fiber is manifold welded, etc. The optical method applied by our group are complementary to the other optical methods of time and microwave frequency transfer [7-10] applied and developed in other research centers.

II. SHORT CHARACTERISTICS OF THE APPLIED METHODS

The both described below methods of time and frequency transfer over optical fiber are two-way methods with the usage of external or internal circulators in fact. In each method, the optical signals in opposite directions are transmitted over the same optical fiber. Currently we use a "dark" fiber, but there is possible to complete the system to use only one channel DWDM. The used lasers are adjusted at the chosen wavelengths around 1550 nm, with precision and stability of about 10 pm each one.

A. Optical method of time transfer

For optical time transfer we use two pairs of electronic-optic converters, i.e. two transmitters and two receivers. The transmitters convert electric 1 pps signals into optical pulses,

and receivers convert the received optical pulses into electric 1 pps signals. The received optical signals are normalized automatically to make the operation of the system independent of the attenuation of the optical path. At each end of the link, external circulators are mounted and TICs are used to measure a difference between 1 pps signal of the local clock and 1 pps signal of the remote clock produced in the output of the optical receivers. Due to interchanging the measurement data, the difference between compared clocks as well as the delay of the fiber can be calculated. This optical method we call TDOTFT (Two-Directional Optical Time and Frequency Transfer) method. The stability of a such time transfer, determined before [3-4] in the loop of 6 km of fiber link in urban telecom network, is at the level of dozen ps (TDEV) (Fig. 2) and, the most probably, is limited mainly by the used TICs, here SR620. A such link of time transfer can be fully calibrated independently of other time transfer methods. Time interval measurements and measurements of chromatic dispersion of the fiber and wavelengths offset of the lasers set in the transmitters are only required to calibrate the link.

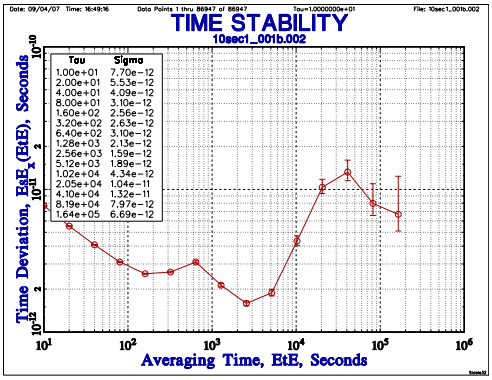

Figure 2. Stability (TDEV) of time transfer of TDOTFT methof determined in the loop of 6 km of fiber link in urban telecom network with the usage of two SR620 counters.

B. Optical method of frequency transfer

For frequency transfer we use one pair of optical equipment (transmitter and receiver) with implemented electronic delay lines, which automatically compensate fluctuations and changes of delay of the fiber to make the total delay between 10 MHz input of the transmitter and 10 MHz output of the receiver almost constant. It is possible due to implementation of auxiliary backward optical transmission between the receiver and the transmitter as well as application of the delay locked loop (DLL). The stability of a such microwave frequency transfer, determined also in the loop of 38 km of fiber link in urban telecom network, is at the level of about 2E-17 (ADEV) for 24-hours averaging time (Fig. 3).

Practically the same results were obtained before during laboratory experiments with optical fiber in the spool [6]. The stability of the phase of the output frequency signal is still maintained at the level of single ps. Within the full range of compensation of delay changes of the fiber, the difference of the phase between the input and output frequency signals can change no more than 30 ps.

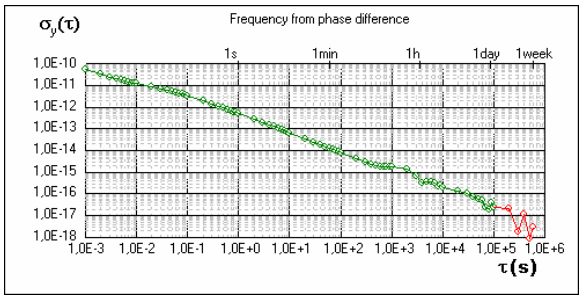

Figure 3. ADEV for relative phase measurements of 10 MHz transmitted in the loop GUM-TP-GUM (38 km of fiber link in urban telecom network), determined with the usage of A7-MX standard frequency comparator.

III. MEASUREMENT RESULTS

For both GUM-NIT and GUM-TP links, the 5071A clock of NIT or TP were compared against UTC(PL) maintained in GUM on the base of the signal taken from the 5071A clock, so it were comparisons of two 5071A clocks, in fact.

For time transfer, linear daily averages of the clocks difference were calculated by fitting regression lines to single common measurements (optical method) or single common observations (GPS CV method – CA code only) for each day. Simultaneously, rms error of linear fitting of regression line for each day and both methods were determined. Also, linear daily averages and rms were determined for calculation of delay of fiber within optical method. For GUM-TP link, single measurements in TDOTFT were synchronized in the both optical ends within a few seconds, whereas for GUM-NIT link, single measurements in TDOTFT in NIT were interpolated on the base of average values of series of 200 single measurements repeated continuously.

For frequency transfer over optical fiber, the stability of the received 10 MHz standard frequency from the remote clock with respective standard frequency from the local clock in GUM were determined only. For this type of measurements a standard frequency comparator of the A7-MX type, with 10 Hz internal filter set, was used.

The exemplary results of measurement for the both GUM-NIT and GUM-TP links are shown in Fig. 4-9. The benefits of applying of the optical methods are clearly visible. Despite the relatively short distance between the laboratories, GPS CV method together with the compared clocks introduce meaningful noise of about 2 ns rms for the GUM-NIT link and of about 4 ns rms for the GUM-TP link, whereas, for the optical methods, it is visible mainly the noise of the compared clocks at the level of below 1 ns for GUM-NIT link and of about 2 ns for GUM-TP link. The reliability of the results of clock comparison obtained in TDOTFT method is confirmed by the accompanying determination of delay of fiber (of link in fact). The observed fluctuations of this delay are relatively small (Fig. 5c and 8c) and of the same range in the both links. So, it follows that these fluctuations are dominated by nonlinearity effects and internal delays inside the used TICs (SR 620).

A. Clock comparison at distance of 16 km (35 km of fiber link) – GUM-NIT

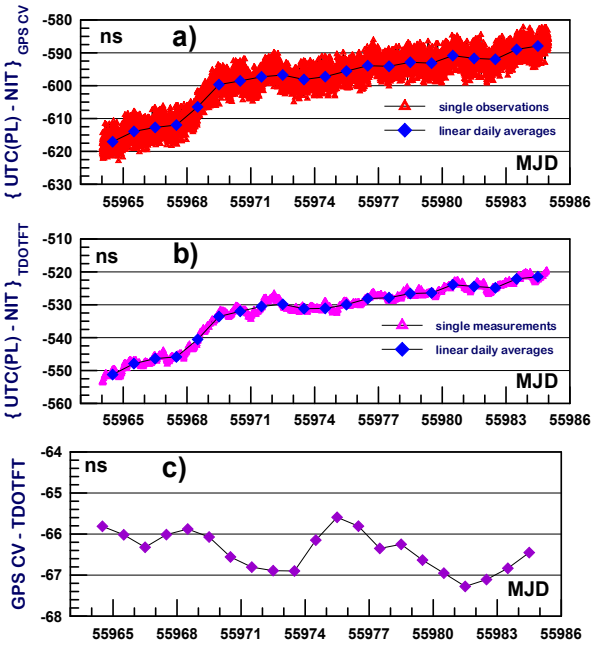

Figure 4. Results of clock comparison between GUM and NIT obtained with GPS CV method (a), TDOTFT method (b) and differences between average daily results obtained from GPS CV and TDOTFT methods (c).

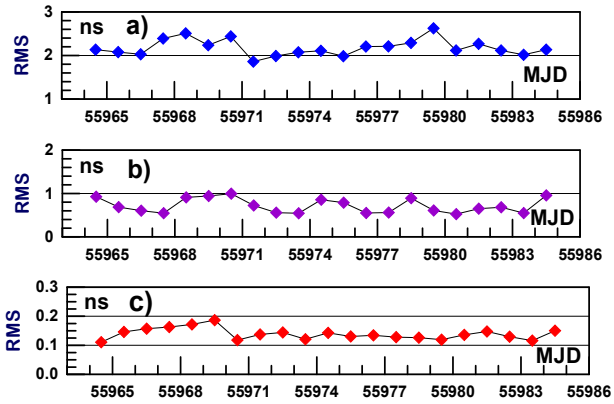

Figure 5. RMS error of linear fitting of regression line for determination of daily averages observed for the link GUM – NIT: clock comparison with GPS CV (a) and TDOTFT (b) methods and fluctuation of delay of fiber in TDOTFT method (c).

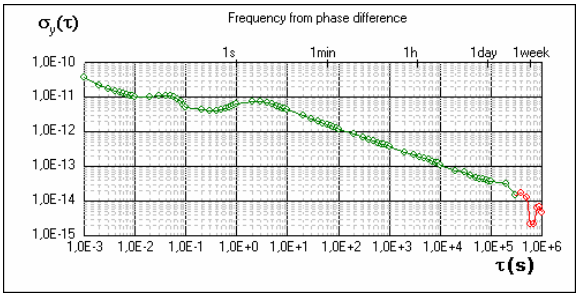

Figure 6. ADEV observed in GUM for the 5071A clock operating in NIT (frequency transfer with DLL).

B. Clock comparison at distance of 7 km (19 km of fiber link) – GUM-TP

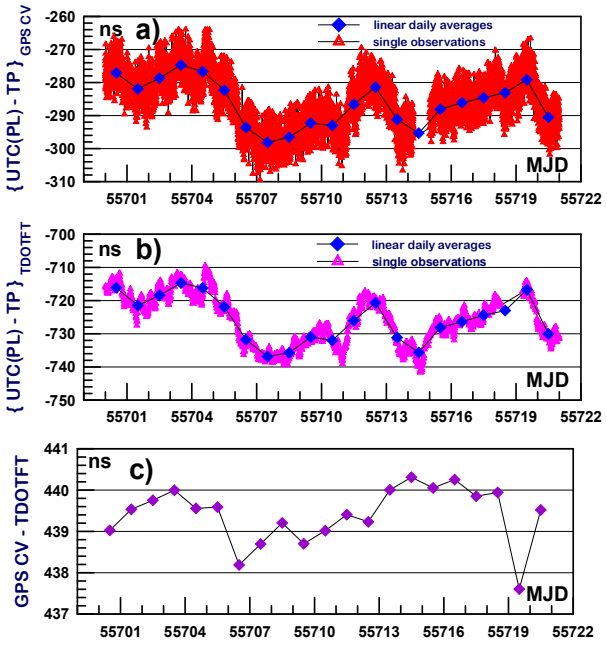

Figure 7. Results of clock comparison between GUM and TP obtained with GPS CV method (a), TDOTFT method (b) and differences between average daily results obtained from GPS CV and TDOTFT methods (c).

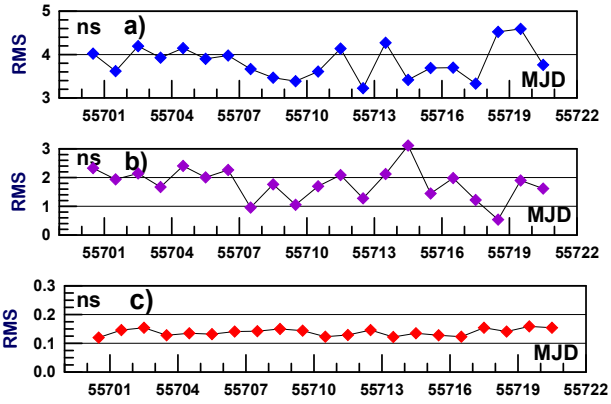

Figure 8. RMS error of linear fitting of regression line for determination of daily averages observed for the link GUM – TP: clock comparison with GPS CV (a) and TDOTFT (b) methods and fluctuation of delay of fiber in TDOTFT method (c).

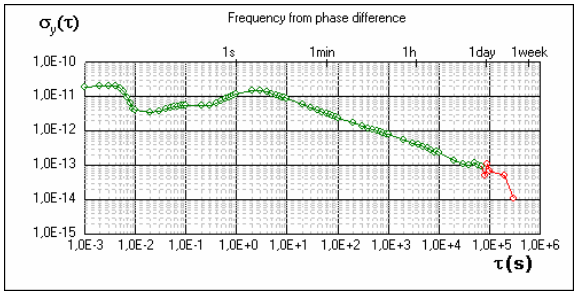

Figure 9. ADEV observed in GUM for the 5071A clock operating in TP (frequency transfer with DLL).

The reasons of the observed visible meaningful difference between the noises present in the both links are the following:

- The 5071A clock operating in NIT has better metrological characteristics than the 5071A clock operating in TP.
- NIT has newer and better time transfer system for GPS CV method (TTS-3 based on dual frequency Javad receiver and the newer antenna) than TP (TTS-2 based on single frequency Motorola receiver).

The results of frequency transfer for the links GUM-NIT and GUM-TP, presented in Fig. 6 and 9, also confirm better characteristics of the clock operating in NIT. In the both cases, the "remotely" observed stability of the 5071A clocks with respective to the 5071A one in GUM comply with or are very close to their technical specifications, approximately.

The comparison of the observed fluctuation of delay of fiber in TDOTFT method (Fig. 5c and 8c), including the local conditions of performing of single measurements, shows the importance of synchronization of partial measurements at the both ends of the optical link in order to maximize the accuracy of optical method. It will have increasing importance in the longer links and/or with compared more stable clocks. For optical frequency transfer with DLL, synchronization is done automatically with a constant delay equal to twice the stabilized delay of fiber link, so it is a valuable benefit with comparison to TDOTFT method.

IV. CONCLUSIONS

The obtained measurement results of optical fiber time and frequency transfer inside urban telecom network in Warsaw allowed to confirm the conservation of metrological characteristics of our optical time and frequency methods as observed in laboratory conditions. Application of optical methods for time and frequency transfer inside urban telecom network is very easy because of no need of application of optical amplifiers typically, whereas the benefits of optical method for time and frequency metrology are significant. For our local needs, it gives the possibility of treating many atomic clocks scattered inside urban telecom network as if clocks were maintained in one laboratory. The possibility of transmission of standard frequency signals without degradation of their metrological characteristics, e.g. for research purposes or to other measurement installations, is very important too. For stronger time and frequency laboratories, it is sufficient to compare cesium fountains and another primary frequency standards.

The obtained measurement results can be also used for precise calibration of the GPS receivers used in NIT and TP for time transfer against the GPS receiver used in GUM and for monitoring the stability of time transfer with the usage of GPS CV method.. We plan to address this issue in the coming months.

REFERENCES

[1] Ł. Śliwczyński, P. Krehlik, M. Lipiński, „Optical fibers in time and frequency transfer", Measurement Science and Technology, vol. 21, 075302, 2010

[2] Ł. Śliwczyński, P. Krehlik, Ł. Buczek, M. Lipiński, "Active propagation delay stabilization for fiber optic frequency distribution using controlled electronic delay lines", IEEE Transactions on Instrumentation and Measurement, vol. 60, pp. 1480-1488, 2011

[3] A. Czubla, J. Konopka, M. Górnik, W. Adamowicz, J. Struś, T. Pawszak, J. Romsicki, M. Lipiński, P. Krehlik, Ł. Śliwczyński, A. Wolczko: "Comparison of Precise Time Transfer With the Usage of Multi-Channel GPS CV Receivers and Optical Fibers Over Distance of About 3 Kilometers", in Proc. 38th Annual Precise Time and Time Interval (PTTI) Meeting, pp. 337-346, December 2006

[4] A. Czubla, J. Konopka, M. Górnik, W. Adamowicz, J. Struś, J. Romsicki, M. Lipiński, P. Krehlik, Ł. Śliwczyński, A. Wolczko: "Two-directional time signal transfer over optical fiber" (in Polish), Pomiary Automatyka Kontrola (PAK), Vol. 53/9bis, pp. 289-292, 2007

[5] A. Czubla, R. Osmyk, P. Szterk: "Comparison of time transfer with usage of GPS CV method and two-directional method with application of optical fibers" (in Polish), Pomiary Automatyka Kontrola (PAK), Vol. 56/09, pp. 1012-1015, 2010

[6] A. Czubla, Ł. Śliwczyński, P. Krehlik, Ł. Buczek, M. Lipiński, J. Nawrocki, "Stabilization of the propagation delay in fiber optics in a frequency distribution link using electronic delay lines: first measurement results", in Proc. 42nd Annual Precise Time and Time Interval (PTTI) Meeting, p. 389-396, November 2010

[7] A. Imaoka, M. Kihara: "Accurate time/frequency tranfer method using biderectional WDM transmission", IEEE Transactions on Instrumentation and Measurement, vol. 47, pp. 537-542, 1998

[8] D. Piester, M. Fujieda, M. Rost, A. Bauch: "Time Transfer Through Optical Fibers (TTTOF): First Results of Calibrated Clock Comparisons", in Proc. 41st Annual Precise Time and Time Interval (PTTI) Meeting, p. 89-99, November 2009

[9] K. Jaldehag, S.-C. Ebenhag, P.O. Hedekvist, C. Rieck: "Time and Frequency Transfer Using Asynchronous Fiber-Optical Networks: Progress Report", in Proc. 41st Annual Precise Time and Time Interval (PTTI) Meeting, p. 383-395, November 2009

[10] V. Smotlacha, A. Kuna, W. Mache: "Time Transfer Using Fiber Links", in Proc 24th European Frequency and Time Forum, Noordwijk, The Netherlands, April 2010

Two-Way Optical Time and Frequency Transfer between IPE and BEV

Vladimír Smotlacha
Research Department
CESNET z.s.p.o.
Prague, Czech Republic
Email: vs@cesnet.cz

Alexander Kuna
Time and Frequency Department
Institute of Photonics and Electronics AS CR, v.v.i.
Prague, Czech Republic
Email: kuna@ufe.cz

***Abstract*—This paper describes our experience with long term two-way optical time transfer between Czech and Austrian national time and frequency laboratories maintaining their national time and frequency standards generating the national time scales UTC(TP) and UTC(BEV), respectively. The optical link utilizes either dedicated optical fibers or Dense Wavelength Division Multiplex (DWDM) channels in all-optical production telecommunication networks. Results from the optical transfer, i.e. clock comparison and link delay including diurnal and seasonal effects are shown and also compared with GPS Common-View and Precise Point Positioning.**

I. Introduction

Global Navigation Satellite Systems (GNSS) play an important role primary in positioning and navigation but they are rather known in a time and frequency community as a means of comparing distant sources of precise time and frequency, e.g. atomic clocks. The uncertainty of the GNSS time transfer depends on the distance between the two observation stations. For instance, the uncertainty of GPS time transfer using a single clock and zero-baseline is in the order of few nanoseconds concerning GPS code measurements and few tens of picoseconds in case of GPS carrier phase measurements [1].

Dedicated optical fibers are commonly used to link atomic frequency sources of a laboratory to a primary frequency standard in a primary metrology unit. Such links have typical length up to few tens kilometers and thus create a local point-to-point network.

The increasing number and coverage of all-optical networks used mainly in telecommunication opens a possibility of using these networks for time and frequency transfer at a distance of hundreds kilometers. Two distant clocks can be compared by use of two-way technique via either single or a pair of optical fibers [2], [3].

II. Background

Our optical time transfers system is an instance of two-way transfer method that relies on known and stable asymmetry of transport delay in both directions. We described the measurement method in [4].

The basic idea is following: two adapters (A and B) are connected by a bidirectional optical link. Each adapter is provided with a 1PPS signal from a local clock and has an output representing the 1PPS signal received from the opposite site. The time interval counter (TIC) measures the interval x_A (resp. x_B) between local and remote 1PPS.

On a symmetrical link, the delay in both directions equals $\delta = \delta_{AB} = \delta_{BA}$. In real network, the fiber length in both directions slightly differs (e.g. due to patch cords in switching boards, fibers compensating the chromatic dispersion), introducing delay asymmetry Δ:

$$\Delta = \delta_{BA} - \delta_{AB}. \tag{1}$$

The clock offset Θ_{AB} may be then calculated as

$$\Theta_{AB} = \frac{x_A - x_B - \Delta}{2}. \tag{2}$$

III. Link Setup

The optical time transfer utilizes two unidirectional optical channels between Institute of Photonics and Electronics (IPE) and Federal Office for Metrology and Surveying (BEV) – see Fig. 1. The whole optical path consists of several segments. The longest part, connecting points of presents (PoPs) in Prague and Brno, utilizes dedicated DWDM (Dense Wavelength Division Multiplexing) channels in Cesnet2 production network. The link between Brno and Vienna University is another DWDM channel in the cross-border link joining CESNET and ACOnet – CESNET is the Czech NREN (National Research and Educational Network), ACOnet is the Austrian NREN. To connect the national laboratories with network points of presence in both metropolises, the rented pairs of dark fiber are used. The total length of the optical path is 550 km and it is equipped with seven optical amplifiers (EDFA – Erbium Doped Fiber Amplifier). Our transmission system uses the same wavelength in both directions – currently, it is 1551.72 nm (i.e. C-band, ITU channel #32). Description of particular segments is summarized in Table I.

IV. Implementation and Instrumentation

We compared the national time scales of the Czech Republic and Austria using an optical link in our experiments and we evaluated the properties of this optical transfer together with time transfer using GPS. The national time scale of the Czech Republic, UTC(TP), is generated from the Cesium beam atomic clock 5071A/001 in IPE in Prague. The clock is housed in dedicated temperature-controlled chamber where

TABLE I
OPTICAL PATH SEGMENTS

Segment	Length	Attenuation	Technology
IPE – CESNET	16 km	7.0 dB	dark fiber
Cesnet PoP – Brno University	309 km	78.6 dB	Cisco ONS (DWDM channel)
Brno University – Vienna University	220 km	50.0 dB	CzechLight booster/preamp (DWDM channel) [7]
Vienna University – BEV	5 km	1.5 dB	dark fiber

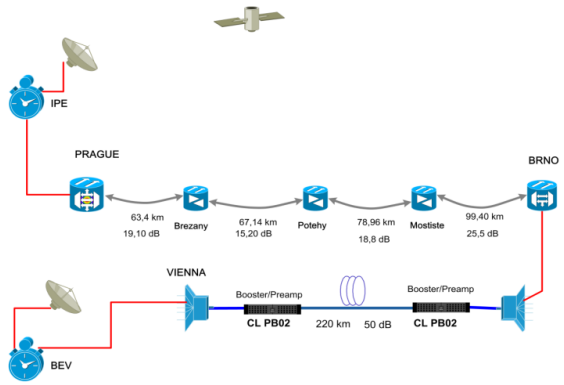

Fig. 1. Schematic of the Optical Link.

the ambient temperature ranges within 0.1C. The Austrian time scale, UTC(BEV) is also generated from the 5071A/001 clock in the BEV in Vienna. Both clocks contribute to the calculation of UTC within the collaboration with the BIPM and thus the 5-day time differences UTC–UTC(k), k = TP, BEV are published monthly in Circular-T [6].

A. Adapters

We designed and manufactured our own time transfer adapters that consist of two main components:

- FPGA chip Virtex 5, which contains all logical circuits;
- SFP (Small Form-factor Pluggable) transceiver, which converts signal between electrical and optical domains.

These adapters encode 1PPS signal from the clock and transport it to the remote site through one of the fibers. Signal from the second fiber is decoded in the adapter and 1PPS referring to the remote clock is provided. Adapter structure is described in [4].

B. Time Interval Counters

In the IPE site, we use Pendulum CNT-91 counter having basic resolution $\approx$ 50 ps, while BEV is equipped with Stanford Research System SR-620 with resolution of $\approx$ 20 ps.

C. GPS Receivers

Both laboratories are equipped with different GPS time transfer receivers: GTR50 (Dicom) in IPE and TTS-2 (Pik-Time Systems) in BEV. Both receivers generate CGGTTS data, thus the Common-View comparison using the GPS code measurements could be done. Unfortunately, comparison using GPS carrier phase measurements couldn't be performed because of the lack of the carrier phase data in the TTS-2 receiver.

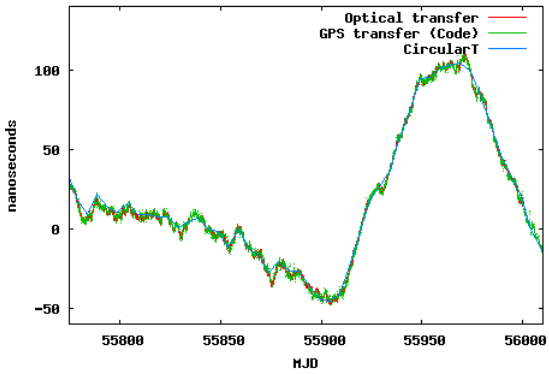

Fig. 2. Measured Time Difference UTC(TP) − UTC(BEV).

V. RESULTS

Our measurements started on August 2, 2011 (MJD 55775), and the data collected until March 14, 2012 (MJD 56000) are presented here. We measured the UTC(TP) and UTC(BEV) time offset every second using the optical method. We are going to present these data and compare them with Common-View GPS (CV GPS), Precise Point Positioning (PPP) [5], and Circular-T values [6].

A. Optical Time Transfer

The graph at Fig 2 provides general overview of all results: red points represent optical measurement data, green points are GPS data, and the blue line shows the time offset between UTC(TP) and UTC(BEV) according to Circular-T. More detailed comparison between optical time transfer and GPS based method is described later.

B. Comparison with GPS transfer

In order to directly compare GPS and optical time transfer, we also processed optical measurement data the same way as CGGTTS does: by calculating the linear regression over interval of 780 s. The difference between optical transfer and CV GPS is shown in Fig. 3 and Fig. 4 shows the detailed comparison for a 5-day period – we can see that optical measurement contains less noise than CV GPS.

Fig. 5 contains measured difference between optical and PPP time transfer. We observed regular diurnal variations in the order of 100 ps, unfortunately the data are available for 18 days only – since the time TTS-4 was installed in BEV. One day results are shown in Fig. 6.

Time stability of all three time transfers in terms of Time Deviation (TDEV) is visualized in Fig. 7. It confirms our observation that optical time transfer has smaller noise than CV GPS and PPP.

Concerning the optical transfer we can identify the white phase modulation noise in averaging intervals of 1–20 s and

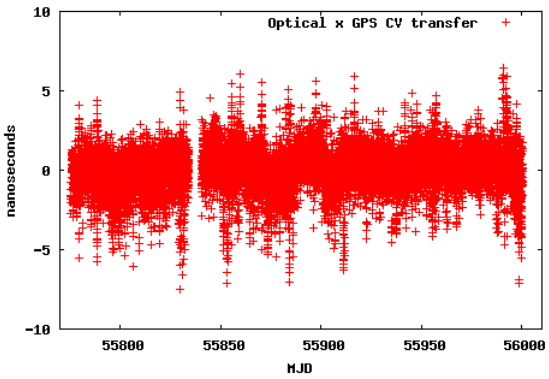

Fig. 3. Difference between optical transfer and GPS CV.

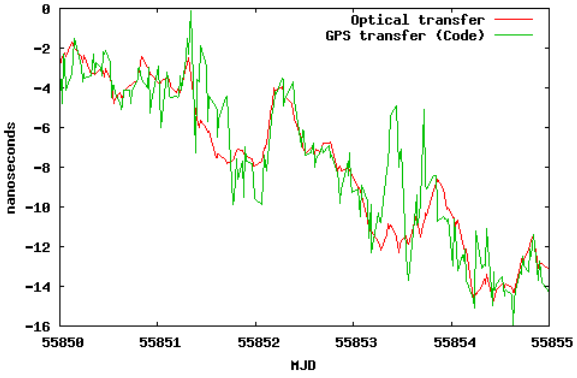

Fig. 4. Detail of optical transfer and CV GPS.

the white frequency modulation noise in averaging intervals of $2 \times 10^1 - 3 \times 10^5$ s. The lowest noise in terms of Time Deviation observed is 30 ps at 20-s averaging interval.

C. Optical link evaluation

Temperature-dependent propagation delay is the important issue of the optical fiber. The dominating effect is caused by the thermal change of the group refraction index, which is about 36 ps/°C/km) [8]. The environmental temperature influence depends on physical installation of optical cable. We

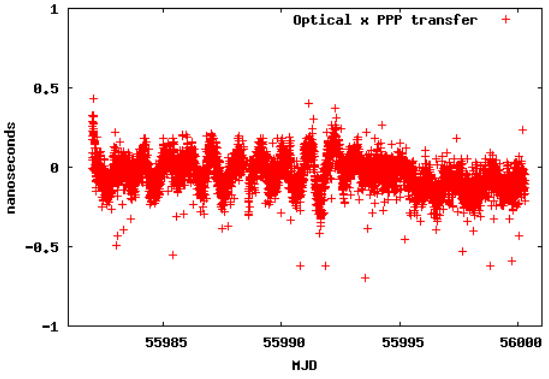

Fig. 5. Difference between optical transfer and PPP.

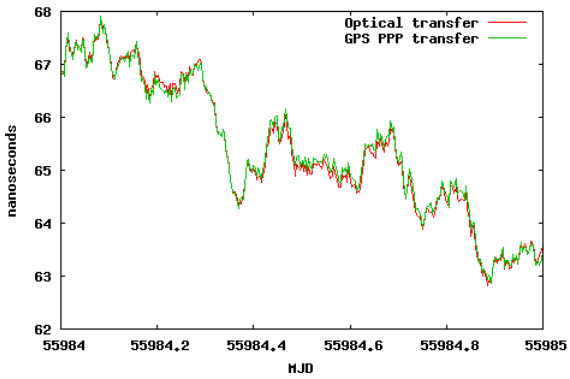

Fig. 6. Detail of optical transfer and PPP.

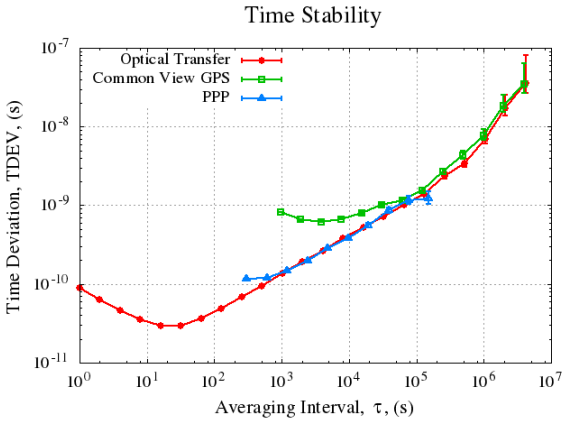

Fig. 7. Time transfer stability.

utilize fiber thread in commercial telecommunication cables which are buried typically 1 m under ground, however part of the technology, namely coils of fiber compensating chromatic dispersion, are installed in technological rooms, usually airconditioned. To describe the delay changes, it is important to distinguish diurnal and seasonal variations. Fig. 8 shows the results of our measurement – data between October 7, 2011 (MJD 55841) and March 14, 2012 (MJD 56000) are displayed. We see the total delay difference is 350 ns during the observation interval. It represents 1.3×10^{-4} of the average propagation delay 2788 μs. Example of diurnal delay changes of 4–7 ns is displayed in Fig. 9.

VI. Conclusion

We implemented optical time transfer system that allows long term time transfer between IPE and BEV and thus provides comparison between UTC(TP) and UTC(BEV). According to the data collected in first eight months of the system operation, the stability of the implemented optical time transfer method in terms of Time Deviation is better than Common View GPS time transfer. The lowest noise is 30 ps at 20-s averaging interval. We are going to continue in evaluating seasonal influence to the time transfer accuracy once data of the whole year will be available.

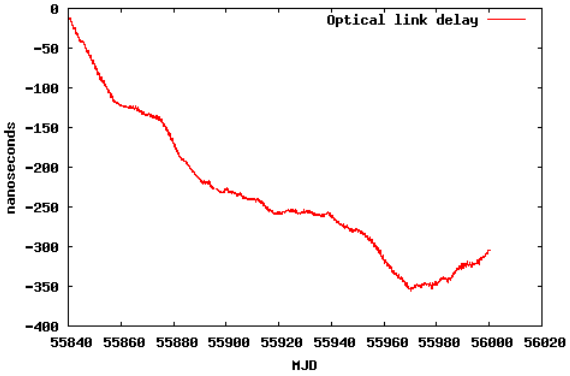

Fig. 8. Seasonal variation in the delay of the optical path.

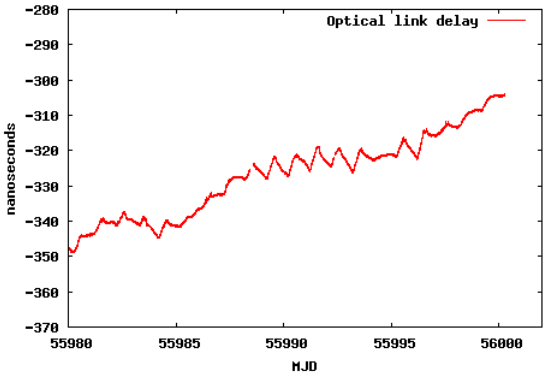

Fig. 9. Diurnal variation in the delay of the optical path.

ACKNOWLEDGMENT

The authors would like to thank Werner Mache and Anton Niessner from the Federal Office for Metrology and Surveying for their participation in this long-term evaluation and for their help with processing the measured data.

This work has been sponsored by the Czech Office for Standards, Metrology and Testing within the Project III/13/11 of the Program of Metrology Development in 2011.

CESNET work was supported by the CESNET Large Infrastructure project (LM201005), funded by the Ministry of Education, Youth and Sports of the Czech Republic.

REFERENCES

[1] M. Lombardi, L. Nelson, A. Novick, and V. Zhang, *Time and Frequency Measurements Using the Global Positioning System*, Cal. Lab. Int. J. Metrology, pp. 26–33, (July–September 2001).

[2] S. C. Ebenhag, P. O. Hedekvist, P. Jarlemark, R. Emardson, K. Jaldehag, C. Rieck, and P. Lothberg, *Measurement and Error Sources in Time Transfer Using Asynchronous Fiber Network*, IEEE Transactions on Instrumentation and Measurement, IM-59, pp. 1918–1924.

[3] S. C. Ebenhag, P. O. Hedekvist, and K. Jaldehag, 2010, *Single-way Fiber-based Time Transfer with Active Detection of Time Transfer Variations*, in Proceedings of the 42nd Annual Precise Time and Time Interval (PTTI) Systems and Applications Meeting, 15–18 November 2010, Reston, Virginia, USA, (U.S. Naval Observatory, Washington D.C.), pp. 413–426.

[4] V. Smotlacha, A. Kuna, and W. Mache, 2010, *Time Transfer in Optical Network*, in Proceedings of the 42nd Annual Precise Time and Time Interval (PTTI) Systems and Applications Meeting, 15–18 November 2010, Reston, Virginia, USA, (U.S. Naval Observatory, Washington D.C.), pp. 427–436.

[5] J. Kouba, and P. Héroux, *GPS Precise Point Positioning Using IGS Orbit Products*, GPS Solutions, vol. 5, no. 2, pp. 12–28, 2001.

[6] BIPM, *Circular-T*, at http://www.bipm.org/jsp/en/kcdb_data.jsp.

[7] Cesnet, 2009, *CzechLight Amplifier devices*, at http://www.optokon.com/datasheets/CActive_devices_for_optical_network/C8-EDFA/ACT_01-07_ENEDFA.pdf

[8] L. G. Cohen and J. W. Fleming, 1979, *Effect of Temperature on Transmission in Lightguides*, Bell System Technical Journal, Vol. 58, No. 4, pp. 945–951.

About time measurements

M. Siccardi, M. Abgrall†, G. D. Rovera†
SKK Electronics, Cuneo, Italia
†LNE-SYRTE, Observatoire de Paris - LNE - CNRS - UPMC, France
e-mail: daniele.rovera@obspm.fr

***Abstract*— When speaking of time measurement often no distinction is made between time and time interval but the difference in accuracy between this two cases can be huge. In this paper we will address some of the aspect related to the accuracy in time-tagging a single or repetitive event.**

INTRODUCTION

The continuous improvement of primary clocks [1] and the increasing requirements in time comparisons in new research areas [2], [3] are the motivation for this paper intended to revisit some of the aspects of the techniques used in time comparisons.

When dealing with frequency comparison/distribution it is evident that there is an interest in distributing a high frequency to get rid of frequency uncertainty. For example at LNE-SYRTE we use optical links to distribute signals at 100 MHz, 1 GHz and at around 9 GHz for feeding atomic fountains, optical clocks and other experiments. However all these links are not suited for transmitting time signals since at every reset of the link the time marker is set to an arbitrary cycle. If we apply the same concept to time comparisons the first idea is to use some features (like the zero crossings) of a high frequency signal as time markers, but this can have some drawback.

Before entering in technical details a short recall on what we call time measurement is presented. SI defines the second: this unit is a time interval and not a time scale. When speaking about time measurements we consider measures that give the position of a particular time event in a given time scale. The worldwide accepted primary timescale Coordinated Universal Time UTC is not available in real time and establishes time markers every 5 days only. In this paper we consider as primary standard the local representation of UTC, usually named UTC(k). We try to address measurement of local events versus UTC(k), including the events that will be used for the evaluation of differences between UTC and UTC(k)

I. UTC(K) LOCAL DEFINITION

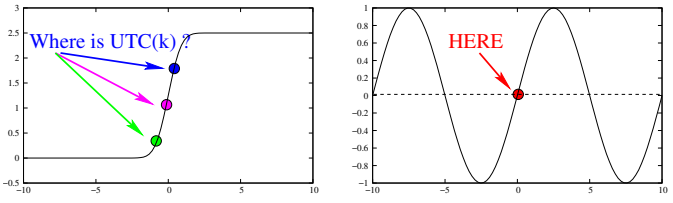

Fig. 1. Examples of time marker in a UTC(k) signal

To account for propagation delay the position in space of the signal must be well defined, at least to a level not being the limiting factor of uncertainty.

Each laboratory has the freedom to chose his own definition of this physical signal, but generally the local time marker is a 1 PPS (one pulse per second) signal crossing a defined trigger level on the rising edge. The signal can be physically available at the output of a 1 PPS distributor (BNC type connector) or (as at LNE-SYRTE) at the input of the counter devoted to clock comparisons. Whatever is the definition of the local physical signal UTC(k), all time measurements must be referenced to this primary time standard, by reporting the time difference between the measured event and one identified time marker of this time scale, associated to the measurement uncertainty.

We deliberately does not differentiate at this point between measures of a periodic event, as the 1 PPS signal generated by a given frequency standard or a single event like the arrival of a T2L2 [4] laser echo. This is to focus mostly on type B uncertainty that are not reduced by averaging results of repeated measurements. Considering that the time events to be measured can have an intrinsic accuracy as good as the local standard, it is very important to chose a definition that allows the best accuracy. Here we consider the advantages and disadvantages of a definition of UTC(k) based on different types of signals: the rising edge of a 1 PPS or the zero crossing of a 100 MHz or 100 MHz signal.

A. Rising edge of 1 PPS

This is largely the most used signal in laboratory dealing with time measurement and up to a few years ago it was the only signal that was suitable to measure a single event. In fact 1 PPS pulses are separated enough to be identified and time-tagged by a technicians. In modern times a time interval counter can measure the delay between a time event and the previous or the following 1 PPS tick, by letting the identification of the tick to a simple computer running a NTP time server. As there is no recognized standard for the 1 PPS signals the interpretation of the time mark depends from laboratory tradition. At the very beginning the 1 PPS was defined only as a “TTL” signal rising from 0 to 5 V. In practice a fast TTL signal can’t propagate over distances exceeding a few centimeters, therefore the signal of 1 PPS has been adapted to propagate on a coaxial line. For this the output impedance of the 1 PPS generator must be adapted to the 50 Ohm of the coaxial line and the line must be terminated over a 50 Ohm load. Here two standard coexists, often in the same laboratory:

5 V at the output of the loaded generator and 5 V before the output resistance, i.e. 2,5 V at the loaded output. Also for the trigger point different "standards" exist, the more common is half of the maximum level, often determined by increasing the trigger level of the counter until he stop to trig. A second one most elegant but very hard to implement is define the time marker at the maximum slope of the 1 PPS rising front. When used in practice the UTC(k) 1 PPS is connected to a device using a fixed trigger level. This level can be manually set with some accuracy if the device receiving the signal is a time interval counter, or set to an arbitrary level, sometime unknown, in other cases like in GPS receivers. Good shaped fast 1 PPS signals can exhibit a rise time of about 500 ps, but in several cases a rise time exceeding 2 ns has been noticed. As an example we can consider that the time marker of the UTC(k) 1 PPS, with a rise time of 1 ns, is defined at 1.25 V. If this signal is used to start (or stop) a nearby counter the cable attenuation/distortion can be neglected, the 50 mV expected as accuracy on trigger setting translates in 20 ps uncertainty. In case the signal is used to reference a device like a GPS receiver an error of 100 ps can be expected. In the case the signal has to travel on a long transmission line the pulse shape can be drastically modified and therefore more uncertainty has to be considered.

B. Zero crossing of a 10 MHz

With the development of electronic devices the problem of identification of a particular zero crossing of a 10 MHz signal can be solved without troubles, therefore the zero crossing of a 10 MHz signal is a good candidate as time marker for the physical realization of a time scale UTC(k). Although the slope of a typical 10 MHz signal is smaller than the slope of a 1 PPS, the trigger level can be well defined and a smaller uncertainty due to the trigger level is expected.

The less obvious, but very important reason to use the 10 MHz, is the fact that many equipments, like GPS receivers, generates their internal time-base from a 10 MHz reference input and accept a 1 PPS input only to identify a particular cycle of the 10 MHz. To better explain this, let us consider the calibration of a GPS receiver by comparison with a distant calibrated device by using a traveling receiver. As calibration of a receiver, we intend the measure of the delay between some reference point in the receiver itself and the received GPS time scale received at the center of phase of the GPS antenna. If the local UTC realization is based on a 1 PPS, and the internal time-base of the GPS receiver is based on the 10 MHz signal, during the campaign it is necessary to measure at least four times the difference between the 1 PPS and the internal time-base of the receivers. In fact, this measure has to be done once for each static receiver at its own site; and twice for the traveling receiver, one at each site also. This difficult operation is specific to each type of receiver, and in some case almost impossible because there is no a physical output of the internal time-base. These four measurements will largely impact on the total uncertainty budget, further increased by the four measurements between the 1 PPS signal feeding the receivers and the local UTC materialization. If the definition of the time markers is given on the zero crossing of the 10 MHz (also for the travel ling receiver) the overall measurement uncertainty is smaller because only the measurement of the 10 MHz against the local UTC are necessary.

When looking more deeply at the uncertainties related to the choice of this definition, we must take into account multiple reflections that can occur in a cable carrying the 10 MHz signal. This source of uncertainty can be neglected when using 1 PPS signals because reflected signals is delayed away from the trigger point, but the sum of the signal sinusoid with the reflected one is a new sinusoid time shifted. The impedance matching at both sides of a cable is never perfect, it can range from the -20 dB for standard good quality equipment to -40 dB for premium special devices. Unfortunately in some cases the reflected wave can reach -10 dB or worse. The maximum time error due to multiple reflections can be roughly estimated with the formula $\Delta_t = |\Gamma_1||\Gamma_2|/(2\pi f)$. As numerical example with a reflection of -20 dB ($|\Gamma = 0.1|$) at both sides the time error can be anywhere between -150 ps and +150 ps, depending on the cable length. We will not discuss in details errors due to the harmonic distortion, but also in this case 30 dB second harmonic can shift the zero crossing of hundreds of picosecond.

From the above considerations it follows that the definition of the time markers on the zero crossing of the 10 MHz does not represent a large improvement in the accuracy of time measurements unless a large effort is carried on avoiding impedance mismatch and harmonic distortion. At this point it is useful to recall that the impedance mismatches on the 10 MHz distribution will also affect the measurement referred to the 1 PPS signal as in many case the real time-base of time measuring devices is based on the zero crossing of the 10 MHz and the offset between the internal time-base and the 1 PPS reference is measured only once at the set-up of the device.

C. Zero crossing of a 100 MHz

In this case there is an improvement of one order of magnitude in accuracy over the zero crossing of 10 MHz. For a signal with a power level around -10 dB the slope near the trigger point is smaller than the slope of a good 1 PPS signal, but not more than a factor two. Hysteresis in the sine-wave to square-wave conversion might introduce severe delay between the zero crossing of the reference signal and the effective time inside the DUT. Delays on the order of 100 ps can arise when 100 MHz, 10 dBm reference signals and 100 mV hysteresis are in play. This delay might be very likely sensitive to input power levels. The drawback of a UTC(k) definition based on this signal is the fact that is very hard to distinguish between two successive zero crossing separated only by 10 ns. A further point is that in practice the majority of the instruments used to time-tag a single or repetitive event requires a 5 MHz or a 10 MHz input as clock signal. Nevertheless new equipment can be developed according to this standard, and in any case a frequency divider can be used as a front end of an old equipment.

D. Composite signal

From the above analysis it is evident that when the needs of absolute time measurement against the local UTC(k) stays in the several hundreds of picosecond range the old 1 PPS is still the good signal, maybe with some clear and measurable definition of the time marker point. When this barrier has to be broken to reach the tens of picoseconds or lower, as required for T2L2 [4], and ACES microwave link [2], the composite signal can be a better choice, especially if it must be propagated from the time laboratory to the roof of the building where the laser or receiver antenna is installed.

The composite signal can be defined as the first zero crossing of a 100 MHz (or 1 GHz) following (or preceding) the 1 PPS. The 100 MHz will provide an accurate series of time markers, while the 1 PPS allows the removal of the 10 ns ambiguity of the accurate measurement. This apparently complex system is in practice greatly simplified by the fact that the majority of the instruments used to perform time measurements already uses an internal time-base built from the reference 10 MHz signal, eventually multiplied to 50 MHz or 100 MHz, like in the case of GPS receivers. For less demanding measurement the 1 PPS alone can be used, accepting that the accuracy is reduced by the uncertainty of the time difference between the primary local time standard (100 MHz) and the working standard (1 PPS). In Fig.2 a simplified schematic of a practical implementation of a composite UTC(k) is presented.

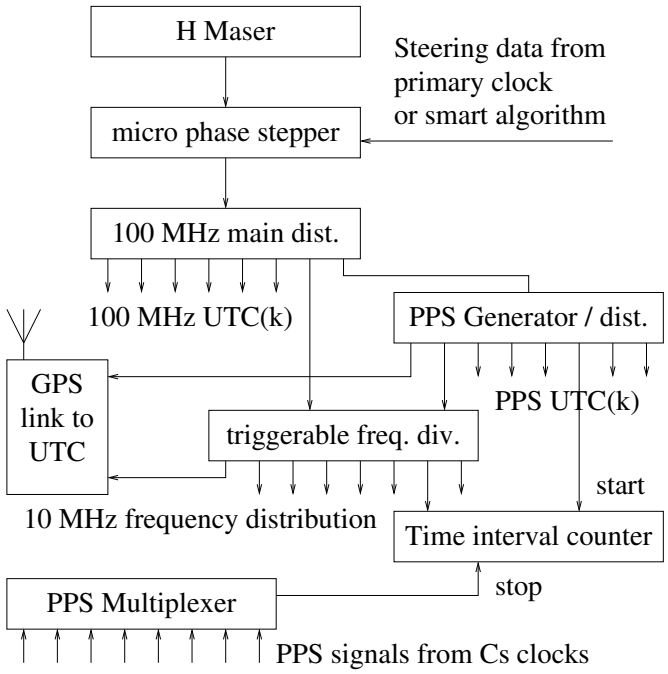

Fig. 2. Implementation of a composite UTC(k)

In this setup the local primary time standard is defined by the zero crossing of the 100 MHz signal on a selected connector of a 100 MHz distribution amplifier. To better define the exact position in space of this reference a symmetrical connector like the APC7 is recommended.

The other outputs of this distributor can be calibrated with an expected accuracy of 30 ps and used as working standards. This level of accuracy requires to use a distribution amplifier with very good performances in impedance matching, harmonic distortion (<-40 dBc), and thermal stability. One of the 100 MHz output will feed a 1 PPS generator / distributor, and one of the 1 PPS output will be chosen as secondary time standard. The measure of time difference between a defined trigger point of this 1 PPS and the primary 100 MHz will be limited mostly by the 1 PPS signal itself, but in case of a fast rise time an accuracy of 200 ps can be expected. All the routine measurement can be referred to this signal, by keeping the traditional set up of clock comparison based on hourly (daily) measurement, therefore this new more accurate UTC(k) definition will not impact the normal time-keeping activity.

The advantages of this composite definition are put in evidence at the end of next session where we consider the case of a GPS receiver used to compare the local time scale UTC(k) with the time scale of a remote laboratory. Similar considerations can be extended to other devices like the Ultra Stable Event Timer Designed for T2L2 [5]

II. Delay measurements

Once the primary time standard based on the zero crossings of a 100 MHz signal has been chosen, the other working standards, based on the same signal or on the 1 PPS, have to be calibrated against this primary one. This calibration has to be done at the setup of the system and repeated when required from equipment drift or failures. We recall the concept that the standards considered here are time series, not only time intervals and that we deal with the absolute position in time of the time markers non only on the time distance between two consecutive events.

In this frame two types of measurements can be identified, the measurement performed between homogeneous signals and the measures between different types, like the 1 PPS and the 100 MHz. In this second case particular care has is necessary to avoid systematic, as an example we can imagine to use a time interval counter to measure the delay between the rising edge of a 1 PPS and the first zero crossing of the 100 MHz. In usual practice to get rid of counter internal delays the two channels are inverted. In this particular case also the trigger level must be changed and it has to be considered that not only channel delays differences but also the reflection coefficient can affect the accuracy.

For demanding measurement to reach the lowest uncertainty the measurement chain has to be taken as short as possible and the choice of the measurement interface is the key element. To show this with an example we reconsider the relative calibration of GPS receivers for establishing a time link between two sites where the UTC(k) is materialized by a 100 MHz signal. The diagram of Fig.3 puts in evidence the interface points of a “Integrated 100 MHz Based GPS Receiver” built around a commercial geodetic GPS receiver.

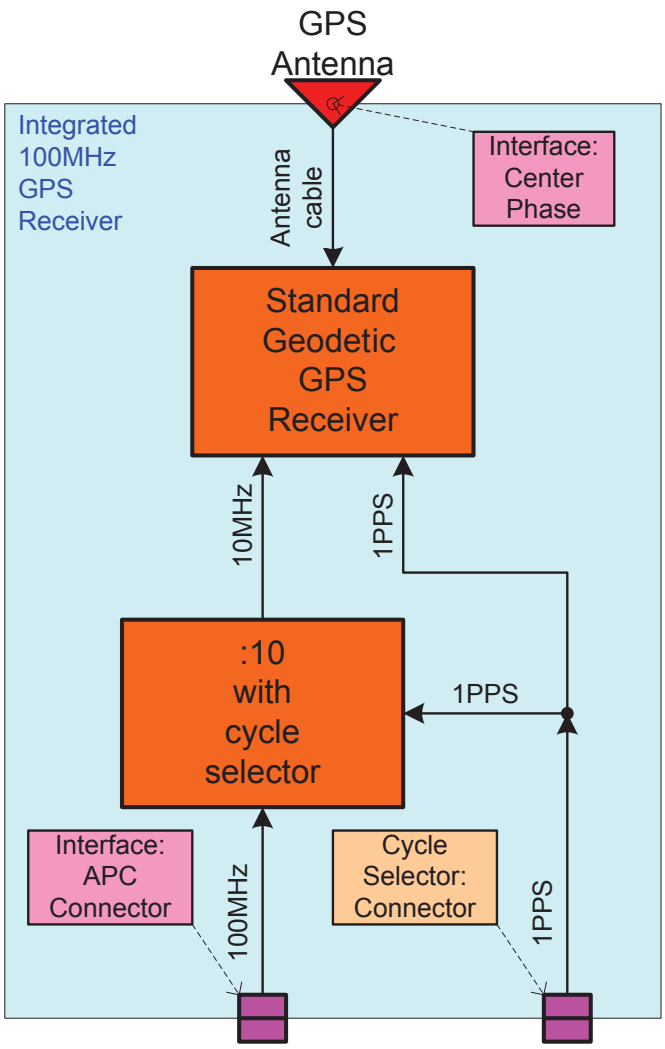

Fig. 3. Integrated 100 MHz Based GPS Receiver

By considering the receiver and the frequency divider as a whole we identify two interfaces point for this device: on one side the 100 MHz input connector (APC 7) and in the other side the center of phase of the antenna. As delay of receiver (for carrier L1 and L2) we intend the delay measured by the receiver when a event (time marker) is applied simultaneously at the 100 MHz input and at the center of phase of the antenna. The third input for the 1 PPS is necessary to chose the right 100 MHz cycle, but does not enter in result of computation.

Lets consider again the case of the calibration transfer between two stationary GPS receivers using a traveling GPS receiver. If the 3 GPS receivers can be represented as in Fig.3, the whole calibration will be reduced to the following steps.

- For the receiver at site A the delay must be known from absolute calibration or chosen at an arbitrary value.
- The delay between UTC(A) and the connector feeding the GPS front end is measured. As this is a fast repeating signal the type A uncertainty can be small, but the type B depends mostly on the impedance matching of the distribution amplifier, of the GPS front-end and of the counter or phase meter.
- The above step is repeated for the traveling GPS.
- The delay of the traveling receiver is calculated by usual technique of common view with the A calibrated receiver. The uncertainty of this delay will be determined by the comparison noise, the sum of uncertainty of the two previous measurements, and by considerations on the stability of the 3 receivers during the calibration campaign.
- At site B the delay between UTC(B) and the front-end of the static and traveling receivers is measured.
- The delay of the receiver B is calculated by common view with the traveling receiver.

The total uncertainty is dominated by the GPS signals, by the receiver behavior, and by the stability of the traveling equipment. On the other hand, the 1 PPS measurement contributions are not present in the error budget. They are substituted by the residual uncertainty of the 100 MHz zero crossing, which should be almost negligible (respect to the GPS contribution). The measurement necessary to define the relationship between the local UTC(k) are reduced to the minimum and in case of good GPS front-end can be accounted for less than four times 100 ps uncertainty. This 100 ps uncertainty will be totally insignificant compared to the other sources that are intrinsic to the GPS technique and the stability of devices.

This simplification of the concept will not mean that other type of measurement are unnecessary, and that the uncertainty of the calibration can be reduced arbitrarily. In fact the hardest point is the estimation of the stability of the traveling receiver along the calibration campaign, considering that in the two sites the set up can differ a lot and therefore several accessory measurement has to be carried out, but will not enter directly on the uncertainty budget. A typical example can be the study of variation of the antenna cable delay due to the temperature and to the stress induced by sharp bending related to the installation. Same of related topics, and the multi-path inside antenna cable have been addressed in the past can be found in literature [6].

REFERENCES

[1] J. Guena, et al."Progress in atomic fountains at lne-syrte," *Ultrasonics, Ferroelectrics and Frequency Control, IEEE Transactions on*, vol. 59, pp. 391 –409, march 2012.

[2] L. Cacciapuoti, et al. "Atomic clock ensemble in space: Scientific objectives and mission status," *Nuclear Physics B - Proceedings Supplements*, vol. 166, pp. 303 – 306, 2007.

[3] OPERA Collaboration, "Measurement of the neutrino velocity with the opera detector in the CNGS beam," 2011.

[4] E. Samain, , et al., "Time transfer by laser link T2L2: Current status and future experiments (invited)," in *2011 Joint Meeting of EFTF-FCS*, pp. 1 –6, may 2011.

[5] E. Samain, P. Fridelance, and P. Guillemot, "An ultra stable event timer designed for T2L2," in *Frequency and Time Forum, Noordwijk, NL, 13-16 April 2010*, 2010.

[6] F. Ascarrunz, T. Parker, and S. Jefferts, "Group-delay errors due to coherent interference," in *1999 Joint Meeting of EFTF-FCS*, vol. 1, pp. 198 –202 vol.1, 1999.

Estimation of COMPASS On-Board Clock Short-term Stability

GONG Hang, NI Shaojie, MOU Weihua, ZHU Xiangwei, WANG Feixue
Satellite Navigation R&D Center, School of Electronic Science and Engineering
National University of Defense Technology
Changsha, Hunan 410073, China
Email: gonghang@nudt.edu.cn

***Abstract*—The short-term frequency stability estimation of GNSS on-board clocks is very important for clock modeling and prediction. Orbit Determination and Time Synchronization (ODTS) method is commonly used to estimate the clock offset, which needs continuous observation by large monitoring ground network and complicate algorithms. COMPASS is on its early stage of construction and has not globally distributed station network for satellites tracking. In this paper, we have analyzed an estimation method based on a single monitoring station observation. Based on this method, a simple method for COMPASS MEO/IGSO on-board clocks estimation using smoothed broadcast ephemeris is presented, and a method for COMPASS GEO on-board clocks estimation using satellite radio ranging (SRR) is also discussed. At the end of this paper, the preliminary estimation results for COMPASS IGSO and GEO on-board clocks by these two methods are presented.**

I. INTRODUCTION

In satellite navigation system, estimation of the performance of satellite on-board atomic clocks will affect the accuracy of satellite clock offset modeling and prediction, and thus directly impact user positioning and timing accuracy. Evaluation of satellite on-board clock performance is of great significance for the control segment. In the application such as satellite clock offset modeling, simulation and prediction, not only characteristics determined by the medium- and long-term stability of the satellite clock need to be known, short-term stability parameters of satellite clock also need to be obtained.

Similar to satellite orbit determination, satellite clock offset solution is very complex, and it is usually carried out by the ODTS (Orbit Determination and Time Synchronization) method, which needs continuous observation of large ground monitoring networks and complex determination algorithms. Precise orbit and clock products provided by IGS analysis centers are derived from post-processing using ODTS method [1].

GPS satellite clock stability estimation is usually implemented using IGS precise clock products for the moment. The sampling interval of 30s typically, even the sampling interval of 5s provided by analysis center COD (Center for of Orbit Determination in Europe), can not meet the need of shorter sampling intervals (e.g. 1s) stability estimation. On the other hand, IGS products are only available for GPS and GLONASS system currently. COMPASS is in its early stage of construction, so there are no globally distributed stations to obtain continuous satellite tracking. In addition, only a few agencies have the measurement data of regional network due to access permission. For COMPASS system, there are certain difficulties for common users to obtain precise satellite clock parameters presently.

In this paper, two simple short-term stability estimation methods for MEO/IGSO and GEO on-board clock are discussed. These methods can be implemented using a single station measurement rather than network observation, and it is simply required that the monitoring receiver clock stability is better than satellite clock. Compared with IGS clock products, the smoothed broadcast ephemeris method is validated using GPS data. Short-term stability of COMPASS IGSO and GEO on-board clock are estimated using these methods at the end.

II. SINGLE STATION ESTIMATION METHODS OF SATELLITE CLOCK STABILITY

For satellite j, the pseudorange and carrier phase observation equations of receiver k are as follows:

$$\rho_k^j = d_k^j + c\left(\Delta t_S^j - \Delta t_R^k\right) + T_k^j + s_k^j + t_j + r_k + m_k^j + \varepsilon_\rho^j \quad (1)$$

$$\varphi_k^j = d_k^j + c\left(\Delta t_S^j - \Delta t_R^k\right) + T_k^j + N_k^j\lambda + \varphi_0^j + s_k^j + t_j + r_k + m_k^j + \varepsilon_\varphi^j \quad (2)$$

Where ρ_k^j is pseudorange; φ_k^i is carrier phase observation; d_k^j is geometric distance of satellite and receiver; Δt_S^j is satellite clock offset; Δt_R^k is receiver clock offset; T_k^j is atmospheric propagation delay, including the ionosphere, troposphere path delay, etc; $N_k^j\lambda$ and φ_0^j are integral and fractional ambiguity of carrier phase; s_k^j is error caused by the Sagnac effect; t_j is transmission delay of

satellite; r_k is receive delay of receiver; m_k^j is multipath error; ε_ρ^j and ε_φ^j are measurement noise of pseudorange and carrier phase.

Like one-way time synchronization method, equations (1) and (2) show that, the following variables should be corrected before the computation of satellite clock offset:

- Geometric distance d_k^j between satellite and receiver;
- Receiver clock offset Δt_R^k;
- Atmospheric propagation delay T_k^j, Sagnac effect s_k^j, and multipath error m_k^j;
- Measurement noise ε_ρ^j and ε_φ^j.

Among these variables, tropospheric delay and Sagnac effect can be determined according to respective models; ionospheric delay can be determined by model or dual-frequency combination method; multipath error can be reduced by improving receiver antenna environment and multipath rejection algorithm; measurement noise is high frequency noise, and it will affect the short-term stability estimation accuracy. Considering that short-term stability computation only require relative variety of clock offset rather than its true value, carrier phase observation with lower measurement noise is preferred, and equations (2) is used.

Because only relative clock offset is needed to estimate satellite clock short-term stability, we can determine the on-board clock offset with respect to receiver clock. In this case, satellite clock stability can be obtained as long as the stability of receiver clock is better than that of satellite clock. It can be achieved easily, such as a receiver with active hydrogen maser reference. If it works in the other way, when the satellite clock stability is better than receiver, this method also provides a receiver clock stability estimation approach.

After all the above variables are corrected, the satellite on-board clock offset with respect to receiver clock is as following:

$$\Delta t_k^j = \frac{1}{c}\left(\varphi_k^j - d_k^j\right) + \Delta\varepsilon_\varphi^j \tag{3}$$

Where $\Delta\varepsilon_\varphi^j$ is residual error. Receiver can obtain carrier phase observation φ_k^j with high sampling rate. According to equation (1.3), satellite clock offset with the same sampling rate can be obtained, as long as geometric distance of satellite and receiver is determined before hand. The short-term stability of on-board clock can be estimated consequently.

Since receiver position can be accurately calibrated, the main problem to determine the geometric distance is how to obtain precise satellite position. There are several ways to determine the satellite position. In the following parts of this paper, the principles of several methods are described, and then the performance of these methods are analyzed and compared.

III. Estimation Method for COMPASS MEO/IGSO On-Board Clock Short-Term Stability

For GPS and GLONASS systems, the accurate satellite position can be obtained directly from IGS precise ephemeris product. IGS final ephemeris has the accuracy of 1~2cm with sampling interval of 15 minutes. Interpolation is required to obtain satellite position with higher sampling rate. Using windowed trigonometric and polynomial interpolation algorithm [2], the interpolation error can be less than 1mm. Its impact on short-term stability estimation can be ignored.

The estimation method based on precise ephemeris is carried out as follows [3, 4]:

1) The transmission time of satellite for each observation is calculated;
2) Satellite position is calculate by precise ephemeris interpolation;
3) Geometric distance of satellite and receiver for each observation is calculated;
4) Carrier cycle slips of carrier phase observations, atmospheric propagation delay, Sagnac effect, and multipath errors are corrected;
5) The satellite on-board clock offset with respect to receiver clock is calculated using equation (1.3), and its short-term stability is computed consequently.

As to COMPASS, there is no precise ephemeris available but broadcast ephemeris. Broadcast ephemeris is predicted results of the post-processed satellite position data using ODTS method. The prediction error of the satellite orbit both in cross-track and along-track direction normally is 5~10m [5], But the prediction error in radial direction which changes relatively slow is much smaller for it is fully observed, with only 1/3 to 1/4 of the error in cross-track and along-track directions [5], which does not affect the estimation of the short-term stability of the satellite clock. Therefore, without precise ephemeris, we can try to use broadcast ephemeris to estimate the stability.

Taking GPS as an example, the broadcast ephemeris is updated every 2h. Each group of ephemeris parameters is available for 4h centered at TOE (Time of Ephemeris). The precision is highest at TOE, and gradually reduces with the aging of ephemeris. Each group of ephemeris parameters is a combination of forecasted fitting results using data of a specific time range. Thus the calculated satellite orbit parameters according to each group of ephemeris parameters jump at the time of ephemeris parameters update. In order to reduce the impact of the jump on the short-term stability estimation, it is needed to smooth the broadcast ephemeris.

For each epoch, there are two groups of ephemeris parameters available. It is possible to use the adjacent two groups of broadcast ephemeris parameters to calculate the satellite positions in order to avoid satellite orbit jumps. As both groups of ephemeris parameters are available at the same time, such smoothing does not introduce additional error. As the predicted error of each group of broadcasted ephemeris is roughly the same, it is suggested here to smooth broadcast

ephemeris using linear weighted method according to the ephemeris age, namely:

$$p = \frac{t_f - t}{t_f - t_b} \cdot p_b + \frac{t - t_b}{t_f - t_b} \cdot p_f \tag{4}$$

Where t is the observation epoch, t_b and t_f are TOE for the two adjacent groups of broadcast ephemeris respectively, and P_b and P_f are satellite positions calculated from the above two groups of broadcast ephemeris for t. Experiments show that the linear weighted smooth method eliminates the jumps of calculated satellite orbit, which helps to improve the estimation accuracy of short-term stability.

Based on the same observation data of GPS L1 carrier phase, the short-term stability of GPS PRN14 on-board clock is estimated using smoothed broadcast ephemeris with linear weighted method as in Fig. 1.

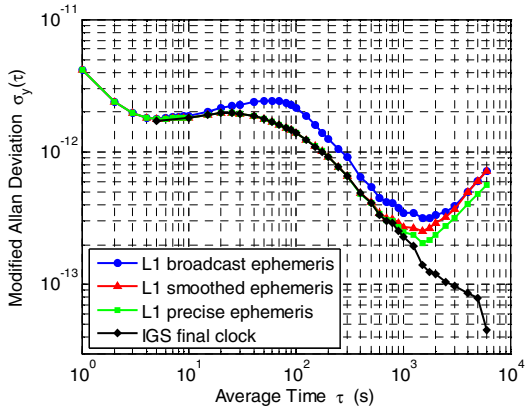

Figure 1. Frequency Stability of GPS PRN14 (MEO) On-board Clock

Fig. 2 shows estimation error of the smoothed broadcast ephemeris method. The estimation error is defined as the relative bias between the estimation result and IGS final clock.

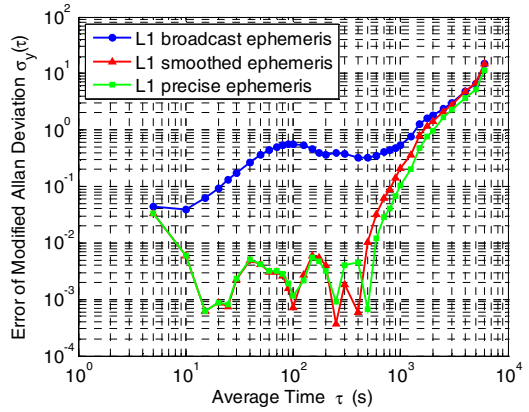

Figure 2. Estimation Error of the Smooted Broadcast Ephemeris Method

From Fig. 2 results, the relative bias of smoothed broadcast ephemeris method and the precise ephemeris method from IGS final clock both are less than 0.1, within the sampling interval of 5~800s, which means that the estimation error of the two methods is a less order of magnitude than the stability itself. Fig. 2 also indicates that the results of smoothed broadcast ephemeris method and the precise ephemeris method are consistent with each other.

The two methods both are applicable to estimate GPS on-board clock short-term stability. But for COMPASS, there is no precise ephemeris available but broadcast ephemeris for the moment. So only the smoothed broadcast ephemeris method is practicable for COMPASS on-board clock estimation.

IV. Estimation Method for COMPASS GEO On-Board Clock Short-Term Stability

For COMPASS MEO/IGSO satellites, we can use smoothed broadcast ephemeris to estimate on-board clock, but for GEO satellites, broadcast ephemeris is not precise enough to estimate clock stability at present due to the difficulty in orbit determination. In this case, the above method is not available for COMPASS GEO satellites any more.

References [6] have researched on estimating the geometry distance of the satellite and receiver using satellite laser ranging (SLR). In GNSS systems, laser ranging is generally used to validate the estimated satellite orbit parameters. Due to the constraints of weather and other factors, laser ranging is unable to achieve continuous observation, which is not adaptive to evaluate the short-term stability. The proposed methods in [6] are not suitable to estimate the short-term stability of GEO on-board clocks.

COMPASS GEO satellites can be observed continuously by the time synchronization monitoring stations. COMPASS GEO satellite has a C-band transponder on it to achieve time synchronization with monitoring stations. Similar to SLR, Satellite Radio Ranging (SRR) works in the way that the monitoring station receives the satellite transferred signal transmitted by the station itself [7]. By measuring the travel delay from the station to the satellite and back, the geometry distance between the satellite and station can be determined. If the GNSS receiver and the monitoring station have the same position and refer to the same clock, then the satellite on-board clock offset can be calculated by equation (3).

Several errors should be corrected before SRR and GNSS carrier phase observations are used to calculate the satellite clock offset: one is the time difference between the observation epochs of the GNSS receiver and the SRR observation station; the other is the distance difference between the antennae centers of the GNSS receiver and the SRR observation station.

From the above discussion, hitherto the SRR method is an effective approach for COMPASS GEO on-board clock stability estimation.

V. Estimation Results

A. *COMPASS IGSO On-Board Colck*

As to COMPASS, there is no precise clock available to validate the estimation results. The observation data obtained from two monitoring stations (Beijing and Sanya) within the same observation period are used to estimate the short-term stability of satellite clock. The estimation results of Beijing

and Sanya are compared to validate themselves one another. The receivers of the two stations both have hydrogen masers synchronized with BDT as reference.

The observation period is from BDT 2011-10-09 06:00:00 to BDT 2011-10-09 18:00:00. The B3 carrier phase observations and broadcast ephemeris are used to estimate the short-term stability of SV09 (IGSO) on-board clock. The estimation results are shown in Fig. 3.

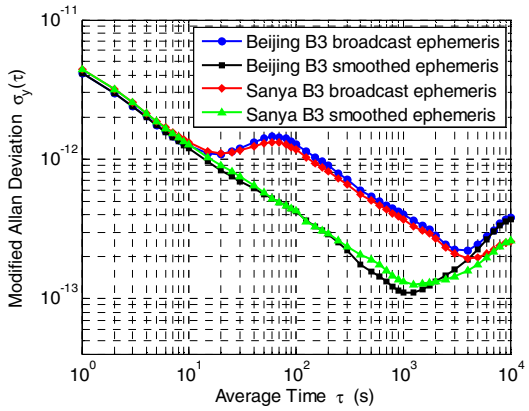

Figure 3. Frequency Stability of COMPASS SV09 (IGSO) On-board Clock

The above result shows that, for SV09 on-board clock, the estimated short-term stability of Beijing station agrees well with Sanya station, and the result based on smoothed ephemeris is better than that based on broadcast ephemeris due to the elimination of jumps of calculated satellite orbit. So the estimated result of Fig. 2 can be considered as actual short-term stability of SV09 on-board clock, at the sample interval of 1~1000s approximately.

B. COMPASS GEO On-Board Colck

For COMPASS GEO satellite on-board clock, using Sanya station SRR and GNSS receiver observation data, the short-term stability of SV01 and SV03 on-board clocks are estimated. Fig. 4 shows the stability results. The observation period is from BDT 2011-10-09 06:00:00 to BDT 2011-10-09 18:00:00.

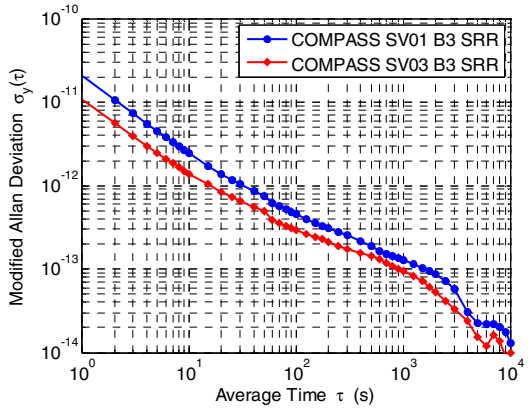

Figure 4. Frequency Stability of COMPASS SV01 (GEO) and SV03 (GEO) On-board Clock

The above result shows that, the estimated short-term stability of GEO on-board clock is consistent with that of IGSO on-board clock at the sampling interval of 10~1000s, and is better at the interval of over 1000s, this maybe due to smoothed broadcast ephemeris method error because the continuous observation time is limited for MEO/IGSO satellites, but there is enough observation for GEO satellites.

On the other hand, but the estimation result of GEO on-board clock is little worse than that of IGSO at the interval of 1~10s, this maybe due to SRR method error, which will be further studied in the future work.

VI. CONCLUSION

Short-term frequency stability estimation of satellite on-board clock is of great significance for GNSS application such as satellite clock modeling and simulation. The ODTS method, which is well-known and commonly used, needs continuous observation from large monitoring networks and complex algorithms. COMPASS is in its early stage of construction and do not have worldwide observation networks to track the satellite continuously. In addition, limited access permission also restricts common users from obtaining precise on-board clock parameters.

Two estimation methods for the short-term stability of COMPASS MEO/IGSO and GEO on-board clock are presented in this paper, which only need observation from one single station. The preliminary short-term stability estimation of COMPASS IGSO and GEO on-board clock are presented using these two methods.

REFERENCES

[1] Dow, J.M., R.E. Neilan, C. Rizos, The International GNSS Service in a changing landscape of Global Navigation Satellite Systems. Journal of Geodesy, 2009. 83: p. 191-198.

[2] Horemuz M, Andersson J V, Polynomial interpolation of GPS satellite coordinates[J]. GPS Solutions, 2006. 10: p. 67-72.

[3] Delporte, J., C. Boulanger, F. Mercier. Straightforward estimations of GNSS on-board clocks. in 2011 Joint Conference of the IEEE International Frequency Control Symposium and European Frequency and Time Forum. 2011. San Francisco, California, USA.

[4] Gonzalez, F.P. Waller. GNSS Clock Performance Analysis Using One-way Carrier Phase and Network Methods. in Proceedings of the 39th Precise Time and Time Interval (PTTI) Applications and Planning Meeting. 2007. Long Beach, California, USA.

[5] Roulston A, Talbot N, Zhang K. An Evaluation of Various GPS Satellite Ephemerides[C]. in Proceedings of the 13th International Technical Meeting of the Satellite Division of The Institute of Navigation (ION GPS 2000). 2000.

[6] LU X F, JIA X L, YANG Z Q, Determination of Navigation Satellite Clock Bias Using SLR and GPS Dual Frequency Phase-Smoothed Pseudo-Range Data[J]. Geomatics and Information Science of Wuhan University, 2008, 33: 237-240. (in Chinese)

[7] Yang, X., L. Ma, B. Sun, H. Lei, L. Sun, Z. Li, W. Zhou. The Method of Time Synchronization Based on the Combination of COMPASS GEO Pseudo-range and Two-way data in 2011 Joint Conference of the IEEE International Frequency Control Symposium and European Frequency and Time Forum. 2011. San Francisco, California, USA.

A Hardware Accelerated 10GbE Primary NTP-Server

Carsten Rieck[1] and Kenneth Jaldehag
Measurement Technology
SP Technical Research Institute of Sweden
Box 857, SE-50115 Borås, Sweden
[1]also with Chalmers University of Technology, Onsala Space Observatory
Email: {carsten.rieck, kenneth.jaldehag}@sp.se

***Abstract*—In this paper we present a primary NTP server design that provides a full line rate packet stream handling with about 50 ns internal timing accuracy independent from packet throughput. The provided solution is replay proof and is intended for NTP services close to backbone of the Internet.**

I. INTRODUCTION

The load on the current set of primary NTP servers on the Internet has increased dramatically during the last decade. This is partly due to the growing number of Internet nodes at large and partly caused by changed NTP usage policies. One example of the latter is the relaxed application of traditional NTP hierarchy rules, where today client nodes directly synchronize to primary servers, regardless of network distance. This scales badly for the primary servers and results in a bad timing performance for the client [1].

NTP servers, including SP's current generation of servers, are often not designed to handle a high rate NTP packet stream, which is a common cause for denial of service (DoS) for NTP. Typical server implementations are built using a user space daemon based on Mills NTP [2,3], a general purpose operating system, such as GNU/Linux or a BSD variant, and general purpose Ethernet interfaces on standard computing hardware; a combination not well suited for regular or malicious overload situations.

An earlier work [4] attempted to move primary NTP from user space into the kernel in order to gain both throughput and timing accuracy. A further step is to decouple NTP completely from general purpose hard- and software, which is presented here.

SP operates, together with NETNOD [5], a number of primary NTP servers based on a FreeBSD system with a custom timing interface [6]. These servers are placed at SP and three of the Swedish NETNOD Internet exchange points, which makes them close to any user node within Sweden but also susceptible to network attacks, in particular DoS. This server park is at the end of life and needs modernization. Fig. 1 depicts today's typical traffic situation for eight of the primary servers SP is responsible for.

Classical NTP solutions are a) not full rate capable and b) hardly traceable. Further, timing accuracy is often a function of throughput, decreasing with the number of incoming packets, which are not necessarily NTP related. Four major design goals are to be met:

1. 10GE line rate capability.
2. Line rate throughput. On a LAN 10GE this would require about 10'964'912 packets per second per interface to be answered for real DoS protection.
3. Accuracy and traceability of NTP timing. Timing for the server timestamps shall be accurate with numerically defined uncertainties. The new server design shall be capable of tracing the NTP timing and individual packets time stamping to UTC.
4. IPv6 capabilities and service flexibility.

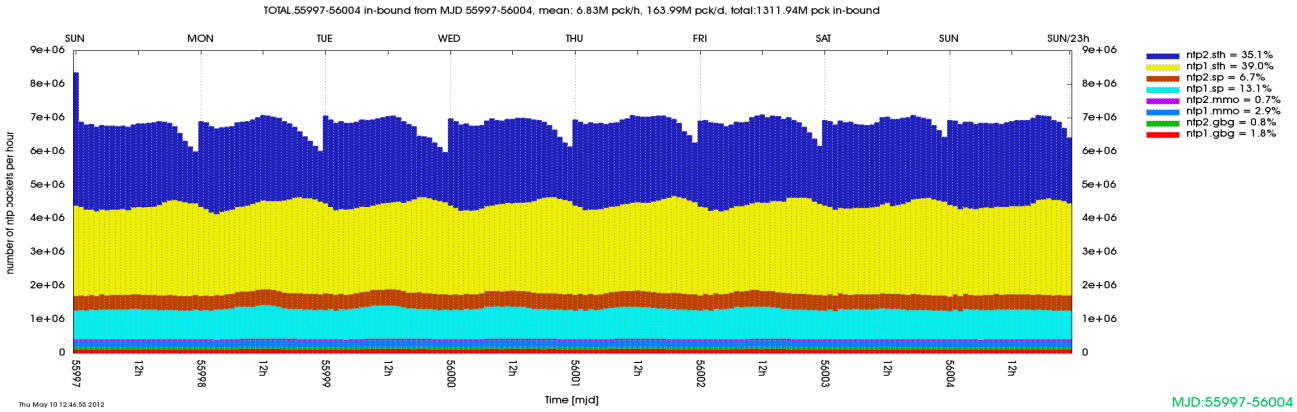

Figure 1. Arbitrary one week snapshot of in-bound traffic of the SP/NETNOD primary NTP servers. The combined mean traffic is less than 2000 packets per seconds, a rather moderate figure compared to the maximal line rate packet stream of about 8x100'000 packets per second. However, individual peek loads occour, which make an individual server drop packets due to insufficient receiving buffers.

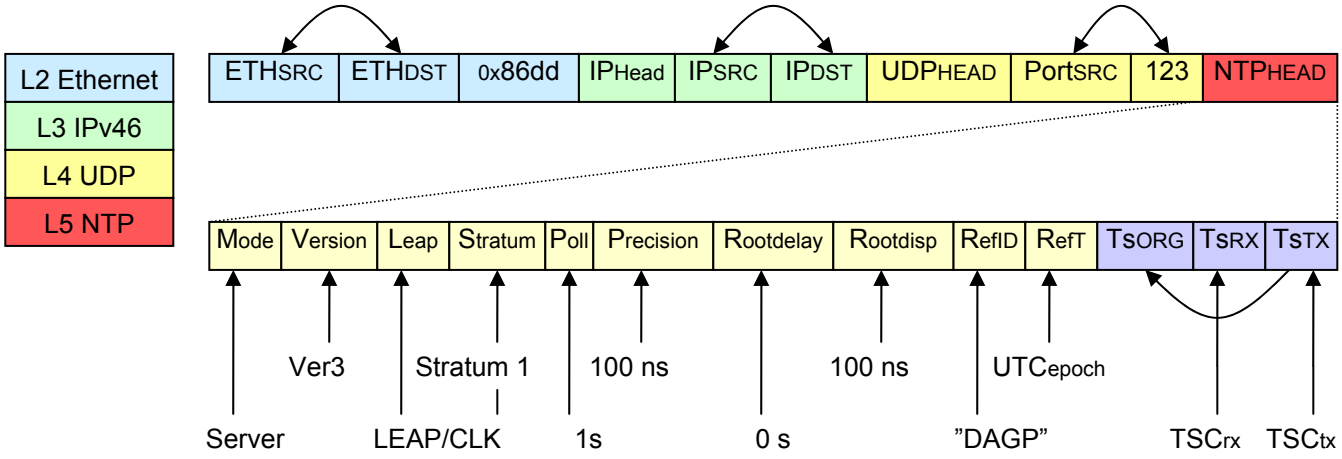

Figure 2. Principle NTP reflection function. L2 checksums are handled in hardware, whereas upper layer checksums are done in software. Prior to the reflection the frame's layers are checked for consistency in order to qualify as a proper NTP client packet. TSCrx represents the NTP epoch corrected receive time of the frame, TSCtx the expected release time of the frame expressed in NTP units. Under normal circumstances the frame realease is uncertain with less than 10 ns (1σ) from the intended value.

II. METHOD

The solution is based on a commercial time stamping network traffic analyzer hardware for 1G and 10G Ethernet from Endace.com [7]. These traffic analyzers can be synchronized to an external time reference using a differentical 1PPS signal. The synchronized internal oscillator drives a 64bit wide time stamp counter (TSC). The counter's least significant bits represent the reference's sub-seconds in units of 2^{-32} s. Its overflow represents the synchronized reference 1PPS, which drives the upper 32bits and is also electrically output. In this way the synchronization can be measured for traceability. The TSC's architecture resembles the timestamp format of NTP, which makes it well suited for the implementation of a high capacity NTP server.

Incoming Ethernet frames are continually captured and individually time stamped using the TSC with a significant resolution of 2^{-27} s, which is about 7.5 ns. The received frames are then hardware load-balanced to a number of receiving channels that efficiently map the received streams to individual memory areas accessible to a user space application. On the other hand, transmitted frames are not time stamped, but a unique replay feature of the hardware allows timely release of frames to the network with the same order of accuracy as the Rx time stamping. In order to account for the varying processing time in user space, due to scheduling, frame distribution and content, a minimal latency between receive and transmit is introduced. For NTP, latency is removed by the two-way principle, thus long latencies (ms) together with large memory buffers contribute to more robust NTP service.

The analyzers network interfaces do not belong to the host system's interfaces, thus network traffic is not handled by the Operating System's (OS) IP stack. This allows the implementation of application specific functions and policies even at lower network layers. For this the analyzer offers an extensive C-language API for frame handling in user space, where the balanced buffering of packets can be utilized to efficiently process the information using a multi-thread technique.

For this NTP realization a specialized IP-stack was developed that asynchronously handles all network traffic. Fig. 3 depicts the architecture of the system. The current implementation provides all necessary functions for a multi-homed IPv4/6 NTP server on VLAN tagged Ethernets. The number of configured hardware-assisted receive channels are matched by the number of frame-handler threads. These handlers receive junks of frames in a poll/timeout fashion and characterize the received data, which results in either a drop or reflect action. NTP client requests, ARP requests, and certain ICMP messages, are replied to with the frame reflector

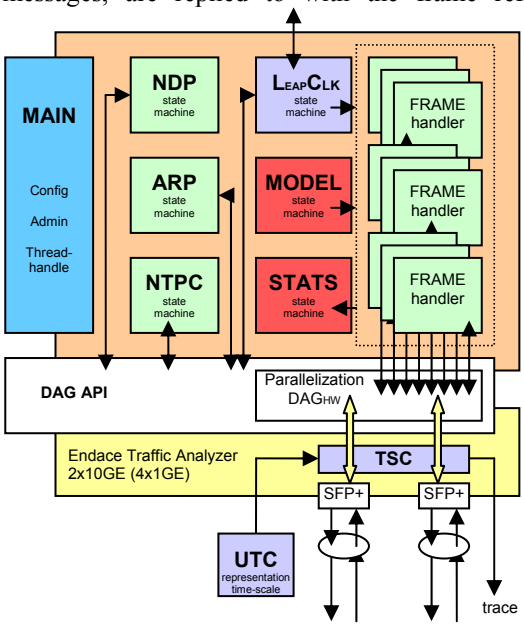

Figure 3. Logical structure of the new server design. The hardware timestamping is governed by a 1PPS PLL synchronization of an internal oscillator on the traffic analyzer. The TSC is 64bit wide with a principal resolution of 2^{-32} s, though the significant resolution is 2^{-27} s, which is about 7.5 ns. The hardware timestamping is originally based on the UNIX epoch (1970/01/01) which has a constant offset to the NTP epoch (1900/01/01). The TCS's overflow of the lower 32bit, representing 1s, is output from the card and can with advantage be used to retrace the synchronization of the card.

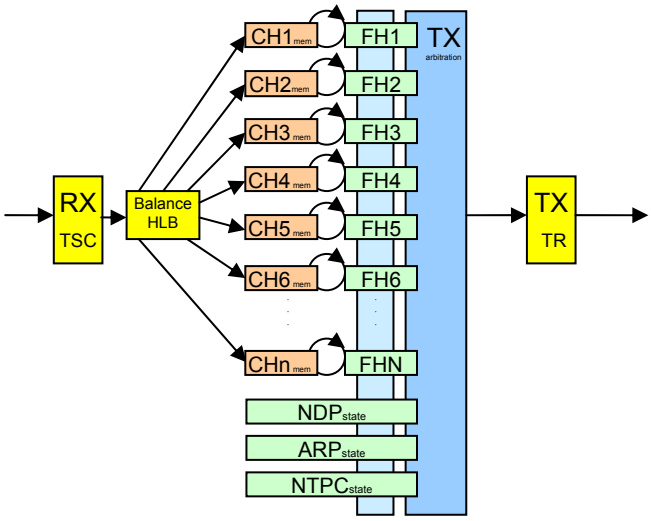

Figure 4. Principle input/output flow of the server. Received frames are timestamped (TSC) and the hardware load balance sorts the packets with the help of a hashing algorithm (HLB) based on the frames L2/L3 layer information into a number of receive channels. The frame data and the timestamps are efficiently transferred to directly mapped memory (CHx). Framehandler (FHx) threads bind to the channel memory from where they are fed a number of frames at a time. For each FH all frames are in consecutive order, but consecutive frames on the wire are likely to be handled by different FH. As soon as a framehandler has processed all frames in a batch it tries to lock the TX arbitration and claimes a time slot for transmit. The transmission is subject to a minimum latency that accounts for the worst case processing time for each batch. In the serialized transmission queue all transmit frames are in timely order. NTP TX timestamps are synchronized with the cards TX scheduled timestamps. The transmit engine (TR) time releases each frame to the wire.

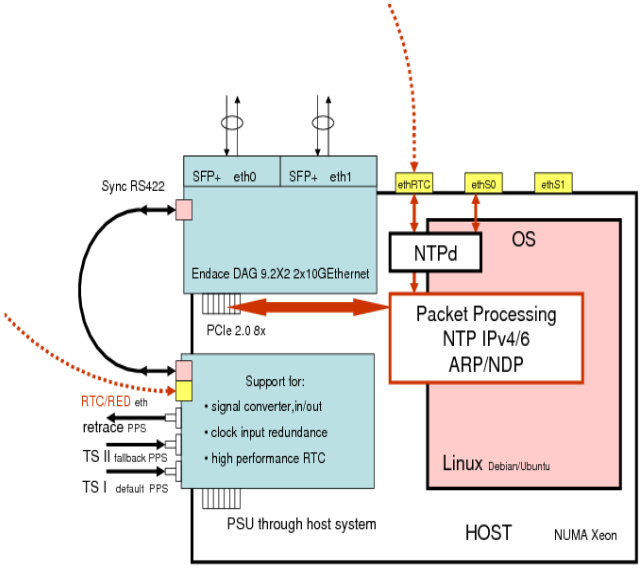

Figure 5. Typical deployment of the analyzer card in a host system. The DAG expects a differential RS422 timing signal. A support card has been designed to handle the signal convertion, which provides single ended coaxial interfaces for PPS_{in} and PPS_{out}. Optional is the integration of a power backuped realtime clock that can provide timecode during startup after a powerdown situation.

Figure 6. Cards of the prototype system.

Top: Endace DAG9.2X2, 2x 10GE pluggable SFP+ transceivers.
Middle: SP support card for signal condioning. The fan is deployed for forced cooling of DAG cards horizontal mounted in 1U servers.
Bottom: Backend view of the test system, with installed SFP+ transceivers, 1PPS in/out connections.

function, which provides outstanding throughput and accuracy, see Fig. 2 for an example regarding NTP. A limitation of this method is that reflected frames have to be the same or of smaller size than the received frame. Larger reply frames have to be handled asynchronously.

Frames that are not reflected, specifically ARP replies, ICMP6 and NTP server packets can nevertheless alter internal data structures, where state changes are asynchronously handled by other handler threads.

Further, a number of state-machines, namely `NDP` and `ARP`, realize network L2/L3 administration and allows the server to act as an ordinary network node. Another vital function is realized in the `LeapClk` state-machine that monitors the state of the clock synchronization and handles leap second instances. The internal oscillator of the network card provides a minimal holdover that covers short interruptions of the synchronization 1PPS. After a configurable time without synchronization the server becomes unsynchronized and stops replying to requests. This server type does not implement any mitigation rules and relies on its single reference clock. Optionally, a model state machine is provided, that allows none-UTC sources, such as free running Rubidium oscillators, to be connected to the system as time references. External time measurements need to characterize the used timescale and update the model state machine with UTC clock models at appropriated time intervals. The state machine regularly computes synchronization phase offsets that are applied by the reflector functions. In this case the traceability of the NTP synchronization is not straight forward anymore, because the phase corrections are applied in software.

Another optional feature is the controlled generation of NTP client packets for a set of NTP servers to be monitored. Due to the excellent and traceable timing properties of the system, this could be used for calibration, or, on synchronized systems, it can measure and monitor latency and delay on network paths.

Fig. 4 shows the principle input/output handling of the system, where hardware time stamping, load balancing and time release are the key features to the performance of the described system.

Fig. 5 depicts the intended architecture for a dual interface 10GE system. The analyzer is supported by a signal conditioner for conversion between single ended and differential (RS422) 1PPS signals. This support card optionally provides synchronization redundancy and an initial time-code source. The system is hosted by general server hardware with PCIe running a GNU/Linux operation system with a late 2.6 kernel. The analyzer expects a PCIe 2.0 x8 lane slot, the support card can be inserted into a PCIe slot for mounting and power supply, but does not interact with the system through PCIe. Actual throughput performance depends on the computing power, bus and memory bandwidth of the host system. A dual port 10GE hosting requires a high end multi processor/multi core system to handle about 22 million[1] NTP packets per second, which presents the worst traffic case on a system with two 10GE interfaces.

Fig. 6 shows the cards used during development. All performance tests were done on a synchronized back-to-back system with two identical setups and cross wired fiber-pairs between the machines, where one machine acts as a client and the other serves as a server. Real life network development and testing was done on 1GE models interfacing a CISCO 12000 router providing IPv4 and IPv6 capabilities. All servers used in the testing run a standard 64-bit Ubuntu 10.04LTS OS.

III. Results

Apart from a functional correct implementation we have focused on the two key requirements: throughput and accuracy. Table 1 presents some experimental tests where also a number of other NTP servers are presented. The DAG back-to-back system performs as expected up to the tested rate of about 2'000'000 packets per second. Higher rates are currently difficult to test, since this assumes a client capable providing and analyzing these data rates. Apart from the 10GE system all other systems are at 100MBit line rate and are connected to a LAN network using standard switches. System A is the SP server type described above, it serves as a benchmark. CPU rate for the `ntpd` process is given, which shows that a typical system starts to saturate at around 10'000 packets per second, still performing well up to 15000 packets.

Table 1 Empirical Behaviour of Different Primary NTP Servers Today. Packet Loss Is the Portion of Sent Client Packets That are not Replied to by the Respective Server Type.

Packets per second	System A[a]		System B[b]	System C[c]	System DAG[d]
	CPU [%]	*Loss [%]*	*Loss [%]*	*Loss [%]*	*Loss [%]*
1	0	0	0	0	0
10	0.01	0	0	0	0
100	0.3	0	0	0	0
500	2.9	0	0	0	0
1000	7.2	0	0	0	0
5000	39.8	0	0.6	0.044	0
7500	58.1	0.0016	9.3	0.26	0
10000	82.2	0.0005	12.1	0.86	0
12500	97.9	0.006	14.2	1.25	0
14000	98.7	0.016	28.5	1.3	0
15000	98.3	0.0086	32.0	2.4	0
16000	no meas	8.6	36.2	4.1	0
17500	no meas	37.7	43.5	40.8	0
20000	no meas	40.8	59.2	50.6	0
22500	no meas	53.4	69.0	58.5	0
25000	no meas	64.8	76.3	67.2	0
27500	no meas	74.7	81.9	76.5	0
30000	no meas	85.1	86.9	85.2	0
40000	no meas	100	96.9	100	0
50000	no meas	100	sys. breaks	100	0
100000	not tested	100	not tested	100	0
1000000	N/A	N/A	N/A	N/A	0
2097152[d]	N/A	N/A	N/A	N/A	0
10000000	N/A	N/A	N/A	N/A	not tested

a. SP Primary NTP server, Intel Pentium III 800MHz, FBSD3.4, ntpd4.0, 1PPS, fastEthernet, no reply for rates > 39k

b. Commercially available system, fastEthernet.

c. Commercially available system, fastEthernet, no replies for rates > 37k.

d. DAG back2back, special test case is 2^{21} pkt/s, single receive channel, 1PPS, 10GE.

[1] A minimal NTP packet in IPv4 with no VLAN tagging on most Ethernets including overhead, but excluding coding, consists of 912bits: (7Pre+1Start+14L2+20IP+8UDP+48NTP+4Check+12Inter)*8 bits

The client for all these tests is software using the DAG 1GE and 10GE hardware in a similar way as the server software described above, by creating client packets at regular time intervals. The client produces histogram statistics of the two-way solution at variable time intervals. All 1PPS synchronized server systems and the client are connected to the same timescale, UTC(SP).

The table does not show any accuracy measures, but all tested conventional systems severely deteriorate in accuracy with growing data rate. It is interesting to note that System B breaks at half the line rate and can only be revived using a cold restart. This is a typical example for a terminal denial of service.

The timing accuracy of the 10GE system is within its expected uncertainty under all test cases. Fig. 7 shows a histogram of about 7 days of data at a data rate of 2^{21} packets per second. Originally the data was collected and statistics were calculated in batches of 600 seconds. Typical standard deviations from the mean are in the order of 8.5 ns. This amounts to peak to peak variations of about 50ns. There is a phase wonder of about 2 ns of the batch mean values over this time period, individual mean values are shown in Fig. 8. The offset values are not calibrated, the estimated clock difference of about -263 ns is due to cabling and the individual delays of the involved components. It is desirable to calibrate each server in order to provide traceability in the order of the time stamp resolution.

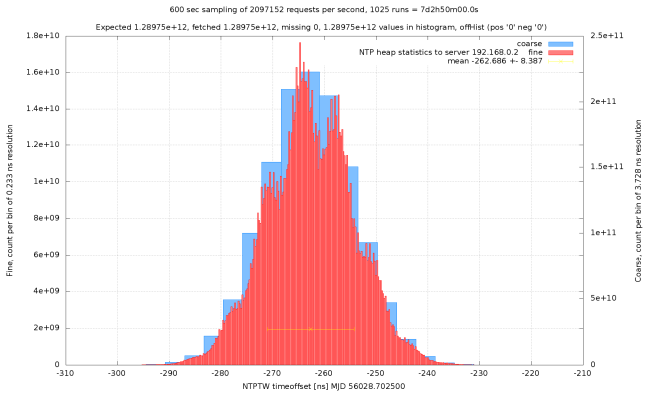

Figure 7. Seven days of NTP time transfer results based on 1025 continuous runs of 600s between two directly connected and synchronized 10GE systems at a rate of 2^{21} NTP packets per second. Client packets were scheduled at evenly spaced intervals. Red bars represent the numerical resolution of the time stamp format in units of 2^{-32} s, i.e. 233 ps, blue bars have a resolution of 2^{-28} s, about 3.73 ns. Features visible in the fine structure indicate the significant resolution of the TSCs and the PPL synchronization of the DAG oscillators. TX release, both on client and server, is uncertain to a about -±3 units of 2^{-27}. The standard deviation of this data set is about 8.5 ns with no outliers or missing values observed. This behaviour is visible at all packet rates tested.

Figure 8. Mean values of the 1025 batches a 600s with a rate of 2^{21} packets per second as presented in the previous graf. Minimum, mean and maximum batch standard deviations are given to illustrate the stability of the NTP solution over long time intervals.

IV. Conclusions and Future Work

The chosen hardware is ideally suited for the design of high capacity NTP services. By hardware assisted time stamping and load balancing it is possible to create line rate capable NTP servers with accurate time stamping independent from packet throughput. Functionality can be tailored to any degree since all network layers are available to the user space application.

Current development is focused on code stabilization and qualification for production environments. A next step is the introduction of different authentication methods to the software, which poses strain on the computing power of the hosting server at high packet rates. Currently, a DNSsec based authentication is being developed. Further the inclusion of other network time protocols, such as IEEE1588, are under discussion.

Acknowledgment

This work was supported by the Swedish Post and Telecom Agency (PTS). Further we would like to thank ntp.org people for their long term commitment to NTP, the Internet Engineering Task Force at large, the Open Source community, and Chris Bone at Endace Europe.

References

[1] D. Mills et al. “Coping with Overload on the Network Time Protocol Public Servers”, PTTI2004

[2] http://www.ntp.org

[3] D.Mills et al. RFC5905 “Network Time Protocol Version 4: Protocol and Algorithms Specification”, http://tools.ietf.org/html/rfc5905

[4] C.Rieck “An Approach to Primary NTP by using the Linux Kernel”, EFTF2007

[5] http://www.netnod.se/other/valueadd/ntp

[6] K. Jaldehag, J. Johansson, G. Lundqvist, C. Rieck, H. Nilsson, P. Löthberg, and H. Nästèn, 2001, “Establishment of Internet Time Servers in Sweden,” EFTF2001.

[7] http://www.endace.com

The Influence of LC components' quality factor Q for GNSS receiver's group delay equalization

Li Pengpeng,Li Yuanling,Chen Lei,Li Baiyu,Ou Gang
Satellite Navigation and Positioning R&D Center, School of Electronic Science and Engineering, National Univ. of Defense Technology, Changsha 410073, China
lipp0808@163.com

***Abstract*—For the satellite navigation receiver, the channel characteristic including amplitude and group delay is a determining factor for ranging and zero estimating accuracy. The technology about group delay equalizing by all-pass network in the RF system is analyzed in this paper. The quality factor Q of LC components, which affects the group delay equalization, is the key of application research. Computer simulation results based on some special RF system shows the way to make a target of the delay equalization and choose LC components with special Q, and give out three important conclusions to guidance the homologous application. Finally, the analytical results are verified, completes the second-order all-pass network circuit hardware, and cascades it with the RF circuit, the entire amplitude and group delay characteristics is im-proved as wish. The test results analyzed with Agilent vector network analyzer show that, group delay fluctuations of the equalization passband is about 7~8ns, amplitude-frequency passband fluctuation is 1.5dBm, the initial value is 137ns and 1dBm. The method could be used to improve the group delay equalization in the wider passband of RF front-end channel, and has important reference value in group delay equalization goal setting, program feasibility study and Q value selection.**

I. INTRODUCTION

Ranging accuracy is an important index of high performance GNSS receiver, zero estimation accuracy will directly affect the ranging accuracy [1][2]. During the procedure of zero estimation, if the channel characteristic is not satisfactory, in particular if group delay is not constant, it will lead to different Doppler signal offset and different zero estimates, making it difficult to ensure zero estimation accuracy.

Group delay and amplitude characteristics of Receiver signal channel are mainly determined by the RF front-end [3][4]. In composition of the RF front-end, low noise amplifier, mixers and amplifiers and other devices are relatively broadband components, group delay and amplitude does not change very much in some narrow channel passband, therefore, the channel characteristics of the RF front-end depends mainly on the part of analog filter. Group delay and nonlinear amplitude of other components superimposed together with filter, forming the characteristics of group delay and amplitude. In premise of not changing amplitude-frequency of filter, relying on the superposition of group delay effects, cascading the filter and equalization all-pass network, it could improve the group delay of the entire network.

Group delay equalization needs appropriate all-pass network, and the characteristics of all-pass network could be directly affected by quality factor Q of the LC components [5][6]. Based on this theory, we analysis the affect of equalization network caused by all-pass network design and Q value, also providing a basis for group delay equalization designed and chose the right Q values..

II. ALL-PASS GROUP DELAY EQUALIZATION NETWORK DESIGN

A. The group delay equalization method

Passband delay curve of passband filter is generally asymmetric. For improving the characteristics of passband group delay curves, we design two-order all-pass group delay equalization network to make group delay equalization, in order to achieve the constant in passband group delay[7].

The idea for the equalization algorithm is like this. First of all, decomposing the asymmetric Parabola into a symmetric parabola L1 and an oblique line L2 which is tangent to L1. Then design two-order independent all-pass network according to the parameters.The first-order characteristics curve in the passband is L3, which is opposite to L1 and called the parabola network equalizer. The second-order characteristics curve in the passband is parabola L4, which is a straight line with the opposite sign of L2, and called the liner network equalizer. At last complete equalization by cascade connection, make group delay function constant, this is called the asymmetric Parabola equalization method [6].

According to the parameters of passband group delay curves, it infers some equalization section parameters as *kn* and *wn*.

B. Main steps of hardware implementation

The commonly hardware structure is T-type, all-pass equalization network and circuit was determined by *kn* and *wn*.

$$\omega_n \geq \sqrt{3} * k_n \tag{1}$$

$$k_n \leq \omega_n < \sqrt{3} * k_n \tag{2}$$

If the relationship between *kn* and *wn* meet formula (1). We should select structure I, if the relationship between *kn* and *wn* meet formula (2). We should select structure Π.

Two kinds of circle structure shows as follow:

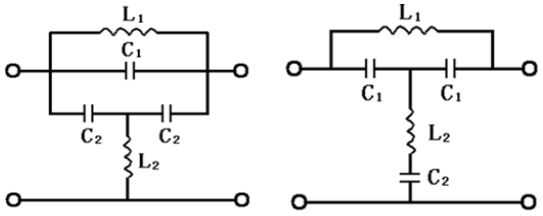

Fig.1 I-type (left) and Π-type (right) circuit

When the circuit was selected，according to *kn* and *wn*, all of LC values needed can be calculated.

C. *The simulation of ADS about all- pass network*

When the circle type and LC values are known, we can make the hardware of all-pass network. For example,the simulation results of ADS[8] about all-pass network shows its characteristics as follow:

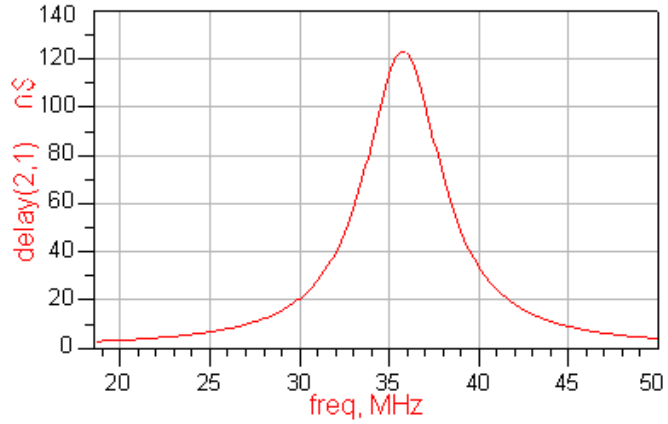

Fig.2 group delay characteristics of all-pass network

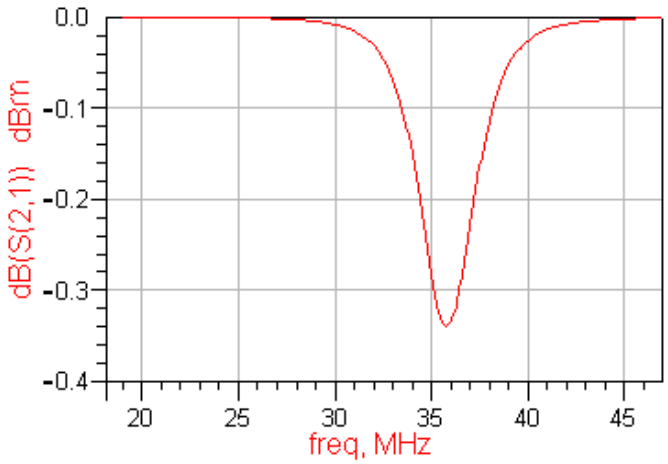

Fig.3 Amplitude characteristics of all-pass network

The simulation results shows that group delay characteristics is relative to the value of LC component, amplitude characteristics is relative to both the Q factor and the value of LC component.

III. INFLUENCE OF GROUP DELAY EQUALIZATION BASED ON Q (QUALITY FACTOR) CHANGING

Amplitude characteristics of all-pass network in the passband can not be a constant, usually there will be a decay point Amax(Fig.3) at the resonant frequency, This Amax point will deteriorate the passband amplitude characteristics, so attention needs to be focused. Its expression is:

$$A_{\max} = 20 * \log \left| \frac{2 * Q * \cos\theta + 1}{2 * Q * \cos\theta - 1} \right| \qquad (3)$$

Discussing group delay characteristics of the network has little significance; it should be connected with the channel group delay characteristics. Therefore, there is no fixed expression.

We simulate the amplitude and group delay parameters of a receiver RF front-end channel by using ADS software, it is connected with the all-pass network, The simulation results of shows that, when the Q value of LC component changes, group delay curve of entire network follows. The results show as follows:

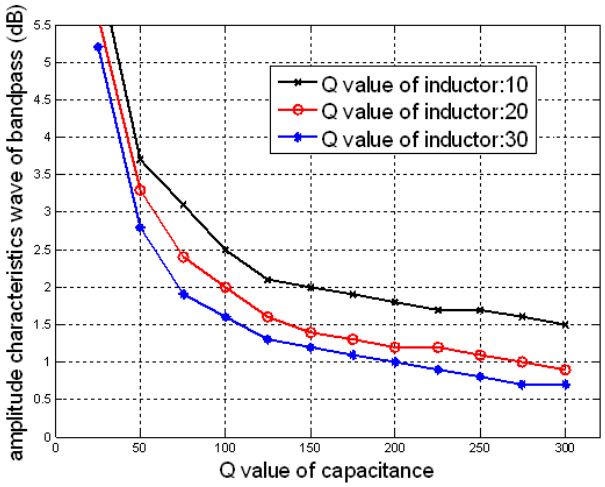

Fig.4 relationship between Q value and channel amplitude characteristics

The simulation results make a lot of sense in practical applications, if the equalization target is known, we just need to choose an appropriate Q value of LC components. The improve effectiveness becomes smaller by increasing the Q value.so, keeping increasing the Q value is not necessary, people can select the appropriate Q value of inductor and capacitor components for their design, and infer the equalization amplitude-frequency by existing Q value. It can be inferred that the equalization results about amplitude and group delay characteristics is suitable or not.

IV. RESULTS OF HARDWARE CIRCLE

When we make some hardware implementation, equalization goal should be set at first: fluctuation within the passband group delay should less than 10ns, amplitude fluctuation in 3dB or less,compared to the initial value of RF front-end is about 137ns and 1dB.

According to the simulation results, when cascade connection of all-pass group delay equalization and the channel was realized, passband fluctuation could be controlled at about 1.2dB or less , and fluctuation could be controlled under 5 ~ 6ns or less. All-pass network design by the asymmetric parabola method can make cascade connection with the RF front-end, two-order all-pass network circuit designed by ADS system shows as follows:

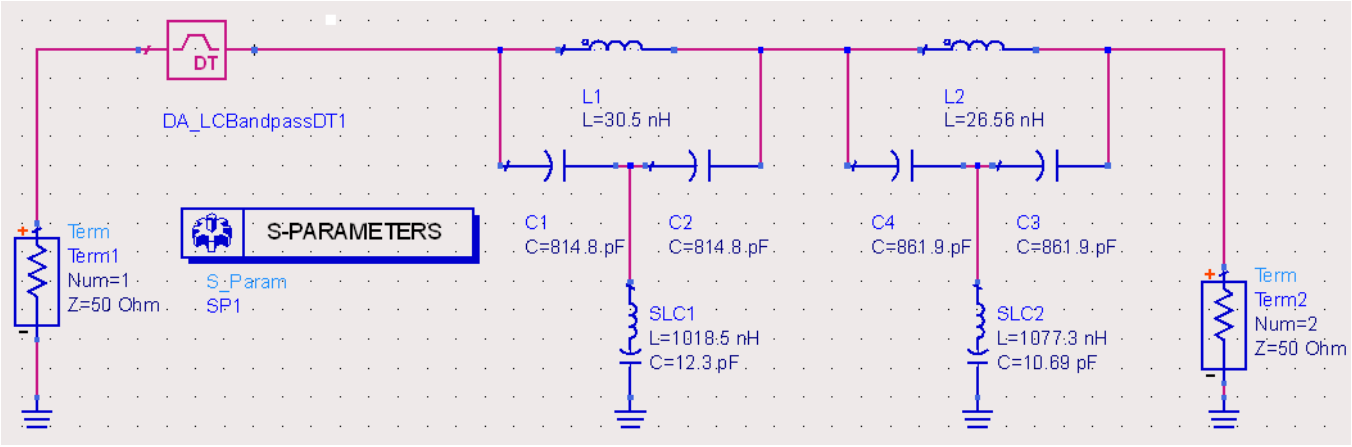

Fig.5 two-order all-pass network circuit design with ADS

After the completed two-order all-pass network circuit hardware cascades the RF circuit, the entire amplitude and group delay characteristics both change, Test results with Agilent vector network analyzer E8362B shows as follow:

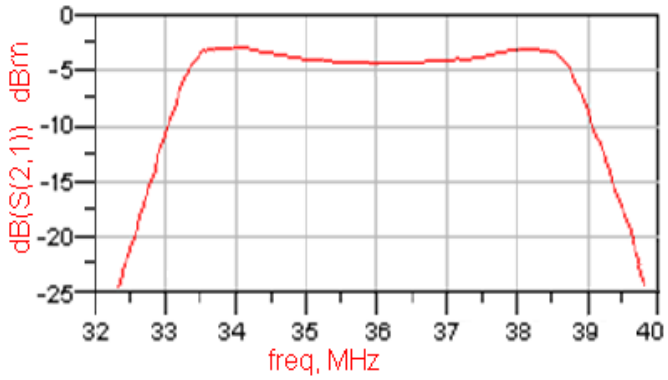

Fig.6 amplitude characteristics of equalized RF front-end

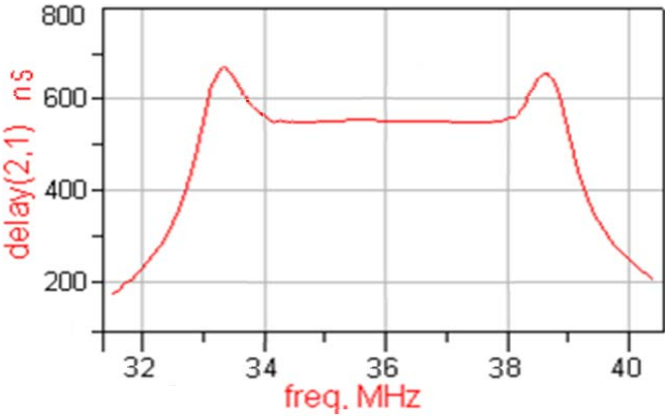

Fig.7 group delay characteristics of equalized RF front-end

There is a small deviation between this result and the simulation results about 1.5dB of amplitude characteristics, 7 ~ 8ns of group delay characteristics, considering the factors of parasitic capacitance and coupled inductors, experimental results and simulation results present a small deviation is acceptable. So conclusion can be simulation results and measured results have good consistency, and simulation results can make good reference.

V. CONCLUSION

Receiver requires high precision, so group delay characteristics of RF front-end need to be equalized. This paper focused on impact of LC components' Q value in group delay equalization, and give out some important conclusions. At last we complete the two-order all-pass network circuit hardware, and cascades it with the RF circuit, the entire amplitude and group delay characteristics is improved as wish.

This paper has important reference value in group delay equalization goal setting, program feasibility study and Q value selection. This paper can be referrence for any system design which needs to achieve the constant in passband group delay characteristics.

REFERENCES

[1] Elliot D. Kaplan, Christopher J. Hegarty, Understanding GPS Principles and Applications, Second Edition[M]. Beijing: Publishing House of Electronics Industry. 2008.

[2] SHA Hai. Research and Application of the Group Delay Measurement Method in Transfer Channel of Satellite Navigation System[D]. Changsha: National University of Defense Technology,2009.

[3] JIANG Shan. Design of Narrow band Little Ripple Group delay

Crystal Filter[J]. Telecommunication Engineering, 2010,50(3):54-58.

[4] Li Peng, Ma Hongmei. Optimization Design of Analog Filters Group delay Inner Equalization[J]. Telecommunication Engineering.2011,5

[5] Arthur B. Williams, Design Handbook of Electric Filter. [M]. Beijing: Publishing House of Electronics Industry. 1986

[6] Wang Qinying, Tian Liqing. Study and Design of IF Group Delay Equalizer[J]. Remote Control and Measure. 2005,11

[7] Chen Shuyuan, Yan Shaoqing. Pahse Shift Equalizer[M]. Beijing: Publishing House of People Postage.1984:224~239

[8] Santa Rosa. Agilent Technologies. Advanced Design System. ADS 2006A Layout Class[M].California USA.2007.121-123.

Optical Frequency Link between Torino and Firenze for remote comparison between Yb and Sr optical clocks

Davide Calonico[1], Cecilia Clivati[1,2], Giovanni A. Costanzo[2], Aldo Godone[1], Filippo Levi[1], Marco Marchetti[3], Alberto Mura[1], Marco Prevedelli[4], Marco Schioppo[3], Guglielmo M. Tino[3], Massimo E. Zucco[1], Nicola Poli[3]
[1]Istituto Nazionale di Ricerca Metrologica, Torino, Italy,
[2]Politecnico di Torino, Torino, Italy
[3]Dipartimento di Fisica e Astronomia and LENS, Università di Firenze, INFN Firenze, Italy,
[4]Dipartimento di Fisica, Università di Bologna, Bologna, Italy
Email: d.calonico@inrim.it, nicola.poli@unifi.it

***Abstract*—The Italian Institute of Metrology (INRIM), the European Laboratory for NonLinear Spectroscopy (LENS), the Physics and Astronomy Department of the University of Firenze (UNIFI) and the Politecnico of Torino started a project to establish a $650\,\mathrm{km}$ optical fiber link that will enable remote frequency comparisons between high accuracy microwave and optical clocks of INRIM and UNIFI-LENS and an absolute measurement of the UNIFI-LENS Sr clock versus INRIM Cesium fountains.**
We report the overall architecture of the project, the present status of the experiment and the preliminary tests performed on the equipments.

I. Introduction

Nowadays, atomic Cs fountains offer an accuracy of few parts in 10^{16} [1], while optical frequency standards demonstrated the possibility of an accuracy even beyond [2], [3]. Presently the most used transfer techniques to compare atomic frequency standards and to disseminate their accuracy and stability rely on satellite techniques, that limit the performances of fountains and even more of optical standards [4]. In fact, satellite techniques give an uncertainty contribution of few parts in 10^{16} only after at least 20 days of continuous measurements, whilst atomic fountains tipically reach this value in half a day and optical frequency standards in 100 s or less. Aside from transportable optical standards, optical fiber links seem the only way to compare remote atomic clocks without a limitation of their possibilities, over continental scale for the moment.
In recent years, the reliability and the performances of optical links have been demonstrated over hauls of several hundreds kilometres, allowing frequency dissemination and remote frequency comparisons with a resolution better than 10^{-19} over few thousands seconds [5], [6], [7]. Presently, several European National Metrology Institutes and research institutes are working to set up the branches of a continental optical network.
Different techniques have been used to obtain frequency dissemination through optical fiber. For example, RF amplitude modulation of an optical carrier has been exploited [8], whereas the direct transfer of an optical carrier, with lower losses and higher resolution, is preferred nowadays. Also, the direct transfer of an optical comb is under study [9], even if at the moment this tecnhique needs a more complex infrastructure, not always available on commercial networks.
To obtain a stable transmission of the optical carrier over long distances, the transmitted radiation has to be frequency stabilized, but also, the phase noise due to temperature variations, vibrations and mechanical noise in the fibers has to be compensated.
INRIM in Torino and UNIFI-LENS in Firenze, in collaboation with Politecnico of Torino and University of Bologna, have started a project to set up an optical fiber link between them. Both institutes are involved in high accuracy atomic clocks experiments: INRIM operates two primary Cs atomic fountains and is developing an optical clock based on laser cooled neutral Ytterbium, whereas at UNIFI-LENS a Sr optical clock is under development and high resolution spectroscopy measurements are being perfomed. The optical link will allow firstly an absolute characterization of the UNIFI-LENS Sr clock with respect to the SI second, that is realized at INRIM through the two Cs fountains; at the same time, a direct comparison between the Yb and Sr optical clocks will be possible, allowing also remote tests of fundamental physics. The experiment will give a contribution to the research on novel techniques for time and frequency transfer through optical fibers, and also to the establishment of a pan-European network of optically-linked laboratories.
The collaboration with Politecnico of Torino and University of Bologna will be beneficial to the development of the optoelectronic equipment to implement the optical link.

II. A $650\,\mathrm{km}$ optical link in Italy

The overall scheme of the optical link is shown in Figure 1. A commercial optical fiber connects INRIM (hereafter, local end) and UNIFI-LENS (remote end) laboratories, and an ultrastable laser radiation in the optical C-band ($1542\,\mathrm{nm}$

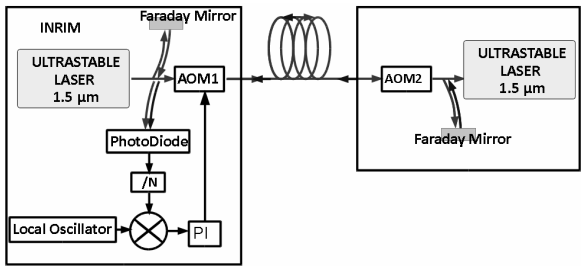

Fig. 1. Conceptual scheme for phase noise cancellation of the optical fiber link. The beatnote between the injected and round-trip radiation is revealed on a fast photodiode, frequency divided (/N) and compared to a stable reference in order to generate an error signal. This signal is then integrated and sent to the acousto-optical modulator AOM1, that acts as actuator for frequency correction. At the remote end, AOM2 shifts the optical carrier in order to distinguish the round-trip signal from spurious reflections along the fiber path.

Fig. 2. The architecture of the Italian $650\ \mathrm{km}$ link under development.

in the present experiment) is sent from INRIM to UNIFI-LENS. In each laboratory, the laser frequency is compared using optical femtosecond combs to the frequency of an atomic frequency standard. The laser source could be either a fiber laser or an External Cavity Diode Laser (ECDL) [10] and it is frequency stabilized on a Fabry-Pérot cavity in vacuum, made of ULE glass, thermally stabilized and suspended in a configuration with low sensitivity to vibrations. The frequency stability of the present experimental set-up could reach an Allan deviation of few parts in 10^{15}, flicker frequency noise limited.

To implement the noise Doppler cancellation technique, at the remote end in Firenze part of the radiation will be reflected back to INRIM and compared with the input signal to actively detect and compensate the phase noise contribution of the optical fiber. An Acousto-Optic Modulator (AOM1) is placed at the local end of the link and used as an actuator for frequency correction. A second modulator at the remote end (AOM2) shifts the frequency of the back-reflected radiation, to distinguish spurious reflections from the round-trip signal.

The optical fiber infrastructure is managed by the Italian National Research and Educational Network (NREN), named GARR. For the first two years of the experiment, the link between INRIM and UNIFI-LENS will have at disposal a couple of dedicated fibers. Then, a Dense Wavelength Division Multiplexing (DWDM) architecture will be implemented, with a dedicated $100\ \mathrm{GHz}$ wide channel (the channel 44 of the International Telecommunication Union grid, ITU44), suitable for transferring radiation at $1542\ \mathrm{nm}$.

This optical fiber structure will also be used for the implementation of GARR-X, the Italian new generation fiber network for data traffic dedicated to research acivities, upgrading the present architecture that is still not full-optical. The overall link length is $650\ \mathrm{km}$, estimated loss is $194\ \mathrm{dB}$ ($0.3\ \mathrm{dB/km}$). This evaluation is provided by GARR on the basis of direct measurements and of design models. Losses compensation will be achieved by 9 optical amplification stations along the fiber haul: bidirectional Erbium Doped Fiber Amplifiers (EDFA) will be used, while at UNIFI-LENS the signal will be regenerated using a local ECDL. The gain of each EDFA will be remotely controlled by GSM drivers, and should be kept as low as $15 - 20\ \mathrm{dB}$ to prevent lasing effects. Therefore we need to place an amplifier each $20\ \mathrm{dB}$ losses to avoid degradation in the Signal/Noise ratio.

Figure 2 shows the effective fiber path; we report the housing possibilities for the amplification stations, together with the attenuation for each span. The housing locations are still under consideration, and a certain degree of freedom is offered to the experiment. In particular, we are working to split the two spans with $30\ \mathrm{dB}$ losses to reduce them to $20\ \mathrm{dB}$, with one more amplification station.

III. Clock developments in the two laboratories

The experiment will compare the Sr optical clock in Firenze with the atomic clock ensemble in Torino. INRIM currently operates two laser-cooled Cs fountains, ITCsF1 and ITCsF2. Since 2003 ITCsF1 has been realizing the SI second at 5×10^{-16} relative accuracy level, and has contributed for more than 25 times to the generation of the Internatinal Atomic Timescale (TAI) of the Bureau International of Poids and Mesures (BIPM). ITCsF2 is a cryogenic fountain designed with the target of 1×10^{-16} relative accuracy level. Both exhibit a frequency instability of about 2×10^{-13} at $1\ \mathrm{s}$ averaging time in terms of Allan deviation [11], [12].

A neutral Yb optical clock is under development. Presently, Ytterbium atoms are prepared in a double stage Magneto Optical Trap (MOT), exciting the dipole transition at $399\ \mathrm{nm}$ and the intercombination line at $556\ \mathrm{nm}$. The first MOT is loaded by a thermal beam pre-slowed by a counterpropagating laser radiation at $399\ \mathrm{nm}$ ($5\ \mathrm{mW}$); the MOT laser intensity is about $2\ \mathrm{mW/cm^2}$ for each beam, while the static magnetic field is 45 G/cm. Up to 5×10^5 atoms are loaded in the first MOT and then 50% are trasferred into the second stage MOT, where they are cooled down to temperature of tens of μK. Currently, we are implementing the off resonance dipole trap at $759\ \mathrm{nm}$ for the Lamb-Dicke regime spectroscopy. The $578\ \mathrm{nm}$ clock laser has been realized [13]. Figure 3 shows the stability of the clock laser, reaching a flicker frequency

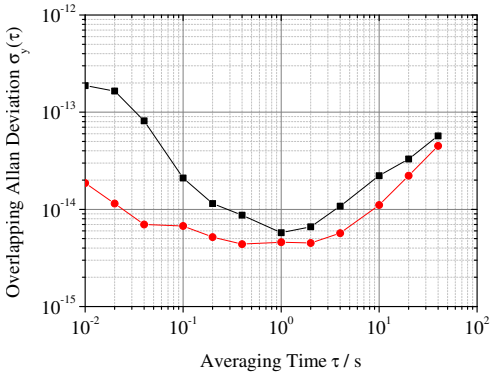

Fig. 3. Allan deviation of the Yb clock laser without (upper curve) and with (lower curve) seismic damping.

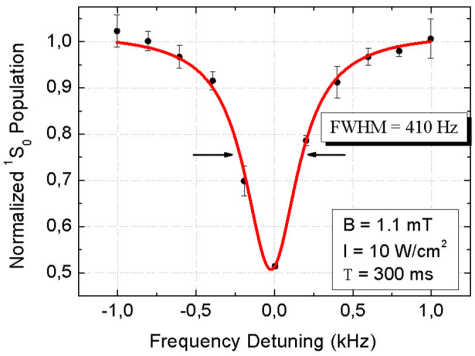

Fig. 4. Magnetic Field induced spectroscopy on the clock transition for ^{88}Sr isotope.

flor of 3×10^{-15} limited by the noise contribution of transfer optical fibers that we are currently going to compensate.

A Ti:Sa optical comb will be used to compare the Yb clock laser at 578 nm with the Cs fountains, whereas a fiber optical comb is going to be used for the optical link.

At UNIFI-LENS, a ^{88}Sr optical clock is in advanced development. Its absolute characterization will be performed by the optical link respect to the SI definition of the second realized at INRIM.

Presently, the double stage MOT at 461 nm (blue MOT) and at 689 nm (red MOT) and a 1D lattice trap at 813 nm have been realized, and prelinary spectroscopic measurements are being carried on.

About 50% of the atoms are transferred from the red MOT into the lattice trap resulting in about 5×10^5 ^{88}Sr atoms. The observed lifetime of the trap is about 1.4 s indicating low heating effects due to amplitude or frequency noise coming from the un-stabilized 813 nm source.

The clock laser at 698 nm is generated by a diode laser locked on a ULE Fabry-Pérot ultrastable cavity and has an estimated frequency stability of 10^{-15} for averaging times between $10 - 100$ s [14].

Applying a magnetic field of 1.1 mT and using an interaction time of T=300 ms, the clock transition has been observed with a linewidth of 410 Hz [15], as shown in Figure 4. For these measurements we applied a constant magnetic field B (along the polarization of the clock laser field and the trapping field) by inverting the current on one of the MOT coils, whereas laser intensity I is estimated from the laser waist w_0 on the atoms and the beam power.

It is possible to find the transition on a day to day basis even without a precise calibration of the laser frequency by adding a 200 kHz chirping on the clock laser frequency (with 2 s period) and by increasing the interaction time on the atomic cloud to 1 s.

IV. Optical link experimental set-up

At INRIM, the laser source at 1542 nm to be transmitted in the link is already operative and characterized, as well as the phase noise compensation system.

The source is a commercial diode laser, frequency locked to a ULE high finesse (120 000) cavity through a Pound-Drever-Hall technique. We evaluated its performances by a beatnote between two identical systems. Residual instability is 10^{-14} at 1 s, limited by acoustic noise and vibrations on the reference cavity. An upgrade of the seismic damping system is ongoing, and from phase noise spectrum evidence we expect to be able to achieve the same results of the Yb clock laser, as the reference system is basically identical.

The phase noise arising in the fiber is compensated by a phase locked loop (PLL) that acts on a AOM. First, a real link was simulated using 100 km of fiber spool in the laboratory and the performances of our noise cancellation loop were evaluated measuring the beatnote between the injected laser and the radiation at the remote end of the link.

Then, the system was demonstrated on a real fiber loop that is part of the urban internet network and has both ends in the laboratory. The link has a DWDM architecture and uses a dedicated (ITU44) channel 100 GHz wide. Total lenght is 47.6 km and losses are ~ 20 dB. Figure 5 shows the noise spectrum of the free running and compensated urban link. The system cancels the fiber noise down to the limitation imposed by the delay, as evaluated in [16].

The interferometer is protected against temperature variations and acoustic noise. Nevertheless, the link stability over long averaging times is limited by residual temperature and pressure variations over the short out-of-loop fibers. Figure 6 reports the fractional instability of the free running and compensated 100 km spooled fiber, acquired with a Λ-type counter; this does not correspond to the Allan deviation in presence of white phase noise. Further discussion and scaling formulas are discussed in [17].

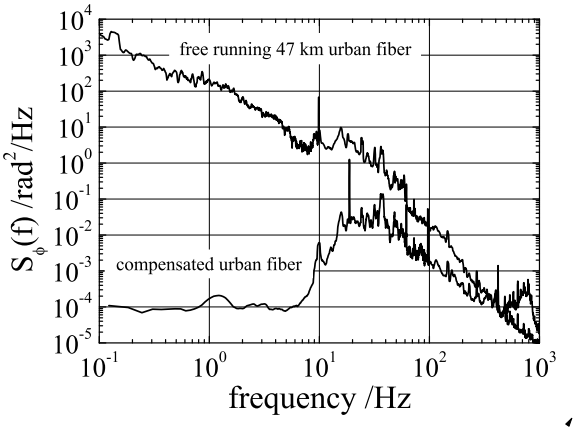

Fig. 5. Phase noise spectra of the free running (upper curve) and compensated (lower curve) urban link.

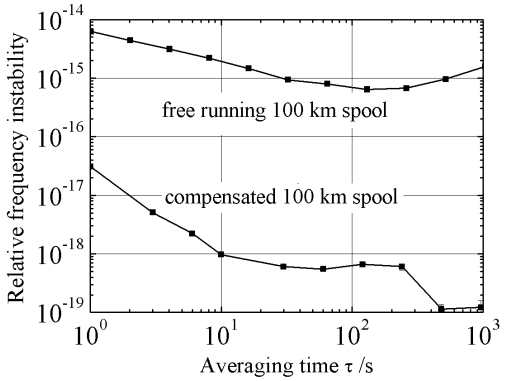

Fig. 6. Relative instability of the free running and compensated $100\ \mathrm{km}$ spool, acquired with a Λ-type counter.

V. Conclusion

We presented the ongoing work to set up a DWDM optical link of about $650\ \mathrm{km}$ that will connect the Italian National Metrological Institute INRIM to the laboratories of UNIFI-LENS. This link will allow remote frequency comparisons between the atomic clocks of the two Institutes and a characterization of the UNIFI-LENS ^{88}Sr clock with respect to the SI second. Moreover, the Torino-Firenze optical link will be the backbone of an Italian Network for optical fiber link dissemination of highly stable and accurate time and frequency signals. This network could be integrated in a wider system of optical links spreading all over Europe, allowing to realize a unique metrological platform composed of the many Cs fountains and optical clocks now present in Europe.

Acknowledgment

The authors would like to acknowledge funding by Compagnia di San Paolo for INRIM link equipments, and Cassa di Risparmio di Firenze for UNIFI-LENS link equipments.

References

[1] T. Parker, "Long-term comparison of caesium fountain primary frequency standards", *Metrologia* vol. 47, pp 1-10, 2010.

[2] C. W. Chou, D. B. Hume, J. C. J. Koelemeij, D. J. Wineland, and T. Rosenband, "Frequency Comparison of Two High-Accuracy Al^+ Optical Clocks, *Phys. Rev. Lett.* vol. 104, pp. 070802-4, Febr. 2010.

[3] N. Huntemann, M. Okhapkin, B. Lipphardt, S. Weyers, C. Tamm, and E. Peik, "High-accuracy optical clock based on the octupole transition in $^{171}Yb^+$, *Phys. Rev. Lett.* vol. 108, pp. 090801-5, Mar. 2012.

[4] A. Bauch, J. Achkar, S. Bize, D. Calonico, R. Dach, R. Hlavac, L. Lorini, T. Parker, G. Petit, D. Piester, K. Szymaniec, P. Uhrich, "Comparison between frequency standards in Europe and the USA at the 10^{-15} uncertainty level", *Metrologia*, vol. 43, pp. 109-120, Febr. 2006.

[5] A. D. Ludlow, T. Zelevinsky, G. K. Campbell, S. Blatt, M. M. Boyd, M. H. G. de Miranda, M. J. Martin, J. W. Thomsen, S. M. Foreman, J. Ye, T. M. Fortier, J. E. Stalnaker, S. A. Diddams, Y. Le Coq, Z. W. Barber, N. Poli, N. D. Lemke, K. M. Beck, C. W. Oates, "Sr Lattice Clock at 1×10^{-16} Fractional Uncertainty by Remote Optical Evaluation with a Ca Clock", *Science* vol. 319, no. 5871, pp. 1805-1808, Febr. 2008.

[6] K. Predehl, G. Grosche, S. M. F. Raupach, S. Droste, O. Terra, J. Alnis, Th. Legero, T. W. Hänsch, Th. Udem, R. Holzwarth, H. Schnatz, "A 920-Kilometer Optical Fiber Link for Frequency Metrology at the 19th Decimal Place", *Science* vol. 336, no. 6080, pp. 441-444, Apr. 2012.

[7] O. Lopez, A. Haboucha, F. Kéfélian, H. Jiang, B. Chanteau, V. Roncin, C. Chardonnet, A. Amy-Klein, G. Santarelli, "Cascaded multiplexed optical link on a telecommunication network for frequency dissemination", *Opt. Expr.* vol. 18, no. 16, pp. 16849-16857, Aug. 2010.

[8] O. Lopez, A. Amy-Klein, M. Lours, C. Chardonnet, G. Santarelli, "High-resolution microwave frequency dissemination on an 86-km urban optical link", *Appl. Phys. B* vol. 98, no. 4, pp. 723-727, 2010.

[9] G. Marra, R. Slavík, H. S. Margolis, S. N. Lea, P. Petropoulos, D. J. Richardson, P. Gill , "High-resolution microwave frequency transfer over an 86-km-long optical fiber network using a mode-locked laser", *Opt. Lett.* vol. 36, no.4, pp. 511-513, 2011.

[10] C. Clivati, D. Calonico, C. E. Calosso, G. A. Costanzo, F. Levi, A. Mura, A. Godone, "Planar-Waveguide External Cavity Laser Stabilization for an Optical Link with 10^{-19} Frequency Stability", *IEEE Trans. Ultrason. Ferroelectr. Freq. Contr.* vol. 58, no. 12, pp. 2582-2587, Dec 2011.

[11] F. Levi, C. Calosso, D. Calonico, L. Lorini, E. K. Bertacco, A. Godone, G. A. Costanzo, B. Mongino, S. R. Jefferts, T. P. Heavner, E. A. Donley, "Cryogenic fountain development at NIST and INRIM: preliminary characterization" , *IEEE Trans. Ultrason. Ferroelectr. Freq. Contr.* vol. 57, no. 3, pp. 600-605, Mar. 2010.

[12] F. Levi, D. Calonico, L. Lorini, A. Godone, "IEN-CsF1 primary frequency standard at INRIM: accuracy evaluation and TAI calibrations", *Metrologia* vol. 43, no. 6, pp. 545, 2006.

[13] M. Pizzocaro, G. A. Costanzo, A. Godone, F. Levi, A. Mura, M. Zoppi, D. Calonico, "Realization of an Ultrastable 578-nm Laser for an Yb Lattice Clock", *IEEE Trans. Ultrason. Ferroelectr. Freq. Contr.* vol. 59, no. 3, pp. 426431, Mar. 2012.

[14] M. G. Tarallo, N. Poli, M. Schioppo and G. M. Tino. "A high stability semiconductor laser system for a ^{88}Sr-based optical lattice clock", *Appl. Phys B* vol. 103, no. 1, pp. 17-25, 2011.

[15] N. Poli, M. G. Tarallo, M. Schioppo, C. W. Oates and G. M. Tino. "A simplified optical lattice clock", *Appl. Phys. B* vol. 97, pp. 27-33, 2009.

[16] P. A. Williams, W. C. Swann, N. R. Newbury, "High stability transfer of an optical frequency over long fiber-optics links", *J. Opt. Soc. Am. B*, vol. 25, no. 8, pp. 1284-1293, Jul. 2008.

[17] S. T. Dawkins et al, "Considerations on the measurementof the stability of oscillators with frequency counters", *IEEE Trans. Ultrason. Ferroelectr. Freq. Control*, vol. 54, no. 5, pp. 918-925, May 2007.

Towards Polish Optical Clock with Cold Strontium Atoms, present status and performance

M. Bober, J. Zachorowski, W. Gawlik
M. Smoluchowski Institute of Physics
Jagiellonian University
Cracow, Poland
jerzy.zachorowski@uj.edu.pl

P. Morzyński, M. Zawada, D. Lisak, A. Cygan, K. Bielska, M. Piwiński, R. S. Trawiński, and R. Ciuryło
Institute of Physics
Nicolaus Copernicus University
Torun, Poland

F. Ozimek, C. Radzewicz
Institute of Experimental Physics, Faculty of Physics
University of Warsaw
Warsaw, Poland

***Abstract*—We report on the status of the work towards cold strontium clock in the Polish National Laboratory of AMO Physics in Toruń. The system consists of: (1) a Zeeman slower and magneto-optical traps (at 461 nm and 689 nm), (2) a frequency comb, and (3) a narrow-band laser coupled to an ultra-stable optical cavity. So far, all parts of the experiment are working and the whole system is tested at the $^1S_0$–$^3P_1$, 689 nm optical transition in ^{88}Sr atoms with 7 kHz linewidth.**

I. INTRODUCTION

Precision timekeeping has been based on atomic clocks for the past half-century. In particular, the SI unit of time, the second, is defined with respect to the frequency of resonance in ^{133}Cs atoms. Techniques of laser cooling and trapping have paved way for much improved atomic clocks: the fountain clocks. A new generation of atomic clocks, using optical transitions instead of the microwave ones offer even higher stability and accuracy(see review [1]). Optical clocks have already surpassed the stability of microwave clocks [2,3] and reached inaccuracies below 10^{-15} with expected control of systematic effects at the 10^{-18} level. They are realized as single ion clocks or neutral atoms in an optical lattice [4]. The use of the lattice limits the atom-atom interactions and offers the possibility of simultaneous measurements of large numbers of atoms increasing the S/N ratio while tuning of the lattice laser to the magic wavelength eliminates the light-shift effects.

The $^1S_0$ – $^3P_0$ transition in alkaline-earth atoms has been proposed as the clock transition and, in particular, the clock using Sr atoms has been realized by the groups in Tokyo, Paris and Boulder [5–7].

In this report we describe the status of the experiment running at the Polish National Laboratory of Atomic, Molecular and Optical Physics in Toruń aiming at the construction of Sr optical lattice clock. At present the first stage has been completed which includes the optical frequency comb, the ultra-narrow band laser stabilized to an optical cavity of high finesse, and the apparatus for cooling and trapping of strontium atoms. All three elements are operating and first spectroscopic measurements have been performed.

II. BLUE MOT SETUP

For ultimate laser cooling to temperatures below 10 μK, atoms have to be already precooled down to a few mK temperature in a blue magneto-optical trap (MOT). For this cooling the strongly allowed transition $^1S_0$–$^1P_1$ is used at 461 nm. To create MOT with reasonable loading rate in good vacuum conditions an atomic oven and a Zeeman slower have to be used due to low strontium vapour pressure. A vacuum set-up was built with an atomic oven, heated to 500ºC. The set-up is presented in Fig. 1. It is divided into two parts. The first one contains the atomic oven producing collimated strontium beam and laser beam collimation stage. The second part, with vacuum in order of 10^{-10} mbar consists of a Zeeman slower and main chamber, where MOT is created. The Zeeman slower construction is described in [8]. It has capture velocity of 450 m/s and produces atoms slowed down to

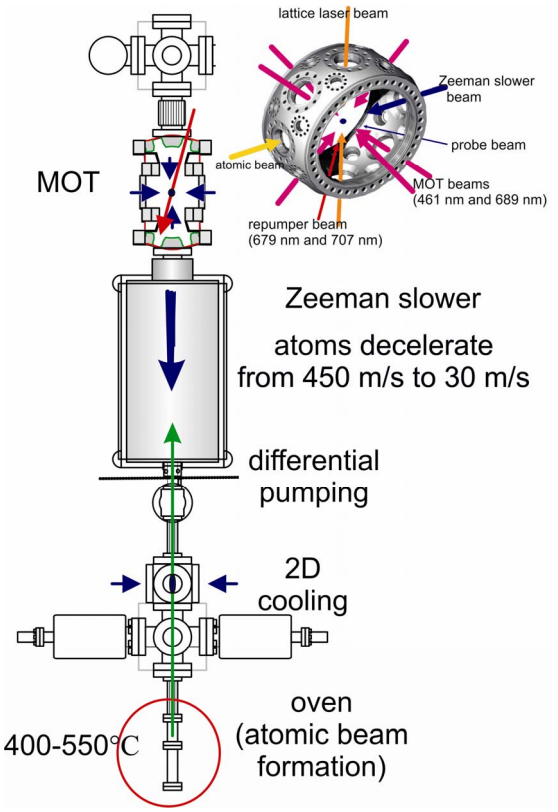

Figure 1. Vacuum set-up. The inset shows the experimental chamber.

30 m/s. The flux at 460ºC is 3.5×10^{9} s^{-1}. Blue MOT beams are detuned 40 MHz below strontium $^{1}S_0$–$^{1}P_1$ transition and have 23 mm in diameter. During the blue MOT stage two repumping lasers are used: 679 and 707 nm. $6–8\times10^{8}$ atoms are loaded into blue MOT and cooled down to 2–3 mK. At the present stage the apparatus is optimized for cooling ^{88}Sr but it can be rearranged for cooling ^{87}Sr.

III. Narrow Band Laser

For ultimate precision spectroscopy on doubly forbidden clock transition an ultra-narrow line width, tunable diode laser system is used as a local oscillator. The details of the system can be found in [9]. The laser is locked to a high-finesse optical cavity used as short-term frequency reference in the Pound-Drever-Hall configuration and thus an efficient laser line width narrowing is achieved. The cavity mirrors and the 100 mm spacer are made of ultra-low expansion glass. The mirrors are optically contacted to a spacer. The FSR of the cavity is 1,5 GHz and its finesse is $F = 62800$. Design of the cavity is optimized with respect to insensitivity to vibrations and is adopted from Webster et al. [10]. The horizontal cylindrical shape with cutouts is chosen and the proper choice of the support points assures immunity to vibrations. Fig. 2 presents a photograph of the bare cavity. The cavity is isolated from the laboratory environment, is enclosed in a vacuum chamber placed in another thermal enclosure. The mechanical isolation is provided by vibration isolation platform (Minus-k, BM-1) and a steel chamber lined with acoustic-damping foam (Nova-scan NanoCube). Two identical cavities are constructed.

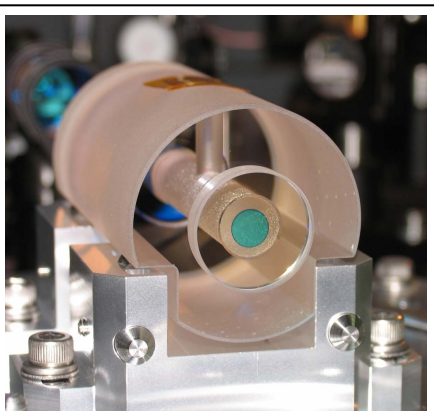

Figure 2. High finesse optical cavity with the support structure.

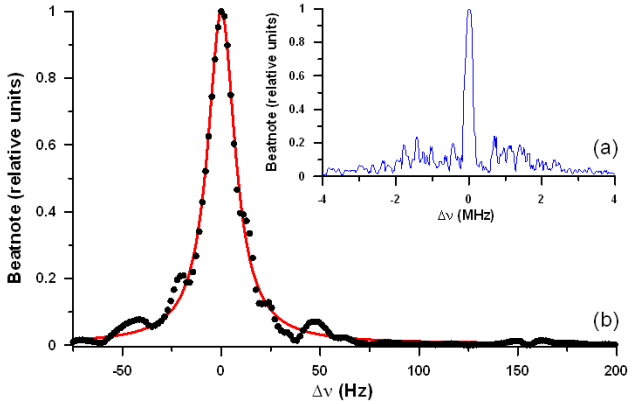

Figure 3. Power spectrum of the beat note of two independently locked lasers: (a) resolution bandwidth 150 kHz, (b) resolution bandwidth 9 Hz. The width of the peak in (b) is 16.8 Hz.

The laser system is based on commercially available external cavity diode lasers, ECDL (Toptica DLpro and DL100) which both provide about 20 mW output power at wavelength 687–693 nm. Each laser is independently locked to its own identical optical cavity with use of the PDH locking method. With this setup optical beat note of two independently locked lasers can be measured. In another configuration (master-slave scheme) one of the lasers is locked to the cavity and the other is phase-locked to the first one with the well-controlled offset. This configuration allows for wide frequency tuning with narrow line width.

We achieved laser line width of about 8 Hz, measured by comparison of two identical systems (see Fig. 3). The relative phase lock of two lasers is better than 150 mHz. The main limitation in the current state of this setup is instability of temperature of the optical cavity. Its active stabilization to a few mK should result in the drift rate of the order of 1 Hz/s.

IV. Spectroscopy and Laser Stabilization on 689 nm Transition

The simplified apparatus used for spectroscopy of 689 nm transition is presented in Fig. 4. Laser beam from one of the ultra-narrow lasers has been sent to room with strontium set-up. Cavity used for ultra-narrow laser was not temperature

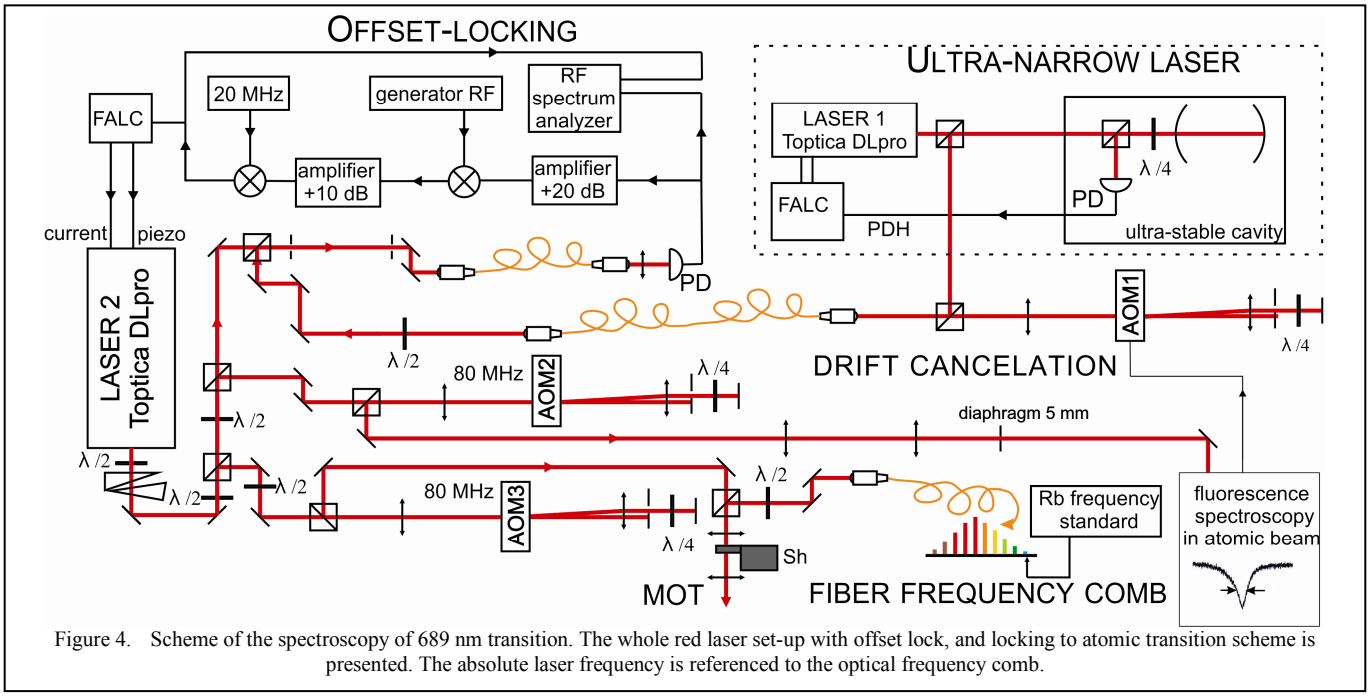

Figure 4. Scheme of the spectroscopy of 689 nm transition. The whole red laser set-up with offset lock, and locking to atomic transition scheme is presented. The absolute laser frequency is referenced to the optical frequency comb.

stabilized and laser frequency was drifting. Five-meter long, single mode, polarization maintaining fiber was used and a second Toptica DLpro laser was locked to the master laser using offset lock technique. This second laser was used for spectroscopy and for creating red MOT. Spectroscopy was done using the laser beam passing twice through AOM (which produced modulation required for spectroscopy). The beam was than expanded to 5 mm diameter, it was crossing the atomic beam perpendicularity and was precisely retro-reflected. Laser beam had π polarization with respect to the magnetic field of 1 mT, directed parallel to the atomic beam. Fluorescence signal was detected with a photomultiplier. Exemplary signal, with narrow sub-Doppler structure of ^{88}Sr $^1S_0(m=0)$–$^3P_1(m=0)$ line at 689 nm, taken at oven temperature of 500ºC is presented in Fig. 5. Using a fiber frequency comb absolute transition frequency was measured with respect to a commercial Rb 10 MHz reference. This measurement, done as a test, was highly limited by the Rb reference accuracy. In the next step cavity drift cancellation system has been build and the laser frequency was locked to atomic transition frequency. Fig. 4 shows the whole red laser set-up with offset lock, and locking to atomic transition scheme. Fig. 6 presents the locking scheme. AOM2 used for creating the beam for spectroscopy is modulated. Level of fluorescence signal from both sides of the atomic resonance are compared and correction is calculated for AOM1 in the ultra-narrow laser path, which cancels the cavity drift. This locking set-up can be also applied, after a few modifications, in future for locking of 698 nm laser to the strontium clock transition.

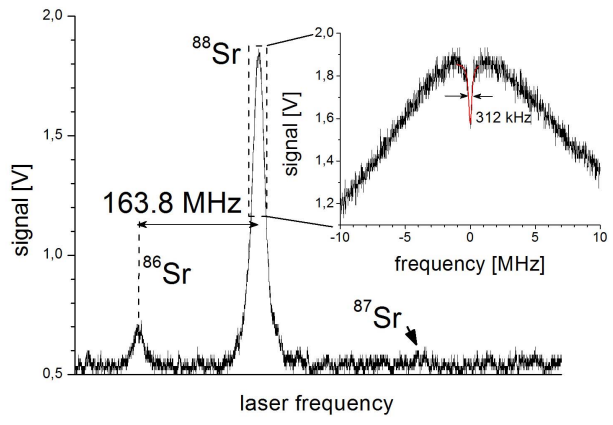

Figure 5. Spectroscopy of the of ^{88}Sr $^1S_0(m=0)$–$^3P_1(m=0)$ line (689 nm). The lower trace shows the wide scan, the inset shows detail of the Doppler-free feature in the center.

V. RED MOT

With 689 nm laser stabilized to strontium transition we created red MOT. The red MOT beams had 8 mm diameter and were superimposed on the blue MOT beams. Magnetic

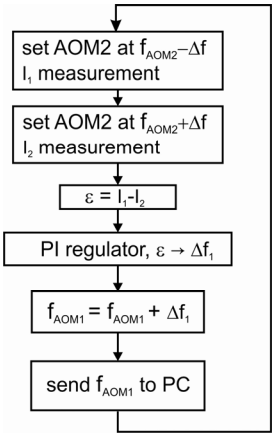

Figure 6. The algorithm of the locking scheme.

field gradient was lowered from around 0.68 T/m during the blue MOT phase to 0.03 T/m at the beginning of the red MOT phase and then the cloud was compressed by linearly ramping the field to 0.10 T/m. In order to transfer as many atoms as possible from the blue trap the narrow band red laser beams were modulated with frequency 16 kHz and modulation depth 1 MHz. Up to 10^7 ^{88}Sr atoms was stored with temperature below 15 μK. Cooled down atoms in red MOT are detected with probe 461 nm laser beam, resonant to $^1S_0$–$^1P_1$ transition.

VI. Conclusion and Outlook

In the first stage of the project the main elements of the apparatus for an optical atomic clock with Sr atoms have been built: the optical frequency comb, the ultra-narrow band laser stabilized to an optical cavity of high finesse, and the apparatus for cooling and trapping of strontium atoms. First spectroscopic measurements have been performed as a test of the system integration. The system is oriented at bosonic ^{88}Sr atoms, but operation with fermionic ^{87}Sr atoms can be achieved after minor modifications.

In a second stage of the project the clock transition $^1S_0$—$^1P_0$ (698 nm) will be investigated. To this end the atoms will be captured in the magic wavelength optical lattice. The ultra-narrow band laser will be tuned to the 698 nm transition and its bandwidth further decreased. The active stabilization of the optical cavity will be implemented assuring low drift of the laser.

Acknowledgment

The research is part of the program of the National Laboratory FAMO in Torun, Poland and was supported by the Polish MNiSW project No. N N202 1489 33 and the Foundation for Polish Science TEAM Project co-financed by the EU European Regional Development Fund.

References

[1] S. A. Diddams, J. C. Bergquist, S. R. Jefferts, and C. W. Oates, "Standards of time and frequency at the outset of the 21st century," Science, vol. 306, pp. 1318–1324, 2004.

[2] A. D. Ludlow et at., "Sr lattice clock at 1×10^{-16} fractional uncertainty by remote optical evaluation with a Ca clock," Science, vol. 319, pp. 1805-1808, 2008.

[3] T. Rosenband et al., "Frequency ratio of Al+ and Hg+ single-ion optical clocks; metrology at the 17th decimal place," Science, vol. 319, pp. 1808–1808, 2008.

[4] H. Katori, T. Ido, and M. Kuwata-Gonokami, "Optimal design of dipole potentials for efficient loading of Sr atoms," J. Phys. Soc. Jpn. vol. 68, pp. 2479–2482, 1999.

[5] M. Takamoto, F. L. Hong, R.Higashi, and H. Katori, "An optical lattice clock," Nature (London), vol. 435, pp. 321-324, 2005.

[6] R. Le Targat et al., "Accurate optical lattice clock with ^{87}Sr atoms," Phys. Rev. Lett., vol. 97, 130801, 2006.

[7] A. D. Ludlow et al., "Systematic study of the ^{87}Sr clock transition in an optical lattice," Phys. Rev. Lett., vol. 96, 033003, 2006.

[8] M. Bober, J. Zachorowski, and W. Gawlik, "Designing Zeeman slower for strontium atoms - towards optical atomic clock," Optica Applicata, vol. 40, pp. 547–555, 2010.

[9] D. Lisak et al., "Ultra narrow laser for optical frequency reference," Acta Phys. Pol. A, vol. 121, pp. 614–621, 2012.

[10] S. A. Webster, M. Oxborrow, P. Gill, "Vibration insensitive optical cavity," Phys. Rev. A, vol. 75, 011801(R), 2007.

Long-term temperature stabilized measurement of ultra-low expansion Fabry-Perot cavity

Radek Šmíd, Martin Čížek, Zdeněk Buchta, Josef Lazar, and Ondřej Číp
Institute of Scientific Instruments of Academy of Sciences of Czech Republic, v.v.i.,
Brno, Czech Republic
smid@isibrno.cz

***Abstract*— The ultra low expansion cavities play a crucial role in laser stabilization, and they are essential in ion clocks. We present a method to measure absolute distance between mirrors of Fabry-Perot cavity (FPC) with a spacer from an ultra low expansion material and the changes of the distance caused by temperature variation with femtometer resolution. The FPC was placed into a temperature-stabilized vacuum stainless steel chamber.**

I. Introduction

The ultra-low expansion materials are crucial in Fabry-Perot cavities. Atom based fountain clocks and ion clocks [1] uses generally lasers prestabilized to the cavity by Pound-Drever-Hall technique [2]. The length stability of the cavity is a crucial in this stabilization. This requires enviroment without any external vibrational source as well as suitable mirror spacer material. The use of any low expansion materials such as Zerodur glass ceramics [3] and ULE glass [4] in combination with temperature stabilized measurement chamber is essential. Thermal dilatation of the cavity of length of 20 cm in laboratory condition temperature stabilized down to 1 mK is around 4 pm. The knowledge of the absolute length of the cavity as well as thermal changes of the cavity length are necessary for any stabilization experiment. In this work we present a method of measurement of length of Fabry-Perot cavities with spacers of ultra-low expansion materials by the use of a femtosecond frequency comb [5].

The method uses a Fabry-Perot cavity (FPC) as a tool for ultra-low expansion material length changes measurement. FPC mirror spacer is made from Zerodur. Temperature of the cavity is stabilized and effects of refractive index of air are suppressed by placing into the evacuated chamber. Any fluctuation of FPC length is demonstrated in the change of free-spectral range (FSR) of the cavity while it exhibits changes in optical domain. Tunable laser follows the changes in the optical frequency transmitted trought the selected mode of FPC. The optical frequency comb stabilized to GPS disciplined oscillator represents a stable source in optical domain and works as a stable frequency rule in optical domain [5]–[10]. Changes of optical frequency are down-converted from the optical domain by the use of optical frequency comb.

II. Theory

The principle of the proposed method employing the optical frequency comb is based on the femtosecond laser and Fabry-Perot optical cavity. The optical frequency comb produces periodically a train of femtosecond pulses. The train of pulses is characterized by the central wavelength, period of pulses, their shape and by pulse to pulse phase shift. In optical frequency domain it produces a frequency spectrum of comb lines around the central optical frequency (wavelength). The frequency f_i of a comb spectral component is represented by expression:

$$f_i = f_0 + i \cdot f_\mathrm{r} \tag{1}$$

where i is the number of the spectral comb component (typically in the order of 10^6) and f_r, and f_0 are frequencies typically set in radio frequency (RF) domain, called repetition and offset frequency, respectively. The repetition frequency f_r is indirectly proportional to the period of the train pulses and the offset frequency f_0 is caused by phase-shifts between envelope of the pulses and their carrier wavelengths [5], [11]. Relative stability of spectral lines of free running femtosecond comb as well as relative stability of frequencies (f_r and f_0) reach the value of 10^{-7}. It is caused by the thermal dilatation of the body of the laser cavity. Therefore a precise stabilization of f_r and f_0 frequencies is necessary for more stable frequency comb spectrum. The stability of i-th optical component (spectral line) of the comb depends multiplicatively (relative stability remains the same) on the stability of the repetition frequency f_r based on (1) and additively on the offset frequency f_0. The repetition frequency is very intensively present in RF spectrum and thus it is easily detected and phase locked to a multiple of an atomic clocks RF signal (typically 10 MHz) by phase-lock servo-loop [5], [11]. The offset frequency has to be retrieved from comb spectrum by self-referencing method called as the f-2f interferometric technique [12]. The offset frequency f_0 is as well as the repetition frequency f_r phase locked to the stable oscillator or atomic clocks RF signal by a servo-loop. The result is the optical comb frequency spectrum with relative stability of all of frequency components coupled to the relative stability of the RF oscillator or atomic clocks (thus more than 10^{-14}).

A. Fabry-Perot cavity

The optical resonator (FPC) consists of two mirrors separated by the geometrical distance L_cav. This distance is represented by the spacer made from the low-expansion material placed between FPC mirrors. The optical resonator is an

instrument which transfers only the precise optical frequencies ν fulfilling the relation:

$$\nu = f_m = m \cdot \nu_{\mathrm{FSR}} = \frac{mc}{4nL_{\mathrm{cav}}} \tag{2}$$

where ν_{FSR} is free spectral range (FSR) of FPC, m-th is a longitudinal mode of the FPC in confocal geometry with mirrors separated by L_{cav} and c is speed of the light and n is the refractive index of air inside the cavity.

III. Tracking of the Cavity Length

The comb spectrum is transmitted through FPC if some of optical frequency spectral lines f_i (1) meets the resonance frequency (2). Reasonable number of lines transmits only if FRS of the FPC is an integer multiple of f_{r} thus $\nu_{\mathrm{FSR}} = x \cdot f_{\mathrm{r}}$ [13], where x is an integer number. The optical signal at the output of the FPC depends on the distance between mirrors in FPC. Other solution is based on separation of very few comb components by the use of ultra-narrow fiber Bragg grating [14]. Otherwise the optical output from FPC represents the similar signal to the white light continuum and the signal doesn't contain any resonance peaks. Nevertheless the problem of mismatch between some separated comb lines is still presented.

These problems can be solved by the use of a single-mode stable laser with the one resonance peak per FSR of the FPC. Because the FPC's FSR is fixed due to the stable low-expansion spacer a tunable laser source searches for the peak resonance. The use of tunable laser source is advantageous for following the small FPC length changes over wide optical spectrum. Optical frequency of the closest optical frequency comb line is used as a precise frequency reference to the tunable laser source. The optical frequency of the tunable laser referenced to optical comb line (1):

$$\nu_{\mathrm{opt}} = f_0 + i \cdot f_{\mathrm{r}} + f_{\mathrm{b}} \tag{3}$$

where f_{b} is the beat frequency between the closest optical comb spectral line and the tunable laser locked to the FPC. The beat frequency could be of both polarities and this polarity is easily evaluated from the measurement results with respect to temperature length variations or for fixed cavity length from variations of beat frequency f_{b} with respect to the offset frequency f_0 or frequency of tunable laser. Let us equal f_m to ν_{opt}, then:

$$\nu_{\mathrm{opt}} = f_m = f_0 + i \cdot f_{\mathrm{r}} + f_{\mathrm{b}} = \frac{mc}{4nL_{\mathrm{cav}}} \tag{4}$$

Extracting the exact length between mirrors of the FPC from (4) then:

$$L_{\mathrm{cav}} = \frac{mc}{4n(f_0 + i \cdot f_{\mathrm{r}} + f_{\mathrm{b}})} \tag{5}$$

Because i and m are integer constants and c is exact speed of the light in vacuum, the exact length L_{cav} of FPC is determined by frequencies f_0, f_{r} and f_{b}. Repetition and offset frequencies are controlled by RF reference by f-to-2f stabilization. The influence of refractive index of air on the result is suppressed when the FPC is inserted into the vacuum chamber where refractive index equals one within precision limits required by the method. The exact length of FPC can be written as:

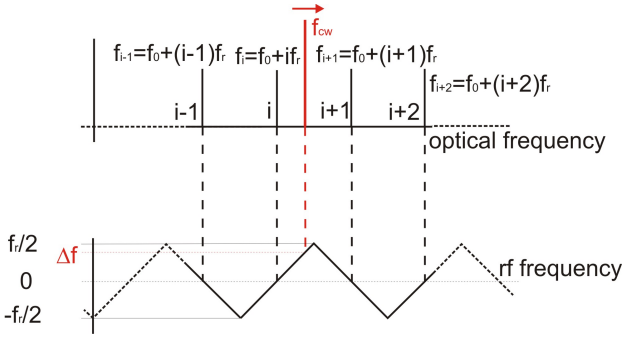

Fig. 1. Principles of measurement of the beat frequency Δf between continuous wave laser source f_{cw} and i-th frequency component.

$$L_{\mathrm{cav}} = \frac{mc}{4(f_0 + i \cdot f_{\mathrm{r}} + f_{\mathrm{b}})} \tag{6}$$

Frequencies f_{r} and f_0 are stabilized and locked to RF reference based on temperature stabilized quartz oscillator disciplined by GPS to cesium atomic clocks. Therefore f_{b} (beat frequency) between optical frequency comb and the tunable laser defines the FPC mirror distance. Variations of the FPC lengths are proportional to variations of beat frequency:

$$\delta L_{\mathrm{cavR}} = \frac{\delta L_{\mathrm{cav}}}{L_{\mathrm{cav}}} = \frac{-\delta f_{\mathrm{b}}}{f_0 + i \cdot f_{\mathrm{r}} + f_{\mathrm{b}}} \tag{7}$$

FPC of initial length L_{cav0} at temperature t is enlarged to length L_{cav1} at temperature $t + \Delta t$ characterized by coefficient of thermal expansion (CTE, α):

$$L_{\mathrm{cav1}}(t + \Delta t) = (1 + \alpha(t) \cdot \Delta t) \cdot L_{\mathrm{cav0}}(t) \tag{8}$$

Thus f_{b} beat frequency variations correspond to temperature variations of the FPC's spacer

$$\alpha(t) \cdot \Delta t = \frac{\Delta L_{\mathrm{cav}}}{L_{\mathrm{cav}}} = \frac{-\Delta f_{\mathrm{b}}}{f_0 + i \cdot f_{\mathrm{r}} + f_{\mathrm{b}}} \tag{9}$$

CTE of low-expansion materials reaches values down to $0.01 \cdot 10^{-6}\mathrm{K}^{-1}$ [3], [4]. Stability in the order of 10^{-12} at 1 s of the RF temperature stabilized oscillator used as a reference of optical frequency comb is equivalent to the temperature change in the order of 0.1 mK. Thus any temperature instabilities of FPC higher than 0.1 mK are easily detected.

Next, the last unknown variable, the integer number i (the number of the comb line component) can be evaluated by tuning the central frequency of the tunable laser f_{cw} to the center of tabled absorption lines in absorption gases [15] where $f_{\mathrm{cw}} = \nu_{\mathrm{opt}}$ in (3). The laser (f_{cw}) tuned to the center of the absorption line could then be rewritten as:

$$f_{\mathrm{ac}} = f_{\mathrm{cw}} = f_0 + i \cdot f_{\mathrm{r}} + f_{\mathrm{b}} \tag{10}$$

where f_{b} is beat frequency between the tunable laser and the closest comb frequency line.

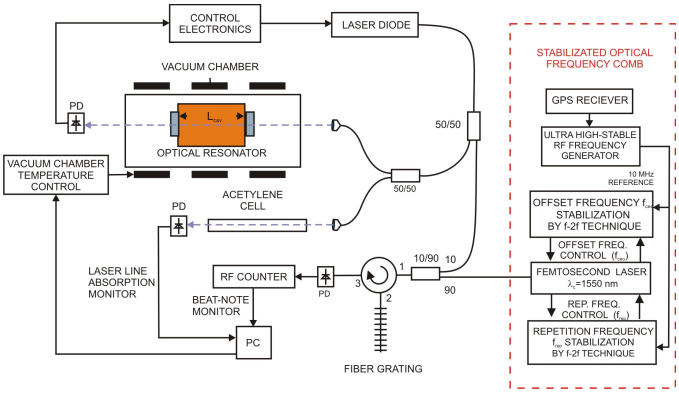

Fig. 2. Scheme of the optical setup for measurement of expansion coefficient of Zerodur material represented by optical resonator using stabilized optical frequency comb and additional laser diode and acetylene cell for exact length evaluation.

The exact number of frequency comb component i can be extracted by tuning at center of absorption lines f_{ac1}, f_{ac2}, f_{ac3}, etc. of absorption gas (for ex. Acetylene):

$$\begin{aligned} \Delta f_{\mathrm{ac1}} &= f_{\mathrm{ac1}} - (f_0 + j \cdot f_{\mathrm{r}}) \\ \Delta f_{\mathrm{ac2}} &= f_{\mathrm{ac2}} - (f_0 + k \cdot f_{\mathrm{r}}) \\ \Delta f_{\mathrm{ac3}} &= f_{\mathrm{ac3}} - (f_0 + l \cdot f_{\mathrm{r}}) \\ &\vdots = \vdots \\ \Delta f_{\mathrm{ac}j} &= f_{\mathrm{ac}j} - (f_0 + i_j \cdot f_{\mathrm{r}}) \end{aligned} \tag{11}$$

The exact number i_j of frequency comb component for each absorption line can be easily extracted. Measurement of the beat frequency between the tunable laser diode and the optical frequency comb with stabilized and known repetition and offset frequencies defines precisely the exact length of the cavity and leads directly from (9) to evaluation of CTE of the FPC spacer.

IV. Experimental Set-up

The piece of Zerodur material in a tube spacer of confocal FPC was measured in temperature stabilized vacuum chamber. Two dielectric mirrors with finesse of 339 deposited on the 10 mm thick fused silica substrates were optically connected to the spacer of 187.5 mm length with inner diameter of 12.7 mm and with the square based outer surfaces of 40 mm$\times$40 mm. The FPC was placed on four points holder in the axis of temperature stabilized stainless steel vacuum chamber. The chamber is evacuated down to 10^{-4} Pa. Temperature stabilization of the vacuum chamber was done by two resistance wires surrounding the chamber and controlled to 0.5 K. The temperature of Zerodur spacer was measured by two sensors inside the vacuum chamber. The temperature remained stable at the FPC surface down to 5 mK within 1 minute of measurement. For better thermal stability of each experimental part were lasers, vacuum chamber and FBG grating closed inside separate boxes with walls made of polyurethane with aluminium foils on both surfaces.

The DFB laser diode was used as a tunable laser source measuring the worked at central wavelength of 1542.14 nm (194.40 THz) and was tuned by the temperature control for more than 2 nm (250 GHz). The diode was supplied by batteries to avoid from additional electrical noises such as 50 Hz noise from the electrical socket. The Er:doped stabilized and Cs clock disciplined [8] mode-locked optical frequency comb with 100 MHz repetition frequency was used as a reference ruler to DFB laser diode. The 100 nm spectral range output of 1560 nm central wavelength of the stabilized fs laser were coupled to the fiber and mixed with DFB laser. DFB laser was supplied by batteries to ensure cut from any external electrical noises. The measurement was restricted to the batteries lifes.

The FBGs with the FWHM of 0.186 nm and 0.096 nm were used to increase SNR during beat-note measurement. Another temperature control within the range from -10°C to 80°C was used for tuning of the FBG's central selective wavelength in the tuning range of the DFB.

Fig. 2 presents the scheme of the set-up with DFB diode laser coupled to the FPC. The DFB laser output signal was splitted into two same parts in the $50/50$ coupler. One part was mixed in 10/90 fiber coupler. The 90% of the optical power of the output from Er:doped mode-locked fiber laser comb interfered with 10% of the DFB laser. Interference signal was coupled to the input port 1 of a fiber circulator. The light from the DFB laser diode was mixed with the optical frequency comb fiber output and the beat signal was through the fiber circulator back-reflected on the FBG (port 2). The light in fiber circulator travels from port 1 to port 2 and from port 2 to port 3 whereas the back-reflection from port 2 to port 1, from port 3 to port 2 as well as from port 3 to port 1 is not possible. The frequency comb components within the range of 0.186 nm or 0.096 represented by FWHM of FBG interfered with single frequency of DFB laser. Beat frequency between the comb components and the DFB laser diode are detected by infrared fast photodetector (PD) at port 3, counted by a RF counter and recorded by the computer.

Second output of 50/50 coupler from DFB laser output light was splitted in 50/50 coupler to the acetylene cell and to the FPC. Infrared PDs monitored absorption at the acetylene cell and the output transmission spectrum of the resonance modes of the FPC. The exact absolute value of the optical frequency of the DFB laser locked to the FPC resonance mode was determined with the help of the absorption cell and the optical frequency comb. The DFB and FBG tuning range covered the range from the center of P(13) to the center of P(11) $^{13}C_2H_2$ absorption lines [15]. The exact number of the closest spectral optical comb component i to the DFB frequency was determined by tuning DFB laser frequency while monitoring the absorption of acetylene cell and recording the the beat signal.

V. Results

The measurement of FPC length variation and hysteresis was caried out in the vacuum chamber at (25.54 ± 0.01)°C. Temperature at the spacer surface was monitored by two resistors and it was stable within 20 mK during several days.

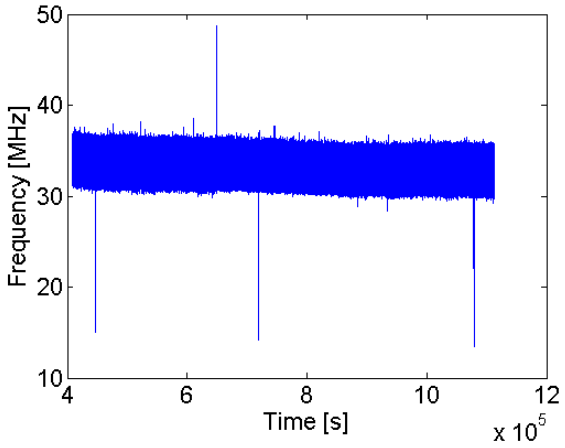

Fig. 3. Frequency beat between tunable DFB diode and the closest optical comb line.

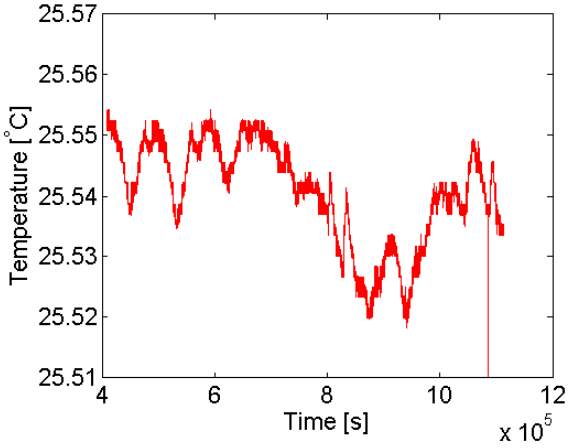

Fig. 4. Temperature stabilization over the measured time.

The measurement followed the measurement of spacer during the cycling process from 22 to 35°C when we had measured the hysteresis up to 8 nm [16]. First measurement of the long-term stability of the material started two weeks after the cycling experiment.

Fig. 3 represents data of the DFB laser diode locked by 1st derivative technique to the FPC over the period of 12 days when batteries could operate without charging. Data are relatively noisy because the 1st derivative technique.

Fig. 4 shows the temperature evolution during the measurement time. Despite on a fact that the FPC is placed into the temperature stabilized vacuum chamber that attenuate any ambient temperature changes we still observed temperature temperature fluctuation with a one-day period representing the temperature changes between the dayligt and night. The temperature never exceeded 30 mK difference between the highest and the lowest value within measured data points.

The level of the relative change of the frequency in the optical domain was hidden under the modulation of the laser diode. Although the long-term stability was reached by Allan variance of the data set. Fig. 5 represents the Allan variance of the data (blue circles). Short-term stability of the laser locked to the cavity was predominantly influenced by the fast modulation of the laser. Temperature changes with one-day period does not seem to have any influence on long term cavity stability. The stability of Zerodur cavity in the temperature stabilized vacuum chamber reached the long term stability of the Cs clock oscillator. We compared the results with the tabled Allan variance of high precision Cs clocks (by Oscilloquartz), long life Cs tube clocks and highly stabilized ovenized crystal oscillator (HS-OCXO) we had used for stabilization of the optical frequency comb. The cavity stability seems to be independent to the ambient temperature although the cycling of the ambient temperature over 10 K can produce hysteresis of the material. If the ambient temperature around the FPC does not overcome 30 mK difference it reaches the long term stability similar to the Cs tube.

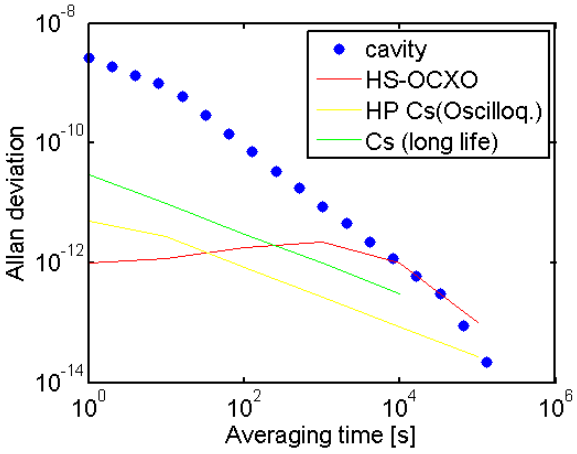

Fig. 5. Allan variance of frequency of the DFB laser locked to the FPC in comparison to the HS-OCXO reference for stabilization of optical comb and high precision (HP) and long life Cs clocks, respectively.

VI. Conclusion

We have measured and presented the stability of Zerodur spacer in teh Fabry-Perot cavity over the period of 12 days in the temperature stabilized vacuum chamber. Allan variance of the DFB laser locked to the cavity decrease and in very long term the stability follows the stability of the high performance Cs standard.

Acknowledgment

The authors acknowledge the support of the AS CR, project No.: AV0 Z20650511, projects of Grant Agency of CR: GA102/12/P962, GAP102/11/P819, GP102/10/1813 and GA102/09/1276 and Ministry of Industry and Commerce, project no.: 2A-1TP1/127. This work was partially supported by European Commission and Ministry of Education, Youth, and Sports of the Czech Republic (project No. CZ.1.05/2.1.00/01.0017.

REFERENCES

[1] S. A. Diddams and T. Udem and J. C. Berquist and E. A. Curtis and R. E. Drullinger and L. Hollberg and W. M. Itano and W. D. Lee and C. W. Oates and K. R. Vogel and D. J. Wineland, An Optical Clock Based on a Single Trapped $^{199}Hg^{+}$ Ion, Science 293, 825 (2001)

[2] R. W. P. Drever, J. L. Hall, F. V. Kowalski, J. Hough, G. M. Ford, A. J. Munley, and H. Ward, Laser Phase and Frequency Stabilization Using an Optical Resonator, Appl Phys B, vol. 31 (2), 97-105 (1983)

[3] Technical information TIE37: Thermal expansion of ZERODUR, http://www.schott.com/advanced_optics/english/download/schott_tie-37_thermal_expansion_of_zerodur_v2_august_2006_en.pdf

[4] ULE Corning Code 7972, Ultra Low Expansion Glass, http://www.corning.com/docs/specialtymaterials/pisheets/UleBro91106.pdf

[5] S. T. Cundiff, J. Ye, Colloquium: Femtosecond optical frequency combs, Rev. Mod. Phys. 75, 325 (2003)

[6] S. A. Diddams, L. Hollberg, L.-S. Ma, L. Robertsson, A femtosecond-laser-based optical clockwork with instability = 6.3x10-16 in 1 s, Opt. Lett. 27(1), 58 (2002)

[7] L.-S. Ma and Z. Bi and A. Bartels and L. Robertsson and M. Zucco and R. S. Windeler and G. Wilpers and C. Oates and L. Hollberg and S. A. Diddams, Optical Frequency Synthesis and Comparison with Uncertainty at the 10-19 Level, Science 303, 1843 (2004)

[8] J. Ye, J. L. Hall, S. A. Diddams, Precision phase control of an ultrawide-bandwidth femtosecond laser: a network of ultrastable frequency marks across the visible spectrum, Opt. Lett. 25(22), 1675 (2000)

[9] S. T. Cundiff, J. Ye, J. L. Hall, Optical frequency synthesis on mode-locked lasers, Rev. Sci. Instrum. 72(10), 3749 (2001)

[10] A. Bauch, H. R. Telle, Frequency standards and frequency measurement, Rep. Prog. Phys. 65, 789 (2002)

[11] H. R. Telle, G. Steinmeyer, A. E. Dunlop, J. Stenger, D. H. Sutter, U. Keller, Carrier-envelope offset phase control: A novel concept for absolute optical frequency measurement and ultrashort pulse generation, Appl. Phys. B 69, 327 (1999)

[12] M. Bellini, T. W. Haensch, Phase-locked white-light continuum pulses: toward a universal optical frequency-comb synthesizer, Opt. Lett. 25, 1049 (2000)

[13] R. Šmíd, O. Číp, J. Lazar, Precise length etalon controlled by stabilized frequency comb, Meas. Sci. Rev. 8, 114 (2008)

[14] R. Šmíd, O. Číp, M. Čížek, B. Mikel, J. Lazar, Conversion of stability of femtosecond mode-locked laser to optical cavity length, IEEE Trans. on Ultrason. Ferroelec. Freq. Control. 57(3), 636-40 (2010)

[15] K. Nakagawa, M. de Labachelerie, Y. Awaji, M. Kourogi, Accurate optical frequency atlas of the 1.5-um bands of acetylene, J. Opt. Soc. Am. B 13(12), 2708 (1996)

[16] O. Číp,R. Šmíd, M. Čížek, Z. Buchta, J. Lazar, Study of the thermal stability of Zerodur glass ceramics suitable for a scanning probe microscope frame, Cent. Eur. J. Phys. 10(2), 447 (2012)

Digital Processing of Beat Note Signals from Optical Frequency Synthesizers

Martin Cizek, Radek Smid, Zdenek Buchta, Josef Lazar and Ondrej Cip
Department of coherence optics,
Institute of Scientific Instruments of the ASCR,
Brno, Czech Republic
E-mail: cizek@isibrno.cz

***Abstract*— The presented work is focused on digital processing of beat note signals from a femtosecond optical frequency comb. The efforts concentrate in two main areas: Firstly, using digital servo-loop techniques for locking free running continuous laser sources on single components of the fs comb spectrum. Secondly, we are experimenting with digital signal processing of the RF beat note spectrum produced by f–2f technique used for assessing the offset and repetition frequencies of the comb, resulting in digital servo-loop stabilization of the fs comb.**

I. INTRODUCTION

While working with RF signals produced by mixing the output of a fs comb with continuous (CW) laser sources the main challenge is to correctly asses the frequency of the beat notes. As the output power of the fs laser is spread over its output spectrum, the levels of single components of the comb are usually very low. Besides the products of non-linear mixing of the continuous laser source and the comb components, the output signal spectrum of the photo detector contains naturally also the products of mixing the single comb components with each other. In case of the RF signal produced by the f–2f detection technique, the situation is very similar: The analyzed spectrum contains a relatively weak offset frequency (f_{ceo}) component together with approx. 20dB stronger repetition rate components originating from nonlinear mixing among the evenly spaced original components of the fs comb. Due to thresholding of the signal, RF counters are more likely to measure the frequency of the strongest spectral component or noise rather than the beatnote. Analyzing the whole spectrum of the output RF signal and using software defined radio (SDR) algorithms instead of measuring beat note frequencies with RF counters appears to be a more flawless technique.

Software capable of computing and analyzing the beat-note RF spectrums using FFT and peak detection was developed. A SDR algorithm performing phase demodulation on the f–2f signal is used as a regulation error signal source for a digital phase-locked loop stabilizing the offset frequency of the fs comb.

II. EXPERIMENTAL SETUP

We are using a stabilized optical frequency comb with 100MHz repetition rate. As can be seen in fig. 1, the 10MHz GPS RF reference signal synchronizes the fs comb and the sampling clock of a high-speed digitizer card. The digitizer processes the signal from a photo detector acting as a non-linear optical mixer for a DFB laser diode and fs comb output. The second channel is used for measuring the RF output of the f–2f detection stage of the fs comb.

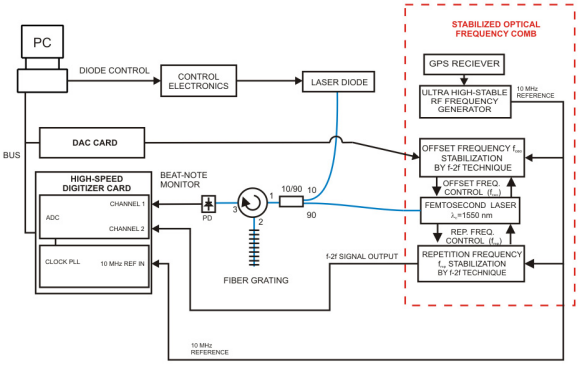

Figure 1. The experimental setup for digital signal processing of signals from a fs comb.

The digitizer card type M3i.3221 is equipped with a 12-bit flash ADC. The sampling clock is generated by an on-board frequency synthesizer slaved to an external 10 MHz GPS RF reference signal. The sampling rate can be set within the interval of 10–250 MS/s with 1Hz resolution.

The digitized data are streamed from the memory buffer on the card and processed in real time by the FFT and SDR algorithms.

The SDR algorithm acting as a digital phase detector pictured in fig. 2 is used as a control error source for a digital regulator stabilizing the offset frequency f_{ceo} of the optical frequency comb.

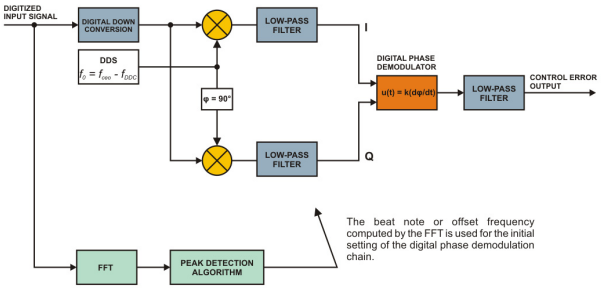

Figure 2. The digital signal processing chain used for real time digital stabilization of the fs comb.

The initial frequency of the beat note is assessed using the FFT algorithm for setting correct parameters of the real-time part of the SDR algorithm. Using digital down conversion, the input signal is then translated to a frequency range, which can be processed by the SDR algorithm in the real time.

The local numeric oscillator (DDS) is tuned to the initial beat-note frequency assessed by the FFT. In-phase and Quadrature components are produced by multiplying the input signal samples with *sin* and *cos* outputs of the local numeric oscillator. The cut-off frequency of the digital low-pass filters in the I and Q branches affects the selective bandwidth of the phase demodulator.

The output of the SDR chain is proportional to the deviation of frequency of the input beat-note signal from the frequency of the local numeric oscillator. It is calculated from the temporal change of the phase angle described by the I and Q components in the Cartesian plane.

III. Experimental Results

Thanks to the recent spread of high-speed multi-core CPUs in personal computers, it is possible to run real-time digital RF signal processing algorithms even on the PC platform. The heart of the pilot experimental SDR system is a computer based on an eight-core AMD FX ™ CPU equipped with a high-speed PCIe digitizer card type M3i.3221 from Spectrum GmbH.

A multithreaded software application performing real-time digital phase demodulation of the f-2f beat-note signal and stabilizing the f_{ceo} of the optical frequency comb was written in the C++ programming language. The bandwidth of the SDR is adjustable in range of 0.1–10 MHz, the SDR can be tuned to any carrier in 0–100 MHz frequency range, the output sampling rate of the software demodulator and digital f_{ceo} regulator can be up to 1 kHz.

The graph in fig. 3 shows an example of locking the f_{ceo} to a desired frequency of 6.25 MHz and stabilizing it for 600 s.

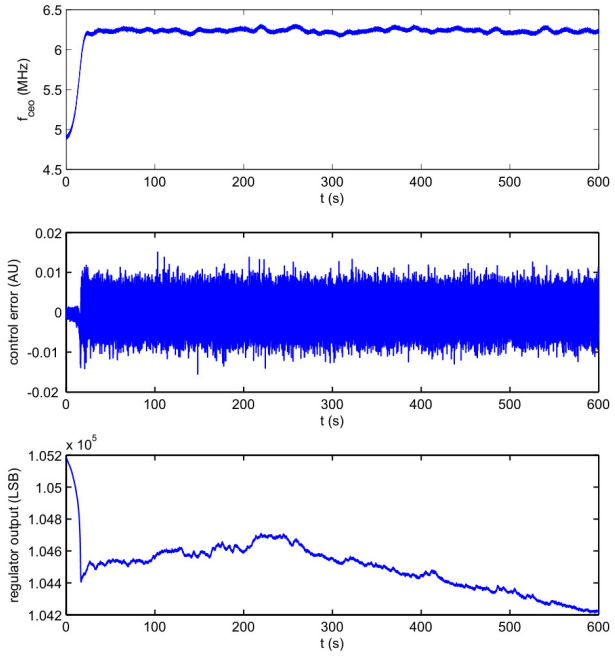

Figure 3. Waveforms of the fceo measured by FFT, control error and regulator output recorded while locking the offset frequency of the comb to a target value of 6.25 MHz.

The first waveform represents the frequency measured by the FFT; the second waveform is the output of the digital phase detector serving as a control error for a digital regulator tuning the pump current of the laser diode in the fs comb. The third waveform is the output of the digital regulator, which is being sent to an 18-bit D/A converter.

Alan deviation was computed from an over-night measurement of digitally stabilized f_{ceo}. The graph in fig. 4 shows its comparison to Alan deviation of f_{ceo} which was left without any stabilization.

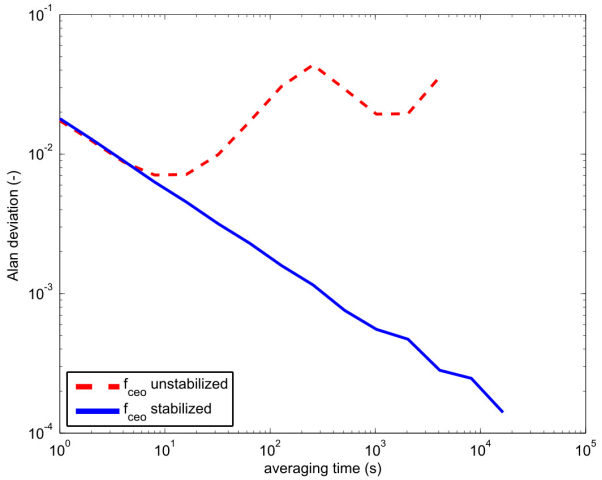

Figure 4. Alan variance of f_{ceo} digitally stabilized to 6.25 MHz compared to Alan variance of unstabilized f_{ceo}. The data were recorded during an overnight 10-hour measurement.

IV. CONCLUSION

We have successfully demonstrated a possibility of using software-defined radio algorithms running on a personal computer for stabilizing an optical frequency comb. The demonstrated SDR is capable of processing signals in 0 – 100 MHz range. Although the experiment shows an application of SDR used for stabilizing the carrier–envelope offset frequency, a very similar setup can be used also for stabilizing the frequency of a beat-note produced by mixing a tunable CW laser source with the output of an optical frequency comb.

ACKNOWLEDGMENT

This work is supported mainly by the Grant Agency of CR projects GPP102/11/P819, GAP102/10/1813 and GPP102/12/P962. The background of the research was supported by the European Commission and Ministry of Education, Youth, and Sports of the Czech Republic project No. CZ.1.05/2.1.00/01.0017 and project LC06007.

REFERENCES

[1] M. Bellini, T. W. Haensch, Opt. Lett. 25, 1049, 2000

[2] O. Cip, R. Smid, M. Cizek, Z. Buchta, J. Lazar, "Study of the thermal stability of Zerodur glass ceramics suitable for a scanning probe microscope frame", Cent. Eur. J. Phys., DOI: 10.2478/s11534-011-0112-6, 2011

The Space Optical Clocks Project:

Development of high-performance transportable and breadboard optical clocks and advanced subsystems

S. Schiller, A. Görlitz, A. Nevsky, S. Alighanbari, S. Vasilyev, C. Abou-Jaoudeh, G. Mura, T. Franzen,
Heinrich-Heine-Universität Düsseldorf (D);
U. Sterr, S. Falke, Ch. Lisdat,
Physikalisch-Technische Bundesanstalt (D);
E. Rasel, A. Kulosa,
Leibniz Universität Hannover (D);
S. Bize, J. Lodewyck,
Observatoire de Paris (F);
G. M. Tino, N. Poli, M. Schioppo,
Università di Firenze and LENS (I);
K. Bongs, Y. Singh,
University of Birmingham (UK);
P. Gill, G. Barwood, Y. Ovchinnikov,
National Physical Laboratory Teddington (UK);
J. Stuhler, W. Kaenders,
TOPTICA Photonics AG (D);
C. Braxmaier,
EADS Astrium Friedrichshafen (D);
R. Holzwarth,
Menlo Systems GmbH (D);
A. Donati,
Kayser Italia Srl (I);
S. Lecomte,
Centre Suisse d'Electronique et de Microtechnique (CH);
D. Calonico, F. Levi,
Istituto Nazionale di Ricerca Metrologica (I);
and members of the SOC2 teams
www.soc2.eu

Abstract— **The use of ultra-precise optical clocks in space ("master clocks") will allow for a range of new applications in the fields of fundamental physics (tests of Einstein's theory of General Relativity, time and frequency metrology by means of the comparison of distant terrestrial clocks), geophysics (mapping of the gravitational potential of Earth), and astronomy (providing local oscillators for radio ranging and interferometry in space). Within the ELIPS-3 program of ESA, the "Space Optical Clocks" (SOC) project aims to install and to operate an optical lattice clock on the ISS towards the end of this decade, as a natural follow-on to the ACES mission, improving its performance by at least one order of magnitude. The payload is planned to include an optical lattice clock, as well as a frequency comb, a microwave link, and an optical link for comparisons of the ISS clock with ground clocks located in several countries and continents. Undertaking a necessary step towards optical clocks in space, the EU-FP7-SPACE-2010-1 project no. 263500 (SOC2) (2011-2015) aims at two "engineering confidence", accurate transportable lattice optical clock demonstrators having relative frequency instability below 1×10^{-15} at 1 s integration time and relative inaccuracy below 5×10^{-17}. This goal performance is about 2 and 1 orders better in instability and inaccuracy, respectively, than today's best transportable clocks. The devices will be based on trapped neutral ytterbium and strontium atoms. One device will be a breadboard. The two systems will be validated in laboratory environments and their performance will be established by comparison with laboratory optical clocks and primary frequency standards. In order to achieve the goals, SOC2 will develop the necessary laser systems - adapted in terms of power, linewidth, frequency stability, long-term reliability, and accuracy. Novel solutions with reduced space, power and mass requirements will be implemented. Some of the laser systems will be developed towards particularly high compactness and robustness levels. Also, the project will validate crucial laser components in relevant environments. In this paper we present the project and the results achieved during the first year.**

I. INTRODUCTION

The principle of an optical lattice clock is shown in Fig. 1. A laser interrogates an ensemble of ultracold atoms, by exciting them to a long-lived atomic state via the clock transition. The atoms are trapped inside a standing-wave laser field ("optical lattice") and possess a temperature of a few micro-Kelvin. The interrogation results in a signal proportional to the absorption of the laser light, which depends on the laser frequency ν. The signal is maximum when the laser frequency coincides with the center of the atomic resonance ν_0. With a feedback control, the laser frequency ν is continuously kept tuned on ν_0. The resulting ultra-stable laser optical frequency ν_0 can be converted to an equally stable radio-frequency by means of a frequency comb.

The operational procedures in a lattice clock are shown in Fig. 1, middle. An atomic beam produced by an oven travels towards the right through a spatially varying magnetic field. In it, the atoms are slowed down by a laser beam (blue arrow, from laser subsystem BB 1, see Fig. 1 bottom) that finally nearly stops and traps the atoms inside the experimental chamber (square), in the 1st stage of a magneto-optical trap (MOT). Subsequently, they are cooled further to a lower temperature of several micro-Kelvin in a 2nd MOT stage by another laser subsystem (BB 2). In a third step, they are then transferred to an "optical lattice" made of counterpropagating laser waves generated by a third laser subsystem (BB 4).

Since the lattice potential "wells" are deeper than the thermal energy of the atoms, they are trapped in the potential minima. There, the atoms are spatially localized in one dimension to well below one wavelength of the clock laser (BB 5) and this condition leads to an excitation spectrum free of 1st-order Doppler spectral broadening or shift. Perturbing effects of the lattice light field on the atomic energy levels of the clock transition are minimized by choosing a so-called "magic" wavelength [1, 2].

The clock transition excitation is performed by the clock laser (BB 5). The laser subsystem BB 3 furnishes auxiliary laser light. The subsystems of a lattice clock are shown in Fig. 1, bottom. The laser light produced by the laser breadboards is transported via optical fibers to diagnostic and frequency stabilization units, to the frequency comb, and to the vacuum chamber containing the atoms.

The work of this project involves developing all subsystems, in part in form of compact breadboards, and integrating them into two transportable clocks, one operating with strontium (Sr), one with ytterbium (Yb).

^{87}Sr and ^{171}Yb are currently considered as the most promising isotopes.

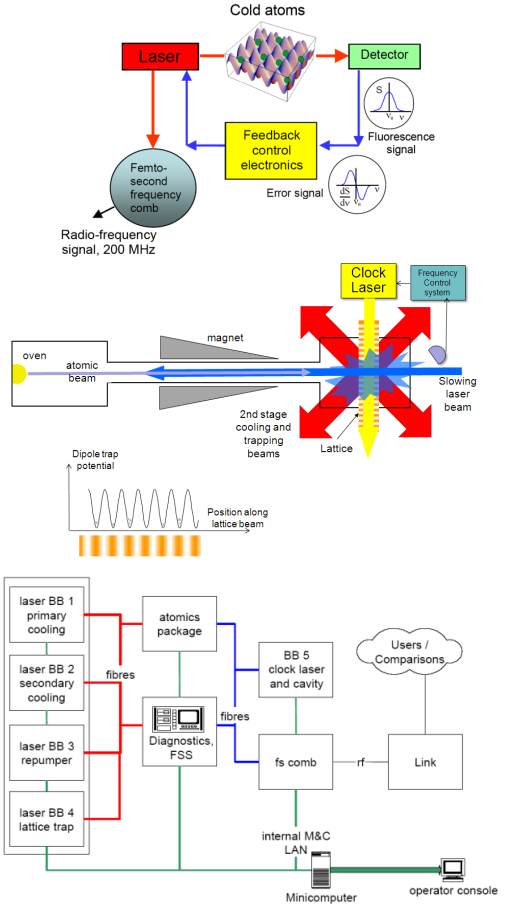

Figure 1. Top left, principle of an optical atomic clock based on atoms trapped by laser light. Top right, schematic of a lattice clock apparatus. Red: laser beams for 2nd stage cooling and trapping in the MOT. Orange-red: lattice laser standing wave; yellow: clock laser wave. Inset: variation of the potential felt by the atoms due to the lattice laser. Bottom, subsystems of a lattice optical clock.

The research leading to these results has received funding from the European Union Seventh Framework Programme ([FP7/2007-2013]) under grant agreement n° 263500.

TABLE I. SPECIFICATIONS FOR THE LASER AND STABILIZATION SUBSYSTEMS FOR THE STRONTIUM CLOCK

Laser breadboard	Wavelength	Frequency stability	Size in cm^3, mass	Power at fiber outputs
BB 1: Cooling #1	461 nm ECDL+SHG	1 MHz	60×45×10 20 kg	140 mW to distribution breadboard
BB 1: Cooling #1 distribution	461 nm	1 MHz	30×45×10 12 kg	50 mW MOT, 30 mW slower, 1 mW detection, 1 mW (IR) FSS
BB 2: Cooling #2	689 nm ECDL	< 1 kHz in 1 h, linewidth < 1 kHz with additional FM	60×45×12 20 kg	10 mW MOT , 1 mW FSS 1 mW to stirring breadboard
BB 2: Stirring and spin polarisation.	689 nm ECDL	Offset phase locked to 689 nm cooling	30×45×10 12 kg	10 mW MOT, 2×1 mW spin polarization
BB 3: Repumper	707 nm, 679 nm ECDL	FM +/- 3 GHz with a few kHz modulation frequency; center: 100 MHz	30×45×10 12 kg	2 mW each wavelength to MOT, 1 mW to FSS
BB 4: Lattice	813 nm ECDL	< 10 MHz in 10 h	30×45×10 12 kg	>200 mW to atomics 1 mW to FSS
BB 5: Clock laser	698 nm ECDL	<1 Hz	60×45×12 20 kg	2 mW to atomics, 2 mW to comb, 0.5 mW to cavity, 1 mW to FSS
BB 5: Clock cavity	698 nm	thermal noise 5×10^{-16}	55×55×55, 30 kg	
FSS: Frequency stabilization system	all, exclud., 698 nm	To levels indicated above	30 × 20 × 10, 10 kg	fiber input for the above fiber outputs

II. LASER SYSTEM FOR STRONTIUM CLOCK

The design of the laser system for the Sr lattice clock is modular, and all modules are connected by optical fibers to the vacuum apparatus. This choice ensures high stability and reliability needed for long-term operation of a clock. Moreover, the modular approach allows for independent testing of the subcomponents and, during the course of the project, simple replacement of components by more advanced components. The developments in the field of commercial lasers have produced impressive improvements in size, mass, stability and reliability of lasers and other optoelectronic components. The result is that the complete laser system for the Sr lattice optical clocks is based on off-the-shelf commercial components of moderate size and high reliability, such as diode lasers. The specifications are given in Table I. Based on ruggedized commercial systems, the lasers (Toptica) have been integrated into compact subsystems where several output beams, controlled in amplitude and frequency via acousto-optical modulators, are produced: a main output to the atomics package, an output for the laser frequency stabilization subsystem, and other additional service outputs. All outputs are provided in single-mode, polarization-maintaining fibers.

The following laser sources have been developed and have been integrated with the atomic package (see Sec. IV): a frequency doubled diode laser (461nm) for 1st cooling (BB 1), a high-power 813 nm laser for the dipole lattice trap (BB 4), two repumper lasers at 679 nm and 707 nm (BB 3). The highly frequency-stable 689 nm laser for 2nd stage cooling on the intercombination transition (BB 2) and the clock laser at 698 nm for the spectroscopy of the clock transition will soon also be integrated.

Fig. 2 shows the Sr laser subsystems developed during the first year of the project. Together, they occupy a volume of ca. 300 liter with an approximate power consumption of 100 W and 150 kg mass.

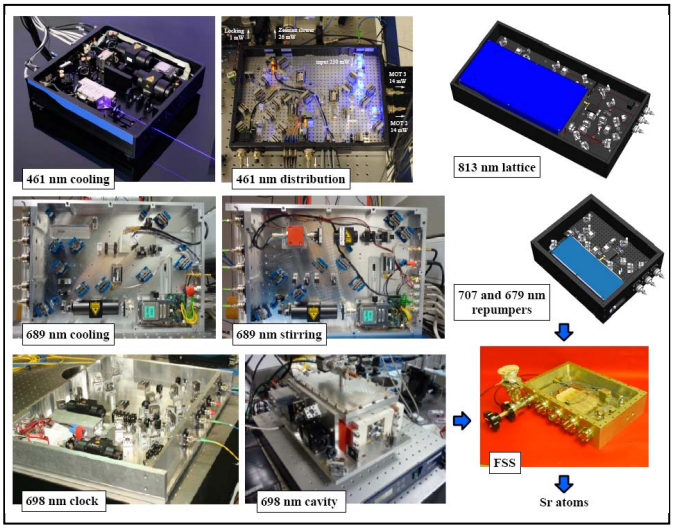

Figure 2. Overview of the laser subsystems for the strontium lattice clock, comprising 7 lasers and the respective frequency stabilization units (698 nm cavity of BB 5 and FSS).

III. LASER SYSTEM FOR THE YTTERBIUM CLOCK

For the operation of an Yb optical lattice clock, lasers with five different wavelengths are required. In the project, we develop compact and transportable laser sources based on state-of-the-art diode and fiber laser technology, see Fig. 3.

For the 1st-stage cooling radiation at 399 nm and for the lattice laser at 759 nm external-cavity-diode-lasers (ECDL) based on narrow-band interference filters [3, 4] are being developed, which promise improved stability compared to the commonly used grating-stabilized ECDLs. A prototype interference-filter ECDL at 399 nm using standard laser diodes and delivering up to 40 mW has already been tested successfully as a master laser. It is used to inject another, free-running laser diode and provides light for initial atom slowing. The higher power of a few 100 mW that is required at the optical lattice wavelength of 759 nm will be achieved using a self-injected tapered amplifier.

A compact repumping laser at 1389 nm, required to reduce fluctuations of the clock interrogation signal, has been developed following the approach at NIST. The unit is based on a DFB laser diode with fiber output, and exhibits a low free-running frequency instability (about 15 MHz/day linear drift) that will allow using the laser without further frequency stabilization.

The postcooling laser at 556 nm is a laser system based on fiber laser technology. It is designed to have a total volume of 3 liter. The all-fiber optical setup consists of three stages. The seed signal at 1111.60 nm is generated by a NKT Photonics BASIK module. The infrared signal is amplified in an amplifier pumped by two pump laser diodes at 974/980 nm. Second harmonic generation (SHG) at 555.80 nm is performed by an all-fiber coupled waveguide periodically poled lithium niobate (PPLN) device. An output power of 20 mW has been achieved.

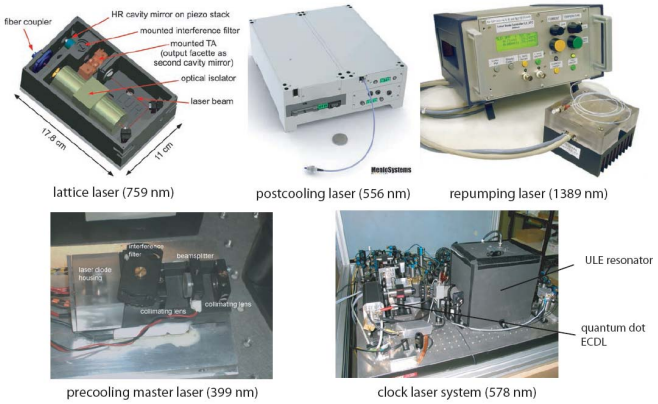

Figure 3. Overview of the laser subsystems developed for the ytterbium lattice clock, comprising 5 lasers.

Our approach for providing the 578 nm clock radiation is based on SHG of the radiation of an external cavity quantum dot laser (QD-ECDL) at 1156 nm in a PPLN waveguide. Stability and linewidth at the 1 Hz level have been achieved by stabilizing the laser to a highly stable ULE reference cavity [5].

IV. STRONTIUM ATOMS PREPARATION AND PRELIMINARY CLOCK SPECTROSCOPY

The design of the first-generation compact vacuum apparatus [6, 7] and the clock breadboard, which is fully operational, are shown in Fig. 4. Strontium atoms are first evaporated by an efficient oven working at 420°C, with a power consumption of 34 W. The atomic beam is then decelerated in a 18 cm long Zeeman slower and finally loaded into a 1st-stage MOT, operating on the dipole-allowed $^1S_0$ - $^1P_1$ transition at 461 nm. Radiation at this wavelength and for repumping at 679 nm and 707 nm are produced by the laser systems described above. Initial work has been performed with ^{88}Sr. The typical number of loaded atoms is about 10^8. By observing the expansion of the atoms from the MOT, an atomic temperature of about 2 mK was determined.

The 2nd-stage MOT operates on the $^1S_0$ - $^3P_1$ transition at 689 nm. Pending availability of the newly developed 689 nm laser, a prototype master-slave laser delivering up to 50 mW has been employed. The slave laser is optically injected with a beam coming from the pre-stabilized master laser. In order to tune the laser frequency on resonance and to provide the necessary power level and frequency modulation for the 2nd-stage MOT, a double-pass acousto-optical modulator (AOM) is used.

As shown in Fig. 5, in the 2nd-stage MOT two phases are implemented, a 120 ms long "broadband" phase during which the frequency of the cooling laser is broadened to 5 MHz to cover the Doppler width of the atomic resonance of the atoms at the end of the 1st-stage MOT, followed by 30 ms of "single-frequency" phase (no broadening). With the broadband phase it is possible to cool and trap about 1 x 10^7 ^{88}Sr atoms at 22 µK, while the "single-frequency phase" further cools the

atomic sample to the 2 μK, with a final population of 1 x 10^6 atoms.

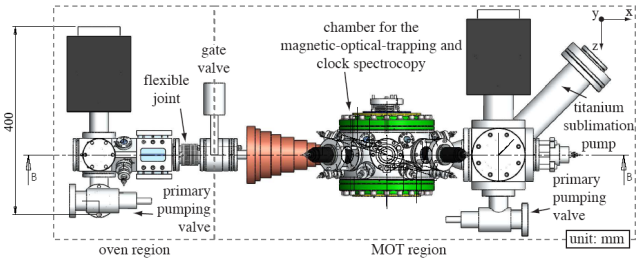

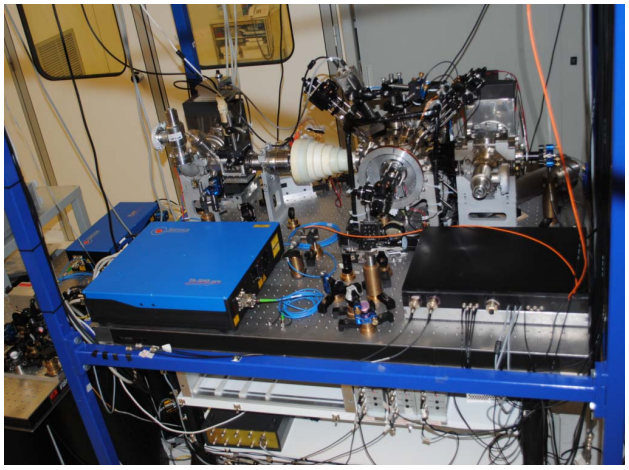

Figure 4. Top: Section view of the 1st generation strontium atomics package. The extension of the vacuum system is ca. 110 cm x 35 cm x 40 cm (150 liters). Bottom: clock breadboard with some of its laser subsystems.

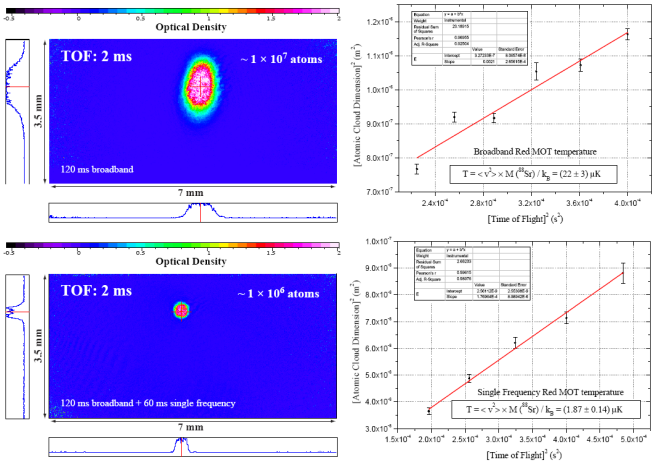

Figure 5. Absorption images of the ^{88}Sr sample and time-of-flight (TOF) measurements of the atom cloud size (graphs) at the end of the "broadband" (top) and "single-frequency" (bottom) phase.

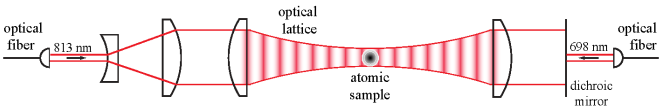

Figure 6. Optical setup of the vertical optical lattice at 813 nm, showing also the clock radiation input.

Subsequently, the ^{88}Sr atoms are then loaded into a vertical 1D optical lattice, realized by means of the external-cavity diode laser at 813 nm developed for this project. In Fig. 6 the design of the optical setup implemented for the vertical 1D lattice is shown. Light coming from the 813 nm laser source is sent through a beam expander, focused on the atomic cloud at the center of the main chamber, recollimated and then retro-reflected. With an available power of 280 mW and a waist of 50 μm, the estimated lattice trap depth is about 5 μK. The infrared beam has been aligned on the cold atomic cloud with the help of a resonant blue beam copropagating with the infrared beam.

Fig. 7 shows an absorption image of the atomic sample trapped in the optical lattice after the single-frequency 2nd stage MOT phase. About 50% of the atoms (5×10^5) are transferred from the latter into the lattice trap. The observed lifetime of the atoms in the trap is about 1.4 s, indicating that heating effects due to amplitude or frequency noise coming from the (unstabilized) 813 nm source are low.

For a preliminary clock spectroscopy test, the stationary 698 nm clock laser developed in Firenze [8] was used, which has a frequency stability of 10^{-15} for integration times between 10 - 100 s. Laser light, resonant with the $^1S_0$-$^3P_0$ clock transition, is coupled through a dichroic mirror along the direction of the lattice (Fig. 6). An AOM is employed to precisely control the timing, frequency and intensity of the excitation pulse on the atomic cloud. Preliminary results of magnetic-field-induced spectroscopy on the clock transition for the ^{88}Sr isotope are shown in Fig. 8. For these measurements we applied a constant magnetic field B (along the polarization of the clock laser field and the trapping field) by inverting the current on one of the MOT coils. By reducing the magnetic field (B = 1.1 mT) and the interaction time (T = 300 ms) we observed a minimum linewidth of about 410 Hz (left plot in Fig. 8).

As demonstrated in [9] it is possible to find the transition on a day-to-day basis even without a precise calibration of the laser frequency by adding a 200 kHz chirping (with 2 s period) on the clock laser frequency and increasing the interaction time to 1 s.

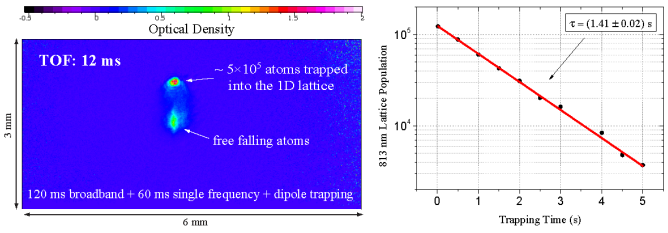

Figure 7. Left: absorption image taken 12 ms after turning off the 689 nm beams, while the 1D lattice (813 nm) is applied. A significant fraction of the atoms remain trapped in the lattice, while the untrapped fraction falls in the gravitational field. Right: Determination of the lifetime of ^{88}Sr atoms trapped in the lattice via measurement of the number of atoms remaining trapped for different durations of the applied optical lattice.

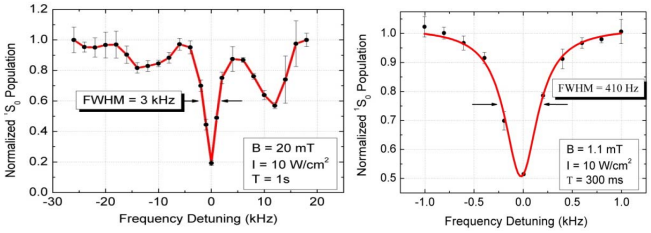

Figure 8. Spectroscopy of the ^{88}Sr clock transition in the optical lattice. The sidebands seen in the left plot indicate confinement of atoms in the lattice.

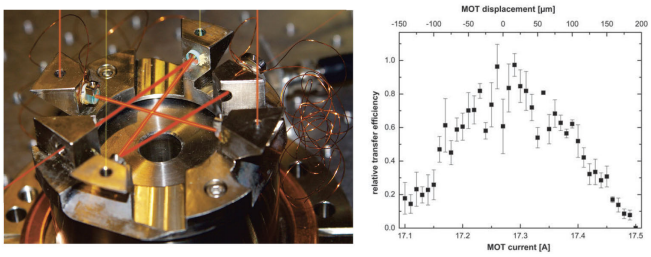

Figure 9. Left, the monolithic resonator setup for 1D and 2D optical lattices. Right, transfer efficiency into the optical lattice as a function of 2nd stage MOT position. The MOT position is controlled via the current through one of the MOT magnetic field coils.

V. Atom Preparation in the Ytterbium Clock

Within the first year of the project we have succeeded in preparing ultracold ensembles of the two isotopes ^{174}Yb and ^{171}Yb in a one-dimensional optical lattice which operates at 759 nm, the magic wavelength for Yb [10]. Our approach for the realization of such a magic-wavelength optical lattice includes enhancement resonators which are placed in the vacuum chamber in which the cold Yb ensembles are prepared. Inside two perpendicular resonators a large-volume optical lattice (either one- or two-dimensional) can be formed with only a few 100 mW power from a diode laser (Fig. 9 left). The resonator mirrors, two of which are mounted on ring piezo actuators, are glued to a monolithic structure, made out of the steel alloy invar, in order to increase the passive stability of the optical lattice. The end mirrors are transparent for the clock transition wavelength of 578 nm, which makes it simple to superimpose the radiation at the clock wavelength with the optical lattice.

Loading of a 1D optical lattice was so far achieved by using one of the two enhancement resonators with a beam waist of ca. 150 µm. We estimate that currently the maximum achievable trap depth is on the order of 50 µK. Yb atoms are loaded into the lattice by carefully aligning the position of the 2nd stage MOT to the lattice position and ramping down the 556 nm cooling light field (see Fig. 9, right). Successful loading of the optical lattice is observed by turning the cooling light field back on after a variable hold time and detecting the fluorescence of the atom that remained trapped in the lattice in the mean time. Without the lattice light field, no atoms are recaptured after roughly 20 ms while with the light field recapturing is possible even after 300 ms. The longest lifetime in the optical lattice observed so far is 130 ms, sufficient for the operation of an optical lattice clock.

In the currently used prototype setup we can transfer more than 20% of the atoms from the 2nd-stage MOT into the optical lattice, amounting to roughly 10^5 atoms, as aimed for. Since the temperature of the atoms in the MOT is typically 30-50 µK, we may infer that the transfer efficiency is limited by the depth of the optical lattice. This limit should be overcome in an advanced resonator setup, which is designed to allow for lattice depths of several 100 µK and higher transfer efficiency.

VI. Next-Generation Subunits

A. Blue light generation

The 461 nm cooling light for Sr is obtained by second-harmonic generation. As a potentially simpler and more robust alternative to the conventional generation in an external enhancement cavity (used in the laser developed for this project), we have tested the single-pass generation in periodically poled KTP waveguides. We could couple fibers with waveguides such that the input coupling efficiency to the waveguide was up to 70% (at 922 nm) and could obtain up to 40 mW of power at 461 nm. The output power could not be increased to more than 100 mW, as required. Therefore, an evaluation of different waveguide types is planned to follow.

B. Vacuum chambers

For a transportable clock, robustness, compactness and moderate mass are desirable. In this respect, we have compared two different techniques for realizing the UHV environment in the atomic package: lead sealing and gluing. Although both techniques have yielded vacuum in the range of 10^{-11}-10^{-12} mbar, the gluing technique has resulted in a more compact and lightweight vacuum chamber which can be baked well above 200 °C. In the process, we have analysed different combinations of materials for the chamber, windows and glues. We have found that although several combinations are possible, MACOR/titanium for the chamber material together with BK7/YAG for windows is a good combination from the thermal expansion point of view. We have also found that the two adhesives H77 and 353ND work quite well.

C. Atom preparation

Two novel approaches for loading atoms into a lattice optical clock are being investigated.

For the first approach, a two-dimensional (2D) MOT loaded from a dispenser is being tested. We have obtained some preliminary results where a 3D MOT is loaded from the 2D MOT system. We have observed clear enhancement in the atom number in the 3D MOT when loaded from the 2D MOT (Fig. 10 inset). Having gained from the above experience, we have made a preliminary design for a 2nd generation compact and lightweight vacuum chamber as required for the project

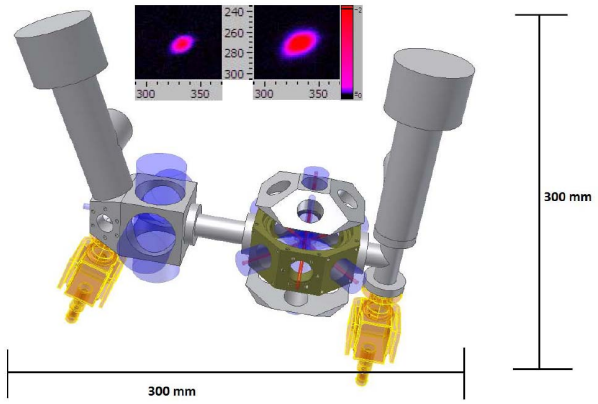

Figure 10. Main figure, preliminary design of the second-generation atomics package, where a 3D MOT (center) will be loaded from a 2D MOT (left side). The design is also adaptable to a Zeeman slower replacing the 2D MOT. Blue: cooling and detection beams; red: 2nd stage cooling and lattice trapping beams; yellow: ion pumps. Inset, two images of a ^{88}Sr 3D MOT loaded without (left) and with (right) a 2D MOT on, in a separate setup. The enhancement of the atom number is clearly visible.

(Fig. 10 main). The design is flexible in the sense that either a 2D MOT or a Zeeman slower can be used for slowing. The ultra-high vacuum will be maintained by ion pumps. In addition to the optical access for lasers for 2nd stage cooling, detection, lattice trapping etc, a thermal enclosure will be designed for the atomics package, which allows control of temperature to better than 0.1 K at the position of the atoms, necessary for controlling the black-body systematic frequency shift. Closed-loop magnetic field control will also be installed.

The second, conventional, approach for capturing atoms and loading them into a lattice trap consists in slowing the hot atoms emitted from the oven using a Zeeman slower, as is done in the 1st generation breadboard (Fig. 4). Typically, in a Zeeman slower a tapered solenoid is used. We have developed a novel transverse magnetic field Zeeman slower [11], which uses permanent magnets situated at adjustable distances from the beam axis (Fig. 11 top), and which works equally well for both ^{87}Sr and ^{88}Sr isotopes. This has potential for achieving a clock apparatus with smaller footprint, reduced mass and no dissipation.

D. Black-body radiation control

Finally, one of the major frequency shifts encountered in neutral atom lattice clocks is the black-body radiation shift due to the surrounding apparatus. Its value needs to be known in order to reach the goal accuracy of the space clock. We have developed a blackbody chamber to test calculations of the Sr black-body shift coefficient. The chamber includes two narrow copper tubes that approximate to well-defined black-body sources (Fig. 11 bottom). Cold Sr atoms at micro-Kelvin temperatures will be transported into either tube by a moving-lattice beam, then transferred into the "magic-wavelength" lattice for interrogation by the clock laser. By sequentially probing the lattice-trapped atoms in the two tubes at different temperatures, the differential blackbody shift is measured, allowing validation of the black-body coefficient.

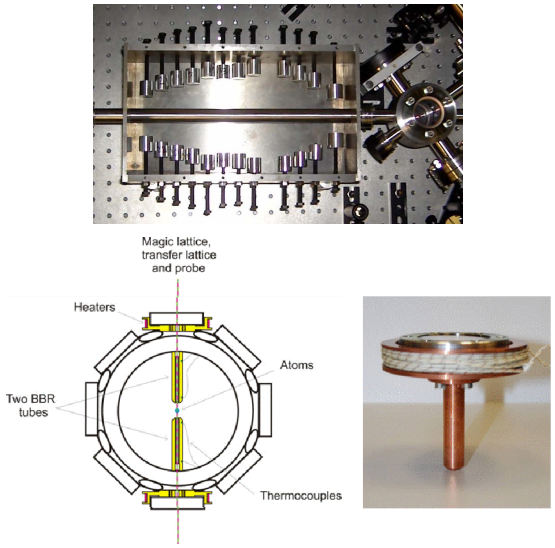

Figure 11. Top, a Zeeman slower using permanent magnets. Bottom left, schematic of MOT/lattice chamber with blackbody tubes. Bottom right, photo of a blackbody tube showing heater section external to the UHV chamber.

VII. CONCLUSION

The newly constructed Strontium laser subsystems have in part been integrated with the atomics subsystem and have already allowed ^{88}Sr atoms to be efficiently cooled, trapped into a 1D optical lattice and interrogated on the clock transition. The subunits of the Yb clock are also working well individually, with the atoms routinely trappable in the optical lattice. The upcoming work for the 2nd year of the project will include: (i) completion of the integration, spectroscopy of the clock transition, initial characterizations of the clocks' performances, and optimization; and (ii) progress on the development of the second-generation subunits (lasers, atomics package components), so that they can be integrated into the clocks in year 3.

Preparatory activities are also in progress for the later robustness testing of lasers and for the full characterization of the transportable optical clocks after moving them from the integration labs to national metrology labs, and for next-generation compact optical frequency combs.

At the end of the project we expect to have an operational lattice clock that will represent the baseline design for the production of the flight model for the ISS space clock.

ACKNOWLEDGMENT

We thank L. Cacciapuoti and O. Minster (ESA) for their continued support.

REFERENCES

[1] H. Katori, M. Takamoto, V. G. Pal'chikov, and V. D. Ovsiannikov, "Ultrastable optical clock with neutral atoms in an engineered light shift trap," Phys. Rev. Lett. 91, 173005 (2003).

[2] S. G. Porsev, A. Derevianko, and E. N. Fortson, "Possibility of an optical clock using the $6\,^1S_0 \rightarrow 6\,^3P_0$ transition in $^{171;173}$Yb atoms held in an optical lattice," Phys. Rev. A 69, 021403 (2004).

[3] X. Baillard, et al., "Interference-filter-stabilized external-cavity diode lasers," Opt. Comm. 266, 609 (2006).

[4] G. Tackmann, et al., "Phase-locking of two self-seeded tapered amplifier lasers," Optics Express 18, 9258 (2010)

[5] S. Vogt, et al., "Demonstration of a Transportable 1 Hz-Linewidth Laser", Appl. Phys. B 104, 741 (2011)

[6] M. Schioppo et al., "Development of a transportable laser cooled strontium source for future applications in space," Proc. EFTF (2010).

[7] M. Schioppo Ph.D. thesis, "Development of a transportable strontium optical clock," Università degli Studi di Firenze (2011), http://coldatoms.lens.unifi.it/optical-atomic-clock/documents.html.

[8] M. G. Tarallo, N. Poli, M. Schioppo, and G. M. Tino, "A high stability semiconductor laser system for a ^{88}Sr-based optical lattice clock", Appl. Phys B 103, 17 (2011).

[9] N. Poli, M. G. Tarallo, M. Schioppo, C. W. Oates and G. M. Tino, "A simplified optical lattice clock", Appl. Phys. B 97, 27 (2009).

[10] Z. W. Barber, et al., "Direct excitation of the forbidden clock transition in neutral ^{174}Yb atoms confined to an optical lattice," Phys. Rev. Lett. 96, 083002 (2006).

[11] Y. B. Ovchinnikov, "A permanent Zeeman slower for Sr atoms," Eur. J. Phys. Special topics 163, 95 (2008).

Iodine based optical frequency reference with 10^{-15} stability

Klaus Döringshoff*, Matthias Reggentin*, Evgeny V. Kovalchuk*, Moritz Nagel*, Anja Keetman†, Thilo Schuldt†, Claus Braxmaier† and Achim Peters*
*Humboldt-Universität zu Berlin
Institut für Physik, 12489 Berlin, Germany
Email: klaus.doeringshoff@physik.hu-berlin.de
†University of Applied Sciences Konstanz
Institute for Optical Systems, 78462 Konstanz, Germany
Email: tschuldt@htwg-konstanz.de

***Abstract*— We present different setups for frequency stabilization of Nd:YAG lasers to absorption lines in molecular iodine featuring frequency stabilities of $3 \cdot 10^{-15}$ at averaging times between 100 s and 1000 s. First results of a semi-monolithic setup, developed aiming at a space qualifiable iodine frequency reference, are shown.**

I. Introduction

Frequency stabilized lasers are a key technology for modern precision metrology related to fundamental physics and earth observation, as well as for optical communication, navigation and ranging. Future space missions rely on stable lasers with high requirements especially on long term stability. Examples are the planned new gravitational wave observatory (NGO), the next generation gravity mission (NGGM) and the gravity recovery and climate experiment (GRACE) follow on mission GRACE-II, where frequency noise below $30\,Hz/\sqrt{Hz}$ at Fourier frequencies between 10 mHz and 100 mHz are required [1].

This level of frequency stability can be achieved by frequency stabilization of the lasers to ultra-stable high finesse cavities [1] or to suitable absorbtion lines in molecules or atoms, that provide absolute optical frequency references.

In particular, molecular iodine provides a rich spectrum of hyperfine transitions in the green spectrum accessible by frequency doubled Nd:YAG lasers [2]. These transition feature strong absorbtion, small natural linewidths and low sensitivity to electric and magnetic fields.

These features in combination with intrinsic frequency and intensity stable Nd:YAG lasers, have enabled the realization of simple and compact optical frequency references. Since their development in the 1990s [2], [3], numerous setups using modulation transfer spectroscopy (MTS) [4] have been realized in the last decades reaching frequency stability of $4 \cdot 10^{-15}$ at 200 s [5]. Compact and simplified versions have been investigated with respect to space missions as well [6]–[8].

Aiming at a compact optical frequency reference with a frequency stability of $1 \cdot 10^{-15}$ we have built and investigated different frequency references based on molecular iodine using MTS technique. Important issues that limit the achievable frequency stability are effects due to residual amplitude modulation (RAM) and beam pointing [9]. We have investigated different setups to minimize these effects by use of a fiber-coupled EOM and an active RAM cancellation scheme. In a cooperative project of the Humboldt-University Berlin with the University of Applied Sciences Konstanz a semi-monolithic setup has been built using an assembly integration (AI) technique taking into account space mission related criteria such as compactness and robustness (see paper by T. Schuldt *et al.* in this proceedings). The special AI also provides the dimensional stability that virtually eliminates any possible beam pointing. This setup is currently investigated and first results on the frequency stability are presented in this paper.

II. Laboratory Setups

A frequency doubled Nd:YAG laser operating at 1064 nm is stabilized to the a_{10} component of the R(56)32-0 transition in iodine ($^{127}I_2$) by means of the MTS technique. In the basic setup, the 532 nm output of the laser is split into a pump- and a probe beam. Both beams pass AOMs, where only the pump is shifted by 80 MHz, and are then fiber coupled to the MTS setup. The collimators provide a beam diameter of 3 mm. Fractions of the pump- and probe beam are split off just before the cell for intensity stabilization via the AOMs and a part of the probe beam is split off before the cell for balanced detection of the MTS signal using a noise cancelling detector [10] (cf. Fig. 1). The iodine cell (ISI Brno, Czech republic) has a length of 80 cm and its cold finger is stabilized to $-15°C$, corresponding to an iodine vapor pressure of 0.76 Pa. Frequency stabilization is then realized via the laser PZT and temperature tuning of the Nd:YAG crystal with with control bandwidth of 30 kHz and 1 Hz, respectively.

Two setups have been realized and investigated, which differ in the realization of the pump beam modulation: In the first

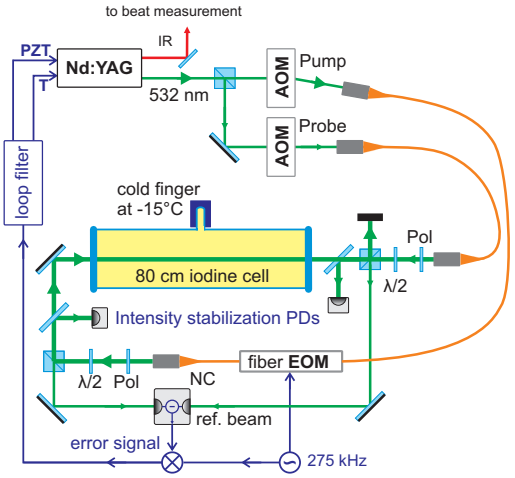

Fig. 1. Schematic of the MTS setup using a fiber-coupled EOM. AOM: acousto-optic modulator, EOM: electro-optic modulator, Pol: Polarizer, PD: photo detector: NC: noise cancelling detector

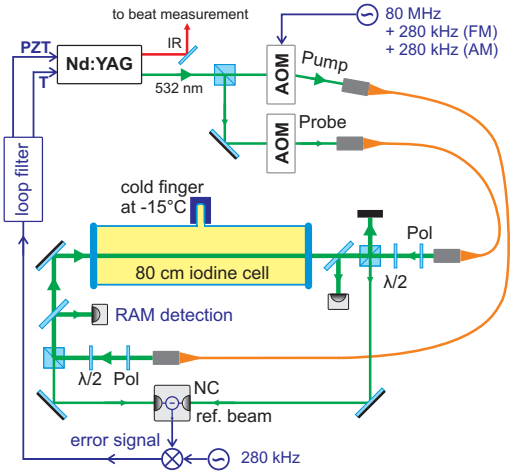

Fig. 2. Schematic of the MTS setup using frequency modulation of the AOM. AOM: acousto-optic modulator, Pol: Polarizer, PD: photo detector: NC: noise cancelling detector

setup (shown in Fig. 1) a fiber-coupled EOM is used for phase modulation providing high modulation indices and low RAM. It was found that unlike in other setups using bulk EOMs [5], [11], for the fiber-coupled EOM, a temperature stabilization was not necessary and no RAM stabilization was applied in this setup. The pump beam is phase-modulated at 275 kHz with a modulation index of 2.4, pump- and probe beam power are 1.8 mW and 0.5 mW, respectively. In this setup the pump power was limited by the fiber-coupled EOM. In the second setup (shown in Fig. 2) the AOM shifting the pump beam is used for frequency modulation. To this end, the 80 MHz rf-signal driving the AOM is frequency modulated at a rate of 280.3 kHz with a frequency deviation of 570 kHz. The residual amplitude modulation, originating at the fiber coupler, is detected before the iodine cell and compensated by an appropriate amplitude modulation at 280.3 kHz applied to the same rf-signal driving the AOM. In this setup, the beams were expanded by a factor of two by telescopes before entering the cell. The pump- and probe power were 6.3 mW and 1.25 mW, respectively. The pump power was stabilized via the temperature of the SHG crystal.

III. Elegant Breadboard Level Setup

Aiming at the development of a space qualifiable iodine frequency reference, an 'elegant breadboard level' (EBB) setup was realized. This setup features a 30 cm cell (ISI Brno, Czech republic) in a triple-pass configuration. The optical setup, shown in Fig. 3, is realized on a mechanically and thermally stable baseplate using a specific assembly integration technique based on a space qualified two component epoxy [12]. For details on the assembly integration please refer to the paper by T. Schuldt *et al.* in this proceedings.

The EBB setup is currently used with the laser system using AOM modulation described above. The pump- and probe light is fiber-coupled to the EBB via individual fibers and the fiber collimators provide beam diameters of 3 mm. Risley-prisms allow for fine tuning of the pump-to-probe beam alignment. Fractions of the light are split off before the cell for balanced detection of the probe beam, for intensity stabilization and for RAM cancellation.

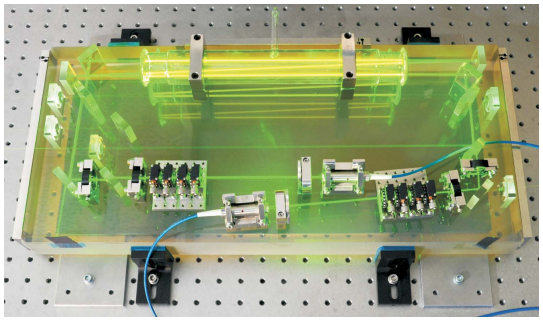

Fig. 3. Photograph of the 'elegant breadboard' spectroscopy setup.

IV. Frequency Stability

The frequency stability of the iodine setups was determined from beat note measurements at 1064 nm between the iodine stabilized laser and a laser stabilized to a high finesse ULE cavity. The frequency stability of the ULE cavity is known from beat measurements with other cavities and exceeds the stability of the iodine setup cf. Fig. 4 (left). For details on the cavity setup please refer to [11].

The frequency stability determined from the beat note measurements between the iodine setups and the ULE cavity is shown in terms of frequency noise spectral density and Allan deviation in Fig. 4 left and right, respectively. A quadratic drift was removed from the timerecords.

The frequency stability of the setup with the fiber EOM shows white frequency noise of $10\,Hz/\sqrt{Hz}$, corresponding

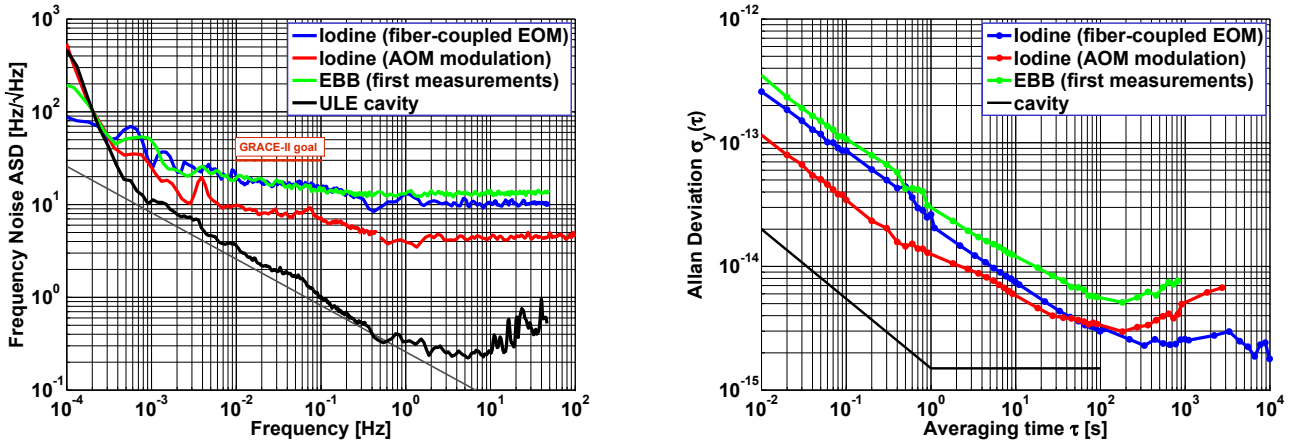

Fig. 4. Frequency stability of the investigated iodine setups. Left: frequency noise amplitude spectral density (ASD). Right: Allan deviation.

to $3 \cdot 10^{-14}/\sqrt{\tau}$ up to averaging times of 100 s and a flicker floor below $3 \cdot 10^{-15}$ between 100 s and 1000 s.

The frequency stability of the setup using AOM modulation and RAM cancellation shows white frequency noise on the level of $5\,Hz/\sqrt{Hz}$ corresponding to $1 \cdot 10^{-14}/\sqrt{\tau}$ up to integration times of 1 s and averages down to $3 \cdot 10^{-15}$ at 200 s. The improvement of the short term stability, with respect to the fiber EOM setup, is attributed to the higher optical powers used in this setup.

The very first measurements of the EBB setup show a frequency stability comparable with the setup using the fiber EOM (cf. Fig. 4), and the performance is currently optimized.

V. Conclusion

In conclusion, two different setups for Nd:YAG laser stabilization to hyperfine transitions in molecular iodine on breadboard level and one on elegant breadboard level have been investigated. The frequency stability achieved with these setups reach white noise levels on the order of $1 \cdot 10^{-14}/\sqrt{\tau}$ and average down to below $3 \cdot 10^{-15}$ at 100 s. The achieved stability is compatible with the requirements on the frequency stability discussed for space missions like NGO or GRACE-II.

First measurements of a semi-monolithic setup show promising results and work is in progress for a direct comparison of two iodine stabilized setups for a unambiguous characterization of the long term stability.

Acknowledgment

This work is supported by the German Space Agency DLR with funds provided by the Federal Ministry of Economics and Technology (BMWi) under grant numbers 50QT1102 and 50OQ0601.

References

[1] R. Thompson, W. M. Folkner, G. de Vine, W. M. Klipstein, K. McKenzie, R. Spero, N. Yu, M. Stephens, J. Leitch, R. Pierce, T. T.-Y. Lam, and D. a. Shaddock, "A flight-like optical reference cavity for GRACE follow-on laser frequency stabilization," in *2011 Joint Conference of the IEEE International Frequency Control and the European Frequency and Time Forum (FCS) Proceedings*. Ieee, May 2011, pp. 1–3. [Online]. Available: http://ieeexplore.ieee.org/lpdocs/epic03/wrapper.htm?arnumber=5977873

[2] J. Ye, L. Robertsson, S. Picard, L.-S. Ma, and J. H. Hall, "Absolute frequency atlas of molecular I_2 lines at 532nm," *IEEE Transactions on Instrumentation and Measurement*, vol. 48, pp. 544–549, 2008.

[3] A. Arie, S. Schiller, E. K. Gustafson, and R. L. Byer, "Absolute frequency stabilization of diode-laser-pumped nd:yag lasers to hyperfine transitions in molecular iodine," *Opt. Lett.*, vol. 17, no. 17, pp. 1204–1206, Sep 1992. [Online]. Available: http://ol.osa.org/abstract.cfm?URI=ol-17-17-1204

[4] J. H. Shirley, "Modulation transfer processes in optical heterodyne saturation spectroscopy," *Opt. Lett.*, vol. 7, no. 11, pp. 537–539, Nov 1982. [Online]. Available: http://ol.osa.org/abstract.cfm?URI=ol-7-11-537

[5] E. J. Zang, J. P. Ciao, C. Y. Li, Y. K. Deng, and C. Q. Gao, "Realization of Four-Pass I_2 Absorption Cell in 532-nm Optical Frequency Standard," *IEEE Transactions on Instruments and Measurement*, vol. 56, no. 2, pp. 673–676, 2007.

[6] V. Leonhardt and J. B. Camp, "Space interferometry application of laser frequency stabilization with molecular iodine," *Applied Optics*, vol. 45, no. 17, p. 4142, 2006. [Online]. Available: http://www.opticsinfobase.org/oe/ViewMedia.cfm?id=90139&seq=0 http://www.opticsinfobase.org/abstract.cfm?URI=ao-45-17-4142

[7] K. Nyholm, M. Merimaa, T. Ahola, and A. Lassila, "Frequency stabilization of a diode-pumped Nd:YAG laser at 532 nm to iodine by using third-harmonic technique," *IEEE Transactions on Instrumentation and Measurement*, vol. 52, pp. 284–287, 2003.

[8] B. Argence, H. Halloin, O. Jeannin, P. Prat, O. Turazza, E. de Vismes, G. Auger, and E. Plagnol, "Molecular laser stabilization at low frequencies for the LISA mission," *Phys. Rev. D*, vol. 81, p. 082002, 2010.

[9] E. Jaatinen, D. J. Hopper, and J. Back, "Residual amplitude modulation mechanisms in modulation transfer spectroscopy that use electro-optic modulators," *Applied Optics*, vol. 025302, 2009.

[10] P. C. Hobbs, "Ultrasensitive laser measurements without tears." *Applied optics*, vol. 36, no. 4, pp. 903–20, Feb. 1997. [Online]. Available: http://www.ncbi.nlm.nih.gov/pubmed/18250756

[11] K. Döringshoff, K. Möhle, M. Nagel, E. Kovalchuk, and A. Peters, "High performance iodine frequency reference for tests of the LISA laser system," in *Proceedings of the 24th European Frequency and Time Forum (2010)*, 2010.

[12] S. Ressel, M. Gohlke, D. Rauen, T. Schuldt, W. Kronast, U. Mescheder, U. Johann, D. Weise, and C. Braxmaier, "Ultrastable assembly and integration technology for ground- and space-based optical systems," *Appl. Opt.*, vol. 49, no. 22, pp. 4296–4303, 2010.

Frequency dissemination at the 19th decimal place

G. Grosche, O. Terra, S.M.F. Raupach, U. Sterr, H. Schnatz,
Physikalisch-Technische Bundesanstalt
Braunschweig, Germany
Gesine.Grosche@ptb.de

A. Pape, J. Friebe, M. Riedmann, E.M. Rasel,
Institute of Quantum Optics
Leibniz University of Hannover
Hannover, Germany

S. Droste, K. Predehl, R. Holzwarth, and Th. Udem
Max-Planck-Institut für Quantenoptik
Garching, Germany

***Abstract*—Optical frequency transmission via phase-stabilized telecommunication fiber is currently the most precise technique available for disseminating frequencies. We summarize some key advances, results and applications for fiber networks spanning up to 1000 km.**

I. INTRODUCTION

The rapid development of ultra-stable lasers and optical clocks, and their application in fundamental physics experiments [1], calls for precise frequency comparisons over long distances. Early work e.g. at the Jet Propulsion Laboratory (JPL) and metrology institutes recognized the potential of optical fibers to transmit radio and optical frequencies. Following demonstration experiments [2,3,4] over distances or order 100 km, optical frequency transmission via phase-stabilized telecom fiber has been adopted worldwide as the most precise technique for frequency dissemination. Here we present some key advances, results and applications for networks spanning up to 1000 km.

II. FIBER TRANSMISSION AND INTERFEROMETER

The method is based on transmitting an ultra-stable optical frequency near 200 THz over standard telecom fiber, while correcting environmental perturbations of the transmission path using interferometric detection. Underground fiber is already well shielded, with passive transmission giving frequency fluctuations typically below 10^{-14} (1…1000 s) for distances up to 100 km. With active phase stabilization, these fluctuations can be suppressed by several orders of magnitude; the noise suppression is fundamentally limited by the round-trip delay of the signal [3], and can be degraded by self-heterodyne noise of the laser source and non-common paths in the interferometer. With careful design of a dedicated fiber interferometer [5] we reached a noise floor of 3×10^{-17} (1s) and $<10^{-20}$ (1h); using this for a 146 km fiber link connecting the University of Hannover and PTB Braunschweig, enabled a transmission accuracy of 10^{-19}. In terms of gravitational red-shift, this corresponds to a 1 mm height difference [1].

III. APPLICATIONS: REMOTE FREQUENCY MEASUREMENTS AND CAMPUS DISTRIBUTION

Applications include remote measurement, e.g. of the transition frequency of the Mg optical clock (Hannover) versus the primary Cs-fountain clock (PTB) [6]. The superb short-term fiber link instability (ADEV $\sim3\times10^{-15}$, Modified ADEV $\sim5\times10^{-17}$ at 1s) and fs-comb techniques have also enabled remote spectroscopy [5], such as the real-time remote comparison at sub-Hz level [7] of two ultra-stable clock lasers, one operating at 914 nm (at University of Hannover) and one at 657 nm (at PTB) via a 73 km phase stabilized fiber link operating at 1540 nm. For ultra-stable lasers with a line-width $\Delta\nu$ of 1Hz or less, the observed phase noise $S\phi(f)$ of the stabilized fiber link [5] remains below that of the laser for all Fourier frequencies $f < 10\times\Delta\nu$, i.e. we can meaningfully "transport" the properties of ultra-stable lasers.

Over distances up to a few km, we expect a link instability (ADEV, measuring bandwidth > 1 kHz) of $\sim5\times10^{-17}/(\tau s^{-1})$. This is because the calculated delay limit [3] results in an instability contribution less than or equal to that of the interferometer for distances up to at least 2 km. Multi-access schemes [8] allow us to establish a network that connects a number of laboratories on the Hannover and Braunschweig campuses, housing the best lasers and clocks. One exciting prospect is the distribution of ultra-stable laser light derived from cryogenic optical cavities [9], with a thermal noise floor below 10^{-16}. This could significantly improve the short term stability of optical clocks [10].

IV. LONG DISTANCE FIBER LINKS

Our goal now is to connect the best clocks in Europe, building on experience gained in several countries [11]. We implemented a novel amplification scheme using stimulated

Work supported by European Space Agency, Centre of Excellence QUEST, and the Deutsche Forschungsgemeinschaft.

Brillouin scattering on a 480 km single-span stabilized link [12] and recently combined this technique with remotely controlled bi-directional fiber amplifiers to establish a 2 × 920 km stabilized fiber link between MPQ Garching and PTB, already leading to a remote measurement of the 1S-2S transition in hydrogen. The transmission properties of the 920 km link [13], with a frequency instability below $5\times10^{-14}/(\tau s^{-1})$ and a relative accuracy of $\sim5\times10^{-19}$, confirm quantitative models for long-distance fiber-links and allow comparisons of the best optical clocks world-wide.

ACKNOWLEDGMENT

We thank T. Legero for building a reliable ultra-stable laser source at 1.54 µm, and A. Koczwara and M. Misera for expert electronics support. G.G. thanks G. Santarelli and F. Riehle for their enthusiasm and encouragement.

REFERENCES

[1] C.W. Chou, D. B. Hume, T. Rosenband, D. J. Wineland, Science **329**, 1630 (2010) and references therein

[2] G.Grosche, B. Lipphardt, H. Schnatz, G. Santarelli *et al.* CMKK1, CLEO (2007)

[3] N.R. Newbury, P.A. Williams, W.C. Swann, Opt. Lett. **32**, 3056 (2007)

[4] F.-L. Hong, M. Musha, M. Takamoto *et al.* Opt. Lett. **34,** 692 (2009)

[5] G. Grosche, O. Terra, K. Predehl *et al.* Optics Letters **34**, 2270 (2009)

[6] J. Friebe, M Riedmann, T Wübbena *et al.* New J. Phys. **13**, 125010 (2011)

[7] A. Pape A, O. Terra, J. Friebe *et al.* Optics Express **18**, 21477 (2010)

[8] G. Grosche, patent registration DPMA 10 2008 062 139 (2008)

[9] T. Kessler, C. Hagemann, C. Grebing *et al.* arXiv:1112.3854v1 (2011)

[10] H. Katori, Nature Photonics **5**, 203 (2011) and references therein

[11] O. Lopez, A. Haboucha, F. Kéfélian *et al.* Optic Express **18,** 16849 (2010) and references therein

[12] O. Terra, G. Grosche, H. Schnatz, Optics Express **18,** 16102 (2010)

[13] K. Predehl, G. Grosche, S.M.F. Raupach, *et al.* Science **336**, 441 (2012)

Fiber optic RF frequency transfer on the distance of 480 km with the active stabilization of the propagation delay

Śliwczyński Ł, Krehlik P, Buczek Ł, Lipiński M, Kołodziej J
Department of Electrical Engineering
AGH University of Science and Technology
Kraków, Poland
(sliwczyn, krehlik, lbuczek, mlipinsk, jackolo)@agh.edu.pl

***Abstract*—In the paper the results of laboratory experiments are presented concerning the time and frequency transfer in 480 km long electronically stabilized fiber optic link. The fiber optic link comprised nine spooled spans with attenuation between 5-15 dB and eight custom-built bidirectional fiber amplifiers. The Allan deviation measured for frequency transfer at one-day averaging was around $4 \cdot 10^{-17}$, whereas time deviation for 1PPS signal was in the range 650-900 fs for averaging times between 10^3-10^5 s.**

I. INTRODUCTION

The propagation delay of the optical fibers is affected by variations of the temperature, degrading the long-term (diurnal and seasonal) stability of the time/frequency transfer. This problem might be solved by stabilizing the propagation delay of the link in the feedback loop exploiting unsurpassed symmetry of the propagation conditions in both directions of the same optical fiber [1]-[5]. Recently our group proposed novel and simple stabilization scheme using the system with two matched electronic delay lines organized in the delay locked loop [6]. The schematic diagram of the stabilized link using this principle is presented in Fig. 1. First measurements showed that the Allan deviation around $2 \cdot 10^{-17}$ at the distance of 20-60 km are possible [7].

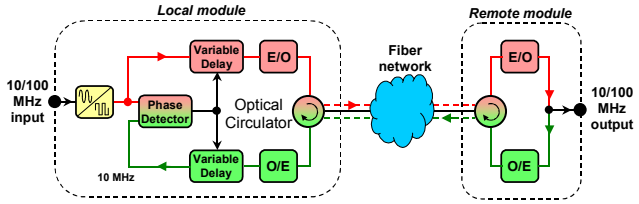

Figure 1. Schematic diagram of fiber optic frequency transfer link with electronic stabilization of the propagation delay

For distances exceeding about 50-70 km the attenuation of the optical fiber must be compensated. Because the operation of stabilized link is based on transmission of signals in both directions in the same fiber the amplifier used to compensate the attenuation must operate bidirectional. Concerning the symmetry of the propagation delay in both directions the best solution is to perform the optical amplification in the same piece of Er-doped fiber [8]. Initial experiments performed with such amplifiers showed that Allan deviation around a few times 10^{-17} with one day averaging is possible [8].

The motivation to perform further experiments was to evaluate the performance of the electronically stabilized link in the laboratory testbed, before its final installation at the target location, i.e. between the Laboratory of Time and Frequency of Polish Central Office of Measures in Warsaw (GUM) and the Astrogeodynamic Observatory of Polish Space Center in Borowiec near Poznan (AOS). Thanks to the availability of both ends of the link at the same place we could verify the stability of the transfer and check the calibration procedures

II. EXPERIMENTAL SETUP

The length of the target link is about 420 km so we decided to perform the laboratory tests on somehow extended baseline equal to 480 km. We used 9 spans of optical fibers spooled on the reels, with lengths of individual spans close to those in the target link. The parameters of the spans are summarized in Table I. The link comprised mostly standard SMF-28 fibers with a few reels of large effective area fibers (LEAF). The total attenuation of entire span exceeded 90 dB, showing total chromatic dispersion around 7300 ps/(nm·km). The simplified schematic diagram of our experimental setup is presented in Fig. 2.

To measure the stability of the frequency transfer we used Agilent DSO81004A high-speed digital oscilloscope, featuring 10 GHz bandwidth and 40 Gs/s real-time sampling rate. We used external 10 MHz oven-controlled crystal reference to synchronize both the DSO and the 10 MHz square-wave generator that was used for frequency transfer.

We would like to thank Telefonika Kable S.A. for giving the access to 500 km of spooled Sumitomo PureGain fibers to set up the fiber link.

TABLE I. PARAMETERS OF EXPERIMANTAL LINK

Span number	*Length [km]*	*Attenuation [dB]*	*Dispersion [ps/(nm·km)]*	*Gain [dB]*	*Fiber type*
L1	50	9.5	850	--------	SMF-28
L2	70	13.3	990	15.4	SMF-28 + LEAF
L3	20	3.8	140	9.2	LEAF
L4	68	12.9	1156	8.3	SMF-28
L5	62	11.8	1054	12.3	SMF-28
L6	70	13.3	990	12.3	SMF-28 + LEAF
L7	68	12.9	1156	12.7	SMF-28
L8	50	9.5	850	10.5	SMF-28
L9	21	4	147	10.0	SMF-28
Total:	**479**	**91**	**7333**	-------	-------

This signal was split into two parts, one supplying the local module, and the second one triggering the oscilloscope. The temporal stability of the transfer was determined on the basis of the histogram of the crossing points of the rising edges of the signal received from the remote module with the reference level.

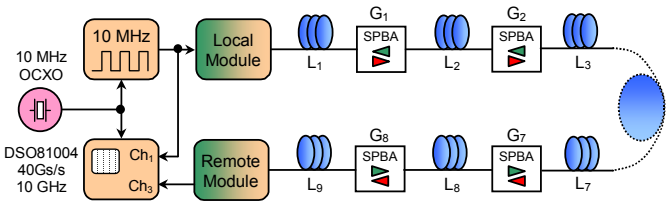

Figure 2. Schematic diagram of experimental setup

III. BIDIRECTIONAL OPTICAL AMPLIFIERS

Bidirectional optical amplifiers are not standard telecommunications equipment so we had to custom-design and built them for our experiments. We investigated a number of possible structures and finally decided to use one where the amplification in both directions occurs in the same piece of erbium doped fiber. Such single path bidirectional amplifier (SPBA) features the best possible symmetry of propagation conditions in both directions and shows negligible thermal dependence of the differences of the propagation delays [8].

The simplified schematic diagram of the SPBAs we used is shown in Fig. 3. The amplifier comprises about 2.5 m of Fibercore M-12 Er-doped fiber, one-sided pumped at 980 nm. The 2x2 95/5 tap couplers at both West and East sides are used to monitor the signal levels and further estimate the gain of the module. Two band-pass filters are used to limit the amplified spontaneous emission (ASE) that originates in the amplifier. The amplifiers are remotely managed via the ethernet port, allowing monitoring the status of the link and setting the gain of each module separately.

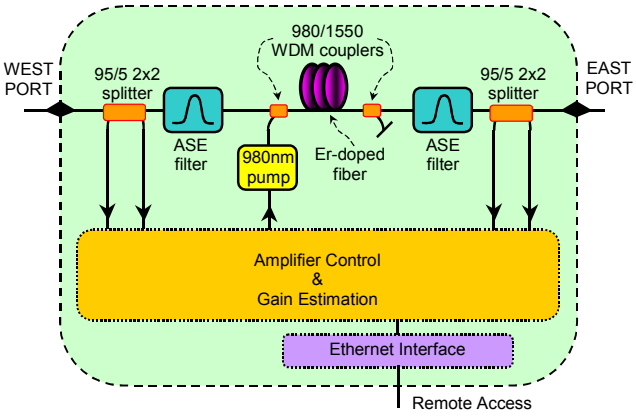

Figure 3. Structure of SPBA used in the experiment

IV. OPTIMIZATION OF THE LINK WITH SPBAS

Bidirectional optical amplifiers used in our experiment allow propagating the backscattering signals originating in the fibers connecting the amplifiers, as well as ASE [8]. These unwanted signals beats with received signals and with itself in the photodiodes, resulting in some electrical noise corrupting transferred signals. Additional factors affecting the quality of the transfer results from conversion of laser phase noise into the intensity noise occurring because of fiber chromatic dispersion [9] and also from electronic noise associated with opto-electronic converters.

To limit the amount of noise generated from beating backscattered signals we detuned laser transmitters in local and remote modules by 100 GHz [10]. We also applied optical band-pass filters in local and remote receivers to cut-off single Rayleigh backscattering. Further, for maximizing the signal to noise ratio (SNR) at both sides of the link the gains of the optical amplifiers should be deliberately chosen [8]. We used the model presented in [11] to calculate the gains of the amplifiers – obtained values are listed in Table I together with other parameters of the link. Basing on the abovementioned model we were able to estimate the SNR to be around 24.3 dB. Simultaneously the sensitivity of SNR to particular values of gains is reasonable – Monte Carlo simulations shows that 5% inaccuracy in gains setting results in deterioration from the optimal SNR not greater than about 1 dB.

V. EXPERIMENTAL RESULTS

During the measurements of the stability of the frequency transfer we placed the oscilloscope with both local and remote modules in the limited-access laboratory where the temperature was kept stable within ±0.5°C. The spools with the optical fibers and all SPBAs were located in another laboratory where diurnal temperature variations around ±4°C were forced. The record of residual fluctuations observed in the link during almost 6 days (from 26.10 to 31.10.2012) is shown in Fig. 4. The rms and peak-to-peak fluctuations of the delay are 2.1 ps and 13 ps, respectively. This gives nearly 4 orders of magnitude improvement of the stability of the transfer, as the fluctuations of the propagation delay observed in the open loop were over 90 ns.

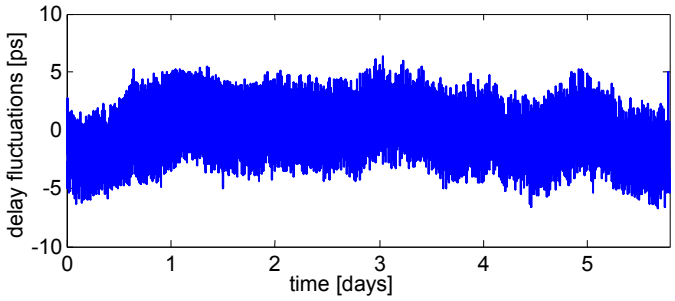

Figure 4. Plot of residual fluctuations of the propagation delay measured in 480 km-long laboratory setup.

Resulting Allan deviation is plotted in Fig. 5, showing value around $4 \cdot 10^{-17}$ at one day averaging. The curve displays monotonic decrease with the slope close to $1/\tau$.

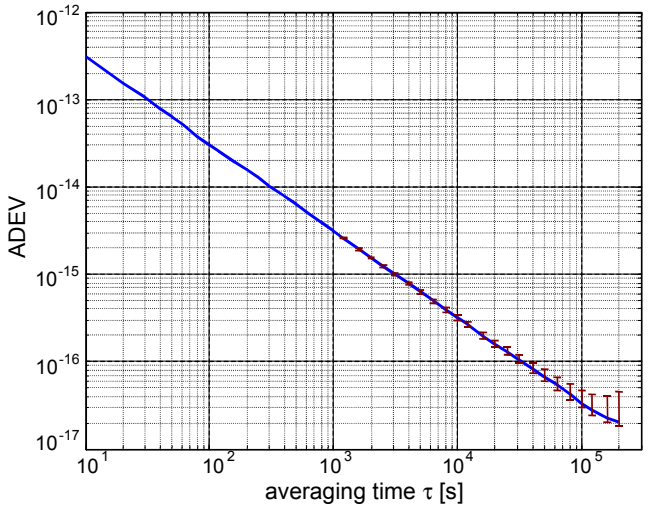

Figure 5. Plot of Allan deviation calculated for data from Fig. 4.

VI. Conclusion

Performed experiments proved that the fiber optic link with electronic stabilization of propagation delay might be successfully used for frequency transfer at the distance close to 500 km. Interfering signals propagating in single path bidirectional amplifiers might be reduced to acceptable level by proper control of amplifiers gains and applying optical filtering at local and remote modules. Comparing the Allan deviation of the link at one day averaging with typical numbers for cesium clocks ($2 \cdot 10^{-14}$) or even cesium fountains ($7 \cdot 10^{-16}$) allow stating that the impairment of the frequency transfer caused by described link should be unnoticeable.

The target link exploiting the equipment described in the paper was launched on 27.01.2012 and since then it continuously operates. The optical path for the link uses the dark fiber from the Polish Optical Internet Consortium PIONER (operated by Poznań Supercomputing and Networking Center - PSNC), with some parts supplied by Polish Telecom operator TP S.A.

The basic function of frequency transfer was extended by adding the capability of the time transfer exploiting the idea described in [12]. The time deviation (TDEV) of the time transfer measured in the laboratory testbed is between 650-900 fs for the averaging times between 10^3-10^5 s.

Acknowledgment

The authors would like to thank Dr. Albin Czubla from GUM for fruitful discussions and many helpful suggestions. The work was realized thanks to the state budget to fund science in the years 2011-2013 under the grant N N515 624639 of the Polish Ministry of Science and Higher Education (MNiSW).

References

[1] F. Narbonneau, M. Lours, D. Chambron, S. Bize, A. Clairon, G. Santarelli, O. Lopez, Ch. Daussy, A. Amy-Klein, Ch. Chardonnet, "High resolution frequency standard dissemination via optical fibre metropolitan network", Review of Scientific Instruments, vol. 77, vol. 77, pp. 064701-8, 2006.

[2] C. Daussy, O. Lopez, A. Amy-Klein, A. Goncharov, M. Guinet, C. Chardonnet, F. Narbonneau, M. Lours, D. Chambon, S. Bize, A. Clairon, G. Santarelli, M. E. Tobar, A.N. Luiten, "Long-Distance Frequency Dissemination with a Resolution of 10-17", Physical Review Letters, vol. 94, pp. 203904-1-4, 2005.

[3] O. Lopez ,A.Amy-Klein, C. Daussy, C. Chardonnet, F.Narbonneau, M.Lours, G. Santarelli, "86-km optical link with a resolution of 2×10−18 for RF frequency transfer", The European Physical Journal D, vol. 48, pp. 35-41, 2008.

[4] O. Lopez, A. Amy-Klein, M. Lours, Ch. Chardonnet, G. Santarelli, "High-resolution microwave frequency dissemination on an 86-km urban optical link", Applied Physics B Lasers and Optics, vol. 98, pp. 723-727, 2010.

[5] M. Fujieda, M. Kumagi, S. Nagano, "Coherent microwave transfer over 204-km telecom fiber link by a cascaded system", IEEE Transactions on Ultrasonics, Ferroelectrics and Frequency Control, vol. 57, pp. 168-174, 2010.

[6] Ł. Śliwczyński, P. Krehlik, Ł. Buczek, M. Lipiński, "Active propagation delay stabilization for fiber optic frequency distribution using controlled electronic delay lines", IEEE Transactions on Instrumentation and Measurement, vol. 60, pp. 1480-1488, 2011.

[7] A. Czubla, Ł. Śliwczyński, P. Krehlik, Ł. Buczek, M. Lipiński, J. Nawrocki, "Stabilization of the propagation delay in fiber optics in a frequency distribution link using electronic delay lines: first measurement results", in 42nd Annual Precise Time and Time Interval (PTTI) Meeting, 2010, pp. 389-396.

[8] Ł. Śliwczyński, P. Krehlik, Ł. Buczek, M. Lipiński, "Frequency transfer in electronically stabilized fiber optic link exploiting bidirectional optical amplifiers", IEEE Transactions on Instrumentation and Measurement, in press, DOI 10.1109/TIM.2012.2188663.

[9] W. Marshall, B. Crosignani, A. Yariv, "Laser phase noise to intensity noise conversion by lowest-order group-velocity dispersion in optical fiber: exact theory", Optics Letters, vol. 25, pp. 165-167, 2000.

[10] Ł. Śliwczyński, P. Krehlik, M. Lipiński, „Optical fibers in time and frequency transfer", Measurement Science and Technology, vol. 21, DOI 10.1088/0957-0233/21/7/075302, 2010.

[11] Ł. Śliwczyński, J. Kołodziej, „Bidirectional optical amplification in long-distance two-way fiber optic time and frequency transfer systems", unpublished.

[12] P. Krehlik, Ł. Śliwczyński, Ł. Buczek, M. Lipiński, "Fiber-optic joint time and frequency transfer with active stabilization of the propagation delay ", IEEE Transactions on Instrumentation and Measurement, in press

A Microwave Frequency Standard Based on the Laser Cooled $^{113}Cd^{+}$ ions

J.W. Zhang, Z.B. Wang, S.G. Wang, K. Miao, L.J. Wang

NIM-THU Joint Institute for Measurement Science(JMI),
Department of Precision Instruments and Mechanology,
Department of Physics,
Tsinghua University, Beijing(100084), P.R. China

Email: zhangjw@tsinghua.edu.cn

Trapped ions are applied to the precision frequency metrology thanks to the long interaction time between ions and radiation field. In the past decades, many groups in the world have built microwave or optical frequency standards based on different trapped ions and achieved great improvements. In this article, a microwave frequency standard developed at JMI is reported, which is based on the laser cooled $^{113}Cd^{+}$ ions.

The energy level structure of the $^{113}Cd^{+}$ ions is shown in Fig. 1. The clock transition is the $\Delta m_F = 0$ transition of the hyperfine splitting of the ground level, and the splitting is about 15.2 GHz. This value is larger than most of the ions applied to microwave frequency standards. A laser connecting the transition between $S_{1/2}(F = 1)$ and $P_{3/2}(F = 1)$ is used to pump ions into the state of $S_{1/2}(F = 0)$; another laser is applied to cool the ions and detect the state of ions via the cycling transition between $S_{1/2}(F = 1, m_F = 1)$ and $P_{3/2}(F = 2, m_F = 2)$. The frequency difference of these two lasers is the hyperfine splitting of the $P_{3/2}$ level which is about 800 MHz. With a acoustooptic frequency shifter, only one laser can accomplish all of the tasks of laser cooling, pump and detection. Thanks to the cycling transition, the ions can be laser cooled and detected with high efficiency. However, during the laser cooling process, ions will be trapped in the dark state of $S_{1/2}(F = 0)$ because of impurity of the circular polariztion of the cooling laser. In order to resolve this problem, a microwave radiation is applied to repump ions from the dark state to $S_{1/2}(F = 1)$ during laser cooling.[1]

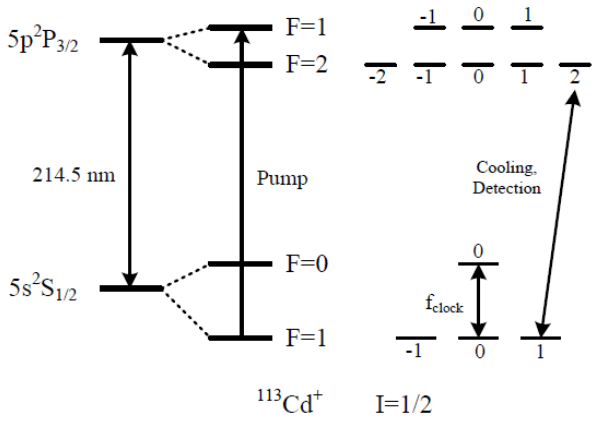

Fig. 1: Schematic energy levels of the $^{113}Cd^{+}$ ions. The $\Delta m_F = 0$ transition of the hyperfine splitting of the ground level is chosed as the clock transition; a laser connecting the transition between $S_{1/2}(F = 1)$ and $P_{3/2}(F = 1)$ is used to pump ions into the state of $S_{1/2}(F = 0)$; another laser is applied to cool the ions and detect the state of ions via the cycling transition between $S_{1/2}(F = 1, m_F = 1)$ and $P_{3/2}(F = 2, m_F = 2)$.

The cadmium ions are trapped in a linear Paul trap. The 214.5nm laser is a frequency-quadrupled diode laser system from Toptica. So far, the $^{113}Cd^{+}$ ions were already trapped and laser cooled down successfully. The Ramsey fringe of the clock transition was measured and the frequency of the transition was obtained with these fringe for odd isotopes of cadmium ions. It is expected to close loop for the frequency standard and to estimate the frequency stability of the experimental setup in the next few months.

[1] U. Tanaka et al., "Laser Cooling of Cd^{+} Ions Using a Microwave Transition as a Repumping Process", Appl. Phys. B, vol. 78, p. 43-47, 2004

High-Speed Reader for Wireless Resonant SAW Sensors

V. Kalinin, J. Beckley, I. Makeev
Transense Technologies plc
Bicester, Oxfordshire, UK
victor.kalinin@transense.co.uk

***Abstract*—A new reader is presented that is based on a narrowband pulsed excitation of two SAW resonators contained in a differential wireless resonant sensor such as a torque senor. Simultaneous excitation of the resonators working at 433-437 MHz allows achieving a flat system frequency response up to Nyquist frequency. An interrogation algorithm and a structure of the reader ensure a torque sampling rate of at least 16 kHz and the system bandwidth of at least 8 kHz achievable at the processor clock of 150 MHz. Systematic errors caused by mutual interference of the two SAW responses, intermodulation products and aliasing are discussed. Random errors caused by the phase noise of the local oscillators are analyzed theoretically. Experimental results are also presented.**

I. INTRODUCTION

Wireless resonant SAW sensors have already found a number of applications in industry to measure temperature in harsh environment, pressure and temperature in car tires and torque in various automotive systems. A number of wireless readers were developed to interrogate the resonant SAW sensing elements. The first designs [1] relied on a close coupling between the sensor antenna and the reader antenna that allowed using the SAW devices as frequency selective elements in the feedback loop of the oscillators contained in the reader. The main problem with this approach was a high variability of the RF coupling between the sensor and the reader that made it difficult to achieve a stable oscillation. More reliable readers were built using CWFM signals and automatic frequency tracking loops [2, 3]. Their interrogation bandwidth was limited by the time constant of the loop. The achieved figures were around 0.6 ms ensuring the sensor bandwidth just over 1.5 kHz.

The use of the continuous interrogation signals in wireless readers either dictates implementation of the front-end circuit in the form of a high-quality directional coupler or a circulator, or requires close coupling between the reader and the sensor antennas. Only in this case a sufficient separation between the interrogation signal and the resonator response is achieved. Pulsed signals are much better suited for wireless interrogation at larger distances between the resonant sensor and the reader antennas. One of the proposed designs was based on the use of a gated PLL in the receiver to track the resonant frequency [4]. This relatively cheap reader had one serious disadvantage – it required the use of several gated PLLs in the case of several resonators per sensor. Even relatively simple temperature sensors usually contain two resonators since differential measurement helps cancelling frequency shifts caused by a variable impedance of the sensor antenna [5] and reduces influence of aging. The number of resonators in a temperature compensated sensor for other physical quantities can be larger than two, up to five as in the case of a torque sensor [6].

Emergence of fast DDS synthesizer chips with a small frequency increment has simplified pulsed interrogation of several resonators in a sequential way, one after another. The usual approach is to launch the RF pulse sufficiently long to reach the steady-state amplitude of oscillation in the resonator and measure free oscillations radiated by the sensor antenna after the interrogation pulse is over. This measurement is repeated at several different frequencies around the resonant frequency and, based on the measured amplitude/phase of the SAW response, the resonant frequency is estimated [7, 8]. The speed of interrogation is limited by the time constant of the resonator loaded with the antenna, $\tau = Q/\pi f = 7\ldots15$ μs at $f =$ 434 MHz for the Q-factor $Q = 5000\ldots10000$. Using the RF pulse width of around 3τ to reach the steady state and the same time to let the free oscillations decay before the next pulse is launched, it takes around 50…100 μs to obtain a reading at one interrogation frequency. The number of the interrogations required for determining one resonant frequency depends on the tracking algorithm implemented in the reader. It was suggested to use three interrogations in [9] and two interrogations in [10] so the minimum time required for measuring one resonant frequency can be as small as $T_1 =$ 100…200 μs in this case.

The problem with the above approach is that the tracking bandwidth Δf_{tr} is limited by the frequency step and the number of interrogation points needed to update the frequency reading. For two or three points it is of the order of $f/2Q =$ 20…40 kHz. Quite often, the peak variation f_m of the resonant frequency in SAW strain sensors is an order of magnitude higher, 200...400 kHz. This means that the highest frequency

of the measurand cannot exceed $F_{max} = \Delta f_{tr}/(2\pi f_m T_1) = 40\ldots320$ Hz in order not to loose tracking. This is a serious limitation for a sensor that measures fast variation of strain, pressure, torque, etc.

The issue of the narrow tracking bandwidth is not critical in the case when the length of the interrogation pulse is smaller than τ (2...3 μs) so that its spectrum covers the whole range of the resonant frequency variation or its significant part. Obviously, this reduces the SAW response magnitude by 5…10 dB but this is tolerable for many short-range applications. The measurements in this case do not rely on the steady-state magnitude/phase but on the spectral analysis of free oscillations of the SAW resonator. This approach was used in a number of works [6, 11-13]. Only one interrogation is needed in this case to update the frequency reading and the measurement time for one resonator is $T_1 \approx 3\tau + T_a$ where T_a is the time needed for spectral analysis and other calculations in the DSP. The smallest achieved value of T_1 = 155 μs was reported in [13] for the DSP chip TMS320F2808 with the clock frequency of 100 MHz. If the physical quantity (e.g. torque) measurement requires interrogation of two resonators then its sampling period is $T_s = 2T_1$ = 310 μs. Due to sequential interrogation of the resonators and effective averaging of the measurand, the system frequency response is not flat up to the Nyquist frequency $0.5/T_s$ although the 3 dB system bandwidth still equals $BW = 0.25/T_1$ = 1.6 kHz [6].

Quite a large number of applications require the sensor bandwidth to be higher than 2 kHz – torque measurement in the power drills, at the IC engine output and in the electronic control units of electric motors, just to name a few. The aim of this paper is to present a high-speed wireless reader working at 420–440 MHz that ensures the bandwidth of the differential resonant sensor significantly exceeding 2 kHz and a flat frequency response up to the Nyquist frequency.

The paper is organized as follows. Section II describes the SAW sensing element, the reader architecture and the interrogation algorithm. Simulation results characterizing systematic and random errors are presented in Section III. Section IV contains some experimental results and conclusions are presented in Section V.

II. Interrogation Method

The main motivation behind the quest for a high-speed reader is to develop a relatively inexpensive torque sensor capable of detecting high-frequency torsion vibrations and transients in automotive applications. The sensor bandwidth should be as wide as possible for a reasonable cost and acceptable resolution comparable to the one already achieved for SAW torque sensors [13].

A. SAW Sensing Element

The ultimate achievable sensor bandwidth BW is limited by the SAW resonator bandwidth. It would be obvious to try increasing BW by reducing the Q-factor of the resonators but this would adversely affect the sensor resolution, which is unacceptable. The sensing element used in this project is the same as the HFSAW element described in [6, 13]. The SAW die made of Y+34° cut quartz contains three resonators (Fig. 1a) with the resonant frequencies $f_1 \approx 437$ MHz, $f_2 \approx 435$ MHz and $f_3 \approx 433$ MHz (Fig. 1b), all connected in parallel. The unloaded Q-factors of all the resonators are above 10000 and the loaded Q-factors are 7000-9000. The first two resonators, M1SAW and M2SAW, have SAW propagation directions at ±45° to the X-axis of quartz coinciding with a shaft axis. The value of $F_m = f_1 - f_2$ linearly depends on torque M applied to the shaft and is used for its measurement. Temperature compensation is achieved by means of an independent measurement of temperature T with the help of the third resonator, TSAW. Measuring the second frequency difference, $F_t = f_2 - f_3$, and solving two simultaneous equations that model the sensor, allows determining both M and T [6].

Since the temperature variation is much slower than the torque variation, it is the value of F_m that needs to be measured with the minimum possible update period while the value of F_t can be measured much less frequently, once every 0.3 s, for instance.

The peak variation of the resonant frequencies f_1 and f_2 due to strain created by the torque applied to the shaft is f_m = 200 kHz and, taking into account their variation with temperature, the maximum deviation of the resonant frequencies does not exceed $\pm f_{max} = \pm 300$ kHz.

B. Reader Architecture

In order to ensure a high-speed tracking of the resonant frequencies varying within the range of $2f_m$, the interrogation by RF pulses lasting for 2.5…3 μs with the subsequent Fourier analysis of the SAW response is selected. Since the resonator time constant cannot be reduced without affecting the sensor resolution, there are only two ways for reducing the torque sampling period T_s: (a) reduce the analysis time T_a and (b) perform simultaneous excitation of the two SAW resonators instead of their sequential excitation. In other words, instead of using the measurement scheme $f_1 - f_2 - f_1 - f_2 - f_1 - \ldots - f_2 - f_1 - f_2 - f_3 - f_1 - \ldots$, implement the scheme $f_{1,2} - f_{1,2} - f_{1,2} - f_{1,2} - \ldots - f_{1,2} - f_{2,3} - f_{1,2} - \ldots$.

The idea of simultaneous excitation of two or more SAW resonators is not new; it was briefly discussed in [14], for instance. However, the excitation was assumed to be performed by a wideband RF pulse with the spectrum covering all the resonators. Obviously the efficiency of such

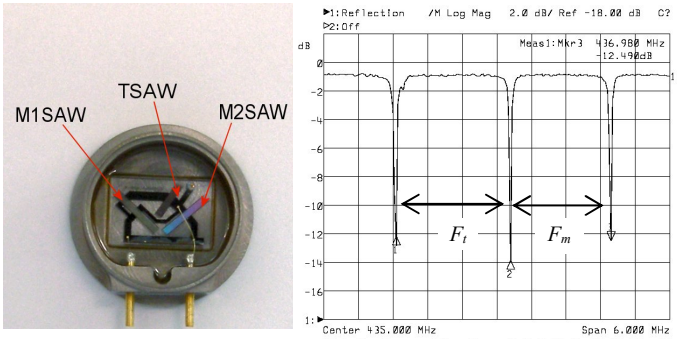

(a) (b)

Figure 1. The SAW torque sensing element (a) and its frequency response (b)

excitation is very low, at least 10 times lower than the one achieved for the relatively narrowband pulse mentioned above. For that reason, the interrogation signal selected for the high-speed reader is the 2.5 μs pulse with two carrier frequencies, f_{i1} and f_{i2} for measuring F_m (or f_{i2} and f_{i3} when F_t is to be measured). They are selected from a discrete set of interrogation frequencies that the Tx synthesizer can generate to be closest to previously measured averaged frequencies f_1, f_2 and f_3 respectively.

Simultaneous interrogation of the two resonators not just reduces the torque sampling period T_s. It also ensures a flat frequency response of the sensor up to the Nyquist frequency which is important for improving the sensor fidelity. This follows from the fact that there is no any averaging over the time interval T_1 involved in determination of F_m in this case.

The simplest implementation of this approach would be to use two sequential readers described in [6] that work synchronously in parallel in such a way that one of them tracks f_1 and another one tracks f_2. In this case $T_s = T_1 = 155$ μs which corresponds to BW = 3.2 kHz. This is an obvious solution although not the best one. Apart from not too impressive bandwidth increase, only by a factor of two, there is a significant drawback associated with the use of two separate receivers for the processing of the SAW responses. As established in [15], one of the main contributions into random frequency measurement errors in the case of closely coupled torque sensors comes from the phase noise of the Rx local oscillator (LO). If the two separate receivers are used for down-conversion of the M1SAW and M2SAW responses then the phase noise translated to the IF will not be correlated and thus the output noise power of the torque signal will be doubled as a result of the differential frequency measurement (as it happens in the case of the sequential interrogation). However, if the sum of the M1SAW and M2SAW responses is down-converted in one receiver, there is a chance that part of random errors will be cancelled due to correlation of the phase noise in the vicinity of $f_1 - f_{Rx}$ and $f_2 - f_{Rx}$ (f_{Rx} is the Rx LO frequency).

A reader performing simultaneous interrogation of two resonators by narrowband RF pulses and down-converting their responses in one receiver can have an architecture shown in Fig. 2a. The superheterodine receiver has quadrature I and Q outputs for more accurate calculation of the resonant frequencies by means of suppressing the spectrum at negative frequencies. The transmit frequencies f_{Tx1} and f_{Tx2} equal f_{i1}, f_{i2} or f_{i3} depending on which pair of the resonators is interrogated. The Rx LO frequency can be selected to be equal to f_{Tx1} or f_{Tx2} or $(f_{Tx1} + f_{Tx2})/2$. In the latter case, the spectrum of the complex signal $I(t) + jQ(t)$ calculated in the DSP is sketched in Fig. 2b. This choice ensures the minimum required bandwidth of the receiver.

A practical implementation of the reader shown in Fig. 2a would however require quite a large number of off-the-shelf components such as synthesizers, LNA, PA, quadrature mixer, etc., so the analogue part of the reader would become quite cumbersome. To minimize the amount of the components on the board, the decision was made to use two transceiver chips of the same type (MLX11006 RF ASIC) as the one used for

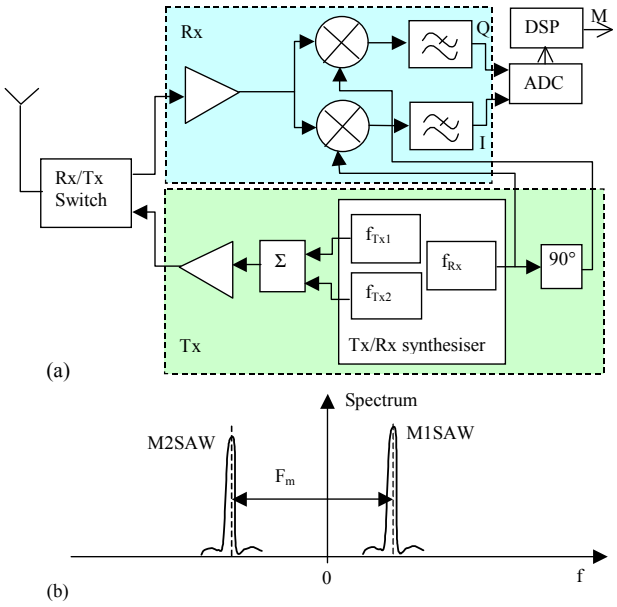

Figure 2. A simplified block-diagram of the reader (a) and the spectrum of the SAW response calculated by the DSP (b)

the low-cost sequential reader [6]. The two chips contain two receivers but only one of them is used for reception of both SAW responses (as shown below this decision gives certain advantages in terms of minimization of the interrogation time). The receiver has a double superheterodine architecture with the 2nd IF image rejection mixer. This does not allow positioning M2SAW response at negative frequencies as shown in Fig. 2b. However, the Rx bandwidth of the RF ASIC is sufficiently wide (at least 3.5 MHz) to allow positioning of both resonant responses at positive IF frequencies. The nominal 2nd IF frequencies for M2SAW and M1SAW responses have been selected to be equal to 0.4…0.9 MHz and 2.3…2.8 MHz respectively.

The Tx synthesizers in the RF ASICs generate interrogation signals at frequencies f_{i1} and f_{i2} (when M2SAW and M1SAW are interrogated) that are added in a combiner circuit. Simultaneous generation of the two interrogation signals requires synchronization of both RF ASICs by the same Tx On/Off command initiated by the DSP.

The digital part of the reader can be implemented in a number of different ways but the aim is to minimize time needed for calculation of the energy spectrum of the two SAW responses by means of DFT:

$$S_n = \left[\sum_{k=0}^{N-1}(I_k \cos\varphi_{kn} + Q_k \sin\varphi_{kn})\right]^2 + \left[\sum_{k=0}^{N-1}(Q_k \cos\varphi_{kn} - I_k \sin\varphi_{kn})\right]^2, \quad \varphi_{kn} = 2\pi\frac{kn}{N} \tag{1}$$

where S_n is the n^{th} line of the energy spectrum and I_k and Q_k are the k^{th} samples of the I and Q signals, N = 512. One obvious option is to replace the cheap DSP TMS320F2808 used in the sequential reader [6] with a more powerful and fast

modern multi-core DSP. It took approximately 50 μs to calculate the spectrum and find one resonant frequency by means of parabolic interpolation for the 2808 processor. Multi-core chips such as TMS320C6472 or TMS320C6474 have from 3 to 6 cores and run at the clock frequencies around 500 MHz. They would reduce the calculation time at least by a factor of 15 but they are expensive, consume too much power (around 10 W) and do not have the necessary periphery (ADC, CAN interface, internal flash memory). Another option would be to use less powerful TMS320C6416 consuming about 1.1 W. When it runs at 720 MHz it can calculate 1024-point complex FFT during just 10 μs. However, it also lacks the necessary periphery and still costs over $100.

Instead of powerful and expensive DSP chips, it was decided to use two relatively cheap processors TMS320F2810 that can run at the clock frequency 150 MHz, 50% higher than the 2808. In order to further alleviate timing constraints, it was decided to add the third, considerably less powerful microcontroller (MC), TMS320F28027. Its role is to manage communications with the RF ASIC1 and RF ASIC2 (setting up their configuration, transmit frequencies, sending Tx On/Off commands, etc.).

The block diagram of the high-speed reader is shown in Fig. 3a. All main components are synchronized by the same 30 MHz clock. The Rx1/Rx2 switch allows the receiver of either RF ASIC1 or RF ASIC2 to pick up the SAW responses. Quadrature outputs of the RF ASIC1 receiver are connected to the ADC inputs of DSP1 while the outputs of the RF ASIC2 receiver are connected to DSP2. Depending on what receiver is operational, either DSP1 or DSP2 calculates the spectrum of SAW responses (see Fig. 3b) and finds the current torque value *M*. DSP2 sends the calculated torque to DSP1 through the fast SPI lines. The latter accumulates four torque samples and transmits them in a single packet through CAN bus. DSP1 is also responsible for synchronization of DSP2 and MC and reading the sensor configuration/calibration file from the EEPROM when the unit is switched on.

Both DSPs initiate Tx On/Off commands through dedicated fast lines and also send the interrogation frequency information through much slower RS232 interface to the microcontroller. The latter generates Tx On/Off and frequency setting commands for the RF ASICs that are sent through a fast 4-line bus. Besides, MC also controls Rx1/Rx2 switch.

C. Interrogation Algorithm

There are three main constraints limiting the interrogation period in the proposed reader: (a) the resonator excitation and response sampling time (26 μs), (b) the time needed for calculation of the spectrum of two SAW responses and finding two resonant frequencies (66 μs), and (c) the time needed to send the interrogation frequency setting commands and the synthesizer switching time (at least 80 μs). The fact that the reader contains two receivers and two DSPs allows offsetting their operation in such a way that effectively halves the torque sampling period.

The timing diagram illustrating the interrogation algorithm is shown in Fig. 4 in its regular part when M1SAW and

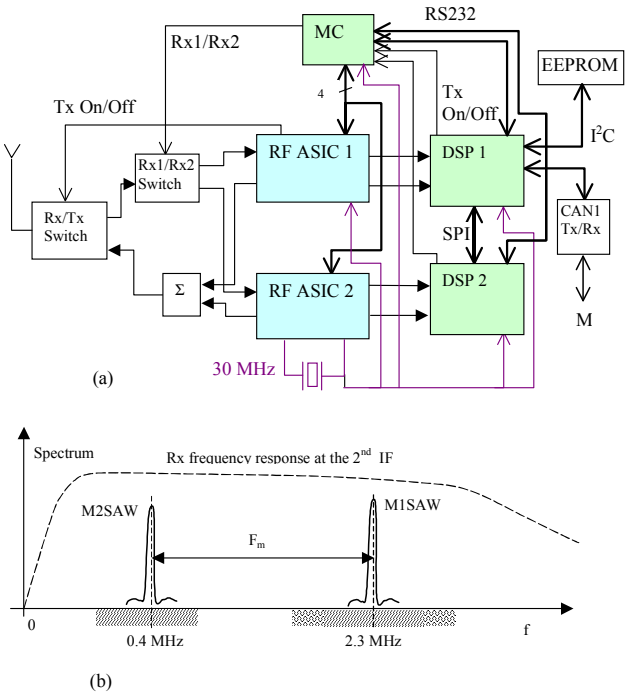

Figure 3. Block diagram of the high-speed reader (a) and the spectrum of the SAW responses received by RF ASIC1 and calculated by the DSP1 (b)

M2SAW frequencies are measured and the temperature is assumed to be known from the previous measurement cycles. Functions of the DSP1, 2 are largely the same. Both of them initiate excitation of the two resonators through the microcontroller MC that generate Tx On and Tx Off commands. These commands are sent from MC to RF ASIC1,2 to activate Tx1,2. After the interrogation pulse is over, either Rx1 in RF ASIC1 or Rx2 in RF ASIC2 are activated to down-convert both SAW responses to their 2nd IF frequencies shown in Fig. 3b. To achieve this, the nominal 1st IF in RF ASIC1, 2 are approximately 15.4 MHz and 17.3 MHz respectively.

If Rx1 is active then it is DSP1 that takes samples of the SAW responses, otherwise DSP2 takes samples of the SAW responses at the output of Rx2. After that the DSPs calculate the spectrum of both SAW responses and find two resonant frequencies. Then the two new interrogation frequencies are determined similarly to how it was done in [13] and the torque value is calculated. The frequency indices are transmitted to MC through RS232 and then the microcontroller sends frequency setting commands to RF ASIC1 and RF ASIC2 in turn. The interrogation frequencies do not need to be updated too often since the aim is to track not the instantaneous resonant frequencies but the averaged ones.

The four sequentially measured torque values M1, M2, M3 and M4 are stored in a buffer as two-byte integers and transmitted in one packet through the CAN interface of RF ASIC1 with the data rate of 1 Mbps. This allows achieving the packet transmission period of 248 μs and the effective torque update period of T_s = 62 μs that corresponds to the sensor bandwidth BW = 8.064 kHz. To our knowledge, at the

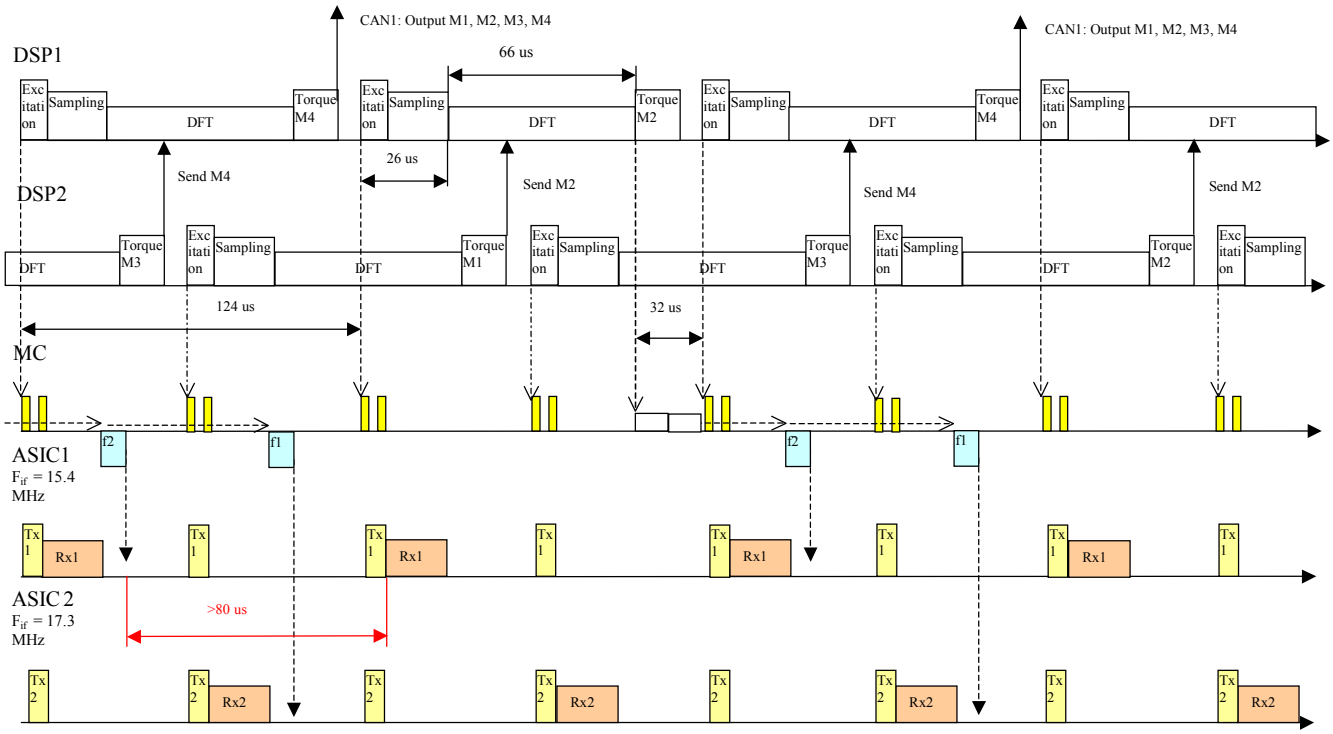

Figure 4. Timing diagram showing the sequence of operations in the DSP1,2, MC and RF ASIC1, 2 when M1SAW and M2SAW are interrogated

moment this is the fastest update rate achieved for the differential SAW resonant sensors.

III. Design Considerations for the Reader

The fact that the two SAW resonators are excited simultaneously and both responses go through one receiver makes it important to consider two issues that were almost irrelevant for the sequential reader.

A. Mutual Influence of the Two SAW Responses

Since the two SAW responses have close magnitudes the spectral sidelobes of one of them can cause a noticeable spectral maximum bias for another one.

System simulations have shown that the bias in F_m can go up to 4 kHz for the loaded Q = 5000 when $f_1 - f_2$ varies from 1.1 MHz to 2.7 MHz (see the shaded areas in Fig. 3b). Bearing in mind that variation of F_m due to strain is around 800 kHz this bias gives a systematic error up to 0.5% FS.

It is possible to reduce the error by multiplying the samples of the SAW responses taken in the DSP by a window function, for instance, Hamming function, before calculating (1). Fig. 5 shows (a) the signal $I(t)$ at the RF ASIC output for F_m = 1.12 MHz, (b) the sampled signal after multiplying by the window and (c) the result of the spectrum calculation in the DSP. As one can see, the measured value of F_m differs from the actual value only by 582 Hz. The signal shown in Fig. 5a corresponds to the case when the SAW response is strongly limited in the 1st IF receiver channel. Simulations show that, for any value of

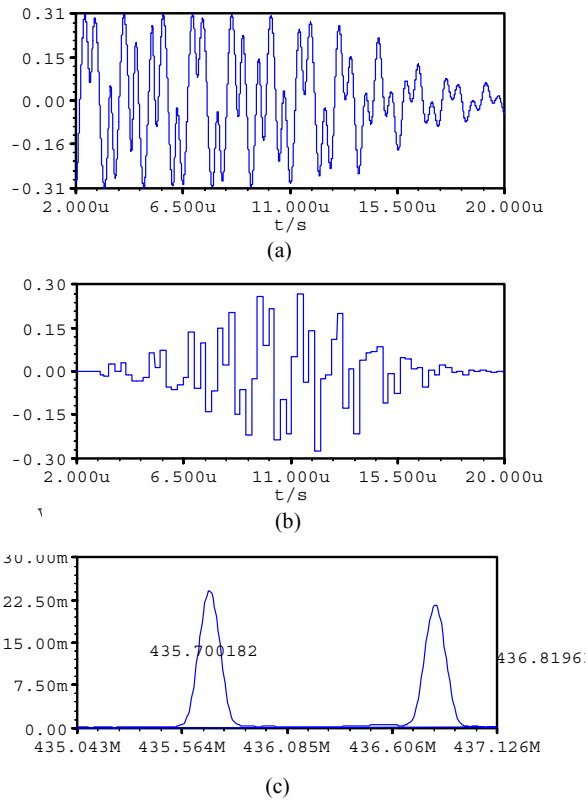

Figure 5. The SAW response $I(t)$ at the Rx output (a), the sampled signal (b) and its spectrum (c) calculated in the DSP

F_m and any amount of limiting, the systematic error does not exceed ±1.3 kHz, which is 0.16% FS. Reduction of the maximum systematic error by a factor of three justifies a small computational overhead associated with the use of the window function.

B. *Errors Due to Aliasing and Intermodulation Products*

The amount of systematic errors also depends on the contribution of the parasitic peaks emerging in the spectrum of the sampled signal due to aliasing. Ideally these peaks should be totally suppressed up to the ADC sampling frequency f_s due to the fact that the spectrum of the complex signal $I(t) + jQ(t)$ should be zero at negative frequency. In reality, however, they will be present because of the de-phasing up to ±1° and ±0.6 dB amplitude imbalance between the I and Q outputs of the RF ASIC according to its specification. Simulations show that, in the worst case, the phase errors cause the spurious spectral lines 39 dB below the main peak and the amplitude imbalance leads to aliases 29 dB below the main peak. When the alias line coincides with the main peak it causes the frequency measurement error. However, its value does not exceed 0.5% FS.

Certain parasitic peaks can also emerge due to non-linearity of the Rx output stage where the signal has the strongest amplitude. Fig. 6 illustrates a typical spectrum of the analyzed signal obtained by MATLAB modeling that takes into account realistic non-linearity of the receiver [15]. The peak input power of the SAW responses is assumed to be quite high, P_{in} = -15 dBm, the resonant frequencies are f_1 = 2.3 MHz and f_2 = 0.4 MHz, the ADC sampling frequency is f_s = 4.166 MHz and the 3 dB cut-off frequency of the anti-aliasing LPF is 3 MHz. It turns out that the strongest parasitic peaks are due to aliases of the 3rd-order intermodulation products $2f_1 - f_2 - f_s$ and $2f_2 - f_1 + f_s$. When the sensor is strained and $f_{1,2}$ vary, the main peaks can cross the parasitic peaks causing non-linearity of the sensor characteristic. Variation of the measurement

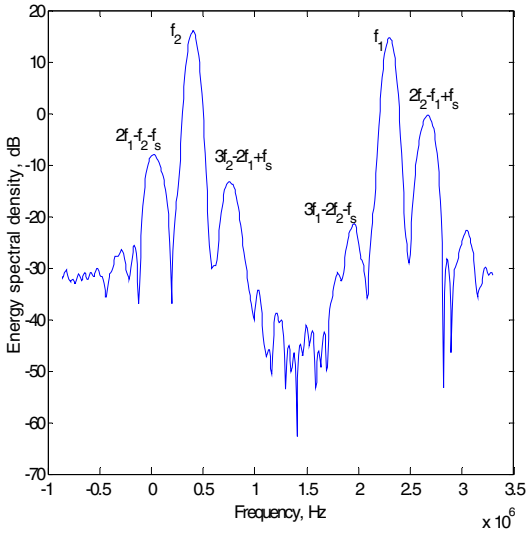

Figure 6. Simulated spectrum of the sampled signal $I + jQ$ at f_s = 4.166 MHz and P_{in} = -15 dBm

error with the torque applied (the sensitivity is $\partial F_m/\partial M$ = 1 kHz/Nm) is shown in Fig. 7 (blue curve). The error can be up to 10 kHz, which is unacceptably high.

By selecting the sampling frequency satisfying the condition

$$f_s > 2(f_1 - f_2)_{\max} = 5.36 \text{ MHz}, \qquad (2)$$

one can move the 3rd-order intermodulation products away from the dangerous range of resonant frequencies. The red curve in Fig. 7 shows the error against applied torque for f_s = 6.25 MHz and P_{in} = -15 dBm. The maximum error is reduced to 2.5 kHz that is only 0.3% FS. It is due to the 5th-order intermodulation products $3f_1 - 2f_2 - f_s$ and $3f_2 - 2f_1 + f_s$ that can still cross the main peaks. They can also be removed if

$$f_s > 3(f_1 - f_2)_{\max} \qquad (3)$$

but this is not achievable for the DSP under consideration. Alternatively, the input power can be reduced. The black curve in Fig. 7 shows the error at f_s = 6.25 MHz and P_{in} = −25 dBm (which is still quite a strong signal). The maximum systematic error is further reduced down to 0.15% FS.

As one can see, it is essential to ensure a good balance and linearity of the quadrature channels of the receiver and select the ADC sampling frequency correctly. It is also important to use high-quality anti-aliasing filters for minimization of systematic errors.

C. *Random Frequency Measurement Errors*

Simultaneous interrogation of two resonators should introduce a certain correlation between the phase noise contained in the two SAW responses at the Rx output and, as a result, correlation between the random errors in the measured values of f_1 and f_2. System simulations show that, for the realistic phase noise of the local oscillator in the 1st IF channel [15], the standard deviation of the measurement errors for $f_{1,2}$ is $\sigma_{f1,2}$ = 560…660 Hz while the standard

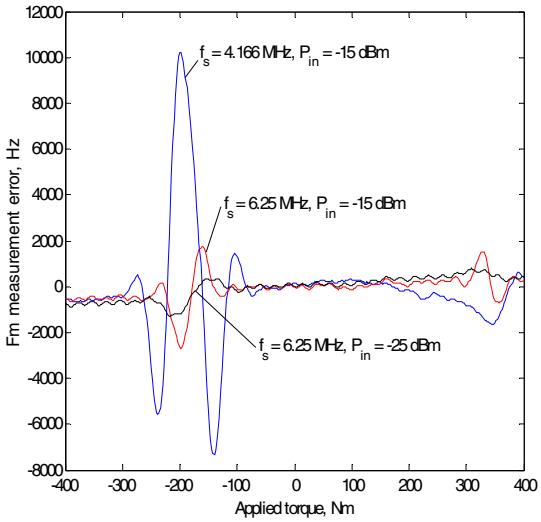

Figure 7. Systematic errors caused by intermodulation products and aliasing at different values of input power and sampling frequency

deviation for the difference frequency is σ_{Fm} = 30…46 Hz. The latter figure is determined, to a great extent, by the quantization and interpolation errors.

In reality, the value of σ_{Fm} is also determined by the additive receiver noise and on-board interference that give uncorrelated contributions to random frequency measurement errors of f_1 and f_2.

IV. Experimental Results

The high-speed interrogator is shown in Fig. 8. It is a single-sided PCB with the on-board 12 V switched mode power supply, CAN buffer and EMC filters in the power supply and CAN lines. Current consumption of the unit is 350 mA.

Samples of a constant torque taken by the reader from a flexplate torque transducer [6] with the range ±800 Nm are shown in Fig. 9 separately for Rx1 (M1 and M3 calculated by DSP1) and Rx2 (M2 and M4 calculated by DSP2). The standard deviation of the measured difference frequency for Rx1 is σ_{Fm} = 380 Hz while the figure for Rx2 is σ_{Fm} = 233 Hz. The standard deviation for the interleaved channels is σ_{Fm} = 326 Hz. The standard deviation for Rx2 is determined by the Rx additive noise as well as the quantization noise and interpolation errors. The higher value of the standard deviation for Rx1 is most likely caused by the fact that the DSP1 takes samples of the Rx1 output signal while transmitting the torque information through the CAN interface of the DSP1. This may cause interference at the ADC input that is absent in the DSP2. Obviously there is room for improvement, for instance, by removing the data transmission function from the DSP1.

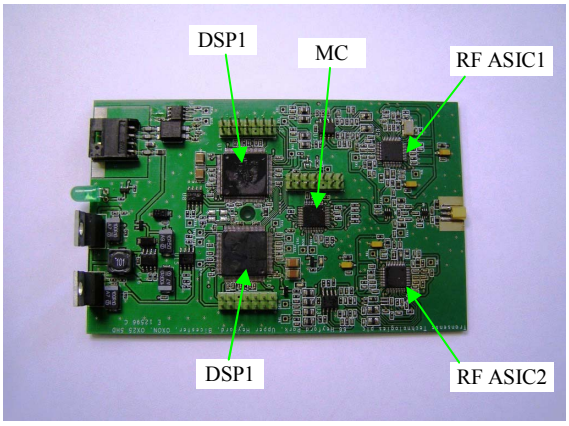

Figure 8. The high-speed reader board

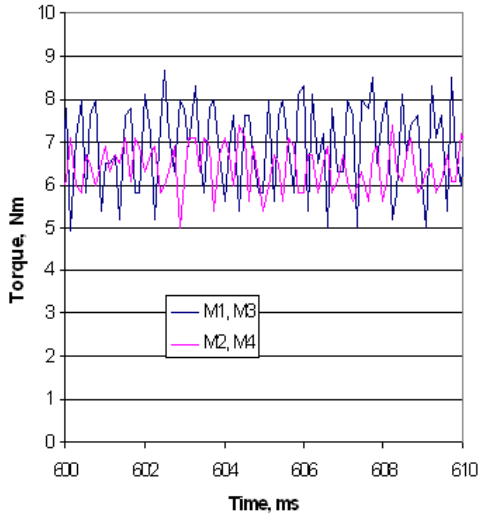

Figure 9. Samples of a constant torque displayed separately for the Rx1 (M1, M3) and Rx2 (M2, M4) outputs

Fig. 10 shows torsion vibrations measured by the flexplate transducer with the high-speed reader connected to it. The vibrations are generated by natural oscillations of a beam attached to the flexplate and used for its calibration in a test rig. The blue trace corresponds to the Rx1+DSP1 channel, the pink one – to the Rx2+DSP2 channel. Both channels output torque sampled with the period of 124 µs and, being interleaved, give the sampling period of 62 µs. The spectrum of the measured torque signal does not contain any higher harmonics that proves a good linearity of the sensor and the reader.

V. Conclusions

A reader for differential wireless resonant SAW sensors working within the range of 420-440 MHz has been developed. It is based on a simultaneous narrowband pulsed excitation of the two resonators that helps achieving a flat frequency response of the sensor up to the Nyquist frequency of 8.064 kHz. The use of two ASIC transceivers and two DSPs working with half-period offset allows achieving the sampling period of 62 µs for two resonators. This is the shortest sampling period reported in literature so far for the differential resonant SAW sensors.

Analysis of systematic errors caused by (a) mutual influence of two strong SAW responses, (b) aliasing and (c) intermodulation products emerging in the receiver due to its

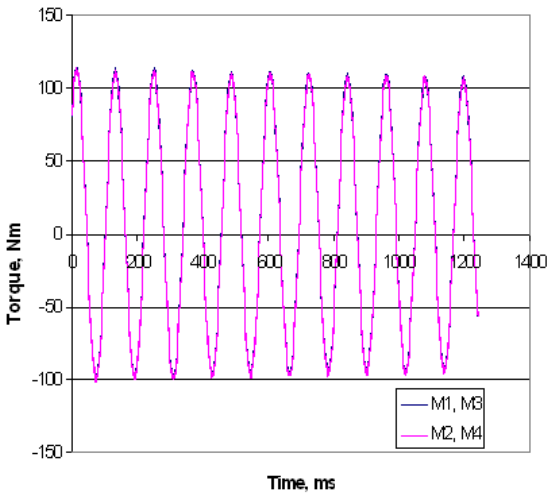

Figure 10. Torsional vibrations measured by the high-speed reader connected to a flexplate torque transducer

non-linearity has been performed and design recommendations suggested that allow reduction of the errors to an acceptable level well below 1% FS.

Random errors in the measured difference frequency have also been modeled using realistic data on the phase noise of the Rx LO. Analysis shows that the errors caused by the phase noise should cancel in the case of both SAW responses received simultaneously by the same receiver.

Experiment has shown that the standard deviation of the random errors for the measured difference frequency is around 330 Hz that is 0.04% FS. The reader provides good linearity of the sensor characteristic and high fidelity of the measured signal. Although it has been used with the SAW torque sensor it can also be used with any other type of wireless resonant SAW sensors relying on measurement of a difference between two resonant frequencies.

REFERENCES

[1] A. Lonsdale and B. Lonsdale, "Method and apparatus for measuring strain", US Patent No. 5585571, Date of patent: 17 Dec 1996, Priority date: 19 Sep 1991.

[2] A. Lonsdale and B. Lonsdale, "Apparatus for tracking resonant frequency", US Patent No. 6467351 B2, Date of patent: 22 Oct 2002, Priority date: 13 Nov 1997.

[3] J. Beckley, V. Kalinin, M. Lee and K. Voliansky, "Non-contact torque sensors based on SAW resonators", Proc. IEEE Int. Freq. Control Symp., pp. 202–213, 2002.

[4] A. Pohl, G. Ostermayer and F. Seifert, "Wireless sensing using oscillator circuits locked to remote high-Q SAW resonators", IEEE Trans. Ultrason., Ferroelectrics and Freq. Control, vol. 45, No. 5, pp. 1161–1168, 1998.

[5] W. Buff, M. Rusko, T. Vandahl, M. Goroll and F. Moller, "A differential measurement SAW device for passive remote sensing", Proc. 1996 IEEE Ultrason. Symp., pp. 343–346, 3–6 Nov 1996.

[6] V. Kalinin, R. Lohr, A. Leigh and G. Bown, "Application of passive SAW resonant sensors to contactless measurement of the output engine torque in passenger cars", Proc. IEEE Int. Freq. Control Symp., pp. 499–504, 29 May – 1 June, 2007.

[7] A. Lonsdale and B. Lonsdale, "Apparatus and method for interrogating a passive sensor", US Patent No. 6765493 B2, Date of patent: 20 Jul 2004, Priority date: 4 Sep 2000.

[8] P. Li, H. Xie, Y. Wen, et al. "A SAW passive wireless sensor system for monitoring temperature of an electric cord connector at long distance", Proc. IEEE Sensors, vol. 6127194 Part ISBN- 978, 2011.

[9] C. Droit, J.-M. Friedt, T. Retornaz and S. Ballandras, "Interrogation strategies for probing wireless passive SAW sensors", Proc. Eurosensors XXV, pp. 1024-1027, 4–7 Sep, 2011.

[10] C. Droit, J.-M. Friedt, G. Martin and S. Ballandras, "Method of rapidly interrogating elastic wave sensors", US Patent Application No. 2011/0241482 A1, Filing date: 5 Apr 2011., Priority date: 6 Apr 2010.

[11] R. Grossman, J. Michel, T. Sachs and E. Schrufer, "Measurement of mechanical quantities using quartz sensors", Proc. European Time and Freq. Forum, pp. 367–381, 5–7 Mar, 1996.

[12] M. Hamsch, R. Hoffmann, W. Buff, M. Binhack and S. Klett, "An interrogation unit for passive wireless SAW sensors based on Fourier transform", IEEE Trans. on Ultrason., Ferroelectrics and Freq. Control, vol. 51, No. 11, pp. 1449-1455, 2004.

[13] V. Kalinin, R. Lohr, A. Leigh, J. Beckey and G. Bown, "High-speed high dynamic range resonant SAW torque sensor for kinetic energy recovery system", Proc. 24th European Freq. and Time Forum, 13–16 April, 2010.

[14] L Reindl, G. Scholl, T. Ostertag, H. Scherr, U. Wolff and F. Schmidt, "Theory and application of passive SAW radio transponders as sensors", IEEE Trans. Ultrason., Ferroelectrics and Freq. Control, vol. 45, No. 5, pp. 1281–1292, 1998.

[15] V. Kalinin, "Influence of receiver noise properties on resolution of passive wireless resonant SAW sensors", Proc. IEEE Ultrason. Symp., pp. 1452 – 1455, 2005.

Eight channel embedded electronic open loop interrogation for multi sensor measurement

David Rabus, Gilles Martin, Émile Carry and Sylvain Ballandras
Dpt. temps-fréquence – Cosyma
FEMTO-ST
Besançon 25044 France
Email: {david.rabus,ballandr}@femto-st.fr

***Abstract*— One strategy in addressing the issue of selectivity in direct detection gas sensors – and specifically when using piezoelectric acoustic transducers – is to use multichannel measurement approaches in which each sensor is functionalized with a different chemical layer and provides different responses when exposed to a given mixture of gasses. Within this context, an 8-channel open loop embedded electronics operating as a transmission-mode radiofrequency network analyzer has been developed. The frequency ranges generated by the synthesizer is 50 to 160 MHz or 200 to 500 MHz. A low noise phase detection scheme was implemented, in addition to magnitude measurement.**

This instrument is used with Surface Acoustic Wave (SAW) and High-overtone Bulk Acoustic Resonator (HBAR) transducers: in the former case, the open-loop approach allows for an improved measurement dynamics, while in the latter case multiple resonances can be probed sequentially, yielding different acoustic penetration depths in the sensing layer. Demonstration of measurement in liquid phase is provided by characterizing the gravimetric sensitivity of HBARs using copper electrodeposition. Values ranging from 2.2 to 13.1 cm^2/g are observed, emphasizing a departure from a perturbative Sauerbrey-like relationship.

I. Introduction

Among the many methods for detecting chemical species in gas phase [1], [2], [3], the need for continuous monitoring (safety regulations [4], [5], quality control [6]) led to the development of direct detection sensors. Using such transducers, including optical and acoustic (bulk acoustic resonator [7], [8], [9], [10], [11], surface acoustic wave delay line [12], [13], [14], [15] and resonator [16]) transduction schemes, a mass loading of a functional chemical coating on the transducer surface is converted to an electrical signal representative of the mass of gas absorbed by the layer. In the case of acoustic transducers, either the velocity of the propagating wave (surface acoustic wave (SAW) device [17]) or boundary condition change (bulk acoustic resonator – BAW [18]) yield a change in the propagation delay of an incoming electromagnetic wave converted to a mechanical wave using the inverse piezoelectric effect. This propagation delay is classically measured as a phase information.

However, the direct detection transducer provides no intrinsic selectivity to the detected compound, and in most cases the selectivity of chemical coatings to small gas molecules is insufficient to identify low concentrations of a single species in a complex mixture of gasses. Thus, one approach commonly named electronic nose [19], [3], [20], [21] is to multiply the detection channels, each being coated with a different compound exhibiting different affinity to the various molecules in the complex mixture. Processing the various responses of the different channels (Principal Component Analysis [22], [23], [24], neural networks [25], [26], [27], [28]) has been demonstrated to yield both the nature and concentration of some compounds in gas phase.

Deployment of these measurements schemes requires dedicated, embedded electronics providing the ruggedness, low power consumption, data processing and communication capabilities hardly found in general purpose laboratory instruments [29]. Since the characterization of the acoustic properties relevant to direct detection transducers is classically performed using network analyzers, an embedded transmission-mode radiofrequency network analyzer with high phase-detection sensitivity is demonstrated. In addition to the multichannel capability provided by multiplexing the radiofrequency source, dedicated software to select a dedicated operating frequency for each channel and periodically probe the phase and magnitude information at this frequency is embedded in the control firmware.

II. Basic principles

Using acoustic wave based sensor for gravimetric measurement requires the measurement of the acoustic velocity as the sensing layer is loaded with the compound to be detected [30], [31], [32]. Using an open loop strategy with a fixed working frequency, the velocity variation is measured as a phase variation. By initially characterizing the phase to frequency relationship (dependent solely on the geometric and material characteristics of the delay line), assuming a locally linear law, the phase measurement is converted to a frequency value in order to provide an information consistent with other measurements results found in the literature (Fig. 3).

A direct digital frequency synthesizer (DDS) is programmed to generate a continuous radiofrequency (RF) signal at a given frequency. This operating frequency, for a given channel, has been selected according to two criteria:

1) following a characterization of the magnitude of the transmission of the acoustic transducer by sweeping the source in the operating frequency band, the maximum of the transfer function magnitude ($|S_{21}|$) is selected,

2) in order to optimize the operating point of the phase detector and analog to digital converters, the nearest phase condition maximizing linearity of the phase-frequency relationship at mid-range of the analog to digital converter operating voltage range is selected. This operating frequency is stored individually for each channel.

The detection circuit includes two separate phase measurement schemes: a rough characterization stage using the AD8302 phase and magnitude detector, and a high sensitivity phase measurement using dedicated phase detectors and variable gain, low noise operational amplifier as presented previously [33]. By increasing the gain on the operational amplifier, one can gradually improve the phase measurement resolution while remaining at a constant operating point. However, doing so also means that the phase range is reduced due to the limited voltage range of the analog to digital converter (ADC). While the AD8302 is tuned to generate a voltage within the ADC range as the phase rotates from +90^o to -90^o, increasing the gain the high sensitivity stage yields measurement ranges reduced to a fraction of the angle range. Thus, a tracking scheme is implemented in which the phase to frequency (locally linear) relationship is identified, and whenever the phase reaches a condition close to the boundary of the operating range of the ADC, the RF source frequency is tuned so that the phase moves back to the middle of the ADC range. This implementation is similar to a digital oscillator, since the frequency tracks a phase condition, with the added advantage than a precise phase measurement is provided as long as the voltage remains within the operating range of the ADC.

Multiplexing the source using a 1 to 8-channel multiplexer allows for probing the response of 8 transducers. One alternate use of the firmware is to connect a single multimode device (HBAR [34], [35]) to the RF output and probe this same device under various operating conditions. The information update rate is fixed to 1 Hz, consistent with the kinetics of chemical reactions considered here. In order to meet power consumption requirements when low update rates is acceptable, powering the electronics is controlled by a dedicated low power (MSP430) microcontroller running a real time clock and in charge of periodically waking up the embedded RF circuits. The total power consumption when all functionalities are running (8-channel measurement and high resolution phase detection) is 4 W with a suppl voltage of at least 7 V.

The capabilities of the system is illustrated by interrogating eight Love-wave delay lines (2.5 μm thick SiO_2 guiding layer on AT-cut quartz), all operating near 125 MHz in order to detect toxic species in composite gas. A second illustration is proposed using two HBAR based transducers at four different frequencies in the range of 50 to 160 MHz and the range of 200 to 550 MHz. The system operation is demonstrated for mass detection and monitoring viscosity change during controlled electrochemical deposition on sensitive surface of the resonators.

The paper is organized as follows: first electronic hardware including the improved phase measurement scheme is described. Then, some measurement results using this embedded electronics are presented when operating on Love mode acoustic delay lines used as gravimetric sensor. Finally, the characterization of the gravimetric sensitivity of various modes of an HBAR is given in liquid phase, using the reversible copper electrodeposition chemical reaction running thanks to an on-board embedded potentiostat.

III. Electronics Hardware

A general overview of the embedded electronics main elements for probing an 8-channel transducer used as gravimetric sensor is given in Fig. 1.

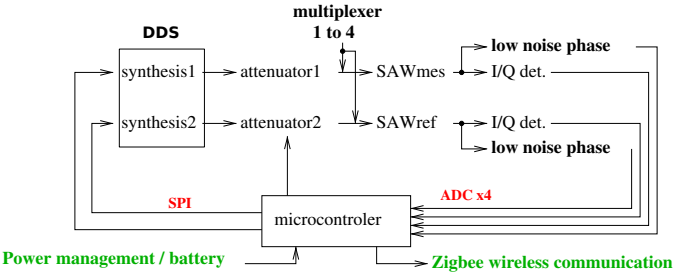

Fig. 1. Electronics overview: a central microcontroller defines the frequency of the signal generated by the two DDS (dual channel system compatible with a differential measurement approach), switches the multiplexer among the various measurement channels, and records the rough phase measurement as provided by an AD8302 phase and magnitude detector, as well as the precise phase output from the low noise phase measurement circuit.

The core control element of the embedded electronics is an Analog Devices ADuC7026 microcontroller. Two Analog Devices AD9954 DDS are controlled through an SPI interface: the two independent sources are used for a differential measurement approach in which two channels of a given sensor are coated with different sensing layers, yielding rejection of correlated noise sources (temperature drift, pressure change) and extracting only the signal of interest (acoustic velocity decrease due to the mass loading of the gas absorbing in the chemical detection layer).

Multi-sensor capability is provided by adding 1 to 4 channel multiplexers on both DDS outputs, using high isolation switches – Hittite Microwave HMC241QS16. Another multiplexer located at the output of the transducer feeds the RF signal to both an AD8302 phase and magnitude detector for recording the magnitude (losses) information and a rough phase estimate (Fig. 2, blue box), as well as to a high resolution phase detector circuit (Fig. 2, red box). The former approach is most significant in providing a high measurement dynamics (-30 to +30 dB with respect to the reference channel, whose power is adjustable on a 32 dB range using a programmable attenuator). The selection of the phase measurement type is realized using a switch – Hittite Microwave HMC349 – which connects the measurement stage to the output of the acoustic sensor. Since only one channel of the reference transducer and one channel of the measurement

transducer are powered at any given time, no RF cross-talk between the signals propagating on adjacent channels is possible.

The on-board 12-bit analog to digital converters are used to digitize the phase and magnitude information and transmit the information to the user through an RS232 link, compatible with wireless transmission interfaces such as radiomodems when installing the embedded electronics in remote areas. The dimensions of the assembled circuit are 25×15×5 cm.

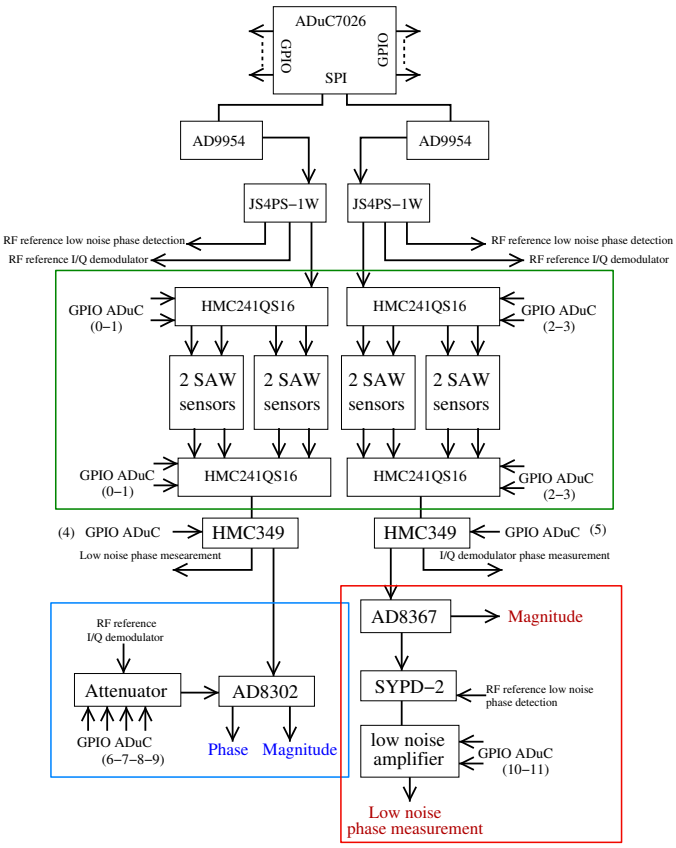

Fig. 2. Description of the electronics using eight surface acoustic wave transducers with open loop strategy and the description of the two types of phase measurement.

The high resolution phase measurement stage is based on an automatic gain detector – Analog Devices AD8367 – which provides the magnitude information and a low noise phase detector – Mini-Circuits SYPD-2 – which provides a voltage output proportional to the phase. This analog signal is amplified by a low noise amplifier with a digitally programmable gain [33]. Gains of 2, 4, 8 or 16 are selected in increasing order to improve the resolution while keeping the tracking capability for fast chemical reactions (e.g. fast phase change during gas injection might require a lower gain). The phase measurement resolution is limited by the noise of the ADC of the ADuC7026 and the frequency tracking capability. With the highest gain, a 8 m^o (millidegrees) standard deviation of the phase measurement is obtained, corresponding to a shift of 16 Hz when using Love wave based transducers.

IV. Results – Implemented Algorithm

Since the electronics is able to probe in an open-loop configuration eight channels, automatic operating frequency identification algorithms are provided at the initialization step (Fig. 3 when using Love mode delay line sensors). The red point (Fig. 3) indicates the result of searching for the maximum of the magnitude. The working frequency is selected automatically near this maximum to yield the best signal to noise ratio by maximizing the transmitted acoustic power. The working frequency is chosen on the decreasing slope of the phase-frequency curve in order to provide a decreasing phase when reducing the acoustic wave velocity (mass loading) of the transducer during chemical detection and thus provide a visual output consistent with the classical Quartz Crystal Microbalance (QCM) frequency output. Beyond the identification of the operating frequency, this characterization of the transfer function of each transducer is also used to qualify the proper operating condition of the sensor and thus provide a quality of service (QoS) information when operating in an autonomous environment.

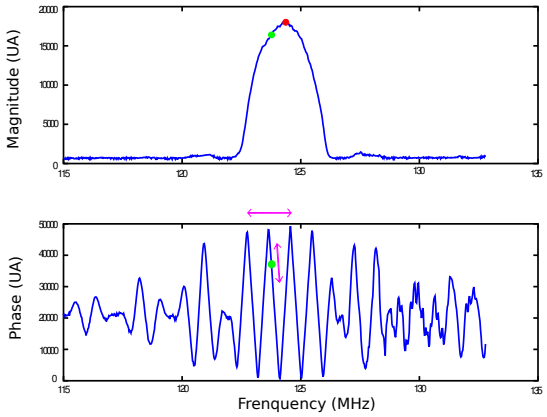

Fig. 3. Magnitude (top) and phase (bottom) S_{21} characterization of a Love mode SAW sensor. In red the automatic search result of the maximum of magnitude and in green the illustration of the result of the automatic search of the working frequency.

The use of different gains of the low noise phase measurement stage is illustrated on Fig. 4. Four S_{21} phase characterizations of a same Love mode transducer using four different gains of the low noise amplifier respectively 2 (blue), 4 (red), 8 (green) and 16 (black) gain values are shown. The improvement of the measurement phase resolution with the increase of the gain is seen, associated with the induced saturation of the measurement when the value is out of the range of the ADC operating range. In the case of large phase variations, the probe signal frequency must be adjusted to track the phase and keep the measured voltage output close to the middle of the operating range of the ADCs. This frequency shift is implemented and can be configured to adapt the frequency shift value to the slope of the measured phase-frequency relationship.

The main limitation of this low noise phase measurement strategy is the time constant of the low noise amplifier

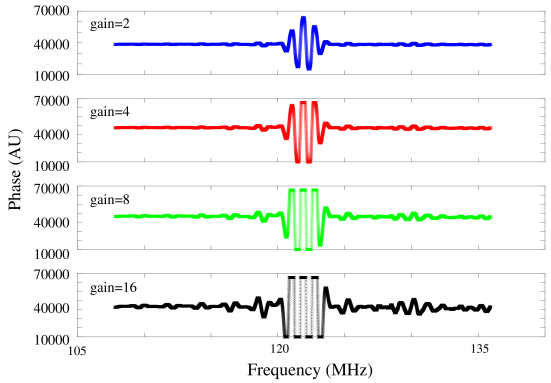

Fig. 4. High resolution of S_{21} phase characterization of Love mode based SAW delay line.

since the noise improvement is obtain by strongly limiting the operational amplifier bandwidth (low pass filtering). The sampling rate of the system is this fixed to 1 Hz for eight sensor measurements.

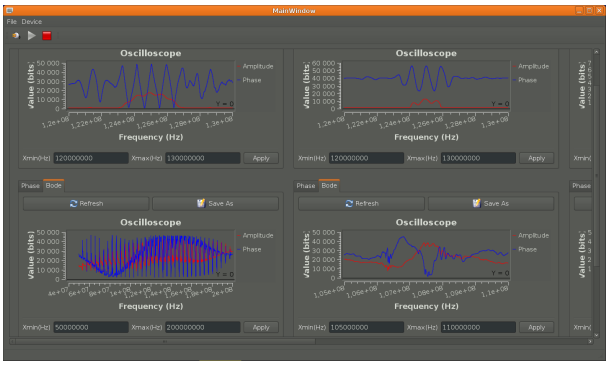

Fig. 5. Screenshot of the graphical interface controling the embedded electronics and displaying measurement results. A Love-mode delay line is connected to one channel (top graphs), and a HBAR resonator to another one (bottom graphs). The initial configuration step displays the transfer function of each device within a user-defined frequency range.

The flexibility of the graphical user interface is demonstrated in Figs. 5 and 6. The frequency range of the acoustic transducer characterization is user defined for each channel, as is the gain applied to the low noise phase detection electronics. Following the initial characterization of each transfer function, the working frequency is either identified automatically or user-defined, before the display switches to a mode in which the time-dependent evolution of the phase is shown.

V. Multi Frequency Measurements

The presented electronic system is now used to probe only two multi-mode sensors in open loop strategy, each at four different frequencies. This approach is most suitable for HBAR transducers whose modes are separated by 10 MHz at most, yielding a reliable selection of the probed mode in a closed loop (oscillator) challenging. No change of either the described hardware or software is needed other than disabling the switching capability of the channel multiplexers.

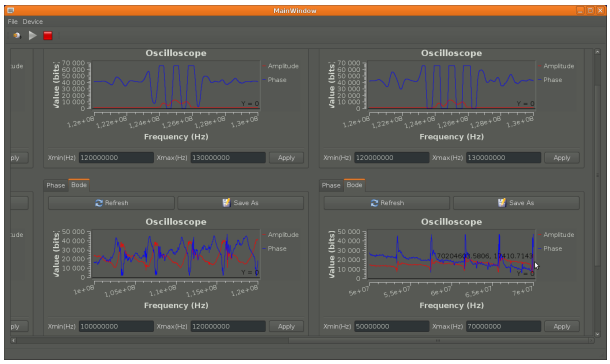

Fig. 6. Second half (last 4 windows) of the graphical user interface, with a characterirazation of the Love mode delay line (top) at various phase gains, and the HBAR (bottom graphs) in different frequency intervals.

We here focus on the characterization of the gravimetric sensitivity characterization of HBAR-sensors in two frequency ranges (50 to 160 MHz and 200 to 550 MHz) using copper electrochemical deposition in an aqueous environment.

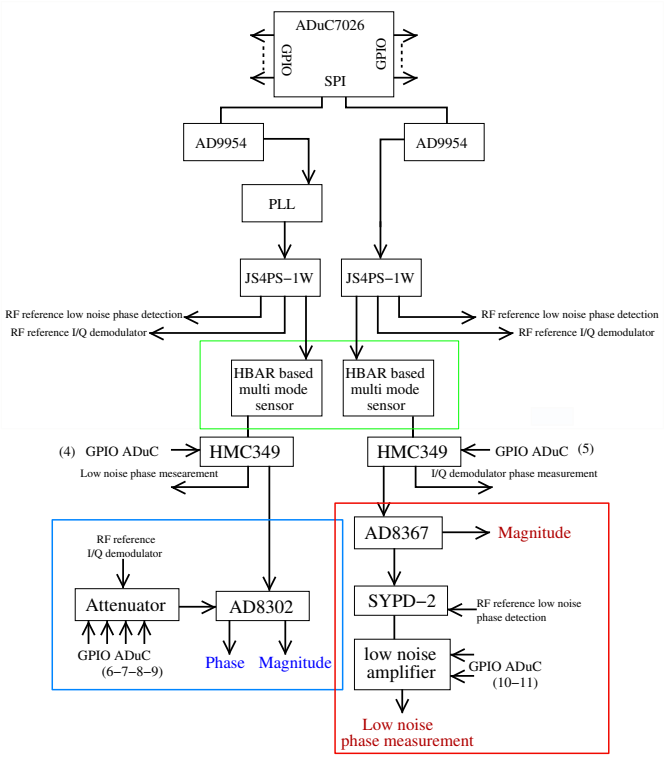

Fig. 7. Description of the electronics using two transducers at four different frequencies with two ranges 200 to 550 MHz (left) and 50 to 160 MHz (right) and the description of the two types of phase measurement.

Fig. 7 illustrates the use of two HBAR transducers (differential measurement) after removing the multiplexing capability. (Fig. 7, green box). Furthermore, the 50 to 160 MHz frequency range (Fig. 7, right) is complemented with a higher frequency RF source operating in the 200 to 550 MHz obtained by Phase Locked Loop (PLL) multiplication (4-times) of the DDS output (Fig. 7, left). Since the SYPD-2 phase detector is only

characterized for operating in the DC to 200 MHz range, the phase measurement in the higher frequency range is only achieved using the AD8302 output.

VI. HBAR GRAVIMETRIC SENSITIVITY CHARACTERIZATION

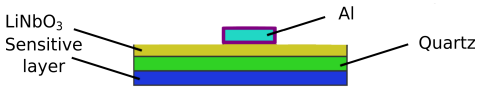

Fig. 8. Stack of layers of an HBAR. The thin active single crystal piezoelectric layer is typically 5 to 50 μm thick (yellow) while the thick substrate (green) is typically 350 μm thick. The sensing surface (blue) is opposite to the electrodes (light blue). The buried electrode between the thin and thick substrates is not shown.

The gravimetric sensitivity of an HBAR is characterized using the multichannel embedded electronics equipped with a 4-operational amplifier embedded potentiostat [36]. The HBAR transducer is made of a stack of single-crystal piezoelectric materials as shown on Fig. 8. From top to bottom, an aluminum electrode excites an active lithium niobate ($LiNbO_3$ $(YXl)/163$) piezoelectric layer to generate the acoustic wave. A thick quartz layer (quartz $(YXl)/32$) is used as low-loss propagation medium. On the free surface of the quartz substrate (backside of the sensor), the sensing functional layer is deposited or, in our case, the electrode to be used as working electrode in the potentiostat on which the copper will be reversibly deposited. In our case, we avoid reaching the buried electrode by using two acoustically coupled resonators (Fig. 9) and thus only bonding electrical connections to the exposed aluminum pads.

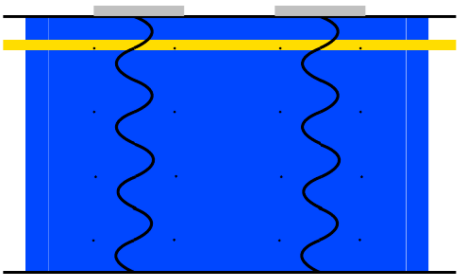

Fig. 9. Transducer based on two acoustically coupled HBARs. The coupled resonator approach is used to avoid reaching the buried electrode (yellow) since all electrical connections are done on the aluminum top electrodes (grey).

As shown on Fig. 10, the open loop strategy is mandatory to select the overtone to be probed. A closed loop strategy would require pass-band filtering each overtone while still meeting the Barkhausen oscillation conditions. The developed system enables the manual selection of any overtone up to four frequencies in the measurement range, corresponding for instance to the four red points on the phase (bottom) characterization on Fig. 10.

These four frequencies are probed sequentially (1 Hz update rate) during a reversible electrochemical deposition of

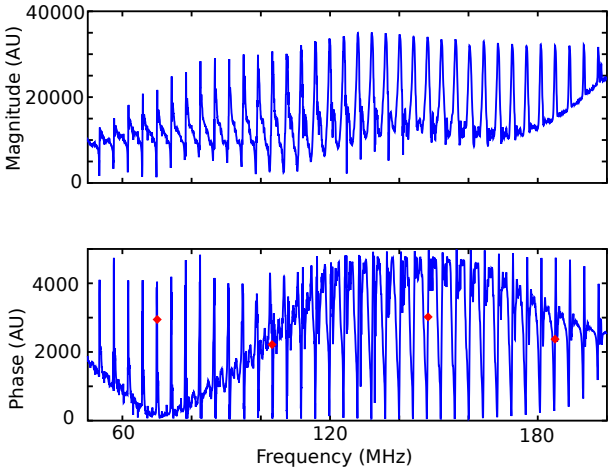

Fig. 10. Magnitude (top) and phase (bottom) S_{21} characterization of a HBAR based transducer. In red the different manually selected working frequencies.

copper (Eq. 1) driven by the microcontroller using an embedded potentiostat. The electrodeposition approach was selected since the simultaneous measurement of the current flowing in the working electrode provides, assuming a 100% yield, an independent estimate of the deposited mass on the sensing surface of the acoustic sensor [37], as shown in Eq. 2. Thus, gravimetric sensitivity [38] is determined for each selected mode using Eq. 3 and defined as the relative frequency shift due to the adsorbed mass per unit area.

$$Cu^{2+} + 2e^- \leftrightarrow Cu \tag{1}$$

$$M_{Cu} = \frac{m_{Cu} \times \Sigma i(t)\delta t}{96440 \times n_e} \tag{2}$$

where

M_{Cu}:	copper deposited mass (g)
m_{Cu}:	molar weight (g/mol)
$\Sigma i(t)\delta t$:	charge transferred during electro-deposition (time interval δt between two samples)
96440:	charge of one mole of electron (C)
$n_e = 2$:	electron transferred during reduction (Eq. 1)

$$S = \frac{\Delta f}{f_0} \times \frac{A}{\Delta m} \tag{3}$$

where

Δf:	frequency shift (Hz)
f_0:	interrogation frequency (Hz)
Δm:	deposited mass (g)
A:	sensitive zone area (cm^2)
S:	gravimetric sensitivity (cm^2/g)

Comparing the gravimetric behavior of each probed overtone is performed by comparing the relative frequency variation (Fig. 11) as measured nearly simultaneously (time lag <1 s) with the embedded electronics. Each color on the graph of Fig. 11 is associated with one mode, for instance blue for the 70 MHz mode and cyan for 148 MHz: the relative

frequency variation is exhibited for each mode during the copper reduction (frequency decrease) and oxidation (frequency rise back to the initial baseline), repeated 5 times during this particular experiment.

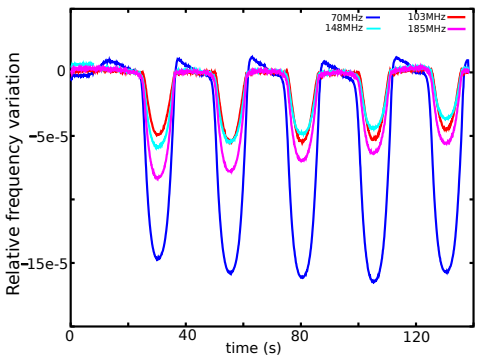

Fig. 11. Relative frequency variation for four modes – 70 MHz (blue) 103 MHz (red) 148 MHz (cyan) 185 MHz (magenta) – as a function of time during the characterization of the gravimetric sensitivity using copper electrochemical deposition.

Different gravimetric sensitivities (Tab. I) for each mode are observed, in contradiction with the prediction of the Sauerbrey relationship [38], emphasizing the inaccuracy in the case of HBAR of the perturbation assumption and thus require proper coupled oscillator modeling to predict the gravimetric sensitivities of the various modes [35]. For instance the relative variation recorded at 148 MHz is three times lower than the relative variation at 70 MHz, thus indicating that the gravimetric sensitivity is three times higher at 70 MHz than at 148 MHz.

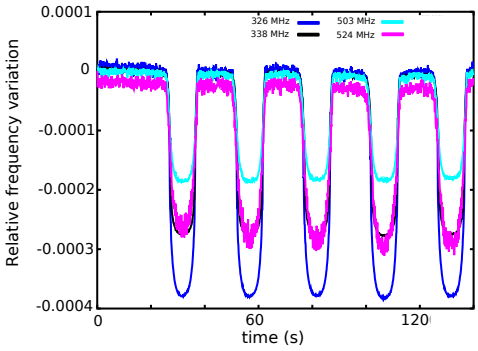

Fig. 12. Relative frequency variation for four working frequencies – 326 MHz (blue) 338 MHz (black) 503 MHz (cyan) 524 MHz (magenta) – as a function of time during the characterization of the gravimetric sensitivity using copper electrochemical deposition.

The same experiment is reproduced on the same sensor in the higher frequency range (Fig. 12). Two modes – 338 MHz (black) and 524 MHz (magenta) – exhibit the same relative frequency variations, thus yielding the same gravimetric sensitivity. However, the gravimetric sensitivity at 326 MHz (blue) is twice that found at 503 MHz (magenta). Using this electronics to characterize simultaneously the gravimetric sensitivity of an HBAR at four different frequencies highlights the different behavior of each overtone. These differences might be due to the viscous load contribution to the phase shift during copper electrodeposition since the surface roughness is increased as the copper layer grows [39].

TABLE I
GRAVIMETRIC SENSITIVITY AS A FUNCTION OF WORKING FREQUENCY

Working frequency (MHz)	Gravimetric sensitivity (cm^2/g)
70	7.6
103	2.2
148	2.2
185	3.6
326	13.1
338	9.7
503	6.6
524	9.7

VII. CONCLUSION

An open loop based electronics has been developed to characterize in transmission radiofrequency acoustic transducers. Eight surface acoustic wave sensors are probed, each one at its optimum operating frequency, or two multi-mode HBAR sensors operating each at four different frequencies. A 1 Hz sampling rate is defined by the bandwidth of a high resolution phase detection scheme. Two operating frequency ranges are available, 50 to 160 MHz and 200 and 550 MHz. A rough phase measurement for transducer characterization is complemented with a high resolution phase measurement strategy for high sensitivity (low concentration) chemical compound detection. This system has been used to characterize the gravimetric sensitivity of a multi-mode HBAR based sensors using an embedded potentiostat to drive an electrochemical reversible copper deposition on the sensing surface of the transducer.

Further developments aim at extending the frequency range to widen the acoustic dispersion relation of the acoustic multimode sensors and adapt the low noise phase measurement strategy to this wide frequency range.

ACKNOWLEDGMENT

The authors thank Jean-Michel Friedt (SENSeOR SAS, Besançon, France) for his help in developing the electronic system. The graphical user interface was developed by Julien Garcia (FEMTO-ST Time & Frequency): its source code is available at `http://serials8.xeme.fr/`.

REFERENCES

[1] *Environmental quality – design, installation and utilization of fixed-fenceline sample collection and monitoring systems*. U.S. Army Corps of Engineers, 1997.
[2] G. Sberveglieri, *Gas sensors: principles, operation and developments*. Kluwer Academic Publisher, 1992.
[3] F. Röck, N. Barsan, and U. Weimar, "Electronic nose: Current status and future trends," *Chem. Rev.*, vol. 108, no. 2, pp. 705–725, 2008.
[4] *NIOSH Pocket Guide to Chemical hazards*. Department of Health and Human Services, Centers for Disease Control and Prevention National Institute for Occupational Safety and Health, 2007.
[5] *A workbook of screening techniques for assessing impacts of toxic air pollutants*. U.S. Environmental Protection Agency, 1988.

[6] *Review of the Process for Setting National Ambient Air Quality Standards*. U.S. Environmental Protection Agency, 2006.

[7] J.-F. Rosenbaum, *Bulk Acoustic Wave Theory and Devices*. Artech House, 1988.

[8] D. Buttry and M. Ward, "Measurement of interfacial processes at electode surface with the electrochemical quartz crystal microbalance," *Chem. Rev.*, vol. 92, pp. 1355–1379, 1992.

[9] S. Fanget, S. Hentz, P. Puget, J. Arcamone, M. Matheron, E. Colinet, P. Andreucci, L. Duraffourg, E. Meyers, and M. Roukes, "Gas sensors based on gravimetric detection – a review," *Sensors and Actuators B: Chemical*, vol. 160, no. 1, pp. 804–821, 2011.

[10] S. Rey-Mermet, R. Lanz, and P. Muralt, "Bulk acoustic resonator operating at 8 GHz for gravimetric sensing of organic films," *Sensors and Actuators B*, vol. 114, pp. 681–686, 2006.

[11] M. Guillemot, F. Dayber, P. Montméat, C. Barthet, and P. Prené, "Detection of explosives vapours on quartz crystal microbalances: generation of very low-concentrated vapours for sensors calibration," *Procedia Chemistry*, vol. 1, pp. 967–970, 2009.

[12] A. J. Ricco, S. J. Martin, and T. E. Zipperian, "Surface acoustic wave gas sensor based on film conductivity changes," *Sensors and Actuators*, vol. 8, pp. 319–333, 1985.

[13] M. S. Nieuwenhuizen and A. J. Nederlof, "Surface acoustic wave gas sensor for nitrogen dioxide using phthalocyanines as chemical interfaces. effects of nitric oxide, halogen gases, and prolonged heat treatment," *Anal. Chem.*, vol. 60, no. 3, pp. 236–240, 1988.

[14] C. Zimmermann, D. Rebière, C. Déjous, J. Pistré, E. Chastaing, and R. Planade, "A love-wave gas sensor coated with functionalized polysiloxane for sensing organophosphorus compounds," *Sensors and Actuators B: Chemical*, vol. 76, no. 1-3, pp. 86–94, 2001.

[15] D. Arn, N. Blom, K. Dubler-Steudle, N. Graber, and H. Widmer, "Surface acoustic wave gas sensors: Applications in the chemical industry," *Sensors and Actuators A*, vol. 25-27, pp. 395–397, 1991.

[16] D. Ballantine, *Acoustic Wave sensors*. Academic Press, 1997.

[17] E. Gizeli, "Study of the sensitivity of the acoustic waveguide sensor," *Analytical chemistry*, vol. 72, no. 24, pp. 5967–5972, 2000.

[18] E. Benes, M. Gröschl, F. Seifert, and A. Pohl, "Comparison between baw and saw sensor principles," 1997.

[19] A. Ricco and S. Martin, "Multiple-frequency SAW devices for chemical sensing and materials characterization," *Sensors and Actuators B*, vol. 10, pp. 123–131, 1993.

[20] J. W. Grate, "Acoustic wave microsensor arrays for vapor sensing," *Chem. Rev.*, vol. 100, no. 7, pp. 2627–2648, 2000.

[21] R. McGill, V. Nguyen, R. Chung, R. Shaffer, D. DiLella, J. Stepnowski, T. Mlsna, D. Venezky, and D. Dominguez, "The "nrl-sawrhino": a nose for toxic gases," *Sensors and Actuators B*, vol. 65, pp. 10–13, 2000.

[22] M. Penza, G. Cassano, F. Tortorella, and G. Zaccaria, "Classification of food, beverages and perfumes by wo_3 thin-film sensors array and pattern recognition techniques," *Sensors and Actuators B*, vol. 73, pp. 76–87, 2001.

[23] M. Penza, G. Cassano, and F. Tortorella, "Gas recognition by activated wo_3 thin-film sensors array," *Sensors and Actuators B*, vol. 81, pp. 115–121, 2001.

[24] G. Peng, U. Tisch, O. Adams, M. Hakim, N. Shehada, Y. Broza, S. Billan, R. Abdah-Bortnyak, A. Kuten, and H. Haick, "Diagnosing lung cancer in exhaled breath using gold nanoparticles," *Nature Nanotechnology*, vol. 4, pp. 669–673, 2009.

[25] D. Donlagić, M. Z. snik snik snik snik, and D. Donlagić, "Low-frequency acoustic resonance level detector with neural-network classification," *Sensors and Actuators A*, vol. 55, pp. 99–106, 1996.

[26] S. Hanaki, T. Nakamoto, and T. Moriizumi, "Artificial odor-recognition system using neural network for estimating sensory quantities of blended fragrance," *Sensors and Actuators A*, vol. 57, pp. 65–71, 1996.

[27] T. Nakamoto, H. Takagi, S. Utsumi, and T. Moriizumi, "Gas/odor identification by semiconductor gas-sensor array and an analog artificial neural-network circuit," *Sensors and Actuators B*, vol. 8, pp. 181–186, 1992.

[28] C.-Y. Shen, H.-C. Huang, and R.-C. Hwang, "Ammonia identification using shear horizontal surface acoustic wave sensor and quantum neural network model," *Sensors and Actuators A*, vol. 147, p. 464Â469, 2008.

[29] A. Nimal, U. Mittal, M. Singh, M. Khaneja, G. Kannan, J. Kapoor, V. Dubey, P. Gutch, G. Lal, K. Vyas, and D. Gupta, "Development of handheld SAW vapor sensors for explosives and CW agents," *Sensors and Actuators B*, vol. 135, p. 399Â410, 2009.

[30] G. Kovacs, M. Vellekoop, R. Haueis, G. Lubking, and A. Venema, "A Love wave sensor for (bio) chemical sensing in liquids," *Sensors and Actuators A: Physical*, vol. 43, no. 1-3, pp. 38–43, 1994.

[31] J. Du and G. Harding, "A multilayer structure for love-mode acoustic sensors," *Sensors and Actuators A: Physical*, vol. 65, no. 2-3, pp. 152–159, 1998.

[32] F. Herrmann, M. Weihnacht, and S. Büttgenbach, "Properties of shear-horizontal surface acoustic waves in different layered quartz-sio_2 structures," *Ultrasonics*, vol. 37, no. 5, pp. 335–341, 1999.

[33] D. Rabus, J.-M. Friedt, S. Ballandras, G. Martin, E. Carry, and V. Blondeau-Patissier, "A high sensitivity open loop electronics for gravimetric acousticwave-based sensors." Noordwijk NL: EFTF, Apr. 2010.

[34] D. Gachon, T. Baron, G. Martin, E. Lebrasseur, E. Courjon, F. Bassignot, and S. Ballandras, "Laterally coupled narrow-band high overtone bulk wave filters using thinned single crystal lithium niobate layers." IFCS-EFTF, May 2011.

[35] G. Mansfeld, "Theory of high overtone bulk acoustic wave resonator as a gas sensor," in *Microwaves, Radar and Wireless Communications. 2000. MIKON-2000. 13th International Conference on*, vol. 2. IEEE, 2000, pp. 469–472.

[36] A. Rowe, A. Bonham, R. White, M. Zimmer, R. Yadgar, T. Hobza, J. Honea, I. Ben-Yaacov, and K. Plaxco, "Cheapstat: An open-source,"do-it-yourself" potentiostat for analytical and educational applications," *PloS one*, vol. 6, no. 9, p. e23783, 2011.

[37] J.-M. Friedt, L. Francis, K.-H. Choi, and A. Campitelli, "Combined atomic force microscope and acoustic wave devices: Application to electrodeposition," *J. Vac. Sci. Tech. A*, vol. 21, no. 4, p. 1500, 2003.

[38] G. Sauerbrey, "Verwendung von schwingquarzen zur wägung dünner schichten und zur mikrowägung," *Zeitschrift für Physik A Hadrons und Nuclei*, vol. 155, no. 2, pp. 206–222, 1959.

[39] J.-M. Friedt, K. Choi, F. Frederix, and A. Campitelli, "Simultaneous atomic force microscope and quartz crystal microbalance measurements: Methodology validation using electrodeposition," *Journal of the Electrochemical Society*, vol. 150, no. 10, pp. H229–H234, October 2003.

Indoor-localization system using a Micro-Inertial Measurement Unit (IMU)

Fabian Höflinger[1], Rui Zhang[2], Leonhard M. Reindl[3]

Laboratory for Electrical Instrumentation
Department of Microsystems Engineering - IMTEK
Georges-Koehler-Allee 106, 79110 University of Freiburg, Germany
{[1]fabian.hoeflinger, [2]rui.zhang, [3]reindl}@imtek.uni-freiburg.de

***Abstract*—In this paper we present a wireless Micro-Inertial Measurement Unit (IMU) which is used for localization of people in indoor areas. The Micro-IMU is built especially for portable applications. The main target of the IMU design was to minimize the size, weight and power consumption, as much as possible whereas the performance is still comparable to commercially available wired IMUs. Through the minimum size the IMU can be integrated into clothes or shoes and provide the full functionality of pedometers. In an experiment the Micro-IMU was mounted on a shoe for detecting the human movement. With sensor data-fusion based on Kalman Filter and ZUPT (Zero Velocity Update) Algorithm we could track a person in an indoor area.**

***Index Terms*—Indoor-Localization system, Inertial Measurement Unit, wireless sensor**

I. Introduction

In recent years, localization systems for indoor areas are becoming more and more popular. To guide people in unknown indoor areas a localization system is needed. This is often useful, in airports to find specific gates, in supermarkets to navigate customers to chosen products and in fairs to navigate visitors to the exhibition stands.
For indoor areas many different localization technologies are available. A brief overview of localization systems is shown in Fig.1 and discuss below.

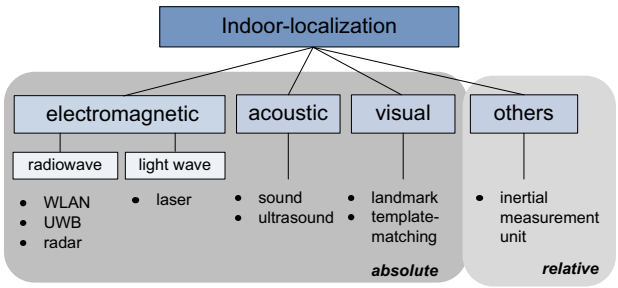

Fig. 1. Overview localization systems

Localization systems based on electromagnetic e.g. WLAN were used to localize people with smartphones and WLAN-Access Points [1]. The positions in such systems is calculated with Time of Flight (ToF) or with RSSI (Received Signal Strength Indication). Systems based on acoustics used ultrasound to locate people. In [2] a system is presented which is calculating the position with Time Difference of Arrival (TDoA) of sound. The disadvantages of electromagnetic and ultrasound systems are the required infrastructure and the accuracy of the system depends on multipath propagation. Visual systems use environment information to estimate the position. In [3] a localization system is presented which compares currently captured images with images in a database. The visual systems have problems to clearly identify positions in dynamic environments.
Relative systems e.g. Inertial Measurement Units (IMUs) detects the movement continuously. The systems rely on inertial sensors, which detects the actual movements with accelerometer, gyroscope and magnetometer. The sensor data is integrated, errors and measurement inaccuracies lead to positioning deviations. Relative systems are good for short distance tracking or for combination with absolute systems in shaded signal ranges.

II. Inertial Measurement Unit (IMU)

Today many different commercially IMUs are available. Fig.2 shows a overview of the dimensions and data performances of state of the art IMUs and IMUs from research groups. Bandwidth, sensor drift, linearity and sample rate describes the performance of an IMU. For precise tracking an IMU with small dimensions and high performance is needed. IMUs with less sensor drift and a high data rate have large dimensions and communicate usually via wire to computers. The IMUs from LITEF are used in civil and military aviation and provides a high end data performance. The μIMU-I [4] is based on a fiber optic gyroscope that provides a high stability and a low drift Factor of $2.8 * 10^{-5\circ}/s$ in a size of $160\,\mathrm{cm}^3$. Most of the commercially available IMUs like the Xsens MTi [5] offer measurement data preprocessing and robust on-board sensor data fusion for 3D orientation. Research groups use these IMUs for developing their own algorithms. However, due to their size, weight, or power consumption, these IMUs are not ideally suitable.
Different research groups works to minimize the size and to use wireless transmission. Barton *et al.* demonstrated a

cubic IMU design with a side length of 10 mm and wireless communication [6]. However, they employ analog sensors which demand for separate analog-to-digital converters. Lin *et al.* presented a system for the analysis of yaw movements with dimensions of 37 mm x 23 mm x 12 mm, integrated with a Bluetooth module and a lithium polymer battery which is comparably large and has limited sampling rate [7]. Tsai *et al.* presented a small wireless IMU without gyroscope in a size of 1 cm^3 [8].

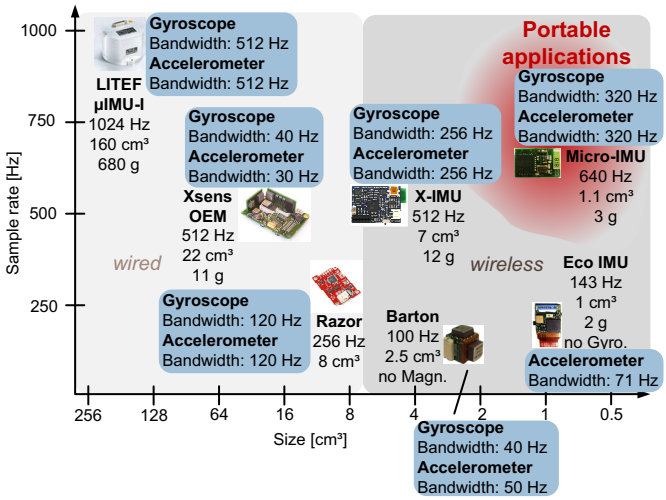

Fig. 2. Overview of size and data performances of state of the art IMUs and IMUs from research groups

III. Design of the Micro-IMU

The main target of the IMU design was to minimize the size, weight and power consumption, as much as possible whereas the performance is still comparable to commercially available IMUs e.g. Xsens MTi IMUs. For the design of the Micro-IMU, we combined the aim of an applicable IMU for portable application and improved the characteristics in size, weight, while the performance is still comparable to state-of-the-art commercially available MEMS IMUs. This becomes possible by using modern MEMS sensors. In our design we used accelerometers and gyroscopes feature three-axis technology and integrated analog-to-digital conversion with automatic temperature compensation in one-chip-design. This saves space in the IMU design as analog converters and 3D packaging are not necessary. Thus, a four-layer PCB is sufficient for integration of all inertial sensors and a microcontroller. Fig.3 shows the block diagram with the components of the IMU.

One important aspect of this design is to move data-processing from the IMU to a base station. Through this, the power consumption of the IMU is reduced, as the demanding computation of sensor data fusion filters and other algorithms to enhance the data quality is moved to more powerful computers with less constraints in size and weight.

A CC430 microcontroller sends the collected raw data to a base station wireless with a maximum sample rate of 640

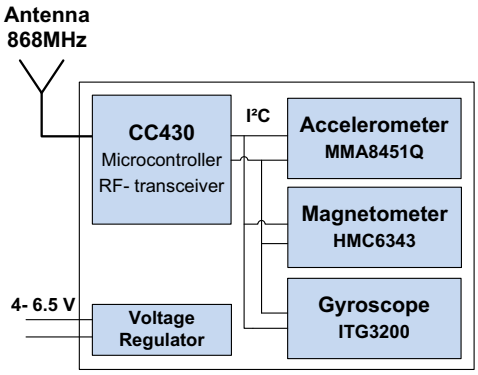

Fig. 3. Block diagram of the Micro-IMU

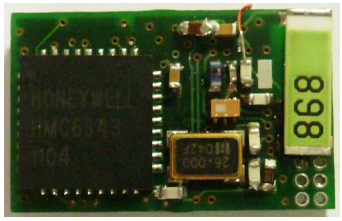

Fig. 4. Micro-IMU with radio cell with a dimension of 18 mm x 16 mm x 4 mm

samples per second. The power consumption of the Micro-IMU is three times lower than the commercially available IMUs. Thereby, the IMU performance is optimized by moving data post processing to the base station. This development offers new possibilities in portable applications with limited size, weight-requirements and battery powering where the position information is not needed on the moving subject.

Fig.4 shows the developed wireless Micro-IMU with an integrated antenna. The presented Micro-IMU with a size of 1.1 cm^3 is 20 times smaller and provides full control over the data of a three-axis accelerometer, a three-axis gyroscope, and a three-axis magnetometer. The Micro-IMU meets the design prerequisites of a space-saving design and eliminates the need of a hard-wired data communication while still being comparable to state of the art commercially available MEMS IMUs.

IV. Performance of the Sensor Data

For the data processing it is important to have a high raw sampling rate. The performance of the raw data is very important for the accuracy of the algorithm. The data quality of the measurement data of the IMU is determined by bias-drift and noise of the sensors. Allan variance approach was used to process the drift and noise information of the sensor. We used the Allan variance to compare the Micro-IMU with the commercial Xsens-MTi IMU [9]. The obtained curve is shown in Fig.5 and the precise characteristics can be found in Table I.

For the gyroscope the Micro-IMU performs better than the MTi concerning drift and noise. The noise level is on average

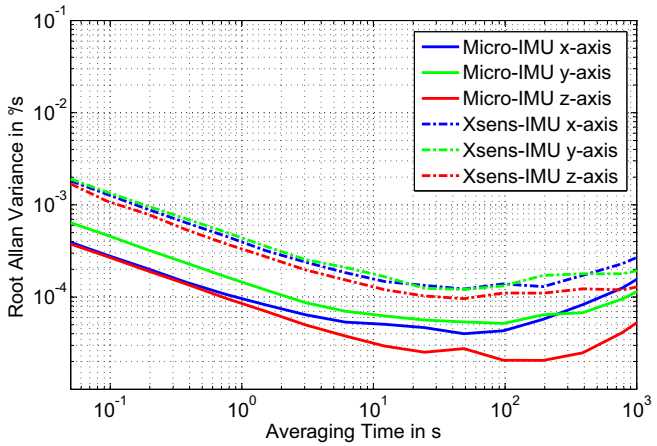

Fig. 5. Allan variance of the Gyroscope of Xsens MTi and Micro-IMU

TABLE I
COMPARISON BETWEEN XSENS [5] AND MICRO-IMU

	Micro-IMU	Xsens MTi
Interface	Wireless	RS232/USB
Sampling Rate	640 sample/sec	100 sample/sec
Bandwidth Acc.	320 Hz	30 Hz
Bandwidth Gyro.	320 Hz	40 Hz
Power Consumption	110 mW	350 mW
Size (OEM)	18 x 16 x 4 mm^3	48 x 33 x 15 mm^3
Weight (OEM)	3 g	11 g
Gyroscope		
Noise in $°/s/\sqrt{Hz}$		
x-axis	0.0055	0.045
y-axis	0.0082	0.041
z-axis	0.0049	0.036
Drift in $°/s$		
x-axis	0.0023	0.0070
y-axis	0.0030	0.0069
z-axis	0.0012	0.0055

six times lower for the Micro-IMU than for the MTi and the drift is lower by a factor of three.

V. SOFTWARE FOR TRACKING

Software part includes three sections. Firstly calibration of sensor is implemented in order to obtain the stable, bias-free, calibrated sensed data from the raw sensed data. Secondly, orientation especially the heading angle is determined by fusing the inertial sensors and magnetic field sensor using Kalman filter. Thirdly, the correct position information is obtained by combining the orientation information and corrected velocity information, which is achieved by "'Zero Velocity Update"' (ZUPT) method.

A. Sensor calibration method

The sensor calibration method is to remove the bias of all the sensors and adjust the orthogonal coordinate of magnetic field sensor. By keep the sensor model still for some time, the bias of gyro and acceleration sensors can be calculated by averaging the sensed data during calibration period. The magnetic field sensor is calibrated by using Merayos technique with a non-iterative algorithm [10], which tries to find the best 3D ellipsoid that fits the sensor data set and returns the parameters of this ellipsoid. The raw data of the magnetic field sensor is shown in Fig.6. Fig.7 shows the result after the calibration with Merayos technique.

After the steps above, a second-order low pass filter is applied for all the sensors so as to remove the noise outliers.

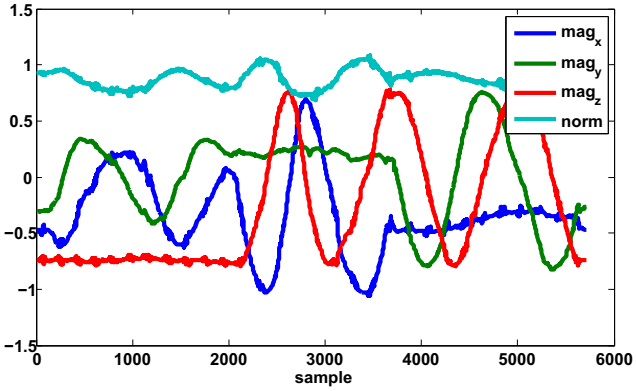

Fig. 6. Raw data of the magnetic field sensor

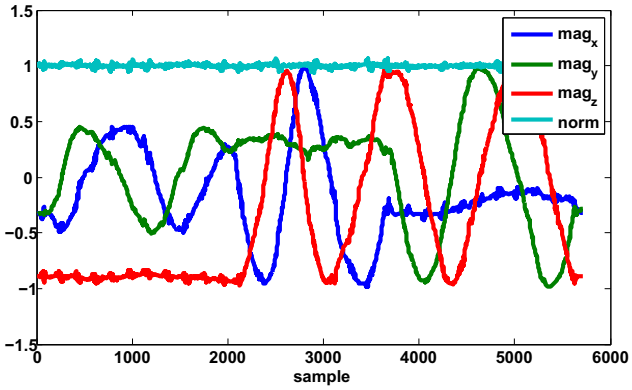

Fig. 7. Output data of the magnetic field sensor after calibration

B. Orientation determination

The study for sensor data fusion include a modified Kalman filter is used, which consists of two functions: the complementary separate-bias Kalman filtering for the motion modeling avoidance and data fusion; the magnetic disturbance detection and minimization for robustness and stability when experiencing local magnetic disturbances. In the complementary Kalman filter the integration of the Euler angles is performed outside of the Kalman filter. The advantage of this structure is that requires a much lower sampling rate and guarantees that the rapid dynamic response of the inertial system will not be compromised by the Kalman filter [11]. The idea of magnetic disturbance detection and minimization is that if magnetic disturbances are detected, the date fusion result will not depend on magnetometers, whose detail can be found in [12].

C. Position calculation

After determining the correct orientation information, the rotation matrix can be obtained to transform the acceleration from sensor body fixed frame to earth fixed frame. After two times integration, the position information can be obtained. However, the accumulated acceleration error will heavily pollute the position data, since the position information is no more correct.

In the whole phases of a stride during normal walking, there exists a time period when the foot is not moving related to the ground. This time period is called sill phase. Ojeda *et al.* [13] showed that the velocity value should be reset when still phase is detected, thus the accumulated errors from the accelerometer output could be effectively removed. This method is called Zero Velocity Update (ZUPT). Experimentally the best indication for still phase could be obtained by observing the three outputs of gyroscopes. If the norm value of gyroscopes outputs is smaller than the predefined threshold, we assume that the foot is experiencing still phase and the velocity can be reset. Fig.8 shows the difference of data output with ZUPT and without ZUPT algorithm.

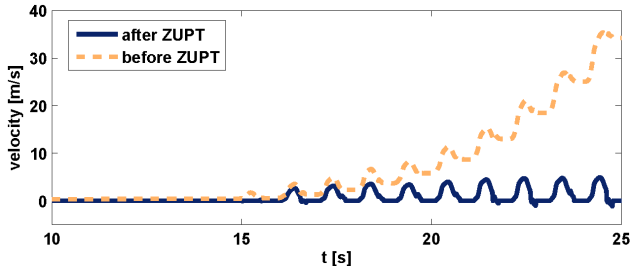

Fig. 8. Comparison between ZUPT applied and not applied velocity determinations

VI. Experiment

In an experiment the Micro-IMU was mounted on a human foot (Fig.9) for detecting a walk of 30 m distance in a floor of a building. During this experiement the yaw angle was oriented around 90 degrees (1.57 rad) four times. The measurement is shown in Fig.10

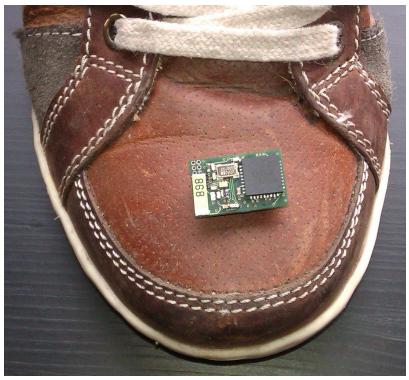

Fig. 9. For an experiment the Micro-IMU was mounted on a shoe

Fig.11 shows the calculated trajectory of the Micro-IMU with sensor data-fusion based on Kalman filter and ZUPT (Zero Velocity Update) Algorithm. The maximum deviation from the real track was 1 m.

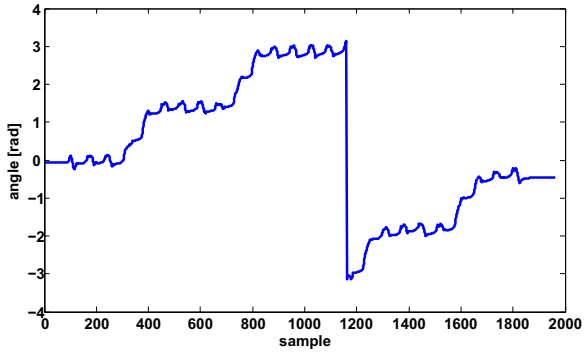

Fig. 10. Yaw angle measurement

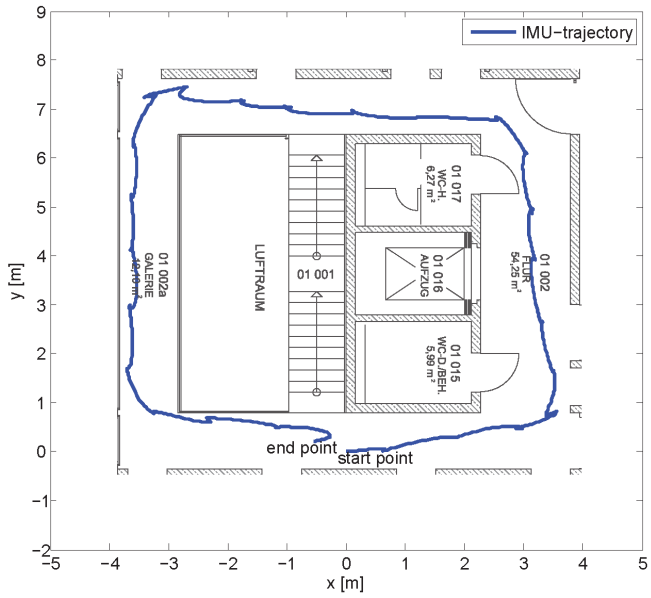

Fig. 11. Measured trajectory of the Micro-IMU from a walk in a floor of a building

VII. Conclusion and Future Work

In this paper, we presented the design of a wireless Micro-IMU that features minimum size and weight. By using highly integrated digital sensors and relocating data post-processing from the IMU to a base station, we are capable of competing with state-of-the-art commercial MEMS IMUs such as the Xsens MTi. This achievement is important for tracking people precisely in indoor areas. In the presented work the miniature size of the designed Micro-IMU made it possible to integrate the IMU into clothes or shoes. In an experiment the Micro-IMU was mounted on a shoe to track a person in a building. After a walk of 30 m the maximum deviation from the real track was 1 m.

In future we will use a motion capture system to measure the real walking track and to improve the filter parameters. Furthermore we will investigate the properties for localization of humanoids with limited load.

ACKNOWLEDGMENT

This work has been supported by the German Research Foundation (DFG) within the Research Training Group 1103 (Embedded Microsystems).

REFERENCES

[1] P. Bahl and V. Padmanabhan, "Radar: an in-building rf-based user location and tracking system," in *INFOCOM 2000. Nineteenth Annual Joint Conference of the IEEE Computer and Communications Societies. Proceedings. IEEE*, vol. 2, 2000, pp. 775 –784 vol.2.

[2] N. B. Priyantha, A. Chakraborty, and H. Balakrishnan, "The Cricket Location-Support System," in *MobiCom '00: Proceedings of the 6th annual international conference on Mobile computing and networking*, 2000, pp. 32–43.

[3] G. Borriello, A. Liu, T. Offer, C. Palistrant, and R. Sharp, "Walrus: wireless acoustic location with room-level resolution using ultrasound," in *Proceedings of the 3rd international conference on Mobile systems, applications, and services*, ser. MobiSys '05. New York, NY, USA: ACM, 2005, pp. 191–203. [Online]. Available: http://doi.acm.org/10.1145/1067170.1067191

[4] "Litef LITEF," 2011, [accessed 2012/04/20]. [Online]. Available: http://www.northropgrumman.litef.com/fileadmin/downloads/Datenblatt$_u$*IMU* − *I.pdf*

[5] "Xsens MTi," 2011, [accessed 2011/11/04]. [Online]. Available: http://www.xsens.com/en/general/mti

[6] J. Barton, A. Gonzalez, J. Buckley, B. O'Flynn, and S. O'Mathuna, "Design, fabrication and testing of miniaturised wireless inertial measurement units (IMU)," in *Electronic Components and Technology Conference, 2007. ECTC '07. Proceedings. 57th*, 29 2007-june 1 2007, pp. 1143 –1148.

[7] Z. Lin, M. Zecca, S. Sessa, L. Bartolomeo, H. Ishii, K. Itoh, and A. Takanishi, "Development of the miniaturized wireless inertial measurement unit wb-4: Pilot test for mastication analysis," in *System Integration (SII), 2010 IEEE/SICE International Symposium on*, dec. 2010, pp. 420 –425.

[8] Y.-L. Tsai, T.-T. Tu, and P. H. Chou, "Ecoimu: A compact, wireless, gyro-free inertial measurement unit based on two triaxial accelerometers." in *IPSN*, X. D. Koutsoukos, K. Langendoen, G. J. Pottie, and V. Raghunathan, Eds. IEEE, 2011, pp. 133–134. [Online]. Available: http://dblp.uni-trier.de/db/conf/ipsn/ipsn2011.htmlTsaiTC11

[9] F. Höflinger, J. Müller, M. Törk, L. Reindl, and W. Burgard, "A Wireless Micro Inertial Measurement Unit (IMU)," in *Proceedings of the IEEE International Instrumentation and Measurement Technology Conference (I2MTC)*, 2012.

[10] J. M. G. Merayo, P. Brauer, F. Primdahl, J. R. Petersen, and O. V. Nielsen, "Scalar calibration of vector magnetometers," *Measurement Science and Technology*, vol. 11, no. 2, p. 120, 2000. [Online]. Available: http://stacks.iop.org/0957-0233/11/i=2/a=304

[11] E. Foxlin, "Inertial head-tracker sensor fusion by a complementary separate-bias kalman filter," *Proceedings of the IEEE 1996 Virtual Reality Annual International Symposium*, vol. 96, pp. 185–194, 1996. [Online]. Available: http://ieeexplore.ieee.org/lpdocs/epic03/wrapper.htm?arnumber=490527

[12] R. Zhang and L. Reindl, "Pedestrian motion based inertial sensor fusion by a modified complementary separate-bias kalman filter," in *Sensors Applications Symposium (SAS), 2011 IEEE*, feb. 2011, pp. 209 –213.

[13] L. Ojeda and J. Borenstein, "Non-gps navigation for security personnel and first responders 1," *Journal of Navigation*, vol. 60, pp. 391–407, 2007.

Laser gyroscopes for very high sensitive applications

Jacopo Belfi*, Nicolò Beverini*, Bachir Bouhadef*, Giorgio Carelli*,
Davide Cuccato§¶, Angela Di Virgilio†, Andrea Licciardi¶, Enrico Maccioni*,
Antonello Ortolan§, Gilberto Saccorotti‡ and Fabio Stefani*
*Physics Department, University of Pisa, Italy
†INFN - Pisa, Italy
‡INGV - Pisa, Italy and Fondazione Prato Ricerche - Prato, Italy
§Laboratori Nazionali di Legnaro, INFN - Legnaro (Padova), Italy
¶Department of Information Engineering, Padova University, Italy

***Abstract*—We present a summary of the recent results obtained with the "G-Pisa" laser gyroscope prototype in the field of rotational metrology. The experimental apparatus consists in an He-Ne laser having a planar square cavity 1.35 m in side that can be operated both in the vertical and in the horizontal plane. For about one year, the ring laser has been utilized by the Virgo gravitational wave interferometer with the aim of estimating and monitoring the local rotational noise which is degrading the performances of its inertial suspensions. Results in the field of environmental monitoring for the improvement of the suspension control as well as the results in the field of rotational seismology are presented. In the last part of the paper we present some considerations about the possibility of performing a ground-based General Relativity test using an array of ring lasers.**

***Index Terms*—IEEEtran, journal, LaTeX, paper, template.**

I. Introduction

Optical interferometers can provide very accurate measurements of absolute rotations. By considering two light beams, counter-propagating inside a closed loop, it is possible to estimate the rotation rate of the local reference frame with respect to an inertial one. According to the Sagnac effect, the two counter propagating beams require different times to complete a round-trip. This time difference is proportional to the flux of the local angular velocity vector through the area enclosed by the optical path.

Among the fully optical rotation sensors, ring laser gyroscopes [1] are nowadays the best performing devices. In these systems two oppositely traveling laser beams are generated inside a ring optical cavity. Since the two beams resonate inside the cavity, the round-trip time difference induced by the rotation is converted into a frequency splitting f_S (Sagnac frequency). For a ring laser of area vector $\vec{A}$, perimeter p, wavelength λ, we have:

$$f_S = \frac{4\vec{A}\cdot\vec{\Omega}}{\lambda p} + f_{sys}, \tag{1}$$

being $\vec{\Omega}$ the angular velocity of the reference frame of the apparatus. The term f_{sys} includes all the non-idealities coming from the laser systematics [2]. They arise mainly from:

-geometrical instabilities in the optical cavity;
-non reciprocities in the cavity and in the active medium of the laser;
-nonlinear coupling between the two oppositely traveling laser modes due to backscattering;

Very large ring lasers, with side lengths of several meters, operate in different part of the world (see [3]) performing very accurate measurements of the Earth rotation rate for geodetic and geophysical purposes. This kind of applications require a very high resolution on the daily time-scale and thus the stability of these devices plays the crucial role. The need of a precise control of systematic errors sets an upper limit to the size of the presently best performing gyroscopes. Too large ring lasers (side lengths larger than 10 m), despite having an outstanding short term sensitivity [4] (directly connected to the area/perimeter ratio), have a degraded stability due to the fluctuation of their cavity geometry and orientation. The best trade-off between short term sensitivity and stability is represented by the ring laser "G", which has a square contour with an area of $16\ \mathrm{m}^2$. It is located at the Geodetic Observatory in Wettzell (Bavaria, Germany), and is manufactured from Zerodur, a glass ceramic with a thermal expansion coefficient less than $5\cdot10^{-9}/\mathrm{K}$. The instrument is installed in a thermally insulated and sealed environment with typical temperature variations of less than 5 mK per day and is kept in a pressure stabilized enclosure allowing the active stabilization of the cavity perimeter at the level of one part in 10^{-10} . During the years G has seen a continuous upgrading, that has made it the most precise Earth based rotation rate measurement device with resolution of about $5\cdot10^{-9}$ of the Earth rotation for an integration time of 30 minutes. The achieved stability of the ring allowed for detection of long-term effects, like the annual and Chandler wobbles [5]. The present stability of "G" is not very far from the threshold below which General relativity tests become possible with ring lasers, which are at the level of 10^{-10} of the Earth rotation. Further improvements in the ring laser technology will require:

-the extension of the active controls to all the relevant physical lengths by the use of ultra stable reference lasers;
-the realization of a tri-axial system for the complete recon-

struction of the local rotation vector;
-the accurate modeling of the systematics errors coming form the dynamics of atom-light interaction in the laser active medium.
In the first part of this paper we summarize the results obtained by operating the meter sized ring laser prototype "G-Pisa" after one year of activity by the Virgo Gravitational waves antenna, as a sensitive detector of the ground rotational motion. In the second part we report about the progresses in the design of a multi-axial ring laser system for the detection of the warping and twisting of local space-time produced by the Earth mass and angular momentum.

II. The "G-Pisa" ring laser

The concept of the ring laser prototype "G-Pisa" (see Fig.1) slightly differs from the one of "G" in Wettzell, the main difference residing in the design. The vacuum chamber hosting the optical cavity is rigidly fixed onto a granite slab which can be transported and arranged both in the vertical and in the horizontal orientation. While "G" has a monolithic structure that ensures an outstanding mechanical passive stability of the ring cavity, G-Pisa is made of modular elements and the requested effective stability is achieved by means of an active stabilization system based on PZT actuators displacing the cavity mirrors. The optical frequency of the laser gyroscope is compared to the optical frequency of another He-Ne laser absolutely stabilized to a selectable optical line of the iodine molecule. The main characteristics of the instrument are reported in table 2. The value of the single mirror total-loss corresponds to a nominal cavity quality factor[1] of $\sim 3.6 \cdot 10^{12}$. We performed an experimental verification of the cavity Q-factor, by means of a measurement of ring-down time of the intra-cavity light. In Fig.3 is reported a typical event of laser intensity decay after switching off the active medium power supply. The fitted value of 660μs corresponds to a Q factor $\sim 1.96 \cdot 10^{12}$. The discrepancy between the measured and the nominal cavity Q factors can be attributed to the insertion losses of the pyrex capillary (4 mm in internal diameter) in the middle of one side of the ring. It has a double role: making it possible to apply the RF discharge to the He-Ne gas and acting as spatial filter for the laser mode. Because of the filtering effect it introduces losses in the cavity and degrades the Q-factor of the optical resonator.

A. Monitoring of ground tilts at the Virgo area

The possibility of very precise measurements of rotations and tilts, not contaminated by translational accelerations, generates a large interest in the field of gravitational waves interferometers. Since the Virgo gravitational waves antenna is highly disturbed by rotational noise, we started a research activity in Pisa for the development of a meter sized ring laser dedicated to pure rotation measurement in the Virgo area as well as for fundamental Physics investigations [6], [7].

The ring laser prototype "G-Pisa" was set in operation in July 2008 [8]. Its concept slightly differs from the one of "G" in Wettzell, the main difference residing in the design. While "G" is made of a zerodur block that ensures an outstanding mechanical stability of the ring cavity, "G-Pisa" is composed by modular elements and the requested effective stability is achieved through the stabilization cavity geometry with respect to a reference laser by using PZT actuators acting on the

[1]The Q factor and the ring down time τ have been calculated according to the following definitions: $Q = \frac{2\pi\nu}{FSR \cdot l}$ and $\tau = \frac{Q}{2\pi\nu}$, where ν is the laser optical frequency, FSR is the cavity free-spectral-range and l is the total losses per round-trip.

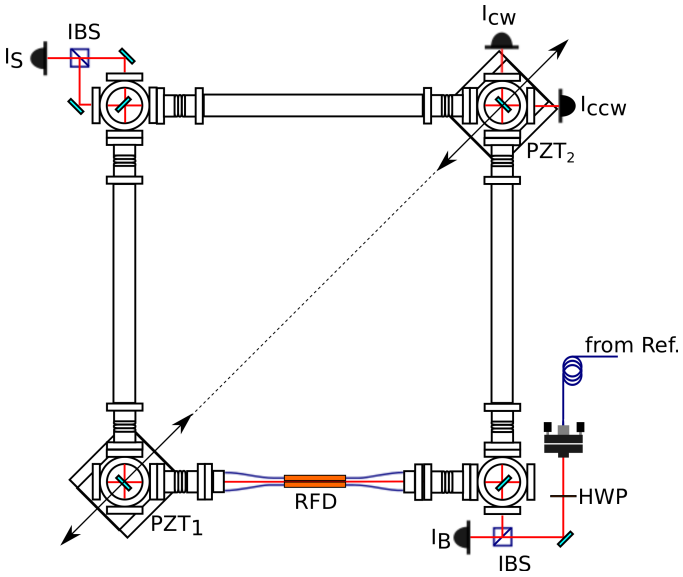

Fig. 1. G-Pisa experimental setup. The cavity vacuum chamber is entirely filled with a mixture of He-Ne and does not contain any intra-cavity element except for the four mirrors. I_S: Sagnac interference signal; I_{ccw}: counter-clockwise single beam intensity; I_{cw}: clockwise single beam intensity; I_B: optical beat intensity; RFD: radio frequency discharge; IBS: intensity beam splitter; HWP: half wave-plate; PZT: piezoelectric transducer.

G-Pisa	
Geometry	
Cavity	square
Side length	1.35 m
Latitude	43 40' 35.86"N
Cavity mirrors	
Radius of curvature	4 m
Total losses	3.7 ppm
Transmission	0.25 ppm
Scatter+absorption	3.5 ppm
Optical properties	
Wavelength	632.8 nm
Output power	1.6 nW (single mode)
Spatial mode	TEM_{00}
Beam waist (s,h)	(1.97 mm, 2.43 mm)

Fig. 2. Main nominal characteristics of the "G-Pisa" apparatus. Mirrors characteristics are the nominal ones (manufacturer information) and refer to an incidence angle of 45, and s-polarized light at 632.8 nm. Beam waists are reported as 4 times the $1/e^2$ beam intensity radius.

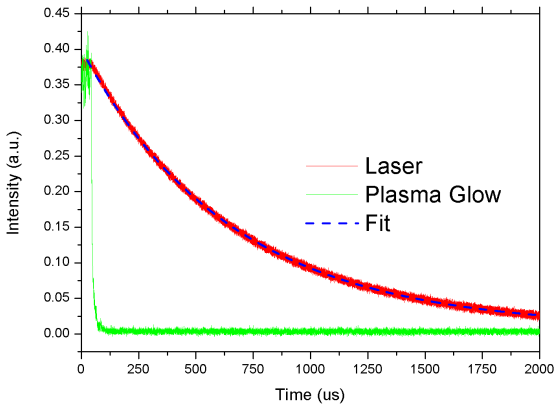

Fig. 3. Measurement of the ring-down time of the laser in the ring cavity. The measurement is performed by abruptly switching of the plasma glow. Both the plasma fluorescence and the laser intensity have been measured simultaneously. The fitted value for the laser decay time is $\tau \simeq 660\mu$s

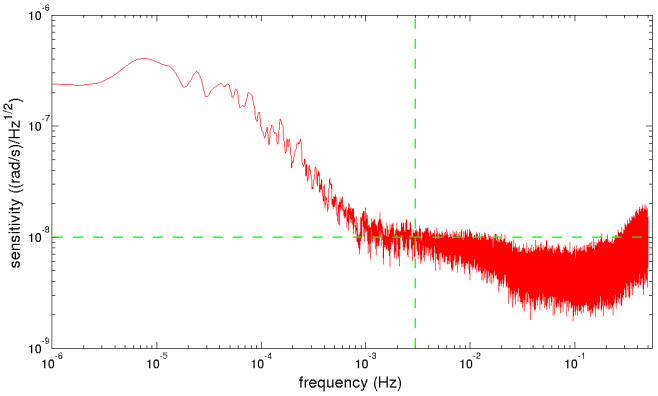

Fig. 4. Linear spectral density of the rotational noise detected at the Virgo site. The markers outline the region of sensitivity better than $10^{-}8\mathrm{rad/s}/\sqrt{\mathrm{Hz}}$ above 30mHz.

cavity mirrors. In 2010 the ring has been installed inside the central area of Virgo to monitor in situ the level of tilts and rotation of the floor of the Virgo central area. The device has been oriented horizontally and vertically, providing in this way measurements of tilts and rotations around the horizontal axis. The monument supporting the ring cavity, and allowing the measurement of horizontal or vertical rotations is described in detail in [9]. The gyroscope acquired data as a stand alone for several months without interruption. The data are kept inside Virgo's data. Fig.4 shows that the measured sensitivity limit was compatible with a noise level $< 10^{-8}(\mathrm{rad/s})/\sqrt{\mathrm{Hz}}$ above 30 mHz, required for studying and controlling the tilts in the Virgo inertial suspensions. Several analysis have been done and reported to Virgo with the precise measurement of the tilt motion induced by the strong wind.

B. Seismology of rotations

During the monitoring activity by the Virgo site, some results in the rising field of rotational seismology [10] have

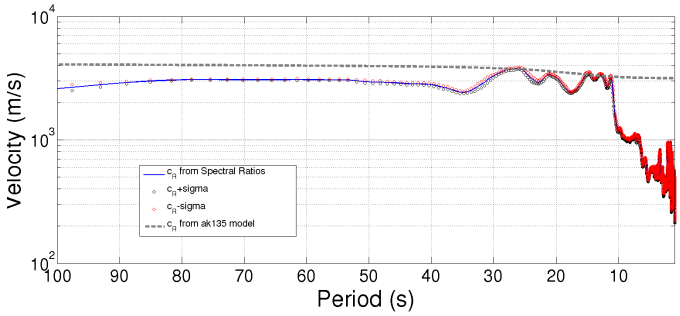

Fig. 5. Reconstructed dispersion curve for the Rayleigh waves at the Virgo site. The curve has been obtained as a spectral ratio between a collocated measurement of vertical acceleration and horizontal rotation.

been achieved. In [11], we performed a dedicated analysis of the Rayleigh waves generated by the $\mathrm{M_w} = 9.0$ Japanese earthquake of march 2011. Taking advantage of the environmental monitoring system of Virgo we have recently conducted some deeper investigations. In Fig.5 is shown the estimate of the Rayleigh waves phase velocity c_R for the above event. It is obtained by evaluating the spectral ratio between the local horizontal rotation detected by the ring laser and the vertical acceleration measured by a collocated accelerometer. The obtained dispersion curve is in agreement with the expectations from a standard model of Earth (ak-135), for time periods around 30 s. For shorter periods the measured dispersion curve deviates for the model predictions due to the local geology. For longer periods (>50 s) we obtain an under estimation of the phase velocity due to the limited response of the accelerometer (force-balanced episensor ES-T).

III. Design optimization: toward a General Relativity test

The recent progresses in the ring laser technology, represented by the performances of the "G" ring laser, triggered a recent proposal [12] to test the gravito-magnetism produced by the Earth using light as a probe. The basic idea of this experiment, named GINGER (Gyroscopes In General Relativity) is to compare two independent estimates of the Earth angular velocity vector: one performed in the Earth-based laboratory reference system with a ring laser array, say it $\vec{\Omega}$, and the other performed with respect to an inertial reference frame (distant observer), say it $\vec{\Omega}'$. According to the Einstein's Relativity predictions, to the leading order, the difference $\delta\vec{\Omega} = \vec{\Omega} - \vec{\Omega}'$ between the two measurements is given by:

$$\delta\vec{\Omega} \sim \frac{GM}{c^2 R}\Omega_E \sin\theta\, \hat{e_\theta} + \frac{G}{c^2 R^3} J_E[\hat{j} - 3\hat{J_E}\cdot\hat{u_r}] \qquad (2)$$

where G is the gravitational constant, R is the Earth mean radius, c is the speed of light, Ω_E is the Earth's angular velocity, M is the Earth mass, J_E is the Earth's angular momentum, θ is the laboratory colatitude,$\hat{j}$ is the direction of the Earth rotation vector, $\hat{e_r}$ and $\hat{e_\theta}$ are respectively the radial and the tangential directions in the local meridian plane. The first term is related to the Earth mass only and corresponds to the geodetic effect, it would be present even in the case of a

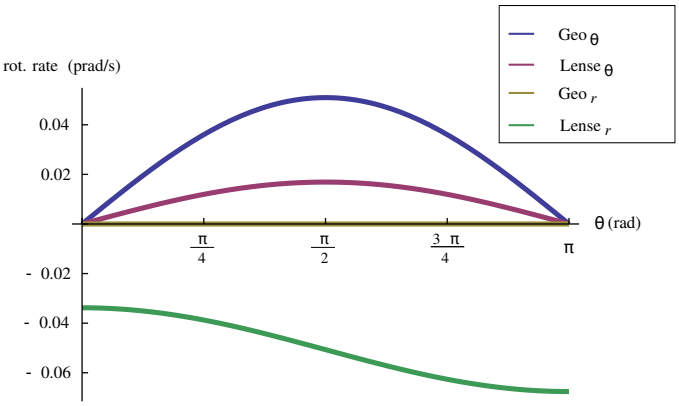

Fig. 6. The geodetic and the Lense-Thirring contributions in function of the colatitude θ of the laboratory. The two components along $\hat{e_r}$ and $\hat{e_\theta}$ are plotted separately.

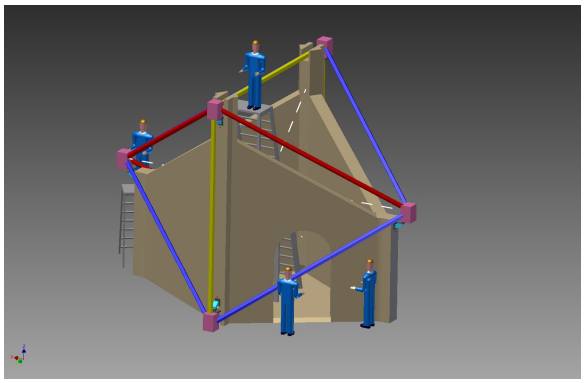

Fig. 7. A possible configuration of the GINGER ring lasers array for the Earth angular velocity measurements. The octahedral geometry allows to access the three components of the vector.

non rotating body. The second term is related to the rotation of the Earth mass and corresponds to the frame dragging or Lense-Thirring effect. In Fig. 6 are shown the contributions of the two terms in function of the colatitude of the laboratory.

A. *Requirements and measurement strategy*

The required resolution of the measurement must be better $10^{-14}\mathrm{rad/s}$ which is equivalent to say that the Earth angular velocity has to be measured better than one part in 10^9 on the surface of the planet. The proposed experiment is based on an array of ring lasers that can locally reconstruct with very high accuracy the Earth angular velocity vector. Such a vector contains both the geodetic and Lense-Thirring contributions of the rotating Earth. On the other hand, VLBI (Very Large Base Interferometer) determines with extremely high accuracy the pure angular velocity of the earth as it rotates with respect to quasars. The results from VLBI include anything perturbing the rotation rate of the planet, such as the effect of the plasticity of the crust and interior of the earth and the influence of the attraction of the moon and the sun, but are only marginally influenced by general relativity through the gravitational delay of clocks. Comparing the data from our ring-lasers array with VLBI, and subtracting the latter from the former we shall be left with the sought for general relativistic terms. The following guidelines for the realization of the proposed test have been defined up to now:

- Since a single ring laser can access only the projection of the angular velocity along one axes (e.g the normal to the ring plane), an array of at least three rings with the same sensitivity are required to gain full information on the angular velocity vector.
- An octahedral configuration (see Fig. 7) of the rings minimizes the number of mirrors (6 mirrors for 3 independent rings) and sets useful constrains to the relative alignment of two orthogonal rings. Octahedral configurations have been used so far for small ring laser systems employed as navigation systems, but not yet for high accuracy apparatus.
- Concerning sensitivity, the larger the ring the higher the Q of the cavity (with equal mirrors quality), the larger the scale factor, and moreover the output power of the laser increases. On the other hand, it is hard to have high mechanical stability of the resonant cavity in a too large ring. A system composed of rings 6 m in side each seems a natural upgrading of G. Larger resonant cavities, with sides of the order of 20 m, have been realized [4] but their performances are limited by the geometry stability.
- The detector design cannot be a simple rescaling of G-Wettzel by a certain factor since it is made of a single block of Zerodur (a glass with thermal expansion coefficient close to zero). Building an array of etherolithic ring lasers, attached to a single monument seems a natural choice. The prototype "G-Pisa", based on a modular mechanical design consisting of four mirror holders connected by a tube has been selected for the implementation of a multi-axial system, rigidly attached to a same monument, made of concrete or granite. The actual material has to be carefully chosen in order to reduce the impact of thermal changes. If necessary, thermal stabilization of the whole apparatus will be provided.
- In order to reduce the influence of the Earth crust motion, due to the wind, rain and weather seasonal changes, pressure loading etc. an underground laboratory (e.g. Gran Sasso or other Laboratories) is highly desirable. In addition a diagnostic apparatus based on mechanical tilt-meters will be necessary for the monitoring of the rotations induced by the environmental fluctuations.

IV. Conclusion

We reported the recent results of the "G-Pisa" ring laser in the field of rotational metrology. It has been shown that a transportable apparatus with meter sized dimensions can be suitably employed in the field of rotational motion control in the large interferometers for gravitational waves as well as a seismic rotation sensor. We also summarized the requirements and the strategy at the base of GINGER, an experiment for detecting general relativistic rotations with a ring laser array

based on ground. The most demanding properties of such apparatus rely with the control of the system geometry and the independent subtraction of the local rotations from the signal given by the Earth rotation rate.

ACKNOWLEDGMENT

We thank U. Schreiber, A. Gebauer and A. Velikoseltsev for the very useful discussions. We acknowledge G. Balestri, G. Petragnani, and A. Soldani from the INFN, section of Pisa, M. Francesconi, F. Francesconi, S. Gennai, M. Marinari and R. Passaquieti from the Physics Department of Pisa.

REFERENCES

[1] G. E. Stedman, *Ring-laser tests of fundamental physics and geophysics*, Reports on Progress in Physics, vol. 60(6):615688, 1997.

[2] F. Aronwitz *Theory of a Traveling-Wave Optical Maser*, Phys. Rev. 139, A635A646, 1965.

[3] http://www.ringlaser.org.nz.

[4] R.B. Hurst et al. *Experiments with a 834 m^2 ring laser interferometer*, Journal of Applied Physics, 105, 113115, 2009.

[5] K. U. Schreiber, T. Klgel, J-P. Wells, R. B. Hurst, and A. Gebauer, *How to detect the chandler and the annual wobble of the earth with a large ring laser gyroscope*, Physical Review Letters, vol. 107(17):1739041 1739044, 2011.

[6] J. Belfi, N. Beverini, A. Di Virgilio, A. Gebauer, A. Ortolan, K. U. Schreiber, A. Tartaglia, J-P. R. Wells, *A laser gyroscope system to detect the Gravito-Magnetic effect on Earth*, GRF2010 essay in the December 2010 Special Issue of Int. J. Mod. Phys. D.19, No. 14, pages 2331-2343, doi:0.1142/S0218271810018360, 2010.

[7] J. Belfi, N. Beverini, F. Bosi, G. Carelli, A. Di Virgilio, D. Kolker, E. Maccioni, A. Ortolan, R. Passaquieti and F. Stefani, *Performance of G-Pisa ringlaser gyro at the Virgo site*, Journal of seismology, DOI: 10.1007/s10950-012-9277-8, 2012.

[8] J. Belfi, et al. *Active control and sensitivity of the G-Pisa gyrolaser*, Il Nuovo Cimento, Vol. 125 B, N. 5-6 , 2010.

[9] J. Belfi ,N. Beverini, F. Bosi, G. Carelli, A. Di Virgilio, E. Maccioni, A. Ortolan and F. Stefani, *A 1.82 m^2 ring laser gyroscope for nano-rotational motion sensing*, Applied Physics B, vol. 106, p. 271-281, 2011.

[10] http://www.rotational-seismology.org

[11] N. Beverini, G. Carelli, A. Di Virgilio, E. Maccioni, G. Saccorotti, F. Stefani and A. Velikoseltsev, *Horizontal rotation signals detected by G-Pisa ring laser for the M_w = 9.0, March 2011, Japan earthquake*, Journal of Seismology, pp. 1-10, doi:10.1007/s10950-012-9276-9, 2012.

[12] J. Belfi, F. Bosi, G. Cella, A. Di Virgilio, A. Ortolan, A. Porzio, S. Solimeno, M. Cerdonio, J. P. Zendri, M. Allegrini, N. Beverini, B. Bouhadef, G. Carelli, I. Ferrante, E. Maccioni, R. Passaquieti, F. Stefani, M. L. Ruggiero, A. Tartaglia, K.U. Schreiber, A. Gebauer, J-P. R. Wells, *Measuring Gravito-magnetic Effects by Multi Ring-Laser Gyroscope*, Phys. Rev. D 84, 122002, 2011.

A small-linewidth absolute optical frequency source

S. M. F. Raupach, T. Legero, A. Bauch, C. Grebing, Ch. Hagemann, T. Kessler, A. Koczwara, B. Lipphardt, H. Schnatz, U. Sterr, and G. Grosche

Physikalisch-Technische Bundesanstalt (PTB),
Bundesallee 100, 38116 Braunschweig, Germany
sebastian.raupach@ptb.de

Abstract— **We describe a system that combines a cavity-stabilized laser, a hydrogen maser and a cesium fountain clock. It provides an optical reference frequency that over the course of half a day drifts with less than 100 µHz/s. Furthermore it allows for a convenient measurement of an absolute frequency in the optical domain**.

I. INTRODUCTION

An absolute optical reference frequency, distributed via fiber networks, would benefit clients both in academia and industry

Lasers stabilized to a Fabry-Pérot cavity [1,2] made e.g. from ultralow expansion (ULE) glass, achieve low fractional frequency instabilities (Allan deviation) of around 10^{-15} or less for averaging times on the order of one second. However, due to aging of the cavity material and residual thermal and mechanical instabilities they exhibit nonlinear as well as linear drifts of their frequency.

Hydrogen masers on the other hand suffer from comparatively high short term noise on the order of 10^{-13} for averaging times of one second, but reach fractional instabilities on the order of 10^{-15} for averaging times of around 3000s and beyond, with exceedingly small long term drifts on the order of 10^{-13}/yr. The maser performance can conveniently be brought to the optical domain by locking the repetition rate of a frequency comb to the maser in analogy to [3].

Here we describe a system, that combines the stabilities provided by a Fabry-Pérot cavity stabilized laser and a hydrogen maser [4]. To achieve absolute frequency accuracy, the maser is furthermore referenced to a primary frequency standard [5]. The maser could in fact be replaced by directly locking the comb to the primary frequency standard, provided that it operates almost continuously.

II. DESCRIPTION

To achieve the desired combination of stabilities, a DFB fiber laser operating at a frequency of 194 THz is phase-locked as a slave laser to a Fabry-Pérot cavity stabilized master laser, which also operates at 194 THz. Typical cavities are made from ULE glass; the ULE used here exhibits a typical linear frequency drift on the order of 100 mHz/s, leading to a monotonical increase in frequency instability (Allan deviation) with increasing averaging time. As illustrated by fig. 1, even after subtracting a linear fit to the frequency time trace, considerable frequency fluctuations exceeding 10^{-14} (at an averaging time of 100 s) remain.

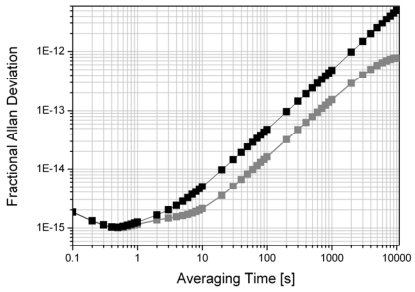

Figure 1. Fractional overlapped Allan deviation of the beat freqeucny between the ULE-cavity stabilized master laser and the Silicon-cavity stabilized master laser (black symbols); after removing a linear fit from the frequency data, strong non-linear frequency variations remain, here visible as stability fluctuation (grey symbols).

Now, simultaneously the beat note of the slave laser against the closest comb mode of a frequency comb is measured. The comb is a commercial, fibre-based femtosecond comb, the repetition rate of which is locked to an active hydrogen maser of PTB.

The beat frequency against the comb is fed into a phase comparator to generate an error signal. The error-signal is low-pass filtered and acts onto the phase-locked loop of the lock to the cavity-stabilized master laser to correct for the master laser's slow frequency variation.

To evaluate the performance, two independent systems with individual masers and master lasers were realized and measured against each other [4], where the second master laser was stabilized to a cryogenic silicon cavity [6].

III. RESULTS

For evaluation, the beat frequency between the two systems' slave lasers was analyzed. Calculating the fractional Allan deviation from the frequency time trace, we observe relative fractional instabilities below 5e-15 for averaging times of less than a second up to several thousands of seconds, with an average frequency drift of less than 100 µHz/s over half a day. Figure 2 demonstrates that the system's stability on longer time-scales is dominated by the maser's frequency behaviour.

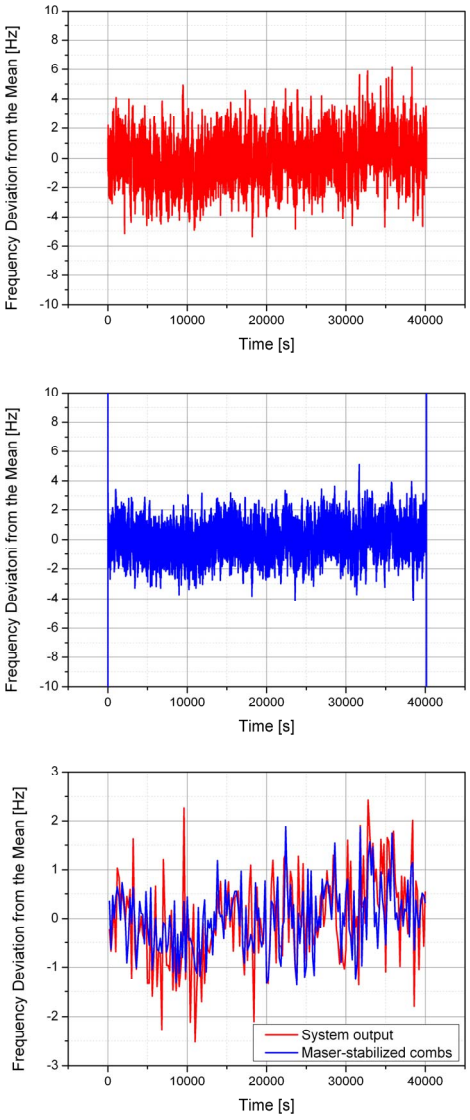

Figure 2. Top panel: Time trace of the beat frequency between the two systems at a gate time of 1 s; middle Panel: time trace (100 s sliding average) of the (virtual) beat note, obtained by beating one of the slave lasers against both combs, where each comb is stabilized to its individual hydrogen maser; bottom panel: time traces of the inter-system beat frequencies (red) and the inter-comb beat frequencies (blue) at a numerical gate time of 200 s.

As the masers were referenced to PTB's cesium fountain clock, a measurement against the system's output would allow for the convenient determination of an absolute optical frequency.

REFERENCES

[1] B. C. Young, F. C. Cruz, W. M. Itano, and J. C. Bergquist, "Visible lasers with subhertz linewidths," Phys. Rev. Lett., vol 82, pp. 3799-3802, 1999

[2] J. Alnis, A. Matveev, N. Kochalevsky, Th. Udem, and T. W. Hänsch, "Subhertz linewidth diode lasers by stabilizaion to vibrationally and thermally compensated ultralow-expansion glass Fabry-Pérot cavities,": Phys. Rev. A, vol. 77, 053809, 2008.

[3] J. Reichert, M. Nierung, R. Holzwarth, M. Weitz, Th. Udem, and T. W. Hänsch, " Phase coherent vacuum-ultraviolet to radio frequency comparison with a mode-locked laser," Phys. Rev. Lett., vol. 84, pp. 3232-3235, 2000.

[4] *S. M. F. Raupach et al, unpublished.*

[5] A. Bauch, S. Weyers, D. Piester, E. Staliuniene, and W. Yang, "Generation of UTC(PTB) as a fountain-clock based time scale," Metrologia, vol. 49, pp. 180-188, 2012.

[6] T. Kessler, C. Hagemann, C. Grebing, T. Legero, U. Sterr, F. Riehle, M. J. Martin, L. Chen, and J. Ye, " A sub-40 mHz linewidth laser based on a silicon single-crystal optical cavity," arXiv1112.3854v1.

Mid-IR frequency measurement using an optical frequency comb and a long-distance remote frequency reference

B. Chanteau, O. Lopez, F. Auguste, B. Darquié, C. Chardonnet, A. Amy-Klein
Laboratoire de Physique des Lasers (LPL)
CNRS and Université Paris 13
Villetaneuse, France
bruno.chanteau@univ-paris13.fr

W. Zhang, G. Santarelli, Y. Le Coq
LNE-SYRTE
Observatoire de Paris, CNRS, UPMC
Paris, France

***Abstract*—We have built a frequency chain which enables to measure the absolute frequency of a laser emitting in the 28-31 THz frequency range and stabilized onto a molecular absorption line. The set-up uses an optical frequency comb and an ultrastable 1.55 µm frequency reference signal, transferred from LNE-SYRTE to LPL through an optical link. We are now progressing towards the stabilization of the mid-IR laser via the frequency comb and the extension of this technique to quantum cascade lasers. Such a development is very challenging for ultrahigh resolution molecular spectroscopy and fundamental tests of physics with molecules.**

I. INTRODUCTION

Ultrahigh resolution molecular spectroscopy is an alternative tool to atoms to perform tests of fundamental physics, such as the search for the non conservation of parity [1], the temporal stability of the electron-to-proton mass ratio [2], or the electron electric dipole moment [3]. Many of these tests rely on the availability of ultrastable and accurate laser sources emitting in the mid-IR where molecules exhibit rovibrational transitions. It is thus very challenging to develop a frequency stabilization or measurement scheme in the mid-IR which does not depend on quite rare frequency secondary references. Such high sensitivity spectroscopy experiments have been performed using an optical frequency comb. In that case, the IR frequency is compared to a high-harmonic of the comb repetition rate with a sum or difference frequency generation in a non linear crystal and a Ti:Sa optical frequency comb. It has been demonstrated at 10 µm with a CO_2 laser [4], at 3.4 µm using a HeNe laser [5], and recently extended to quantum cascade lasers at 5 µm [6], and 3.4 µm using a fiber comb [7].

II. EXPERIMENTAL SET-UP

In our case, we have built a frequency chain with two fiber femtosecond lasers, a remote optical reference and an optical link, which enables to measure the absolute frequency of a CO_2 laser, emitting in the 28-31 THz frequency range, against an optical reference from the LNE-SYRTE (Fig. 1). The CO_2 laser, located at LPL, is stabilized onto a molecular absorption line.

The optical reference is a fiber laser, emitting at 1.55 µm, locked to a very high finesse cavity with the Pound-Drever-Hall method. A fiber femtosecond laser, centered at 1.55 µm, is phase-locked to the ultrastable laser. The repetition rate of this femtosecond laser is then compared to the primary standards of LNE-SYRTE (H-maser, cryo-oscillator, caesium fountain). This scheme enables to measure the absolute frequency of the ultrastable laser and therefore compensate the cavity drift, which is critical for some high sensitive spectroscopy experiments, as for example the parity violation experiment [1]. This optical reference is then sent through a 43-km long optical link to LPL [8].

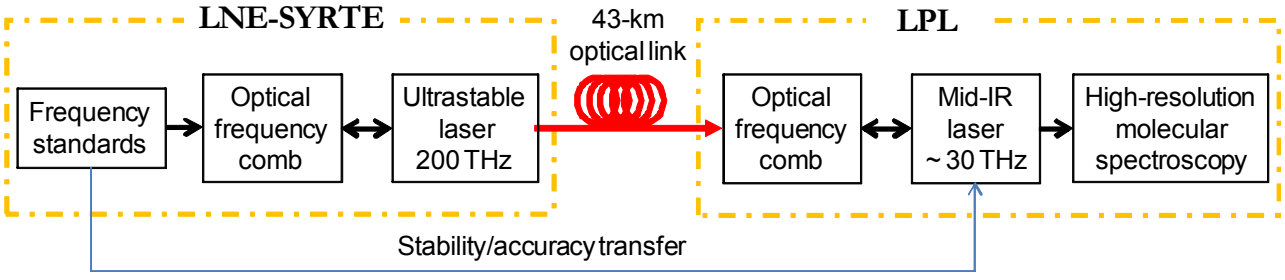

Figure 1. Mid-IR frequency measurement principle

The authors acknowledge funding support from *ANR*, *LNE*, *CNRS* and *Université Paris 13*.

At LPL, we aim at measuring ?? the frequency of a CO_2 laser, at around 10 µm, locked to an absorption line of the molecule OsO_4. A fiber femtosecond laser at 1.55 µm is used to transfer the optical reference stability and accuracy to the IR laser. The modes frequencies can be written as:

$$\nu_p = p\, f_{rep} + f_{CEO} \quad (1)$$

where p is an integer near 780 000. The optical reference is used to lock the repetition rate of the comb. After removing the offset frequency f_{CEO}, we have:

$$f_{rep} = \frac{1}{N}(\nu_{ref} - \Delta_{ref}) \quad (2)$$

with f_{rep} the repetition rate, N an integer near 780 000, ν_{ref} the optical reference frequency, and Δ_{ref} the beatnote between the ultrastable laser and the femtosecond laser. Then, low-frequency modes are generated in a non linear fiber in order to obtain a comb centered around 1.85 µm. This comb is mixed with the CO_2 laser in a non linear crystal leading, via sum frequency generation, to a shifted comb of frequencies:

$$\nu_q + \nu_{CO_2} = q\, f_{rep} + f_{CEO} + \nu_{CO_2} \quad (3)$$

with ν_q the frequency of one mode of the comb, ν_{CO_2} the CO_2 laser frequency, q an integer around 660 000. The beatnote Δ_{CO_2} between this shifted comb and the comb directly issued from the femtosecond laser, with modes ν_p gives:

$$\begin{aligned}\Delta_{CO_2} &= (q\, f_{rep} + f_{CEO} + \nu_{CO_2}) - (p\, f_{rep} + f_{CEO}) \\ &= \nu_{CO_2} - (p-q) f_{rep}\end{aligned} \quad (4)$$

In combination with (2), we obtain:

$$\nu_{CO_2} = \frac{p-q}{N}(\nu_{ref} - \Delta_{ref}) - \Delta_{CO_2} \quad (5)$$

with $p-q$ is near 120 000. Thus the CO_2 laser frequency is compared to a high-harmonic of the comb repetition rate [4]. Finally, the CO_2 laser frequency can be measured against the frequency standards of LNE-SYRTE.

III. Results and Perspectives

With this set-up, we measured the frequency of a CO_2 laser, locked to an OsO_4 saturation line, with a relative stability of 6×10^{-14} after 1 s integration time, not limited by the measurement set-up [9], even without compensating the optical link used for the experiments (Fig. 2). The measurements duration is however limited by the chemical stability of OsO_4 molecules, which degrade after a few hours. We have also measured the absolute frequency of the CO_2 laser, and we obtained a value consistent with the previous measurements [10]-[11].

We are now progressing towards the stabilization of the CO_2 laser via the frequency comb. Because molecules degrade over a few hours, the CO_2 laser frequency drifts. First results of stabilization show that this drift has been removed. The next step is to lock the CO_2 laser directly to the optical reference,without prestabilization on a molecular absorption line. This is necessary for the parity non conservation experiment since left- and right-handed molecules lines are alternately measured in a supersonic beam [1].

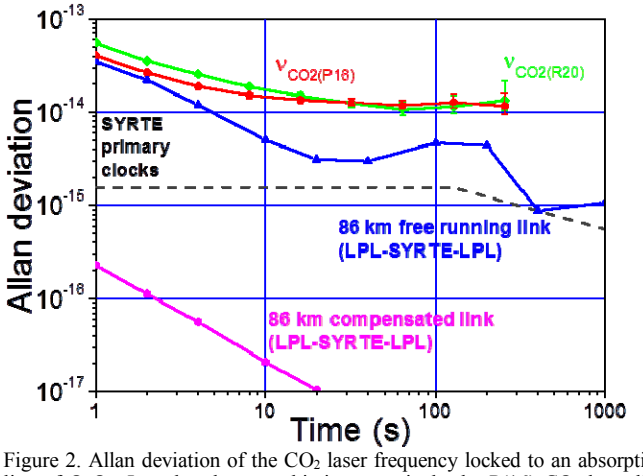

Figure 2. Allan deviation of the CO_2 laser frequency locked to an absorption line of OsO_4. In red and green, this is respectively the P(16) CO_2 laser line near the $^{190}OsO_4$ P(55) line and the R(20) CO_2 laser line near the $^{192}OsO_4$ R(67) line. In blue and magenta, typical stability of optical link used for the IR frequency measurement experiments. Dashed line : combination of the ultrastable laser and primary standards of LNE-SYRTE stabilities.

In the future, we will extend this stabilization/measurement scheme to quantum cascade lasers. Among several constraints, the ideal molecule for the parity violation experiment must have a rovibrational absorption line in the spectral range of an ultrastable laser. Till now, we were limited to the CO_2 laser, which emits in spectral windows about 1 GHz wide every 30-50 GHz, between 9 and 11 µm. With a quantum cascade laser, we can access a continuous spectral range of 200 GHz, at any wavelength between 2 and 20 µm. This would simplify the optical scheme of any ultrahigh sensitivity IR spectroscopy measurement.

References

[1] B. Darquié et al, "Progress toward a first observation of parity violation in chiral molecules by high-resolution laser spectroscopy," Chirality, vol. 22, pp. 870-884, 2010.

[2] A. Shelkovnikov, R.J. Bucher, C. Chardonnet, A. Amy-Klein, "Stability of the Proton-to-Electron mass ratio," Phys. Rev. Lett., vol. 100, p. 150801-150803, 2008.

[3] J. J. Hudson, D. M. Kara, I. J. Smallman, B. E. Sauer, M. R. Tarnutt, E. A. Hinds, "Improved measurement of the shape of the electron," Nature, vol. 473, pp. 493-497, 2011.

[4] A. Amy-Klein, A. Goncharov, M. Guinet, C. Daussy, O. Lopez, A. Shelkovnikov, C. Chardonnet, "Absolute frequency measurement of an SF_6 two-photon line using a femtosecond optical comb and sum-frequency generation," Opt. Lett., vol. 30, p. 3320-3322, 2005.

[5] S. M. Foreman et al., "Demonstratin of a HeNe/CH4-based molecular clock," Optics Letters, vo. 30, pp. 570-572, 2005.

[6] S. Borri et al., "Direct link of a mid-infrared QCL to a frequency comb by optical injection," Optics Letters, vol.37, pp. 1011-1013, 2012.

[7] M. A. Gubin et al., "Femtosecond fiber laser based methane optical clock," Appl. Phys., vol. 95, pp 661-666, 2009.

[8] O. Lopez et al., "Cascaded multiplexed optical link on a telecommunication network for frequency dissemination," Opt. Expr., vol. 18, p. 16849-16857, 2010.

[9] V. Bernard et al, "CO_2 laser stabilization to 0.1-Hz level using external electrooptic modulation," IEEE J. of Quant. Electr., vol. 33, pp. 1282-1287, 1997.

[10] O. Acef, F. Michaud, and G.D. Rovera, "Accurate determination of OsO_4 absolute frequency grid at 28/29 THz," IEEE Trans. Instr. Meas., vol. 48, pp. 567-570, 1999.

[11] A. Amy-Klein, A. Goncharov, C. Daussy, C. Grain, O. Lopez, G. Santarelli, C. Chardonnet, "Absolute frequency measurement in the 28-THz spectral region with a femtosecond laser comb and a long-distance optical link to a primary standard," Appl. Phys., vol. 78, pp. 25-30, 2004.

Cr:ZnSe Laser with 0.03 Hz/Hz$^{1/2}$ Frequency Noise for Compact Methane Based OFS

M. Gubin, M. Frolov, A. Kireev, Yu. Korostelin, V. Kozlovskyi, Yu. Podmar'kov, A. Shelkovnikov, D. Tyurikov
P.N. Lebedev Physical Institute
Moscow, Russia
Email: gubin@sci.lebedev.ru

V. Lazarev, A. Pnev
Bauman Moscow State Technical University
Moscow, Russia

***Abstract*— The mid-IR cw tunable solid state Cr^{2+}:ZnSe laser with spectral density of intrinsic frequency noise less than 30 mHz/Hz$^{1/2}$ was created. The laser was applied for sub-Doppler spectroscopy of ($\nu_1+\nu_4$) vibrational-rotational band of methane and narrow resonances of saturated dispersion at $\lambda = 2.36$ μm were demonstrated for the first time. Characteristics of resonances and low frequency noise of the laser pave the way to a short-term frequency stability at the level of $10^{-15} - 10^{-16}$.**

I. INTRODUCTION

The development of compact optical frequency standards (OFS) with a short/long-term stability at the level of $\sigma = 10^{-15}$-10^{-16} (σ - Allan standard deviation) for averaging time $\tau = 1$-10^5 s is one of the hot demands in time-frequency metrology, navigation, fundamental experiments [1-3]. High-stability frequency standards based on cooled atoms in optical traps or ions in Paul traps with accuracy 10^{-17} and higher need an interrogative oscillator with radiation linewidth at sub-Hertz level. Another important problem is associated with creation of permanently working clocks (flywheels) with middle and long-term stability comparable or better than that of the active H-masers but more compact and with less severe requirements to environmental conditions.

There are two well developed concepts for new generation of superstable interrogative oscillators: (1) lasers stabilized over superhigh-Q ULE/Silicon cavities [4]; (2) microwave whispering gallery mode cryocooled sapphire oscillators [5]. Each concept has its own advantages and disadvantages: temporal drift after averaging time $\tau > 10$ s for ULE cavities, or big mass and power consumption for commercially available cryocooled sapphire oscillator - ULISS model [6]. Here we propose another way for realization of superstable interrogative oscillator based on lasers stabilized over narrow saturated absorption/dispersion resonances (SA, SD) at methane spectral lines in 2.3-3.4 μm wavelength region.

There are a number of attractive features of methane stabilized laser as compared to other gas-cell OFS (Nd:YAG/I_2 for example): (1) small natural linewidth - $\gamma_{nat} = 0.1$-10 Hz; (2) high absorption coefficient - (0.2-20) cm^{-1}Torr^{-1} (for ν_3 band lines at 300K-77K); (3) spherical symmetry and as a consequence - absence of linear Zeeman shift and reduced collisional shift; (4) chemical passivity, i.e. no "windows chemistry".

Accidental coincidence of a He-Ne laser radiation wavelength (3.39 μm) with $F_2^{(2)}$ component of P(7) line of methane ν_3 band initiated a lot of research started with pioneer papers of V.Letokhov, J.Hall and V.Chebotayev with colleagues since 1967 [7, 8 and references therein]. Among numerous results of these research portable He-Ne/CH_4 OFS with stability $\sigma = 1\cdot10^{-14}$ for $\tau = 1$ s, and repeatability of $1\cdot10^{-13}$ were realized [9, 10].

The new stage for CH_4 based OFS started when low loss mid-IR laser crystals operating in 2.0-3.5 μm spectral range have been grown [11]. With Cr^{2+}:CdSe, Cr^{2+}:ZnSe crystals cw generation at room temperature was demonstrated [12, 13]. It means that any of several hundreds of CH_4 lines in these range with typical intensities (10^{-19}-10^{-21}) cm^{-1}/mol·cm^{-2} [14] is accessible and can be tested as a frequency reference.

One of the main peculiarities of Cr^{2+}:CdSe and Cr^{2+}:ZnSe lasers is 2-3 orders higher output power as compared to traditional He-Ne laser: 10-100 mW instead of 50-100 μW. It means that very low Schawlow-Townes noise limit (~0.001 Hz/Hz$^{1/2}$) is achievable with these lasers. This is a significant detail because in our case the ultimate achievable frequency stability is directly determined by Schawlow-Townes noise.

The high output power of Cr-doped solid state laser also simplifies the connection between this laser and a femtosecond frequency comb.

At the same time there is a problem of oversaturation of CH_4 transition in the case of an intracavity absorption cell. It

This research is funded in part by Russian Academy of Science under programs "Fundamental optical spectroscopy and its application" and "Extreme light fields and their application" and by Russian Ministry of Education and Science under contract no. 16.513.11.3115

can be solved by different methods and one of the ways is to select less intensive lines.

In the methane vibrational-rotational absorption bands ν_3 and $(\nu_1+\nu_4)$ lying in the spectral range of interest (2.2-3.5 μm, Fig. 1) it is possible to find transitions which have appropriate line strength, absorption coefficient, simple structure and are perspective for further frequency stabilization of solid state lasers based on the Cr-doped CdSe and ZnSe crystals.

II. EXPERIMENT

In present work we developed a tunable solid state optically pumped Cr^{2+}:ZnSe laser for registration of narrow saturated dispersion resonances at $(\nu_1+\nu_4)$ vibrational-rotational band of methane at 2.3-2.5 μm.

A. Scheme of the Cr^{2+}:ZnSe Laser

For the implementation of the Cr^{2+}:ZnSe /CH_4 OFS we plan to use two-mode method of saturation spectroscopy which was successively applied in our He-Ne/CH_4 systems [15]. As a first step we developed a two-mode cw Cr^{2+}:ZnSe laser. The laser resonator is an astigmatically compensated [16] four mirror folded cavity with 2% output coupler (Fig. 2). A Lyot filter is used for laser wavelength tuning and an intracavity Fabry-Perot etalon (uncoated 8-mm CaF_2 plate) serves as a fine selector. The laser operates at two adjacent longitudinal modes with frequency difference $\omega_{12} \sim 150$ MHz. A cw Tm fiber laser at 1.94 μm with maximum output power 2.8 W is used for optical pumping. Typical output power of the Cr^{2+}:ZnSe laser is in the range of 60-80 mW through the 2.3-2.5 μm tuning spectral range.

Two principal experiments were carried out in present research: (1) measurement of intrinsic frequency noise of the Cr^{2+}:ZnSe solid state laser; (2) observation of SD resonances at R(2) CH_4 line at 2.36 μm.

B. Measurement of the Beat Frequency Noise Spectral Density

The intermode beat signal at 150 MHz was detected by InAs photodiode, demodulated by frequency-to-voltage converter and analyzed with FFT spectrum analyzer. Spectral density of beat frequency fluctuations $\delta\omega_{12}$ for the free running Cr^{2+}:ZnSe laser at 75 mW output power is presented in Fig. 3 (curve 2). For estimation of the laser natural frequency noise it is necessary to exclude residual technical frequency fluctuations at Fourier frequencies less than 2 kHz. The minimum observed value of spectral density $\delta\omega_{12} = 0.03\text{-}0.05$ Hz/Hz$^{1/2}$ at Fourier frequencies 2-10 kHz gives the upper limit of the laser natural frequency noise.

The F/V converter frequency noise was measured with a signal generator and is depicted in Fig. 3 by curve 1. It is seen that the laser real frequency noise does not exceed frequency noise of the F/V converter used for measurements. Calculated Shawlow-Townes spontaneous fluctuations limit shown by the dashed line in Fig. 3 is at millihertz level (0.008 Hz/Hz$^{1/2}$). Estimation has been made for the laser power 75 mW and the resonator round trip losses 10%.

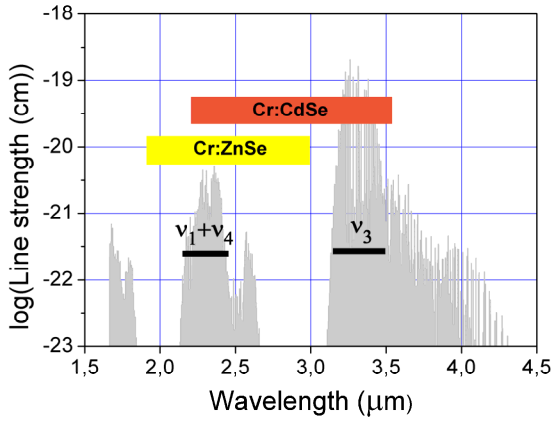

Fig. 1. CH_4 spectrum of interest.

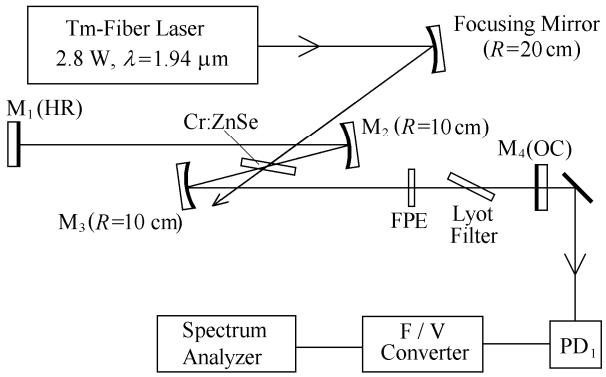

Fig. 2. The scheme of the cw two-mode Cr^{2+}:ZnSe laser. FPE – Fabry-Perot etalon, PD – photodetector.

C. Resonances of Saturated Dispersion at E-Component of the R(2) Line Methane $(\nu_1+\nu_4)$ Band

For the second experiment the laser scheme was slightly changed: Lyot filter and the output mirror were replaced with diffraction grating (600 grooves/mm) for more precise wavelength tuning and FP etalon was replaced with PZT tuned air-spaced interferometer (15 GHz free spectral range). Also a 20 cm long CH_4 absorption cell with liquid nitrogen cooled jacket was placed inside the laser cavity. In this scheme we observed methane lines in 2.3-2.5 μm spectral range. The SD resonances at E - component of the R(2) line ($\lambda = 2.36$ μm) at room and liquid nitrogen temperatures are shown in Fig. 4. Two factors make this line attractive as a frequency reference: first – it has no hyperfine structure and second – it belongs to a transition with low rotational number J = 2. The latter means that the absorption coefficient can be significantly increased by methane cooling.

At 300K and methane pressure $p_{CH4} = 10$ mTorr the observed SD resonance peak-to-peak amplitude was $\Delta\omega_{12} = 2$ kHz . At 77K and $p_{CH4} = 1$ mTorr we obtained $\Delta\omega_{12} = 20$ kHz, i.e. methane cooling from 300K to 77K led to about two orders rise of the absorption coefficient.

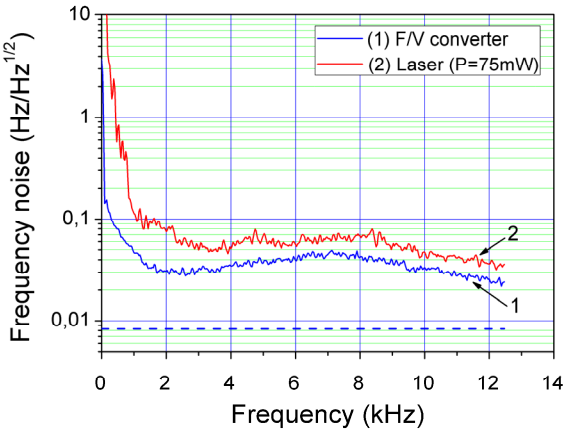

Fig. 3. Spectral density of the beat frequency noise. Dashed line - calculated Shawlow-Townes limit.

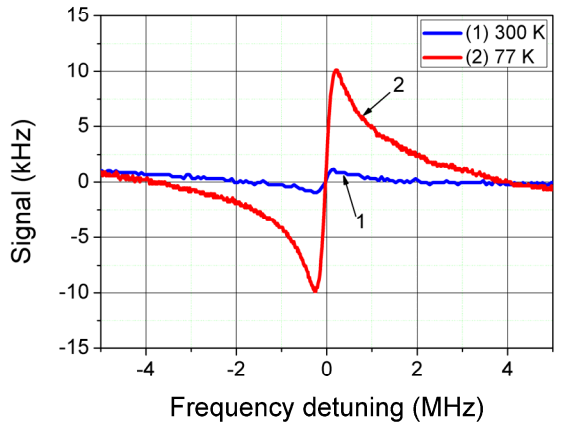

Fig. 4. SD resonances at E-component of the R(2) line ($\nu_1+\nu_4$) band: 1 - T = 300K, p_{CH4} = 10 mTorr; 2 – T = 77K, p_{CH4} = 1 mTorr.

The full width 2γ of the SD resonances was measured by comparison with a transmission peak of an analyzing interferometer (234 MHz free spectral range and finesse 35). The obtained value $2\gamma \approx 400$ kHz is determined mainly by the laser resonator mechanical fluctuations.

The slope of the SD resonance at its center at 77K is $S = \Delta\omega_{12}/\gamma = 0.1$. For the laser frequency stabilization on this resonance the Allan standard deviation for white frequency noise can be estimated as:

$$\sigma(1s) = \frac{\delta\omega_{12}}{S\omega\sqrt{2\tau}} \approx 2\cdot 10^{-15}$$

where $\omega = 127$ THz is a frequency of the Cr^{2+}:ZnSe laser.

For the next laser resonator design the resonance width is expected to be $2\gamma \approx 100$ kHz and the slope $S \approx 1$. So ten times better Allan standard deviation will be possible.

III. Conclusion

There are two well developed directions in creation of very low phase noise and high short-term frequency stability interrogative oscillators: lasers stabilized by superhigh-Q ULE/Silicon cavities and microwave whispering gallery mode cryocooled sapphire oscillators. The experiments carried out in the present work show that two-mode cw solid state Cr^{2+}:ZnSe, Cr^{2+}:CdSe lasers stabilized by narrow saturated dispersion resonances of methane spectral lines in 2.3-3.4 μm wavelength region also can be used for the implementation of interrogative oscillator with frequency stability at the level of 10^{-15}-10^{-16} (τ = 1 s).

References

[1] Y. Y. Jiang et al, "Making optical atomic clocks more stable with 10^{-16}-level laser stabilization," Nature Photonic, vol. 5, pp. 158-161, 2011.

[2] T. Rosenband et al, "Frequency ratio of Al+ and Hg + single-ion optical clocks; metrology at the 17th decimal place," Science, vol. 319, pp. 1808-1812, 2008.

[3] M. Nagel, K. Möhle, K. Döringshoff, E. Kovalchuk, and A. Peters, "Ultra-stable cryogenic optical sapphire resonators for tests of fundamental physics," IQEC/CLEO Pacific Rim 2011, 28 August – 1 September 2011, Sydney, Australia.

[4] T. Kessler et al, "A sub-40 mHz linewidth laser based on a silicon single-crystal optical cavity," arXiv:1112.3854v1.

[5] J.G. Hartnett, D.L. Creedon,1 D. Chambon, and G. Santarelli, "Stability measurements of microwave frequency synthesis with liquid helium cooled cryogenic sapphire oscillators," arXiv:1004.0775v1.

[6] http://www.uliss-st.com

[7] V.S. Letokhov and V.P. Chebotayev, Nonlinear Laser Spectroscopy, Springer-Verlag, Berlin, 1977, p. 466.

[8] J.L.Hall, "Frequency-stabilized lasers: from the beginning toward the future", Laser Physics, vol. 4, pp. 306-318, 1994.

[9] M. Gubin et al, "Absolute frequency measurements with a set of transportable He-Ne/CH_4 OFS and prospects for future design and applications," Proc. of the 6th International Symposium on Frequency Standards and Metrology, 9-14 September 2001, St.Andrews, Scotland, World Scientific Publishing Ltd, ed. P.Gill., pp.453-460.

[10] S. N. Bagayev, A. K. Dmitriyev, and P. V. Pokasov, "Transportable He-Ne/CH_4 frequency standard for precision measurements," Laser Physics, vol. 7, pp. 989-992, 1997.

[11] V.A. Akimov et al, "Vapour growth of II-VI single crystals doped by transition metals for mid-infrared lasers," Phys. Stat. Sol., vol. 3, pp.1213-1216, 2006.

[12] G.J. Wagner, T.J. Carrig, R.H. Page, K.L. Schaffers., J. Ndap, X. Ma, and A. Burger, "Continuous-wave broadly tunable Cr^{2+}:ZnSe laser," Opt. Lett., vol. 24, pp. 19-21, 1999.

[13] V.A. Akimov et al , "Efficient cw lasing in a Cr^{2+}:CdSe crystal," Quantum Electronics, vol, 37, pp. 991-992, 2007.

[14] L.R.Brown et al, "Methane line parameters in HITRAN," Journal of Quantitative Spectroscopy and Radiative Transfer, vol. 82, pp. 219-238, 2003.

[15] M.A. Gubin and E.D. Protsenko, "Laser frequency standards based on saturated-dispersion lines of methane," Quantum Electronics, vol. 27, pp. 1048-1062, 1997.

[16] H.W. Kogelnik, E.P. Ippen, A. Dienes, and C.V. Shank, "Astigmatically compensated cavities for cw dye lasers," IEEE J.Quantum.Electron., vol. 8, pp. 373-379, 1972.

State-of-the-Art Time Link Calibration with a mobile TWSTFT Station

Thorsten Feldmann, Arvind Balu, Cédric Molard, Wolfgang Schäfer
TimeTech GmbH
Stuttgart, Germany
Thorsten.Feldmann@timetech.de

Dirk Piester
Physikalisch-Technische Bundesanstalt (PTB)
Bundesallee 100
38116 Braunschweig, Germany

***Abstract*—Two-Way Satellite Time and Frequency Transfer (TWSTFT) using geostationary telecommunication satellites has become an important technique for comparing remote timescales. There is a need for periodic calibration of the signal delays along the links which are part of the network for the realization of the International Atomic Time (TAI). In order to minimize the efforts of such TWSTFT calibration campaigns, TimeTech GmbH has assembled a mobile station on a trailer. The trailer contains the usual TWSTFT equipment, including the two-way modem, the up/down converters, filters, and amplifiers, as well as monitoring systems, air conditioner, and weather sensors. The steerable antenna is mounted on top of the trailer. The 1 PPS and 10 MHz signals required as input to the TWSTFT equipment are transferred from inside the timing laboratory by an optical link and two reference generators in a master-slave configuration.**

I. INTRODUCTION

The Coordinated Universal Time (UTC), is calculated by the Bureau International des Poids et Mesures (BIPM) and published as UTC-UTC(k) on a five day basis in the monthly Circular T [1], where UTC(k) is a physical approximation realized by laboratory "k". This requires accurate knowledge of the internal delays of the equipment used for comparing the timescales of the participating laboratories or the delays of the complete links.

The timescale comparisons for the generation of UTC are done either by utilizing signals of Global Navigation Satellite Systems (GNSS) or by Two-Way Satellite Time and Frequency Transfer (TWSTFT) using telecommunication satellites [2]. In GPS based relative calibration campaigns performed between 2008 and 2011 using traveling receivers, uncertainties of less than 2 ns, valid at the time of calibration, have been reported (see [3], [4], and [5]). The TWSTFT links operated in parallel with the GPS equipment were calibrated by comparing them to the newly calibrated GPS links.

However, calibrating operational TWSTFT links by means of portable TWSTFT equipment has advantages over the indirect calibration by comparison to GPS links:

- TWSTFT is an independent method for timescale comparisons and calibrations should ideally also be done by means of TWSTFT.
- The statistical uncertainty of a TWSTFT link calibrated by comparison to a GNSS link is the combination of the GNSS calibration uncertainty, the noise of the GNSS link, and the TWSTFT link noise. Only a calibration of TWSTFT by means of TWSTFT itself provides the lowest possible uncertainty.
- Although the calibration values for the TWSTFT links obtained by comparison with GPS, e.g. reported in [3] and [4], were in agreement with previously conducted TWSTFT calibrations [6] within the combined 1-σ uncertainties, systematic effects related to the operational GPS links between the remote sites, which are perhaps not fully understood, could lead to incorrect results.
- Portable TWSTFT calibration equipment allows for calibrating links between laboratories, which operate only TWSTFT and are not equipped with GNSS receivers. The TimeTech set-up presented here is particularly suitable as it allows verification of success of the campaign in *real-time*.

The uncertainties of the relative calibration campaigns reported in [6], [7], and [8] are at the sub-nanosecond level. If the ground installations were not touched and the communication satellite was not changed, the delays were shown to be stable at the 0.5 ns level within one year [7]. However, changes of the laboratory configuration are sometimes unavoidable and the lifetime of communication satellites is limited. In order to keep the time-transfer uncertainties in the international TWSTFT network at the sub-nanosecond level, periodical calibrations of the links are needed.

The calibrations of the European links reported in [7] were conducted with portable equipment provided by the Technical University Graz, Austria [9]. The installation at the timing laboratories required labor extensive mounting of an outside satellite terminal and setting up a lot of heavy weighting inside equipment. In view of minimizing the efforts of TWSTFT link calibrations, TimeTech GmbH has assembled a portable station based on a trailer containing the satellite terminal, and other major parts of the equipment.

II. DESCRIPTION OF THE EQUIPMENT

The portable calibration station primarily comprises of a trailer with the satellite antenna mounted on top. A photograph of the trailer is shown in Fig. 1.

When the trailer is transported by car, the antenna is stowed and covered with protective metal enclosure. The adjustment of the antenna is completely motorized. Only the position of the communication satellite has to be provided to the electronic control system. The position and attitude of the trailer can be estimated with sufficient precision with an inbuilt single frequency GPS receiver and a compass.

Inside, the trailer comprises the TWSTFT modem, the up/down converters, filters, a computer server to record the measurement data and control the TWSTFT system, the control system for the antenna, a slave 1 PPS and 10 MHz reference signal generator, which is synchronized by means of optical fibers to the master inside the timing lab, and a satellite simulator. The satellite simulator will be used for an on-site verification of the stability of the internal delays of the TWSTFT equipment.

An air conditioner dissipates the heat produced by the electronics and keeps the temperature in a stable state. The system has to be connected to electrical power with an alternating voltage of 230 V. The overall power consumption is about 700 W. An uninterrupted power supply and a battery backup guarantee about two hours of autonomous operation in case of external power failures. In the event a 230 V power connection is not available an electrical generator with gasoline engine will be provided.

In the clock room of the laboratory only a small rack is needed. It contains the optical master reference generator with integrated time interval counter (TIC), a 1 PPS distribution amplifier with pulse regeneration, and a data switch to enable remote access to the computer inside the trailer via optical fiber.

The laboratory rack and the rack inside the trailer are shown in Fig. 2. The optical cable between the rack in the laboratory and the trailer consists of four fibers. One pair is used for the metrological signal link between master and reference generator, the second pair is deployed for data communication. The connection with the trailer is secured by waterproof optical plug and socket.

At each laboratory participating in a calibration campaign the mobile station operates simultaneously with the fixed TWSTFT equipment in common-clock mode. The assembly scheme of the mobile station at a timing laboratory is depicted in Fig. 3. The laboratory provides the 5/10 MHz reference frequency for the optical link master generator and a 1 PPS signal coherent to the local UTC(k) (1 PPS Ref). After passing the distribution amplifier (PDA) two 1 PPS signals are connected to the pulse input of the optical master and the stop channel of the TIC inbuilt inside the master.

Figure 1. Photograph of the trailer.

Before the TWSTFT measurement starts the start channel of the TIC is temporarily connected to the local UTC(k), which is in practice a 1 PPS signal with known delay and uncertainty with respect to UTC(k). Thus, at each laboratory the TWSTFT measurement can be referenced to the local UTC(k). Since the TIC is part of the traveling equipment, no additional uncertainty due to different internal delays of local TICs is introduced. This procedure is similar to that described in [5] in the context of a GPS link calibration, but due to the pulse regenerating distribution amplifier the signal characteristic (rise time, amplitude) of the signal at the stop channel of the TIC is the same in all laboratories and no trigger related uncertainty [5] has to be taken into account.

Due to the optical two-way fiber link the signals generated by the optical slave signal generator inside the trailer are coherent to the input signals at the optical master. In order to synchronize the measurement timestamps of the TWSTFT modem the UTC epoch information can be transmitted from the master to the slave, if the master is synchronized by Network Time Protocol (NTP). In case that network connection is impossible or forbidden, the time can also be manually set or alternately can be obtained from a second single frequency GPS receiver in the slave.

Figure 2. The equipment inside the laboratory (left photo) and the equipment rack inside the trailer (right photo).

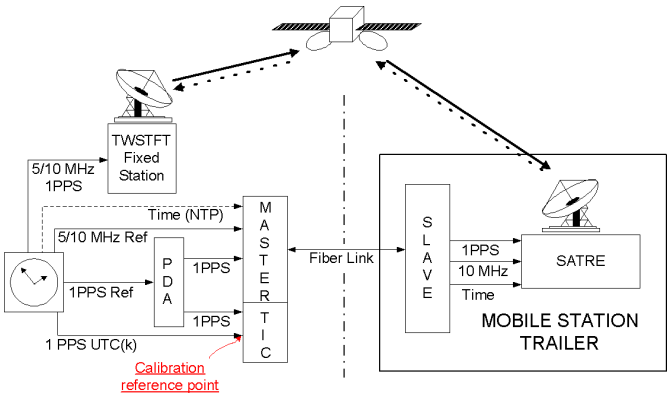

Figure 3. Assembly scheme of mobile station at timing laboratory.

III. Brief Review of TWSTF Calibrations

TWSTFT between two remote laboratories 1 and 2 is based on the exchange of modulated radio signals via a communication satellite, which are coherent to the respective timescales UTC(1) and UTC(2). At both sites the signal of the remote site is compared to the local UTC(k). It is thus ensured that the measurements at both sites are performed at virtually the same time. The difference between the measurements at laboratory 1 and 2 reflects the difference UTC(1) − UTC(2) plus the delays due to the ground station equipment, asymmetries of the signal path, and the Sagnac effect [10].

In mathematical term the two remote measurements are given by [6]

$$\begin{aligned} TW(1) = {} & UTC(1) - UTC(2) + TX(2) + SP(2) \\ & + RX(1) + SCU(1) + SCD(1) \end{aligned} \qquad (1)$$

and

$$\begin{aligned} TW(2) = {} & UTC(2) - UTC(1) + TX(1) + SP(1) \\ & + RX(2) + SCU(2) + SCD(2). \end{aligned} \qquad (2)$$

TX(k) and RX(k) are the signal delays of the transmission and reception part of the respective ground station, SP(j) is the signal path delay from site j to site k, and SCU(k) and SCD(k) are the Sagnac delays for up and downlink, respectively. According to [11] the Sagnac effect is corrected with sufficient precision by applying fixed values calculated from the station positions and the nominal position of the satellite after setting SCU(k) = −SCD(j). Thus, the Sagnac delay is not further considered in the following and left out from all equations. However, the other delays are a priori unknown and have to be determined by calibrations.

A. Single Transponder Setup

In single transponder setup the same satellite antenna covers both stations 1 and 2, respectively (see Fig. 4).

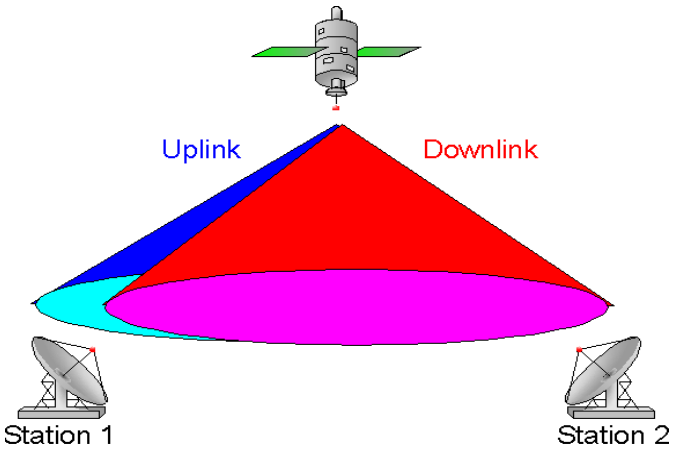

Figure 4. Scheme of single transponder setup TWSTFT.

This is e.g. the case for the European TWSTFT network. The signals of both stations are relayed by the same satellite equipment. Thus, the signal path delays are equal: SP(1) = SP(2). In TWSTFT the delays through the Earth atmosphere cancel to first order. The timescale comparison is performed by exchanging the measurement data and reads

$$\begin{aligned} UTC(1) - UTC(2) = {} & \tfrac{1}{2}[\,TW(1) - TW(2)] \\ & + \tfrac{1}{2}[\,DLD(1) - DLD(2)], \end{aligned} \qquad (3)$$

where DLD(k) denotes the station dependent delay difference defined by DLD(k) = TX(k) − RX(k).

In order to measure [DLD(1) − DLD(2)] the mobile station is operated for several days at site 1 in parallel with the fixed TWSTFT equipment in common-clock mode according to Fig. 3. The common-clock difference (CCD) between the mobile and the fixed station is given by

$$CCD1 = \langle TW_M - TW(1) \rangle = DLD(1) - DLD_M\,, \qquad (4)$$

with TW_M and DLD_M the measurements of the mobile station and the mobile station dependent delay difference, respectively. <…> denotes averaging over several measurements.

In a second step, the mobile station is transported to station 2 and a second CCD measurement takes place:

$$CCD2 = \langle TW_M - TW(2) \rangle = DLD(2) - DLD_M\,. \qquad (5)$$

The difference between the CCDs yields the calibration value for the TWSTFT link:

$$C_{TW} = \tfrac{1}{2}[\,CCD1 - CCD2] = \tfrac{1}{2}[\,DLD(1) - DLD(2)]. \qquad (6)$$

The DLD_M delays cancel out if the mobile station is properly referenced to the local UTC(k) at both laboratories (see Fig 3). Finally, the calibrated time transfer is given by

$$\begin{aligned} \mathrm{UTC(1)-UTC(2)} &= \tfrac{1}{2}\left[\mathrm{TW(1)-TW(2)}\right] \\ &+ \tfrac{1}{2}\left[\mathrm{DLD(1)-DLD(2)}\right] - \mathrm{C_{TW}}\,. \end{aligned} \tag{7}$$

B. *Separated Transponder Setup*

In the separate transponders case the two ground stations are within the coverage of different antennas of the satellite, as sketched in Fig. 5. The signal path lengths within the satellite can differ from each other. The satellite providers usually do not measure this delay difference prior to launch, since it is not relevant for communication applications. However, in terms of TWSTFT it is a presumption in the timescale difference computation (3) and has to be taken into account if it is not fulfilled.

For the separated transponder configuration the timescale difference is explicitly given by

$$\begin{aligned} \mathrm{UTC(1)-UTC(2)} &= \tfrac{1}{2}\left[\mathrm{TW(1)-TW(2)}\right] \\ &+ \tfrac{1}{2}\left[\mathrm{DLD(1)-DLD(2)}\right] + \tfrac{1}{2}\left[\mathrm{SP(1)-SP(2)}\right]. \end{aligned} \tag{8}$$

Another complicating factor for calibrations is that two stations located at the same site cannot receive their respective signals. In [13] it is proposed to solve both problems by measuring with two mobile stations, locating one at each site, and exchanging them for a second measurement. This procedure requires precise scheduling of the campaign, as well as a second mobile station.

However, usually the timing laboratories operate TWSTFT and GNSS equipment in parallel. Thus, the TWSTFT link with separated transponder configuration can be calibrated by using one mobile TWSTFT station and a calibrated GNSS link. This procedure enables separating station dependent delays and signal path delay differences, and the GNSS noise and uncertainty affect only the computation of the signal path delay differences.

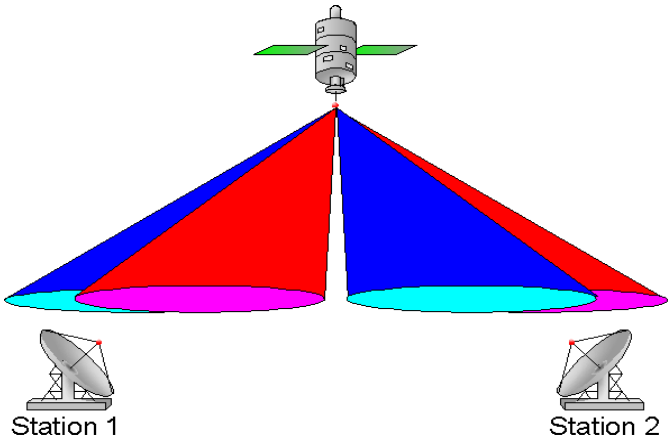

Figure 5. Scheme of separated transponder setup TWSTFT.

Operated at laboratory 1 the mobile station provides a second TWSTFT link with the remote laboratory 2:

$$\begin{aligned} \mathrm{UTC(1)-UTC(2)} &= \tfrac{1}{2}\left[\mathrm{TW_M-TW(2)}\right] \\ &+ \tfrac{1}{2}\left[\mathrm{DLD_M-DLD(2)}\right] + \tfrac{1}{2}\left[\mathrm{SP(1)-SP(2)}\right]. \end{aligned} \tag{9}$$

The signal path delay difference [SP(1) − SP(2)] is the same for the link between the two fixed stations (8) and the link between mobile station and remote fixed station (9) and cancels out in the combination of (8) and (9), which is equivalent to (4). The measurements performed when the mobile station is at laboratory 2 yield a result equivalent to (5), and a calibration value similar to (6) can be formed from the difference. The timescale difference now reads

$$\begin{aligned} \mathrm{UTC(1)-UTC(2)} &= \tfrac{1}{2}\left[\mathrm{TW(1)-TW(2)}\right] - \mathrm{C_{TW}} \\ &+ \tfrac{1}{2}\left[\mathrm{DLD(1)-DLD(2)}\right] + \tfrac{1}{2}\left[\mathrm{SP(1)-SP(2)}\right], \end{aligned} \tag{10}$$

where [SP(1) − SP(2)] is still unknown. It can be computed by comparing (10) to a calibrated GNSS link, which requires an additional GNSS calibrator combined with the mobile station, in order to achieve the lowest possible uncertainty.

IV. Results of a Test CCD Measurement

In 2011 the mobile station was transported to the Physikalisch-Technische Bundesanstalt (PTB), Braunschweig, Germany, and operated in common-clock mode (cf. Fig. 3) together with the fixed TWSTFT equipment at PTB, using the communication satellite Telstar 11N.

The results of a seven-day CCD measurement are depicted in Fig. 6. During each even hour, measurement data were taken on a second-by-second basis for about one minute and an average by employing polynomial fitting was calculated, similar to the procedure recommended in [11] and [12] and used for evaluating the links between the institutes participating in the European TWSTFT network.

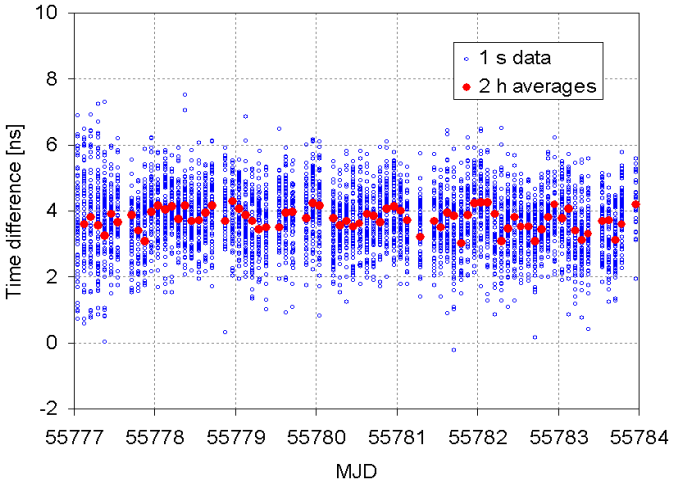

Figure 6. Seven day common-clock time difference measurements between mobile and fixed station at PTB (Telstar 11N).

The aim of a calibration measurement is to calculate the CCD as mean value of all measurements, according to (4) and (5). This can be done in two (or more) steps in order to get rid of the Gaussian distributed white phase noise. For this purpose, the complete time series of measurement data is split in multiple data blocks of equal length. Then the averages of each data block are calculated, constituting a new time series. The CCD value and the related standard deviation (SD), which is identical with the statistical uncertainty, are calculated from the new time series. The length of the data blocks is estimated from the minimum of the time deviation (TDEV) [14] calculated from the original time series. The minimum of the TDEV itself shall not be used as statistical uncertainty, since measurement uncertainty is not defined that way [15]. Practical applications of this data and uncertainty evaluation scheme are given in [5].

By definition, the usual TWSTFT data collection method [11] already provides a first averaging. In order to prove that the calibration can be done with the two-hour averages, all 1 s data have been concatenated and the TDEV for averaging times up to 100 s has been calculated (Fig. 7).

The double logarithmic plot (Fig. 7) shows a decreasing TDEV between 1 s and approximately 20 s averaging time, which indicates that the measurements are dominated by white phase noise. The following flat slope identifies flicker phase noise being dominant and each interval between 20 s and 100 s can be used for a first averaging of the 1 s data.

In real calibration campaigns the mobile station will probably stay not any longer than two or three days at each participating laboratory and the number of two-hour averages will not suffice for further averaging. For this reason, also for the seven-day test measurement only the SD of the two-hour averages was calculated. The result is

$$\sigma = 0.33 \text{ ns}. \qquad (11)$$

In case of a real campaign this would be the statistical uncertainty of the CCD measurement at PTB. It has to be noted that (11) composes of the noise of the fixed PTB equipment, as well as of the complete mobile set-up, including the optical link between PTB´s measurement room and the outside parking place of the trailer.

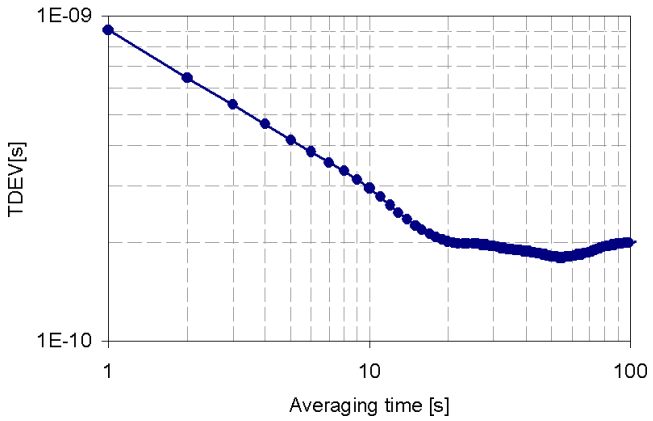

Figure 7. Time deviation of concatenated 1 s data

The operational TWSTFT links are evaluated by storing the two-hour data in files and exchanging them by means of internet communication. However, the modern TWSTFT modems are also capable of exchanging their measurements in quasi real-time via the telecommunication satellite along with the metrological signal. In [6] it is pointed out that the mean difference between the real-time solution and the usual method based on data file exchange is below 10 ps. This enables on-site verification and control of the measurements. Any errors can be immediately corrected.

V. Optical Link

The optical link between the laboratory rack and the trailer is a critical part of the equipment. Originally, the optical master and slave generator were intended for campus time and frequency distribution up to a few kilometers, free of attenuation and dispersion effects occurring along electrical cables.

The local oscillator inside the slave generator is compared and synchronized to the master reference generator by means of two-way, currently using a pair of unidirectional operated optical fibers. For the calibration it is essential that the delay between the 1 PPS master input signal and the slave 1 PPS output remains stable during the campaign. Otherwise, the mobile station dependent delay difference DLD_M would not cancel correctly from (6) and the systematic uncertainty would be increased to excessively high values.

The stability of the optical 1 PPS transfer was locally tested by splitting a 1 PPS signal and connecting it to the optical master as well as to the start channel of a TIC, while the 1 PPS output signal of the slave was connected to the stop channel (Fig. 8). A series of turn off and on sequences of master and slave generator was performed within 2.5 hours. While the devices were turned on, the TIC measurements were recorded on second-by-second basis. The momentary temperature values inside the master generator were recorded in parallel.

The results are depicted in Fig. 9. The temperature measurements are colored in red. The uncompensated TIC measurements (blue) are strongly coupled to the temperature variations. The data plotted in green color are corrected for the temperature measurements inside the master using a linear coefficient of 0.09 ns/°C. A temperature compensation of the slave is not necessary since all variations are already actively compensated by the optical two-way measurement.

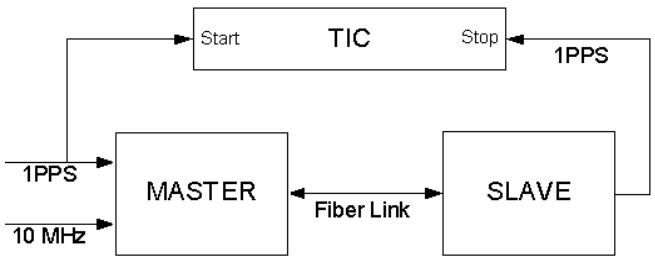

Figure 8. Setup for testing the optical link.

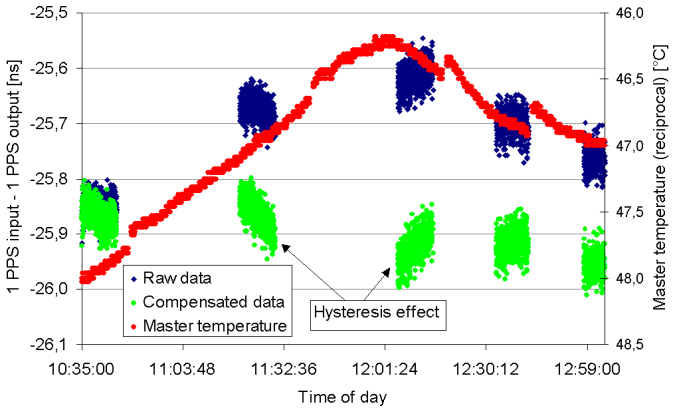

Figure 9. Input 1 PPS of optical master device measured with respect to 1 PPS output of slave generator (blue: uncorrected measurements, green: linear temperature compensation applied) and temperature inside the master generator (red, y-axis values are reciprocally depicted).

The optical link is subject of continuous development. The goal is to generate a remote signal with the same phase noise and instability characteristic as the input signal. Potential effects due to changes of the differential delay between the two unidirectional fibers will be examined in detail in the future. In principle it is possible to extend optical master and slave generator with optical circulators and to perform the two-way measurements using a single bidirectional optical fiber, similar to the optical link setup described in [16].

If the sign of the slope of the temperature measurements has not changed between two adjacent measurement sequences, the averages of these two sequences are in good agreement. However, if the slope has changed a "hysteresis" effect is visible. A simple linear compensation is obviously not sufficient and a more advanced compensation algorithm will be implemented in the internal control software of the master reference generator.

Besides the temperature effect no additional phase jumps are introduced due to turning off and on the devices. Thus, the optical link can be effectively considered as a cable with fixed delay.

VI. Next Working Steps

Real link calibration campaigns are to be started as soon as possible. These campaigns will include PTB, since it is the pivot laboratory within the network of the links used for the computation of UTC by the BIPM [17]. The list of other candidates consists of the Instituto Nazionale di Ricerca Metrologica (INRIM), Italy, the Federal Office of Metrology (METAS), Switzerland, the Astrogeodynamical Observatory (AOS), Poland, and the Swedish National Testing and Research Institute (SP).

In order to produce valuable results a detailed evaluation of the systematic uncertainty budget will be conducted, taking into account all critical parts of the mobile equipment and the procedure as a whole, similar to the evaluation done for PTB´s GPS calibrator [5].

A very promising step forward in TWSTFT is the use of the carrier-phase for remote frequency comparisons [18]. The carrier-phase short-term stability is about 100 times better than that of the modulated signals. If this could be harnessed for calibration measurements, the time interval for which the mobile station has to stay at the laboratories could be reduced without affecting the statistical uncertainty. However, this requires a method to determine the a priori unknown initial phase by the help of the code measurement, e.g. by applying a Kalman Filter [19]. The execution of special calibration measurements during the odd hours when no regular TWSTFT sessions take place is discussed in order to provide long continuous measurement time series.

VII. Conclusion

A mobile TWSTFT for relative time link calibrations has been introduced. Main parts of the equipment are assembled on a trailer, including the satellite terminal. The trailer will be transported by car between the laboratories participating in a calibration campaign. The antenna is steered by motors and only a parking place with free sight to the dedicated communication satellite is required. This avoids labor intensive assembling and disassembling of heavy weighted equipment.

Inside the laboratories only a small rack with few equipment enabling local optical two-way time and frequency transfer with the trailer and optical data connection is needed. At the time of writing this publication the optical two-way link equipment is improved with the goal of providing output signals with the same signal quality as the input signals.

Calibration campaigns involving several European timing laboratories are scheduled to start very soon.

Acknowledgment

We would like to thank PTB staff for supporting the test measurement at PTB and Andreas Bauch (PTB) for some valuable corrections to the manuscript.

References

[1] T. J. Quinn, "The BIPM and the accurate measurement of time," Proc. IEEE, vol. 79, no. 7, pp. 894-905, 1991.

[2] J. Levine, "Time and frequency distribution using satellites," Rep. Prog. Phys., vol. 65, pp. 1119-1164, 2002.

[3] H. Esteban, J. Palacio, F.J. Galindo, T. Feldmann, A. Bauch, and D. Piester, "Improved GPS based time link calibration involving ROA and PTB," IEEE Trans. UFFC, vol. 57, no. 3, pp. 714-720, 2010.

[4] T. Feldmann, A. Bauch, D. Piester, A. Stefanov, L.-G. Bernier, C. Schlunegger, and K. Liang, "On improved GPS based link calibration of the time links between METAS and PTB," Proc. EFTF, Nordwijk, NL, April 13-16, 2010.

[5] T. Feldmann, A. Bauch, D. Piester, M. Rost, E. Goldberg, S. Mitchell, and B. Fonville, "Advanced GPS Based Time Link Calibration with PTB´s New Calibration Set-Up," Proc. 42nd PTTI, Reston VA, USA, pp. 509-526, November 15-18, 2010.

[6] D. Piester, A. Bauch, L. Breakiron, D. Matsakis, B. Blanzano, and O. Koudelka, „Time transfer with nanosecond accuracy for the realization of International Atomic Time," Metrologia, vol. 42, no. 2, pp. 185-198, 2008.

[7] A. Bauch, D. Piester, B. Blanzano, O. Koudelka, E. Kroon, E. Dierikx, P. Wibberly, J. Achgar, D. Rovera, L. Lorini, F. Cordara, and C. Schlunegger, "Results of the 2008 TWSTFT Calibration of Seven European Stations," Proc. EFTF – IEEE FCS Joint Conference, Besançon, France, pp. 1209-1215, April 20-24, 2009.

[8] D. Piester, A. Bauch, J. Becker, T. Polewka, A. McKinley, and D. Matsakis, "Time Transfer between USNO and PTB: Operation and Calibration Results," Proc. 35th PTTI, San Diego CA, USA, pp. 93-101, December 02-04, 2003.

[9] D. Kirchner, H. Ressler, P. Hetzel, A. Söring, and W. Lewandowski, "Calibration of three European TWSTFT stations using a portable station and comparison of TWSTFT and GPS common-view measurement results," Proc. 30th PTTI, Reston Va, USA, pp. 365-376, December 01-03, 1998.

[10] E.J. Post, "Sagnac Effect," Rev. Mod. Phys., vol. 39, no. 2, pp. 475-493, April 1967.

[11] ITU Radiocommunication Sector, "The operational use of two-way satellite time and frequency transfer employing PN codes," Recommendation ITU-R TF.1153-2, Geneva, Switzerland, 2003.

[12] A. Bauch, D. Piester, M. Fujieda, and W. Lewandowski, "Directive for operational use and data handling in two-way satellite time and frequency transfer (TWSTFT)," Rapport BIPM-2011/01, Bureau International des Poids et Mesures, Sevres, France, 2011.

[13] D. Piester, T. Feldmann, A. Bauch, M. Fujieda, and T. Gotoh, "Concept for an Accurate Calibration of Long Baseline Two-Way Satellite Time and Frequency Transfer (TWSTFT) Links via Two Separated Transponders on One Telecommunication Satellite," Proc. EFTF – IEEE FCS Joint Conference, Besançon, France, pp. 1076-1081, April 20-24, 2009.

[14] W. Riley, "Handbook of Frequency Stability Analysis," NIST Special Publications 1065.

[15] Joint Committee for Guides in Metrology (JCGM), "Evaluation of measurement data – Guide to the expression of uncertainty in measurement," JCGM 100:2008.

[16] D. Piester, M. Rost, M. Fujieda, T. Feldmann, and A. Bauch, "Remote atomic clock synchronization via satellites and optical fibers," Adv. Radio Sci., vol. 9, pp. 1-7, 2011.

[17] Z. Jiang, F. Arias, W. Lewandowski, and G. Petit, "Toward new procedures in TWSTFT and GNSS delay characterization for UTC time transfer?," Proc. EFTF, Nordwijk, NL, April 13-16, 2010.

[18] B. Fonville, D. Matsakis, A. Pawlitzki, and W. Schäfer, „Development of Carrier-Phase-based Two-Way Satellite Time and Frequency Transfer (TWSTFT)," Proc. 36th PTTI, Washington DC, USA, pp. 149-164, December 07-09, 2004.

[19] R.J. Meinhold and N.D. Singpurwalla, „Understanding the Kalman Filter," The American Statistician, vol. 37, no. 2, pp. 123-127, 1983.

Delay Calibration System For A Two Way Satellite Time & Frequency Transfer Station

Faisal Mubarak, Erik Dierikx
VSL
P.O. Box 654, 2600 AR, Delft, The Netherlands
fmubarak@vsl.nl

***Abstract*—A completely automated system has been designed to calibrate path delays in a two way satellite time and frequency transfer (TWSTFT) ground station. The heart of this delay calibration system is a dual bidirectional up/down converter that converts the modulated pseudo random noise (PRN) code from 70 MHz to Ku-band (10 GHz to 14 GHz) frequencies and vice versa. Besides the usual transmit (Tx) and receive (Rx) paths in the TWSTFT system, the dual bi-directional up/down converter offers two additional independent transmit and receive paths. These additional paths allow performing different independent loop delay measurements within the station from which the individual path delays can be calculated.**

I. INTRODUCTION

The TWSTFT station at VSL is located at three separate locations (see figure 1). Time scale generation, signal encoding and decoding to and from a pseudo random noise (PRN) code and modulation and demodulation on a 70 MHz carrier are performed in the Time & Frequency (TF) laboratory. The TF laboratory is connected to a room on the other side of the building in which a Ku-band up converter (U/C) and down converter (D/C) are installed. The laboratory is connected to this room by coaxial cables of approximately 100 meter. The transmit (Tx) cable and the receive (Rx) cable are indicated with cable-A and cable-B respectively.

The U/C converts the 70 MHz transmit signal to about 14 GHz and the D/C converts the received signal at about 11 GHz down to 70 MHz. The up converter and down converter are connected to a solid state power amplifier (SSPA) and a low noise amplifier (LNA) respectively, that are both mounted on the antenna arm on the rooftop. The coaxial cables for these connections are approximately 20 meter long.

All equipment and all cables in the transmit and receive paths of the station introduce delays. For the operation of the TWSTFT station it is important to calibrate and monitor the delay difference between the transmit path and the receive path.

The aim of this work has been to develop an automated system for calibration and monitoring of the path delays in the TWSTFT from the modem up to a reference plane in front of the dish antenna.

This work has been financed by the Dutch Ministry of Economic Affairs, Agriculture and Innovation.

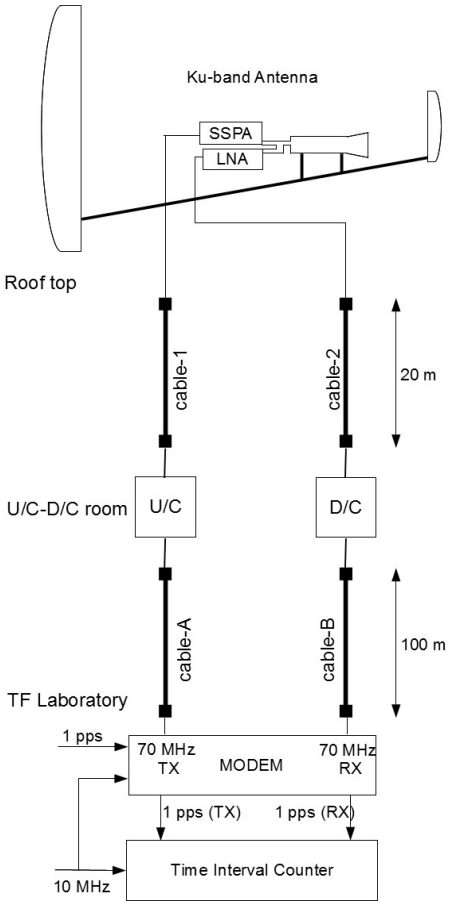

Figure 1. A simplified diagram of the TWSTFT station at VSL.

II. DELAY CALIBRATION PRINCIPLE

The delay calibrations in our system are based on the three-corner-hat method [2]. With three cables, three independent loop delays can be measured as shown in figure 2. With the combination of these measurements, the delay of the individual cables can be calculated.

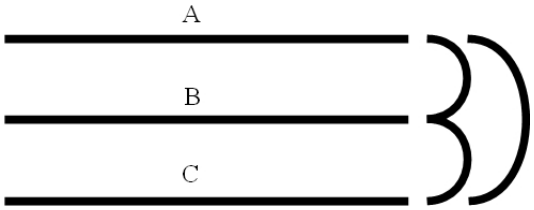

Figure 2. Schematic diagram of the three corner hat method

If M_{XY} is the loop delay of cable X + cable Y including a small correction the interconnection link, then (1) can be derived for the delay of cable A, T_A.

$$T_A = \frac{M_{AB} + M_{CA} - M_{CB}}{2} \quad (1)$$

And similar equations can be derived for the delays of cables B and C.

To apply this method in the TWSTFT station, the system is divided in two segments. The first segment includes the modem and the 100 meter cables from the TF laboratory to the U/C and D/C room carrying the 70 MHz modulated PRN code signals. The second segment includes the U/C and D/C, the 20 meter cables to the rooftop, SSPA, the LNA and the antenna. These two segments will be discussed in the following sections.

III. Delay Calibration in the 70 MHz Paths

To implement the method described above in the 70 MHz segment of the system, a third cable C needs to be installed in parallel to cables A and B as shown in figure 3. Furthermore, for automated configuration of the different loops, two sets of remote controlled transfer switches are required. One set (switches S1 and S2) is installed in the TF laboratory near the modem and the other set (switches SA, SB and SC) is installed close to the U/C and D/C.

Switch S1 connects the Tx port of the modem to either cable A or cable C. Switch S2 connects the Rx port of the modem to either cable A or cable B. Switches SA, SB and SC at the far end of the cables are used to interconnect the cables A, B and C to create the loops. The interconnections between the switches are realized through short (10 cm) coaxial cables and a power splitter/combiner. Using this splitter/combiner not only improves the symmetry between the three paths, but also reduces the power to the input port of the modem, thus avoiding overload.

Although the interconnection cables are short and the power splitter/combiner is small, they will introduce an additional delay in the loop measurements for which a correction is required. These correction values need to be determined in advance; preferably before the installation of the switchboxes in the TWSTFT system.

The measurement paths are indicated in figure 3, resulting in the (corrected) loop delays M_{AB}, M_{CA} and M_{CB}.

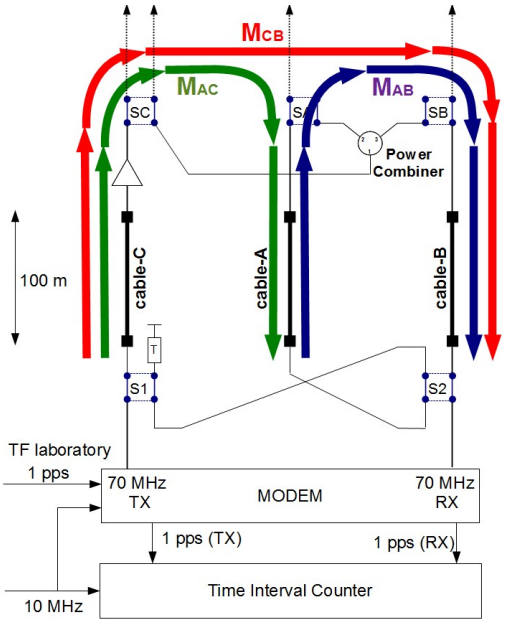

Figure 3. Delay calibration in the 70 MHz segment

From these the cable delays T_A, T_B and T_C are given by (2).

$$T_A = \frac{M_{AB} + M_{CA} - M_{CB}}{2}$$
$$T_B = \frac{M_{AB} + M_{CB} - M_{CA}}{2} \quad (2)$$
$$T_C = \frac{M_{CA} + M_{CB} - M_{AB}}{2}$$

IV. Delay Calibration in the Ku-Band Paths

A. Requirements

Calibration of the Ku-band paths in the system, including the U/C and D/C by implementing the three-corner-hat method is more complicated for two reasons.

- Each loop measurement must include at least three frequency shifts: from 70 MHz to the Ku-band Tx frequency (near 14 GHz), from the Tx frequency to the Rx frequency (near 11 GHz) and from the Rx frequency back to 70 MHz.
- At least one of the paths needs to be bi-directional.

B. Hardware implementation

Knowing that the commercial U/C and D/C can be used in only one direction requires that at least two bi-directional parallel paths are created in the system. To implement these bi-directional paths including the required frequency transformations, we have developed a dual bi-directional up/down converter. A schematic diagram of this device, also known as delay calibration unit (DCU) is shown in figure 4.

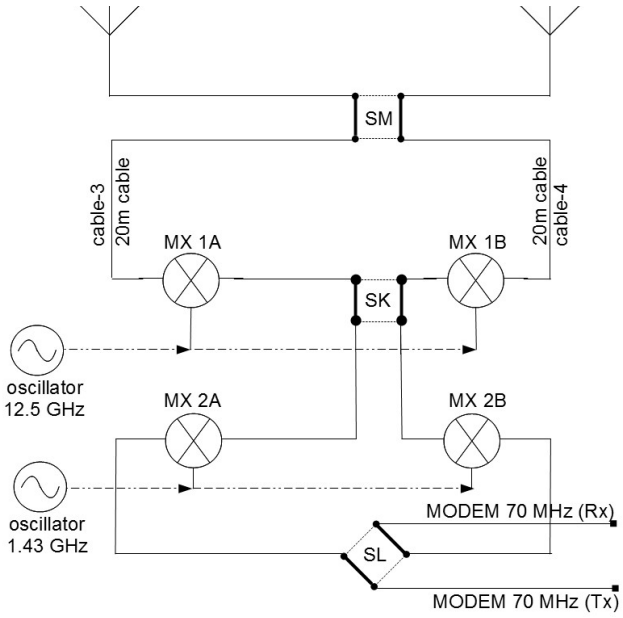

Figure 4. Dual bi-directional up/down converter

The DCU consists of two parallel paths: on the left via cable-1 and mixers MX 1A and MX 2A and on the right via cable-2, MX 1B, MX 2B. The signal direction in each of the paths can be either from top to bottom (Rx) or from bottom to top (Tx). The direction of the signals in each path is determined by the position of switch SL. If the left path is connected toward the Tx port of the modem, the right path will be connected towards the Rx port of the modem and vice versa.

The frequency conversion is realized in a two-stage process, first from 70 MHz to an intermediate frequency f_{INT} in the L-band (1 GHz to 2 GHz) using MX 2A and MX 2B and then from L-band to Ku-band, using MX 1A and MX 1B. The signal generator driving mixers 1A and 1B, is set at frequency f_1 at the average of the Ku-band Tx and Rx frequencies f_{TX} and f_{RX} (3).

$$f_1 = \frac{f_{TX} + f_{RX}}{2} \tag{3}$$

Using this method, one signal generator is used for down-converting from 11 GHz receiver frequency and up-converting to 14 GHz transmission frequency.

From f_{TX} or f_{RX} and f_1, f_{INT} can be derived by (4).

$$f_{INT} = f_{TX} - f_1 \tag{4}$$

And hence, the frequency f_2 required to drive MX 2A and MX 2B is given by (5).

$$f_2 = f_{INT} - 70\,\text{MHz} \tag{5}$$

The frequencies f_1 and f_2 are fixed and do not need to be adjusted during normal operation.

C. *Implementation in the TWSTFT station*

Implementing this DCU in the TWSTFT station provides us with two additional independent paths from the modem to the reference plane at the antenna. This is shown in figure 5.

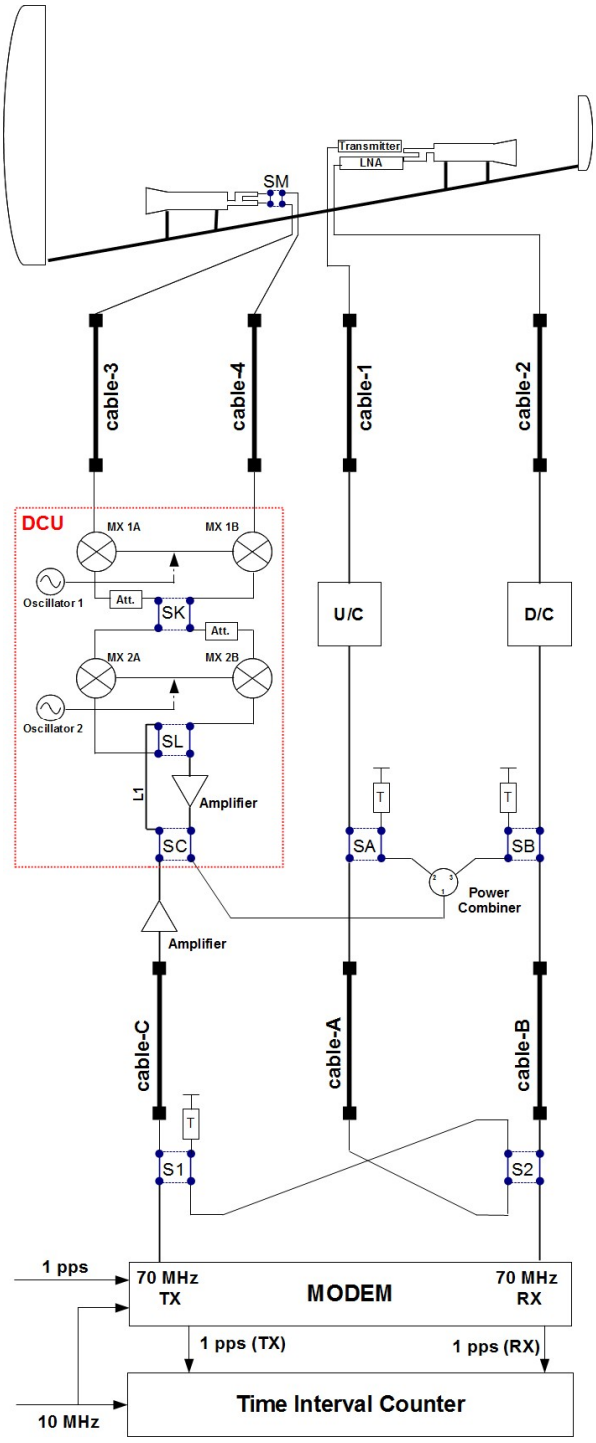

Figure 5. TWSTFT station including the delay calibration unit

Note that two amplifiers have been included for signal level conditioning to and from the DCU.

Path delays in this system, including the usual Tx and Rx paths, are defined in table 1.

ID	Description
T_{KU}	from SA, U/C, cable-1, SSPA, horn, antenna
T_{KD}	from SB, D/C, cable-2, LNA, horn, antenna
T_{PL}	from SC, DCU-left, cable-3, SM, horn
T_{PR}	from SC, DCU-right, cable-4, SM, horn
T_{TX}	$T_{KU} + T_A$; total transmit delay
T_{RX}	$T_{KD} + T_B$; total receive delay

Table 1: Path delay definitions

With these paths, loop delays are defined by (6) that need to be measured for the three-corner-hat method:

$$\begin{aligned} M_2 &= T_{KU} + T_{PL} + T_A + T_B \\ M_3 &= T_{KU} + T_{PR} + T_A + T_B \\ M_4 &= T_{KD} + T_{PL} + T_C + T_B \\ M_5 &= T_{KD} + T_{PR} + T_C + T_B \\ M_6 &= T_{PL} + T_{PR} + T_C + T_B \end{aligned} \tag{6}$$

D. *Rx path calibration*

Figures 6 and 7 show the measurement loops M_4, M_5 and M_6 required for the calculation of the Rx path delay.

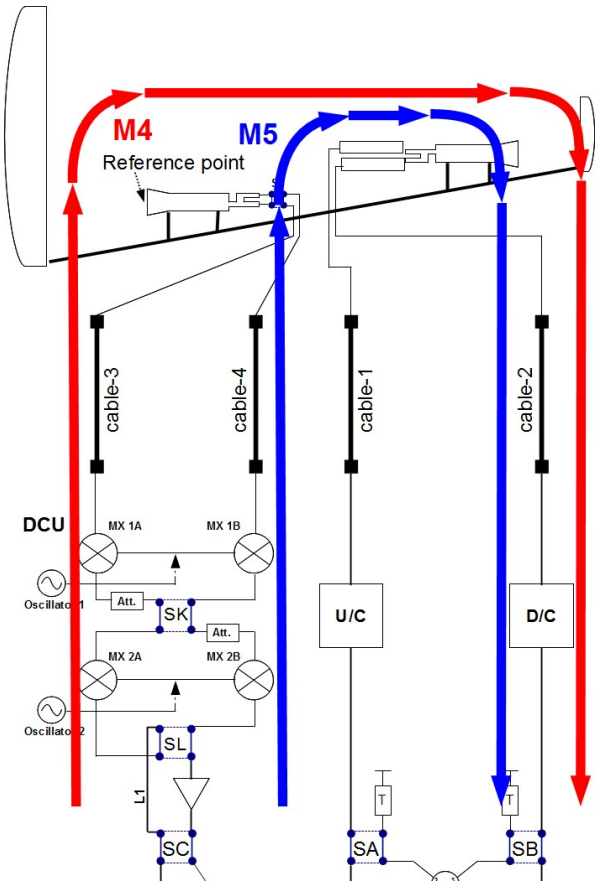

Figure 6. Measurement loops M_4 and M_5 required for the Rx path calibration of the Ku-band segment.

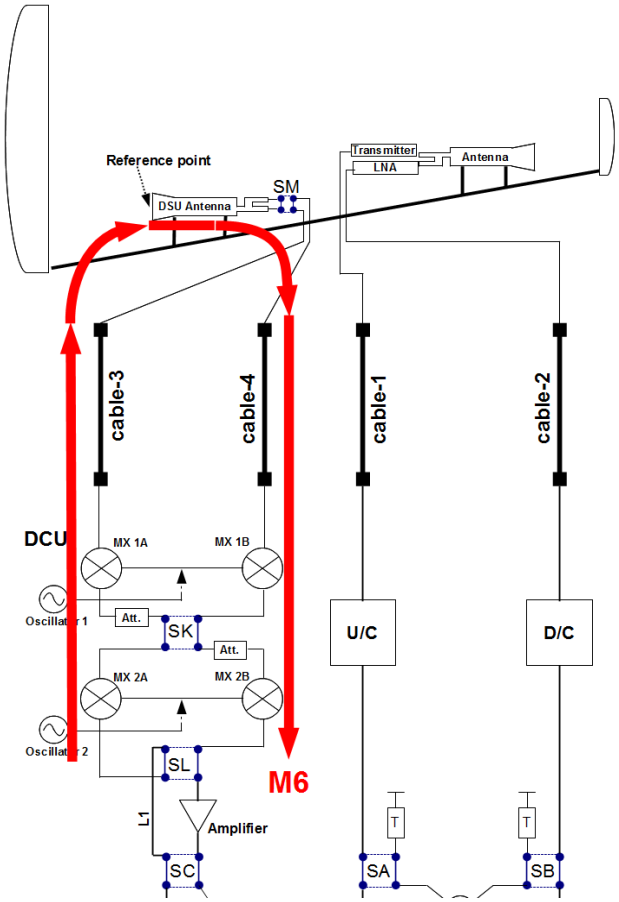

Figure 7. Measurement loop M_6 is required for both the Tx and Rx path calibration of the Ku-band segment.

The total delay of the receive path from the antenna down to the modem, T_{RX}, was defined in table 1. From (2) and (6), T_{RX} can be derived as in (7):

$$T_{RX} = \frac{M_4 + M_5 - M_6 - M_{AB} + M_{AC}}{2} \tag{7}$$

E. *Tx path calibration*

Similarly, for the Tx path calibration measurement loops M_2, M_3 (figure 8) and M_6 are required.

The total delay of the transmit path from the modem up to the antenna, T_{TX}, was defined in table 1. From (2) and (6), T_{TX} can be derived as in (8):

$$T_{TX} = \frac{M_2 + M_3 - M_6 - M_{AC} + M_{AB}}{2} \tag{8}$$

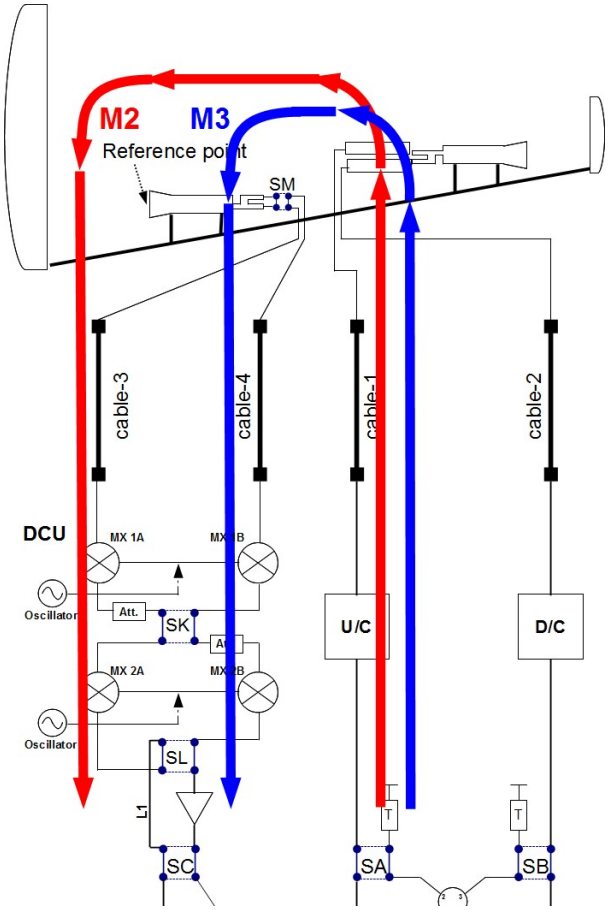

Figure 8. Measurement loops M_2 and M_3 required for the Tx path calibration of the Ku-band segment.

V. TWSTFT Station Calibration Parameter

The difference T_{TX} - T_{RX} is the parameter that is important for the station calibration and has a direct influence on all TWSTFT links to and from this station. When two TWSTFT stations have performed this type of station calibration, the results can be combined to find the link calibration parameter, CALR, as defined in the TWSTFT ITU report format [3]. Up till now, CALR values are commonly determined in calibration campaigns using a travelling TWSTFT station. Typically, a TWSTFT station is visited by a travelling station once in 5 years. If all TWSTFT stations would become equipped with an automated delay calibration system as described in this paper, it would be much easier to maintain the link calibration values, CALR, and any station delay variations would be detected easier.

VI. Results

More than 8 months of measurement data has been recorded. Automated measurements have been performed 12 times per day, during the odd hours. Each measurement consists of 30 s of data. To verify the performance of the delay calibration system, all measurements were performed using PRN code modulation at 1 MHz chip rate. For all measurements a signal-to-noise ratio (SNR) of higher then 60 dB was achieved.

All loop measurements of the cables A, B and C at 70 MHz have been found to be extremely stable with time deviations (TDEV) down to 10 ps over 1 day to 10 days averaging.

In Figure 9 results of M_2 and M_3 configuration are presented. Both of these configurations include stations traditional Tx-path delay.

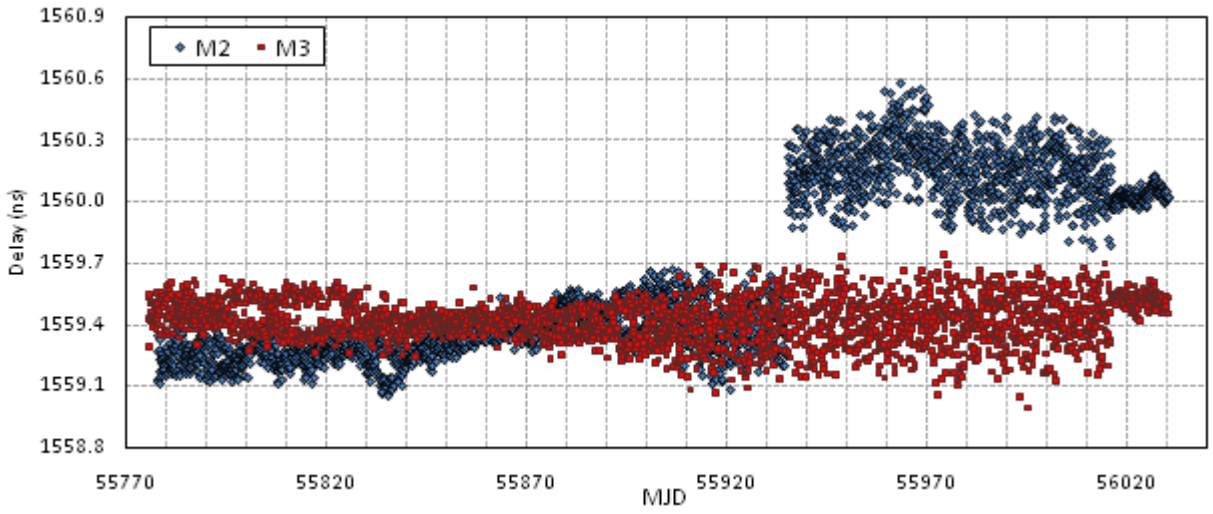

Figure 9. Measurement results of M_2 and M_3 configuration.

In Figure 10, results of M_4 and M_5 configuration are shown. These two configurations include stations traditional Rx-path delay.

In Figure 11, measurement results of M_6 configuration are presented, showing the round trip delay of the calibration system itself.

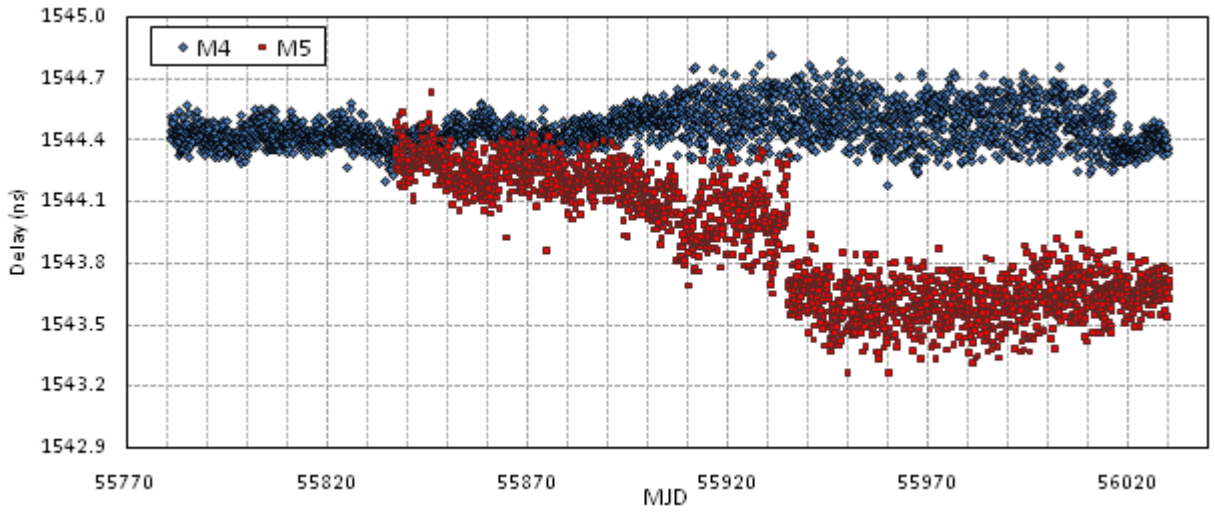

Figure 10. Measurement results of M_4 and M_5 configuration.

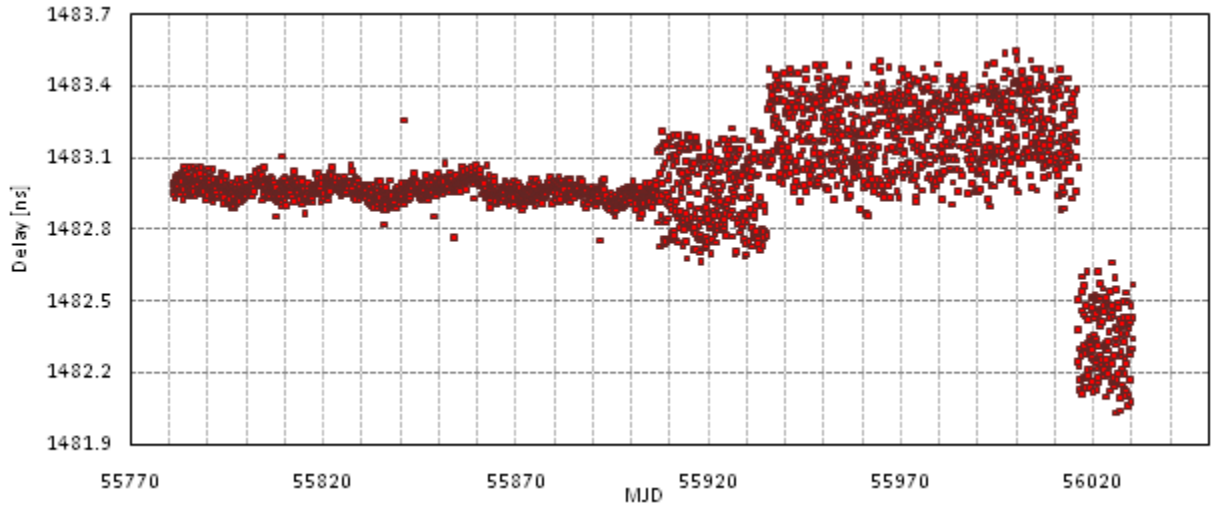

Figure 11. Measurement results of M_6 configuration.

Abrupt changes in measured delay values of M_2 to M_6 are due to various hardware modifications. Almost no drift component is noticeable on the delay measurements. The low drift level has been achieved by installing delay calibration unit inside in the U/C and D/C room. The SSPA used for transmission is one of the most temperature susceptible devices in the TWSTFT station [1][4]. During test-measurements the SSPA and the LNA were installed in a temperature stabilized environment. The low drift values lead to superior long-term stability of the TWSTFT station.

Random fluctuations are mainly caused by system noise, harmonic distortion and non-linearity. To make the signal less susceptible to noise, PRN code modulation is used to achieve a high post-correlation signal-to-noise ratio, which is directly limited by the modulator's chip-rate frequency. For the measurement data presented, the same chip-rate of 1 MHz is selected as for the usual station to station measurements. The harmonic distortion of the system is minimized by selecting highly linear devices and keeping the signal generators fixed on a single frequency. Random fluctuations of less than 100 ps have been achieved for all measurement configurations presented.

In Figure 12 time deviation plots of the station's Tx- and Rx-path delays are shown. For 1 day averaging time, a time stability of less than 70 ps was achieved.

In Figure 13 a time deviation plot is shown for the calculated station delay calibration parameter (T_{TX}-T_{RX}). The time stability is less than 70 ps for 1 day averaging time.

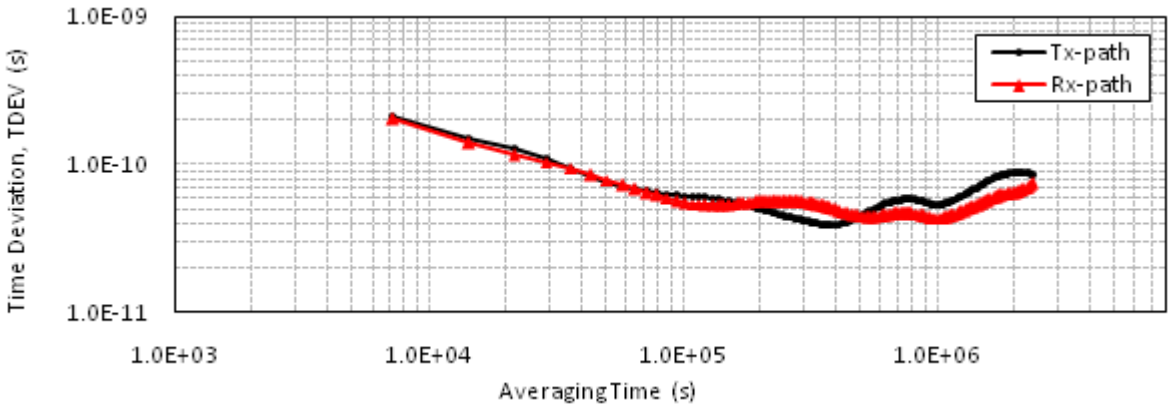

Figure 12. Time Deviation (TDEV) result for Tx & Rx measurements.

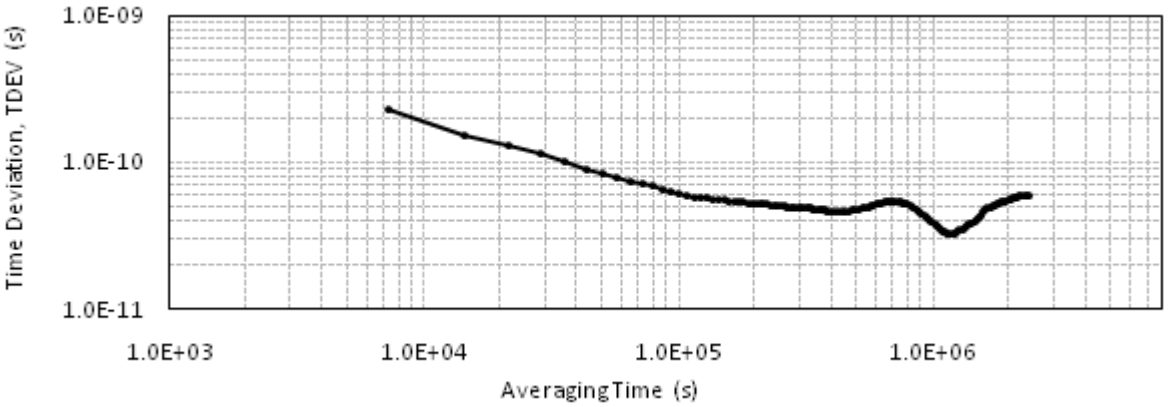

Figure 13. Time Deviation (TDEV) result for (T_{TX}-T_{RX}).

VII. Discussion of the Results

The results presented in the previous section have been obtained in an indoor test bench, in which the dish antenna has been replaced with a small Ku-band horn antenna. It is to be expected that the performance of the system will be somewhat deteriorated when operated in an outdoor environment. The stability is to be expected mostly affected by the influence of temperature fluctuations on the SSPA and the LNA.

The DCU contains several short interconnection cables between the switches and other parts of the system. These short cables introduce small systematic deviations in the measured loop delays. These deviations can be calibrated in advance before installing the DCU in the TWSTFT station. Similarly, the delays of the two amplifiers connected to switch SC need to be calibrated in advance and corrections need to be applied in the computations to determine the Tx and Rx path delays. These corrections will introduce some additional contributions in the overall station calibration uncertainty. This uncertainty evaluation is still in progress.

The DCU is a bi-directional device. However, the signal in the Tx direction has a different Ku-band frequency than the signal in the Rx direction. In the computations, it is assumed that the delay in the cables and the DCU shows no or very small frequency dependence in the range from 11 GHz to 14 GHz.

Reflections caused by impedance mismatch in the Ku-band segment of the system may cause systematic delay offsets. Any influence from these reflections still needs to be investigate in further delay.

VIII. Conclusions

An automated delay calibration system for a TWSTFT station has been developed and evaluated in a test bench. The heart of the system is a dual bi-directional 70 MHz to Ku-band up/down converter. This device allows measuring of additional independent delay loops in the station, covering all components from the modem to the antenna dish.

From measurement data acquired over several months, the stability of the station including the delay calibration unit has been evaluated. The delay stability (TDEV) of all different loops and of the transmit and receive path in the station is typically less than 60 ps over 1 day averaging.

Absolute delay calibration of TWSTFT station as proposed in this paper can become a useful alternative to the traditional TWSTFT link calibrations by means of a travelling TWSTFT station.

REFERENCES

[1] F. Mubarak, E. Dierikx, "Dual-Stage Quad-Mixer Satellite Simulator for a TWSTFT Station", IFCS &EFTF, 2011, San Fransisco, California, USA.

[2] Gerrit de Jong, et. All., "Automated Delay Measurement System For An Earth Station for two-Way Satellite Time and Frequency Transfer", PTTI , 1994, Reston VA, USA.

[3] ITU- 7/67-E, "The operational use of a two-way satellite time and frequency transfer employing PRN codes", 14th September 2009.

[4] T.E.Parker, V.Zhang, "Sources of Instabilities in Two-Way Satellite Time Transfer", IEEE, 2005.

Characterization of OP TWSTFT stations in colocation based on combined use of code and carrier phase data

Amale Kanj, Joseph Achkar, Daniele Rovera
LNE-SYRTE
Observatoire de Paris
Paris, France
amale.kanj@obspm.fr

***Abstract*— The TWSTFT carrier phase technique permits to improve the short term stability of the two-way links. The basic idea of this method is to calculate the offset between the frequencies of the two remote clocks in comparison. The frequency of the local oscillator on-board and Doppler coefficients are also determined. By applying the carrier phase method using the two OP ground stations in a common clock mode, a frequency stability of 1×10^{-12} is reached at 1 s while with the OP satellite simulator, a value of $4\text{x}10^{-13}$ is achieved.**

I. INTRODUCTION

Two-way satellite time and frequency transfer (TWSTFT) is one of the most precise methods for comparing remote time scales and frequency standards. Today, TWSTFT comparisons between Time institutes contribute to the realization of the International Atomic Time (TAI), calculated by the Bureau International des Poids et Mesures (BIPM), with a combined uncertainty of about 2 ns.

Each two-way ground station is equipped by a SATRE modem which applies the spread spectrum method over a generated intermediate frequency carrier modulated by a pseudo random noise code sequence at 1 Mchips/s carrying the clock signal. The two stations in comparison emit simultaneously a microwave signal which is transmitted to the remote station through a geostationary telecommunication satellite. The delay difference between the signal transmission from one site and the reception of the signal transmitted from the other site is determined by the Time Interval Counter (TIC) of each station.

The relationship of the two time scales in comparison can be written as [1]:

$$T_1 - T_2 = \frac{1}{2}(\Delta T_1 - \Delta T_2) + \frac{1}{2}\left[\left(\sigma_1^{Tx} - \sigma_1^{Rx}\right) - \left(\sigma_2^{Tx} - \sigma_2^{Rx}\right)\right] + \frac{1}{2}\left[(\sigma_1^{U} - \sigma_1^{D}) - (\sigma_2^{U} - \sigma_2^{D})\right] + \frac{1}{2}(\sigma_{21} - \sigma_{12}) + \frac{1}{2}\left[\left(\sigma_{R1}^{U} - \sigma_{R1}^{D}\right) - \left(\sigma_{R2}^{U} - \sigma_{R2}^{D}\right)\right] \quad (1)$$

ΔT_1 and ΔT_2 are the propagation delays measured by the TIC of station 1 and 2 respectively.

The phase difference between the two clocks is deduced by the combination of the two measurements.

σ_1^{Tx}, σ_1^{Rx}, σ_2^{Tx}, σ_2^{Rx} are the propagation delays in ground stations, σ_1^{U}, σ_1^{D}, σ_2^{U}, σ_2^{D} are the signal path uplink and downlink delays, σ_{21} and σ_{12} are the satellite path delays through the transponder from one station to another. σ_{R1}^{U}, σ_{R1}^{D}, σ_{R2}^{U}, σ_{R2}^{D} are the delays caused by the Sagnac effect.

In the past, we have reached a frequency stability of 8.10^{-16} at one day on the Ku band link [2].

Nowadays, the improvement of the stability of the TWSTFT technique must follows the improvement of the frequency stability of atomic clocks and primary frequency standards. Previous works [3][4] demonstrated that the TWSTFT carrier phase improves the short term stability of the two-way links. In this paper, we describe the principle of the two-way carrier phase technique based on the work developed in [4] and present the results of applying the carrier phase method in colocation using two two-way ground stations at LNE-SYRTE.

II. PRINCIPLE OF THE TWSTFT CARRIER-PHASE TECHNIQUE

The two-way carrier phase technique permits to compare remote atomic clocks by carrier phase measurements. The same equipments are used in both carrier and code phase methods.

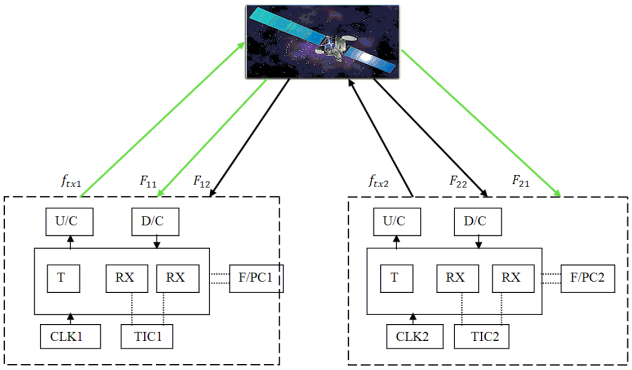

Figure 1. TWSTFT carrier phase principle.

The two remote stations in comparison emit a signal in the same time with a frequency f_{tx1} for station 1 and f_{tx2} for station 2, each station measures the frequency of the two-way signal received from the other station. In addition of the signal transmitted by the remote station, each station receives its own signal coming from the satellite. The frequency of the transmitted signal is shifted because of the Doppler effect due to the slight motion of the geostationary satellite and the unknown satellite local oscillator frequency.

As shown in Fig. 1, $F_{11}$and F_{22} are the ranging frequencies, F_{12} and F_{21} are the two-way signals frequencies received at station 1 and station 2 respectively.

Considering the clock frequency of station 1 as the reference system frequency fsys, the clock frequency of station 2 is shifted from this frequency by a value df. To calculate this frequency offset between the two clocks in comparison, the equation system of the two-way carrier phase method must be established.

A. Doppler Effect

The Doppler effect is the perceived change in frequency of an electromagnetic signal resulting from the relative movement of the source and receiver. In our case, the relative speed of the satellite is the origin of the Doppler shift in the carrier frequency transmitted from the ground stations.

The station 1 emits a signal with a frequency f_{tx1}. When the signal reaches the satellite, the frequency received on board is calculated as follows:

$$f_{rs} = f_{tx1} + k_1 f_{tx1} \quad (2)$$

With

$$k_i = \frac{v_i}{c} \quad (3)$$

v_i : Projection of the satellite velocity in the direction of station i.

c : Velocity of light.

The received frequency on board is then mixed with the satellite local oscillator frequency f_{slo}:

$$f_s = f_{tx1} + k_1 f_{tx1} - f_{slo} \quad (4)$$

The signal is emitted from the satellite to the station 2 from one side and back to the station 1 from the other side.

Thus, the received frequency at station 2 calculated in the reference of station 1 is:

$$(F_{21})_1 = f_{tx1} + k_1 f_{tx1} - f_{slo} + k_2(f_{tx1} + k_1 f_{tx1} - f_{slo}) \quad (5)$$

The ranging frequency is calculated in the same way as follows:

$$F_{11} = f_{tx1} + k_1 f_{tx1} - f_{slo} + k_1(f_{tx1} + k_1 f_{tx1} - f_{slo}) \quad (6)$$

B. Frame of reference

For the purpose of calculating the expression of the received frequencies at each station, a frame of reference should be defined.

In fact, both timescales must be in the same frame of reference to be compared.

In order to convert a given frequency f_m as defined by a frame of reference m to its equivalent frequency f_n in a frame of reference n the following transformation equation is used:

$$f_n = f_m \frac{f_{mref}}{f_{nref}} \quad (7)$$

Where f_{mref} and f_{nref} are the instantaneous frequencies of the reference clock at the transmitter and the receiver respectively.

Considering station 1, the oscillation period is equal to $\frac{1}{f_{sys}}$, while for the station 2 the oscillation period is equal to $\frac{1}{f_{sys}+df}$.

Therefore, the duration of fsys cycles in station 2 is equal to $\frac{f_{sys}}{f_{sys}+df}$.

As an example, the expression of f_{tx1}calculated in the frame of reference of station 2 is equal to:

$$(f_{tx1})_2 = (f_{tx1})_1 \frac{f_{sys}}{f_{sys}+df} \quad (8)$$

We will proceed further on by calculating all the frequencies in the frame of reference of the receiver.

C. Equation system

By applying the transformation presented in equation 7 to the equation 5, the expression of the received frequency from station 1 measured at station 2 is obtained:

$$(F_{21})_2 = f_{tx1}\left(\frac{f_{sys}}{f_{sys}+df}\right)(1+k_1)(1+k_2) - f_{slo}\left(\frac{f_{sys}}{f_{sys}+df}\right)(1+k_2) \quad (9)$$

By proceeding in the same way to calculate the ranging frequency of station 2 and the frequency of the signal received by station 2 from station 1, we build the TWSTFT carrier phase equation system:

$$\begin{aligned} F_{11} &= f_{tx1}(1+k_1)^2 - f_{slo}(1+k_1) \\ F_{22} &= f_{tx2}(1+k_2)^2 - f_{slo}\left(\frac{f_{sys}}{f_{sys}+df}\right)(1+k_2) \\ F_{21} &= f_{tx1}\left(\frac{f_{sys}}{f_{sys}+df}\right)(1+k_1)(1+k_2) - f_{slo}\left(\frac{f_{sys}}{f_{sys}+df}\right) \\ F_{12} &= f_{tx2}\left(\frac{f_{sys}}{f_{sys}+df}\right)(1+k_1)(1+k_2) - f_{slo}(1+k_1) \end{aligned} \quad (10)$$

The constructed equation system is a nonlinear system with four unknowns: f_{slo} , k_1 , k_2 and df . To find the solution of this system, several means can be used.

III. SOLVING THE EQUATION SYSTEM

By referring to the equation system presented in equation 10, we deduce that the received frequencies satisfy the following equality:

$$F_{11}F_{22} - F_{12}F_{21} = 0 \quad (11)$$

As a result of this dependency, using three of the four equations will be sufficient to calculate the frequency offset. Considering the case of two different transmitted frequencies, a solution for the clock offset in terms of F_{11} , F_{12} , F_{22} and f_{slo} is calculated as follows:

$$\Delta f = -1 + \sqrt{\frac{2F_{12}\,f_{tx1}}{F_{22}\,f_{tx2}}}\frac{\sqrt{{f_{slo}}^2+2f_{tx1}F_{12}+f_{slo}\sqrt{{f_{slo}}^2+4f_{tx1}F_{11}}}}{\left(f_{slo}+\sqrt{{f_{slo}}^2+4f_{tx1}F_{11}}\right)} \quad (12)$$

With:

$$\Delta f = \frac{df}{f_{sys}}$$

Different solutions could be defined in the same way using other equations combinations.

However for equal uplink frequencies, another solution can be calculated by applying the Taylor theorem [5] in order to linearize the four system's equations. We proceed by calculating multiple differences between the equations as follows:

$$\begin{aligned} F_a &= F_{11} - F_{22} = 2kf_{tx} - (\Delta f + k)f_{slo} \\ F_b &= F_{12} - F_{21} = 2.\Delta f.f_{tx} - (\Delta f + k)f_{slo} \\ F_c &= F_{12} - F_{22} = (f_{tx} - f_{slo})(\Delta f + k) \end{aligned} \quad (13)$$

With:

$$\begin{aligned} k &= k_1 - k_2 \\ f_{tx} &= f_{tx1} = f_{tx2} \end{aligned}$$

The equation of Δf is then determined:

$$\Delta f = -\left[\frac{F_a - F_b}{2} - \frac{f_{tx}}{f_{tx}-f_{slo}}F_c\right]\frac{1}{2f_{tx}} \quad (14)$$

To calculate Δf, the value of the satellite LO frequency must be known.

By using the first equation of the carrier phase system, we calculate the satellite LO frequency:

$$f_{slo} = -\left[\frac{F_{ii}}{1+k_i} - (1+k_i)f_{tx}\right](1+\Delta f) \quad (15)$$

k_i is determined through the ranging delay.

With i =1, 2 for station 1 and station 2 respectively.

IV. SYSTEM SETUP AND EXPERIMENTAL VALIDATION

All measurements reported further on have been realized in colocation between two two-way ground stations at LNE-SYRTE using two SATRE modems and the same Hydrogen Maser clock.

The experiments were made using the satellite TELSTAR 11N in the Ku band. As the two-way regular sessions are scheduled during even hours, the carrier phase tests were made during odd hours. We also did three days of continuous 1 s measurements.

The experiments consisted on emitting the same microwave frequency from the two stations using a chip rate of 1 Mchips/s and recording 1 s time delay and carrier frequency data.

We used the equation 14 to calculate the frequency offset. The Doppler coefficients and the frequency of the satellite local oscillator will be determined.

A. Experimental validation of the system setup

The experimental validation has consisted to verify if the transmitted microwave frequencies from the two stations are known and if the relationship presented in the equation 11 is satisfied.

An unknown frequency offset has been detected between the transmitted frequencies from the two TWSTFT ground stations at LNE-SYRTE that means that the value of one of the transmitted microwave frequencies was not exactly identified. To determine this frequency, we have applied small frequency shifts on the transmitted frequency of the station. Fig. 2 shows that the variation of the frequency offset is a function of the applied frequency shifts. As the value of the determined offset is non constant and can change in amplitude depending on the used microwave frequency, we have replaced the frequency converters of one of our stations by spare equipments permitting to achieve a precise transmitted microwave frequency.

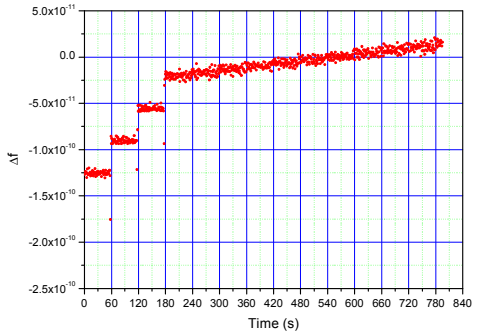

Figure 2. Microwave frequency shifts applied on one station permitting the determination of the frequency offset.

On the other side, the variation of the difference between the ranging frequencies and the two-way frequencies is illustrated in Fig. 3, we can easily observe that there is no offset nor drift. In consequence, the relationship is fully satisfied.

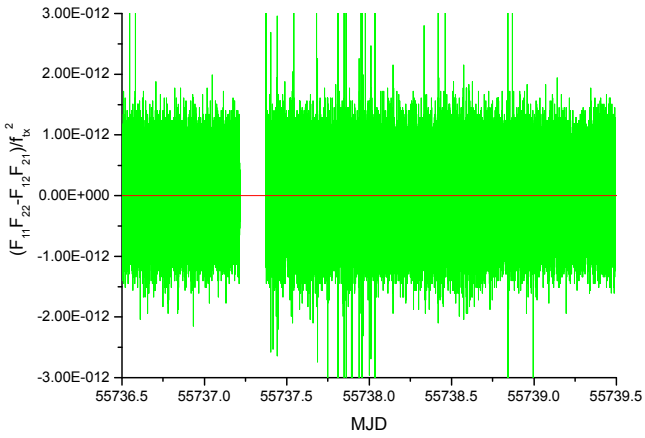

Figure 3. Variation of $F_{11}F_{22} - F_{12}F_{21}$ versus time expressed in MJD.

B. *Ranging delay measurement and Doppler coefficients evaluation*

Ranging measurements were made using one station during three days. The geostationary satellite revolves around the earth at the same angular velocity of the earth itself, 360 degrees every 23 h 56 min 4 s in an equatorial orbit, and therefore it seems to be in a fixed position over the equator. However, many effects cause the alteration of its orbit, such as force of gravity of the sun and the moon, and the non circular form of the equator. The satellite has then a back and forth movement around a fixed position. Fig. 4 shows that this movement is the origin of a sinusoidal delay variation with peak to peak of about 160 µs.

In the same figure, the variation of the associated Doppler coefficient is shown during three days. However, the satellite velocity is calculated from the ranging delay.

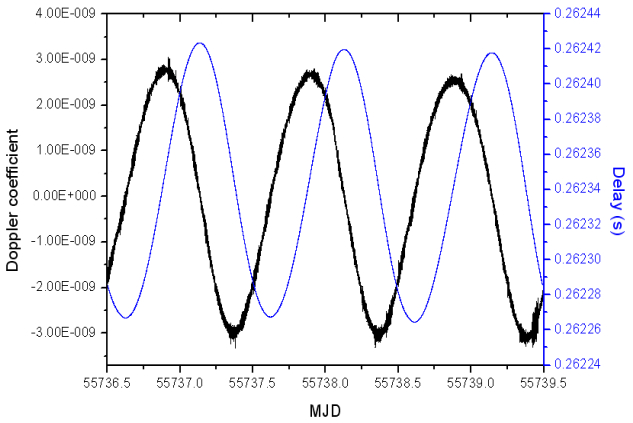

Figure 4. Variation of the measured ranging delay and associated Doppler coefficient.

C. *Determination of satellite LO frequency*

The frequency of the satellite local oscillator is calculated using the equation 15, and shown in Fig. 5, we observe a sine wave variation with a period of about 24 h and a peak to peak amplitude of about 300 Hz. We also observe a distortion on the signal frequency which is repeated in the same time every day. This is caused by the temperature variation on the board of the satellite.

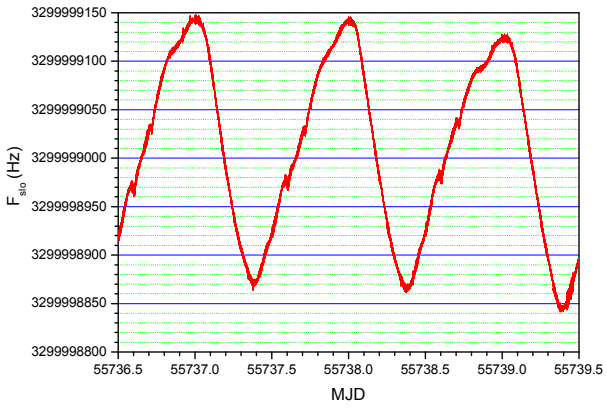

Figure 5. Variation of the calculated frequency of the satellite local oscillator versus time.

V. *CHARACTERIZATION OF THE TWO-WAY CARRIER PHASE LINKS*

We present the characterization of the OP-OP link in term of frequency stability in common clock mode.

According to Fig. 6, the measurement noise of continuous two-way carrier phase measurements during three days reached a frequency stability of 1.78×10^{-12} at 1 s . After an averaging time equal to 300 s, a degradation on the link stability appears.

The best performance achieved with two-way carrier phase measurements is shown in the same figure. The frequency

stability reached 1.13×10^{-12} at 1 s. After an averaging time of 128 s, a frequency stability equal to 2.41×10^{-14} is obtained. However, a simple interpolation reveals a frequency stability around 10^{-17} at one day. Actually, with our system set up we are still far from this performance.

To compare the performance of the TWSTFT carrier phase against the GPS carrier phase, we used two geodetic dual frequency receivers in common clock mode, the associated frequency stability is reported in Fig. 6. It is clearly shown that the short term stability of the two-way carrier phase link is better than the GPS carrier phase link.

However, to understand the origin cause of the frequency stability degradation on the two-way carrier phase links, we used the satellite simulator developed in our laboratory [6]. This device permits to measure the delay in the equipments of the two-way earth Station. Therefore, by using the satellite simulator, the atmospheric propagation and the satellite noise can be eliminated.

Fig.6 shows that the measurement noise of the simulator-station path is extremely low, less than 4×10^{-13} at 1 s. However, a degradation of the link stability appears in the same averaging time as the carrier phase links stability, which leads us to limit the causes of this degradation at two-way station equipments and local environmental conditions.

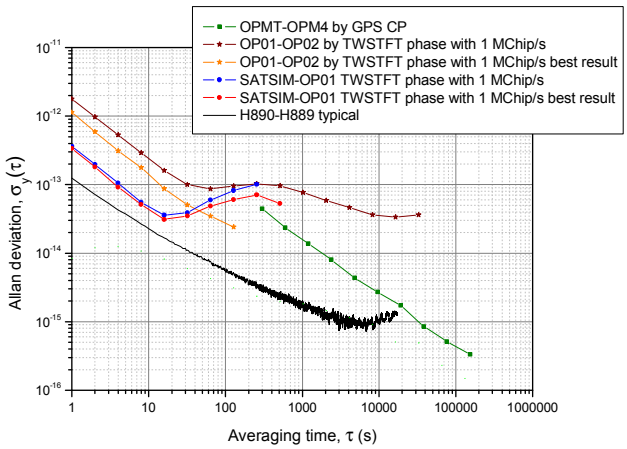

Figure 6. Frequency stability of OP-OP link using different techniques (TW, GPS). As a reference, stability of local Hydrogen Maser clock is also reported.

VI. CONCLUSION AND OUTLOOKS

It has been demonstrated that the use of the phase measurements in TWSTFT technique improves the short term stability of the two-way links.

In this paper, we have presented the first results of application of TWSTFT carrier phase method in colocation by using two two-way stations at LNE SYRTE. The following performances are achived in terms of frequency stability :

- 1×10^{-12} at 1 s.
- 3×10^{-14} at 100 s.
- Degradation at 300 s.

We used the satellite simulator developped in our laboratory to better understand the causes of the stability degradation on the two-way carrier phase links. This work is not completely achieved and must be continued. In this context, further studies of atmospheric effects impact on TWSTFT carrier phase should be releazed.

Otherwise, considering the carrier phase equation system by using phase data instead of frequency data permits once the phase ambiguity is fixed to overcome the need for doing continuous measurements as in present case. However, this task requires a hardware development at the SATRE modem level.

ACKNOWLEDGMENT

The authors would like to thank B. Fonville, D. Matsakis (USNO), W. Schaefer (Timetech) and the CCTF working group on TWSTFT for their support.

This work was partially funded by the French Space Agency (CNES).

REFERENCES

[1] "The operational use of two-way satellite time and frequency transfer employing pseudorandom noise codes," Rec. ITU-R TF.1153-3, 2010.

[2] V. Zhang et al. "Two-way satellite time and frequency transfer using 1 MCHIP/S codes ", 41st Annual Precise Time and Time Interval (PTTI) Meeting, 2009.

[3]W. Schaefer, A. Pawlitzki and T. Kuhn, "New trends in two-way time and frequency transfer via satellite," Technical report, Proceedings of the 31 Annual Precise Time and Time Interval (PTTI) Systems and Applications Meeting, pp. 505-514, 1999.

[4] B. Fonville, D. Matsakis, A. Pawlitzki and W. Shaefer, "Development of carrier-phase-based two-way satellite time and frequency transfer (TWSTFT)," Technical report, Proceedings of the 36th Annual Precise Time and Time Interval (PTTI) Systems and Applications Meeting, pp. 149-164, 2005.

[5] W. Press, B.Flannery, S.Teukolsky and W.Vetterling, "Numerical recipes in C : The art of scientific computing," 1992.

[6] J. Achkar "Design, realization and application of a satellite simulator in a TWSTFT station," 40th European Microwave Conference, pp. 1516-1519, 2010.

Two Way Time Transfer with Picoseconds Precision and Accuracy

Jan Kodet[1,3], Ivan Prochazka[1], Josef Blazej[1]
Dep. Of Physical electronic
[1]Czech Technical University in Prague
Prague, Czech Republic
kodet@fjfi.cvut.cz

Petr Panek[2]
[2]Academy of Sciences of the Czech Republic,
Prague, Czech Republic

Ulrich Schreiber[3], Pierre Lauber[3]
[3]Technical University Munich, Wettzell Observatory,
Bad Koetzting, Germany

Abstract — **The first results of a two way time transfer between two timing devices over modest distances with sub-ps precision and a few ps accuracy were the major tasks of this work. The two way time transfer scheme employing a single coaxial cable was applied. Based on our previous results we have designed and constructed a timing device which allows registration of Times of Arrivals of pulses with sub-ps timing resolution, linearity, and stability. The concept of the timing devices enables to carry out time tagging of pulses of interest in parallel to the comparison of the time scales of these timing devices. The two timing devices were located in different laboratories and buildings within one institution. The common clock 5 MHz was referenced to a Cesium clock. The analysis of systematic errors contribution shows that the accuracy of the time transfer well below 10 ps may be achieved. The time transfer was accomplished over distances of the order of hundreds of meters. The main limitation for longer distances is the quality of the coaxial cable used for time transfer together with the amount of radiofrequency interference within the experiment.**

I. INTRODUCTION

Event timing systems are often used in a number of experimental techniques. Commonly, measurement of Times-of-Arrival (ToA) of pulses generated from two or more different sources (detectors, clocks, ...) with respect to a common time scale is required in order to evaluate delays between these pulses. This could be a quite easy task if all the pulse sources are situated at the same place. Then all event timers can be placed in the same rack together with a common time base and their inputs are connected to the pulse sources via relatively short cables. The cable delays are supposed constant thus they can be simply corrected in the ToA measurements.

This approach cannot be used in the cases when one or more pulse sources are so remote that the cable delays variations cannot be neglected. The temperature dependence of a high performance semirigid coaxial cable of the length of 100 m can be expected in the range of ±5 ps/K and other coaxial cables have commonly the temperature dependence much higher [1]. The event timer which was developed in out laboratory provides sub-picosecond precision and the temperature dependence lower than 0.2 ps/K [2]-[6]. Evidently the use of long cables can completely degrade the performance of the whole timing system.

The solution is to place the event timers beside the pulse sources and keep the length of the cables as short as possible. But in this case an extremely accurate time distribution, i.e. time transfer between the event timers must be guaranteed. Because the time distribution must be insensitive to changes of cable delays, the only possible approach is the Two Way Time Transfer Technique (TWTT) [7], [8].

II. TIMING DEVICE

Based on the previous results [2]-[6] we have designed and constructed an Event Timer (ET) which allows measurement and registration of Times of Arrival (ToA) of input pulses with respect to a local time base. A new concept of the SAW filter excitation allowed a further improvement of the device performance. The single shot precision of the registration of synchronously generated time markers lower than 490 fs RMS was achieved, see Figure 1.

When two equal ETs (channels) are used and ToAs of split asynchronous pulses are measured, the resulting single shot precision is 700 fs RMS per channel, see Figure 2. This result contains all the nonlinearity effects of the time interpolation in addition.

Operating the device in a common laboratory environment without temperature stabilization, the TDEV better than 4 fs is routinely achieved for averaging times from 300 s to 3000 s [9].

To be able to check the measurement performance and do experiments such as synchronous triggering of laser fire or the two way time transfer, a reference time mark generator has

been included into the timing device. It generates low jitter pulses synchronously to the local time base. The repetition frequency of these pulses and number of generated pulses are programmable. The timing jitter of the pulses is below 280 fs RMS.

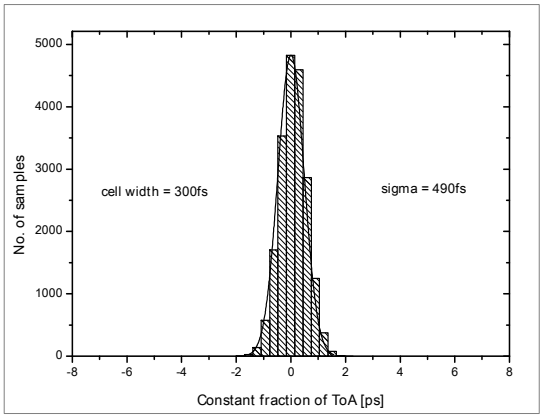

Figure 1. The constant fraction of synchronous ToA was recorded. The normal distribution function was plotted to show good agreement with normal distribution. The rms of the measured data is 490 fs, this figure contains also jitter of the time mark generator which is roughly ~280 fs. Distracting the rms jitter of time mark generator one get the rms of measurement 400 fs.

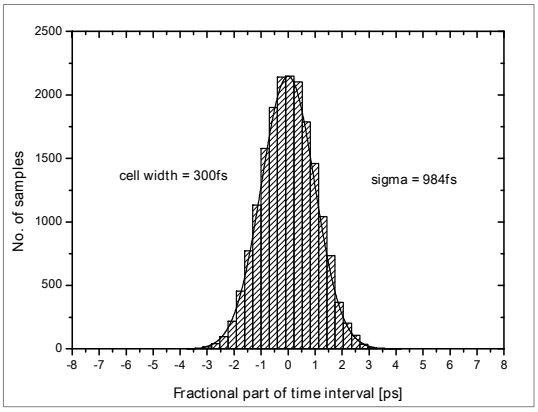

Figure 2. Times of arrival of pulses generated from pulse generator were measured on two channels. The pulses were passively divided and were fed in to two independent channels. The normal distribution function was plotted to show good agreement with normal distribution. The rms of the measured data is 984fs, i.e. ~696fs per channel.

To be able to check the measurement performance and do experiments such as synchronous triggering of laser fire or the two way time transfer, a reference time mark generator has been included into the timing device. It generates low jitter pulses synchronously to the local time base. The repetition frequency of these pulses and number of generated pulses are programmable. The timing jitter of the pulses is below 280 fs RMS.

The Figure 3. shows the PCB design of the event timing device.

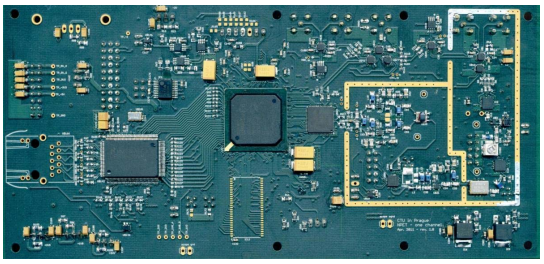

Figure 3. The figure shows the bottom side of PCB, the FPGA si located in the middle of the PCB, the exciter and filter is located at right side – inside the shielding box.

III. TWTT PRINCIPAL

The technique of the Two Way Time Transfer (TWTT) via single coaxial cable was inspired by the comparison of the two event timers using split pulses. Using this technique the pulse is split into two equal pulses and connected to the ET A using cable C_1 and to ET B using cable C_2; ToAs at both devices are measured and time difference is computed ($Diff_1$). Then the cables are exchanged (ET A -> C_2 and ET B -> C_1) and time difference ($Diff_2$) of ToAs is computed again. The time scales difference between both event timers is computed using formula

$$\hat{\Delta}_c = \frac{1}{2}\left(Diff_1 + Diff_2\right) \quad .$$

The advantage of exchanging of the cables is that the time scales difference do not depends on the length of the cables C_1 and C_2.

Inspired by the described method we have implemented the TWTT technique according to the Figure 4. .

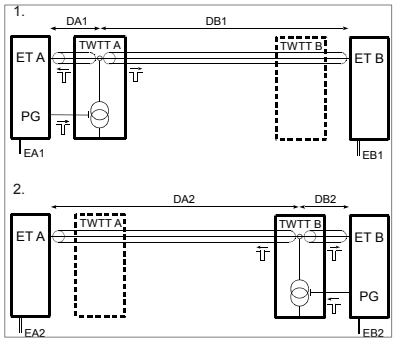

Figure 4. Block scheme of the Two Way Time Transfer via a single coaxial cable: 1st step when the TWTT module A is generating the test pulse, 2nd step when the TWTT module B is generating the test pulse.

The operating scheme is the following: two identical Event Timers ET A and ET B are equipped with TWTT modules, which are located close to them. These modules are interconnected by a single coaxial cable. The measurement is carried out in two steps. In the first step the ET A generates a pulse, using a current driver the pulse is implied in to an interconnecting cable and the ToA of the received pulse is measured by both event timers (ToA_{A1} and ToA_{B1}). In the second step the role of the devices is exchanged. The ET B generates equal pulse as to the pulse generated by ET A. The pulse propagates toward both devices where the pulse is time tagged (ToA_{A2} and ToA_{B2}). The timescales difference can be then computed according to

$$\hat{\Delta} = \frac{1}{2}\left((ToA_{B1} - ToA_{A1}) + (ToA_{B2} - ToA_{A2})\right),$$

and as a side product one obtains a delay of the cable

$$\tau_c = \frac{1}{2}\left((ToA_{B1} - ToA_{A1}) - (ToA_{B2} - ToA_{A2})\right).$$

The precision of the resulting time scales difference will obviously depend on the precision of both event timers, reproducibility of pulses generated by TWTT modules and on the influence of noise induced on the interconnecting cable. The event timers and TWTT modules used in our experiments exhibited sub-picoseconds timing resolution, linearity and long term stability. Therefore the sub-picoseconds precision of the TWTT is routinely achieved.

IV. INPUT BOARD

In developing of a new input board the main attention was put on enabling TWTT implementation in parallel with standard ToA measurement. The input board serves as an extension board which is put in front of the event timing device. The input board consists of two equal input channels which shares one event timing device and a pulse current source which is triggered by pulse generate implemented inside event timing device. The photograph of the input board electronic is in Figure 5.

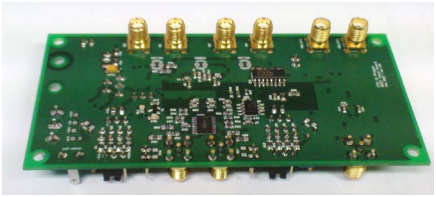

Figure 5. The photograph of TWTT extension input board for event timer. The input board has two input channels with adjustable trigger levels and slopes. The TWTT driver provides a fast output pulses with slew rates of 2 V/ns. The input board enables to operate the device in a standard event timing regime in parallel with TWTT.

V. SYSTEMATIC ERRORS VERIFICATION

The systematic errors needed to be verified using independent method. Two event timers were put besides and the same clock was connected to both devices. At first the time scales difference was measured using split pulses. The cables used for connecting these pulses were exchanged to distract the different length of the cables; a 1000 measurement was done in each step with precision on 1.3 ps RMS. As a second step the time scales difference was measured using TWTT method, the precision is dependent on the slew rate of the pulses which appears at the second end of the interconnecting cable. The jitter of the TWTT method was not higher then 1.8 ps RMS for slew rates of pulses up to 0.1 V/ns. Those two time scales differences were obtained for two different length of interconnecting cables (slew rates); and sequence of measurement was made. Between two consequent measurements the cables needed to be 3 times exchanged; entire data set was collected during several days. The results are plotted in Figure 6.

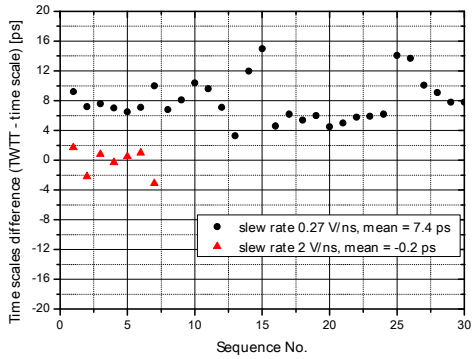

Figure 6. The figure shows the comparison of the TWTT method with classical comparison using split pulses. The comparison was done for two different lengths of the interconnecting cables. The first (short) cable had the slew rate of the sent pulses at the far end of the cable very close to TWTT driver itself (2 V/ns). The second cable (long) had slew rate of 0.27 V/ns.

The experimental results show that absolute time transfer for the short cable can be achieved below 5 ps with mean value of -0.2 ps. The reproducibility is mostly influenced by the reproducibility of the connection of the SMA connectors.

The comparison of the TWTT using long cable shows slight offset of systematic errors with the mean value of 7.4 ps. The offset is caused by the non-symmetry of trigger levels at the inputs of the input comparators. The absolute time transfer can be achieved below 20 ps.

VI. EXPERIMENTS

To test the performance of the TWTT method we have implemented the experiment shown in Figure 7.

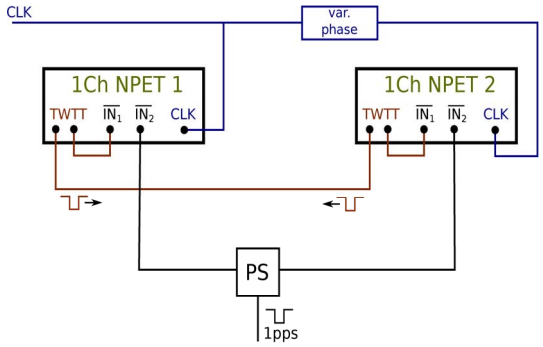

Figure 7. Testing of the performance of the TWTT method. The same clock was used and phase variation was achieved by heating one of the clock distributions.

The two event timers were connected to the same clocks. One part of the distribution of the clocks had phase variation which was performed by heating of the cables. In to the second input of the event timers the split 1PPS pulses were connected. Between each measurement of the 1PPS pulses the TWTT was made and the time scales difference was subtracted from time difference of the 1PPS pulses. The result is in Figure 8.

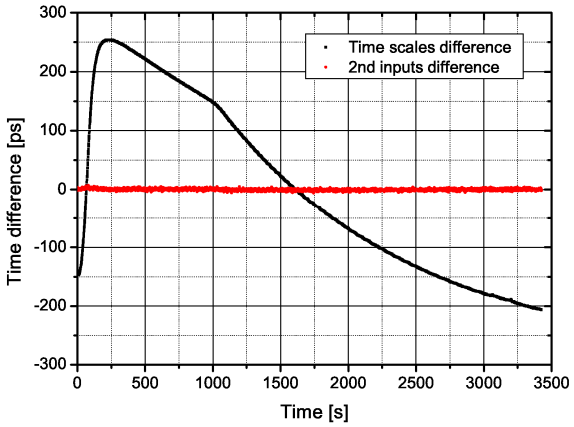

Figure 8. The graph shows time scales variation and the difference of the event timers after application of the measured calibration. The difference of the event timers was measured in second input.

The TWTT preliminary experiment was carried out in Fundamental Station Wettzell. At first the TWTT setup was installed in SLR building. The clock sources were derived from master clocks and both devices were connected to different places of clock distribution network. The TWTT was performed during several hours, see Figure 9.

Then the same experiment was done within two buildings, master cock room and SLR building. The coaxial cable Andrew Heliax LDF50 was used for interconnecting both event timers.

The time scales difference changed by 200 ps within 16 hours, see Figure 10.

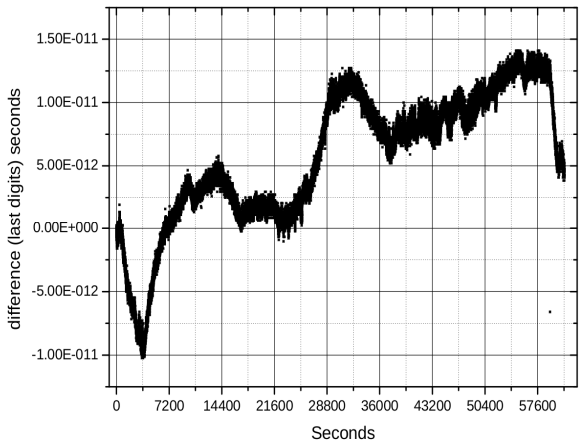

Figure 9. Difference of the two time scales formed by NPET timing systems in the field experiment within one building.

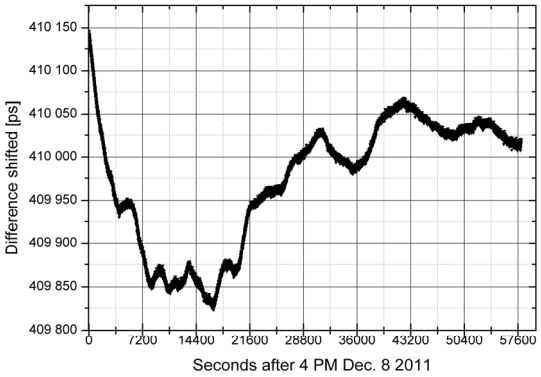

Figure 10. Difference of the two time scales formed by NPET timing systems in the field experiment within master clock room and SLR building.

VII. SUMMARY

A Two Way Time Transfer technique for modest distances with an accuracy of a few picoseconds has been designed, analyzed, and experimentally verified. It uses a single coaxial cable driven by pulse current sources. The ToAs are measured with respect to local time scales at both ends of the cable and the difference between the time scales computed using the TWTT procedure eliminating the cable delay influence.

The key requirement was to keep the possibility of using the device as a standard event timer in parallel with the time transfer. Therefore the input board has two independent channels and TWTT drivers.

The systematic errors of the time transfer were analyzed. The main requirement put on TWTT method to be comparable with classical comparison of two event timers (time scales) is keeping the symmetry of the input connectors delays, trigger

levels, and slew rates of the pulses, which are used for TWTT. Those symmetries must be kept as good as possible.

The TWTT method was compared with classical comparison based on splitting of pulses. The measurement with a short cable with slew rate close to the 2 V/ns proved that when the trigger levels are correctly adjusted than systematic error in comparison with classical method is very close to be zero and the reproducibility depends mainly on the quality of the connectors. Using a long cable with slew rate of 0.27 V/ns the comparison within the classical method was 7.4 ps. Using this TWTT system several experiments in Prague and Wettzell laboratories were done.

ACKNOWLEDGMENT

This work has been carried out at the Czech Technical University in Prague. Numerous grants were provided by the Czech Grant Agency, Czech Ministry of Education and by international agencies. Recently, the research and development of time transfer technologies is supported by SMT CR grant LH12005. The support of the Fundamental Station Wettzell, Germany, operated jointly by Federal Bureau Cartography and Geodesy and the Technical University Munich is highly appreciated.

REFERENCES

[1] Heliax Coaxial Cables. Andrew Ltd., USA

[2] Pánek P.; "Time Interval Measurement Based on SAW Filter Excitation". IEEE Trans. Instr. Meas, vol. 57, no. 11, pp. 2582-2588, Nov 2008

[3] Procházka, I. - Pánek, P.; "Nonlinear effects in the time measurement device based on surface acoustic wave filter excitation". Review of Scientific Instruments. 2009, vol. 80, no. 7, p. 076102

[4] Pánek, P. - Procházka, I. - Kodet, J.; "Time measurement device with four femtosecond stability". Metrologia. 2010, vol. 47, no. 5, p. L13-L16

[5] Pánek, P. - Procházka, I.; "Time interval measurement device based on surface acoustic wave filter excitation, providing 1 ps precision and stability". Review of Scientific Instruments, vol. 78, no. 9, Sep 2007.

[6] Pánek, P.; "Random Errors in Time Interval Measurement Based on SAW Filter Excitation. IEEE Transactions on Instrumentation and Measurement". vol. 57, no. 6, pp. 1244-1250, Jun 2008.

[7] Sullivan D.B. - Levine J.; "Time Generation and Distribution. Proceedings of the IEEE", vol.79, no.7 (July 1991), pp.907-913.

[8] Levine J.; "A Review of Time and Frequency Transfer Methods". Metrologia, vol.45 (2008), pp. S162-S174.

[9] Procházka, I. - Kodet, J. - Pánek, P. - Schreiber, U.; "Novel concept of sub-picosecond timing system and its applications in fundamental metrology". In Proceedings of 2011 Joint Conference of the IEEE International Frequency Control and the European Frequency and Time Forum (FCS), 2011, 161-164

Studies of a short and long - term stability of an active hydrogen maser with stand alone cavity auto tuning

N. Demidov, V. Vorontsov, A. Belyaev
"Vremya-CH " JS company
Nizhny Novgorod, Russia
demidov@vremya-ch.com

I. Blinov
"VNIIFTRI"
Mendeleevo, Russia

***Abstract* — This paper outlines the evolution of the stand alone cavity auto tuning of the active hydrogen maser using microwave cavity frequency switching technique. Analysis of basic destabilizing factors limiting short- term, long- term frequency stability and phase noise of output signal of this technique is given. The effect of cavity tuning on short and medium term stability characteristics is negligible. Long-term frequency stability of (3÷5) × 10^{-16} at averaging time 1÷20 days has been achieved.**

I. INTRODUCTION

Hydrogen masers are widely used for various scientific and high technology applications due to their high both short-term and long- term frequency stability.

In experimental physics there are plenty of problems where the demands for the highest oscillator's frequency stability are critical: for example, to specify the fundamental physical constants' values, to verify the special and general relativity theories. Hydrogen masers are also used in very long baseline interferometry (VLBI), because they provide the best frequency stability at the typical averaging time from 10^2 to 10^3s. On July 18, 2011 the spacecraft «Zenit-2SB» with the unique radio-observatory «Spektr-R» has been successfully launched. The satellite contains two active hydrogen masers produced by «Vremya-CH» company. One of them is used as a reference signal for VLBI.

The role of active hydrogen masers is now increasing in time keeping applications. Active hydrogen masers have been widely used in Russia for time keeping since 1970s [1]. Since 1990s many of time keeping centers have started including them into atomic clocks ensembles.

Bureau International des Poids et Mesures (BIPM) has been using data from more than one hundred masers all over the world to form International Atomic Time (TAI).

The active hydrogen maser frequency stability is determined by the expression [2]:

$$\sigma_y(\tau) = \frac{1}{Q_a\sqrt{\tau}}\sqrt{\frac{kT}{2P_a}}\ , \qquad (1)$$

where P_a is a power delivered by the atoms to the cavity, k - Boltzmann's constant (1.38×10^{-23} JK^{-1}), T- absolute temperature, Q_a - hydrogen atomic line quality factor, τ-averaging time. This expression describes hydrogen maser stability at averaging time τ > 10s.

Typical value Q_a=2×10^9 and P_a ~ 2×10^{-13} W.

Stability of H-maser is $\sigma_y(\tau) \approx 5\times10^{-14} \times \tau^{-1/2}$ at τ > 10s.

At less averaging time the electronic circuit noise is determinant and the up-to-date maser 1s stability is ~(0.8÷1.0) × 10^{-13}. According to the equation (1) hydrogen maser frequency stability depends on the averaging time as $\tau^{-1/2}$. But it is correct only till a number of physical perturbation factors starts acting. The most important of them are shown in Table 1.

The perturbation factors given in Table 1 influence in different ways. Though the second order Doppler's effect gives a bigger frequency shift, it is well controlled. The spin-exchange shift is proportional to the atomic density in the bulb n_a and usually there is no any problem to control it as well. The two last factors have a great importance for achieving the long-term frequency stability, especially the last one.

The method of the atomic line quality modulation Q_a was used in previous generations of our masers for cavity tuning. The stability (noise floor) with this technique on a daily basis was ~2×10^{-15} [3] and the main reason limiting further improvement of frequency stability, was possibly related to the big time constant of this cavity tuning method: $\mathfrak{T}$>1day [4].

Cavity frequency switching method has much less time constant $\mathfrak{T}$~3×10^3s [4] and potentially allows to get better long-term stability. This system was proposed by B. Gaigerov and G. Elkin [5] first and then was successfully developed by H. Peters [6].

We performed cavity frequency switching method in hydrogen maser of CH1-75A model for the first time and now we have developed a new model of the active hydrogen maser VCH-1003M with that cavity tuning method which allowed us to considerably improve both short-term and long-term stability.

TABLE I. HYDROGEN MASER STABILITY PERTURBATION FACTORS

Perturbation factors	Equation	Fractional frequency offset	stability floor
Second order Doppler's effect	$\frac{\Delta\nu_D}{\nu} = \frac{-3kT}{2mc^2}$	-4.31×10^{-11}	$\sim10^{-16}$
Spin-exchange shift	$\frac{\Delta\nu_D}{\nu} = \alpha n_a$	2×10^{-13}	$\sim10^{-15} \div 10^{-16}$
Magnetic field dependence	$\frac{\Delta\nu_m}{\nu} = \frac{2.773\times10^{11}\times B_0^2}{\nu_0}$	2×10^{-13}	$\sim10^{-15} \div 10^{-16}$
Wall shift	$\frac{\Delta\nu_w}{\nu} = \frac{K}{D}$	$-(0.5\div2)\times10^{-11}$	$\sim10^{-15} \div 10^{-17}$ per day
Cavity pulling	$\frac{\Delta\nu_c}{\nu} = \frac{Q_c}{Q_a}\times\frac{(\nu_c-\nu_0)}{\nu_0}$	~0	$\sim10^{-14} \div 10^{-16}$

II. OVERALL DESIGN OF VCH-1003M ACTIVE HYDROGEN MASER

Figure 1 shows physics package schematic diagram.

The main features of the VCH-1003M are the following:

-high-precision digital control of the maser cavity ovens with temperature stability of the order 10^{-5} ºC;

- the cavity, as well as in our previous maser models, is made of sitall — the special glass having a very low thermal expansion less than 2×10^{-7}/ºC. This cavity material and precision ovens control allows very low maser temperature sensitivity less than $(1\div2)\times10^{-14}$/ºC to be obtained;

-five layer magnetic shields provide low magnetic sensitivity $<1\times10^{-14}/10^{-4}$T;

- light and compact vacuum system consists of getter and ion pumps. Getter contains pressed titanium cuttings or pressed titanium-vanadium powder as a pumping substance and has two separate chambers. The first one serves the discharge dissociator and state selector magnet section. Another part pumps out the hydrogen from the storage bulb region.

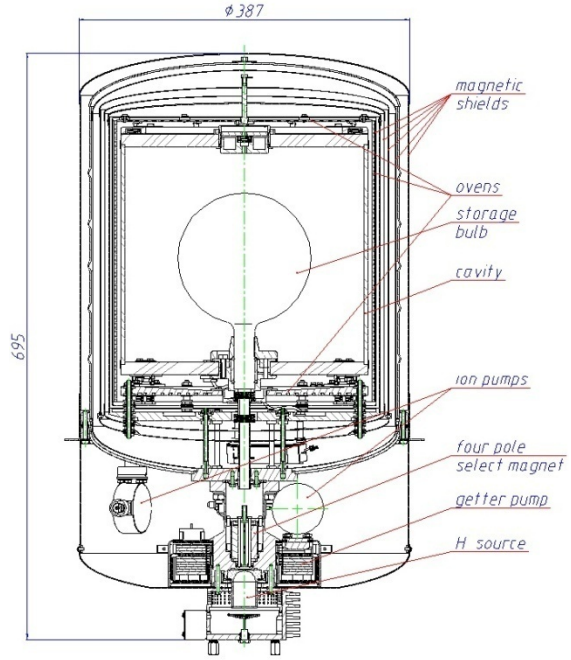

Figure 1. H-maser physics package schematic diagram

Two small ion pumps of 2 l/s capacity are used for pumping out residual gases from the getter and from the cavity, ovens and magnetic shields system.

To start up the getter the built-in heater is used to provide the temperature up to 800ºC. The practical usage of getters with external heaters when the inside temperature hardly reached 450ºC discovered their unreliable operation. This design permits to reach the vacuum better then 10^{-6} Pa in storage bulb providing high long-term stability of the hydrogen maser. This design of the vacuum system has been used also in passive hydrogen masers since 2012.

III. CAVITY FREQUENCY SWITCHING SYSTEM

Figure 2 shows principle of operation and an electronics block diagram of the cavity tuning system.

This is a traditional active maser scheme. The Microwave Receiver coupled to the cavity transmits the RF signal to PLL Unit to lock the 5MHz crystal oscillator. Circuit contains Modulation Period Generator (Modulator) which forms square wave signal of 87.2 Hz frequency. Digital-to-Analog Converter (DAC2) produces two-level voltage Um, which drives the varactor modulating the cavity resonant frequency within about 15 kHz range. When the average cavity frequency differs from the atomic hydrogen line frequency, the maser output signal level is modulated. After being detected from IF signal 20.405 MHz and amplified, low frequency signal goes to Synchronous Detector input as a mistuning signal.

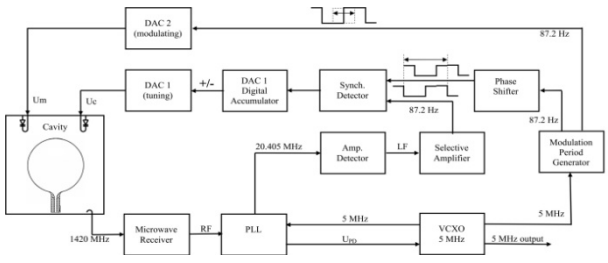

Figure 2. Schematic diagram of a cavity tuning system based on the cavity frequency switching method

Signal to another Synchronous Detector input passes from Modulator through Phase Shifter. The last one eliminates the signal propagation delay through the

electronic circuitry. Phase Shifter resolution is one 1024th of modulation period.

Synchronous Detector produces "+" or "-" counting pulses depending on coincidence or noncoincidence of both its input signals and sends them to DAC1 Digital Accumulator, operating as a "digital integrator". This Accumulator controls the DAC1, changing step by step its output voltage U_c, applied to tuning varactor. Thus average cavity frequency is tuned to atomic hydrogen line frequency. Digital Accumulator determines the time constant of the cavity tuning system as well. Usually it is set from 3×10^3 s to 7×10^3 s .

Though the cavity is tuned on the atomic line frequency the output maser frequency is left dependent on atomic flux (due to spin-exchange shift of the hydrogen emission line). This frequency shift can reach the value $\sim1\times10^{-12}$. The Modulation Period Generator has a function to reduce this dependence by precision setting the duration of the two half periods of modulation. The step of this setting is 200 ns or 0.0035% of the half period. This gives the resolution of spin-exchange shift compensation about $(2\div4)\times10^{-15}$. Therefore the maser output frequency practically does not depend on beam flux [6].

During the development of this cavity tuning system a particular attention was paid to the modulation frequency choice. Relatively high modulation frequency enables to filter the amplitude modulation at the output of the phase detector more efficiently, thus minimizing spurious at the modulation frequency and its harmonics in the phase noise of the maser's output signals. But further increasing the modulation frequency, for example, up to 348 kHz, leads to growth of the maser temperature sensitivity, likely due to the raising of the transient process influence in the cavity.

On the other hand, the precision digital-to-analog converters with a very low voltage temperature coefficient (less than 5ppm FSR/ºC) and very low aging drift of output voltage were used to reach an excellent long-term stability. Resolution of modulating DAC2 in output fractional frequency is about 5×10^{-15}, resolution of tuning DAC1 is less than 1×10^{-16}.

IV. SHORT-TERM STABILITY

Figure 3 shows the results of short-term stability measurements.

Short-term stability of 5 MHz output signal was measured by frequency comparator model VCH-314 with band pass 3Hz.The masers were placed in the room with temperature change range ±0.5ºC

Typical maser stability with the described above cavity tuning system at averaging time 1s is $(0.9\div1.3)\times10^{-13}$. And it is worth notice that turning on cavity tuning system operation (switching on the modulation) does not degrade 1s stability though the maser output power reduces for 7÷10%.

As it was mentioned above time constant ($\mathfrak{T}$) of the cavity tuning system was selected within

$\mathfrak{T}= 3\times10^3\div7\times10^3$s.

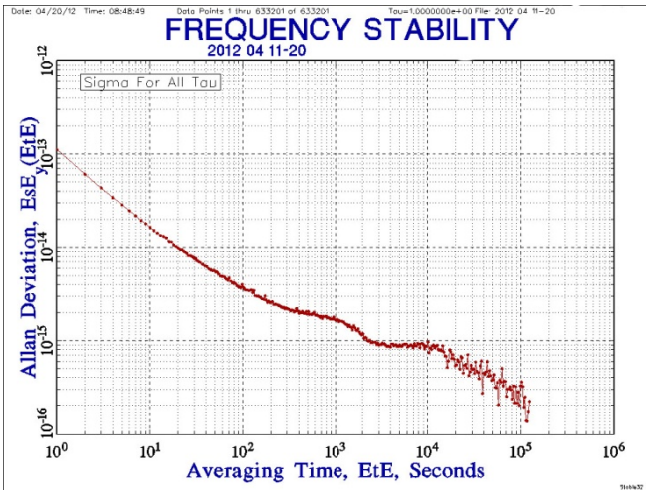

Figure 3. Short- term stability of hydrogen maser (Allan deviation).

At averaging time $2\times10^3\div2\times10^4$ s the flat part of stability plot can be observed due to random frequency noise of cavity tuning system and room temperature variations.

At averaging time one day the maser stability is better than 5×10^{-16}.

V. LONG - TERM STABILITY

Eight hydrogen masers with the similar cavity tuning system have been delivered to VNIIFTRI in 2008-2009. Frequency stability comparison of the masers versus the atomic scale TA (SU) has been started since January 2009.

Figure 4 shows the results obtained for individual masers. Three corner hat method was used to calculate the stability at averaging time from 1 up to 15 days, which was equal to $(3\div5)\times10^{-16}$.

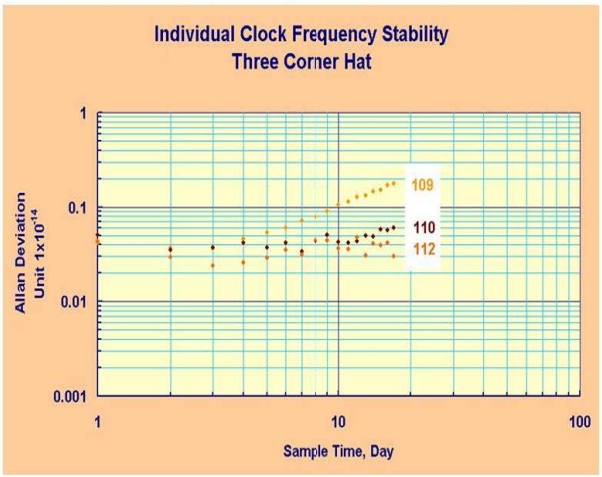

Figure 4. Individual stability of the masers delivered to VNIIFTRI

Figure 5 shows long-term stability of VNIIFTRI masers in 1 year after production. Figure 6 shows the long-term stability of masers in about 3 years of uninterrupted continuous operation.

Data next to the plots are calculated frequency drifts of the masers. It is clearly seen that both rather new masers and the masers which has been operated for a few years have a frequency drift about $(1\div3)\times10^{-16}$/day and some of them even less 1×10^{-16}/day.

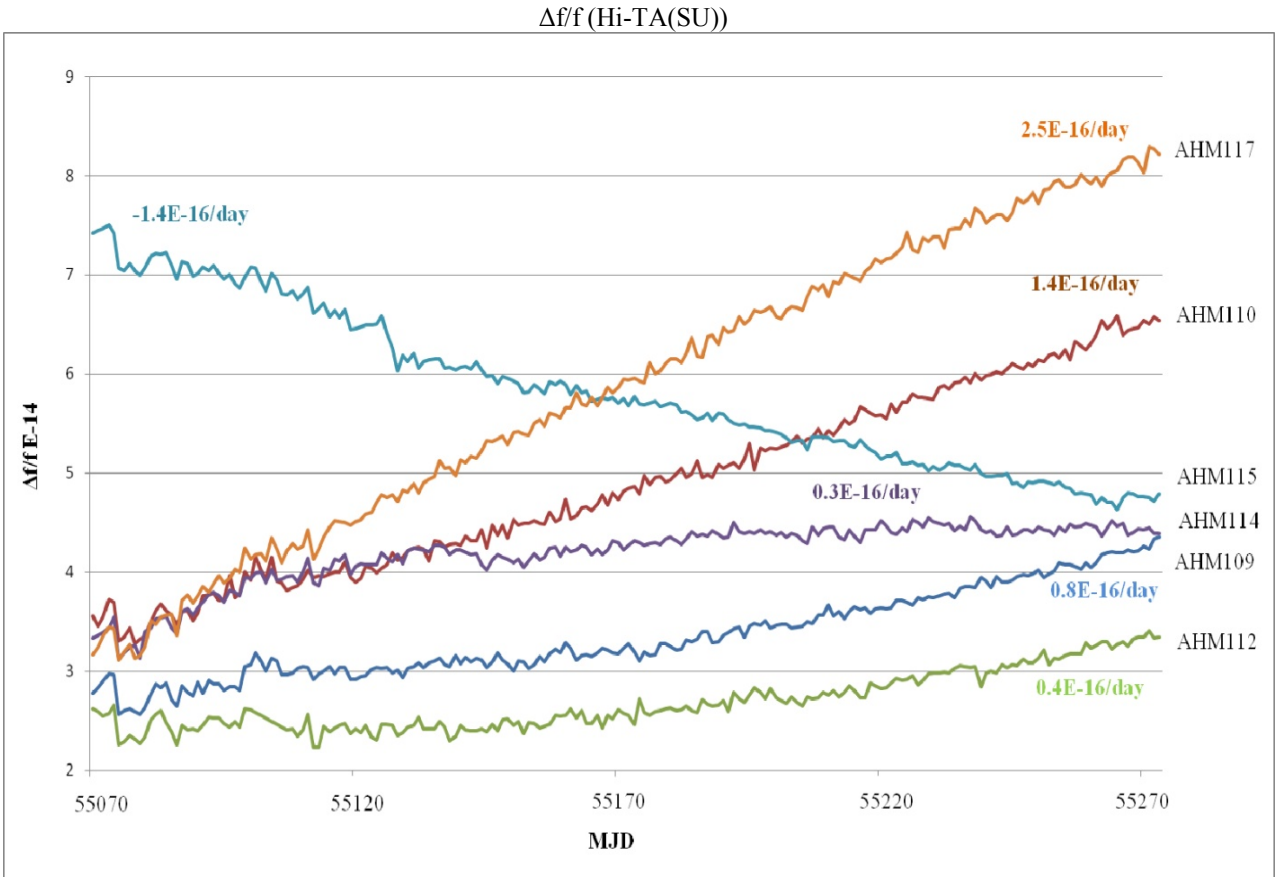

Figure 5. Long-term stability of the masers delivered to VNIIFTRI in 1 year after production

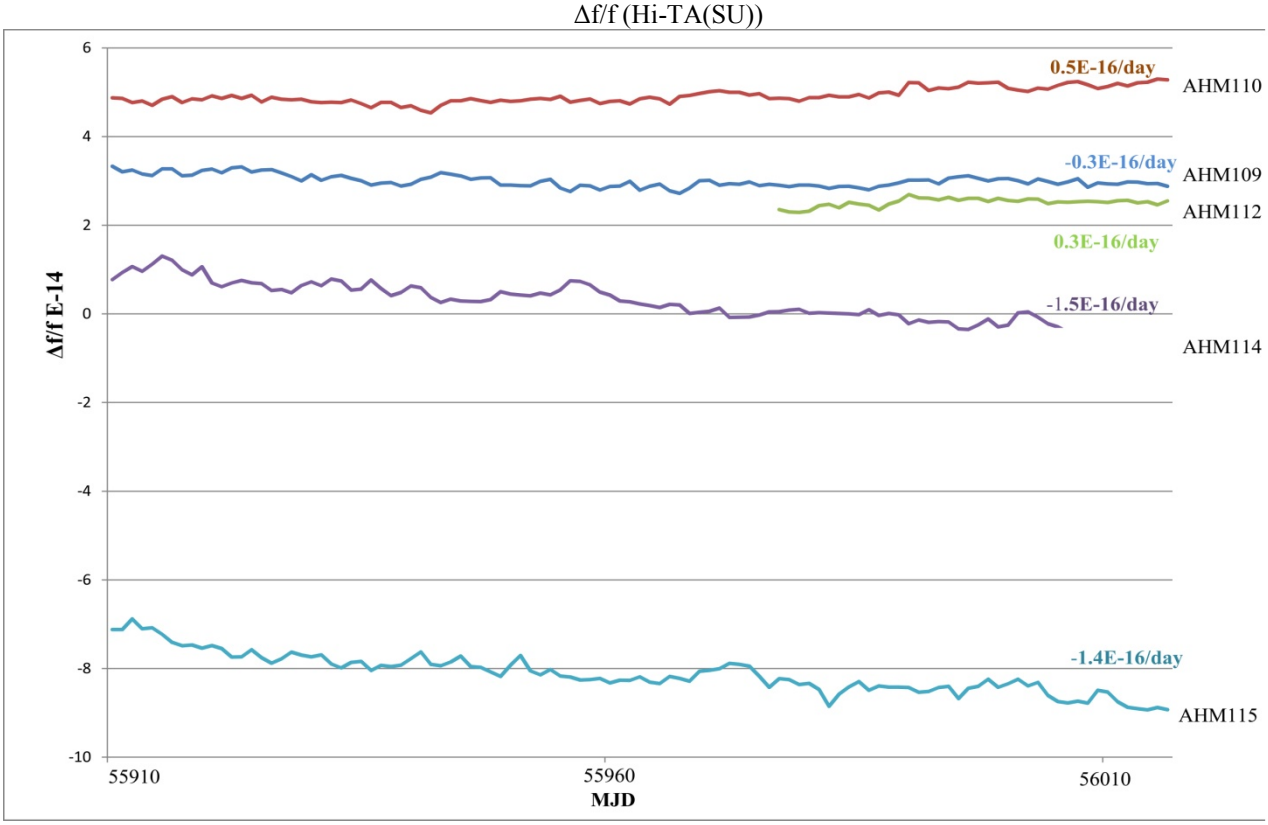

Figure 6. Long-term stability of masers delivered to VNIIFTRI in 3 years of uninterrupted continuous operation

As it was mentioned above modulation period pulse ratio is set at position where maser output frequency doesn't depend on hydrogen beam intensity. After 2 or 3 years of operation masers don't require this procedure to be revised. It demonstrates excellent long-term cavity autotuning system stability.

VI. PHASE NOISE OF OUTPUT SIGNALS

When cavity modulation is switched on the amplitude modulation of the intermediate frequency signal can cause spurious components in the output maser's signal. Therefore, this problem was of special concern. Relatively high modulation frequency 87.2 Hz is able to be trapped by a notch filter very effectively.

Figure 7 shows the typical phase noise of 5 MHz output signal.

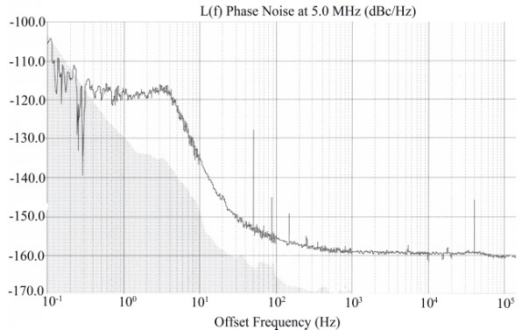

Figure 7. Typical phase noise of 5 MHz output signal

Figure 8 shows the phase noise of the maser's output signal when low noise crystal oscillator model BVA 8607 from Oscilloquartz is used (ULN option).

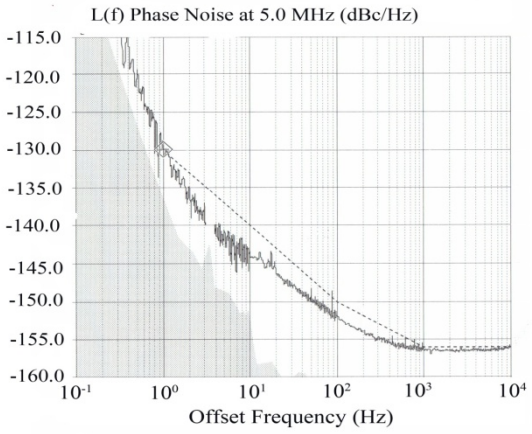

Figure 8. Phase noise when low noise crystal oscillator is used

The level of spurious components at 87.2 Hz and its harmonics are below -145dBc. Low phase noise is especially important when the masers are used in VLBI systems.

VII. TEMPERATURE SENSITIVITY

Figure 9 shows typical temperature sensitivity of 1.2×10^{-15}/ºC.

The maser was placed into the temperature controlled chamber and it had been kept there for about 20 hours at temperature +35ºC. The maser output frequency was checked and after that internal temperature in the chamber was decreased for 5ºC. Each temperature level had been kept for about 6÷7 hours and after the frequency had been checked again the following temperature change had been done. This procedure was repeated for 5 times till the temperature reached +10ºC. It is clear visible that each time after the temperature had been rather roughly changed, the cavity tuning system tried to reproduce the output maser frequency.

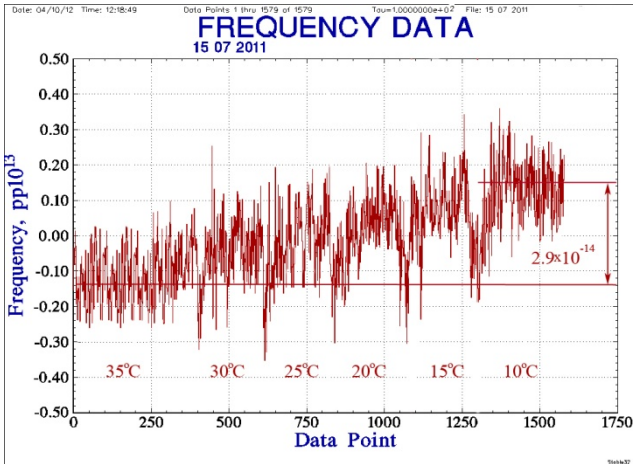

Figure 9. Typical temperature sensitivity of the maser (1.2×10^{-15}/ºC)

Tests of 25 masers with this cavity tuning system show that temperature sensitivity is less than $\pm 2 \times 10^{-15}$/°C

VIII. MAGNETIC SENSITIVITY

Figure 10 shows the maser under magnetic test.

Helmholtz coil creates magnetic field of about $(0.5 \div 1) \times 10^{-4}$ Tesla value. The output maser frequency in this test changes less than $1 \times 10^{-14}/10^{-4}$T.

Figure 10. Hydrogen maser under magnetic test

IX. CONCLUSION

Cavity auto tuning of the active hydrogen maser using microwave cavity frequency switching technique has been developed. The cavity tuning system operation does not degrade short-term stability (at averaging time τ=1s - 10^3s) and phase noise of the maser output signal. This is particularly important when the maser is used for VLBI and as a reference for fountain clocks.

At averaging time more than 10^4 s the described cavity tuning system considerably reduces the maser output frequency drift due to cavity offset and the frequency stability about (3÷5) x 10^{-16} at averaging time $\tau \geq 10^5$s has been reached.

High long-term stability and predictable behavior of the maser frequency allows the masers to be effectively used in precision time keeping systems. Low temperature sensitivity permits the masers to be used without special temperature stabilizing chambers.

REFERENCES

[1] N. Koshelyeaevsky. H-masers in the USSR. Proc. 5 European Time and Frequency Forum. - 1991, p.415-434.

[2] L.S. Gatler, C.L. Searle. Some aspects of the theory and measurement of frequency fluctuations in frequency standards. // Proc. of the IEEE, - 1966, v.54, p.p. 136-154.

[3] N.A. Demidov and A.A. Uljanov. Design and Industrial Production of Frequency Standards in the USSR. Proc. Of the 22-nd Annual Precise Time and Time Interval (PTTI) Applications and Planning Meeting, USA, 1990, p.p. 187-207.

[4] J. Vanier and C. Audoin,. The quantum physics of atomic frequency standards. – 1989,Bristol Adam Hilger

[5] B. Gaigerov, G. Elkin "Cavity autotuning in hydrogen frequency reference", Measurement equipment, 1968, No 6.

[6] H.E. Peters. Design and construction of new hydrogen masers using cavity frequency switching servos. Proc. Of the 38th Annual Frequency Control Symposium, CIIIA, 1984, p.p.420-427.

[7] N. Demidov, V. Logatchev, V. Gorev, V. Vorontsov. Investigation of the frequency stability of active hydrogen maser with autonomous cavity autotuning using frequency switching method. Proc. Of the 19th European Frequency and Time Forum, France, 2005.

[8] Domnin Yu., Koshelyaevsky N., Kostromin V., Krasovsky P., Palchikov V. , Activities and Updates at the State Time and Frequency Standard of Russia, Proceedings of the 41th Annual Precise Time and Time Interval Systems and Applications Meeting, November 16 - 19, 2009, Hyatt Regency Tamaya Resort, Santa Ana, Pueblo, New Mexico, USA.

Laser-pumped high-performance compact gas-cell Rb standard with < $3\times10^{-13}\ \tau^{-1/2}$ stability

Thejesh Bandi, Christoph Affolderbach, and Gaetano Mileti
Laboratoire Temps – Fréquence (LTF)
Institut de Physique, Université de Neuchâtel
2000 Neuchâtel, Switzerland
Email: thejesh.bandi@unine.ch

Camillo Stefanucci, Francesco Merli, and Anja K. Skrivervik
Laboratoire d'Electromagnétisme et d'Acoustique (LEMA),
École Polytechnique Fédérale de Lausanne (EPFL),
1015 Lausanne, Switzerland

Claudio E. Calosso
Optics division
Istituto Nazionale di Ricerca Metrologica (INRIM)
10135 Torino, Italy

***Abstract* — We demonstrate a high-performance laser-pumped rubidium-cell atomic frequency standard exhibiting a short-term stability of < $3\times10^{-13}\ \tau^{-1/2}$. The key components of this standard are a Rb vapor cell of 25mm diameter and a newly developed compact microwave resonator cavity. The overall volume of the clock's physics package – including the frequency-stabilized laser head and physics package – is < 3 liters, which shows the potential of this compact clock for future portable applications.**

I. Motivation

There is an increasing interest in improving the performances of portable atomic frequency standards, e.g. in view of next generation GNSS applications [1]. Presently, the best clock onboard GNSS navigation systems is the Passive Hydrogen Maser (PHM) with a short-term stability < $7\times10^{-13}\ \tau^{-1/2}$ and reaching the 1×10^{-14} level at 1-day timescale. State-of-the-art lamp-pumped space Rb standards (RAFS) exhibit ≈ 2×10^{-12} at τ = 1 s, reaching ≤ 4×10^{-14} over one day [2,3]. However, the superior stability of the PHM comes with a compromise on the mass, volume, and power consumption of the clock, key figures that exceed the values for a Rb standard by a factor of 5.5, 11, and 4.5, respectively. Recent works on laser-pumped Rb atomic clocks using noise-cancellation in 14mm-size cells [4] and Pulsed Optical Pumping (POP) [5] approaches have demonstrated short-term clock stabilities of < $6\times10^{-13}\ \tau^{-1/2}$ and $1.6\times10^{-13}\ \tau^{-1/2}$, respectively.

In this work, we aim to develop a laser-pumped Rb standard that can reach stabilities of < $6\times10^{-13}\ \tau^{-1/2}$ (1 s < τ < 10'000 s) and < 1×10^{-14} over one day. This clock uses an enlarged Rb cell (25mm diameter and 25mm length) placed inside a newly developed compact magnetron-type microwave cavity. Thanks to this new cavity, the clock can maintain the compact volume, low mass, and low power consumption of a conventional lamp-pumped RAFS.

II. Experimental Setup and Clock Components

Fig. 1 shows the schematics of our experimental clock setup. This setup consists of three main parts: the frequency stabilized Laser Head (LH), the Physics Package (PP), and the microwave synthesizer (Local Oscillator, LO).

The laser head is based on a distributed feed-back (DFB) diode laser emitting at 780nm (Rb D2 transition). The LH also contains an evacuated Rb reference cell. Narrow sub-Doppler saturated-absorption spectroscopy lines obtained from this reference cell are used for frequency stabilization of the laser light. The overall volume and mass of the laser head are 0.9 liters and 0.6 kg, respectively. Further details on the laser head were reported in [6-8].

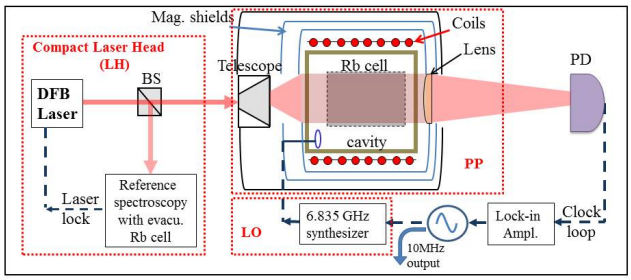

Figure 1. Schematics of the double-resonance (DR) clock setup. PD: photo detector; BS: beam splitter.

This work was supported by the Swiss National Science Foundation (SNSF), the Swiss Space Office (SER-SSO), and the European Space Agency (ESA).

The Physics Package is similar to the one presented in [7], except for the Rb cell and the magnetron-type cavity. At the heart of the PP is a 25mm-diameter Rb cell filled with atomic Rb and a mixture of buffer gases. A novel magnetron-type microwave cavity was designed to surround the cell. This design exploits electrodes placed inside the cavity in order to make it resonate at the ^{87}Rb clock transition of ≈ 6.835 GHz, and sustain a TE_{011}-like mode structure of the microwave magnetic field. A microwave field simulation of this resonant TE_{011}-like mode is shown in Fig. 2. Based on these simulations and design, a microwave resonator was fabricated and characterized (for further details see [9]). Thanks to the magnetron-type cavity design, the overall volume of the cavity is < 0.04 liters (outer cavity dimensions), which is much smaller than for a fundamental-mode resonator with comparable mode structure (≈ 0.14 liters). The complete Physics Package (including heaters and magnetic shields) has a total volume of < 0.8 liters, and a mass of < 1.4 kg.

The microwave source (LO) and the digital lock-in and clock loop electronics were realized at INRIM and are described in detail in [10]. The phase noise of this LO at 6.835 GHz carrier is measured to be S_φ = -108 dBrad^2/Hz. From this value, the LO contribution to the clock instability via the intermodulation effect is calculated as ≈ 8×10^{-14} at 1s integration time.

We used in-house made temperature control modules based on digital electronics for the PP and the laser head, and a low-noise current driver and lock-in loop for operation of the DFB laser head.

III. Double Resonance (DR) Signal and Clock Stability

A. Double resonance signal and stability prediction

Fig. 3 shows our typical measured double resonance signal, with a linewidth of 361 Hz (FWHM) and a signal contrast of 25%. Here contrast is defined as the DR line peak amplitude divided by the background level outside the microwave resonance condition. The photocurrent of 1.7 μA at FWHM corresponds to a shot-noise limited frequency

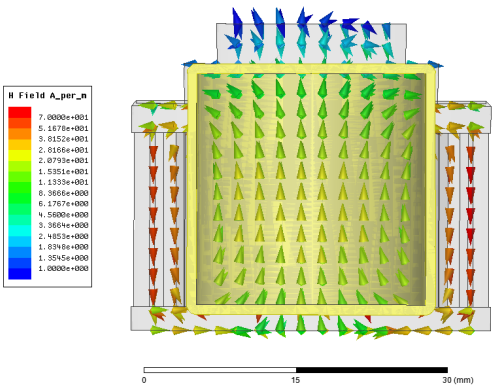

Figure 2. Microwave field simulations showing the TE_{011}-like resonant mode [9].

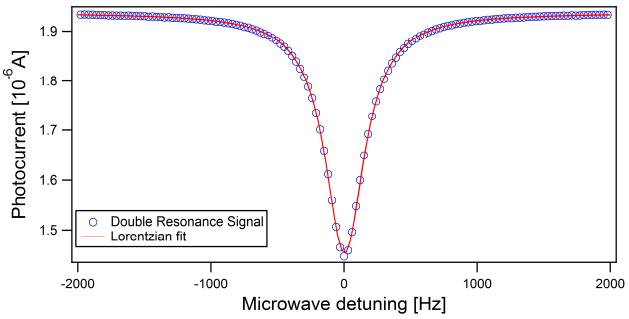

Figure 3. Measured DR clock signal, showing a linewidth of 361 Hz and a contrast of 25%.

stability of $5.5\times10^{-14}\ \tau^{-1/2}$ [1]. However, presently the estimated signal-to-noise (S/N) stability of our clock is limited to $2.4\times10^{-13}\ \tau^{-1/2}$, mainly due to FM-to-AM noise conversion of laser FM noise in the atomic vapor [11].

B. Measured clock stability

The output frequency of the microwave LO is locked to the center of the DR signal using a clock loop as shown in Fig. 1, and the 10 MHz output of the OCXO quartz oscillator is compared to the reference signal from an active Hydrogen Maser. The measured stability of our clock is $2.4\times10^{-13}\ \tau^{-1/2}$ (see Fig. 4), which is in excellent agreement with the predicted S/N limit. For this result, the clock was operated in standard laboratory conditions (no vacuum enclosure or thermal chambers used). The clock stability at longer time-scales ($\tau \geq$ 1000 s) remains to be studied.

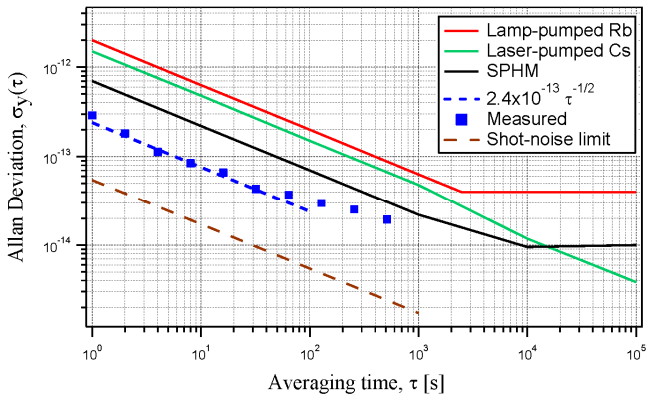

Figure 4. Measured clock short-term stability (blue squares) compared to other clocks.

IV. Conclusions

We have demonstrated a conceptually simple and compact continuous-wave laser-pumped DR clock, showing a short-term frequency stability of $2.4\times10^{-13}\ \tau^{-1/2}$ when operated in laboratory conditions. This clock has a fundamental shot-noise limit of $5.5\times10^{-14}\ \tau^{-1/2}$ that could be approached by noise-subtraction technique [4] or by using a laser source with reduced FM noise [12]. Studies on the medium- to long-term stability of the clock remain to be done by evaluating, for

instance, the impact of light-shifts, temperature shifts, and microwave power shifts. A previous clock realization with a similar physics package (but using a different cavity) has already reached the level of $1x10^{-14}$ at 10^4s integration times [1].

This clock has the potential for future portable applications, such as in GNSS (satellite navigation), high-speed telecommunication, deep space missions, and as LO reference for portable optical synthesizers or optical frequency standards.

ACKNOWLEDGMENT

We thank F. Gruet, M. Pellaton, P. Scherler and M. Durrenberger (all at LTF-UniNe) for their contributions to this work.

REFERENCES

[1] T. Bandi, C. Affolderbach, C. E. Calosso, and G. Mileti, "High-performance laser-pumped rubidium frequency standard for satellite navigation", Electronics Letters, vol. 47, no. 12, pp. 698-699 (2011).

[2] P. Rochat et al., "The Onboard Galileo Rubidium and Passive Maser, Status & Performance", Proc. IEEE Int. Freq. Control Symposium, Vancouver, Canada, August 29-31 2005, pp. 26-32.

[3] R. T. Dupuis, T. J. Lynch, J. R. Vaccaro, "Rubidium Frequency Standard for the GPS IIF Program and Modifications for the RAFSMOD Program", Proc. joint IEEE Int. Freq. Control Symposium and European Frequency and Time Forum, Toulouse, France, April 22-25 2008, pp.655-660.

[4] C. Affolderbach, T. Bandi, R. Matthey, F. Gruet, M. Pellaton, G. Mileti, "Compact, High-Stability Rb Atomic Clocks for Space", Proc. of the 3rd International Colloquium - Scientific and Fundamental Aspects of the Galileo Programme, August 31st – September 2nd 2011, Copenhagen, Denmark. ESA proceedings WPP-326, paper 1400.

[5] S. Micalizio, A. Godone, C. Calosso, F. Levi, C. Affolderbach and F. Gruet, "Pulsed Optically Pumped Rubidium Clock with High Frequency-Stability Performance", IEEE Trans. Ultrason. Ferroelectr. Freq. Control, vol. 59, no. 3, pp.457-462 (2012).

[6] C. Affolderbach, G. Mileti, "A compact laser head with high-frequency stability for Rb atomic clocks and optical instrumentation", Review of Scientific Instruments, Volume 76, 073108, (2005).

[7] T. Bandi, F. Gruet, C. Affolderbach, C. E. Calosso and G. Mileti, "Investigations on Improved Rb cell standards", Proc. of the Joint IEEE Int. Freq. Control and European Frequency and Time Forum, San Francisco, California, USA, May 2-5 2011, no. 7254.

[8] R. Matthey, C. Affolderbach, G. Mileti, "Methods and evaluation of frequency aging in DFB laser diodes for Rubidium atomic clocks",Optics Letters, Vol. 36, No. 17, p. 3311-3313, (2011).

[9] C. Stefanucci, T. Bandi, F. Merli, M. Pellaton, C. Affolderbach, G. Mileti and A. K. Skrivervik, "Comact microwave resonator for high-performance rubidium frequency standards", submitted for publication (2012).

[10] C. E. Calosso, S. Micalizio, A. Godone, E. K. Bertacco, and F. Levi, "Electronics for the pulsed rubidium clock: design and characterization", IEEE Trans. Ultrason. Ferroelectr. Freq. Control, vol. 54 (9), pp. 1731-40, 2007.

[11] J. C. Camparo, "Conversion of laser phase noise to amplitude noise in an optically thick vapor," J. Opt. Soc. Am. B, vol. 15, pp. 1177-1186, 1998.

[12] G. Mileti, J. Deng, F. L. Walls, D. A. Jennings, R. E. Drullinger, "Laser-Pumped Rubidium Frequency Standards: New Analysis and Progress", J. Quantum Electronics, Vol. 34, pp. 233-237, 1998.

The Opto-Electronic Oscillator (OEO): Review and Recent Progress

Lute Maleki
OEwaves, Inc.
465 N. Halstead Street, Suite 140
Pasadena, California 91107

***Abstract*—This paper reviews developments over the past two decades related to the Opto-Electronic Oscillator (OEO). Various approaches for realization of the OEO architecture are discussed. Recent advances related to generation of spectrally pure signals with a compact configuration of OEO, based on optical whispering gallery mode (WGM) resonators are discussed. Finally, based on the current development, future versions of the OEO, which combine the optoelectronic feedback loop with a Kerr comb frequency generator made with a crystalline WGM resonator, are mentioned.**

I. Introduction

Spectrally pure and frequency stable microwave and mm-wave reference signals have widespread applications in diverse fields of science and technology ranging from metrology to communications, sensing, and radar. The need for high performance sources in this spectral domain is growing at an increasing rate in response to advances in technology related to radio astronomy, mm-wave metrology, and high rate data transmission networks with associated wider bandwidth requirements. The traditional approach for generating spectrally pure signals relies on multiplication of lower frequency signals generated with high performance quartz or surface acoustic wave (SAW) oscillators, or direct generation using high quality factor (Q) microwave and mm-wave resonator oscillators, but these approaches have inherent limitations. In the case of multiplied signals, the multiplied noise of the high performance oscillator at 20 log N, with N the multiplication factor, limits achievable performance; in the direct generation scheme, the high Q cavity is bulky, highly sensitive to environmental perturbations, and for the highest performance requires cryogenic cooling, thus limiting applications where size, weight, and power are restricted.

II. The Opto-Electronic Oscillator (OEO)

A. General Scheme

In the last fifteen years, generation of spectrally pure microwave and mm-wave signals has been achieved using optical schemes. The most widespread approach is based on the opto-electronic oscillator (OEO) where high Q optical cavities with extremely low loss are used with opto-electronic feedback loops. The generic OEO consists of a light source (usually a laser), light modulator, optical cavity, and a photodetector; the output of which is fed back to the modulator to achieve a closed loop configuration (see Figure 1). This feedback loop can generate self-sustained oscillation if its overall gain is larger than the loss, and the waves circulating in it add up in phase. The former requirement can be met with insertion of gain in the loop and, the latter, by controlling the phase. Since the loop can support waves circulating once, twice, …n-times, the oscillator is fundamentally multi-mode, with the mode spacing determined by the free spectral range of the cavity. By adding a filter in the loop with a prescribed center frequency ν, the output of the oscillator can be obtained at that frequency. In this way, any frequency supported by the bandwidth of the components can be generated. The close-to-carrier phase noise of the OEO is fundamentally determined by the Q of the optical resonator, while its white noise floor is determined by the shot noise of the optical power on the photodetector. In practice, the noise is ultimately limited by the 1/f noise of the amplifier in the loop, and the 1/f noise of the photodetector.

The power of the OEO architecture is in its flexibility as it can be configured in a variety of ways with different optical and electrical components to optimize the performance. The

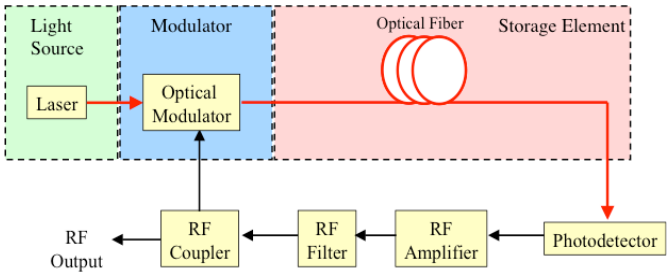

Figure 1 Generic configuration for Opto-Electronic Oscillator (OEO)

gain, the filter, the phase shifter can be placed either in the optical segment or the electrical segment of the loop. The light source can be of any suitable type, including a laser or a source of amplified spontaneous emission (ASE); modulation of light can be achieved directly with the current of the laser, or with an external modulator. The signal can be generated with phase, amplitude, or polarization modulation. The high Q cavity can be a Fabry-Perot, a whispering gallery mode optical resonator, or a long fiber delay with an equivalent $Q = \pi \tau \nu_0$, where ν_0 is the oscillator frequency, and τ is the delay given by nL/c, with L the length of the fiber, c the speed of light, and n the index of refraction of the fiber. The operation

frequency can be fixed by a fixed filter or tuned by changing the RF filter's center frequency, or the cavity's "optical length" through controlling dispersion, or the wavelength of the laser. Finally, even the light source can be a laser external to the loop, or a source produced by placing gain in a second optical loop that is coupled to the electrical loop through the modulator, which is shared by both loops. This latter configuration is known as the coupled opto-electronic oscillator or COEO.

An attractive feature of the OEO architecture is that its noise can be accurately modeled with analysis and with numerical simulations. In the original paper describing the OEO, a model for the noise of the oscillator was presented [2]. This model has been modified by various authors to include the effect of noise in the components such as amplifiers and detectors on the overall spectral purity [4]. Noise models based on Laplace transform formalism and Langevine equations have also been developed [23]. A recent paper has studied the optical noise associated with the use of the fiber in the loop, and experimentally verified what has been previously asserted regarding the influence of Rayleigh scattering and Brillouin effect [22].

Variations of the OEO architecture by several research groups around the world have been employed to generate high performance microwave and mm-wave signals. In the fiber based OEO, the length of the fiber is related to the Leeson frequency given by:

$$f_L = \frac{\nu_0}{2Q}$$

where ν_0 is the frequency of the oscillator. A 16 km long fiber was used to obtain the highest achieved spectral purity of -163 dBc/Hz in a 10 GHz free-running oscillator, at 7 kHz from the carrier [4]. This performance was limited by the flicker noise of the photodetector the loop. One of the features of a fiber delay is that oscillations at frequencies that are multiples of the fundamental frequency associated with the length of fiber (the analog of longitudinal modes of a laser resonator) are also supported. This multi-mode oscillation, mentioned above, can be suppressed if the bandwidth of the filter in the loop is narrow enough so that only a single mode of oscillation survives in the loop. Such a narrow-band filter, however, is not practical, especially when the length of the fiber is long and the operation frequency is in the microwave and mm-wave range. For example, for a 4 km length of fiber the frequency associated with these modes is about 90 kHz; a filter with this bandwidth is hard to realize at frequencies above a GHz.

One approach to mitigate this problem is to utilize optical (instead of electronic) filters in the OEO. This scheme is particularly attractive since Fabry-Perot cavities and whispering gallery mode (WGM) optical resonators can have narrow bandwidth. A low noise OEO has been recently demonstrated with a Fabry-Perot as a filter in the optical loop [5]. A 39 GHz OEO utilizing a WGM resonator as an optical filter has also been demonstrated [6]. Another approach for reducing the amplitude of unwanted modes surviving the filter bandwidth and appearing as "supermodes" in the phase noise spectrum is to use multiple lengths of fiber as an optical filter [7]. These extra loops essentially represent a finite impulse response filter. Such an approach was recently somewhat modified to achieve the overall filtering effect in optics, rather than in combination with the electrical loop [8]. Finally, an OEO utilizing an atomic transition in rubidium was also demonstrated; this oscillator was designed to also achieve high stability of operation derived from the atom [9].

A limitation of multi-loop approach is that filtering is best accomplished when the two fiber lengths are different so that the FSR related to each length is at a proper ratio to ideally provide only a single mode coinciding in frequency in both loops. This condition dictates that one of the fiber lengths is shorter than the other, so the resultant Q of the combined loops is lower than the Q of the longest length of fiber. A modified version of multi-loop configuration to reduce or eliminate the unwanted noise peaks while providing the best performance and lowest degradation of high Q of the long fiber was assembled as a pair of coupled OEO injection locked to each other [11]. This scheme was recently modified to optimize the performance by careful control of phase and amplitude of mutually injected signals of the OEO pair [21].

It is desirable to reduce the unwanted supermodes by decreasing the length of the fiber to increase the frequency of the modes so that they might lie outside the filter bandwidth. This, however, reduces the high Q associated with the length of the fiber delay. A way around the problem is the COEO scheme. In the COEO, the active optical loop essentially functions as a Q multiplier of the oscillator. So a shorter fiber length in the COEO can produce a lower phase noise than with the same length of fiber in the OEO, while at the same time practically eliminating the unwanted supermodes. This scheme also has the desirable feature of a more compact size associated with the short length of fiber, with the added benefit of lower sensitivity to environmental perturbations [10].

With advances in technology of optical modulators and detectors, the operating frequency of the OEO is also on the rise. Early on, operation at 39 GHz was demonstrated [12], but recently an OEO operating at 50 GHz has also been produced [13]. As the frequency of operation increases, effect of laser noise and dispersion on the phase noise produced by the oscillator must be taken into account [14].

B. OEO Based on WGM Resonators

A new direction in OEO technology is the application of WGM resonators, both, as the filter and the high Q element. The basic configuration is depicted in Figure 2. Because a semiconductor laser can be locked to the high Q resonator, as well, this scheme has the added benefit of small size and low operation power. These are important benefits for applications where size and power are important. There are two basic approaches for realization of the WGM resonator-based OEO: direct modulation of the laser current or external modulation using a resonator made with electro-optic material. In the former case, the resonator can be fabricated with crystalline

material, such as calcium fluoride or magnesium fluoride, to achieve extremely high Qs.

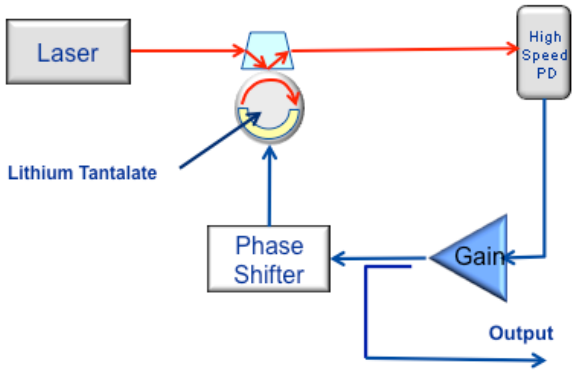

Figure 2 Schematic diagram of the OEO based on a lithium niobate modulator made with a whispering gallery mode resonator

Optical resonators with Q exceeding 10^{11} have been demonstrated with these materials [15]. The noise corresponding to this high Q is quite low, but the frequency of the oscillator is limited to the bandwidth of the modulation frequency of the laser, and is typically limited to x-band frequencies. Given the growing interest in higher frequency oscillators, the WGM resonator serving as a modulator can be more attractive. Here, the resonator is fabricated with electro-optic material, such as lithium niobate or lithium tantalate, and provided with electrodes that can be used to apply the modulation voltage. The narrow resonance of the resonator serves to provide low phase noise in the oscillator circuit; it also leads to highly efficient modulation and thus reduction for needed amplification. It should be mentioned that an OEO with a WGM resonator as filter and an external phase modulator has also been demonstrated.

The latest advance in the technology of WGM based OEO is the use of a both TE and TM modes of the resonator. A modulator transferring photons from a single TE mode to TM modes has been shown to perform as a true single sideband (SSB) modulator. The SSB modulator is fundamentally more efficient, and thus can improve the performance of the oscillator. Furthermore, since the indices of refraction of the modes respond differently to a forcing function, such as temperature change or an applied voltage, the modulation frequency can be tuned. This approach has been recently implemented, and a tunable oscillator with a WGM resonator was demonstrated [16].

An different approach for generation of microwave and mm-wave signals takes advantage of the fact that a frequency comb generated with a femtosecond mode locked laser is essentially equivalent to a large number of narrow linewidth lasers that are separated in frequency by a fixed amount, and are all coherent with respect to each other. Such a comb can generate a signal at the output of a fast photodetector as a result of the beat generated by its tines. Because of the coherence of the very narrow comb lines, the signal produced has outstanding spectral purity, and can be combined with a stable optical reference to also provide high stability [19]. Recent work in this area has shown stand alone femtosecond combs with very high stability producing unmatched spectral purity at 1 and 10 GHz [18].

One of the shortfalls of the technique with femtosecond combs is that they are large, requiring a pump laser, and are generally limited to application in the laboratory environment. They also produce signals at frequencies around 10 GHz and lower. A recent advance in the generation of optical frequency comb using a WGM resonator has opened the door for generation of high spectral purity signals at virtually any desired microwave or mm-wave (and even THz) frequency. This is based on Kerr nonlinearity in the resonator material, which through the process of four-wave mixing and hyper-parametric oscillation allows excitation of many modes when one mode of the resonator is pumped with laser light. Moderate laser powers combined with the high Q of the resonator make this process possible [19]. Using the Kerr frequency comb, high spectrally pure mm-wave signals have been produced at about 35 GHz [20]. A clear advantage of this scheme is the small size of the Kerr comb oscillator that can support a wide variety of applications in science and engineering [25].

Advances made with the comb oscillator appear to make the need for the OEO configuration less important. In fact, it can be shown that combining the OEO feedback loop with the comb will result in a regenerative architecture, similar to COEO. The outcome will be higher performance, by perhaps tens of dB, beyond what is achievable with the Kerr comb oscillator. This area represents a new focus for OEO research in the future, and will likely provide new results within the next few years.

In summary, the OEO architecture for generation of spectrally pure microwave and mm-wave signals has advanced considerably in the past few years. New schemes for realization of the OEO and use of optical combs promise to serve emerging applications to meet the ever stringent performance requirement of emerging applications.

ACKNOWLEDGMENT

The author wishes to express his gratitude to members of the Quantum Sciences and Technology Groups at JPL, and those at OEwaves who have made important and extensive contributions to the development and advancement of the OEO technology. In particular, I wish to thank Jerry Byrd, Danny Eliyahu, Shuhua Huang, Vladimir Ilchenko, Wei Liang, Andrey Matsko, Enrico Rubiola, Anatoliy Savchenkov, David Seidel, Meirong Tu, Steve Yao, and Nan Yu for their contributions, and for enriching my understanding and knowledge in this field.

REFERENCES

[1] X. S. Yao and L. Maleki, “Optoelectronic oscillator for photonic systems,” IEEE J. Quantum Electron., 32, Jul 1996, pp. 1141–1149.

[2] X. Steve Yao and Lute Maleki, "Optoelectronic microwave oscillator," JOSA B, 13, 1996, pp. 1725-1735.

[3] X. Steve Yao and L. Maleki, “Dual microwave and optical oscillator,” Opt. Lett., 22, 1997, pp. 1867-1869.

[4] D. Eliyahu, D. Seidel D, and L. Maleki “RF amplitude and phase-noise reduction of an optical link and an opto-electronic oscillator,” IEEE Trans. Microwave Theory Tech., Feb. 2008, pp 449-456.

[5] I. Ozdur , D. Mandridis, N. Hoghooghi , et al. “Low Noise Optically Tunable Opto-Electronic Oscillator With Fabry-Perot Etalon,” J. Lightwave Tech., 28, Nov. 2010, pp. 3100-3106; Kim JM, Cho D., “Optoelectronic oscillator stabilized to an intra-loop Fabry-Perot cavity by a dual servo system,” OPTICS EXPRESS, 18, Jul. 2010, pp.14905-14912.

[6] S. Fedderwitz, A. Stohr, S. Babiel, et al., “Optoelectronic K -Band Oscillator With Gigahertz Tuning Range and Low Phase Noise” IEEE Photon.Tech. Lett., 22, Oct. 2010, pp. 1497-1499.

[7] X. S. Yao and L. Maleki, “Multiloop optoelectronic oscillator,” IEEE J. Quantum Electron., 36, 2000, pp. 79–84.

[8] Ji. Yang, Y. Jin-Long, W. Yao-Tian, Z. Li-Tai, and Y. En-Ze. “An Optical Domain Combined Dual-LoopOptoelectronic Oscillator,” Photon.Tech. Lett., 19, Jun. 2007, pp.807-812.

[9] Strekalov D, Aveline D, Yu N, et al., “Stabilizing an optoelectronic microwave oscillator with photonic filters,” J. Lightwave Tech., 21, Dec. 2003, pp. 3052-3061.

[10] D. Eliyahu and L. Maleki, “Modulation response (S21) of the coupled opto-electronic oscillator,” in IEEE International Frequency Control Symposium/PDA Exhibit, Vancouver, BC, Canada, 2005, pp.850-856; E. Salik, N. Yu, and L. Maleki, “An ultralow phase noise coupled optoelectronic oscillator,” IEEE Photon. Technol. Lett., 19, 2007, pp. 444–446,; F. Quinlan, S. Gee, et al., “Self-Stabilization of the Optical Frequencies and the Pulse Repetition Rate in a Coupled Optoelectronic Oscillator” J. Lightwave Tech., 26, Aug. 2008, pp. 2571-2575.

[11] W. M. Zhou, G. Blasche, “Injection-locked dual opto-electronic oscillator with ultra-low phase noise and ultra-low spurious level,” IEEE Trans. Microwave Theory Tech., 53, Mar. 2005, pp 929-933.

[12] Chang DH, Fetterman HR, Erlig H, et al., “39-GHz optoelectronic oscillator using broad-band polymer electrooptic modulator,” IEEE Photon.Tech. Lett., 14, Feb. 2002, pp. 191-193.

[13] Sascha Fedderwitz, Andreas Stöhr, Sebastian Babiel, Vitaly Rymanov and Dieter Jäger, “Opto-Electronic Dual-Loop 50 GHz Oscillator with Wide Tunability and Low Phase Noise,” 2010 IEEE Topical Meeting on Microwave Photonics (MWP), Montreal, Quebec, Canada, 5-9 Oct. 2010.

[14] Volyanskiy K, Chembo YK, Larger L, et al., “Contribution of Laser Frequency and Power Fluctuations to the Microwave Phase Noise of Optoelectronic Oscillators,” J. Lightwave Tech., 28, Sept. 2010, pp. 2730-2735.

[15] L. Maleki, V. S. Ilchenko, A. A. Savchenkov, and A. B. Matsko, in A. B. Matsko, ed. Practical Applications of Microresonators in Optics and Photonics, CRC Press, 2009, chap. 3.

[16] V. S. Ilchenko, W. Liang, D. Eliyahu, A. B. Matsko,* D. Seidel, and L. Maleki, “Voltage-controlled photonic oscillator,”A. A. Savchenkov, OPTICS LETTERS, 35, May 2010, pp. 1572-1574.

[17] A. Bartels, S. A. Diddams, C. W. Oates, G. Wilpers, J. C. Bergquist, W. H. Oskay, and L. Hollberg, “Femtosecond-laser-based synthesis of ultrastable microwave signals from optical frequency references,” Opt. Lett. 30, 6, 2005, 667–669.

[18] S. A. Diddams, M. Kirchner, T. Fortier, D. Braje, A. M.Weiner, and L. Hollberg, “Improved signal-to-noise ratio of 10 GHz microwave signals generated with a mode-filtered femtosecond laser frequency comb” OPTICS EXPRESS, Mar. 2009, 17, pp. 3331-3340.

[19] A. B. Matsko, A. A. Savchenkov, D. Strekalov, V. S. Ilchenko, and L. Maleki, "Optical hyper-parametric oscillations in a whispering gallery mode resonator: threshold and phase diffusion", Phys. Rev. A 71, 033804 (2005).

[20] L. Maleki, V. S. Ilchenko, A. A. Savchenkov, W. Liang, D. Seidel, and A. B. Matsko, “High Performance, Miniature Hyper-parametric Microwave Photonic Oscillator,” in 2010 IEEE International Freq. Control Symp., June 2010. pp. 558-563.

[21] O. Okusaga, E. J. Adles, E. C. Levy, W. Zhou, G. M. Carter, C. R. Menyuk, and M. Horowitz, “Spurious mode reduction in dual injection-locked optoelectronic oscillators,” Optics Express, 19, pp.5839-5854 (2011).

[22] A. David, and M. Horowitz “Low-frequency transmitted intensity noise induced by stimulated Brillouin scattering in optical fibers,” Optics Express, 19, pp.11792-11803 (2011).

[23] K. Voliyanskiy, L. Larger, E. Rubiola, and P. Colet, “Determination of Phase Noise Spectra in Optoelectronic Microwave Oscillators: A Langevin Approach,” J. Quant. Electron., 45, pp. 178-186 (2009).

[24] Kirill Volyanskiy, Patrice Salzenstein, Herv´e Tavernier, Maxim Pogurmirskiy, Yanne K. Chembo, and Laurent Larger, “Compact Optoelectronic Microwave Oscillators Using Ultra-high Q Whispering Gallery Mode Disk-Resonators and Phase Modulation,” Optics Express, 18, pp. 2359-2363 (2010).

[25] L. Maleki, “The Optoelectronic Oscillator,” Nature Photonics, 5, pp. 728–730 (2011).

Long-Term Behavior of Rubidium Clocks in Space

James C. Camparo
Physical Sciences Laboratories
The Aerospace Corporation
El Segundo, CA, USA
James.C.Camparo@aero.org

James O. Hagerman
Integrated Systems & Global Solutions - Defense
Schriever AFB, CO, USA
James.o.hagerman@lmco.com

Thomas A. McClelland
Frequency Electronics, Inc.
Uniondale, NY, USA
Thomas.mcclelland@freqelec.com

***Abstract*— The generic, very long duration performance of rubidium (Rb) atomic clocks in space has implications ranging from deep-space missions to the outer planets to global-navigation satellite systems like Galileo and GPS. Here, using telemetry and frequency tuning data collected from spacecraft clocks that have been in operation continuously for anywhere from 2 to 11 years, we consider the performance and viability of Rb atomic clocks for very long duration space missions. While the results that we present are general in nature, and in no way system specific, they are nonetheless important and rarely available for space-mission planners.**

I. INTRODUCTION

A. Rb Atomic Clocks In Space

The space segments of many (if not most) satellite systems employ quartz oscillators as the stable frequency and time reference. Only a few systems, (e.g., GPS, Glonass, Milstar, and Galileo), have employed atomic clocks as their stable frequency and time reference. This situation is primarily due to the established reliability of quartz-crystal oscillators, as well as the very conservative approach to using new technologies in space applications. However, over the last 25 to 30 years, considerable experience using atomic clocks in space has accumulated on the programs mentioned above, and over this time span most of the experience has been with rubidium (Rb) vapor-cell atomic clocks and cesium (Cs) atomic beam clocks.

Understanding the true performance of atomic clocks in space is important for the planning of satellite-system upgrades as well as the design of next-generation space systems. This is particularly true given the fact that most systems engineers and electrical engineers likely "feel comfortable" with the technology of crystal oscillators. Unfortunately, and to the detriment of space system performance, systems and electrical engineers may not fully appreciate the benefits that reliable atomic clocks can bring to their space-system's performance. For instance, while it is well known that quartz crystal clocks are sensitive to various forms of radiation, systems engineers may not be aware that atomic clocks are fundamentally *insensitive* to space radiation environments (i.e., solar flares), as demonstrated quite clearly for Rb atomic clocks [1].

TABLE I. TYPICALLY ASSUMED RB AND CS ATTRIBUTES

Parameter	Rb Clock	Cs Clock
Size (in^3)	100	1000
Weight (lbs.)	5	40
Power (W)	20	50
Frequency Aging (day^{-1})	10^{-12} to 10^{-13}	$< 10^{-14}$

Rb atomic clocks are attractive candidates for space programs due to their small size, low weight, and low power consumption. However, "common knowledge" (at least in the atomic clocks community) suggests that their long-term frequency stability is poorer than other candidate atomic clocks, in particular Cs atomic beam devices. To illustrate the point, Table 1 shows the typical trade-offs that are *assumed* when choosing between Rb and Cs technologies.

In this paper, we consider the long-term performance of Rb atomic clocks that have flown in space for a number of years. For each of the six clocks we consider, we evaluate the clock's fractional-frequency history over the long term, and these data are then compared with the Rb clock's rf-discharge lamp history and the clock's overall temperature history. As we will show, common knowledge regarding the Rb atomic clock's long-term frequency stability (i.e., the clock's frequency aging) is grossly pessimistic compared to the level of performance these spacecraft devices can actually deliver.

B. *Milstar Rb Atomic Clocks*

For this study, we had access to the Milstar satellite clock data. The Rb clocks flown on Milstar satellites are all manufactured by Frequency Electronics, Inc. They are conventional Rb vapor devices, and a functional generic diagram of the clock's physics package is shown in Fig. 1. Resonance light from a Rb^{87} RF discharge lamp is used to optically pump Rb^{87} atoms in a resonance cell located inside a microwave cavity. The resonance light transmitted through the resonance cell is used to detect the magnetic resonance signal of the Rb atoms, and this signal locks a voltage controlled quartz oscillator (VCXO) to the Rb atomic reference frequency. The Milstar Rb clocks are remotely tunable with a resolution of $<1 \times 10^{-12}$, in order to correct for frequency aging [2].

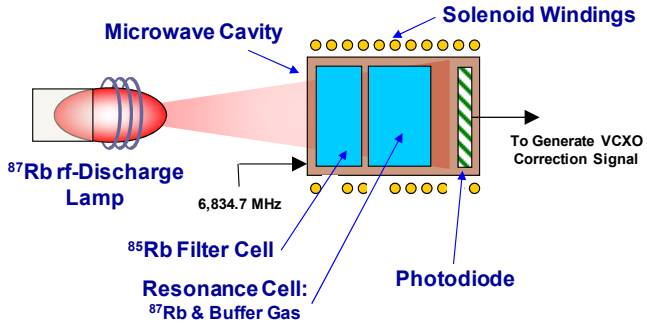

Figure 1. Functional diagram showing the key elements of the conventional Rb atomic clock physics package.

II. Data Collection Process

The stable output frequency of the Rb atomic clocks on each Milstar satellite can be adjusted by the constellation-control ground station (see Fig. 2.). The ground station maintains precise time with a Cs atomic clock, which is tied to UTC(USNO) via GPS [3]. Frequency and telemetry data, including a record of frequency tuning corrections, are collected by the ground station and archived. This archived data is the raw material upon which our analysis is based. We note that all Milstar specific information in the data has been removed, so as to better understand the performance of the Rb clocks un-influenced by the details of the space system.

III. Results

One of the major potential contributors to a Rb clock's frequency variations is the change that occurs in the RF discharge lamp's light output. This is due to the fact that the magnetic resonance frequency of the optically pumped Rb atoms in the clock's resonance cell is altered by the light-shift effect [4], a phenomenon where the spectral profile and intensity of the lamp's light alter the energy-level structure of the Rb atom [5]. Lamp intensity, as well as lamp temperature, was therefore analyzed over the full operational time for each of the Rb clocks. We note that the Rb lamps are maintained in a temperature controlled oven.

Rubidium atomic clocks are also sensitive to ambient temperature (albeit slightly compared to crystal oscillator clocks), so that we also considered the Rb clocks' baseplate temperature over the full measurement interval.

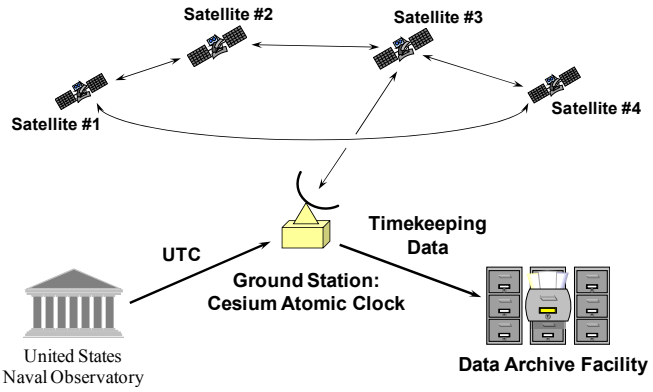

Figure 2. Notional diagram depicting the control of satellite Rb atomic clocks from the ground.

A. *Rb Satellite Clock A*

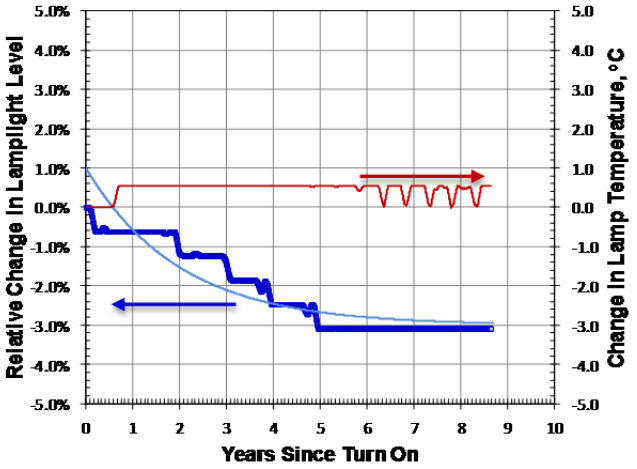

Figure 3. Rb lamp characteristics as a function of time for Rb satellite clock A. Each data point represents an average over 30 days.

As illustrated in Fig. 3, continuous measurement information over almost 9 years of operation is provided for Rb satellite clock A. The light intensity data of Fig. 3 are fit to a function of the form:

$$I = I_{\infty} + \delta I \, e^{-t/\tau_L}, \qquad (1)$$

and for this clock we find that $\delta I = 4\%$, and $\tau_L \cong 2$ years. The baseplate temperature is shown in Fig. 4, where a semi-annual (seasonal) temperature variation of about 4°C can be observed on top of a gradual temperature increase of ~4°C over the 9 year interval.

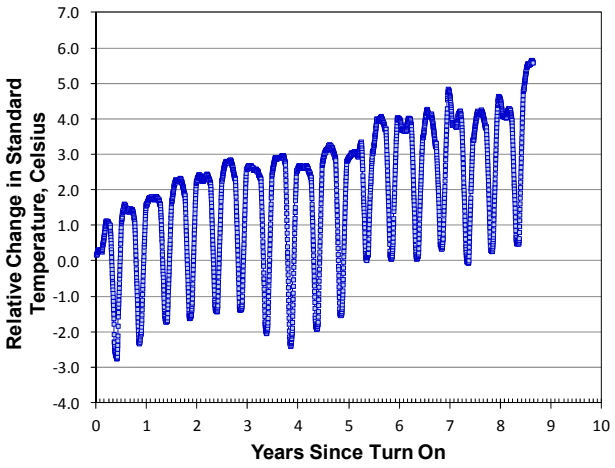

Figure 4. Baseplate temperature monitor as a function of time for Rb satellite clock A. Each data point represents a 30 day average.

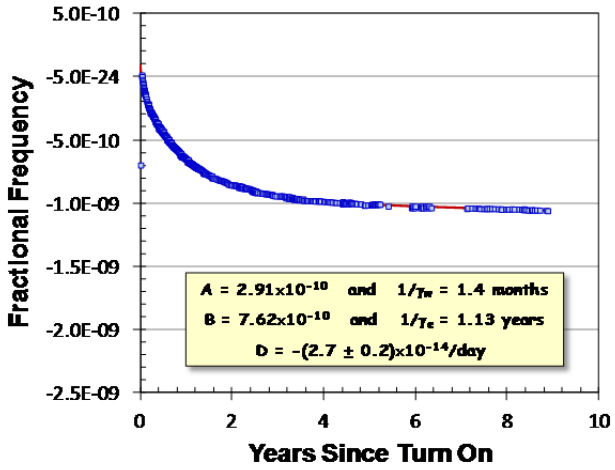

Figure 5. Relative frequency as a function of time for Rb satellite clock A. Data derived from commanded frequency corrections are shown in blue. The data are fit to a function of the form shown in Eq. (2), which is in red.

The Rb clock's fractional-frequency data over the 9 year period is shown in Fig. 5, and the data are fit to a function of the form:

$$y(t) = Ae^{-\gamma_w t} + Be^{-\gamma_e t} + Dt \qquad (2)$$

Empirically, it is found that the long-term frequency data for Rb clocks is often described well by this equation [4]. The "A" term has a relatively fast time constant, and is thought to be as associated with the migration of liquid Rb in the lamp or resonance cell to the "cold point." The "B" term has a slower time constant, and may be due to effects such as permeation of helium through the glass walls of the resonance cell [4]. The "D" term is a linear frequency aging term, the source of which is not well understood. In the following sections it will be seen that all the Rb clocks in this study are reasonably well described by Eq. (2), though with varying values for the adjustable parameters.

In the case of Rb satellite clock A (see Fig. 5), the "A" term has a time constant of ~1.4 months, and the "B" term has a time constant of ~1.13 years, neither of which agree well with the time constant associated with the lamp's light (~ 2 years). This suggests that for Rb satellite clock A, effects in addition to the light shift are important for determining the long-term frequency behavior of the clock. The asymptotic frequency aging term, D, is negative with a magnitude less than 3×10^{-14}/day.

B. Rb Satellite Clock B

Like Rb satellite clock A, continuous measurement information over almost 9 years is provided for this clock. The Rb lamp data over this interval are shown in Fig. 6. It is clear from this figure that in this case the lamp's light intensity was extremely stable over the full measurement interval (at least compared to Rb clock A).

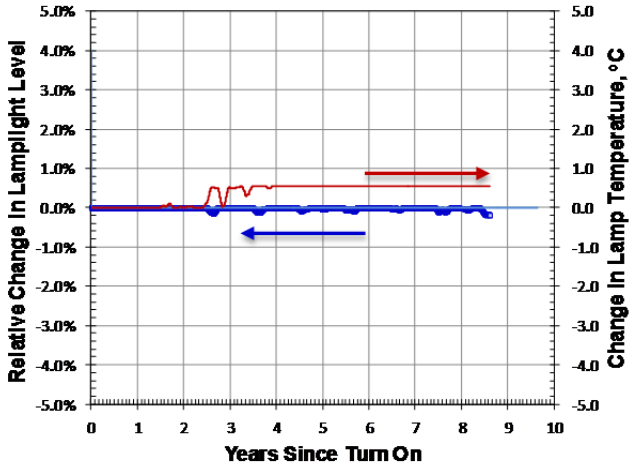

Figure 6. Rb lamp characteristics as a function of time for Rb satellite clock B. Each data point represents an average over a 30 days.

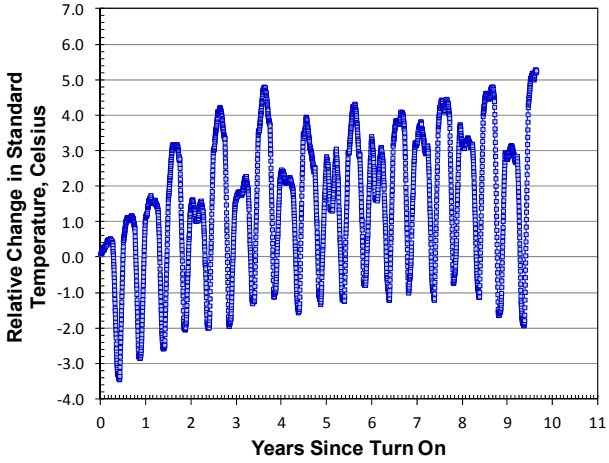

Figure 7. Baseplate temperature monitor as a function of time for Rb satellite clock B. Each data point represents a 30 day average.

The baseplate temperature is shown in Fig. 7, and semi-annual (seasonal) temperature variations of about 4°C are observed (similar to Rb satellite clock A) on top of a gradual temperature increase (in this case ~3 to 5°C) over the 9 year period. Notice that there is some indication that the average temperature actually begins to decrease starting in year 7.

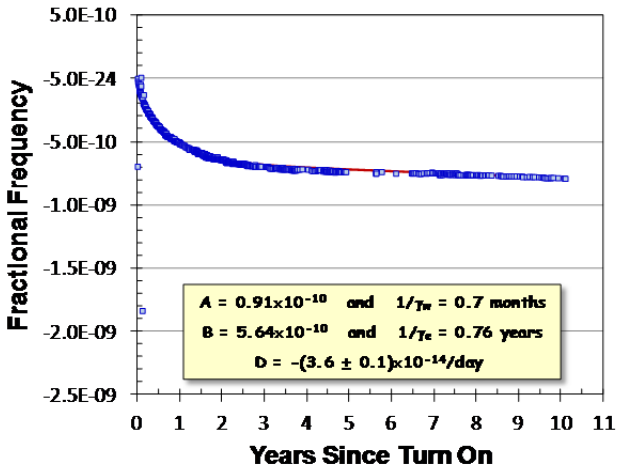

Figure 8. Relative frequency as a function of time for Rb satellite clock B. Data derived from commanded frequency corrections are shown in blue. The data are fit to a function of the form shown in Eq. (2), which is in red.

In the case of Rb satellite clock B's fractional frequency (see Fig. 8), the "A" term of Eq. (2) has a time constant of ~0.7 months, and the "B" term has a time constant of ~0.76 years. As with Rb satellite clock A, the frequency vs. time data do not appear to be well correlated with the lamp's light intensity data. This suggests that for Rb satellite clock B, similar to clock A, effects in addition to the light shift are important for determining the long-term frequency behavior of the clock. The asymptotic frequency aging term, D, is again negative with a magnitude of $\sim 3.6\times10^{-14}$/day.

C. Rb Satellite Clock C

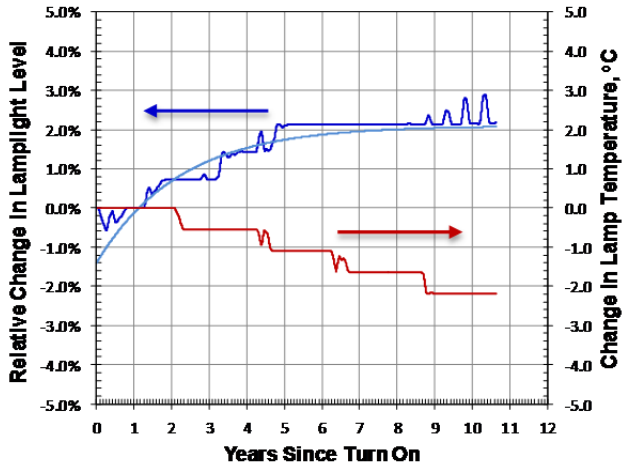

Figure 9. Rb lamp characteristics as a function of time for Rb satellite clock C. Each data point represents an average over 30 days.

This clock has the longest continuous data record, approximately 11 years. The light intensity data over this time interval are shown in Fig. 9, where it should be noticed that the light intensity actually increased in time. Similar to Rb clock A, the light intensity change is reasonably well described by Eq. (1) with $\delta I = -3.5\%$ and $\tau_L \cong 2.2$ years.

The baseplate temperature for Rb satellite clock C is shown in Figure 10. As with Rb satellite clocks A and B, the temperature shows a seasonal variation of ~4°C on top of a gradual temperature increase (in this case of ~5°C) over the 11 year interval.

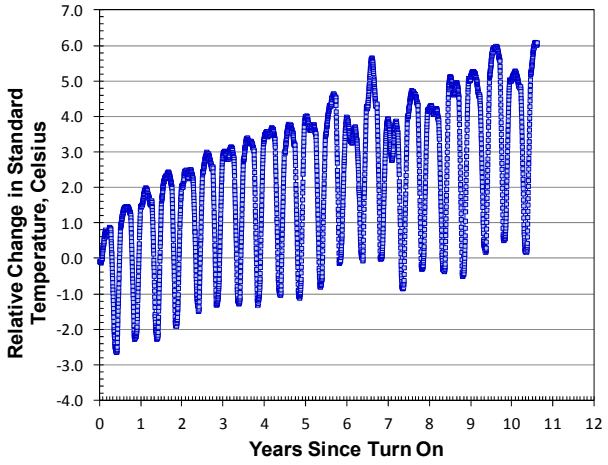

Figure 10. Baseplate temperature monitor as a function of time for Rb satellite clock C. Each data point represents a 30 day average.

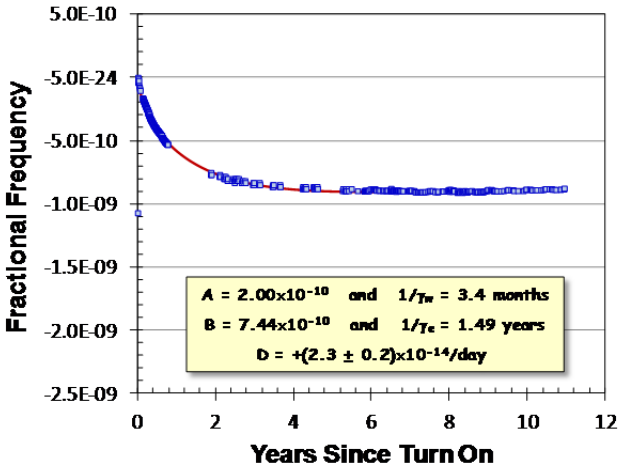

Figure 11. Relative frequency as a function of time for Rb satellite clock C. Data derived from commanded frequency corrections are shown in blue. The data are fit to a function of the form shown in Eq. (2), which is in red.

The frequency vs. time data for Rb satellite clock C is shown in Figure 11. For this clock, the "A" term of Eq. (2) has a time constant of 3.4 months, and the "B" term has a time constant of 1.49 years. As with Rb satellite clocks A and B, neither of these time constants correlates well with the time constant associated with the variation of lamp's light intensity. Furthermore, the "A" and "B" exponential terms are associated with negative frequency equilibration, like the other units; whereas the lamp's light intensity for this clock actually increases in time, unlike the other units. The asymptotic frequency aging term, D, is *positive* in this case with a magnitude of 2.3×10^{-14}/day.

Rb Satellite Clock D

This clock has operated continuously for only 5 years, less than the previous clocks that we've discussed. The lamp's light intensity data are provided in Fig. 12. Over the 5 year

period of operation for this clock the light intensity decreased almost linearly with time, even though there was no visible change in the lamp's oven temperature. Notice that the light intensity change over this time was ~7%, which is more than what was exhibited for the three previous units.

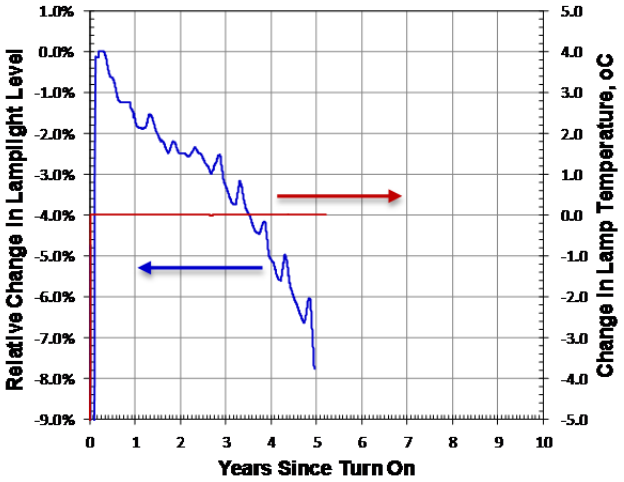

Figure 12. Rb lamp characteristics as a function of time for Rb satellite clock D. Each data point represents an average over 30 days.

The baseplate temperature record for this clock is shown in Fig. 13. It is more or less consistent with the record of the other clocks, exhibiting a gradual positive increase in temperature of ~3°C.

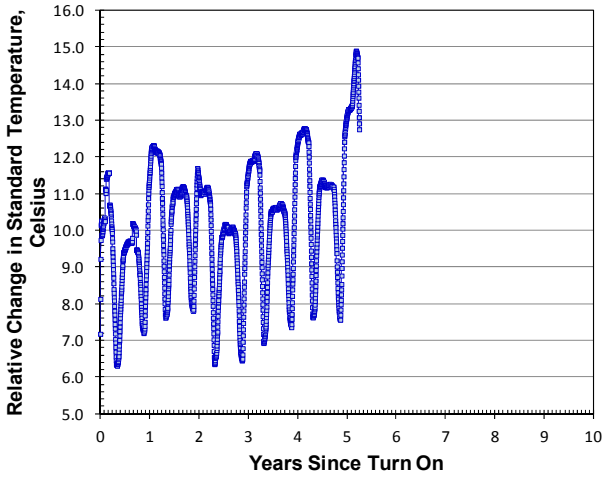

Figure 13. Baseplate temperature monitor as a function of time for Rb satellite clock D. Each data represents a 30 day average.

The frequency record for Rb satellite clock D is shown in Fig. 14. This record is quite interesting, in that the asymptotic aging rate, D, cannot be distinguished from zero at the 95% confidence level. It is to be noted that the (effectively) zero frequency aging rate is obtained in spite of the fact that the lamp's light intensity during this period was decreasing faster than for clocks A, B, or C.

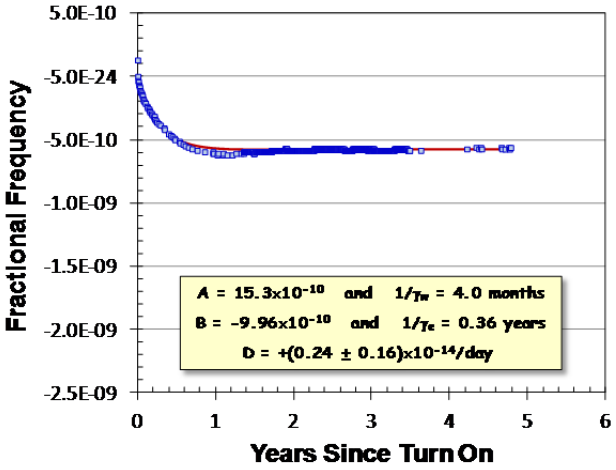

Figure 14. Relative frequency as a function of time for Rb satellite clock D. Data derived from commanded frequency corrections are shown in blue. The data are fit to a function of the form shown in Eq. (2), which is in red

D. Rb Satellite Clock E

The lamp intensity record for this clock is shown in Fig. 15. This clock was operated for approximately 2 years in STANDBY mode, a mode of operation in which the clock is powered ON but with its RF output disabled. A clock operated in this mode can be activated quickly, without the need for a lengthy warm-up period. After operating in the STANDBY mode for 2 years, this clock was powered completely OFF for ~3 years, before being powered on again for a period of almost 3 years. The lamp intensity, using the entire 7-plus year record, is well described by Eq. (1), with $\delta I = 5\%$, and $\tau_L \cong 2$ years. This functional fit suggests that the lamp intensity variation in time is controlled by factors which are independent of whether or not the lamp is operating; a conclusion that likely points to the underlying mechanism of the lamplight's change with time. One possible mechanism that is consistent with the data is loss of noble gas density in the lamp bulb [6]. Nevertheless, this is a question that will require further study.

The baseplate temperature record is shown in Fig. 16, and is in general consistent with the baseplate temperature record of the other clocks. The frequency record for this clock, during the nearly 3 year time period during which its RF output was enabled, is shown in Fig. 17. As the data demonstrate, for the full three year period the linear frequency aging term, D, is statistically indistinguishable from zero. This result suggests that frequency equilibration [4] must have completed during the STANDBY and OFF periods, an observation that may point to the mechanism of frequency equilibration. More importantly, perhaps, the data of Fig. 17 demonstrate that Rb vapor cell clocks have the ability to achieve frequency aging rates of ~10^{-15}/day or lower. In other words, linear frequency aging is not a *necessary* condition for Rb vapor-cell clock technology. Of course, how one routinely achieves such a low frequency-aging rate for a Rb atomic clock is the million-dollar question.

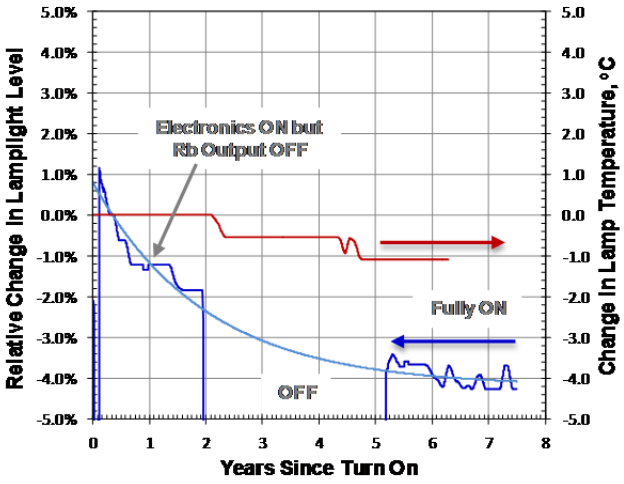

Figure 15. Rb lamp characteristics as a function of time for Rb satellite clock E. This device was operated in STANDBY mode (i.e., electronics powered, including physics package, but with the RF output disabled) for approximately two years; then, the device was powered OFF for ~ three years; then it was powered fully ON (including the RF output). Each data point represents an average over 30 days.

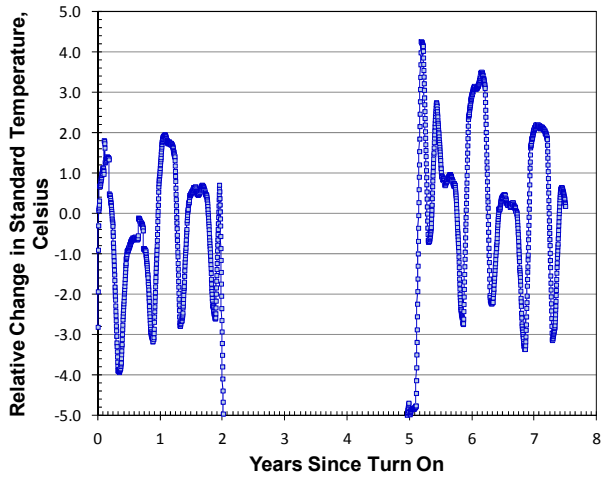

Figure 16. Baseplate temperature monitor as a function of time for Rb satellite clock E. The device was operated in STANDBY mode (i.e., electronics powered, including physics package, but with the RF output disabled) for approximately two years, then powered OFF for ~ 3 years, then powered fully ON. Each data point represents an average of 30 days.

E. Rb Satellite Clock F

The lamp light record for this clock is shown in Fig. 18. As indicated in the figure, this unit was operated for ~2.5 years, then powered OFF for ~1 year, then powered back ON, but without the Rb RF output. Similar to Rb satellite clock E, this unit's complete lamplight intensity history is reasonably well described by a single exponential function. This unit's lamp intensity changed much more than any of the other units that we studied: ~8% during the 2.5 years of operation and ~18% over 8 years.

The baseplate temperature record for this unit is shown in Fig. 19. The seasonal temperature variations are similar to the other clocks, however, the average temperature shifted down by ~3°C six months after the start of the record. The frequency record for this clock during the initial 2.5 years of operation is shown in Fig. 20. Fitting the data to Eq. (2) indicates that the "A" term is not present, that the "B" term has a time constant of 0.59 years, and that the linear frequency aging rate, D, is -7.3×10^{-14}/day.

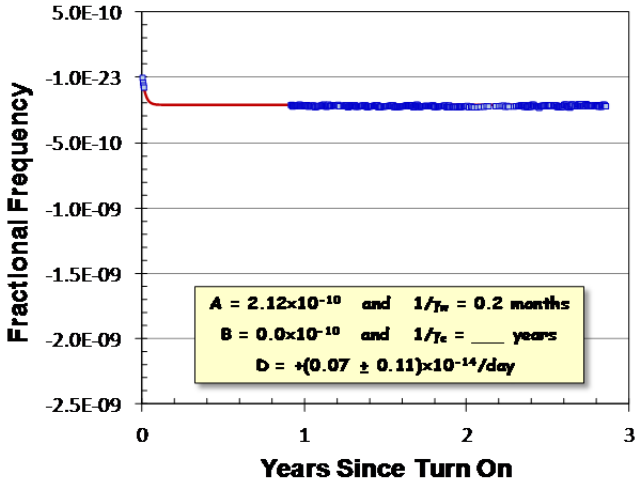

Figure 17. Relative frequency as a function of time for Rb satellite clock E. Data derived from commanded frequency corrections are shown in blue. The data are fit to a function of the form shown in Eq. (2), which is in red

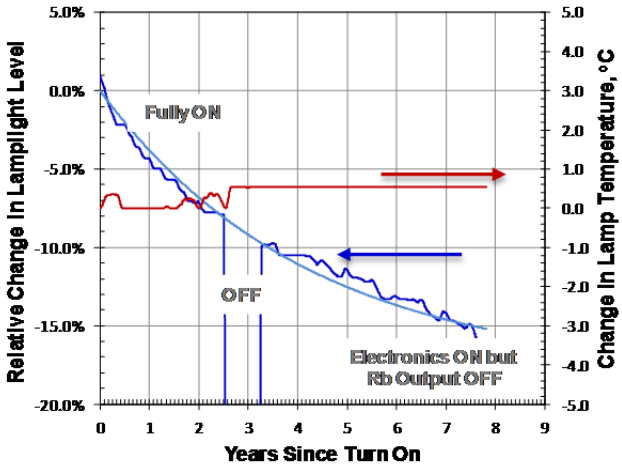

Figure 18. Rb lamp characteristics as a function of time for Rb satellite clock F. This device was operated normally for approximately 2.5 years, then powered OFF for almost one year, then operated without the RF output. Each data point represents a 30 day average.

IV. Discussion

The fractional-frequency time histories for our sample of spacecraft Rb atomic clocks are all fairly well described by Eq. (2). It is clear that these clocks all experience an exponential equilibration period of several years before exhibiting a much smaller, approximately linear, frequency aging. It is interesting to note (based on the record of Rb satellite clock E) that the equilibration appears to be a onetime process; which is absent if the clock's power is cycled after the equilibration is complete.

None of the clocks in our study exhibited a clear correlation between the lamp's light intensity change and the clock's fractional-frequency change. Typically, Rb vapor-cell

atomic clocks are designed to operate near a "zero light shift" condition [7]. This is achieved empirically by adjusting the operating temperatures of the physics package ovens, as well as the buffer gas contents of the Rb cells. The lack of correlation between frequency and light intensity suggests that this design strategy is effective for achieving long-term frequency stability, at least for the spacecraft clocks considered here. This observation also suggests that some other, un-identified process(es) contribute to the frequency equilibration and frequency aging.

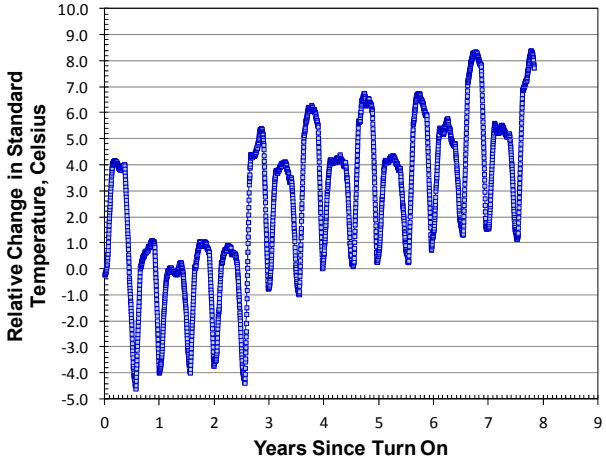

Figure 19. Baseplate temperature monitor as a function of time for Rb satellite clock F. This device was operated normally for approximately 2.5 years, then powered OFF for almost one year, then operated without RF output. Each data point represents an average over 30 days.

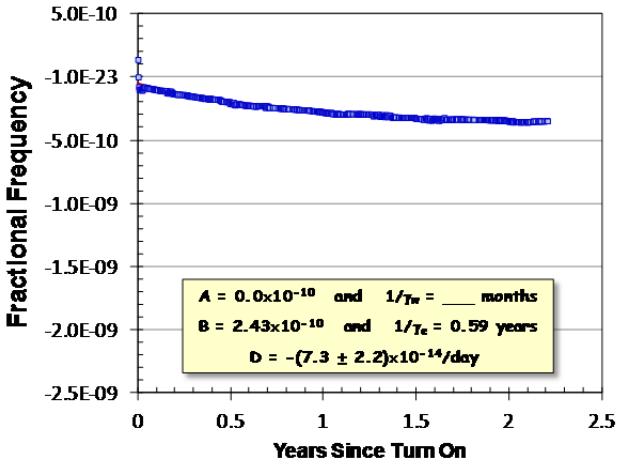

Figure 20. Relative frequency as a function of time for Rb satellite clock F. The data are shown in blue, and these were fit to the functional form shown in Eq. (2), which is in red.

Figure 21 shows the linear frequency aging rate, D, for all six of the Rb clocks discussed in this report. Note that these frequency aging rates are all smaller than what has generally been thought to be the norm for Rb vapor-cell atomic clocks (see Table I).

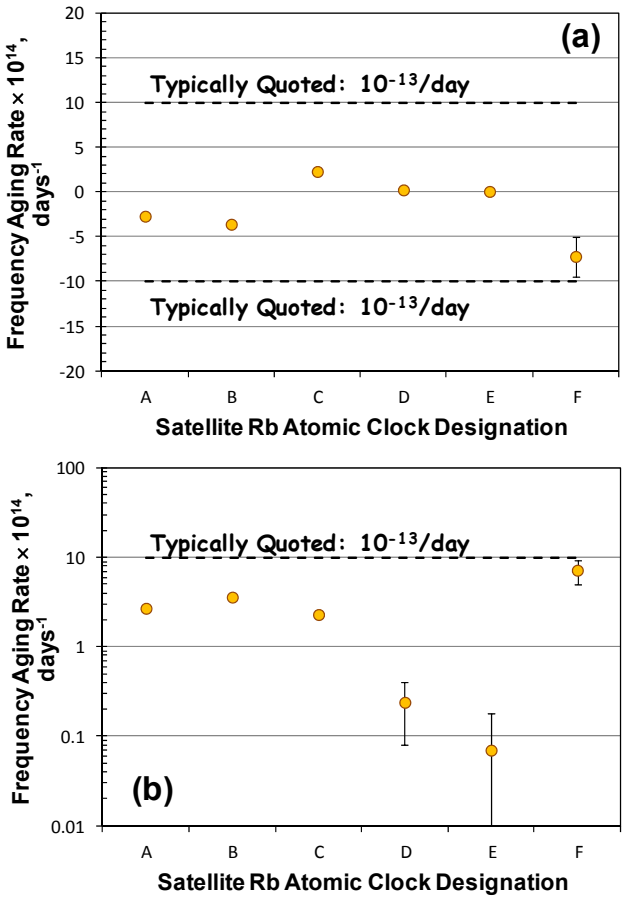

Figure 21. Summary plots showing asymptotic linear frequency aging coefficients, D, for each of the satellite clocks studied: (a) is a linear plot, and for greater clarity (b) shows the same data on a log plot.

V. CONCLUSION

This paper supplements what is in fact a very limited literature regarding the performance of Rb atomic clocks in space. The availability of such data is important for many systems engineers as they plan the next generations of GNSS and satellite communication systems. In summary, the data discussed here demonstrates a number of issues regarding well-designed Rb atomic clocks.

- Rb atomic clocks can operate in space for extended periods of time. In particular, one of the clocks in our study continues to operate after 11 years of operation, and two others continue to operate after approximately 9 years of operation. Further, these clocks are operating with no indication of an approaching end-of-life.
- For the Rb atomic clocks considered here, frequency equilibration is a very slow process, which can take 2 to 3 years.
- The asymptotic linear frequency aging rate of Rb atomic clocks can be much slower than what clock researchers typically think.

In particular, two of the clocks studied here exhibited an un-measurable frequency aging for about two years: at the

95% confidence level, the linear frequency aging rate, D, for one of these clocks was -0.7×10^{-15}/day < D < $+5.5\times10^{-15}$/day and for the other clock -1.5×10^{-15}/day < D < $+2.9\times10^{-15}$/day. Saying this differently, *over two years of continuous operation* one of these clocks could have suffered a total fractional-frequency change no greater than 4×10^{-12}, while the other could have suffered a total fractional-frequency change no greater than 2×10^{-12}.

References

[1] J. Camparo, S. Moss, & S. LaLumondiere, "Space-system timekeeping in the presence of solar flares," IEEE Aerospace and Electronic SYSTEMS Magazine, 19(5), 3-8 (2004).

[2] T. McClelland, I. Pascaru, M. Meirs, "Development of a Rb Frequency Standard for the MILSTAR Satellite System," 41st Annual Symposium on Frequency Control, 1987, p. 66.

[3] J. Camparo, R. Frueholz, and A. Dubin, "Precise time synchronization of two Milstar communications satellites without ground intervention," Internat. J. Sat. Commun., 15, 135-139 (1997).

[4] J. Camparo, C. Klimcak, and S. Herbulock, "Frequency equilibration in the vapor-cell atomic clock," IEEE Trans. Instrum. Meas. 54(5), 1873-1880 (2005).

[5] S. Pancharatnam, "Light shifts in semiclassical dispersion theory," J. Opt. Soc. Am. 56(11), 1636 (1966); B. S. Mathur, H. Tang, and W. Happer, "Light shifts in the alkali atoms," Phys. Rev. 171(1), 11-19 (1968).

[6] S. Kazantsev, V. Khutorshchikov, G. Guthohrlein, and L. Windholz, *Practical Spectroscopy of High-Frequency Discharges* (Plenum, New York, 1998) Ch. 8.

[7] J. Vanier, R. Kunski, P. Paulin, M. Tetu, and N. Cyr, "On the light shift in optical pumping of rubidium 87: the techniques of 'separated' and 'integrated' hyperfine filtering," Can. J. Phys. 60, 1396-1403 (1982).

Asymmetric Spectra of Phase Modulated Transitions of Square Waves

Michael J Underhill

Underhill Research Ltd, Lingfield, UK,
Email: mike@underhill.co.uk

***Abstract*—Square waves have instantaneous transitions between fixed upper and lower levels. The timing of the rising and falling transitions or 'edges' may be modulated in time and phase separately and independently. The resulting spectrum sidebands are a combination of the two transition modulations. In general the modulation spectrum is asymmetric with different upper and lower sideband spectra. This paper reports an investigation into why this should be so. New methods of single sideband modulation and demodulation are proposed.**

I. Introduction

Asymmetric phase noise spectra can be seen on the square wave output of the Anti Jitter Circuit as shown in Fig. 1, originally shown at EFTF/IFCS in Tampa 2003 [1]. Here the applied phase jitter signal was swept over a span of 10MHz on a 40MHz signal. The AJC suppressed the phase noise more on one transition than on the other. The phase noise is seen to be suppressed unequally on the two sidebands. The presence of unequal sidebands is a sign of simultaneous AM and PM on a carrier.

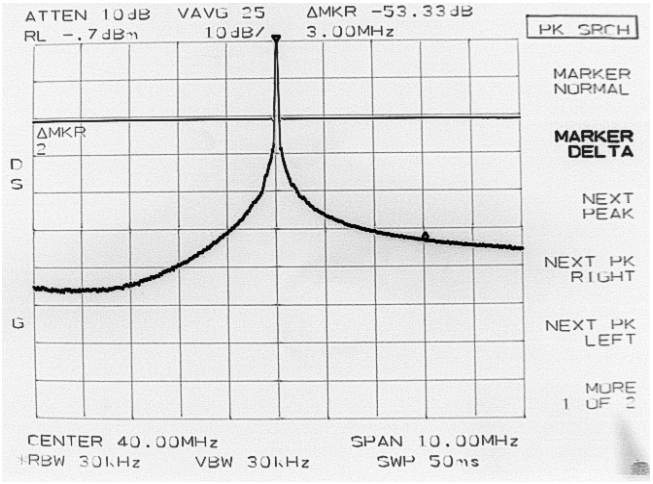

Figure 1. Measured asymmetric suppression of upper and lower sidebands of an input spectrum of an Anti-Jitter Circuit.

Fig. 2 shows a schematic block diagram of the EF-AJC (Enhanced Feedback Anti-Jitter Circuit), together with the key waveforms that explain its operation in suppressing phase and time jitter.

The Basic AJC has a floating charge integrator that creates a ramp waveform, with local feedback to maintain the operating point. The comparator output has much reduced jitter (on the rising edge).

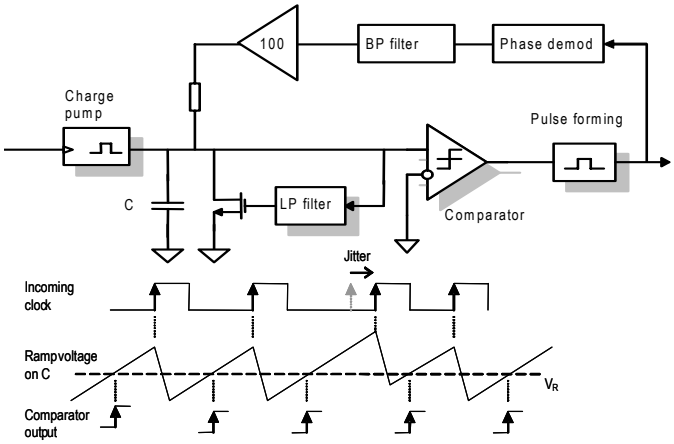

Figure 2. EF-AJC schematic diagram above with key wave forms explaining AJC operation below.

The EF-AJC loop in the upper part of the block diagram has an Extra Feedback loop around a Basic AJC. It lowers the cut-off frequency, and improves the jitter suppression, intrinsic noise and residual jitter.

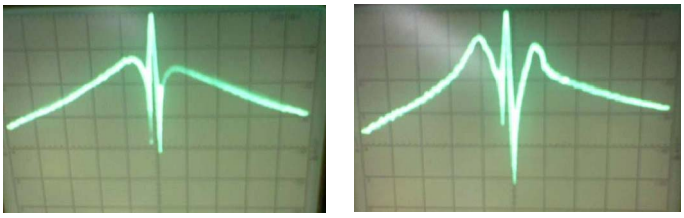

Figure 3. Left: Spectrum of suppression transfer function of comparator noise with no EF feedback, Fc = 10.2MHz, 5KHz/div, 300Hz RBW spectrum of suppression transfer function of comparator noise with EF feedback.

Fig. 3 also shows asymmetric spectra from the EF-AJC.

All AJCs have square-wave outputs switching between logic levels and in general are found to give spectra that are asymmetric.

II. Investigation of the Reasons for Asymmetric Spectra

The assumption that was investigated is that asymmetric spectra are caused by simultaneous amplitude and phase modulation by the same modulating signal. To confirm this tests were carried out using an HP8657D signal generator at 100MHz with a modulation frequency 1MHz that could be applied to amplitude (AM) or phase (PM) modulate or both

amplitude and phase modulate (AM+PM). For the tests the PM level was set to a modulation index of 1. The AM level was then adjusted to give the maximum imbalance of the first modulation sidebands at 99MHz and 101MHz, as observed on an HP8560A spectrum analyzer. The best suppression of the lower sideband was achieved with an AM modulation index of 57%. The asymmetry between the two first sidebands was then 13dB as shown in Fig. 4.

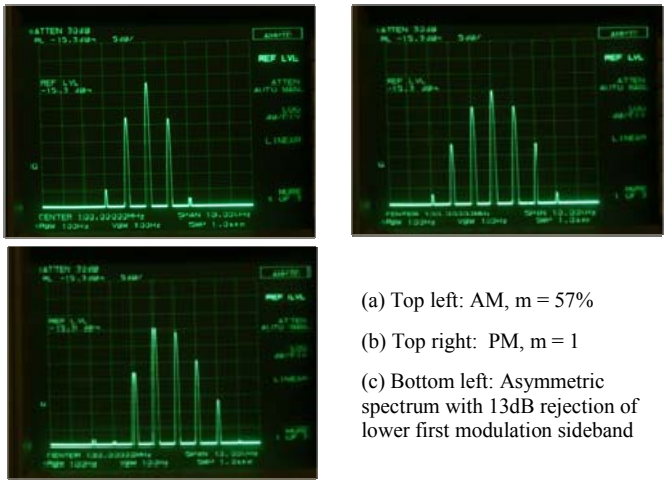

(a) Top left: AM, m = 57%

(b) Top right: PM, m = 1

(c) Bottom left: Asymmetric spectrum with 13dB rejection of lower first modulation sideband

Figure 4. Asymetric spectrum of 100MHz carrier (a) AM modulated with 1MHz sine wave at 57%, (b) PM modulated with 1MHz with m = 1, and (c) simultaneous AM and PM, all as observed on an HP8560A spectrum analyzer with 5dB/div vertical scale.

Fig. 4 is supporting evidence for the proposition that *an asymmetric spectrum can only occur if there is simultaneous AM and PM modulation*. Note that the individual AM and PM spectra individually are perfectly symmetrical.

Simultaneous AM-PM noise modulation of oscillators with asymmetric spectra have been investigated and reported, particularly by V. N. Kuleshov [2]. But the creation of simultaneous AM and PM by edge modulation of square-waves seems not to have been investigated to any extent.

III. MATHCAD SIMULATOR OF EDGE MODULATED SQUARE-WAVES

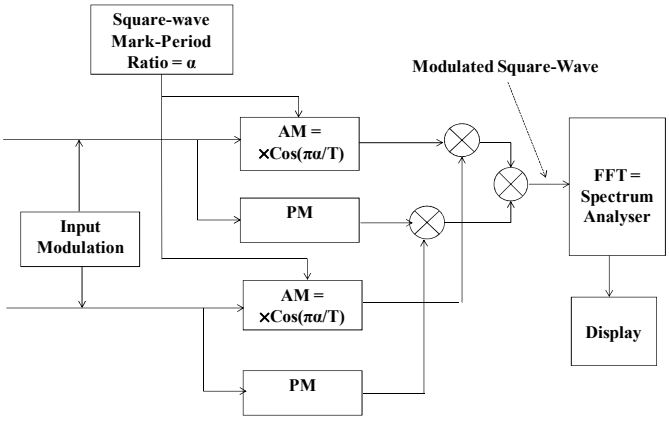

Figure 5. Transition Position Modulation System Process Diagram as implemented as a Mathcad simulation.

Fig. 5 shows the system process block diagram of a Mathcad simulator constructed to investigate edge modulation of square-waves.

At top left there is a source for the square-waves with provision for setting the frequency *f* and the mark-period ratio α of the test waveform (the latter as described below). The frequency scale internally in the simulation was chosen to be integer for convenience. For display there was a post-correction factor which for engineering credibility was set so that the display was in units of 1MHz. The carrier frequency for most of the tests was then set to 1GHz on the display. The input modulation to the left can be set to modulate the two edges independently in phase and amplitude as indicated by the four central blocks. The mark-period ratio was actually set by adjustable DC biases superimposed on the two edge modulation signals.

It is important to note that the AM modulation process gains G_{AM} from modulation amplitude to sideband amplitude are proportional to Cos(πα/T) where α is the mark-period ratio and T is the period. This has a null and a phase reversal when the mark-period ratio α is 0.5. This can be deduced by inspection for example of the final waveform of Fig. 6.

$$G_{AM} = Cos(\pi\alpha/T) \qquad (1)$$

Also of importance is that the carrier amplitude C is proportional to Sin(πα/T). This has a maximum at α = 0.5.

$$C = Sin(\pi\alpha/T) \qquad (2)$$

These processes are combined to create the modulated square-wave signal sent to the FFT spectrum analyzer.

Fig. 6 shows the key waveforms involved in generating the edge modulated square-wave signal.

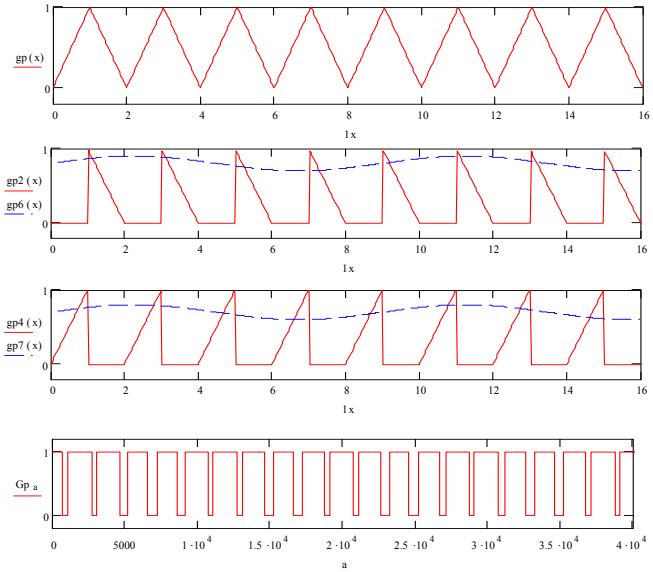

Figure 6. Key waveforms for generating the edge modulated square-wave signal. Top: triangular wave at carrier frequency. 2nd and 3rd from top: separated sloping edges compared with the modulation levels (blue dashed lines) for the up and down transitions. Bottom: the resultant edge-modulated square wave passed to the FFT. (α= 0.75, m_u = 0.1, m_d = -0.1)

In Fig. 6 the DC bias values in the modulator were 0.7 and 0.8. The mean of these is the mean mark to period ratio α = 0.75. The up and down sine-wave modulation peak values (modulation indices) were m_u = 0.1 and m_d = -0.1. The opposite signs indicate that the modulations are in anti-phase.

The number of bits in the FFT shown in Fig. 5 was made adjustable, so that a compromise could be made between accuracy and simulation time. A simulation run with 18 bits typically took 5 to 15 seconds on a DELL studio laptop and about two to three times as long on a Samsung NC10 notebook. Usually the Samsung was used with 16 or 17 bits with some loss of FFT spectrum quality.

IV. MATHCAD SIMULATOR INVESTIGATION OF SIMULTANEOUS EDGE MODULATION OF SQUARE-WAVES

The Mathcad simulator was used for a large number of trials of different values of the up and down modulation indices m_u and m_d, and the mark-period ratio α. The following selection of results has been made to illustrate the main points of discovery or confirmation of what could be expected.

The general objective was to find values of the modulation parameters that would generate single sideband with a minimum of the opposite unwanted sideband.

A. Example 1: Perfect Square-Wave

Fig. 7 shows the 18 bit FFT spectrum of a perfect 1GHz square-wave with mark-period ratio of exactly α = 0.5. Note that there is no second harmonic. The third harmonic is at its theoretical value of -9.54dB (one third) relative to the carrier amplitude.

From the depth of the troughs of the FFT spectrum relative to the peak value the dynamic range of the simulation with the 18 bit FFT was estimated from Fig. 7 to be about 60dB.

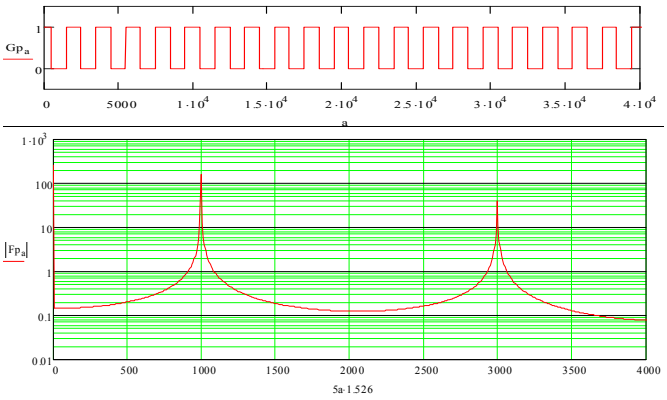

Figure 7. Spectrum of perfect square-wave at 1GHz at bottom. Waveform at top

B. Example 2: First Trial with 102.2 MHz Modulation

Fig. 8 shows first upper sideband USB suppression of 23dB, but unacceptably high second harmonic sidebands. The sum of the modulation indices was 2.9 which is thus shown to be too high for acceptable performance as an SSB generation method.

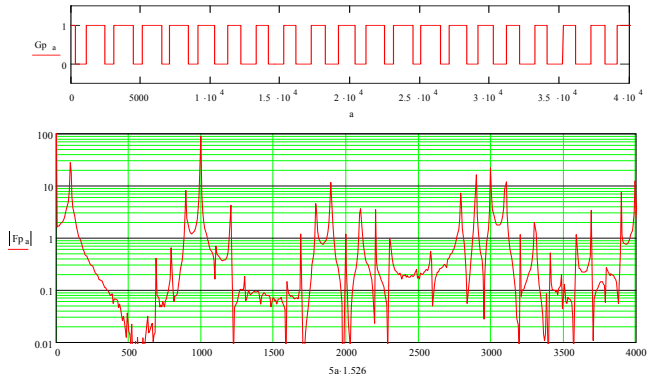

Figure 8. Square-waveform at top, spectrum at bottom, , for carrier at 1GHz and 102.2MHz Modulation Parameters: Mark-Period-Ratio α = O.555 Mod-up m_u = +0.09, Mod-down m_d = -0.2. LSB/USB = 23dB

C. Example 3: Perfect Square Wave EqualPhase (Time-Shift) Modulation at Low Level

Note no carrier second harmonic in Fig. 10. The surprise is the 15dB first sideband asymmetry.

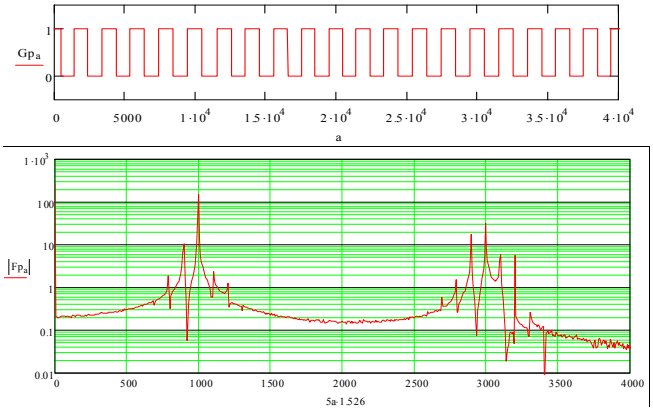

Figure 9. Carrier at 1GHz and 102.2MHz with Modulation Parameters: Mark-Period-Ratio α = 0.5, Mod-up m_u = +0.1, Mod-down m_d = -0.1

D. Example 4: Perfect Square Wave Equal In-Phase (Time-Shift) Modulation at High Level

Fig. 19 shows increased levels of modulation harmonics.

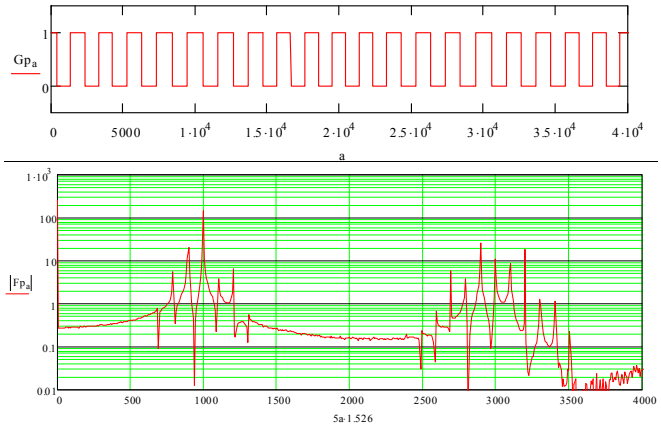

Figure 10. Carrier at 1GHz and 102.2MHz Modulation Parameters: Mark-Period-Ratio α = O.5, Mod-up m_u = +0.2, Mod-down m_d = +0.2

E. Example 5: Perfect Square Wave Equal High Level 0.2 Out-of-phase Modulation

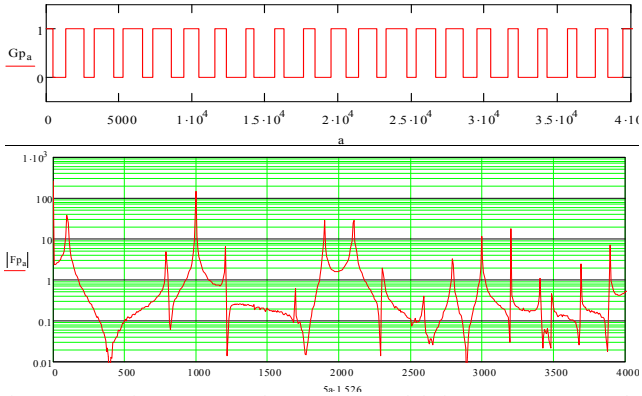

Figure 11. Carrier at 1GHz and 102.2MHz Modulation Parameters: Mark-Period-Ratio α = O.5, Mod-up m_u = +0.2, Mod-down m_d = -0.2

Fundamental frequency sidebands have cancelled, but not the second harmonic sidebands. But the fundamental remains in the mean level of the waveform and at left of spectrum.

F. Example 6: Single Edge Modulated Spectrum

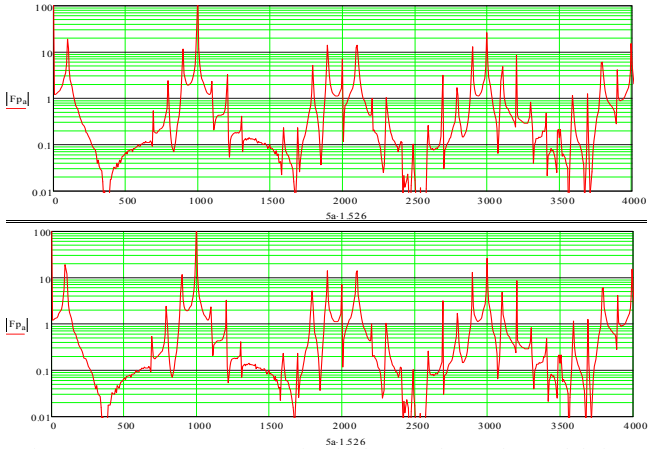

Figure 12. Same LSB spectrum for single up or down edge modulation compared top and bottom

For either one of the two edges modulated we get the same spectrum, where the lower sideband dominates by about 18dB.

G. Example 7: High Mark-Period Ratio Gives USB

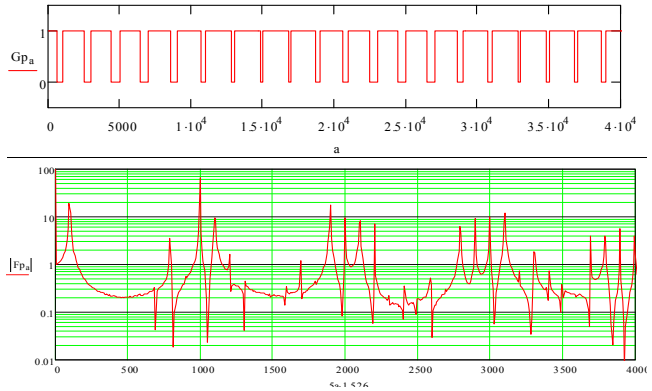

Figure 13. USB if Mark-Period-Ratio α = 0.8125, Mod-up m_u = 0.00, Mod-down m_d = +0.2

Note a dominant fundamental frequency USB with the LSB at -30dB. But the LSM 2nd harmonic is poor at -12dB.

H. Example 8: Low Mark-Period Ratio Gives LSB

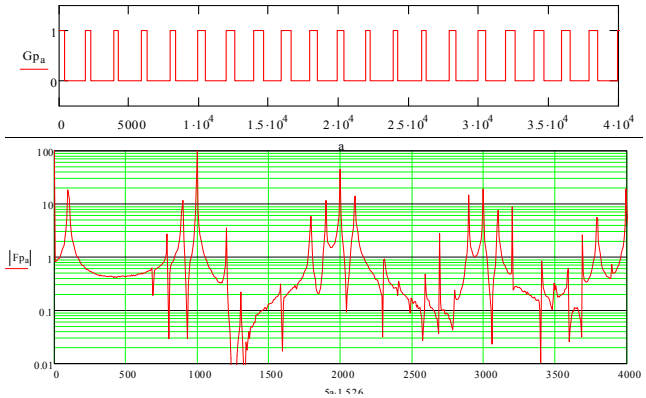

Figure 14. LSB if Mark-Period-Ratio α = 0.26, Mod-up m_u = 0.00, Mod-down m_d = +0.20

The dominant fundamental is LSB, with USB at -30dB. But note the poor USB second harmonic at -12dB.

I. Example 9: Optimised Asymmetric Modulation

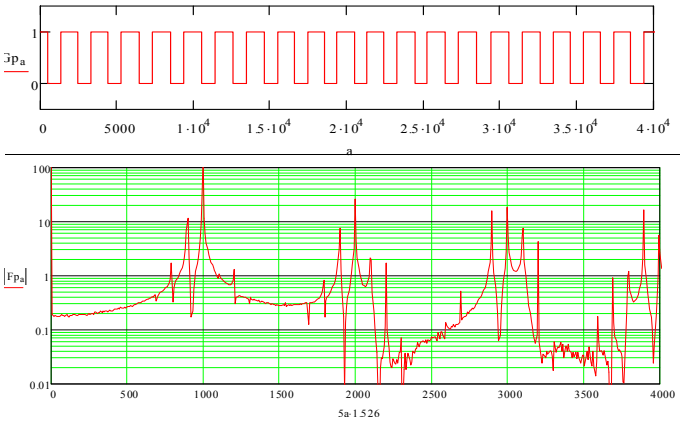

Figure 15. Optimum LSB if Mark-Period-Ratio α = 0.573, Mod-up m_u = 0.01, Mod-down m_d = -0.20

In Fig. 15 we get fundamental LSB, with USB at -30dB. Note the improved LSB second harmonic at -19dB.

J. Example10: Optimised LSB at 2.222MHz

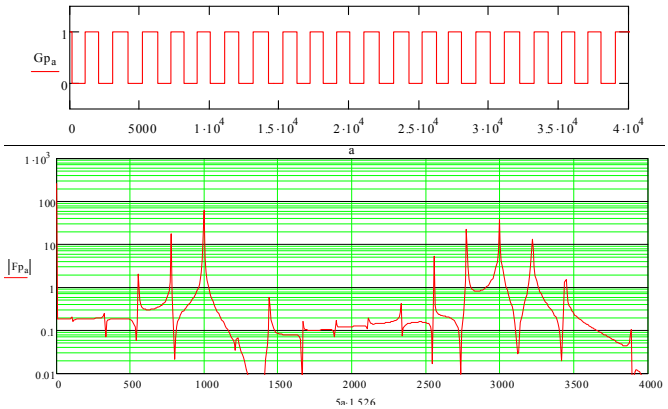

Figure 16. Optimum LSB if Mark-Period-Ratio α = 0.8, Mod-up m_u = +0.1, Mod-down m_d = +0.1

The modulation frequency has been doubled to 2.222MHz. The fundamental sideband is an LSB, with the USB at better than -40dB. Note the improved LSB second harmonic at -35dB.

K. Example11: Optimised USB at 2.222MHz

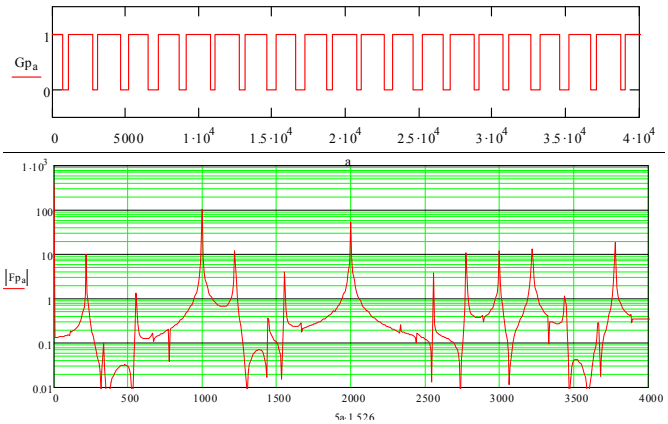

Figure 17. Optimum USB if Mark-Period-Ratio $\alpha = 0.75$, Mod-up m_u = +0.1, Mod-down m_d = -0.1

In Fig. 17 we get fundamental LSB, with USB at better than -40dB. Note the improved LSB second harmonic at -35dB.

The last two examples show that at the doubled frequency of 2.22MHz the FFT appears to have greater dynamic range. It indicates that all previous results may be pessimistic. Thus the prognosis for devising an SSB modulation method based on edge modulation of square waves may be better than first thought at the commencement of this project.

V. CONCLUSIONS

The transitions of square waves can be independently time-shift modulated to give SSB spectra that are by definition asymmetric.

The resulting spectrum sidebands are a combination of the two transition modulations and also depend heavily on the waveform mark-period ratio.

A Mathcad simulation including an 18 bit FFT has proved to be a good tool for investigation of this type of modulation technique and for the optimisation of modulation parameters.

The modulation method is significantly non-linear. The unwanted generation of second and higher order modulation sidebands is a problem. The easiest cure is to use low modulation levels.

Carrier cancellation and removal, also using square waves, is in principle possible but it could introduce even more harmonic distortion. One possible technique for further investigation is the interlacing of a pair of modulated short mark square waves. The dominant energy would then be at the second harmonic of the carrier and this could be low pass filtered.

Performance at higher modulation frequencies appears to be significantly better. The simulation may not be so representative at lower frequencies?

In the future new square wave methods of single sideband modulation (and demodulation) remain as possibilities. Future work looks worth pursuing on the basis of the results achieved so far.

Image recovery mixers (giving 3dB image noise reduction in principle) are a potentially useful area of application for this technique. This technique requires only about 15dB of opposite sideband rejection.

REFERENCES

[1] M. J. Underhill, "The Noise and Suppression Transfer Functions of the Anti-Jitter Circuit", Joint IFCS and 17th EFTF, Tampa, USA, 5-8 May 2003.

[2] V.N.Kuleshov "New development of PM and AM noiseanalysis in crystal oscillators: an influence of wide-band noisesources," Proc. of 19th EFTF, Besancon, France, 2005

On the Impact of Group Delay Variations on GNSS Time and Frequency Transfer

Tobias Kersten
Institut für Erdmessung (IfE)
Schneiderberg 50, D-30167 Hannover, Germany
phone: +49 511 762 5711, fax: +49 511 762 4006
Email: kersten@ife.uni-hannover.de

Steffen Schön[1,2] and Ulrich Weinbach[1,2]
[1]Quantum Engineering and Space
Time Research QUEST
[2]Institut für Erdmessung (IfE)
Email: {schoen, weinbach}@ife.uni-hannover.de

***Abstract*—Group Delay Variations (GDVs) are azimuth and elevation dependent code delays that can limit the accuracy of the GNSS code observables. This contribution focuses on the GDV determination and discusses several solutions with respect to repeatability and separability. On-site tests at a laboratory network as well as simulations of several time links are discussed analyzing the stochastic processes apparently introduced by GDV. The stability of the P3 links are not effected. However, offsets up to 0.6 ns can occur.**

In a detailed study, GDVs are applied to an inter-continental Precise Point Positioning (PPP) time transfer link. This analysis shows that GDV are not an issue for the stability of the PPP links, since small weights reduce the impact of the P3 GDV. It can be shown that the stochastic process, induced by GDV in a PPP analysis, is similar to a random walk noise, well below the L3 carrier phase observation noise of $\sigma_\phi = 6$ mm. Offsets for the receiver clock estimates of up to 0.4 ns are reported for the link WTZS (Wettzell) and Boulder (NIST).

I. Introduction

Global Navigation Satellite Systems (GNSS) are not only used for navigation and positioning but are also widely adopted by timing laboratories for international time and frequency transfer. In addition to the Two Way Satellite Time and Frequency Transfer (TWSTFT), three GNSS based techniques are in use: (1) GPS Common View (CV), (2) All-In-View, and recently (3) Precise Point Positioning (PPP), cf, e.g., [8], [13], or [14].

Using the GPS precise P code has two advantages. First, the noise level of the P code is considerably smaller than that one of the clear access (C/A) code. Second, the first order ionospheric delays can be eliminated forming the ionosphere free linear combination P3, since the P code is modulated on both frequencies as signal L1 P(Y) and L2 P(Y). Generally, lower signal to noise ration (SNR) at low elevation may show large variations [19] and furthermore the P code is modulated with the encrypted Y code. Therefore efforts have been made by manufacturers to develop different strategies for tracking this signal.

For time and frequency transfers, different error sources related to the receiver-antenna combination have to be considered, like e.g., hardware delays in the cable and receiver as well as the temperature sensitivity of the equipment. In this paper we will discuss the impact of the so called Group Delay Variations (GDV), i.e. delays that are dependent on the receiver antenna and the azimuth and elevation of the incoming signal. In literature, GDV have been addressed, e.g. in the context of GNSS based landing approaches [18], or satellite orbit determination [9]. But also time and frequency transfer methods can be affected, especially when combining the two orders of magnitude more precise carrier phase observables with code observables [4], [5], [20]. First experiments using the absolute antenna calibration unit to determine the elevation dependent variations of the code Group Delays were discussed in [26] for several antennas and receivers. Within these studies GDV for geodetic GNSS antenna with magnitudes in the order of 1 m (3.3 ns) were obtained with an accuracy of about 5 cm (0.17 ns).

The paper is organized as follows: In the first section the methodology to determine the GDV is explained. In section III the obtained GDV for several geodetic antennae are discussed and validated experimentally. In the last section we analyze the possible impact of the GDV on time and frequency transfer for European and transatlantic links using simulations and real data processed with a PPP approach.

II. Concept of GDV Determination

With the Hannover Concept of absolute antenna calibration a well-established experiment and calibration facility exists. Since 2000, Phase Center Variations (PCV) for GPS and GLONASS carrier phases on L1/L2 are successfully and routinely determined as described in detail in, e.g., [17], [25], or [16]. For this investigation, we made use of this technique and expanded the processing algorithms in our IfE GNSS software to use this approach to recover GDV with the actual available GNSS signals in the field. The facility as well as the concept of this approach are shown in Figure 1.

A. Observation Model of Group Delay Variations (GDV)

For accessing GDV at the observation level, we apply an approach similar to that one used for carrier phase

observations as shown in [25] and [11]. The undifferenced code observation P_A^j in meters from a satellite j to a station A reads:

$$P_A^j = \rho_A^j + c(\delta t_A - \delta t^j) + T_A^j + I_A^j + d_A - d^j + REL_A^j + MP_A^j + GDV(\alpha, e) + \epsilon_A^j, \quad (1)$$

with the geometric distance ρ_A^j, the receiver and satellite clock error in meter $c\,\delta t_A$, $c\,\delta t^j$, the signal delay in the receiver d_A and in the satellite d^j, the relativistic effect REL_A^j, the multipath error MP_A^j, and code noise ϵ_A^j, as well as the tropospheric path delay T_A^j and the ionospheric path delay I_A^j, [22]. In addition, we introduce the Group Delay Variations $GDV(\alpha, e)$ to the code observables as a function of the elevation e and azimuth α of the incident ray.

For the elimination of distance dependent effects as well as effects induced by the satellite clock, inter-station single differences $SD_{AB}^j = P_A^j - P_B^j$ are formed:

$$SD_{AB}^j(t_\iota) = GDV_{AB}^j(\alpha, e, t_\iota) + MP_{AB}^j(t_\iota) + c\delta t_{AB}(t_\iota) + \epsilon_{AB}^j(t_\iota), \quad (2)$$

with the differential Group Delay Variation $GDV_{AB}^j(\alpha, e, t_\iota)$, the effect of multipath at both stations $MP_{AB}^j(t_\iota)$, the differential receiver clock error $c\delta t_{AB}(t_\iota)$ in meters, as well as the code noise $\epsilon_{AB}^j(t_\iota)$ with a magnitude of $\sqrt{2} \cdot \epsilon^j(t_\iota)$. The observation epoch is denoted by t_ι.

A Stanford Rubidium FS725 was used as common oscillator, thus the differential receiver clock error is constant. Its amount equals the initial clock offset between both receivers.

Simply using inter-station single differences, like in equation (2), would largely reduce the GDV as well. However, if the orientation of the antenna under test is changed in very precise and predictable steps between subsequent epochs, we eliminate the impact of the reference antenna and access the GDV of the test-antenna at epoch t_ι like

$$\Delta SD_{A,B}^j(t_\iota, t_{\iota-1}) = SD_{AB}^j(t_{\iota-1}) - SD_{AB}^j(t_\iota) \quad (3)$$

$$= \Delta GDV_A^j(t_{\iota-1}, t_\iota) + \Delta MP_{AB}(t_{\iota-1}, t_\iota) + \Delta\epsilon_{AB}^j(t_\iota). \quad (4)$$

Due to a maximum offset of 5^s between subsequent epochs, the multipath term at station B is eliminated and largely reduced for the antenna under test mounted on the robot. Since both receivers are connected to the same oscillator (Stanford Rubidium FS725), the differential receiver clock error is eliminated - the impact is at least below the noise level of the code observation of $1\text{-}2{\cdot}10^{-9} \cdot \tau^{-1}$.

The robot arm itself was calibrated with a LEICA laser tracker LTD 640 at the Geodetic Institute of Hannover (GIH). It was proven, that the positioning is accurate at the 0.25 mm level, [15].

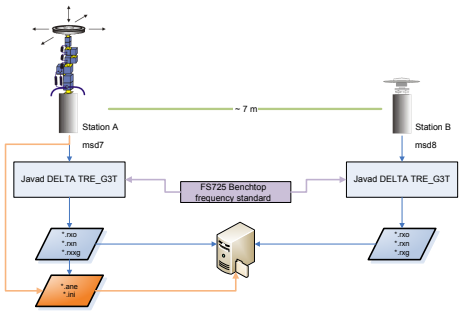

Figure 1. Calibration facility of the Hannover Concept for absolute antenna calibration at the Institut für Erdmessung, University of Hannover.

B. Mathematical Model of Group Delay Variations (GDV)

In analogy to the approach for the determination of PCV, we use continuous expansions on a sphere for the suitable modeling of GDV as variations with orthogonal base - functions. The model reads:

$$GDV(\alpha, e) = \sum_{n=0}^{n_{\max}} \sum_{m=0}^{m_{\max}} \begin{Bmatrix} A_{nm}\,\bar{R}_{nm}(\alpha, e) \\ B_{nm}\,\bar{S}_{nm}(\alpha, e) \end{Bmatrix}, \quad (5)$$

with: A_{nm}, B_{nm} := unknown coefficients, and

$$\begin{Bmatrix} \bar{R}_{nm}(\alpha, z) \\ \bar{S}_{nm}(\alpha, z) \end{Bmatrix} = \begin{Bmatrix} \cos(m\alpha) \\ \sin(m\alpha) \end{Bmatrix} N_{nm}\,(P_{nm}\sin(e))$$

the fully normalized harmonics $\bar{R}_{nm}$ and $\bar{S}_{nm}$, of degree n and order m. These are functions of the elevation angle e and azimuth angle α of a satellite in the antenna system. The normalization factor is denoted by N_{nm} and the associated Legendre functions by $P_{nm}\,(\sin(e))$, [10].

The estimation procedure is implemented in the software package developed at the Institut für Erdmessung. Details as well as results of a co-variance analysis of the estimable parameters are described in [11] or [12]. The corrections were computed from a synthesis of the spherical harmonics.

III. Discussion of Group Delay Variations (GDV)

Applying the methodology, described above, we estimate parameter sets for different non-geodetic and geodetic antennae with different characteristics.

In Figure 2 the determined GDV are depicted for some exemplary antennae . The P1 and P2 GDV for an Ashtech Marine ASH700700B antenna are depicted in Figures 2(a) and 2(d). The plots show that elevation-dependent variations are present with magnitudes from $-2\,\text{ns} < \text{GDV} < +2.6\,\text{ns}$, mainly caused by azimuth-dependent variations, cf. Figure 2(a). A similar GDV pattern was obtained for the P2 code, especially when comparing the P1 and P2 GDV at 300° in azimuth. Azimuthal variations are smaller for P2 with magnitudes

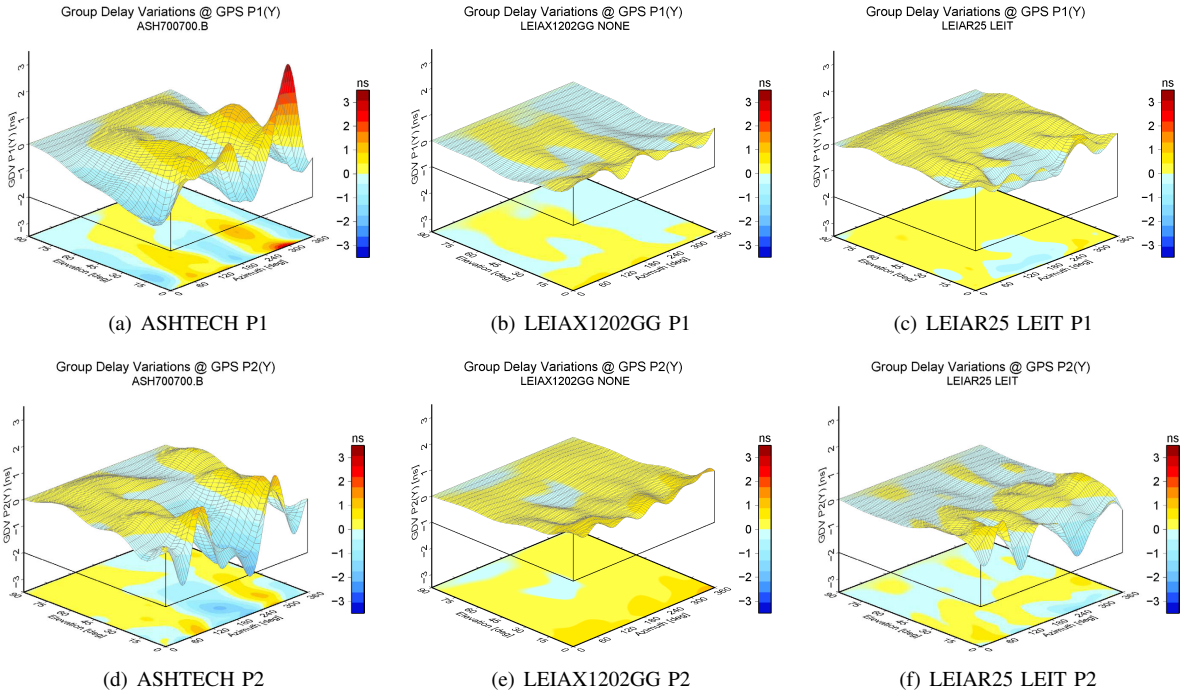

(a) ASHTECH P1 (b) LEIAX1202GG P1 (c) LEIAR25 LEIT P1

(d) ASHTECH P2 (e) LEIAX1202GG P2 (f) LEIAR25 LEIT P2

Figure 2. Determined GDV for exemplary antennas.

of approximate $-1.5\,\text{ns} < \text{GDV} < +1.5\,\text{ns}$, cf. Figure 2(d).

The Figures 2(b) and 2(e) show the determined GDV of the Leica Rover LEIAX1202GG antenna which exhibits no significant elevation dependency, but small azimuthal variations at elevations below 15°. The behavior on P1 is very similar to the GDV on P2, with magnitudes below 1 ns, cf. Figure 2(e).

The GDV for the Leica choke ring LEIAR25 antenna, depicted in Figures 2(c) and 2(f) appear to be not elevation-dependent. However, small azimuthal variations occur. Here the GDV show marginal differences between P1 and P2, apart from small variations at elevation angles below 15°.

For a calibrated μBlox antenna azimuthal variations on C/A have magnitudes of up to 2-3 ns for elevation angles between 90°-30°, cf. Figure 3(b). These azimuthal variations produce the overall effect, which can be seen in the single differences depicted in Figure 3(d) and 3(e). However, the GDV for the Javad Dual Depth choke ring antenna are very small and show only elevation dependencies below 1 ns at elevations below 15°, but not significant azimuthal variations as depicted in Figure 3(c).

Furthermore, some similarities of the GDV pattern exist with respect to their corresponding PCV pattern for the antennae used in this study. This is especially true for antennae, which show large azimuthal variations in their PCV like e.g. the Ashtech Marine ASH700700B or the μBlox patch antenna.

Plausibility checks

Since the code noise is large compared to the pattern, the following plausibility checks for the determined GDV were carried out.

A short baseline setup as depicted in Figure 3(a) was used to verify the obtained results. For this test, the corrections per epoch and line-of-sight were calculated and applied to the observed minus computed values (OMC) of the inter - station single differences of the C/A code. A Javad Dual Depth JPS_REGANT_DD_E antenna was used on pillar MSD8 while a μBlox ANN-MS_GP antenna with a ground plane was installed on pillar MSD7. The OMC of the C/A inter-station single differences (SD) are depicted in the Figures 3(d) and 3(e) versus GPS time. In addition the elevation of the satellites and the Group Delay Variations are indicated by a solid line. As shown in Figures 3(f) and 3(g) the root - mean - square (RMS) of the OMC C/A SD could be improved by up to 6% by applying the corrections.

Further tests were carried out using the same setup with a Trimble Zephyr I TRM41249.00 and a Leica AR25 LEIAR25 antenna mounted on pillars MSD7 and MD8, respectively. It turns out that applying the GDV for both antennae on a short baseline improves the code observation in the mean elevations about 0.6 - 0.8 ns.

In a third evaluation, estimated GDV were applied to the observations as corrections during the calibration processing. Several calibrations were repeated, showing that GDV are significant and estimable, [12].

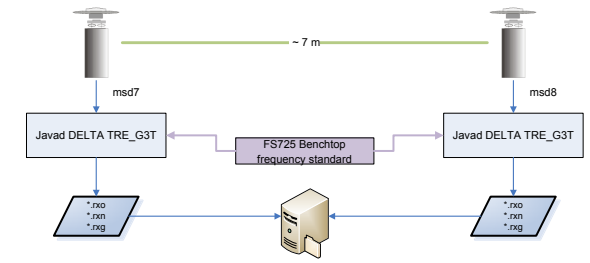

(a) short baseline setup

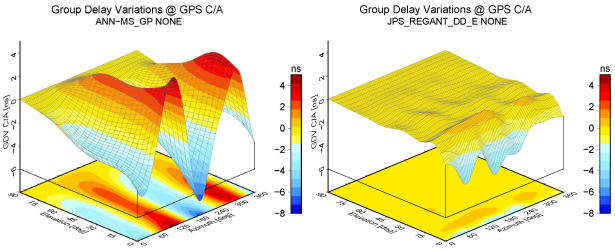

(b) GDV C/A UBLOX (c) GDV C/A JAVAD DualDepth

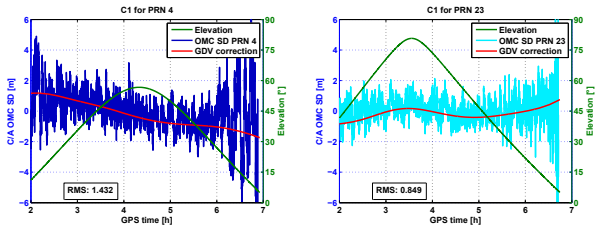

(d) SD on short baseline (e) SD on short baseline

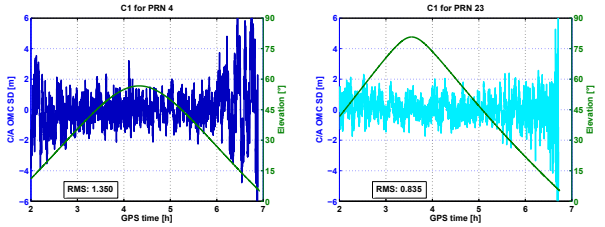

(f) GDV applied (g) GDV applied

Figure 3. (a) Short baseline common clock mode set up, (b) GDV of a μBlox ANN-MS_GP, (c) GDV of a Javad Dual Depth JPS_REGANT_DD_E antenna, (d,e) inter - station SD for two exemplary satellites PRN4 and PRN23, (f,g) SD after applying GDV to the code observable.

IV. Application to Time Transfer

To analyze the impact of GDV on time and frequency transfer two scenarios were studied: (1) a simulation for continental and inter-continental time links, (2) a frequency transfer scenario using Precise Point Positioning (PPP) with code observations corrected for GDV.

A. Simulation Strategy

The GDV are introduced in a simulation. We processed 14 days in daily batches with a sampling rate of 15 seconds for 7 IGS (or ITRF) stations, (Table I). Besides inner - European links stations outside Europe were used to study the impact of varying GPS satellite geometry. For each station we assume four scenarios with different antennae: (1) Ashtech Marine ASH700700.B, (2) Leica AR25 LEIAR25, (3) Trimble Zephyr I TRM41249.00 and (4) Trimble 2d choke ring TRM59900.00 antenna to evaluate the possible impact of different antenna combinations on different links. The receiver clocks are estimated using the ionosphere - free linear combination P_3,

$$P_3 = \left(\frac{f_1^2}{f_1^2 - f_2^2}\right) \cdot P_1 - \left(\frac{f_2^2}{f_1^2 - f_2^2}\right) \cdot P_2, \qquad (6)$$

with the carrier frequencies f_1 and f_2 and the corresponding code observations P_1 and P_2.

From experiments at the laboratory network at the IfE rooftop with different antennae and receivers a P_3 code noise of $\sigma_{P_3} \approx 0.6$ m was obtained, as indicated by a slope of τ^{-1} in Figure 5(a).

Precise orbits from the IGS [7] as well as the software developed at IfE were used for the simulations. The applied time transfer methodology equals the All - In - View technique, since all satellites visible above an elevation of 5° are considered. The advantage of using All - In - View w.r.t Common - View techniques are discussed in detail in [24]. For every station, receiver clock solutions with four antennae are obtained, each set with 80640 epochs with a 15 s sampling rate. Exemplary results for the receiver clock differences are depicted in Figure 4. Typical patterns are induced by the changing satellite geometry which repeats with the well known sidereal repetition time of 24 h - (3 min 56 sec). The induced time transfer error for the link PTBB - BRUS with the same antenna is +0.05 ns whereas for an inter-continental link PTBB - UNS3 equipped with the same antenna this increases to -0.08 ns. However, the largest impact is obtained for the inter - continental link PTBB - UNS3 and different antennae (ASH700700.B vs. TRM59900.00) with a time offset of -0.35 ns.

In Figure 5(a) the Allan Deviation [1] of several links, for simulation purposes equipped with same antenna type, a Trimble 2d choke ring (TRM59900.00) are shown. It is obvious that the Allan deviation starts with a white frequency modulation (WFM), with a characteristic slope of $\tau^{-0.5}$ until $\tau = 10^3$ sec ($\approx$ 20

Table I
Stations used in the simulation scenario.

Station	Location	Institution	Length [km]
PTBB	Braunschweig, Germany	PTB	0
BRUS	Brüssel, Belgium	ROB	479
MIZU	Mizusawa, Japan	GFZ	8785
ONSA	Onsala, Sweden	LMV	552
UNSA	Salta, Argentinia	GFZ	11242
USN3	Washington, USA	USNO	6520
WAB2	Wabern, Switzerland	METAS	679

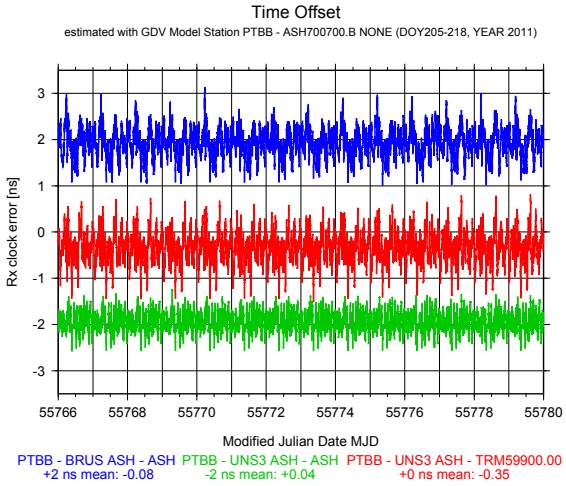

Figure 4. Simulated time series of the estimated receiver clock error for three exemplary links from PTBB are shown. Please note that the links PTBB-BRUS and PTBB UNS3 were shifted by +2 ns and -2 ns, resp. for readability.

minutes). A noise of $\sigma_{P_3} = 2 \cdot 10^{-9}$ at $\tau = 1\,\text{sec}$, is assumed, which is quite reasonable for the observation noise of P_3 links shown in [6] as well as [19]. It is obvious that the values of the Allan deviation for all kinds of links are definitely below the WPM of the code observation. In addition, the modified Allan deviation [3] depicted in Figure 5(b) shows, that the apparent noise induced by GDV behaves like WPM.

For a inner - European link PTBB - BRUS and for the same antenna, the plot of the Allan deviation shows a stability of $\sigma_y = 3.5 \cdot 10^{-13}$ at $\tau = 10^3$ seconds. For an inter - continental link PTBB - UNS3 this transition point changes to $\sigma_y = 1.5 \cdot 10^{-13}$ at $\tau \approx 3.6 \cdot 10^3$ seconds. This shows that significant differences for larger τ occur due to the different GPS satellite geometry and variations accentuate for increasing distance of the link. The behavior of the Allan deviation is very similar for all tested antennae, especially concerning the transition point. The transition between the different noise processes always occur around $\tau = 10^3$ seconds for short links below 1000 km, cf. Table I, and changes to $\tau = 3.6 \cdot 10^3$ seconds for links of more than 6000 km, cf. Figure 5(a). For all antenna combinations the impact is well below the P_3 observation noise of the links and thus has no impact on the stability.

To provide comparable values within the time and frequency transfer, the simulated time series were analyzed using the GPS time transfer standard GGTTS format. This format is a unique standard for GPS time receiver software and applications. One track of the GGTTS formats consists of 780 seconds (13 minutes) length. The reason for the 13 minutes are (1) usually a receiver required 2 minutes to lock on one satellite, (2) approx 10 minutes are necessary to transmit the full content of the navigation message and (3) one minute is usefully

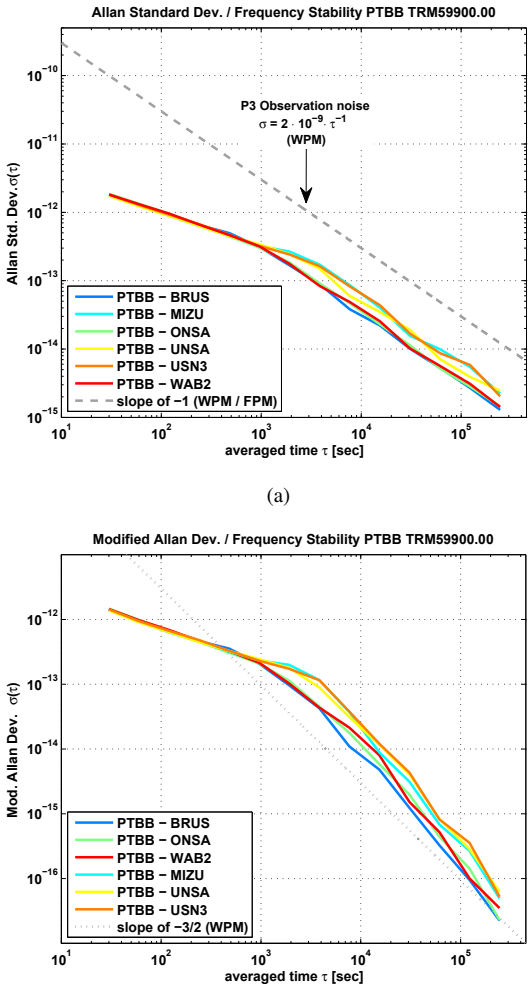

Figure 5. Allan standard deviation (a) and modified Allan deviation (b) of simulated time series for several baselines.

for data processing and preparation of a new track [2].

Simulated time series for several antennae and links are transformed into the GGTTS format and are depicted in Figure 6. For all antennae and links the apparent noise induced by the GDV is characterized by a slope of $\tau^{-3/2}$. As expected, the smallest mod. Allan deviation is obtained for the short link PTBB - BRUS, with the same antenna, since the impact of GDV is largely reduced because of the similar satellite geometry. The mod. Allan deviation [3] of the several links are very similar. For inter - continental links the mod. Allan deviation starts with a white frequency modulation (WFM) of $\sigma_y = 5 \cdot 10^{-12}\,\tau^{-0.5}$, cf. also Figure 6, followed by a white PM with $\sigma_y = 2 - 6 \cdot 10^{-10}\,\tau^{-3/2}$ for $\tau > 10^3$ sec. As described above, the mod. Allan deviation of the GGTTS time series is moreover well below the P_3 observation noise.

To summarize this subsection: the best results can be achieved assuming that both stations of a short link are

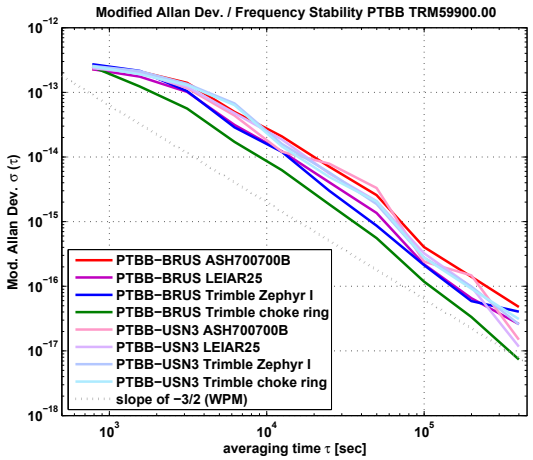

Figure 6. Modified Allan deviation of GGTTS formatted time series for several baselines and different equipment.

equipped with the same antennae. For long links the impact depends on the GDV as well as on the changing satellite geometry. Within our analysis the GDV of antenna have a quite similar impact. Since the P_3 code noise is larger than the effect introduced by the GDV, they are not yet an issue for the stability of the link. The same holds for the GGTTS time format.

However the apparent noise induced by the GDV is close to the noise, achievable by combining carrier phase and code observables. The phase noise of the Code plus Carrier linear combination (CPC) is reduced by a factor of about 20 with respect to the P_3 code noise, [5]. Also potential GDV for the Galileo E5a,b AltBOC signal could have an impact on time transfer since this signal is more robust against external influences.

B. PPP frequency transfer

In order to study the impact of GDV on PPP frequency transfer, the GDV corrections were introduced into a Precise Point Positioning (PPP) link between Wettzell, Germany (WTZS) and Boulder, USA (NIST). This link is of special interest since (1) the GDV could be determined for the antennae, which are actually located at these stations, (2) the receivers at these stations are connected to active H - Maser frequency standards, which provide the necessary frequency stability, and (3) from the simulation study the largest impact is expected for a inter - continental link.

The station WTZS is equipped with a Leica AR25.R3 LEIT 3d choke ring antenna and a Septentrio PolaRx2 receiver connected to an external H - Maser EFOS 39. The station NIST uses a Novatel NOV702 antenna in combination with a Novatel NOV OEM4 - G2 receiver also connected to an external H - Maser. In our study, a LEIAX1202GG is used for NIST instead of a NOV702 but the antennae are nearly identical.

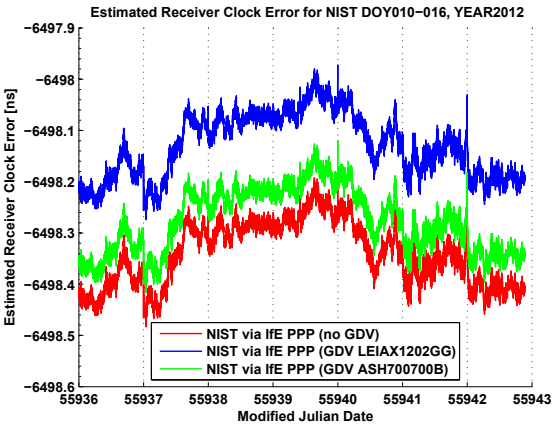

(a) Estimated receiver clock error at NIST

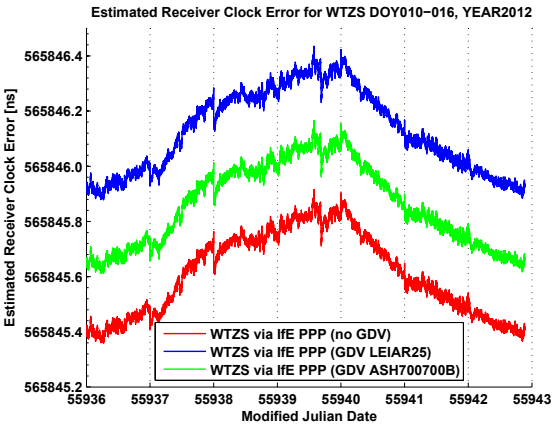

(b) Estimated receiver clock error at WTZS

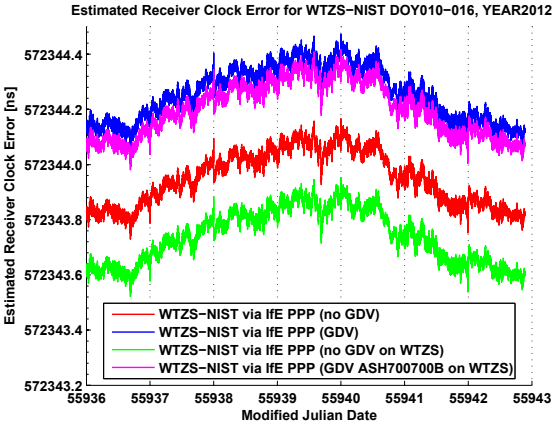

(c) Estimated receiver clock error for the link WTZS-NIST

Figure 7. PPP receiver clock estimates for station NIST and WTZS (linear drift removed) with different GDV applied.

The PPP analysis is carried out with a PPP software, developed at IfE [23] using a Kalman filter approach. The precise orbits, clocks, and Earth rotation parameter (ERP) for the DOY010 up to DOY016, 2012 were obtained from the IGS, [7]; corrections for ocean tide loading (Model FES2004) origin from the Onsala Space

Observatory (OSO), cf. [21].

For this study, several scenarios were calculated: (1) only one day is processed in order to analyze the impact on a daily solution, (2) one week of data were processed continuously and (3) in both scenarios a third antenna, Ashtech Marine ASH700700B which has a more pronounced GDV pattern than the LEIAR25.R3 and LEIAX1202GG antennae is introduced.

Figures 7(a) and 7(b) show the receiver clock error calculated for both stations separately. The three time series are obtained from (1) applying no GDV correction, (2) applying the GDV correction corresponding to the antenna in use, and (3) applying arbitrarily the correction for an Ashtech Marine antenna. A common linear drift is removed. It can be noted that the time series of the receiver clock estimates of station NIST are nearly identical except to an offset of 0.2 ns between with and without considering the GDV. The same behavior is depicted for the estimated receiver clock of station WTZS, where an offset of up to 0.5 ns can be noticed. As shown in Figure 7(c) the impact of the GDV corrected code observable introduce an offset with a magnitude of 0.35 ns on the inter - continental link WTZS - NIST. Additionally, we have introduced a second antenna correction (Ashtech Marine ASH700700.B) to see the impact of a more pronounced GDV pattern. In conclusion, the difference between the solutions with and without consideration of GDV introduces an offset, but the patterns of the receiver clock estimates are very similar, cf. Figures 7(a) - 7(c).

Concerning the frequency stability of the link, we compare two scenarios. First we start with a daily solution, the modified Allan deviation for different scenarios is depicted in Figure 8(a). The stability for one day resembles a flicker phase modulation (FPM) process of $1.5 \cdot 10^{-12} \cdot \tau^{-1}$ for the whole day. Significant differences between the several PPP processing scenarios could not be detected. But if we take a look onto the stability of the difference between w/o GDV consideration, one summarize, that the process is mapped as a white frequency modulation (WFM) with $3.5 \cdot 10^{-15} \cdot \tau^{-0.5}$.

In the second scenario, data of one week from the PPP link WTZS - NIST is depicted in Figure 8(b). The modified Allan deviation starts with a white phase modulation (WPM) and transitions into a flicker phase modulation (FPM) process with $5 \cdot 10^{-13} \cdot \tau^{-1}$ down to $8.46 \cdot 10^4$ sec (one day). For $\tau > 8.46 \cdot 10^4$ seconds the frequency stability turns into a flicker frequency modulation (FFM) process with a magnitude of about $8 \text{ - } 9 \cdot 10^{-16} \cdot \tau^0$, which is typical for PPP frequency transfer, since this level of FFM process reflects the frequency stability of the used H - Masers.

To sum up, in currently used PPP links GDV leads to offsets of few tens of nanoseconds. However, GDV are not an issue for the stability of the link since the code weighting with $\sigma_{P_3} = 0.6$ m downweights the impact of the P3 GDV magnitudes when using geodetic antennae.

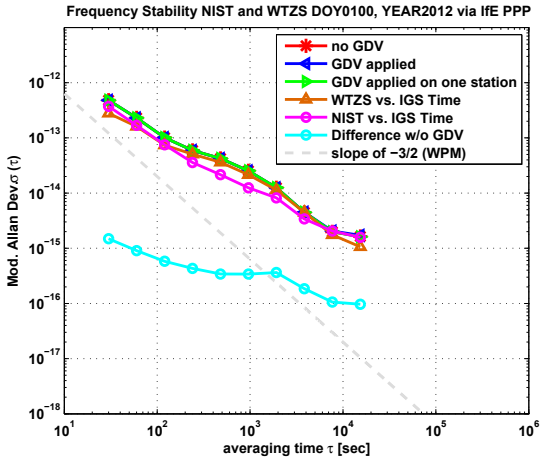

(a)

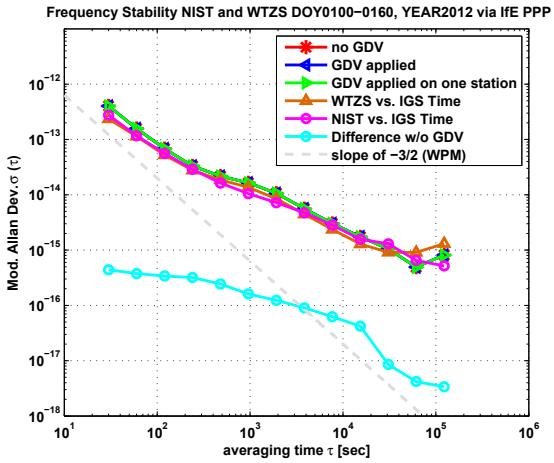

(b)

Figure 8. Frequency Stability for intercontinental time link WTZS and NIST for one day (a) and one week (b). Data, origin from daily IGS station files, processed with IfE PPP software to analyze the impact of GDVs.

V. Conclusion

In this study we have shown that significant systematic errors on code observables can be caused by Group Delay Variations (GDV). GDV vary with the elevation as well as the azimuth of the incident ray and are specific for each antenna type. Furthermore it could be shown that GDV can be estimated by the Hannover Concept of absolute antenna calibration. The method provides a precision of 0.15 ns. Furthermore, it could be shown that the RMS of the code OMC could be reduced by up to 6% when applying these corrections.

Simulation studies reveal that the effect of GDV equals a white PM / white FM and a stability of $\sigma_y = 3.5 \cdot 10^{-13}$ at $\tau = 10^3$ seconds. The same behavior is obtained when applying the GGTTS standard format for time and frequency transfer. It could be shown, that the GDV introduce a white PM on the GGTTS formatted time series. Since the noise level of P3 is rather high

($\sigma_{P_3} \approx 2 \cdot 10^{-12}$ at $\tau = 10^3$ sec), the impact of the GDV on the stability of P3 time and frequency links can be neglected up to now. However, GDV can induce time offsets in the links of up to 0.5 ns.

Furthermore the introduction of GDV in a PPP frequency comparison on an inter - continental link between Wettzell WTZS and Boulder NIST shows, that GDV are not a limiting factor for the stablility of the link, however offsets of up to 0.4 ns can be introduced.

Finally, further investigations are necessary to analyze the impact of GDV on code and carrier phase combinations. Here GDV may become an issue because of the new generations of code modulation, such as Galileo E5 AltBOC, which provides a very low code noise. This new signals will be fully available within the next years and improve time and frequency transfer as well. Therefore GDV can become an issue, so that they have to be modeled accurately for the use in precise applications.

DISCLAIMER

Although the authors dispense with endorsement of any of the products used in this study, commercial products are named for scientific transparency. Please note that a different receiver / antenna unit of the same manufacturer and type may show different characteristics.

ACKNOWLEDGMENT

The work within this project is supported by the German Aerospace Center (DLR) with the project label 50NA0903, funded by the Federal Ministry of Economics and Technology (BMWI), based on a resolution by the German Bundestag.

REFERENCES

[1] D. W. Allan. Statistics of Atomic Frequency Standards. *Proceedings of the IEEE*, 54(2):221–230, 1966.

[2] D. W. Allan and C. Thomas. Technical Directives for Standardization of GPS Time Receiver Software to be implemented for improving the accuracy of GPS common-view time transfer. *Metrologia*, 31:69–79, 1994.

[3] L. G. Bernier. Theoretical Analysis of the Modified Allan Variance. In *41st Annual Frequency Control Symposium*, pages 116–121, 1987.

[4] G. Cerretto, A. Perucca, P. Pavella, A. Mozo, R. Píriz, and M. Romay. Network Time and Frequency Transfer With GNSS Receivers Located in Time Laboratories. *IEEE Transactions on Ultrasonics, Ferroelectronics and Frequency Control*, 57(6):1276–1284, 2010.

[5] P. Defraigne. GNSS Time and Frequency Transfer: state of the art and possible evolution. In *Workshop on Development of Advanced TFT Techniques, Bureau Internationale des Poids et Measurements (BIPM), June 28*, 2011.

[6] P. Defraigne and G. Petit. Time transfer to TAI using geodetic receivers. *Metrologia*, 40:184–188, 2003.

[7] J. M. Dow, R. Neilan, and C. Rizos. The International GNSS Service in a changing Landscape of Global Navigation Satellite Systems. *Journal of Geodesy, Springer Verlag, New York*, 83:191–198, 2009.

[8] A. Gifford. One Way GPS Time Transfer 2000. In *32nd Annual Precise Time and Time Interval (PTTI) Meeting*, 2000.

[9] B. Haines, Y. Bar-Sever, W. Bertiger, S. Desai, N. Harvey, and J. Weiss. Improved Models of the GPS Satellite Antenna Phase and Group Delay Variations Using Data from Low-Earth Orbiters, Abstract #G54A-05. In *presented at 2010 Fall Meeting, AGU, San Francisco, Calif., 13-17 Dec*, 2010.

[10] E. Hobson. *The Theory of Spherical and Ellipsoidal Harmonics*. Cambridge, University Press, 1931.

[11] T. Kersten and S. Schön. Towards Modeling Phase Center Variations for Multi-Frequency and Multi-GNSS. In *5th ESA Workshop on Satellite Navigation Technologies and European Workshop on GNSS Signals and Signal Processing (NAVITEC), 8.-10. December ESTEC, Noordwijk, The Netherlands December*, 2010.

[12] T. Kersten and S. Schön. GNSS Group Delay Variations - Potential for improving GNSS based Time and Frequency Transfer? In *Proceedings of the 43rd Annual Precise Time and Time Interval (PTTI) Meeting, Long Beach, CA, USA*, 2011.

[13] J. Levine. A Review of Time and Frequency Transfer Methods. *Metrologia*, 45:162–174, 2008.

[14] M. A. Lombardi, L. M. Nelson, A. N. Novick, and V. S. Zhang. Time and Frequency Measurements Using the Global Positioning Systems. *Cal. Lab. Int. J. Metrology*, 3:26–33, 2001.

[15] V. Meiser. Kalibrierung des GNSS-Antennenkalibrierroboters des Institut für Erdmessung mittels Lasertracking. Technical report, Geodätisches Institut Hannover, 2009.

[16] F. Menge. *Zur Kalibrierung der Phasenzentrumsvariationen von GPS Antennen für die hochpräziese Positionsbestimmung*. PhD thesis, Wisschschaftliche Arbeiten der Fachrichtung Vermessungswesen der Universität Hannover, 2003.

[17] F. Menge, G. Seeber, C. Völksen, G. Wübbena, and M. Schmitz. Results of the absolute field calibration of GPS antenna PCV. In *Proc. Int. Tech. Meet ION GPS-98, Nashville Tennesee*, 1998.

[18] T. Murphy, P. Geren, and T. Pankaskie. GPS Antenna Group Delay Variation Induced Errors in a GNSS Based Precision Approach and Landing Systems. In *Proc. ION GNSS 20th International Technical Meeting of the Satellite Division, 25-28 September, Fort Worth, Texas*, 2007.

[19] H.-M. Peng, C.-S. Liao, and J.-K. Hwang. Perfomance Testing of Time Comparison Using GPS-smoothed P3 Code and IGS Ephemeries. *IEEE Transactions on Instrumentation and Measurement*, 54(2):825–828, 2005.

[20] J. Ray and K. Senior. IGS/BIPM pilot project: GPS carrier phase for time/frequency transfer and timescale formation. *Metrologica*, 40:270–288, 2003.

[21] H.-G. Scherneck. A parameterized Solid Earth Tide Model and Ocean Tide Loading Effects for global geodetic baseline measurements. *Geophys. J. Int.*, 106(3):677–694, 1991.

[22] G. Seeber. *Satellite Geodesy, Foundations, Methods and Applications*. Walter de Gruyter, 2003.

[23] U. Weinbach and S. Schön. GNSS receiver clock modeling when using high Precision oscillators and its impact on PPP. *Advances in Space Research*, 47(2):229–238, 2011.

[24] M. A. Weiss, G. Petit, and Z. Jiang. A Comparison of GPS Common-View Time Transfer to All-in-View. In *Frequency Control Symposium and Exposition, 2005. Proceedings of the 2005 IEEE International. 29-31 Aug.*, 2005.

[25] G. Wübbena, M. Schmitz, F. Menge, V. Böder, and G. Seeber. Automated Absolute Field Calibration of GPS Antennas in Real-Time. In *ION GPS 2000, Salt Lake City, 19-22. September 2000, USA*, 2000.

[26] G. Wübbena, M. Schmitz, and M. Propp. Antenna Group Delay Calibration with the Geo++ Robot - extensions to code observable. In *IGS Analysis Workshop, Poster, June 2-6 Miami Beach Florida, USA*, 2008.

Very Precise Synchronization of Distributed Pseudolites

Werner R. Lange
Lange-Electronic GmbH
Gernlinden, Germany
T.: +49-8142-2845820
WLange@lange-electronic.de

ABSTRACT
Pseudolites are GNSS transmitters that have a fixed position on the ground and transmit original satellite signals. Very often pseudolites are used around airports and harbors to ease the navigation and increase integrity and availability of satellite navigation systems. Pseudolites are also used in the European „Gate"-Projects. „GATE" is the name of a Galileo test bed where several pseudolites are located around a valley in southeast Bavaria transmitting Galileo signals so that receivers are able to use Galileo signals for testing purpose in "real live" before the satellites are in the sky. Besides this first Gate project a number of similar pseudolite projects have been established. One of these projects is named "aviation gate" and is located at the research airport of Braunschweig.

This project shall show the use of Galileo signals in aviation – from approach to landing to taxiing. It is extremely important to synchronize the pseudolites as good as possible to minimize the navigation errors.

The system in Braunschweig consists of 9 pseudolites and a reference station. The pseudolites are mounted in an inner circle of 5 systems around the airport and 4 systems in distances between 30 and 60 km. The full pseudolite constellation is working now, the results are remarkeable.

The paper describes the basics and goals of the project and includes the latest results of the project – 9 free running GPS-receivers are synchronizing 9 pseudolites. The results look very promising – the receivers are far better synchronized than anticipated, they work in the low nanosecond range.

To enhance the accuracy of the timing receivers into the sub-nanosecond range the receivers have a remote adjustment capability: The reference station continuously measures the range of the pseudolites and is able to adjust the phase of the GPS receivers 10 MHz output with a resolution of 25 ps over a WLAN link.

This type of application is ideally suited at locations where independent stations require a very high degree of synchronization.

THE PROJECT

About 30 years ago the Airport of Braunschweig was used as small local airport, the most traffic was originated by the fleet of Volkswagen, the scientific flights done by the research organization DLR, the German research organization for aviation and space technology and the Luftfahrtbundesamt, the people who are the next to appear at airplane accidents after fire brigades and police has done the first jobs.

About 15 years ago the airport received a new name – Research Airport. That lead to an extraordinary growth – several institutes of the Technical University and a variety of small and medium companies, all related to air and space settled around the airport – it is in the meantime an extremely important spot of aerospace development in Germany.

In preparation of the European satellite program Galileo several test beds have been installed. The Institute of Flight Guidance of the TU Braunschweig had the idea to establish an area to test the

possibilities of the developing Galileo satellite system. The aim was to taxi, take off and land under a ground based Galileo system made up by 9 pseudolites. For this purpose they built two circles of pseudolites, the outer circle of 4 and the inner circle of 5 pseudolites

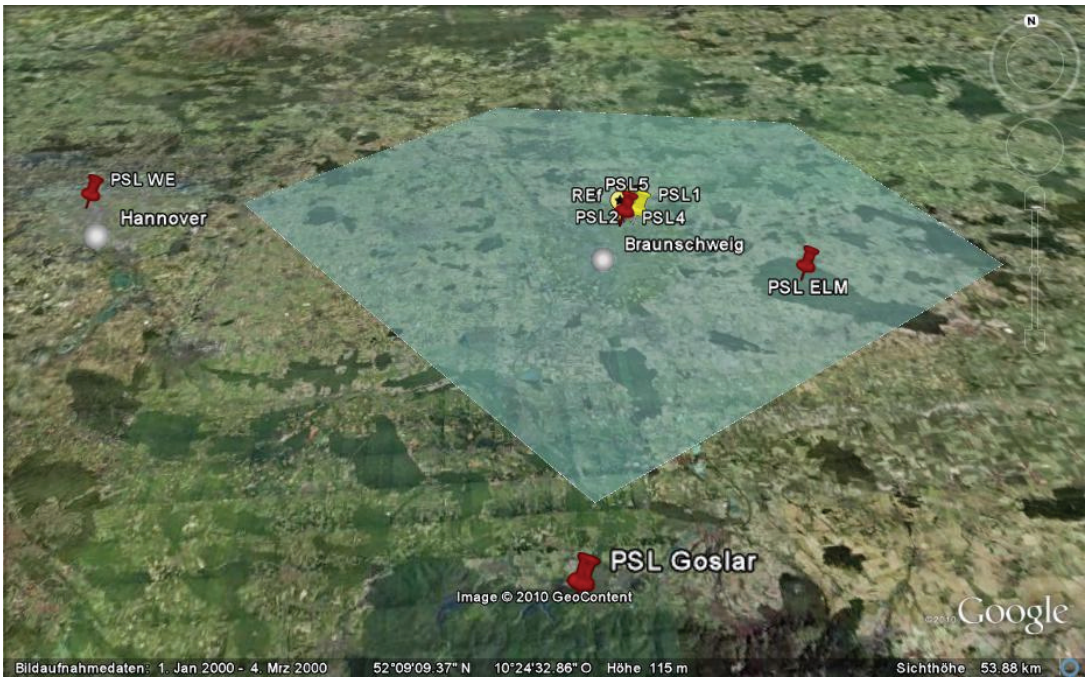

Picture 1: overview of the greater airport area

Picture 2: The inner circle

Picture 3: The view from a pilot's seat

THE SOLUTION

The inner circle is mainly used during the final approach, the roll- and taxiways and the tarmac, all antennas except one are directed into the inner circle, the transmission angle is 180°. The fifth antenna has a 360° pattern. The outer circle uses three 90° antennas and one with 360°. This antenna is relatively close to the airport and shall deliver a closer signal during final approach.

The advantage of such a GBAS (Ground Based Augmentation System) is to test and verify the versatility of the codes, data, signal structure and not at least the receivers in a real life environment. There are disadvantages, too. The position of the pseudolites is, by all means, flat, so the geometry i.e. the VDOP is very bad. Than there are near/far effects - the received signal strength varies drastically – while GPS L1 is received at about -120 dBm +-2 dBm the pseudolite signals are between -50 and -125 dBm – far too much for the receivers. Thus the signals have to be pulsed – another problem because the design of the coding structure is not designed for this while for instance GPS is. Another disadvantage is that the calculation of the precise position requires the evaluation of the raw data of the receiver.

A mayor problem is to synchronize the pseudolites in a way that the expectations of accuracy are met – +-30 cm of navigation means about +-1ns all the time. And the pseudolites are up to 60 km apart.
This means the transmitted information's code modulation, the time synchronization and navigation data has to be selected carefully.

The modulation and time synchronization has to include
- PRN
- time of transmission
- Doppler frequency

thus allowing to measure the precise distance from receiver to pseudolites.

A few remarks to the architecture of the system:
- Besides the 9 pseudolites there are 2 reference receivers
- The total area covers about 5000 km²

- Frequencies used are E1, E5a and E5 where E1 and E5a/b are produced in separate signal generators
- Navigation message and time synchronization are modified for this application.

The modification of the navigation message means that they contain no real ephemerides and use the possibility that part of the content of the data can be freely defined.

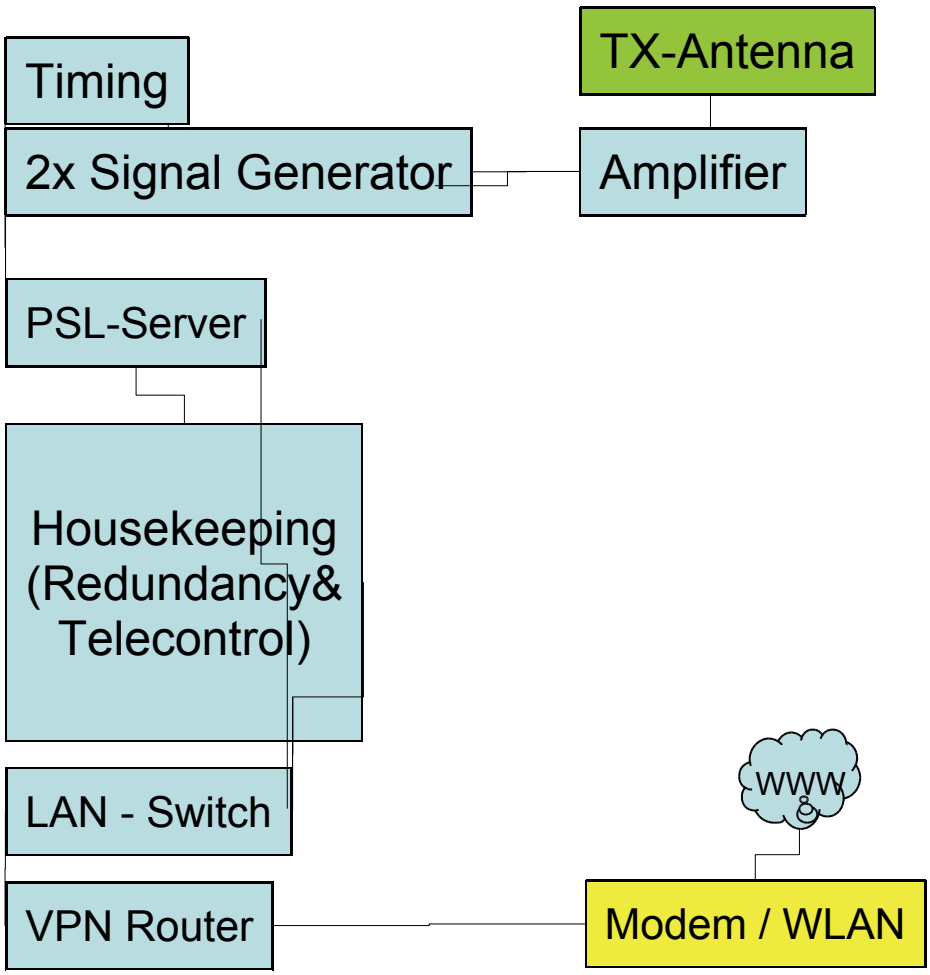

Picture 4: Block diagram of a pseudolite

Synchronization

Each of the pseudolites has its own GPS timing receiver equipped with a double-oven OCXO delivering phase coherent 10MHz and 1pps signals to each of the signal generators. The GPS signal shall warrant the long term stability to within +-5ns, for compensation of the resulting offset and the internal drifts of the 9 timing receivers each of them has a second reference oscillator (also DOCXO) that can be remote controlled. The mathematical resolution of this fine adjustment via remote control is 25ps.

The fine adjust may be done in different ways – a direct control with fast regulation leads to a fast compensation of errors, a deferred, strongly absorbed and continuous control gives more stable signals and keeps the “real” errors. Both methods have to be optimized during the progress of the tests. The second method is presently used at the system.

The pictures 5, 6 and 7 show the difference of the pseudorange of E1signals of 3 pseudolites taken from the reference station, uncompensated free running at picture 5, compensated with a 10 min time constant at picture 6 and picture 7 shows the same results picture 6 but with a low pass filter applied.

The green horizontal line in picture 7 show the limits set by the experiment – plus/minus 30 cm or ~ +-1ns – mission accomplished?

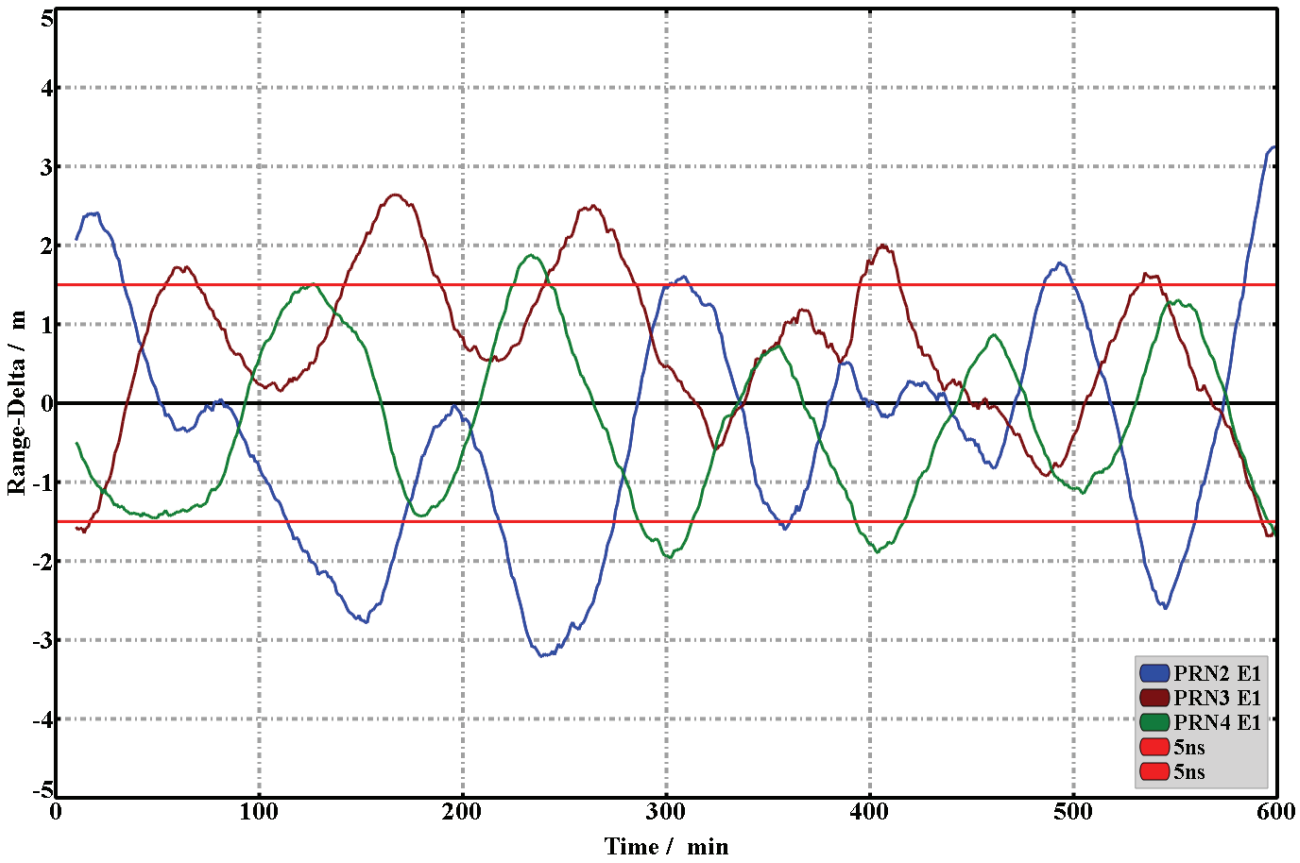

Picture 5 shows 3 of the pseudolites timing receiver running “uncoordinated” within 10 hrs

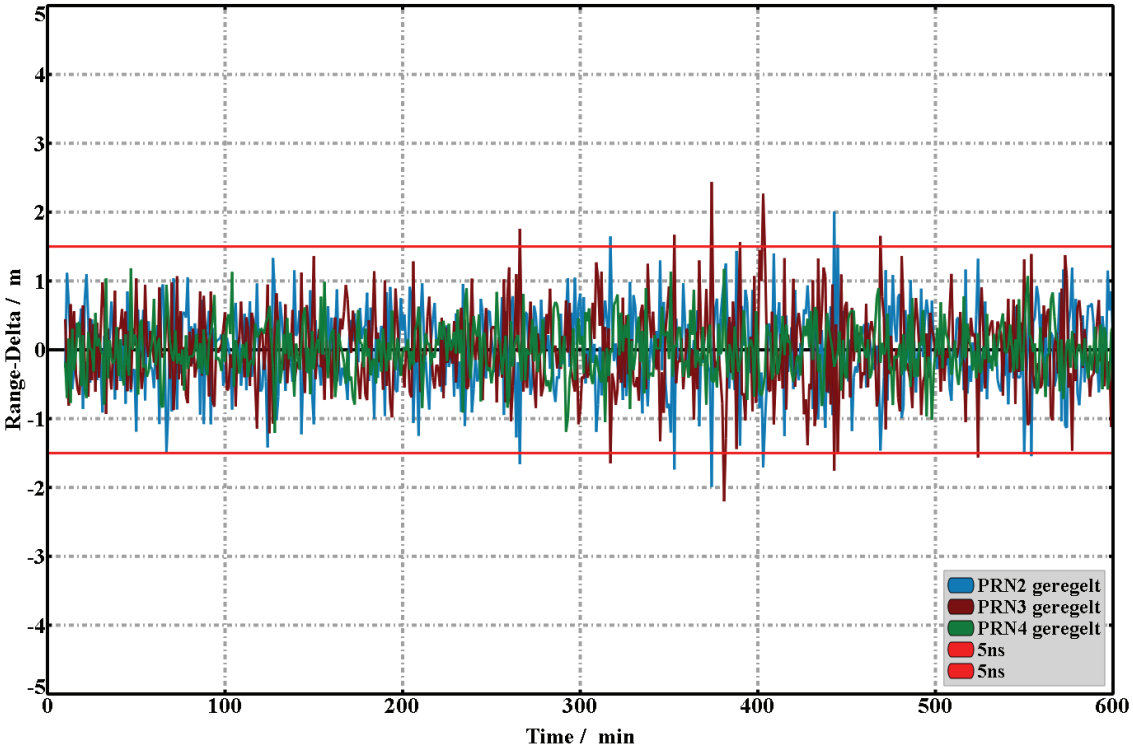

Picture 6 shows the same receivers with a 10 min control time constant, including noise

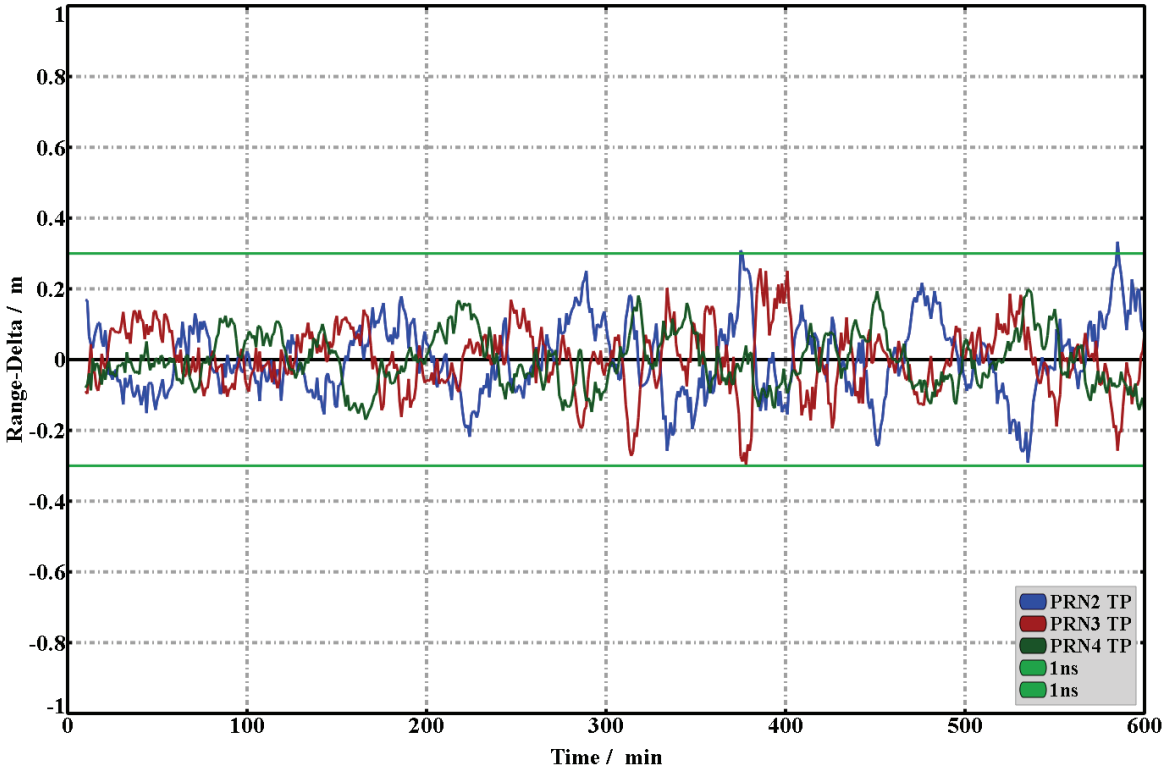

Picture 7 shows the same receivers with a 10 min control time constant, results low pass filtered

WHAT COMES NEXT?

Well, we are not really satisfied with the uncompensated drifts seen in picture 5. We are presently working on the next generation receiver with a Rubidium atomic clock as primary oscillator – this may make the curves smoother and narrow the extremes at least as far as they are a result of the behavior of the timing receivers. One has to take into account that these results include an error line starting with the GPS antenna, the timing receiver, the signal generators, the transmission antennas, the transmission path, the receiving Galileo antenna and the Galileo receiver. Besides this it may be helpful to equip the reference receiver with a timing receiver, too.

Thanks to Dipl.-Ing Benedikt von Wulfen, Institute of Flight Guidance of the Technical University of Braunschweig for help, tests and pictures

Picture 8: The two types of antennas used, the 360° antenna (left) and the 180° Antenna (right)

Study and Development of a New GNSS Receiver for Time and Frequency Transfer

LIANG Kun, ZHANG Aimin, GAO Xiaoxun,
WANG Weibo, NING Dayu
National Institute of Metrology
Beijing, China, 100013
Email: liangk@nim.ac.cn

ZHANG Side

Beijing Trust GPS Science&Technology Development Co. Ltd
Beijing, China, 100107

Abstract—Time and frequency transfer techniques based on GPS and GLONASS were studied. On the basis of Topcon GNSS receiver module, one new type of GNSS time and frequency transfer receiver named NIMTFGNSS-1 has been developed and its scheme has been accounted for. Compared with several popular GPS time and frequency transfer receivers made aboard in the world by the common clock difference experiments and the long baseline experiments, the performance of the receiver has been tested and verified. Its time and frequency transfer noise level can match those of the several commercial receivers and the time stabilities from the GPS code and carrier phase results in the common clock difference experiments using two NIMTFGNSS-1 receivers during a few days are separately within 1 ns and 100 ps and the GLONASS code results is with 4 ns.

I. INTRODUCTION

GPS(Global Positioning System) time and frequency transfer is one of the most useful tools for time and frequency transfer. With the quick development of GLONASS(GLObal NAvigation Satellite System), it has been the most significant supplementary means for GPS time and frequency transfer. BIPM(Bureau International des Poids et Mesures) has published UTC results with GLONASS involved in Cir.T[1] since January 2010. GNSS (Global Navigation Satellite System) time and frequency transfer receiver is the significant research direction in time and frequency area.

II. PRINCIPLES OF TIME AND FREQUENCY TRANSFER WITH GNSS

Time and frequency transfer methods by GNSS are divided into three types that are C/A code, P3 code and carrier phase time and frequency transfer according to the measurement signals. And the basic principle is as shown in fig. 1.

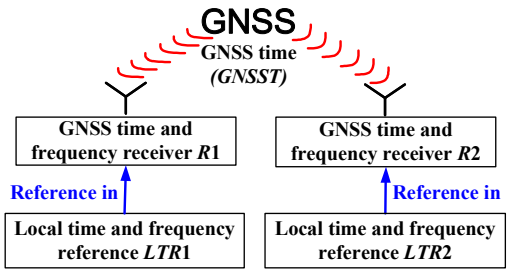

Figure. 1 Time and frequency transfer by GNSS

The two stations use the GNSS time and frequency transfer receivers R1 and R2 separately referenced to the corresponding local time and frequency standards LTR1 and LTR2[2]. The reference methods can be different in terms of the operation modes of the receivers. Thus, time and frequency transfer can be realized and the calculation is shown as (1)-(3). First, we can get the time and frequency transfer results $\Delta T1$ and $\Delta T2$ for each station, that is to say, the difference between the local time and frequency standard and GNSS time(GNSST). Then the difference

between $LTR1$ and $LTR2$ can be calculated by the difference between $\Delta T1$ and $\Delta T2$.

$$\Delta T1 = LTR1 - GNSST \quad (1)$$

$$\Delta T2 = LTR2 - GNSST \quad (2)$$

$$LTR1 - LTR2 = \Delta T1 - \Delta T2 \quad (3)$$

III. GNSS TIME AND FREQUENCY TRANSFER RECEIVER

GNSS time and frequency transfer receiver especially for time and frequency transfer implements the comparison by measuring difference between the external time and frequency reference and GNSS time, while the general GNSS receiver cannot get this value other than the position. For the moment, in general, there are two kinds of operation modes for GPS time and frequency transfer receivers. In the first mode (mode 1), the receiver, e.g. a Septentrio Polarx2eTR, Polarx3eTR or Ashtech Z12-T, is operated with time and frequency directly synchronized to the local reference time scale by a internal phase lock loop. In the second mode (mode 2), the receiver, e.g. a AOA TTR6 or Dicom GTR50, is operated in a free running status without synchronization, and the link between the receiver time scale and the local reference time scale is established with a time interval counter(TIC). The operation mode of the time and frequency transfer receiver is indicated in fig. 2[3] and compared in [3].

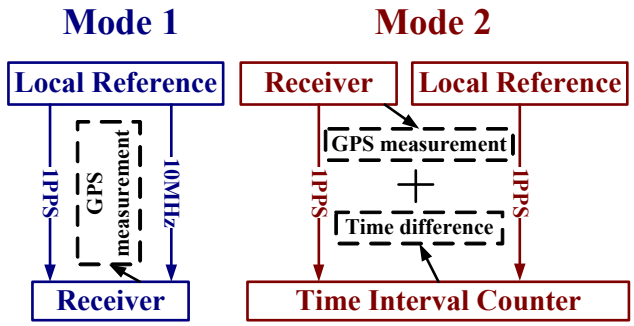

Figure. 2 Operation mode

IV. DESIGN AND REALIATION

Based on the GNSS module of Topcon company, one new type of GNSS time and frequency receiver named NIMTFGNSS-1 for rack using or portable using is designed with mode 1, with which the receiver noise performance is better[3], as shown in fig. 3. The scheme of the receiver is illustrated as follows in fig. 4. After temperature sensitivity evaluation[3] of the receiver engine, we have the receiver engine board located in one temperature chamber so that its ambient temperature can be controlled within the stability of less than 0.3(1 sigma) degrees, which would decrease the measurement uncertainty of the receiver due to the variation of the environmental temperature.

Figure. 3 NIMTFGNSS-1 receiver

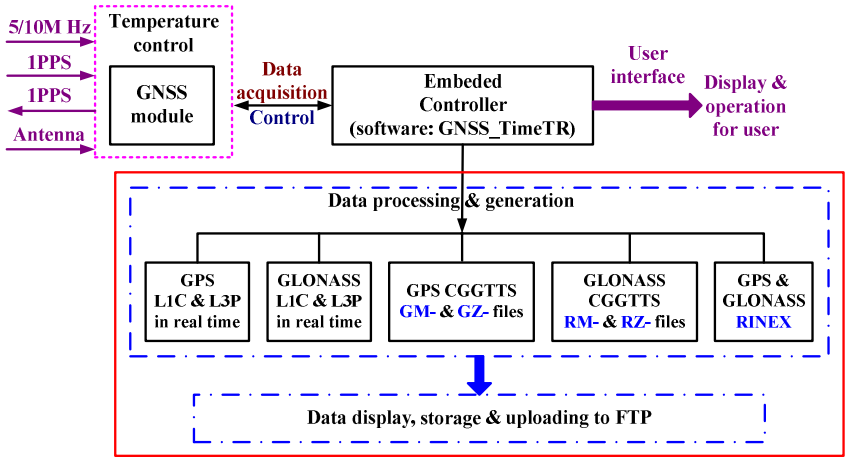

Figure. 4 Scheme of the receiver

The receiver can generate the C/A and P3 code CGGTTS files(GM- file for GPS C/A code, GZ- file for GPS P3 code, RM- file for GLONASS C/A code and RZ- file for GLONASS P3 code) and Rinex files of GPS and GLONASS, and generate and show the real-time time difference data in at least 1 second as shown in fig. 5. The receiver interface software named GNSS_TimeTR is shown in fig. 6.

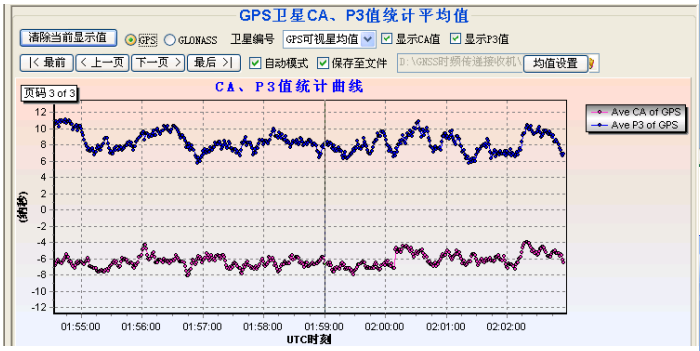

(a) GPS

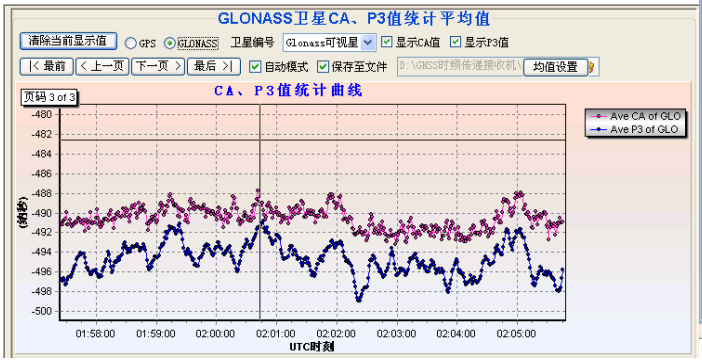

(b) GLONASS

Figure. 5 Real-time time difference in one second

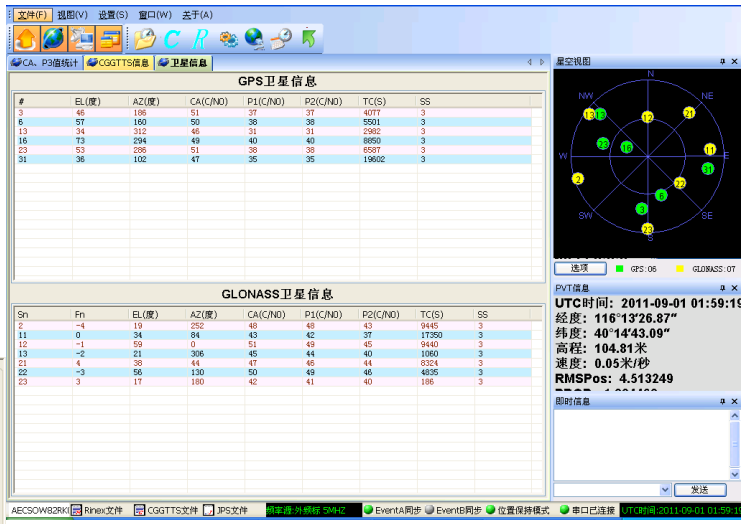

(a) Interface display 1

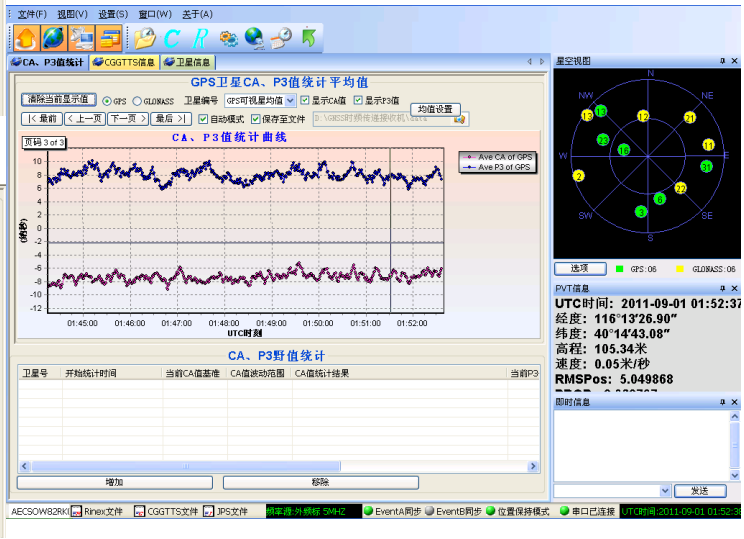

(b) Interface display 2

Figure. 6 Interface software (GNSS_TimeTR)

V. PERFORMANCE VERIFICATION

The CCD(Common Clock Difference) experiments among one NIMTFGNSS-1 receiver(IM07, rack using type) and another two kinds of time and frequency transfer receivers including Septentrio PolaRx2eTR(IM2P) and PikTime TTS-4(TTS4) receivers have been implemented at NIM Hepingli campus. However, only GPS P3 transfer performance can be compared because Septentrio PolaRx2eTR receiver just generates GPS P3 CGGTTS file. The results during the same period show that the GPS P3 transfer performance of the new time and frequency transfer receiver can match that of the other two receivers in fig. 7. As seen in the fig., the standard deviation during 7 days is about 1ns using the common view(CV) processing method. As well, the CCD experiments among another NIMTFGNSS-1 receiver (IM03, portable using type) Septentrio PolaRx3eTR(BJ2P) and Dicom GTR50(IM06) receivers at NIM Changing campus have been implemented. We can get the similar conclusion in fig. 8 to that from fig. 7. All the receivers used in the experiments haven't been calibrated, and the time difference values for some links between two receivers in the following figures are removed by some different offsets for better view.

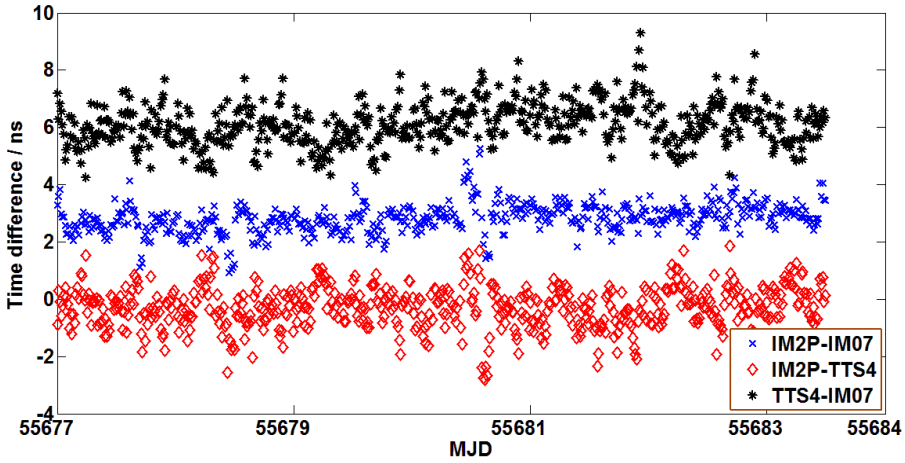

Figure. 7 Performance comparison 1

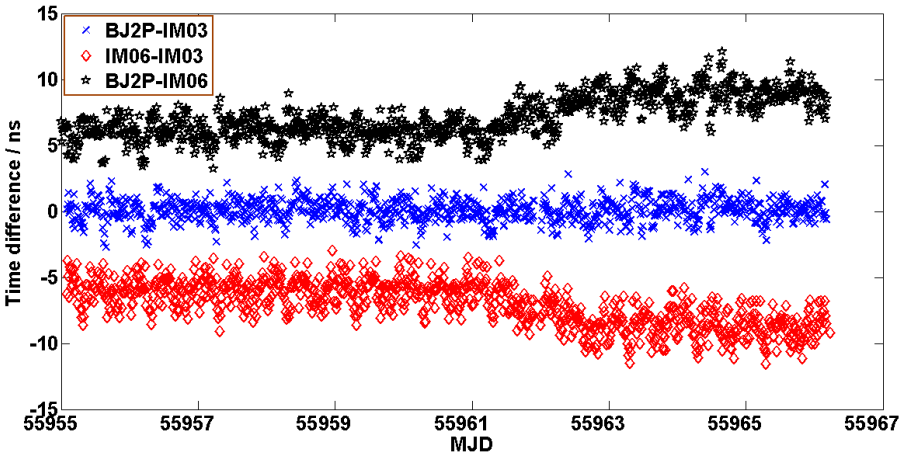

Figure. 8 Performance comparison 2

We have also done the CCD experiments among the IM03 and IM07 and IM2P. The CCD results between IM03 and IM07 by GPS carrier phase using PPP(Precise Point Position) technique are shown in fig. 9 and the standard deviation is 85 ps. And the CCD results between IM03 and IM07 using GPS C/A code(L1C) and P3 code(L3P) are shown in fig. 10 and the standard deviation are 0.89 ns and 0.81 ns separately.

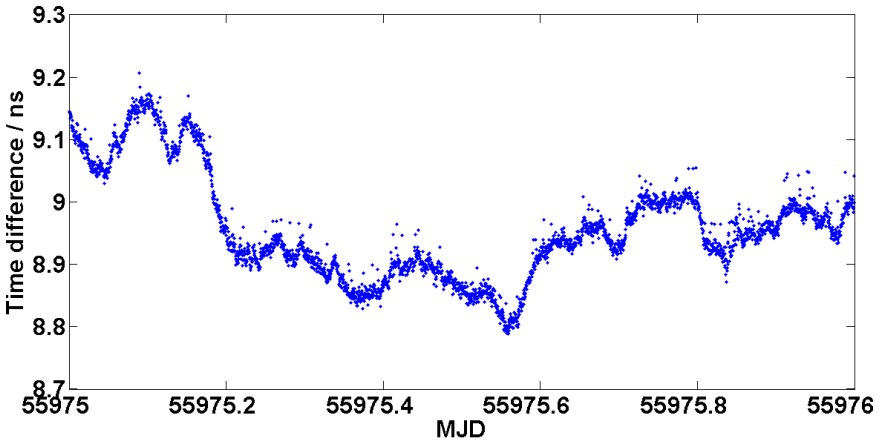

Figure. 9 Performance comparison 3

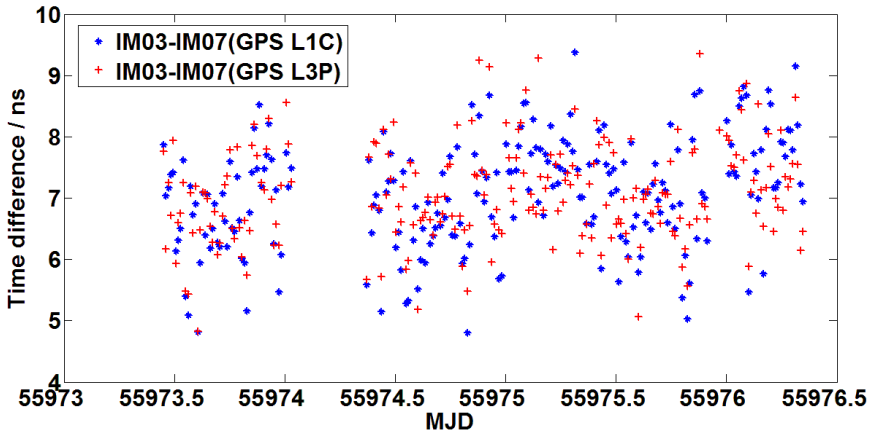

Figure. 10 Performance comparison 4

And the CCD results between IM03 and IM07 using GLONASS C/A code(L1C) and P3 code(L3P) are shown in fig. 11 and the standard deviation are 3.7 ns and 3.4 ns separately. They are much bigger than those using GPS probably due to the inter-frequency bias for GLONASS system[4,5].

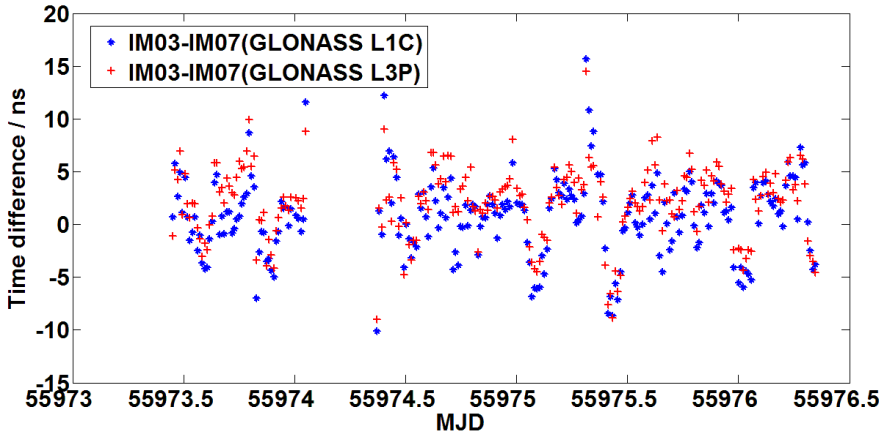

Figure. 11 Performance comparison 5

VI. LONG BASELINE EXPERIMENTS

For the long baseline performance of time and frequency transfer, we use the data of the link between Ashtech Z12-T receiver(PT02) in PTB and IM03 receiver in NIM, and we use the data of the link between PikTime TTS-3 receiver(PT05) and IM2P for comparison in fig. 12. We have got the link data between IM03 and IM07, located separately in Hepingli campus and Changping campus that is about 40 km baseline, and used IM2P and IM06 for comparison in fig. 13 and partial enlarged view in fig. 14.

We also compared the results for the GLONASS P3 link between IM07 and PT05 and the GLONASS P3 link between TTS4 and PT05 in fig. 15, and IM07 and TTS4 were both referenced to UTC(NIM). By comparison, generally we can see that the link data using NIMTFGNSS-1 receiver are similar to those using another types of the time and frequency transfer receivers in terms of fig. 12~15. That states that GPS or GLONASS transfer noise level performance of NIMTFGNSS-1 in the long base line can match the other types of time and frequency transfer receivers. The data gaps in fig. 12 and 13 came from the tests of the interface software after some new modification.

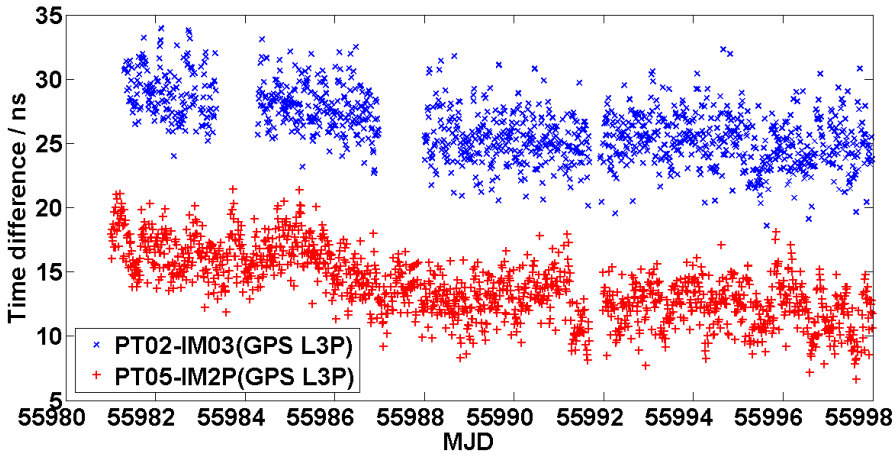

Figure. 12 Performance comparison 6

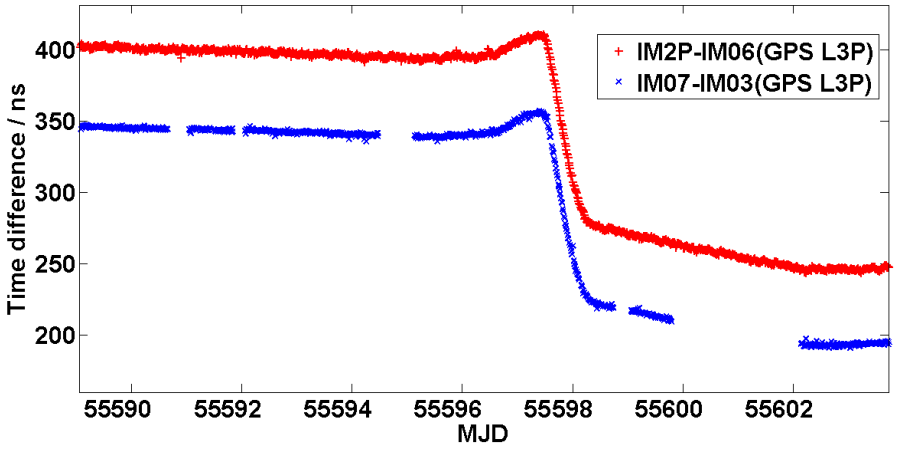

Figure. 13 Performance comparison 7

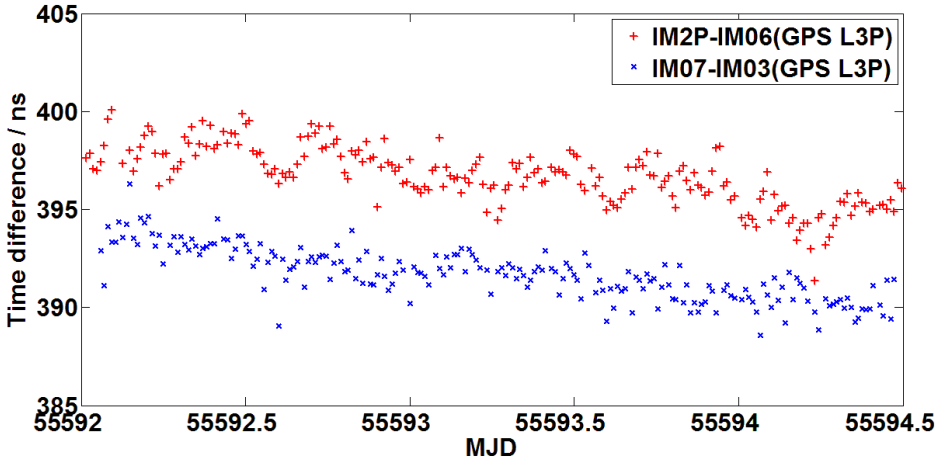

Figure. 14 Performance comparison 8

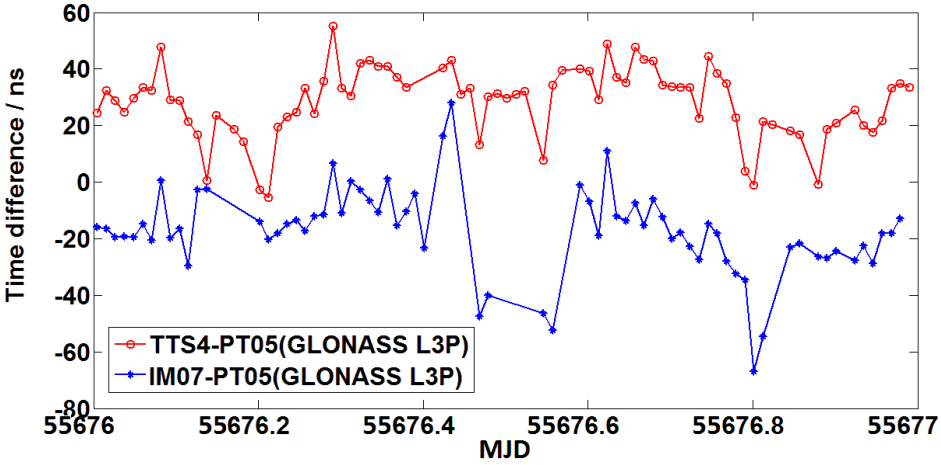

Figure. 15 Performance comparison 9

VII. CONCLUSION

The operation modes of GNSS time and frequency transfer receivers have been described and GNSS receivers including portable using type and rack using type for time and frequency transfer have been developed. The noise performance of the receiver itself and the long baseline performance have been verified by the CCD experiments in NIM and the long baseline time and frequency transfer experiments in the links between NIM and PTB and between the two campuses of NIM. The time stabilities (standard deviation) of GPS C/A and P3 code CCD experiments using CV method in 16-min interval for several days data are within 1 ns and those of GLONASS C/A and P3 code are within 4 ns. The corresponding time stabilities of GPS carrier phase CCD experiments using PPP method in 30-s interval for one day data is within 100 ps. The noise level performance for time and frequency transfer using the self-developed new receivers can match that using the present types of the main commercial time and frequency transfer receivers, including Septentrio PolaRx2eTR and PolaRx3eTR receivers, PikTime TTS-3 and TTS-4 receivers, Ashtech Z12-T receiver and Dicom GTR50 receiver.

ACKNOWLEDGMENT

We thank a lot the Royal Observatory of the Spanish Navy (ROA) for providing the GPS P3 CV program for reference. We want to appreciate Physikalisch-Technische Bundesanstalt (PTB) and Wuhan Institute of Physics and Mathematics (WIPM), Chinese Academy of Sciences (CAS) separately for using data of PT02 and PT05 and TTS4. We thank PikTime and AOS for some helpful discussion about GLONASS system.

REFERENCES

[1] BIPM. Cir.T 263[N].2009.

[2] Kun Liang, Aimin Zhang. Study on Time and Frequency Transfer by GLONASS[J]. ACTA METROLOGICA SINICA. 2011 32(2).

[3] Kun Liang, Thorsten Feldmann, Andreas Bauch, Dirk Piester, Aimin Zhang, Xiaoxun Gao, "Performance Evaluation of NIM GPS Receivers in Use for Time Transfer with PTB," Proc. of the 24th EFTF, Noordwijk, The Netherlands, April 2010, P1.46

[4] J. Azoubib and W. Lewandowski, 2000, Test of GLONASS precise-code time transfer, Metrologia, 37, pp. 55-59.

[5] W. Lewandowski, J. Azoubib, A.G. Gevorkyan, P.P. Bogdanov, J. Danaher, G. de Jong, and J. Hahn, 1997, *"First Results from GLONASS Common-View Time Comparisons Realized According to the BIPM International Schedule,"* in Proceedings of the 28th Annual Precise Time and Time Interval (PTTI) Applications and Planning Meeting, 3-5 December 1996, Reston, Virginia, USA (U.S. Naval Observatory, Washington, D.C.), pp. 357-366.

Smartphone application for the near-real time synchronization and monitoring of clocks through a network of GNSS receivers

D. Calle, R. Píriz
GMV, Madrid, Spain
rpiriz@gmv.com

C. Plantard, G. Cerretto
INRiM, Torino, Italy
g.cerretto@inrim.it

Abstract— **The promising potentialities for time and frequency transfer of a network solution of geodetic GNSS receivers located in National Timing Laboratories aiming at comparing their time scales at the maximum level of precision is presented**.[1]

I. INTRODUCTION

In time metrology, different techniques are used for time and frequency transfer, basically TWSTFT (Two Way Satellite Time and Frequency Transfer), GPS CV (Common View) and GPS AV (All in View) [1].

In recent years, many national timing laboratories have collocated geodetic GPS receivers together with their traditional GPS/GLONASS CV/AV receivers and TWSTFT equipments. Time and frequency transfer using GPS code and carrier-phase, is an important research activity for many institutions involved in time applications, basically due to the fact that carrier phase measurements generated are two orders of magnitude more precise than the GPS code data. This was recognized when the International GNSS Service (IGS) and Bureau International des Poids et Mesures (BIPM), formed a joint pilot study to analyze the IGS Analysis Centers clock solutions and recommend new means of combining them. In addition, the CCTF (Consultative Committee for Time and Frequency), in 2006, passed a recommendation "Concerning the use of Global Navigation Satellite System (GNSS) carrier phase techniques for time and frequency transfer in International Atomic Time (TAI)". Moreover, the BIPM in 2002 started a project named TAIP3 [2] aiming at the use of the phase and code GPS measures.

Many of geodetic GNSS receivers hosted in national timing laboratories, operate continuously within the International GNSS Service (IGS) and their data are regularly processed by IGS Analysis Centers. Whereas participating stations must agree to adhere to certain strict standards and conventions which ensure the quality of the IGS Network, a number of products and tools have been developed in order to allow time and frequency transfer without taking part to the IGS.

One standalone GPS carrier phase analysis technique is Precise Point Positioning (PPP), in which dual frequency code and phase measures are used to compare the reference clock of a single receiver to a reference time scale. Several works [3],[4],[5],[6] were carried out to evaluate the time and frequency transfer capabilities of PPP, leading the BIPM to start a pilot experiment which aims to evaluate the possibility to regularly compute some TAI links with the PPP algorithm, to obtain an improved statistical uncertainty [7]. The PPP algorithm used for the BIPM pilot experiment has been developed by the Natural Resources Canada (NRCan) [8].

In this paper we want to investigate a possible network solution, similar to the IGS analysis center solutions, that can be easily managed by a network of timing centers to solve in a unique system all the clock differences (besides other quantities) to understand the feasibility and the advantages of this approach in time and frequency transfer. The investigation is based on a web-based tool named *magicGNSS* (magicgnss.gmv.com), which is a suite of GNSS software products developed by GMV in Madrid, that allows the users to perform a wide range of calculations and analyses related to GNSS, from the evaluation of performances at user level, to the computation of precise GNSS orbits and clocks, including the calculation of precise receiver coordinates. The time and frequency transfer capabilities or the network solution (named Orbit Determination & Time Synchronization, ODTS) are evaluated and compared to PPP solutions as well as to other

[1] This work is mainly based but not exclusively on the paper G.Cerretto, P.Tavella, A.Perucca, A.Mozo, R. Piriz, M. Romay, "Time and Frequency Transfer through a network of GNSS receivers located in Timing Laboratories", in Proc. of EFTF/IEEE FCS, April 2009, Besançon, France.

time transfer results. A dedicated *magicGNSS* web page allows the visualization of estimated clocks in near-real time, including an adaptation of such web page to smartphone screens. Examples of web and smartphone visualization are presented below.

II. MAGICGNSS

magicGNSS is a web application for high-precision GNSS data processing. It allows the calculation of GPS satellite orbits and clocks, and also of station/receiver coordinates, tropospheric delay and clocks. The user can upload his own station data (RINEX measurement files) or use data from a global network of pre-selected *core stations* from IGS.

magicGNSS is available at http://magicgnss.gmv.com. A one-month trial account can be requested online for free. After the trial period, the usage of *magicGNSS* is subject to a yearly fee. In Table I, the characteristics of the *magicGNSS* account are summarized.

TABLE I. CHARACTERISTICS OF MAGICGNSS ACCOUNT

	magicGNSS account
Available algorithms	PPP, ODTS, COMP
Disk quota	10 Gb
Core station data	from 2008/01/01
IGS products(1)	from 2008/01/01
Navigation messages(2)	from 2008/01/01
User station data in ODTS	yes
Max. no. of stations in ODTS	60
Max. no. of stations in PPP	60
Max. data span in PPP	5 days
Max. data span in ODTS	5 days
Ftp upload	yes
Deletion of user station data	never
Usage of public station data	PPP and ODTS
Share your station data	yes
Technical support by email	next-day basis

(1) Orbits and clocks needed for PPP and COMP

(2) Needed for ODTS initialization

With *magicGNSS*, the user can analyze results in a convenient way through comprehensive PDF reports and organize the processing scenarios and history within his account in an easy way with a generous disk quota [9]. At present, *magicGNSS* supports GPS and GLONASS data both in ODTS and PPP, while Galileo processing is planned for the near future. One of the most interesting characteristics of *magicGNSS* is the easy way to use it. Inside *magicGNSS* account, one has just to click on *New* to define a new scenario (network), then click on *Save*, and then click on *Run* to process the data and generate results.

The algorithms that process station data to generate products in *magicGNSS*, are called ODTS, which stands for *Orbit Determination & Time Synchronization*, and PPP. ODTS is a *network solution* requiring a set of stations distributed worldwide. PPP is a *single-station solution* (although several stations can be processed together for convenience). In ODTS the stations must be static, while PPP supports static and kinematic processing. The advantages of a network solution like ODTS as compared to PPP are that the estimates of each station can benefit from the measures of all stations being in principle more robust and precise. In addition, all clock differences are available in a single solution instead of asking a time consuming series of PPP single station solutions.

There are two types of station data within *magicGNSS*: *core station* data and *user station* data. For ODTS, the server maintains data from 36 IGS core stations distributed worldwide. Current *core station* data is available with a latency of typically one hour. The user can also upload his own station data (daily, hourly, or 15-min RINEX files) via the web or ftp. Batch upload and automation are possible using ftp. Normal or compressed data files can be uploaded, and if the RINEX file does not have P1, the C1 code will automatically be converted to P1 using the CC2NONCC tool from IGS. Station data uploaded and shared by other users can also be processed.

The GPS and GLONASS operators inform the users about events affecting satellite availability by publishing messages named NANUs. *magicGNSS* automatically downloads NANUs as they are issued and extracts the relevant information so that only healthy satellites will be considered in the data processing.

An additional module, called COMP, allows comparing *magicGNSS* products with IGS and among themselves.

In Table II, *magicGNSS* generated products are indicated.

TABLE II. MAGICGNSS PRODUCTS

Product	ODTS	PPP	Format	Accuracy (RMS)
Report	✓	✓	pdf	N/A
Satellite orbits	✓	×	sp3	~2/6/4 cm(*)
Satellite clocks	✓	×	clk	~0.15 ns
Station clocks	✓	✓	clk	~0.15 ns
Station tropo	✓	✓	txt	<1 cm (zenith)
Station coords	✓	✓	snx	<1 cm

(*) In the Radial/Along/Normal directions

III. DATA PROCESSING AND PRODUCTS

The basic ODTS and PPP input measurements are pseudorange (code) and phase L1-L2 dual-frequency iono-free combinations. On L1, the P1 code is used in order to be consistent with IGS. The raw input code and phase measurements are decimated and used internally by ODTS and PPP at a typical rate of 5 minutes (down to 30 sec can be also used). The core measurements are smoothed using the phase with a *Hatch* filter, thus reducing the code error from the meter lever to typically 25 cm.

ODTS and PPP are based on a batch least-squares algorithm, that minimizes measurement residuals solving for orbits, satellite and station clock offsets, phase ambiguities and station tropospheric zenith delays. In the case of PPP, satellite orbits and clocks are not solved for, but fixed to IGS products (*ultra-rapid*, *rapid* or *final*) or GMV internal products (that support GPS and GLONASS). For this reason PPP is not a total independent technique, conversely to ODTS that, autonomously, provides all products.

Clocks are calculated as snapshot values, i.e., as instantaneous values at the measurement time epoch, without correlation with previous estimates. Clocks are estimated at the same rate as the measurements (typically every 5 minutes).

In ODTS, satellite and station clock offsets are estimated with respect to a reference clock, provided by one of the stations. In PPP, the station clock is referred to the IGS Time scale (IGST), as derived from the satellite clocks in the IGS products. From subsequent differentiation, the differences between station clocks can be inferred.

The satellite and Earth dynamics are based on high-fidelity models that follow IERS recommendations. Modelled effects include a full Earth gravity model, Sun, Moon and planetary attractions, solid Earth tides, ocean loading, and solar radiation pressure (SRP), including eclipses. Radiation force discontinuities during eclipse entry/exit are smoothed in order to improve orbit accuracy. The satellite attitude is modelled as a generic nadir-pointing yaw-steering law applicable to all GNSS satellites. In ODTS, the orbit fit is based on the estimation of the initial state vector (position and velocity) and 8 *empirical* SRP parameters. Earth Rotation Parameters (ERPs) are automatically downloaded from the IERS server, but they can also be estimated by ODTS itself. The tropospheric correction is based on the estimation of a zenith delay per station (a constant value every hour), using a mapping function to account for the satellite-station signal elevation. Small effects such as relativity and carrier-phase wind-up are also modelled.

For the core stations, a priori station coordinate values come from ITRF or IGS solutions, and they can be refined within the ODTS process. For user stations, the precise coordinates from PPP can be used as input values for ODTS. Satellite and station antenna offsets and phase centre variations are taken into account, the latest ANTEX file from IGS is always used.

IV. DESCRIPTION OF THE ODTS ALGORITHM

The ODTS processing can be summarized as follows:

1. Given a satellite position and velocity at a certain starting epoch, an orbit can be produced on the basis of dynamic information, by numerical integration of the equations of motion of the satellite over a certain period. Furthermore, the partial derivatives of the satellite position with respect to the estimated dynamical parameters are produced.
2. For the epochs within that period at which tracking data is available, a tracking observation can be reconstructed numerically, using the known station position, the satellite position coming from the integrated orbit, and precise models for the effects affecting the tracking signal propagation. Also, the partial derivatives of the reconstructed measurements with respect to the estimated parameters are produced.
3. The measurement residuals (difference between the pre-processed tracking observations and the associated calculated observations) are computed.
4. The sum of squares of all available residuals is minimized by estimating corrections to the various model parameters in a least squares sense. To accomplish that, the computation of the partial derivatives of the expected measurements with respect to the estimated parameters is needed.

The process described is iterated until one of the following criteria is met:

- the number of iterations exceeds a certain threshold defined by configuration;
- the RMS of the weighted measurement residuals is below a certain threshold defined by configuration;
- the difference between two consecutive solutions is below a certain margin established by configuration.

The next sections describe those steps in detail.

Orbit Computation

The orbit propagation consists of computing the satellite state vector for a whole integration arc, given an initial state vector at the epoch t_0 and a model of forces acting on the satellite. The solution of the problem is achieved by integrating the equations of motion, which can be expressed in matrix form as follows:

$$\frac{d\vec{y}}{dt} = \vec{f}(t, \vec{y})$$
$$\vec{y}(t_0) = \vec{y}_0$$

being

$$\vec{y} = \begin{pmatrix} \vec{r} \\ \vec{v} \end{pmatrix}, \quad \vec{y}_0 = \begin{pmatrix} \vec{r}_0 \\ \vec{v}_0 \end{pmatrix}$$

$$\vec{f}(t, \vec{y}) = \begin{pmatrix} \vec{v} \\ \vec{a} \end{pmatrix}$$

where $\vec{r}$ and $\vec{v}$ are the satellite position and velocity, $\vec{a}$ is the acceleration and $\vec{y}_0$ is the state vector at the epoch t_0.

The numerical integration of this differential equation is performed using a 8th-order Gauss-Jackson method.

The state vector $\vec{y}_0$ at the end of the estimation arc is one of the sets of parameters that have to be estimated during the ODTS process. After a preliminary integration using an approximate state vector (from navigation messages), the integration is always performed backwards, using the estimated state vector at the end of the arc as initial value.

The integration process is based on physical models, which provide the satellite acceleration at each moment in time, as a sum of all the contributions, namely earth and third

body gravity, solar radiation pressure and relativistic correction to acceleration.

Measurement modelling

The main goal of this part of ODTS is to provide the least squares module with the measurement residuals and partial derivatives of the measurements with respect to the parameters to be estimated.

This process has three parts, which have to be performed observation by observation:

- compute the measurement expected from the computed satellite orbit, the (possibly estimated) station positions and an estimation of the different biases between the direct measurement and the geometric station-satellite distance: tropospheric delay, satellite and station clock biases, phase ambiguity, plus a relativistic correction,

- compute the residual, that is, the difference between the actual measurement and the expected one,

- get the partial derivatives of the expected measurement with respect to all the estimated parameters, using the partial derivatives of the orbit with respect to the dynamical parameters computed in the orbit integration.

The GNSS measurements accepted by ODTS can be of four different types:

- Raw iono-free pseudorange.
- Smoothed iono-free pseudorange.
- Iono-free carrier phase.
- Ambiguity-free iono-free carrier phase.

The tropospheric delay can be configured to be removed either in pre-processing (which means they are "tropo-free") or estimated within the ODTS process.

Note that the GNSS measurements have to be corrected to be referred to the centre of mass of the satellite, and not to the satellite antenna phase centre.

Expected measurement computation

All the computations are performed in the Inertial Reference Frame. To obtain the geometrical range d (in meters) for a measurement at reception time τ, the following operations are necessary:

- compute actual reception time $\tau - b_{sta}$, where b_{sta} is the station clock bias

- compute station position at reception time: $\vec{x}(\tau - b_{sta})$

- compute travel time: $\Delta t = d_0/c + \Delta/c$, where Δ is the total correction to the travel time, in meters, due to different biases, and c the velocity of light.

- satellite emission time is approximately

$$(\tau - b_{sta}) - \Delta t = (\tau - b_{sta}) - d_0/c - \Delta/c,$$

where d_0 is an initial value for the geometric range which is chosen to be ρ (the actual measurement), since the convergence is faster. Note that it would also converge to the solution taking $d_0 = 0$ instead of $d_0 = \rho$.

- compute satellite position at emission time:

$$\vec{r}(\tau - b_{sta} - d_0/c - \Delta/c)$$

- get geometrical range:

$$d = \left\| \vec{x}(\tau - b_{sta}) - \vec{r}(\tau - b_{sta} - d_0/c - \Delta/c) \right\|$$

This formula has to be iterated to obtain the correct value:

$$d_{n+1} = \left\| \vec{x}(\tau - b_{sta}) - \vec{r}(\tau - b_{sta} - d_n/c - \Delta/c) \right\|$$

Finally, the expected measurement (in meters) is just the final travel time (in meters), corrected by the effect of the clock biases:

$$\rho_{\exp} = d + \Delta + \delta t_{rel} + b_{sta} - b_{sat}$$

where b_{sat} is the satellite clock bias, and δt_{rel} is the relativistic correction to the satellite clock.

When the measurement is carrier-phase, the formula is slightly different:

$$\varphi_{\exp} = d + \Delta + \delta t_{rel} + b_{sta} - b_{sat} - Amb$$

where Amb is the estimated ambiguity (pass-dependent bias).

The corrections included in the term $\Delta = D_{Tropo} + c \cdot \Delta t_r$ are:

- D_{Tropo} - tropospheric delay, either computed in pre-processing or to be estimated in ODTS.

- Δt_r - relativistic correction to the travel time.

Note that δt_{rel} and Δt_r are different terms: the first one is a correction to the satellite clock, and Δt_r is the correction to the travel time.

Station and satellite position computation

For the process described above, we should be able to get the satellite and station position at any time. In the case of the satellite, we just use the orbit obtained by the orbit integrator at fixed steps, and interpolate at required time using Lagrange of order 8.

The station positions passed to ODTS are in ECEF coordinates. These are not the geodetic marker coordinates, but the antenna phase centre. In order to get the station position in the inertial frame, the Earth Rotation Matrix is also interpolated by Lagrange at required time: [*ERM(t)*]. The station position in IRF (Inertial Reference Frame) results from applying the Earth Rotation Matrix to the estimated station position in ECEF:

$$\vec{x}_{STA\_IRF} = \left[ERM(t) \right] \vec{x}_{STA\_ECEF}$$

The station position is subject to periodic variations due to solid tides, ocean loading and atmospheric loading. ODTS only retains the first contribution, the instantaneous

deformation of the solid Earth under the tidal potential of the Sun and the Moon. The vector displacement of the station due to degree 2 Solid Earth Tides expressed in the inertial reference frame is given by:

$$\Delta\vec{x}_j = \sum_{k=1}^{2} \frac{GM_k a_e^4}{GM_\oplus \left\|\vec{x}_{P,k}\right\|^3} \left\{ h_2 \vec{x}_j \left(\frac{3}{2}\left(\vec{x}_{P,k} \cdot \vec{x}_j\right)^2 - \frac{1}{2} \right) + 3l_2 \left(\vec{x}_{P,k} \cdot \vec{x}_j\right)\left[\vec{x}_{P,k} - \left(\vec{x}_{P,k} \cdot \vec{x}_j\right)\vec{x}_j\right] \right\}$$

where:

GM_1	Gravitational constant of the Sun
GM_2	Gravitational constant of the Moon
R_e	Equatorial radius of the Earth
$\vec{x}_{P,1} = \vec{x}_{Sun}$	Inertial position of the Sun
$\vec{x}_{P,2} = \vec{x}_{Moon}$	Inertial position of the Moon
h_2	Degree 2 Love number (= 0.6026)
l_2	Degree 2 Shida number (= 0.0831)

This formula comes from the IERS 1996 conventions, and corresponds to the elastic Earth approximation.

Clock biases

A satellite or station clock is supposed to be a realization of its local time, but in fact it has a bias with respect to the true time *t (*which a perfect clock would provide) :

$$\tau = t + b$$

where τ is the time lecture of the clock and b is the clock bias.

The clock bias is estimated by the least-square process for each observation epoch. The relativistic effect on the satellite clocks has been also considered, whose most important part is the eccentricity correction:

$$\delta t_{rel} = +\frac{2\vec{r} \cdot \vec{v}}{c^2}$$

Corrections to travel time

In the previous description of the measurement reconstruction, the term Δ consists of the several corrections to the travel time, namely:

Tropospheric delay:

The tropospheric delay can be either computed by the pre-processing algorithm or estimated in ODTS.

In the first case, the delay is just taken from the observations input structure.

In the second case, the tropospheric zenith delay is the parameter to be estimated during the ODTS process. The tropospheric delay for a given elevation angle is obtained from the zenith delay by a mapping function, chosen by configuration between the Saastamoinen model and an external model.

The Saastamoinen model has the following mapping function:

$$D = \frac{D_Z - 0.002277 * B * (\cot E)^2}{\sin E}$$

where E is the elevation angle and D_Z is the zenith delay. The correction term B depends on the station altitude, and can be interpolated from a table.

Relativistic correction:

This is the correction due to general relativity theory, whose most important effect is the Shapiro delay.

Note that the ionospheric delay is not computed, since the ODTS input observable is iono-free.

Residuals computation

The residuals are the difference between the expected measurements $\rho_{\exp}$ and the actual measurements ρ obtained at the receivers. If there were no measurement noise, and if our orbits, clocks and corrections were the exact ones, the residuals should be zero. If our estimation of orbits, clocks and our corrections are accurate, the residuals contain essentially the measurement noise. The residuals computation is simply, for any measurement type:

$$res = \rho - \rho_{\exp}$$

$$res = \varphi + ambiguity - \varphi_{\exp}$$

V. TIME AND FREQUENCY TRANSFER EVALUATION SCENARIO

A preliminary evaluation of the time transfer capabilities of *magicGNSS* has been carried out selecting a network of 8 GNSS stations belonging to Time and Frequency laboratories, as indicated in Table III. Note that 7 stations are located in Europe and one in the USA, thus we are facing not a global network with worldwide coverage but a so-called *regional* network.

Hourly RINEX files generated by the participating stations and uploaded into a dedicated *magicGNSS* account, have been processed by means of the ODTS algorithm, with respect to the clock of the PTB station chosen as reference.

A comparison with the estimates generated by the *magicGNSS* PPP algorithms, using the IGS *rapid* products, has been performed in terms phase offsets and Allan deviation.

For the present work, the following period has been considered:

- 2012 April 19th (MJD 56036 , DOY 110) - 2012 April 22th (MJD 56039 , DOY 113) included

TABLE III. LABORATORIES CONSIDERED IN THE WORK

Lab.	*Country*	*Station*	*Receiver type*	*Reference*
ORB	Belgium	BRUS	Ashtech Z-XII3T	UTC(ORB)
INRiM	Italy	IENG	Ashtech Z-XII3T	UTC(IT)
PTB	Germany	PTBB	Ashtech Z-XII3T	UTC(PTB)
ROA	Spain	ROAP	Septentrio PolaRx2	UTC(ROA)
SP	Sweden	SP01	Javad	UTC(SP)
SP	Sweden	SP02	Javad	UTC(SP)
SP	Sweden	SPT0	Javad	Maser
USNO	U.S.A	USN3	Ashtech Z-XII3T	UTC(USNO)

VI. RESULTS

The figures presented in this section are results of the *magicGNSS* ODTS clock solution and the *magicGNSS* PPP computation (using IGS *rapid* products). Figure 1. shows the phase offset estimates issued from the ODTS algorithm using the UTC(PTB) time scale as reference, while Figure 2. shows the overlapped Allan deviation obtained from the ODTS clock estimates.

Figure 3. and Figure 4. show respectively the same entities (i.e., the phase offset clocks estimates and the overlapped Allan deviation), but obtained with *magicGNSS* PPP algorithm instead of ODTS. Please note that the PPP algorithm uses the IGS time scale as reference, consequently, in order to compare the ODTS and PPP algorithms, the UTC(PTB) solution from PPP has been subtracted from all other clocks from PPP.

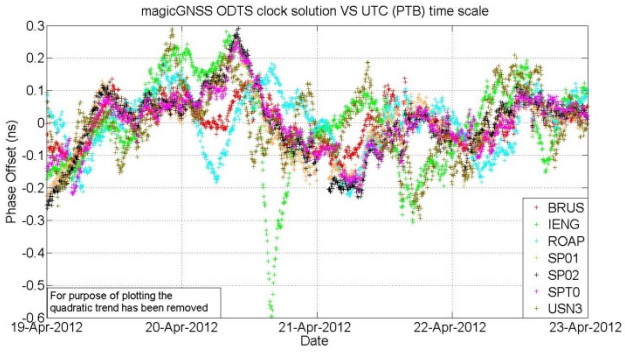

Figure 1. Baseline clock estimates as obtained with *magicGNSS* ODTS algoritm using UTC(PTB) time scale as reference

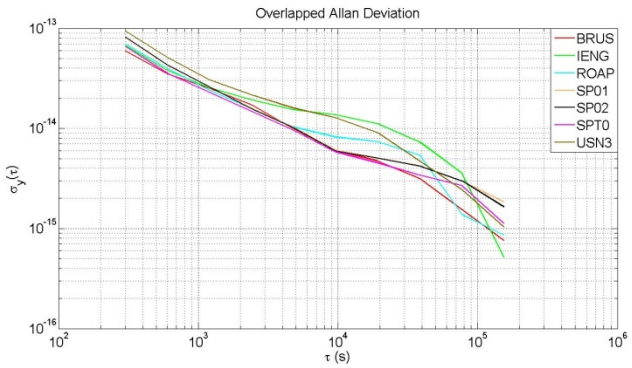

Figure 2. Overlapped Allan deviation of the clock estimates as obtained with *magicGNSS* ODTS

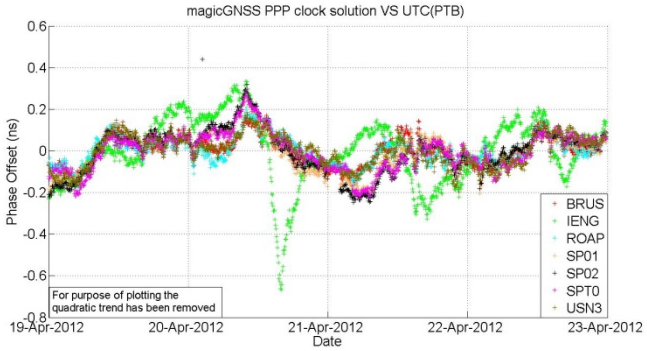

Figure 3. Baseline clock estimates as obtained with *magicGNSS* PPP algorithm using UTC(PTB) time scale as reference

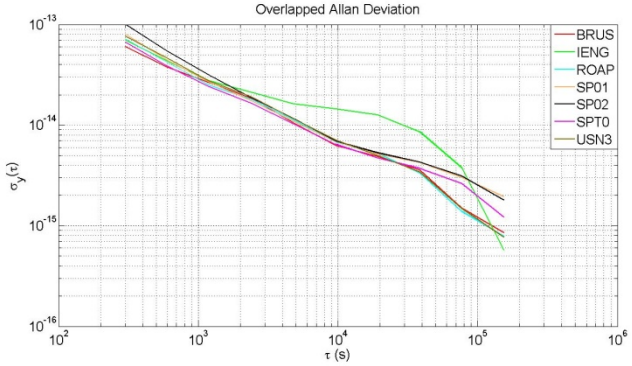

Figure 4. Overlapped Allan deviation of the clock estimates as obtained with *magicGNSS* PPP algorithm

The trend comparison between Figure 1. and Figure 3. (for this purpose the quadratic trend has been removed) and between Figure 2. and Figure 4. show a good overall agreement among the estimates generated by the ODTS and PPP algorithms. In both cases, the phase offset analysis show the same behavior: the variations are comprised between -0.4 ns and -0.7 ns, and the main variations are visible on the two plots.

Only the Allan deviation comparison shows a visible difference between the PPP and ODTS algorithms, notably,

comparing the USN3 and ROAP results. For USN3 the difference is probably due to the fact that this station is the only station which is not on the European continent. However, except USN3 and ROA for which a slight difference is depictable, the global behavior of the other stations is approximately the same irrespective of the algorithm used.

In order to evaluate the difference between the two algorithms, the estimates obtained from the ODTS algoritm has been subtracted from the estimates obtained from the PPP computation. The result is shown in Figure 5.

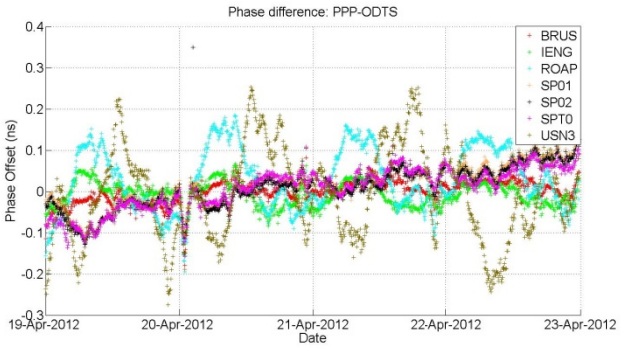

Figure 5. Clock estimates difference between the *magicGNSS* PPP algorithm and the *magicGNSS* ODTS alogorithm

Figure 5. shows that the variations between the two algorithms are always comprised between -0.3 ns and 0.3 ns, moreover this interval can be dived by 2 excluding ROAP and USN3 stations which show higher daily variations. We note, also on Figure 5. a very low drift, however this one does not perturb significantly the ODTS estimates.

To conclude about these results, even in case of a limited network of 8 stations, the ODTS technique offers clock comparisons with precision which is comparable to the state of the art techniques, such as PPP using IGS products.

However with respect to ODTS, for PPP two disadvantages can be pointed out, namely the dependency on external products (IGS) and latency of those products. In principle, RINEX data from all time and frequency laboratories can be uploaded in real time and a global clock synchronization with ODTS achieved in near real time. Latency can be improved using 15 min RINEX files; fast execution time (1 min). Also take note that any clock noise is added due to the sat clock interpolation (30-sec rate is possible).

The ODTS algorithm presents very good results and aspects to use this one to monitoring time scales with a high precision and reactivity.

VII. Operational Aspects

Within the *magicGNSS* account, a Scheduler is available to automate ODTS or PPP processes. The user can choose how often the executions shall be done (from every day to every hour), and how many minutes after the integer hour the execution is to be started. This last feature has been envisaged in order to accommodate for late arrival of RINEX files.

In the experiment described in this paper, each of the timing laboratories upload their hourly RINEX files to the *magicGNSS* server using a shared *magicGNSS* account. This is done via ftp protected by username and password. The laboratories take care of the ftp upload automation, and ultimately it is their responsibility the smooth and continue RINEX file upload. Then, on the server side, the ODTS is executed every hour 20 minutes after the hour (this gives plenty of time for RINEX upload). The ODTS execution time for 8 station and 2 days of data is only around 1 minute, therefore clock results for the last hour are available around 21 minutes past the hour.

A dedicated *magicGNSS Timing* web page allows the visualization of estimated clocks in near-real time. This web page presents the clock results from ODTS executions coming from the Scheduler, as described above. The *Timing* web page focuses on station clock results exclusively, thus all the ODTS complexity is hidden and other estimated parameters (orbits, troposphere, etc.) are ignored (however the standard full PDF report from ODTS is also available in case troubleshooting is necessary). The *Timing* web page is shown in Figure 6.

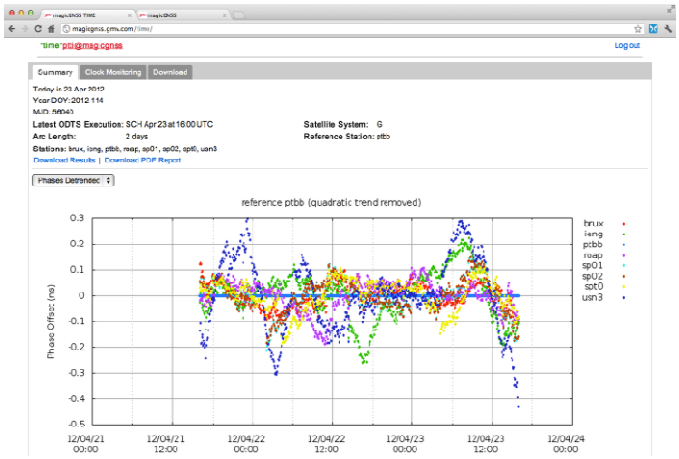

Figure 6. The *magicGNSS Timing* web page

The *Timing* page contains three areas: “Summary”, “Clock Monitoring”, and “Download”. The “Summary” area contains the clock results of the latest ODTS execution, with plots for phase offset, frequency, and Allan deviation. Individual clocks or all clocks together can be visualized. The Summary page refreshes every few minutes so that the page shows at any time the latest results. This is useful for example to display this page continuously on a computer display at the lab.

The “Clock Monitoring” area is similar to the “Summary” area but instead of the latest results it allows dynamically plotting multiple days of the past clocks evolution, also in

terms of phase offset, frequency, and Allan deviation, for one or several clocks. It is also possible to change the Reference Clock dynamically without the need of re-executing ODTS.

Finally, the "Download" area allows downloading via ftp all the clock estimates generated by ODTS over the days, in CLK RINEX format (daily files). These daily files are actually feeding the dynamic plots generated under "Clock Monitoring".

The *Timing* web page has been optimized for visualization on smartphone screens, and all the functionality is available on the go. An example is shown in Figure 7. The phone app allows the lab operator to monitor the clocks also when out of the office or home, and in such a way quickly react to possible anomalies.

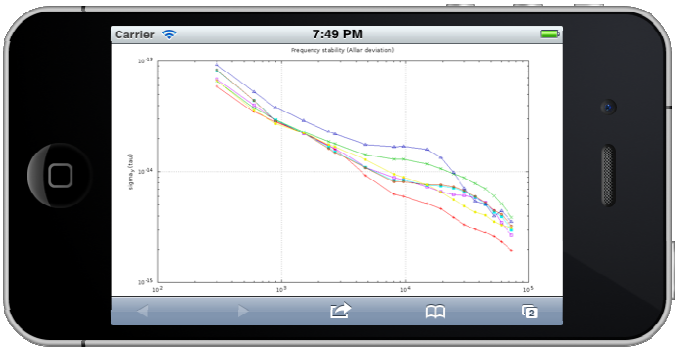

Figure 7. The *Timing* web page on a smarthphone screen

VIII. CONCLUSION

The presented work represents an investigation about the time/frequency transfer capabilities of the ODTS algorithm included in *magicGNSS*. Results show promising performances. More investigations are in progress taking into account different periods and different types of network, looking also at the robustness and reliability of the algorithm.

IX. AKNOWLEDGMENTS

Authors wish to thank all the personnel in timing laboratories involved in this experiment, for the effort in providing regularly their station data to the *magicGNSS* account.

REFERENCES

[1] J. Levine, "A review of time and frequency transfer methods", Metrologia, Vol 45, pp S162-S174, 2008.

[2] P. Defraigne, G. Petit, and C. Bruyninx, 2002, "Use of geodetic Receivers for TAI," in Proceedings of the 33rd Precise Time and Time Interval (PTTI) Meeting, Nov 2001, Long Beach, California, USA (U.S. Naval Observatory, Washington, D.C.), pp. 341-348

[3] D. Orgiazzi, P.Tavella, F. Lahaye, "Experimental assessment of the Time Transfer Capability of Precise Point Positioning (PPP)", in Proceedings of the 2005 Joint IEEE International Frequency Control Symposium and Precise Time and Time Interval (PTTI) Systems and Applications Meeting, 29-31 August 2005, Vancouver, BC, Canada.

[4] N. Guyennon, G. Cerretto, P. Tavella, F.Lahaye, "Further Characterization of the Time Transfer Capabilities of Precise Point Positioning (PPP)", to appear in UFFC IEEE Transactions on Ultrasonics, Ferroelectrics, and Frequency Control, 2009, in press

[5] P. Defraigne, C. Bruyninx, and N. Guyennon, "PPP and phase only GPS frequency transfer," in Proceedings of the IEEE International Frequency Control Symposium Jointly with the 21st European Frequency and Time Forum (EFTF '07), pp. 904–908, Geneva, Switzerland, May-June 2007.

[6] P.Defraigne,Q. Baire, and N. Guyennon, "GLONASS and GPS PPP for time and frequency transfer," in Proceedings of the IEEE International Frequency Control Symposium Jointly with the 21st European Frequency and Time Forum (EFTF '07), pp. 909–913, Geneva, Switzerland, May-June 2007.

[7] G. Petit and Z. Jiang, "Precise Point Positioning for TAI computation", International Journal of Navigation and Observation, Volume 2008, Article ID 562878.

[8] J. Kouba and P. Héroux, "Precise Point Positioning Using IGS Orbit and Clock Products", GPS Solutions, vol. 5 n. 2, 2001, pp. 12-28.

[9] R. Piriz, A. Mozo, P. Navarro, D. Rodriguez, "magicGNSS: Precise GNSS Products Out of the Box", in Proceedings of the 21st International Technical Meeting of the Satellite Division of the Institute of Navigation ION GNSS 2008.

[10] P. Defraigne and C. Bruyninx, "On the link between GPS pseudorangenoise and day boundary discontinuities in geodetic time transfer solutions," GPS Solut., vol. 2, 2007.

[11] Z. Jiang, G. Petit, and P. Defraigne, "Combination of GPS carrier phase solution with a calibrated time transfer link," in Proceedings of the IEEE International Frequency Control Symposium Jointly with the 21st European Frequency and Time Forum (EFTF '07), pp. 1182–1187, Geneva, Switzerland, May-June 2007.

A Simple, Configurable, Permanent Magnet Zeeman Slower for Sr

Ian R. Hill*†, Yuri B. Ovchinnikov*, Elizabeth M. Bridge*‡, E. Anne Curtis*†, Sean Donnellan†*, and Patrick Gill*†‡
*NPL, Hampton Road, Teddington, TW11 0LW, UK
†Blackett Laboratory, Imperial College London, South Kensington Campus, London, SW7 2AZ, UK
‡Clarendon Laboratory, University of Oxford, Parks Road, Oxford, OX1 3PU, UK
Email: ian.hill@npl.co.uk

***Abstract*— We report the successful demonstration and characterisation of a Zeeman slower based on an array of permanent magnets, implemented for atomic Sr on the $^1S_0 \rightarrow {}^1P_1$ transition at 461 nm. Measurements of longitudinal velocity distributions and MOT loading characteristics are presented. In particular, we highlight a simple transverse-field slower, which is both compact and highly tunable, light weight ($\leq$ 2 kg), and with no power load, as a favourable option for space-borne operation. For optimum parameters of this slower we achieve a slow flux of $\sim 3.5 \times 10^9$ atom/s at $\sim$ 30 m/s for ^{88}Sr and load $\sim 2.5 \times 10^7$ atoms into a magneto-optical-trap (MOT) operating on the same $^1S_0 \rightarrow {}^1P_1$ transition, which scales approximately with the relative isotopic natural abundances of Sr. With the addition of repumpers at 707 nm and 679 nm, we achieve a factor of $\sim$ 17 enhancement to MOT number with loading time $\sim$ 0.5 s.**

I. Introduction

Rapid loading of a magneto-optical trap (MOT) is an essential first step in optical lattice clock operation [1]. A high flux of slow atoms is therefore required, which is often achieved with an atomic beam apparatus exploiting the Zeeman slowing technique [2]. Conventional Zeeman slowers utilise current carrying tapered solenoids to generate the required magnetic field profile for compensation of the varying Doppler shift experienced during slowing [3]. Such slowers often require a significant current, and therefore large power supply, and consequently the added complication of water cooling the apparatus. In addition, the field profile is difficult to tune and the coil windings fully enclose the atomic beam tube restricting both optical access and the ability to remove the slower from the vacuum apparatus without disassembly.

Recently, alternative designs which circumvent these issues, using permanent magnets to generate the required field distribution, have been proposed [4], [5], [6]. The original proposal of Ref. [4] is for a transverse field Zeeman slower consisting simply of a 2D array of permanent magnetic dipoles, positioned accordingly either side of the atomic beam tube (Fig. 1). In this paper we characterise the performance of such a slower for Sr, which serves as part of the optical lattice clock apparatus at the National Physical Laboratory (NPL).

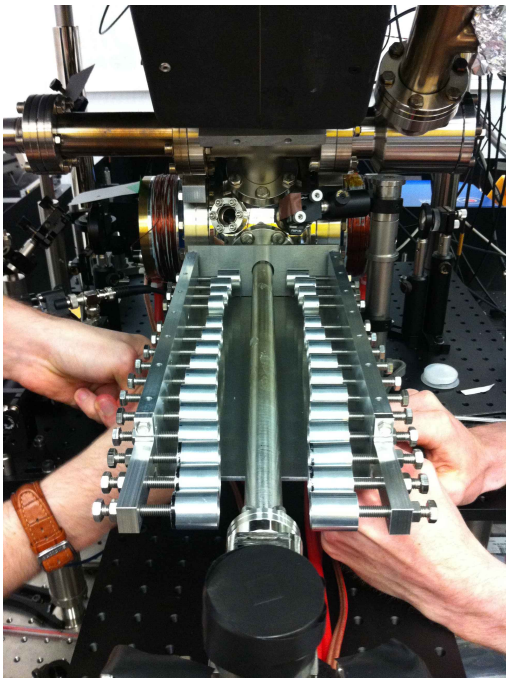

Fig. 1. Installation of the Zeeman slower

II. Zeeman Slowing Atomic Strontium

A. General theory of Zeeman slowing

A formal treatment of Zeeman slowing relevant to the design of a Zeeman slower for Sr can be found in Ref. [4]. The level structure relevant to laser cooling Sr is shown in Fig. 2. The slower operates on the $^1S_0 \rightarrow {}^1P_1$ transition at 461 nm, which has photon scattering rate $\Gamma = 1.90 \times 10^8$ s^{-1} allowing efficient slowing over relatively short lengths of a few tens of centimetres.

B. Zeeman shift of the $^1S_0$ and $^1P_1$ states

For the bosonic isotopes of Sr, with zero nuclear spin, the $^1S_0$ ground state has Landé g-factor $g_J = 0$, and so no first order Zeeman shift occurs. The $^1P_1$ excited state has $g_J = 1$ and magnetic substates $M_J = 0, \pm 1$, which are shifted in energy, E_M, by the applied field, B_z, according to $\Delta E_M = \mu_B g_J M_J B_z$, where μ_B is the Bohr magneton. The resulting

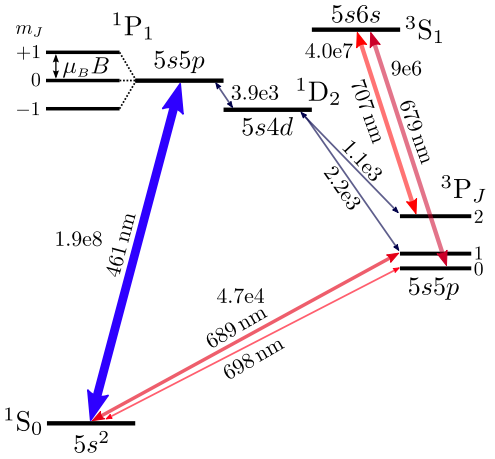

Fig. 2. Energy levels used in laser cooling Sr, shown for the bosonic isotopes. Decay rates are in unit s^{-1}.

frequency shift of the $^1\mathrm{S}_0 \rightarrow {}^1\mathrm{P}_1$ transition is thus,

$$\Delta\nu \simeq 1.4589\, M_J \quad [\mathrm{MHz/Gauss}] \tag{1}$$

The situation for the fermionic isotope, ^{87}Sr, with nuclear spin $I = 9/2$, is a little more complex, owing to the additional hyperfine interaction. The $^1\mathrm{P}_1$ excited state is split into 3 hyperfine components with total angular momentum $F = 7/2, 9/2$, and $11/2$. For slowing and cooling we operate on the $F \rightarrow F+1$ transition from the $|F = 9/2\rangle$ ground state to the stretched $|F = 11/2, M_F = -11/2\rangle$ excited state. Here, calculation of the appropriate g-factors must include the nuclear g-factor, g_I, which is a small number given by $g_I = \frac{\mu_I(1-\sigma_d)}{\mu_B |I|}$, where $\mu_I = -1.0924\mu_N$ is the nuclear magnetic moment and $\sigma_d = 0.00345$ the diamagnetic correction [7], $\mu_N = \frac{e\hbar}{2m_p}$ is the nuclear magneton, and m_p the proton mass. For the $^1\mathrm{P}_1$ state $g_F \simeq 2/11$, which provides a Zeeman shift of the stretched state equivalent to the bosonic case. The addition of nuclear spin results in a Zeeman splitting of the ground state which, if significant, could result in optical pumping issues for a spin-flip (magnetic field crossing zero) transverse-field slower, such as that presented here. In the transverse field configuration we require linearly polarised light, aligned orthogonal to the magnetic field direction, which is decomposed into $\sigma^{\pm}$ light. For the majority of the slowing only σ^- light is resonant with the Zeeman tuned atomic resonance, however, interaction with the σ^+ component could lead to atoms lost from the slowing process by optical pumping in the ground state. Crucially, for cooling ^{87}Sr, the resulting Zeeman splitting of the $^1\mathrm{S}_0$ $F = 9/2$ ground state is small enough ($\Delta\nu_g \simeq 830$ Hz/G for $M_F = 9/2$) in comparison to the $^1\mathrm{S}_0 \rightarrow {}^1\mathrm{P}_1$ transition width to not pose a problem.

C. Slower length

The length of the slower is set by capture and exit velocities, and ϵ parameter [4], which is constrained by the available slowing beam power. The ϵ parameter describes the ratio of the local deceleration, $a(s)$, to the maximum achievable local deceleration, $a_{max}(s)$. for a given local saturation, s, as,

$$\epsilon = a(s)/a_{max}(s), \tag{2}$$

and is used to characterise the design of the slower.

Typically, we operate with an approximately effusive oven source (see Fig. 5) heated to $\sim 600\,^\circ$C, which produces a thermal atomic beam with a roughly Maxwellian longitudinal velocity distribution and most probable velocity ~ 500 m/s. For capture in the MOT we require a slow atom flux < 50 m/s, to which, in principle, we may slow all atoms. Typically, we choose the ϵ parameter to be in the range 0.6 to 0.8 to satisfy the condition for stable slowing, calculated for the average local laser intensity. We may adjust ϵ by means of varying the laser intensity for a given field gradient, or by adjusting the field gradient for a given laser intensity.

A potential limit to the slowing length is imposed by a small branching probability (~ 1 in 50 000) of the excited $5s5p\,^1\mathrm{P}_1$ state to decay to the $5s4d\,^1\mathrm{D}_2$ state. From here 2/3 of atoms decay to the ground state via the $5s5p\,^3\mathrm{P}_1$ state ($4.7\times 10^4\ s^{-1}$), and the remaining 1/3 are shelved in the metastable $5s5p\,^3\mathrm{P}_2$ state (see Fig. 2). In each case, the time for such a detour is significant compared to the total slowing time ($<$ 2 ms), and atoms are unlikely to return to the slowing process following this decay. We consider these atoms as shelved in a dark state and lost from the slowing process. The efficacy of the slower is therefore reduced at long lengths due to the increasing significance of branching losses. As a result, the maximum slowing efficiency for an infinitely long slower is 40 %, regardless of configuration. If we assume a limit to the slowing length due to branching losses, a change in velocity of 490 m/s, corresponding to scattering 50 000 photons, may be efficiently achieved, or slowing from 520 m/s to 30 m/s. For a source temperature of 600 °C, this corresponds to a slower capture of ~ 50 % of the atoms within the thermal distribution. For a slower operating at $\epsilon = 0.7$, and with $s = 1$ at the slower exit (slowing beam convergence ~ 30 mrad), slowing over this velocity range is achieved for a slower length of 32 cm, with magnetic field varying from -460 G to $+300$ G.

D. Optimum field profile

The optimum magnetic field profile of the slower is calculated according to Eq. 6 in Ref. [4] for constant ϵ. For efficient use of the slowing laser power, the slowing beam is convergent towards the source of the atomic beam, providing an increased saturation, s, and thus local deceleration, towards the slower entrance. Counter to this, the laser power is reduced throughout the slower, towards the slower entrance, by absorption of the slowing light by the resonant atomic flux. For a typical atomic beam flux $\sim 1\times 10^{11}$ atoms/s, this reduction in power is estimated to be ~ 10 % which is sufficiently small to be neglected in calculation of the field profile.

The slower described here is designed for $\epsilon = 0.7$, with capture velocity $v_c \simeq 430$ m/s and exit velocity $v_f \simeq 25$ m/s, for 35 mW slowing beam power (in reality 70 mW is required as only half is resonant) with $1/e^2$ beam waist ~ 5 mm at slower exit converging to ~ 1.5 mm at the entrance

25 cm upstream (convergence half angle ~ 14 mrad). At the slower exit the beam size is limited by the vacuum apparatus geometry, and is intended to overlap well with the diverging atomic beam. The field profile varies over a range of ~ 600 G, which is implemented from approximately -300 G to 300 G to minimise the maximum magnitude of field which must be produced. The high exit field also ensures the slowing beam detuning is far from resonance with atoms extracted from the slower exit, allowing relatively unimpeded operation of the MOT.

III. A Zeeman Slower for Sr based on Permanent Magnets

Conventionally, the slowing field is implemented using a tapered solenoid electro-magnet with the field direction collinear with the slowing beam. The slower described here is based on an array of permanent magnetic dipoles generating a transverse slowing field, as proposed in Ref. [4].

A. Realising the field with permanent magnets

The magnetic flux density from a magnetic dipole placed at the origin of a Cartesian coordinate system and oriented along the x-axis, is described by the following set of equations,

$$B_x = \frac{\mu_0 m}{4\pi}\left[\frac{2x^2 - y^2 - z^2}{r^5}\right] \tag{3}$$

$$B_y = \frac{\mu_0 m}{4\pi}\left[\frac{3xy}{r^5}\right] \tag{4}$$

$$B_z = \frac{\mu_0 m}{4\pi}\left[\frac{3xz}{r^5}\right], \tag{5}$$

where $r = \sqrt{x^2+y^2+z^2}$, μ_0 is the vacuum permeability ($\mu_0 = 4\pi \times 10^{-7}$), and m is the magnetic moment. A suitable spatially varying magnetic field profile, transverse to the atomic beam direction z, can then be easily produced by an array of transversely oriented magnetic dipoles (MD) positioned at equal intervals, dz, along the atomic beam tube, and with symmetrical distribution at distances x_i (see Fig. 3).

One further note concerns the transverse field curvature along x and y, which is greatest along x and at regions of high field. For the magnetic configuration presented here (Fig. 3), the variation across the slower exit provides a symmetrical ~ 15 G increase at the transverse extremities of the atomic beam tube (± 8 mm from axial centre), which corresponds to a maximum variation of exit velocity of 5 m/s. Such variations should be accounted for by conservative choice of ϵ, and are minimised, for a given desired field, by use of a higher strength magnet positioned further from the atomic beam tube, and thus do not pose a significant concern.

B. Construction of the slower

The dipole model of the Zeeman slower is well realised using stacks of neodymium disc magnets [8]. Neodymium iron boron ($Nd_2Fe_{14}B$) permanent magnets offer an extremely high magnetic flux per unit volume, high coercivity, and are widely available at a low cost. They come in various grades such as N35, N38, N42, etc., with higher numbers generally

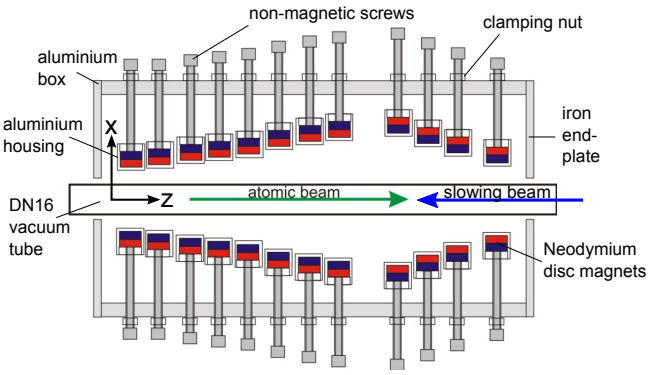

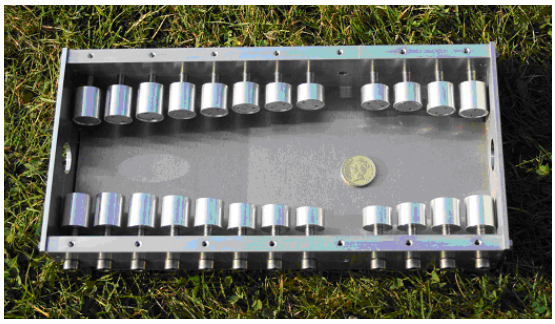

Fig. 3. Magnetic dipole (MD) Zeeman slower. The slower pictured is designed for a Sr space optical clock as part of the EU FP7 SOC2 project [9].

implying a 'stronger' magnet. The 'strength' of the magnet is determined by its residual induction (or flux density), B_r, and is typically of the order 12 kG for the common grade N35. The magnetic field strength, H, is then given by,

$$H = B_r/\mu_0 \qquad [\mathrm{A/m}] \tag{6}$$

which for a cylindrical magnet of radius r and height h provides a magnetic moment,

$$m = H\pi r^2 h \qquad [\mathrm{A.m^2}] \tag{7}$$

The construction of the slower is extremely simple. We use disc magnets with individual dimensions $r = 15$ mm and and $h = 2$ mm, which are stacked according to the required field strength at points along the slower. Each stack is housed inside a small aluminium cylindrical case which is attached to a screw thread for tuning of position x_i. The magnet dipole array is supported by an all aluminium frame into which each magnet is screwed. The only exception is at the slower exit where the frame end cross-plate is made from iron to provide magnetic shielding of the end field. Without the shield, or any other additional compensation, the transverse field configuration provides a rapid decay of the end slowing field. The addition of the shield serves to increase this further, and with the correct positioning also provides a slight enhancement to the end slowing field, aiding the realisation of the ideally steep field gradient at the slower exit. The residual field contributed to the MOT region ~ 20 cm downstream of the slower exit

is ~ 160 mG in both x and z directions and ~ 20 mG in y, which is small and can be easily compensated.

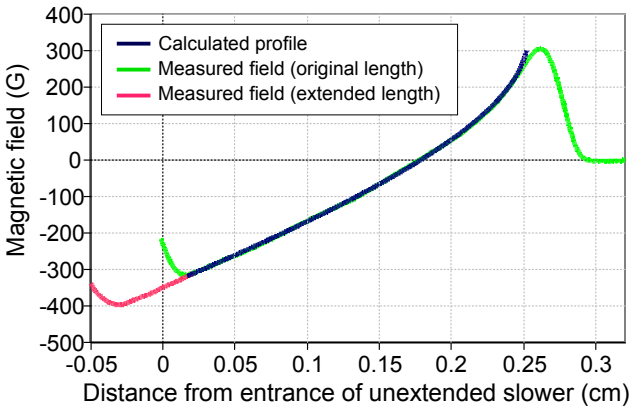

Fig. 4. Measured centre-line field profile of the transverse-field MD Zeeman slower fitted to the theoretical curve for the parameters given in the text. An extension was added to the slower to increase the field magnitude at the slower entry by ~ 82 G.

For rapid tuning of the slower, we measure the magnetic field profile using a commercial gaussmeter (Bell 610 gaussmeter) and transverse hall probe mounted to a motorised linear actuator, and iteratively adjust the magnet positions. The measured field profile of the tuned slower is shown in Fig. 4 for two lengths of slower; one with 12 pairs of magnets and entrance field -315 G, and an extended version with 3 additional magnet pairs providing -397 G entry field. The exit field is measured at 304 G, requiring a detuning $\Delta = -510$ MHz for an exit velocity of 25 m/s (for $\epsilon = 0.6$ and $s \sim 1$ as previously stated). The corresponding expected capture velocities are therefore $v_c \sim 447$ m/s and 502 m/s respectively. Assuming an initial Maxwellian thermal distribution of atomic velocities, the extension provides access to an additional 32 % of atoms.

IV. Characterisation of the Slower

The slower performance is characterised by measurements of the longitudinal velocity distribution recorded in the MOT region downstream of the slower exit, and by loading of a MOT operating on the same $^1S_0 \rightarrow {}^1P_1$ transition at 461 nm.

The vacuum apparatus used for MOT loading is detailed in Fig. 5, with the position of cooling and trapping beams required for clock operation shown. The initial atomic beam is produced by expansion through a 1 mm diameter channel of length 11 mm, which provides a high flux, $\sim 10^{14}$ atoms/s, in the spectroscopy cell immediately following the oven. For further collimation, the centre-line flux is sampled by an additional 1 mm aperture placed 10 cm downstream of the channel exit, which provides a highly collimated beam with typical flux $\sim 10^{11}$ atoms/s for source temperature $\sim 600\,^{\circ}$C, and divergence half angle ~ 10 mrad, which flows to the MOT region 69 cm downstream.

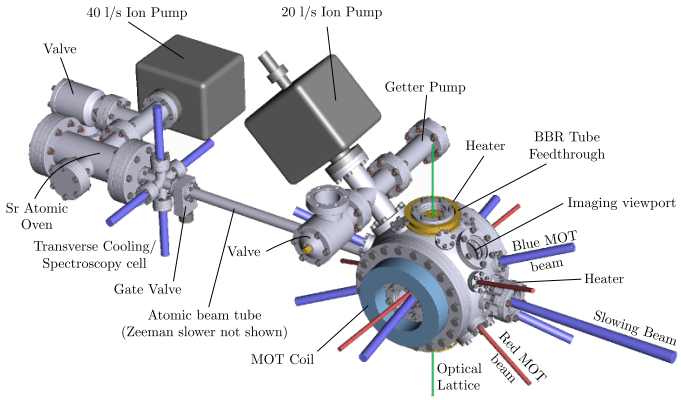

Fig. 5. The NPL Sr vacuum apparatus

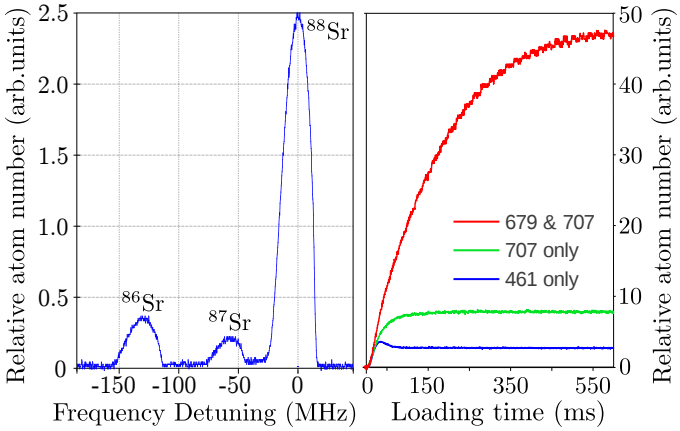

Fig. 6. Validation of MOT loading for isotopes of Sr and MOT loading curves with and without repumpers

For the intended slowing conditions, a slow flux $\sim 3.5 \times 10^9$ atoms/s centred at ~ 30 m/s (slowing beam detuning $\Delta \simeq -535$ MHz), is produced. The velocity of the slow peak varies linearly with slowing beam detuning, by, ~ 2.17 MHz/ms^{-1}, as expected. Measurements of the useful slow flux exiting the slower was investigated by loading of the MOT, which is operated with typical parameters: detuning $\Delta = -40$ MHz, $1/e^2$ beam waist ~ 6 mm, power ~ 4 mW per beam (retroreflected). We routinely load $\sim 2 \times 10^7$ atoms into the MOT and have observed a factor of ~ 17 enhancement with the application of repump light resonant with 707 nm and 679 nm transitions, shown in Fig. 6. The extension to the entrance field of the Zeeman slower provides a 30 % increase in MOT atom number, in line with calculations, which demonstrates the full length of the slower is working efficiently.

To validate the performance of the slower for the fermionic isotope, ^{87}Sr, we have loaded MOTs of the ^{88}Sr, ^{87}Sr, and ^{86}Sr isotopes and compared relative abundances, see Fig. 6. A continuous, synchronous scan of the slowing beam and MOT beam detunings is carried out and the isotopically separated MOTs are formed. The loaded number of atoms scale approximately according to relative abundances and are positioned according to the relevant isotope shift, indicating the hyperfine structure of the fermion does not cause a problem

TABLE I

COMPARISON OF ZEEMAN SLOWER ATTRIBUTES.

Parameter	MD ZS	Solenoid ZS	unit
Power consumption	zero	14	[W]
Heat dissipation	zero	14	[W]
Laser power (calculated for)	70	36	[mW]
Mass	< 2	~ 7 + PSU	[kg]
Dimensions (approx)	30x15x5	18x12x12	[cm]
Capture velocity, v_c	500	390	[m/s]

for the transverse-field spin flip slower configuration.

V. CONCLUSION

The design, construction, and characterisation of a simple transverse-field permanent magnet Zeeman slower has been described. The performance of the slower is validated by measurements of the longitudinal velocity distribution and by loading of a magneto-optical-trap. The slower apparatus is light, compact, easily shielded, and consumes zero power; attributes which are well suited to space-borne operation. To highlight this a comparison of the MD Zeeman slower against a compact solenoid Sr Zeeman slower [10] is made in Tab. I. The slower also benefits from ease of tuning, which can be carried out in situ, or with the slower separated from the apparatus. Optical access is available along the full length of the slower which may be of benefit for transverse cooling. Finally, we achieve a slow flux of 3.5×10^9 atoms/s for an atomic beam flux of $\sim 1 \times 10^{11}$, which is in relative agreement with other reported slowers for Sr [3].

ACKNOWLEDGMENT

The authors would like to thank Alastair Sinclair and Guido Wilpers for providing an additional laser at 461 nm for measurement of the longitudinal velocity distribution. This work was funded in part by the iMERA OCS project, the EU FP7 SOC2 project, and the UK NMO programme.

REFERENCES

[1] H. Katori et al., *Spectroscopy of strontium atoms in the Lamb-Dicke confinement*, Proceedings of the 6th Symposium in Frequency Standards and Metrology, 323-330 , 2001.

[2] W. D. Phillips and H. Metcalf, *Laser Deceleration of an Atomic Beam*, PRL **48**, 9, 1982.

[3] I. Courtillot et al., *Efficient cooling and trapping of strontium atoms*, Optics Letters **28**, 6, 2003.

[4] Y. B. Ovchinnikov, *A Zeeman slower based on magnetic dipoles*, Optics Communications **276**, 261-267, 2007.

[5] Y. B. Ovchinnikov, *Longitudinal Zeeman slowers based on permanent magnetic dipoles*, Optics Communications **285**, 1175, 2011.

[6] P. Cheiney et al., *A Zeeman slower design with permanent magnets in a Halbach configuration*, Rev. Sci. Instrum. **82**, 063115, 2011.

[7] M. M. Boyd et al., *Nuclear spin effects in optical lattice clocks*, Phys. Rev. A **76**, 022510, 2007

[8] Y. B. Ovchinnikov, *A permanent Zeeman slower for Sr atomic clock*, Eur. Phys. J. Special Topics **163**, 95100, 2008

[9] S. Schiller et al., *The Space Optical Clocks Project: Development of high-performance transportable and breadboard optical clocks and advanced subsystems*, Proceedings of European Frequency and Time Forum 2012, IEEE, 2012

[10] M. Schioppo, *Development of a transportable strontium optical clock*, PhD thesis, University of Florence, 2010

Characterization of an ultra-stable optical cavity developed in the industry for space applications.

B. Argence, S. Bize, P. Lemonde and G. Santarelli
LNE-SYRTE
Observatoire de Paris, CNRS, UPMC
Paris, France
Berengere.Argence@obspm.fr

E. Prevost and R. Le Goff
SODERN
20 Av. Descartes
Limeil-Brevannes, France

T. Lévèque
CNES, Centre National d'Etudes Spatiales
18 Av. Edouard Belin
Toulouse, France

***Abstract*— We report the main characteristics and performances of the first – to our knowledge – prototype of an ultra-stable cavity designed and produced by industry with the aim of space missions. Finite element modeling was performed in order to minimize thermal and vibration sensitivities. The system was designed to be transportable, acceleration tolerant (up to several g) and temperature range compatible (ΔT ~ 40 K). The optical axis of the 100 mm long cavity is vertical. The spacer is made from Ultra-Low Expansion (ULE) glass and mirrors substrate from fused silica to reduce the thermal noise limit to $4x10^{-16}$. The axial vibration sensitivity was evaluated at $(4 \pm 0.5)\ x10^{-11}$ /(ms^{-2}), while the transverse one is $< 1x10^{-11}$ /(ms^{-2}). The fractional frequency instability is ~ $1x10^{-15}$ from 0.1 to few seconds.**

I. INTRODUCTION

Frequency-stable lasers are important tools whose present applications include modern frequency metrology [1-4], gravitational wave detection [5], fundamental physics tests [6,7], coherent optical links [8] and related space applications [9]. Frequency stability can be achieved by locking the laser to a rigid Fabry-Perot (FP) cavity. Recently, significant progress towards cavity designs with low vibration sensitivity [10], transportability [11] and robustness [12] has been achieved.

This work presents the characterization of a full industrial engineering model of FP cavity assembly for space applications. This cavity was realized by SODERN company under CNES (French Space Agency) procurement and tested at SYRTE. Extensive thermo-mechanical modeling was performed to obtain low thermal and vibration sensitivities.

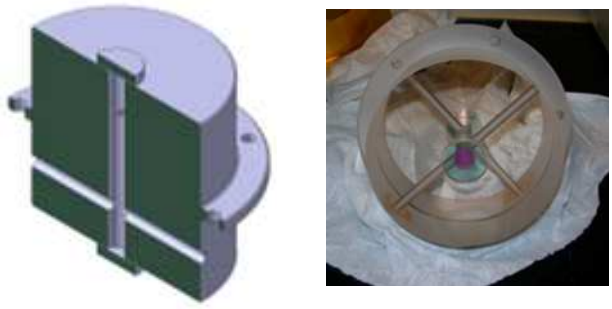

Figure 1. Drawing (left) and photography (right) of the cavity

The system was designed to support acceleration up to several g. The total mass is 40 kg dominated by the mass of the external vacuum enclosure (~20kg). The transportability is already demonstrated since the system was assembled at SODERN facilities and moved to SYRTE, 25km away. This study was a mean to transfer knowhow from laboratory to industry and also a first step toward a space qualified system.

II. GENERAL CONSIDERATIONS

The cavity has a cylinder geometry of length 100 mm and diameter 110 mm (see Fig. 1). The reflection coating of the mirrors allows operation at 1.542µm, in the telecom wavelength region. The free spectral range is 1.5 GHz. The linewidth of the cavity is measured to be 3.9 ± 0.1 kHz, corresponding to a finesse of ~ 380 000. The optical contrast is ~ 70%. The mirror configuration is plano-concave (radius of curvature of 500mm). The spacer is made from Ultra-Low Expansion (ULE) glass, with Fused Silica (FS) mirrors substrates in order to reduce thermal

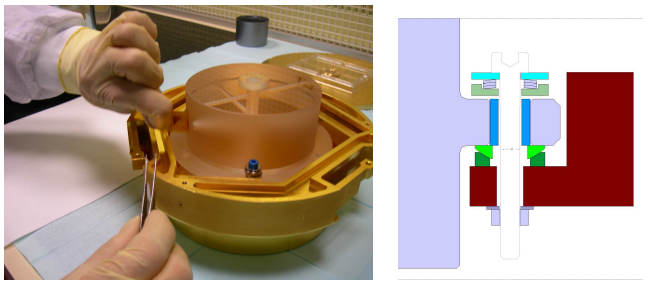

Figure 2. (Left) Photography of the cavity and its CFD, see text for details. (Right) Drawing of the setup used to fix the cavity to the CFD.

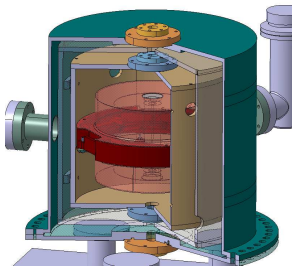

Figure 3. Drawing of the system including cavity, interface, shields and vacuum chamber.

noise floor [13,14]. For the present geometry, the calculated flicker thermal noise is ~ $4x10^{-16}$, dominated by the coatings. This is a factor > 2 better than an all-ULE cavity. The drawback is an increase of the thermal sensitivity – coefficient of thermal expansion (CTE) – to about ~ 10^{-7}/K, a value that we verified experimentally.

III. Finite Element Modeling

A. Cavity geometry

The shape of the cavity is a 100 mm long cylinder with an edge/ring at the middle allowing to rigidly attach the cavity (see Fig. 2). The cylinder and ring are machined from a monolithic block of ULE. The cavity is then held symmetrically in three points (at 120 degrees) by a mechanical interface, see paragraph C. The shape of the central ring (thickness and diameter) was optimized to minimize deformations of the cavity. The diameter of the spacer was designed to minimize the transverse vibration sensitivities and the position of the vents holes was determined to maintain stiffness.

B. Thermal Shields

The cavity is protected against thermal perturbations by three gold coated aluminum shields inside a stainless steel vacuum chamber, as presented in Fig. 3. Aluminum provides low temperature gradient while maintaining good mechanical stiffness. For the vacuum chamber, stainless steel was preferred to aluminum to obtain a good level of vacuum. This passive thermal shielding can be modeled by a 2^{nd} order low pass filter with a time constant of ~ 2 days. To keep the first mechanical resonance as high as possible and to be compatible with the requirements of transport, each shield is rigidly fixed to the upstream one. The vacuum chamber is a cylinder of a radius of 170 mm and a height of 300 mm. A 2 liter/second ion pump ensures a vacuum level $<10^{-6}$ mbar. A residual gas analysis revealed that the molecular hydrogen H_2 from the stainless steel can limit the vacuum level.

C. Mechanical Interface

A critical part of the system is the interface between this cavity and the internal shield. Indeed, it's quite challenging to rigidly hold the 2.2kg of the cavity without transmitting thermal and vibration perturbations or breaking its symmetry. Much efforts have been devoted to modelizing this part called CFD (Cavity Fastening Device), represented in Fig. 2. This interface is made of Invar, chosen to reduce the differential temperature expansions and consequently constraints and deformations applied to the cavity. Internal cantilevers allow to rigidly attach the cavity to the CFD while external ones fix the CFD to the internal shield. Studies have been performed to optimize their geometry and their flexibility. These cantilevers can thus filter the constraints and deformations due to temperature variations or vibrations. To avoid any permanent moment of force and to prevent any break of ULE glass, studies were conducted to optimize the interface between the glass and the internal cantilevers. The cavity and the CFD are bolted with an optimized stack of washers, see right drawing on Fig. 2. The first mechanical resonance of the whole system – including cavity, CFD, shields and vacuum chamber – was designed to be ~ 300Hz, quite high considering the mass of the system.

IV. Experimental test Setup

The experimental setup to lock a laser onto the cavity is the classical Pound Drever Hall (PDH) method [15]. The scheme is presented in Fig 4. We use a low noise extended cavity diode laser with an output optical power of 15mW. A fibered voltage controlled Variable Optical Attenuator (VOA) is used to control the optical power sent into the cavity. A 10/90 splitter extracts 90% of the frequency stabilized beam. A polarized beam splitter and a half waveplate allow fine tuning of the optical power. After passing through an optical isolator, the beam is phase modulated at 61MHz using an Electro-Optical Modulator (EOM). We optimize the polarization before the EOM to minimize the residual amplitude modulation. After two lenses used to realize the mode-matching, the beam is injected into the cavity. The reflected beam is sent to an avalanche photodiode. This PDH signal is then mixed to a local oscillator to produce the error signal. The control loop only acts on the current of the diode with a bandwidth of 600 kHz.

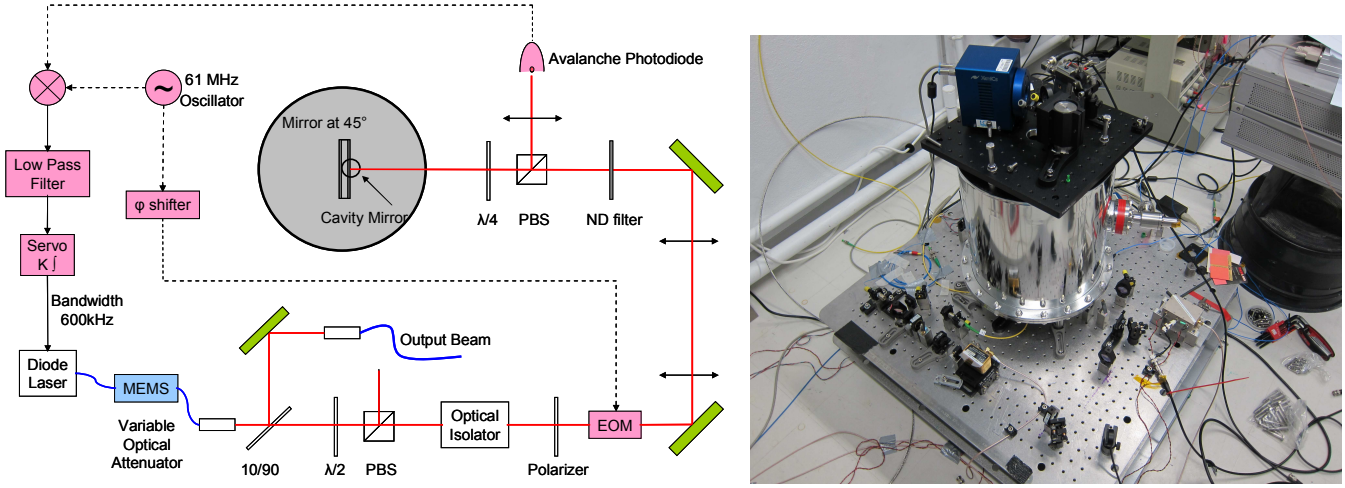

Figure 4. (Left) Experimental Setup used to lock the diode laser onto the cavity following the PDH locking technique.
Blue line: Optical fiber path, Red line: Free space path, Black line: Electrical path
PBS: Polarizer Beam Splitter, λ/2(4): half (quarter) waveplate, EOM: Electro-Optical Modulator, ND: Neutral Density
(Right) Photography of the experimental setup.

This setup is protected against environmental perturbations by a ~ 1.2 m^3 aluminum box with an acoustic absorber not shown in the photography of Fig. 4.

We measure the optical power to frequency conversion coefficient to be about ~ 200 Hertz per µWatt transmitted. Consequently, to avoid frequency noise degradation due to optical power fluctuations, the injected power is actively controlled by the VOA. This system maintains a relative intensity noise (RIN) below -100 dB from 1 Hz to 1 kHz (bandwidth limited). This ensures that frequency fluctuations induced by optical power are lower than $1x10^{-16}$ at 1s.

V. Preliminary Results

A. Vibration sensitivity measurements

The vibration measurement setup is presented in Fig 5. The cavity setup is shaken with either sinusoidal or chirped signals from 2 to 50 Hz using an active vibration isolation platform. The acceleration modulation is measured with a piezoelectric sensor. The induced frequency modulation is measured using the beat-note between the diode laser locked to the cavity and another ultra stable reference laser. Frequency fluctuations are then converted with a frequency-to-voltage converter. Both acceleration and frequency modulations are simultaneously measured with a vector signal analyzer. The vibration sensitivity Γ is then defined by the following equation:

$$\Gamma = \frac{1}{\nu_0}\sqrt{\frac{S_\nu(f)}{S_a(f)}} \qquad (1)$$

where $S_\nu(f)$ and $S_a(f)$ are respectively the frequency and acceleration power spectral densities and ν_0 is the optical frequency equal to 194 THz.

With this setup, we evaluate the vertical vibration sensitivity at $(4 \pm 0.5)\ x10^{-11}$ /(ms^{-2}). The horizontal sensitivity is more difficult to evaluate due to a strong coupling between the three orthogonal axes of the platform when a horizontal excitation is applied. Nevertheless, by modulating at frequency where the cross-coupling is minimum, we can evaluate the horizontal vibration sensitivity at $(6 \pm 3)\ x10^{-12}$ /(ms^{-2}).

B. Frequency Stability

The frequency stability of the laser locked to the cavity is evaluated by comparison with an Ultra Stable Laser. Preliminary measurements show a stability of the beat-note of ~ $1x10^{-15}$ from 0.1 to few seconds (linear drift removed).

VI. Conclusion and Prospects

We present the preliminary characterization of the first ultra-stable Fabry-Perot cavity totally developed by a space industry. Extensive thermo-mechanical modeling was performed to reduce thermal and vibration sensitivities. The system was designed to be robust, transportable, and able to stand acceleration (up to several g) and temperature variations (up to 40K).

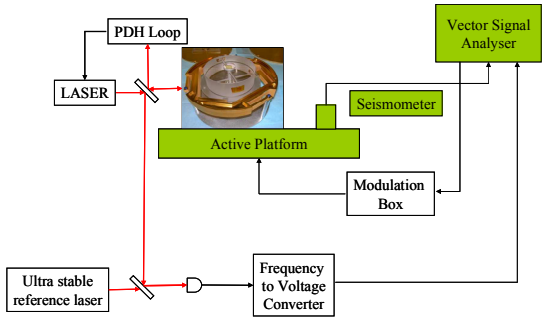

Figure 5. Vibration Sensitivity measurement setup.

The measured sensitivities are adapted to quiet satellite environment, but need to be reduced for future versions. The laser locked onto this cavity shows fractional frequency stability ~ 10^{-15} from 0.1 to few seconds. A new version is in preparation for the ultra-stable laser interrogation oscillator of a Strontium lattice clock (698nm), in the FP7/SOC2 European project framework.

ACKNOWLEDGMENT

Authors thank W. Zhang, Z. Xu and Y. Le Coq for their contribution to the frequency stability measurements and J. Pinto and M. Lours for their assistance with electronics.

REFERENCES

[1] H. Katori, "Optical lattice clocks and quantum metrology", Nature Photon., vol. 5, pp. 203, 2011

[2] M. D. Swallows, M. Bishof, Y. Lin, S. Blatt, M. J. Martin, A. M. Rey and J. Ye "Suppression of Collisional Shifts in a Strongly Interacting Lattice Clock", Science, vol. 331, pp. 1043, 2011.

[3] N. Huntemann, M. Okhapkin, B. Lipphardt, S. Weyers, Chr. Tamm and E. Peik, "High-Accuracy Optical Clock Based on the Octupole Transition in 171Yb+", Phys. Rev. Lett., vol. 108, pp. 090801, 2012.

[4] J.A. Sherman, N.D. Lemke, N. Hinkley, M. Pizzocaro, R.W. Fox, A.D. Ludlow and C.W. Oates "High-Accuracy Measurement of Atomic Polarizability in an Optical Lattice Clock", Phys. Rev. Lett., vol. 108, pp. 153002-5, 2012.

[5] F. Acernese et al., "Virgo status", Class. Quantum Grav., vol 25, pp. 184001, 2008.

[6] S. Herrmann, A. Senger, K. Mohle, M. Nagel, E.V. Kovalchuk and A. Peters, "Rotating optical cavity experiment testing Lorentz invariance at the 10^{-17} level", Phys. Rev. D, vol. 80, pp. 105011, 2009.

[7] C. W. Chou, D. B. Hume, T. Rosenband and D. J. Wineland, "Optical Clocks and Relativity", Science, vol. 329, pp. 1630 – 1633, 2010.

[8] H. Jiang et al., "Long-Distance frequency transfer over an urban fiber link using optical phase stabilization", J. Opt. Soc. Am. B, vol. 25, issue 12, pp. 2029, 2008.

[9] K. Danzmann and A. Rüdiger, "LISA technology – concept, status, prospects", Class. Quantum Grav., vol 20, S1, 2003.

[10] S. Webster and P. Gill, "Force-insensitive optical cavity", Opt. Lett., vol. 36, pp. 3572-3574, 2011.

[11] S. Vogt, C. Lisdat, T. Legero, U. Sterr, I. Ernsting, A. Nevsky and S. Schiller, "Demonstration of a Transportable 1 Hz-Linewidth Laser," Appl. Phys. B, vol. 104, pp. 741-745, 2011.

[12] D. R. Leibrandt, M. J. Thorpe, J. C. Bergquist, and T. Rosenband, "Field-test of a robust, portable, frequency-stable laser," Opt. Express, vol. 19, pp. 10278-10286, 2011.

[13] J. Millo et al., "Ultrastable lasers based on vibration insensitive cavities", Phys. Rev. A, vol. 79, pp. 053829, 2009.

[14] K. Numata, A. Kemery and J. Camp, "Thermal-Noise Limit in the Frequency Stabilization of Lasers with Rigid Cavities", Phys. Rev Lett., vol. 93, pp. 250602, 2004.

[15] R. W. Drever et al., "Laser phase and frequency stabilization using an optical resonator", Appl. Phys. B: Lasers Opt., vol. 31, pp. 97, 1983.

An Ultra-Stable Optical Frequency Reference for Space Applications

Thilo Schuldt*, Anja Keetman*, Klaus Döringshoff†, Matthias Reggentin†, Evgeny Kovalchuk†, Moritz Nagel†, Martin Gohlke†, Ulrich Johann‡, Dennis Weise‡, Achim Peters† and Claus Braxmaier*
*University of Applied Sciences Konstanz
Institute for Optical Systems, 78462 Konstanz, Germany
Email: tschuldt@htwg-konstanz.de
†Humboldt-University Berlin
Institute for Physics, 12489 Berlin, Germany
Email: klaus.doeringshoff@physik.hu-berlin.de
‡Astrium GmbH – Satellites, 88090 Immenstaad, Germany
Email: ulrich.johann@eads.astrium.net

***Abstract*— A variety of future space missions require ultra-stable optical frequency references. Setups based on Doppler-free spectroscopy of molecular iodine offer frequency stabilities in the 10^{-15} domain at longer integration times and have the potential to be realized space compatible on a relatively short time scale. We present a compact optical frequency reference using modulation-transfer spectroscopy of molecular iodine near 532 nm. Using a specific assembly-integration technology, this setup takes into account space mission related criteria such as compactness, robustness, MAIVT and environmental influences. With this setup, a frequency stability of $3 \cdot 10^{-15}$ at integration times between 100 s and 10.000 s was demonstrated in a first measurement.**

I. Introduction

A variety of future space missions related to fundamental science, geoscience, Earth observation, navigation and ranging, rely on the availability of ultra-stable frequency references, especially in the optical domain. Lasers stabilized to atomic or molecular transitions are preferred due to high long-term frequency stability and the provision of an absolute frequency reference. While single-ion clocks and neutral atom lattice clocks have the potential of ultimate frequency stability down to the 10^{-18} level, their complexity prevents their immediate development for space compatibility. Setups based on Doppler-free spectroscopy offer frequency stabilities in the 10^{-15} domain at longer integration times (up to several hours) and have the potential to be developed space compatible on a relatively short time scale. Their frequency stability is comparable to the hydrogen maser in the microwave domain.

Iodine-based frequency standards using modulation transfer spectroscopy at a wavelength near 532 nm are commonly used laboratory equipment, cf. e.g. [1], [2], [3], developed also in compact setups [4], [5], [6]. State-of-the-art setups – as developed at the Humboldt-University Berlin – reach noise levels of $2 \cdot 10^{-14}$ at an integration time of 1 s and below $3 \cdot 10^{-15}$ at integration times between 100 s and 1000 s using an 80 cm long iodine cell in single-pass configuration in combination with a frequency-doubled Nd:YAG laser.

With the goal to realize a space qualifiable iodine frequency reference, a compact setup on elegant breadboard level was realized using a baseplate made of Clearceram-Z HS, a glass ceramics with an ultra-low coefficient of thermal expansion of $2 \cdot 10^{-8}\,\mathrm{K}^{-1}$. The optical components are joint to the baseplate using adhesive bonding technology. This setup ensures higher long-term frequency stability due to enhanced pointing stability. Also, the assembly-integration (AI) technology takes into account space mission related criteria such as compactness, robustness, MAIVT (the process of manufacturing, assembly, integration, verification and test) and environmental influences (shock, vibration and thermal vacuum tests). The AI technology was already successfully environmentally tested and demonstrated in a previous setup of a compact fiber-coupled heterodyne interferometer. With this setup, which serves as a demonstrator for the optical readout of the LISA (Laser Interferometer Space Antenna) gravitational reference sensor, noise levels below $5\,\mathrm{pm}/\sqrt{\mathrm{Hz}}$ in translation measurement and below $10\,\mathrm{nrad}/\sqrt{\mathrm{Hz}}$ in tilt measurement, both for frequencies above 10^{-2} Hz, were demonstrated in experiment.

II. Laboratory Setup at HUB

A state-of-the-art laboratory setup of an iodine-based frequency reference was developed at the Humboldt-University Berlin (HUB) over the last years [7], [8]. As light source, a non-planar ring-oscillator (NPRO) type Nd:YAG laser with a wavelength of 1064 nm, frequency-doubled to 532 nm, is used (model 'Prometheus' by InnoLight GmbH). The schematic of the setup using modulation-transfer spectroscopy (MTS) is shown in Fig. 1. The laser output beam is split into pump and probe and both beams are passing AOMs which are used for intensity stabilization. Also, the pump beam is shifted in frequency by 80 MHz. Pump and probe beams are fiber-coupled and sent to the spectroscopy unit. A fiber electro-optic modulator (EOM, by Jenoptik GmbH) is used for phase modulation of the pump beam at a frequency of 275 kHz. An 80 cm long iodine cell (provided by ISI Brno, Czech Republic) is used in single-pass configuration. After fiber outcoupling,

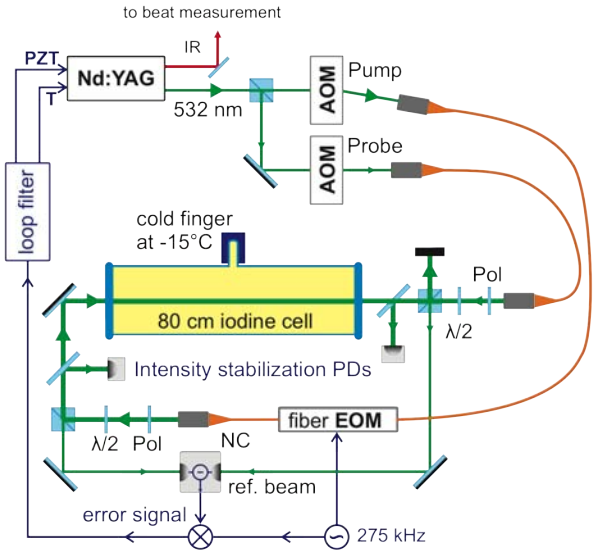

Fig. 1. Schematic of the frequency stabilization setup at HUB using modulation transfer spectroscopy.

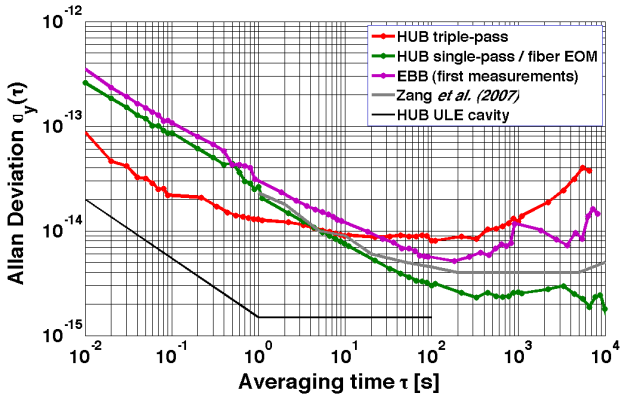

Fig. 2. Stability measurements of different iodine-based frequency references, given in root Allan deviation. Shown are the stability curves for the single- and triple-pass laboratory setup at HUB, the best published iodine system by Zang et al [3] and the stability of the ULE cavity setup at HUB used as reference for the HUB iodine setups [7]. Also included is the first measurement with the newly developed setup on elegant breadboard (EBB) level.

part of each beam is sent to a monitoring photo diode used for intensity stabilization. For error signal generation, balanced detection is implemented where part of the probe beam, split-off before the iodine cell, is used as reference beam. The mixed down error signal is input to a servo control loop actuating the laser frequency via the temperature of the laser crystal (slow actuation) and a PZT mounted to the laser crystal (fast actuation).

With this setup, a frequency stability of $3 \cdot 10^{-15}$ at integration times between 100 s and 10.000 s was achieved, cf. Fig. 2. The beat measurement was carried out by comparing the iodine setup to a reference ULE cavity setup. It is assumed that the stability of the iodine setup is limited by residual amplitude modulation (RAM) effects at these longer integration times. Also, a measurement in triple-pass configuration – yielding to an interaction length of 2.4 m in the iodine cell – was performed (cf. Fig. 2). Due to enhanced signal-to-noise ratio, the short-term stability was improved, compared to single-pass configuration. The long-term stability decreased due to pointing effects of the two overlapped counter-propagating beams in the iodine cell.

III. Setup on Elegant Breadboard Level

For its future application in space missions, a more compact and more robust setup on 'elegant breadboard (EBB)' level was developed. This setup is realized using a mechanically and thermally highly stable baseplate made of OHARA Clearceram-Z HS, a glass ceramics with a coefficient of thermal expansion (CTE) of $2 \cdot 10^{-8}\,\mathrm{K}^{-1}$. The optics (such as mirrors and beamsplitters) are directly integrated on the board using a specific assembly-integration technology based on a space qualified two component epoxy. Optical components such as fiber collimators and waveplates are placed in specific highly stable mounts made of Invar, a nickel iron alloy with a CTE of $2 \cdot 10^{-6}\,\mathrm{K}^{-1}$.

Compared to the HUB laboratory setup, this setup insures a higher mechanical and thermal stability yielding to a higher pointing stability and therefore a higher long-term frequency stability. This assembly-integration technology also takes into account specific space mission related criteria such as compactness, robustness and environmental influences (thermal-vacuum, vibration, shock).

A. Assembly-Integration Technology

The assembly-integration (AI) technology should take into account aspects, such as high thermal and mechanical stability, high long-term stability, alignment feasibility of the optical components, and space qualification of the AI technology. Using an ultra-low CTE glass ceramics baseplate – such as Zerodur or Clearceram – two methods are conceivable: hydroxide-catalysis bonding [10] and adhesive bonding [11].

Hydroxide-catalysis bonding technology was originally developed by Stanford University for jointing the Gravity-Probe B star-tracking telescope made of fused quartz components [12]. The bonding procedure can be applied to materials where a silicate-like network can be created between two flat surfaces with a planeness better $\lambda/10$. The bond thickness is 20 nm to 100 nm, depending on the bonding solution. The settling time (i.e. the time after which the component can not be moved) of the bonding procedure is depending on the pH-value of the bonding solution. Values are between 1 min and 10 min with a typical value of 2 min. Hydroxide-catalysis bonding was applied to the optical bench (OB) of the LISA Technology Package (LTP) aboard LISA Pathfinder where translation and tilt must be measured with pm/$\sqrt{\mathrm{Hz}}$ and nrad/$\sqrt{\mathrm{Hz}}$ sensitivity. The integrated OB was successfully subjected to environmental tests (thermal and vibration) [13].

Adhesive bonding is a well known technology, also used for optical assemblies with components made of glasslike materials (such as Zerodur, ULE, fused silica). Also components

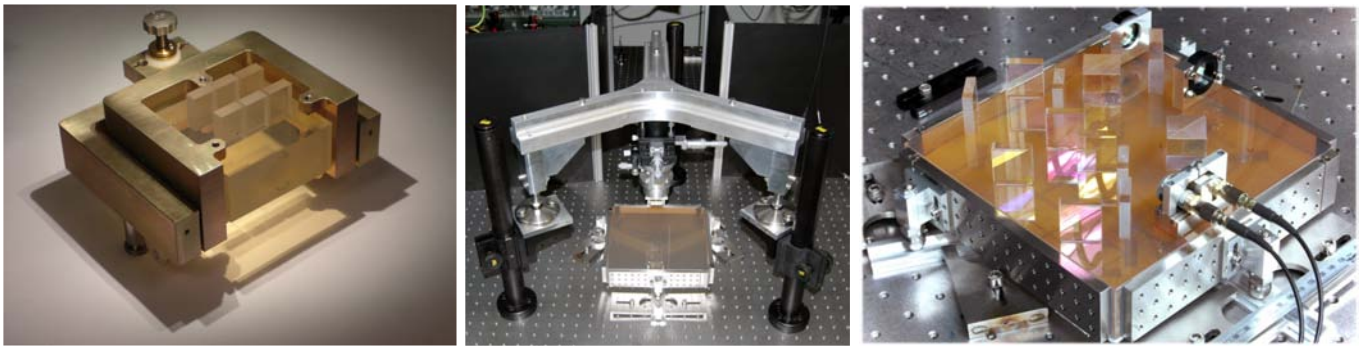

Fig. 3. Left: Photograph of the testboard for comparing hydroxide-catalysis bonding and adhesive bonding technology. Four mirrors are joint to the Zerodur baseplate using hydroxide-catalysis bonding technology, the other two mirrors using adhesive bonding technology [9]. Middle: Photograph of the integration of the heterodyne interferometer. A specific alignment jig was developed for adjusting and fixing the optical components during the integration and curing process. Right: Photograph of the completely integrated interferometer setup. The optical components are joint to the 20 cm × 20 cm Zerodur baseplate using adhesive bonding technology.

made of Invar can be integrated. First tests – carried out in comparison to hydroxide-catalysis bonding – were performed using a space-qualified two-component epoxy (Hysol EA 9313). A bond layer thickness of a few μm was measured and environmental tests with a testboard were performed, cf. Fig. 3, left. On this testboard, mirrors were integrated using both integration technologies. After thermal cycling and vibrational testing, the relative alignment of the optical components was measured using a heterodyne interferometer with pm/$\sqrt{\text{Hz}}$ and nrad/$\sqrt{\text{Hz}}$ sensitivity. No difference between both integration technologies was seen. The settling time (i.e. alignment time) of adhesive bonding can be up to several hours, depending on the ambient temperature. This integration technology does not necessarily require clean-room environment but can be performed in a standard laboratory with a flow-box.

Adhesive bonding has clear advantages which mainly include the settling time and the required process environment. The integration process can be carried out faster and with less complexity. Using this AI technology, a heterodyne interferometer was developed at Astrium (Friedrichshafen) in a collaboration with the Humboldt-University Berlin and the University of Applied Sciences Konstanz [14], [9], [15] as shown in Fig. 3. This setup is realized as a demonstrator for the optical readout of the LISA gravitational reference sensor. With this setup, noise levels below 5 pm/$\sqrt{\text{Hz}}$ in translation and below 10 nrad/$\sqrt{\text{Hz}}$ in tilt measurement, both for frequencies above 10^{-2} Hz, were demonstrated. For integration of the interferometer, a specific jig was developed which offers the possibility of adjusting the optical component in tilt and translation, cf. Fig. 3. Also the jig applies a dedicated force to the substrate which is perpendicular to the bonding surface. This ensures a thin and homogenous bonding layer.

The EBB iodine setup is integrated using adhesive bonding technology. The jig was adapted for our purposes and used for fixing the components during the curing process. Our setup includes the possibility of aligning the overlap in the iodine cell also after integration of all optical components using four pairs of wedged glass plates. Therefore, the tilt alignment of the optical components is not as critical as for the heterodyne interferometer setup. The mounts made of Invar are also integrated using the same epoxy (Hysol EA 9313).

B. Design and Realization

The iodine setup consists of the laser system, the spectroscopy unit and the corresponding electronics, where the spectroscopy unit is realized on EBB level. For the first measurements, the laser system and the electronics of the HUB laboratory setup are used, for details cf. [8]. The setup for spectroscopy is realized using adhesive bonding technology as described above. Specific ultra-stable mounts made of Invar are used for components such as collimators, waveplates, polarizers and the iodine cell. The optic substrates are made of fused silica and have dimensions of 35 mm × 25 mm × 8 mm with a 1° wedge.

The baseplate is made of OHARA Clearceram-HS with dimensions of 550 mm × 250 mm × 50 mm. Plates made of Invar are bonded to the sides of the glass ceramics board for integration of the detectors and the iodine cell cooling. A 30 cm long iodine cell (provided by ISI Brno, Czech Republic) is used in triple-pass configuration.

A schematic of the spectroscopy unit is shown in Fig. 4, left. Pump and probe beam are fiber-coupled to the board using polarization-maintaining single-mode fibers with pigtailed fiber collimators (provided by OZOptics Inc.). The output beams are collimated with a beam diameter of 3 mm. The collimators are placed in ultra-stable mounts made of Invar. Shims enable a tilt of the collimator and therefore the parallelism of the output beam with respect to the baseplate. Polarizers after fiber output ensure a clean polarization.

As all optics are directly joint to the baseplate and do not have any possibility for adjustment, four wedged AR-coated glass plates are placed in probe and pump beam, respectively. They enable an independent adjustment of both beams in two perpendicular directions. The wedges are mounted in commercial rotation mounts which are screwed to an adapter plate made of Invar.

The polarization of the pump beam is adjusted in a way that part of the laser light is transmitted at the first thin

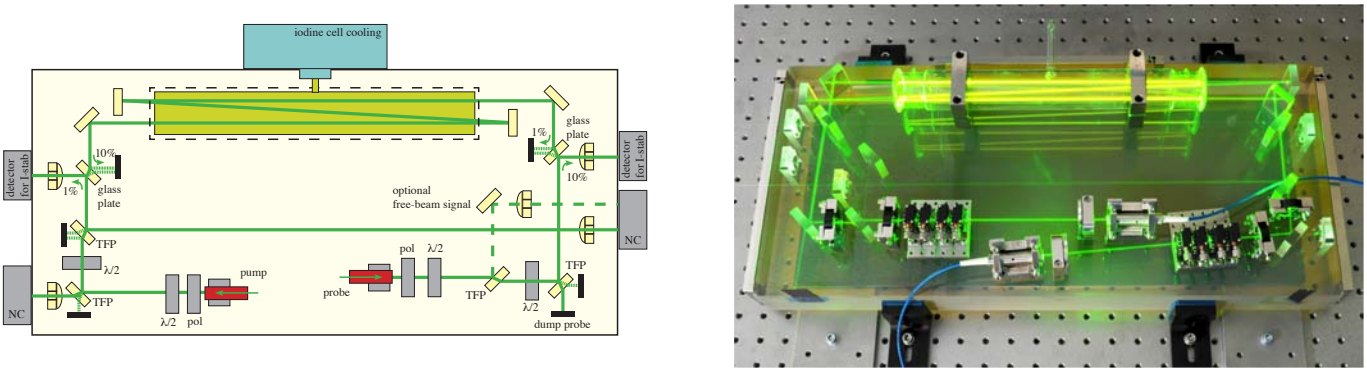

Fig. 4. Schematic (left) and photograph (right) of the spectroscopy setup on EBB level. The 30 cm long iodine cell is used in triple-pass configuration. The dimensions of the Clearceram baseplate are 550 mm × 250 mm × 50 mm, the components are integrated using adhesive bonding technology. Not shown in the photograph are the detectors and the cell cooling.

film polarizer (TFP) towards a noise-cancelling detector (NC). This detector is used for RAM-stabilization with feedback to the RF-amplitude of the corresponding AOM. Part of the pump laser light is split-off at a glass plate (with uncoated front surface and AR-coated back surface) and detected for intensity stabilization (which is carried out by feedback to the temperature of the frequency doubling crystal).

Corresponding to its polarization, the probe beam is split at a first TFP, where the reflected beam can be taken as free-beam reference signal for the noise-cancelling detection of the spectroscopy signal. Part of the probe beam is split-off at a glass plate for intensity stabilization (analog to the pump beam). After passing thrice the iodine cell, the beam is outcoupled at a TFP towards a noise-cancelling detector for generating the error signal. In front of each detector, a lens is integrated which focuses the 3 mm laser beam onto the photo diode. The lenses are bonded to fused silica substrates which is adhesive bonded to the baseplate.

C. First Measurements

For characterizing the frequency stability of the EBB setup, it was combined with the laser system and the electronics of the laboratory setup at HUB. As the fiber EOM showed degraded transmission after one year operation, an alternative modulation scheme was implemented where the AOM in the pump beam was frequency modulated. The resulting RAM was suppressed by the RAM stabilization as detailed above.

With this setup, a beat measurement with a ULE cavity setup was performed. A frequency stability of $5 \cdot 10^{-15}$ was obtained at an integration time of 100 s, cf. the measurement shown in Fig. 2. Compared to the laboratory setup at HUB in single-pass configuration, the frequency stability of the EBB setup at integration times longer than 100 s is degraded. This is most probably caused by remaining RAM of the AOM where the RAM stabilization is not yet fully optimized.

IV. Outlook

The EBB setup is currently combined with a dedicated laser system for obtaining an independent and transportable frequency reference. This setup is further optimized and possible limitations in frequency stability are analyzed.

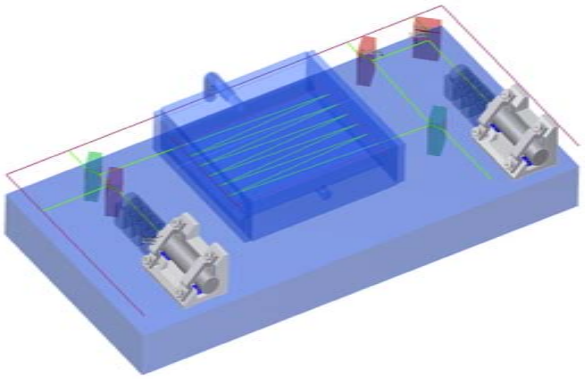

Fig. 5. Possible design of a more compact iodine spectroscopy setup on engineering model (EM) level using a compact multipass iodine cell with internal reflection.

In a next activity, the EBB setup will be the basis for a more compact setup on engineering model (EM) level. This setup will be further improved with respect to mass, dimension and mechanical and thermal stability. This setup will be subjected to environmental tests (vibration, thermal-vacuum). Main issue for reducing the size of the setup, is the implementation of a compact multipass iodine cell. Different design options for the multipass cell are currently investigated including internal vs. external reflection and an alternative cooling concept. A preliminary EM design is shown in Fig. 5 with a multipass cell with a total optical pathlength of about 1 m.

Acknowledgment

This work is supported by the German Space Agency DLR with funds provided by the Federal Ministry of Economics and Technology (BMWi) under grant numbers 50QT1102, 50OQ0601 and 50OQ0701.

REFERENCES

[1] J. Ye, L. Robertsson, S. Picard, L.-S. Ma, and J. H. Hall, "Absolute frequency atlas of molecular I_2 lines at 532nm," *IEEE Transactions on Instrumentation and Measurement*, vol. 48, pp. 544–549, 2008.

[2] J. Ye, L.-S. Ma, and J. L. Hall, "Molecular iodine clock," *Phys. Rev. Letters*, vol. 87, p. 270801, 2001.

[3] E. J. Zang, J. P. Ciao, C. Y. Li, Y. K. Deng, and C. Q. Gao, "Realization of Four-Pass I_2 Absorption Cell in 532-nm Optical Frequency Standard," *IEEE Transactions on Instruments and Measurement*, vol. 56, no. 2, pp. 673–676, 2007.

[4] K. Nyholm, M. Merimaa, T. Ahola, and A. Lassila, "Frequency stabilization of a diode-pumped Nd:YAG laser at 532 nm to iodine by using third-harmonic technique," *IEEE Transactions on Instrumentation and Measurement*, vol. 52, pp. 284–287, 2003.

[5] T. Schuldt, C. Braxmaier, H. Müller, G. Huber, A. Peters, and U. Johann, "Frequency stabilized Nd:YAG laser for space applications," in *Proceedings of the 5th International Conference on Space Optics (ICSO 2004)*, ESA Publications, 2004, pp. 611–617.

[6] B. Argence, H. Halloin, O. Jeannin, P. Prat, O. Turazza, E. de Vismes, G. Auger, and E. Plagnol, "Molecular laser stabilization at low frequencies for the LISA mission," *Phys. Rev. D*, vol. 81, p. 082002, 2010.

[7] K. Döringshoff, K. Möhle, M. Nagel, E. Kovalchuk, and A. Peters, "High performance iodine frequency reference for tests of the LISA laser system," in *Proceedings of the 24th European Frequency and Time Forum (2010)*, 2010.

[8] K. Döringshoff, M. Reggentin, M. Nagel, E. Kovalchuk, A. Keetman, T. Schuldt, C. Braxmaier, and A. Peters, "Iodine based optical frequency reference with 10^{-15} stability," in *this Proceedings (EFTF 2012)*, 2012.

[9] M. Gohlke, T. Schuldt, D. Weise, U. Johann, A. Peters, and C. Braxmaier, "A High Precision Heterodyne Interferometer for Relative and Absolute Displacement Measurement," in *ISOT 2009: International Symposium on Optomechatronic Technologies*, 2009.

[10] E. J. Ellife, J. Bogenstahl, A. Deshpande, J. Hough, C. Killow, S. Reid, D. Robertson, S. Rowan, H. Ward, and G. Cagnoli, "Hydroxide-catalysis bonding for stable optical systems for space," *Class. Quantum Grav.*, vol. 22, pp. S257–S267, 2005.

[11] S. Ressel, M. Gohlke, D. Rauen, T. Schuldt, W. Kronast, U. Mescheder, U. Johann, D. Weise, and C. Braxmaier, "Ultrastable assembly and integration technology for ground- and space-based optical systems," *Appl. Opt.*, vol. 49, no. 22, pp. 4296–4303, 2010.

[12] D.-H. Gwo, S. Wang, K. A. Bower, D. E. Davidson, P. Ehrensberger, L. Huff, E. Romero, M. T. Sulivn, K. Triebes, and J. A. Lipa, "The Gravity Probe-B Star-Tracking Telescope," *Adv. Space Res*, vol. 32, no. 7, pp. 1401–1405, 2003.

[13] G. Heinzel, C. Braxmaier, M. Caldwell, K. Danzmann, F. Draaisma, A. Garcia, J. Hough, O. Jennrich, U. Johann, C. Killow, K. Middleton, M. te Plate, D. Robertson, A. Rüdiger, R. Schilling, F. Steier, V. Wand, and H. Ward, "Successful testing of the LISA technology package (LTP) interferometer engineering model," *Class. Quantum Grav.*, vol. 22, pp. 1–6, 2005.

[14] T. Schuldt, M. Gohlke, D. Weise, U. Johann, A. Peters, and C. Braxmaier, "Picometer and nanoradian optical heterodyne interferometry for translation and tilt metrology of the LISA gravitational reference sensor," *Class. Quantum Grav.*, vol. 26, p. 085008, 2009.

[15] T. Schuldt, M. Gohlke, H. Kögel, R. Spannagel, A. Peters, U. Johann, D. Weise, and C. Braxmaier, "Picometre and nanoradian heterodyne interferometry and its application in dilatometry and surface metrology," *Meas. Sci. Technol.*, vol. 23, p. 054008, 2012.

ATTENDEE LIST